CURRENT DEBATES ON NATURAL AND ENGINEERING SCIENCES

5

Hikmet Y. ÇOĞUN
İshak PARLAR

Editors

Hikmet Y. ÇOĞUN

İshak PARLAR

Contents

Automatic Classification of Neuromuscular Diseases With Random Forest (Rf) Algorithm

Erdem TUNCER

Introduction

Neuromuscular diseases; It is a disease that affects the peripheral nervous system, is acquired or develops genetically, and is characterized by muscle wasting or weakness later on. Electromyography (EMG), one of the most important tools for the correct diagnosis of neuromuscular diseases, is used. (Bekiroglu & et al. 2016). Separation of EMG signs and classification of similarly shaped ones by grouping provide valuable information in terms of neuromuscular pathology evaluation. Neuromuscular disorder is a general term that refers to diseases that affect any part of the nerve or muscle. Myopathy and neuropathy are two important types of neuromuscular diseases. The symptoms of these two diseases can be very similar to each other. In the complaint of not being able to move the muscles, this movement disorder in neuropathy is caused by the nerves going to the muscle, while in myopathy, movement disorder occurs due to a problem in the muscle. The purpose of electromyography in the diagnosis of these diseases is to support the clinical diagnosis. EMG signals, which have a complex structure, do not contain easily understandable information. Therefore, these signs need to be classified by computer (Lee & et al. 2021, Kucuk & et al. 2019).

In this study, a classification structure consisting of five processing steps was arranged for the diagnosis of neuropathy and myopathy, which are the most common types of neuromuscular diseases. EMG signals were preprocessed, windowed, feature extraction and classification stages before being classified. 80% of the EMG signals analyzed in 0,2 second windows were used for training and the rest for testing. Afterwards, 10 features were calculated and the feature vector was obtained. Finally, the data were classified with the Random Forest (RF) algorithm. With the proposed features and classification algorithm, a success rate of 96,6% was achieved in the classification of normal, myopathy and neuropathy EMG data.

Materials and Method

The open access PhysioNet EMG dataset was used in this study. Data were collected with the Medelec Synergy N2 EMG Monitoring System (Oxford Instruments Medical) by placing a 25 mm. concentric needle electrode on the tibialis anterior muscle of all subjects. Two analog filters, 20 Hz. high-pass and 5 KHz. low-pass filters, were used during the recording process. Figure 1 shows three 0,2 second samples of EMG data. Figure 1(a) a 44 year old man with no history of neuromuscular disease; Figure 1(b) 57 year old man with myopathy due to a long-standing history of polymyositis; male subject EMG. Data were recorded at 50 KHz. and then downsampled to 4 KHz. (Goldberger & et al. 2000).
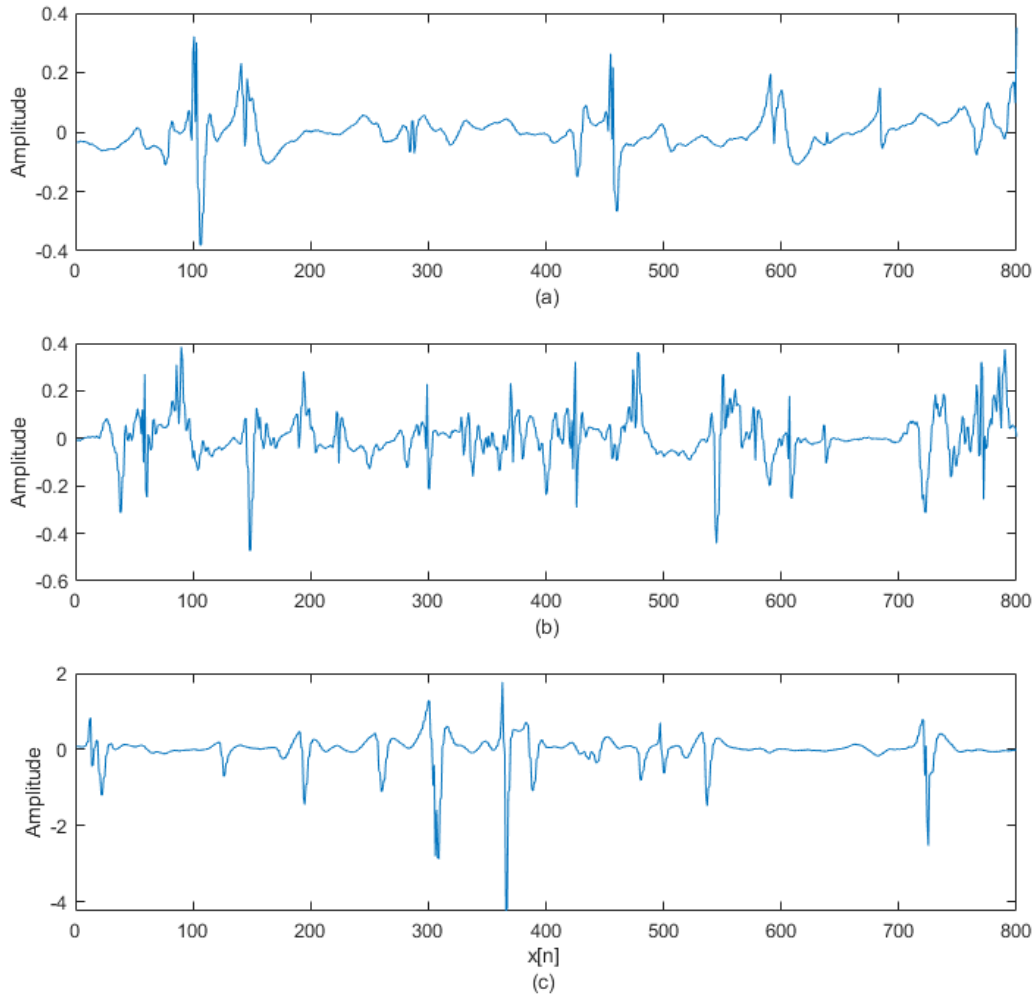
Fig 1. Typical EMG patterns of Normal (a), Myopathic (b) and Neuropathy (c) with 800 samples.

The data are split in 0,2 second windows with no overlap. The number of windows and data set information obtained from the data are given in Table 1.

Table 1. Information about the EMG dataset

Data type	Number of epochs	Total time (Second)
Normal	63	12,6
Myopathy	137	27,4
Neuropaty	184	36,8
Total	**384**	**384**

Various features are extracted for each window using the discrete wavelet method. 7-level wavelet transform is used to separate the EMG signal into lower frequency bands. The wavelet transform structure using the Symlets (Sym) 2 wavelet is shown in Figure 2.
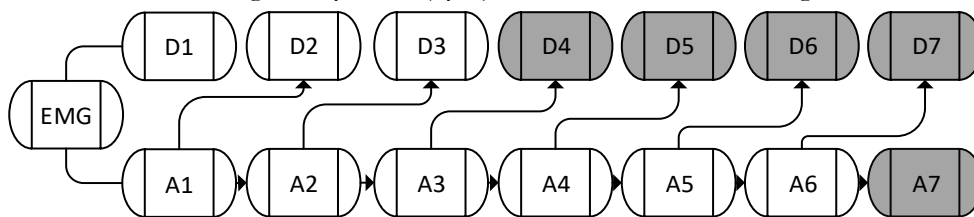
Fig. 2. Wavelet decomposition tree

Detail (D) and Approximation (A) coefficients were obtained from the EMG signal using the discrete wavelet transform. The approximation coefficients are obtained by calculating the low frequency components, and the detail coefficients are obtained by calculating the other frequency components (Tuncer E. 2022). 10 different features of these wavelet coefficients are extracted. In Figure 2, the wavelet coefficients from which the features are extracted are shown in bold. The list of obtained features is given in Table 2. With 2 features obtained from 5 different wavelet coefficients, a feature matrix was created for each window data.

Table 2. Feature list obtained from each window

No.	Feature Name	The wavelet coefficient from which the feature is obtained	No.	Feature Name	The wavelet coefficient from which the feature is obtained
1	Shanon Entropy	A7	6	Standard deviation	D4
2	Shanon Entropy	D7	7	Standard deviation	D5
3	Shanon Entropy	D6	8	Standard deviation	D6
4	Shanon Entropy	D5	9	Standard deviation	D7
5	Shanon Entropy	D4	10	Standard deviation	A7

The created feature matrix is given as input to the classifier algorithm. 80% of the data was used as training and the rest as testing. RF algorithm was used as the classifier algorithm. The RF algorithm is an improved version of the bagging method. Instead of branching out each node using the best branch among all the variables, it branches each node using the best among the randomly selected variables at each node. Each dataset is generated by displacement from the original dataset. Trees are then developed using random feature selection. Developed trees are not pruned (Archer & et al. 2008, Breiman & et al. 2001). With this strategy, the RF algorithm achieves successful results. RF is also very fast, resistant to overfitting and can work with as many trees as desired. Two parameters are defined by the user to start the RF algorithm. These parameters are the number of variables used at each node and the number of trees to be developed to determine the best split (Breiman & et al., Edla &et al. 2018).

Results and Discussion

In this study, a machine learning technique has been proposed to help the correct diagnosis of neuromuscular diseases from EMG data. In this study using the PhysioNet data set, normal-myopathy-neuropty data were classified.

EMG data are divided into windows and classified by calculating 2 features from 5 different wavelet coefficients. Data are classified with the RF algorithm. From the RF algorithm parameters; Batch size 40, max. depth 10 and number of trees 50. As a result of the study, 96,10% success was achieved with the RF algorithm in the correct classification of neuromuscular diseases. In terms of misdiagnosis rate, the error rate was again determined as 3,90%. The comparison of this study and the studies in the literature is given in Table 3.

Kucuk H. et al. focused on 2-class study rather than 3-class study. According to the results of binary classification using 25 features, they achieved an average success rate of 92,9%. Belkhou A. et al. similarly made a 2-class classification in their study. As a result of classification, they achieved a high success rate by using 55 features. However, the proposed model was used only to differentiate normal-disease data. Istenic R. et al. achieved a success rate of 70,4% with 40 features using SVM. Subasi A. et al. achieved a success rate of 99% using 47 features in their study. In this study, 10 features were used. Compared to the studies in the literature, the number of features used is quite low. This provides advantages with faster classification performance and less processing overhead. The success rate obtained was close to or higher than the success rates in the literature.

Considering the number of features used with success rates, it is understood that the model can be classified with few features and high accuracy.

Table 3. Accuracy comparison

Author	Dataset	Class types	Classifier	Number of Features	Acc.
Kucuk H. et al.	EMGLAB	Neuropathic -Normal Neuropathic -Myopathic Myopathic - Normal	SVM	25	97,39% 94,57% 86,74% Avg. 92,9%
Subasi A. et al.	EMGLAB	Myopathic-Neuropathic-Normal	Bagging Ensemble with SVM	47	99%
Istenic R. et al.	-	Myopathic-Neuropathic-Normal	SVM	40	70,4%
Belkhou A. et al.	EMGLAB	Normal- Neuropathic Normal-Miyopati	SVM KNN	55	99.34% 99.07%
This work	**PhysioNet**	**Myopathic-Neuropathic-Normal**	**RF**	**10**	**96,10%**

Although artificial intelligence is used in many sectors, its use in the health sector is increasing day by day. Expanding the use of machine learning algorithms, especially in the early diagnosis of high-cost chronic diseases, will positively affect the quality and cost of the delivery of health services. By using the created model on different data sets and increasing the data volume and size, it can give priority to the diagnosis and treatment process studies of diseases.

REFERENCES

Archer, K. J. (2008) Emprical characterization of random forest variable importance measure, computational statistical data analysis. *Computational Statistics & Data Analysis*, *52* (4), 2249-2260.

Bekiroglu, S., Cifci, E. G. (2016) The Evaluation Concerning Patient Complaint Systems Depend On General Secretary Hospitals. *Journal of Medical Social Work*, *0* (7), 32-42.

Belkhou, A., Jbari, A., Badlaoui, O. E. (2021) A computer-aided-diagnosis system for neuromuscular diseases using Mel frequency Cepstral coefficients. *Scientific African*, *13*, e00904.

Breiman, L. (2001) Random forests,machine learning. *Kluwer Academic Publishers*, *45* (1), 5-32.

Edla, D. R. Mangalorekar, K., Dhavalikar, G., Dodia, S. (2018) Classification of EEG data for human mental state analysis using Random Forest Classifier. *Procedia Computer Science*, *132*, 1523-1532.

Goldberger, A., Amaral, L., Glass, L., Hausdorff, J., Ivanov, P. C., Mark, R., ... & Stanley, H. E. (2000) PhysioBank, PhysioToolkit, and PhysioNet: Components of a new research resource for complex physiologic signals. *Circulation*, *101* (23), e215–e220.

Istenic, R., Kaplanis, P. A. (2010) Multiscale entropy-based approach to automated surface EMG classification of neuromuscular disorders. *Med Biol Eng Comput*, *48*, 773–781.

Kucuk, H., Eminoglu, I., Balci, K. (2019) Classification of neuromuscular diseases with artificial intelligence methods. *Journal of the Faculty of Engineering and Architecture of Gazi University*, *34* (4), 1725-1741.

Lee, J. W., Shin, M.J., Jang, M.H., Jeong, W.B., Ahn, S. J. (2021) Two-stage binary classifier for neuromuscular disorders using surface electromyography feature extraction and selection. *Medical Engineering and Physics*, *98*, 65-72.

Subasi, A., Yaman, E., Somaily, Y., Alynabawi, H.A., Alobaidi, F., Altheibani, S. (2018) Automated EMG Signal Classification for Diagnosis of Neuromuscular Disorders Using DWT and Bagging. *Procedia Computer Science*, *140*, 230-237.

Tuncer, E. (2022) Ictal-Interictal Epileptic State Classification with Traditional and Deep Learning Architectures. *International Journal of Research Publication and Reviews*, *3* (9), 1972-1977.

Performing Heart Rhythm With Iot Using Ecg Sensor

Çağatay ERSİN
Mehmet KARAYEL

Introduction

Today, cardiovascular diseases have become widespread due to unhealthy diets and sedentary lifestyles. Detection of cardiovascular diseases can be done with EKG devices in health institutions. In this study, a device that can measure and remotely monitor heart rhythm was designed and realized for individuals with cardiovascular disease. In the study, the ESP8266 wifi module was used for remote monitoring of the ECG heart sensor, microcontroller development board, and IoT (Internet of Things) channels over the internet. When the individual with heart disease or heart rhythm disorder places the probes of the ECG sensors in the heart region, instant measurements are made with the controller and sent to the previously opened channels on the thingspeak internet address, which is an IoT interface. Thanks to this study, the healthcare team will be able to follow the heart rhythm even when the patient is away. Cardiovascular diseases commonly cause death worldwide [1,3,4] Deaths due to heart diseases in Turkey constitute 45% of total deaths. Time is of the essence in any disease that occurs in the cardiovascular system. Anomalies occurring in the patient should be identified quickly and communicated to healthcare professionals. For this reason, continuous timed ECG recordings are of vital importance in patients with heart disease who have problems in the cardiovascular system [1].

Early diagnosis or preliminary inference is very important in the health sector. While this is important for the quality and effectiveness of the treatment, it also means vital interventions for critical diseases. The most important step necessary for the realization of preliminary inference and early diagnosis is the continuous monitoring of the data. Continuous monitoring and analysis of people's data can enable immediate detection of abnormal situations [2].

cardiovascular diseases occur due to dangerous factors such as smoking, hypertension, blood lipids, hereditary heart disease from the family, obesity and diabetes. To reduce the mortality rates brought about by these disorders, an Electro Cardiograph device was made. With this device, electrical activities occurring in the heart are observed, and with the data received, diseases in the heart can be detected beforehand and necessary precautions can be taken. With the EKG device, the flow rate and pulse of the heart can be easily measured [4]. The ECG is one of the most widely available and routinely performed diagnostic tools in modern medicine for non-invasive cardiovascular diseases [5]. Instant display of ECG data is of great importance for patients with heart disease [1]. In this study, a system that can send instant data to the thingspeak IoT interface with an ECG sensor has been designed. The heart rate graphs of the sick individual were monitored remotely with this system.

Material and Method

Heart signals are an important and effective biological signal used in the diagnosis of cardiovascular diseases [6]. The EKG, which is used for the diagnosis of cardiovascular diseases, is a device that provides a graphical recording of the electrical activity that occurs during the contraction of the heart. A weak electrical activity occurs during the contraction and relaxation of the atria and ventricles, also known as the heartbeat. This activity contains a lot of data on heart rhythm, frequency and spread. Electrocardiography, or in other words, an EKG device, is used to measure electrical activity. Electrodes attached to the skin on the chest, arms and legs allow the electrical activity of the heart to be measured [7]. In this study, the heart rhythm data from the ECG sensor were instantly measured and sent to the Thingspeak IoT interface via the ESP82266 wifi module. Arduino Uno microcontroller development board was used in the study and the ECG sensor was connected to the microcontroller development board. The power of the study was provided by a lithium-polymer battery with a voltage of 7.4 volts. The ESP8266 wifi module is connected to Arduino's microcontroller development board to send instantaneous data measured from the ECG sensor to the Thingspeak IoT interface. The block diagram of the study is shown in figure 1.
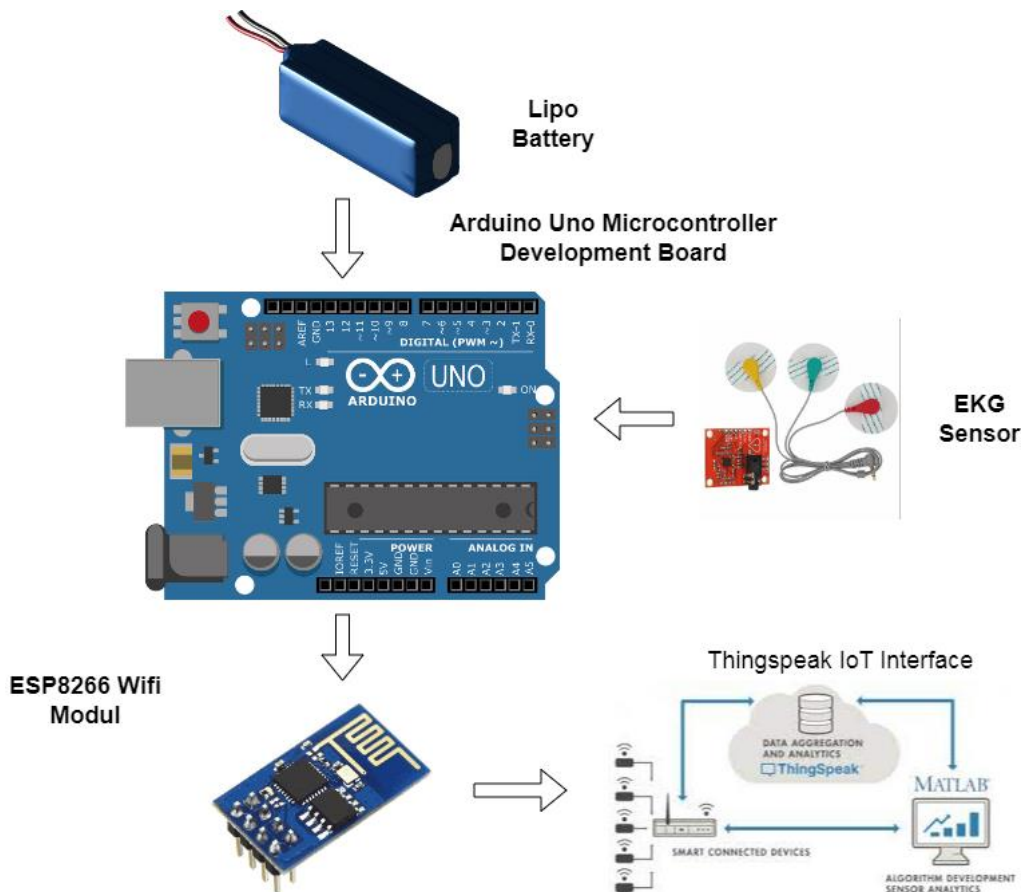
Figure 1. Block diagram of the system

2.1. Internet of Things

The detection provided by Wireless Sensor Network (WSN) technologies, which is the main area of use of IoT (Internet of Things), is encountered in many areas of today's life. This offers the ability to measure, infer and understand environmental indicators from sensitive natural resources

to urban environments. The proliferation of these devices in a communicative network creates the Internet of Things (IoT). Here, sensors and actuators seamlessly interact with the environment and enable information to be shared across platforms to develop a common language of communication. Fueled by the adoption of various wireless technologies such as RFID tags and embedded sensor and actuator nodes, IoT has evolved day by day from the beginning [8] The Internet of Things (IoT) allows physical objects to see, hear, and think, It allows coming together and "talk". IoT is the transformation of basic technologies such as embedded devices, communication protocols, sensor networks, internet protocols and applications from traditional to smart ones [9,10]. The concept of the Internet of Things was first used by Kevin Ashton in 1999 in a presentation on the benefits of Radio Frequency Identification (RFID) technology for P&G [11]. Internet of Things; It is used in applications such as e-health, home automation, smart environment, smart water, smart agriculture, smart livestock, smart energy, smart cities, smart measurement, industrial control, security and emergencies, shopping, and logistics. Relevant data are collected from sensors to provide better quality service in these areas and to increase efficiency and productivity. These data are stored in Cloud Computing systems, creating "Big Data". They are analyzed by machine learning methods and contribute to making related improvements. The most prominent application areas include the smart industry, where the development of smart manufacturing systems and connected manufacturing spaces is often discussed under the heading Industry 4.0. While smart energy applications focus on smart electricity, gas and water meters; In the smart home or building field, smart thermostats and security systems are attracting a lot of attention in the context of the Internet of Things applications [12]. In the study, the heart rate data was sent to the thingspeak internet of things interface by using the internet of things technology. Thanks to the study, the heart rate data of the patient, whose ECG sensor is attached to his body, will be able to be monitored remotely.

2.2. Thingspeak IoT Interface

Thingspeak is a free data platform for the Internet of Things (IoT) that remains popular today. Thingspeak is also a web-based open API IoT-based information platform that converts external components used for IoT into their data and is used to store sensor data. Thingspeak communicates between the internet connection and the cloud as a 'data packet' carrier and takes the detected graphic from the connected sensor to the main microcontroller, records, analyzes, observes and works. Thingspeak Arduino, TI CC3200 module, Raspberry-pi etc. It helps build the social network of development photos, sensor-based daily apps, location/location tracking apps, and updated objects. The main feature of the Thingspeak function is the Data field, location field, and Channel field, which is the status field. Thingspeak, mechanical mechanisms can be created, and the information you choose and information can be processed and visualized alternately and matched with MATLAB's use of tweets and other warning forms. It also offers the ability to create a general channel for general analysis and forecasting. It takes advantage of graphic visualization operations for sensors/actuators and can be used for objects. IoT helps bring everything together and allows us to communicate with our things, and more interestingly, allows objects to interact with other objects. This is the platform. Thingspeak offers the use of real data, graphic visualization, as well as plug-ins used to collaborate with web services, social networks or API. The main feature of Thingspeak is the Thingspeak Channel. On a page that will send the channel to Thingspeak for channelling. Programs loaded on the microcontroller transmit to the thingspeak channel within a certain period on the sensor screen. Programs uploaded to the microcontroller have a 15-second period to transmit the latest sensor values to the Thingspeak Channel. As the internet of things progressed, the wireless sensor network became more and more acceptable. As the Internet of Things progresses, the wireless sensor network is used. [13].

In this study, heart rate data is taken with a microcontroller development board and sent to the thinkspeak channel with ESP8266. By opening an account in the Thingspeak IoT interface, a channel was created and heart rate data was sent to this channel. In addition, the position of the patient with an ECG sensor is entered in thingspeak, the channel is opened and the position information is shown in this channel.

2.3 Design of the System

In this study, a biomedical device was designed using a microcontroller development board. With this designed device, heart data can be obtained and monitored while the person with heart disease is away. ECG sensor pads (green, red, yellow) are placed on the person's body. The yellow electrode was placed on the heart of the patient, the red electrode was placed on the right side in line with the heart, and the green electrode was placed on the abdomen. The regions where the electrodes are placed are shown in figure 2.
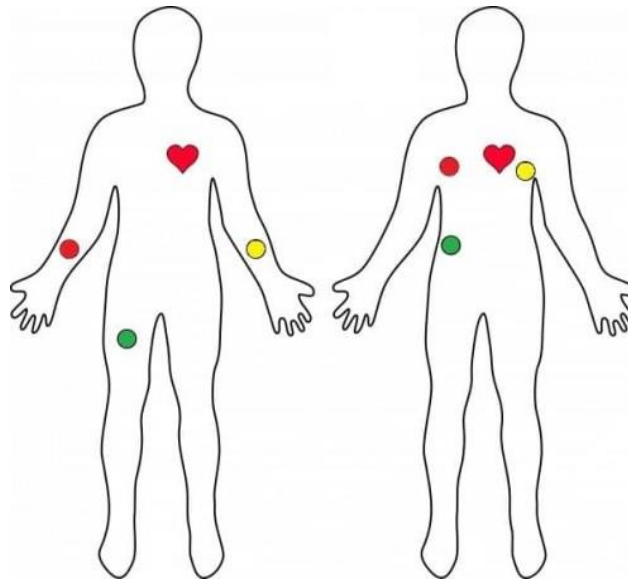
Figure 2. Areas where ECG electrodes are placed

The system is connected electronically and instant data is taken with the electrodes. The electronic circuit of the system in the study is shown in Figure 3.
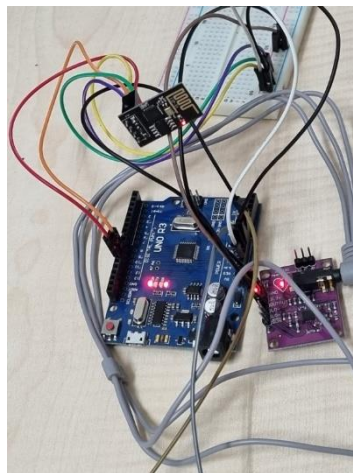
Figure 3. The electronic circuit of the system

Data from the system was received with the code written to the Arduino ide software. The data obtained with the electrodes attached to the person were instantly monitored on the serial monitor. The graphical representation of the data on the serial plotter is given in figure 4.
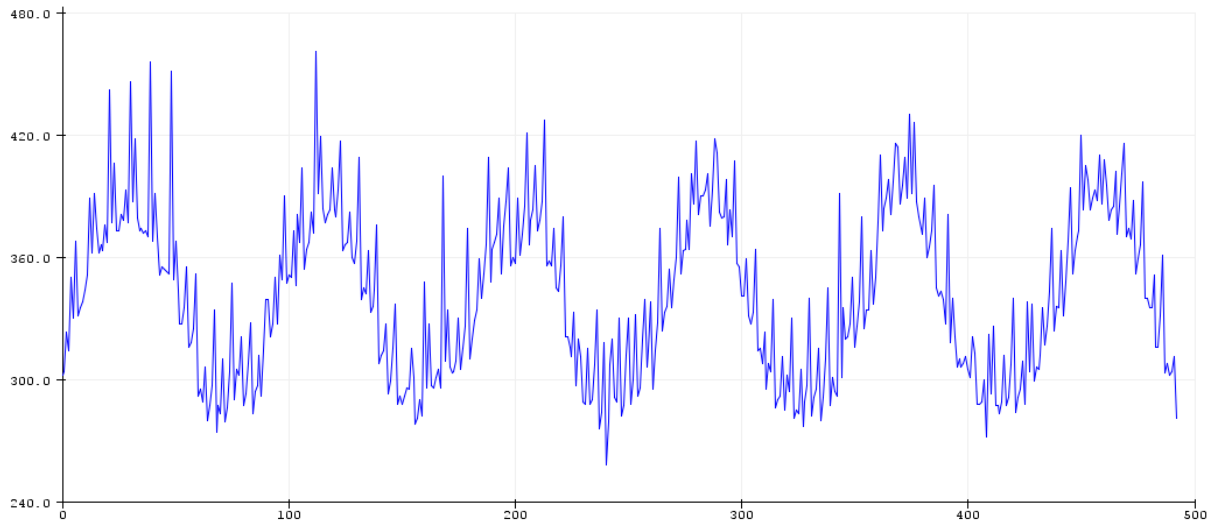
Figure 4. ECG graph

In the study, this instantaneous data was sent to the Thingspeak IoT channel using the ESP8266 wifi module. The device is connected to the internet with the wifi name and password and the data is sent to the thingspeak IoT interface IP address. The image of the sent data is shown in figure 5.

```
Data Send.
112.33
128.67
GET https://api.thingspeak.com/update?api_key=1FNPNELLDGNUKX5B&field1=128.67


Data Send.
98.67
95.67
GET https://api.thingspeak.com/update?api_key=1FNPNELLDGNUKX5B&field1=95.67
```

Figure 5. Data sent to Thingspeak IoT interface

These sent data were transferred to the Thingspeak IoT channel, which was opened before. It is shown graphically in the channel. In addition, the data of the person received through the electrodes are displayed on the screen by entering the location information. The location and graphical representation of the data sent to the Thingspeak IoT interface are shown in figure 6.
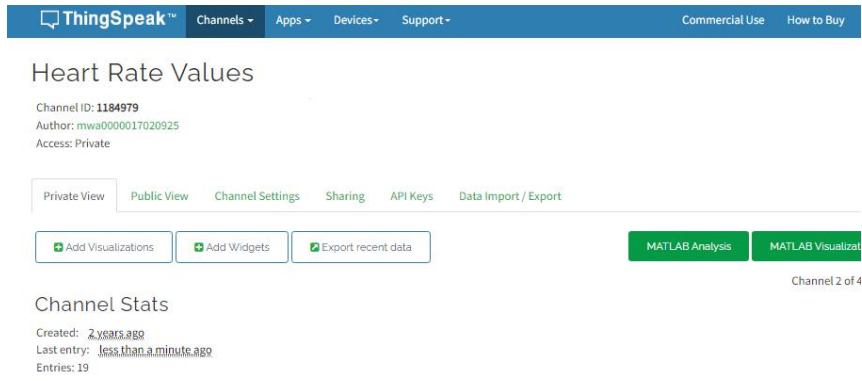
Figure 6. Thingspeak IoT interface, 2022

In the study, heart data was taken from the user and displayed as date and time on the thingspeak channels with an IoT interface. The location where the user's data is taken is also shown on a different screen. The display of the user's heart rate graphics and location over the channel is given in figure 7.
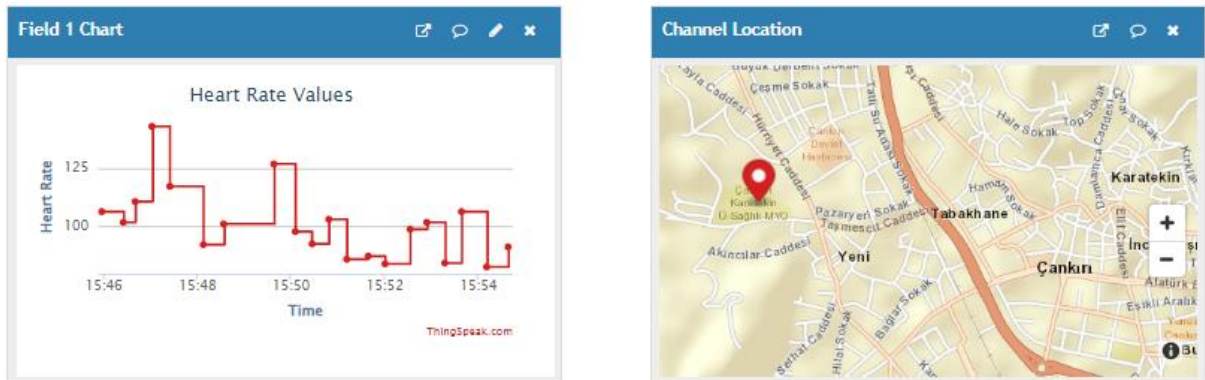
Figure 6. Data and location in the Thingspeak IoT interface channel

The healthcare team will be able to follow the patient remotely through this study. In addition, the thingview, which is an android software, is graphically shown in the interface for the tracking of the data sent to the Thingspeak interface with the android device. The graphical representation of the data coming to the Thingview interface is given in figure 7. Here, it is seen that the instantaneous heart rate is 106.33 and the maximum and minimum values are given.

Figure 7. Android IoT interface,

3. Results and Evaluation

In this study, a biomedical device was designed. The device received heart rate data with the ECG sensor and sent it to Thingspeak, which is used as an IoT interface with the internet of things technology. In the designed system, an ECG heart sensor, microcontroller development board for data acquisition and control, and EPS8266 wifi module are used to send data to the internet. With this study, the heart rhythm of the user can be monitored remotely with the Thingspeak internet address or android device. The study has been tested on the user and the data has been taken. The user's heart rate graph is shown in the system. In addition, with the location channel performed in this study, the information from which region the user's ECG data were obtained is also reached.

REFERENCES

Bilgin, SN, & Çamurcu, AY (2017). Wireless ECG and Pulse Oximeter Application System Design.

Akleylek, S., KILIÇ, E., Söylemez, B., Aruk, E., & Aksaç, C. (2020). A Study on Internet of Things Based Health Monitoring Systems. Journal of Engineering Sciences and Design, 8(5), 80-89.

İlhan, İ. (2017). Mobile device controlled EKG holter. Dicle University Engineering Faculty Journal of Engineering, 8(1), 101-110.

Farmer, B., Zeynep, S. EN, & AKKAS, M. (2021). Internet of Things Based Wireless Portable ECG Device. European Journal of Science and Technology, (26), 91-95.

Abdioğlu, S., Acar, B., & Kavsaoğlu, AR (2021). Wireless ECG Device Design and Website Design for the Evaluation of Attributes Using Signal Processing Techniques. European Journal of Science and Technology, (26), 144-150.

Arslan, Ö., & Karhan, M. (2022). Effect of Hilbert-Huang transforms on classification of PCG signals using machine learning. Journal of King Saud University-Computer and Information Sciences.

medicalpark.com.tr

Ersin, C., Yaz, M.,., & Karhan, M. (2019). An Example IoT Application for the Defense Industry. Electronic Letters on Science and Engineering, 15(3), 66-73.

Aktaş, F., Ceken, C., & Erdemli, YE (2016). Applications of IoT technology in the field of biomedicine. Düzce University Journal of Science and Technology, 4(1), 37-54.

Gökrem, L., & Bozuklu, M. (2016). Internet of Things: Studies and current situation in our country. Gaziosmanpaşa Journal of Scientific Research, (13), 47-68.

Ercan, T., & Kutay, M. (2016). Internet of Things (IoT) applications in industry. Afyon Kocatepe University Journal of Science and Engineering, 16(3), 599-607.

Altinpulluk, H. (2018). The use of internet of things technology in educational environments. Journal of Open Education Applications and Research, 4(1), 94-111.

Ersin, C., & Ali, O. Z. (2020). IoT-based embedded system design and implementation for occupational health and safety. European Journal of Science and Technology, (18), 494-504.

Improvement of Satellite Optimization Parameters with Lagrange Multipliers

Enes ÇELİK[1]

Introduction

With the beginning of the space age, satellites began to use in communication, earth observation and navigation. Satellite design, analysis, optimization, production, integration and operation have become essential areas. The problems that arise in satellite research and development are becoming increasingly complex. Satellite system design features, satellite orbiting and security design are still being developed today. Comprehensive design is to design and optimize at the system level. In this process, the design plan is according to the needs. Effective payload, reliability, launch and orbit are designed simultaneously in satellites. In addition, the effective load is limited for reliability reasons. Thus, the satellite system consists of many subsystems and becomes a problem involving a series of complex calculations. One of these subsystems is to optimize the design. Our limitations here may be parameters such as budget, lifespan and weight. The research aims to optimize the satellite performance and operation under the relevant rule constraints with the help of optimization subsystems of the overall satellite design (Larson & Wertz, 1999). The thrust of the satellites has increased thanks to the batteries with the latest technology (Dutta et al., 2013). In addition, mini, micro and nano satellites have developed. Earth's outermost satellites or satellites close to the Van Allen belt are exposed to severe radiation with long transfer times and sunrays causing damage to satellite devices (Dutta et al., 2014). To better model the satellite system, the transfer trajectory design should be calculated along with the station holding strategy, power, state control, thermal control, and outer construction material (Sobieszczanski-Sobieski, 1995). Therefore, multidisciplinary design optimization is preferred to deal with satellite system design problems (Sobieszczanski-Sobieski & Haftka, 1997).

Related Works

Shi et al. proposed a surrogate-assisted multidisciplinary design optimization framework for the multidisciplinary design optimization problem of electrified geostatic orbital satellites, consisting of multidisciplinary modeling, multidisciplinary analysis, and surrogate-assisted optimizer (Shi et al., 2017). Appel et al. were interested in the optimization problem of multi-satellite orbit transfer. The solution was carried out using functional optimization techniques. This algorithm is based on a combination of first-order gradient and neighbor-extremal algorithms (Appel et al., 2014). Conway, in a study, examined numerical optimization methods in the satellite optimal orbit problem. He proposed a solution to this optimization process with calculus of variations, nonlinear programming, parametric optimization and evolutionary algorithms (Conway, 2010). In one of his studies, George used a genetic algorithm and simulated annealing methods together to minimize the revisit time of constellation-shaped satellites (George, 1997). Wu et al. used the collaborative optimization method for the optimization problem of the remote sensing

[1] Instructor, Computer Science, Babaeski Vocational School, Kırklareli University, orcid: 0000-0002-3282-865X

satellite, which includes power, attitude control, thermal control and infrastructure systems (Wu et al., 2013). Huang et al. developed the nested cooperative optimization method to solve the optimization problem of manoeuvrable satellites (Huang et al., 2014).

Material and Methods

Lagrange multipliers are there to solve the constraints incrementally, incrementally. It is a precise method that optimizes the objective function to meet Kuhn-Tucker conditions (Luenberger & Ye, 1984). Since the main framework of the discrete Lagrange multipliers theory is similar to continuous lagrange multipliers, it is preferred for satellite optimization problems with continuous lagrange multipliers.

Continuous Lagrange Multipliers

Continuous Lagrange multipliers were initially developed to address constrained optimization problems. This method tries to find a local minimum by transforming an equality-constrained issue into an unconstrained problem space with the help of the Lagrangian function, where the objective function is expressed as follows.

$$\text{Minimize } f(x)$$

$$h_i(x) = 0 \qquad i = 1, \dots, m$$

$$x \in X$$

$$L(x, \lambda) = f(x) + \lambda^T h(x)$$

Then the x's are minimized to obtain an extreme point of the Lagrangian function (Avriel, 2003).

Discrete Lagrange Multipliers

Discrete Lagrange Multipliers provide a mathematical basis for handling discrete-constrained optimization. This theory extends the concept of a straight saddle point to discrete space. It provides the initial conditions for a saddle point to be a local minimum by defining a Lagrangian factorization formulation. Discrete Lagrange multipliers attempt to concentrate on generic theorems and lemmas related to discrete constrained optimization that do not answer according to the problem structure. Here d denotes a random set of discrete values. To find discrete Lagrangian factors, the generalized Lagrangian function defines in discrete space.

$$L_d(x, \lambda) = f(x) + \lambda^T H\big(h(x)\big)$$

H is the continuous transformation function. The lambda equality constraints and h(x) represent the corresponding vector of Lagrangian multipliers. Unlike straight Lagrange multipliers, it has been proven that the Discrete Lagrange Factors and the concept of the saddle point are intertwined. Thus, the conditions for a saddle point can change to be sufficient conditions for the local minimum solution (Wu, 1998).

Parameters of an available satellite system that need to be optimized; economy, outer shell, pneumatics, orbit, reliability, thermal control, thrust, weight, and electromagnetism. Numerical solutions for several representative cases are present for use in optimization processes. According to the weight function and constraint function consisting of impulse (x), budget (y), and electromagnetism (z) variables, what can be the x, y, and z variables to minimize the weight?

$$f(x, y, z) = x + y + 2z$$

$$g(x, y, z) = x^2 + y^2 + z^2 = 3$$

$$\nabla f = (1, 1, 2)$$

$$\nabla g = (2x, 2y, 2z)$$

$$1 = 2\lambda x$$

$$1 = 2\lambda y$$

$$2 = 2\lambda z$$

$$x^2 + y^2 + z^2 = 3$$

λ cannot be zero,

$$x = \frac{1}{2\lambda}$$

$$y = \frac{1}{2\lambda}$$

$$z = \frac{1}{\lambda}$$

substituting x, y, z in the equation,

$$\frac{1}{4\lambda^2} + \frac{1}{4\lambda^2} + \frac{1}{\lambda^2} = 3, \lambda = \pm\frac{\sqrt{2}}{2}$$

If λ substitute in the equations, in order of x, y, z,

$$(x,y,z) = (\frac{\sqrt{2}}{2}, \frac{\sqrt{2}}{2}, \sqrt{2}) \text{ or } (x,y,z) = (-\frac{\sqrt{2}}{2}, -\frac{\sqrt{2}}{2}, -\sqrt{2})$$

substituting x, y, and z in the weight function,

$$f\left(\frac{\sqrt{2}}{2}, \frac{\sqrt{2}}{2}, \sqrt{2}\right) = x + y + 2z = 3\sqrt{2}$$

$$f\left(-\frac{\sqrt{2}}{2}, -\frac{\sqrt{2}}{2}, -\sqrt{2}\right) = x + y + 2z = -3\sqrt{2}$$

These critical points $(-\frac{\sqrt{2}}{2}, -\frac{\sqrt{2}}{2}, -\sqrt{2})$ select to minimize the weight function.

According to the age function and constraint function consisting of the orbit (x) and thermal level (y) variables, what can be the x and y variables to maximize the age?

$$f(x, y) = xy$$

$$g(x, y) = 3x^2 + y^2 = 6$$

$$\nabla f = (y, x)$$

$$\nabla g = (6x, 2y)$$

$$y = 6\lambda x$$

$$x = 2\lambda y$$

$$3x^2 + y^2 = 6$$

23

x in the equation is substituted for x in the other equation,

$$y = 6\lambda(2\lambda y) = 12\lambda^2 y$$

x and y cannot be zero, simplifying the equation with y,

$$12\lambda^2 = 1$$

$$6 = 3x^2 + (6\lambda x)^2$$

$$6 = 3x^2 + 36\lambda^2 x^2$$

$$6 = 3x^2 + 3(12\lambda^2)x^2$$

$$6 = 3x^2 + 3x^2$$

$$x = \pm 1, y = \pm\sqrt{3}$$

Critical points are $(1, \sqrt{3})$, $(-1, \sqrt{3})$, $(1, -\sqrt{3})$, $(-1, -\sqrt{3})$. If x, y, pairs are written in place of the age function,

$$f(1, -\sqrt{3}) = xy = -\sqrt{3}$$

$$f(-1, \sqrt{3}) = xy = -\sqrt{3}$$

These critical points can select to minimize the age function.

$$f(1, \sqrt{3}) = xy = \sqrt{3}$$

$$f(-1, -\sqrt{3}) = xy = \sqrt{3}$$

These critical points can select to maximize the age function. Since we aim to maximize the age function $(1, \sqrt{3})$, $(-1, -\sqrt{3})$, these critical points are selected.

According to the cost function and constraint function consisting of pneumatic (x), outer shell (y), and weight by mass (z) variables, What can be the x, y, and z variables to minimize the cost?

$$f(x, y, z) = x^2 + y^2 + z^2$$

$$g(x, y, z) = x + y + z = 1$$

$$h(x, y, z) = x + 2y + 3z = 6$$

$$\nabla f = (2x, 2y, 2z)$$

$$\nabla g = (1,1,1)$$

$$\nabla h = (1,2,3)$$

$$x = \frac{\lambda + \mu}{2}$$

$$y = \frac{\lambda + 2\mu}{2}$$

$$z = \frac{\lambda + 3\mu}{2}$$

$$x + y + z = 1$$

$$x + 2y + 3z = 6$$

x, y, and z are substituted in the equation,

$$\frac{\lambda+\mu}{2} + \frac{\lambda+2\mu}{2} + \frac{\lambda+3\mu}{2} = 1, \; 3\lambda + 6\mu = 2$$

$$\frac{\lambda+\mu}{2} + 2\left(\frac{\lambda+2\mu}{2}\right) + 3\left(\frac{\lambda+3\mu}{2}\right) = 6, \; 3\lambda + 7\mu = 6$$

μ=4 from the equations. If μ is substituted in the other equation,

$$3\lambda + 7(4) = 6, \; \lambda = -\frac{22}{3}$$

If λ and μ are substituted in the equations,

$$x = \frac{\lambda + \mu}{2} = \frac{-\frac{22}{3} + 4}{2} = -\frac{5}{3}$$

$$y = \frac{\lambda + 2\mu}{2} = \frac{-\frac{22}{3} + 8}{2} = \frac{1}{3}$$

$$z = \frac{\lambda + 3\mu}{2} = \frac{-\frac{22}{3} + 12}{2} = \frac{7}{3}$$

Thus, the critical points are $(-\frac{5}{3}, \frac{1}{3}, \frac{7}{3})$, respectively. Substituting the x, y, and z cost function,

$$f\left(-\frac{5}{3}, \frac{1}{3}, \frac{7}{3}\right) = x^2 + y^2 + z^2 = \frac{25}{3}$$

The value in the equation is the minimum point. There is no maximum point. These critical points $\left(-\frac{5}{3}, \frac{1}{3}, \frac{7}{3}\right)$ choose to minimize the cost function.

Results

Satellite design, analysis, optimization, production, integration, and operation are critical subjects. Satellite systems consist of many subsystems and become a problem involving a series of complex calculations. Our primary constraints here are budget, life span, and weight parameters. In this study, satellite design optimization parameters were optimized under minimal possibilities. In this optimization process, the minimum and maximum points of the parameters related to Lagrange Multipliers have been determined. Since many parameters exist in satellite systems, successful results have been observed using Lagrange Multipliers in optimization processes. This study applied Lagrange Multipliers to artificial world data, not real-world data. In future studies, Lagrange Multipliers can be used in satellite optimization processes under constrained conditions.

References

Appel, L. Guelman, M. & Mishne, D. (2014) Optimization of satellite constellation reconfiguration maneuvers. *Acta Astronautica,* 99, 166-174.

Avriel, M. (2003) Nonlinear programming: analysis and methods. *Courier Corporation.*

Conway, B. A. (2010) A brief survey of methods available for numerical optimization of spacecraft trajectories. *In 61st International Astronautical Congress,* (pp. 1848-1862).

Dutta, A. Libraro, P. Kasdin, N. J. Choueiri, E. & Fracken, P. (2013) Design of next-generation all-electric telecommunication satellites. *In 31st AIAA International Communications Satellite Systems Conference* (pp. 5625).

Dutta, A. Sreesawet, S. Vijayan, S. & Foster, A. (2014) On the design of power and propulsion subsystems of all-electric telecommunication satellites. *In 32nd AIAA International Communications Satellite Systems Conference* (pp. 4243).

George, E. R. (1997) Optimization of satellie constellations for discontinuous global coverage via genetic algorithms. *Astrodynamics,* (pp. 333-346).

Huang, H. An, H. Wu, W. Zhang, L. Wu, B. & Li, W. (2014) Multidisciplinary design modelling and optimization for satellite with maneuver capability. *Structural and Multidisciplinary Optimization,* 50(5), 883-898.

Larson, W. J. & Wertz, J. R. (1999) Space mission analysis and design. *Space*, 5(14), 110.

Luenberger, D. G. & Ye, Y. (1984) Linear and nonlinear programming (Vol. 2). Reading, MA: Addison-wesley.

Shi, R. Liu, L. Long, T. Liu, J. & Yuan, B. (2017) Surrogate assisted multidisciplinary design optimization for an all-electric GEO satellite. *Acta Astronautica,* 138, 301-317.

Sobieszczanski-Sobieski, J. (1995) Multidisciplinary design optimization: an emerging new engineering discipline. *In Advances in structural optimization* (pp. 483-496) Springer.

Sobieszczanski-Sobieski, J. & Haftka, R. T. (1997) Multidisciplinary aerospace design optimization: survey of recent developments. *Structural optimization,* 14(1), 1-23.

Wu, Z. (1998) *Discrete Lagrangian methods for solving nonlinear discrete constrained optimization problems.* Doctoral dissertation, M. Sc. Thesis, University of Illinois, Urbana, IL.

Wu, W. Huang, H. Chen, S. & Wu, B. (2013) Satellite multidisciplinary design optimization with a high-fidelity model. *Journal of Spacecraft and Rockets,* 50(2), 463-466.

Potent Matrices

Hasan KELEŞ[1]

Introduction

This section is about the justification of (iii), which is one of the conditions for the algebraic structure that forms the basis of abstract algebra. The structure monoid of and how it is displayed on the structure is investigated. The definition of the idempotent element on a monoid structure is discussed. The algebraic structures according to the binary operation of multiplying square matrices in matrices, $(\mathbb{R}, \cdot)$ and $(\mathbb{R}, +)$ are known that are monoids. The <u>real numbers</u> $\mathbb{R}$, with the usual operations of addition and multiplication, also form a field. In order to make the study more understandable, first the structures in $\mathbb{R}$ and then the structures of square matrices according to the multiplication operation in the matrix are included. The situation of the equations that provide idempotent element formation in these structures in their own structures was examined. The solution of the equation $x^2 = x$ in real numbers is 0 and 1. Also, the solution of the equation $x^k = x$ in integer numbers is the number 0 and, If $k \in \mathbb{Z}^+$ is odd, the set of solution to the equation $x^k = x$ is $\{0, 1\}$, if k is even, it is $\{-1, 0, 1\}$.

The solution of the equation $x^2 = 1$ in real numbers is $x = \pm 1$. The solution of the equation $x^2 = x$ is 0 and 1. The solutions of this equation, 0 and 1, are idempontent numbers.

$$x^2 = x \Rightarrow x^2 - x = 0$$

$$x(x-1) = 0 \Rightarrow x = 0 \lor x = 1.$$

Let F be a field and $\mathbb{M}_n(F) = \left\{ \left[a_{ij} \right]_n \middle| a_{ij} \in F, n \in \mathbb{Z}^+ \right\}$. Here $\mathbb{M}_n(F)$ is considered as set of square matrices. The equation $AX = B$ is written for $A, X, B \in \mathbb{M}_n(\mathbb{R})$ matrices.

If $A = X = B$ matrix is taken in $AX = B$ equation, $X^2 = X$ equation is obtained. Necessary conditions in the solution of this equation necessitated the following definition.

$$X^2 - X = [0] \Rightarrow X(X - I_n) = [0]$$

$$X^2 - X = [0] \Rightarrow X = [0] \lor X = I_n.$$

Also, the solutions of the equation $X^2 = X$ are zero dividing matrices,

$$X(X - I_n) = [0] \Rightarrow X \neq [0] \lor X \neq I_n.$$

---

[1] Lecturer, Karadeniz Technical University

In this section, the forces resulting from the multiplication of matrices and hence the forces of matrices are examined. For the special matrices existing in the literature, the conditions for being written for some orders are given.

Let us start with the row co-divisor definition that I gave in the study in [10-11].

Let A^T denote the transpose of $A \in M_n(F)$. Let A and B be two regular square matrices of order n. The determinant of the new matrix obtained by writing the ith row of the matrix A on the jth row of the matrix B is called the *co-divisor by row* of the matrix A by the row on the matrix B. It is denoted by $\underset{ij}{AB}$. Their number is n^2. The matrix co-divisor by row is $\left[\left(\underset{ij}{AB} \right)_{ij} \right]$ [9].

For the two matrices satisfying the above conditions, the matrix division is also given by

$\dfrac{A}{B} := \dfrac{1}{|B|} \left[\left(\underset{B}{^A i_j} \right)_{ji} \right]$ and at the same time, the solution of the equation $AX = B$ is $X = \dfrac{B}{A}$.

The row co-divisor definition is related to the product XA, and the column co-divisor definition is related to the AX product. The same expression is written in terms of powers when the solutions of the expressions here are repeatedly divided into the same matrix.

Let $A \in \mathbb{M}_n(\mathbb{R})$ be a regular matrix then there are at least two regular matrices A_1 and A_2 which satisfies the following equation,

$$A = A_1 A_2 \ [12].$$

Every regular matrix can be written as the product of an infinite number of regular matrices. Briefly, for any regular matrix A

$$A = \prod_{i=1}^{+\infty} A_i \text{ where } A_1, A_2, \dots \text{ are regular.}$$

An $n \times n$ matrix A is called inuolutoy iff $A^2 = I_n$, where I_n is the $n \times n$ identity matrix [16].

The broader perspectives are presented for the involutive mind by taking $X^k = X^{-1}$, the periodic mind by taking $X^{k+1} = X$ and the the idempotent mind by taking $X^k = I_n$ in the equation $X^k = X$.

Any power of a matrix other than an integer of 2 is equal to the unit matrix. To generalize this situation, the following definition is given.

Defination 1. An $n \times n$ matrix A is called k^{th} order involutive iff $A^k = I_n$, where $k \geq 2$.

Example 2. Let the matrix $A = \begin{bmatrix} 1 & 1 \\ -1 & 0 \end{bmatrix}$ be given. The matrix A is the 6th order infolutive matrix by

$$A^6 = \begin{bmatrix} 1 & 0 \\ 0 & 1 \end{bmatrix} = I_2.$$

$$X^k = \begin{cases} idempotent, & if \ X^k = I_n \\ involutive, & if \ X^k = X^{-1} \\ nilpotent, & if \ X^k = [0] \\ peryodik, & if \ X^{k+1} = X \end{cases}$$

There is sufficient information in the literature about nilpotent, periodic and involutive matrices.

Matrıces Idempotent Degree k^{th}

Definition 1. A group is a set G equipped with a binary operation $\cdot : G \times G \to G$ that associates an element $a.b \in G$ to every pair of elements $a, b \in G$, and having the following properties: $\cdot$ is associative, has an identity element $e \in G$, and every element in G is invertible (w.r.t. $\cdot$). More explicitly, this means that the following equations hold for all $a, b, c \in G$:

i. $a.(b.c) = (a.b).c$. (associativity);

ii. $a.e = e.a = a$. (identity);

iii. For every $a \in G$, there is some $a^{-1} \in G$ such that $a.a^{-1} = a^{-1}.a = e$. (inverse) [11].

A set M together with an operation $\cdot : M \times M \to M$ and an element e satisfying only Conditions (G1) and (G2) is called a *monoid* [2, 17].

An element $a \in G$ is an idempotent (element) of G if $a * a = a$. We note $P(G)$ the set of idempotents of G in [1, 2, 17]. This set is the set of 2nd order idempotent elements. Shortly,

$$P^2(G,*) = \{a * a = a, a \in G\}.$$

If a is element $P^2(G,*)$, then processing a, $k-$times is still equal to a, for a positive integer $k \geq 3$.

$$\underbrace{a * a \cdots * a}_{k-times} = a.$$

The set $P^k(G,*)$ is the set of *idempotent elements* of *degree* k^{th}. Likewise,

$$P^k(G,*) = \left\{ a \middle| \underbrace{a * a \cdots * a}_{k-times} = a, a \in G \right\}.$$

The set $P^2(\mathbb{R},+)$ of the monoid $(\mathbb{R},+)$ is $\{0\}$ and the set $P^2(\mathbb{R},\cdot)$ of the monoid $(\mathbb{R},\cdot)$ is $\{0,1\}$.

The set of square matrices order n^{th} of a field F is denoted by $\mathbb{M}_n(F)$. The set of idempotent elements of the monoid $\mathbb{M}_n(F)$ is

$$P^k(\mathbb{M}_n(F),\cdot) = \left\{ [a_{ij}]_n \middle| A^k = A, A = [a_{ij}]_n \in \mathbb{M}_n(F) \right\}$$

$$= \{[0]_n, I_n, ...\}$$

If $n = 2$, this set is

$$P^2\left(\mathbb{M}_2(F),\cdot\right) = \left\{ \left[a_{ij}\right]_2 \Big| A^2 = A, A = \left[a_{ij}\right]_2 \in \mathbb{M}_2(F) \right\}.$$

In this study, $F = \mathbb{R}$ is taken.

$$P^2\left(\mathbb{M}_2(\mathbb{R}),\cdot\right) = \left\{ \left[a_{ij}\right]_2 \Big| A^2 = A, A = \left[a_{ij}\right]_2 \in \mathbb{M}_2(\mathbb{R}) \right\}.$$

Example 2. The matrix $A = \begin{bmatrix} 2 & -8 \\ \frac{1}{4} & -1 \end{bmatrix} \in P^2\left(\mathbb{M}_2(\mathbb{R}),\cdot\right)$ is the idempotent elements of degree 2nd

. This matrix A is a second order second-degree idempotent matrix since this matrix provides the definition of idempotent,

$$A^2 = \begin{bmatrix} 2 & -8 \\ \frac{1}{4} & -1 \end{bmatrix}\begin{bmatrix} 2 & -8 \\ \frac{1}{4} & -1 \end{bmatrix} = \begin{bmatrix} 2 & -8 \\ \frac{1}{4} & -1 \end{bmatrix} = A.$$

Lemma 3. Let $A \in P^2\left(M_2(\mathbb{R}),\cdot\right)$. Then,

$$A^k = A, \text{ where } k \in \mathbb{Z}^+.$$

Proof. The proof of this Lemma 3 is done by induction method. The given statement is true for $k = 1$.

$$A = A.$$

Assume that given lemma 3 is true for $k - 1$. Then

$$A^{k-1} = A \Rightarrow \left(A^{k-1}\right)A = AA = A$$

$$A^k = A.$$

Lemma 4. Let $A \in P^2\left(M_2(\mathbb{R}),\cdot\right)$. The elements in the positions of this matrix satisfying the conditions (i) and (ii) given below,

i. $a_{11} = \dfrac{1}{2} \pm \dfrac{1}{2}\sqrt{1 - 4a_{12}a_{21}} = a_{22}, a_{11} + a_{22} = 1$.

ii. $a_{21} \neq 0 \Rightarrow \begin{cases} a_{21} > 0 \Rightarrow \dfrac{1}{4a_{21}} > a_{12} \\ a_{21} < 0 \Rightarrow \dfrac{1}{4a_{21}} < a_{12} \end{cases}$

$$a_{21} = 0 \Rightarrow A = \begin{bmatrix} 0 & 0 \\ 0 & 0 \end{bmatrix}.$$

Proof. If the matrix $A \in P^2\left(M_2(\mathbb{R}),\cdot\right)$, then $A^2 = A$.

$$A^2 = \begin{bmatrix} a_{11} & a_{12} \\ a_{21} & a_{22} \end{bmatrix}\begin{bmatrix} a_{11} & a_{12} \\ a_{21} & a_{22} \end{bmatrix} = \begin{bmatrix} a_{11} & a_{12} \\ a_{21} & a_{22} \end{bmatrix}$$

$$a_{11}^2 + a_{12}a_{21} - a_{11} = 0$$

$$a_{11}a_{12} + a_{12}a_{22} - a_{12} = 0$$

$$a_{11}a_{21} + a_{21}a_{22} - a_{21} = 0$$

$$a_{22}^2 + a_{12}a_{21} - a_{22} = 0$$

$$a_{11} = \frac{1}{2} \pm \frac{1}{2}\sqrt{1 - 4a_{12}a_{21}} = a_{22}$$

$$1 - 4a_{12}a_{21} \geq 0 \Rightarrow a_{12} \neq 0 \Rightarrow \begin{cases} \dfrac{1}{4a_{12}} > a_{21}, a_{12} > 0 \\[2mm] \dfrac{1}{4a_{12}} < a_{21}, a_{12} < 0 \end{cases}$$

$$a_{12} = 0, a_{11} + a_{22} = 1.$$

Lemma 5. Let $A \in P^3\left(\mathbb{M}_2(\mathbb{C}),\cdot\right)$. The elements in the positions of this matrix satisfing the conditions (i), (ii) and (iii) given below,

    i. $|a_{11}| \leq \dfrac{2}{\sqrt{3}}\sqrt{1 - a_{12}a_{21}}, 1 > a_{12}a_{21}$.

    ii. $a_{12} = \dfrac{a_{11} - a_{11}^3}{a_{21}a_{22} + 2a_{11}a_{21}}$, where $a_{21}a_{22} \neq -2a_{11}a_{21}$.

    iii. $a_{11} = -\dfrac{1}{2}a_{11} \mp \dfrac{1}{2}\sqrt{4 - 3a_{11}^2 - 4a_{12}a_{21}}$.

Proof. If the matrix A is the third-degree idempotent matrix, then $A^3 = A$.

$$A^3 = \begin{bmatrix} a_{11} & a_{12} \\ a_{21} & a_{22} \end{bmatrix}\begin{bmatrix} a_{11} & a_{12} \\ a_{21} & a_{22} \end{bmatrix}\begin{bmatrix} a_{11} & a_{12} \\ a_{21} & a_{22} \end{bmatrix} = \begin{bmatrix} a_{11} & a_{12} \\ a_{21} & a_{22} \end{bmatrix}.$$

$$a_{11} = \begin{cases} \mathbb{C}, a_{12} = 0 \\[2mm] -\dfrac{a_{22}}{2} \pm \dfrac{a_{22}}{2}\sqrt{4 - 3a_{22}^2 - 4a_{12}a_{21}}, a_{12} \neq 0 \end{cases}$$

$$a_{12} = \begin{cases} \dfrac{a_{11} - a_{11}^3}{2a_{11}a_{21} + a_{21}a_{22}} \vee \dfrac{a_{22} - a_{22}^3}{2a_{11}a_{21} + a_{21}a_{22}}, 2a_{11}a_{21} + a_{21}a_{22} \neq 0 \\[1em] \mathbb{C}, a_{21}a_{22} = 0 \wedge a_{11} = 0 \\[1em] \varnothing, a_{11} = 0 \wedge 2a_{11}a_{21} + a_{21}a_{22} = 0 \end{cases}$$

$$a_{12} = \begin{cases} \mathbb{Z}, a_{12} = 0 \\[0.8em] -\dfrac{a_{11}}{2} \pm \dfrac{1}{2}\sqrt{4 - 3a_{11}^2 - 4a_{12}a_{21}}, a_{12} \neq 0 \wedge -\dfrac{a_{11}}{2} \pm \dfrac{1}{2}\sqrt{4 - 3a_{11}^2 - 4a_{12}a_{21}} \in \mathbb{Z} \\[0.8em] -\dfrac{a_{11}}{2} + \dfrac{1}{2}\sqrt{4 - 3a_{11}^2 - 4a_{12}a_{21}}, a_{12} \neq 0 \wedge -\dfrac{a_{11}}{2} + \dfrac{1}{2}\sqrt{4 - 3a_{11}^2 - 4a_{12}a_{21}} \in \mathbb{Z} \wedge -\dfrac{a_{11}}{2} - \dfrac{1}{2}\sqrt{4 - 3a_{11}^2 - 4a_{12}a_{21}} \in \mathbb{C} \setminus \mathbb{Z} \\[0.8em] -\dfrac{a_{11}}{2} - \dfrac{1}{2}\sqrt{4 - 3a_{11}^2 - 4a_{12}a_{21}}, a_{12} \neq 0 \wedge -\dfrac{a_{11}}{2} - \dfrac{1}{2}\sqrt{4 - 3a_{11}^2 - 4a_{12}a_{21}} \in \mathbb{Z} \wedge -\dfrac{a_{11}}{2} + \dfrac{1}{2}\sqrt{4 - 3a_{11}^2 - 4a_{12}a_{21}} \in \mathbb{C} \setminus \mathbb{Z} \\[0.8em] \varnothing, a_{12} \neq 0 \wedge -\dfrac{a_{11}}{2} - \dfrac{1}{2}\sqrt{4 - 3a_{11}^2 - 4a_{12}a_{21}} \in \mathbb{C} \setminus \mathbb{Z} \wedge -\dfrac{a_{11}}{2} + \dfrac{1}{2}\sqrt{4 - 3a_{11}^2 - 4a_{12}a_{21}} \in \mathbb{C} \setminus \mathbb{Z} \end{cases}$$

$$a_{21} = \begin{cases} \left\{0, \dfrac{1 - a_{11}^2 - a_{22}^2 - a_{11}a_{22}}{a_{12}}\right\}, a_{12} \neq 0 \\[1em] \mathbb{C}, 1 - a_{11}^2 - a_{22}^2 - a_{11}a_{22} = 0, a_{12} = 0 \\[1em] \left\{0, a_{12} = 0, 1 - a_{11}^2 - a_{22}^2 - a_{11}a_{22} \neq 0\right\} \end{cases}$$

Example 6. Conditions (i), (ii) and (iii) are fulfilled for $a_{11} = 1, a_{22} = -2$ and $a_{11} = 1, a_{22} = -2$. Indeed, the matrix $A \in P^3\left(\mathbb{M}_2(\mathbb{R}), \cdot\right)$ ise, since

$$A^2 = \begin{bmatrix} 1 & 2 \\ -1 & -2 \end{bmatrix}\begin{bmatrix} 1 & 2 \\ -1 & -2 \end{bmatrix} = \begin{bmatrix} -1 & -2 \\ 1 & 2 \end{bmatrix} \neq A$$

The matrix A is not the matrix idempotent degree 2nd.

$$A^3 = \begin{bmatrix} 1 & 2 \\ -1 & -2 \end{bmatrix}\begin{bmatrix} 1 & 2 \\ -1 & -2 \end{bmatrix}\begin{bmatrix} 1 & 2 \\ -1 & -2 \end{bmatrix} = \begin{bmatrix} 1 & 2 \\ -1 & -2 \end{bmatrix} = A.$$

But, matrix A is the matrix idempotent elements of 3th degree.

Lemma 7. Let $A \in P^3\left(\mathbb{M}_2(\mathbb{C}), \cdot\right)$. Then,

$$A^{2k+1} = A, \text{ where } k \in \mathbb{Z}^+.$$

Proof. The proof of this Lemma 7 is done by induction method. It is true for $k = 1$.

$$A^3 = A.$$

Assume that given Lemma 7 is true for $2k-1$.

$$A^{2k-1} = A \Rightarrow \left(A^{2k-1}\right)A^2 = AA^2 = A$$

$$A^{2k+1} = A^3 = A.$$

Theorem 8. An regular matrix $A \in P^3\left(\mathbb{M}_n(\mathbb{R}),\cdot\right)$ if and only if the A matrix is involutive 2nd degree.

Proof. $\Rightarrow$: If $A \in P^3\left(\mathbb{M}_n(\mathbb{R}),\cdot\right)$, then

$$A^3 = A \Rightarrow A^2 = I_n.$$

$\Leftarrow$ If the A matrix is involutive 2nd degree, then,

$$A^2 = I_n \Rightarrow A^3 = A.$$

CONCLUSIONS AND DISCUSSIONS

It is obvious that the concept of "idempotent elements of degree k^{th}", which has just been defined, will find many application areas. The studies on the set of square regular matrices is carefully observed whether it adds a new feature to their algebraic structures. A more general expectation is the expansion of algebraic structures. For example, group, object, ring, etc.

REFERENCES

Herstein, I. N. (1975). Topics in Algebra 2nd Edition, , Wiley, İnternational-Editions, John Wiley & Sons Inc, Printed in the United States of America.

Brawley, J. V., Gamble, R. O. (1978). lnvolutory Matrices over Finite Commutative Rings, Linear Algebra and It is Applicauons, 21, 175-188.

Gallier, J., and Quaintance, J. (2019). Algebra, Topology, Differential Calculus, and Optimization Theory For Computer Science and Engineering, University of Pennsylvania, PA 19104, USA.

Keles, H. (2010). The Rational Matrices, New Trends in Nanotechnology and Nonlinear Dynamical Systems, Ankara, paper58.

Keleş, H. (2017). Different Approaches on the Matrix Division and Generalization of Cramer's Rule, Journal of Scientific and Engineering Research 4(3):105-108.

Keleş, H. (2015). Lineer Cebire Giriş-I-, Bordo Puplication, Trabzon, Turkiye.

Keleş, H. (2018). On Matrix Division and Rational Matrices, SOI: 1.1/IM DOI: 15863/IM, International Scientific Journal Intelligent Mathematics, 1(7).

Keleş, H. (2022). On Results Divisibility and Multipliers of Regular Matrices of Order n^{th}, 8. International Istanbul Scientific Research Congress March 12-13, İstanbul, Turkiye, Pages 712-718.

Keleş, H. (2022). On The Relationship Between Transpose and Division, 8. International Istanbul Scientific Research Congress March 12-13, Pages 719-722, İstanbul, Turkiye.

Keleş, H. (2022). On Some Simplification and Extension of Rational Matrices, Türkiye.

Porter, Duane, A. (1976). Solvability of the Matric Equation $AX = B$, Linear Algebra and Its Applzcatzons 13. 164-177.

Rafael Bru., Maria T. Gassó., Isabel Giménez, and José A. S. (2015). The Hadamard Product of a Nonsingular   General H-Matrix and Its Inverse Transpose is Diagonally Dominant, Hindawi Publishing   Corporation Journal of Applied Mathematics Volume, Article ID 264680, 6 pages.

Volodymyr, P. Shchedryk. (2020). A greatest common divisor and a least common multiple of solutions of a linear matrix equation, Pidstryhach Institute for Applied Problems of Mechanics and Mathematics, National Academy of Sciences of Ukraine, Math. Gm.

Thabet KH. (2012). AL-Ghuribi SU., Matrix Multiplication Algorithms, IJCSNS International Journal of Computer Science and Network Security, 12, 74-79.

Alvaro   Rittatore.   (1998).   Algebraic   Monoids   And   Group   Embeddings, Arxiv:Math/9802073v1 [Math.Ag].

Keleş, H. (2023). On the Involutive Matrices of the kth Degree, Iraqi Journal for Computer Science and Mathematics, Vol. 4, No. 1,   p. 10-14.

The Role Of Machıne Learnıng Algorıthms For Spam E-Maıl Fılterıng

Bekir PARLAK[1]

Introduction

Programs called MAILBOX on the Massachusetts Institute of Technology (MIT) computers dating back to 1965 are the first examples of electronic mail. A networked system was created by ARPANET and e-mail started to be used in 1972. Emails are defined as "username@computername". In a few years 75% of ARPANET traffic was sent via email. With the invention of e-mail, the world has moved from ARPANET to the Internet. With the discovery of the internet, e-mails have provided users with an easy way to exchange information on a global level. The simple message transfer protocol (SMTP: Simple Mail Transfer Protocol) is the e-mail standard that was first introduced. SMTP does not check whether the email sender is a contact. Because of this, some problems such as forgery and fraud arose in e-mail communication. This simplicity in the SMTP protocol is exploited by viruses, fraudsters and spammers.

The continuous increase in the number of e-commerce companies with the rise of e-commerce has led to an increase in the number of advertising emails(Cormack, 2008). Online shoppers receive emails from untrusted senders to hunt for their passwords or bank account information. These randomly sent unsolicited bulk e-mails are called spam. Symantec states that the total spam rates in 2015, 2016 and 2017 were 52.7%, 53.4% and 54.6%, respectively(Cleary et al., 2018). Kaspersky also reported the rate of spam emails as 53.49% at the end of the third quarter of 2018(Vergelis et al., 2019).

The ease of use of e-mails and the ability to reach thousands of people at the same time have brought some disadvantages. One of these disadvantages is unsolicited(spam) messages(Bhowmick and Hazarika, 2018). Thanks to its cost and speed advantage, e-mails are used for purposes such as advertising, promotion, marketing, creating public opinion, sharing inappropriate content, obtaining personal information by sending malicious software, and dozens of spam e-mails are sent to e-mail boxes every day. The rate of spam e-mail is increasing day by day in the researches conducted by most of the research companies. While this situation causes loss of time and effort for users, it also causes unnecessary occupation of network traffic. In addition, from the point of view of enterprises, it is seen that it causes huge financial losses. Many different methods and techniques are used to filter spam and successful results are obtained. Despite this, they continue to use their e-mail systems, developing new strategies and methods to overcome the filters or techniques applied to spam users. For this reason, it is essential to carry out current studies in this field, to develop different methods and techniques, to create different data sets and to support analyzes.

---

[1] Dr. Öğr. Üyesi, Amasya Üniversitesi

In order to solve many problems, computers aim to provide machines with abilities such as learning and interpretation inspired by the behavior of the human brain. Different methods and techniques are used to reveal spam. However, such studies are usually carried out with English datasets. Studies on Turkish datasets are not serious. The reason for this is the inadequacy of data sets or the scarcity of researchers working in this field. There are many techniques for detecting and removing spam. These techniques can be grouped into two groups, namely artificial intelligence and machine learning. Machine learning techniques are examined in two groups as supervised or unsupervised. However, it is supervised learning that is widely used. In order to detect whether an e-mail is spam or regular e-mail, a large data set must be prepared as spam and regular e-mail, with each document labeled according to its class.

In this study, it aims to contribute to the spam filtering studies and the literature by determining the most successful classification algorithms and feature selection methods using a Turkish and English datasets available in the literature. In order to classify Turkish and English e-mails as spam or normal, firstly, a Turkish and English e-mail datasets containing text-based spam and normal e-mail samples were used. Then, the content of each e-mail was analyzed and different words or terms appearing in each e-mail were found. After applying some preprocessing techniques to these words, scores were assigned with three successful feature selection methods, Gini-Index(GI), Max-Min Ratio(MMR), and Extensive Feature Selector (EFS). The feature vectors obtained by these methods are classified by two successful classifiers.

E-mail System and Spam E-mail

Electronic mail (e-mail) is the name given to an electronic message, usually in the form of a simple text, image or video, that a user sends to a computer and forwards it to another user who can read it over a computer network(Altunyaprak, 2006). Email messages consist of a header and a body. The title includes the sender, recipient, subject, and date. Spam are messages sent in bulk by strangers, malware, or bot accounts. These can also be defined as messages sent to e-mail accounts without the request of the person. Unwanted e-mails can be used for purposes such as advertising, promotion and propaganda, as well as for purposes such as stealing personal information and crashing companies' systems. When we look at our e-mail addresses in daily life, we encounter dozens of advertising messages every day, and some of them come from addresses we do not know. In addition, some spam messages may send viruses or computer-damaging links to capture our personal information and bank account information. They can steal our information when they copy trusted web addresses and make us trust them. Another reason why we face spam today is the email trade. Companies that offer e-mail services usually offer it for free. However, while providing this service, it can provide access to many data, especially an e-mail address. E-mail addresses belonging to millions of people are marketed to different businesses and cause us to receive unsolicited messages from companies we do not know. While companies are always looking for ways to communicate with their customers more accessible, cheaper or faster, they offer all three with the e-mail service available on the internet. In this case, the marketing of email addresses is one of the reasons for the increase in spam. Today, many different methods are used and new techniques are being developed to filter unsolicited (spam) e-mails. Some of these methods are Word Filtering, Rule-Based Filtering, Blacklists and Antivirus Scanning.

There are some common features when examining spam. These are;

• The contents are up to date.

• They can talk about human feelings and ask for the e-mail to be forwarded to many people.

• Often their content is misleading.

• It is sent for promotional purposes.

Related Works

Although there are many studies to filter spam written in English(Ahmed, 2020; Sharma and Kaur, 2016; Venkatraman et al., 2019), such studies are relatively few with Turkish(Dedeturk and Akay, 2020; Ergin et al., 2012; Ozgur et al., 2004), an agglutinative language with a much more complex morphological structure than English. For the Turkish language, Özgür et al.(Ozgur et al., 2004) used a rooting operator to classify Turkish emails and applied two different classifiers, with a success rate of approximately 90%. Tunga and Kitik(Güngör and Çıltık, 2007) proposed methods based on the n-gram method and the first n-word heuristic. The best success rates with their approach were about 97% for a Turkish dataset. In the study of Ates(Ates, 2014), two different content-based filtering methods were carried out using the supervised learning algorithm Support Vector Machines and the unsupervised learning algorithm Gaussian Mixture Models, using both Turkish and English datasets. Deniz et al.(Deniz et al., 2019) Attribute extraction was performed using the TurkishEmail e-mail dataset and algorithms belonging to the Doc2Vec library were used. Doc2Vec includes two different algorithms called Distributed Bag of Word (DBoW) and Distributed Memory (DM). Classification was made with six different pattern classifiers. The highest performance DBoW+DM feature selection and support vector machine machine learning resulted in a score of 78.75%. Karamollaoğlu et al.(Karamollaoglu et al., 2018) aimed to analyze the content information of e-mails written in Turkish, to determine whether these e-mails are spam e-mails and to classify them with the help of Naive Bayes Classifier and Vector Space Model, one of the machine learning methods. Both methods were subjected to different evaluation criteria and their performances were compared. Experimental results showed higher performance of Naïve Bayes Classifier method compared to Vector Space Model. Unlike other studies, Kaynar et al.(Kaynar et al., 2016) proposed an automatic encoder-based deep learning machine, which is one of the modern machine learning approaches for the classification of spam. Autoencoders are actually multilayer sensors where the inputs and outputs have the same dataset. The classifier using the automatic encoder deep learning machine has been shown to have an extremely high success rate of 98% accurate classification. Ergin et al.(Ergin et al., 2012) applied a Turkish anti-spam filter to identify text-based Turkish spam emails (junk or bulk email). In the study, a database containing spam and normal e-mail samples in Turkish was created. The content of each e-mail was analyzed and different words from all e-mails were identified. The content of each e-mail was analyzed and different words from all e-mails were identified. Then, a Turkish root extraction function was used to obtain the root forms of different words. Mutual Information (MI= Mutual Information) scores of different words were calculated, so that two types of feature vectors were created according to the MI scores. After this process, binary and probability based models of Bayesian classifier were tested and success rates of binary and probability based models were compared.

In addition to the Turkish spam filtering studies, there are also English e-mail filtering studies in the literature. In one study(Renuka et al., 2015), spam classification in the proposed system was carried out using the Naive Bayes classifier, which is a conditional probability-based probabilistic classifier applicable to more complex classification problems. The application of feature selection using Hybrid Ant Colony Optimization also serves to be efficient and yielding good results for the system proposed in this study. Venkatraman et al.(Venkatraman et al., 2020) proposed the integration of the Naive Bayes classification with the conceptual and semantic similarity technique to combat the uncertainty posed by polysemy in spam detection. To analyze the effectiveness of the approach, experiments were performed on comparative datasets such as Spambase, PU1, Enron1 and Lingspam. It is clear from the experimental results that the proposed system achieves

a higher accuracy of 98.89% than existing approaches. In another study(Bhuiyan et al., 2018), related to Machine Learning Techniques (MLT=Machine Learning Techiques) such as Naive Bayes, SVM, K-Nearest Neighborhood, Bayesian Additive Regression, KNN Tree and rules shows a survey of the different email spam filtering system available. However, this study presents the classification, evaluation and comparison of different spam filtering systems and summarizes the general scenario regarding the accuracy of the different approaches available. Bhowmick et al.(Bhowmick and Hazarika, 2018), presented a comprehensive review of the latest and successful content-based spam filtering techniques. Their focus is mainly on machine learning-based spam filters and their inspired derivatives. They came to the conclusion by examining techniques, evaluation criteria and exploring promising branches of the latest developments and making recommendations for future research. Subasi et al.(Subasi et al., 2018) proposed an approach for spam filtering based on simple and better accuracy decision tree algorithms. From the experimental results, the proposed random forest classifier outperformed other decision tree methods for public datasets.

Feature Extraction

The word bag-of-words (BoW) approach(Li et al., 2020) is one of the methods used for feature extraction in text classification studies. In this approach, the order of the terms in the documents is ignored, while the frequency of their occurrence is used. Therefore, each unique word in a text collection is considered a different attribute. As a result, a document is represented by a multidimensional feature vector(Parlak and Uysal, 2021). In a feature vector, each dimension corresponds to a value weighted by term frequency (TF) or term frequency-inverse document frequency (TF-IDF)(Parlak and Uysal, 2018).

In addition, it should not be forgotten that some pre-processing steps(Uysal and Gunal, 2014) are necessary for performance during feature extraction from text documents. Commonly used preprocessing steps are the "removal of stop-words" and the "stemming" algorithm. In this study, both pre-processing steps were applied. For stemming, Zemberek(Akın and Akın, 2007) and Porter stemmer(Porter, 1980) algorithm and term frequency-inverse document frequency (TF-IDF) were used as weighting approach.

Feature Selection

In addition, it should not be forgotten that some pre-processing steps(Uysal and Gunal, 2014) are necessary for performance during feature extraction from text documents. Commonly used preprocessing steps are the "removal of stop-words" and the "stemming" algorithm. In this study, both pre-processing steps were applied. For stemming, Zemberek(Akın and Akın, 2007) and Porter stemmer(Porter, 1980) algorithm and term frequency-inverse document frequency (TF-IDF) were used as weighting approach.

Feature selection techniques generally fall into three categories: filters, wrappers, and embedded methods. Filter techniques are computationally fast; however, they usually ignore attribute dependencies. Filter-based techniques are widely preferred especially for text classification field. There are many filter-based techniques for the selection of distinctive features in text classification. In this study, three different feature selection techniques, namely Gini Index (GI), Normalized Difference Measure (NDM) and Extensive Feature Selector (EFS) were used. Table 1 explains the notations in the formulas of these methods. Also, the methods are detailed below:

Table 1. *Notations for feature selection methods*

Notation	Meaning
$p(t\mid C_j)$	Probability of term t when class C_j exists
$p(\bar{t}\mid C_j)$	Probability of absence of term t when class C_j exists
$p(t\mid \overline{C_j})$	Probability of absence of of term t when class C_j does not exists
$p(\bar{t}\mid \overline{C_j})$	Probability of term t when class C_j does not exists
$p(C_j\mid t)$	Probability of class C_j when t term is present
$p(\overline{C_j}\mid t)$	Probability of absence of class C_j when t term is present
$p(C_j\mid \bar{t})$	Probability of class C_j when t term is not present
$p(\overline{C_j}\mid \bar{t})$	Probability of absence of class C_j when t term is not present

Gini Index(GI)

GI is an improved version of the method originally used to find the best feature distribution in decision trees(Singh et al., 2010). It is an accurate and fast method. The formula is as follows:

$$GI(t) = \sum_{j=1}^{M} P(t\mid c_j) * P(c_j\mid t) \tag{1}$$

Max-Min Ratio(MMR)

MMR(Rehman, Javed, Babri, & Asim, 2018) provides better performance on datasets including highly skewed classes. The method is a combination of true positives, false positives and their differences. According to the method, the feature score is calculated as follows:

$$MMR(t) = \sum_{j=1}^{M} \frac{|P(t\mid c_j) - P(t\mid \overline{C_J})|}{\min(P(t\mid c_j), P(t\mid \overline{C_J}))} \cdot \max(P(t\mid c_j), P(t\mid \overline{C_J})) \tag{2}$$

Extensive Feature Selector(EFS)

The EFS method(Parlak and Uysal, 2021) selects more important features by using both class-based and collection-based probabilities of the feature. Its formula is a bit more complex than other methods:

$$EFS(t) = \sum_{j=1}^{M} \left(\frac{P(t\mid C_j)}{P(\bar{t}\mid C_j) + P(t\mid \overline{C_J}) + 1} \right) \cdot \left(\frac{P(C_j\mid t)}{P(\overline{C_J}\mid t) + P(C_j\mid \bar{t}) + 1} \right) \tag{3}$$

Datasets

In this study, "TurkishEmail"(Ergin et al., 2012) and "Enron1"(Uysal and Gunal, 2014) datasets were used. There are a total of 800 e-mails in this dataset, which consists of normal and spam e-mails in the Turkish dataset. In the English dataset (Enron1), there are 5172 e-mails in total in this dataset, which consists of regular and spam e-mails. The distribution of training and test data of these datasets is given in Table 2-3 below.

Table 2. *Turkish Email Dataset*

	Train	Test
Ham	300	100
Spam	300	100

Table 3. *English Email Dataset*

	Train	Test
Ham	1836	1836
Spam	750	750

Classifiers

In this study, it is employed two successful classifiers. These classifiers Multinomial Naive Bayes(MNB) and Decision Tree(DT).

A particular naive Bayes classifier called MNB was created specifically for classifying texts. This naive Bayes classifier's event model was specifically represented by the multinomial term. For text categorization, multinomial and multi-variate Bernoulli event models are frequently used(Zhao et al., 2016). The way a portion of the formula is calculated varies across multinomial and multi-variate Bernoulli event models. Multi-variate Bernoulli event model employs document frequencies in this calculation, whereas multinomial model considers term frequencies.

The widely-used DT classifier(Quinlan, 1986) creates a hierarchy of decision rules from data automatically. Each path in the tree structure used to express these decision criteria leads to the assignment of a class label. After making Yes/No decisions along a path of nodes inside a tree structure, classification is carried out. One of the most effective decision tree classification methods is C4.5.

Experimental Study

Different sized vectors of the features selected by each selection method were fed with MNB and SVM classifiers. Stop-words removal and stemming were applied in the experiments. The widely known Zemberek algorithm has been implemented as a stemming algorithm for Turkish dataset. Also, Porter-stemmer algorithm has been employed as a stemming algorithm for English dataset. In this study, GI, MMR and EFS were used as feature selection methods. The total number of features was 18650 and 27521 for Turkish and English datasets, respectively. However, in terms of size; dimension reduction was performed by creating 100, 250, 500 and 1000 feature vectors. In addition, the F score(Goutte and Gaussier, 2005) was used as a measure of success. This score is presented predominantly, not in a class-specific form. The F-Scores obtained are listed in Table 4-7. The best ones in the results are shown in bold.

Given the highest weighted average F scores, it outperformed the GI, MMR, and EFS methods overall in most cases. In the Turkish dataset, GI has the highest performance in the MNB classifier, while MMR has the highest performance in the DT classifier. However, the methods are more successful when the feature size is low in the MNB classifier, while the methods are more successful when the feature size is high in the DT classifier. In the English dataset, EFS has the highest performance in the MNB classifier, while GINI has the highest performance in the DT classifier. However, the methods are more successful when the feature size is high in the MNB classifier, while the methods are more successful when the feature size is low in the DT classifier.

Table 4. *F Scores for Turkish E-mail Dataset with MNB Classifier*

Turkish E-mail	100	250	500	1000
GINI	**0.977**	0.940	0.930	0.930
MMR	0.970	0.925	0.935	0.915
EFS	0.970	0.940	0.915	0.930

Table 5. *F Scores for Turkish E-mail Dataset with DT Classifier*

Turkish E-mail	100	250	500	1000
GINI	0.950	0.960	0.970	0.965
MMR	0.955	0.965	**0.975**	0.970
EFS	0.960	0.965	0.970	0.965

Table 6. *F Scores for English E-mail Dataset with MNB Classifier*

English E-mail	100	250	500	1000
GINI	0.877	0.904	0.916	0.921
MMR	0.869	0.901	0.918	0.917
EFS	0.884	0.902	0.916	**0.923**

Table 7. *F Scores for English E-mail Dataset with DT Classifier*

English E-mail	100	250	500	1000
GINI	**0.911**	0.897	0.889	0.889
MMR	0.888	0.893	0.880	0.871
EFS	0.894	0.888	0.890	0.890

Conclusions

In this study, the performances of two widely known classifiers were extensively analyzed using three different feature selection methods. This analysis was carried out on datasets consisting of Turkish and English e-mail documents. Experimental results were obtained with the combination of MNB classifier and GI Feature Selector of the most successful scheme for the Turkish dataset. For the English dataset, the most successful schema was obtained with the combination of MNB classifier and EFS Feature Selector. As a future study, a new Turkish e-mail dataset in this field will be gained and analyzed with different attribute selection techniques.

REFERENCES

Ahmed, B. (2020). Wrapper Feature Selection Approach Based on Binary Firefly Algorithm for Spam E-mail Filtering. *Journal of Soft Computing and Data Mining 1*, 44-52.

Akın, A.A., Akın, M.D. (2007). Zemberek, an open source NLP framework for Turkic languages. *Structure 10*, 1-5.

Altunyaprak, C. (2006). Bayes yöntemi kullanarak istenmeyen elektronik postaların filtrelenmesi. Yüksek Lisans Tezi, Muğla Üniversitesi Fen Bilimleri Enstitüsü.

Ates, N. (2014) Support vector machine and gauss mixture model detection of unsolicited e-mails. Master's thesis, Suleyman Demirel Universitesi, Fen Bilimleri Enstitusu, Bilgisayar Muhendisligi Anabilim Dali.

Bhowmick, A., Hazarika, S.M. (2018). E-Mail Spam Filtering: A Review of Techniques and Trends, Advances in Electronics, *Communication and Computing. Springer*, pp. 583-590.

Bhuiyan, H., Ashiquzzaman, A., Juthi, T.I., Biswas, S., Ara, J. (2018). A survey of existing e-mail spam filtering methods considering machine learning techniques. *Global Journal of Computer Science and Technology*.

Cleary, G., Corpin, M., Cox, O., Lau, H., Nahorney, B., O'Brien, D., O'Gorman, B., Power, J.-P., Wallace, S., Wood, P. (2018). Internet security threat report. Symantec Corporation, California, USA, Tech. Rep.

Cormack, G.V. (2008). Email spam filtering: A systematic review. Foundations and Trends® in *Information Retrieval 1*, 335-455.

Dedeturk, B.K., Akay, B. (2020). Spam filtering using a logistic regression model trained by an artificial bee colony algorithm. *Applied Soft Computing 91*, 106229.

Deniz, E., Erbay, H., Coşar, M. (2019). Türkçe e-postaların Doc2Vec ile sınıflandırılması.

Ergin, S., Sora Gunal, E., Yigit, H., Aydin, R. (2012). Turkish anti-spam filtering using binary and probabilistic models. Global Journal on Technology 1.

Goutte, C., Gaussier, E. (2005). A probabilistic interpretation of precision, recall and F-score, with implication for evaluation, European conference on information retrieval. Springer, pp. 345-359.

Güngör, T., Çıltık, A. (2007). Developing methods and heuristics with low time complexities for filtering spam messages, International Conference on Application of Natural Language to Information Systems. Springer, pp. 35-47.

Karamollaoglu, H., Dogru, İ.A., Dorterler, M. (2018). Detection of Spam E-mails with Machine Learning Methods, 2018 Innovations in Intelligent Systems and Applications Conference (ASYU). IEEE, pp. 1-5.

Kaynar, O., Görmez, Y., Işık, Y. (2016). Oto Kodlayıcı Tabanlı Derin Öğrenme Makinaları İle Spam Tespiti. Uluslararası Yönetim Bilişim Sistemleri Konferansı 44.

Li, P., Mao, K., Xu, Y., Li, Q., Zhang, J. (2020). Bag-of-Concepts representation for document classification based on automatic knowledge acquisition from probabilistic knowledge base. *Knowledge-Based Systems 193*, 105436.

Ozgur, L., Gungor, T., Gurgen, F. (2004). Adaptive anti-spam filtering for agglutinative languages: a special case for Turkish. *Pattern Recognition Letters 25*, 1819-1831.

Parlak, B., Uysal, A.K. (2018). On feature weighting and selection for medical document classification, Developments and Advances in Intelligent Systems and Applications. Springer, pp. 269-282.

Parlak, B., Uysal, A.K. (2021). A novel filter feature selection method for text classification: Extensive Feature Selector. *Journal of Information Science*, 0165551521991037.

Porter, M.F. (1980). An algorithm for suffix stripping. Program 14, 130-137.

Quinlan, J.R. (1986). Induction of decision trees. Machine learning 1, 81-106.

Renuka, D.K., Visalakshi, P., Sankar, T. (2015). Improving E-mail spam classification using ant colony optimization algorithm. *Int. J. Comput. Appl 22*, 26.

Sharma, R., Kaur, G. (2016). E-Mail Spam Detection Using SVM and RBF. *International Journal of Modern Education and Computer Science (IJMECS) 8*, 57.

Singh, S.R., Murthy, H.A., Gonsalves, T.A. (2010). Feature Selection for Text Classification Based on Gini Coefficient of Inequality. Fsdm 10, 76-85.

Subasi, A., Alzahrani, S., Aljuhani, A., Aljedani, M. (2018). Comparison of decision tree algorithms for spam e-mail filtering, 2018 1st International Conference on Computer Applications & Information Security (ICCAIS). IEEE, pp. 1-5.

Uysal, A.K., Gunal, S. (2014). The impact of preprocessing on text classification. *Information Processing & Management 50*, 104-112.

Venkatraman, S., Surendiran, B., Kumar, P.A.R. (2019). Spam e-mail classification for the Internet of Things environment using semantic similarity approach. *The Journal of Supercomputing*, 1-21.

Vergelis, M., Shcherbakova, T., Sidorina, T., Kulikova, T. (2019). Spam and phishing in 2018. Secure List.

Zhao, L., Huang, M., Yao, Z., Su, R., Jiang, Y., Zhu, X. (2016). Semi-supervised Multinomial Naive Bayes for text classification by leveraging word-level statistical constraint, Proceedings of the Thirtieth AAAI Conference on Artificial Intelligence. AAAI Press, pp. 2877-2883.

Rised CO₂ And Climate Change Effects On Wheat

Uğur KEKEÇ
Burçak KAPUR
Eser çeliktopuz
Levent KOÇ
Müge Erkan CAN

Introduction

Short-wave radiation from the sun, retained as long-wave radiation in the earth and atmosphere; dispersed on earth by ocean circulation and given back to the atmosphere as ground radiation. Part of it absorbed by clouds and greenhouse gases in the atmosphere and released back to the atmosphere. In this way the earth's surface and the lower atmosphere are warming. Earth warming more than expected this process, which provides and regulates the heat balance, is called the natural greenhouse effect (Türkes, Sümer & Çetiner, 2000). Today, the aforementioned global climate change as a result of the strengthening the natural greenhouse effect of the rapid increase in greenhouse gas accumulations released into the atmosphere increase in the average surface temperature of the Earth and reveals changes in climate.

The average temperature of the earth and water bodies has been increasing since 1861. The increase is around 0.8 °C during the 20th century (IPCC, 2001). Globaly, from 1861 to the 1990s was the warmest decade and 1998 was instrumental measurement It was recorded as the hottest year of the process. Every 10 years between 1950-1993 the average daily-nightly maximum surface air temperatures increased by 0.2 °C. The specified increase is 0.1°C higher than the 10-year increase in the daily maximum temperature is too much. The prolongation of frost-free seasons in many mid and high latitudes seen as a result of temperature increase. Since 1880, the temperature of the Earth has risen by 0.08 °C per decade, but since 1981, the pace of warming has increased by more than twice that, to 0.18 °C per decade (NOAA, 2022). According to NOAA's temperature data, 2021 was the sixth-warmest year ever. Nine years between 2013 and 2021 are among the ten warmest on record (NOAA, 2022). Clearly indicates that the negative effects of human actions on the climate in recent years shows its effects (Figure 1). The extraordinary development of the industry in recent years and increased use of fossil fuels, increasing CO₂ emissions; 120 years of the past the increase in temperature during the last 20 years of today.
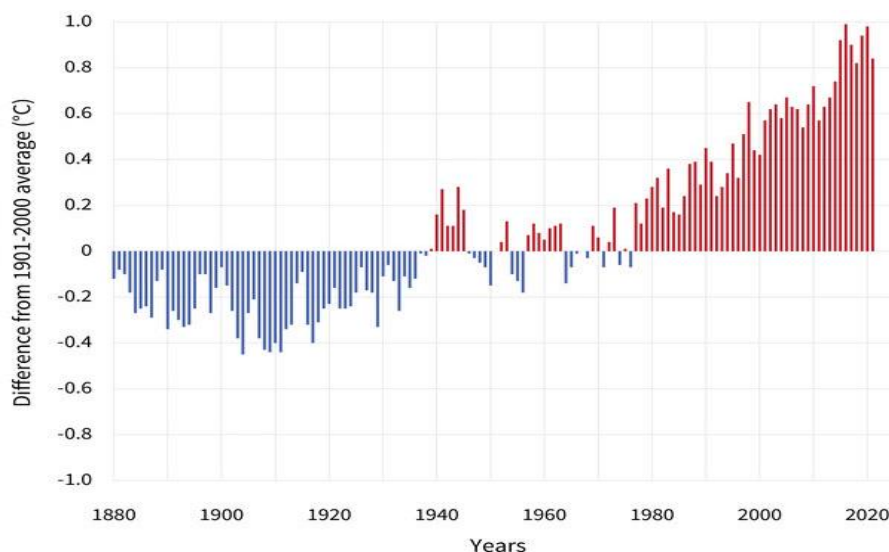
Figure 1. Annual surface temperature as compared to the average for the 20th century (1880–2021). Red bars reflect years that were warmer than normal, and blue bars show years that were cooler than usual. NOAA Climate.gov graph, based on data from the National Centers for Environmental Information. (NOAA, 2022).

In this context, Turkey is at risk for the potential effects of global warming group of countries. The most striking changes observed in Turkey characterized by increases in summer temperatures. Summer temperatures, mostly, increases in the western and southwestern regions. In addition, the last 50 years the amount of precipitation on the western provinces of Turkey in the winter season decreased (Karaca, Deniz & Tayanç, 2000).

The last 70 years, according to the data recorded at the meteorological stations, the increase in annual average temperatures in Turkey tends to; especially in the Mediterranean and Southeast Anatolian regions increase between 0.07-0.34 degrees every 10 years (WorldData, 2022). 1930-2003 in a study using Mann-Kendall trend analysis significant increases in annual average temperatures in the Çukurova region (Kapur et al., 2007) were detected.

Agro-economic systems (agriculture, forestry, fisheries and water resources) are vital to human development and is highly sensitive to climate change. The annual average increasing temperature will enhance desertification, salinization, erosion and thus, arid and semi-arid areas. The type of crop, yield and growth time and duration are determined by atmospheric conditions. Within this context, wheat is a crucial plant that needs to be protected from the harmful impacts of climate change. It occupies 15% of the world's agricultural areas and provides 25% of the protein and 20% of the calories needed for food. Turkey, which meets 3.6% of the world wheat production, is among the most important wheat producer and consumer countries in the world. Wheat is cultivated on an area of approximately 9.5 million hectares in our country. Although it changes from year to year in production, it is around 20 to 21 million tons. An average of 225 kg of wheat per year is required to feed one person considering that, for our 80 million population (OECD/FAO, 2021).

Possible effects of global climate change on wheat crop

In wheat, a positive effect could be seen due to the increase in CO$_2$ when it transfers the growth which affects positively to the expanding leaf area. Thus, the plant receives more light and CO$_2$, positively affecting its development. This positive development, in addition to CO$_2$, depends on the competition for light, water, temperature and plant nutrients (Gifford & Morrison, 1993).

However, in the field, such a high increase in yield should not be expected due to the competition in the field. The positive effect of CO_2 on the development of wheat decreased due to the limited water and plant nutrients, decreased aeration in the plant root zone and increased salinity levels. With these limitations, the plant negativly effected and could not responde to the positive effect of CO_2 and this is known as the plant's capacity to use assimilates (Sink Effect). Root development acts as a depot for photoassimilation and thus, the reason for the limitation of plant growth depends on the limited storage of roots. Stitt (1991), reveals that the limited phytosythesis despite to the increasing CO_2 level attributed to the effect of deficit root storage capacity. Thus, plant responses determined by long-term, experimental studies could be explained according to the capacity of the plant, which depends on the plant variety, development process and growing conditions.

Due to the increase of CO_2, enhanced plant growth and leaf area also causes a rise in the loss of CO_2 by respiration. As a result of this, more larger plants, in other words, plants that grow faster, so that more respiration they do (Gifford & Morison, 1993). Another negative effect is the plant shading itself. Allows larger leaf surface area to benefit from more light however, increasing leaf sizes shade each other. Thus,this reduces the photosynthesis in the unit area. All these positive and negative factors combined effects reveals the actual vegetation growth rate was positive in the trials against the CO_2 increase (Reddy & Hodges 2000). Table 1 displays the anticipated effects on wheat yield under two fold CO_2 climatic scenarios developed using global circulation models, taking into account the studies that are currently published worldwide.

Table 1. Wheat production with Global Circulation Model in conditions of double CO₂ increase (IPCC, 2001).

Region	Yield Change(%)	Countries
Europe	-10 to +10	France, UK, and Northern Europe
South America	-61 to +5	Argentina, Brazil, Chile, and Mexico
Former Soviet Union	-19 to +41	---
North America	-100 to +234	USA and Canada
Africa	-65 to +6	Egypt, Kenya, South Africa, Zimbabwe
South Asia	-61 to +67	Bangladesh, India, Philippine, Thailand, Indonesia
China	-78 to +28	---
Asia	-41 to +65	Australia and Japan

Effects of CO_2 and possible CO_2 increase on plant physiology and productivity

The effect of the rised CO_2 on the plant is varies from the microscopic level (at the cell level) to the macroscopic agro-ecosystem level. The study of the increase level of CO_2 in C3 crops such as wheat is complex to explain the physiology and the process. Photosynthesis, respiration and transpiration is one of the most important processes which the plants are directly affected by the increase in CO_2. Some of these primary effects is positive; some will have negative effects on wheat. The general effects of increased CO_2 on the plant are schematicly illustureted in Figure 2. With increasing carbon dioxide, if plant nutrients and climatic factors are suitable an increase in yield could be possible. However, how plants respond to increased carbon dioxide under restrictive

conditions will depend on the level of negative conditions. Examining the level these interactions of possible changes are very important in determining the adaptation approaches.
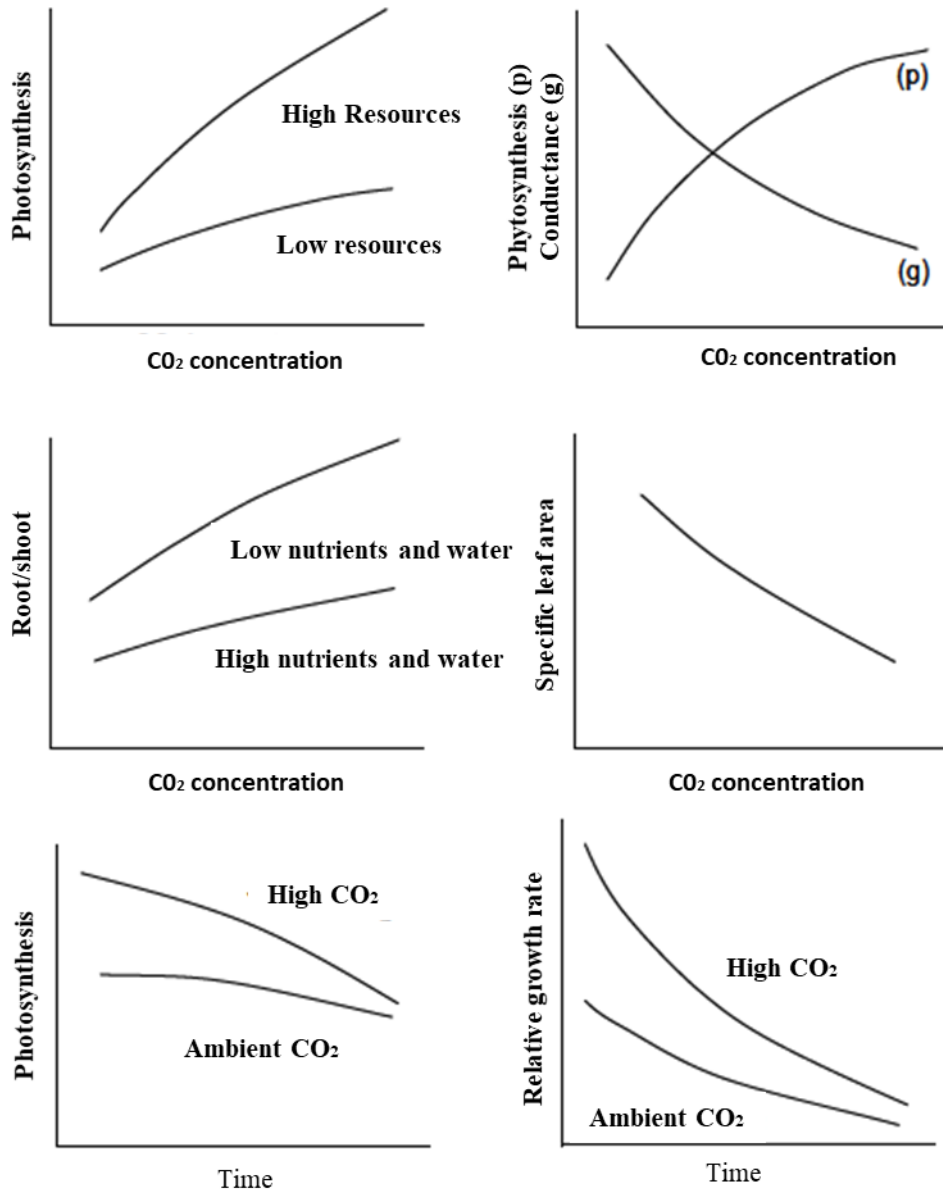
Figure 2. The response of plants to CO_2 concentration (Bazzaz, 1990).

Photosynthesis and respiration

The net relationship of photosynthesis and respiration between the atmosphere and terrestrial ecosystems which is clearly known that it affects the direction of carbon flow.

Photosynthesis: Despite the rise in atmospheric CO_2, it is thought that this increase may benefit agriculture if changes in temperature and precipitation regime do not actually occur. CO_2 is an absolute requirement for photosynthesis and life on earth. The increased CO_2 concentration in the atmosphere, enhance the CO_2 concentration differences between the atmosphere and inside

uptake of CO_2 by diffusion and thus, chloroplasts CO_2 difusion increases in leaves and conversions of carbohydrates rised. In C3 plants, including wheat, the increase in CO_2 increases the rate of photosynthesis at both leaf and vegetation levels (Lemon, 1983; Acock & Allen, 1985; Drake & Leadley, 1991).

Due to the different photosynthetic mechanisms of the plant species to CO_2 increases causes different respond. In some species, photosynthesis takes the C3 pathway. The reason why this pathway is called the C3 is because the first formed in the biochemical process phosphoglyceric acid which has three carbons. In other species, this path is conversely, since the first product has four carbons, the C4 path and called C4 plants. The C4 plants affected less than C3 plants versus CO_2 increase in photosynthesis action as reflected in Figure 3 (Akita & Moss, 1973).
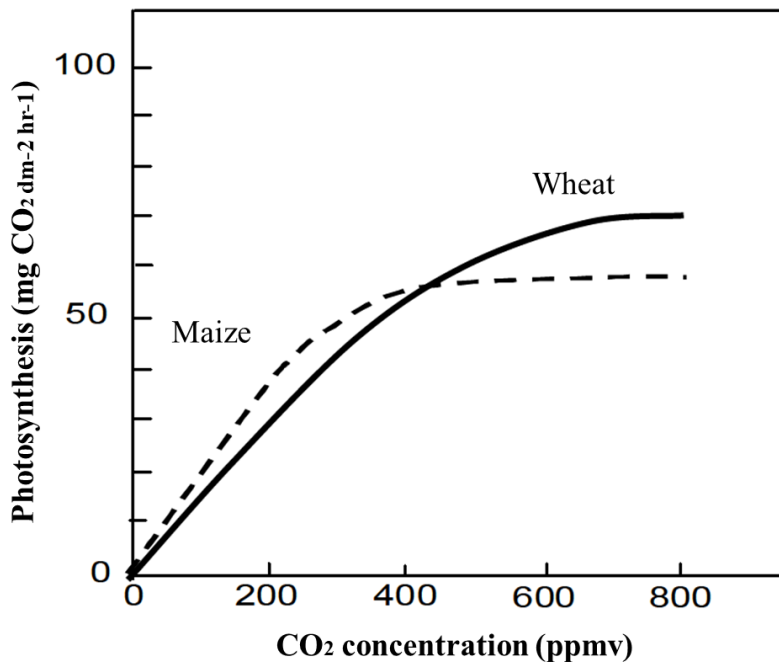
Figure 3. The rate of photosynthesis in maize and wheat change depending on CO2 (Akita & Moss, 1973)

Respiration: Photosynthetic carbon uptake response to atmospheric CO_2 changes can be easily understood and modeled at many scales. However, the mechanism of respiration change versus to CO_2 increse (in a short time-second or minute; long in the process-seasonal) is less understood. Photosynthesis, growth and substrate increases in enhance the respiration rate per unit area. This situation could be explained as the higher biomass requires higher energy support to grow. On the other hand, increasing levels of CO_2 in the atmosphere could reduces the level of CO_2 that released via respiration (Amthor, 1989). So these two opposing effects interaction is unknown. Some researchers think twice the CO_2 concentration reversing the outward, net movement of CO_2 in plant tissue found to decrease. Some researchers also found that increased CO_2 concentrations increased CO_2 use efficiency on phytosynthesis (Gifford & Morrison, 1993). In addition, increasing CO_2 levels in wheat, in the long term, controlled-condition studies and field trials demonstrating reduced respiration Reddy & Hodges (2000). However, today short-term metabolic changes has not been fully determined with the relations in the long-term and permanent changes.

Climate adaptations of photosynthesis and respiration (aclimation): Depending on the increase of CO_2 level cause an increase in the rate of photosynthesis however, it is stated that this initial reaction will decrease in the long run (Stitt, 1991). An organism's adaptation to changing

environmental conditions is often inherited (Hale & Orcutt, 1987). Plants adapt the rate of photosynthesis and respiration to high CO$_2$ levels. However, adaptability of the plants is insufficiently defined today. Photosynthetic adaptation causes a decrease in Rubisco enzyme production. This process is more linked with the high levels of carbohydrates in the leaves (Stitt, 1991). Another important factor affecting the photosynthesis rate of the plant is depends on the effectively storing capacity of photosynthesis products as refered physiological capacity. In other words, higher persistence of photosynthesis at high levels, or continuous/stable formation depends on the biomass storages such as fruit, tuber and grain. These depots provide increasingly fixed carbohydrates. Even in the process of adaptation level, photosynthesis is generally increases as the CO$_2$ concentration increase in the atmosphere. On the other hand, long-term adaptation is necessary for photosynthetic capacity and respiration (Reddy & Hodges 2000).

Stoma resistance and water use efficiency

Another important physiological effect of CO$_2$ increase is on the movement of stomata is the effect. CO$_2$ absorption from stomatal pores on leaf surfaces and water vapor is released. In this context, due to atmospheric CO$_2$ increase, transpiration level may decrease. A 30% decrease in conductivity stoma was detected in a double CO$_2$ increase environment. (Cure & Acock, 1986) (Table 2).

Table 2. Percentage change in transpiration in plants against increased CO$_2$ (300 ppm CO$_2$ increase) (Cure & Acock, 1986).

Reaction Type	Wheat	Barley	Rice	Corn
Transpiration	-17 $\pm$ 17	-19 $\pm$ 6	-16 $\pm$ 9	-26 $\pm$ 6
Type Reaction	Sorghum	Soy Beans	Cotton	Potatoes
Transpiration	-27 $\pm$ 16	-23 $\pm$ 5	-18 $\pm$ 17	-51 $\pm$ 24

Thus, the water use efficiency (WUE) is increased by this two fold increase in CO$_2$ together, it will cause a decrease in transpiration. WUE is defined as the biomass rate to the water lost by the plant through evapotranspiration. Proportionality rise of CO$_2$ affects positively C3 crops such as wheat under limited irrigation conditions than the sufficient water conditions due to smaller stomatal openings of C3 plants. Increases between 70-100% in water use efficiency in wheat which was determined by Kimball & Idso (1983) and Morison (1985).

At the leaf level, in the conducted studies on fifty different plants, CO$_2$ increases effects C3 and in C4 plants on gymnosperms, angiosperms, monocotyledons and dicotyledons as different stoma responses (Morison, 1985). However, an increase in CO$_2$ or the stomatal behavior associated with the reduction and the related physiological mechanism not fully understood. Contrary to past information, the stomata of C3 and C4 plants in a linear relationship against the 2 fold CO$_2$ increase and that, on average, both C3 and C4 plants have showed a 40% decrease in stomatal opening to double CO$_2$ increase. (Figure 4.) (Rosenzweig & Hillel, 1998).
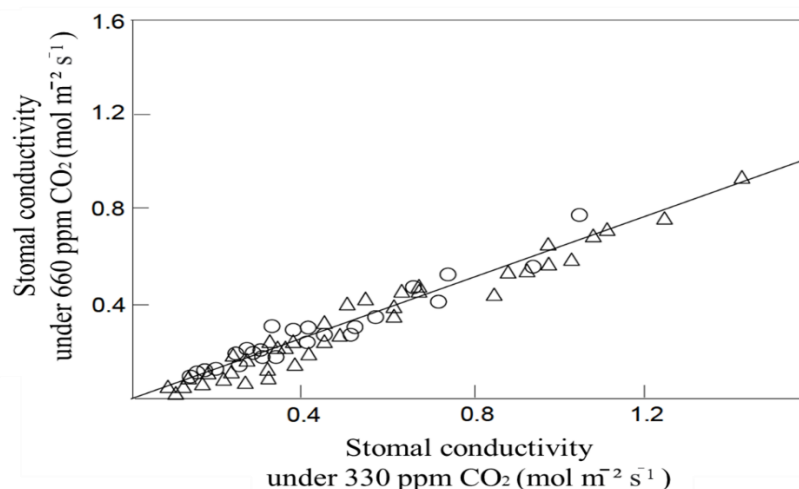
Figure 4. Change of stomatal conductivity due to CO2 increase (⊿= C3 plant, O=C4 plant) (Morison, 1985).

The stomatal response to the increase in CO_2 varies according to many factors. These are leaves age, light intensity, atmospheric humidity, and temperature (Morison, 1985). Determining the stomatal response with the relationship between CO_2 is difficult because of the interaction between CO_2, temperature and plant hormones. The relationship between stomatal regulation and gas exchange also presents similar difficulties for the explanation.

The closure of stomata and the parallel as a result of decreased transpiration and latent heat loss associated with the leaf temperature increase is a well known aspect. Leaf and vegetation temperatures under controlled climate chambers increase 1-3 °C depending on the CO_2 increase (Chaudhuri et. al., 1986; Idso, Kimball & Mauney, 1987). Reduction in transpiration associated with closure of stomata (25-35%), is not equal to the decrease in stomatal conduction (40%) (Allen, Jones & Jones, 1985; Morison, 1985). The reason for this is the increased vapor pressure inside the leaf, partial it increases the vapor pressure gradient from the leaf to the air in order to compensate for the decreasing conductivity. Thus, the leaf temperature is also increases the metabolism and leaves (including respiration and physiological development) causes tissue aging.

The relationship between photosynthesis and stomatal movements can be considered at three levels. These can be considered as leaves, plants and vegetation. At the leaf level, certain increased transpiration efficiency (photosynthetic water use) as a result of the increase in CO_2 increases net assimilation between 60% - 160% with a decrease in transpiration (Morison, 1985).

At the plant level, photosynthetic water use efficiency do not increase as much as water use efficiency during longer growth periods. This is caused due to the photosynthetic adaptation, adverse temperature effect, amount of product and transpiration. Under double CO_2 increased conditions, Morison (1985) reported a plant growth increase of about 30% together with a decrease in transpiration, in which case both factors mentioned (plant growth and transpiration) water use efficiency in the plant between 70% and 100% increases.

At the vegetation level, the water use efficiency in the field is planted per unit area biomass accumulation to the total water level used by plants in that area (ETc) ratio. The total amount of water used by the plant directly affected by CO_2 increase but by vegetation cover and plant water uptake both affected by stomatal inclusions and soil evaporation and transpiration.

Another change in the hydrological regime under increasing CO_2 conditions is the water balance interaction due to the increase of leaf area. In arid environments this cause a direct transpiration rise significantly. Thus, at the vegetation level at the field, on the water use efficiency more complex relationships and effects occur. With double CO_2 increase, the increases in WUE causes increase by approximately 30% to 50% in products and vegetation.

Biological yield and grain yield

Increased photosynthesis at high atmospheric CO_2 concentration provides increased biomass accumulation as expected (Kimball & Idso, 1983; Cure & Acock, 1986; Poorter, 1993). With a doubling of CO_2 in trials under controlled conditions (today 350 ppm), yield levels of plants such as wheat differs. Response (yield level) of most plants is positive, but small some of them were negative (Table 3). Some researchers have conducted their experiments to verify controlled conditions (Lawlor & Mitchell, 1991; Hendrey, 1993).

Table 3. The rate of the yield change in different crops against increasing CO_2 (%) change (300 ppm CO_2 increase) (Cure and Acock, 1986).

Wheat	Barley	Rice	Corn	Soy Beans	Cotton	Potato	Dessert potato	Weighted average
+35±14	+70±9	+15±3	+29±64	+29±8	+209±20	+51±11	+83±12	+41

Response to increased CO_2, different plants and even different varieties of the same plants varies. Varieties of the same cultivar different response to CO_2 is depending on the genetics of plant varieties, experimentation technique and to the pattern. C3 and C4 photosynthetic pathways seem to be the general variation reason for differences between plants.

Biomass formed in the crops is the difference between photosynthesis and respiration via accumulation in the form of carbon products, plus mineral accumulation. Therefore biomass increase parallels concurrent to net photosynthesis impact as expected. On the other hand, under real conditions, plant nutrients, the amount of soil water content and other factors, should also be at an optimum level. Example;the promotion of root and vegetative parts growth means additional resource use. This on the contrary, increased carbon assimilation makes nutrients more restrictive for growth. Growth at low temperatures is probably not by assimilation, rather it will be limited by its photosynthetic capacity. If these factors are sufficient CO_2 increase could rise the wheat yield from 0% to 40%. Earlier field studies found that doubling CO_2 could be increased to 30%, and an increase of 20% can be achieved by quadrupling. In trials simulating field temperature in England, The biomass value of winter wheat is between 15-27% with a doubling of CO_2 and if the CO_2 level is doubled in graduated temperature tunnels, the reaction was between 6-34% (Lawlor & Mitchell, 2000). Nine regions in Europe under Open Top Chambers (OTC) 25 studies were conducted with wheat, starting at 10% of CO_2 320 µmol/mol encourage biomass production, the trials and regression analysis using all data reflects for each 100 µmol/mol 13% of the above-ground biomass increase detected (Lawlor & Mitchell, 2000).

Wheat's response to increased carbon assimilation is resilient and all plant organs could growth. The main stems are usually the least affected organs which is also mentioned by Kapur (2010) for the wheat under climate change effects. On the other hand, tiller growth and viability and root growth were the most encouraged are organs. However, the leaf area, the number of grains per spike and the grain weight was determined by the variety and environmental conditions. From rised CO_2 the grain yield increase is similar with the increase of the biomass. Reproductive

period in comparison to the vegetative growth period grain yield is more sensitive to biomass production, especially during flowering. Summer wheat variety Minaret in multi-site OTC trials reveals 11% grain weight increase per 100 μmol/mol CO_2 enrichment. These results are similar which obtained on the wheat variety Mersia (Lawlor & Mitchell 2000).

Kimball (1983) investigated the effect of CO_2 on wheat in more than seventy studies on pot experiments, yield levels also increased around 90% of the studies. These increases are varies between 0-100%. Although a few negative results were mentioned, but the reason was not disclosed. Gifford and Morison (1993) stated that the negative results of the experiment are due to the mixing of CO_2 with other gases such as ethylene may be a decrease in yield. Kimball (1983) and Cure & Acock (1986) found that C3 plants on average yields were reported with a twofold increase in CO_2 an increase of 35% yield reported. On the other hand, this increase was detected as 10% in C4 plants. For C3 plants, this means biomass of 0.1%/ppmv increase to CO_2 rise. The increase in C4 plants is not directly related to photosynthesis, may be due to the improvement of the efficiency of water use. Despite several trials on yield quality, the increase in CO_2 appears to have little effect (Reddy & Hodges, 2000).

In general, the increase in wheat yield, tillering and more depends on the grain (Lawlor & Mitchell,1991; Kapur, 2010). Experimental CO_2 increase also changes in organs were observed. These changes are related with the stem and root length, the increase in leaf area and thickness.

If not always also, generally increased leaf thickness, which is due to increased starch levels and the specific leaf surface area (Reddy & Hodges, 2000). These two effect could reduces the potential assimilation of unit leaf area via lowering the rise of photosynthesis (Rosenzweig & Hillel, 1998).

Temperature and possible temperature rise effect on plant physiology, growth and yield

High temperature stress processes in plant is the least understood subject. Soil and air temperatures although they are not simultaneously rise often show a high level of variation. Therefore the roots and branches grow in changing environments. The metabolism of field crops is highly affected by these environmental temperatures. Significantly the temperature affects the crop morphology, degradation of photosynthetic products and root-branch ratio. 'Critical Temperatures' that used in the empirical description of plant growth, covers the average minimum and maximum diurnal temperatures and the total temperature above a certain limit as well as in the growth period. Different physiological processes and plant development periods have different temperature responses (Reddy & Hodges, 2000).

The effect of CO_2 increase on plant growth has been studied extensively, however, the interaction of CO_2 with temperature increase in this regard has not been well studied. Genarally the studies covering the effect of temperature change in controlled environments taking into account without nighttime changes. In the field, high temperatures are often associated with high radiation and increased water requirements and thus, it is difficult to understand the effects of climatic factors separately on the plant (Reddy & Hodges, 2000).

Global climate models over the growth period of any plant, gives the number of days in the season that the total temperature and tolerance limit value required will be exceeded. This reflects only the potential effects of high temperature on the amount of yield (Reddy & Hodges, 2000).

Effect of temperature on physiological processes

High temperatures mostly in modarate climatic regimes is expected to decrease the yield. This type of damage in plant production systems is difficult to detect and temperatures are generally within out of optimal ranges in many agricultural regions. For example, optimum growth of wheat temperature is 15 ºC as the period average, however, in the Great Plains in the USA. It is also grown when the daily temperature maxima reaches 25 ºC during the grain filling process (Paulsen, 1994).

Plants balance the temperature rise, long-wavelength radiation and heat energy by spreading through transpiration and close their stomata when exposed to drought stress (Gates, 1980). These closures reduce transpiration and, as a result, the cooling effect of water loss disappears, so plant temperatures increase. Thus, water and temperature stresses often occur together and they affect.

Hot dry winds (North African Sirocco or Middle East Chamsin) often increase high temperature damage. Temperatures between 45-55ºC for at least 30 minutes are damage the leaves many environments. Even if temperatures of around 35 ºC and 40 ºC last longer, they show aproximately the same effect (Fitter & Hay, 1987) and above 40 ºC temperatures also affect the closure of stomata (Shibles, Anderson & Gibson 1975). Considering the effects of high temperatures on major crops such as wheat that vernalization is reversed in temperature periods of 30 ºC and above for more than eight hours (Acock & Acock, 1993).

Root temperature is more effective than above soil surface temperature because the roots optimal temperature values are lower and to rapid temperature fluctuations shows less adaptations (Paulsen, 1994). Reduction of metabolic substrates, increase in the levels of respiration affects the root activity and the other physiological processes negatively. Therefore, root growth and function are highly affected under high temperature.Temperature affects the uptake of plant nutrients and water, as well as the displacement of root carbohydrates. Prolonged high temperatures ultimately result in completely stop the root growth.

The sensitivity of photosynthesis to temperature is higher than the respiration. The leaf photosystem II (PS2) reaction center in their chloroplasts and thylakoid membranes is very sensitive and responds quickly to high temperature and high luminous (especially during the grain filling process) (Paulsen, 1994).

In many studies, net photosynthesis in wheat is limited at 5 °C that it increases over a wide optimum range as the temperature increases (>25 °C) and stopped around 40 °C (Lawlor and Mitchell, 2000). Due to the nature of Rubisco, the sensitivity of net photosynthesis to $CO_2$was found to increase significantly with temperature. Optimum temperature with elevated CO_2 increases by a few degrees. This is related with the kinetic parameters of Rubisco that due to temperature and the proportional solubility of CO_2 and oxygen (O_2). This means that photorespiration increases with temperature. The most important effect of the climate change is the higher temperature accelerates the leaf formation and aging, thus shortening the active photosynthesis period (Lawlor & Mitchell, 2000).

Above a minimum limit value, the plants' resistance to rising temperature tends to be positive up to the optimum temperature value. Optimum temperature value is the maximum rate of plant growth when all other variables are optimum. These other variables are humidity, aeration, plant nutrients (BBM), light and CO2 of the environment (Fitter & Hay, 1987). When this optimal range is exceeded, plants react negatively and significant reduction in growth and yield occurs (Fig. 5). Different Optimal temperatures vary according to plants. For example, a semi-arid region plant optimal temperature required by corn for photosynthesis is higher than the wheat and grows in a

more temperate climate (Figure 6). Generally plants maintained the temperature of the leaves according to the ambient temperature, if the usable water level is sufficient.
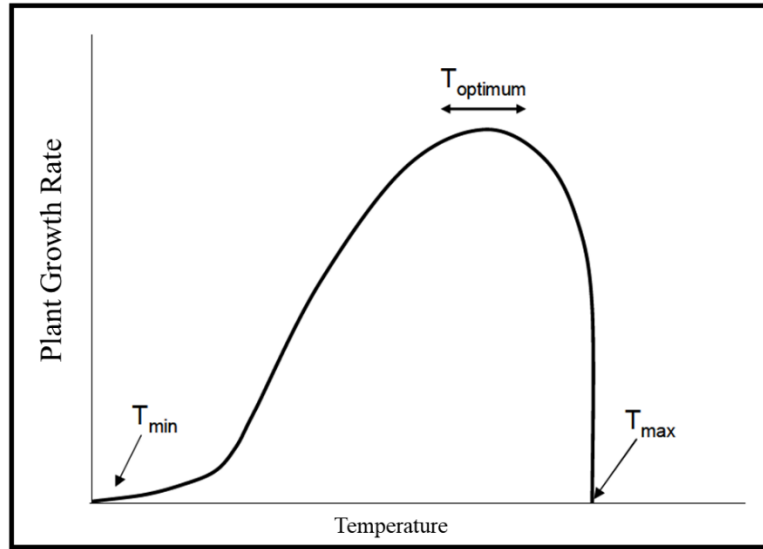
Figure 5. The relationship between plant growth rate and temperature (Rosenzweig & Hillel,1998)
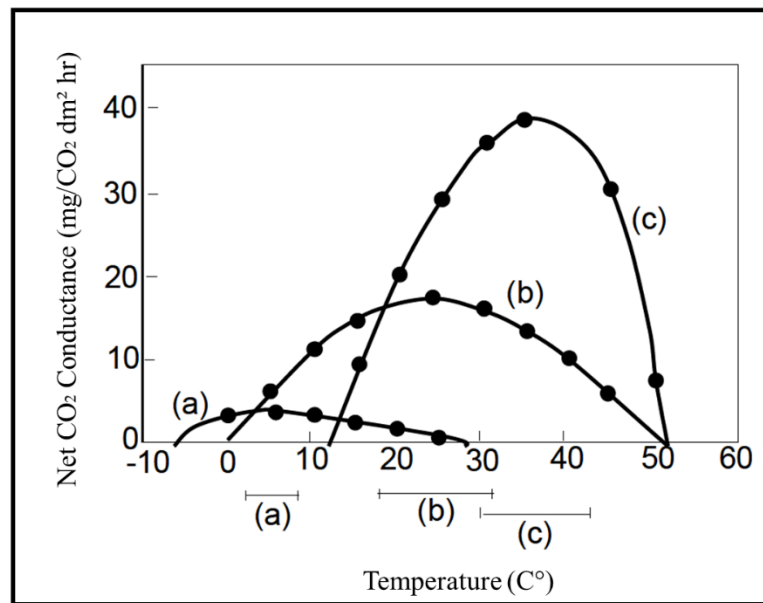
Figure 6. Relationship between net photosynthesis rate and temperature (a: grass; b: wheat,c: maize; horizontal lines indicate optimum range) (Rosenzweig & Hillel, 1998)

Rising temperatures increase the metabolic activities of plant cells, however, extremely high temperatures can damage enzymes (Fitter &Hay,1987). Rapid reaction levels are useful up to a certain level, above which temperatures can damage some plant processes. Balancing both effects serves to determine the general response of the plant to the increase in temperature. Optimum temperature above the range photoplasmic proteins, cellular enzymes and membranes decompose and a cessation or decrease in the rate of cytoplasmic flow occurs.

In temperate zone varieties, respiration rates are 20 °C below the temperature is low and with the rise in temperature it reaches the 'equilibrium point' until 40 °C. At this temperature point, the respiration rate is equals the rate of photosynthesis; and a net carbon build-up does not occur

at this point which stops the growth. The net level of photosynthesis is obtained when the gross carbon is subtracted from the respiration carbon consumption. This relation were reflected in Figure 7 (Fitter & Hay,1987). Accelerated respiration reduces net biomass accumulation and lowers the efficiency of economical product. In an example given by Paulsen (1994), wheat grains was reduced by the increased respiratoion at high temperature levels. Under increased CO_2 conditions respiration rate changes may partly contribute to reduce the photosynthesis. On the other hand, plants have a certain respiration adaptation to warmer conditions, without an increase in rate (Reddy & Hodges, 2000).
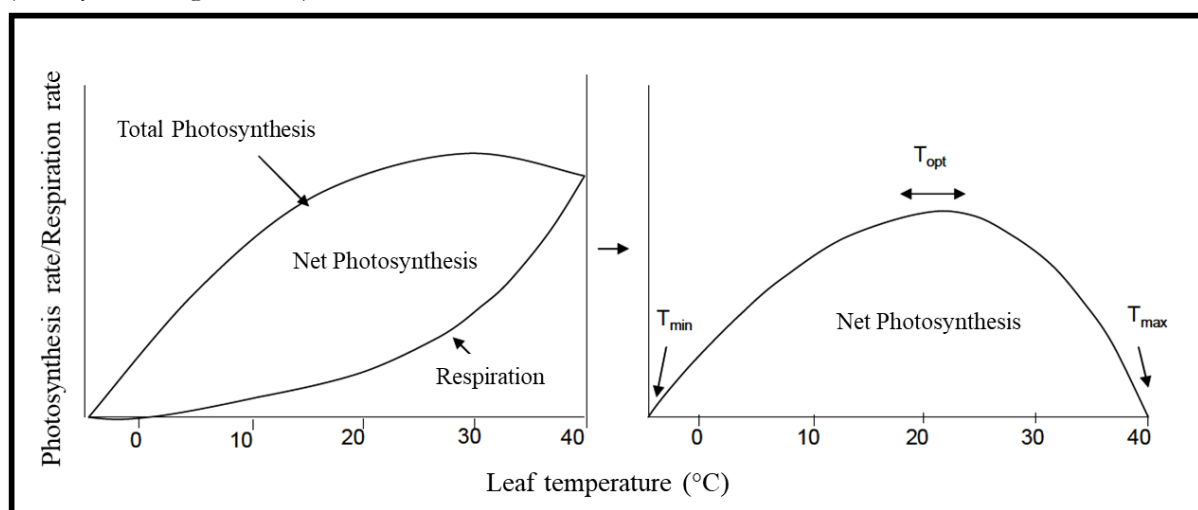
Figure 7. The effect of temperature on plant photosynthesis and respiration and net production (Pisek et al., 1973)

The susceptibility of plants to high temperature damage may be affected vegetative and reproductive development periods differently by their prolongation. Especially during the reproductive development of the plant the high temperatures could damage the plant. Possibly, it can affect grain filling in wheat. In the Anthesis process and just before, the changes that may cause many types of infertility, however, it was determined that wheat was less sensitive to this change (Paulsen, 1994).

Low yield depends on low assimilation rates, accelerated plant development and shortened daily temperature changes. High temperatures can accelerate ripening and effect the functional quality properties of wheat. After near-optimal temperatures in the main products negative effects of rised temperatures, will be higher. In the double CO_2 scenario when the predicted temperature rise reaches its upper limit, plant breeders must be to develop temperature-tolerant varieties (approximately 4 °C temperature rise).

The effects of temperature on wheat phenology are more than the effects of extreme temperatures. Extreme cold can damage wheat; or late frosts promote sterility. During flowering temperatures above freezing (lower than 5 °C) and extreme temperatures (more than 30 °C) can damage pollen formation. This, as a result, may reduce yield while reducing grain settling. Climate change is likely can lead to low yields due to extreme temperatures; because of climate change due to the frequency of extreme temperatures, especially in short development stages to which plant growth is sensitive, may change over time (Lawlor & Mitchell, 2000).

As the effects of changing climate, winter death, vernalization, respiration levels and high temperature stress may vary. High night temperatures can stop the accumulation of carbohydrates of plant organs (Hall & Allen, 1993), and thus, flowering and grain filling may be adversely affected.

In some field crops, the tissues are resistant to low temperatures and thus they become more resistant to the harmful effects of frost. Warmer or milder autumns reduce winter strength and infrequent cold could increases the yield damage sensitivity in this periods. Some studies reveals that 'Winter Deaths' may increase with warming scenarios (Mearns, Rosenzweig & Goldberg, 1992).

In some crops, such as winter wheat, 'full blooming' cannot occur without passing the cooling period. This process is called 'vernalization'. In winter ss temperatures rise, vernalization is negatively affected. Farmers can adapt to the change by switching to the 'summer wheat variety' (Rosenzweig, 1985). This situation changes the marketing, processing and quality of wheat.

Rising temperatures during the night increase respiration so increase the use of plant carbohydrates storage and thus yield decreased. This effect, limits some tropical crop yields in agricultural areas. In a simulation study, the effects of the minimum and maximum temperature changes were investigated by Rosenzweig & Tubiello (1996) and they reveal, the minimum temperature increase negatively effects the wheat yield in the USA more than the maximum temperature rise. Plant responses to adverse effects of climate change are variable, however if a north-south section consideration, the southern part of USA has more negative effects due to decreases in vernalization on wheat Rosenzweig & Tubiello (1996).

Effect of temperature on growth and development period

In mid and high latitude areas Increased warming could be beneficial as increase the duration of the potential growth season. A prolonged potential growing season could provide early sowing in spring, accelerated growth and early ripening with the harvest. As a result, multiple cropping can take place.

The main environmental factor controlling plant growth is temperature. High temperatures generally affect the phenological development of plants and accelerates maturation (Ellis et. al., 1990). Shortened growth period of time due to rised temperature can reduce the potential yield of annual crops (Rosenzweig, 1990; Butterfield & Morison, 1992). In this context, the length of the growth period and the the total amount of light input is main determinants of the total dry matter and yield (Monteith, 1981). Early plant growth in warm environments effects the potential grain yield in the plant growth period (Paulsen, 1994).

With high temperature, the lengths of all developmental stages are shortened. Especially if the period from double ring formation at the apex to flowering is shortened more causes a decrease in the number of grains of each spike and a decrease in grain yield Reddy & Hodges (2000). High temperatures often reduce the number of leaves and spikes due to rapid growth (Paulsen, 1994). Optimum photosynthesis temperature for wheat is between 20-30 ℃, whereas it is 15 ℃ on average for grain yield during the growing period. This temperature difference reveals the importance for maximum yield for temperate plant varieties via photosynthetic activity and temperature process in wheat (Paulsen, 1994). High temperature it also reduces the number and weight of grains that can be harvested. Figure 8 shows the effects of high and low temperatures (Acock & Acock,1993).
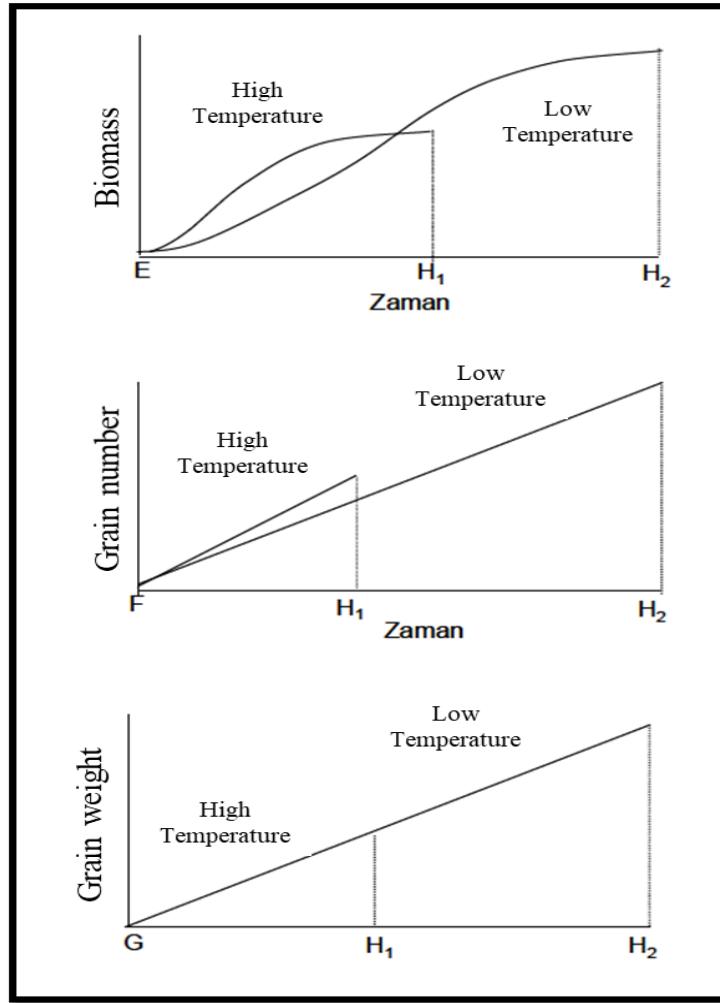
Figure 8. Effects of low and high temperatures on plant growth and yield (E: Germination, F: Beginning of development of plant organs for harvest, G: Beginning of Dry matter accumulation, H: End of dry matter accumulation) (Acock & Acock, 1993).

Researchers have determined the need for thermal time for a plant during its development period as various linear and nonlinear indices. Thermal indices are usually 'degree days of growth' (Thermal Time = Total Temperature defined as Growing Degree Days, GDD) and calculated based on total daily or monthly maximum and minimum temperatures. Some of these have been changed as day length, solar radiation and water stress. These indices are used in calculating the effects of seasonal temperatures according to plant growth, crop and geographical region.

Phenological development and growth processes of plants as seed germination, leaf formation, growth and the beginning of the spike period are directly related to the temperature. The plant total temperature need for each development period is called Thermal Time. Effective thermal process cannot accumulate and plant growth cannot progress below from a certain base or sub-temperature level. Thermal time, accumulation level and plant growth level are increasing with optimal temperature. A forementioned above this optimal temperature, basic process accumulation and plant growth decreases and with the increase in temperature, the accumulation inhibited and accordingly the development of the plant stops.

Effects of temperature on biological yield and grain yield

High temperatures shorten all development cycles. In this context, there is more limited time to obtain resources such as the light water and nutrients, and thus biomass production decreases with increasing temperature. The size of influence depends on which growth cycle is affected. Because the maximum shortening of the growth rate period compared to the shortening of the first growth period, has greater impact on biomass. In a study in England, a 3.5 °C icrease throughout all growth periods reduces the biomass of winter wheat 16% and grain yield by 35% with greatly shortened growth period (Reddy & Hodges, 2000). Further more according to Kapur (2010), vegetative parts (leaf, stem and root weight) per plant, under warm conditions increased more rapidly than in cooler conditions with reached to the highest value early and consequently the weight is lower in hot conditions than in cool conditions. Generally, in the greenhouse trails where the ambient temperature changes, the effects of increasing temperature on biomass were more negatively detected. However, this situation varies greatly between seasons and varieties (Lawlor & Mitchell, 2000).

The negative effect of increasing temperature on grain yield is higher than on the biomass. So the harvest index decreases more in rised temperature. This means that particular the grain yield is sensitivity to grain filling period. During the grain filling period 1 °C increase in temperature shortens the time by 5% and thus, harvest index and grain yield reduced. If the high temperatures promote sterility in flowering period also this reduces yield. In open air growth chamber using minaret summer wheat variety trials at 9 different regions, statistical analysis, reflects 6% of grain yield and biomass decreased for each 1 °C increase throughout growing season (from emergence to maturity). Also these effects can be estimated very well with simulation models (Lawlor & Mitchell, 2000).

Water and possible drought effects on growth and yield

Precipitation is the primary source of soil moisture and in arid regions it is the major factor that influencing the plant yield. An overall average precipitation estimater global climate model results also reflect the potential changes of hydrological regimes in each location. A change in climate parameters affects the total seasonal precipitation. In addition, also this situation affects the seasonal distribution and inter-seasonal distribution change. For plant productivity, the seasonal distribution of precipitation degradation may be even more effective than the reduction in total precipitation. Yield, beside amount of water, is also sensitive to potential daily or seasonal 'ET' variation.

Crop water stress depends on the cellular water activity, reduced energy potential in plants, low cell turgor pressure, increased solution densities, decreased cell pressure and lost hydration of tissues (Hale & Orcutt, 1987). After all, the cell expansion and division, cell wall formation, protein and chlorophyll synthesis, and photosynthesis slows down. When significant water stress occurs, the respiratory level rises, sugar and proteins accumulate and metabolism is disrupted (Fitter & Hay,1987).

As water stress increases, the potential osmotic pressure in plant cells decreases. This process adjusts the regulation of turgor. Osmotic regulation allows cell growth at low water levels (Kramer, 1983). Conservation of turgor features are the lowering osmotic pressure, deposition of solute capacity, and elasticity properties of cells (Hale & Orcutt, 1987).

In the initial stages of drought stress, crop could be protected via turgor osmotic regulation. If water stress persists, plants may lose their adaptive properties and yield levels are more likely to suffer from drought, especially during the reproductive development period. In water stress, leaves, which absorb water rapidly during the dry period can draw water from the grain (Rosenzweig &

Hillel, 1998). Drought in leaves accelerates aging and leaf fall. The water tension during the flowering, pollen release and grain filling phases affects the yield especially in wheat. In wheat, leaf formation and spike formation are affected by water stress.

Wheat studies on the interaction of CO_2 and drought under field conditions are quite a few and can be summarized as follows (Bauer,1972);

a) In elevated CO_2 application, the water use of the wheat plant is may decrease slightly in moist environment, however, in dry conditions could increase slightly

(b) Stimulation of biomass and grain yield with elevated CO_2 tends to be greater in dry conditions compared to humid conditions.

CO_2, climate change and wheat yield

CO_2 temperature and precipitation variations change the growing conditions of crops. The physiological effect of increased CO_2 on the plant may be beneficial to agriculture. Under changing conditions, in environments where plant nutrients and water are not limited, the water use efficiency and photosynthesis increased in the short periods. However, in field conditions, there is often a lack of water and plant nutrients and so productivity may not be an increase (Rosenzeweig & Hillel, 1998).

A combination of changes in key factors in plant physiological processes, understanding of the reasons for the yield change is very powerful. In order to determine the effects of climate change realistically, with CO_2 more research is needed on the interaction between temperature and drought. Furthermore, conducting such studies for each agro-ecosystem could give reasonable results.

References

Acock, B. & Acock, M. C. (1993). Modeling approaches for predicting crop ecosystem responses to climate change. In D. R. Buxton, R. Shibles, R. A. Forsberg, B. L. Blad, K. H. Asay, G. M. Paulsen, and R. F. Wilson (eds.).lntemational Crop Science I. Crop Science Society of America. Madison, Wl. pp. 299-306.

Acock, B. & Alien, L. H. (1985). Crop responses to elevated CO2 concentrations. In B. R. Strain and J. D. Cure (eds.). Direct Effects of Increasing CO2 on Vegetation. DOE/ER-0238. U.S. Department of Energy. Washington, DC. pp. 53-97.

Akita, S. & Moss, D. N. (1973). Photosynthetic responses to CO2 and light by maize and wheat leaves adjusted for constant stomatal apertures. Crop Science 13:234-237.

Allen, L. H., Jones, P. & Jones, J. W. (1985). Rising atmospheric CO2 and evapotranspiration. In Advances in Evapotranspiration. Proceedings of the National Conference on Advances in Evapotranspiration. December 16-17, 1985. American Society of Agricultural Engineers. St. Joseph, MI. pp. 13-27.

Amthor, J. S. (1989). Respiration and Crop Productivity. Springer-Verlag. New York. 215 pp.

Bauer, A. (1972). Effect of Water Supply and Seasonal Distribution on Spring Wheat Yields. Bulletin 490. North Dakota Agricultural Experiment Station. Fargo, ND.

Bazzaz, F. A. (1990). The response of natural ecosystems to the rising global CO2 levels. Annual Review of Ecology and Systematics 21: 167- 196.

Bulterfield, R. E. & Morison, J. I. L. (1992). Modeling the impact of climatic warming on winter cereal development. Agriculture and Forest Meteorology 62:241-261.

Chaudhuri, U. N., Burnelt, R. B., Kanemasu, E. T. & Kirkham, M. B. (1986). Effect of Elevated Levels of CO2 on Winter Wheat Under Two Moisture Regimes. Response of Vegetation to Carbon Dioxide. 029. U.S. Department of Energy. Washington, DC. 71 pp.

Cure, J. D. & Acock, B. (1986). Crops responses to carbon dioxide doubling: A literature survey. Agriculture and Forest Meteorology 38: 127-145.

Drake, B. G. & Leadley, P. W. (1991). Canopy photosynthesis of crops and native plant communities exposed to long-term elevated CO2. Plant, Cell and Environment 14:853-860.

Ellis, R. H., Hadley, P., Roberts, E. H. & Summerfield, R. J. (1990). Quantitative relations between temperature and crop development and growth. In M. T. Jackson, B. V. Ford-Lloyd, and M. L. Parry. (eds). Climatic Change and Plant Genetic Resources. Belhaven Press. London. pp. 85-115.

Fitter, A. H. & Hay, R. K. M. (1987). Environmental Physiology of Plants. Second Edition. Academic Press. London. 423 pp.

Gates, D. M. (1980). Biophysical Ecology. Springer-Verlag. New York. 611 pp.

Gifford, R. M. & Morison, J. I. L. (1993). Crop responses to the global increase in atmospheric CO2 concentration. In International Crop Science I. Crop Science Society of America. Madison, Wl. pp. 325-331.

Hale, M. G. & Orcutt, D. M. (1987). The Physiology of Plants Under Stress. Wiley. New York. 206 pp.

Hale, M. G. & Orcutt, D. M. (1987). The Physiology of Plants Under Stress. Wiley. New York. 206 pp.

Hall, A. E. & Alien, L. H. (1993). Designing cultivars for the climatic conditions of the next century. In International Crop Science I. Crop Science Society of America. Madison , WI. pp. 291-297.

Hendrey, G. R., (1993). Free-air CO2 Enrichment for Plant Research in the Field. C. K. Smoley. Boca Raton, FL. 308 pp.

Idso, S. B., Kimball, B. A. & Mauney, J. R. (1987). Atmospheric carbon dioxide enrichment effects on cotton midday foliage temperature: Implications for plant water use and crop yield. Agronomy Journal 79:667-672.

IPCC, (2001). Climate Change: Impacts, Adaptation and Vulnerability. Contribution of Working Group II to the Third Assessment Report of Interngovernmental Panel on Climate Change.pp 398-400.

Kapur, B. (2010). Enhanced CO2 and Global Climate Change Effects on Wheat Yield in Çukurova Region. Ph. D. Thesis, Çukurova University, Adana, Turkey (in Turkish).

Kapur, B., Topaloğlu, F., Özfidaner, M. & Koç, M. (2007). Çukurova bölgesinde Küresel İklim Değişikilği ve Buğday Verimliliği Üzerine Etkilerine Genel Bir Bakış. Küresel İklim Değişikliği ve Çevresel Etkiler Konferansı, 18-20 Ekim, 2007. Konya Büyükşehir Belediyesi, Bildiriler Kitabı, Konya, s. 35-45.

Karaca, M., Deniz A. & Tayanc, M. (2000). Cyclone Track Variability over Turkey in Association with Regional Climate, Int. J. of Climatology, No: 20.

Kimball, B. A. & Idso, S. B. (1983). Increasing atmospheric CO2: Effects on crop yield, water use, and climate. Agricultural Water Management 7:55-72.

Kimball, B. A. (1983). Carbon dioxide and agricultural yield: An assemblage and analysis of 430 prior observations. Agronomy Journal 75:779-788.

Kramer, P. J. (1983). Water Relations of Plants. Academic Press. San Diego.

Lawlor, D. W. & Mitchell, R. A. C. (1991). The effects of increasing CO2 on crop photosynthesis and productivity: A review of field studies. Plant, Cell and Environment 14:807-818.

Lawlor, D. W. & Mitchell, R. A. C. (2000). Crop Ecosystem Responses to Climate Change: Wheat. In: Reddy, K.R., Hodges, H.F. (eds), Climate Change and Global Crop Productivity. CABI Publishing, Cab International, Wallingford, UK, 57-80 pp.

Lemon, E. R., (1983). CO2 and Plants: The Response of Plants to Rising Levels of Atmospheric Carbon Dioxide. Westview Press. Boulder, CO. 280 pp.

Mearns, L. O., Rosenzweig, C. & Goldberg, R. (1992). Effect of changes in interannual climatic variability on CERES-Wheat yields: Sensitivity and 2xCO2 general circulation model studies. Agricultural and Forest Meteorology 62: 159-189.

Monteith, J. L. (1981). Climatic variation and the growth of crops. Quarterly Journal of the Royal Meteorological Society 107:749-774.

Morison, J. I. L. (1985). Sensitivity of stomata and water use efficiency to high CO2. Plant, Cell and Environment 8:467-474.

NOAA. (2022). National Centers for Environmental Information, State of the Climate: Monthly Global Climate Report for 2021, published online January 2022, retrieved on September 22, 2022 from https://www.ncei.noaa.gov/access/monitoring/monthly-report/global/202113/supplemental/page-3.

OECD/FAO, (2021). OECD-FAO Agricultural Outlook 2021-2030, OECD Publishing, Paris, https://doi.org/10.1787/19428846-en.

Paulsen, G. M. (1994). High temperature responses of crop plants. In K. J. Boote, J. M. Bennett, T. R. Sinelair, and G. M Paulsen (eds.). Physiology and Determination of Crop Yield. American Society of Agronomy. Madison, Wl. pp. 365-389.

Pisek, A., Larcher, W., Vegis, A. & Napp-Zinn, K. (1973). The Normal Temperature Range. In: Temperature and Life. Springer, Berlin, Heidelberg. https://doi.org/10.1007/978-3-642-65708-5_4

Poorter, H. (1993). Interspecific variation in the growth response of plants to an elevated ambient CO2 concentration. Vegetation 104/105:77-97.

Reddy, K. R., & Hodges, H. (2000). Climate Change and Global Crop Productivity. Wallingford: CABI. https://doi.org/10.1079/9780851994390.0007

Rosenzweig, C. (1990). Crop response to climate change in the Southern Great Plains: A simulation study. Professional Geographer 42:20-37.

Rosenzweig, C. & Tubiello, F. N. (1996). Effects of changes in minimum and maximum temperature on wheat yields in the central U.S.: A simulation study. Agricultural and Forest Meteorology 80:215-230.

Rosenzweig, C. (1985). Potential CO2-induced climate effects on North American wheat producing regions. Climatic Change 7:367-389.

Rosenzweig, C., & Hillel, D. (1998). Climate Change and the Global Harvest: Potential Impacts of the Greenhouse Effect on Agriculture. Oxford University Press. New York, N.Y.

Rosenzweig, C., & Hillel, D. (1998). Climate Change and the Global Harvest: Potential Impacts of the Greenhouse Effect on Agriculture. Oxford University Press. New York, N.Y.

Shibles, R. M., Anderson, I. C. & Gibson., A. H. (1975). Soybean. In L. T. Evans (ed.). Crop Physiology. Cambridge University Press. London. pp. 151-189.

Stitt, M. (1991). Rising CO2 levels and their potential significance for carbon flow in photosynthetic cells. Plant, Cell and Environment 14:741-762.

Türkeş, M., Sümer, U. M. & Çetiner, G. (2000). 'Küresel iklim değişikliği ve olası etkileri', Çevre Bakanlığı, Birleşmiş Milletler İklim Değişikliği Çerçeve Sözleşmesi Seminer Notları (13 Nisan 2000, İstanbul Sanayi Odası), 7-24, ÇKÖK Gn. Md., Ankara.

WorldData, (2022). The Climate in Turkey. https://www.worlddata.info/asia/turkey/climate.php (Erişim: Ekim, 2022)

Petrographıc Features Of The Upper Trıassıc-Lower Jurassıc Kızılören Formatıon Dolostones (Konya Northwest, Türkiye)

Ali Müjdat Özkan[1]
Levent Kenan Kibar[2]

Introduction

The study area covers Ardıçlı District and its surroundings, located in the northwest of Konya province. Previous studies were mainly stratigraphic and mineral exploration, and the Kızılören Formation dolostones were not studied in detail. Özkan and Kibar (2015) studied the Kızılören Formation carbonates in detail (sedimentological and geochemical) in the study area. In this study, the petrographic features of Kızılören dolostones were studied in detail. In the study, thin sections were carried out under a polarizing microscope for all samples and a scanning electron microscope was performed for some samples. Alizarin red-s test was applied to separate dolomite and calcite minerals on thin sections of dolostone. Thus, the mineralogical compositions, textural properties, and depositional environments of the dolostones were determined.

In accordance with the purpose of the study, 3 measured stratigraphic sections were measured from the Kızılören Formation, samples were collected from appropriate levels and the measured sections were correlated (Özkan and Kibar, 2015).

According to the petrographic characteristics of the Kızılören Formation dolomites: (1) unimodal, very fine to fine crystalline planar-s (subhedral) mosaic dolomite, (2) medium to coarse crystalline planar-e (euhedral) mosaic dolomite, (3) medium crystalline planar-e (euhedral) replaced dolomite, (4) unimodal, medium to coarse crystalline non-planar-s-a (subhedral-anhedral) mosaic dolomite, (5) fine-crystalline planar-e-s (euhedral-subhedral) mosaic dolomite, (6) polymodal planar-e-s (euhedral-subhedral) mosaic dolomite, (7) coarse-very coarse crystalline non-planar-c (cement) saddle dolomite and (8) defined as microbrecciated dolomite (Özkan and Kibar, 2015).

Results

Petrographic Properties of the Samples Taken from Karagüneytepe Measured Stratigraphic Section (A)

The Kızılören carbonates at Karagüney Tepe start with dolomitic limestone at the bottom, continue as limestone-dolostone alternation in the middle sections and continue as dolostone towards the top after the dolomitic limestone, and end with limestone at the top. Considering the microscopic properties of the samples taken from the Karagüneytepe measured stratigraphic

section, it was observed that they were dolomitic limestone, limestone (mudstone), dolomicsparite, dolosparite, and crystalline limestone according to Dunham's (1962) classification (Table 1).

Table1. Microscopic properties of samples taken from Karagüneytepe measured stratigraphic section

Sample	Calcite content%	Dolomite content %	Allochems				Orthochems		Name of the rock (Dunham,1962)
			Fossil %	Intraclast %	Ooid %	Pellet %	Sparite %	Micrite %	
A-1	82	18	10	5	-	7	25	53	dolomitic limestone
A-5	85	15	5	-	-	-	10	85	dolomitic limestone
A-9	92	8	9	-	-	-	7	84	limestone
A-20	94	6	7	5	-	-	15	73	limestone
A-25	80	20	-	-	-	-	100	0	dolomitic limestone
A-33	5	95	-	-	-	-	50	50	dolomicsparite
A-41	91	9	-	-	-	-	0	100	mudstone
A-57	8	92	-	-	-	-	90	10	dolomicsparite
A-67	95	5	-	-	-	-	-	100	mudstone
A-85	82	18	-	-	-	-	2	98	dolomitic limestone
A-120	7	93	-	-	-	-	100	0	Dolosparite
A-160	91	9	-	-	-	-	100	0	crystalline limestone

In thin sections, idiotopic, hibidiotopic, and xenotopic textured dolomite crystals are observed in the form of euhedral-subhedral and anhedral grains in sizes varying from micro to coarse (Table 2).

Table 2. Textural properties of samples taken from Karagüneytepe measured stratigraphic section

Sample	Calcite content%	Dolomite content %	Primary texture preservation rate	Dolomite Crystal					Texture
				Size	Sorting	Shape			
						Eu	Su	Xe	
A-1	82	18	Mimetic	fine	good	yes	yes	yes	xenotopic
A-5	85	15	Mimetic	fine	good	-	-	yes	xenotopic
A-9	92	8	Mimetic	fine	good	-	-	yes	xenotopic
A-20	94	6	Mimetic	fine	good	-	-	yes	xenotopic
A-25	80	20	non-mimetic	fine	good	yes	yes	yes	subhedral
A-33	5	95	Mimetic	fine - coarse	kötü	yes	-	yes	euhedral
A-41	91	9	Mimetic	fine	good	yes	-	yes	xenotopic
A-57	8	92	Mimetic	fine - coarse	poor	yes	yes	yes	subhedral
A-67	95	5	Mimetic	fine - coarse	poor	-	yes	yes	xenotopic
A-85	82	18	Mimetic	fine	good	-	-	yes	xenotopic
A-120	7	93	non-mimetic	fine-medium	good	yes	yes	-	euhedral
A-160	91	9	non-mimetic	fine	good	yes	yes	-	subhedral

Eu: euhedral, Su: subhedral, Xe: xenotopic

As a result of petrographic examinations, it was observed that they were in the form of fine to very fine crystalline dolomite (Figure 1a), calcite-cemented brecciated dolomites (Figure 1b), fine-to-coarse crystalline (polymodal, Figure 2a) dirty, euhedral and subhedral dolomite rhombs, medium-crystalline, euhedral replaced dolomite (Figure 2b), subhedral, fine-to-very fine-crystalline dolomites (Figure 3a), subhedral-xenotopic, medium-coarse crystalline and mostly in the form of dirty dolomites (Figure 3b), fine crystalline dolomitic limestone (Figure 4a) and crystalline limestone (Figure 4b).
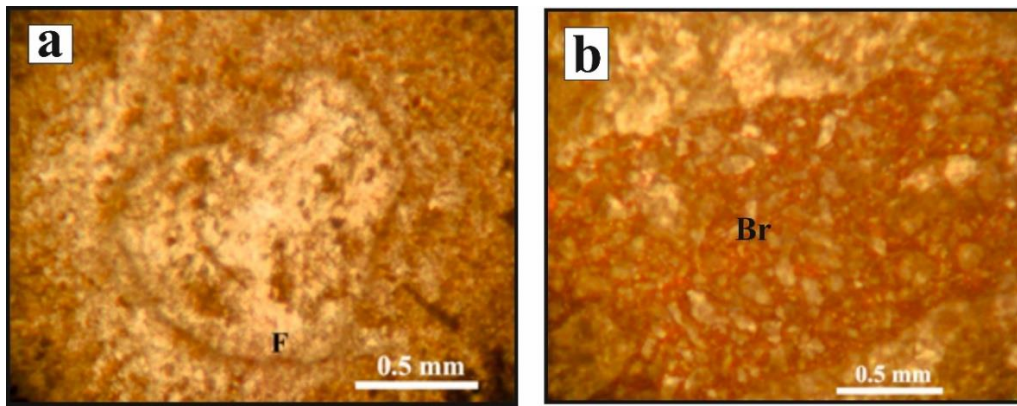
Figure 1. a) Very fine to fine crystalline, subhedral mosaic dolomite (df-1), fossiliferous dolomitic limestone. F: fossil (PPL, Sa:A-1; dolomitic limestone), b) Calcite-cemented brecciated (Br) dolomite (df-8) and dolomicsparite (df-1) (PPL, Sa: A-57 dolomite)
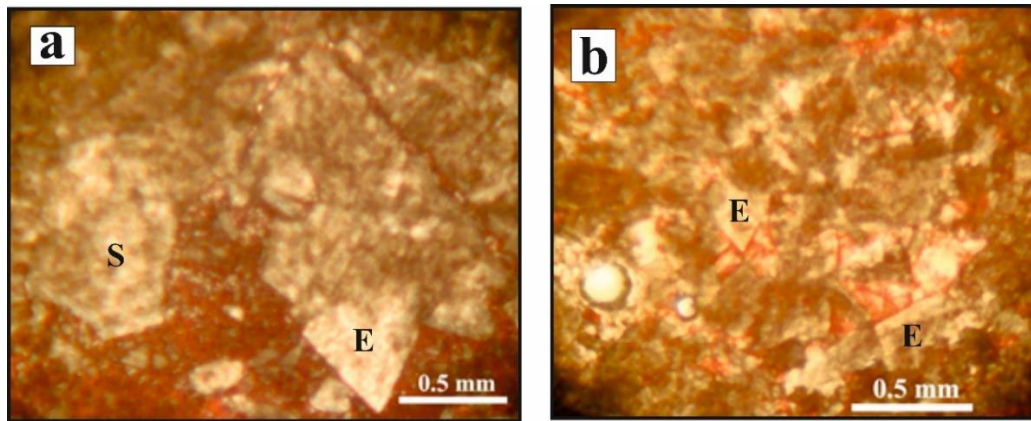
Figure 2. a) Thin-coarse crystalline (polymodal; df-6), euhedral (E) and subhedral (S) dolomite rhomboids (PPL, Sa: A-57 dolomite), b) Medium-crystalline (df-3), euhedral dolomite rhombs (PPL, Sa: A-33; dolomite)
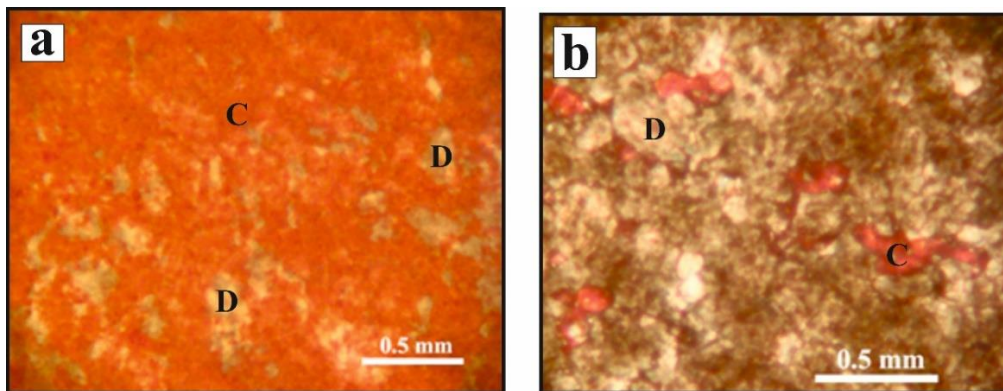
Figure 3. a) Fine-crystalline (df-1), xenotopic dolomite (PPL, Sa: A-85; dolomitic limestone) b) Subhedral-xenotopic, medium-coarse crystalline (df-4) and mostly dirty dolomite (PPL, Nu: A-120; dolomite), C: calcite, D: dolomite
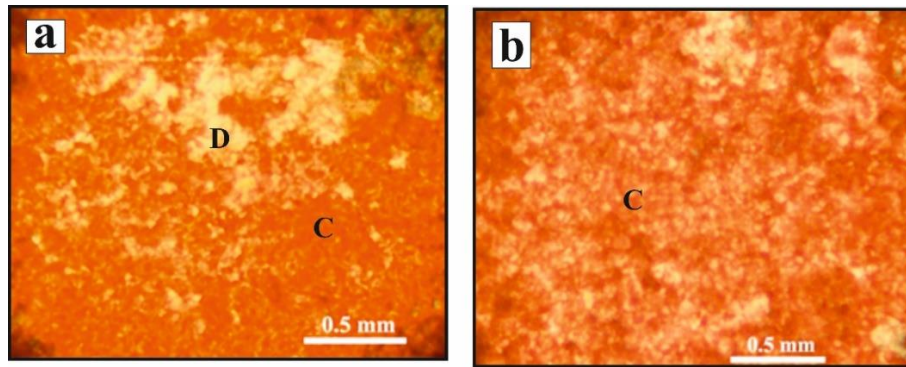
Figure 4. a) Fine crystalline dolomitic limestone (PPL, Sa: A-160; limestone), b) Crystalline limestone (PPL, Sa: A-160; limestone), C: calcite, D: dolomite

As a result of the SEM (scanning electron microscope) examination made from a sample (A-33) taken from the Karagüneytepe measured stratigraphic section, fine-medium crystalline subhedral dolomite crystals, and the EDX diagram is seen (Figures 5 and 6).
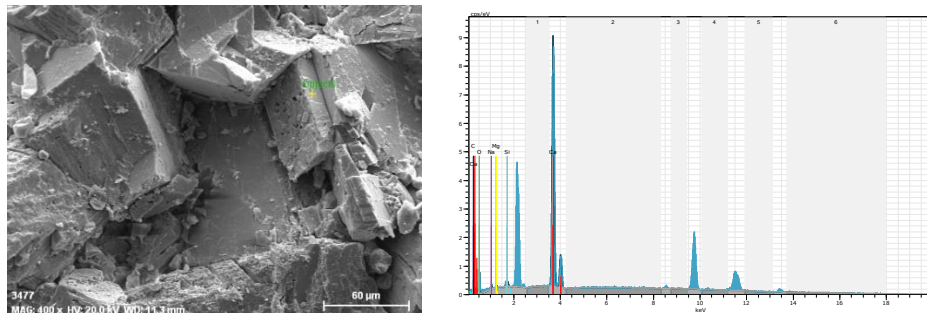
Figure 5. Fine-medium-crystalline, euhedral, subhedral dolomite crystals, intracrystalline and intercrystalline porosity (SEM) and energy dispersion X-Ray spectra (EDX)

Figure 6. Fine-crystalline, euhedral dolomite crystals, intracrystalline and intercrystalline porosity (SEM), and energy dispersion X-Ray spectra (EDX)

Petrographic Properties of the Samples Taken from the Doğudağ Measured Stratigraphic Section (B)

The carbonates in the Doğudağ measured stratigraphy section begin with dolostone at the base, contain intercalations of calcitic dolomite upwards, and end with dolostones. Fossils (5-25%) are observed in some dolostones and calcite dolomites, and there are 0-90% micrite and 10-100% sparite in the dolostones (Table 3).

In thin sections, euhedral, subhedral, and anhedral dolomite crystals of varying sizes from micro to large are observed (Table 4).

Table 3. Microscopic properties of samples taken from Doğudağ measured stratigraphic section (B)

| Sample | Calcite content % | Dolomite content % | Allochems | | | | Orthochems | | Name of the rock (Dunham,1962) |
			Fossil %	İntraclast %	Ooid %	Pellet %	Sparite %	Micrite %	
B-1	3	97	25	-	-	-	100	0	dolosparite
B-15	2	98	5	-	-	-	55	40	dolomicsparite
B-33	1	99	15	3	-	5	17	60	dolomicsparite
B-60	4	96	-	-	-	-	10	90	dolomicsparite
B-80	35	65	14	-	-	-	86	0	calcitic dolomite
B-100	3	97	-	-	-	-	85	15	dolomicsparite
B-120	2	98	-	-	-	-	80	20	dolomicsparite
B-160	2	98	-	-	-	-	65	35	dolomicsparite
B-195	2	98	-	-	-	-	55	45	dolomicsparite
B-235	45	55	-	4	-	2	84	10	calcitic dolomite
B-257	6	94	-	14	-	-	60	26	dolomicsparite
B-300	8	92	-	15	-	-	70	15	dolomicsparite

Table 4. Textural properties of samples taken from Doğudağ measured stratigraphic section (B)

| Sample | Calcite content % | Dolomite content % | Primary texture preservation rate | Dolomite Crystal | | | | | Texture |
| | | | | Size | Sorting | Shape | | | |
						Eu	Su	Xe	
B-1	3	97	non-mimetic	fine-coarse	kötü	yes	yes	-	euhedral
B-15	2	98	mimetic	fine-medium	good	yes	yes	yes	Subhedral
B-33	1	99	mimetic	fine-medium	good	yes	yes	yes	Subhedral
B-60	4	96	mimetic	fine	good	yes	yes	yes	xenotopic
B-80	35	65	non-mimetic	fine-medium	good	yes	yes	-	Subhedral
B-100	3	97	mimetic	fine-medium	good	yes	yes	yes	Subhedral
B-120	2	98	mimetic	fine-medium	good	yes	yes	yes	Subhedral
B-160	2	98	mimetic	fine-medium	good	yes	yes	yes	Subhedral
B-195	2	98	mimetic	fine-medium	good	yes	yes	yes	Subhedral
B-235	45	55	mimetic	fine-coarse	poor	yes	-	-	euhedral
B-257	6	94	mimetic	fine	good	yes	yes	yes	Subhedral
B-300	8	92	mimetic	fine-coarse	poor	yes	yes	yes	Subhedral

Eu: euhedral, Su: subhedral, Xe: xenotopic

As a result of the petrographic examination of the samples, it was observed that they were in the form of rhomboids of medium to coarse crystalline (df-2) euhedral dolomite (Figure 7a), dolomicsparitic (polymodal; df-6) dolomite (Figure 7b), fine crystalline (df-1) dolomicsparite (Figure 8a), fine crystalline (df-1) calcitic dolomite (Figure 8b), fine-crystalline (df-1) dolomicsparite and replacement with iron oxide (Figure 9a), dedolomitization in dolosparites (Figure 9b), intraclastic dolomite and calcite cement (Figure 10a), fine-crystalline (Figure 9a) df-1)

dolomicsparite with calcite veins and partially replaced by dolomite (10b), medium to coarse crystalline (df-2) euhedral, zoned dolomite rhomboids (Figure 11a) and fossiliferous dolomicsparite (11b; df-1).
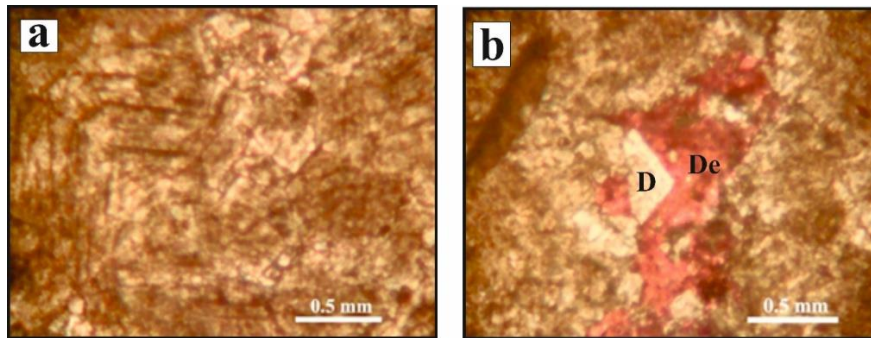
Figure 7. a) Euhedral, medium-coarse crystalline (df-2), dirty dolomite rhombs (PPL, Sa: B-1; dolomite), b) Euhedral-subhedral, polymodal (df-6) dolomite crystals and dedolomite (PPL, Sa: B-15; dolomite), D: dolomite, De: dedolomite
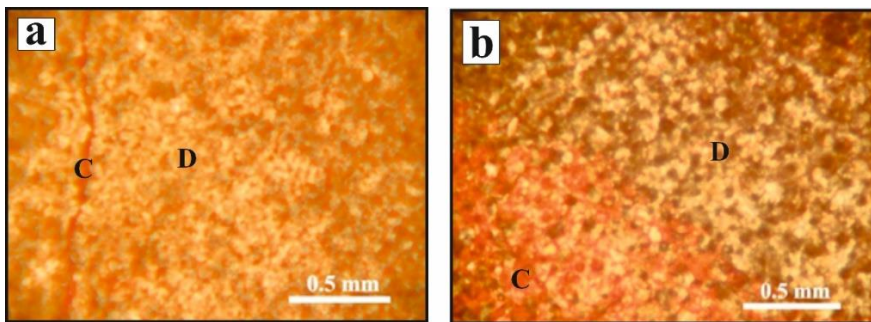
Figure 8. a) Fine-crystalline (df-1) dolomicsparite and calcitic vein (PPL, Sa: B-60; dolomite) b) Fine-crystalline (df-1) calcitic dolomite (PPL, Sa:B-80; calcitic dolomite), C: calcite, D: dolomite
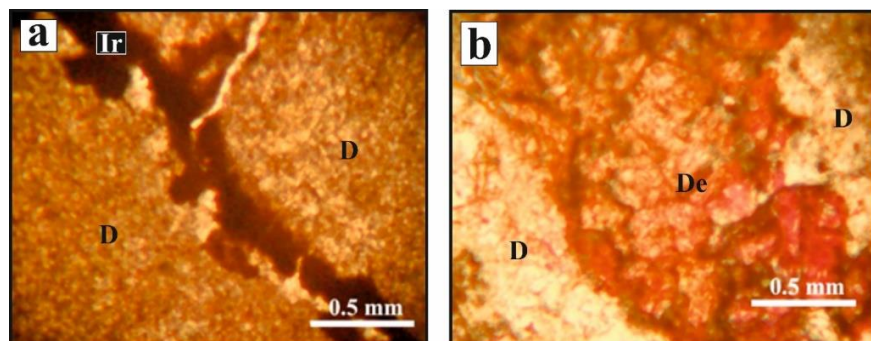
Figure 9. a) Replacement by fine crystalline (df-1) dolomicsparite and iron oxide. (PPL, Sa: B-100; dolomite), b) Dedolomitization in dolomicsparite (PPL, Sa: B-160; dolomite), D: dolomite, De: dedolomite, Ir: iron oxide
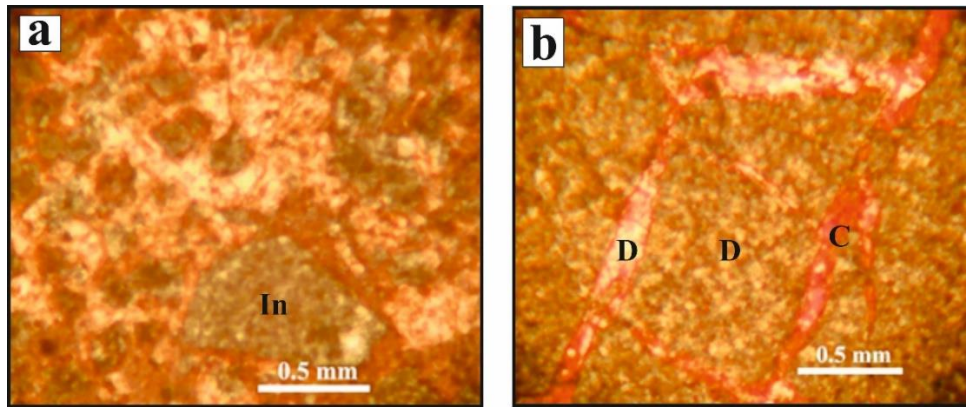
Figure 10. a) Intraclastic dolomite and calcite cement (PPL, Sa: B-235; calcitic dolomite), b) Calcite vein in fine crystalline (df-1) dolomicsparite and partially replaced by dolomite (PPL, Sa: B-257; dolomite), D: dolomite, C: calcite, In: intraclast
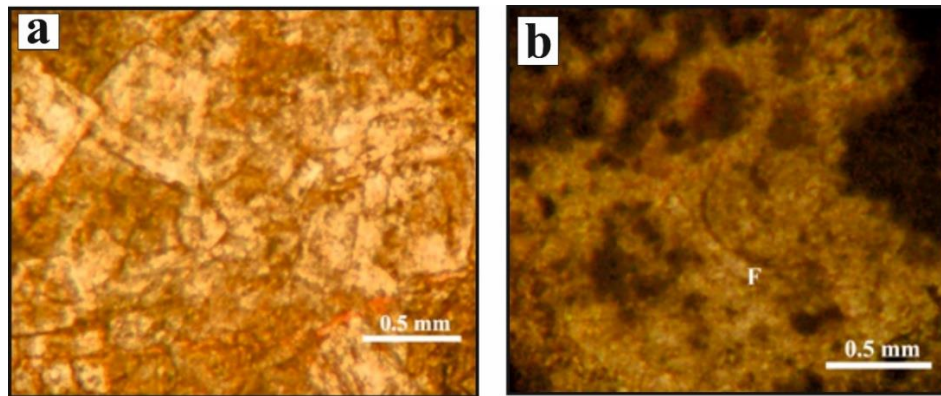
Figure 11. a) Medium-coarse crystalline (df-2), euhedral, zoned dolomite rhombs (PPL, Sa: B-300; dolomite), b) Fine-crystalline (df-1), fossiliferous dolomicsparite. F: fossil (XPL, Sa: B-33; dolomite)

As a result of the SEM (scanning electron microscope) examination of two samples (B-1, B-120) taken from the Doğudağ measured stratigraphic section, fine crystalline, subhedral (Figure 12), and euhedral (Figure 13) dolomite crystals and EDX diagram are seen.
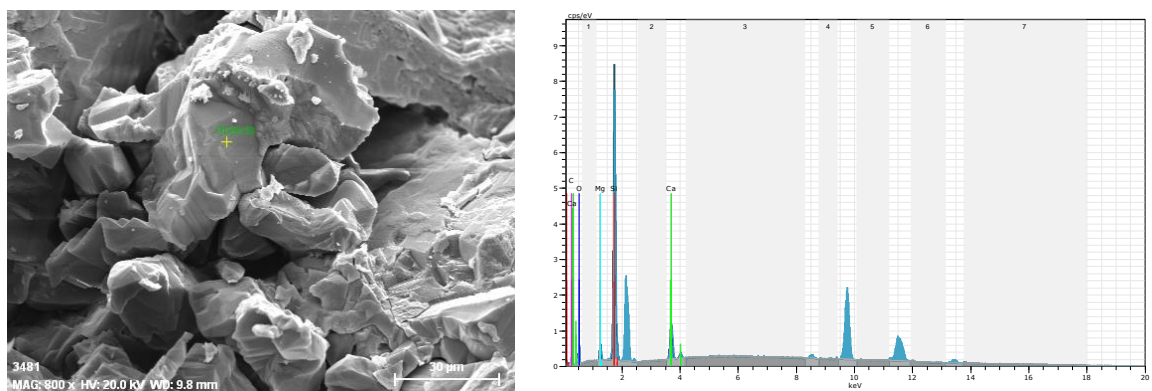
Figure 12. Fine-crystalline, subhedral dolomite crystals, intercrystalline porosity (SEM), and energy dispersion X-Ray spectra (EDX; B-1)

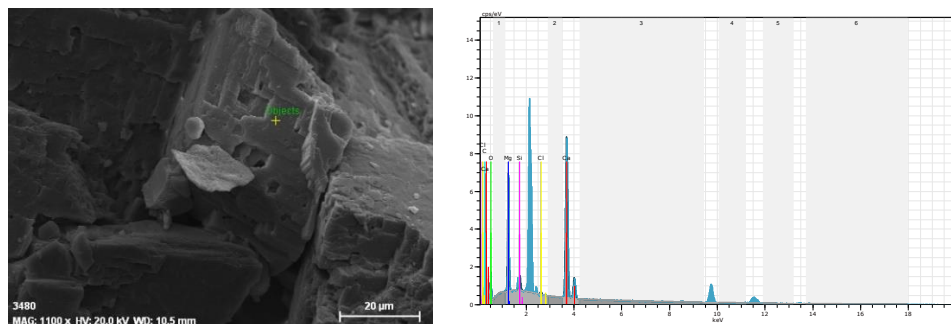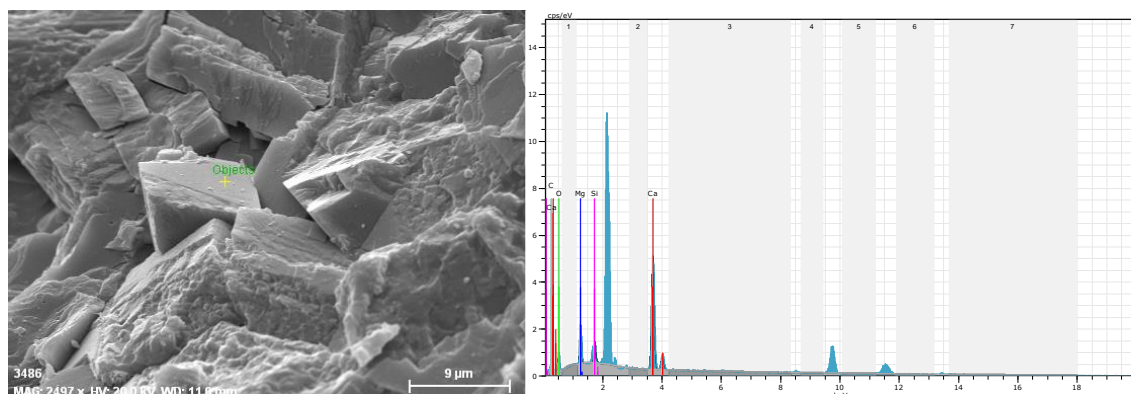*Figure 13. Fine-crystalline, euhedral dolomite crystals, intercrystalline porosity (SEM), and energy dispersion X-Ray spectra (EDX; B-120)*

Petrographic Properties of the Samples Taken from the Sarıbayırsırtı Measured Stratigraphy Section (C)

The carbonates in the Sarıbayırsırtı measured stratigraphic section (C) start with dolostone at the base, continue with dolomitic limestone interbedded limestone in the middle sections, and end with dolostone at the top, after the alternation of calcitic dolomite-dolostone (Table 5). Thin-crystalline, subhedral and anhedral dolomite crystals with hibidiotopic and xenotopic textures are observed in thin sections (Table 6).

Table 5. Microscopic properties of samples taken from Sarıbayırsırtı measured stratigraphic section (C)

| Sample | Calcite content % | Dolomite content % | Allochems | | | | Orthochems | | Name of the rock (Dunham,1962) |
			Fossil %	İntraclast %	Ooid %	Pellet %	Sparite %	Micrite %	
C-7	9	91	10	8	-	-	60	22	dolomicsparite
C-17	25	75	-	-	-	-	85	15	calcitic dolomite
C-25	6	94	-	15	-	-	50	35	dolomicsparite
C-30	9	91	-	10	-	-	60	30	dolomicsparite
C-39	45	55	5	-	-	-	100	0	calcitic dolomite
C-50	100	0	8	-	-	-	44	48	mudstone
C-56	93	7	7	-	-	-	46	47	mudstone
C-62	60	40	-	-	-	-	85	15	dolomitic limestone
C-67	94	6	-	-	-	-	100	0	crystalline limestone
C-73	92	8	-	-	-	-	100	0	crystalline limestone
C-87	9	91	-	-	-	-	100	0	dolosparite
C-109	8	92	8	-	-	-	100	0	dolosparite

Table 6. Textural properties of samples taken from Sarıbayırsırtı measured stratigraphic section (C)

Sample	Calcite content %	Dolomite content %	Primary texture preservation rate	Dolomite Crystal					Texture
				Size	Sorting	Shape			
						Eu	Su	Xe	
C-7	9	91	mimetic	fine	good	yes	yes	yes	subhedral
C-17	25	75	mimetic	fine	good	yes	yes	yes	subhedral
C-25	6	94	mimetic	fine-coarse	poor	yes	yes	yes	subhedral
C-30	9	91	mimetic	fine-coarse	poor	yes	yes	yes	subhedral
C-39	45	55	non-mimetic	fine	good	yes	yes	-	subhedral
C-50	100	0	mimetic	fine	good	-	-	-	xenotopic
C-56	93	7	mimetic	fine	good	-	yes	yes	xenotopic
C-62	60	40	mimetic	fine	good	-	yes	yes	subhedral
C-67	94	6	non-mimetic	fine	good	-	yes	-	subhedral
C-73	92	8	non-mimetic	fine	good	-	yes	-	subhedral
C-87	9	91	non-mimetic	fine	good	yes	yes	-	subhedral
C-109	8	92	non-mimetic	fine	good	yes	yes	-	subhedral

Eu: euhedral, Su: subhedral, Xe: xenotopic

As a result of the petrographic examination, it was observed that they were in the form of dolomicsparite (Fig. 14a; df-1), calcitic dolomite (Fig. 14b), dolomitic limestone (Fig. 15a), euhedral-subhedral, fine-crystalline (df-5) sugary dolosparite and dedolomite (Fig. 15b, 16a), dolomitic limestone (Fig. 16b), euhedral-subhedral, fine-crystalline (df-5) dolomite crystals-dolomicrite, calcite fossil and void fill calcite cement (Figure 17a) and coarse-very coarse crystalline (df-7) saddle (cement) dolomite (Fig. 17b).
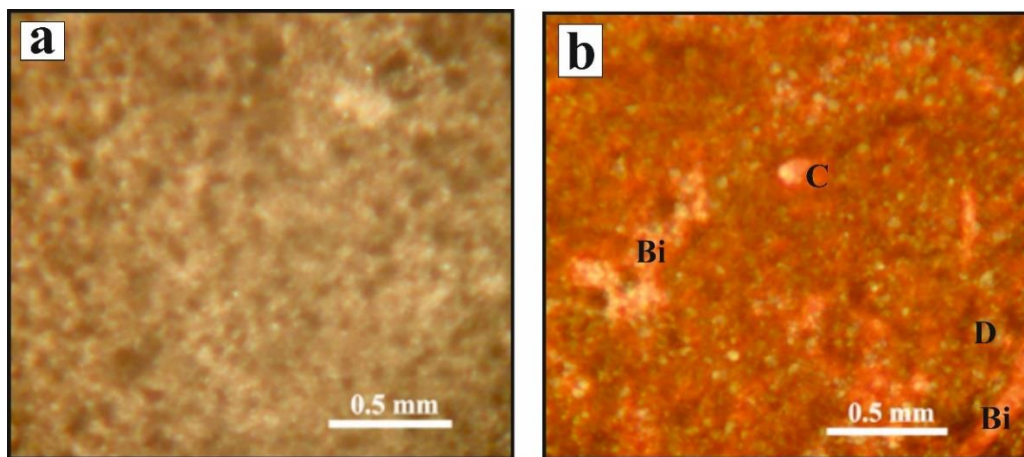
Figure 14. a) Fine to very fine crystalline (df-1), Dolomicsparite (PPL, Sa: C-7; dolomite), b) Bioclast, fine crystalline (df-1) dolomicsparite and calcite cement (PPL, Sa: C -7; dolomite), C: calcite, D: dolomite, Bi: bioclast
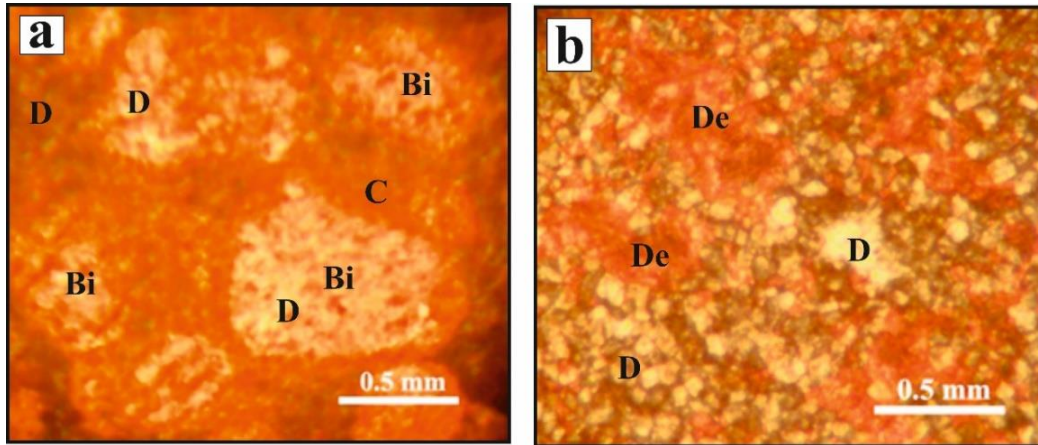
Figure 15. a) Bioclasted, calcite-cemented dolomicsparite (df-1, PPL, Sa: C-7; dolomite), b) Euhedral-subhedral, fine-crystalline (df-5) dolosparite and dedolomite (PPL, Sa: C-39) ; calcitic dolomite), C: calcite, D: dolomite, De: dedolomite, Bi: bioclast
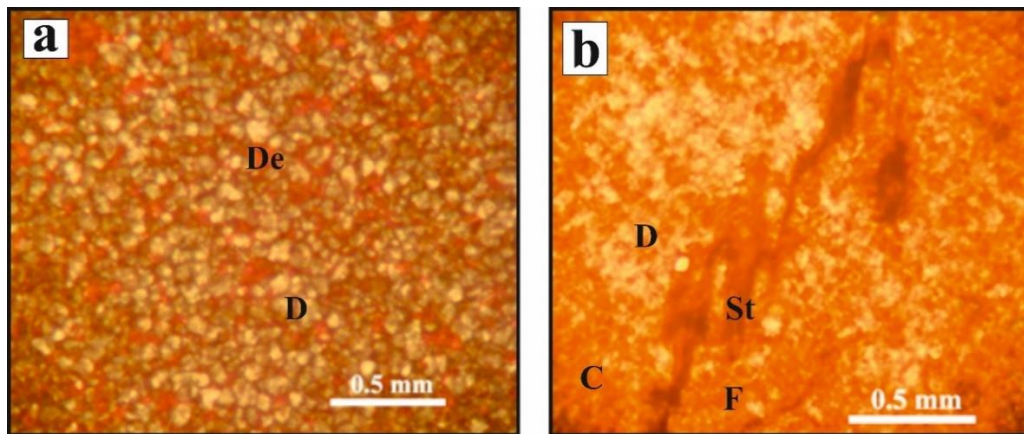
Figure 16. a) Euhedral to subhedral, fine crystalline (df-5) suggary dolosparite and dedolomite (PPL, Sa: C-39; calcitic dolomite), b) Sparicalcite, fossil (F), stylolite, and dolomite crystals (PPL, Sa: C-67; limestone),), C: calcite, D: dolomite, De: dedolomite, St: stylolite
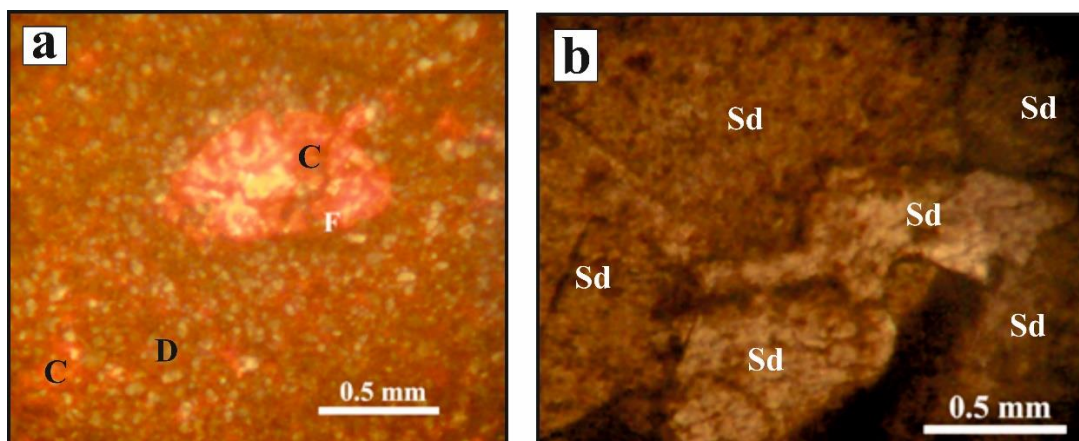
Figure 17. a) Euhedral-subhedral, fine-crystalline (df-5) dolomite crystals-dolomicrite, calcite fossil, and void-filling calcite cement, (PPL, Sa: C-109; dolomite) F: fossil, b) Coarse–very coarse crystalline (df-7), (nonplanar-c) saddle dolomite cement. (PPL, Sa: C-25; dolomite), C: calcite cement, D: dolomite, Sd: saddle dolomite

Discussion

Unimodal, very fine to fine crystalline planar-s (subhedral) dolomites (df-1); small crystal sizes (<60 µm) indicate limited subtidal to supratidal environments (Amthor and Friedman, 1991). It may develop by early replacement of fine crystalline early diagenetic dolomite or concurrent neomorphic or original peritidal carbonate mudstones (Zenger, 1983; Amthor and Friedman, 1991). Crystal size is controlled by the ratio relationship of the two functions; nucleation and growth rate (Spry, 1969; Amthor and Friedman, 1991). Dolomite often selectively replaces fine crystalline $CaCO_3$ (Murray and Lucia, 1967; Sibley et al., 1987; Amthor and Friedman, 1991). The fine particles have a very large surface area compared to their volume and therefore the nucleation rate is fast. If the nucleation rate is high compared to the growth rate, the resulting crystal size will be small (Amthor and Friedman, 1991). This can be explained, among others, by selective dolomitization of finer crystalline calcium carbonate and early dolomitization of subtidal and supratidal carbonate muds (Amthor and Friedman 1991). We can emphasize that the fine crystalline dolomites in the Kızılören Formation were formed by early diagenetic replacement of carbonates in tidal and subtidal environments.

Medium to coarse crystalline planar-e (euhedral) mosaic dolomites (df-2); are often presented as evidence of pre-dolomitization texture. Because the crystal size in individual mosaics is unimodal and it can be stated that the nucleation sites for dolomite are homogeneously distributed (Sibley, 1982; Schofield, 1984; Amthor and Friedman, 1991). The fact that the dolomite crystals show the sharing of reconciled boundaries indicates that they are formed in situ. They develop simultaneously to form congruent crystal boundaries and the development of planar-e mosaics is achieved by the combined growth of zones in adjacent crystals (Schofield, 1984; Amthor and Friedman, 1991). The absence of intracrystalline chipping features, continuity, and zones of equal width indicate the continued development of the crystals. We can say that the medium-coarse crystalline planar-e (euhedral) mosaic dolomites (df-2) of the Kızılören Formation developed simultaneously and in situ.

Medium-crystalline planar-e (euhedral) replaced dolomites (df-3); dirty core and clean margin texture can be observed widely in rocks of all ages (Sibley, 1982; Amthor and Friedman, 1991). Intercrystalline chipping in dolomite rhombs indicates dissolution after dolomitization. Late diagenetic crack-filled dolomites are formed at high temperatures (burial origin). The crack fillings that cut the dolomite rhombs in the mid-crystalline euhedral replacement dolomites of the late diagenetic phase indicate a high temperature (burial origin) formation. The euhedral form of dolomite rhombs suggests formation at temperatures below 50–100°C (approximately critical temperature), since higher temperatures develop anhedral forms (Sibley and Gregg, 1987; Ramadan, 2014). Also, planar dolomite crystals may form along chemical compaction dissolution wrinkles. We can state that the medium crystalline planar-e (euhedral) replaced dolomites (df-3) of the Kızılören Formation are of late diagenetic burial origin.

Unimodal, medium to coarse crystalline non-planar-s-a (subhedral-anhedral) replaced dolomites (df-4); it develops as a replacement for the original limestone or dolostone. This type of replacement usually completely destroys the original depositional tissues (Amthor and Friedman, 1991). This type of dolomite corresponds to the xenotopic-a dolomite described by Gregg and Sibley (1984) and Sibley and Gregg (1987) (Ramadan, 2014). They propose that the xenotopic dolomite texture results from the neomorphic recrystallization of pre-existing dolomite or the replacement of limestone at high temperatures. Folk (1959) described non-planar-a dolomite as the replacement of the original limestone in the burial setting. Such a replacement can occur only in certain zones and originally had high porosity and permeability. This coarse non-planar dolomite cement is generally called saddle dolomite (Radke and Mathis, 1980; Amthor and Friedman, 1991).

It has been emphasized that almost all of these dolomites consist of high temperatures (60-150°C; Radke and Mathis, 1980) and high salinity basinal waters (Ramadan, 2014). No conclusive evidence of saddle dolomite formation at low temperatures from marine or hyposaline waters has been demonstrated so far (Amthor and Friedman, 1991; Ramadan, 2014). We can say that the unimodal, medium to coarse crystalline non-planar-s-a (subhedral-anhedral) replacement dolomites (df-4) in the Kızılören Formation developed in a high-temperature burial environment.

Fine-medium crystalline planar-e-s (euhedral-subhedral) mosaic dolomites (df-5); fine crystalline matrix dolomite usually develops as a fabric destroyer (Lonnee, 1999). At this stage, the micritic matrix and fossil components in the mud-supported sediments are replaced. The fine crystalline matrix dolomite was restricted to formation after the initial chemical compaction but formed approximately simultaneously with the medium crystalline matrix dolomite. The mid-crystalline matrix dolomite in the Kızılören Formation developed as fabric-destructive replaced dolomite.

Polymodal planar-e-s (euhedral-subhedral) mosaic dolomites (df-6); are formed by mimetic and non-mimetic replacement of fossils and unimodal matrix (Sibley and Gregg, 1987). If the dolomitization solution is slightly less supersaturated with respect to dolomite, the matrix may become dolomitized but the fossils may remain undolomitized (Sibley and Gregg, 1987). The fossils remain undolomitized because at less saturation very few dolomite cores are formed on very coarse calcite. If these fossils remain as calcite, the resulting rock will be in the form of unimodal, planar-s dolomite with unreplaced allochemes (Sibley and Gregg, 1987). If allochemes are resistant to dolomitization, they then dolomitize above the critical temperature or critical saturation, and the resulting texture may be polymodal with non-planar dolomite, non-mimetic replacement allochemes, and planar-s matrix (Sibley and Gregg, 1987). Another possibility is that non-replaced fossils will dissolve leaving patterns either during or after dolomitization (Sibley and Gregg, 1987). If the non-dolomitized matrix and allochemes dissolve, the resulting dolomite will be unimodal, planar-e dolomite. This form of dolomite is commonly referred to as sugary. It may develop similarly to the situation described by Sibley and Gregg (1987), but the dolomite may continue to evolve until the void is completely filled, resulting in unimodal, planar-s dolomite (Sibley and Gregg, 1987; Ramadan, 2014). We can say that the Kızılören Formation was formed by the mimetic replacement of the original limestones in the polymodal planar-e-s (euhedral-subhedral) mosaic dolomites (df-6).

Coarse–very large anhedral cement dolomites (df-7) are generally referred to as saddle dolomite (Radke and Mathis, 1980). Almost all of these dolomites have been interpreted as formed by brines at elevated temperatures (60–150°C; Radke and Mathis, 1980) and high salinity (Amthor and Friedman, 1991). Saddle dolomites, for which conclusive evidence has not been provided so far, may form in hyposaline water, or at lower temperatures than seawater (Radke and Mathis, 1980; Machel, 1987). In this lack of evidence, anhedral cement dolomite has also been interpreted as being formed at higher salinities than seawater and elevated temperatures from brine (Amthor and Friedman, 1991). It is thought that the saddle dolomites observed in the Kızılören Formation dolomites are formed from basinal saline waters at elevated temperatures with medium-deep burial.

Microbrecciated dolomites (df-8); the time of formation of fractures and cracks reflect the state of the rock or sediment while providing evidence of local or regional tectonic events (Boillot et al., 1988). They are helpful in determining relative chronology and can sometimes determine the time, and they may also be important in restoring porosity (Boillot et al., 1988). Fractures and fissures are therefore of great importance in a diagenetic study. The chronological order establishes the relation of the original rock to the petrification state and its relation to the stylolitization. The crack line is used to distinguish two types of cracks: (1) zig-zag cracks with jagged or irregular edges

without specific geometries, (2) roughly linear cracks with zig-zag, smooth, or irregular (on close examination) edges (Boillot et al., 1988). We think that the Kızılören Formation developed as brecciated dolomites within the local and/or regional tectonic fractures in the microbrecciated dolomites (df-8).

The beginning of the stylolitization in the limestones is about 500 m (Dunnington, 1967; Lind, 1993; Duggan 2004). Horizontal stylolites with amplitudes of 10 cm or greater are found, although they are less than 1 cm in most lithofacies. It suggests that the larger amplitude stylolites cut the smaller amplitude stylolites, suggesting that the stylolization in a given lithology occurred during the progressive middle and deep burial (Duggan, 2004). Since the amplitudes of the stylolites observed in the Kızılören Formation dolomites are <1 cm, they suggest shallow-medium burial. The dark coloration observed at the borders of the stylolites was thought to be probably of organic origin.

The characteristics of the Kızılören Formation dolostones suggest formation at low temperatures in the shallow-buried (in-tidal-subtidal) mixed water area in a shallow marine carbonate environment in the early diagenesis, and at high temperatures from altered seawater in the mid-deep burial area in the late diagenesis. Dedolomitization occurred by meteoric water affection in the Kızılören Formation.

REFERENCES

Amthor, J. E. & Friedman, G. M. (1991) Dolomite–rocks textures and secondary porosity development in Ellenburger Group carbonates (Lower Ordovician), west Texas and southeastern New Mexico. *Sedimentology*, *38,* 343-362.

Boillot, G. Comas, M. C. Girardeau, J. Kornprobst, J. Loreau, J. P. Malod, J. Mougenot, D. Moullade, M. (1988) Preliminary results of the Galinaute Cruise: dives of the submersible *Nautile* on the western Galicia Margin, Spain. *Ocean Drilling Program*, 37-51.

Duggan, J. P. (2004) Burial dolomites at Swan Hills Simonette NTEf, West-central Alberta Basin. *Can. Soc. Petrol. Geol.*, *2004 Dolomite Conference*, 29 p.

Dunham, R. J. (1962) Classification of carbonate rocks according to depositional texture. In: classification of carbonate rocks, (ed. W. E. Ham). *Amer. Assoc. Petrol. Geol. Memoir*, *1*, 108-121.

Dunnington, H. V. (1967) Aspects of diagenesis and shape in stylolitic limestone reservoirs. In: origin of oil. *Geology and Geophysics, Proc. Seventh World Petroleum Congres*, *2*, 339-352.

Folk, R. L. (1959) Thin-section examination of pre-simpson Paleozoic rocks. In: stratigraphy of the pre-simpson Paleozoic subsurface rocks of Texas and southeast New Mexico (eds. V. E. Barnes, P. E. Cloud, Jr, L. P. Dixon, R. L. Folk, E. C. Jonas, A. R. Palmer & E. J. Tynan), University of Texas. *Bur. Econ. Geol. Publ.*, *5924*, 95-130.

Gregg, J. M. & Sibley, D. F. (1984) Epigenetic dolomitization and the origin of xenotopic dolomite texture. *Jour. Sedim. Petrol.*, *54*, 908-931.

Lind, I. L. (1993) Stylolites in chalk from leg 130, Ontong Java Plateau. *Proceedings of the Ocean Drilling Program, Scientific Results*, *130*, 445-451.

Lonnee, J. S. (1999) Sedimentology, dolomitization and diagenetic fluid evolution of the Middle Devonian Sulphur Point Formation, northwestern Alberta. *University of Windsor,* MSc. Thesis, p. 133.

Murray R. C. & Lucia, F. J. (1967) Cause and control of dolomite distribution by rocks selectivity. *Bull. Geol. Soci. Amer.*, *78*, 21-35.

Özkan, A. M. & Kibar, L. K. (2015) Konya kuzeybatısındaki Kızılören formasyonundaki (Üst Triyas-Alt Jura) dolomitlerin sedimantolojik ve jeokimyasal incelenmesi. *Selçuk Üni. Fen Bil. Enst.* Yüksek Lisans Tezi, 93 s. (Unpublished)

Radke, B. M. & Mathis, R. L. (1980) On the formation and occurrence of saddle dolomite. *Jour. Sedim. Petrol.*, *50*, 1149-1168.

Ramadan, F. S. (2014) Petrographic and diagenetic characteristics of the dolomites at Um Bogma Formation (Early Carboniferous), West-central Sinai, Egypt. *World Applied Sciences Journal*, *31*, 12-30.

Schofield, K. (1984) Are pressure solution, neomorphism and dolomitization genetically related? In: stylolites and associated phenomena–relevance to hydrocarbon reservoirs. *Spec. Publ. Abu Dhabi Nat. Reservoir Res. Found.*, 183-201.

Sibley, D. F. (1982) The origin of common dolomite fabrics, clues from the Pliocene. *Jour. Sedim. Petrol.*, *52*, 1087-1100.

Sibley, D. F. & Gregg, J. M. (1987) Classification of dolomite rock textures. *Jour. Sedim. Petrol.*, *57*, 967-975.

Sibley, D. F. Dedoes, R. E. Bartlett, T. R. (1987) Kinetics of dolomitization. *Geology*, *15*, 1112-1114.

Spry, A. (1969) Metamorphic textures. Oxford, *Pergamon Press.*

Zenger, D. H. (1983) Burial dolomitization in the Lost Burro Formation (Devonian), east-central California, and the significance of late diagenetic dolomitization. *Geology*, *11*, 519-522.

Özkan, Ali Müjdat & Kibar, Levent Kenan; Petrographıc Features Of The Upper Trıassıc-Lower Jurassıc Kızılören Formatıon Dolostones (Konya Northwest, Turkiye)

79

Geochemical Propertıes Of The Saytepe Formatıon (Upper Cretaceous) Carbonates Around Hadım And North (Konya, Turkiye)

Ali Müjdat Özkan[1]
Görkem Kırkan[2]

Introduction

The aim of the study is to study the geochemical properties of the Saytepe Formation (Upper Cretaceous) carbonates around Hadim (Konya, Türkiye) located in the Central Taurus Mountains. In this context, major, trace, and rare earth element analyzes were made from the Saytepe Formation carbonate samples, in which environment this formation was deposited, how it was altered in its diagenetic history, it was determined how the climate was during the deposition process, whether there was terrigenous material input to the basin during the deposition of carbonates, and which rocks were the origin of detrital.

Previous studies have shown that the distribution and amounts of some major and trace elements in fine-grained rocks can be used to determine paleoclimatic conditions (Cao et al., 2012; Wang et al., 2017; Ding et al., 2018). It has been stated by many researchers (Cao et al., 2012; Wang et al., 2017; Ding et al., 2018) that elements such as Fe, Mn, V, Cr, Co, and Ni show relative enrichment in humid climatic conditions. Ding et al. (2018) emphasized as a result of the increase in alkalinity of water due to evaporation in arid climate conditions, the storage of salty minerals increases, and elements such as Ca, Mg, Na, K, Ba, and Sr are concentrated.

The geochemical properties of the Saytepe Formation carbonates were tried to be revealed by making main, trace and rare earth element analyses of the samples taken at appropriate intervals along the lines of two measured stratigraphic sections (Büyükkaratepe ÖSK and Dedetepe ÖSK) selected around Bağbaşı-Hadim (Konya). In this framework, the determination of the environmental conditions (oxic to anoxic) in which the Saytepe Formation carbonates were deposited, whether there were continental detritus (stream and/or wind blow) development into the basin during the deposition, whether there were hydrothermal entrances to the basin, whether the original characteristics of the carbonate phase were preserved if there are terrestrial inputs, studies have been carried out to determine their source rock (felsic, mafic or mixed) types, to determine to what extent the limestones have been affected in the diagenetic process, whether they have undergone metamorphism and paleoclimatic conditions.

[1] Doç. Dr. Konya Teknik Üniversitesir
[2] Jeoloji Müh. Konya Teknik Üniversitesi,

Results

Major Element Geochemistry

The lithogeochemical results of Saytepe carbonates are given in Tables 1, 2, and 3. In some of the carbonate samples, the measurable element values that are very low or below the limit values may be due to the adsorbing of these elements to the clay minerals. Elements below the limit value were evaluated by taking the limit values in this study.

The Saytepe carbonate samples present, %0.10-1.03 SiO_2, %0.01-0.45 Al_2O_3, %0.04-0.48 Fe_2O_3, %0.01-0.12 K_2O, %0.01-0.02 TiO_2, %0.01-0.02 P_2O_5, %0.01 MnO, %0.01-0.03 Na_2O, %34.53-55.76 CaO ve %0.34-18.09 MgO (Table 1).

In the Saytepe samples, there is a strong positive correlation between SiO_2 and Al_2O_3, Fe_2O_3, Na_2O, K_2O, TiO_2, moderate negative correlation with CaO, moderate positive correlation with MgO, no correlation with P_2O_5 and MnO (Table 4).

Table 1. Major element (%) concentrations of the Saytepe Formation carbonates

Sample	SiO₂	Al₂O₃	Fe₂O₃	MgO	CaO	Na₂O	K₂O	TiO₂	P₂O₅	MnO	Cr₂O₃	LOI	SUM
B-80	0.16	0.02	0.06	0.71	55.02	<0.01	<0.01	<0.01	<0.01	<0.01	<0.002	44.0	99.69
B-68	0.22	0.04	0.11	1.46	53.74	<0.01	<0.01	<0.01	0.01	<0.01	0.002	44.3	99.96
B-55*	0.20	0.04	0.13	18.09	34.53	0.02	<0.01	<0.01	<0.01	<0.01	<0.002	46.7	99.95
B-49	0.32	0.15	0.04	0.55	54.80	<0.01	0.05	0.01	0.02	<0.01	0.002	44.0	99.96
B-43	0.40	0.19	0.08	0.61	54.48	<0.01	0.06	0.01	0.02	<0.01	0.002	44.1	99.95
B-30	0.16	<0.01	0.05	0.39	55.25	<0.01	<0.01	<0.01	<0.01	<0.01	<0.002	44.1	99.94
B-19	0.10	<0.01	0.04	0.34	55.76	<0.01	<0.01	<0.01	<0.01	<0.01	<0.002	43.7	99.96
B-15	0.20	<0.01	0.04	0.37	55.50	<0.01	<0.01	<0.01	<0.01	<0.01	<0.002	43.8	99.94
B-10	0.16	<0.01	0.07	0.41	55.34	<0.01	<0.01	<0.01	<0.01	<0.01	<0.002	44.0	99.67
B-6	0.19	0.03	0.11	0.56	55.06	<0.01	<0.01	<0.01	<0.01	<0.01	<0.002	44.0	99.92
B-1*	1.03	0.45	0.48	16.39	34.92	0.03	0.12	0.02	<0.01	<0.01	<0.002	46.3	99.95

*dolostone

Table 2. Trace element (ppm) concentrations of the Saytepe Formation carbonates

Sample	Ba	Rb	Sr	Zr	U	V	Th	Mo	Cu	Ni	Pb	Zn	Sc	Co	Cs
B-80	11	<0.1	263.3	5.6	1.5	<8	<0.2	<0.1	1.5	3.9	2.5	3	<1	<0.2	<0.1
B-68	16	0.3	357.0	4.8	2.4	20	<0.2	0.1	1.7	4.7	2.5	3	<1	0.2	<0.1
B-55*	7	<0.1	178.7	6.0	2.2	16	<0.2	0.2	2.4	4.4	2.3	12	<1	0.4	<0.1
B-49	10	1.4	311.2	8.4	0.3	<8	<0.2	<0.1	1.2	3.2	1.4	5	<1	<0.2	<0.1
B-43	5	1.9	240.2	6.2	0.6	<8	0.2	<0.1	1.5	4.1	1.6	4	<1	<0.2	<0.1
B-30	4	<0.1	307.5	5.2	1.1	8	<0.2	<0.1	1.4	3.6	2.0	4	<1	<0.2	<0.1
B-19	5	<0.1	320.7	3.9	0.5	<8	<0.2	<0.1	0.9	3.3	2.9	3	<1	<0.2	<0.1
B-15	6	<0.1	268.3	6.6	0.6	<8	<0.2	<0.1	1.3	3.1	2.0	3	<1	<0.2	<0.1
B-10	7	<0.1	367.8	3.5	0.6	<8	<0.2	<0.1	1.0	2.7	2.3	4	<1	<0.2	<0.1
B-6	9	0.2	211.6	4.2	0.9	<8	<0.2	0.2	1.5	2.7	10.6	11	<1	<0.2	<0.1
B-1*	7	4.2	142.7	5.4	3.4	24	0.4	9.2	3.9	9.1	12.5	21	<1	0.6	0.1

Table 2. Continued

Sample	Ga	Be	Hf	Nb	Ta	Sn	Hg	As	Tl	Se	Bi	Sb	Cd
B-80	<0.5	<1	0.1	<0.1	<0.1	<1	0.10	2.1	<0.1	<0.5	<0.1	0.1	0.3
B-68	<0.5	<1	0.1	<0.1	<0.1	<1	0.05	1.9	<0.1	<0.5	<0.1	0.3	0.4
B-55*	<0.5	<1	0.2	<0.1	<0.1	<1	0.06	2.6	<0.1	<0.5	<0.1	0.6	0.4
B-49	<0.5	<1	0.1	<0.1	<0.1	<1	0.05	1.9	<0.1	<0.5	<0.1	0.2	0.8
B-43	<0.5	<1	0.2	0.1	<0.1	<1	0.04	1.5	<0.1	<0.5	<0.1	0.1	0.4
B-30	<0.5	<1	<0.1	<0.1	<0.1	<1	0.08	2.5	<0.1	<0.5	<0.1	0.2	0.3
B-19	<0.5	<1	<0.1	<0.1	<0.1	<1	0.03	1.9	<0.1	<0.5	<0.1	0.5	0.3
B-15	<0.5	<1	0.2	<0.1	<0.1	<1	0.02	1.3	<0.1	<0.5	<0.1	0.4	0.3
B-10	<0.5	<1	<0.1	<0.1	<0.1	<1	0.09	1.3	<0.1	<0.5	<0.1	0.4	0.2
B-6	<0.5	<1	<0.1	0.2	<0.1	<1	0.29	3.0	<0.1	<0.5	<0.1	1.2	0.7
B-1*	<0.5	<1	0.1	0.3	<0.1	<1	2.62	9.3	<0.1	<0.5	<0.1	3.3	0.2

Table 3. Rare earth element (ppm) concentrations of the Saytepe Formation carbonates

Sample	La	Ce	Pr	Nd	Sm	Eu	Gd	Tb	Dy	Y	Ho	Er	Tm	Yb	Lu	TREE
B-80	<0.1	0.2	<0.02	<0.3	<0.05	<0.02	<0.05	<0.01	<0.05	0.2	<0.02	<0.03	<0.01	<0.05	<0.01	0.92
B-68	0.6	0.6	0.05	0.5	0.09	<0.02	0.10	0.01	0.10	1.7	0.02	0.08	<0.01	<0.05	<0.01	2.24
B-55*	0.1	0.2	<0.02	<0.3	<0.05	<0.02	<0.05	<0.01	<0.05	0.3	<0.02	<0.03	<0.01	<0.05	<0.01	0.92
B-49	0.3	0.9	0.07	0.4	<0.05	<0.02	0.07	<0.01	0.06	0.4	<0.02	0.04	<0.01	<0.05	<0.01	2.01
B-43	0.6	1.1	0.10	0.6	0.10	<0.02	<0.05	<0.01	0.08	0.6	<0.02	0.05	<0.01	<0.05	<0.01	2.80
B-30	0.2	0.2	<0.02	<0.3	<0.05	<0.02	<0.05	<0.01	<0.05	0.7	<0.02	0.03	<0.01	<0.05	<0.01	1.02
B-19	0.2	0.2	<0.02	<0.3	<0.05	<0.02	<0.05	<0.01	0.06	0.5	<0.02	<0.03	<0.01	<0.05	<0.01	1.03
B-15	0.1	0.3	<0.02	<0.3	<0.05	<0.02	<0.05	<0.01	<0.05	0.6	<0.02	0.04	<0.01	<0.05	<0.01	1.01
B-10	0.3	0.2	0.05	<0.3	<0.05	<0.02	<0.05	<0.01	0.06	0.8	<0.02	0.03	<0.01	<0.05	<0.01	1.16
B-6	0.4	0.5	0.02	0.3	<0.05	0.04	0.08	<0.01	0.09	1.1	<0.02	0.08	<0.01	<0.05	0.02	1.67
B-1*	0.9	1.9	0.18	0.8	0.14	<0.02	0.14	0.01	0.08	0.9	<0.02	0.07	<0.01	0.06	<0.01	4.34

Table 4. Major element (%) correlation of the Saytepe Formation carbonates

	SiO_2	Al_2O_3	Fe_2O_3	MgO	CaO	Na_2O	K_2O	TiO_2	P_2O_5	MnO	TREE	LOI
SiO_2	1											
Al_2O_3	0.98	1										
Fe_2O_3	0.93	0.86	1									
MgO	0.59	0,54	0.73	1								
CaO	-0.63	-0,58	-0.76	-0.99	1							
Na_2O	0.83	0.78	0.93	0.92	-0.93	1						
K_2O	0.96	0.99	0.81	0.47	-0,517	0.72	1					
TiO_2	0.95	0.89	0.97	0.63	-0.66	0.89	0.86	1				
P_2O_5	0.14	0.30	-0.19	-0.22	0.20	-0.21	0.37	-0.15	1			
MnO	.c	.c	.c	.c	.c	.c	.c	.c	.c	.c		
TREE	0.92	0.94	0.81	0.38	-0.43	0.63	0.92	0.81	0.31	.c	1	
LOI	0.57	0.53	0.71	0.99	-0.99	0.89	0.46	0.60	-0.19	.c	0.39	1

Trace Element Geochemistry

Trace element analysis results of the Saytepe Formation samples: Sr 143-368 ppm, Rb 0.1-4.2 ppm, Ba 4-16 ppm, Zr 3.5-8.4 ppm, U 0.3-3.4 ppm, V 8-24 ppm, Mo 0.1-9.2 ppm, Ni 2.7-9.1 ppm, Co 0.2-0.6 ppm, Th 0.2-0.4 ppm, Zn 3-21 ppm, Pb 1.4-12.5 ppm, Cu 0.9-3.9 ppm, Hf 0.1-0.2 ppm, Nb 0.1-0.3 ppm, Cs 0.1 ppm and Ga 0.5 ppm (Table 2).

In the Saytepe carbonate samples, strong positive correlation between Rb and K_2O (R=0.99), SiO_2 (R=0.97), Al_2O_3 (R=0.99), Fe_2O_3 (R=0.84), TiO_2 (R=0.88), Na_2O and Rb (R=0.74), strong positive correlation between Rb and Th (R=0.88), Mo (R=0.87), Ni (R=0.84), Hg (R=0.86), As (R=0.82), Rb a moderate positive correlation was observed between Na_2O (R=0.74), Cu (R=0.76), Zn (R=0.70), Co (R=0.74), Nb (R=0.75) (Table 5). Moderate positive correlation between Sr and CaO (R=0.74), SiO_2 (-0.61), Fe_2O_3 (R=-0.66), MgO (R=-0.73), Na_2O (R=-0.74), Cu (R=-0.77) moderate negative correlation between Pb (R=-0.64), Co (R=-0.74), Nb (R=-0.67), Hg (R=-0.61), As (R=-0.67), Sr and Zn (R=-0.82), a strong negative correlation is observed. Ba and Zr elements do not show strong or moderate correlations with any major or trace element (Table 5).

Table 5. Major (%) and trace element (ppm) correlation of the Saytepe Formation carbonates

	SiO2	Al2O3	Fe2O3	MgO	CaO	Na2O	K2O	TiO2	P2O5	MnO	Ba	Sr	Zr	U	V	Th	Mo	Cu	Ni	Pb	Zn	Co	Hf	Nb	Hg	As	Rb
SiO2	1																										
Al2O3	0.98	1																									
Fe2O3	0.93	0.86	1																								
MgO	0.59	0.54	0.73	1																							
CaO	-0.65	-0.58	0.7	0.8	1																						
Na2O	0.83	0.78	0.93	0.92		1																					
K2O	0.96	0.99	0.98	0.47	-0.52	0.72	1																				
TiO2	0.95	0.89	0.97	0.63		0.82	0.86	1																			
P2O5	0.14	0.30	-0.19	-0.22	0.20	-0.21	0.37	-0.15	1																		
MnO	.c	.c	.c	.c	.c	.c	.c	.c	.c	.c																	
Ba	-0.06	-0.08	0.01	-0.09	0.08	0.12	-0.13	-0.09	-0.06	.c	1																
Sr	0.61	-0.59	0.6	0.7	0.74	0.7	0.54	0.59	0.04	.c	0.25	1															
Zr	0.19	0.27	-0.07	0.10	-0.11	0.05	0.31	-0.01	0.67	.c	0.05	-0.21	1														
U	0.63	0.54	0.81	0.76	0.78	0.81	0.45	0.71	-0.42	.c	0.33	-0.52	-0.10	1													
V	0.68	0.61	0.81	0.74	0.6	0.79	0.53	0.72	-0.27	.c	0.37	-0.40	-0.05	0.94	1												
Th	0.95	0.89	0.97	0.63		0.82	0.86	1	-0.15	.c	-0.09	-0.59	-0.01	0.7	0.72	1											
Mo	0.95	0.89	0.97	0.63		0.82	0.86	1	-0.15	.c	-0.09	-0.59	-0.01	0.7	0.72	1	1										
Cu	0.86	0.81	0.9	0.5	0.8	0.9	0.74	0.88	-0.18	.c	0.03	0.77	0.09	0.89	0.85	0.88	0.89	1									
Ni	0.91	0.84	0.9	0.7		0.8	0.82	0.93	-0.12	.c	0.06	0.59	0.06	0.8	0.86	0.93	0.93		1								
Pb	0.66	0.59	0.7	0.42	-0.44	0.6	0.54	0.74	-0.30	.c	0.02		-0.28	0.48	0.74	0.75		0.59	1								
Zn	0.79	0.74	0.9	0.8		0.9	0.68	0.83	-0.18	.c	-0.10	0.82	-0.01	0.68	0.83	0.84		0.77	0.83	1							
Co	0.83	0.78	0.9	0.9	1.0		0.72	0.89	-0.21	.c	-0.12	0.74	0.05	0.79	0.89	0.89		0.89	0.63	0.92	1						
Hf	-0.05	-0.03	-0.13	0.26	-0.24	0.06	-0.03	-0.19	0.24	.c	-0.36	0.37	0.38	-0.1	-0.07	-0.19	-0.19	0.05	-0.07	-0.32	-0.03	0.06	1				
Nb	0.83	0.76	0.9	0.51	-0.55	0.76	0.72	0.88	-0.21	.c	-0.03	0.67	-0.15	0.6	0.58	0.89	0.89	0.75	0.96	0.89			-0.27	1			
Hg	0.94	0.88	0.9	0.62	0.65	0.8	0.84	0.99	-0.17	.c	-0.07	0.61	-0.04	0.7	0.99	0.99	0.99	0.91	0.80	0.86			-0.23		1		
As	0.90	0.84	0.9	0.68		0.9	0.80	0.97	-0.21	.c	-0.06	0.67	0.04	0.5	0.72	0.97	0.97	0.91	0.90	0.90			-0.24			1	
Rb	0.97	0.9	0.8	0.48	-0.53	0.7	0.99	0.88	0.33	.c	-0.32	0.55	0.27	0.5	0.57	0.88	0.87	0.84	0.57	0.70		-0.04					1

In the Saytepe Formation samples, strong positive correlation between rare earth elements La and SiO_2 (R=0.81), Al_2O_3 (R=0.81), moderate positive correlation between Fe_2O_3 (R=0.75), K_2O (R=0.78), TiO_2 (R=0.71) is observed. Strong positive correlation between La and Ce (R=0.88), Pr (R=0.87), Nd (R=0.92), Sm (R=0.93), Gd (R=0.84), La and Dy (R=0.79), a moderate positive correlation was observed between Er (R=0.75), Yb (R=0.71) (Table 6). Strong positive correlation between Ce and SiO_2 (R=0.95), Al_2O_3 (R=0.97), Fe_2O_3 (R=0.80), K_2O (R=0.97), TiO_2 (R=0.81), La (R=0.88) moderate positive correlation between Na_2O (R=0.65), Gd (R=0.79), strong positive correlation was observed between Ce and Pr (R=0.96), Nd (R=0.95), Sm (R=0.89), Yb (R=0.81) (Table 6). No strong or moderate correlation was observed between Eu and any major and trace element (Table 6).

Table 6. Major (%) and rare earth element (ppm) correlation of the Saytepe Formation carbonates

	SiO₂	Al₂O₃	Fe₂O₃	MgO	CaO	Na₂O	K₂O	TiO₂	P₂O₅	MnO	La	Ce	Pr	Nd	Sm	Eu	Gd	Tb	Dy	Y	Ho	Er	Tm	Yb	Lu
SiO₂	1																								
Al₂O₃	0.98	1																							
Fe₂O₃	0.93	0.86	1																						
MgO	0.59	0.54	0.73	1																					
CaO	0.4	-0.58	0.76	0.4	1																				
Na₂O	0.83	0.78	0.95	0.9		1																			
K₂O	0.9	0.99	0.81	0.47	-0.52	0.72	1																		
TiO₂	0.9	0.89	0.97	0.63	0.6	0.89	0.86	1																	
P₂O₅	0.14	0.30	-0.19	-0.22	0.20	-0.21	0.37	-0.15	1																
MnO	.c	.c	.c	.c	.c	.c	.c	.c	.c	.c															
La	0.8	0.81	0.75	0.27	-0.32	0.52	0.78	0.71	0.20	.c	1														
Ce	0.9	0.97	0.80	0.40	-0.45	0.65	0.97	0.89	0.39	.c	0.8	1													
Pr	0.9	0.97	0.82	0.44	-0.48	0.69	0.97	0.85	0.33	.c	0.87	0.9	1												
Nd	0.91	0.92	0.80	0.42	-0.47	0.65	0.91	0.79	0.29	.c	0.92	0.95	0.95	1											
Sm	0.88	0.87	0.82	0.44	-0.49	0.66	0.85	0.81	0.14	.c	0.93	0.89	0.91	0.98	1										
Eu	-0.12	-0.14	0	-0.15	0.15	0.14	-0.17	-0.1	-0.15	.c	0.07	-0.04	0.21	0.20	-0.18	1									
Gd	0.80	0.75	0.86	0.45	-0.48	0.67	0.69	0.82	-0.12	.c	0.84	0.79	0.74	0.77	0.78	0.14	1								
Tb	.c	.c	.c	.c	.c	.c	.c	.c	.c	.c	.c	.c	.c	.c	.c	.c	.c								
Dy	0.34	0.35	0.37	-0.03	-0.01	0.09	0.30	0.25	0.10	.c	0.79	0.51	0.42	0.56	0.59	0.43	0.66	.c	1						
Y	0.14	0.07	0.25	-0.12	0.09	0.01	0.02	0.15	-0.25	.c	0.59	0.23	0.18	0.33	0.40	0.31	0.58	.c	0.81	1					
Ho	.c	.c	.c	.c	.c	.c	.c	.c	.c	.c	.c	.c	.c	.c	.c	.c	.c	.c	.c	.c	.c				
Er	0.44	0.40	0.49	0.09	-0.12	0.23	0.35	0.38	-0.03	.c	0.75	0.55	0.41	0.55	0.58	0.54	0.77	.c	0.9	0.81	.c	1			
Tm	.c	.c	.c	.c	.c	.c	.c	.c	.c	.c	.c	.c	.c	.c	.c	.c	.c	.c	.c	.c	.c	.c	.c		
Yb	0.9	0.89	0.97	0.63	0.6	0.89	0.8	1.0	-0.15	.c	0.71	0.81	0.85	0.72	0.86	0.1	0.82	.c	0.25	0.15		0.38	.c	1	
Lu	-0.12	-0.14	0	-0.15	0.15	0.14	-0.17	-0.1	-0.15	.c	0.07	-0.05	0.21	0.20	-0.18	1.0	0.14	.c	0.43	0.31	.c	0.54	.c	0.1	1

Some elemental ratios such as Mo/U, V/Cr, Ni/Co, U/Th, and V/(V+Ni) are used to reveal redox conditions (Hatch and Leventhal, 1992; Jones and Manning, 1994) (Table 7). Mo/U, V/Cr, Ni/Co, U/Th, and V/(V+Ni) ratios of the Saytepe Formation samples vary between 0.04-2.71, 0.58-1.75, 11-23.5, 1.5-12, and 0.66-0.81, respectively. (Table 8; Figure 1).

Table 7. Some elemental concentrations used to evaluate paleoredox conditions

Element ratio	Oxic	Dysoxic	Anoxic	Euxinic	Writers
Ni/Co	<5	5-7	>7		
V/Cr	<2	2-4.5	>4.5		Jones & Manning (1994)
U/Th	<0.75	0.75-1.25	>1.25		
V/(V+Ni)	<0.46	0.46-0.60	0.54-0.82	>0.84	Hatch & Leventhal (1992)

Table 8. Redox susceptibility trace element concentrations and geochemical ratios of the Saytepe Formation carbonate samples (dolostone)*

Sample	Mo/U	V/Cr	Ni/Co	U/Th	V/(V+Ni)	Mn/Sr	K/Rb	Si/Al	Al/Ti	Ce/Ce*	Eu/Eu*	Pr/Pr*	La/La*	(La/Sm)N	(Dy/Sm)N
B-80	0,07	0,58	19,5	7,5	0,67	0,29	0,083	7,047	1,77	0,70	1,88	0,399	-0,24	0,29	1,18
B-68	0,04	1,46	23,5	12	0,81	0,22	0,028	4,849	3,53	0,705	0,98	0,508	-1,25	0,97	1,32
B-55*	0,09	1,17	11	11	0,78	0,43	0,083	4,405	3,53	1,03	1,88	0,399	-0,24	0,29	1,19
B-49	0,33	0,58	16	1,5	0,71	0,25	0,029	1,883	13,23	0,96	1,54	0,686	42,74	0,87	1,42
B-43	0,16	0,58	20,5	3	0,66	0,32	0,026	1,859	16,75	1,02	1,29	0,678	-11,04	0,87	0,95
B-30	0,09	0,58	18	5,5	0,69	0,25	0,083	14,094	0,88	0,67	1,88	0,399	-0,48	0,58	1,19
B-19	0,2	0,58	16,5	2,5	0,71	0,24	0,083	8,811	0,88	0,67	1,88	0,398	-0,48	0,58	1,42
B-15	0,16	0,58	15,5	3	0,72	0,29	0,083	17,622	0,88	1,54	1,88	0,359	-0,24	0,29	1,19
B-10	0,16	0,58	13,5	3	0,75	0,21	0,083	14,094	0,88	0,37	1,88	0,997	-11,04	0,87	1,42
B-6	0,22	0,58	13,5	4,5	0,75	0,37	0,041	5,585	2,65	0,99	2,83	0,299	-0,96	1,16	2,13
B-1*	2,71	1,75	15,2	8,5	0,73	0,54	0,024	2,021	19,84	1,09	0,67	0,859	1,69	0,93	0,68

Table 8. Continued

| Sample	Al₂O₃/TiO₂	Y/Ho	Er/Nd	(Nd/Yb)N	Eu/Sm	Rb/Sr	Sr/Ba	Sr/Rb	Ga/Rb	Sr/Cu	Th/Co	La/Sc	Mg/Ca	Fe/Al	K/Na	Th/U
B-80	2	10	0,10	0,50	0,4	0,0004	23,9	2633		175	1	0,1	0,011	3,962	1,119	0,133
B-68	4	85	0,16	0,83	0,22	0,0008	22,3	1190	1,7	210	1	0,6	0,023	3,627	1,119	0,083
B-55*	4	15	0,10	0,50	0,4	0,0006	25,5	1787	5	74	0,5	0,1	0,442	4,288	0,559	0,091
B-49	15	20	0,10	0,66	0,4	0,0045	31,1	222,3	0,4	259	1	0,3	0,008	0,353	5,594	0,667
B-43	19	30	0,08	0,99	0,2	0,0079	48,0	126,4	0,3	160	1	0,6	0,009	0,556	6,713	0,333
B-30	1	35	0,10	0,50	0,4	0,0003	76,9	3075	5	220	1	0,2	0,006	6,604	1,119	0,182
B-19	1	25	0,10	0,50	0,4	0,0003	64,1	3207	5	356	1	0,2	0,005	5,283	1,119	0,400
B-15	1	30	0,13	0,50	0,4	0,0004	44,7	2683	5	206	1	0,1	0,006	5,283	1,119	0,333
B-10	1	40	0,10	0,50	0,4	0,0003	52,5	3678	5	368	1	0,3	0,006	9,245	1,119	0,333
B-6	3	55	0,27	0,50	0,8	0,0009	23,5	1058	2,5	141	1	0,4	0,008	4,836	1,119	0,222
B-1*	22,5	45	0,08	1,11	0,14	0,0294	20,4	34,0	0,1	36	0,7	0,9	0,396	1,410	4,476	0,118
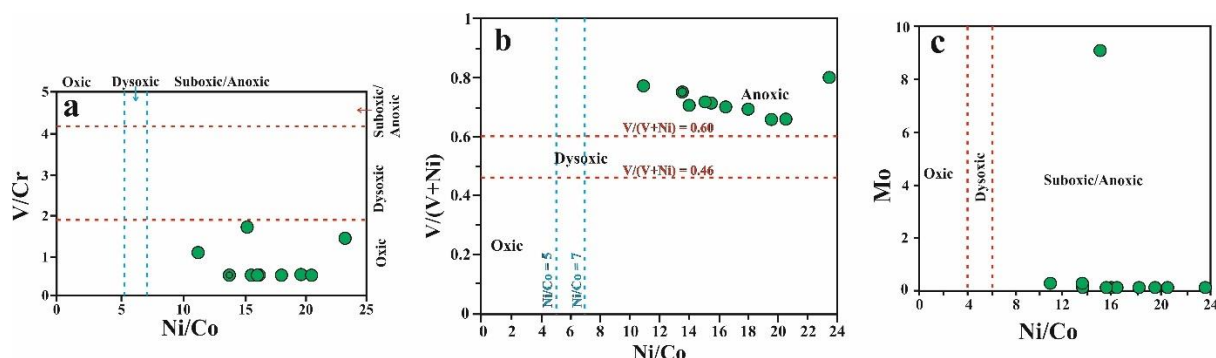
Figure 1. a) The Saytepe Formation samples fall into the suboxic-anoxic area in the V/Cr–Ni/Co diagram, b) The Saytepe Formation samples fall into the anoxic area in the V/(V+Ni–Ni/Co diagram, c) Mo–Ni/Co In the diagram, the Saytepe Formation samples fall into the suboxic-anoxic area.

The total rare earth element values of the Saytepe carbonate samples are 0.92-4.34 ppm (average 1.74 ppm), which is very low compared to present-day marine sediments and Post-Archaean Average Australian Shale (PAAS). The values of the Saytepe carbonate samples normalized to Post-Archaean Australian Shale (McLennan, 1989) show depletion and moderate positive Y anomaly in all samples (Graph 1).
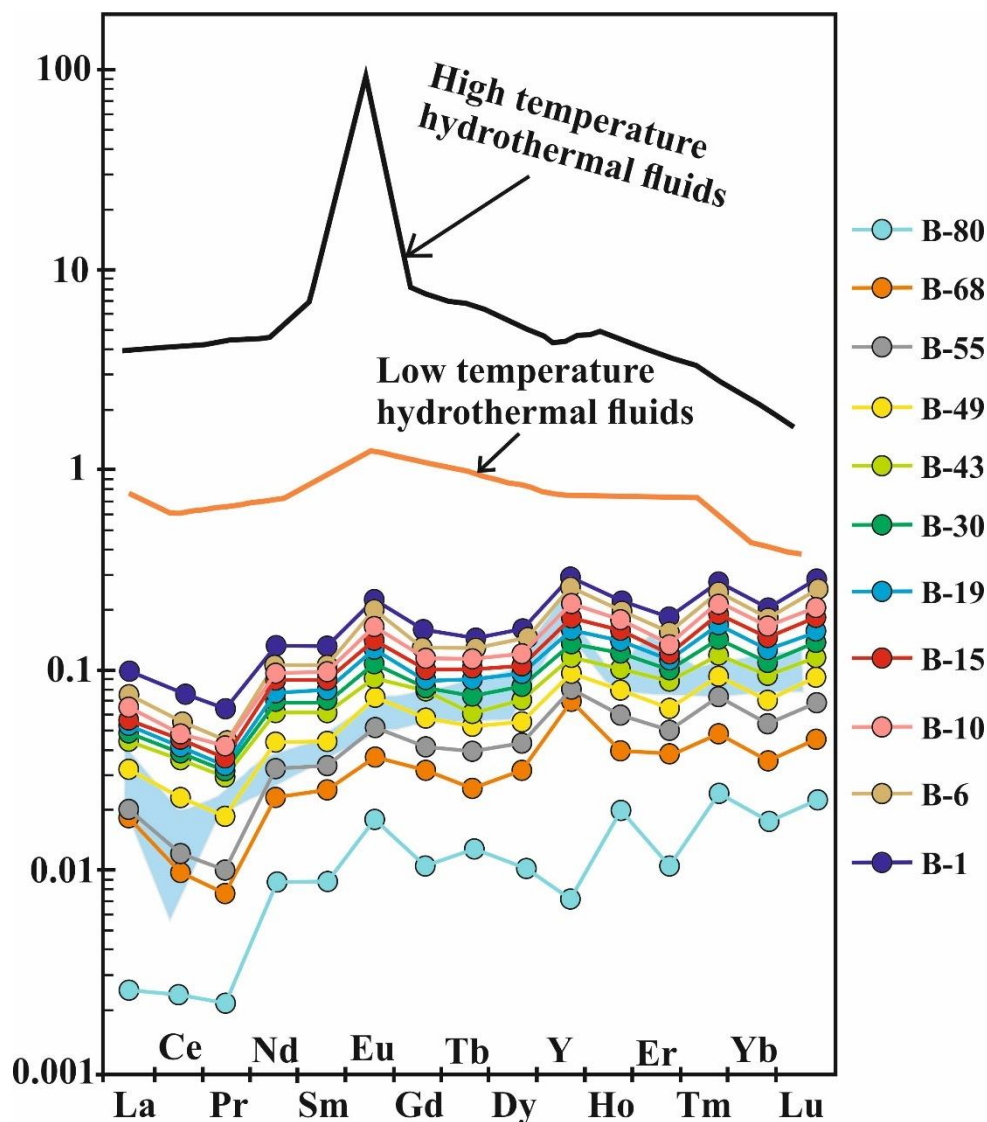
Graph 1. Shale normalized (PAAS) REE+Y diagram of the Saytepe carbonate samples. The blue area denotes present-day seawater

In addition, the REE+Y values of the Saytepe carbonate samples normalized to Post-Archaean Australian Shale show that a small number of samples exhibit current seawater characteristics, most of them exhibit higher values than current seawater by light rare earth elements and a few samples show lower values than current seawater (Graph 1). Again, we can say in Graph 1 that Saytepe carbonate samples were not exposed to any hydrothermal fluid effects and present moderately negative Ce, positive Eu anomaly, and positive Y anomaly.

Discussion

Evaluation of Sample Conservation

During the diagenesis process, some elements show enrichment and some elements show depletion, so it becomes necessary to determine the degree of change in our samples. Some tests are used to determine the degree of this change.

The textural change in carbonate rocks is mostly in the form of the transformation of unstable minerals into stable minerals (Brand and Veizer, 1980; Wang et al., 2017). Micritic and/or sparitic calcite minerals can transform into neomorphic coarse sparicalcite as a result of diagenetic alteration. Although the Saytepe carbonate samples were deposited as micritic mudstone, they were neomorphized into microsparitic and sparitic limestones during the diagenetic change process, but it was observed that the primary texture was preserved in most samples.

Some elemental ions (such as Sr, Mg, Fe and Mn) can be incorporated into calcite mineral lattices. Meteoric waters contain low Sr^{+2} but high Fe^{+2} and Mn^{+2} elements (Brand and Veizer, 1980; Wang et al., 2017). Therefore, in the diagenetic alteration process, an increase in Fe^{+2} and Mn^{+2} content, a decrease in Sr^{+2} content, while a decrease or increase may be observed in Mg^{+2} depending on the nature of the primary carbonate mineral (Brand and Veizer, 1980; Wang et al., 2017). From this, we can say that the changes of trace elements are important markers and they can reflect the degree of diagenetic alteration (Wang et al., 2017) that took place after deposition.

Again, Wang et al. (2017) stated that Sr and Mn are important elements of diagenetic alteration. While meteoric diagenesis can remove Sr^{+2} from the carbonate mineral structure, it can ensure the incorporation of Mn^{+2} into the carbonate mineral structure (Brand and Veizer, 1980; Gilleaudeau and Kah, 2013; Wang et al., 2017). Therefore, we can state that Mn/Sr values are very useful indicators in determining the diagenetic alteration of carbonate rocks due to the contradictory properties of Sr and Mn elements.

If the Mn/Sr values are less than 3, it is stated by some researchers that the primary deposition feature of the rock is preserved, if it is between 3-10, it has undergone low diagenetic alteration, and if it is >10, it indicates severe alteration (Kaufman and Knoll,1995; Wang et al., 2017). Mn/Sr values of the Saytepe carbonate samples are between 0.21 and 0.54, and we can say that they preserve their primary deposition characteristics. Although it is known that hydrothermal effects show positive Eu and high Ba values, positive Eu (Graph 1) and low Ba values (Table 2) are observed in the Saytepe carbonate samples, and we can state that positive Eu values are caused by terrigenous feldspars rather than hydrothermal effect. Because no hydrothermal effect is observed in our samples in Graph 1.

The K/Rb values were high (≥500) in highly metamorphosed rocks, 230 in unmetamorphized igneous rocks (except oceanic tholeiites) and 200 in shales, Rudnick et al. (1985) and Bauernhofer et al. (2009) emphasized. Since the K/Rb values of the Saytepe samples vary between 0.024 and 0.083 (Table 8), we can state that they did not undergo metamorphism.

The Sr/Ca versus Na diagram of the Saytepe carbonate samples also shows some diagenetic alteration in the Saytepe Formation samples (Figure 2).
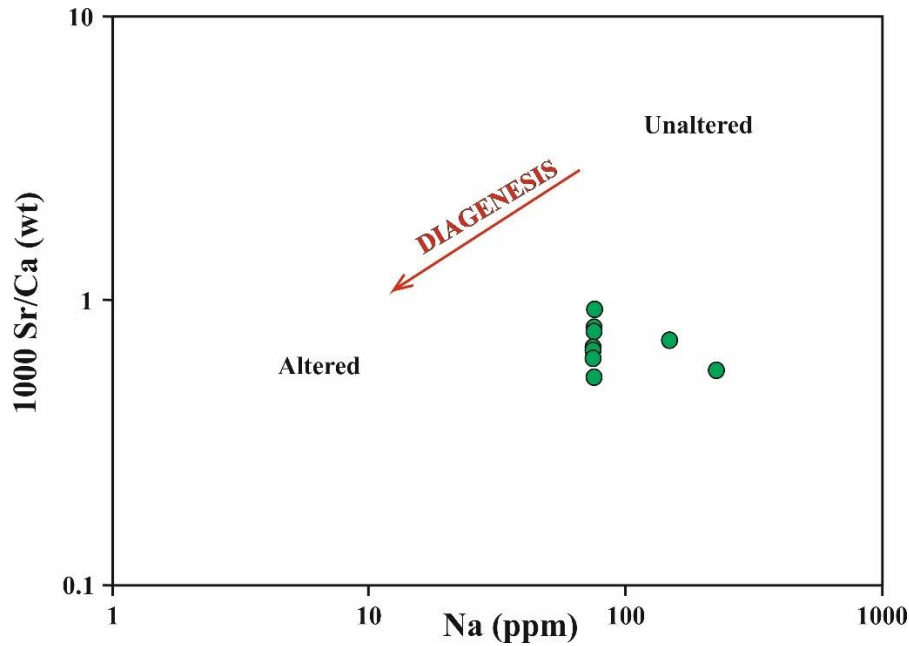
Figure 2. Sr/Ca vs. Na diagram of the Saytepe carbonate samples

Major and Trace Element Evaluation of the Saytepe Formation Carbonates

It has been emphasized by many researchers such as Garrels and Mackenzie (1971), Nesbitt ve ark. (1980), Taylor ve McLennan (1985), and Wronkiewicz ve Condie (1990) that the behavior of trace elements is complex depending on processes such as weathering, physical sorting, adsorption, provenance, diagenesis, and metamorphism.

It is known that the major and trace elements contained in the limestones are greatly affected by the terrigenous contribution (Kuchenbecker et al., 2016). It is observed that the terrigenous contribution of Si, K, Al, Ti, Rb, Sr, Ba, Nb, Ta, Th, U, and REEs in the Saytepe samples is generally low (Tables 1, 2, and 3; Figure 3). Again, the distribution of the Saytepe carbonate samples in the Si versus Zr diagram shows that Si is entire of terrestrial origin rather than biogenic (Figure 4).

Calcium is predominantly biogenic and strongly negatively correlated with almost all other major and trace elements (Zhang et al., 2017), it functions as a diluent of other components. This situation is clearly observed in the form of carbonate tendency in the SiO_2-Al_2O_3-CaO diagram of the Saytepe samples (Figure 3). While Al_2O_3 values did not show any correlation with MnO and P_2O_5 in the Saytepe limestone samples, they were strongly positive correlation with SiO_2 (R=0.98), Fe_2O_3 (R=0.86), Na_2O (R=0.78), K_2O (R=0.99), TiO_2 (R=0.97)(Table 4) indicates that Si, Fe, Na, K, Ti are mostly provided by clay minerals.
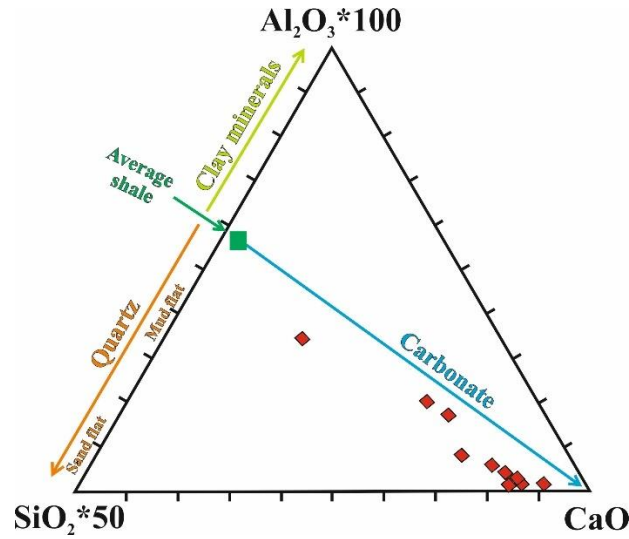
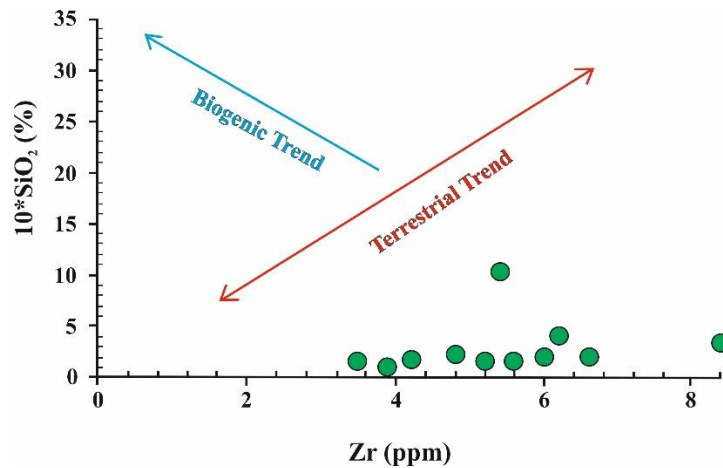*Figure 3. In the Al-Si-Ca triangular diagram, all the Saytepe Formation samples show a carbonate rock tendency*

Figure 4. In the SiO₂ vs. Zr diagram, the silica in the Saytepe carbonates has a terrestrial tendency and is not of biogenic origin

Kuchenbecker et al. (2016) stated that Rb/Sr ratios reflect the relative abundance of terrigenous content and carbonate fraction. The Rb/Sr values of the Saytepe Formation samples are 0.0003-0.030 (mean 0.0042) (Table 5), indicating that some Sr loss has occurred as a result of diagenetic alteration. Because Kuchenbecker et al. (2016) are slightly higher than the expected 0.0008 Rb/Sr value in carbonate rocks.

It is emphasized that Th/U values are very useful indicators in determining the provenance of contamination in chemical sedimentary rocks. Chemically formed sedimentary rocks can contain debris such as volcanic ash, detrital material, and phosphate (Thurston et al., 2011).

Thurston et al. (2011) emphasized that the ratio of phosphate pollution in chemical rocks occurs when having a Th/U>5 value, while other contaminations are represented by Th/U values between 3-5 (Condie, 1993; Thurston et al., 2011). Since the Th/U values observed in the Saytepe samples vary between 0.08 and 0.67, it indicates the absence of phosphate contamination.

Zhang et al. (2017) stated that using the Rb-Sr-Ba triangle diagram, it is possible to distinguish between freshwater limestones, shallow marine limestones, and open ocean limestones. When the Rb-Sr-Ba triangle diagram is used for the Saytepe samples, the samples show the offshore environment (Figure 5). Again, Zhang et al. (2017), the graph of Sr/Ba versus Sr/Rb can be used to distinguish between limestones deposited in fresh water and limestones deposited in shallow marine environments. When we reduced the Saytepe samples to the Sr/Ba versus Sr/Rb plot, all of the samples indicated deposition in the shallow marine (continental margin) environment (Figure 6).
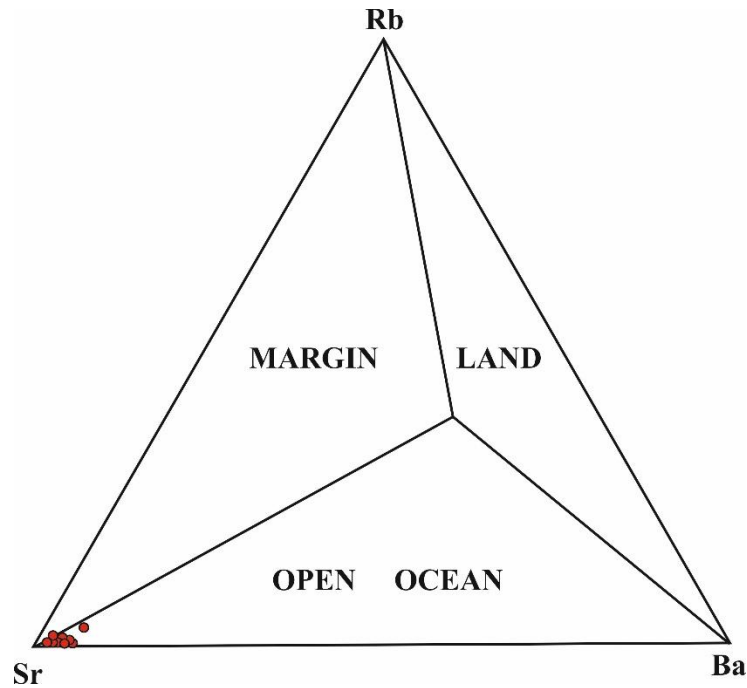

Figure 5. Rb-Sr-Ba triangular diagram of the Saytepe carbonate samples. Diagram showing various limestone depositional environments (from Zhang et al., 2017)
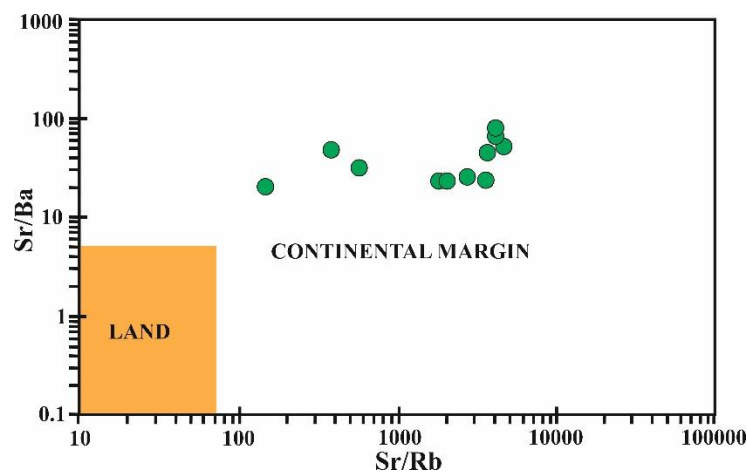

Figure 6. Sr/Ba versus Sr/Rb diagram of the Saytepe carbonates

Roy and Roser (2013), Yandoka et al. (2015), Xie et al. (2018), and Ding et al. (2018) stated that Sr/Cu and Ga/Rb values can also be used to determine the paleoclimate. Ga is mostly enriched in clay minerals (especially kaolinite) and indicates a warm-humid climate (Ding et al., 2018). Ding et al. (2018) emphasized that the Rb element is closely related to the illite mineral and reflects the cold and dry climate. The very low Ga/Rb values in the sediments indicate that the climate is cold and dry. Generally, in warm and humid climatic conditions, fine-grained sediments exhibit low Sr/Cu values and high Ga/Rb values (Ding et al., 2018). Ding et al. (2018) emphasized that Sr/Cu values between 1.3-5 indicate a warm humid environment, while values above 5 indicate hot-arid climate conditions.

Figure 7 shows the Ga/Rb vs. Sr/Cu graph of the Saytepe samples, with Ga/Rb 0.11-5 (mean 3.17), Sr/Cu 36-368 (average 200) values. Therefore, Sr/Cu values of the Saytepe samples indicate warm-arid climatic conditions.
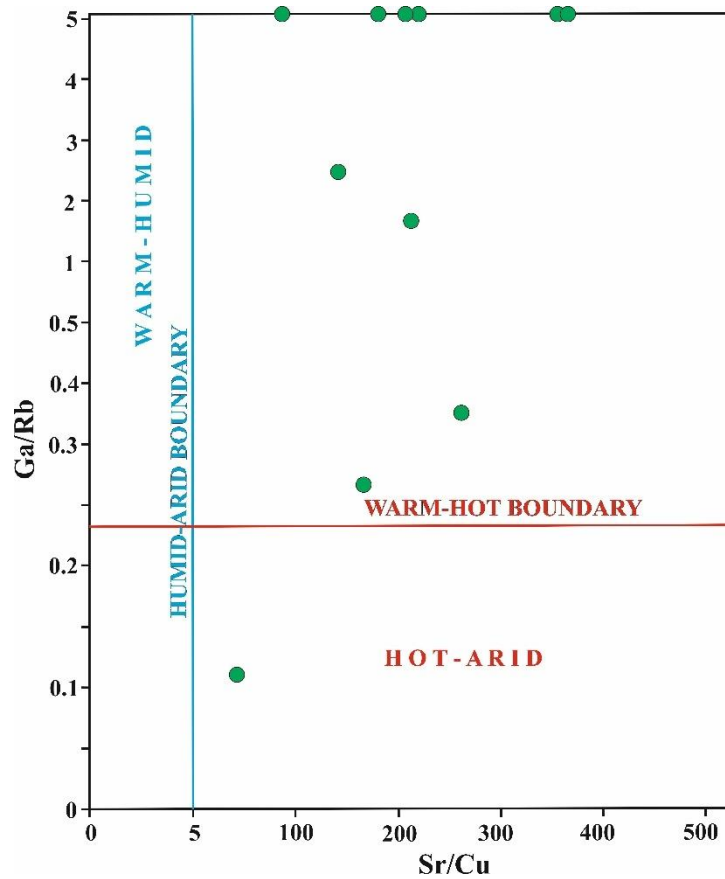
Figure 7. Ga/Rb versus Sr/Cu diagram of the Saytepe carbonate samples. Diagram shows paleoclimatic conditions (diagram from Ding et al., 2018)

The presence of rare earth elements in carbonates can be affected by many factors. (1) The introduction of terrigenous detrital into the basin (Piper, 1974; McLennan, 1989), (2) the biogenic deposition from the water column in the basin (Murphy and Dymond, 1984), and (3) the interaction process related to the depth, salinity, and oxygen content of the water in the basin (Elderfield, 1988; Piepgras and Jacobsen, 1992; Bertram and Elderfield, 1993; Greaves et al., 1999), (4) eutigenic removal of rare earth elements from the water column in the basin and due to early diagenesis (Sholkovitz, 1988).

Seawater contributes very little REE to chemical sediments, but sediments that do not have marine water characteristics can have very high REE concentrations due to contamination by non-carbonate materials (Nothdurft et al., 2004) such as silicates, Fe-Mn oxides, phosphates and sulfides during the chemical filtration process (Zhao et al., 2009).

Positive correlation with total rare earth elements SiO_2, Al_2O_3, TiO_2, and Fe_2O_3 (R=0.62, R=0.48, R=0.67, R=0.45, respectively) in terrestrial and shallow marine limestones indicates that REE is under the influence of siliciclastic input (Zhang et al. et al., 2017). The strong positive correlation between TREE of the Saytepe samples and SiO_2 (R=0.92), Al_2O_3 (R=0.94), TiO_2 (R=0.81), Fe_2O_3 (R=0.81) (Table 6) also highlights the effect of siliciclastic input on REE.

Zhang et al. (2017) stated that the size of the Ce anomaly of the limestones increased significantly from spreading ridges to continental coastal seas. In the graph of Ce/Ce* versus Al_2O_3 and Fe_2O_3 (Figure 8) the Saytepe Formation samples mostly point to the terrestrial margin and partly to the open sea environment. However, in Figure 8a, two samples fall into the terrestrial environment, possibly indicating an intertidal or supratidal environment.
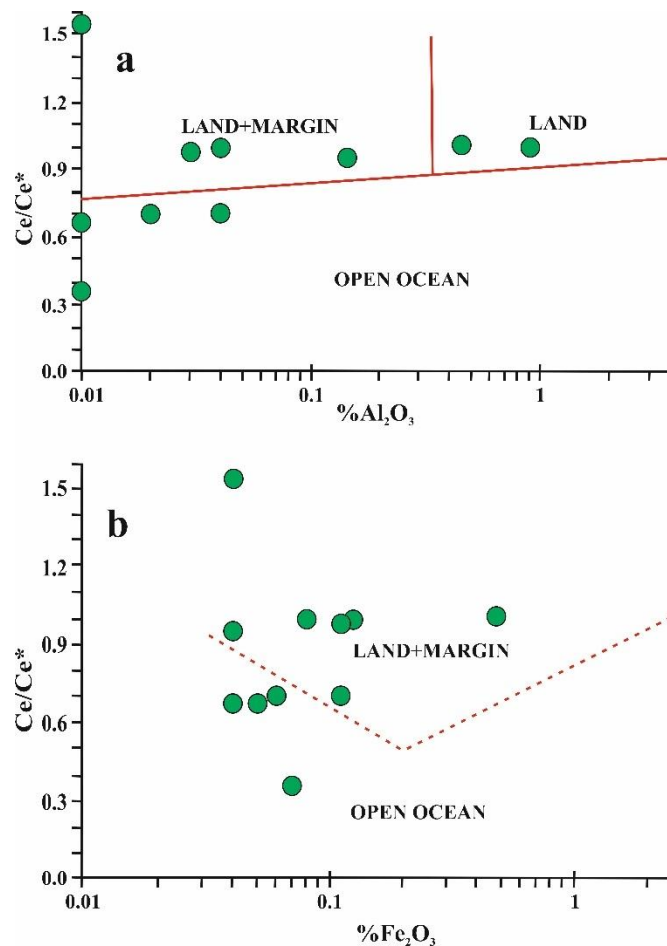

Figure 8. Ce/Ce* versus Al₂O₃ and Fe₂O₃ diagram of the Saytepe carbonate samples. Limestones deposited in various storage environments (Taylor and McLennan, 1985)

Murray et al. (1990, 1991) stated that Ce anomaly depends on the deposition environment, high Ce values indicate oxic conditions, while low Ce values indicate anoxic conditions. During the transgression process, the bottom waters become anoxic and the whole rock Ce anomaly becomes negative (Wilde et al., 1996). In the regression process, any fixed point in the base becomes shallow; therefore, the bottom waters will be oxic and the whole rock Ce anomaly will be positive.

Since the characteristics of the Saytepe Formation sediments occur in a transgressive shallow marine (carbonate-dominated shelf) depositional environment, Wilde et al. (1996) suggest the applicability of the model proposed in this study. From this, we can say that the Ce values contained by the Saytepe carbonate samples are negative values (Graph 1), indicating transgressive and anoxic carbonate deposition. In the Ce/Ce* vs. Nd graph in Figure 9, all of the Saytepe samples fall into the anoxic area, and in the Ce/Ce* vs. La_N/Sm_N diagram in Figure 10, all the samples fall into the anoxic area, supporting the above interpretation. In addition, the fall of the Saytepe carbonate samples into the anoxic area in the Pr/Pr* versus Y/Ho diagram in Figure 11 also indicates the dominance of anoxic conditions during the deposition process.
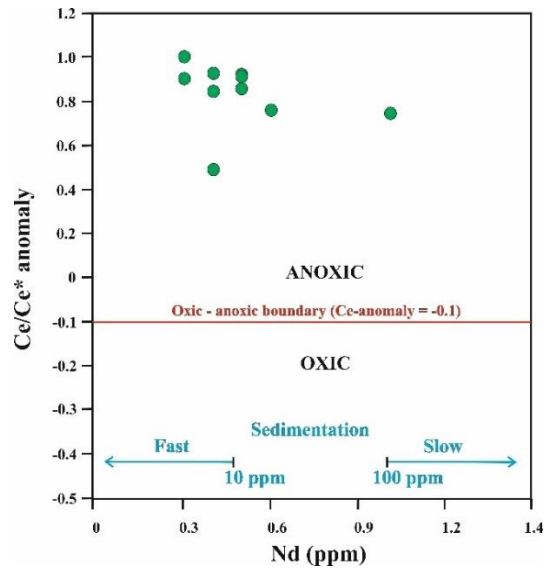

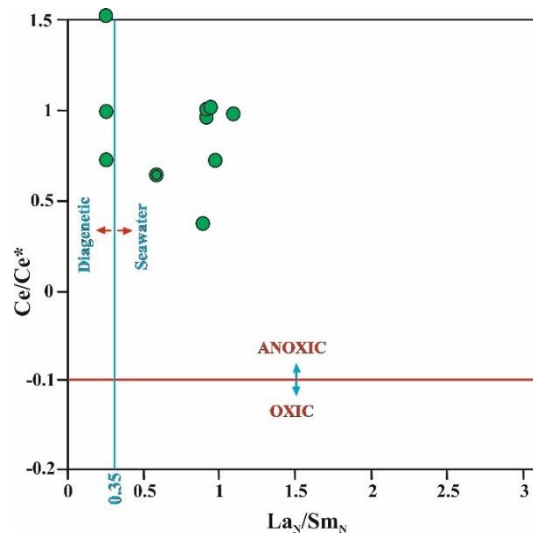*Figure 9. Ce/Ce* vs. Nd diagram of the Saytepe carbonates*

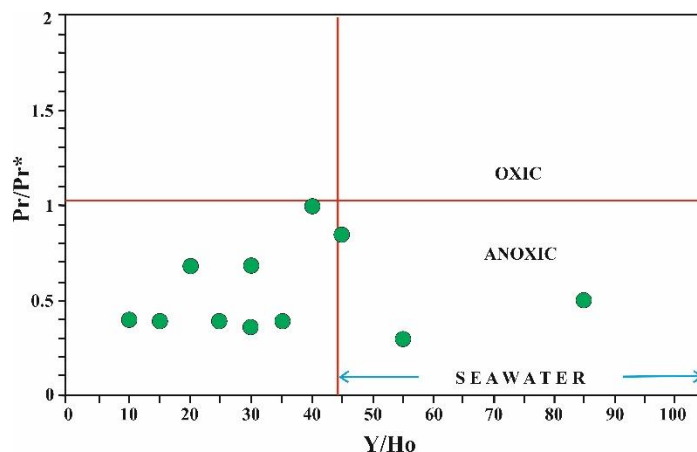*Figure 10. Ce/Ce* versus $(La/Sm)_N$ diagram of the Saytepe carbonates*

Figure 11. Pr/Pr* vs. Y/Ho diagram of the Saytepe carbonate samples

Ali and Wagreich (2017) stated in their study that limestone Ce anomalies are close to 1 and differ from seawater (0.1-0.4) values. They stated that (1) the presence of small amounts of clay (from detrital input) minerals in pure and impure samples, (2) may have resulted from the increase in LREEs due to the degradation of Ce-containing organic matter a few cm deep in the sediment column below the seafloor. Ce anomaly values in the Saytepe carbonate samples vary between 0.37-1.54 (mean 0.88) (Table 8) and are higher than seawater values. We can say that the increase in Ce anomaly in the Saytepe samples is due to the presence of clay minerals in the limestones and/or the degradation of organic matter containing Ce in the seafloor sediments.

The redox potential of Eu/Eu* in aqueous solutions is highly dependent on temperature and less on the variation of pressure, pH, and REE (Bau, 1996; Bau and Dulski, 1996), and positive Eu anomalies may be associated with acidic, reducing hydrothermal fluids.

Eu/Eu* in the Saytepe carbonate samples vary between 0.67-2.83 (mean 1.69; Table 8), and they show great differences. In addition, although these samples show positive Eu anomaly, we cannot say that they indicate any hydrothermal fluid effect. Because positive Eu anomaly can be caused not only by hydrothermal fluids but also by the input of detrital feldspars. In addition, Graph 1 shows that Saytepe carbonate samples have not undergone hydrothermal alteration. Observation of >1 Eu anomaly in all Saytepe carbonate samples (except for two samples) indicates that this positivity originates from detrital feldspars. Positive Eu anomalies, which are not common in seawater, are mostly (1) an increased influx of hydrothermal fluids into the ocean at mid-ocean ridges (German et al., 1990); (2) a slight increase in the primary or detrital feldspar component (Madhavaraju et al., 2010); (3) due to diagenetic alteration of limestones (Brand and Veizer, 1980).

In the Eu/Eu* vs. Ce/Ce* graph of the Saytepe carbonate samples (Figure 12), our samples mostly show deposition in the marginal-offshore environment.

Bau (1996), and Bau and Dulski (1996) stated that the Y/Ho values (44-74) in seawater are high, while a constant chondritic Y/Ho value of ~28 is observed in terrigenous detrital and volcanic ash. The Y/Ho value is between 60-90 in open sea water and varies depending on the salinity (Lawrence et al., 2006). Recent seawater Y/Ho values are significantly higher than stream and estuary water (Nozaki et al., 1999; Lawrence et al., 2006).
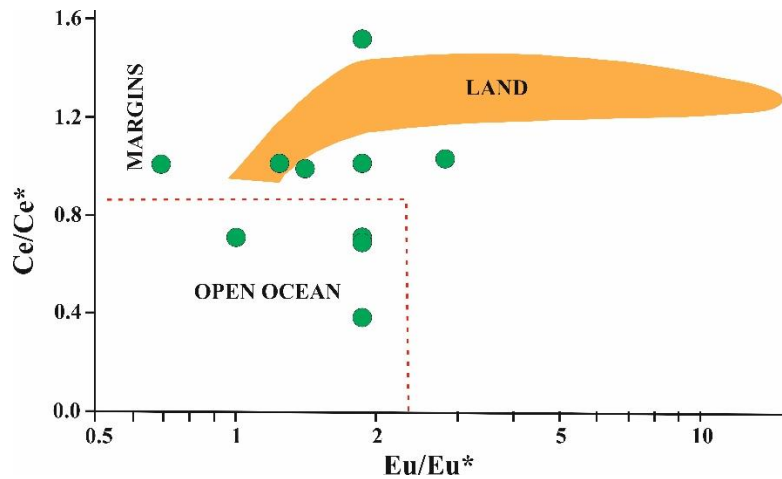
Figure 12. Positions of Saytepe carbonate samples in Ce/Ce* vs. Eu/Eu* diagram according to various storage environments. The diagram is taken from Zhang et al. (2017)

The Y/Ho ratios of the Saytepe Formation samples (Table 8) have an average value of 35 (between 10-85), which is considerably lower than the open sea water value (60-90), and it is observed that at some stages during the deposition of the carbonate, the freshwater suspension load and/or the eolian states that the powders are mixed effectively (Kuchenbecker et al., 2016). In addition, the low Y/Ho values of the Saytepe carbonate samples (10-85), Song et al. (2014) maintained the seawater values at a low rate (only 1 sample). This situation is observed in the Y/Ho versus TREE diagram in Figure 13, indicating predominantly terrestrial input for REE.
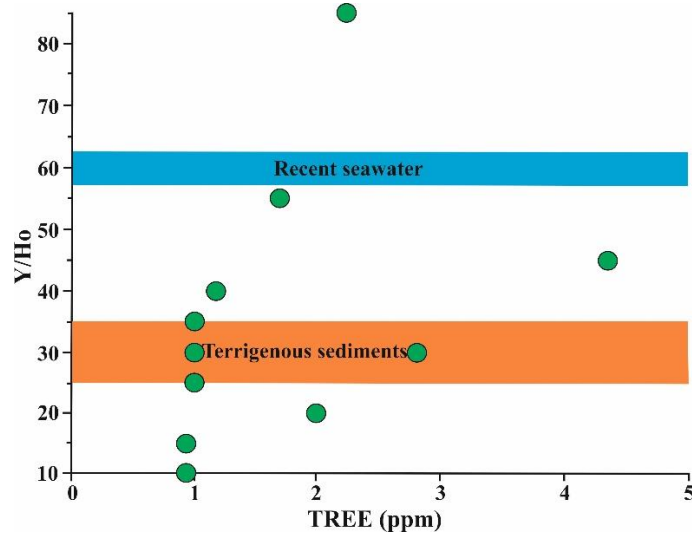
Figure 13. The Saytepe carbonate samples in the Y/Ho-TREE diagram indicate a high degree of siliciclastic contamination

Y/Ho values in the Saytepe samples were found to be low at levels with siliciclastic addition (in impure limestones) and higher at levels without siliciclastic additions (≥ 36 in relatively pure limestones) (Figure 13).

Ali and Wagreich (2017) stated that in previous studies, they found that the Y/Ho values in seawater were approximately two times higher than those of chondritic and shale values. Researchers believe that this value is affected by redox conditions; they stated that due to the

preferential adsorption of Ho to Y by Fe and Mn oxyhydroxide particles dissolved under anoxic conditions, it decreased from 102 in oxic waters to 67 in anoxic waters (Bau et al., 1997). We can say that during the deposition of the Saytepe carbonates, the oxic conditions on the shallow shelf turned into anoxic conditions on the deep shelf (offshore) and the Y/Ho values may have decreased from 102 to an average of 35 (between 10-85). This is also consistent with the fact that Saytepe carbonate samples show the development under anoxic conditions in Figures 9, 10, and 11.

Possible Sources of Detritic Materials in the Saytepe Formation Carbonates

Major oxides in sediments can be attributed to their origin, but some trace elements, including Na, K, Ca, Mg, and Fe, are not fully compatible with source rocks due to variable weathering and diagenetic processes (McLennan, 1989; Xing et al., 2021). Stable elements such as Ti, Si, Al, and Zr are relatively immobile during diagenetic processes and are often used as markers to reflect terrigenous input (Hatch and Leventhal, 1992; Xing et al., 2021). For instance, in sediments Ti is commonly found in the minerals ilmenite ($FeTiO_3$) or rutile (TiO_2), Si is most commonly associated with siliciclastics, including quartz, feldspar, and clay minerals (Kidder and Erwin, 2001; Xing et al., 2021), and in Al feldspars, clay minerals and other aluminum silicate minerals (Rimmer, 2004; Xing et al., 2021).

The strong (R=0.98) positive relationship between SiO_2 and Al_2O_3 in the Saytepe carbonate samples indicates that feldspar and quartz are derived from terrestrial input from the same source (Table 4).

Al_2O_3/TiO_2 values are used to reveal the provenance of clastic rocks, and these values range from 3-8 for mafic igneous rocks, 8-21 for intermediate rocks, and 21-70 for felsic igneous rocks (Hayashi et al., 1997). The Al_2O_3/TiO_2 ratios of the Saytepe samples are 3-8 (3 samples), 9-19 (2 samples), and 22 (one sample) (Table 8), with 5 samples <3 and emphasizing the source rock composition from mixed source rocks.

In addition, Al/Ti ratios are also used to determine whether the terrigenous input is of a stream or eolian origin. The Al/Ti ratios of the Saytepe carbonate samples range from 1 to 20 (average 6) (Table 8), and the fact that they are lower than the upper crust average value (27), indicates that terrigeneous input to the basin during the deposition process is via wind transport rather than streams.

In addition, the source of terrigenous input in the Saytepe samples falls into the arid climate zone (Figures 7 and 14), and the terrigenous material arriving in the basin during the deposition of the Saytepe Formation shows a low level of input depending on the climate.
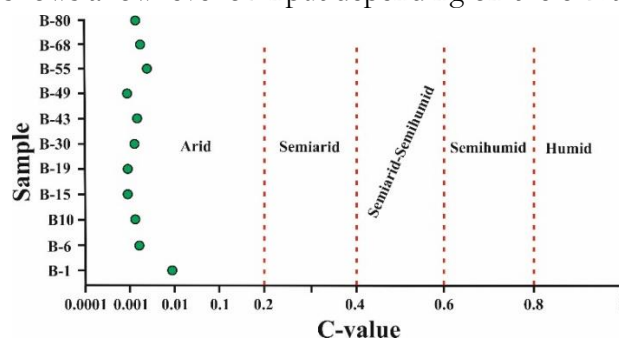

Figure 14. The Saytepe Formation samples show the arid climate zone according to the C-value [Σ(Fe+Mn+Cr+Ni+V+Co) / Σ(Ca+Mg+Sr+Ba+K+Na)]

Many authors (McLennan, 1989; McLennan and Taylor, 1991; McLennan et al., 1980; Wronkiewicz and Condie, 1990) have suggested Th and La elements as indicators of felsic origin, Sc and Cr elements as indicators of mafic origin, and used to make a distinction between felsic and mafic provenance.

In the La versus Th diagram (Figure 15a), the Saytepe carbonate samples fall into the mafic source area. The TiO_2/Zr ratio is another indicator of source rocks (Mclennan et al., 1993; Xing et al., 2021), where TiO_2/Zr ratios of mafic rocks are higher than 200 and felsic rocks are lower than 55. Since the TiO_2/Zr ratios of Saytepe carbonate samples are $<<1$, it indicates that the terrigenous fragments were taken from the felsic source. In the TiO_2 vs. Zr diagram (Figure 15b), all of the Saytepe Formation samples fall into the source area of felsic rocks. Therefore, the detrital that came to the basin during the deposition of Saytepe carbonates was taken from mixed provenance.
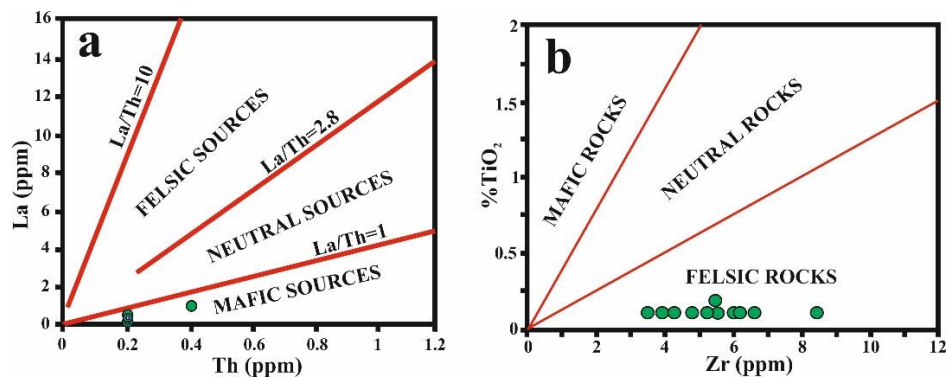
Figure 15. (a) Th versus La diagram for Saytepe carbonate samples, (b) TiO₂ versus Zr diagram

It was emphasized by Cullers (2002) that the provenance of detrital rocks can be determined in the plot of Th/Co versus La/Sc. When the Saytepe carbonate samples are reduced to the Th/Co versus La/Sc plot, it indicates that the detrital input originates from felsic rocks (Figure 16a).

The Na_2O versus K_2O separation diagram of the Saytepe Formation carbonates (Bhatia, 1983) indicates the high richness of quartz in the clastic inputs (Figure 16b). This situation is also consistent with the quartz abundance observed in the petrographic examinations of our samples.
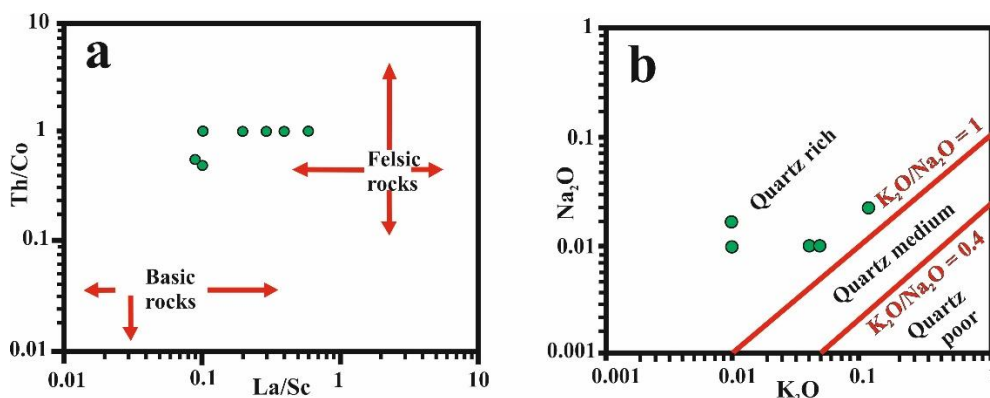
Figure 16. (a) La/Sc vs. Th/Co diagram for the Saytepe carbonate samples (diagram taken from Cullers, 2002), b) Na₂O vs. K₂O diagram

REFERENCES

Ali, A. & Wagreich, M. (2017) Geochemistry, environmental and provenance study of the Middle Miocene Leitha limestones (Central Paratethys). *Geologica Carpathica*, *68*(3), 248-268.

Bau, M. (1996) Controls on fractionation of isovalent trace element in magmatic and aqueous systems: evidence from Y/Ho, Zr/Hf, and lanthanide tetrad effect. *Contributions to Mineralogy and Petrology*, *123*, 323-333.

Bau, M. & Dulski, P. (1996) Distribution of yttrium and rare-earth elements in the Penge and Kuruman iron-formations, Transvaal Supergroup. *Precambrian Res., 79*, 37-55.

Bau, M. Möller, P. Dulski, P. (1997) Yttrium and lanthanides in eastern Mediterranean seawater and their fractionation during redox-cycling. *Mar. Chem., 56*, 123-131.

Bauernhofer, A. Hauzenberger, C. Wallbrecher, E. Muhongo, S. Hoinkes, G. Mogessie, A. Opiyo-Akech, N. Tenczer, V. (2009) Geochemistry of basement rocks from SE Kenya and NE Tanzania: Indications for rifting and early Pan-African subduction. *International Journal of Earth Sciences, 98*(8), 1809-1834.

Bertram, C. J. & Elderfield, H. (1993) The geochemical balance of the rare earth elements and Nd isotopes in the oceans. *Geochim. Cosmochim. Acta, 51*, 1957-1986.

Bhatia, M. R. (1983) Plate tectonics and geochemical composition of sandstones. *J Geol., 91*, 611-627.

Brand, U. & Veizer, J. (1980) Chemical diagenesis of a multi-component carbonate system: trace elements. *Jour. Sediment. Petrol., 50*, 1219-1236.

Cao, J. Wu, M. Chen, Y. Hu, K. Bian, L. Z. Wang, L. G. Zhang, Y. (2012) Trace and rare earth element geochemistry of Jurassic mudstones in the northern Qaidam Basin, northwest China. *Chem. Erde-Geochem., 72*, 245-252.

Condie, K. C. (1993) Chemical composition and evolution of the upper crust: Contrasting results from surface samples and shales. *Chem. Geol., 104*, 1-37.

Cullers, R. L. (2002) Implications of elemental concentrations for provenance, redox conditions, and metamorphic studies of shales and limestones near Pueblo, CO, USA. *Chemical Geology, 191*(4), 305-327.

Ding, J. Zhang, J. Tang, X. Huo, Z. Han, S. Lang, Y. Zheng, Y. Li, X. Liu, T. (2018) Elemental Geochemical Evidence for Depositional Conditions and Organic Matter Enrichment of Black Rock Series Strata in an Inter-Platform Basin: The Lower Carboniferous Datang Formation, Southern Guizhou, Southwest China. *Minerals, 8*(11), 1-29.

Elderfield, H. (1988) The oceanic chemistry of the rare earth elements. *Philos. Trans. R. Soc. Lond., A 325*, 105-126.

Garrels, R. M. & Mackenzie, F. T. (1971). *Evolution of sedimentary rocks*. NY:W.W. Norton and Co.

German, C. R. Klinkhammer, G. P. Edmond, J. M. Mitra, A. Elderfield, H. (1990) Hydrothermal scavenging of rare earth elements in the ocean. *Nature, 345*, 516-518.

Gilleaudeau, G. J. & Kah, L. C. (2013) Carbon isotope records in a Mesoproterozoic epicratonic sea: carbon cycling in a low-oxygen World. *Precambrian Res., 228*, 85-101.

Greaves, M. J. Elderfield, H. Sholkovitz, E. R. (1999) Aeolian sources of rare earth elements to the Western Pacific Ocean. *Marine Chemistry, 68*, 31-38.

Hatch, J. R. & Leventhal, J. S. (1992) Relationship between Inferred Redox Potential of the Depositional Environment and Geochemistry of the Upper Pennsylvanian (Missourian) Stark Shale Member of the Dennis Limestone, Wabaunsee Country, Kansas, USA. *Chemical Geology, 99*, 65-82.

Hayashi, K. I. Fujisawa, H. Holland, H. D. Ohmoto, H. (1997) Geochemistry of ~1.9 Ga sedimentary rocks from northeastern Labrador, Canada. *Geochim. Cosmochim. Acta, 61*(19), 4115-4137.

Jones, B. & Manning, D. A. C. (1994) Comparison of Geochemical Indices Used for the Interpretation of Palaeoredox Conditions in Ancient Mudstones. *Chemical Geology, 111*, 111-129.

Kaufman, A. J. & Knoll, A. H. (1995) Neoproterozoic variations in the C-isotopic composition of seawater: stratigraphic and biogeochemical implications. *Precambrian Research, 73*, 27-49.

Kidder, D. L. & Erwin, D. H. (2001) Secular Distribution of Biogenic Silica through the Phanerozoic: Comparison of Silica-Replaced Fossils and Bedded Cherts at the Series Level. *The Journal of Geology, 109*(4), 509-522.

Kuchenbecker, M. Babinski, M. Pedrosa-Soares, A. C. Lopes-Silva, L. Pimenta, F. (2016) Chemostratigraphy of the Lower Bambuí Group, Southwestern São Francisco Craton, Brazil: Insights on Gondwana Paleoenvironments. *Brazilian Journal of Geology, 46*, 145-162.

Lawrence, M. G. Greig, A. Collerson, K. D. Kamber, B. S. (2006) Rare earth element and yttrium variability in South East Queens-land waterways. *Aquatic Geochemistry, 12*(1), 39-72.

Madhavaraju, J. González-León, C. M. Lee, Y. I. Armstrong-Altrin, J. S. Reyes-Campero, L. M. (2010) Geochemistry of the Mural Formation (Aptian-Albian) of the Bisbee Group, Northern Sonora, Mexico. *Cretaceous Research, 31*, 400-414.

McLennan, S. M. Nance, W. B. Taylor, S. R. (1980) Rare earth element-thorium correlations in sedimentary rocks, and the composition of the continental crust. *Geochim. Cosmochim. Acta, 44*(11), 1833-1839.

McLennan, S. M. (1989) Rare Earth Elements in Sedimentary Rocks: Influence of Provenance and Sedimentary Process. *Review of Mineralogy, 21*, 169-200.

McLennan, S. M. & Taylor, S. R. (1991) Sedimentary Rocks and Crustal Evolution: Tectonic Setting and Secular Trends. *The Journal of Geology, 99*(1), 1-21.

McLennan, S. M. Hemming, S. McDaniel, D. K. Hanson, G. N. (1993) Geochemical approaches to sedimentation, provenance, and tectonics, in Processes Controlling the Composition of Clastic Sediments, edited by M. J. Johnsson, and A. Basu. *Spec. Pap. Geol. Soc. Am., 284*, 21-40.

Murphy, K. & Dymond, J. (1984) Rare earth element fluxes and geochemical budget in the eastern equatorial Pacific. *Nature, 307*, 444-447.

Murray, R. W. Buchholz Ten Brink, M. R. Jones, D. L. Gerlach, D. C. Russ, G. P. (1990) Rare Earth Elements as Indicators of Different Marine Depositional Environments in Chert and Shale. *Geology, 18*, 268-271.

Murray, R. W. Brink, M. R. B. Brumsack, H. J. Gerlach, D. C. (1991) Rare earth elements in Japan Sea sediments and diagenetic behavior of Ce/Ce∗: Results from ODP Leg 127. *Geochimica et Cosmochimica Acta, 55*(9), 2453-2466.

Nesbitt, H. W. Markovics, G. Price, R. C. (1980) Chemical processes affecting alkalies and alkaline earth during continental weathering. *Geochim. Cosmochim. Acta, 44*, 1659-1666.

Nothdurft, L. Webb, G. E. Kamber, B. S. (2004) Rare earth element geochemistry of Late Devonian reefal carbonates, Canning Basin, Western Australia: Confirmation of a seawater REE proxy in ancient limestones. *Geochimica et Cosmochimica Acta, 68*, 263-283.

Nozaki, Y. Alibo, D. S. Amakawa, H. Gamo, T. Hasumoto, H. (1999) Dissolved rare earth elements and hydrography in the Sulu Sea. *Geochim. Cosmochim. Acta, 63*, 2171-2181.

Piepgras, D. J. & Jacobsen, S. B. (1992) The Behavior of Rare Earth Elements in Seawater: Precise Determination of Variations in the North Pacific Water Column. *Geochimica et Cosmochimica Acta, 56*, 1851-1862.

Piper, D. Z. (1974) Rare Earth Elements in the Sedimentary Cycle: A Summary. *Chemical Geology, 14*(4), 285-343.

Rimmer, S. M. (2004) Geochemical paleoredox indicators in Devonian–Mississippian black shales, central Appalachian Basin (U.S.A.). *Chem. Geol. 206*, 373-391.

Roy, D. K. & Roser, B. P. (2013) Climatic control on the composition of Carboniferous–Permian Gondwana sediments, Khalaspir basin, Bangladesh. *Gondwana Res., 23*, 1163-1171.

Rudnick, R. L. McLennan, S.M. Taylor, S.R. (1985) Large iron lithophile elements in rocks from high-pressure granulite facies terrains. *Geochimica et Cosmochimica Acta, 49*,1645-1655.

Sholkovitz, E. R. (1988) Rare earth elements in the sediments of the North Atlantic Ocean, Amazon Delta, and the East China Sea: the reinterpretation of terrigenous input patterns to the oceans. *American Journal of Science, 288*(3), 236-281.

Song, C. Herong, G. Linhua, S. (2014) Geochemical characteristics of REE in the Late Neo-Proterozoic limestone from northern Anhui Province, China. *Chin. Jour. Geochem., 33*, 187-193.

Taylor, S. R. & McLennan, S. M. (1985) The Continental Crust: Its Composition and Evolution. Cambridge: Blackwell.

Thurston, G. Ito, K. Lall, R. A. (2011) Source apportionment of U.S. fine particulate matter air pollution. *Atmos. Environ., 45*(24), 3924-3936.

Wang, Z. W. Fu, X. G. Feng, X. L. Song, C. Wang, D. Chen, W. B. Zeng, S. Q. (2017) Geochemical features of the black shales from the Wuyu Basin, southern Tibet: Implications for palaeoenvironment and palaeoclimate. *Geol. Jour., 52*, 282-297.

Wilde, P. Quinby-Hunt, M. S. Erdtmann, B. D. (1996) The Whole-rock Cerium Anomaly: a Potential Indicator of Eustatic Sea-level Changes in Shales of the Anoxic Facies. *Sediment. Geol., 101*(1–2), 43–53.

Wronkiewic, D. J. & Condie, K. C. (1990) Geochemistry and mineralogy of sediments from the Ventersdorp and Transvaal Supergroups, South Africa: Cratonic evolution during the early Proterozoic. *Geochim. Cosmochim. Acta, 54*, 343-354.

Xie, G. L. Shen, Y. L. Liu, S. G. Hao, W. D. (2018) Trace, and rare earth element (REE) characteristics of mudstones from Eocene Pinghu Formation and Oligocene Huagang Formation in Xihu Sag, East China Sea Basin: Implications for provenance, depositional conditions, and paleoclimate. *Mar. Petrol. Geol., 92*, 20-36.

Xing, K. Shu, Q. Lentz, D. R. (2021) Constraints on the Formation of the Giant Daheishan Porphyry Mo Deposit (NE China) from Whole-Rock and Accessory Mineral Geochemistry. *J. Pet. 62*, 1–26.

Yandoka, B. M. S. Wan, H. A. Abubakar, M. B. Hakimi, M. H. Adegoke, A. K. (2015) Geochemical characterization of Early Cretaceous lacustrine sediments of Bima Formation, Yola Sub-basin, Northern Benue Trough, NE Nigeria: Organic matter input, preservation, paleoenvironment and palaeoclimatic conditions. *Mar. Petrol. Geol., 61*, 82-94.

Zhang, K. J. Li, Q. H. Yan, L. L. Zeng, L. Lu, L. Zhang, Y. X. Hui, J. Jin, X. Tang, X. C. (2017) Geochemistry of limestones deposited in various plate tectonic settings. *Earth-Science Reviews, 167*, 26-47.

Zhao, Y. Zheng, Y. F. Chen, F. (2009) Trace element and strontium isotope constraints on the sedimentary environment of Ediacaran carbonates in southern Anhui, South China. *Chemical Geology, 265*, 345-362.

Bearıng Capacıty And Elastıc Settlement Of Shallow Foundatıons

Mustafa AYTEKIN[1]

Introduction

There are many methods proposed to estimate the bearing capacity and elastic settlement of shallow foundations. In author's opinion, a reliable method of bearing capacity estimation among all is the effective area method that is also known as Meyerhof's theory. For the settlement estimations, the Schmertmann Method is among others is the best estimation approaches. However, application of these methods as they have proposed originally are a little bit time consuming. In this chapter, you will find these methods are modified to overcome their shortages since these methods are modified by the author to be able to apply in an easy way.

In this chapter, the author has concentrated on the bearing capacity of two-way eccentric shallow foundations. In rectangular/square based and two-way loaded (two-way eccentric) shallow foundations, four zones in which the resultant load might act are defined in the effective area method. Three out of the four zones that are employed in the determination of the effective areas overlap around kern. Only one zone that has a triangular-shaped effective area (called as case 1 in the literature) out of the four zones has no overlap with the others. The resultant load will always be out of the kern for case 1, and also it might be out of the kern for the remaining three cases. Design of foundations is not acceptable in general if the resultant load acts out of the kern. In the present study, the four cases are reconsidered. The zones on which the resultant load can be acting for the four cases are modified because these zones are overlapped partly. The modification has been made to have clear borders between the zones. On top of that, zone 4 is divided into two. A new zone corresponding to the area of kern is defined as zone 5. The design will be accepted if the resultant load acts within zone 5 (the kern). Also, the graphs in use to determine the dimensions of the effective areas are eliminated since it is not precise. Formulae are derived to determine the dimensions of the effective areas instead of using the graphs. Two new criteria are discovered and proposed to check whether the resultant load acts outside, inside or on the borderline of zone 5 (the kern).

One of the methods intensively employed in many practical projects to estimate the immediate (elastic) settlement of shallow foundations is the Schmertmann-Hartman-Brown method (1978). In the method, two approaches are given as a function of type of the shallow foundation either a square/circular (axisymmetric condition) or a strip (plain strain condition) foundation. Thus, two sets of equations are provided to estimate the settlements for these types of shallow foundations. If a shallow foundation has a shape of rectangular, some approximations are suggested in the technical literature to estimate the elastic settlement of rectangular based shallow foundations. These approximations are tedious and time consuming. In this study, the Schmertmann – Hartman – Brown method (1978) is modified and only one set of equations used for any type (square, circular, rectangular, and strip) of shallow foundations is introduced. The

---

[1] Prof., University of Bahain, Department of Civil Engineering,

modified method estimates the immediate settlement as precise as the original form of the method that is more complicated. Also, some hypothetical cases are considered to figure out the effect of width and length/width ratios of foundations on elastic settlement.

Bearing Capacity

The bearing capacity estimation on the geotechnical design of two-way loaded (two-way eccentric) foundations are as follows:

a. Determine the eccentricities of e_B and e_L seen in Fig.1 in both directions of B and L, respectively.
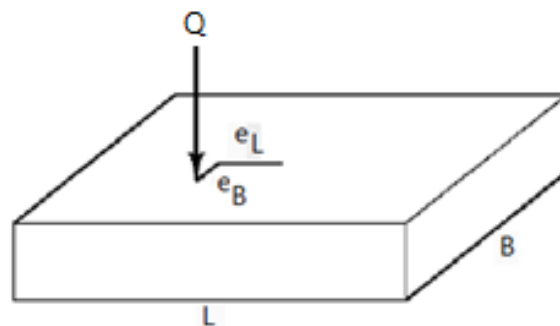
Fig.1 Two-way loaded square/rectangular foundation

b. Determine the dimensions of the kern as seen in Fig.2 and check the location of the resultant load (Q) whether it acts inside, outside or on the border line of the kern.
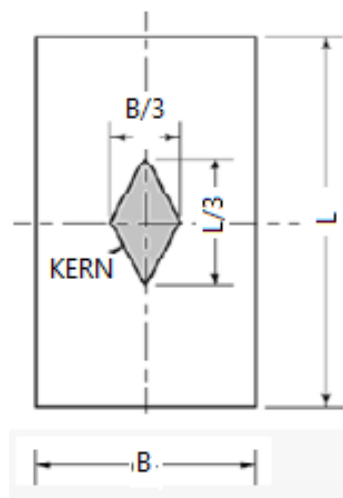
Fig.2 *Dimensions of the kern*

Use the criteria seen below to find out the location of the resultant load (Eq.1).

$$\left(\frac{6e_B}{B} + \frac{6e_L}{L}\right) \le 1 \tag{1}$$

If Eq. (1), which is actually the last two terms of second parenthesis of Eq.(2) has the value equal to one, the minimum bearing pressure would be nil whereas if the value is more than one, it would be a negative number, which means the minimum bearing is tension. In other words, if Eq. (1) is satisfied, the minimum bearing pressure is either compression or nil. Otherwise, the minimum bearing is a negative value that reflects a gap between the base of the foundation and underlying

soil. Since no gap in the design is accepted under any foundation, there must be some solutions to avoid this situation like increasing dimensions of foundation or reducing the eccentricities physically.

  c. Use the sign (+ or -) in Eq. (2) to calculate the maximum and minimum bearing pressures at the base of foundation according to the position of the load (inside, or on the border line of the kern).

$$q = \left(\frac{Q+W_f}{BL} - u_D\right)\left(1 \pm \frac{6e_B}{B} \pm \frac{6e_L}{L}\right) \tag{2}$$

where

Q: Load from superstructure

W_f : Weight of foundation

B and L: Width and length of foundation, respectively

U_{Df} : Pore water pressure at the base level of the foundation

e_B and e_L: eccentricities on B and L directions, respectively.

  In the design, the maximum bearing pressure must be less than or equal to the allowable bearing capacity of soil, and at the same time the minimum bearing pressure must be compression or at least zero but not tension. Once, the maximum and minimum bearing pressures are estimated, allowable bearing capacity of the foundation must be determined too.

  The bearing capacity of foundation can be estimated by a number of methods. Terzaghi's bearing capacity equation (Terzaghi, 1943) is widely used to estimate ultimate bearing capacity of foundations even it has many limitations in practical applications. In order to minimize these limitations, many proposals have been made by researchers (Meyerhof, 1963; Prakash and Saran, 1971; Saran and Agarwal, 1993; Vesic, 1973; Sawwaf and Nazir, 2012; Krabbenhoft and others, 2012; Loukidis and others, 2008). One of these methods has been proposed by Meyerhof (1963) and his proposed method is known as *Meyerhof Bearing Capacity Equation, General Bearing Capacity Equation, or The Effective Area Method.* Vesic, 1973 has also proposed an equation almost identical with Meyerhof's equation. Meyerhof's general bearing capacity equation is seen below:

$$q_u = c'N_cF_{cs}F_{cd}F_{ci} + qN_qF_{qs}F_{qd}F_{qi} + 0.5\gamma B'N_\gamma F_{\gamma s}F_{\gamma d}F_{\gamma i} \tag{3}$$

  Then, the ultimate bearing load can be estimated as follows.

$$Q_{ult} = q_u A' \tag{4}$$

  A procedure to determine the effective area (A') and effective width (B') that would be used in the Meyerhof's general bearing capacity equation was proposed by (Highter & Anders, 1985) in addition to one proposed by Meyerhof (1963).

  It is the common practice to employ the proposed *effective area* determination on the design of two-way loaded foundations. In the determination of effective area, four cases are provided to design a square/rectangular based and two-way loaded foundations by Highter &Anders in 1985. In the determination of the four cases, the criteria are the ranges of the ratios of e_B/B, and e_L/L. In general, nothing is mentioned for these four cases about the application points of the resultant

loads whether it is in or out of the kern. However, anything may occur in terms of eccentricity. It means that the resultant force can be in, out or on the border line of the kern except case 1 in that eccentricity is always out of the kern.

Cases defined in the effective area method

When one has a closer look into the four cases mentioned in the effective area method, the resultant load is always out of the kern in case 1 seen in Fig. 3, mostly out of the kern in cases 2 (Fig.4), and 3 (Fig. 5), some area out of the kern even in case 4 (Fig.6). Thus, the cases should be modified in order to have a clear border between the cases. Only case 1 has the areas not overlap with the areas of the rest of the cases. There are overlaps of the areas in the cases of 2, 3, and 4 as seen in Figs. 4, 5, and 6. The zone 4 seen in Fig. 6 is the common zone in the cases of 2, 3, and 4. The shapes and borders of the effective areas are taken from Das, 2007.

CASE 1: $[(e_L/L) > (1/6)$ and $(e_B/B) > (1/6)]$ As it is seen in Fig. 3, the resultant acts within the zones 1.
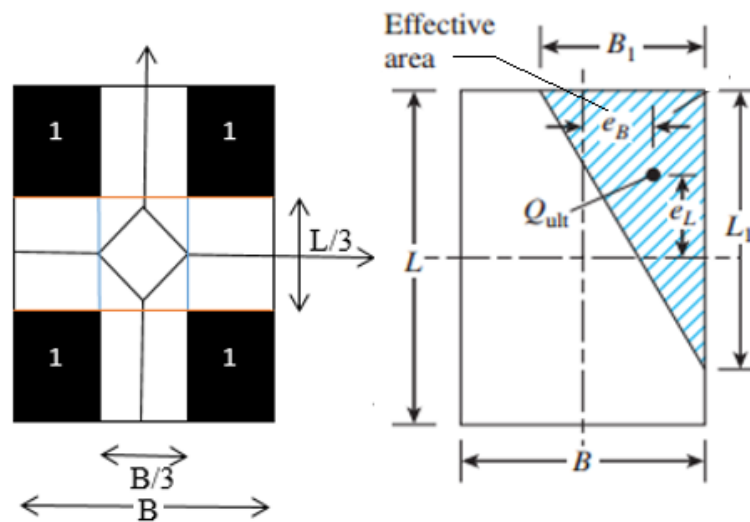
Fig. 3 Resultant load acts in zones 1 (Case 1)

It is obvious that the resultant acts out of the kern so that minimum bearing pressure would be tension and a gap between the base of foundation and the underlying soil would occur.

CASE 2: $[(e_L/L) < 0.5$ and $0 < (e_B/B) < (1/6)]$ As it is seen in Fig. 4, the resultant load acts within the zone 2. Again, it is obvious that the resultant load is not always acting within or border line but mostly out of the kern so that minimum bearing pressure would be tension mostly and a gap between the base of foundation and the underlying soil would occur.

CASE 3: $[(e_L/L) < (1/6)$ and $0 < (e_B/B) < 0.5]$ As it is seen in Fig. 5, the resultant load acts within the zone 3. Again, it is obvious that the resultant load not always acting within or border line but mostly out of the kern so that minimum bearing pressure would be tension mostly and a gap between the base of foundation and the underlying soil would occur.
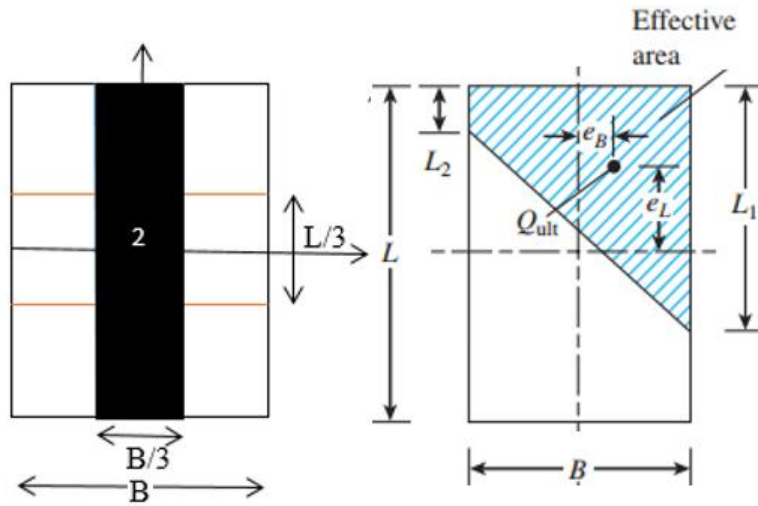
Fig. 4 Resultant load acts in zone 2 (Case 2)
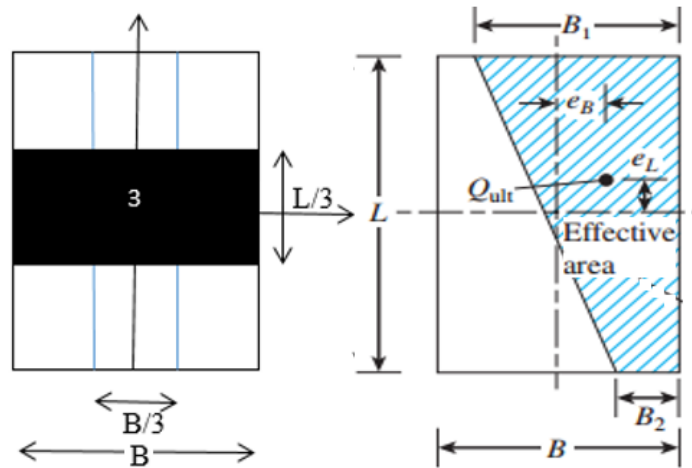
Fig. 5 Resultant load acts in zone 3 (Case 3)

CASE 4: $[(e_L/L) < (1/6)$ and $(e_B/B) < (1/6)]$

As it is seen in Fig. 6, the resultant load acts within the zone 4. The resultant load not always acting within or border line but it might be out of the kern so that minimum bearing pressure might be tension and a gap might occur between the base of foundation and the underlying soil.
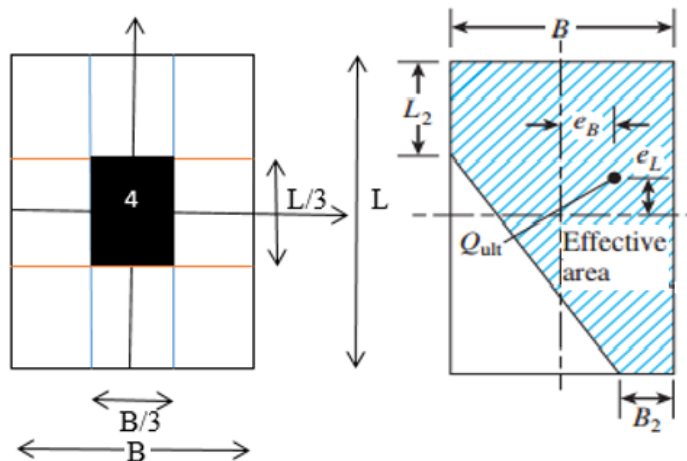
Fig. 6 Resultant load acts in zone 4 (Case 4)

Modified Cases

CASE 1 is not modified so that it will remain as it is. In the modified cases of 2, 3, 4, the resultant load is out of the kern mostly, and it is always out of the kern in case 1. Thus, these cases may be employed for any research or other purposes except the design that would be applied in the field because there would be tension between the base of foundation and underlying soil.

In this study, a new case is defined as _case 5_ (Fig.11) that is actually representing the kern so that case 5 can be used to design foundations that would be applied in the field because the resultant load acts in the kern so that the minimum bearing pressure would be a positive value or at least nil.

Modified CASE 2: Modified and redefined as seen below

[(1/6) < (e_L/L) < 0.5 and 0 < (e_B/B) < (1/6)]. When these ranges are applied to zone 2, it will become as seen in Fig.7. You can see the difference by comparing Figs.4 and 7.
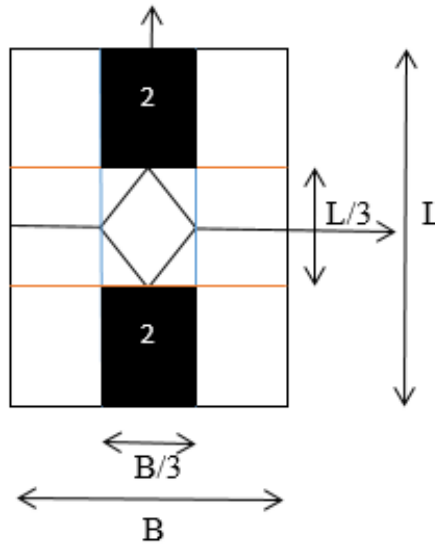
Fig. 7. Zone 2 to after the modification

The dimensions of the effective area seen in Fig. 4b can be calculated by the Eqs. (5 to 9) instead of using the graph generated in the original effective area method.

$$A_o = \frac{B - 6e_B}{B + 6e_B} \tag{5}$$

$$L_1 = \left(\frac{1.5 - 3eL/L}{1 + A_o + A_o^2}\right)(A_o + 1)L \leq L \tag{6}$$

$$L_2 = A_o L_1 \leq L \tag{7}$$

The effective area;

$$A' = \frac{1}{2}(L_1 + L_2)B \tag{8}$$

and the effective width;

$$B' = \frac{A'}{L_1 \, or \, L_2 \, (larger \, one)} \tag{9}$$

Modified CASE 3: Modified and redefined as seen below $[(e_L/L) < (1/6)$ and **(1/6)** $< (e_B/B) \leq 0.5]$.

When these ranges are applied to zone 3, it will become as seen in Fig.8. The difference can be seen by comparing Figs.5 and 8.
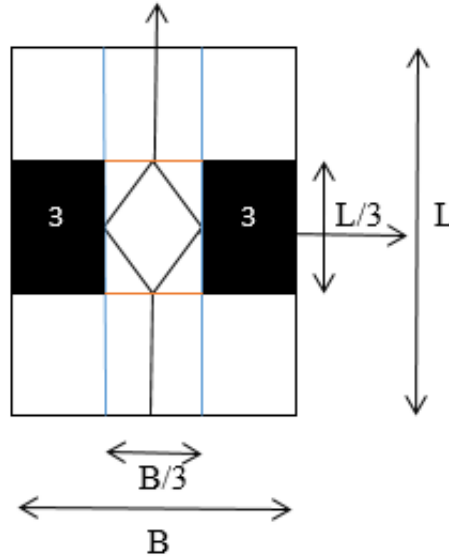
Fig. 8 Zone 3 to after the modification

The dimensions of the effective area seen in Fig. 4b can be calculated by the Eqs. (10 to 14) instead of using the graph generated in the original effective area method.

$$A_1 = \frac{L+6e_L}{L-6e_L} \tag{10}$$

$$B_1 = \left(\frac{1.5-3e_B/B}{1+A_1+A_1^2}\right)(A_1 + 1)B \leq B \tag{11}$$

$$B_2 = A_1 B_1 \leq B \tag{12}$$

The effective area;

$$A' = \frac{1}{2}(B_1 + B_2)L \tag{13}$$

and the effective width:

$$B' = \frac{A'}{L} \tag{14}$$

Modified CASE 4: The four dark triangular zones seen in Fig. 9 represent zone 4. The eccentricity of the resultant load would be within the following borders for this case.

$$e > e_{max}, \text{ and } \frac{e_B}{B} \leq \frac{1}{6} \text{ and } \frac{e_L}{L} \leq \frac{1}{6}$$

where e and e_{max} are calculated from Eqs.(19 & 18), respectively. The effective area and effective width for this case would be calculated just like the procedure given in case 5.
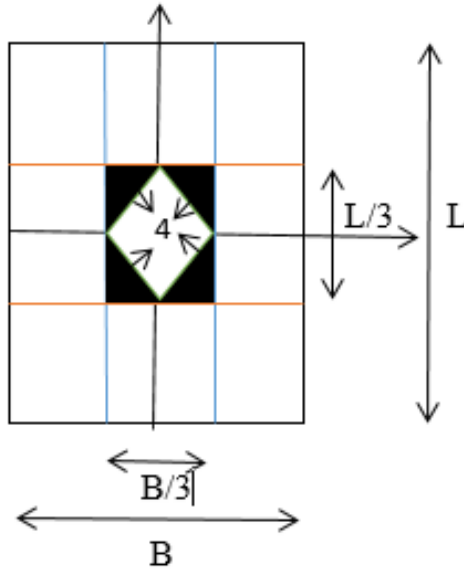
Fig. 9 *Zone 4 to after the modification*

CASE 5 (New): A newly considered case in that only the zone of kern will be considered (see Fig. 10). Two criteria for this zone have been determined by the author and given below. One of the criteria can be employed to determine whether the resultant load is in, on or out of the border line of kern.

Criteria 1:

The kern is seen in Fig, 11a (zone 5), and one of the four parts of the kern is shown in Fig. 11b. To create a criteria that would be employed for the case 5 in the effective area method, the steps are as follows.

1. Find angles ⬜⬜⬜⬜⬜ and⬜⬜ in Fig.11b as seen below.

$$\alpha = tan^{-1}\left(\frac{B}{L}\right) \tag{15}$$

$$\beta = tan^{-1}\left(\frac{e_B}{e_L}\right) \tag{16}$$

$$\gamma = 180 - \alpha - \beta \tag{17}$$
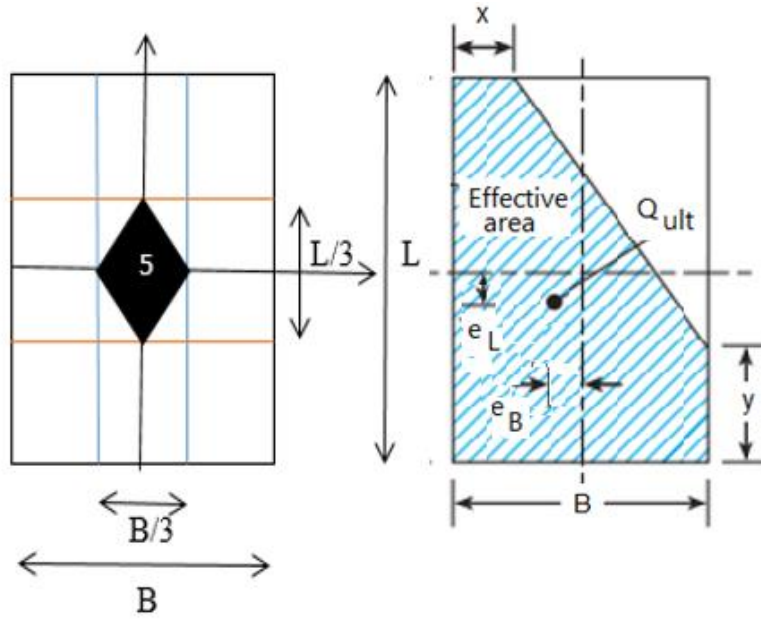
Fig. 10. Zone 5 newly defined
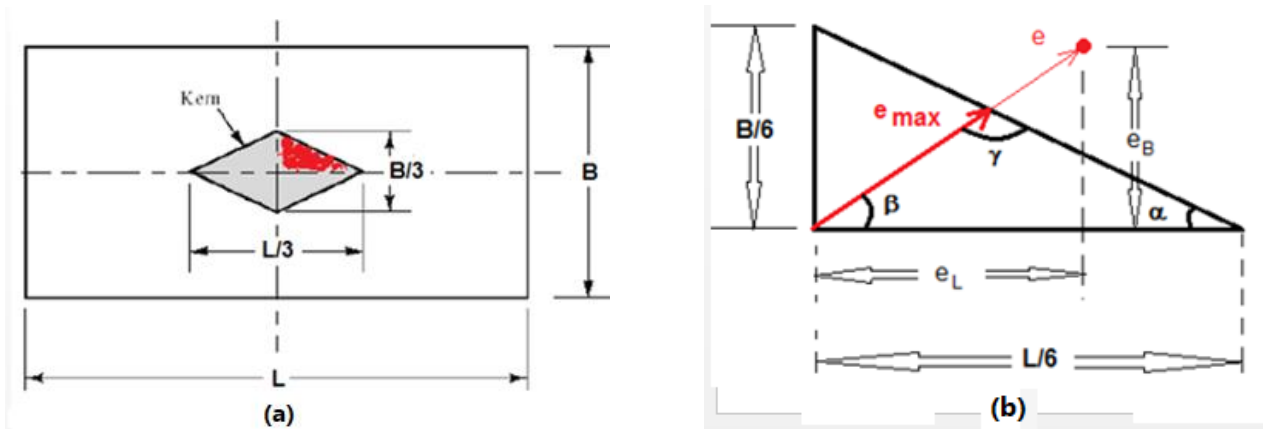
Fig. 11 The value of eccentricities on a foundation

2. Find maximum value of eccentricity within the kern:

$$e_{max} = \frac{sin\alpha}{sin\gamma} \cdot \frac{L}{6} \qquad (18)$$

3. Find the existing eccentricity;

$$e = \sqrt{(e_L^2 + e_B^2)} \qquad (19)$$

Application of resultant load is within the kern if

$e < e_{max}$

Application of resultant load is on the borderline of the kern if

$e = e_{max}$

Application of resultant load is outside of the kern if

$e > e_{max}$

Finally, check the criteria of the modified cases given here. If e is less than or equal to e_{max}, then, employ the procedure for case 5.

Criteria 2:

In order to have the application point of the resultant load within the kern, when the eccentricity on B-direction only, maximum value of $e_B = B/6$, the eccentricity on L-direction must be equal to zero ($e_L = 0$) or wise versa if the eccentricity on L-direction only (see Fig.12).
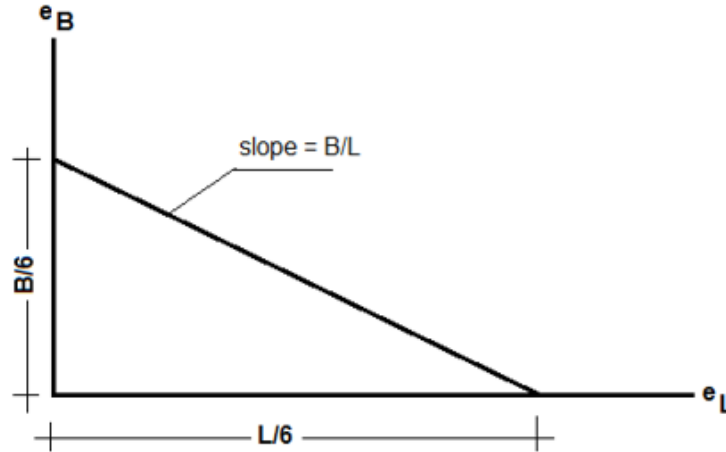
Fig. 12 One fourth of the kern

Thus, the following relationships can be written:

$$\left[0 \leq \frac{e_B}{B} \leq \left(\frac{1}{6} - \frac{e_L}{L}\right)\right] \tag{20}$$

Or

$$\left[0 \leq \frac{e_L}{L} \leq \left(\frac{1}{6} - \frac{e_B}{B}\right)\right] \tag{21}$$

If this is the case of eccentricities, the resultant load acts either in the kern or on the borderline of the kern. If this criterion is not satisfied, it means that the location of resultant load is out of the kern. In this case, minimum value of the bearing pressure would be tension so that the foundations with a tension under it should not be designed in general because there will be a gap between the base of the foundation and soil under lying instead tension stress.

If the resultant load acts in zone 5, which is actually the kern, the shape of the effective area would be similar to one seen in Fig. 13b. Coordinates of the effective area can be located from 0 to 5 that must be numbered clockwise as seen in Fig 13a. The coordinates of the points (0 to 5) are numbered as follows:

$0(x_o,y_o)$, $1(x_1,y_1)$, $2(x_2,y_2)$, $3(x_3,y_3)$, $4(x_4,y_4)$, $5(x_5,y_5)$

Actually, $x_o = x_5$, and $y_o = y_5$. From Fig. 13b:

$0(0,0)$, $1(0, L)$, $2(x, L)$, $3(B, y)$, $4(B,0)$, $5(0,0)$ can be written.
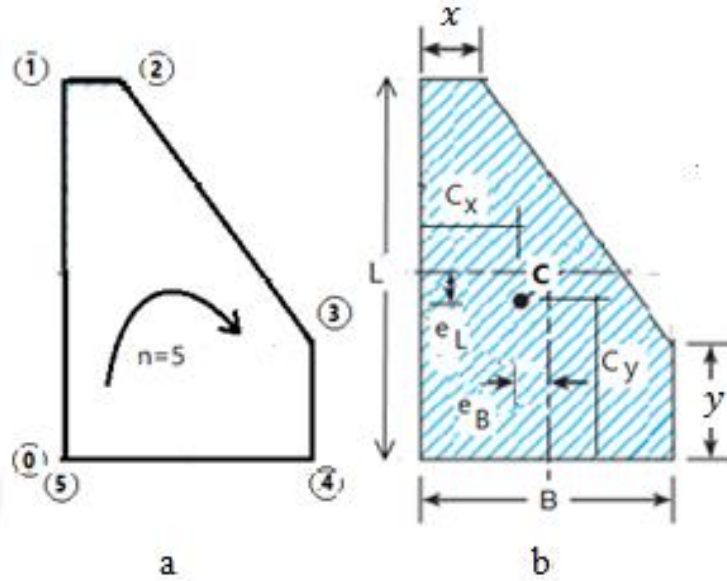
Fig.13 Coordinates of effective area

Coordinates (C_x, and C_y) of the centroid of effective area can be written as follows (see Fig.13b):

$$C_x = \frac{B}{2} - e_B \tag{22}$$

$$C_y = \frac{L}{2} - e_L \tag{23}$$

Also, these coordinates can be written as follows:

$$A = \frac{1}{2}\sum_{i=0}^{n-1}(x_i y_{i+1} - x_{i+1} y_i) \tag{24}$$

$$C_x = \frac{1}{6A}\sum_{i=0}^{n-1}(x_i + x_{i+1})(x_i y_{i+1} - x_{i+1} y_i) \tag{25}$$

$$C_y = \frac{1}{6A}\sum_{i=0}^{n-1}(y_i + y_{i+1})(x_i y_{i+1} - x_{i+1} y_i) \tag{26}$$

The right side of Eq. (25) is equal to the right side of Eq. (20), and Eq.(26) is equal to Eq.(23). Therefore, Eqs. (27) and (28) can be derived as follows:

$$-x^2 L + (x + B)(xy - BL) - 2B^2 y - 3\left(\frac{B}{2} - e_B\right)(-xL + xy - BL - By) = 0 \tag{27}$$

$$2xL^2 + (L + y)(xy - BL) - By^2 - 3\left(\frac{L}{2} - e_L\right)(-xL + xy - BL - By) = 0 \tag{28}$$

Eqs. (27), and (28) can be solved for unknowns of x and y numerically by a proper method. In this study, a MATLAB code has been developed to solve these equations and normalized values are given in Table 1. The effective area can be determined from:

$$A' = \frac{1}{2}(BL + xL + By - xy) \tag{29}$$

Or

$$A' = \frac{1}{2}(B + x)(L - y) + By \tag{30}$$

Or

$$A' = BL - \frac{1}{2}(B - x)(L - y) \tag{31}$$

And the effective width;

$$B' = \frac{A'}{L} \tag{32}$$

Tables 1 and 2 can be used to determine effective area for this case just like newly described case 5.

Table 1. x / B values

eL/L	0.027	0.053	0.080	0.107	0.133	0.160
eB/B	x/B values					
0.02	0.4614					
0.04	0.7380	0.3408	0.0625			
0.06	0.7323	0.5006	0.2389	0.0519		
0.08	0.6966	0.5352	0.3303	0.1491	0.0124	
0.10	0.6539	0.5250	0.3628	0.2027	0.0688	
0.12	0.6090	0.4982	0.3633	0.2244	0.1000	
0.14	0.5636	0.4642	0.3475	0.2259	0.1125	0.0144
0.16	0.5184	0.4272	0.3232	0.2150	0.1120	0.0204

Table 2. y / L values

eL/L	0.027	0.053	0.080	0.107	0.133	0.160
eB/B	y / L values					
0.02	0.7819	0.7823	0.7256	0.6634	0.6006	0.5386
0.04	0.3254	0.6211	0.6249	0.5830	0.5304	0.4747
0.06	0.0477	0.3894	0.4853	0.4812	0.4469	0.4021
0.08		0.1901	0.3303	0.3655	0.3540	0.3232
0.10		0.0167	0.1902	0.2495	0.2584	0.2419
0.12			0.0756	0.1439	0.1667	0.1623
0.14				0.0530	0.0833	0.0879
0.16					0.0100	0.0204

Elastic settlement

It has been a principal issue to estimate the settlement of foundations for civil engineers. Thus, many researchers have studied the problem to get a reliable solution of it. Terzaghi and Peck (1948) proposed an empirical relationship between the settlement (Se) of a prototype foundation measuring B×B in plan and the settlement of a test plate. Bjerrum and Eggestad (1963) provided the results of 14 sets of load settlement tests. Bazaraa (1967) also provided several field tests results. Both gave correlation of settlements between with size of plate used in the tests and size of foundation that would be designed. Jeyapalan and Boehm (1986) and Papadopoulos (1992) summarized the case histories of 79 foundations. DeBeer and Martens (1957) and DeBeer (1965) proposed another formula to estimate the elastic settlement of a foundation. Burland and Burbidge (1985) proposed a method for calculating the elastic settlement of sandy soil using the field standard penetration number N_{60}.

The Schmertmann-Hartman-Brown method (1978) is commonly used for the estimation of elastic (immediate) settlement of shallow foundations. In the procedure on the estimation of immediate settlement, two approaches are used. One for axisymmetric (square and circular foundations) cases, and the other is for plane strain (strip foundations) condition as seen in Fig.14. In case of rectangular foundations, there is an approximation in the method by using both axisymmetric and plane strain conditions.
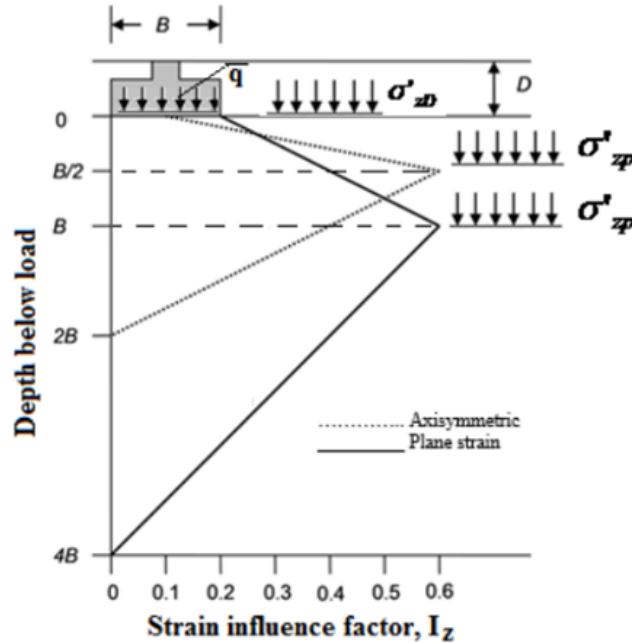
Fig. 14 *Variation of stress influence factors (a) square/circular based and strip foundations (Sschmertmann, 1978), (b) Proposed variation of strain influence factor (u-line) for any shape of shallow foundation.*

Schmertmann – Hartman - Brown Method (1978)

In this method, immediate (or elastic) settlements (S$_e$) of shallow foundations are calculated by Eq. (1) seen below.

$$S_e = C_1 C_2 C_3 \left(q - \sigma'_{zD}\right) \sum_{i=1}^{n} \frac{\Delta z_i I_{zi}}{E_{si}}$$

(33)

Where

$$C_1 = 1 - 0.5 \left(\frac{\sigma'_{zD}}{q - \sigma'_{zD}}\right)$$

(34)

Correction for strain relief due to excavation,

$$C_2 = 1 + 0.2 \log\left(\frac{t}{0.1}\right)$$

(35)

Correction for creep,

114

$$C_3 = 1.03 - 0.03\left(\frac{L}{B}\right) \geq 0.73 \tag{36}$$

q = gross contact pressure of footing,

σ'_{zD} = Effective stress at the base level of footing before the construction

Δz_i = thickness of soil layer i.

Iz_i = strain influence factor of layer i.

Es_i = elasticity modulus of layer i.

B = width of foundation

L = length of foundation

According to Fig.1a, the exact value of Izi at any depth can be determined as follows; For square and circular footings (L/B=1)

$$I_z = 0.1 + \frac{z}{B}(2I_{zp} - 0.2) \quad if \quad \left(0 \leq z \leq \frac{B}{2}\right) \tag{37}$$

$$I_z = 0.667 I_{zp}\left(2 - \frac{z}{B}\right) \quad if \quad \left(\frac{B}{2} \leq z \leq 2B\right) \tag{38}$$

For strip (continuous) footings $\frac{L}{B} \geq 10$

$$I_z = 0.2 + \left(\frac{z}{B}\right)(I_{zp} - 0.2) \quad if \quad (0 \leq z \leq B) \tag{39}$$

$$I_z = 0.333 I_{zp}\left(4 - \frac{z}{B}\right) \quad if \quad (B \leq z \leq 4B) \tag{40}$$

For rectangular footings in which the length is greater than ten times the width, the plane strain approach is used. For rectangular loads in which the length is less than ten times the width, a linear interpolation between the axisymmetric and plane strain case is performed, dependent on the length to width ratio. For the rectangular foundations $\left(1 < \frac{L}{B} \leq 10\right)$

$$I_z = I_{zp} + 0.111(I_{zc} - I_{zs}) * \left(\frac{L}{B} - 1\right) \tag{41}$$

where

I_{zc} = strain influence factor for strip footing that has a width of B,

I_{zs} = strain influence factor for square footing that has a width of B, this value must be at least zero or larger

As it is seen above, the calculations of strain influence factors are complicated and time consuming. To avoid these problems, the method is modified and a procedure much simpler than the original Schmertmann et al. method.

Modification of the Schmertmann-Hartman-Brown (1978) Method

In this paper, the Schmertmann – Hartman - Brown (1978) method is modified by considering boundary conditions of the square/circular (L/B = 1) and strip (L/B > 10) foundations. Equations on the calculation of strain influence factors for any type of shallow foundation such as rectangular, square, circular, strip in Eq. (33) have been re-driven. Thus, the following procedure has been prepared to estimate immediate settlements of any type of shallow foundations. In the modified method, the assumed variation of the strain influence factor is seen in Fig. 15. The user should not be worried about the problem whether it is an axisymmetric or plane strain problem. The data that are needed to be used in the modified method are the size, depth of foundation, load (or bearing pressure), unit weight of soil, number and thickness of soil layers and their modulus of elasticity values under the foundation within the depth of 2B or maximum 4B. The author suggests to users that consider the layers only within the depth of z_{max} that can be calculated by Eq. (18) from the base of foundation.
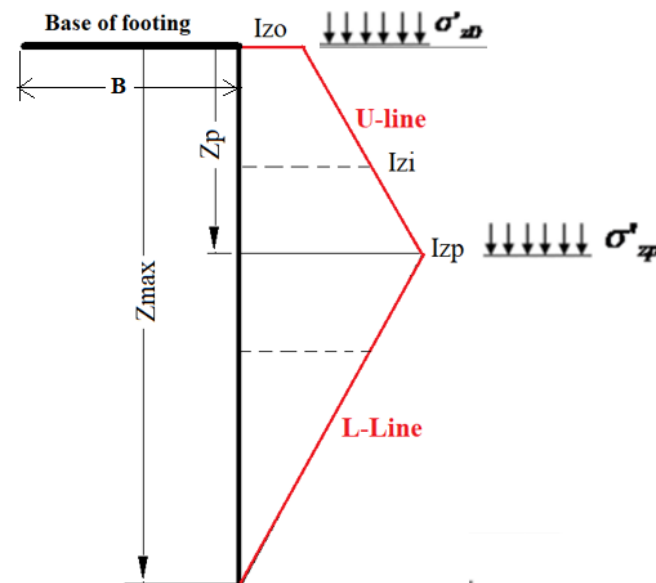
Fig. 15 *Variation of the strain influence factor for any type (square, circular or rectangular) of shallow foundation in the modified method*

Calculation steps of the modified approach for any type of shallow foundations:

1. Calculate the followings:

    1. Total bearing pressure (contact pressure):

$$q = \frac{P + W_f}{A} \tag{42}$$

Where
P = Column load
W_f = Weight of footing
A = Base area of footing (BxL)

2. Effective overburden pressure at the base level of foundation:

$$\sigma'_{ZD} = \gamma D_f - u_D \tag{43}$$

3. Net bearing pressure

$$q_{net} = q - \sigma'_{zD} \tag{44}$$

Where
u_D = pore water pressure at base level of footing

C_1, C_2, and C_3 would be calculated from Eqs. 34, 35, and 36, respectively.

Up to this point, all the procedure and calculations are same as the original method. After this point the modifications would take place.

4. Depth of z_p at which the peak of the strain influence factor (I_{zp}) occurs (see Fig. 15). Its value must be B/2 and B for square/circular based footings and strip footings, respectively. The following equation can be used for any type of shallow foundations to get the depth of which peak strain influence factor occurs.

$$z_p = \left(\frac{L}{B} - 1\right)\frac{B}{18} + \frac{B}{2} \qquad\qquad (B/2) \leq z_p \leq B$$

(45)

As an alternative, Fig. 16 can be used to get z_p value as follows.

$$z_p = B\, Cp \tag{46}$$

Where C_p is a coefficient that can be taken from Fig.16.
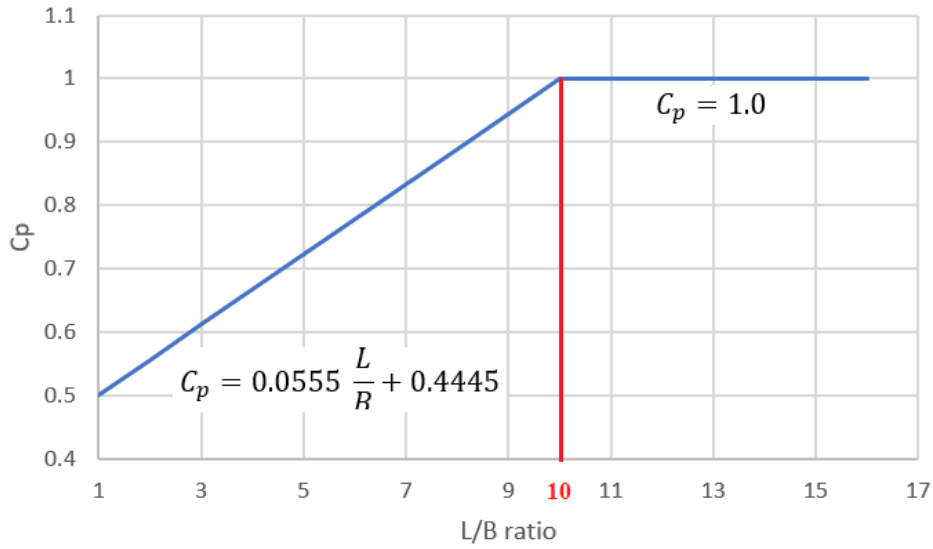
Fig. 16 *C_p-coefficient as a function of L/B ratio*

5. Effective overburden pressure at the depth of z_p. at which peak of strain influence factor takes place:

$$\sigma'_{zp} = z_p \, \gamma' \tag{47}$$

Where
γ' = submerged unit weight of soil

6. The strain influence factor, I_{zo} (at the base of any shape of a shallow foundation) is seen in Eq.16. Its value must be between 0.1 and 0.2 (Fig. 17).

$$I_{zo} = \frac{8}{90} + \frac{1}{90}\left(\frac{L}{B}\right) \qquad\qquad \frac{L}{B} \leq 10 \tag{48}$$

As an alternative, I_{zo} can be taken from Fig.4 as a function of L/B ratio.
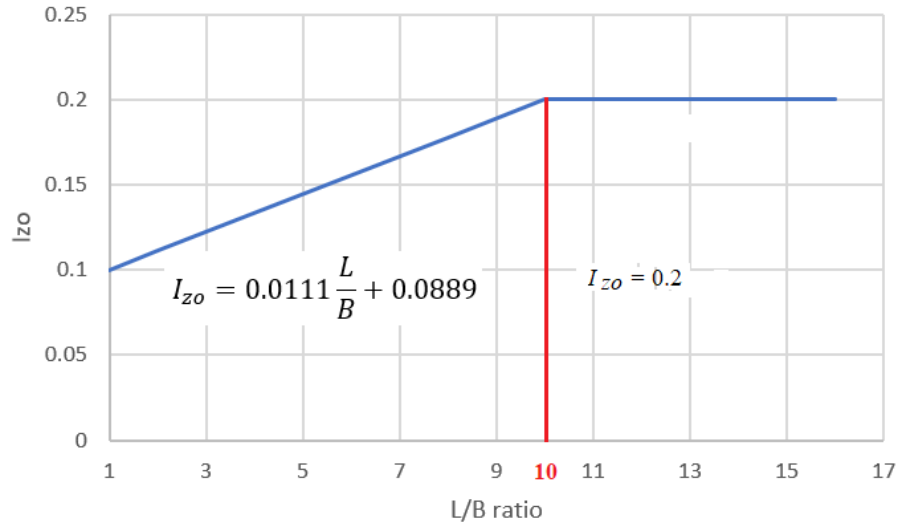
Fig. 17 *Variation of I zo as a function of L/B-ratio*

7. The peak value of strain influence factor same as Schmertmann et all. (1978) method:

$$I_{zp} = 0.5 + 0.1 \sqrt{\frac{q_{net}}{\sigma'_{zp}}} \qquad (49)$$

8. Depth z_{max} at which the strain influence factor would be reduced to zero.

$$z_{max} = \frac{2}{9}L + \frac{16}{9}B \qquad (2B \le z_{max} \le 4B) \qquad (50)$$

As an alternative Fig.5 can be used to get z_{max} value as follows.

$$z_{max} = B \, C_m \qquad (51)$$

Where C_m is a coefficient that can be taken from Fig.18.
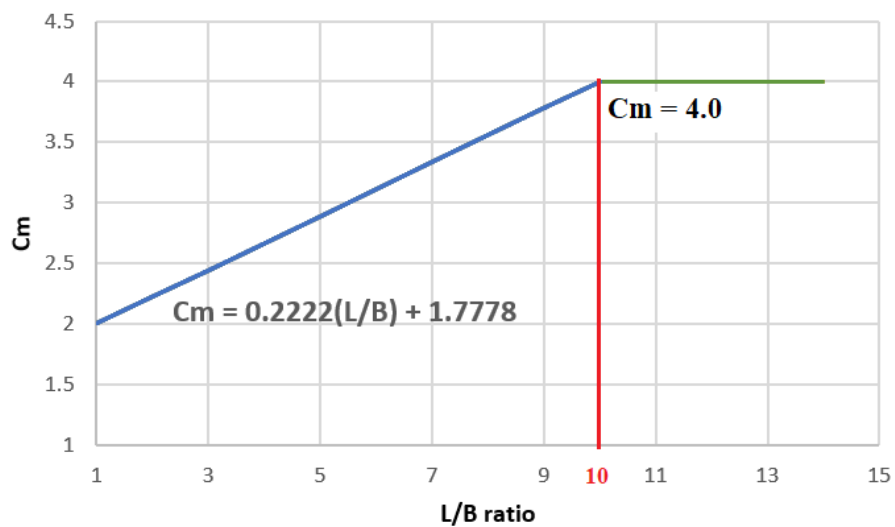
Fig. 18 *Coefficient of Cm as a function of L/B ratio*

9. Calculation of I_{zi} values on U-line in Fig. 15 by Eq. (52)

$$I_{zi} = I_{zo} + \left(\frac{I_{zp} - I_{zo}}{z_p}\right) z_i$$

if $\left(0 \le z_i \le z_p\right)$

(52)

10. Calculation of I_{zi} values on L-line in Fig. 15 by Eq. (53)

$$I_{zi} = I_{zp} - \left(\frac{I_{zp}}{z_{max} - z_p}\right)(z_i - z_p) \qquad \text{if } \left(z_p \le z_i \le z_{max}\right) \qquad (53)$$

2. Modulus of elasticity is estimated by tip resistance, q_c, of Cone Penetration Test, CPT, if E_s values are not known Eq. (54).

$$E_s = q_c \left(2.389 + 0.111\frac{L}{B}\right) \qquad \frac{L}{B} \le 10 \qquad (54)$$

Terzaghi, Peck and Mesri, 1996) suggest using the following equation.

$$\frac{E_{s(L/B)}}{E_{s(L/B=1)}} = 1 + 0.4\log\left(\frac{L}{B}\right) \le 1.4$$

where $E_{s(L/B=1)} = 3.5q_c$

Note: If the modulus of elasticity of soil layers are known, no need the estimation by Eq. (54).

Elastic (immediate) settlement calculation is same as Schmertmann, et all. (1978) method Eq. (1) seen below:

$$S_e = C_1 C_2 C_3 q_{net} \sum_{i=1}^{n} \frac{\Delta z_i I_{zi}}{E_{si}} \qquad (1)$$

Hypothetical Cases:

Once modification of Schmertmann's method was completed, calculations of the elastic (immediate) settlements became quite simple with a simple computer code prepared. Then, the effect of L/B (length/width ratio) and B (width) on elastic settlement is investigated. For the hypothetical case, the foundation and soil profile seen in Fig. 19 are employed.
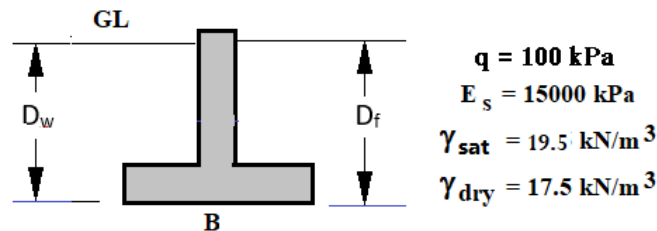
Fig.19 *Soil profile and foundations in hypothetical cases*

The variation of settlements with L/B starting from 1 to 12 for B =1, 3, 5 meters have been estimated by the code and plots are given in Fig. 20. As it is seen in Fig. 7, when L/B is increased, settlement increases too until L/B=10. Then, there is no change on the settlement. Similarly, when B is increased, settlement increases too.
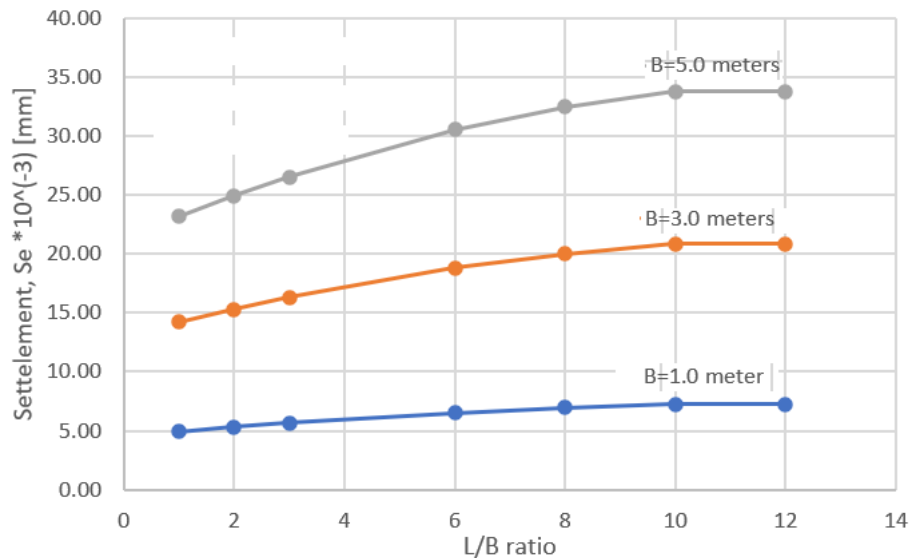
Fig. 20 *Settlement/Width versus L/B ratios*

However, once the settlements are normalized as $\left(\frac{S_e}{B}\right)$, it has been seen that when B is increased, $\left(\frac{S_e}{B}\right)$ ratios are decreased as seen in Fig. 21.

CONCLUSIONS

The following conclusions are drawn after the analytical and numerical work done in this study.

1. Clear borders among the four zones are established without overlaps. That means borders of the zones given in the technical literature are modified.

2. Zone 4 is divided into two. In other words, zone 4 has been modified and a new zone (zone 5) is defined.
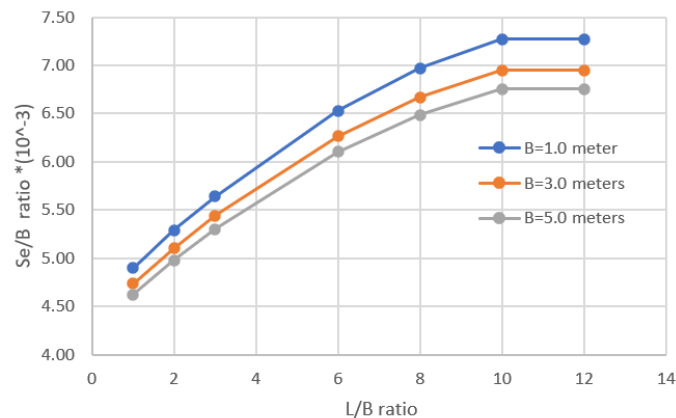
Fig. 21 *Settlement/Width versus L/B ratios*

1.   To check whether the resultant load acts in zone 5 (kern), two more criteria have been derived in addition to one in use.

2.   To calculate the effective areas for the defined five zones, formulas have been derived instead of employing the graphs in calculation of effective areas for all of the cases.

3.   Since the hand solution of formulas for zone 4, and 5 is impossible, a MATLAB code is generated, and the equations are solved. However, any other numerical technique can be employed to solve the equations of (27) and (28).

4.   The Schmertmann, et al (1978) method is modified, and a more convenient approach is proposed, so that there would be no worries about the foundation whether it is ab axisymmetric problem or plain strain problem. Also, only two equations would be employed to calculate the strain influence values in place of five equation in the original method.

5.   The settlements increase from $L/B = 1$ until it is 10, after that ($L/B > 10$) no more settlement would occur.

6.   Settlement/width ratio would be decreasing while the width of footing is increased. This result shows that angular distortion of footings with larger width (B) would be less than the angular distortion of footings with smaller B.

REFERENCES

Badakhshan E, Noorzad A (2017). A simplified method for prediction of ultimate bearing capacity of eccentrically loaded foundation on geogrid reinforced sand bed. International Journal of Geosynthetics and Ground Engineering, 3(2), 1-15.

Bazaraa ARSS (1967). Use of the Standard Penetration Test for Estimating Settlements of Shallow Foundations on Sand. Ph.D. Thesis, University of Illinois, Champaign-Urbana, Illinois.

Bjerrum L, Eggestad A (1963). Interpretation of load test on sand. European Conference on Soil Mechanics and Foundation Engineering, Weisbaden, West Germany, 1, 199.

Burland JB, Burbidge MC (1985). Settlement of foundations on sand and gravel. Institution of Civil Engineers, 78(1), 1325-1381.

Das BM, Atalar C, Shin FC (2009). Developments in elastic settlement estimation procedures for shallow foundations on granular soil. 2nd International Conference on New Developments in Soil Mechanics and Geotechnical Engineering, Near East University, Nicosia, North Cyprus, 9-41.

Das MB (2007). Principles of Foundation Engineering. 6th edition, CENGAGE Learning, Hampshire, UK.

DeBeer E, Martens A (1957). Method of computation of an upper limit for the influence of heterogeneity of sand layers in the settlement of bridges. 4th International Conference on Soil Mechanics and Foundation Engineering, London, 1, 275-281.

DeBeer EE (1965). Bearing capacity and settlement of shallow foundations on sand. Symposium on Bearing Capacity Settlement of Foundations, Duke University, Durham, NC, 15-33.

Higher WH, Anders JC (1985). Dimensioning footings subjected to eccentric loads. Journal of geotechnical engineering. Journal of Geotechnical Engineering, ASCE, 111(5), 659-665.

Jeyapalan JK, Boehm R (1986). Procedures for predicting settlements in sands. In W.O. Martin (ed.), Settlements of Shallow Foundations on Cohesionless Soils: Design and Performance, ASCE, Seattle, 1-22.

Krabbenhoft S, Damkilde L, Krabbenhoft H (2012). Lower-bound calculations of the bearing capacity of eccentrically loaded footings in cohesionless soil. Canadian Geotechnical Journal, 49(3), 298-310.

Loukidis D, Chakrabory T, Salgado R (2008). Bearing capacity of strip footings on purely frictional soil under eccentric and inclined loads. Canadian Geotechnical Journal, 45(6), 768-787.

Meyerhof GG (1953). The bearing capacity of foundations under eccentric and inclined loads. Proceedings, 3rd International Conference on Soil Mechanics and Foundation Engineering, Zurich, Vol. 1, 440-445.

Meyerhof GG (1963). Some recent research on the bearing capacity of foundations. Canadian Geotechnical Journal, 1(1), 16-26.

Papadopoulos BP (1992). Settlements of shallow foundations on cohesionless soils. Journal of Geotechnical Engineering, ASCE, 118(3), 377-393.

Prakash S, Saran S (1971). Bearing capacity of eccentrically loaded footings, Journal of the Soil Mechanics and Foundation Division, ASCE, 97(SM1), 95-117.

Sahu R, Patra CR, Sobhan K, Das BM (2019). Ultimate Bearing Capacity Prediction of Eccentrically Loaded Rectangular Foundation on Reinforced Sand by ANN. In: Meguid M, Guler E, Giroud J (eds) Advances in Geosynthetics Engineering. GeoMEast 2018. Sustainable Civil Infrastructures. Springer, Cham.

Schmertmann JH, Hartman JP, Brown PR (1978). Improved strain influence factor diagrams. Journal of Geotechnical Engineering Division, ASCE, 104(8), 1131-1135.

Terzaghi K (1943). Theoretical Soil Mechanics. Wiley, New York.

Terzaghi K, Peck RB (1948). Soil Mechanics in Engineering Practice. 1st Edition, John Wiley and Sons, New York.

Terzaghi K, Peck RB, Mesri G (1996). Soil Mechanics in Engineering Practice. 3rd Edition, John Wiley & Sons, New York.

Vesic AS (1973). Analysis of ultimate loads of shallow foundations. Journal of the Soil Mechanics and Foundation Division, ASCE, 99(SM1), 45-73

Evidential Fuzzy Multi-Criteria Decision Making Based On Belief Entropy

Galip Cihan YALÇIN[1]

Introduction

The decision-making process is the process of selecting the best alternative by evaluating alternatives according to one or more criteria. The decision maker will need to combine the data at hand while evaluating the alternatives according to the criteria. Data aggregation is the process of obtaining information about different situations or events from various and different data sources and then integrating them from a single data source to reach final results with higher accuracy. In other words, data aggregation is an approach to handle various sources of information that are imperfect in various ways, and ultimately to obtain a clearer view of the situation, thus reducing uncertainty. Much of this data to be combined is uncertain. Common causes of uncertainty are imprecision, randomness and vagueness. We can express the errors arising from the measurements made as the state of being imprecise. The reason for ambiguity is the uncertainties arising from verbal or linguistic expressions such as "good", "bad" during decision making. There are many methods developed to combat situations such as incompleteness, uncertainty and inconsistency that negatively affect the decision-making process. The basis of these methods is Probability Theory, Fuzzy Set Theory and Dempster-Shafer Mathematical Proof Theory. And the main purpose of these methods is to combat the uncertainty in the decision-making process. Among these methods, Fuzzy Set Theory and DST are the strongest theories (Kalcı, 2008). Fuzzy Set Theory helps to select the most appropriate evidence from different sources at different times, while DST helps consolidate evidence for the final assignment process (Chatterjee & Namin, 2021).

Fuzzy sets, rough sets, DST and many similar methods are used to identify information that is currently uncertain. And many of these methods can be translated into a framework on evidence theory. DST stands out because it can better represent information that is uncertain by using basic probability assignment (bpa) and applying uncertainty reasoning. DST not only provides a mathematical framework for modeling uncertainty, but also provides a method of combining data from different sources (Deng, Xiao & Deng, 2017). DST can effectively combine the uncertainty of conflict information, but it still has some shortcomings in conflict between different sources of evidence (Xiong, Su & Qian, 2021). DST offers several advantages, including the ability to transfer probabilistic measures to focal elements and assign probabilistic values to the proof-of-discrimination framework (Chatterjee & Namin, 2021).

Method

DST, which emerged with A.P.Dempster's work on determining the lower and upper limits of probability in 1967, was developed in 1976 with some additions in G.Shafer's book titled Mathematical Theory of Proof. At the beginning of these additions; opinion function (belief function) definition comes. For this reason, the theory was named DST, taking the name of both

[1] PhD. Student, Kirikkale University, Institute of Science and Technology, Mathematics Program, Kirikkale, Turkiye,

fathers of ideas. This theory is a numerical method and was developed to deal with incomplete and uncertain information. DST has successful applications in many areas from artificial intelligence to medical diagnosis, from statistical classification to data fusion, from face identification to risk assessment, from target identification to multi-criteria decision analysis (Çerçioğlu, 2004). DST has been widely studied and applied because of its advantage of effectively handling uncertainty problems in combining multi-source information. Many in-depth studies have been carried out with DST, which is presented as an effective method to solve the uncertainty problem (Zhu & Xiao, 2021).

As an extension of probability theory, proof theory can better handle unknown and imprecise information. Because of its advantages, evidence theory has more flexibility and efficiency for modeling and processing uncertain information. The uncertainty measurement plays an important role in both evidence theory and probability theory. In probability theory, Shannon entropy provides a new perspective for measuring uncertainty. Various entropies are available to measure the uncertainty of the bpa in proof theory (Deng, Xiao & Deng, 2017).

DST is an advanced version of Bayesian probability theory. It has the advantage of showing "uncertainty" by distributing probability to multiple event hypotheses rather than a single event (Zhu & Xiao, 2021). There are some features that distinguish Bayesian inference and DST, which has many common denominators. In Bayesian inference, the weights assigned to the situations are called "probability", while in DST they are called "mass". The most important distinguishing feature is; In DST, there is no obligation to give a clear value to the variables as in Bayesian inference. For example, in Bayesian inference, everything takes a net value such as "0" and "1", "black" and "white", while in DST it can take any value between 0 and 1 (Seçkin, 2015).

If Θ is a set containing all possible possible values of a variable and the elements in Θ are mutually exclusive, then Θ is referred to as the perceptual frame (Xiong, Su & Qian, 2021).

Considering Θ ($\Theta = \{A_1, A_2, \ldots, A_i, \ldots, A_N\}$) as the frame of discernment and 2^Θ ($2^\Theta = \{\emptyset, \{A_1\}, \{A_2\}, \ldots, \{A_N\}, \{A_1, A_2\}, \ldots, \{A_1, A_2, \ldots, A_i\}, \ldots, \Theta\}$) as all subsets of Θ, the function in $m: 2^\Theta \to [0,1]$ format is a bpa function if the following conditions are met (Büyükyazıcı & Sucu, 2009):

$$m(\emptyset) = 0$$

$$\sum_{x \in 2^\Theta} m(x) = 1$$

We can define the values of the bpa function here as the probabilities of each element in the frame of discernment Θ. The function m is called the function bpa and $m(x)$ is called the fundamental probability of x (Xiong, Su & Qian, 2021).

When x is treated as any subset of Θ and the fundamental probability value is different from 0, x is a focal element (Xiong, Su & Qian, 2021). The value received for any focus element belonging to the belief function is called the degree of belief (Büyükyazıcı & Sucu, 2009).

There are two confidence criteria: the belief function (bel) and the plausibility (pls) function. As the first confidence criterion, the one-to-one opinion function is defined as $bel: 2^\Theta \to [0,1]$

and this value is obtained from the sums of the propositions in question (Beynon, Curry & Morgan, 2000).

$$bel\,(A) = \sum_{B \subseteq A} m(B), \qquad \forall A \subseteq \Theta$$

Another of the confidence criteria, the one-to-one plausibility (pls) function, is defined as $pls: 2^{\Theta} \rightarrow [0,1]$.

$$pls\,(A) = 1 - bel(\bar{B}) = \sum_{B \cap A \neq \emptyset} m(B), \qquad \forall A \subseteq \Theta$$

bel(A) and pls(A) are lower and upper limits of function A. The lower limit indicates the degree of support for the hypothesis, and the upper limit indicates the maximum degree of support expected to be assigned to the hypothesis (Xiao, 2020).

The relationships between the variables whose mass values are observed and their relationships with the values obtained from previous observations are made using Dempster's rule of combination (Çavdur, 2005). Information obtained from different information sources can be easily combined with the Dempster's rule of combination (Xiong, Su & Qian, 2021).

When the independent evidence sources m_1 and m_2 are combined, the $m = m_1 \oplus m_2: 2^{\Theta} \rightarrow [0,1]$ toa function is obtained (Xiao, 2020). The $\oplus$ operator has commutation and union properties (Tong, Xu & Denœux, 2021).

$$m(A) = \begin{cases} \mathbf{0} & A = \emptyset \\ \dfrac{\sum_{B,C \in 2^{\Theta} | B \cap C = A} m_1(B)m_2(C)}{1 - K} & A \neq \emptyset \end{cases}$$

Here K can be expressed as the conflict coefficient (amount of conflict) between m_1 and m_2 and is calculated with the help of the following formula:

$$K = \sum_{B,C \in 2^{\Theta} | B \cap C = \emptyset} m_1(B)m_2(C)$$

The operations in the DST method are shown below step by step:

Step-1: Alternatives are given values in line with the verbal expressions shown below by the decision makers (Shemshadi et al., 2011):

Table 1. Linguistic variables for the fuzzy rates of the alternatives

Linguistic Variables	Abbreviations	Fuzzy Number Values
Very Poor	VP	(0.0, 0.0, 0.1, 0.2)
Poor	P	(0.1, 0.2, 0.2, 0.3)
Medium Poor	MP	(0.2, 0.3, 0.4, 0.5)
Fair	F	(0.4, 0.5, 0.5, 0.6)
Medium Good	MG	(0.5, 0.6, 0.7, 0.8)
Good	G	(0.7, 0.8, 0.8, 0.9)
Very Good	VG	(0.8, 0.9, 1.0, 1.0)

Step-2: A decision matrix is created by assigning fuzzy number values to linguistic variables.

Step-3: The decision matrix of the criteria is created.

$$W = [w_1 \ldots w_j \ldots w_n]$$

In addition, the decision matrix containing the values taken by the $i\,th$ alternative according to the $j\,th$ criterion is prepared by the $k\,th$ decision maker.

$$\tilde{X}_k = \begin{bmatrix} \tilde{x}_{11k} & \cdots & \tilde{x}_{1jk} & \cdots & \tilde{x}_{1nk} \\ \vdots & \cdots & \vdots & \cdots & \vdots \\ \tilde{x}_{i1k} & \cdots & \tilde{x}_{ijk} & \cdots & \tilde{x}_{ink} \\ \vdots & \cdots & \vdots & \cdots & \vdots \\ \tilde{x}_{m1k} & \cdots & \tilde{x}_{mjk} & \cdots & \tilde{x}_{mnk} \end{bmatrix}$$

Step-4: The elements of the weighted decision matrix are calculated with the following formulas

$$x_{ijk1}^w = x_{ijk1} * w_j$$

$$x_{ijk2}^w = x_{ijk2} * w_j$$

$$x_{ijk3}^w = x_{ijk3} * w_j$$

$$x_{ijk4}^w = x_{ijk4} * w_j$$

The weighted decision matrix is created as follows:

$$\tilde{D}_k = \begin{bmatrix} \tilde{x}_{11k}^w & \cdots & \tilde{x}_{1jk}^w & \cdots & \tilde{x}_{1nk}^w \\ \vdots & \cdots & \vdots & \cdots & \vdots \\ \tilde{x}_{i1k}^w & \cdots & \tilde{x}_{ijk}^w & \cdots & \tilde{x}_{ink}^w \\ \vdots & \cdots & \vdots & \cdots & \vdots \\ \tilde{x}_{m1k}^w & \cdots & \tilde{x}_{mjk}^w & \cdots & \tilde{x}_{mnk}^w \end{bmatrix}$$

Step-5: Aggregated weighted decision matrix elements are calculated with the following formulas.

$$x_{ij1}^{w} = min_k\{x_{ijk1}^{w}\}$$

$$x_{ij2}^{w} = \frac{1}{t}\sum_{k=1}^{t} x_{ijk2}^{w}$$

$$x_{ij3}^{w} = \frac{1}{t}\sum_{k=1}^{t} x_{ijk3}^{w}$$

$$x_{ij4}^{w} = max_k\{x_{ijk4}^{w}\}$$

The aggregated weighted decision matrix is created as follows:

$$\widetilde{D} = \begin{bmatrix} \tilde{x}_{11}^{w} & \cdots & \tilde{x}_{1j}^{w} & \cdots & \tilde{x}_{1n}^{w} \\ \vdots & \cdots & \vdots & \cdots & \vdots \\ \tilde{x}_{i1}^{w} & \cdots & \tilde{x}_{ij}^{w} & \cdots & \tilde{x}_{in}^{w} \\ \vdots & \cdots & \vdots & \cdots & \vdots \\ \tilde{x}_{m1}^{w} & \cdots & \tilde{x}_{mj}^{w} & \cdots & \tilde{x}_{mn}^{w} \end{bmatrix}$$

Step-6: Combined fuzzy values are calculated separately for benefit and cost criteria. For this, the following formula is used:

$$x_{ij4}^{w+} = \max_i\{x_{ij4}^{w}\} \text{ , for benefit criteria } (BC_j)$$

$$x_{ij1}^{w-} = \min_i\{x_{ij1}^{w}\} \text{ , for cost criteria } (CC_j)$$

$$\bar{\tilde{x}}_{ij}^{w} = \begin{cases} \left(\frac{x_{ij1}^{w}}{x_{ij4}^{w+}}, \frac{x_{ij2}^{w}}{x_{ij4}^{w+}}, \frac{x_{ij3}^{w}}{x_{ij4}^{w+}}, \frac{x_{ij4}^{w}}{x_{ij4}^{w+}}\right), for\ BC_j \\ \left(\frac{x_{ij1}^{w}}{x_{ij1}^{w-}}, \frac{x_{ij2}^{w}}{x_{ij1}^{w-}}, \frac{x_{ij3}^{w}}{x_{ij1}^{w-}}, \frac{x_{ij4}^{w}}{x_{ij1}^{w-}}\right), for\ CC_j \end{cases}$$

The normalized aggregated weighted decision matrix is created as follows:

$$\overline{\overline{D}} = \begin{bmatrix} \bar{\tilde{x}}_{11}^{w} & \cdots & \bar{\tilde{x}}_{1j}^{w} & \cdots & \bar{\tilde{x}}_{1n}^{w} \\ \vdots & \cdots & \vdots & \cdots & \vdots \\ \bar{\tilde{x}}_{i1}^{w} & \cdots & \bar{\tilde{x}}_{ij}^{w} & \cdots & \bar{\tilde{x}}_{in}^{w} \\ \vdots & \cdots & \vdots & \cdots & \vdots \\ \bar{\tilde{x}}_{m1}^{w} & \cdots & \bar{\tilde{x}}_{mj}^{w} & \cdots & \bar{\tilde{x}}_{mn}^{w} \end{bmatrix}$$

Step-7: The elements of the normalized aggregated decision matrix are calculated with the help of the following formula:

$$Def\left(\bar{\bar{x}}_{ij}^{w}\right) = \frac{\int \mu(x)xdx}{\int \mu(x)dx} = \frac{\int_{\bar{x}_{ij1}^{w}}^{\bar{x}_{ij2}^{w}}\left(\frac{x-\bar{x}_{ij1}^{w}}{\bar{x}_{ij2}^{w}-\bar{x}_{ij1}^{w}}\right).xdx+\int_{\bar{x}_{ij2}^{w}}^{\bar{x}_{ij3}^{w}} xdx+\int_{\bar{x}_{ij3}^{w}}^{\bar{x}_{ij4}^{w}}\left(\frac{\bar{x}_{ij4}^{w}-x}{\bar{x}_{ij4}^{w}-\bar{x}_{ij3}^{w}}\right).xdx}{\int_{\bar{x}_{ij1}^{w}}^{\bar{x}_{ij2}^{w}}\left(\frac{x-\bar{x}_{ij1}^{w}}{\bar{x}_{ij2}^{w}-\bar{x}_{ij1}^{w}}\right)dx+\int_{\bar{x}_{ij2}^{w}}^{\bar{x}_{ij3}^{w}} dx+\int_{\bar{x}_{ij3}^{w}}^{\bar{x}_{ij4}^{w}}\left(\frac{\bar{x}_{ij4}^{w}-x}{\bar{x}_{ij4}^{w}-\bar{x}_{ij3}^{w}}\right)dx} =$$

$$\frac{-\bar{x}_{ij1}^{w}\bar{x}_{ij2}^{w}+\bar{x}_{ij3}^{w}\bar{x}_{ij4}^{w}+\frac{1}{3}\left(\bar{x}_{ij4}^{w}-\bar{x}_{ij3}^{w}\right)^{2}-\frac{1}{3}\left(\bar{x}_{ij2}^{w}-\bar{x}_{ij1}^{w}\right)^{2}}{-\bar{x}_{ij1}^{w}-\bar{x}_{ij2}^{w}+\bar{x}_{ij3}^{w}+\bar{x}_{ij4}^{w}}$$

The normalized aggregated decision matrix is created as follows:

$$Def\left(\bar{\bar{D}}\right) = \begin{bmatrix} Def(\bar{\bar{x}}_{11}^{w}) & \cdots & Def(\bar{\bar{x}}_{1j}^{w}) & \cdots & Def(\bar{\bar{x}}_{1n}^{w}) \\ \vdots & \cdots & \vdots & \cdots & \vdots \\ Def(\bar{\bar{x}}_{i1}^{w}) & \cdots & Def(\bar{\bar{x}}_{ij}^{w}) & \ldots & Def(\bar{\bar{x}}_{in}^{w}) \\ \vdots & \cdots & \vdots & \cdots & \vdots \\ Def(\bar{\bar{x}}_{m1}^{w}) & \cdots & Def(\bar{\bar{x}}_{mj}^{w}) & \ldots & Def(\bar{\bar{x}}_{mn}^{w}) \end{bmatrix}$$

Step-8: The defuzzification process is performed by applying the following procedure to the normalized aggregated decision matrix elements:

$$\overline{Def}\left(\bar{\bar{x}}_{ij}^{w}\right) = \frac{Def\left(\bar{\bar{x}}_{ij}^{w}\right)}{\sum_{s=1}^{m} Def\left(\bar{\bar{x}}_{sj}^{w}\right)}, \ j = 1, 2, \ldots, n$$

The defuzzified matrix is created as follows:

$$\overline{Def}\left(\bar{\bar{D}}\right) = \begin{bmatrix} \overline{Def}(\bar{\bar{x}}_{11}^{w}) & \cdots & \overline{Def}(\bar{\bar{x}}_{1j}^{w}) & \cdots & \overline{Def}(\bar{\bar{x}}_{1n}^{w}) \\ \vdots & \cdots & \vdots & \cdots & \vdots \\ \overline{Def}(\bar{\bar{x}}_{i1}^{w}) & \cdots & \overline{Def}(\bar{\bar{x}}_{ij}^{w}) & \ldots & \overline{Def}(\bar{\bar{x}}_{in}^{w}) \\ \vdots & \cdots & \vdots & \cdots & \vdots \\ \overline{Def}(\bar{\bar{x}}_{m1}^{w}) & \cdots & \overline{Def}(\bar{\bar{x}}_{mj}^{w}) & \ldots & \overline{Def}(\bar{\bar{x}}_{mn}^{w}) \end{bmatrix}$$

To calculate the degree of uncertainty of the criteria;

Step-9: The belief entropy $(E_d(C_j))$ of the C_j $(j = 1, 2, \ldots, n)$ criterion is calculated with the following formula (Kang & Deng, 2016):

$$E_d(C_j) = - \sum_{i=1}^{m} \overline{Def}\left(\tilde{x}_{ij}\right) log \frac{\overline{Def}(\tilde{x}_{ij})}{2^{|A_i|}-1}$$

As a result of applying the following procedure to the calculated belief entropy, the uncertainty degree of the criterion is calculated:

$$U\left(C_j\right) = e^{E_d(C_j)} = e^{- \sum_{i=1}^{m} \overline{Def}(\tilde{x}_{ij}) log \frac{\overline{Def}(\tilde{x}_{ij})}{2^{|A_i|}-1}}$$

Step-10: The degree of uncertainty of the C_j criterion is normalized with the help of the following formula:

$$\bar{U}\left(C_j\right) = \frac{U(C_j)}{\sum_{h=1}^{n} U_h}, \ j = 1, 2, \ldots, n$$

Step-11: In terms of C_j criterion, the bpa value of A_i alternative is calculated with the help of the following formula (Sun, Li & Deng 2020):

$$m_{C_j}(\emptyset) = 0$$

$$m_{C_j}(A_i) = \overline{Def}\left(\bar{\tilde{x}}_{ij}^w\right) * (1 - \overline{U}_j)$$

$$m_{C_j}(\Theta) = 1 - \sum_{i=1}^m m_{C_j}(A_i), i = 1, 2, \dots, m; j = 1, 2, \dots, n$$

Step-12: Multiple proofs are combined with Dempster's rule of combination as follows:

$$m_C = \left(\left(m_{C_1} \oplus m_{C_2}\right)_1 \oplus \dots \oplus m_{C_n}\right)_{(n-1)}$$

Thus, it returns the belief (confidence) values of the $A_i (i = 1, 2, \dots, m)$ alternatives in terms of the C_j criterion:

$$Bel(A_i) = m_C(A_i)$$

Step-13: A_i alternatives are ranked according to their belief (confidence) values and thus the best alternative is decided:

$$\propto = \operatorname*{argmax}_{1 \leq i \leq m}\{Bel(A_i)\}$$

Conclusions

In this study, a new method has been described and a different perspective has been brought to multi-criteria decision making methods. The weights of the criteria were determined by the entropy method. The alternatives were listed by evaluating the criteria for each alternative by the decision makers. The values expressed verbally by the decision makers were converted into numerical values and the alternative ordering process was facilitated. This method, which was put forward to combat uncertainty, is preferred more than many multi-criteria decision-making methods because of its superior features.

References

Beynon, M., Curry, B., & Morgan, P. (2000). The Dempster–Shafer theory of evidence: an alternative approach to multicriteria decision modelling. *Omega*, *28*(1), 37-50. doi: https://doi.org/10.1016/S0305-0483(99)00033-X.

Büyükyazıcı, M., & Sucu, M. (2009). Matematiksel kanıt kuramı'nda uzlaşma üretici yöntemler için bir çerçeve. *İstatistikçiler Dergisi: İstatistik ve Aktüerya*, *2*(1), 19-27.

Chatterjee, M., & Namin, A. S. (2021). A fuzzy Dempster–Shafer classifier for detecting Web spams. *Journal of Information Security and Applications*, *59*, 102793. doi:10.1016/j.jisa.2021.102793.

Çavdur, F. (2005) Arama Motorları Kullanıcı Oturumlarındaki Konu Değişikliklerinin Tespit ve Tahmin Yöntemleri. Master's Thesis. *Uludağ Üniversitesi Fen Bilimleri Enstitüsü*, Bursa.

Çerçioğlu, H. (2004). Dempster Shafer Teorisi Kullanılarak Tedarikçi Seçimi Uzman sistemi Uygulaması. Master's Thesis. *İstanbul Teknik Üniversitesi Fen Bilimleri Enstitüsü*, İstanbul.

Deng, X., Xiao, F., & Deng, Y. (2017). An improved distance-based total uncertainty measure in belief function theory. *Applied Intelligence*, *46*(4), 898-915. doi: https://doi.org/10.1007/s10489-016-0870-3.

Kalcı, K. (2008). Gemi Savunma Sistemlerinde Tehdit Değerlendirme ve Silah Atama Uygulamaları. Master's Thesis. *Ankara Üniversitesi Fen Bilimleri Enstitüsü*, Ankara.

Kang, B., & Deng, Y. (2019). The maximum Deng entropy. *IEEE Access*, *7*, 120758-120765. **doi:** 10.1109/ACCESS.2019.2937679.

Seçkin, F. (2015). Sürdürülebilir Tedarik Zinciri Yönteminde Alıcı-Tedarikçi Regresyon Seviyelerinin Değerlendirme Kriterlerinin Formülasyonuna Yönelik Bir Model Geliştirilmesi. PhD Thesis. *Hava Harp Okulu Havacılık ve Uzay Teknolojileri Enstitüsü*, İstanbul.

Shemshadi, A., Shirazi, H., Toreihi, M., & Tarokh, M. J. (2011). A fuzzy VIKOR method for supplier selection based on entropy measure for objective weighting. *Expert systems with applications*, *38*(10), 12160-12167. doi: 10.1016/j.eswa.2011.03.027.

Sun, C., Li, S., & Deng, Y. (2020). Determining weights in multi-criteria decision making based on negation of probability distribution under uncertain environment. *Mathematics*, *8*(2), 191. doi: https://doi.org/10.3390/math8020191.

Tong, Z., Xu, P., & Denoeux, T. (2021). An evidential classifier based on Dempster-Shafer theory and deep learning. *Neurocomputing*, *450*, 275-293. doi: 10.1016/j.neucom.2021.03.066.

Xiao, F. (2019). EFMCDM: Evidential fuzzy multicriteria decision making based on belief entropy. *IEEE Transactions on Fuzzy Systems*, *28*(7), 1477-1491. doi: 10.1109/TFUZZ.2019.2936368.

Xiong, L., Su, X., & Qian, H. (2021). Conflicting evidence combination from the perspective of networks. *Information Sciences*, *580*, 408-418. doi: https://doi.org/10.1016/j.ins.2021.08.088.

Zhu, C., & Xiao, F. (2021). A belief Hellinger distance for D–S evidence theory and its application in pattern recognition. *Engineering Applications of Artificial Intelligence*, *106*, 104452. doi: https://doi.org/10.1016/j.engappai.2021.104452.

Pandemics

Cihat Furkan Göv[1]
Hulya Celik[2]

INTRODUCTION

The emergence and spread of infectious diseases with pandemic potential has occurred regularly throughout history. Many infectious diseases that lead to pandemics are caused by zoonotic pathogens transmitted to humans due to increased contacts with animals through breeding, hunting and global trade activities. Understanding the mechanisms of transmission of pathogens to humans allowed the creation of methods of preventing and controlling infections. For centuries, the implementation of public health measures such as isolation, quarantine and border control have helped control the spread of infectious diseases and maintain the community structure. Global friction programs of waterborne pathogens, vector-borne diseases and zoonotic spreads in the animal-human interface are of primary importance for rapidly detecting the emergence of infectious threats. In the event of a pandemic, new technologies are needed for rapid diagnostic tests, contact monitoring, reuse of drugs, biological markers of disease severity, and new platforms for the development and production of vaccines. In this research project, we review the major pandemics that have affected humanity throughout history, such as plague, cholera, influenza and coronavirus diseases, how they were contained in the past and how these diseases are managed today.

Virüs

The virus is a small agent that causes infection with only one of the deoxyribo nucleic acid or ribonucleic acids packaged in the protective sheath, which consists of a protein or complex structure. Viruses are not considered alive because they need host cells to grow and multiply. Since viruses do not independently have proliferation mechanisms and molecules, they depend on host cells for reproduction and are considered parasitic cells. Viruses often have a limited host range that they can infect, and viruses can only infect certain bacteria, plants or animals. Viruses depend on the metabolic molecules of the host cell. Viruses alter the host's normal metabolic reactions, allowing new virus particles to form. In order for viruses to survive, they must infect a cell and synthesize their own viral proteins and genetic material by capturing the mechanisms of the cell (Takz,2019).

---

[1] Ağrı Ibrahim Cecen University, Faculty of Pharmacy Basic Pharmaceutical Sciences Department / Fundamental Sciences of Pharmacy 03200 Agri/TURKEY
[2] Ağrı Ibrahim Cecen University, Faculty of Pharmacy Basic Pharmaceutical Sciences Department / Fundamental Sciences of Pharmacy 03200 Agri/TURKEY

Ways Viruses Are Transmitted

-Direct contact

-Injection of blood or contaminated liquids

-Tissue transplants

-Respiratory tract

-Fecal-oral pathway

Factors Affecting The Ways Viruses Are Transmitted

-Source of the virus

-Resilience of the virus

-Environmental conditions

-How the virus reaches the target tissues of the body (Basustaoglu,2010).

Proliferation of Viruses

When viruses encounter a host cell that can multiply by entering the body of the living creature, they activate their proliferation mechanisms. When the virus encounters a suitable host cell where it can multiply, it immediately clings to it. After viruses cling to the host cell, certain enzymes are used to break down the cell membrane and transfer genetic material into the cell. This genetic material can be a chain of ribonucleic acid or deoxyribonucleic acid, which contains information that provides the synthesis of proteins necessary to initiate the process of developing new viruses. The genetic material of the virus captures the mechanisms of the cell through enzymes belonging to the virus. The mechanisms of the cell are used to create new genetic material belonging to the virus and to create protein sheaths. New viruses in the cell usually come out when the cell breaks down. When the cell disintegrates, the cell dies. This cycle, which viruses use to multiply and cause the cell to die, is called a lytic (disruptive) cycle.

Viruses with membranes on protein bristles do not choose the way to break down the body in order to multiply. Unlike other viruses, such viruses pass through the cell membrane and enter the cell. These viruses, which enter the cell as a whole, multiply and then come out without breaking down the cell. Once the virus enters the cell, it stores its genetic material as part of the cell deoxyribonucleic acid. In this way, the virus continues to transfer genetic material to the baby cells every time the cell multiplies without revealing its presence to the cell. It can secretly transfer the genetic material of the virus from cell to cell without causing any signs of disease, and suddenly the virus starts the cycle of proliferation. This cycle is called the lysogenic cycle (Freudenric and Kiger 2020).

Pandemi

The word pandemic is derived from the ancient Greek words pan and demos, and 'pan' means 'demos' and people mean (Pandemic). Wikipedia, free encyclopedia,2022).

The effect is not a specific country or region; Infectious diseases that are effective all over the world are called pandemics. According to the World Health Organization, the pandemic is a rapidly spreading and unseasonal infectious disease in which the human population does not have immunological resistance (Qiu et al.2017).

General Characteristics of Pandemics

- Appearance in various geographical areas

- The emergence of many diseases that can be a precursor to infectious diseases

- Caused by mutated viruses

- Inadequate or no social immunity

- Formation of diseases resulting in death

- Causing changes and measures in the lifestyles of society

- Spreading without seasonal conditions (Özkoçak et al. 2020).

Major Pandemics in Human History

Amvâs Tâ:

The plague, which occurred in the Palestinian settlement of Amvâs during the reign of Omar, spread rapidly and was also seen in the territory of Syria and Iraq. Syria was the most common settlement of the epidemic.

The plague of cucumbers spreading in Amvâs is the most common of the plague species. It is defined by the Arabs as a blessing.

Since it appeared in Amvâs, the epidemic was called Amvâs tuânu.

There are three types of this plague, bubonic, septicaemia and pneumonic, caused by a bacterium called Yersinia pestis, which passes from one rodent infected with fleas to another. Tâun is a bubonic species also known as cucumber, which is one of the plague species.

The bacterium pestis, which enters the human body with the bite of fleas, causes the lymph node to become inflamed and stretched.

In the later stage of the disease, with the growth of lymph nodes, inflamed and severe pain-causing bulges appear in the body

Swelling is more common in the armpits, behind the ear, earlobe and groin areas where the skin is thin in the body

Swellings can be red, yellow, black in color. In the mildest type of the disease, the silus is red in color. With the increase in disease severity, the swellings turn yellow and then black.

In the Middle Ages, medical examiners did not know much about the treatment of taun disease. If the swellings in the bodies of those infected with Taun's disease spontaneously exploded

without intervention and the blood and pus in the boil emptied out, the patient had a chance of recovery. Otherwise, patients usually die within three days.

According to the imam shafi, he thought that the patient would be healthy by applying the ointment obtained by crushing the violet flower in the treatment of taun disease or by boiling the violet and containing it in the patient (Genghis,2020).

Black Plague

The disease was seen between 1347 and 1351. The disease is called black plague because of the appearance of black swelling in the body (Glitter, 2020).

Yersinia pesticide is the cause of the plague epidemic that has killed many people in Europe (Jarus,2020).

Doctors who treated the plague also wore some special costumes. The protective costume consisted of a polished fabric coat, a beak-shaped mouthpiece usually filled with herbs, straw and spices, and a mask with a glass eye part. These doctors studied ways to treat blood draw, frog or leech (Byfield, 2010).

Cholera

Cholera is an infection whose factor is Vibrio Cholerae, which causes the body to lose high rates of water, showing signs of diarrhoea that starts suddenly and suddenly intensifies. When the bacteria, which is resistant to stomach acid, is taken into the body at high rates with liquid, the bacteria escapes stomach acid and reaches the intestines, causing infection (Undored and Altinbas 2020).

The outbreak was seen in Japan in 1817, Moscow in 1826, Berlin in 1831, Paris and London, Hamburg in 1892 and Canada. Many people have lost their lives in these outbreaks. Treatment for cholera, which has a high mortality rate, is quite simple.

Cholera patients recover in a short time with oral fluid treatment. Salt and glucose mixtures are given to eliminate the lack of electrolytes such as sodium, potassium, chlorine and bicarbonate lost in the treatment and to provide the necessary energy in patients with nutritional problems. In patients whose condition is too severe to meet the nutritional needs, the mixture is applied into the vein. In even more serious and urgent cases, tetracycline and tetracycline-like antibiotics are used (Aslan,2020).

Spanish Flu

The influenza epidemic, a subtype of H1N1 virus, was the cause of the H1N1 virus between 1918 and 1921. The surprising thing about the epidemic is that it affects more healthy young adults than the weak, the elderly and children. The reason the outbreak is called spanish flu is because Spain did not take part in World War I and there was no mention of the outbreak in other European states due to censorship, and the Spanish press brought up the outbreak for the first time (Aslan,2020).

Doctors used vaccines against the hemophilus influenzae and pneumococcal species to treat the outbreak. They gave oxygen to the patients. Although they resorted to ancient applications such as bleeding the patient, they could not find a definitive treatment in every intervention.

In order to reduce the spread of the epidemic, measures such as quarantine, isolation, mask use, closure of public areas were taken but were unsuccessful.

The vaccines and drugs used in the treatment were not effective. Although blood transfer from recovering patients to new patients was a silver lining, there was no definitive solution (Temel, 1918).

Hong Kong Flu

The disease was first seen in Hong Kong. It is the influenza epidemic that caused the deaths of nearly 1 million people between 1968 and 1969.

The disease-causing type A H3N2 virus is derived from the H2N2 virus with an antigenic deviation called the merger of many subtypes of the virus to produce different viruses than the original.

The new type of virus carries the genes of H2N2, one of the bird flu virus variants (Aslan, 2020).

Symptoms of Hong Kong flu include fever, muscle pain, weakness. These symptoms usually lasted 4-6 days. The mortality rates of children and elderly patients with Hong Kong flu are high. Although a vaccine for the virus was produced, it benefited after the outbreak affected people on a global scale (Hsieh et al.2006).

Smallpox

Variola virus is the cause of smallpox. Variola virus is in the Poxviridae family. When a case of smallpox is encountered, it is obligatory to be reported internationally. Smallpox falls into the group of infectious diseases among the types of diseases (Özer and Suna 2020).

The first vaccine produced in history is the smallpox vaccine (Badur,2020).

In 1966, as a result of the campaign led by the World Health Organization, the use of smallpox vaccines was mandatory worldwide. The World Health Organization has reported that the infection that causes smallpox worldwide has ceased permanently. The World Health Organization has recommended that the smallpox vaccine be removed from routine practice after the end of the disease. Smallpox is the only disease that has ever ended among human infectious diseases (Özer and Suna 2020).

Swine influenza

The cause of the disease is a virus in the family Orthomyxoviridae. The other name of the disease is "swine influenza virus", i.e. SIV.

Known swine flu types are usually Influenzavirus A, which is rarely type C influenza virus.

Swine flu is constantly changing its structure to spread among humans.

In 2009, an outbreak of swine flu was observed. The outbreak, which began in 2009, originated in Mexico and affected 191 countries worldwide. The outbreak that started in Mexico was caused by H1N1, a subspecies of influenza A virus.

The disease is transmitted to humans from those who come into contact with poultry and pigs closely and without protective clothing. When the meat of the sick animal is cooked under favorable conditions, the disease is not transmitted (Kara, 2010).

Symptoms of the disease are fever, cough without phlegm beats, unbearable pain throughout the body, fever, weakness, shortness of breath and sudden symptoms with a temperature of 38.30 °C. Sudden symptoms are high fever, pain, ache, diarrhea, which develop between 3-6 hours. Although these symptoms vary from person to person, they can usually vary between 4-7 days.

Oseltamivir or zanamivir drugs used to treat flu can be used in the treatment. These drugs should be used within the first 2 days after the onset of symptoms. Drugs should be administered under the supervision of a doctor and used in accordance with risk groups. Paracetamol should be used instead of aspirin as a painkiller. It is not recommended to consume medicines when going abroad for pandemic prevention purposes (Sanli,2010).

Bird Flu

Bird flu is a deadly disease transmitted from animals with the virus. Other names of the disease are Avian Influenza, Pestis Avium, Bird Flu, Avian Flu, Chicken Plague. The type of virus that is deadly to humans is H5N1 (Aslan,2020).

Bird flu is an infectious disease caused by influenza viruses found in birds. Disease-causing viruses are carried in the intestines of birds, are found in their feces and often do not show symptoms of the disease.

The virus that causes bird flu has been proven to be transmitted between pigs and humans, between chickens and humans, but there is no certainty about whether there is transmission between wild birds and humans (Goldrick and Goetz 2007).

Symptoms of the disease include fever, cough, sore throat, muscle aches and pain in the lung. Cases with pneumonia and respiratory distress are at risk of death. The disease is called blue death because the body begins to turn blue when not enough oxygen enters the cells.

There is no definitive treatment for the disease. Protection is provided by vaccination. Animals with disease factors need to be killed. Due to antigen changes in influenza virus, the activity of the virus should be monitored and the content of influenza vaccines should be updated every year (Aslan,2020).

Ongoing Pandemics

Hiv/Aids

The hiv virus is the cause of the disease. Hiv virus is known as the human immunodeficiency virus. Hiv virus affects the mechanisms of the immune system in humans, causing the system to collapse. The disease that hiv virus is a factor in is called AIDS. AIDS is known as acquired immunodeficienicience syndrome. AIDS is an infectious disease in the zoonotic group (Undored and Altinbas 2020).

HIV virus, which is a factor in AIDS disease, is the virus that causes the collapse of the immune system by affecting cells involved in vital functions such as T cells, macrophages and dendritic cells, which are auxiliary cells in the human immune system (Özer and Suna 2020).

Ways hiv/aids are transmitted

HIV virus, which is a factor in AIDS disease, is found in the blood of people infected with the highest rates. Genital secretions, phlegm, breast milk, saliva, tears and cerebral spinal fluid may also be a disease factor. The most important factors that are effective in the transmission of the disease factor are blood, genital secretions and breast milk.

Stages and Cemptons of HIV Infection

Primary Infection

Hiv virus, which is a factor in AIDS disease, first acts on macrophage/dendritic cells in submucosal layers;

Approximately 87% of people infected with HIV 2-4 weeks after entering the body show flu-like symptoms. . People infected with this stage have high rates of HIV in their genital fluids and have a high amount of transmission (Lewthwaite and Wilkins 2009).

Serokonversiyon

This period, known as seroconversion, is the stage at which the body begins to produce antibodies to the virus (Card et al.2008).

Asymptomatic Infection

The stage of asymptomatic infection is known as the latent period. At this stage, the disease progresses quite insidiously. It does not show symptoms or symptoms. The duration of this period varies from person to person. The reason for the difference in duration is due to the difference in the health status and immune system functions of the person (Lever,2009).

Advanced HIV Infection/ Clinical AIDS

It is the stage where there is a significant reduction in immune system mechanisms, increased proliferation of HIV virus, cessation of antigen production and increased susceptibility to infections (Hazenberg et al.2003).

HIV /AIDS Treatment

The aim of the treatment, known as antiretroviral, is to suppress HIV replication and increase immune functions by using drugs that control the proliferation of HIV virus, to keep the life expectancy of infected people at normal level and to normalize the quality of life. Effective viral suppression has a positive effect on the general health of the community by reducing the risk of disease transmission among individuals (Akgül et al. 2018).

Drugs Used to Treat HIV/ AIDS

Nükleozid Revers Transkriptaz İnhibitörleri (NRTİ)

Nucleoside Revers Transcriptase Inhibitors interact with the catalytic region of the revers transcripttase enzyme found in the HIV virus, a cause of AIDS disease (De Clercq,2007).

Nucleoside Revers Transcripttase Inhibitors have analogues 2',3'-dideoxynucleosine (ddN), and the effects of drugs in this group are similar. After nucleoside Revers Transcriptal Inhibitors enter the cell, they turn into 5'-monophosphate (ddNMP), 5'-diphosphate (ddNDP) and 5'-triphosphates (ddNTP), respectively. The transformation process occurs before ddNMP acts as a competiative inhibitor/alternative substrate of normal deoxynucleosite triphosphate (dNTP).

As a compelling inhibitor of the normal substrate, ddNTP inhibits the merging of the normal substrate with the DNA chain and participates in this chain as an alternative substrate in the form of ddNMP. Thus, it acts as a de-chain terminator (De Clercq,2009).

Non-Nükleozid Revers Transkriptaz Enzim İnhibitörleri (NNRTİ)

The first two classes of Non-Nucleoside Reversal Transcardase Enzyme Inhibitors are known as 1-[(2hydroxytoxy)methyl]-6-(phenylticyo)timin-structured compounds i.e. 4,5,000 with HEPT6.7-tetrahydro-5-methylimidazo[4,5,1-jk][1,4]benzodiazepin-2(1H)-on, i.e. TIBO derivatives (Pauwels et al. 1990).

Compounds of this nature primarily interact with the allosteric region of HIV-1 revers transcriptasis. The drugs in this gup are also called specific inhibitors of HIV-1 (De Clercq,2004).

Protease Inhibitors (PI)

Protease Inhibitors carry a hydroxyetylene skeleton opened by the HIV protease enzyme, which resembles a peptide bond but cannot be opened itself. The mechanism of action of drugs in this group prevents HIV protease from performing its normal function; thus, the proteolytic process of precursor viral proteins to mature viral proteins is prevented (Madruga et al.2007).

Fusion Inhibitors (FI)

Hiv virus, which is a factor of AIDS disease, creates fusion with normal cells thanks to gp41 in the membrane, transferring its viral RNA and viral enzymes to normal cells. Enfuvirtite, a physio intibitary, was produced to prevent this fusion (Matthews et al. 2004).

The mechanism of action of drugs in this group is to prevent the virus molecule from fusing with the outer cell membrane (De Clercq,2009).

Co-receptor Inhibitors (CRİ)

Co-receptor inhibitors must enter the target cells to show their effects, and the correlators used in M (macrophage)-tropical and T (lymphocyte)-tropical HIV lineages) should interact with CCR5 or CXCR4. The mechanism of action of drugs in this group is the interaction of the co-receptor and viral glycoprotein gp120, the interaction of gp120 with the CD4 receptor and the fusion of gp41 and the outer cell membrane (Westby and van der Ryst 2005)

The only CRİ drug approved for use is maravirocytose (Perros, 2007), an antagonist ccr5.

Integrators (II)

The enzyme integral has attracted attention in the development of drugs against hiv virus. The first clinically approved integral inhibitor (II) is raltegravir. The effect of raltegarvirin is on thread transfer. This is the effect of elvitegravir. Elvitegravirin is effective in reducing viral loading in people infected with HIV (Sulukan et al. 2009).

Covid-19

Coronaviruses are single-chain, positive polarity, enveloped RNA viruses in the Coronavirinae subfamily of the Coronaviridae family in the Nidovirales class. The reason these viruses are called coronaviruses is due to the latin word "corona", which means "crown" due to the bar-shaped extensions found on the surface of the virus (Chen et al.2020).

The four structural proteins found in coronaviruses - the S (Spike) protein, the E (Envelope) protein, the M (Membrane) protein and the N (Nucleocapsid) protein -- are responsible for the formation of mature virus particles (virions) and the emergence of infection. The S protein is responsible for the formation of spikes on the surface of the coronavirus. The protrusions on the surface are responsible for the virus's adhesion to the host cell septators and its entry into the cell M protein, which allows the virus particle to form with three different transmembrane regions, to allow the virus to curve the cell membrane and bind to the nucleocap. Protein E is involved in the packaging and release of the virus and viral pathogenesis. The N protein contains regions connected to the viral genome in the RNA structure (Alpine and Unal 2020).

Ways Covid-19 Is Transmitted

The main way of transmission of coronavirus is the droplet path. The virus found in respiratory secretions can make the healthy individual sick by direct contact with the mucous membrane, while the infected individual coughs, sneezes or speaks through droplets. In finding a new host for the virus, the contact of another individual is effective with the droplets that the sick individual emits through coughing and sneezing (Gürsu,2020).

Stages and Cemptons of Covid-19 Infection

The severity of infection is divided into 5 groups: asymptomatic infection, mild form, moderate form, severe infection, critical infection.

Asymptomatic Infection

It is defined for cases that have tested positive for coronavirus and do not show clinical symptoms. Asymptomatic infection plays an important role in social transmission. This is due to the absence of clinical symptoms in those infected.Babies and children who do not show clinical symptoms play an important role in interpersonal transmission.

Mild Form Symptoms

Fever, fatigue, muscle pain, cough, sore throat, runny nose, sneezing, symptoms of acute upper respiratory tract

Symptoms of Medium Form

Pneumonia, usually fever and cough, wheezing in some cases

Symptoms of Severe Infection

Dyspnea, central cyanosis, decreased oxygen saturation, hypoxemia

Critical Signs of Infection

Acute respiratory distress syndrome, respiratory failure, multiple organ failure (Happy, 2020).

Covid-19 Treatment

The main goal in the treatment of coronavirus is supportive and symptomatic treatment. First of all, the infected persons should be removed from the community and quarantined. Cases with mild symptoms should be managed by home counseling without going to health centers. In treatment, the body's water and electrolyte level should be kept to a certain extent, nutrition should be taken care of, fever and cough should be checked. In cases where the body does not receive enough oxygen, the face mask, high-flow nasal cannula, oxygen should be provided through non-invasive ventilation. Mechanical ventilation and oxygen support may be required, and kidney replacement therapy may be required in some patients. Antibiotics and antifungal should be used in cases with two or more infections in the body at the same time (Jin et al. 2020).

Vaccines are the most effective way to prevent epidemics in the form of infections. This is because it takes both costly and a long time to develop drugs suitable for treatment. Vaccines are both a way to be used in the prevention of global epidemic diseases (DG et al. 2020).

Drugs Used to Treat Covid-19

Klorokin (CQ), Hidroksiklorokin (HCQ)

Although chloroquine has not been approved by the FDA in the treatment of coronavirus, it has allowed use if doctors deem it appropriate. The FDA has not approved any therapeutic agents or drugs for the treatment and prevention of coronavirus. Clinical efficacy and safety of chloroquine in the treatment of coronavirus is unclear. Since doctors are successful in the treatment of different diseases, they have approved the use of chloroquine.

Hydroxychloroquine is a chloroquine-derived drug.The mechanism of action of the drug inhibits the enzyme polymerase, preventing the merger by interfering with the glucocytion of the virus and cell receptors by increasing the ph of the place where the intracellular digestion of the substance formed and taken by the combination of phagosome and lysosome occurs.

Hydroxychloroquine is recommended in patients who will be monitored with outpatient treatment and treated by hospital in the coronavirus treatment guide of the Ministry of Health in our country.

Favipiravir

Favipiravir RNA viruses have an effect by inhibiting the enzyme RNA-dependent RNA polymerase. Favipiravir is an antiviral drug. Favirpiravir forms favipiravir ribofuranosyl-5B-triphosphate, an active form of the body. For this activation process, favipiravir intraselecular phosphoribosylasion occurs. Favipiravir ribofuranosyl-5B-triphosphate is a substrate of RNA-dependent RNA polymerase and inhibits RNA polymerase enzyme activity. Since the RNA-dependent RNA polymerase enzyme is found in many RNA viruses, favipiravir expands its spectrum by affecting this enzyme.

Remdesivir

Remdesivir is in the antiviral drug group. It is used in the treatment of Ebola and marburg virus infections. This drug is the precursor to nucleotide analoma, which is metabolized into the intracellar adenosine triphosphate analogue, which inhibits the enzyme viral RNA polymerase. Remdesivir is a wide-spectrous drug. It has a preventive and therapeutic effect in non-clinical studies against coronaviruses.

Lopinavir/ritonavir(LPV/R)

Lopinavir, a combination of ritonavir, is used to treat HIV infection. It is a protease inhibitor, one of the drugs used to treat AIDS. The enzyme protease plays a role in the processing of coronavirus polyprotein. Lopinavir and rheaavirin have contrasting effects against coronavirus separately and together.

Nitazoksanid

The drug nitazoksanid has strong in vitro activity against coronavirus. Apart from the coronavirus, this drug has broad-spectrum antiviral activity against influenza, respiratory sysnsityal virus, parainfluenza, rotavirus and norovirus The mechanism of action of the drug is associated with the pathways regulated with the host during the proliferation of the virus.

Tosilizumab

The effect of the drug tosilizumab is caused by monoclonal antibodies due to membrane or inhibiting soluble interleukin-6 receptors (rIL-6). This drug has been approved for use in the treatment of rheumatoid arthritis patients.

İvermektin

Ivermectin is a broad-spectrum FDA-approved drug effective against parasites. It has had an effect on many viruses in studies on the drug. The mechanism of action of the drug ivermectin inhibits the nuclear intake of the host and viral proteins. Ivermectin both acts on some Rna virus infections and has an effect on some DNA viruses. In studies on the drug, the coronavirus has a reducing effect on its effectiveness (Mutlu et al. 2020).

Factors Affecting Viral Pandemics

Vaccines

Viral pandemics can be effectively prevented with inexpensive and effective vaccination strategies. Vaccines protect against pathogens by stimulating primary defense mechanisms.

Vaccination is the process of applying a small amount of an infectious agent, such as viruses or bacteria, to stimulate the immune system to recognize and respond to this agent. Vaccines are often used to prevent infectious diseases. Vaccines are administered by injection. Vaccines are often designed to stimulate the production of antibodies, proteins that neutralize foreign invaders in the body.

To improve the specific immunological system through vaccination, the human body can produce white blood cells (B and T cells) that can fight the pathogen (especially) in response to the immune system, allowing the adaptive immune system to grow.

Since the disease is mostly a new type of virus in virus-induced pandemics, it is impossible to produce a vaccine before the pandemic begins.

In the production of vaccines against pandemics, the disease factor is primarily stated. After the disease factor is determined, it is replicated in the cultural environment and the vaccine is produced. The spread of pandemics increases in the time spent in vaccine production. The vaccine produced is specific to the disease factor determined. Vaccines are effective on the black virus. The treatment of the infected person with the vaccine is limited (Şahin and Demir 2020).

Antiviral Drugs

Antiviral drugs are used in virus-induced infections. It is used in the prevention and treatment of virus-induced infections. In viral pandemics, the treatment of the disease is either through the application of vaccines or the use of antiviral drugs to prevent the disease before the disease occurs (Carrasco et al. 2011).

Virus-Related Protein Use

The protein associated with the virus contains anti-idiotypical antibodies, natural ligands of the receptor and anti-receptor antibodies. The mechanism of action prevents the virus from binding to host cell receptors and entering the cell before the viral infection begins.

Reverse Transcription Inhibitors/ Revers Transcription Inhibitors

Nucleotide or nucleoside analogues, similar to the building blocks of ribonucleic acid or Deoxyribo nucleic acid, are used as antiviral drugs. Since the mechanism of action is not 3'OH in analogues, viral Ribonucleic acid or Deoxyribo blocks enzymes that synthesize nucleic acid.

Antisense

When the virus genome becomes active in the host cell, it produces mRNA molecules that play a role in the synthesis of viral proteins. mRna production begins by proteins. Antisensors are

drugs made from short segments of DNA or RNA that can bind to their viral genomes as a complement and prevent transcription of the viral genome.

Ribozim

When the virus genome becomes active in the host cell, it produces mRNA molecules that play a role in the synthesis of viral proteins.mRna production begins by proteins. Antisensors are drugs made from short segments of DNA or RNA that can bind to their viral genomes as a complement and prevent transcription of the viral genome.

Protease Inhibitors

Protease inhibitors developed for the treatment of HIV/ AIDS and hepatitis C are widely used in the treatment of these diseases. Some viruses break down viral protein chains after translation with the enzyme protease within the target cell, creating virions and spreading them in cells that are not infected with disease factors. Protease inhibitors take effect by inhibiting the enzyme viral protease.

İnterferonlar

Interferons suppress the disease-causing virus factor by strengthening the body's immune system instead of attacking the disease-causing virus factor.Interferon viruses prevent their proliferation.Interferons are signaling proteins produced due to the presence of several viruses in the body.Interferons are cytokines synthesized by cells in viral infection. It shows its effect by enabling communication between cells to strengthen the immune system against disease-causing factors.Interferons have opposite effects on the proliferation of viruses by protecting cells from virus infections.

Conventional Plasma Treatment

Conventional plasma therapy, which is used to treat and prevent epidemic diseases, is the treatment of the disease by taking blood from people who have suffered from the disease, separating antibodies and giving them to sick people (Şahin and Demir 2020).

3. RESULTS AND RECOMMENDATIONS

Pandemiler epidemics that are effective worldwide. An epidemic pandemic not only is it widespread and the mortality rate is high, but it is also contagious must be high. Affecting human history pandemilere Although various methods have been applied in the treatment of related diseases for centuries, there is no definitive treatment method. Her pandemiye there is a unique way of treating the disease. These semptomatik and supportive treatment, lac treatment and vaccination of healthy people pandeminin to reduce the effects. Pandemileri investments in preventing factors increase,Ar-Thanks to the development of ge studies, we may face in the future pandemic we strengthen our hand in their dangers.

Acknowledgement

4. REFERENCES

AKGÜL, Ö., ÇALŞKAN, R., & ÖNER, YA (2018). HIV/AIDS: Current Approaches. Journal of Medical School Clinics , 1 (1), 19-31.

ALP, S., & ÜNAL, S. (2020). Pandemic caused by the new coronavirus (SARS-CoV-2): developments and current situation. Flora Magazine, 25.

Aslan, R. (2020). From history to the present, epidemics, pandemics and Covid-19. Journal of Detail, 8(85), 35-41.

Badur, S. (2010). H1N1 epidemiology and virus. ANKEM Derg , 24 , 190-5.

Basustaoglu,A.C,2010.Medical Microbiology.Atlas Bookseller Tic.Ltd.Sti,947,Ankara

Byfield T. (2010) . Renaissance: God in Man, A.D. 1300 to 1500: But Amid Its Splendors, Night Falls on Medieval Christianity, Christian History Project, p. 37.

Card, J.J., Amarillas, A., Conner, A., Akers, D.D., Solomon, J., DiClemente, R.J. (2008). TheComplete HIV/AIDS Teaching Kit: With CD-ROM, Springer Publishing Company, New York, 25-71.

Carrasco, LR, Lee, VJ, Chen, MI, Matchar, DB, Thompson, JP and Cook, AR (2011). Antiviral stockpiling strategies for future influenza pandemics: a global epidemic-economic perspective. Journal of the Royal Society Interface , 8 (62), 1307-1313.

Genoa, E. (2020). Amvas taunu and its effects that occurred during the Period of Omar. Journal of Caucasus University Faculty of Theology, 7(13), 129-150.

Chen, Y., Liu, Q., & Guo, D. (2020). Emerging coronaviruses: genome structure, replication, and pathogenesis. Journal of medical virology, 92(4), 418-423.

Craig Freudenrich, PhD & Patrick J. Kiger "How Viruses Work" 2020. https://science.howstuffworks.com/life/cellular-microscopic/virus-human.htm

 (Accessed:14 February 2022)

De Clercq, E. (2004). Non-nucleoside reverse transcriptase inhibitors (NNRTIs): past, present, and future. Chemistry & biodiversity, 1(1), 44-64.

De Clercq, E. (2007). "Anti-HIV drugs" Verh. K. Acad. Healed. Belgian, 69, 81-104.

De Clercq, E. (2009). Anti-HIV drugs: 25 compounds approved within 25 years after the discovery of HIV. International journal of antimicrobial agents, 33(4), 307-320.

DG, A., HJ, S., & MH, K. (2020). Lee S, Kim HS, Myoung J, et al. Current Status of Epidemiology, Diagnosis, Therapeutics, and Vaccines for Novel Coronavirus Disease 2019 (COVID-19). J Microbiol Biotechnol [Internet], 30(3), 313-24.

Goldrick, BA and Goetz, AM (2007). Pandemic flu: what infection control specialists need to know. American journal of infection control , 35 (1), 7-13.

GÜRSU,E. (2020). CoronavirusPandemisi.
https://www.researchgate.net/profile/ElifGuersu/publication/341599760_Koronavirus_Pande
misi_ve_SarsCoV2_Virusune_Genel_Bakis/links/5ec95c0392851c11a8820702/Koronavirues-
Pandemisi-ve-Sars-CoV-2-Viruesuene-Genel-Bakis.pdf

Hazenberg, MD, Otto, SA, van Benthem, BH, Roos, MT, Coutinho, RA, Lange, JM, ... & Miedema, F. (2003). Permanent immune activation in HIV-1 infection is associated with progression to AIDS. Aid , 17 (13), 1881-1888.

Hsieh, YC, Wu, TZ, Liu, DP, Shao, PL, Chang, LY, Lu, CY, ... & Huang, LM (2006). Flu outbreaks: past, present and future. Journal of formosan Medical Association , 105 (1), 1-6.

Jarus O. 20 of the worst epidemics and pandemics in history. Live Science, All About History March 20, 2020. https://www.livescience.com/worst-epidemics-and-pandemics-in-history.html

 (Access 16.02.2022)

Jin, YH, Cai, L., Cheng, ZS, Cheng, H., Deng, T., Fan, YP, ... & Wang, XH (2020). A quick recommendation guide to the diagnosis and treatment of pneumonia (standard version) infected with the new coronavirus (2019-nCoV) in 2019. Military Medical Research , 7 (1), 1-23.

Kara, A. (2010). Swine Flu (Pandemic Influenza 2009, Influenza 2009 H1N1). Journal of Child Health and Diseases, 53(1).

Kutlu, R. (2020). What we have learned about the new coronavirus pandemic, current approaches to diagnosis and treatment and the situation in Turkey. Turkish Journal of Family Medicine and Primary Care, 14(2), 329-344.

Lever, AM (2009). HIV: virus. Medicine , 37 (7), 313-316.

Lewthwaite, P. and Wilkins, E. (2009). Natural history of HIV/AIDS. Medicine , 37 (7), 333-337.

Madruga, J. V., Cahn, P., Grinsztejn, B., Haubrich, R., Lalezari, J., Mills, A., ... & DUET-1 Study Group. (2007). Efficacy and safety of TMC125 (etravirine) in treatment-experienced HIV-1-infected patients in DUET-1: 24-week results from a randomised, double-blind, placebo-controlled trial. The Lancet, 370(9581), 29-38.

Matthews, T., Salgo, M., Greenberg, M., Chung, J., DeMasi, R., & Bolognesi, D. (2004). Enfuvirtide: the first therapy to inhibit the entry of HIV-1 into host CD4 lymphocytes. Nature reviews Drug discovery, 3(3), 215-225.

MUTLU, O., UYGUN, İ., & ERDEN, F. (2020). Drugs used to treat coronavirus disease (COVID-19). Kocaeli University Journal of Health Sciences, 6(3), 167-173.

Özer, M., & Suna, H. E. (2020). Covid-19 pandemic and education. Şeker, Özer, A. and C. Korkut (Der.), Anatomy of the global epidemic: Within the future of man and society, 171-192.

Özkoçak, V., Koç, F., & Gültekin, T. (2020). Anthropological View of Pandemics: Example of coronavirus (Covid-19). Electronic Turkish Studies , 15 (2).

Pandemic.Wikipedia, liberation. https://tr.wikipedia.org/wiki/Pandemi(Access:14.02.2020)

Glitter, H. (2020). Infectious disease outbreaks in history. Tepecik Education and Research Hospital Journal, 30, 19-26.

Pauwels, R., Andries, K., Desmyter, J., Schols, D., Kukla, M. J., Breslin, H. J., ... & Janssen, P. A. (1990). Potent and selective inhibition of HIV-1 replication in vitro by a novel series of TIBO derivatives. Nature, 343(6257), 470-474.

Perros, M. (2007). CCR5 antagonists for hiv infection and AIDS treatment. Advances in Antiviral Drug Design , 5 , 185-212.

Qiu, W., Rutherford, S., Mao, A., & Chu, C. (2017). Pandemic and its effects. Health, culture and society , 9 , 1-11.

SULUKAN, E. E., KÜÇÜKOĞLU, K., & GÜL, H. İ. (2009). AIDS and the drugs used to treat it. Ankara Faculty of Pharmacy Journal,38 (1) 47- 78.

Şahin, F., & Demir, S. (2020). Viruses, Factors and Consequences Affecting Viral Pandemics. Muzaffer Şeker, Ali Özer and Cem Korkut. Turkish Academy of Sciences, 55-76.

Sanli, K. (2010). Influenza virus and swine flu. Istanbul Legal Sultan Suleyman Medical Journal (IKSST), 2(1), 4-12.

Don't wear it, S. (2019). Review of Virus Subject in Secondary Education from the Point of View of Program, Teacher and Student. Master's Thesis, Hacettepe University Institute of Educational Sciences, Ankara.

UNMASKED, Ö. L., & ALTINBAS, SK (2020). Microorganisms existed long ago on the blue planet: the history of pandemics. Turkish Journal of Women's Health and Neonatology , 2 (2), 53-69.

Temel, M. K. (1918). Flu Pandemic. Istanbul University Institute of Health Sciences Master's Thesis, Istanbul.

Westby, M., & van der Ryst, E. (2005). CCR5 antagonists: host-targeted antivirals for the treatment of HIV infection. Antiviral chemistry and chemotherapy, 16(6), 339-354.

An Application of Distributed Order Differential Equations to a HIV Infection Model

Mehmet KOCABIYIK[1]
Mevlüde YAKIT ONGUN[2]
İlkem TURHAN ÇETİNKAYA[3]

1.Introduction

In many fields of science and engineering, fractional differential equations are frequently encountered. Since fractional order differential equations are more realistic than ordinary differential equations, the researches give more attention to this subject, recently. The distributed order differential equations (DODEs) are also one of the important subjects in fracture analysis because of the density function included. Detailed information about distributed order fractional operators and their applications is given in (Ding et al., 2021). A numerical method for the DODEs in which the derivative is Caputo type is presented in (Diethelm & Ford, 2009). Some theorems are given for the convergence of the presented method. The study is supported by numerical examples. Dielectric induction and diffusion problems are modeled by DODEs in (Caputo, 2001). Katsikadelis presented a numerical method to linear and non-linear distributed order fractional differential equations in (Katsikadelis, 2014). Another efficient method for linear and non-linear distributed order fractional differential equations is presented in (Jibenja et al., 2018). This method is based on a hybrid of block-pulse functions and Taylor polynomials. The effectiveness of the method is presented by numerical examples. Najafi et.al. gives detailed theorems and definitions about distributed order fractional differential equations including non-negative density function in (Najafi et al., 2011). The proposed procedure is applied to a model of the solar-wind-driven magnetosphere-ionosphere to check the stability.

Many methods are available in literature to solve mathematical models. NSFD schemes developed by Mickens are very popular methods in solving differential equations leads from engineering and science (Mickens, 1989; Mickens, 1994; Mickens, 2002). The method is very popular since it is simple to construct and it gives opportunity to resolve the numerical instabilities. The basic procedure for determining denominator function and some applications is given in (Mickens, 2007). For detailed literature survey, one can check (Patidar, 2005; Patidar, 2016).

Recent studies show that NSFD schemes can be applied to the DODEs. A model of distributed order fractional multi strain Tuberculosis is considered in (Sweilam et al., 2020). The system of differential equation is discretized by NSFD scheme and midpoint quadrature. Numerical simulations are presented. A smoking model of distributed order is presented in (Kocabiyik & Ongun, 2021). NSFD shemes are used to discrete the model. Some theorems are given to analyze the stability of the model. Numerical simulations and phase portraits are presented. To present the

---

[1] Res. Asst., Burdur Mehmet Akif Ersoy University, Department of Mathematics, Orcıd: 0000-0002- 7701-6946.
[2] Prof. Dr., Süleyman Demirel University, Department of Mathematics, Orcıd: 0000-0003-2363-9395.
[3] Asst. Prof. Dr., Kütahya Dumlupınar University, Department of Mathematics, Orcıd: 0000-0002-5520-310X.

effect of the NSFD schemes, comparison with another two methods is done. A distributed order Malaria-Ross model is presented in (Kocabıyık, 2022). The model is discretized by NSFD schemes. In the view of the Jury conditions, the stability analysis is examined. As another example of DODE, SVIR model can be given (Kocabıyık et al., 2021). Numerical analysis and stability analysis is presented by using NSFD schemes. The numerical results for the different density functions are presented in graphical form.

In this study, it is aimed to give an application of DODEs on a biological model. So, the nonlinear system of ordinary differential equation given in (Perelson et al., 1993) and (Perelson & Nelson, 1999) is considered. The model presents the effect of the HIV infection on CD4$^+$ T cells which has an important role on immune regulation. The same model is considered in (Ongun & Turhan, 2013) and it is approached by NSFD schemes developed by Mickens (Mickens, 1990) and (Mickens, 1993). They also present the stability analysis of the model. In this study, we rewrite the HIV model in distributed order form. The distributed order model is discretized by NFDS schemes. The equilibrium points are determined and stability analysis is performed. The detailed comparison is presented with the results obtained in (Ongun & Turhan, 2013).

2. Basic Definitions on Differential Equations of Fractional and Distributed Order

This section presents the basic definitions of fractional and DODEs. Some of them can be listed as below:

Definition 2.1. (Podlubny, 1999) Assume that $f(t)$ is a continuous in the range of $[a,t]$ and *(n+1)*-th times differentiable function. Let *n* be an integer and *a* satisfy *n < a < n + 1*. Then Grünwald-Letnikov fractional derivatives of order *a* is defined by

$$_{GL}D_t^\alpha f(t) = \lim_{h \to 0} h^{-\alpha} \sum_{i=0}^{n} (-1)^k \binom{\alpha}{i} f(t - ih)$$

$$= \sum_{k=0}^{n} \frac{(t-a)^{-\alpha+k} f^{(k)}(a)}{\Gamma(-\alpha+k+1)} + \frac{1}{\Gamma(-\alpha+n+1)} \int_a^t (t-\tau)^{n-\alpha} f^{(n+1)}(\tau) d\tau.$$

Definition 2.2. (Podlubny, 1999) Assume that $f(t)$ is an integrable function in the range of $[a,t]$ and $n-1 < \alpha \leq n$, $n \in \mathbb{N}^+$ Then, Riemann Liouville fractional derivative of order α is defined by

$$_{RL}D_t^\alpha f(t) = \frac{1}{\Gamma(n-\alpha)} \frac{d^n}{dt^n} \int_a^t \frac{f^{(n)}(\tau)}{(t-\tau)^{\alpha-n+1}} d\tau.$$

Definition 2.3. (Podlubny, 1999) Assume that $f(t)$ is an integrable function in the range of $[a,t]$ and $n-1 < \alpha \leq n$, $\boldsymbol{n} \in \mathbb{N}^+$. Then, Caputo fractional derivative of order α is defined by

$$_{C}D_t^\alpha f(t) = \frac{1}{\Gamma(n-\alpha)} \int_a^t \frac{f^{(n)}(\tau)}{(t-\tau)^{\alpha-n+1}} d\tau.$$

Let us give the definition of approximate Grünwald-Letnikov formula since it will be used in this study:

Definition 2.4. (Meerschaert & Tadjeran) For DODEs, the approximate Grünwald-Letnikov formula is defined as

$$_{GL}D_t^\alpha f(t) = \lim_{h \to 0} h^{-\alpha} \sum_{i=0}^{n} (-1)^i \binom{\alpha}{i} f(t - ih)$$

or

$$_{GL}D_t^\alpha f(t) = \sum_{i=0}^{n} q_i^\alpha f(t_{n-i}), n = 1, 2, ..., \frac{t - \alpha}{h},$$

where h is very small; and for $i = 0, 1, 2, ..., n$, $q_i^\alpha = \left(1 - \frac{1+\alpha}{i}\right) q_{i-1}^\alpha$ and $q_0^\alpha = h^{-\alpha}$.(Dorciak, 1994).

3. An Application of DODEs

In this section, an epidemic model for the HIV infections of CD4$^+$ T cells given in (Perelson et.al., 1993) and (Perelson & Nelson, 1999) is considered. The model is converted to the distributed order form. The model is discretized by using NSFD schemes. Equilibrium points and Jacobian matrix of the discrete model are determined. Applying Schur-Cohn criteria, the stability analysis is presented. Also, some numerical comparisons are given to present the effect of the NSFD schemes for different step sizes.

The reason of the prefer NSFD schemes which is first developed in 1989 by Mickens (Mickens, 1989) is to be a very useful method since it has a big role in dynamical consistency. Also, NSFD schemes lead to obtain the effective results with less effort.

Let us give short procedure about the application of the NSFD schemes to an ordinary differential equation. Taking into consideration of the first order ordinary differential equation given as

$$\frac{dx}{dt} = g(x, \lambda),$$

the discretization procedure can be expressed in the following form:

$$t \to t_n, \ x(t) \to x_n, \ g(t) \to g(t_n), \ \frac{dx}{dt} \to \frac{x_{n+1} - x_n}{\psi},$$

where λ is a parameter and ψ is the denominator function which can be determined as

$$\psi = \frac{1 - e^{-h\kappa}}{\kappa}.$$

One can see more details about constructing NSFD schemes, determining denominator functions and the extended applications of the method in (Mickens,1989; Mickens, 1994, Mickens; 2002; Mickens, 2005; Mickens 2007).

3.1. Discretization of Distributed Order Model

In this section, we rewrite the model of HIV infections of CD4+ T cells presented in (Perelson et.al., 1993) and (Perelson & Nelson, 1999) in the form of DODEs as

$$D_t^{d(\alpha)} T(t) = p - \alpha T(t) + r T(t) \left(1 - \frac{T(t) + I(t)}{T_{max}}\right) - kV(t)T(t)$$

$$D_t^{d(\alpha)} I(t) = kV(t)T(t) - \beta I(t),$$
(1)

$$D_t^{d(\alpha)} V(t) = N\beta I(t) - \gamma V(t),$$

where, $T(t)$, $I(t)$ and $V(t)$ are the size of uninfected CD4$^+$ T cells, the size of infected CD4$^+$ T cells by the HIV viruses, and the size of HIV virus particles in the blood, respectively. The positive parameters k and N are the rate constant of infection and number of the produced virus particles by each infected CD4+ T cells (Wang & Li, 2006). The maximum level of CD4+ T cell population in the body and the rate of average specific T-cell growth are denoted by the parameters Tmax and r (Perelson et.al. 1993). The positive constants p, α, β, and γ denotes the source of CD4+ T cells within the body, the death rate of CD4+ T cells, the death rate of the infected cells, and the rate of viral clearance, respectively (Naresh et.al., 2009), (Nowak & May, 1991) and (Yang & Xiao, 2010). $d(a)$ is the density function.

Applying NSFD schemes to the model (1) and considering approximate Grünwald-Letnikov derivative formula which is obtained by definition of DODE, the following discrete system is obtained:

$$\sum_{k=1}^{m} \frac{d(a_k)}{m} \sum_{j=0}^{n+1} q_j^{a_k} T_{n+1-i} = p + (r-a)T_{n+1} - r\frac{T_{n+1}}{T_{max}}(T_n + I_n) - kV_n T_{n+1},$$

$$\sum_{k=1}^{m} \frac{d(\alpha_k)}{m} \sum_{j=0}^{n+1} q_j^{\alpha_k} I_{n+1-i} = kV_n T_n + \beta I_n,$$
(2)

$$\sum_{k=1}^{m} \frac{d(\alpha_k)}{m} \sum_{j=0}^{n+1} q_j^{\alpha_k} V_{n+1-i} = N\beta I_n - \gamma V_n.$$

In this discrete system, for $i = 1, 2, 3$ and $0 < \alpha_k < 1$, it is obtained that $q_0^{\alpha_k} = (\theta_i(h))^{-\alpha_k}$ with approximate Grünwald-Letnikov derivation formula. The expressions $\theta_i(h)$ are the denominator functions obtained by NSFD schemes and for this system, the denominator functions are chosen as

$$\theta_1(h) = \frac{e^{(a-r)h}-1}{a-r}, \quad \theta_2(h) = \frac{e^{\beta h}-1}{\beta}, \quad \theta_3(h) = \frac{e^{\gamma h}-1}{\gamma}.$$

To rearrange the discrete system (2), by expanding first term of the sum

$$\sum_{j=0}^{n+1} q_j^{\alpha_k} T_{n+1-i} = q_0^{\alpha_k} T_{n+1} + \sum_{j=1}^{n+1} q_j^{\alpha_k} T_{n+1-i}$$

and with the help of Grünwald-Letnikov formula, $(\theta_1(h))^{-\alpha_k}$ can be written instead of $q_0^{\alpha_k}$. So the first term of the discrete system is

$$\sum_{k=1}^{m} \frac{d(\alpha_k)}{m}\left((\theta_1(h))^{-\alpha_k} T_{n+1} + \sum_{j=1}^{n+1} q_j^{\alpha_k} T_{n+1-i}\right) = p + (r-a)T_{n+1} - r\frac{T_{n+1}}{T_{max}}(T_n + I_n) - kV_n T_{n+1} \qquad .$$
(3)

Substituting $\sum_{k=1}^{m} \dfrac{d(\alpha_k)}{m} = M$ into Eq. (3), T_{n+1} is obtained as

$$T_{n+1} = \frac{p - M\left(q_1^{\alpha_k} T_n + \sum_{j=2}^{n+1} q_j^{\alpha_k} T_{n+1-i}\right)}{M\left(\theta_1(h)\right)^{-\alpha_k} + a - r + r\dfrac{T_n + I_n}{T_{\max}} + kV_n}.$$

Let us apply the same procedure to the second or third equations of Eq. (2) :

$$\sum_{j=0}^{n+1} q_j^{\alpha_k} I_{n+1-i} = q_0^{\alpha_k} I_{n+1} + \sum_{j=1}^{n+1} q_j^{\alpha_k} I_{n+1-i} = q_0^{\alpha_k} I_{n+1} + q_1^{\alpha_k} I_n + \sum_{j=2}^{n+1} q_j^{\alpha_k} I_{n+1-i}$$

$$\sum_{j=0}^{n+1} q_j^{\alpha_k} V_{n+1-i} = q_0^{\alpha_k} V_{n+1} + \sum_{j=1}^{n+1} q_j^{\alpha_k} V_{n+1-i} = q_0^{\alpha_k} V_{n+1} + q_1^{\alpha_k} V_n + \sum_{j=2}^{n+1} q_j^{\alpha_k} V_{n+1-i}$$

Inserting these expressions into the system, finally, the discrete system is obtained as

$$T_{n+1} = \frac{p - M\left(q_1^{\alpha_k} T_n + \sum_{j=2}^{n+1} q_j^{\alpha_k} T_{n+1-i}\right)}{M\left(\theta_1(h)\right)^{-\alpha_k} + a - r + r\dfrac{T_n + I_n}{T_{\max}} + kV_n},$$

$$I_{n+1} = \frac{kV_n T_n - M\left(q_1^{\alpha_k} I_n + \sum_{j=2}^{n+1} q_j^{\alpha_k} I_{n+1-i}\right)}{M\left(\theta_2(h)\right)^{-\alpha_k} + \beta},$$

(4)

$$V_{n+1} = \frac{N\beta I_n - M\left(q_1^{\alpha_k} V_n + \sum_{j=2}^{n+1} q_j^{\alpha_k} V_{n+1-i}\right)}{M\left(\theta_3(h)\right)^{-\alpha_k} + \gamma}.$$

3.2. Equilibrium Points and the Jacobian Matrix of the Discrete System

In this section, the equilibrium points and the Jacobian matrix of Eq. (4) will be determined. The following equations should be solved to determine the equilibrium points of Eq. (4):

$$T_n = \frac{p - MQT_n}{M\left(\theta_1(h)\right)^{-\alpha_k} + a - r + r\dfrac{T_n + I_n}{T_{\max}} + kV_n},$$

$$I_n = \frac{kV_n T_n - MQI_n}{M\left(\theta_2(h)\right)^{-\alpha_k} + \beta},$$

(5)

$$V_n = \frac{N\beta I_n - MQV_n}{M\left(\theta_3(h)\right)^{-\alpha_k} + \gamma}$$

where $\sum_{j=0}^{n+1} q_j^{\alpha_k} = Q$.

Firstly, choosing $I_n = V_n = 0$ and solving the first equation of Eq. (5) the equilibrium points E_1 and E_2 are obtained as

$$E_1 = \left(\frac{-T_{max}\left(M\eta_1 + a - r\right) + \sqrt{\left(T_{max}\left(M\eta_1 + a - r\right)\right)^2 - 4rT_{max}p}}{2r}, 0, 0 \right),$$

$$E_2 = \left(\frac{-T_{max}\left(M\eta_1 + a - r\right) - \sqrt{\left(T_{max}\left(M\eta_1 + a - r\right)\right)^2 - 4rT_{max}p}}{2r}, 0, 0 \right),$$

where

$$\eta_1 = Q + \left(\theta_1\left(h\right)\right)^{-\alpha_k}.$$

Secondly, in the case of $I_n \neq V_n \neq 0$, the equilibrium point can be expressed as $E_3 = \left(e_{31}, e_{32}, e_{33}\right)$, where

$$e_{31} = \frac{\left(M\eta_2 + \beta\right)\left(M\eta_3 + \gamma\right)}{N\beta k},$$

$$e_{32} = \frac{e_{32}^*}{N\beta k\left(\theta_2\left(h\right)\right)^{\alpha_k}\left(\theta_3\left(h\right)\right)^{\alpha_k}\left(\beta + M\eta_2\right)\left(Mr\eta_3 + kT_{max}N\beta + r\gamma\right)},$$

$$e_{33} = \frac{e_{33}^*}{k\left(\theta_2\left(h\right)\right)^{\alpha_k}\left(\theta_3\left(h\right)\right)^{2\alpha_k}\left(\beta + M\eta_2\right)\left(M\eta_3 + \gamma\right)\left[r\left(M\eta_3 + \gamma\right) + kT_{max}N\beta\right]},$$

$$\begin{aligned}
e_{32}^* = &\left(\theta_2\left(h\right)\right)^{\alpha_k}\left(\theta_3\left(h\right)\right)^{\alpha_k}\Big\{-r\eta_2^2\eta_3^2 M^4 + \eta_2\eta_3\left(-T_{max}N\beta k\eta_1 - 2r\left(\gamma\eta_2 + \beta\eta_3\right)\right)M^3 - \Big[T_{max}N\beta k\left(\eta_1\left(\gamma\eta_2 + \beta\eta_3\right)\right. \\
&+\eta_1\eta_3\left(a - r\right)\Big) - r\left(\eta_1\left(\gamma\eta_2 + \beta\eta_3\right) + \eta_3\left(a - r\right)\right)\Big]M^2 - \Big[T_{max}N\beta k\left(a - r\right)\left(\gamma\eta_2 + \beta\eta_3\right) + \eta_1\gamma\beta \\
&+2r\beta\gamma\left(\gamma\eta_2 + \beta\eta_3\right)\Big]M + \beta^2\left[T_{max}Nk\left(Npk - \gamma\left(a - r\right)\right) - r\gamma^2\right]\Big\},
\end{aligned}$$

$$\begin{aligned}
e_{33}^* = &\left(\theta_2\left(h\right)\right)^{\alpha_k}\left(\theta_3\left(h\right)\right)^{2\alpha_k}\Big\{-r\eta_3^2\eta_2^2 M^4 - \eta_2\eta_3\left(T_{max}N\beta k\eta_1 + 2r\left(\eta_2\gamma + \eta_3\beta\right)\right)M^3 \\
&-\Big[T_{max}N\beta k\left(\eta_1\left(\eta_2\gamma + \eta_3\beta\right) + \left(a - r\right)\eta_2\eta_3\right) + r\left(\left(\theta_3\left(h\right)\right)^{-\alpha_k}\eta_2\gamma\left(4Q\beta + 4\beta + \gamma\eta_2^2\right) + \beta^2\eta_3^2\right)\Big]M^2 \\
&-\beta\Big[T_{max}Nk\left(\left(a - r\right)\left(\eta_2\gamma + \eta_3\beta\right) + \eta_1\beta\gamma\right) + 2\gamma r\left(\left(a - r\right)\left(\eta_2\gamma + \eta_3\beta\right) + \eta_1\beta\gamma\right)\Big]M \\
&+\beta^2\left[T_{max}Nk\left(\left(r - a\right)\gamma + pNk\right) - r\gamma^2\right]\Big\},
\end{aligned}$$

$$\eta_2 = Q + \left(\theta_2\left(h\right)\right)^{-\alpha_k},$$

$$\eta_3 = Q + \left(\theta_3\left(h\right)\right)^{-\alpha_k}.$$

Also, the Jacobian matrix which is necessary to analyze the equilibrium points of the discrete distributed order HIV model is obtained as

$$J(T,I,V) = \begin{pmatrix} j_{11} & j_{12} & j_{13} \\ j_{21} & j_{22} & j_{23} \\ 0 & j_{32} & j_{33} \end{pmatrix},$$

where

$$j_{11} = \frac{-Mq_1^{\alpha_k}\left(M(\theta_1(b))^{-\alpha_k} + a - r + r\frac{T_n + I_n}{T_{\max}} + kV_n \right) - \frac{r}{T_{\max}}\left(p - M\left(q_1^{\alpha_k} T_n + \sum_{j=2}^{n+1} q_j^{\alpha_k} T_{n+1-i} \right) \right)}{\left(M(\theta_1(b))^{-\alpha_k} + a - r + r\frac{T_n + I_n}{T_{\max}} + kV_n \right)^2},$$

$$j_{12} = -\frac{r}{T_{\max}}\frac{p - M\left(q_1^{\alpha_k} T_n + \sum_{j=2}^{n+1} q_j^{\alpha_k} T_{n+1-i} \right)}{\left(M(\theta_1(b))^{-\alpha_k} + a - r + r\frac{T_n + I_n}{T_{\max}} + kV_n \right)^2},$$

$$j_{13} = -k\frac{p - M\left(q_1^{\alpha_k} T_n + \sum_{j=2}^{n+1} q_j^{\alpha_k} T_{n+1-i} \right)}{\left(M(\theta_1(b))^{-\alpha_k} + a - r + r\frac{T_n + I_n}{T_{\max}} + kV_n \right)^2},$$

$$j_{21} = \frac{kV_n T_n}{M(\theta_2(b))^{-\alpha_k} + \beta},$$

$$j_{22} = \frac{-Mq_1^{\alpha_k}}{M(\theta_2(b))^{-\alpha_k} + \beta},$$

$$j_{23} = \frac{kT_n}{M(\theta_2(b))^{-\alpha_k} + \beta},$$

$$j_{32} = \frac{N\beta}{M(\theta_3(b))^{-\alpha_k} + \gamma},$$

$$j_{33} = \frac{-Mq_1^{\alpha_k}}{M(\theta_3(b))^{-\alpha_k} + \gamma}.$$

3.3. Stability Analysis of Equilibrium Points of HIV System

In this section, the stability of the model will be examined. The following Lemma and Theorem are one of the important lemmas and theorems for determining locally asymptotically stability of the equilibrium points. One can find some detailed definitions and theorems about locally asymptotically stability in (Jury, 1964), (Elaydi, 1999), (Gopal, 2009), (Richter, 2002), (Allen, 2007).

Theorem 3.1. (Richter, 2002) Let the equilibrium point of the difference equation $x_{n+1} = F(x_n)$ be $\tilde{x}$ and assume that the function F is a continuously differentiable function defined on some open neighborhood of an equilibrium point $\tilde{x}$. The equilibrium point $\tilde{x}$ is locally asymptotically stable, if absolute values of all the roots of the characteristic polynomial are less than one. Otherwise, the equilibrium point $\tilde{x}$ is unstable.

Lemma 3.1 (Schur-Cohn criterion for n=3). (Elaydi, 1999) Let the characteristic polynomial be $p(\lambda) = \lambda^3 + c_1\lambda^2 + c_2\lambda + c_3$. The solutions λ_i, $i = 1, 2, 3$ of $p(\lambda) = 0$ lie inside the unit disk if the conditions below are satisfied:

i. $1 + c_1 + c_2 + c_3 > 0$.

ii. $1 - c_1 + c_2 - c_3 > 0$.

iii. $1 - c_3^2 > |c_2 - c_3 c_1|$.

In the view of Theorem 3.1, the following theorem can be given.

Theorem 3.2. The equilibrium point E_1 of HIV system (1) is locally asymptotically stable if following conditions are satisfied.

i.

$$\left| 2(\theta_1(b))^{\alpha_k} \left[T_{\max} QM^2 + (\theta_1(b))^{\alpha_k} QT_{\max}(a-r)M + (\theta_1(b))^{\alpha_k} rp \right] \right| < \left| T_{\max} \left(1 + (\theta_1(b))^{2\alpha_k} Q^2 \right) M^2 \right.$$
$$\left. + M(\theta_1(b))^{\alpha_k} \left(-2T_{\max}r - Q(\theta_1(b))^{\alpha_k} + \varpi \right) + \left((\theta_1(b))^{2\alpha_k} \right) \left((-r+a)\varpi + T_{\max}(-r+a)^2 - 2rp \right) \right|,$$

ii.

$$\left| MQ \left[M \left((\theta_3(b))^{-\alpha_k} + (\theta_2(b))^{-\alpha_k} \right) + \beta + \gamma \right] - \left\{ M^2 Q^2 \left(\beta - M \left((\theta_3(b))^{-\alpha_k} - (\theta_2(b))^{-\alpha_k} \right) - \gamma \right)^2 \right. \right.$$
$$\left. \left. + M^2 (\theta_2(b))^{-\alpha_k} (\theta_3(b))^{-\alpha_k} \varsigma + M(\theta_2(b))^{-\alpha_k} \gamma\varsigma + \beta M(\theta_3(b))^{-\alpha_k} \varsigma + \beta\gamma\varsigma \right\}^{1/2} \right|$$
$$< 2 \left| \left(M + \gamma(\theta_3(b))^{-\alpha_k} \right) \left(M + \beta(\theta_2(b))^{-\alpha_k} \right) \right|,$$

iii.

$$\left| MQ \left[M \left((\theta_3(b))^{-\alpha_k} + (\theta_2(b))^{-\alpha_k} \right) + \beta + \gamma \right] + \left\{ M^2 Q^2 \left(\beta - M \left((\theta_3(b))^{-\alpha_k} - (\theta_2(b))^{-\alpha_k} \right) - \gamma \right)^2 \right. \right.$$
$$\left. \left. + M^2 (\theta_2(b))^{-\alpha_k} (\theta_3(b))^{-\alpha_k} \varsigma + M(\theta_2(b))^{-\alpha_k} \gamma\varsigma + \beta M(\theta_3(b))^{-\alpha_k} \varsigma + \beta\gamma\varsigma \right\}^{1/2} \right|$$
$$< 2 \left| \left(M(\theta_3(b))^{-\alpha_k} + \gamma \right) \left(M(\theta_2(b))^{-\alpha_k} + \beta \right) \right|,$$

where,

$$\varpi = \sqrt{T_{\max} \left[T_{maz} \left(\left(Q + (\theta_1(b))^{-\alpha_k} \right) M + (-r+a) \right)^2 - 4rp \right]},$$

$$\varsigma = \frac{2kN\beta\left(-T_{\max}\left(\left(Q+\left(\theta_1(b)\right)^{-\alpha_k}\right)M+a-r\right)+\varpi\right)}{r}.$$

Remark 3.1. Since the equilibrium point E_3 of HIV system (1) leads to complicated process, the examination of stability of the equilibrium point E_3 is given in the numerical results section.

3.4. Numerical Results

In the view of Lemma 3.1 and Theorem 3.2, the stability of the model will be examined for the equilibrium points E_1 and E_3 which have biological meanings. So, the parameters given in (Wang & Li, 2010) and also used in (Ongun & Turhan, 2013) are considered to be able to compare the stability results. These parameters are given as

$k = 0.0027, \beta = 0.3, T_{\max} = 1500, p = 0.1, a = 0.2, \gamma = 2.4, , N = 10$.

During the analysis the step size is chosen as $h = 0.01$. In addition, to show that DODEs are the general case of ordinary differential equations in some way, the density function is chosen as $d(\alpha) = 1$. To compare the results with (Ongun and Turhan, 2013) in which the system is ordinary differential equations the parameter of the average specific T-cell growth rate is chosen as $r = 0.05$. So, by substituting equilibrium point E_1 into Jacobian matrix, the characteristic equation is obtained as follows:

$$p(\lambda) = \lambda^3 - 0.012081\lambda^2 - 979898.33\lambda + 6517.47.$$

According to Schur-Cohn criteria, it can be seen that

1. $1 - 0.012081 - 979898.33 + 6517.47 = -973379.87 < 0.$
2. $1 + 0.012081 - 979898.33\lambda + 6517.47 = -986414.80 < 0.$
3. $\left(1 - 6517.47^2\right) - \left|-979898.33 - \left(-0.012081 \times 6517.47\right)\right| = -4345.10 < 0$

Since none of the condition of the Schur-Cohn criteria is satisfied, the equilibrium point E_1 is not stable as in (Ongun & Turhan, 2013). At the same time, the solution of characteristic equation is

$\lambda_1 = 0.006651, \quad \lambda_2 = 989.89, \quad \lambda_3 = -989.89$.

Since all of the absolute values of eigenvalues λ_i, $i = 1, 2, 3$ is not smaller than 1, it is approved that the equilibrium point is not stable.

For another comparison, by choosing $r = 0.8$, it is obtained that

$$p(\lambda) = \lambda^3 + c_1\lambda^2 + c_2\lambda + c_3$$

where

$c_1 = 3495.7956, c_2 = -24.5591, c_3 = 19399.67520$.

By using the values in the Schur-Cohn criteria,

1. $1 + c_1 + c_2 + c_3 = -15927.4386 < 0$

2. $\qquad 1 - c_1 + c_2 - c_3 = 15880.3203 > 0$,

3. $\qquad 1 - c_3^2 - |c_2 - c_3 c_1| = -0.4441.10^9 < 0$

is obtained. So, similarly, the equilibrium point E_1 is not stable as in (Ongun & Turhan, 2013).

Now, let us choose the parameter as $r = 0.001$. The characteristic equation for the equilibrium point E_1 is obtained as

$$p(\lambda) = \lambda^3 + 0.005382\lambda^2 - 0.002145\lambda - 0.000022.$$

The root of the characteristic equation is obtained as $\lambda_1 = -0.01093$, $\lambda_2 = 004851$, $\lambda_3 = -0.04296$. Since $|\lambda_i| < 1$, in this case, the equilibrium point is locally asymptotically stable as in (Ongun & Turhan, 2013). In addition, using Schur-Cohn criteria, it is satisfied that

1. $\qquad 1 + c_1 + c_2 + c_3 = 1.00321 > 0$.

2. $\qquad 1 - c_1 + c_2 - c_3 = 0.99249 > 0$.

3. $\qquad 1 - c_3^2 - |c_2 - c_3 c_1| = 0.99785 > 0$.

Now, let us compare the stability of the equilibrium point E_3 by choosing $r = 0.8$. The characteristic equation is obtained as

$$p(\lambda) = \lambda^3 - 0.00543\lambda^2 - 147344.33\lambda + 0.01474.$$

According to Schur-Cohn criteria

1. $\qquad 1 + c_1 + c_2 + c_3 = -147343.3411 < 0$.

2. $\qquad 1 - c_1 + c_2 - c_3 = -147343.3597 < 0$.

3. $\qquad 1 - c_3^2 - |c_2 - c_3 c_1| = -147343.3505 < 0$.

is obtained and it is seen that the equilibrium point E_3 is not stable.

On the other hand, as is known, discretization is depended to density function. So, under different circumstance, the density function can be chosen different. Due to this reason, unlike the other examples, let us choose the density function and the parameter r as $d(\alpha) = 3\alpha + 1$, $\alpha = 0.1$ and $r = 0.003$, respectively. For the equilibrium point E_1, the characteristic equation is

$$p(\lambda) = \lambda^3 + c_1\lambda^2 + c_2\lambda + c_3,$$

where $c_1 = -0.15658$, $c_2 = -0.05652$ and $c_3 = 0.00842$. Considering Schur-Cohn criteria

1. $\qquad 1 + c_1 + c_2 + c_3 = 0.79531 > 0$.

2. $\qquad 1 - c_1 + c_2 - c_3 = 1.09163 > 0$.

3. $\qquad 1 - c_3^2 - |c_2 - c_3 c_1| = 0.94472 > 0$.

The equilibrium point E_1 is locally asymptotically stable because of satisfying all three conditions.

As another example by choosing $d(\alpha)=2\alpha-1$, $\alpha=0.005$ and $r=0.05$, the characteristic equation of the equilibrium point E_3 is found as

$$p(\lambda)=\lambda^3+0.0056\lambda^2-1.0093\lambda+0.0035.$$

Since the roots of the interested equation are $\lambda_1=0.00358$, $\lambda_2=1.00004$, $\lambda_3=-1.00922$, the equilibrium point E_3 is not stable.

As mentioned before, NSFD schemes are very effective methods. To show the effectiveness, finally we present the comparison of the convergency of the method in Table1 and Table 2. The compatibility of the results with (Ongun & Turhan, 2012) is seen.

Table 1. Stability of equilibrium point E_1 under application of different methods for different step-size h. ($r=0.001$, $d(\alpha)=1$)

h	Theta Method	Fourth-Order Runge-Kutta Method	Distributed Order NSFD schemes
0.0001	Conv.	Conv.	Conv.
0.001	Conv.	Conv.	Conv.
0.1	Conv.	Conv.	Conv.
0.8	Conv.	Conv.	Conv.
1	Div.	Conv.	Conv.
5	Div.	Div.	Conv.
10	Div.	Div.	Conv.

Table 2. Stability of equilibrium point E_3 under application of different methods for different step-size h .($r=0.05$, $d(\alpha)=1$)

h	Theta Method	Fourth-Order Runge-Kutta Method	Distributed Order NSFD schemes
0.0001	Conv.	Conv.	Conv.
0.001	Conv.	Conv.	Conv.
0.1	Conv.	Conv.	Conv.
0.8	Div.	Conv.	Conv.
1	Div.	Div.	Div.
5	Div.	Div.	Div.

10	Div.	Div.	Div.

CONCLUSION

In this study, a model defines the HIV infection of CD4$^+$T cells is rewritten in distributed order form. The advantage of rewriting HIV system by DODEs leads from the density function included in the derivative. By density function, DODEs can be regarded as the general case of the interested ordinary differential equation. So, under different circumstances, the behavior of the differential equation can be interpreted. In the discretization of the model, NSFD schemes are used. The stability analysis of the equilibrium points is presented. The stability results correspond to ordinary differential equation model is compared with the results in literature. Also, the efficiency of NSFD schemes for big step-size is presented in Table 1 and Table 2 by comparing with Theta method and Fourth-Order Runge-Kutta method. The effect and the importance of the NSFD schemes on convergency can be clearly seen from Table 1 and Table 2 for the big step size. By making detailed comparison of the stability results with the results given in literature, it is concluded that NSFD schemes can be applied to the system of DODEs.

REFERENCES

Allen, L. J. S. (2007). *An introduction to mathematical biology*. Department of Mathematics and Statistics Texas Tech University, Pearson Education.

Caputo, M. (2001). Distributed order differential equations modelling dielectric induction and diffusion. *Fractional Calculus and Applied Analysis*, *4*(4), 421-442.

Diethelm, K., & Ford, N. J. (2009). Numerical analysis for distributed-order differential equations. *Journal of Computational and Applied Mathematics*, *225*(1), 96-104.

Ding, W., Patnaik, S., Sidhardh, S., & Semperlotti, F. (2021). Applications of distributed-order fractional operators: A review. *Entropy*, *23*(1), 110.

Dorciak L. (1994). Numerical models for simulation the fractional-order control systems. *UEF-04-94, The Academy of Sciences, Institute of Experimental Physic, Kosiice, Slovak Republic.*

Elaydi, S. (1999). *An introduction to difference equations*. Springer, New York, NY, USA.

Jury, E. I. (1964). *Theory and Application of the z-Transform Method*. Wiley.

Gopal, M. (2009). *Digital Control and State Variable Methods, Conventional and Intelligent Control Systems*. New Delhi: Tata McGraw-Hill Publishing Company Limited.

Jibenja, N., Yuttanan, B., & Razzaghi, M. (2018). An efficient method for numerical solutions of distributed-order fractional differential equations. *Journal of Computational and Nonlinear Dynamics*, *13*(11).

Katsikadelis, J. T. (2014). Numerical solution of distributed order fractional differential equations. *Journal of Computational Physics*, *259*, 11-22.

Kocabıyık, M. (2022). Nonstandard Discretization and Stability Analysis of a novel type Malaria-Ross Model. *Journal of the Institute of Science and Technology*, *12*(2), 1023-1033

Kocabiyik, M., & Yakıt Ongun, M. (2021). Construction a distributed order smoking model and its nonstandard finite difference discretization. *AIMS Mathematics, 7*(3), 4636-4654.

Kocabıyık, M., Yakıt Ongun, M. & Turhan Çetinkaya, İ. (2021). Numerical analysis of distributed order SVIR model by nonstandard finite difference method . *Journal of Balıkesir University Institute of Science and Technology,* 23 (2), 577-591 . (In Turkish)

Meerschaert, M. M., & Tadjeran, C. (2004). Finite difference approximations for fractional advection-dispersion flow equations. *Journal of computational and applied mathematics*, *172*(1), 65-77.

Mickens, R. E. (1989). Exact solutions to a finite-difference model of a nonlinear reaction-advection equation: Implications for numerical analysis. *Numerical Methods for Partial Differential Equations*, *5*(4), 313-325.

Mickens, R. E. (1994). *Nonstandard finite difference models of differential equations*. World Scientific Publishing, Atlanta, Ga,USA.

Mickens, R. E. (2002). Nonstandard finite difference schemes for differential equations. *Journal of Difference Equations and Applications*, *8*(9), 823-847.

Mickens, R. E. (2005). *Advances in the applications of nonstandard finite difference schemes*. World Scientific.

Mickens, R. E. (2007). Calculation of denominator functions for nonstandard finite difference schemes for differential equations satisfying a positivity condition. *Numerical Methods for Partial Differential Equations: An International Journal*, *23*(3), 672-691.

Najafi, H. S., Sheikhani, A. R., & Ansari, A. 2011. Stability analysis of distributed order fractional differential equations. *Abstract and Applied Analysis* (Vol. 2011). Hindawi.

Naresh, R., Sharma, D., & Tripathi, A. (2009). Modelling the effect of tuberculosis on the spread of HIV infection in a population with density-dependent birth and death rate. *Mathematical and computer Modelling, 50*(7-8), 1154-1166

Nowak, M. A., & May, R. M. (1991). Mathematical biology of HIV infections: antigenic variation and diversity threshold. *Mathematical Biosciences, 106*(1), 1-21.

Patidar, K. C. (2005). On the use of nonstandard finite difference methods. *Journal of Difference Equations and Applications,* 11(8), 735-758.

Patidar, K. C. (2016). Nonstandard finite difference methods: recent trends and further developments. *Journal of Difference Equations and Applications, 22*(6), 817-849.

Podlubny, I., 1999. *Fractional Differential Equations*, Academic Press, New York.

Richter, H. (2002). The generalized Henon maps: Examples for higher-dimensional chaos. *International Journal of Bifurcation and Chaos, 12*(06), 1371-1384.

Sweilam, N., AL-Mekhlafi, S. M., & Albalawi, A. O. (2020). On the Distributed Order Fractional Multi-Strain Tuberculosis Model: A Numerical Study. *Statistics, Optimization & Information Computing, 8(*1), 175-186.

Wang, L., & Li, M. Y. (2006). Mathematical analysis of the global dynamics of a model for HIV infection of CD4+ T cells. *Mathematical Biosciences, 200*(1), 44-57.

Yakıt Ongun, M., & Turhan, İ. (2013). A numerical comparison for a discrete HIV infection of CD4+ T-Cell model derived from nonstandard numerical scheme. *Journal of Applied Mathematics,* 2013.

Yang, Y., & Xiao, Y. (2010). Threshold dynamics for an HIV model in periodic environments. *Journal of Mathematical Analysis and Applications*, *361*(1), 59-68.

Analysis of the Charge Transport Properties of Bis Chalcone Derivative from the Reorganization Energy, Band Gap under the Different Electric Fields and Results of Bond Length Alternation for Efficient Organic Field Effect Transistors

Gül YAKALI[1]
Abdullah BİÇER
Günseli TURGUT CİN

Introduction

The π-conjugated organic molecules especially including polyaromatic systems have attracted considerable attention in the optoelectronic field due to having properties of stability, flexibility and delocalization of charges, etc (Siddiqui et al, 2012: 339, Cias et al, 2011:14519). These properties provide enhancing the charge transport rate therefore optoelectronic device performance by decreasing band gap (ΔE). Especially, π-conjugated containing thiophene backbone have considerably attention in semiconducting materials recently (Zhang et al., 2012: 879, Zhang et al., 2008: 5148).

Theoretical and experimental studies including Marcus Electron Transfer Theory and Density Functional Theory (DFT), single crystal x-ray crystallography (SCXRD) are very important methods to evaluate the charge transport properties of the molecules. Marcus Electron Transfer Theory is the powerful way for understanding the electron and hole transfer behavior of the organic semiconductor molecules in material science (Chai et al, 2011:3219). According to Marcus Electron Theory, the charge transfer rate strongly depends on the parameters of reorganization energy and charge transfer integral. The reorganization energy (λ) can be said that the change in the molecular geometry when an electron is added or removed from a molecule (inner reorganization) (Zhu et al, 2016:1078). For efficient electron or hole injection in the optoelectronic device form, it is desirable that reorganization energy is small (Qi et al, 2020:3677). Beside the reorganization energy, HOMO and LUMO orbitals, energy band gap value under the different electric fields play an important role to determine the mobility since electronic devices are operated under the electric field. Evaluation of theoretical results give the comprehensive information about the organic pi-conjugated molecules for their device forms whether they can be used as an optoelectronic device or not.

The charge transfer integral of the conjugated molecules is highly desirable large that it is evaluated from the molecular arrangements of the molecules in solid phase obtained from SCXRD data. Solid film or the crystal phase of the molecules give the excellent information the device performance by considering their aggregation phase which created noncovalent interactions intra-intermolecular hydrogen bonding, intra-intermolecular π ⋯ π stacking interactions, short

---

[1] Assoc. Prof. Dr. Gül Yakalı, Izmir Katip Çelebi University, Engineering Sciences, Orcıd: 0000-0002-0015-5948

interactions between the atoms and $C-H\cdots\pi$ interactions in the crystal structure not only single molecule since molecules display aggregation in their solid phases through collective interactions between each other (Yao et al, 2018:9, Herman et al, 2016:3). High intermolecular overlaps and close intermolecular contacts in the crystal structure are benefical for better performance of organic devices especially, organic semiconductors. According to reported results about the $\pi\cdots\pi$ stacking modes ,the antiparallel H type stacking which shows more overlap between the rings and J type stacking mode which shows less overlap or parallel displaced mode between the rings increases the optoelectronic device performance (Banerjee et al, 2019:2248, Li et al, 2020:970). Therefore, the high performance for n-type organic semiconductor with the small reorganization energy may be attributed to favourable $\pi\cdots\pi$ stacking mode with the close perpendicular distance (3.0Å- 4.0 Å) between the rings and structural rigidity with the perfect planar structure.

Ionization potential (IP), electron affinity (EA) are the important parameters to define electron and hole injection barriers. The IP value must be small for efficient hole injection into the HOMO of the molecule while EA value must be large to obtain efficient electron injection into LUMO of the molecule. The lower the IP of the hole transport layer (HTL), the easier will be the injection of holes from ITO (indium tin oxide) to HTL, the higher the EA of the electron-transport layer (ETL), and the easier the injection of electrons from the cathode to ETL (Lin et all, 2003:5241, Chai et all, 2017:697, Brückner et al, 2017:17603).

In present work, to analyze optical and electronic properties of the molecule, results of the theoretical calculations and SCXRD datas were interpereted and structure property relationship of the molecule was studied. Experimental and theoretical results demonstrated that this molecule can be used as an efficient electron transport material for OFET applications with the excellent properties in terms of small reorganization energy, high electron affinity value and desirable pi…pi stacking interactions mode in solid phase giving the information about charge transfer integral and modified to decrease reorganization energy and increase charge transfer integral.

Method

Density functional Theory Calculations including B3LYP functional and 6-311G basis set were performed to evaluate electronic and optical properties of the molecule for the use an organic semiconductors devices by using the cif file data obtained SCXRD experiment with the Gaussian software (Taydakov, 2016:32, Tsiper, 200:47).

According to Marcus Theory, the charge transfer rate is determined by the following equation.

$$W = \frac{V^2}{h}(\pi/\lambda\,k_BT)^{1/2}\exp\left(-\lambda/4k_BT\right)$$

Here, V and λ are the transfer integral and reorganization energy, respectively The λ is divided into two parts as λ_{rel}^1 which represents to the geometry relaxation energy of one molecule from neutral to charged state and λ_{rel}^2 represents to the geometry relaxation energy from charged to neutral state.

$$\lambda = \lambda_{rel}^1 + \lambda_{rel}^2$$
$$\lambda_{anion} = \lambda_{rel}^1 + \lambda_{rel}^2 = \left[E^{(1)}(M) - E^{(0)}(M)\right] + \left[E^{(1)}(M^-) - E^{(0)}(M^-)\right]$$

$$\lambda_{cation} = \lambda_{rel}^1 + \lambda_{rel}^2 = \left[E^{(1)}(M) - E^{(0)}(M)\right] + \left[E^{(1)}(M^+) - E^{(0)}(M^+)\right]$$

Here $E^{(1)}(M)$ is the neutral energy the optimized charged geometry, $E^{(0)}(M)$ is the energy of the neutral geometry. $E^{(1)}(M^-)$-$E^{(1)}(M^+)$ are the energies of the charged state at the optimized neutral geometry and $E^{(0)}(M^-)$- $E^{(0)}(M^+)$ are the neutral energies of charged states. In the calculaion of ionization energy, the adiabatic ionization potential (IPa) and vertical ionization potential (IPv) have been calculated as the following equation.

$$IPa = E^0(M)^+ - E^0(M) \text{ and } IPv = E^0(M)^+ - E^0(M)$$

The adiabatic/vertical electron affinity (EAa)/(EAv) of all molecules have been calculated as following equation;

$$EAa = E^0(M) \text{-} E^0(M)^- \text{ and } EAv = E^0(M)^- - E^1(M)^-$$

Results and Discussion

The optimized geometries of the compound in the neutral state created through the cif file of the single crystal x-ray diffraction data are demonstrated in the Figure 1. The moieties of the molecule have a slightly twisting and rigid molecular geometry in solid phase with the dihedral angle of 75° between the molecule plane and cyclohexane ring. The main aim of this study is to examine the molecular geometry and noncovalent interactions on its energy levels and charge transport properties. Therefore, HOMO and LUMO levels, ionization potential, reorganization energy, electron affinity were interpreted by taking into account the geometry and interactions of the molecule in solid phase. In addition, The electronic properties of the molecule under the different electric fields were investigated in the y direction which is the possible direction of charge transfer channels since the pi…pi stacking interactions are created along the y axis in its solid phase or crystal structure.

The molecule shows symetrical structure with the central cyclohexane ring and tiyophene rings at the ends of the molecule skeleton. Since the molecule is symmetrically twisted from the molecule plane it can be visualized as a propeller. The optimized geometric parametersof the molecule in neutral, anion and cation states are presented in Table 1.
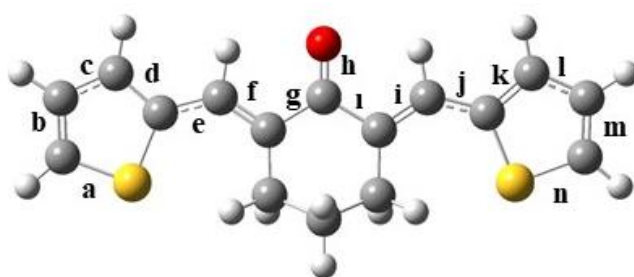

Figure 1. The optimized geometries of the studied compound.

Table 1. Bond Length Alternation Values of the compound

Index	Notr	Anion	Cation	$\Delta(C-N)$	$\Delta(A-N)$
a	1.72796	1.74615	1.71584	0.01212	0.01819
b	1.36811	1.36911	1.38465	0.01654	0.0010
c	1.41490	1.41311	1.39469	0.02021	0.00059
d	1.38305	1.39508	1.40679	0.02374	0.01203
e	1.43944	1.42518	1.41167	0.02777	0.01426
f	1.35429	1.37604	1.37920	0.02491	0.02175
g	1.50143	1.47283	1.49347	0.00796	0.0286
h	1.22652	1.25818	1.22335	0.00297	0.03166
ı	1.50144	1.47280	1.49355	0.00789	0.02864
i	1.35428	1.37605	1.37922	0.02494	0.02177
j	1.43943	1.42516	1.41166	0.02777	0.01427
k	1.38303	1.39507	1.40686	0.02383	0.01204
l	1.41491	1.41310	1.39467	0.02024	0.00181
m	1.36811	1.36910	1.38469	0.01658	0.00099
n	1.72797	1.74616	1.71586	0.01211	0.01819

The reorganization energy of the molecule can be predicted from the change in the molecular geometry optimized neutral, anion and cation states. When a molecule gains or loses charges, it will relax its molecular geometry for a new charge distribution. Due to the extended pi system, the change in the molecular parameters of the studied molecule are observed over the entire molecule. The bond length alternation (BLA) based on reduction and oxidation displayed small changes that BLA values upon reduction for the molecule are considerably larger than that of oxidation; this result verify the reorganization energy for electron is greater than those for hole of the molecule which support the results obtained from reorganization energy calculations (Table 2). In addition, the torsion angles about the cyclohexane ring in the molecule are 173.80, 174.46 and 158.86 for the neutral anionic and cationic states, respectively which supports the creation smaller geometrical changes in the anionic state than that of cationic state, also. According to following equation, the small reorganization energy (λ) which is supported by a smaller geometrical relaxation with respect to the neutral geometry is favorable to get high charge transport rate. Therefore, it can be predicted that studied molecule has electrons as a charge carriers and feature of the n-type molecule due to small electron reorganization energy value (0.20 eV).

$$W = \frac{V^2}{h}(\pi/\lambda\, k_B T)^{1/2}\exp\left(-\lambda/4k_B T\right)$$

Table 2. The value of the reorganization energies of the compound.

Compound	Boşluk reorganizayon enerjisi (eV)	Elektron reorganizasyon enerjisi (eV)
Bis-chalcone	0.23	0.20

Table 3. The value of the iyonization potenteial and electron affinitiy of the compound.

Strong stacking interactions of the compound				
Stacking parameters	Cg1 ··· Cg1 (pathway 1)	Cg2···Cg2 (pathway 2)	Cg2···Cg2 (pathway 3)	Cg1 ··· Cg1 (pathway 4)
Pitch angle (P: °)	26.7	21.3	18.6	24.1
Roll angle (R: °)	3.9(2)	5.3(2)	5.3(2)	3.9(2)
Pitch distance(d_p: Å)	1.95	1.55	1.30	1.78
Roll distance (d_r: Å)	0.26	0.36	0.36	0.26
Slipping angle (β: °)	24.1	18.6	21.3	26.7
Interplanar distance ($d_{\pi\pi}$: Å)	3.875	3.982	3.875	3.982

In device applications of organic π-conjugated systems beside the taking into account the reorganization energy, the molecular arrangement and assembly of molecules are considered to determine the charge transfer integral given in the equation 1 which is the parameter defined the molecular interaction between the adjacent fragments of the molecule through noncovalent interactions in solid phase. Molecular arrangements in solid phase created by pi..pi (ring…ring) stacking interactions provide charge transport channels between the aggregated molecules. In this molecule, the antiparallel H type with helical stacking interactions in the solid phase of the molecule forms the charge transport channel for the molecule that this type stacking is a favourable to increase the charge transport rate, therefore transfer integral value since high transfer integral result in high charge mobility in the optoelectronic field (Figure 2). The pi..pi stacking type of the studied molecule was decided by evaluating the stacking and interactions parameters given in the Table 4. In addition, the stacking interactions of the molecule are consolidated by the nonlassical hydrogen bonds.

Compound	IPa(eV)	IPv(eV)	EAa(eV)	EAv(eV)
Bis-chalcone	7.19	7.31	1.15	1.05

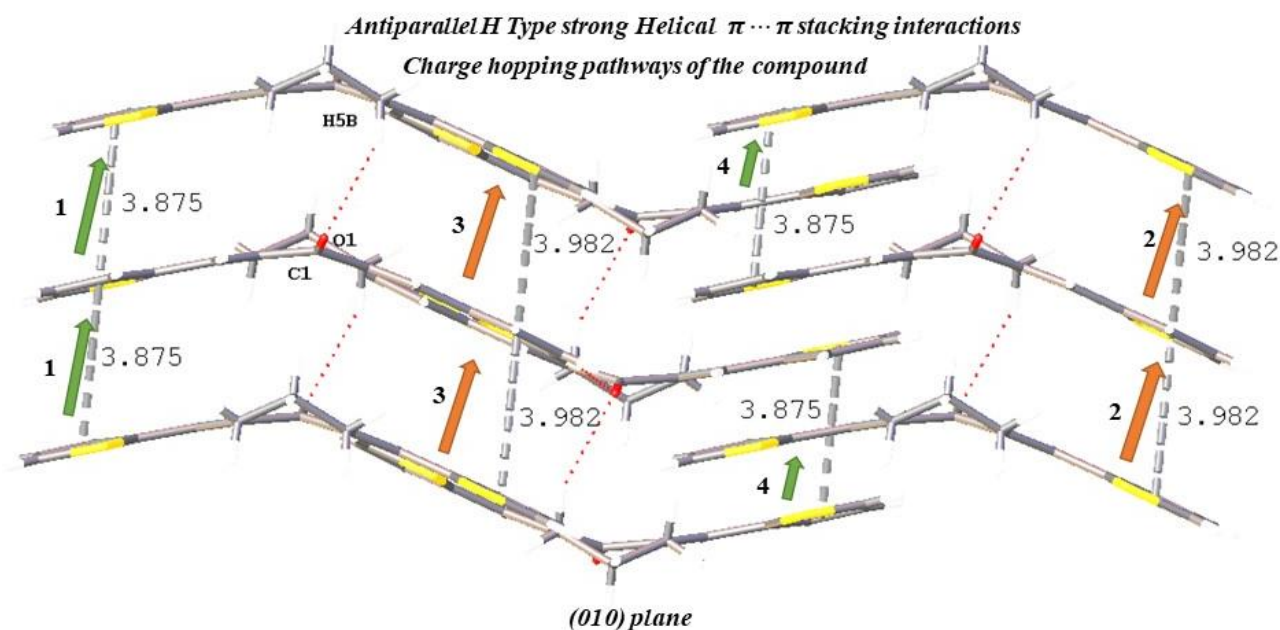**Table 4.** Crystallographic stacking data of the compound.

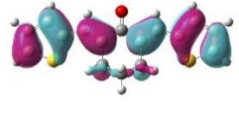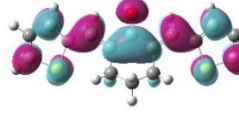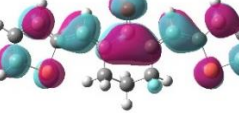**Figure 2.** The favourable charge hopping pathways of the compund.

To further understanding the optoelectronic device performance of the molecule, injection of hole and electron into an organic molecule should be considered through evaluating IP and EA values. The IP value must be small for efficient hole injection into the HOMO of the molecule while EA value must be large to obtain efficient electron injection into LUMO of the molecule. The lower the IP result in easier the injection of holes, the higher the EA result in easier the injection of electrons .The calculated results of the IPs and EAs, HOMO-LUMO energy levels and band gaps are shown in Table 5 and 6. In our study, it is clear that IPv has higher value, whereas vertical electron affinity has a lower value when we compare the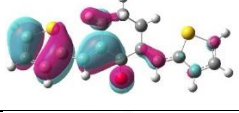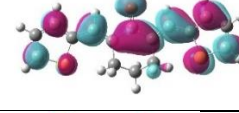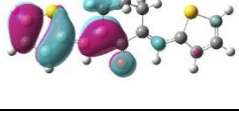 results with other studied similar molecules given in the literature (Wang et al, 2016:8405, Navamani et al, 2013:17948). The low electron affinity of molecule means large barrier for electron injection, which will result in a high threshold voltage. The LUMO level of the molecule should be lowered for easy electron injection. As a result our molecule are suitable for electron transport with the high EA value and hole transport material with the small IP value. It could be good candidate material to obtain efficient ambipolar (n type and p type) type charge transport material in optoelectronic field.

The distribution of the HOMO and LUMO of the molecule at different electric fields from 0.0 eV to 0.40 eV were calculated in the y direction which is the possible direction of charge transfer since the pi…pi stacking interactions are created along the y axis in its solid phase or crystal structure. (Figure 2) . Since HOMO and LUMO orbitals are delocalized over the entire molecule, it has good conducting channel for the electron transfer. The total dipole moment of the molecule has been found as small 2.078 debye when there is no electric field. It means that the molecule has high polarizability. Its dipol moment value decreased as the electric field applied that the electron transport property of the molecule is strengthened as electric field increased. The change in the electric field has the effect on the HOMO and LUMO energy levels and band gap value (Table 5 and Table 6). It has also been observed that the increase in electric field leads to the decrease in band gap and the HOMO and LUMO start localizing at the opposite side of the molecule showing that the molecule under electric field is a better electron transport material.

Table 5. HOMO, LUMO, band gap and Total dipol momens of the molecule under the different electric fields.

Electric Fields (eV)	HOMO (eV)	LUMO (eV)	Band Gap (eV)	Dipole Moment (debye)
0.00	-5.9749	-2.4136	-3.5613	2.078274
0.10	-6.4974	-3.0764	-3.4210	2.629898
0.20	-6.9722	-3.6557	-3.3165	3.509276
0.30	-7.4506	-4.2846	-3.1660	4.756478
0.40	-7.9023	-4.8432	-2.1798	5.922111

Table 6. Spatial distrubution of HOMO and LUMO under the various electric fields.

Electric Fields $(V/Å)$	HOMO	LUMO
0.00		
0.10		
0.20		
0.30		
0.40		

Conclusions

In conclusion, the electronic and charge transport properties of the bischalcone derivative have been studied by considering the Marcus Electron Theory and DFT calculations from the crystallographic data. The electron reorganization energy of the molecule was defined smaller than that of hole that the molecule displays feature of n type organic molecule due to having the electrons as a charge carrier. In addition, electron injection barrier of the molecule was predicted as a small since it has high EA value when we compared it with similar molecules given in the literature. The small IP value makes the molecule durable for optoelectronic devices. Beside the reorganization energy to verify the charge transfer integral of the molecule which is shown in the mobility formula, the molecular arrangements of the molecule in solid phase was considered. According the crystallographic stacking data and stacking view of the molecule , it displayed antiparallel stacking type with the helical formation in solid phase which is a favourable type to create efficient optoelectronic device. The HOMO-LUMO behavior of the molecule was observed in the different electric fields via calculation of DFT because the organic semiconductors are

conducted under the electric field. As the electric field increased from 0.0 eV to 0.40 eV band gap value decreases and situation of the orbitals changes that they are located opposite sides of the molecule. Also, its dipol moment value decreased as the electric field applied that the electron transport property of the molecule is strengthened as electric field increased. Experimental and theoretical results demonstrated that this molecule can be used as an efficient electron transport material for OFET applications and modified to decrease reorganization energy and increase charge transfer integral.

Acknowledge

References

Banerjee, A.; Saha, A.; Saha, B. K. *Crystal Growth and Design* **2019.** Understanding the Behavior of π-π Interactions in Crystal Structures in Light of Geometry Corrected Statistical Analysis: Similarities and Differences with the Theoretical Models, 19(4), 2245–2252. https://doi.org/10.1021/acs.cgd.8b01857.

Brückner, C.; Walter, C.; Stolte, M.; Braïda, B.; Würthner, F.; Engels, B.; Brückner, C.; Walter,

C.; Stolte, M.; Braïda, B.; Meerholz, K.; Bru, C.; Walter, C.; Stolte, M.; Meerholz, K. *Jounal of Physical Chemistry C,* **2017.** Structure – Property Relationships for Exciton and Charge Reorganization Energies of Dipolar Organic Semiconductors : A Combined Valence Bond Self-Consistent Field and Time-Dependent Hartree-Fock and DFT Study of Merocyanine Dyes*, 119, 31, 17602–17611, https://doi.org/10.1021/acs.jpcc.5b06206.

Chai, S.; Wen, S. H.; Huang, J. D.; Han, K. L. *Journal of Computational Chemistry* **2011** Density Functional Theory Study on Electron and Hole Transport Properties of Organic Pentacene

Derivatives with Electron-Withdrawing Substituent, *32* (15), 3218–3225. https://doi.org/10.1002/jcc.21904.

Chai, S.; Chen, D.; Huang, J. *Research Papers.* **2017**, Charge-transport properties of 4-(1,2,2-triphenyl-vinyl)aniline salicylaldehyde hydrazone: tight-packing induced molecular 'hardening' 695–699. https://doi.org/10.1107/S2052252517010685.

Cias, P.; Slugovc, C.; Gescheidt, G. Hole Transport in Triphenylamine Based OLED Devices: From Theoretical Modeling to Properties Prediction. *Journal of Physical Chemistry A* 2011, *115* (50), 14519–14525. https://doi.org/10.1021/jp207585j.

Hermann, J.; Alfè, D.; Tkatchenko, A. *Nature Communications* **2017**, Nanoscale π-π Stacked Molecules Are Bound by Collective Charge Fluctuations. *8* (14052), 1-8. https://doi.org/10.1038/ncomms14052.

Li, Q.; Li, Z. *Accounts of Chemical Research,* **2020.** Molecular Packing: Another Key Point for the Performance of Organic and Polymeric Optoelectronic Materials., *53* (4), 962–973. https://doi.org/10.1021/acs.accounts.0c00060.

Lin, B. C.; Cheng, C. P.; Ping, Z.; Lao, M. *Journal of Physical Chemistry A*, **2003**. Reorganization Energies in the Transports of Holes and Electrons in Organic Amines in Organic Electroluminescence Studied by Density Functional Theory, 5241–5251. https://doi.org/10.1021/jp0304529

Navamani, K.; Saranya, G.; Kolandaivel, P.; Senthilkumar, K. *Chemical Physics* **2013**. Effect of Structural Fluctuations on Charge Carrier Mobility in Thiophene, Thiazole and

Thiazolothiazole Based Oligomers. Physical Chemis*try 15* (41), 17947–17961. https://doi.org/10.1039/c3cp53099j.

Qi, Y.; Chen, C.; Zheng, C.; Tang, Y.; Wan, Y.; Jiang, H.; Chen, T.; Tao, Y.; Chen, R. *Physical Chemistry Chemical Physics* **2020.** Heteroatom-Bridged Heterofluorenes: A Theoretical Study on

Molecular Structures and Optoelectronic Properties, *22*(6), 3675–3682. https://doi.org/10.1039/c9cp06458c.

Siddiqui, S. A.; Al-Hajry, A.; Al-Assiri, M. S. *International Journal of Quantum Chemistry* **2016.** Ab Initio Investigation of 2,2'-Bis(4-Trifluoromethylphenyl)-5,5'-Bithiazole for the Design of Efficient Organic Field-Effect Transistors, *116* (5), 339–345. https://doi.org/10.1002/qua.25034.

Taydakov, I. V.; Akkuzina, A. A.; Avetisov, R. I.; Khomyakov, A. V.; Saifutyarov, R. R.;

Avetissov, I. C. *Journal of Luminescence* **2016**. Effective Electroluminescent Materials for OLED Applications Based on Lanthanide 1.3-Diketonates Bearing Pyrazole Moiety. *177*, 31–39. https://doi.org/10.1016/j.jlumin.2016.04.017.

Tsiper, E. V.; Soos, Z. G.; Gao, W.; Kahn, A. *Chemical Physics Letters* **2002**. Eletronic Polarization at Surfaces and Thin Films of Organic Molecular Crystals: PTCDA. 360 (1–2), 47–52. https://doi.org/10.1016/S0009-2614(02)00774-1.

Yao, Z. F.; Wang, J. Y.; Pei, J. *Crystal Growth and Design* **2018**. Control of π-π Stacking via Crystal Engineering in Organic Conjugated Small Molecule Crystals. 18 (1), 7–15. https://doi.org/10.1021/acs.cgd.7b01385.

Wang, L.; Li, T.; Shen, Y.; Song, Y. A. *Physical Chemistry Chemical Physics* **2016**. Theoretical Study of the Electronic Structure and Charge Transport Properties of Thieno[2,3-b]Benzothiophene Based Derivatives, 18 (12), 8401–8411. https://doi.org/10.1039/c5cp07879b.

Zhang, M.; Zhao, G. Ming-Xing Zhang and Guang-Jiu Zhao. *ChemSusChem* **2012**. Modification of n-Type OrganicSemiconductor Performance of Perylene Diimides by Substitution in Different Positions: Two- Dimensional π- Stacking and Hydrogen Bonding, *ChemSusChem 2012,* 5, 879 – 887. https://doi.org/10.1002/qua.25034

Zhang, Y.; Cai, X.; Bian, Y.; Li, X.; Jiang, J. *Journal of Physical Chemistry C* 2008. Heteroatom Substitution of Oligothienoacenes: From Good p-Type Semiconductors to Good Ambipolar Semiconductors for Organic Field-Effect Transistors. *112* (13), 5148–5159. https://doi.org/10.1021/jp710123r.

Zhu, R.; Duan, Y. A.; Geng, Y.; Wei, C. Y.; Chen, X. Y.; Liao, Y. *Computational and Theoretical Chemistry* **2016**. Theoretical Evaluation on the Reorganization Energy of Five-Ring-Fused Benzothiophene Derivatives. 1078, 16–22. https://doi.org/10.1016/j.comptc.2015.12.017.

Assembly Line Balancing using Lean Techniques and Mathematical Modeling: A Case Study

Betül KAYIŞOĞLU[1]
İsmet SÖYLEMEZ[2]
Özgül DEMİREL[3]
Gamzenur ARIKAN[3]
Kübra KURTOĞLU[3]

Introduction

The competitiveness of companies is determined as a result of the efficient and effective use of resources. The efficient and effective use of resources in the production sector is possible as a result of the balanced distribution of workloads to workstations on assembly lines. The assembly line balancing problem in institutions with assembly lines is to arrange the workstations during the assembly process, taking into account the priority relations between the works.

Assembly lines can be defined as systems in which small modular transport systems called conveyor belts are added one after the other and the product is transported either automatically or manually (Soylemez, 2020). Each product becomes the final product after the successive processes called "tasks" are completed. In the technical relations of the tasks with each other, that is, in the priority relations, other tasks cannot be started before some tasks are completed. In the assembly line balancing problem, 3 different objectives take these constraints into account. Type-1 is to find the minimum number of stations in the given cycle time, Type-2 is to find the cycle time in the given number of stations, and Type-E is to maximize line efficiency that considers not the only number of stations but also cycle time. In this study, the type-2 assembly line balancing problem is handled. The amount of time it takes to complete a product from start to finish is defined as cycle time. A new product is processed in each cycle. The final product is obtained by completing the processes at all stations.

Lean manufacturing was born in the Toyota Factory. The lean manufacturing system is also called Toyota Production System. The general definition of Lean according to the Lean Institute that "Lean is a way of thinking about creating needed value with fewer resources and less waste. And lean is a practice consisting of continuous experimentation to achieve perfect value with zero waste." (https://www.lean.org/explore-lean/what-is-lean/). There are generally 7 wastes in the production systems. These are Inventory, Waiting, Quality Defects, Overproduction, Over-processing, Motion, and Transportation. Experts are also talking about an 8th waste these days. This is about Unused Talent or Skills. Lean manufacturing techniques are used to eliminate these

[1] Dr, Abdullah Gül Üniversitesi, Endüstri Mühendisliği, 0000-0001-9979-5269
[2],* Dr, Abdullah Gül Üniversitesi, Endüstri Mühendisliği, 0000-0002-8253-9389, Corresponding Author
[3] Abdullah Gül Üniversitesi, Endüstri Mühendisliği

wastes. 5S and Kaizen are the two lean manufacturing techniques that are applied to eliminate wastes.

In this study, the simple assembly line balancing problem (ALB) is discussed. The system, which was simplified by using lean techniques first, was then balanced using a mathematical model. A case study is conducted in a company producing ovens. With lean techniques, wastes are eliminated and the process time of the tasks is achieved. With the precedence relation of the tasks, a mathematical model is run to achieve a balanced assembly line. Different computational experiments are conducted with different numbers of workstations. According to the results of the mathematical model, cycle time and the number of workstations both decreased.

The rest of the study is organized as follows: The literature about assembly line balancing is discussed in Section 2. Section 3 gives the current system and first solution approach which is lean techniques discussed. The mathematical model is presented in Section 4. Section 5 gives the mathematical modeling results. Section 6 concludes the study.

Literature Review

Some literature review studies about the ALB problem that have been carried out are as follows: Baybars (1986); Becker and Scholl (2006); Boysen, Fliedner, and Scholl (2007); Battaia and Dolgui (2013); Sivanankaran and Shahabudeen (2014); Hazır, Delorme, and Dolgui (2014); Eghtesadifarda, Khalifehb, and Khorrama (2020).

Ertürk et al. (2014) performed the "Ranked Positional Weight Assembly Line Balancing Method" which is one of the heuristic methods for the ALB problem. Sahin et al. (2018) handled multi-manned assembly line balancing problem which also handled the number of required resources. The authors applied a simulated annealing algorithm for the solution methodology. Delice et al. (2018) handled two-sided U-type assembly lines with sequence-dependent set-up times. In this article, the ant colony optimization method was applied.

Sahin and Kellegoz (2019) handled multi-manned assembly lines with walking workers. In this article, they developed mathematical modeling and used Electromagnetic Field Optimization Algorithm as a solution methodology.

Yıldız et al. (2020) discussed the line balancing problem with a two-stage approach. In the first stage, the determination of whether the workers can perform the work elements and the necessary equipment determination was completed, and then the line balancing problem was solved in the existing system with mathematical modeling (using LINGO). In the second stage, a simulation model was designed in ARENA to determine whether the balanced assembly line in the new system complies with the real conditions, thanks to the data obtained in the first stage.

In the study by Campana et al. (2022), different from simple assembly line balancing, assignments were made by considering hierarchical worker assignments. In the article, mathematical models and heuristic methods are used and heuristic methods are compared.

The study by Qattawi Madathil (2019) consists of two phases; the first phase is applying lean manufacturing principles to reduce waste and improve the overall assembly-line efficiency. In this phase, Heijunka (production leveling), Muda elimination, and supermarket are applied. The second is line balancing using optimization modeling. After the second phase, the number of stations decreases from 27 to 21, and the total number of workers decreases from 27 to 23.

Case Study

A case study is conducted in an oven company. This company produces different types of gas and electrical cooking ranges. Firstly, lean manufacturing studies were carried out in the production area, and the studies related to the optimization mentioned in section 4 were developed.

Company has an assembly line that is used for the assemble process for the ovens. There are 28 workstations in the assembly line. Figure 1 shows the operation times in each station after wastes are eliminated. The longest operation time in the workstations gives us the cycle time that is 70 in the current system. It can be easily observed that the workers in the workstations do not do the same amount of work, some do less work, while others work longer than average. Figure 1 shows us how unbalanced the assembly line is in the current system.

One of the most basic assumptions of the assembly line balancing problem is that task times are standard. That is, there is a standard time for the time spent in producing each product. Assembly line balancing in the current production system does not mean achieving very good results. Because current task times need to be analyzed in detail. Thanks to detailed video analysis; value-added, non-value-added, and waste times are revealed in detail. With small touches, shorter standard times can be reached thanks to productivity increases in the processes. For this reason, processes with lean manufacturing techniques were analyzed first. Standard times are reached in a shorter time. Then, it is aimed to reach the optimum assembly line with the help of a mathematical model. The studies on lean manufacturing are given, firstly.
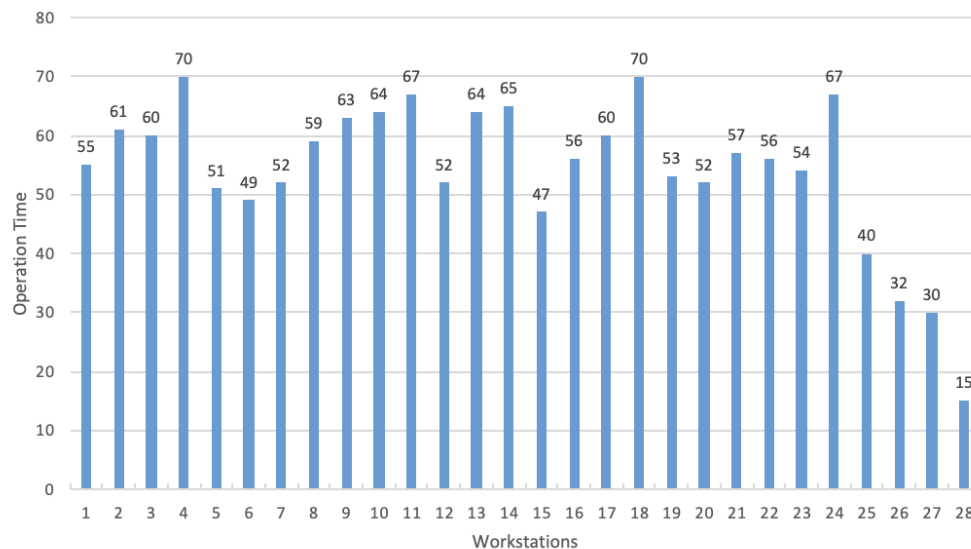
Figure 1. Operation time in each workstation in the current system

Lean Manufacturing

Before starting the analysis, it is necessary to choose which product family to work with first. The product group with the highest demand was selected according to the previous year's demand. Secondly, the determination of job elements by microanalysis was done.

While using the video analysis method, the business processes of the selected product family were determined. Then, videos of the processes were taken. Each video is examined in detail and

detailed with the microanalysis method. As a result of the video analysis, each process was divided into 3 basic parts. These are value-added, non-value-added, and waste activities. "Cutting, bending, screwing, welding, painting" will be given as value-added activities (VA). "Turn on, close, fix, check, control" are the non-value added activities (NVA). Waste activities (W) will be "walking, repairing or looking for" etc. Figure 2 shows different types of process times. Task i takes 62 seconds. However, NVA and W activities must be completely or partially eliminated. Firstly, waste time should be completely eliminated. When the first stage is completed, it is aimed to shorten the times that NVA in lean manufacturing. Even in VA activity, the time can be shortened with kaizens.

Figure 2. Types of task process times

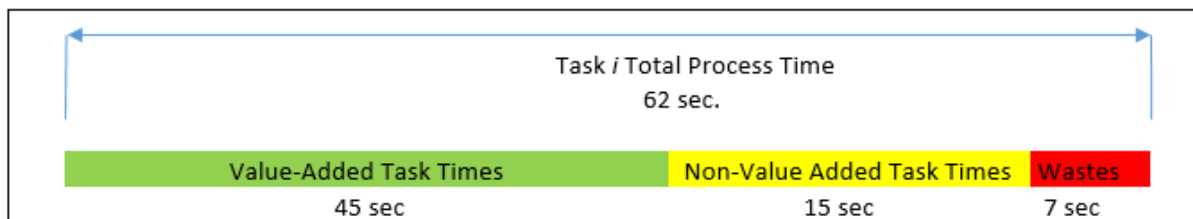With small touches, wastes are eliminated. And also small kaizens were carried out to remove some non-value adding activities. After eliminating unnecessary activities, it will be possible to move on to the mathematical modeling part for assembly line balancing.

An example of improving processes with the microanalysis method is as follows:

Hitting the bottom and side hairs of the oven with a hammer is one activity and takes 35 seconds. Turning and holding the hammer takes 2 seconds in the current system. Instead of the operator turning around and picking up the hammer every cycle, placing the hammer on the side of the assembly line table or with a top-hanging system can be achieved more easily. In this way, a gain of 2 seconds will be provided for each product/cycle. Another waste minimization example is "placing the oven in the packing carton". In the current situation, it takes about 40 seconds. When this preparation time is eliminated, the processing time is halved which is about 20 seconds waste time. Elimination of this process for the assembly line is an important gain for assembly line balance.

Two detailed video analysis gains are mentioned above. There are 48 work items in the selected product group. Video microanalysis was performed for all items. The total processing time has been reduced from 1341 to 1072. In this way, about 20% efficiency increase was achieved before the line balance was made.

After these analyses, new processing times are obtained for 48 tasks. After this stage, a better line balance was achieved with the help of mathematical modeling. In the following part, the mathematical modeling approach is presented.

Methodology

After the necessary improvements were completed with lean techniques, the optimization phase was started. There are three main constraints for the assembly line balancing problem. these constraints; assignment of all tasks to stations, ensuring priority relations, and not exceeding the number of stations given. It is aimed to reach the best cycle time by satisfying these constraints.

Mathematical Modeling

In this study, the type-2 assembly line balancing problem is studied in which the cycle time is minimized with the given number of stations. Let N denote the set of tasks where $i, j \in N$, and S denote the set of workstations where $k \in S$. P_j is the set of immediate predecessors of task i in the precedence network where $Pj \subset N. t_i$ is the operation time of task i. The last parameter c is the cycle time. x_{ik} is defined as a binary variable that takes the value 1 if task i is assigned to Workstation k, 0 otherwise.

With these definitions, the type-2 assembly line balancing model (T2ALBM), is given below:

Model T2ALBM:
$$Z^* = Min \; c \tag{1}$$

s.t.

$$\sum_{k \in S} x_{ik} = 1 \qquad \forall i \in N \tag{2}$$

$$\sum_{i \in N} t_i x_{ik} \leq c \qquad \forall k \in S \tag{3}$$

$$\sum_{k \in S} k \, x_{ik} - \sum_{k \in S} k \, x_{jk} \leq 0 \qquad \forall j \in N, \forall i \in P_j \tag{4}$$

$$x_{ik} \in \{0,1\} \qquad \forall i \in N, \forall k \in S \tag{5}$$

The objective function defined in Equation (1) minimizes the cycle time. Constraints (2) ensure that every task is assigned to a workstation. Constraints (3) guarantee that the total time in a station does not exceed the cycle time. Constraints (4) satisfy the precedence relations between tasks. Constraints (5) define decision variables.

Results

There are 48 different tasks done on the assembly line of the company in which we conduct our case study. Process time of these tasks and the precedence relation between them are defined. We run the model (T2ALBM) type-2 assembly line balancing model for this problem. We consider the different number of workstations from 17 to 30. We run with CPLEX and obtain the optimal solution for each instance in seconds. Figure 3 gives the cycle times achieved with the mathematical model for the different numbers of stations.
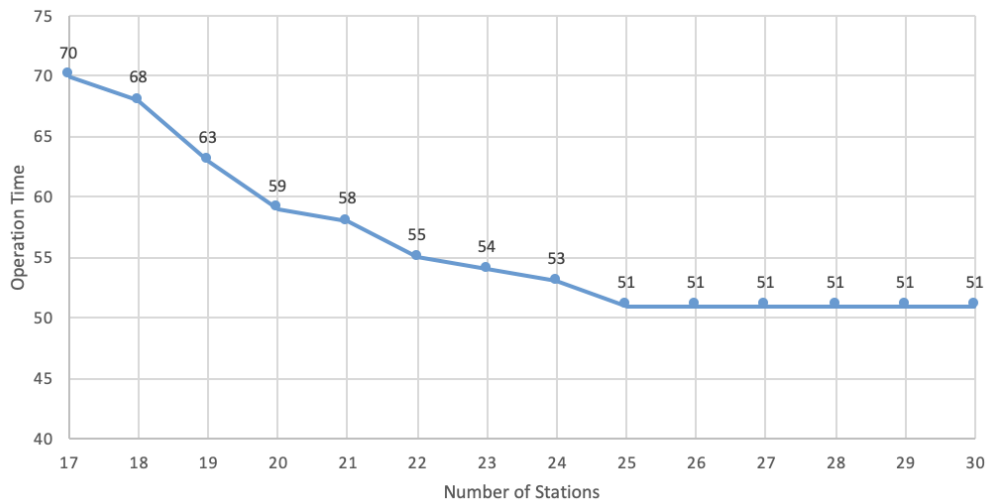
Figure 3. Cycle times achieved with T2ALBM for different numbers of stations

When Figure 3 is examined, it is seen that cycle time decreases as the number of stations increases as expected. However, when the number of stations is 25, there is no improvement in the cycle time even if we increase it more. The operation time of one of the tasks is 51 seconds. For that reason, we do not get any improvement as much as we increase the number of workstations. In the current system, the number of workstations is 28 with cycle time 70 seconds. When we check the mathematical model solution with 28 workstations, the cycle time is 51 seconds which is 27% lower than the current cycle time. Moreover, with the mathematical model, we are able to achieve the same cycle time with the lower number of workstations. Decreasing the number of stations from 28 to 25 is possible with cycle time 51. This means that we also have an improvement in the number of employees. It can be easily seen from Figure 4 that there is a more balanced assembly line with the solution achieved with T2ALBM.

Figure 4. Operation time in each workstation in the solution achieved with T2ALBM for the number of workstations 25.

If the company does not need to decrease the cycle time in the current system. In other words, if the cycle time 70 is appropriate for their current production system, then we can check the number of workstations needed for this cycle time from the solutions of the mathematical model. In this case, 17 workstations are enough instead of 28 workstations which imply 39% improvement in the workforce.

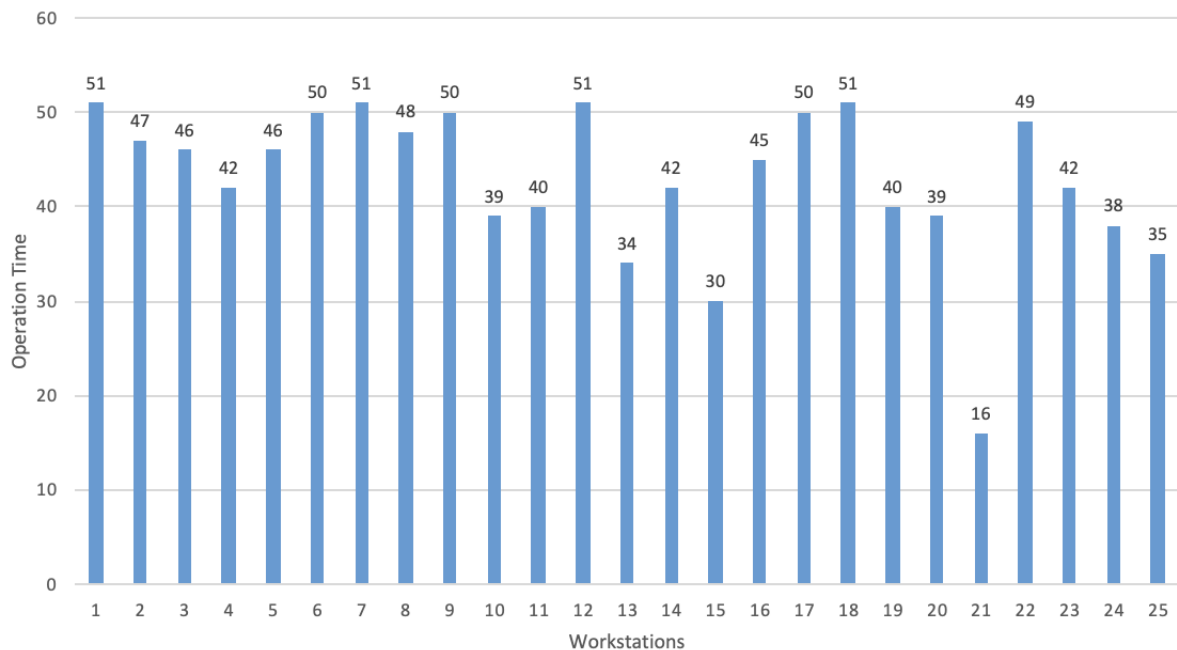## Conclusion

In this study, a simple assembly line balancing problem is studied. A case study is conducted in a company producing ovens. The product group with the highest demand is chosen to study. All the tasks conducted to produce this product group are listed. Non-value added and waste activities are determined and eliminated with small kaizens. The operation time of each task and precedence relations of these tasks are obtained. In the current system, the assembly line is examined. The operation times in each workstation are observed and it is seen that the assembly line is not balanced effectively. Cycle time is directly related to the task assignments to workstations. For that reason, it is crucial to be able to obtain balanced assembly lines.

To be able to solve ALB problem, the mathematical model is given. The mathematical model is solved for the different number of workstations. The cycle time achieved by the mathematical model with the same number of workstations in the current system is 27% lower than the current cycle time. Moreover, when we analyze the results of the mathematical model, we see that the number of workstations required to achieve the same cycle time in the current system is 39% lower than the number of workstations in the current system. To sum up, with the mathematical model, the cycle time or/and the number of workstations in a system can be improved significantly.

References

Battaïa, O. and Dolgui, A. (2013). A taxonomy of line balancing problems and their solution approaches. International Journal of Production Economics, 142(2), 259-277.

Baybars, I., (1986). A survey of exact algorithms for the simple assembly line balancing problem. Management Sciences, 32, 909–932.

Becker, C. and Scholl, A. (2006). A survey on problems and methods in generalized assembly line balancing. European Journal of Operational Research, 168(3), 694- 715.

Boysen, N., Fliedner, M., and Scholl, A. (2007). A classification of assembly line balancing problems, European Journal of Operational Research, 183, 674-693.

Campana, N. P., Iori, M., & Moreira, M. C. O. (2022). Mathematical models and heuristic methods for the assembly line balancing problem with hierarchical worker assignment. International Journal of Production Research, 60(7), 2193-2211

Delice, Y., Aydoğan, E. K., Söylemez, İ., & Özcan, U. (2018). An ant colony optimisation algorithm for balancing two-sided U-type assembly lines with sequence-dependent set-up times. Sādhanā, 43(12), 1-15.

Eghtesadifard, M., Khalifeh, M., and Khorram, M. (2020). A systematic review of research themes and hot topics in assembly line balancing through the web of science within 1990–2017. Computers and Industrial Engineering, 139, 106-182.

Eryürük, S. H., Kalaoğlu, F., & Baskak, M. (2011). Assembly line balancing by using statistical method in clothing production. Textile and Apparel, 21(1), 65-71.

Hazır, Ö., Delorme, X., and Dolgui, A. (2014). A survey on cost and profit oriented assembly line balancing. International Federation of Automatic Control Proceedings, 47 (3), 6159-6167.

Qattawi, A., & Chalil Madathil, S. (2019). Assembly line design using a hybrid approach of lean manufacturing and balancing models. Production & Manufacturing Research, 7(1), 125-142.

Sahin, M., Kellegoz, T., & Soylemez, I (2018). Çok işçili montaj hatlarında istasyon ve kaynak yatırımı maliyetinin enküçüklenmesine yönelik tavlama benzetimi ve tam sayılı doğrusal programlamaya dayalı yeni bir algoritma. Dicle Üniversitesi Mühendislik Fakültesi Mühendislik Dergisi, 9(2), 727-739.

Sahin, M., & Kellegoz, T. (2019). Balancing multi-manned assembly lines with walking workers: problem definition, mathematical formulation, and an electromagnetic field optimization algorithm. International Journal of Production Research, 57(20), 6487-6505.

Sivasankaran, P. and Shahabudeen, P. (2014). Literature review of assembly line balancing problems. The International Journal of Advanced Manufacturing Technology, 73, 9- 12, 1665-1694.

Soylemez, I (2020). Kaynak Paylaşımlı Kaynak Kısıtlı Montaj Hattı Dengeleme Problemi için Bir Çözüm Yaklaşımı, Gazi University, PHD dissertation.

Topaloğlu Yıldız, Ş., & Yıldız, G., & Cin, E. (2020). A mathematical programming and simulation modeling based solution approach to the worker-assigned assembly line balancing problem in an electronics company. Kocatepe İİBF Journal, June 2020, 22(1), 57-73.

Access time: 29.11.2022, https://www.lean.org/explore-lean/what-is-lean/.

Nonlinear Deformation Capacities of RC Frames Under Seismic Loads and Pushover Analysis.

Mehmet Fatih Yilmaz[1]

1.Introduction

The most important part of the building in Turkey are composed of Reinforced Concreate structures. Considering the seismic event in the region, it is require to determine the seismic behavior of the RC structures with a more proper and correct methods. For these purposes many linear and nonlinear analysis approach are investigated. With the new specification about seismic design of building the design approach changes from strength base design to displacement base design. Displacement based design approach allow engineer to consider the nonlinear deformation capacities of the structures and economically design structure under seismic loads. The equal displacement rule are the critical acceptance of these approach. It accept that the elastic models and nonlinear model of building have equal displacement demand under seismic loads. There for if the structure design to reach the demand displacement of the seismic load without crashing, it can safely carry the seismic loads.

For these purpose determining nonlinear response of the RC structure become critical and many affords are focuses on this. Rasheed and Dinno [1] develop a new method for reinforced concrete structural elements, taking into account the nonlinear behavior capacities, and with the help of these approaches, more economical designs can be made. Rasheed and Dinno [1] conduct a study, in order to determine the nonlinear behavior of reinforced concrete structures, analytical models were created with the help of the Sap 2000 program by using the experimental data in the literature and testing the compatibility of these models with experimental studies. Most literature research presumes that the frame systems' flexibility is simply the bending of the columns and beams. Although the bending of columns and beams is modeled with the generally used plastic hinge, it is impossible to predict the joint's flexibility. For this reason, there is a need for advanced models that will take into account the joint's flexibility and better represent the structure's lateral deformations and earthquake responses [2]. Rajasankar, Iyer, and Prasad [3] developed formulations of lumped plastic behavior and nonlinear behavior to calculate reinforced concrete sections. The effect of shear force on the collapse in reinforced concrete elements is generally neglected in nonlinear analysis approaches. However, shear force and axial loads have significant effects on bending failure.

Shayanfar and Akbarzadeh Bengar [4] conduct a study presenting a spring model describing the bending behavior and the effects arising from the shear effect was proposed, and the reality of the proposed model was examined with parametric studies. Habibi and Moharrami [5] conduct a study to determine the nonlinear sensitivity analysis of reinforced concrete moment frame structure. Nonlinear pushover analysis with both material and geometric nonlinearity was considered. The improved computer technology makes more advanced structure analysis available, and the specification requirements are changed from static analysis to nonlinear analysis. Moreover,

[1] Mehmet Fatih Yilmaz, Assit Prof Dr,Ondokuz Mayis University, Civil Engineering Department

the probabilistic uncertainties should be determined in the structure's design. For these purposes, some efforts are presented in the literature to determine the reliability analysis of structure with the first-order reliability methods and nonlinear analysis [6].

One of the important factor effecting the nonlinear behavior of the RC structure is the reinforcing details. The proper detailing of the reinforcement include both longitudinal and transverse reinforcing. For this purpose a detailed study conducted to determine the reinforcing configuration and minimum and maximum reinforcing requirement of the RC structure. This study discusses a reinforced concrete frame beam system, which has been experimentally studied in the literature. Firstly, pushover analyzes of the RC frame system were performed with the help of Sap 2000 and Seismo-struct programs, and its compatibility with the experimental data was observed. Thus, it has been shown that the mathematical model is compatible with the actual model. Then, real earthquake records were applied to the frame system, and the base shear force and peak displacement values of the frame beam were obtained under the near-fault and far-fault earthquake records. Earthquake records were scaled so that elastic earthquake forces exceeded the beam base shear capacity, and analyzes were performed for new records. In addition, pushover analyzes were carried out by forming different transverse reinforcement details, and the effects of the change in transverse reinforcement details on the frame deformation capacity and ductility were examined.

2.FE model of the frame structure

2.1.Description of the frame structure

A reinforced concrete frame system, which can make large deformations under the effect of bending, has been examined in this study. Studies on both analytical and mathematical models were carried out by the examined system [7], and a system with details in the literature was selected. The purpose of choosing this system is to compare the results obtained from the model created in the computer environment with the results obtained from the experimental study and to determine the compatibility of the model created with the real model, taking into account the assumptions to be made during modeling.

The studied system consists of a two-story frame. This system has a foundation section with a width of 800 (mm) and a height of 400 (mm) at the bottom. In the experimental studies, the foundation section was attached to the strong floor in the laboratory with the help of pre-stressed bolts. Thus moment-transmitting fixed support was obtained. The height of the first floor is 2200 (mm) between the beam axis and the column foundation connection points, and the height of the second floor is 2000 (mm) between the beam axes. The horizontal distance between the column axes is taken as 3500 (mm).

A 40 cm height and 30 cm width section was used as the column-reinforced concrete section. Column longitudinal reinforcements were formed with the help of 8 Q20 reinforcements. Moreover, Q10 reinforcement was used as transverse reinforcement, and it was formed with 125 (mm) intervals. The clearance distance from the center of the longitudinal reinforcements to the outer surface of the column is taken as 40 (mm). Also, the beam element with 40 cm height and 30 cm width was selected. As transverse reinforcement, Q10 reinforcement was formed at 125 (mm) intervals. In both elements, transverse reinforcement is formed with two stirrup arms in both directions, which are formed from a single stirrup. The depth of concrete cover in the beams is taken as 50 (mm). Concrete material strength was determined as C30 in the tests performed by Güner and the concrete elasticity module was obtained as 23674 MPa [7]. The material properties

of the reinforcement were determined as 418 MPa and 454 MPa, respectively, for the yield strengths for Q20 and Q 10 reinforcements [7].
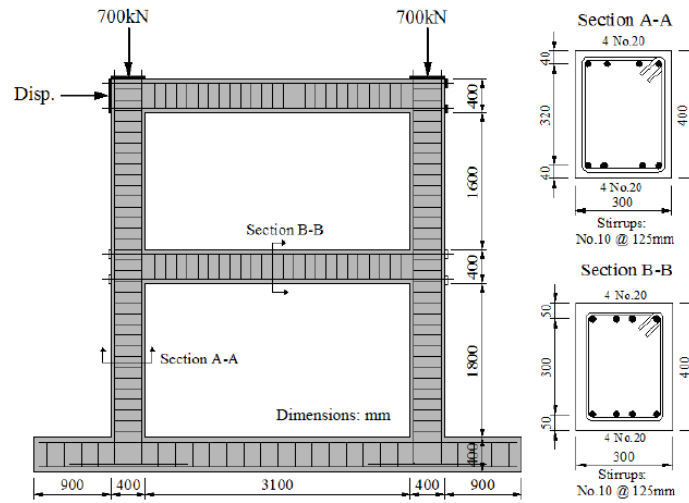
Figure 1 Details of Vecchio and Emara Frame [7]

2.2. FE model of the frame structure.

The finite element model of the structure was created with the help of both Sap 2000 and Seismo Struct programs. Since both programs are widely and effectively used in nonlinear structural analysis applications, they were preferred within the scope of this study. The SeismoStruct program allows users to define a more advanced material and plastic joint description in creating nonlinear models. However, the interface used in modeling large structures brings some difficulties. The Sap 2000 program, on the other hand, has significant advantages and conveniences in terms of the interface used and provides little opportunity for the assumptions made for the mathematical model and the modification of the parameters used.

Güner [7] in their study, the behavior of the frame system under the effect of experimental lateral thrust was investigated in the laboratory environment, and obtained the shear force and top peak displacement of the frame system. In addition, the mathematical model of the framework was obtained with the help of two different programs. Experimental data and mathematical models were compared. The mathematical model produced within the scope of this study was verified with experimental data. Figure 2 contains a comparison of experimental data and mathematical models. Although it is seen that experimental data and mathematical models have specific separations, they have acceptable differences from each other.
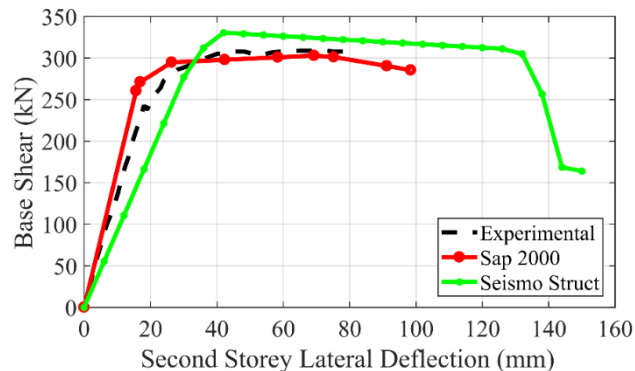
Figure 2 Comparison of Load Deflection Response of Vecchio and Emara Frame.

2.3. Plastic hinge formation and moment-curvature relation.

It is seen that the first plastic hinge for the analyzed frame system occurs in the first-floor beams. Then the second plastic hinges are formed at the column foundation connection points. Followinh hinge formation occurs at the endpoints of the first-floor beam and the endpoints of the second-floor column, respectively. It has been determined that the system has six plastic hinges in the pre-failure condition as shown in the Figure 3.
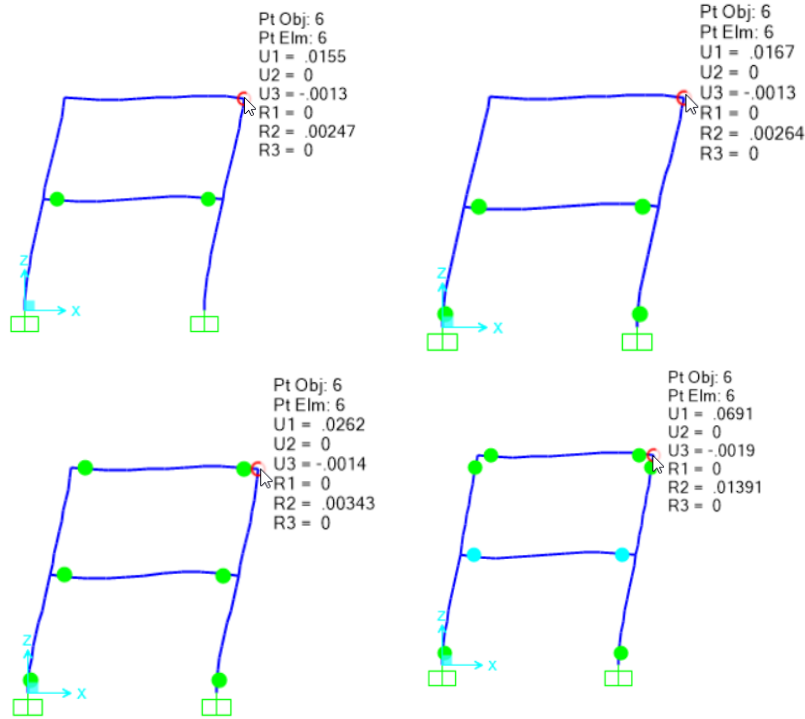
Figure 3 Propagation of the plastic hinge on the frame structure

The stress-strain capacities of the reinforcement of the frame system sections were obtained with the help of the Mander approach. It is seen that with the increase of the confinement reinforcement in this model, the concrete reaches a large deformation capacity and can carry large stresses. Suppose the moment-curvature relationship of the section is calculated considering the behavior of the confined concrete and its strain capacity. In that case, it can be seen that there will be significant decreases in the moment capacity of the section after the reinforcement starts to yield, as can be seen in Figure 4. However, the section can undergo large deformations until collapse occurs in the section.
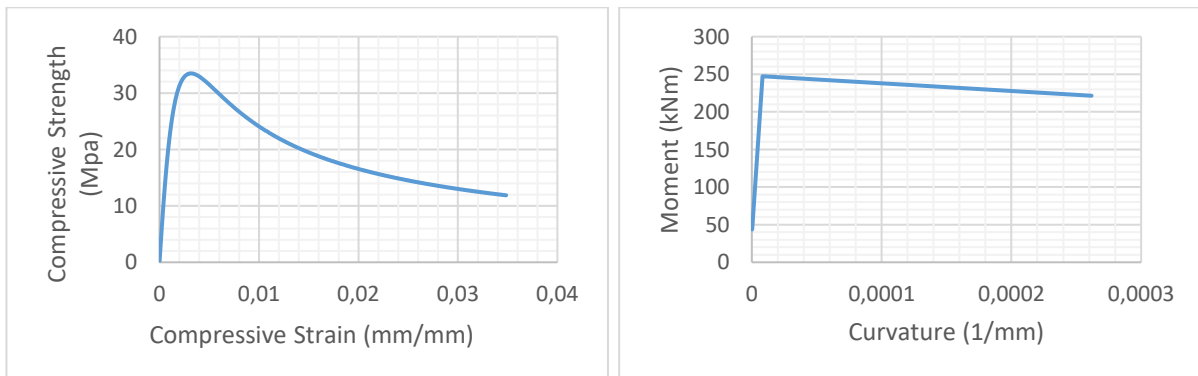
Figure 4 Moment curvature relation of the Beam section

Selection of the Earthquake records.

3.1. 3.1.Selection of the earthquake records.

Within the scope of this study, a total of 10 real earthquake records, five near faults and five far faults, were selected to determine the behavior of the reinforced concrete frame system under the earthquake loads. If the distance of the measurement station to the earthquake center is 15 km or less, it is considered a near fault, and if it is above, it is considered a far fault. Earthquake records with Mw 6 and above were selected in order to ensure that the earthquake intensity is at a level that can cause damage to the structure. Selected near earthquake records are given in Table 1, and far fault earthquake records are given in

Table 2.

Table 1 Near-fault ground motion records.

| No	Earthquake	Year	Station	Mw	Dist. (km)	VS30 (m/s)
1	Loma Prieta	1989	Corralitos	6.93	3.85	462.2
2	Imperial Valley-02	1940	El Centro Array #9	6.95	6.09	213.4
3	Cape Mendocino	1992	Petrolia	7.01	8.18	422.2
4	Morgan Hill	1984	Gilroy Array #6	6.19	9.87	663.3
5	Kobe, Japan	1995	KJMA	6.90	0.96	312.0

Table 2 Far-field ground motion records.

No	Earthquake	Year	Station	Mw	Dist. (km)	VS30 (m/s)
1	Landers	1992	Amboy	7.28	69.21	382.9
2	N. Palm Springs	1986	Anza Fire Station	6.06	42.36	360.5
3	Loma Prieta	1989	Monterey City Hall	6.93	44.35	638.6
4	Northridge	1994	Castaic-Old Ridge Route	6.69	20.72	450.3
5	El Mayor-Cucapah, Mexico	2010	Salton City	7.20	72.63	324.5

3.2.Frequency content of the records.

The spectral acceleration graphs obtained by taking the FFTs of the selected earthquake records are shown in Figure 4. It is seen that extreme acceleration values are observed in the 0-1.5 sec frequency range in the near fault earthquake records. In the far fault earthquake records, it is seen that extreme acceleration values are observed in the frequency range of 0-0.5 seconds, except for the Kobe earthquake. The frequency contents and acceleration values of earthquake records show that near-fault earthquake records are expected to be more devastating for low and medium-rise buildings.
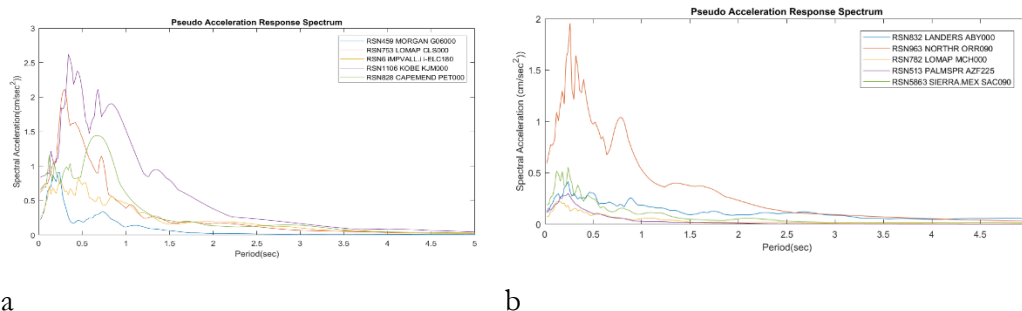

a   b

Figure 5 Spectral Acceleration graph of the a) Near field and b) Far field earthquake records.

4.Time history analysis of the Frame

4.1. 4.1.Nonlinear deformation capacities of the frames.

By using the obtained mathematical model and selected earthquake records, the behavior of the frame system under the near and far fault earthquake records was simulated. While performing the time history analysis, the structure's elastic base shear forces and elastic top lateral displacement values were determined using the linear time history. Then, nonlinear analyzes of the structure were performed in the time domain by using both material and geometry nonlinearity.

Elastic base shear force V_E obtained from these analyses, base shear force V_{max} obtained from nonlinear time history analyses, and elastic peak displacement δ_e and peak displacement δ_{max} obtained from nonlinear time history analyses are presented in Table 3, Table 4, Table 5, and Table 6 separately.

Table 3 Near Field Records

Record Name	V_E (kN)	V_{max} (kN)	δ_e (cm)	δ_{max} (cm)
MORGAN G06000	110.953	68.147	0.4929	0.3119
LOMAP CLS000	17.635	18.393	0.0772	0.0772
iMPVALL.i_i ELC180	49.452	54.572	0.207	0.207
KOBE KJM000	37.475	41.5	0.1572	0.1572
CAPEMEND PET000	19.024	19.582	0.0843	0.0843

Table 4 Far Field Records

Record Name	V_E (kN)	V_{max} (kN)	δ_e (cm)	δ_{max} (cm)
Landers_ABY_000	13.911	51.817	0.0624	0.0239
Northridge_Orr_090	24.833	25.984	0.1082	0.1082
Palms_AZF_225	12.59	13.004	0.0557	0.0557
LOMA_MCH_000	8.974	9.06	0.0402	0.0402
Sierra_mex_Sac_000	12.513	13.094	0.0548	0.0548

As a result of the analyses, it was determined that the system exhibited elastic behavior in some earthquake records. , the earthquake records were scaled with the coefficients determined to have an elastic base shear force of 400 kN to examine the frame system's nonlinear behavior. The analysis results for the scaled earthquake records are shown in Table 5 Increased Near Field RecordsTable 5 and Table 6.

Table 5 Increased Near Field Records

Record Name	V_E (kN)	V_{max} (kN)	δ_e (cm)	δ_{max} (cm)
MORGAN G06000	400	242.107	0.4929	0.3119
LOMAP CLS000	400	258.761	0.0772	0.0772
iMPVALL.i_i ELC180	400.001	298.544	0.207	0.207

KOBE KJM000	400.002	382.57	0.1572	0.1572
CAPEMEND PET000	400.002	294.371	0.0843	0.0843

Table 6 Increased Far Field Records

Record Name	V_E (kN)	V_{max} (kN)	δ_e (cm)	δ_{max} (cm)
Landers_ABY_000	400	180.243	1.7952	0.6875
Northridge_Orr_090	399.999	360.297	1.743	1.4233
Palms_AZF_225	400.014	325.198	1.7695	1.3416
LOMA_MCH_000	399.985	251.754	1.7935	1.0229
Sierra_mex_Sac_000	400.002	347.627	1.7515	1.6785

4.2. Calculating the ductility of the frame with different confinement reinforcements.

As seen from the analyzes performed in the time domain, the elastic base shear force gives higher values than the nonlinear base shear force. According to the equal displacement rule, the displacement value obtained in elastic behavior is expected to be equal to the displacement value in the nonlinear ideal model. It has been determined that the equal displacement rule is met in the frame system examined under the effect of the near-fault, but this rule is not fully satisfied in the far fault.

The equal displacement rule allows structural engineers to economically dimension their buildings by using base shear values much smaller than the elastic base shear force. For this, the structure is expected to not collapse during an earthquake, and it must be able to deform sufficiently to meet the peak displacement demand of the earthquake safely. In reinforced concrete structures, crushing concrete under pressure is the most critical factor limiting this deformation capacity. For this reason, it should be ensured that the deformation capacity of the concrete is increased by using reinforcement detail and that the building can safely carry the loads under the demanded top displacement.

In order to better understand the effect of the confinement reinforcement, static pushover analyzes were carried out considering different confinement reinforcement configurations, and the ductility values of the frame system for each confinement reinforcement were calculated as in

Table 7. Figure 6 shows the pushover analysis results obtained for the respective confinement reinforcements.
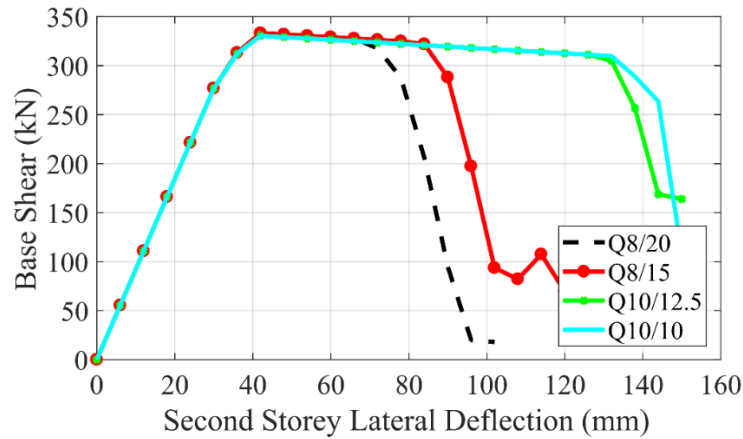
Figure 6 Push-over analysis of different confinement reinforcement configuration of frame sections.

Table 7 Effect of confinement reinforcement in to the ductility of the concreate section

Confinement Reinforcement	δ_y (mm)	δ_{max} (mm)	μ
Φ8/20	36	84	2.3
Φ8/15	36	90	2.5
Φ10/12.5	36	132	3.7
Φ10/10	36	132	3.7

5.Conclusion.

Within the scope of this study, a reinforced concrete frame system, which has been experimentally analyzed in the literature, is discussed, and the pushover analyzes of this system were carried out with the help of Sap2000 and Seismo-Struct programs. The mathematical model and the experimental model of the selected structure were compared, and the accuracy of the mathematical model was determined. Then, time history analyzes were performed under the selected near and far fault earthquake records, and elastic and nonlinear base shear forces and peak displacements formed in the structure were examined. In addition, different confinement reinforcement details were examined to determine the ductile demand of the frame system with the help of static pushover analyses.

When the confinement reinforcement decreases, the maximum deformation rate that the RC frame can achieve without crushing decreases, so the ductility of the frame system decreases significantly. The ductility value of the frame system is determined as $\mu = 2.3$ and $\mu = 3.7$ for the Φ8/20cm and Φ10/12.5cm confinement reinforcement respectively. After this value, stirrups were placed at Φ10 10 cm intervals, but no change was observed in the ductile response capacity of the frame system. In this case, it has been observed that the deformation capacity of the section is no longer limited by the crushing of the concrete, but by the yielding and rupture of the reinforcement, so that large deformations can occur in the section.

References

[1]   Rasheed HAS, Dinno KS. An improved nonlinear analysis of reinforced concrete frames. Comput Struct 1994;53:625–36. doi:10.1016/0045-7949(94)90106-6.

[2]   Birely AC, Lowes LN, Lehman DE. A model for the practical nonlinear analysis of reinforced-concrete frames including joint flexibility. Eng Struct 2012;34:455–65. doi:10.1016/j.engstruct.2011.09.003.

[3]   Rajasankar J, Iyer NR, Prasad AP. Modelling inelastic hinges using CDM for nonlinear analysis of reinforced concrete frame structures. Comput Concr 2009;6:319–41. doi:10.12989/cac.2009.6.4.319.

[4]   Shayanfar J, Akbarzadeh Bengar H. Nonlinear analysis of RC frames considering shear behaviour of members under varying axial load. Bull Earthq Eng 2017;15:2055–78. doi:10.1007/s10518-016-0060-z.

[5]   Habibi AR, Moharrami H. Nonlinear sensitivity analysis of reinforced concrete frames. Finite Elem Anal Des 2010;46:571–84. doi:10.1016/j.finel.2010.02.005.

[6]   Dimitri V, Bljuger F, Yankelevsky D. Reliability evaluation in nonlinear analysis of reinforced concrete structures. Struct Saf 1997;19:203–17. doi:10.1016/s0167-4730(96)00025-2.

[7]   Guner S. Performance Assessment of Shear-Critical. University of Toronto, 2008.

Impacts of Remote Working on Productivity of Civil Engineers during the COVID-19 Pandemic

Ayşegül TEPE[1]
Bengi AYKAÇ[2]
Murat AYHAN[3]

Introduction

The first cases of COVID-19 disease, caused by the novel coronavirus, were reported in December 2019 in Wuhan, China. Due to the spreading speed and severity of the disease, the World Health Organization (WHO) declared that COVID-19 is qualified as a pandemic (WHO, 2020). Unfortunately, this highly contagious disease has spread to more than 200 countries and has caused more than 600 million confirmed cases, with more than 6.5 million deaths worldwide as of 21 November 2022 (WHO, 2022). Besides the adverse effects of the pandemic on the public health, commercial establishments, including the construction industry, were also affected severely (Ogunnusi et al., 2020: 120). Due to the contagious nature of the disease, social distancing was needed to slow the spread of COVID-19 and therefore all business activities were initially suspended or limited, except in essential sectors such as the medical and supply sectors (Gamil and Alhagar, 2020: 122-123). For this reason, commercial organizations have resorted to alternative forms of work and many companies had to switch to remote work, which can also be called Work-From-Home (WFH). Several on-site activities in the construction industry were stopped or postponed and employees were encouraged to work remotely to fulfill their ongoing tasks (Esa et al., 2020: 977). Besides on-site activities that cannot be performed remotely (i.e., concrete casting), there is no other option but to switch to remote work in order to carry out activities such as design and management in the construction industry.

Aim of the Study

Considering that remote working has a significant impact on employee performance due to various factors (Mardianah and Hidayat, 2020: 1043-1044), investigating the productivity during remote working period has become an issue that needs to be taken into consideration. In the construction industry, which makes a significant contribution to the country's economy and Gross Domestic Product, the effects of the COVID-19 on productivity should be examined in order to prevent performance loss and to continue business activities as before. In this study, it is thought that working remotely or WFH will have direct effects on the productivity of civil engineers. The study has two major objectives. First, it is aimed to provide empirical evidence showing whether there is an increase or a decrease in the productivity of civil engineers during the remote working period using the data collected from the construction industry. Secondly, is it aimed to identify the

---
[1] Student, Gazi University, Civil Engineering Department, Orcıd: 0000-0002-5220-0309
[2] Assoc. Prof., Gazi University, Civil Engineering Department, Orcıd: 0000-0002-6285-5667
[3] Asst. Prof., Gazi University, Civil Engineering Department, Orcıd: 0000-0002-2011-4190

factors affecting the engineering productivity in the construction industry during the remote working period and to reveal improvement opportunities for the sector.

Research Background

The impact of remote working on employee productivity has been discussed in the literature for more than a decade (Mustajab et al., 2020: 14). Recent studies on this subject have revealed two opposing findings. It was stated that the COVID-19 pandemic caused disruptions in the performance of employees in various activities (Mardianah and Hidayat, 2020: 1043-1044). In a study that examines the effects of the COVID-19 on companies from the Ghana construction industry, Agyekum et al. (2021: 231) stated that there were delays in project deliveries due to COVID-19. Kutluay Tutar et al. (2021: 705-706) stated that the works in the construction industry were disrupted during the COVID-19 period. In another study, the results of a questionnaire conducted with 71 civil engineers, the positive and negative experiences of the participants in the process of WFH were revealed (Ogunnusi et al., 2020: 126-127). It is also claimed that the virtual working environment provided during the pandemic period can be considered as a new normal. Shibani et al. (2020: 57), investigated the effects of the pandemic on the construction industry in the United Kingdom and observed an increment in the office productivity during the remote working period. There are other researchers claiming that remote work can increase employee productivity (Akça and Tepe Küçükoğlu, 2020: 79-80; Angelici and Profeta, 2020: 23-24; Galanti et al., 2021: 430-431).

Previous Studies on Productivity in the Construction Industry

Productivity includes all factors that can affect the progress, development, and production outputs of construction processes (King et al., 2021: 5). Considering the competitive nature of the construction industry, it is clear that achieving higher productivity is critically important and performance improvements are a constant requirement for construction companies to remain competitive and profitable (Zhang etal., 2018: 1). In a broad perspective, productivity is the ratio of output produced to all or some of the input resources expended in the production process, or vice versa (Hughes and Thorpe, 2014: 211; Poirier et al., 2015: 75; Ayele and Fayek, 2019: 195-198). In the literature, the productivity measurement levels in the construction industry are classified as (1) Activity level (i.e., the productivity of steel elements' assembly activity), (2) Project level (i.e., the productivity of the construction of a new building), and (3) Industry level (i.e., the productivity of a country's construction industry as a whole). Regardless of the measurement level, the productivity of the construction industry can be divided into three: (1) Single factor productivity, (2) Partial factor productivity, and (3) Multi-factor productivity. If productivity corresponds to the ratio of output to a single particular input (i.e., labor force only), then this measurement is considered as a single factor productivity measure. On the other hand, the ratio of output to all relevant inputs is considered as a multi-factor productivity measure (Huang et al., 2009: 2139). Partial factor productivity is the ratio of output to some of the expended inputs spent (i.e., labor and capital resources). The tendency in the literature is to focus on single-factor productivity measures and on the labor productivity in particular (Ellis Jr and Lee, 2006: 317; Poirier et al., 2015: 74-84; Vereen et al., 2016: 2). Labor productivity; corresponds to the ratio of output to the working hours required to install a unit of that output (as cited in Hughes and Thorpe, 2014: 211). Labor productivity is an adequate way of monitoring the performance of an activity; however, activity-based labor productivity may not represent the true state of productivity at project or industry levels (Bernstein, 2003: 47-50). In other words, the overall performance to produce an output can be affected by various factors that need to be considered and it may not reveal the whole picture based solely on the performance of certain activities (AlChaer and Issa,

2020: 1). Therefore, in the case of performance monitoring on labor productivity, measurements at the project level are more appropriate than measurements at the activity level.

Based on the findings of the literature review, a single factor productivity approach over labor productivity is adopted in this study. Labor productivity will be measured at the project level.

Previous Studies on Engineering Productivity in the Construction Industry

Engineering productivity is the ratio of output to input; however, output has intangible aspects, unlike tangible products in the construction process (Sacks and Barak, 2008: 440). Rather than dealing with intangible inputs and outputs, previous studies have used simplified approaches for quantifications and measurements. In one of the earliest studies on design and engineering productivity by Thomas et al., (1999: 1), the amount of design sheets produced was used as the output and the hours required to create these sheets were used as the amount of input, and the productivity was measured in hours per design sheet. Song and AbouRizk (2005: 362) mentioned that working hours are the primary inputs in design work, since working hours are measurable, easily traceable, and most engineering companies keep records of working hours.

$$Engineering\ Productivity = \left(\frac{Output}{Input}\right) = \left(\frac{Construction\ Quantity}{\sum Direct\ Engineering\ Work\ Hours}\right) \tag{1}$$

In this study, engineering productivity will be compared using a project-level measurement approach, considering that the selected cases should have similar project scopes. In the study, (1) the engineering productivity before remote working will be compared with the engineering productivity during the remote working period, and (2) the productivity of similar projects undertaken by the same team before and during the pandemic will be compared, instead of comparing the project-level productivity values of different projects between companies or industries. The study's dataset will compare similar with similar, which removes output heterogeneity. Therefore, the sample cases in the dataset were selected based on similar project scope constraints.

Methodology

In the study, the Impacts of WFH/Remote Working Process on Civil Engineering Productivity during the COVID-19 Pandemic Period are quantitatively determined and evaluated. The basis of the study is primarily the determination of the factors affecting the productivity of an employee. A questionnaire was designed to categorize the factors affecting employee productivity for data collection and statistical analysis. Productivity was measured by conducting a questionnaire with the construction industry employees who produced similar works before and during the COVID-19 Pandemic in Ankara and comparing the works produced by the individuals in unit time. The questionnaire was sent to the participants online and then confirmed by phone. 102 people were reached, but 12 people were not included in the study because they filled the questionnaire incompletely. The study was completed with a total of 90 participants. In the first part of the questionnaire, there are questions to collect demographic information. In other sections, questions are categorized related to sub-factors which are affecting productivity.

Research Findings

While evaluating the data obtained in the study, SPSS (Statistical Package for Social Sciences for Windows) 22.0 program was used for the statistical analysis. Shapiro Wilk-W test and Kolmogorov Smirnov test were used to show the normality distribution of the data. In addition,

skewness and kurtosis values were used to understand the shape of the distribution. Descriptive statistics were expressed as mean and standard deviation for continuous variables and were given as frequency and percentage for categorical data. Chi-square test was used for comparisons of categorical data. In the comparison of quantitative data, Independent Samples T-Test and One-Way Analysis of Variance (ANOVA) test were used for variables that met the assumption of normal distribution. When significance was detected in the ANOVA test, the significance was evaluated with Tukey measure as a post-hoc test. Statistical significance was accepted as $p < 0.05$. For those who did not meet the normal distribution assumption, the Mann-Whitney U test, which is the non-parametric equivalent of the Independent Samples T-Test, and the Kruskal-Wallis H test, which is the non-parametric equivalent of the One-Way ANOVA, were used.

The questionnaire was based on a 5-point Likert-scale. The Cronbach Alpha (α) coefficient was used in the reliability and internal consistency analysis of the factors. Cronbach Alpha (α) coefficient, which takes a value in the range of 0 to 1, provides acceptable reliability for any value greater than 0,7 (Kılıç, 2016: 47). The Cronbach Alpha (α) values calculated for all the sub-factors were either very close to the threshold of 0,7 or higher. This indicates that the sub-factors are adequately reliable.

Table 1 shows the percentages and frequency distributions of the socio-demographic variables from the first part of the questionnaire .

Table 1 - Distribution of Participants' Socio-Demographic Characteristics

Variables and Corresponding Categories		n (%)
Gender	Male	47 (%52,22)
	Female	43 (%47,78)
Marital Status	Single	55 (%61,11)
	Married	35 (%38,89)
Position	Project Engineer	41 (%45,56)
	Center Office Engineer	13 (%14,44)
	Architect	17 (%18,89)
	Project Director	6 (%6,67)
	Draftsman	9 (%10,00)
	Other	4 (%4,44)
Professional Experience	0-2 Years	21 (%23,33)
	2-4 Years	20 (%22,22)
	5-9 Years	26 (%28,89)
	10 Years and Over	23 (%25,56)
Designated-Separate Room as a Workstation	No	14 (%15,56)
	Yes	76 (%84,44)
Support of Government	No	28 (%31,11)
	Yes	28 (%31,11)
	No idea	34 (%37,78)
Changes in Work Duration	Decreased	22 (%24,44)
	Not Changed	35 (%38,89)
	Increased	33 (%36,67)
Use of Building Information Modeling Tools	No	41 (%45,56)
	Yes	49 (%54,44)

The mean and standard deviation values for the continuous variables and factor scores are given in Table 2.

Table 2 - Mean, Standard Deviation, and Median Scores of Sub-Factors

	Mean & Standard Deviation	Median (minimum-maximum)
Employee	2,911±0,934	2,93 (1-4,43)
Manager	2,929±0,767	3 (1,33-5)
Equipment	3,27±1,32	3 (1-5)
Financial	2,86±1,27	3 (1-5)
Project	2,64±1,25	2,5 (1-5)
Environment	3,14±0,95	3,2 (1,2-5)
Productivity Change Percentage	0,626±6,018	0 (-13,01-16)

The distribution of the responses of participants for each variable is given in Table 3.

Table 3 - The Distribution of the Responses

Sub-Factor	Question	Strongly Disagree n (%)	Disagree n (%)	Neither agree nor disagree n (%)	Agree n (%)	Strongly Agree n (%)
Employee	Job Discipline	23 (%25,56)	14 (%15,56)	21 (%23,33)	19 (%21,11)	13 (%14,44)
	Changes in the Methods of Communication	20 (%22,22)	21 (%23,33)	19 (%21,11)	16 (%17,78)	14 (%15,56)
	Remote Control of CAD Files	22 (%24,44)	13 (%14,44)	20 (%22,22)	11 (%12,22)	24 (%26,67)
	Same Workplace and Living Space	17 (%19,1)	25 (%28,09)	10 (%11,24)	22 (%24,72)	15 (%16,85)
	External Stimuli in the House	16 (%17,78)	23 (%25,56)	12 (%13,33)	22 (%24,44)	17 (%18,89)
	The Disappearance of Control Pressure	30 (%33,33)	12 (%13,33)	11 (%12,22)	11 (%12,22)	26 (%28,89)
	Changes in Work Duration	23 (%25,56)	17 (%18,89)	15 (%16,67)	19 (%21,11)	16 (%17,78)
Manager	Not Familiar with the WFH Process	13 (%14,44)	20 (%22,22)	21 (%23,33)	11 (%12,22)	25 (%27,78)
	Motivation Enhancing Flexibility	14 (%15,56)	11 (%12,22)	34 (%37,78)	21 (%23,33)	10 (%11,11)
	Online Meeting Productivity	4 (%6,56)	8 (%13,11)	10 (%16,39)	29 (%47,54)	10 (%16,39)
	Status of Hiring a New Person	35 (%42,17)	16 (%19,28)	22 (%26,51)	4 (%4,82)	6 (%7,23)
Equipment	Lack of Infrastructure and Materials	15 (%16,67)	21 (%23,33)	10 (%11,11)	13 (%14,44)	31 (%34,44)
	Need for Technical Support	5 (%8,06)	18 (%29,03)	13 (%20,97)	13 (%20,97)	13 (%20,97)
Financial	Payment Problems	5 (%10,2)	9 (%18,37)	13 (%26,53)	5 (%10,2)	17 (%34,69)
	No Overtime Pay	25 (%40,98)	13 (%21,31)	6 (%9,84)	7 (%11,48)	10 (%16,39)
	Not Receiving the Expected Raises	12 (%23,53)	8 (%15,69)	10 (%19,61)	7 (%13,73)	14 (%27,45)
Project	Repetition of Work	23 (%26,14)	12 (%13,64)	20 (%22,73)	14 (%15,91)	19 (%21,59)
	Unforeseen Changes in the Project	33 (%36,67)	20 (%22,22)	17 (%18,89)	11 (%12,22)	9 (%10)
Environment	Decreased Health Concern	2 (%2,22)	17 (%18,89)	10 (%11,11)	22 (%24,44)	39 (%43,33)
	Lack of Coordination	13 (%14,44)	19 (%21,11)	14 (%15,56)	28 (%31,11)	16 (%17,78)
	Home Office Performance Drop	20 (%22,22)	17 (%18,89)	9 (%10)	32 (%35,56)	12 (%13,33)
	Work-Life Balance	17 (%18,89)	22 (%24,44)	12 (%13,33)	28 (%31,11)	11 (%12,22)
	Chores	27 (%30)	14 (%15,56)	16 (%17,78)	21 (%23,33)	12 (%13,33)

Hypotheses of the Research

The hypothesis of the study is listed below. The statistical analysis with respect to these hypotheses can be seen in Table 4.

H₁: Socio-demographic characteristics have a direct effect on productivity sub-factors.

H₁₁: Gender has a direct effect on the environment-related sub-factors related to productivity.

H₁₂: Presence of a designated-separate room as a workstation directly affects the changes in the productivity.

H₁₃: Changes in the work duration has a direct effect on the changes in the productivity.

Table 4: Statistical evaluation of H_{1_1}, H_{1_2} and H_{1_3} hypotheses

		Mean & Standard Deviation	Median (minimum-maximum)	t\F	p
Gender	Male	3,40±0,90	3,60 (1,40-5,00)	t=2,796	**0,006**
	Female	2,86±0,93	2,80 (1,20-4,20)		
Designated-Separate Room as a Workstation	No	-2,49±5,46	-1,45 (-13,01-9,00)	t=-2,150	**0,034**
	Yes	1,19±5,97	0,00 (-11,56-16,00)		
Changes in Work Duration	Decreased	4,73±5,05	4,78 (-3,67-16,00)	F=23,193	**<0,001** p^{ac}**<0,001** p^{bc}**<0,001**
	Not Changed	2,30±4,76	0,00 (-6,44-12,05)		
	Increased	-3,89±4,92	-3,50 (-13,01-7,40)		

A statistically significant difference was identified between male (3.40±0.90) and female (2.86±0.93) participants related to the environmental sub-factor scores with respect to gender (t=2.796; p=0.006). In terms of environment-related variables, the productivity of males was affected more severely than the productivity of females.

A statistically significant difference was identified between those who have a designated-separate room as a workstation at home (1.199±5.971) and those who do not (-2,489±5.464) with respect to the change percentage in the productivity **(t=-2,150; p=0,034)**. The productivity of those who do not have a designated-separate room as a workstation in their home is lower than those who have.

A statistically significant difference was identified between the change percentage in the productivity and the change in work duration **(F=23,193; p<0,001)**. Tukey's test was performed as a post-hoc analysis to determine which groups originated the difference. There is a difference between those whose working hours have decreased (4.733±5.046) and those whose working hours have increased (-3.892±4.922). There is also a difference between those whose working hours did not change (2.304±4.758) and those whose working hours increased (-3.892±4.922) **(p^{ac}<0,001; p^{bc}<0,001)**. The productivity of those whose working hours increased was lower than the productivity of those whose working hours decreased or did not change.

In the light of these explanations, hypothesis H_{1_1}, H_{1_2} and H_{1_3} were accepted.

Discussion of Findings

This study aims to determine how the transition to remote working, which is a new way of doing business, has affected employees' productivity in the construction industry during the COVID-19 pandemic. In addition, it is aimed to determine the factors affecting engineering productivity during the remote working period and to make improvement suggestions for the industry. Limitations of the study include the dataset being collected from a specific region only and the questionnaire being applied to people who produced similar projects before and during the COVID-19 pandemic. In other words, the dataset was collected from participants that produced similar projects before and during the pandemic period in Ankara.

Impact of Gender on Productivity

Transitions to remote work with the COVID-19 pandemic reduced health concerns as well as limiting people's social interactions. This exposed people at high levels of loneliness. In

particular, remote workers may suffer more from the process of staying at home because they do not have the opportunity to socialize with their colleagues. This situation reflects negatively on their work performance (Larson et al., 2020: 3; Toscano and Zappalà, 2020: 14; Wang et al., 2021:27). While people, who work in a regular office environment but had to switch to remote working due to the pandemic, may have a negative impact on their desire to work and their productivity may decrease. In addition, the same working and living space makes it difficult to determine the boundaries and balance between home responsibilities and work duties (Awada et al., 2021:1173). Work-related stress, role ambiguity arising from responsibilities between home and work, family-work conflict, disagreements with other people living at home are reflected in the performance of employees and affect their work productivity and work commitment (Galanti et al., 2021:427; Tong et al., 2021: 1). In a study that acknowledges work-family conflicts as gender-related, it is stated that such conflict attributes to women due to women being primary responsible of housework and childcare. The same study argued that men are affected by family-work conflict as much as women in the transition to WFH with the COVID-19 pandemic (Galanti et al., 2021: 427). Today, although men contribute more to housework, the traditional gender roles of society, which places childcare and housework responsibilities on women (Cerrato and Cifre, 2018: 9; Baert et al., 2020: 9). Therefore, WFH facilitates the balance of women's responsibilities between family-work-home and meeting the demands of other household members at home (Awada et al., 2021: 1183; Farooq and Sultana, 2021: 309). In another study, it was stated that while WFH, women were able to balance their work-home-child care responsibilities better than when they worked at the office and this was contributing to their productivity (Colley and Williamson, 2020: 23). It has been observed that women are more willing to work remotely than men and have higher productivity during the remote working period (Awada et al., 2021: 1185; Pérez et al., 2002: 273).

Impact of Having a Designated-Separate Room as a Workstation on Productivity

WFH during the COVID-19 pandemic has also highlighted the need for physical space in home-office environments. The point to be noted is that not all individuals working from home have a designated area for work. In this case, it may be necessary to use other areas in the house, such as the dining table or areas such as the kitchen counter and the coffee table. The lack of a special work area can affect the person both physically and mentally and reduce her/his performance at work (Xiao et al., 2021: 182-189). Working in a designated room for work ensures that the employee is isolated from distractions and gets the work done without interruption. Employees need to leave the living space and distractions to focus on their own work (Mello, 2007: 258). Huls et al., (2022: 84) found that participants, who have a designated-separate room at home and work there all day, had a higher productivity than those without a designated-separate room at home, or only use a designated-separate room for part of the day.

Impact of Changes in Work Duration on Productivity

Labor productivity depends on long working hours (Maqsoom et al, 2018: 16). Continuing overtime period throughout the project causes a decrease in labor productivity (Acıkara, 2016: 43). Employees who work overtime feel stress and fatigue that do not only decrease their productivities but also it causes them to make mistakes and get sick (Pencavel, 2015: 2073). Considering a certain hourly working time per week, overtime hours longer than 3 or 4 weeks cause fatigue and lead to productivity losses (Thomas and Raynar, 1997: 184-187). Moreover, the long working hours and the fact that individuals have to work outside of working hours negatively affect the work-life balance (Suvacı and Şimşek, 2021: 186). Work-life balance is the balancing of expectations at the work and private life of employees (Bekmezci et al., 2021: 3-4). Failure to establish a work-life balance causes an elevated level of stress in employees and accordingly negatively affects

motivation, performance, and productivity (Yılmaz and Sağlam, 2021: 522). Some of the employees believe that working fewer hours will reduce distraction and increase productivity as it will establish a better work-life balance (Colley and Williamson, 2020: 10).

Conclusion

In the fight against the COVID-19 pandemic, it has become a significant issue to continue the normal flow of life and work without interruption. Therefore, examining the changes in the productivity of employees during the transition to remote work has become a necessity for both managers and employees. This study aims to reveal how remote work, which is a new way of doing business after the COVID-19 pandemic, affects the productivity of employees in the construction industry. At the same time, it is aimed to determine the factors affecting productivity and to make suggestions for the improvements. Limitations of the study include the dataset being collected from a specific region only and the questionnaire being applied to people who produced similar projects before and during the COVID-19 pandemic.

If the productivity of the employees is increased and they are required to work with maximum efficiency, the first thing to do is to determine the factors affecting employee productivity. Therefore, within the scope of this study, the factors affecting the productivity of an employee, mostly a construction industry employee, were examined. With the results obtained from the literature review, the factors affecting the engineering productivity were categorized and a questionnaire was designed. The results of the questionnaire were analyzed statistically, and the acceptance-rejection status of the hypotheses was determined.

It was concluded that gender has a direct effect on the environment-related sub-factors of productivity. In other words, it was concluded that women are more productive than men during the remote working period. This shows that the remote working provides an advantage for women to establish a more comfortable home-work-life balance. In this regard, although the fact that men stay at home more and become more involved in the routines at home during the pandemic, this interrupts them although it is not an insurmountable situation.

Another hypothesis is that having a designated-separate room at home affects productivity. Having a designated-separate room as a workstation increases productivity. However, a designated-separate room as a workstation may not be in everyone's home. In this case, great sacrifice falls on the employee and the household members who lives with them. Employees, who do not have a designated-separate room, can use any room in the house as a workstation. Appropriate work duties may be assigned to employees, who do not have a designated-separate room, by managers. For example, they may attend only mandatory meetings and not included in every meeting.

The last hypothesis is the changes in working duration having an effect on productivity. It has been concluded that employees whose working durations decrease or do not change are more productive than those that increase. Working overtime does not always mean the work is perfect. After a while, working overtime gets tiring and wears out the employee. It also makes them more prone to mistakes. Although remote working provides flexibility, managers observing a decrease in the performance of their employees should intervene in this situation and certain time schedule for work should be arranged similar to the normal office environment.

References

Acıkara, T. (2016). Türk inşaat sektöründe verimlilik faktörleri uygulamalarının değerlendirilmesi: en iyi verimlilik uygulamaları endeksi, Master's Thesis, Antalya: Akdeniz University.

Agyekum, K., Kukah, A. S., and Amudjie, J. (2021). The impact of COVID-19 on the construction industry in Ghana: the case of some selected firms. Journal of Engineering, Design and Technology, 20(1), p. 222-244. http://dx.doi.org/10.1108/JEDT-11-2020-0476,

Akça, M., and Tepe Küçükoğlu, M. (2020). COVID-19 ve iş yaşamına etkileri: evden çalışma. Journal of International Management Educational and Economics Perspectives, 8(1), p. 71-81.

AlChaer, E., and Issa, C. A. (2020). Engineering productivity measurement: a novel approach. Journal of Construction Engineering and Management, 146(8), 04020087, p. 1-11, https://doi.org/10.1061/(ASCE)CO.1943-7862.0001875.

Angelici, M., and Profeta, P. (2020). Smart-Working: work flexibility without constraints. CESifo Working Paper, No. 8165, Center for Economic Studies and info Institute (CESifo), p. 1-116.

Awada, M., Lucas, G., Becerik-Gerber, B., and Roll, S. (2021). Working from home during the COVID-19 pandemic: Impact on office worker productivity and work experience. Work, (Preprint), p. 1-19, doi: 10.3233/WOR-210301

Ayele, S., and Fayek, A. R. (2019). A framework for total productivity measurement of industrial construction projects. Canadian Journal of Civil Engineering, 46(3), p. 195-206. http://dx.doi.org/10.1139/cjce-2018-0020.

Baert, S., Lippens, L., Moens, E., Sterkens, P., and Weytjens, J. (2020). The COVID-19 crisis and telework: a research survey on experiences, Expectations and Hopes. IZA Discussion Papers, p. 1-37, Bonn: Institute of Labor Economics (IZA).

Bekmezci, M., Mert, İ. S., and Abubakar, M. (2021). İş-yaşam dengesinin yaşam tatminini yordamasında çalışılan sektörün düzenleyici etkisi. Anadolu Üniversitesi Sosyal Bilimler Dergisi, 21(1), p. 1-22, https://doi.org/10.18037/ausbd.902535.

Bernstein, H. M. (2003). Measuring productivity: An industry challenge. Civil Engineering (N.Y.), 73(12), p. 46-53.

Cerrato, J., and Cifre, E. (2018). Gender inequality in household chores and work-family conflict. Frontiers in psychology 9,1330, p. 1-11. https://doi.org/10.3389/fpsyg.2018.01330.

Colley, L., and Williamson, S. (2020). Working during the pandemic: From resistance to revolution? Canberra, Australia: UNSW Canberra.

Ellis Jr, R. D., and Lee, S.-h. (2006). Measuring project level productivity on transportation projects. Journal of construction engineering and management, 132(3), p. 314-320. https://doi.org/10.1061/(ASCE)0733-9364(2006)132:3(314).

Esa, M. B., Ibrahim, F. S., and Kamal, E. B. (2020). Covid-19 pandemic lockdown: The consequences towards project success in Malaysian construction industry. Advances in Science, Technology and Engineering Systems Journal Vol. 5(5), p. 973-983. https://dx.doi.org/10.25046/aj0505119.

Farooq, R., and Sultana, A. (2021). The potential impact of the COVID-19 pandemic on work from home and employee productivity. Measuring Business Excellence, p. 308-325. http://dx.doi.org/10.1108/MBE-12-2020-0173.

Galanti, T., Guidetti, G., Mazzei, E., Zappalà, S., and Toscano, F. (2021). Work from home during the COVID-19 outbreak: The impact on employees' remote work productivity, Engagement, and Stress. Journal of occupational and environmental medicine, 63(7), p. 426-432. https://doi.org/10.1097/jom.0000000000002236.

Gamil, Y., and Alhagar, A. (2020). The impact of pandemic crisis on the survival of construction industry: A case of COVID-19. Mediterranean Journal of Social Sciences, 11(4), p. 122-128. https://doi.org/10.36941/mjss-2020-0047.

Huang, A. L., Chapman, R. E., and Butry, D. T. (2009). Metrics and Tools for Measuring Construction Productivity: Technical and Empirical ConsiderationsMetrics and Tools for Measuring Construction Productivity: Technical and Empirical Considerations. Gaithersburg, MD: Special Publication (NIST SP) National Institute of Standards and Technology.

Hughes, R., and Thorpe, D. (2014). A review of enabling factors in construction industry productivity in an Australian environment. Construction Innovation, Vol. 14 (2), p. 210-228. https://doi.org/10.1108/CI-03-2013-0016.

Huls, S. P., Sajjad, A., Kanters, T. A., Hakkaart-van Roijen, L., Brouwer, W. B., and van Exel, J. (2022). Productivity of working at home and time allocation between paid work, unpaid work and leisure activities during a pandemic. Pharmacoeconomics, 40(1), p. 77-90. https://doi.org/10.1007/s40273-021-01078-7.

Kılıç, S. (2016). Cronbach's alpha reliability coefficient. Psychiatry and Behavioral Sciences, 6(1), p. 47-48.

King, S. S., Rahman, R. A., Fauzi, M. A., and Haron, A. T. (2021). Mechanisms for addressing the impact of COVID-19 on infrastructure projects. 4th National Conference on Wind and Earthquake Engineering In IOP Conference Series: Earth and Environmental Science, Vol. 682 (1), p. 1-9, http://dx.doi.org/10.1088/1755-1315/682/1/012047.

Kutluay Tutar, F., Ekici, M., Balkaya, D., and Tutar, N. F. (2021). Öğrenen ekonomi bağlaminda kendisi küçük ama tahribati büyük. International Academic Social Resources Journal, (e-ISSN: 2636-7637), 6 (24), p. 699-712, doi: 10.31569.

Larson, B. Z., Vroman, S. R., and Makarius, E. E. (2020). A guide to managing your (newly) remote workers. Harvard Business Review, p. 1-6.

Maqsoom, A., Mughees, A., Khan, A. K., and Arif, M. I. (2018). Labor productivity in construction industry: investigating the influence of internal psychosocial stressors. In ICCREM (International Conference on Construction and Real Estate Management) 2018: Analysis of Real Estate and the Construction Industry, p. 10-17. Reston, VA: American Society of Civil Engineers.

Mardianah, L., and Hidayat, S. (2020). Empirical study of the impact of work from home (WFH) policy and top management support on employee performance. Journal of Research in Business, Economics, and Education, 2(5), p. 1039-1045.

Mello, J. A. (2007). Managing telework programs effectively. Employee responsibilities and rights journal, 19(4), p. 247-261. https://doi.org/10.1007/s10672-007-9051-1.

Mustajab, D., Bauw, A., Rasyid, A., Irawan, A., Akbar, M. A., and Hamid, M. A. (2020). Working from home phenomenon as an effort to prevent COVID-19 attacks and its impacts on work productivity. TIJAB (The International Journal of Applied Business), 4(1) , p. 13-21.

Ogunnusi, M., Hamma-Adama, M., Salman, H., and Kouider, T. (2020). COVID-19 pandemic: the effects and prospects in the construction industry. International journal of real estate studies, 14(Special Issue 2)., p. 120-128.

Pencavel, J. (2015). The productivity of working hours. . The Economic Journal, 125(589), p. 2052-2076. https://doi.org/10.1111/ecoj.12166.

Pérez, M. P., Carnicer, M. P., and Sánchez, A. M. (2002). Differential effects of gender on perceptions of teleworking by human resources managers. Women in Management Review, p. 262-275.

Poirier, E. A., Staub-French, S., and Forgues, D. (2015). Measuring the impact of BIM on labor productivity in a small specialty contracting enterprise through action-research. Automation in construction, 58, p. 78-84. http://dx.doi.org/10.1016/j.autcon.2015.07.002.

Sacks, R., and Barak, R. (2008). Impact of three-dimensional parametric modeling of buildings on productivity in structural engineering practice. Automation in Construction, 17(4), p. 439-449. http://dx.doi.org/10.1016/j.autcon.2007.08.003.

Shibani, A., Hassan, D., and Shakir, N. (2020). The effects of pandemic on construction industry in the UK. Mediterranean Journal of Social Sciences, 11(6), p. 48-60. https://doi.org/10.36941/mjss-2020-0063.

Song, L., and AbouRizk, S. M. (2005). Quantifying engineering project scope for productivity modeling. Journal of construction engineering and management, 131(3), p. 360-367. https://doi.org/10.1061/(ASCE)0733-9364(2005)131:3(360).

Suvacı, B., and Şimşek, M. C. (2021). İş-Yaşam dengesi, örgütsel bağlılık ve çalışanların işten ayrılma niyetleri arasındaki ilişkinin belirlenmesi. Social Sciences Research Journal, 10(1), p. 185-194.

Thomas, H. R., and Raynar, K. A. (1997). Scheduled overtime and labor productivity: Quantitative analysis. Journal of construction engineering and management, 123(2), p. 181-188.

Thomas, H. R., Korte, Q. C., Sanvido, V. E., and Parfitt, M. K. (1999). Conceptual model for measuring productivity of design and engineering. Journal of architectural engineering, 5(1), p. 1-7.

Tong, R., Wang, L., Cao, L., Zhang, B., and Yang, X. (2021). Psychosocial factors for safety performance of construction workers: taking stock and looking forward. Engineering,

Construction and Architectural Management, p. 1-19. https://doi.org/10.1108/ECAM-09-2021-0786.

Toscano, F., and Zappalà, S. (2020). Social isolation and stress as predictors of productivity perception and remote work satisfaction during the COVID-19 pandemic: The role of concern about the virus in a moderated double mediation. Sustainability, 12(23), 9804, p. 1-14. https://doi.org/10.3390/su12239804.

Vereen, S. C., Rasdorf, W., and Hummer, J. E. (2016). Development and comparative analysis of construction industry labor productivity metrics. Journal of Construction Engineering and Management, 142(7), 04016020, p. 1-9. http://dx.doi.org/10.1061/(ASCE)CO.1943-7862.0001112.

Wang, B., Liu, Y., Qian, J., and Parker, S. K. (2021). Achieving effective remote working during the COVID-19 pandemic: A work design perspective. Applied psychology, 70(1), p. 16-59. https://doi.org/10.1111/apps.12290.

WHO. (2020). World Health Organization, Retrieved from (https://covid19.who.int/), on (November 21, 2022).

WHO. (2022). World Health Organization, Retrieved from (https://covid19.who.int/), on (November 21, 2022).

Xiao, Y., Becerik-Gerber, B., Lucas, G., and Roll, S. C. (2021). Impacts of working from home during COVID-19 pandemic on physical and mental well-being of office workstation users. Journal of Occupational and Environmental Medicine, 63(3), p. 181-190. https://doi.org/10.1097/jom.0000000000002097.

Yılmaz, B., and Sağlam, M. (2021). COVID-19 algılanan stres ve tehdidinin, çalışanların iş yaşam dengesi ve motivasyonu üzerindeki etkisi. Akademik Araştırmalar ve Çalışmalar Dergisi (AKAD), 13(25), p. 518-538. https://doi.org/10.20990/kilisiibfakademik.977745.

Zhang, L., Wen, M., and Ashuri, B. (2018). BIM log mining: Measuring design productivity. Journal of Computing in Civil Engineering, 32(1), 04017071, p. 1-13. https://doi.org/10.1061/(ASCE)CP.1943-5487.0000721.

Investigation of Energy Management Studies in Specified Microgrid Applications

Fatma Yaprakdal[1]

Introduction

The great increase in the world population in the last twenties and the rapidly developing technology cause a great increase in the global electrical energy demand. Fossil fuels such as natural gas, oil and coal, which are among the sources that meet a large part of the global energy demand, have many environmental side effects, especially greenhouse gas emissions [1]. In addition, the existing coal reserves in the world are expected to expire in approximately one hundred and twenty years, and oil reserves in approximately fifty years [2]. The importance of using renewable energy sources instead of fossil fuels which is leading to rapidly declining reserves and significantly large environmental problems is gradually increasing. In order to increase awareness on this issue and to achieve a cleaner world, clean and sustainable energy generation is encouraged in many countries with the help of the World Bank and local leading companies of the countries [3]. In this context, with the increase in the integration of distributed renewable energy sources into the grid, traditional grids have started to become inadequate. As an alternative solution to this situation, a great increase is observed in the use of more reliable, highly efficient and energy-saving MGs [4]. Apart from these advantages of MGs, the fact that they are systems that can control the electricity supply to a significant extent is among the most striking features. Thanks to these features, MGs have the ability to meet its own energy and sell surplus energy production back to the main grid, making the system economically very profitable. In addition, MGs can ensure the continuity of the system by using this energy stored for a certain period in case of sudden interruptions in electrical energy [5]. However, the high cost of renewable energy sources and the fact that they have some disadvantages such as providing intermittent energy due to climatic conditions can negatively affect the MGs in which these resources are integrated [6].

MGs can operate in grid-tied or islanded mode. In case of any problem in the main grid, the usage of islanded mode in MGs is more preferred since the MGs can continue to operate safely by switching to islanded mode. MGs increase the efficiency of the main grid by exchanging the energy with other MGs connected to the grid in the mode of grid-tied operation mode [7]. However, MGs must have the same phase and voltage with other networks that switch to island mode in case of any failure, and then with this network when reconnecting to the main grid [8]. In the MG applications examined here, MGs operated in island mode are more common. In order to use distributed energy resources in MGs at an optimal scale with smart, safe, reliable and accurate coordination, energy management is required. In addition, energy management studies in MGs are carried out especially to minimize financial cost and electrical power losses. These energy management studies in MGs vary according to the power system application area. In this chapter, a research study is conducted on energy management studies for specific MG applications. MGs have mainly been considered in two segments as on-grid and off-grid as first stage. Then, on-grid

[1] Fatma Yaprakdal, Assistant Prof., Kırklareli University, Electrical and Electronics Engineering

MGs are divided into community-level and residential-level categories. MGs in the the area of regional-rural, industrial-commercial, hospital, university campus and military are included in the community-level MG category while private residential customers that can be found in a particular residential area, as well as individual homes, buildings and structures like farms are included in the residential-level MG category. In off-grid MG applications, all remote MG varieties have been examined. The main reason for categorizing MGs in this way is that energy management studies vary considerably depending on the location of MGs, internal dynamics such as user profiles, and whether they are connected to the grid or not.

The rest of the paper is organised as follows. General characteristics of MGs are mentioned in Section 1 while energy management system definition, mission and aims are emphasized in Section 2. After these general definitions, detailed information on energy management and control architecture in MGs are given in Section 3. In the 4th Section, MG applications are categorized in on-grid and off-grid and the some studies regarding energy management of these applications are mentionedConclusions are given in Section 5.

1.Microgrid Structure

According to the IEEE 2030.7 standard, an MG is defined as 'a group of interconnected loads and distributed energy resources with clearly defined electrical boundaries that act as a single controllable entity with respect to the grid and can be connected to and disconnected from the grid to operate in both grid-tied mode and islanded-mode'. Based on this definition, the basic units that form the MGs are distributed conventional energy generation units (micro turbines and diesel generators), distributed renewable energy resources, energy storage systems, electric vehicle charging stations, intelligent devices such as circuit breakers (CBs) and intelligent switches, and energy end-users.

Distributed energy resources in MGs are composed of micro turbines, internal combustion engines, fuel cells and combined cycle gas turbines and renewable energy generation units such as solar panels and wind turbines [11]. Renewable energy sources are increasingly preferred in distributed power generation to compensate for the disadvantages of centralized power generation such as high cost, transmission line losses and environmental impacts. However, problems such as weakening of the reliability index of the power system occur when integrating it into the main grid due to the intermittent nature of the RE sources. Problems that may arise due to such reasons in the power system can be overcome by using a correct protection scheme and isolation systems and a redundant generation system diversified with traditional DERs.

Distributed power generation units operate at low voltage (1V-1kV) and medium voltage (1kV-35kV) levels. Their installed power values vary between 1W and 100MW and in this respect; they are examined in four groups as micro scale (1W-5kW), small scale (5kW-5MW), medium scale (5MW-50MW) and large scale (50MW-100MW). Micro turbines and solar cells are in the micro-scale power group, while wind systems are in the small-scale power group [11], [12].

Main battery technologies used in large-scale applications are lead-acid batteries, lithium-ion batteries, sodium–sulfur batteries and flow batteries. Lithium-ion batteries and sodium–sulfur batteries have high power, energy densities and high efficiency while lead-acid batteries low power density and capital cost. Althouh flow batteries show high energy density, independent power and energy ratings, they have low storage capacity. The main use of ESSs in MG applications is to minimize the discontinuity in energy supply caused by the intermittent nature of renewable energy sources, that is, to ensure system reliability.

Electric vehicle charging stations also support a more eco-friendly system by integrating to the MGs, enabling the electrical energy required for the vehicle to be produced with renewable and clean energy [13]. In MGs integrated with electric vehicles, the direction of power flow is from vehicle to grid or from grid to vehicle. The power flow from the vehicle to the grid occurs during periods of high demand or high electricity pricing hours, and while this system is not suitable for every electric vehicle, battery and fuel cell electric vehicles are the most suitable vehicle types for such use [14].

Energy end-users are group of interconnected loads belong to factories, campuses, hospitals or residences who meet their energy needs such as cooling, heating and lighting in the MG. While traditional power grids have a communication network from the generation units to the consumers, an MG has a bi-directional communication network in addition to that network. With this two-way network, energy production units such as fuel cells, solar panels, wind turbines and energy storage systems can instantly provides feedback about their energy generation and filling rates to the end-users (responsive loads) [9].

MG-wide control and coordinated operation is performed by the MG central controller and local controllers. Control, coordination and efficient management of DERs in MG increases system performance and supports continuity in development. The MG's connection to main grid is provided by a point of common coupling (PCC). The DERs are connected to the system via power electronic interface (PEI) in grid-tied or islanded modes for control, measurement and protection purposes thanks to their plug-and-play features. While an MG connected to the grid enjoys the advantage of energy exchange with the main grid under normal operating conditions, it switches to islanded mode in case of failure in the main grid, thus maintain the system stability. In this mode, DERs perform efficient integrated operation with demand response and load shedding, providing uninterrupted power to critical loads.

MGs are located in remote areas, in areas belonging to certain consumer groups and divers sectors, in line with their aim, taking into account the load types, geographical and climatic conditions. Except for operating mode, MGs can be grouped according to the type of electrical power type, supply phases, integrated renewable energy sources variety, application area and supervisory control system type.

2. Energy Management System (EMS)

Regarding EMS application program interface in power systems management, an EMS is described as "a computer system comprising a software platform providing basic support services and a set of applications providing the functionality needed for the effective operation of electrical generation and transmission facilities so as to assure adequate security of energy supply at minimum cost" in the standard IEC 61970 by the International Electrotechnical Commission.

Energy management supports the power system in terms of supply-demand security, increasing the integration of renewable energy sources into the system, minimizing power losses and producing quality electrical energy [21]. In this context, energy management includes many different optimization types such as cost optimization, carbon dioxide emission minimization and energy generation-consumption optimization. One of the most important distinguishing features for these optimization applications is the time period that will be taken as a basis in the work to be done. The time period in which the energy management will be implemented is an important criterion. Setting very short-term periyods (seconds-30mins) for dynamic control of renewable energy sources, short-term periyods (30min-6hrs) for the relationship between source and storage systems, medium-term periyods (6hr-24hrs) for market pricing and long term periods (1 day – 1

week) should be set for load dispatch and maintenance scheduling [22]. For the studies in these time periods, various data types such as camera, meteorological data, power system data are used. It is the duty of the energy management system to process such data and make the necessary optimizations regarding these types of datas [23].

The mathematical methodologies used within the scope of the energy management system can be examined under three basic categories: classical methods, meta-heuristic methods and intelligent methods. Classic methods do not have branch, bound, and integer constraints. As an optimization method, these methods can use linear and non-linear optimization techniques. These techniques, on the other hand, are used to solve two basic optimization problems under certainty and uncertainty. Linear programming, mixed integer programming and nonlinear programming are used in optimization problems under certainty while dynamic programming and stochastic programming are used in optimization problems under uncertainty [25].

Meta-heuristic methods are heuristics that can work with missing or redundant data, with or without constraints. These methods are unlikely and iterative; the desired value is obtained by taking the average of the studies performed many times. Particle swarm optimization, rule-based bat optimization, genetic algorithm, gray wolf optimization, artificial bee colony, crow search algorithm, teaching-learning-based-optimization, adaptive differential evaluation, gravity search algorithm (GSA), modified firefly algorithm, social spider algorithm and whale optimization algorithm (WOA) are types of meta-heuristic algorithms [26].

The last mathematical methodology used within the scope of the energy management system is artificial intelligence (AI) based methods. AI based methods include problem-based classification, fuzzy control and neural networks, multi-agent based on model prediction, game theory and deep learning and they are the most advanced and comprehensive mathematical methods. All numerical methods are given in Figure 1.
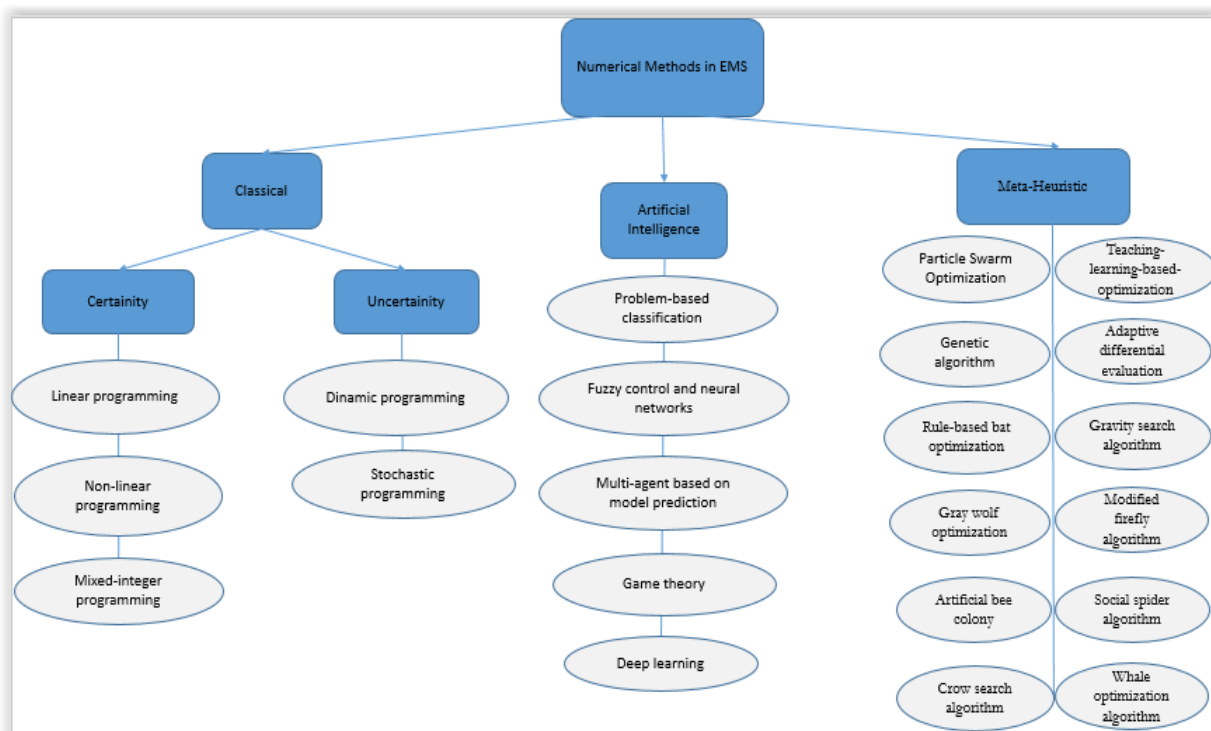

Fig. 1 Numerical methods used for energy management studies

3. MG Control and EMS

The MG-EMS or control system has been defined as follows by the reputable major institutions. IEEE standard 2030.7 defines a MG control system as 'A system that includes the control functions that define the MG as a system that can manage itself, operate autonomously, and connect to and disconnect from the main distribution grid for the exchange of power and the supply of ancillary services; it includes the functions of the MG-EMS; it is the MG controller if implemented in the form of a centralized system' [6]. An MG-EMS is defined as 'System operating and controlling energy resources and loads of the MG' in IEC-TS 62898-1 [11]. In order to provide certain functional needs and necessary benefits in microgrids, an EMS, which is an advanced real-time control and optimization system, must be implemented to operate at the grid-tied and the islanded mode. An EMS mainly preserves grid efficiency and economy based on DERs' power generation, devices on the grid, electrical and climatic forecast data, and electricity-energy market in MGs.

A MG control system includes software and hardware systems and could be physically centralized or distributed. MGs have their own control systems, defined as hierarchical control, and each MG has an MG central control that collects and processes data, operates according to control procedures, and regularly checks the system. If there is one of this control system in the established MG system, it is called a central control system, if each unit in the system is designed to be connected to a different control system, it is called a decentralized control system [16]. These systems are flexible systems that can be expanded in parallel with the increase in the number of consumers. Control levels in MG are divided into three main groups as primary, secondary and tertiary control levels according to their important characteristics such as response, communication and operation [17].

The primary control level can be called field control and is based on system changes and local measurements. The main purpose of this system is to increase reliability, improve performance and realize power distribution. As a standard power dispatch method it provides voltage tracking, active and reactive power mode control, frequency and voltage tracking, but it cannot prevent voltage and frequency fluctuations [18]. The secondary control level improves the parts where the primary control level falls short. At this control level, voltage and frequency fluctuations are damped. It has the characteristics of improving the quality of the power system, taking into account the cost. The system can change the target according to the geographical environment, the preferences of the users and manufacturers, and the equipment costs [19]. The last and top level control, the tertiary control level, is the most advanced control level. This level particularly interested in cost between MG and main grid, electricity market operations and optimal power dispatch. This control level adjusts the cost based on meteorological forecasts. It strengthens the prediction model by incorporating many algorithms such as the K-nearest neighbor algorithm [20], machine learning, long short-term memory, k-nearestneighbors, generalized regression neural network, neural network community and deep recurrent neural networks.

4. EMS in Specified MG Applications

MG applications have different optimization purposes within the scope of energy management, such as maximizing the renewable energy generation, minimizing operating costs, maximizing the life of the system used, and minimizing environmental costs [15]. These purposes vary depending on the campus designed as an MG. In this study, MG applications containing the EMSs have been examined in two basic categories as on-grid (grid-tied) and off-grid (islanded) according to their connection to the main grid. On-grid MG applications are grouped under 2 main subgroups; including community-level and building (individual) level MG applications in this scope

of work. The aim here is to examine regional MG-EMS application studies according to campus types and the relevant needs specific to these campuses. Since there are not many off-grid MG application studies, these studies are examined in a single category.

4.1. EMS in On-Grid MG Applications

An EMS in on-grid MG applications uses the information it receives from the energy generation sources, energy end-consumers and also the energy market to program the generation of its DERs and the net energy it will import from or export to the upstream electricity grid at an optimal level since it has to achieve many objectives like minimizing net power importation from the upstream electricity grid, energy cost and emissions maximizing renewable energy generation and thereby maximizing profits on energy exports to the upstream electricity grid at the same time.
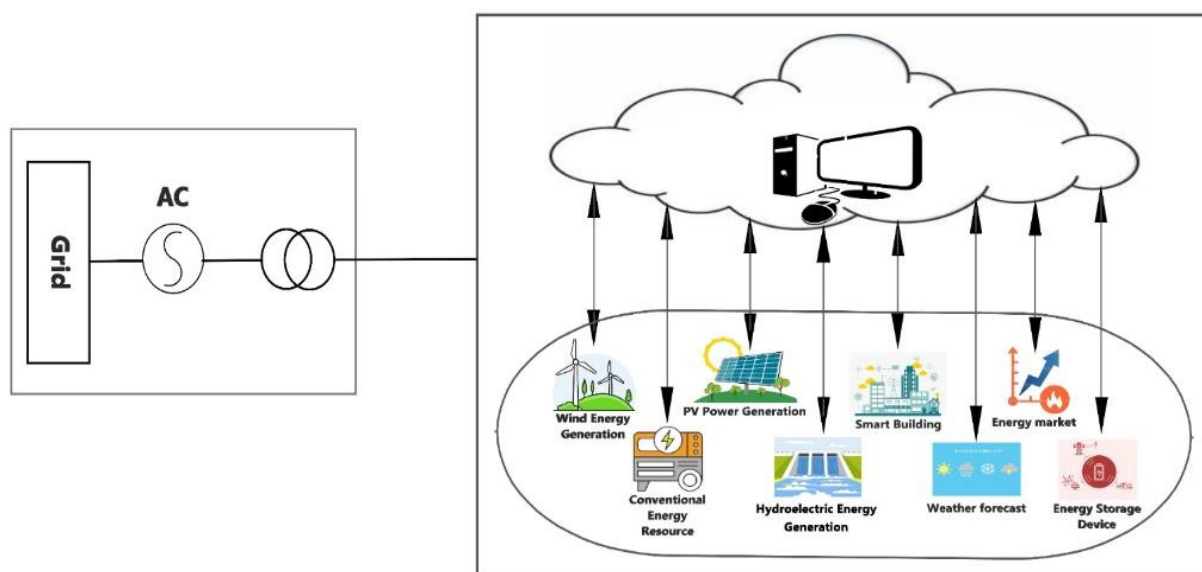

Fig. 2 On-grid MG components and connection

4.1.1. Community – Level MG Applications

Community-level MG application areas consist of regional and rural, industrial and commercial, hospital, university campus and military, and they are connected to the upstream power grid at single point of common coupling (PCC) to ensure system reliability and economy. The most important basic elements that should be in a community microgrid; being self-sufficient in energy production, reliability and sustainability in the supply of energy, and being able to produce low- cost energy. In ordinary operating circumstances, each MG community supports seperate MGs to decrease power losses and improve system stability by sharing resources internally [6]. In case of extraordinary conditions, each MG community is able to operate independently of the main grid to ensure its own unity and reliability.

4.1.1.1. Regional - Rural MGs

As of 2021, the number of people without access to electricity is 768 million. The regions with these communities are mostly rural areas and distributed villages far from the main power

grid. It is very expensive to extend the power grid up to these regions and many technical problems may occur in these regions, such as voltage drop more than acceptable voltage drop values. Therefore, establishing independent systems such as renewable energy-based MG in these regions will be very beneficial in terms of technical, economic, social and environmental aspects. Wind-photovoltaic power generation systems are a convenient preference to meet the electrical energy needs of rural areas away from the main grid.

On the other hand, cities and especially capitals are among the most preferred campuses in terms of MG studies. The biggest reason for this is that such important metropolises should not be interrupted during power cuts. Then, there are reasons such as improved resilience, being advantageous in cost and independence in energy. In this context, some developed countries have initiated pilot regional MG programs. For example, in October 2020 the Australian Government announced that it would support regional MG pilot programs with an investment of $50 million. Another example can be given from Sweden; here, too, the first trial steps for the transition to local energy systems (LESs) are being carried out in the Swedish town of Simris with a LES composed of local wind turbine, the PV farm, and the containers hosting the battery energy storage system (BESS) and the backup generator and EMS. While Europe is currently facing an energy crisis, the race to catch up with the deadlines of the Paris Agreement continues in the energy sector. Therefore, energy utilities everywhere are striving to make the best strategic plan to accelerate energy transitions. Transition steps to (LESs) are gaining importance in this sense. In [41], instead of using the secondary control level, particle swarm optimization has been performed to reduce frequency and voltage fluctuations in MG. The renewable energy sources of this system, which is established for Beijing, are created with a wind turbine of 2500kW and 3 PV panels of 200kW. It has been announced that the use of preferred sources prevents frequency and voltage fluctuations. Azaza and Wallin designed the MSC with a wind turbine and a PV panel. The load profiles that may occur if the obtained MSs are used for different cities in Sweden for 6 months were analyzed by particle swarm optimization [43]. Minimizing the cost through the linear programming method is studied in [31] for a small region in Colombia, used PV panels as a renewable energy source. Cases such as different battery sizes and installation of PV panels have been examined and it is explained that the cost increases in proportion to the battery size. MG study is carried out in [32] for the Kallar Kahar region in Pakistan. Mixed integer linear programming is used as an optimization algorithm. A 500kW wind turbine and a 2000kW PV panel have been used to energize the region, which has a power of 73.6MW. With the help of the HOMER program, the microgrid size and total cost have been minimized and electrical load peak shaving is realized. In [34], an MG operating in three modes called continuous operation mode, power sharing mode and on/off mode is designed. The system, which includes a 200kW PV panel and 2x 100kW solid oxide fuel cells, has determined a mixed-mode energy management strategy and optimum battery size to ensure minimum operating cost. As a result of the study, it is announced that PV panel powers reduce the operating cost and the low charge level causes an increase in the energy cost in the MG.

4.1.1.2. Industrial-commercial MGs

Interest in MGs is also increasing rapidly by large commercial companies and industrial enterprises such as mining company, independent power producer, oil&gas company, datacenter, hotels&resorts and food&beverage company. The primary purpose of commercial and industrial segments is to increase reliability against potential energy interruptions and then to minimize corporate energy costs. Therefore, the commercial and industrial MG sector is a rapidly growing and developing segment among other MG segments. In commercial and industrial (C&I) microgrids, optimization studies can be applied in order to meet their own energy needs, which are their priority targets according to energy market pricing in general in the context of energy management. In fact, the general tendency for the last few years has been to sell energy to the main

grid operator in case of surplus power generation or during peak energy pricing times, and to buy energy from the main grid during periods of low energy prices.

Industrial plants use large step changes under normal and sensitve loading. To protect the system from failures caused by lack of power supply, DERs must be sized satisfactorily and have adequate EMS that provides the system the essential robustness and resilience.

4.1.1.3. Hospital MGs

The devices used in hospitals are of vital importance. In this respect, hospital loads are critical electrical loads and also the electrical energy demand in hospitals is at a very high level in line with the size of hospitals. Hospitals connected to the conventional grid use backup diesel generators and UPS to meet their energy needs in case of power outages just for a limited period. However, besides the depletion of fossil fuel reserves in the near future, there is also an unforeseen fluctuation in diesel prices. Moreover, these generators have risk of error to start up. Therefore, in hospitals where both heat and electrical energy demand is quite high, cogeneration systems that can efficiently produce both electricity and heat energy, especially in which renewable energy sources such as solar power, biomass and wind energy plants are integrated, are quite necessary systems. If a hospital is regulated as MG, its ESSs will store the electrical energy produced by DERs integrated cogeneration system primarily for use in critical situations. While this system supports resilience of power supply for the hospital power demand, it also provides financial benefits to the hospital.

The issues such as capacity planning and solar system efficiency of a general hospital located in New Jersey, with a 3,642kW photovoltaic (PV) panel and energy storage system have been worked in [27]. As a result of this study; It has been determined that as the efficiency of PV panels rises above 16%, the payback period increases, the payback of PV panels operating with 16% efficiency will take 50 months. Besides, the energy cost of the PV panels used decreases by 30%.

In [29], an MG system is designed in a hospital with PV panels, Li-ion energy storage units and diesel generators. Optimization of the dimensions of the structures in the MG system has been carried out by using REopt® software, taking into account the economic benefit of the system and the endurance capacity of the system elements. With the MG hospital application designed in this way, approximately $ 440,191 savings have been obtained from the power losses prevented during power outages and from the energy provided by the main-grid.

4.1.1.4. University Campus MGs

University campus MGs are parts of the utility grid consisting of a group of DERs and energy consumers. The multiple uncertainties in an MG, such as limited solar generation, fluctuations in market prices, and controlling different loads, are challenging points in managing campus energy with an MG system, and therefore this type of application study is very open to research and development. MGs established in a campus can be successfully operated with the robust energy management system to overcome these challenges by offering a variety of solutions to minimize greenhouse gas emissions, maintenance costs and peak load demands of the microgrid infrastructure. Therefore, today, universities generally provide their basic requirements in order to transform their energy supply systems into campus MGs. University campus MGs have been pioneered the service as a testing ground for observing the economic, technical and environmental benefits of using an MG system in the electrical grid. The operational management of electrical consumption and generation units of each building within the campus is monitored by a central controller.

An energy management system (EMS) parametric optimization application for the efficient and traceable coordination of distributed energy resources consisting of wind turbine and solar panels has been implemented in [30] at a residential level MG in Lambton College, Canada. In this MG, which has an energy storage unit as well as distributed energy sources, the energy management study is presented as a two-level parametric-mixed integer linear programming problem to provide significant improvement in uncertainty management with the aim of net cost minimization. It is concluded that the proposed system can make smart decisions in the face of current uncertainties without violating operational constraints, and it is emphasized that this proposed approach can be easily applied in real-time applications.

In [2], a three-phase AC microgrid system including a solar panel that can generate a maximum total of 100 kW of energy for 24 hours of operation and an energy storage unit with the capacity of 175 kWh or 300 kWh to examine different operating scenarios, at Eskişehir Osmangazi University. In order to reduce the total amount of electricity consumption for the phasor mode, which is a new application model that allows the analysis of the 24-hour time interval of the modeling in the Matlab / Simulink environment, the cost optimization study was carried out by utilizing the multi-time tariff. Instead of meeting most of MG's energy needs from the electricity grid, different scenarios have been studied on to provide support from the PV energy generation unit and energy storage unit, and a remarkable cost minimization is achieved.

In [44], a real-time MG study with both a wind turbine and a PV panel connected to a 380kW load is presented. It is envisaged that this system, which is carried out at Aalborg University MG Research Laboratory in Denmark, will be put into island mode or switch to normal mode at a specified time in order to keep the balance between the amount of energy production and consumption stable.

4.1.1.5. Military MGs

Some MGs may be operated by organizations serving or elements of the armed forces. This is usually the smallest of the various MG markets. However, it is a market that is often of prime importance to national security, as individual bases may rely on these MGs for energy independence for enhanced resilience (often up to 2 weeks or more) and to improve cybersecurity in an age where military equipment is rapidly becoming highly technical. National Defence Departments own many local installations from sensitive scientific search facilities like microelectronics and biological laboratories to major industrial facilities like dockyards and aviation warehouses and those facilities are connected to the national power grid. Prolonged power outages in the national power grid will adversely affect National Defence Departments' operational mission, while creating significant finansial losses. Therefore, MGs integrated with a proper and cyber secure EMS are a good opportunity for military applications.

Some military MGs are mobile, which means they can be deployed quickly and easily on a battlefield, in turn reducing the need for fuel to be transported over long distances to remote locations. These types of military MG applications will be mentioned within the scope of off-grid MG applications segment.

4.1.2. Residential-Level MG Applications

Under this MG segment, private residential customers that can be found in a particular residential area, as well as individual homes, buildings and structures like farms, are considered. These MGs are connected to the main grid and they may include centralized or distributed power generation and distribution systems, energy storage devices and electrical vehciles charge units.

They can sell the excess of the energy they generate and participate in the energy market as 'prosumers'. In an MG system where there is more than one individual residence, it may take longer to take decisions regarding operation and development of the system due to the large number of people involved in the system and, accordingly, the high number of decision makers. In these MG systems, since each home has its own internal energy dynamics, the main difficulty in terms of energy management is that neither renewable generation nor the electrical consumption can be controlled.

In [35], a usable, 3-tier hierarchical MG system is implemented in Australia. An EMS device is placed in each of the houses connected to the MG and it is followed by this system. As a result of the study, the continuity of the system is ensured by giving electricity to the houses with electricity production, more than electricity consumption, to neighbors in need of electricity, and then to the system. The design of an MS according to the residential profile is carried out in [36], using a DC-PV panel and an AC-wind turbine. It is aimed that to increase the life of the system used by using genetic algorithm. In addition, optimization study has been expanded to reduce radiation and CO2 emissions. In [37], an MG study is carried out for a house powered by a PV panel. In the Matlab environment, the energy management system is implemented using real user data. The reason for giving importance to real user data is to show that the MG system is actually usable. A new graphical method is proposed to show the change of energy flow. In [38], a control study is carried out for MG, which has an electric vehicle charging station that can be used as commercial and residential. In this system, where PV panels are located, the importance of the batteries to be used has emphasized that the electricity production is insufficient from time to time. It has been proven that electric vehicles provide a significant increase in energy needs. The biggest reason for this is the inability to provide a power flow from the vehicle to the grid. Zhuo suggested using MC for an Australian farm with PV panels and a wind turbine. The purpose of existence of MG is to meet the energy needs while minimizing the cost. For this study, he made the system close to reality with the constantly changing electrical peaks and weather conditions in the system. As a result of the study, it is announced that the system has been optimized in terms of financial and electrical load [39].

4.2. EMS in Off-Grid MG Applications

These microgrids will be similar to community microgrids with the main difference being that they will not usually be connected to a utility national grid. They will instead operate as an "island" microgrid system, usually because of economic issues or their geographical location – they may be located some distance away from national transmission lines. Examples of remote microgrids are for communities in remote regions like Alaska, Western Australia or islanded nations around the world. Their main function will be reliability and resilience. Due to their remoteness, system maintenance and access to parts can be challenging and needs to be considered when designing such a system. This means that they will often be designed to operate autonomously and are even more likely than other MGs to draw on distributed and diverse generation technologies. This needs to be balanced with the MG needs and levelized cost of electricity (LCOE).

Moreover remote military applications are in off-grid MG segment and they are installed in an ad-hoc way. Security of forward operating bases are in the most important point in the framework of MG setup. This security issue, which is of priority and importance, determines the installation location of the MG, energy requirements, generator and building layouts. Bases have the potential to evolve in an ad-hoc manner, which can double or even halve overnight due to modifications in mission and force needs. Therefore, these systems are powerfull but not well organized. They meet their energy needs by means of diesel generators and these generators are usually over-sized for their energy needs. This decreases performance and leads to wet stacking,

which damages the generator motor. Load planning is not possible in advance, as these MGs are systems that are built in an ad-hoc way.

5.CONCLUSION

Smart grids consisting of MGs are expected to replace traditional power systems in the near future. Energy crisis and increasing greenhouse gas emission are key issues accelerating this situation. Due to the increasing importance of MGs in this respect, there have been many relevant research studies and on-going studies. In this chapter, the studies carried out in the field of energy management in MGs are examined by grouping them according to their locational feature. Therefore, this study will be a guide for researchers and practitioners who will carry out an MG study or installation in any of the categories described, in terms of energy management studies and also in terms of giving an idea for the relevant MG installation. In the relevant literature, these studies are handled one by one according to the campuses where MG is applied, while energy management studies for all campus types are discussed here. In the examined studies, it has been determined that the researchers who implement and plan the MG project have goals and preferences in line with their specific needs. These are briefly as follows;

• An MG design with integrated charging station for EV technology that remains popular,

• Cost optimization is one of the priorities in the implemented systems. In this context, in order to keep the cost in the desired balance, issues such as fuel cost optimization and battery size optimization should be handled as a priority,

• Even though the optimization goals are the same in the studies, the methods and software programs used differ.

• System life and maintenance costs are important. In order to reduce these expenses, the choice of quality and appropriate equipment, taking into account cost optimization,

• Solar panels and wind turbines are preferred because they have reliable, sustainable, widespread technology and have less investment costs compared to other energy sources,

• Providing an appropriate system design for this situation as the voltage/frequency stability of the system is of critical importance especially when the MG transitions from island mode to grid-tied mode and vice versa.

REFERENCES

[1] Hu, N. Xie, D. Fang, and X. Zhang. (2018). The role of renewable energy consumption and commercial services trade in carbon dioxide reduction: Evidence from 25 developing countries, Applied Energy, 211, 1229-1244.

[2] G. Tarihi, İ. Çetinbaş, B. Tamyürek, M. Demirtaş. (2018). Eskişehir Osmangazi Üniversitesi Kampüsünde Elektrik Tüketim Maliyetinin Azaltılmasına Yönelik FV Üretim ve Enerji Depolama Biriminden Oluşan bir Mikro Şebekenin Optimal Tasarımı G. Üniversitesi, Teknoloji Fakültesi 1. Ulusal Elektrik Enerjisi Dönüşümü Kongresi Bilimsel Makalesi. 8, 41-49.

[3] Y. Zahraoui, M. R. Basir Khan, I. Alhamrouni, S. Mekhilef, and M. Ahmed.(2021). Current status, scenario, and prospective of renewable energy in algeria: A review. Energies, 14,907-916

[4] Güven D. (2019). Verimliliği düşmüş bataryaların hizmet sektöründe Kullanımı: Akıllı tesis uygulaması, Yüksek Lisans Tezi, İstanbul Teknik Üniversitesi, Enerji Enstitüsü, İstanbul,

[5] K. Normandeau,(2020) Microgrids for Hospitals and Healthcare Microgrids in Hospitals. Microgrid Knowledge

[6] K. Shivarama Krishna and K. Sathish Kumar, (2015).A review on hybrid renewable energy systems, Renewable and Sustainable Energy Reviews. 52,907–916.

[7] M. F. Zia, E. Elbouchikhi, and M. Benbouzid,(2018). Microgrids energy management systems: A critical review on methods, solutions, and prospects. Applied Energy, 222, 1033–1055.

[8] İ.Anabilim,(2021). ENERJİ DEPOLAMA ÜNİTELİ TRİJENERASYON MİKRO ŞEBEKE SİSTEMİNDE ÇİZELGELEME OPTİMİZASYONU: HASTANE, Yüksek Lisans Tezi, İstanbul Teknik Üniversitesi, Lisansüstü Eğitim Enstitüsü, İstanbul

[9] Burhan.B,(2017). YENİLENEBİLİR ENERJİ KAYNAKLARINI İÇEREN MİKRO-ŞEBEKE SİSTEMLERİN AKILLIYÖNETİMİ, Doktara Tezi, İnönü Üniversite, Fen Bilimleri Enstitüsü, Malatya

[10] B. Kocaman, (2014). Mikro Şebekeler için Örnek Bir Enerji Yönetimi Uygulaması, Bitlis Eren Üniversitesi Fen Bilimleri Dergisi. 3, (35-52)

[11] A. Basa Arsoy, F. M. Nuroğlu. (2009) Dağıtılmış Üretim Kaynağı İçeren Dağıtım Sistemlerinde Sürekli Durum ve Kısa Devre Analizi. 3, (104)

[12] T. S. Ustun, C. Ozansoy, and A. Zayegh, (2011).Recent developments in microgrids and example cases around the world - A review, Renewable and Sustainable Energy Reviews, 15, (4030–4041).

[13] D. A. Savio, V. A. Juliet, B. Chokkalingam, S. Padmanaban, J. B. Holm-Nielsen, and F. Blaabjerg,(2019) .Photovoltaic integrated hybrid microgrid structured electric vehicle charging station and its energy management approach. Energies (Basel). 12, (168-186)

[14]   C. B. Robledo, V. Oldenbroek, F. Abbruzzese, and A. J. M. van Wijk, (2018).Integrating a hydrogen fuel cell electric vehicle with vehicle-to-grid technology, photovoltaic power and a residential building. Applied Energy, 215, (615–629).

[15]   Y. E. G. Vera, R. Dufo-López, and J. L. Bernal-Agustín,(2019).Energy management in microgrids with renewable energy sources: A literature review, Applied Sciences (Switzerland),. 9, (384-412).

[16]   L. Meng et al, (2017).Review on Control of DC Microgrids and Multiple Microgrid Clusters, IEEE Journal of Emerging and Selected Topics in Power Electronics, 5,(928–948).

[17]   M. F. Zia, M. Benbouzid, E. Elbouchikhi, S. M. Muyeen, K. Techato, and J. M. Guerrero, (2020).Microgrid transactive energy: Review, architectures, distributed ledger technologies, and market analysis, IEEE Access, 8.(19410–194329).

[18]   P. Borazjani, N. Izzri, A. W. Hashim, B. H. Azura. (2014). A Review on Microgrid Control Techniques. 2014 IEEE Innovative Smart Grid Technologies - Asia (ISGT Asia) Conference, 8, (749-753)

[19]   S. K. Sahoo, A. K. Sinha, and N. K. Kishore, (2018).Control Techniques in AC, DC, and Hybrid AC-DC Microgrid: A Review,IEEE Journal of Emerging and Selected Topics in Power Electronics, 6, (738–759).

[20]   D. Y. Yamashita, I. Vechiu, and J. P. Gaubert,(2020). A review of hierarchical control for building microgrids," Renewable and Sustainable Energy Reviews, 118.

[21]   B. Kocaman, (2014). Mikro Şebekeler için Örnek Bir Enerji Yönetimi Uygulaması, Bitlis Eren Üniversitesi Fen Bilimleri Dergisi,3, (35-52)

[22]   J. Ma and X. Ma,(2018)A review of forecasting algorithms and energy management strategies for microgrids," Systems Science and Control Engineering, 6, (237–248).

[23]   L. Liu, Y. Wang, L. Liu, and Z. Wang, (2018). Intelligent Control of Micro Grid: A Big Data-Based Control Center, IOP Conference Series: Earth and Environmental Science, 108.

[24]   O. Kahouli, H. Alsaif, Y. Bouteraa, N. ben Ali, and M. Chaabene,(2021). Power system reconfiguration in distribution network for improving reliability using genetic algorithm and particle swarm optimization, Applied Sciences (Switzerland),11, (3092-3107)

[25]   H. Karimi and S. Jadid,(2020).Optimal energy management for multi-microgrid considering demand response programs: A stochastic multi-objective framework, Energy, 195,(1-13).

[26]   S. Leonori, M. Paschero, F. M. Frattale Mascioli, and A. Rizzi,(2020). Optimization strategies for Microgrid energy management systems by Genetic Algorithms, Applied Soft Computing Journal, 86, (19-56)

[27]   K. Chau, K. Mahani, M. A. Jafari, and S. Haghani,(2018) Solar-Powered Microgrid Capacity Planning for a General Hospital. IEEE Green Energy and Smart Systems Conference (IGESSC),18(1-6)

[28]   K. Sirviö, K. Kauhaniemi, A. A. Memon, H. Laaksonen, and L. Kumpulainen,(2020)Functional analysis of the microgrid concept applied to case studies of the sundom smart grid, Energies (Basel), 13, (4223-4234)

[29]   A. Lagrange, M. de Simón-Martín, A. González-Martínez, S. Bracco, and E. Rosales-Asensio, (2020). Sustainable microgrids with energy storage as a means to increase power resilience in critical facilities: An application to a hospital, International Journal of Electrical Power and Energy Systems, 119, (1-12).

[30]   E. C. Umeozor and M. Trifkovic, (2016), Energy management of a microgrid via parametric programming," in IFAC-PapersOnLine, 7, (272–277).

[31]   C. A. Correa, G. Marulanda, and A. Garces, (2016) Optimal Microgrid Management in the Colombian Energy Market with Demand Response and Energy Storage.1944.

[32]   J. Ahmad *et al.*, (2018).Techno economic analysis of a wind-photovoltaic-biomass hybrid renewable energy system for rural electrification: A case study of Kallar Kahar, *Energy*, 148, (208–234).

[33]   V. N. Coelho, M. Weiss Cohen, I. M. Coelho, N. Liu, and F. G. Guimarães,(2017). Multi-agent systems applied for energy systems integration: State-of-the-art applications and trends in microgrids, *Applied Energy*,187, (820–832).

[34]   S. Sukumar, H. Mokhlis, S. Mekhilef, K. Naidu, and M. Karimi, (2017). Mix-mode energy management strategy and battery sizing for economic operation of grid-tied microgrid, *Energy*,118, (1322–1333).

[35]   M. N. Akter, A. Mahmud, Amanullah M. T. (2016) A Hierarchial Transactive Energy Managment System for Microgrid IEEE Power & Energy Society. General Meeting (2016 : Boston and Institute of Electrical and Electronics Engineers. 8

[36]   A. S. O. Ogunjuyigbe, T. R. Ayodele, and O. A. Akinola, (2016).Optimal allocation and sizing of PV/Wind/Split-diesel/Battery hybrid energy system for minimizing life cycle cost, carbon emission and dump energy of remote residential building,.171, (153–171)

[37]   S. Leonori, A. Martino, F. M. Frattale Mascioli, and A. Rizzi, (2020). Microgrid Energy Management Systems Design by Computational Intelligence Techniques, *Applied Energy*, 277.

[38]   J. L. Torres-Moreno, A. Gimenez-Fernandez, M. Perez-Garcia, and F. Rodriguez, (2018). Energy management strategy for micro-grids with PV-battery systems and electric vehicles, *Energies (Basel)*, vol. 11, (552-565).

[39]   W. Zhuo, (2018). Microgrid energy management strategy with battery energy storage system and approximate dynamic programming. Proceedings of the 37th Chinese Control Conference.1 (7581-7587)

[40]   Mohamed S. Taha, Yasser A.-R. I. Mohamed, (2016) Robust MPC-Based Energy Management System of a Hybrid Energy Source for Remote Communities .IEEE Power Electronics Society, IEEE Power & Energy Society, and Institute of Electrical and Electronics Engineers, 1, (1-6)

[41]	H. Li, A. T. Eseye, J. Zhang, and D. Zheng, (2017). Optimal energy management for industrial microgrids with high-penetration renewables,. *Protection and Control of Modern Power Systems*, 2,(2-12)

[42]	M. S. Behzadi and M. Niasati, (2015). Comparative performance analysis of a hybrid PV/FC/battery stand-alone system using different power management strategies and sizing approaches, *International Journal of Hydrogen Energy*, 40, (538–548)

[43]	M. Azaza and F. Wallin, (2017). Multi objective particle swarm optimization of hybrid micro-grid system: A case study in Sweden, *Energy*, 123, (108–118).

[44]	A. C. Luna, L. Meng, N. L. Diaz, M. Graells, J. C. Vasquez, and J. M. Guerrero, (2018). Online Energy Management Systems for Microgrids: Experimental Validation and Assessment Framework, *IEEE Transactions on Power Electronics*, 33, (2201–2215).

[45]	R. R. Nivedha, J. Govind Singh, and W. Ongsakul,(2018) PSO based Economic Dispatch of a Hybrid Microgrid System. IEEE, 5,(18-23).

[46]	B. Papari, C.S. Edrington, T. V. Vu, F. Diaz-Franco,(2017). A Heuristic Method for Optimal Energy Management of DC Microgrid, *2017 IEEE Second International Conference on DC Microgrids 17, (337-343).*

[47]	X.-F. Lin, X. Yan-Zhao, C.-N. Song, S.-J. Song, and L. Bin,(2016)An Experiment And Research Platform For DC Micro-grid. Proceedings of the 35th Chinese Control Conference. 1, (8588-8595)

[48]	J. Jimeno, J. Anduaga, J. Oyarzabal, and A. G. de Muro, (2011).Architecture of a microgrid energy management system, *European Transactions on Electrical Power*,21, (1142–1158)

The effect of the use of different materials and design optimization in the connecting rod on fatigue analysis

Berkay KARAÇOR[1]
Ali Kemal DUMAN [2]
Mustafa ÖZCANLI [3]

1. INTRODUCTION

The connecting rod in internal combustion engines plays a noteworthy role in transferring the vertical force it receives from the piston as a result of combustion events to the rotational force of the crankshafts (Joakim, 2020: 1). The connecting rod is exposed to multidirectional amplitude bending loads, gas and mass forces, inertia forces and buckling loads, axial tension and compression loads during operation. From the moment the engine starts to move, the connecting rod is subjected to repetitive loads millions of times. For this reason, it is important for the life of the connecting rod to be strong enough to withstand the high stresses that will occur while moving in the engine (Acar, 2016: 1-2). This situation can be applied with design optimizations as a result of using new generation materials and performing detailed stress-strain analysis on engine components in the optimization to be carried out in the connecting rod, efforts to increase the strength, decrease in weight, and reduce the production cost come to the fore (Ismail *et al.*, 2021: 8728). Long connecting rod life and low deformation critically depend on material selection and material quality. Among these material choices, titanium materials have become particularly interesting in the automotive industry in areas where hardness and toughness are required. (Ajayi *et al.*, 2020: 4390). Modern connecting rods are also manufactured from alloying elements of magnesium, aluminum, and polymeric connecting rods, especially titanium. In the automotive field, connecting rods are traditionally produced by forging from powder metal or forged steel, as well as being produced as a casting type (Kaliappan S *et al.,* 2018*:* 14599). Many elements such as poorly made design, fatigue, application of excessive load to critical stress areas, excessive bending, as well as material selection can cause failure in connecting rod parts (Gök and Cihan, 2021: 222-223). In this case, the researchers simulate real fatigue tests in the finite element analysis of connecting rod designs. For this, firstly, a three-dimensional design model is created, then the material is defined to the design, and after the limitations and loads are defined, the necessary analysis data for the results are obtained from the process (Zhang *et al.,* 2019*:* 1) . In the literature, there are many studies on the optimization of the connecting rod design, the use of different materials, and the comparison of static and fatigue analysis. In a study of these, Vijayvergiya et al. analyzed the connecting rod design using the finite element method, using three different sections in the connecting rod. They observed that the I-type section design gave the best results in terms of deformation, equivalent stress, equivalent elastic strain, and factor of safety (Vijayvergiya *et al*, 2008: 239-243). Sathish and Muthulakshmanan examined how to improve the design in terms of strength,

[1] Research Assistant, Cukurova University, Department of Automotive Engineering, Orcid: 0000-0001-5208-366X

[2] Bachelor's degree, Cukurova University, Department of Automotive Engineering, Orcid: 0000-0002-3722-2868

[3] Prof. Dr., Cukurova University, Department of Automotive Engineering, Orcıd:0000-0001-6088-2912

weight, and safety with numerical analysis by using Aluminum alloys and AISI 4340 steel instead of traditional materials in connecting rod design (Sathish and Muthulakshmanan, 2018: 1123-1125). In their study, Basavaraj et al. simulated connecting rod fatigue analysis in ANSYS using four different materials. It has been determined that 42CrMo4 steel gives 1.01 times better results in terms of safety factor and 10 times better in terms of the number of cycles, while the deformation and equivalent stress values are the same compared to the second-best material after itself (Basavaraj, *et al.*, 2021: 2812-2814). In another connecting rod numerical analysis study, they aimed to find the optimum material both dynamically and cost-effectively by changing the connecting rod material (Ali H. and Haneef. 2016: 1273-1275). Seralathan et al. performed static analysis on an I-type connecting rod they designed. In their comparison of equivalent stress, total deformation, and equivalent elastic strain, they discovered that the best results were obtained with A356-5%SiC-10% Flyash stir cum squeeze casting material. It was found that this material gave better results in terms of equivalent stress, total deformation, and equivalent strain results by 0.11%, 62.6%, and 61.32%, respectively, compared to the base material (Seralathan, *et al.*, 2020: 3724-3728). While testing the connecting rods both experimentally and numerically, Gao et al. tried to come up with a design that did not compromise safety while reducing the weight of the connecting rod. They concluded that verifying the real tests they conducted with simulated tests would provide an opportunity to provide an economic advantage with longer cycle numbers while reducing the weight of the connecting rod and increasing the strength (Gao *et al.*, 2022: 3–23). In this study, C45 Carbon Steel, AISI 4340 Steel, and Titanium alloys, which are not used together in the literature, were defined as connecting rod materials. The connecting rod design has been optimized depending on the effects of the 3 different materials applied on the static and fatigue analysis effect. A study was carried out to increase the efficiency of connecting rods to be used in vehicles by researching the most suitable material and design combination.

2. MATERIAL

In this study, C45 steel and AISI 4340 steel and Titanium alloy materials were preferred as connecting rod materials. The mechanical characteristics of the materials defined in the ANSYS software program are indicated in Table 1 (Ajayi *et al.*, 2020: 4393; Hagos,2018: 23).

Table 1. Material Characteristics

	Density (kg/m³)	Tensile Ultimate Strength (MPa)	Young's Modulus (GPa)	Tensile Yield Strength (MPa)	Poisson Ratio
C45 Steel	7850	565	200	310	0.3
AISI 4340 Steel	7850	745	200	470	0.3
Titanium Alloy	4620	1070	96	930	0.36

3. METHOD

Finite element methods were used to find mechanical properties in connecting rod analysis. The finite element method helps the designer to simulate real analysis. Errors and deficiencies in the model can be determined in advance in this way and necessary precautions can be taken in the actual design and analysis (Godara *et al.*, 2022: 1896). The calculation tools that customize the

outlines of the design, taking into account certain design limits, are Finite Element Analysis. With this method, very small elements are needed in the analysis while solving the most fundamentally complex components within certain limits (Muhammad and Shanono, 2019:25-26). FEM is a practical method used for fatigue analysis and evaluation of part life, which has many pros compared to other processes used in many diverse analyses. By means of this method, critical points can be determined and the stress/strain distribution in the whole part can be found, as well as providing great benefits to the designer in case the loading conditions are complex or the part does not have a regular geometric shape (Mirehei *et al.*, 2008: 22) . In this study, ANSYS 2020 R2 Static Structural module was used for static and fatigue analysis, and connecting rod designs were designed in CATIA V5 R20. The distance between the inner diameter of the small end and inner diameter of the big end is 146 mm. While the inner diameter of the small end is 18 mm, the outer diameter of the small end is 24 mm. In parallel, the inner diameter of the big end is 17 mm, the outer diameter of the big end is 21 mm. The width of the section design is 60 mm. Also, the thickness of the design is 10 mm. The visuals of the connecting rod design are given in Figure 1. According to the results of the design analysis, optimization was achieved by reducing the connecting rod width by 1.3 times and increasing the thickness by 1.1-1.2 times.
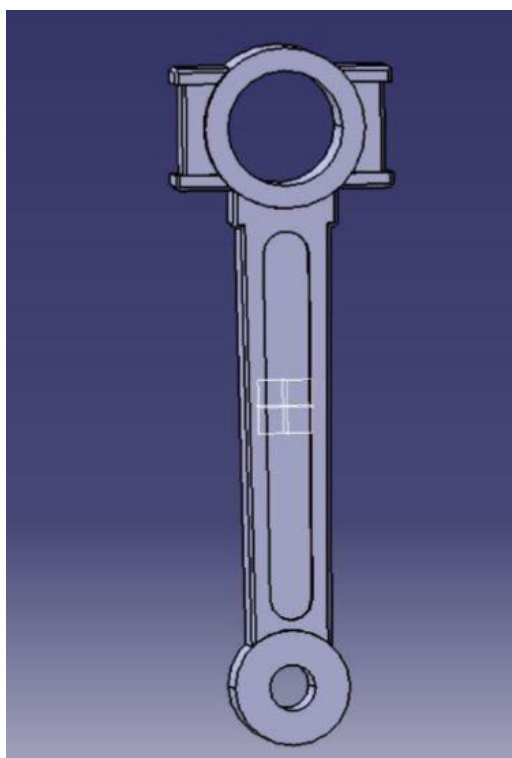

Figure 1. 3D model of connecting rod design

Figure 2 and Figure 3 indicate the cylindrical support region and applied force region for analysis. The assumptions applied in the analysis are: The connecting rod head was fixed with the fixed support command. According to ideal gas calculations and gas force calculations, the force on the connecting rods is accepted as 25000 N in the -Z direction (Basavaraj, *et al.*, 2021: 2809-2810). The module is meshed with the lowest possible element size to find the best mesh quality. The mesh should be thinner only in certain areas and key areas such as re-entered corners, holes, and areas where stress concentration is expected.

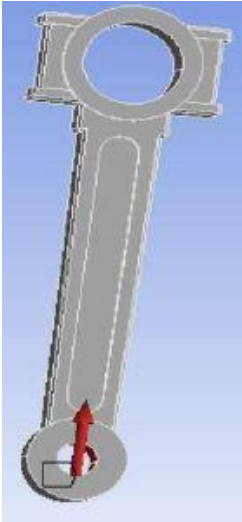Figure 2. Fixed support region for design

Figure 3. Applied force region for design

Figure 4 indicates mesh images of the connecting rod design. In design mesh statistics, the connecting rod design has 425726 nodes and 284306 elements.
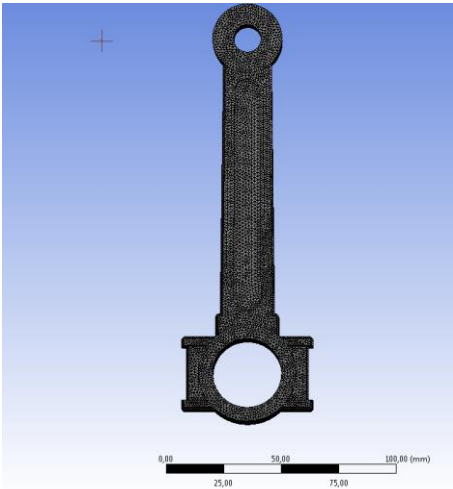

Figure 4. Mesh view of connecting rod design

4. RESULT AND DISCUSSIONS

The total deformation, equivalent stress, equivalent elastic strain, safety factor, lifetime, and damage values obtained as a result of the analysis are given in Table 2. In the comparison of total deformation values, the lowest value was obtained in C45 steel with 0.042 mm. In the results of equivalent stress values, the lowest value was found with a value of 81.836 MPa when titanium alloy material was used. When the safety factor results are examined, it is seen that the highest number is reached in the titanium alloy material design. Equivalent elastic strain results also indicate that the lowest value was reached with C45 steel material, as in total deformation. This value is 0.5 times the highest equivalent elastic strain value obtained with Titanium alloy. The highest value in damage values was determined in Titanium alloy and the lowest value in AISI4340 steel. The damage value of C45 steel is 1.2 times higher than that of AISI 4340 steel. Figure 5, Figure 6, and Figure 7 indicate the total deformation, Von-Mises stress, and safety factor distribution, respectively, of the three materials, used.

Table 2. Results of Analysis

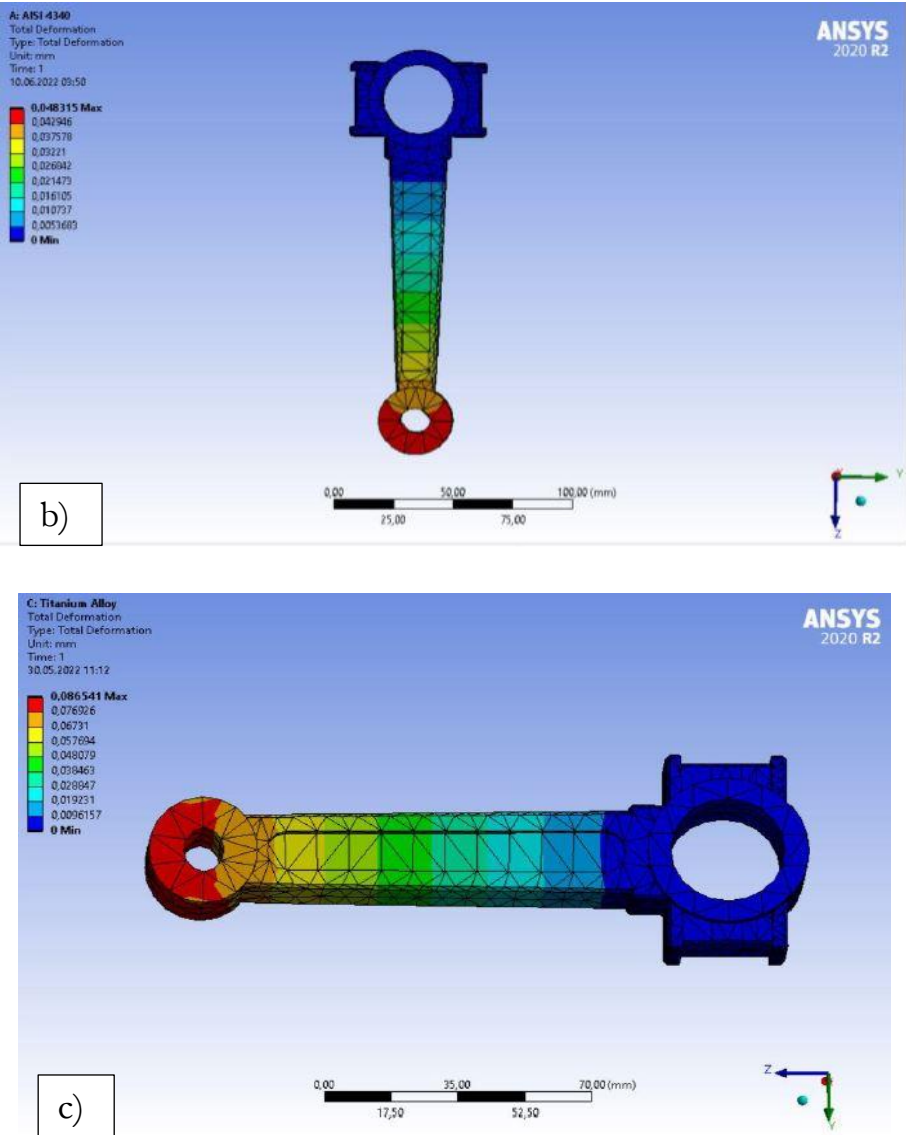|	C45 Steel	AISI 4340 Steel	Titanium Alloy
Total Deformation(mm)	0.042	0.048	0.086
Equivalent Von-Mises Stress (MPa)	82.096	113.94	81.836
Equivalent Elastic Strain(mm/mm)	0.0004	0.0006	0.0008
Safety Factor	3.776	4.125	11.364
Life (Cycle)	100×10^5	100×10^5	100×10^4
Damage	120.58	100	100×10^{30}

a)
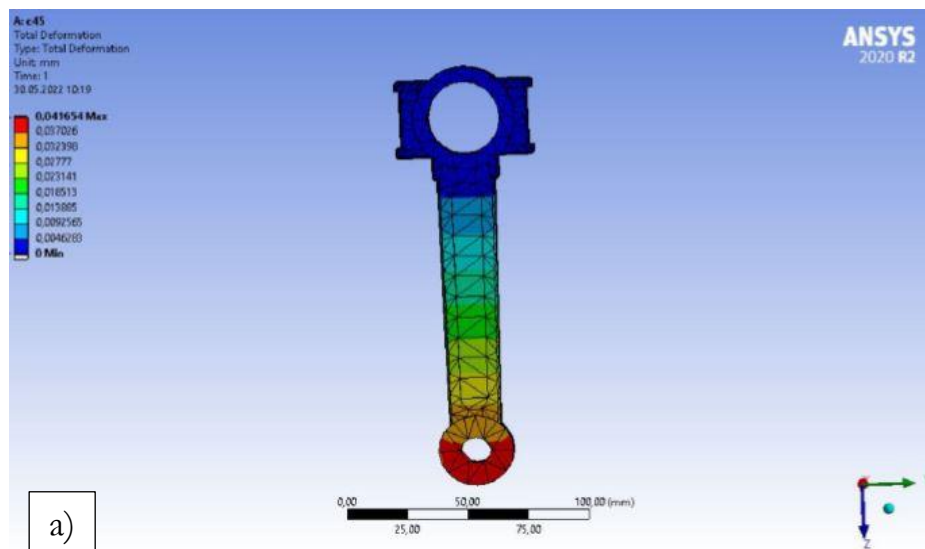
Figure 5. Total deformation in connecting rod design of (a) C45 steel (b) AISI 4340 steel c) Titanium alloy

As indicated in Figure 5a, Figure 5b, and Figure 5c, the C45 steel design has the lowest deformation value, this value is 0.49 times lower than the Titanium alloy design, which reaches the highest value. AISI 4340 steel design has 1.14 times higher deformation value than C45 steel design.
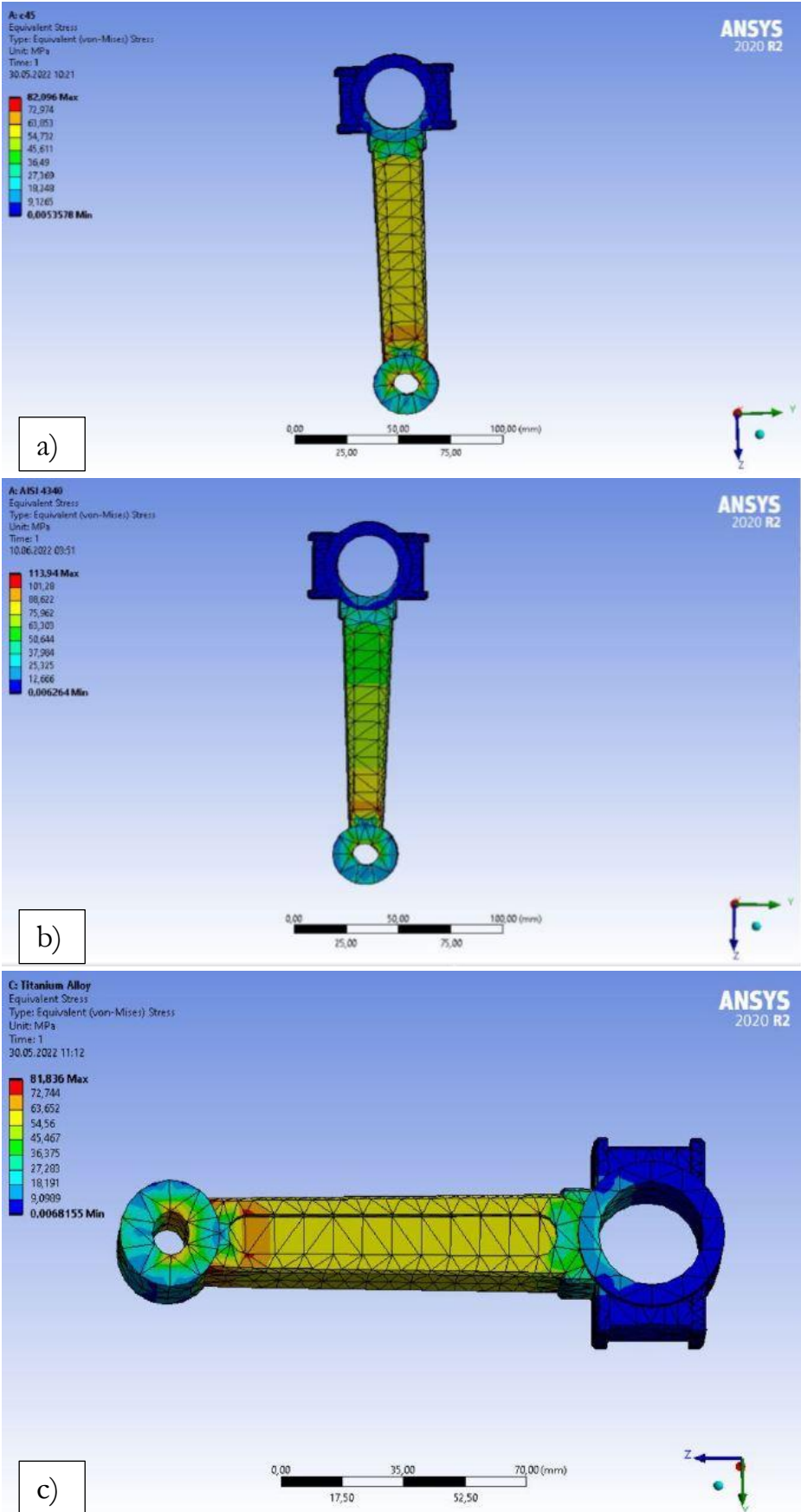
Figure 6. Equivalent stress in connecting rod design of (a) C45 steel (b) AISI 4340 steel c) Titanium alloy

Equivalent stress distribution values are given in Figure 6a, Figure 6b, and Figure 6c. While the lowest value is reached with the titanium alloy design, this value is 0.72 times lower than the AISI 4340 steel design, which has the highest value. The C45 steel design has an equivalent stress value of 0.72 times lower than the AISI 4340 steel design.
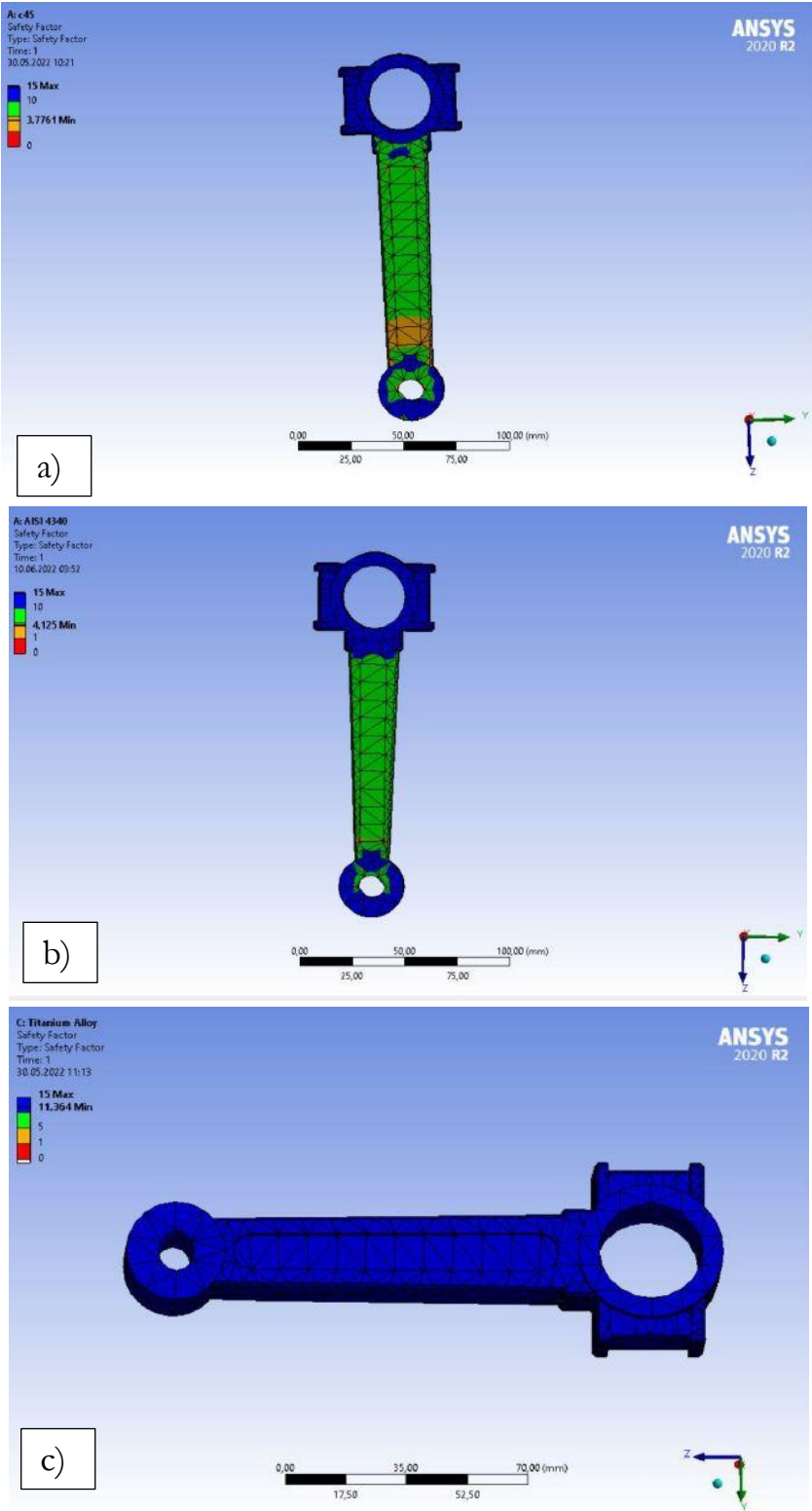

Figure 7. Safety factor in connecting rod design of (a) C45 steel (b) AISI 4340 steel c) Titanium alloy

In Figure 7a, Figure 7b, and Figure 7c, the safety factor values of the three materials are presented. Titanium alloy design has the highest factor of safety value, which is 3 times higher than the lowest factor of safety value obtained with C45 steel. The titanium alloy design showed a factor of safety 2.75 times higher than the AISI 4340 steel design.

Table 3 presents the data obtained from the fatigue graphs of the three materials. It is seen that AISI 4340 and C45 steel have 1.8 times and 2.7 times more cycles at final loading conditions, respectively than titanium alloy. In the design of C45 steel, the first ruptures occur at loading between 0.75 times and 1 time, while in the design of AISI 4340 steel, the first ruptures are observed at loading between 1 layer and 1.25 times. It has been determined that there is no change in the number of lifetimes up to 1.5 times loading in the titanium alloy design.

Table 3. Fatigue Sensitivity Results

	Material	Loading History				
		0.5	0.75	1.0	1.25	1.5
Life Cycle Values	C45 Steel	100×10^5	100×10^5	75×10^5-87.5×10^5	37.5×10^5	18.39×10^5
	AISI 4340 Steel	100×10^5	100×10^5	100×10^5	50×10^5-60×10^5	27.04×10^5
	Titanium Alloy	100×10^4	100×10^4	100×10^4	100×10^4	100×10^4

5. CONCLUSION

Considering the repeated loads that the connecting rod is exposed to in internal combustion engines, it is very critical to know the performance of the engine throughout its life. In this study, three different materials such as C45 steel, AISI 4340 steel, and titanium alloy were used and the results of the static and fatigue analyzes of these materials in the connecting rod were compared. It is understood from the analysis results that C45 steel material can also be used instead of titanium alloy, which is generally preferred in the design of the connecting rod. The following numerical results during the study also support this indicator:

1. The total deformation value is 51.16% less deformation value in C45 steel design compared to the Titanium alloy design.
2. In the comparison made in terms of equivalent elastic strain, the C45 steel design showed 50% less equivalent elastic strain than the Titanium alloy design.
3. Both the C45 material design and the AISI 4340 material design have 10 times more cycles than Titanium alloy.

Numerical analyzes have shown that C45 material can also be used in connecting rod design in light of all analysis results. However, these analyzes should be verified with real tests and the parts to be optimized in the design should be revealed with real tests.

REFERENCES

Acar, H. (2016). *Biyel kolu analizi, optimizasyonu ve yorulma davranışının incelenmesi.* Master Science Thesis. Bursa Technical University, Bursa.

Ajayi, O. K. Malomo, B. O. Paul, S. D. Adeleye, A. A. Babalola, S. A. (2021). Failure modeling for titanium alloy used in special purpose connecting rods. *Materials Today: Proceedings*, *45*(January),4390–4397.

Ali, H. M. M. Haneef, M. (2015). Analysis of fatigue stresses on connecting rod subjected to concentrated loads at the big end. *Materials Today: Proceedings*, *2*(4–5),2094–2103.

Basavaraj, Y. Joshi, R. Setty, G. R. Samiullah, M. Museb, M. Tayab, M. Banu, H. (2021). FEA of nx-11 unigraphics modeled connecting rod using different materials. *Materials Today: Proceedings*, *46*(October),2807–2813.

Gao, W. Wang, G. Zhu, J. Fan, Z. Li, X. Wu, W. (2022). Structural optimization design and strength test research of connecting rod assembly of high-power low-speed diesel engine. *Machines*, *10*(9),815.

Godara, S. S. Brenia, V. Soni, A. K. Singh Shekhawat, R. Saxena, K. K. (2022). Design and analysis of connecting rod using ANSYS software. *Materials Today: Proceedings*, *56*,1896–1903.

Gök, M. G. Cihan, Ö. (2021). Investigation of failure mechanism of a DCI engine connecting rod. *European Journal of Technic*, *11*(2),222-228.

Hagos, T. (2018). *Static structural and life prediction analysis of feeder table head shaft for wonji-shoa sugar factory using Ansys.* Addis Ababa University, Addis Ababa.

Ismail, I. Abdelrazek, S. M. Ismail, M. Emara, A. (2021). Enhancing the durability of connecting rod of a heavy-duty diesel engine. *International Journal of Automotive and Mechanical Engineering*, *18*(2), 8728–8737.

Joakim, A. (2020) *Design optimization of a connecting rod for internal combustion engine.* California State University, California.

Kaliappan, S. Revanth Raam, A. B, C. Asswin, S. Mohammed Ibrahim, Dr. T. Mothilal, M.D. Rajkamal (2018). Modal and kinematic analysis of a connecting rod for different modal and kinematic analysis of a connecting rod. *International Journal of Pure and Applied Mathematics*, *119*(12),14599–14608.

Mirehei, A. Hedayati Zadeh, M. Jafari, A. and Omid, M. (2008). Fatigue analysis of connecting rod of universal tractor through finite element method (ANSYS). *Journal of Agricultural Technology*, *4*(2),21–27.

Muhammad, A. Shanono, I. H. (2019). Static analysis and optimization of a connecting rod. *International Journal of Engineering & Technology Sciences*, *6*(June),24–40.

Sathish, T. Muthulakshmanan, A. (2018). Design and simulation of connecting rods with several test cases using al alloys and high tensile steel. *International Journal of Mechanical and Production Engineering Research and Development*, *8*(1),1119–1126.

Seralathan, S. Mitnala, S. V. Sahith Kumar Reddy, R. V. Venkat, I. G. Reddy, D. R. T. Hariram, V. Micha Premkumar, T. (2020). Stress analysis of the connecting rod of compression ignition engine. *Materials Today: Proceedings*, *33*, 3722–3728.

Vijayvergiya, A. Kumari, E. Lal, S. (2021). Design and shape optimization of connecting rod end bearing through ANSYS. *International Research Journal on Advanced Science Hub*, *3*(11),235–242.

Zhang, M. Zhao, C. Yan, Z. Yao, L. Yang, Z. Hassa, M. (2019). The structure, stress and modal analysis of 1.6-liter gasoline engine connecting rod based on finite element analysis. *IOP Conference Series: Materials Science and Engineering, 677*(3), 032094.

Ballistic evaluation of armor plates at different angles

Umut KUMLU[1]
Mustafa Atakan AKAR[2]
Doğukan BAŞER[3]
Ömer HÜKÜMDAR[4]
Berkay KARAÇOR[5]

1. INTRODUCTION

Human has been in need of protection throughout their history. As a result of this need, they have been in constant work to discover the better, both in their daily life and in war situations. For this, they developed weapons that started with the use of stones and sticks (Demir, 2008: 1). The proliferation of armaments has created the need for protection against the threat of weapons. In line with these needs, human beings have had to use personal protective shields and armors (Robinson, 1967: 45-50). It has been through wars throughout history and has used new weapons and armor equipment that it has produced with developing technology (Yavas, 2009: 3-5). Taking precautions against threats and attacks of ammunition and weapons is always among the top priorities in the defense industry, which is the sector in which technology is developing the fastest (Agrawal, 2011: 1-4). From the past to the present, the ballistic performance of various materials has been the subject of constant research. Along with the development of weapons and ammunition, armors that can show ballistic performance against the threats they may pose have also been developed (Murray *et al.,* 2008: 1-23). On the other hand, according to the place where the armor in question will be used, a suitable armor material should be selected or an appropriate armor design should be made. For example, in some armor applications, the weldability of the armor is very important. Therefore, it is not possible to use a material with weak welding ability, no matter how much ballistic protection it provides and no matter how light it is (Ashby *et al.,* 1998*:* 3-161-219-263). In some applications; continuity of the armor is desired. In other words, a similar protection should be provided each time against successive threats. In such cases, ceramics, etc., which often provide one-time protection due to their fragile structure. The materials are not suitable for use (Carlucci and Jacobson, 2008: 3). In short, in order to select the most suitable material to meet the need, there is always a need for ballistic examination of many different materials or a system formed by these materials. While the ballistic performance definition of armors can be realized through FEM (Finite Element Method), it helps in determining critical design parts and material performance during the design phase (Kartikeya, *et al.,* 2019:514-520). The effect of the order of plates against bullet impact were studied by several authors. Teng et al. (Teng, *et al.,* 2008: 870-884) performed the ballistic tests through the analysis program in order to

[1] Research Assistant, Cukurova University, Department of Automotive Engineering, Orcıd: 0000-0001-7624-6240

[2] Assoc. Prof. Dr., Cukurova University, Department of Automotive Engineering, Orcıd: 0000-0002-0192-0605

[3] Bachelor degree, Cukurova University, Department of Automotive Engineering, Orcıd: 0000-0002-1530-3595

[4] Bachelor degree, Cukurova University, Department of Automotive Engineering, Orcıd: 0000-0002-0806-3562

[5] Research Assistant, Cukurova University, Department of Automotive Engineering, Orcıd: 0000-0001-5208-366X

find the strong and weak configurations in the double-plate armors. It created ideal properties for the strongest configuration in the low strength and high ductility front layer and the high strength and low ductility back sheet. Babaei et al. (Babaei, *et al.* 2011*:* 208-217) tried the ballistic test application to examine which material should be placed in the front and rear positions on the plates made of steel and aluminum plates. They found that the aluminum-steel sequence did not perform well in providing ballistic protection compared to the steel-aluminum sequence. Yunfei et al. (Yunfei, *et al.*, 2014: 38-49) examined the effect of plate order on ballistic performance in double-layer steel plates by real ballistic test. With the presence of high strength and low ductility material in the first layer, it gives better ballistic results than the presence of low strength and high ductility material in the first layer. In a study by Iqbal et al. (Iqbal *et al.*, 2010: 185–195) it was aimed to see the effect of 1100-H12 aluminum alloy plates and Weldox steel plates on ballistic tests. They discovered that not only the change in curvature but also the thickness of the material affects the ballistic limit of the formed plates. When the literature is examined, it is seen that there is no study showing the change of directional deformation in armor plates at varying angles. For this reason, in this study, three different angles (0°, 30°, 60°) were used for the target multi-material hybrid plates, and the directional deformation of the plates was determined by explicit dynamic analysis. As a result, the results of this study will be developed and will provide important findings in terms of ballistic performance evaluation that can be used in the defense industry.

2. MATERIAL

In this study, Ramor 500 and Armox 500T were used as plate material and lead material was used for 7.62 x 51 NATO bullet design. The mechanical properties of the materials defined in the ANSYS software program are presented in Table 1 (Ssab,2022: 5; Ssab,2022: 4).

Table 1. Material Characteristics

	Density (kg/m³)	Tensile Ultimate Strength (MPa)	Young's Modulus (GPa)	Tensile Yield Strength (MPa)	Poisson Ratio
Ramor 500	7850	1700	-	1450	1.
Armox 500T	7760	1650	209	1300	0.3

Johnson-Cook material models are commonly used in ballistic impact simulations. While the material properties are given in Table 1, a simplified Johnson Cook model is used for plate materials in these models. The following equation describes the flow voltage as:

$$\sigma_y = (A + B\varepsilon^n)(1 + Cln\dot{\varepsilon}^*)$$
(1)

A, B, C and m are the constants in the equation; σ_y represents the effective stress, ε the effective plastic strain, $\dot{\varepsilon}^*$ the normalized effective plastic strain rate, and n the work hardening exponent (Dietenberger *et al.*, 2005: 1-10). Model factors for Ramor 500 and Armox 500T are listed in Table 2 and Table 3.

Table 2. Model parameters for Armox 500T

	A_A(MPa)	B_A (MPa)	n	C
Armox 500T	1372.48	835.021	0.2467	0.0617

where A_A B_A n and c are Johnson-Cook parameters for Armox 500T. A_A is the yield stress, B_A is the hardening stress, n is the strain hardening, and c is the strain-rate hardening (Iqbal *et al.*, 2016: 146-164).

Table 3. Model parameters for Ramor 500

	A_R(MPa)	B_R (MPa)	n	C
Ramor 500	1021	965	0.057	0.001

where A_R B_R n and c are Johnson-Cook parameters for Ramor 500. A_R is the yield stress, B_R is the hardening stress, n is the strain hardening, and c is the strain-rate hardening (Scazzosi *et al.*, 2021: 14).

3. METHOD

The FEM is a numerical analysis process frequently used in engineering and mathematical models (Seshu, 2019: 1-15). The finite element method consists of three main stages. The first stage is the preprocessing stage, where a finite element mesh is improved and material characteristics and boundary conditions are used to subdivide the subject geometry for mathematical analysis. The second stage is the stage that includes the solution stage of the program by deriving the basic matrix equations from the main example and solving the basic quantities. The post-processing and third stage include examining the base quantity values, such as stresses and displacements, for which the solution is verified, and the derivation and investigation of additional quantities, such as error index and particular stresses. The created geometric models are transferred in order to execute Finite Element Analysis. In the program interface, element type selection on the mathematical model, creation of the mesh form, determination of the contact areas, boundary conditions, environmental and material properties and analysis type were performed (Hutton, 2014) In this study, ANSYS 18.0 Explicit Dynamics module was used for dynamic collision analysis, while bullet and plate designs were designed in CATIA V5 R20. The target plate is 100x200 mm in size and 14.5 mm thick, designed in CATIA V5 R20 and then transferred to ANSYS 18.0 Workbench for analysis. Images of the projectile and plate design are given in Figure 1 and Figure 2. The 7.62 × 51 mm bullet is a specially designed bullet with a diameter of 7.62 mm, a sleeve length of 51.2 mm.
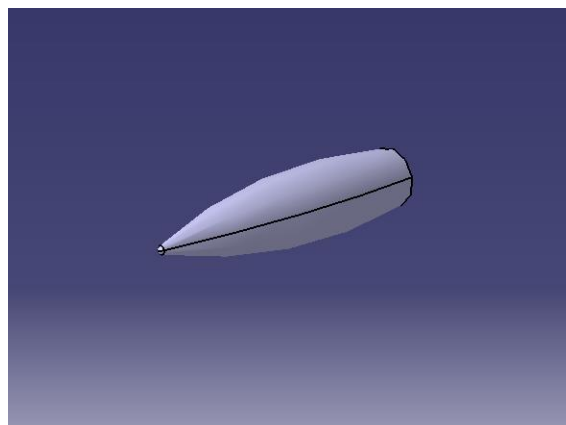

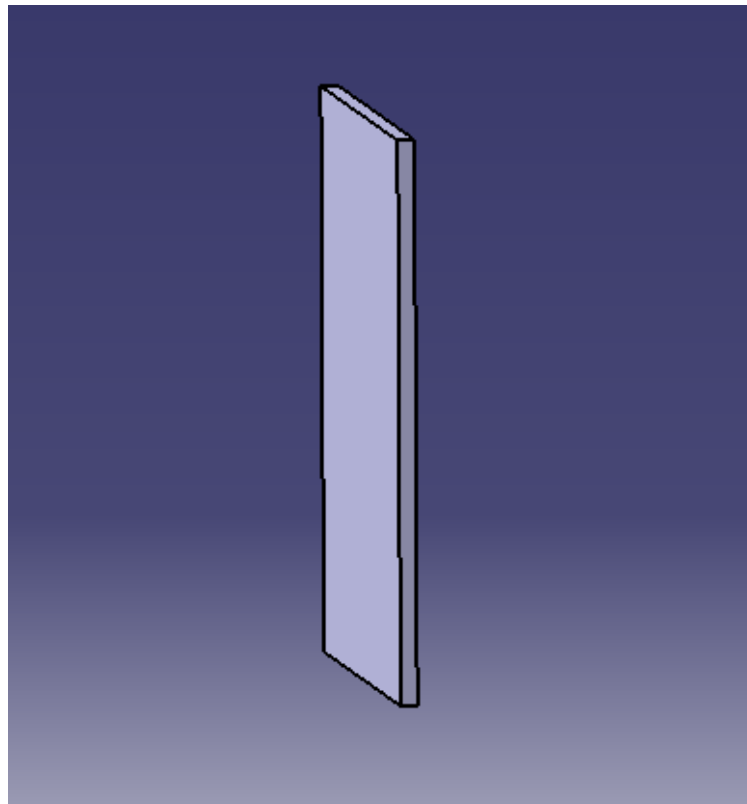Figure 1. CATIA view of 7.62x51 mm bullet

Figure 2. CATIA view of the designed plate

The most important step in finite element analysis is the meshing phase. The selecting and implementation the appropriate- mesh enables easy analysis for users (Uçtu, *et al.,* 2017: 37-43). Figure 3 shows mesh images of the steel plate and bullet. In plate and bullet mesh statistics, the target plate is 2162846 elements, the bullet core is 9036 elements, and the bullet jacket is 6888 elements.
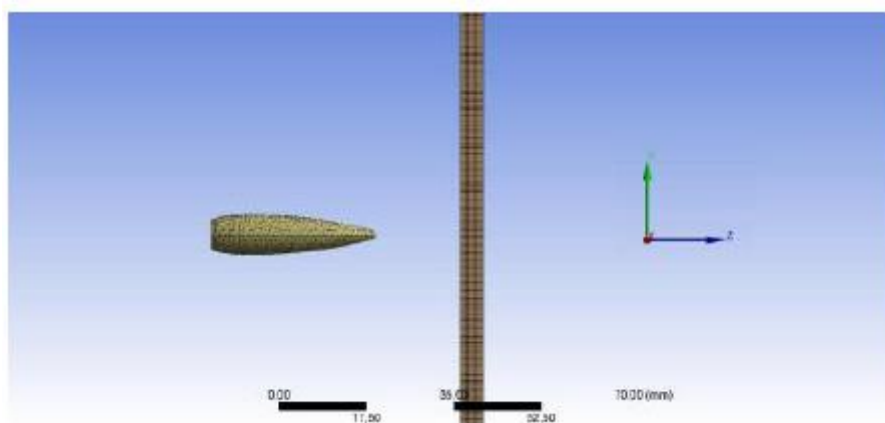

Figure 3. Mesh view of 7.62x51mm bullet and plate

In Figure 4, ANSYS images of the boundary conditions given to the target layer are given. The analysis was applied according to the following assumptions:
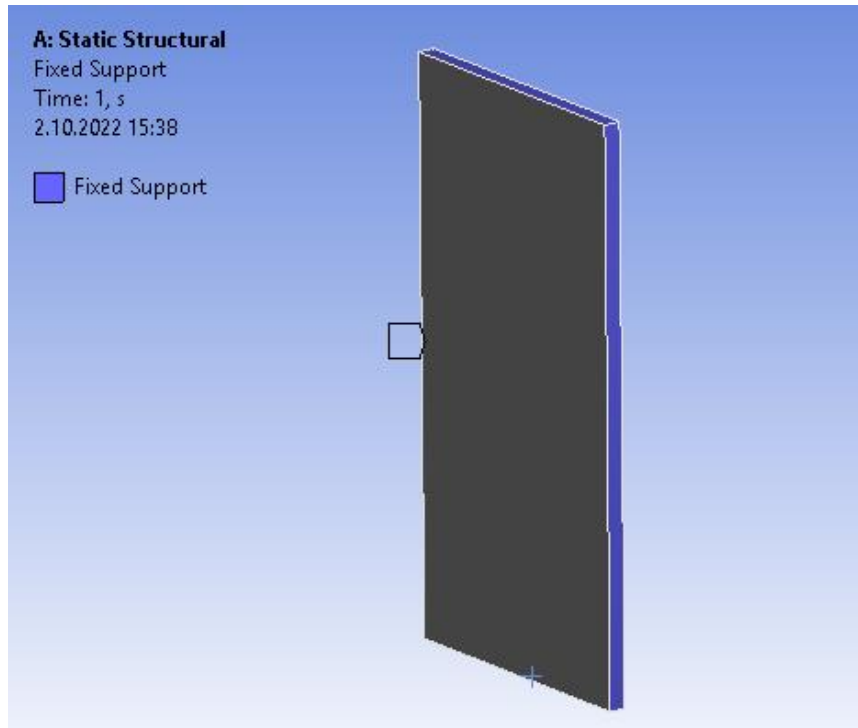
Figure 4. Boundary conditions for plate

In the mesh phase, the bullet models were updated on ANSYS and mesh was applied, and then the plate was supported from 4 side surfaces. In this explicit dynamic analysis, the lead was first applied to hit Armox 500T and then Ramor 500. The rate of fire of the bullet varies according to the type and caliber of the bullet, the diameter of the barrel and the groove sets in the gun. In order to achieve the most ideal result, 850 m/s average velocity is accepted for 7.62x51 mm bullet.

4. RESULT AND DISCUSSIONS

Explicit dynamic analysis through finite element analysis showed that the lowest directional deformation value occurs in the layer combination with 60°. In the numerical analysis of the layer combination with 0°, the highest directional deformation value was obtained. The results of the analysis are shown in Table 4. Figures 5 to 7 show the distribution of directional deformation values of the plate. When the plate angle increased from 0° to 30°, a decrease of 20.68% was observed in the amount of directional deformation, while a significant decrease of 197.25% was observed in the angle increasing from 30° to 60°. For the plate angle of 60°, the minimum deformation value is obtained, the deformation value is 3.385 mm, while for the plate angle of 0°, the angle with the maximum deformation value is obtained, the deformation value of 12.143 mm. It is seen that the minimum deformation value is 3.59 times less than the maximum deformation value.

Table 4. Results of Analysis

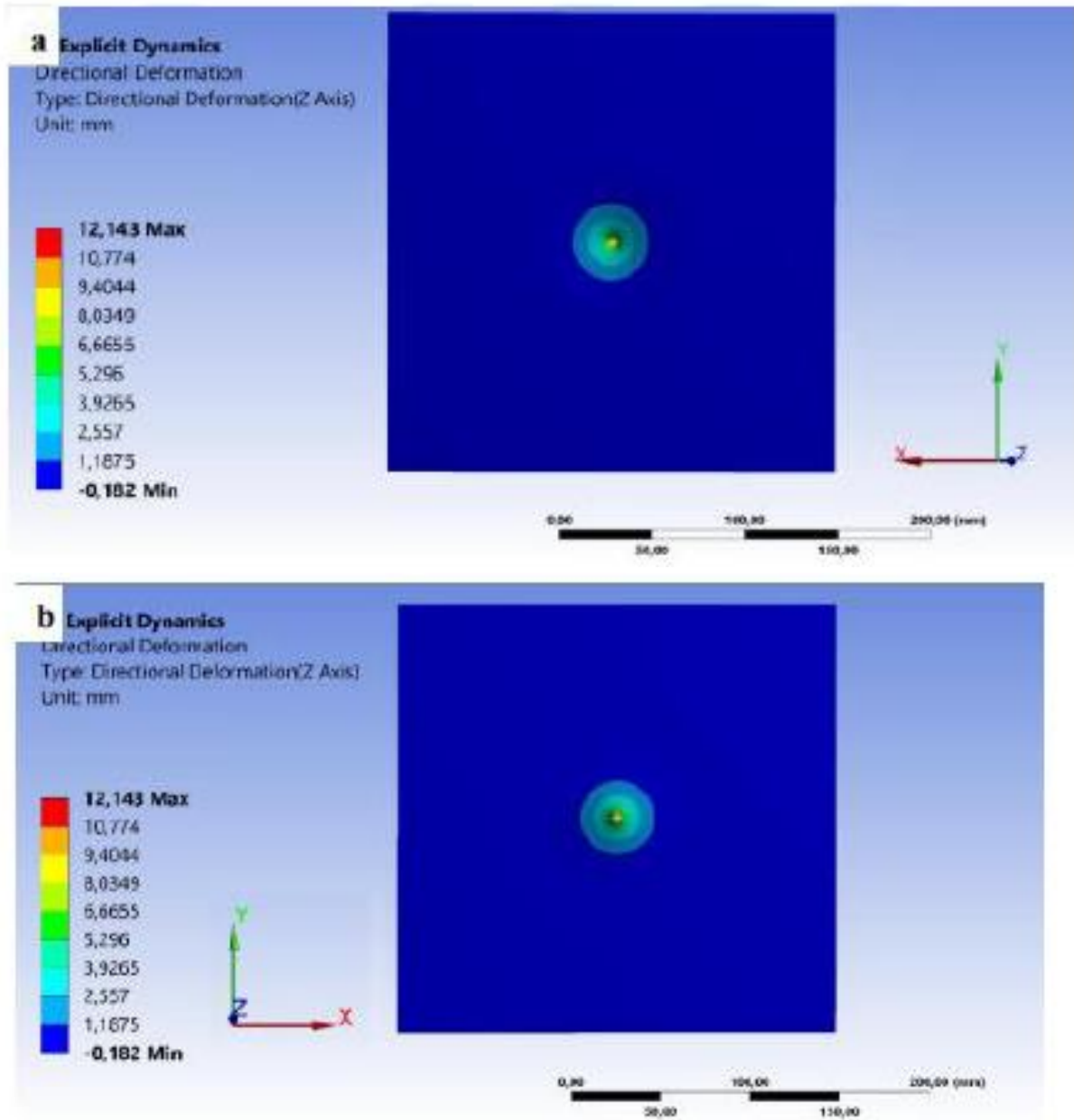| Angle	Directional Deformation (mm)
0°	12.143
30°	10.062
60°	3.385

Figure 5. Directional deformation on the front (a) back (b) surfaces in the Z direction at 0° angle on the plate

As seen in Figure 5a and Figure 5b, the directional deformation value was found to be 12.143 mm in the explicit dynamic analysis made at 0° angle and the plate was pierced by the bullet as in the test. In this case, it has the maximum directional deformation value in the explicit dynamic analysis made with 0° angle.
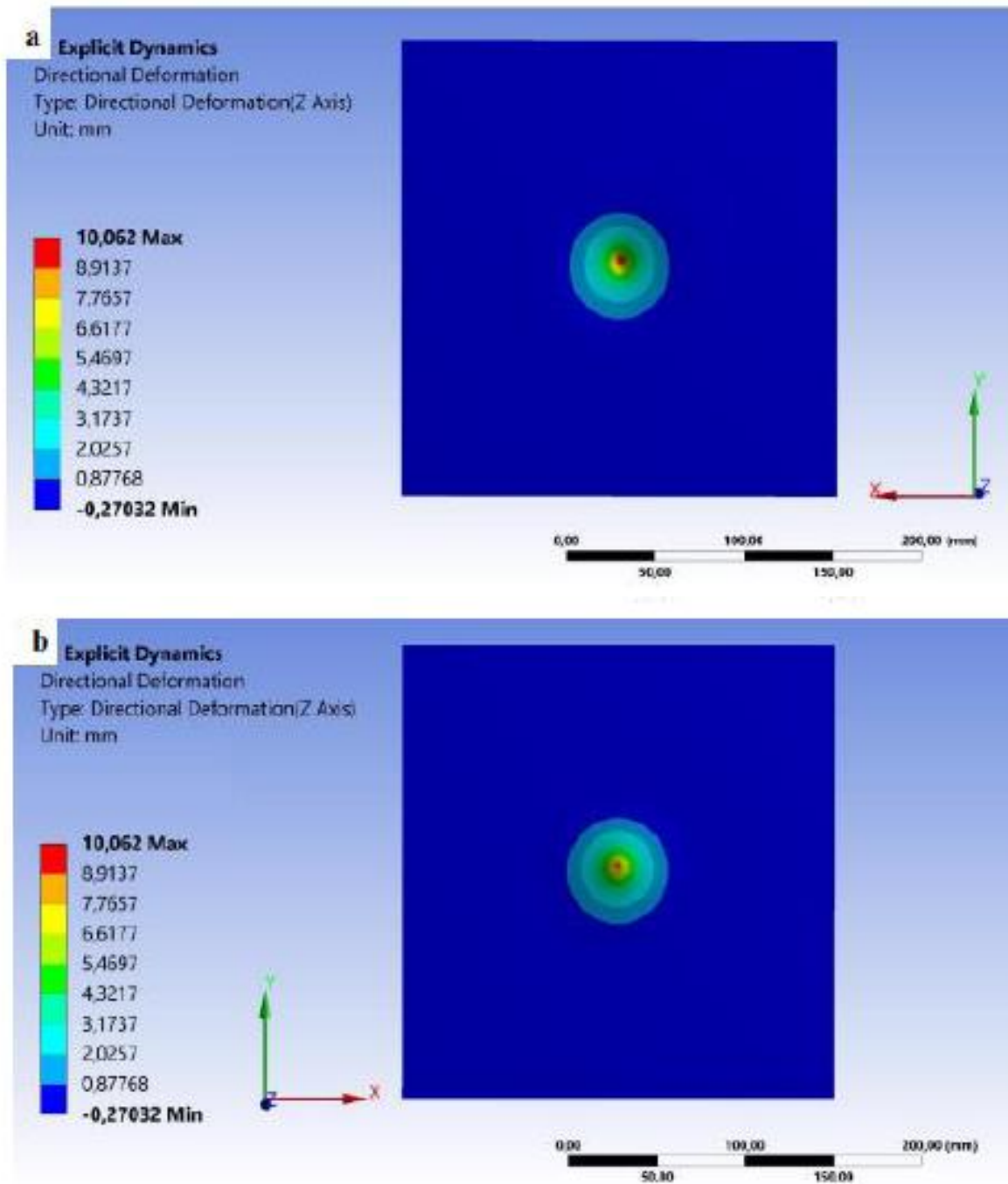
Figure 6. Directional deformation on the front (a) back (b) surfaces in the Z direction at 30° angle on the plate

As seen in Figure 6a and Figure 6b, the directional deformation value was found to be 10.062 mm in the explicit dynamic analysis made with an angle of 30° and the plate was not pierced by a bullet as in the test.
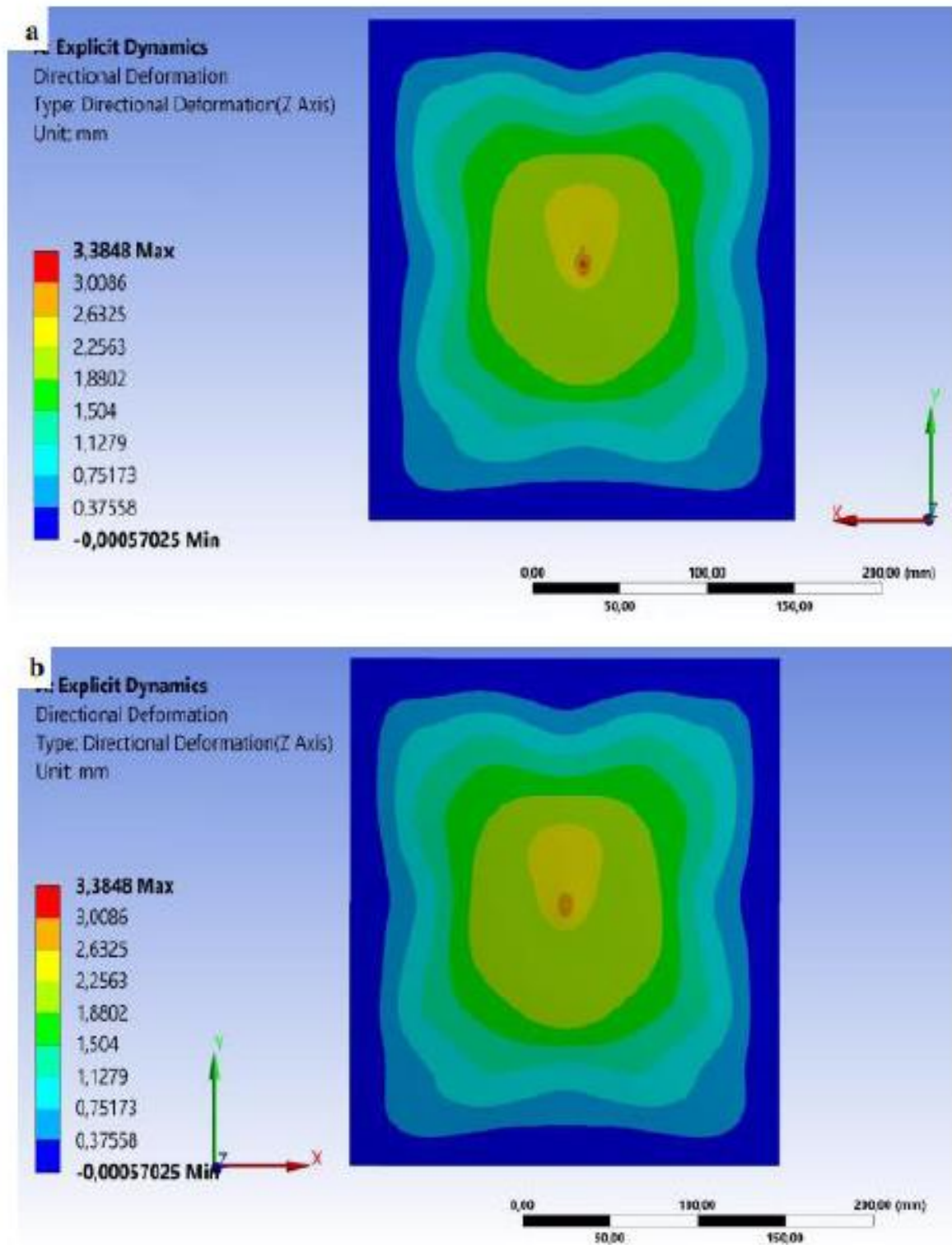
Figure 7. Directional deformation on the front (a) back (b) surfaces in the Z direction at 60° angle
on the plate

As seen in Figure 7a and Figure 7b, the directional deformation value was found to be 3.3848 mm in the explicit dynamic analysis made with an angle of 60°, and the plate could not be pierced by the bullet and bounced, as in the test. In this case, it has a minimum directional deformation value in the explicit dynamic analysis made with an angle of 60°.

5. CONCLUSION

It is very important to know the ballistic performance of engineering materials in order to choose armor materials that provide full ballistic protection in civil and military applications. Ballistic protection is an increasingly developing situation in the defense industry. In this study, the effects on finite element analysis were shown by performing explicit dynamic analysis at three different angles (0°, 30°, 60°) for the hybrid plate obtained by using Armor 500T and Ramor 500 materials. It was found in the analysis results that the directional deformation results decreased as the angle increased. The following results were obtained during the study:

1. In the analyses made at 0° collision angle, the result of 12.143 mm directional deformation was reached. At this angle, the plate was pierced with 7.62x51mm bullets and the failure mode was observed. The maximum deformation value at this angle is 258.73% higher than the minimum deformation value.

2. In the analyses made at 30° collision angle, the result of 10.062 mm directional deformation was reached. At this angle, the plate was not pierced by 7.62x51mm bullets and a significant bulge was observed on the back of the target.

3. In the analyses made at 60° collision angle, the result of directional deformation of 3.3848 mm was reached. At this angle, the plate was not pierced by 7.62x51mm bullets and no obvious protrusion was observed on the back of the target. With this, the least deformation value occurred.

REFERENCES

Agrawal, B. J. (2011). High performance textiles for ballistic protection, *Defense Science Research Conference and Expo (DSR)*, Singapore, 1-4.

Ashby, M. F., Jones, D. R. H. (1998). *Engineering materials 2*, 2nd ed., Butterworth-Heinemann, Oxford.

Babaei, B. Shokrieh, M.M. Daneshjou, K. (2011). The ballistic resistance of multilayered targets impacted by rigid projectiles, *Mater. Sci. Eng. A, 530* 208–217.

Carlucci, D. E., Jacobson, S. S., (2008). *Ballistics; theory and design of guns and ammunition*, Taylor and Francis Group, New York.

Demir, T. (2008). *Metal ve katmanlı zırh malzemelerinin 7,62 mm lik zırh delici mermiler karşısında balistik başarımlarının incelenmesi*, Master's Thesis, TOBB Ekonomi ve Teknoloji Üniversitesi, Ankara.

Dietenberger, M., Büyük, M. Kan, C.D. (2005). Development of a high strain-rate dependent vehicle model. *LS-Dyna Anwenderforum*, *1*, 1–10.

Hutton, D.V. (2004). *Fundamental of finite element analysis*, Mc Graw Hill, New York.

Iqbal, M.A., Senthil K., Sharma P., Gupta N.K. (2016). An investigation of the constitutive behavior of Armox 500T steel and armor piercing incendiary projectile material. *Int. J. Impact Eng.*, 146–164.

Iqbal, M.A. Chakrabarti, A. Beniwal, S. Gupta, N.K. (2010). 3D numerical simulations of sharp-nosed projectile impact on ductile targets. *Int. J. Impact Eng.*, 185–195.

Kartikeya, Prasad, S. Bhatnagar, N. (2019). Finite element simulation of armor steel used for blast protection. *Procedia Struct. Integrity.*, *14* (2018), 514–520.

Murray, G. White, C. V. Weise, W. (2008). *Introduction to engineering materials*, 2nd ed., CRC Press, New York.

Robinson, H.R. (1967). *Oriental armour*, Walker, New York.

Scazzosi, R. Giglio, M. Manes, A. (2021). Experimental and Numerical Investigation on the Perforation Resistance of Double-Layered Metal Shield under High-Velocity Impact of Armor-Piercing Projectiles, *Materials*, *14*, 626.

Seshu, P. (2009). *Textbook of finite element analysis*, PHI Learning Pvt. Ltd.

Ssab, (2022). *Armox 500T*. [Access available:28.09.2022]: https://www.ssab.com/tr-tr/products/brands/armox/armox-500t.

Ssab, (2022). *Ramor500*. [Access available:28.09.2022]: https://www.ssab.com/en/brands-and-products/armox/product-offer/ramor-500.

Teng, X. Wierzbicki, T. Huang, M. (2008). Ballistic resistance of double-layered armor plates, *Int. J. Impact Eng.*, 870–884.

Uçtu, Ö. Sevim, İ. Karataş, B. Şahin, B. (2017). Determination of optimum mesh size to measure tooth root stress of spur gear using finite element analysis", *Turkish Journal of Engineering (TUJE), 1* (1), 37-43.

Yavaş, M. O. (2009). *Hafif silahlara karşı bireysel savunma amaçlı kompozit malzeme tasarımı ve balistik dayanımı*, Master's Thesis, Selçuk Üniversitesi, Konya.

Yunfei, D. Wei, Z. Yonggang, Y. Lizhong, S. (2014). Experimental investigation on the ballistic performance of double-layered plates subjected to impact by projectile of high strength, *Int. J. Impact Eng.*, 38–49.

Does Hardun Change Colors?: A Preliminary Study on Ventral Color Alterations of Anatolian Harduns

Melodi YENMİŞ[1]
Yusuf BAYRAKCI[2]

Introduction

Reptilian integument is specialized for terrestrial life. It consists of two main layers as epidermis and dermis. Epidermis is a hard cover of the body with its keratinized and cornified structure. Dermis, on the other hand, is thicker than the epidermis and consists of chromatophores and cells that supports epidermis. Chromatophores are the cells that give the skin it's color and they vary according to their structures and pigments they carry (Ligon and McCartney, 2016).
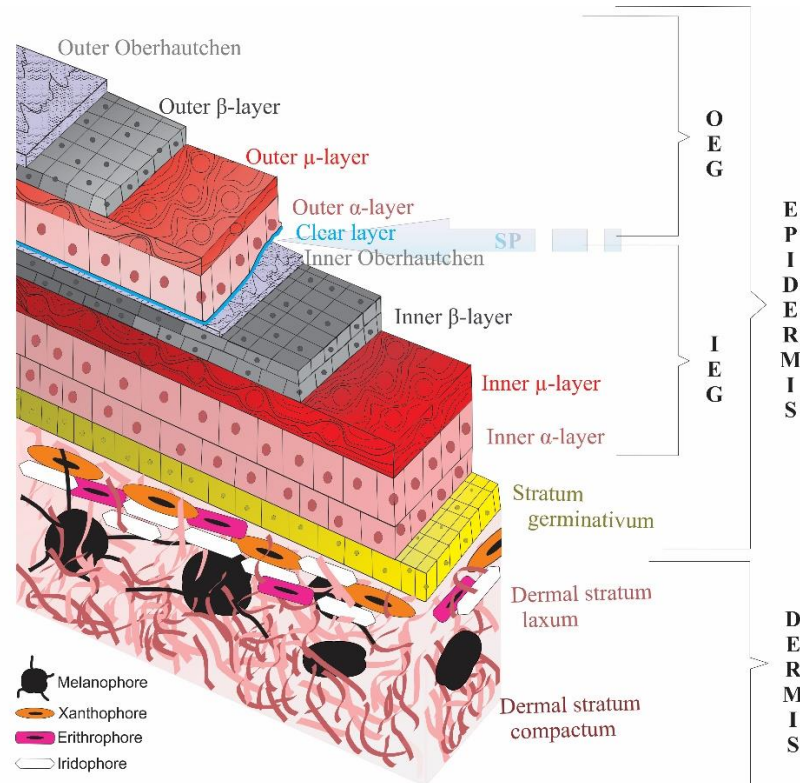

Figure 1 - Illustration of the layers, shedding pane (SP) and the chromatophores of reptile skin. OEG: Outer epidermal generation, IEG: Inner epidermal generation.

[1] Melodi Yenmiş, Dr., Ege University, Science Faculty, Biology Dept., 0000-0003-2627-6008
[2] Yusuf Bayrakcı, Dr., Ege University, Science Faculty, Biology Dept., 0000-0001-5992-0643

There are four types of chromatophores in the dermis (Figure 1). Xanthophores which are the closest ones to epidermis comprise pteridine pigments. They are responsible for yellow-orange colors of the skin. Erythrophores comprise carotenoid pigments which produce red and orange colors. When xanthophores and erythrophores are close and covering each other, they produce various color combinations. Iridophores (guanophores, granulophores) are different from the previous chromatophores in terms of structure and function. They have reflective properties due to the crystal guanine pigments they contain. The density and the deployment of the crystals designate the way of diffraction of light (iridescence). The primer color they produce is blue, due to the reflection of blue wavelengths. Green coloration is produced by the combination of this blue reflection of the iridophores and orange color of the carotenoids (Bagnara et al., 1979; Kuriyama et al., 2006; Schartl et al., 2015; De Mello et al., 2021).

Melanophores lie deeper in the dermis, beneath the former chromatophores. The pigments of melanophores are called melanin and they are responsible for brown and black coloration. Melanophores have dendrites which are facing toward the epidermis, and they can be dispersed or aggregated along with their melanin bearing melanosomes. Aggregation of the dendrites makes the skin area look lighter while dispersion makes it look darker (Ligon and McCartney, 2016) (Figure 2).
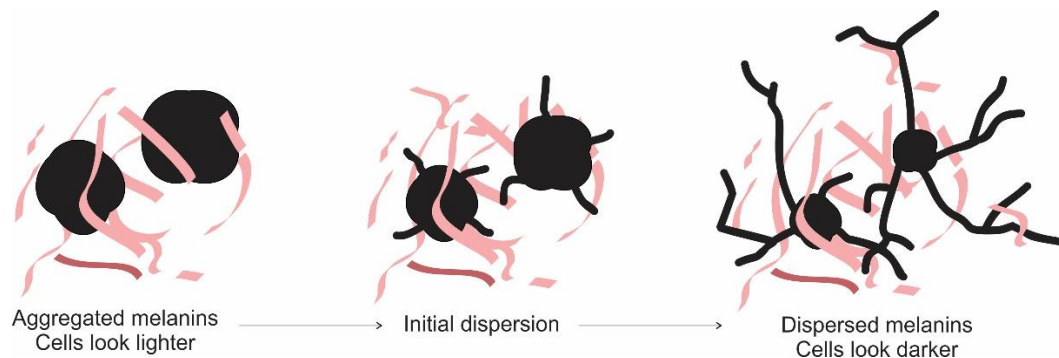

Aggregated melanins
Cells look lighter   Initial dispersion   Dispersed melanins
Cells look darker

Figure 2 - Movement of the melanophores' dendrites showing lighter look with aggregation and darker look with dispersion.

Color changing abilities are vital for many reptiles since it helps to avoid predators and provide disguise for preys as in aposematism, crypsis and mimicry. It is also a signaling instrument among conspecifics as in mating and territorial behaviors. It is more distinct in males since they change into eyeful colors during mating seasons both for attracting females and intimidating other male counterparts. Although rare, females are also observed to change color. For example, some gravid female members of Agamidae and Chamaeleonidae families reflect distinctive colors to avoid disturbance from their conspecifics (Olsson et al., 2013; Assis et al., 2020). Some members of Testudines and crocodiles are also known to have the ability to change color. Snakes are the only extant reptiles which are unable to alter their coloration (Merchant et al., 2018).

Hardun, Starred agama or *Laudakia stellio* is the most abundant Agamid in Turkey. Their total length can be up to 40 cm. The scales in the ventral body region are rectangular. Scales of the dorsal body and the head are carinated (spiny). Tails consisting of two rows of scales arranged in rings. The head is a triangular form expanding towards the body. They are one of the rock agamas of Euroasia and even though some relatively close species were shown to have color changing abilities (Panov and Zykova, 1997), there are very limited information about the color change of the Hardun (Brammah et al., 2010; Baig et al., 2012). Here we show that Anatolian Harduns change their ventral color during morphological observations.

Material and Methods

We have recorded 5 individuals from four different localities (Figure 3). The studies were made with the permission of Ege University Animal Experiments Local Ethics Committee (Permission no: EGE HADYEK 2017-065) and Ministry of Forestry and Water Affairs, General Directorate of Nature Conservation and National Parks (Permission no: 72784983-488.04). All the individuals were immediately released to their habitats after taking photos and videos. The details of the localities and the individuals are given in Table 1.

Figure 3 - Localities of the individuals studied (Made via Google Earth Pro)

The individuals were recorded during ventral color change. Canon EOS 6D (WG) camera, Canon Zoom Lens (24-105 mm) and Canon Macro Lens EF (100 mm) were used for photography and video shooting.

Table 1 - Localities (east to west), GPS data and the individual numbers and sexes studied.

Locality	GPS	Individuals
Hatay	36°28'55.2"N 36°29'20.6"E	1 ♂ ,1 ♀
Konya	37°42'48.5"N 33°34'47.0"E	1 ♂
Manisa	38°29'17.5"N 28°02'25.4"E	1 ♂
İzmir	38°28'34.6"N 27°11'11.4"E	1 ♂

Results

Some males and females were ventrally spotless to begin with. And some were spotted with randomly distributed darker scales (Figure 4). Among the spotted individuals which are the main subject of the present study, it was noted that the spots on the ventral body disappeared in an average of 7 minutes.
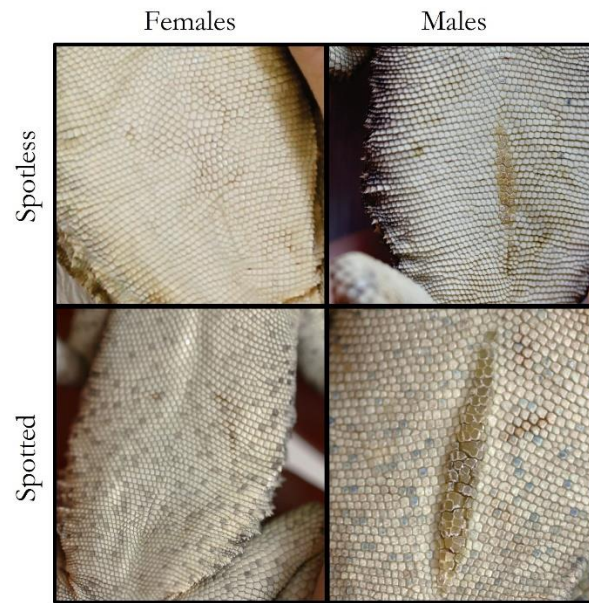
Figure 4 - Examples of male and female individuals that are spotless and spotted at the ventral body.

During the study period, individuals stood in the hands of the researcher. Spotted scales, which appeared randomly scattered among the rectangular ventral scales, gradually changed color during this time, turning into the general ventral color which is milky white or gray (Figure 5). No variations in the process were observed between male and female individuals.
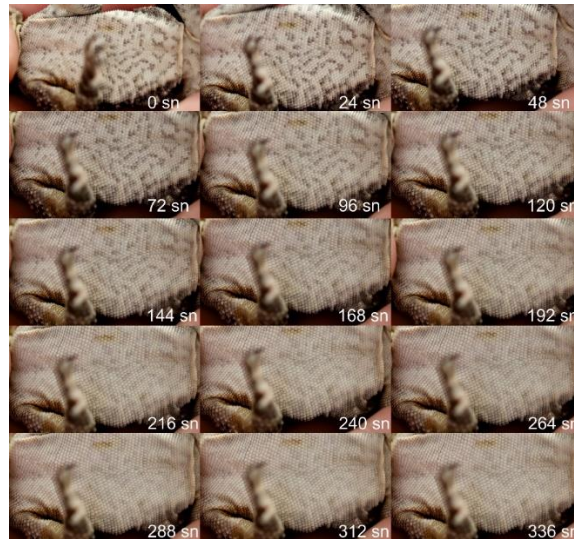

Figure 5 - Frames taken every 24 seconds from the ventral body of a female individual showing the disappearance of the spots in approximately 6 minutes.

Discussion

The ventral body patterning in *L. stellio* is completely spotless with milky white or gray background color in the vast majority of individuals. Only some has spots at the ventral body. The frequency of the spots and the darkness of their colors differ between individuals.

Previous studies have mentioned the color change of the rock agamas of Eurasia. In addition to the signaling context of this change, they said it was a response to changes in physiological state and the air temperature (Panov and Zykova, 1997). However, there are limited information on the color change of *L. stellio*: Brammah et al., (2010) stated that *L. stellio* changes color rapidly depending on the temperature and said that it takes lighter colors in hot and darker colors in cold. Baig et al. (2012) stated that different color variations are seen in one of the subspecies, *L. stellio stellio*, depending on the physiological color change, but further studies are needed. Yet no previous study reported visual proof for this change in *L. stellio* and no such change has been reported for the Anatolian populations.

Here we showed ventral color change in *L. stellio* from Anatolia. In the five ventrally spotted individuals studied, we found that the spots disappeared in an average of 7 minutes. That is, individuals changed the color of the ventral body during the examination period. And in about 7 minutes, the body has taken on a completely spotless, milky white appearance. Since it is a change of brown-black coloration, it can be stated that the melanophores are responsible for these spots and these results indicate that the melanophores beneath these scales aggregate under certain conditions (Ligon and McCartney, 2016).

The contribution of melanophores to physiological color change in reptiles is very important due to their dynamic nature. The dynamism in terms of dispersion/aggregation of melanosomes is controlled by hormones (e.g., α-MSH) and neurotransmitters (e.g., EPI), (Summers and Greenberg, 1994; Ligon and McCartney, 2016). Therefore, further detailed studies are needed to understand the conditions that effect such controllers for a ventral color change in Hardun.

We should state that this study is preliminary and was conducted under noncontrollable field conditions, and no tissue samples were taken from the individuals. Therefore, along with the above-mentioned hormonal studies, live animal experiments under different temperature and light and genetic research (especially for MC1R and Agouti genes that influence adaptive coloration) (Hoekstra, 2006; Hubbard et al., 2010) are needed as well as histological studies to understand the status of melanophores during this change. Having said that, it is important to note this phenomenon, because ventral coloration has been used as a taxonomical character for years for *L. stellio* (e.g., Göçmen et al., 2003; Almog et al., 2005; Ilgaz et al., 2005; Gül and Tosunoğlu, 2011).

Ventral patterning of Hardun should not be considered a permanent morphology and should not be included in intra- or inter-population studies. Further research of this phenomenon will provide new insights into the physiology of color change in Harduns and under what conditions it occurs.

Acknowledgements

Conflict of interest

There are no competing interests to declare.

References

Almog, A., Bonen, H., Herman, K., & Werner, Y. L. (2005). Subspeciation or none? The hardun in the Aegean (Reptilia: Sauria: Agamidae: *Laudakia stellio*). *Journal of Natural History*, *39*(7), 567-586. doi: 10.1080/00222930400001293

Assis, B.A., Jarrett, B.J., Koscky, G., Langkilde, T. and Avery, J.D. (2020). Plastic sexual ornaments: Assessing temperature effects on color metrics in a color-changing reptile. *PloS one*, *15*(5):p.e0233221.

Bagnara, J.T.; Matsumoto, J.; Ferris, W.; Frost, S.K.; Turner, W.A.; Tchen, T.T.; Taylor, J.D. (1979). Common Origin of Pigment Cells. *Science*, *203*, 410–415.

Baig, K.J., Wagner, P., Böhme, W. and Ananjeva, N. B. (2012) A morphologybased taxonomic revision of *Laudakia* Gray, 1845 (Squamata: Agamidae), *Vertebrate Zoology*, *62*(2): 213-260.

Brammah, M., Hoffman, J. I., Amos, W. (2010). Genetic divergence between and within two subspecies of *Laudakia stellio* on islands in the Greek Cyclades. *The Herpetological Journal*, *20*(2), 91-98.

De Mello, P.L.H.; Hime, P.M.; Glor, R.E. (2021). Transcriptomic Analysis of Skin Color in Anole Lizards. *Genome Biology and Evolution*, *13*, doi:10.1093/gbe/evab110

Göcmen, B., Tosunoglu, M., Taskavak, E. (2003). A taxonomic comparison of the Hardun, *Laudakia stellio* (Reptilia, Agamidae), populations of southern Turkey. *Zoology in the Middle East*, *28*, 25-32.

Gül, Ç., Tosunoğlu, M. (2011). External morphological and osteological features of Turkish populations of *Laudakia stellio* (Lınnaeus, 1758). *Herpetozoa*, *24*, 73-88.

Hoekstra, H. E. (2006). Genetics, development and evolution of adaptive pigmentation in vertebrates. *Heredity*, *97*(3), 222–234. https://doi.org/10.1038/sj.hdy.6800861

Hubbard, J. K., Uy, J. A. C., Hauber, M. E., Hoekstra, H. E., Safran, R. J. (2010). Vertebrate pigmentation: From underlying genes to adaptive function. *Trends in Genetics*, *26*(5), 231–239. https://doi.org/10.1016/j.tig.2010.02.002

Ilgaz, Ç., Baran, İ., Avcı, A., Olgun, K., Kumlutaş, Y. (2005). On *Laudakia caucasia* (Eichwald, 1831)(Sauria: Agamidae: *Laudakia*) specimens collected from northeastern Anatolia. Russian Journal of Herpetology, 12(3), 184-187.

Kuriyama, T.; Miyaji, K.; Sugimoto, M.; Hasegawa, M. (2006). Ultrastructure of the Dermal Chromatophores in a Lizard (Scincidae: *Plestiodon latiscutatus*) with Conspicuous Body and Tail Coloration. Zoological Science, 23, 793–799. https://doi.org/10.2108/zsj.23.793

Ligon, R. A., McCartney, K. L. (2016). Biochemical regulation of pigment motility in vertebrate chromatophores: a review of physiological color change mechanisms. *Current Zoology*, *62*(3):237-252. https://doi.org/10.1093/cz/zow051

Merchant, M., Hale, A., Brueggen, J., Harbsmeier, C., Adams, C. (2018). Crocodiles alter skin color in response to environmental color conditions. *Scientific Reports*, *8*(1), 1–10. https://doi.org/10.1038/s41598-018-24579-6

Olsson, M., Stuart-Fox, D., Ballen, C. (2013). Genetics and evolution of colour patterns in reptiles. *Seminars in cell & Developmental Biology*, *24*(7): 529-541. https://doi.org/10.1016/j.semcdb.2013.04.001.

Panov, E.N., Zykova, L.Y. (1997). Differentiation and interrelations of two representatives of *Laudakia stellio* complex (Reptilia: Agamidae) in Israel. *Russian Journal of Herpetology*, *4*(2):102-114.

Schartl, M.; LaRue, L.; Goda, M.; Bosenberg, M.W.; Hashimoto, H.; Kelsh, R. (2015). What is a vertebrate pigment cell? *Pigment Cell Melanoma Research.*, *29*, 8–14. https://doi.org/10.1111/pcmr.12409

Summers, C. H., & Greenberg, N. (1994). Somatic correlates of adrenergic activity during aggression in the lizard *Anolis carolinensis*. *Hormones and Behavior*, *28*(1), 29–40.

Software-Defined Network Application With AI Techniques

Fatih Şahin

1.Introduction

Data centers are getting bigger and bigger with the developing technology. In growing data centers, large volumes of complex and irregular information begin to take place. This information in big data needs to be processed in order to be meaningful and valuable. Big data cannot be processed, managed and stored with traditional methods. In other words, the traditional network management approach is insufficient at this stage. With a better network approach, new methods and a wider bandwidth, this data becomes processable. Software Defined Network (SDN) emerges as a method that meets these needs. SDN provides ease of management, hardware independence, dynamic, flexible and scalable network architecture. Therefore, it offers an effective solution to large and complex network management.

Installing and managing networks requires skilled specialists in configuring multiple network elements. A systems-based approach is needed where communication between network elements (switches, routers, etc.) is complex. This is difficult to achieve with the current programming interfaces in most of today's networking equipment. In order to achieve this, a new network model was needed and the concept of LTA emerged in the meantime (Sezer et al., 2013). The Open Networking Foundation is a non-profit organization dedicated to the development, standardization and commercialization of SDN. The Foundation gives the definition that best explains SDN as follows: SDN is a new network architecture where network control is separated from transmission and can be directly programmed (Xia et al., 2015).

SDN architecture consists of three layers, namely application, control and data layers, and two interfaces between application-control and control-data layers. The control layer is basically where the sending of packets takes place. In the data layer, the traffic flow that occurs during the transmission of packets is regulated.

In traditional network traffic, routers and switches determine the destination of the packet. These, in turn, are located on the same hardware, integrated with each other in the control and data layers. SDN is mainly focused on separating these two layers. In SDN, the control plane is moved to a high-performance server and network management is performed by a central controller software. The data layer ensures that routers and switches are only responsible for stream routing. The control layer is known as the network operating system. In this layer, communication between network applications and data layer takes place. The communication between the control layer and the data layer is provided by the open source network protocol OpenFlow (Niyaz et al., 2015). SDN architecture not only enables the network to be programmed directly, but also creates the necessary infrastructure for network services and applications.

The main purpose of the communication network is to transfer information packets from one point to another. Since transmission occurs to more than one node in the network, this causes a heavy traffic flow. In the meantime, effective and efficient traffic flow can be ensured thanks to the controller using SDN. Thus, a simpler and easier management approach is offered by avoiding the confusion caused by the traffic that causes density and diversity.

In this study, it is aimed to realize the traffic flow in the networks depending on the SDN controller and to optimize the data obtained here by using artificial intelligence optimization techniques. In the light of the obtained data, it is aimed to develop an application on prediction by using artificial neural networks (ANNs). The content of the study continues as follows: General information about the tools and methods used in the 2nd chapter, the application steps of the proposed method in the 3rd chapter, the results obtained from the application in the 4th chapter, and finally the conclusion and discussion about the subject in the 5th chapter.

1.1. Software Defined Networking

Work on advancing computer networks can be divided into three phases in terms of programmability:

• Active networks: (mid 1990s to early 2000s) leads to the addition of programmable functions in the network. Where switching devices can perform operations to process packets.

• Control and data plane separation (2001 to 2007) leading to new capabilities such as predicting or controlling routing behavior.

• OpenFlow API (2007 to 2010) which is the first common southbound interface to handle L2-L4 network flows between control and data plane. However, to handle L5-L7 flows to give the ability to support Network Virtualization Function (NVF), OpenFlow protocol needs to be extended. Each flow chart consists of (i) header fields, (ii) counters, and (iii) movements. If there is no packet match, a PACKET-IN message is sent to the controller over a secure channel, which is encrypted using Transport Layer Security (TLS) to notify the controller about this packet, as shown in Figure 1.

The first OpenFlow version, OF 1.0, was released in March 2008 with support for a single flow table. Later versions of OpenFlow, such as OF 1.1, support more advanced features such as various flow tables, which involve using the "goto" command as a pointer to another flow table. OF 1.2 includes IPv6, which is extensible mapping using the TLV structure, giving switches the ability to communicate with multiple controllers simultaneously. Added OF 1.3m tables for QoS support. Later OF 1.4 TLV structures were used more to support optical ports on switches and were optimized to save time spent communicating between switch and controller if the flow table was full.
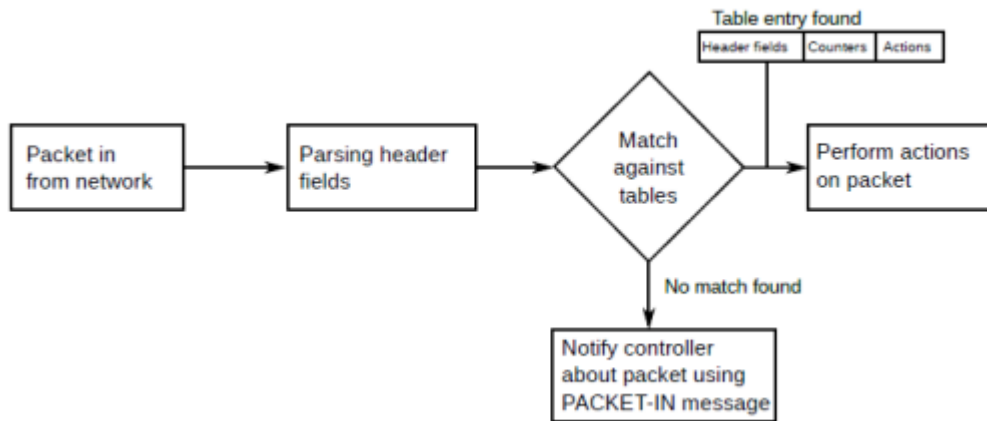
Figure 1. Open vSwitch basic packet routing

Decomposition of the network system provides the ability to manage it through a high level of abstraction. SDN, the latest paradigm of programmable networks, facilitates network operations such as routing or adding rules to routing devices with a single central controller. This means that the routing units will implement the decisions made by this controller. A comparison between the SDN architecture shown in Figure 2 and the traditional network architecture . The main abstraction concepts defined by SDN are: 1. Routing, 2. Distribution, and 3. Specification. The routing abstraction allows any routing action to be performed by the controller while hiding low-level processing with switching devices. Distribution abstraction involves replacing the traditional distributed control plane with a logically centralized plane. Routing abstraction hides low-level use with switching devices during which any forwarding action is performed by the controller. Specification abstraction allows developers to write network applications by defining desired flow actions and configurations without dealing with low-level or physical configurations.

The logically centralized control plane shown in Figure 2 provides a global view of the network, which opens the door for more optimized control of the guiding elements. It can be achieved with a single or distributed controller(s). In addition, FlowVisor, a proxy controller, provides a logical localization for network virtualization purposes. A brief comparison of the controller platforms shown in Table 1.

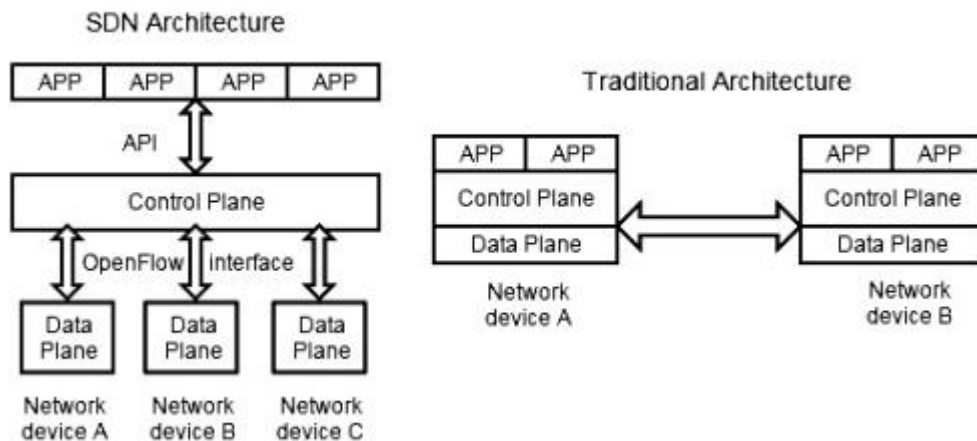Common SDN simulators and emulators such as Mininet, NS-3 and Estinet are described and compared in Table 2

Figure 2. Comparison of traditional network architecture with SDN.

Table 1. A comparison of controller platforms

Controller	Language	Created by	OpenFlow version
NOX[17]	Python, C++	Nicira	1.0, 1.3
POX[18]	Python (2.7)	Nicira	1.0
Beacon[19]	Java	Stanford university	1.0.1
Maestro[20]	Java	Rice university	1.0
Floodlight[21]	Java	Big Switch Networks	1.0
Floodlight-plus[22]	Java	Big Switch Networks	1.3
Ryu[23]	Python	NTT Labs	1.0 to 1.4
(ODL)OpenDaylight[24]	Java	Linux Foundation	1.0, 1.3

Table 2. Comparison of SDN simulators and emulators

Simulator/ emulator	Open source	Language	Platform	OpenFlow version
Mininet (Emulator)	Yes	Python	BSD open source	OF 1.3 of the reference user switch and NOX from CPqD and Ericsson
NS-3 (Simulator)	Yes	C++, Python	GNU GPLv2	Pre OF 1.0 and version of OF-SID that support MPLS
EstiNet (emulator/ simulator)	No	–	–	OF 1.3 and 1.0

The ability of SDN to program the routing plane by the SDN controller can reduce the cost required to add custom networking devices such as firewalls, load balancers, and Intrusion Detection Systems (IDS). Also, the SDN approach provides more dynamic and less expensive solutions for technologies used in WANs such as path computing technology, extending these solutions as an SDN application allows network operators to program the Path Computing Element (PCE) directly. As a result, the controller is a virtual machine manager in different environments, for example a private cloud.

1.2. Artificial Intelligence on SDN

Recently, soft computing and artificial intelligence methods have started to play an important role in most modern systems such as intelligent transportation. This gives us a chance to improve the performance of existing computer networks. Integration between the concept of abstraction in the SDN paradigm and AI techniques can lead to more adaptive behavior of network elements. It will also introduce new mechanisms to deal with both traditional networking issues and new SDN related issues. This section will discuss recent efforts in this regard.

1.2.1.Load Balance and Flow Routing

The load balance function is a requirement to minimize latency and maximize throughput in computer networks that support multiple routing approaches. Load balancing is also considered a defense technique against some network attacks such as DDoS attack. In the SDN approach, abstraction provides a significant advantage for the global view and discovery of the topology of the network. In Back Propagation Neural Network (BPNN), which is used to provide real-time dynamic load balance and delay, it is reduced by 19.3% compared to DLB and static Round Robin methods. The input vector for the neural network contains the following path information: 1. Bandwidth utilization rate 2. Packet loss rate 3. Transmission delay and 4. Transmission hops. The authors also proposed a BPNN-based approach for load balancing in data centers. BPNN is implemented internally within Open vSwitch, which reduces the time it takes to send the routing decision from the controller to Open vSwitch. The input vector consists of: 1. Available bandwidth and 2. Packet loss. And from that, it proposes a genetic algorithm in SDN-based client-server architecture. The fitness function defined by formula (1):

$$\text{Min} \quad \sqrt{\frac{\left(\sum_{j=1}^{k} X[j]^2\right) - \left(\frac{\sum_{j=1}^{K} X[j]}{K}\right)^2}{K}} \Bigg/ \frac{\sum_{j=1}^{k} X[j]}{K} \tag{1}$$

K stands for servers and each has X workload sets. Performance comparison was made with random and cyclic trial methods and showed better performance. In addition, a genetic algorithm for SDN-based voice stream routing optimization over IP network is introduced. Network defined as a connected graph. The problem is to show that the graph satisfies the demand with the bandwidth and latency requirements of the source and destination. The fitness function given by the formula shown in equation (2).

$$\text{Max} \frac{\sum \textbf{embedded demands}}{\sum \textbf{demands}} \tag{2}$$

Due to time consumption issues, the authors did not apply the crossover operation. Population size and non-allocation probability were the most important parameters for the algorithm. Also, since the genetic algorithm was implemented in python, the time efficiency was 10 times less than the mixed integer linear programming algorithm implemented in C++. The advantage of using the genetic algorithm approach is to obtain a partial solution of the problem during the solution phase, while this is not possible in a linear program; this partial solution helps to evaluate other algorithms. In another context, an Ant Colony Optimization (ACO) approach for QoE-sensitive flow routing. ACO is a swarm intelligence method that uses metaheuristic optimization. Quality of Experience (QoE) in computer networks specifies requirements for customers to measure the value of the service provided from the customer's perspective. In SDN applications, it passes user session parameters to the controller, which runs the ACO algorithm on a weighted graph; where the weights between the peaks are the latency and loss rate for each network device. The fitness function depends on the type of stream and the estimated value of the corresponding QoE model (ie: audio, video or data). ACO achieved a 24.1% increase for the maximum QoE achieved with the shortest path routing approach.

1.2.2.Network security

The SDN approach introduces a number of new security issues and seems to be one of the biggest problems with SDNs. Possible threats include targeting the controller by programming vulnerabilities in the secure channel, error configurations, and DDo attacks, as shown in Figure 3. In addition, SDN has advantages over traditional networks in terms of security as shown in Table 3. Artificial intelligence and data mining techniques, which were previously used in conventional network architectures to solve routing problems and optimize the performance of packet filters, are playing an important role in SDN-based networks after adding programming ability as authors to a proposed information security management. It is a system based on the combination of fuzzy inference system and both TRW-CB and Rate Limiting algorithms in SDN environment.
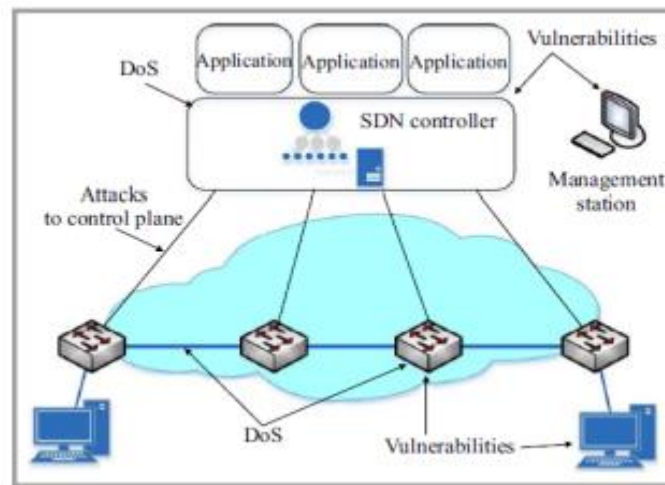

Figure 3. Potential attack vector in SDN.

Table 3. SDN security benefits.

SDN Characteristic	Security Use
Global Network View	– Network-Wide Intrusion Detection – Detection of Switch's Malicious Behavior. – Network Forensics.
Self-Healing Mechanisms	– Reactive Packet Dropping. – Reactive Packet Redirection.
Increased Control Capabilities	– Access Control.

TRW-CB algorithm that detects SYN Flooding caused by a host based on the idea that a benign host will achieve a higher probability of successful connection than a malicious host. The degree of attack obtained as input and output for the fuzzy logic module obtained by the specified algorithms. The decision making system is implemented as SDN controller application with short-term learning module as shown in Figure 4. The proposed system showed better results compared to a non-fuzzy logic approach.

It is a BPNN-based collaborative intrusion prevention system, taking advantage of the global view in the SDN paradigm. Each Open vSwitch is responsible for collecting data to perform input for several ANNs. The system is offline trained by MATLAB. Open vSwitches need to

communicate with each other as it is a collaborative system. Unfortunately in the SDN paradigm Open vSwitchs cannot talk to each other. Therefore, a neural routing table has been implemented in each Open Vswitch and the controller can assist in the creation of these tables. Figure 5 shows the pattern of a neural message, and the experimental results show that as the network grows, the detection rate of DDoS attack increases and the false positive rate decreases.

Whereas, Self-Organizing Maps (SOM) approach has been proposed to detect DDOS attack. SOM is a kind of artificial neural networks based on unsupervised learning. SOM can be used as a classification mechanism when processing with unlabeled input vector. The training in SOM is based on a set of features required from streaming inputs of Open vSwitches. The detection cycle consists of three phases: 1. Stream collection, which requests stream inputs from all Open vSwitches. 2. It is feature extraction that takes the output of the stream collection module and extracts the most important features that constitute a possible DDoS attack. These features include: Average of Packets per Stream (APf), Average Bytes per Stream (ABf), Average Time per Stream (ADf), Even Percentage Streams (PPf), Odd Streams Growth (GSf), and Differential Ports Growth (GDP), and (iii) the SOM classification used as the classification method. These stages are implemented as application level modules in the SDN controller. Compared to different methods run on the well-known KDD-99 dataset, the proposed approach showed a lower overhead.

1.2.3.Smart Network Applications

Integration between SDN and AI space opens the door to building smarter network applications. As the authors suggest, it is a reinforcement learning approach for adaptive video streaming in the SDN paradigm. The controller represents a periodic decision maker that determines when to choose a new path and when the server should change the quality of the video. The decision Markov process used to model decision-making actions. It is a Q-learning technique used in case of unknown rewards for moving between the current and next state. The percentage of packet losses and the number of quality changes represent the most important parameters for defining the reward. The Q values are updated by the function shown in Equation (3) and stored in the Q-table, where γ and η represent the discount factor and the learning factor, respectively.

$$\hat{Q}(s_t, a_t) = \hat{Q}(s_t, a_t) + \eta(r_{t+1} + \gamma$$

$$\max_{a_{t+1}} \hat{Q}(s_{t+1}, a_{t+1}) - Q(s_t, a_t)) \quad (3)$$

And the softmax function shown in Equation (4) represents the probability of choosing an action at state t at time s.

$$P(a|s) = \frac{\exp\left[\frac{Q(s,a)}{T}\right]}{\sum_{b \in A} \exp\left[\frac{Q(s,b)}{T}\right]} \quad (4)$$

Here T represents a random motion currently used in the simulated annealing method to escape the local optimum problem. The controller can modify the existing path and/or adaptively remove/add selected layers based on available bandwidth to increase the QoE of the video

streaming service. The aforementioned approach showed a reduction in frame loss rate of 89% and 70%, respectively, compared to the shortest path forwarding and greedy-based approaches.

2.General Information

In the subheadings of this section, basic explanations about the concept of the controller from which the data required for the application part is obtained and its functioning in the network environment, the preferred ANN method for using the collected network data, the Tabu Search Algorithm and the Annealing Simulation Algorithm, which are among the artificial intelligence optimization techniques used to determine the regions where the flow is the most intense on the network, are given respectively.

In SDN architecture, control and management operations are performed by a central controller. This controller has full control of the network topology and address information. When a switch sends a packet send request to the controller for a packet that is not in the flow table, the controller receives those requests. The controller then takes actions and listens for traffic and defines packet forwarding routes on demand. OpenFlow controllers are programmed by network operators with a control interface. MILLER and YILTAŞ KAPLAN 10.21923/jesd.676110 1001 As shown in Figure 1, large networks are being built to include more SDN controllers, that is, SDN application layers. This application layer is responsible for network virtualization, traffic engineering, routing, monitoring and quality of service services.

Communication between the application layer and the SDN controllers is handled by a set of application programming interfaces (APIs) called the Northern Interface. Similarly, the interface between the SDN controller and OpenFlow network devices is called the Southern Interface (Kutay and Ercan, 2016). SDN architecture provides ease of transmission, control and management over complex networks. In addition, thanks to the interactions between the network layers, it has an important place in today's technology as a powerful control platform in terms of traffic flow.
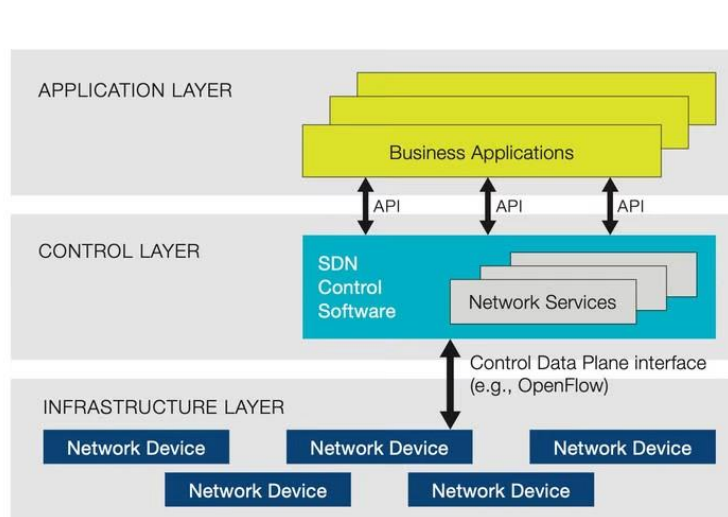
The application, control, and infrastructure layers are kept separate in SDN and communicate through APIs. Source: Open Networking Foundation

2.1.Artificial Neural Networks (Artificial Neural Networks)

Artificial intelligence is divided into various sub-titles according to the solutions it brings to different types of problems. The most common types of artificial intelligence are knowledge-based expert systems, fuzzy logic approach and ANNs. The preferred method used in this study is ANNs.

When the neurological structure of the human brain was examined, it was understood that it had a completely different working mechanism than digital computers, and the concept of ANN emerged. The information processing system of the human brain is quite complex. The nerve cell in the brain, called a neuron, performs certain calculations even faster than the computer, which is considered the fastest by humans today. A neural network is a massively parallel distributed processor composed of simple processing units, which has a natural disposition that experiential information is made available for storage and use (Haykin, 2009). ANNs, on the other hand, are systems where artificial neurons come together in the same way as neurons in the human brain, collect information about the problem and solve the problem. In short, ANN is a network system structure formed by connecting artificial neurons using different geometrical paths (Staub et al., 2015). ANN is similar to the human brain in two fundamental ways. The first is the acquisition of knowledge by the network through a learning process from the environment. The second is the use of internal neuron connection strengths, also known as synaptic weights, to store acquired information. While the ANN structure allows learning nonlinear relationships, it also adapts to changing environments. Among the most preferred features of ANNs is the ability to handle missing parameter values. Thanks to this feature, an ANN based on a limited number of training sets can be a good classifier (Mourrain et al., 2006). ANNs have the ability to make decisions using what they have learned when faced with a problem. In ANNs, information is acquired by the network and this information is stored using the connections between neurons. In ANNs, the network can be defined as a processor that stores information and makes this information functional (Taşhan, 2017).

In a study designed with the help of ANNs related to a different problem area, there is a general representation of the ANN example as input layer, hidden layer and output layer (Abu Salam and Keskin, 2018). It is also emphasized here that there are different ANN models such as back propagation.

2.2.Artificial Intelligence Optimization Techniques

Effective results are obtained by using artificial intelligence optimization techniques, also known as meta-heuristics, for the solution of optimization problems. A heuristic algorithm tries to find a particular example of a solution that maximizes profit by recursively calling a heuristic function. The example solution that maximizes profit will be the optimal solution for the optimization problem. Heuristic techniques are methods that perform different solution modifications to reach a solution that is either superior or superior (Oommen & Rueda, 2005). Artificial intelligence optimization techniques are a promising technique for solving optimization problems. Because it can imitate the operations of the brain and use parallel processing to save computation time (Shih et al., 2004). These techniques, which consist of computer algorithms, aim to find the one that will give the best result from the various moves available to reach the best solution. Since many of the problems do not have a final solution and the time required to solve these problems is very large, the researchers tried to find the fastest algorithm that gives a result close to the final solution. As a result, artificial intelligence optimization techniques have emerged. These techniques are also important because they create an upper or lower limit for exact solution methods. They also aim to find the best possible solution, although they do not reach a definitive solution.

2.2.1. Taboo Search Algorithm

Tabu search algorithm, which was put forward by Fred Glover in 1986, was created to overcome the shortcomings of local search methods. Some complex problems could not be best solved by local search methods. Taboo search aims to bring the most effective heuristic solution to this type of problem. Tabu search is an intelligent search procedure that starts from an initial possible point and tries to reach an optimal solution by constructing a finite sequence. Neighboring subsets of the initially selected possible solution point are created and the next point is determined as the best solution. Tabu movements are listed under the name of the tabu list in order to prevent a return to some previous points, as tabu search allows ascending movements. Due to the exit movement, the procedure avoids traps in the local optimum (Kovačević-Vujčić et al., 1999). To summarize briefly, the working principle of tabu search is to continue tracking through local search by allowing this non-optimal solution when the local optimum is encountered (Gendreau and Potvin, 2010). The tabu search algorithm uses some restrictions when searching. For this reason, the algorithm is called "taboo", that is, "forbidden search". Constraints are created by making use of memory structures (Aladağ, 2009). Thanks to these constraints, normally acceptable difficult situations are bypassed and the best result is achieved. An adaptive memory and sensitive research are required for problem solving in taboo search to qualify as intelligent. Tabu search algorithm, which gains the ability to produce problem-specific solutions with these features, is accepted as a meta-heuristic search algorithm (Michalska et al., 2016).

2.2.2. Simulated Annealing Algorithm

The annealing simulation algorithm, which is a probability-based heuristic algorithm, was created by Kirkpatrick, Gelatt, and Vecchi. The annealing simulation algorithm is a technique created to find a good solution of the optimization problem by using a random variation around the existing solution (Zhao et al., 2013). This algorithm, which is based on the physical annealing process of solid objects, is used in solving complex optimization problems. After heating the solid body to its melting point, the process of gradually cooling the body until it crystallizes is called annealing. The energy of the system decreases to the minimum level while the atoms of the objects with high energy levels at high temperatures pass into a regular crystal. The temperature is also reduced to reduce the energy of the system. If this cooling process is acted too quickly, the crystallized structure of the object will deteriorate and an irregularity will occur in the structure of the object (Kalınlı, 2003).

The annealing simulation algorithm, which is designed to find the largest or smallest values of the function in multivariate functions, finds the best solution in the shortest time. For this reason, it is preferred in the optimization of problems that cannot be expressed with a mathematical model. In the annealing simulation algorithm, the objective function value tends to decrease (Çakır, 2006). However, in some cases, this function can be accepted at high values in order not to be stuck with the local minimum. In this way, a better global solution can be sought without being stuck with the local minimum (Kılıçaslan, 2019).

3. Application of the Proposed Method

Within the scope of this study, Floodlight VM, Eclipse, MATLAB and nntool tools were used while developing an application for monitoring the flow traffic depending on the SDN controller. Floodlight, which has become widespread worldwide as a constantly developing project among SDN controller software, is open source and an application that supports the Java programming language (Floodlight, 2020). On the official website of the Floodlight project, all necessary steps and installations for software developers are presented in detail. Eclipse

environment, which is open source code and especially Java-based software is designed, is used for the program stages of the proposed method. Eclipse comes integrated with the Floodlight VM during installation. In fact, there are Floodlight v1.0, Eclipse, Mininet v2.2.0, Open vSwitch v3.2.1, Wireshark w/openflow software in the Floodlight VM installed during this study. The topologies created in the application are created with the Python programming language on Mininet. Another alternative example that can be preferred as a Java platform for mutual transactions with Floodlight is IntelliJ IDEA. Instead of all these application environments, different tools can be used for different controller software. For example, the POX controller is designed with the Python programming language (Author, 2013). Likewise, the Ryu controller requires basic knowledge of Python. After deciding on the most suitable controller and programming environments in the proposed study, MATLAB and nntool, which are more efficient and easier to use, were preferred for operations based on artificial intelligence techniques.

The data required to spy on the traffic in the application are the key, port number, the amount of packets received and transmitted, bandwidth, drops, collisions and the time in seconds (sec) that they occur. This data is accessed through the Floodlight project in the Floodlight VM. In order to increase the accuracy, statistical data were obtained over various topologies. For this, five different topologies consisting of different numbers of switches and machines (hosts) were created in the Mininet environment. Five different data sets were obtained by running each of the created topologies for 27 seconds. By selecting the duration of 27 seconds, thousands of rows of data were obtained, which was considered sufficient during the processing of the data. Since it was observed that an excessive increase in the amount of data occurred with increasing the time, and this would pose a problem during the processing of the data, the 27-second period was preferred. Key, port, received and transmitted packet amount and time columns of the data transferred on matrix structures in MATLAB were selected and other columns were ignored. A separate point to be noted here is that data transmission in LTAs is in the form of flows. Since a stream has many packet contents, conceptual confusion may arise in studies related to classical network structures. Therefore, within the scope of this study, the term "packet amount", which is the concept in classical computer networks, has been preferred to express the amount of data obtained through Floodlight. Thus, the main focus is on the obtained data sets and the application processes on them. The factors that will make the difference for the application part of the study are the algorithms used and the approach in the analysis of the results.

The application part of the study is based on artificial intelligence. The aim here is to try to estimate how many packets are received and forwarded from a given switch and port at a given moment. This estimation part was carried out with ANN, which is one of the artificial intelligence methods. With nntool, which is a MATLAB tool, data is processed on ANN. With the help of MATLAB matrix operations, 80% of the data sets are reserved for training and 20% for testing. The key, port and time columns of the data sets are set as input data, and the received packet and transmitted packet columns are set as output data. Networks were created by selecting the necessary parts on nntool. The first created network is a network with three inputs and two outputs. However, since the prediction success is low, the networks are designed to be three-input and one-output. Thus, separate networks were created for each topology according to received packets and transmitted packets. A two-layer ANN with ten neurons was sufficient because there were no very complex data sets. The accuracy of the predictions of the ANNs created for five different topologies at certain moments was compared. Accuracies were calculated using MAPE (Mean Absolute Percentage Error) and R2 (R-squared) functions.

The last part of the application consists of optimization. The problem to be optimized, that is, the value desired to be obtained as the optimum result, is which route in the topology has the highest density. For this purpose, optimization was carried out with four different methods and

their results were compared. The first of these is the traditional search method linear search, the second tabu search, the third modified tabu search, and the fourth is a mixture of annealing simulation and tabu search algorithms (hereinafter, it will be called the mixing algorithm). The last two methods are the methods revealed for the first time within the framework of this study. As a result of these four different optimization methods, the route with the highest packet traffic was determined. The important criteria for the choice of the algorithms used at this stage are that they can be functionally adapted to the network problem, that is, they can compare the density in the regions on the network with each other and be fast. The process created by the optimization step in this study is to prioritize the shortest time to go to the correct solution of the problem. For this purpose, it was tried to find the most suitable methods. In a previous different network study (Yıltaş, 2007), genetic algorithm, which is among the evolutionary algorithms, was used. Genetic algorithm is a particularly suitable method for routing, assignment or placement based optimization problems, and there are other examples in the literature such as the solutions of Ünsal and Yiğit (2018) and Yiğit and Aydemir (2018). However, the steps such as generation, crossover, mutation in the genetic algorithm are incompatible with the determination of dense network regions in a short time, which is the main purpose of this study. By considering the tabu search and annealing simulation algorithms, which are seen to be able to perform appropriate and fast operations through the programs created in this study, two additional models (modified tabu algorithm and mixing algorithm) are proposed, and it is planned to compare them with the linear search algorithm. The modified tabu search algorithm was obtained by subtracting the tabu list from the tabu search algorithm. When the tabu search algorithm is examined, it is observed that the tabu list is unnecessary for this problem and slows down the optimization. An increase in performance was observed when the list was removed from the algorithm. From here, it has been observed that although artificial intelligence optimization techniques are convenient, they are not always successful because they are problem-specific. In another problem, for example the traveling salesman problem, this algorithm, which is very convenient, causes poor performance in the current study problem.

The first part of the mixing algorithm, which is the last method, comes from the tabu search algorithm. Instead of the randomly chosen initial solution in the annealing simulation algorithm, the case of assigning the first value in the tabu search algorithm as the initial solution is preferred. Taboo search is not included in the following sections. In the remaining part, neighboring solutions were created and the change in the objective function, that is, in the total packet value, was observed. In addition, a change has been made in this section. Normally, if there is a decrease in the objective function, while the solution is the current solution, the opposite is taken into account in this algorithm. In other words, if there is an increase in the objective function, the solution becomes the current solution. Because the basis of the problem is the region densities in the network, that is, the excess of the packet flow is observed.

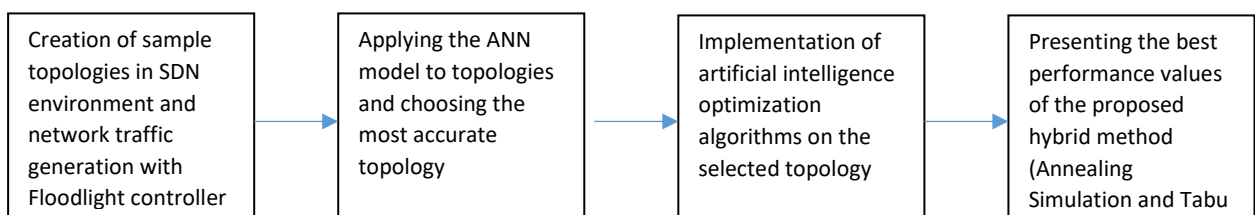The connection of the processing elements in the application part with each other is briefly seen in Figure 2.

| Creation of sample topologies in SDN environment and network traffic generation with Floodlight controller | → | Applying the ANN model to topologies and choosing the most accurate topology | → | Implementation of artificial intelligence optimization algorithms on the selected topology | → | Presenting the best performance values of the proposed hybrid method (Annealing Simulation and Tabu |

Figure 2: Application Operations

References

Abu Salam, Z. K. A., Keskin, M. E., 2018. Level Estimation of Dibis Dam with Artificial Neural Networks. Journal of Engineering Sciences and Design, 6(4), 564-569.

Aladag, C. H., 2009. Tabu Search Algorithm for Architecture Selection of Artificial Neural Networks. Doctoral Thesis. Hacettepe University, Institute of Science and Technology, Department of Statistics, Ankara, Turkey.

Çakır, B., 2006. Annealing Simulation Algorithm for Assembly Line Balancing with Stochastic Process Time. Master Thesis, Industrial Engineering, Gazi University, Institute of Science, Ankara.

Değirmenci, Ş., 2018. Packet Surveillance Application and Optimization Connected to Software Defined Network Controller. Master Thesis. Istanbul University, Institute of Science and Technology, Department of Computer Engineering, Istanbul, Turkey

Floodlight. Project Floodlight-Floodlight Controller-Installation Guide, [Online]. Available: https://floodlight.atlassian.net/wiki/spaces/floodlightcontroller/pages/1343544/Installation+G uide#InstallationGuideLinux.

Gendreau, M., Potvin, J.-Y., 2010. Handbook of Metaheuristics, 2nd ed. Springer Science+Business Media.

Haykin, S., 2009. Neural Networks and Learning Machines, Third ed. New Jersey, USA: Pearson Education, Inc., [Online]. Available: http://dai.fmph.uniba.sk/courses/NN/haykin.neural-networks.3ed.2009.pdf

Kalınlı, A., 2003. Training of Elman Network Using Simulated Annealing Algorithm. Erciyes University Journal of Science Institute, 19(1), 28-37.

Kılıçaslan, K. Heat Treatment Algorithm (Simulated Annealing), [Online]. Available: Ders.kilicaslan.nom.tr/doc/19/52/Isıl%20Operation%20Algorithm.docx

Kovačević-Vujčić, V. V., Čangalović, M. M., Ašić, M. D., Ivanović, L., Dražić, M., 1999. Taboo Search Methodology in Global Optimization. Computers & Mathematics with Applications, 37, 125-133

Kutay, M., Ercan, T., 2016. An Overview of Software Defined Campus Networks. Selcuk University Journal of Engineering, Science and Technology, 4(2), 155-164.

Michalska, M., Zufferey, N., Mattevelli, M., 2016. Taboo Search For Partitioning Dynamic Dataflow Programs. The International Conference on Computational Science, Procedia Computer Science, 80, 1577-1588.

Mourrain, B., Pavlidis, N. G., Tasoulis, D. K., Vrahatis, M. N., 2006. Determining the Number of Real Roots of Polynomials Through Neural Networks. Computers & Mathematics with Applications, 51(3-4), 527-536.

Niyaz, Q., Sun, W., Alam, M., 2015. Impact on SDN Powered Network Services Under Adversarial Attacks. The 2015 International Conference on Soft Computing and Software Engineering (SCSE 2015), Procedia Computer Science, 62, 228 – 235.

Oommen, B. J., Rueda, L. G., 2005. A Formal Analysis of Why Heuristic Functions Work. Artificial Intelligence, 164, 1-22.

Sezer, S., Scott-Hayward, S., Chouhan, P. K., Fraser, B., Lake, D., Finnegan, J., Viljoen, N., Miller, M., Rao, N., 2013. Are We Ready for SDN? Implementation Challenges for Software-Defined Networks. IEEE Communications Magazine, 51(7), 36-43.

Shih, H. S., Wen, U. P., Lee, E. S., Lan, K. M., Hsiao, H. C., 2004. A Neural Network Approach to Multiobjective and Multilevel Programming Problems. Computers & Mathematics with Applications, 48, 95-108.

Staub, S., Karaman, E., Kaya, S., Karapınar, H., Güven, E., 2015. Artificial Neural Network and Agility. World Conference on Technology, Innovation and Entrepreneurship, Procedia - Social and Behavioral Sciences, 195, 1477 – 1485.

Taşhan, B., 2017. Road Lane Detection System With Convolutional Neural Network. Master's Thesis. Bahçeşehir University, Graduate School of Natural and Applied Sciences, Computer Engineering, İstanbul, Turkey.

Ünsal, Ö., Yiğit, T., 2018. Optimization of School Bus Routing Problem by Using a Method with Artificial Intelligence and Clustering Techniques, Journal of Engineering Sciences and Design, 6(1), 7-20.

Xia, W., Wen, Y., Foh, C. H., Niyato, D., Xie, H., 2015. A Survey on Software-Defined Networking. IEEE Communication Surveys & Tutorials, 17(1), 27-51.

Author, S., 2013. Using OpenFlow Protocol and Pox Controller in Network Switches. Master Thesis. University of Trakya. Graduate School of Natural and Applied Sciences, Department of Computer Engineering, Edirne, Turkey.

Yıltaş, D., 2007. Design of a New Routing Algorithm in Low-Orbit Satellite Systems. Doctoral Thesis. Istanbul University. Graduate School of Natural and Applied Sciences, Department of Computer Engineering, Istanbul, Turkey.

Yiğit, T., Aydemir, M., 2018. Container Loading Problem Optimization By Using Genetic Algorithm Without Rotating The Package, Journal of Engineering Sciences and Design, 6(1), 21-28.

Zhao, X., Lin, W., Yu, C., Chen, J., Wang, S., 2013. A New Hybrid Differential Evolution with Simulated Annealing and Self-Adaptive Immune Operation.

Open Networking Foundation. Software-defined networking: The new norm for networks. Available from: https:// www.opennetworking.org/images/stories/downloads/sdnresources/white-papers/wp-sdn-newnorm.pdf

Astuto BN, Mendonca M, Nguyen XN, Obraczka K, Turletti T. A survey of software-defined networking: past, present, and future of programmable networks. IEEE Communications Surveys and Tutorials. 2014; 16(3):1617–34

Bakshi K. Considerations for Software Defined Networking (SDN): Approaches and use cases. IEEE Aerospace Conference, Big Sky; MT. 2013 Mar. p. 1–9.

Shinde MB, Tamhankar SG. Review: software defined networking and OpenFlow. International Journal of Scientific Research in Network Security and Communication. 2013Jun; 1(2):18–20.

Feamster N, Zegura E, Rexford J. The road to SDN: An intellectual history of programmable networks. ACM SIGCOMM Computer Communication Review archive. 2014; 44(2):87–98.

Kreutz D, Ramos FMV, Verissimo P, Rothenberg CE, Azodolmolky S, Uhlig S. Software-defined networking: A comprehensive survey. Proceedings of the IEEE. 2015; 103(1):14–76.

Basta A, Kellerer W, Hoffmann M, Hoffmann K, Schmidt E-D. A virtual SDN-enabled LTE EPC architecture: A case study for S-/P-gateways functions. Future Networks and Services (SDN4FNS); Trento. 2013 Nov. p. 1–7.

Jammal M, Singh T, Shami A, Asal R, Li Y. Software defined networking: State of the art and research challenges. Computer Networks. 2014; 72:74–98.

Rowshanrad S, Namvarasl S, Abdi V, Hajizadeh M, Keshtgary M. A survey on SDN, the future of networking. Journal of Advanced Computer Science and Technology. 2014; 3(2): 232–48.

Braun W, Menth M. Software-defined networking using OpenFlow: Protocols, applications and architectural design choices. Future Internet. 2014; 6(2):302–36.

OpenFlow Switch Specification Version 1.0.0. Available from: https://www.opennetworking.org/images/stories/ downloads/sdn-resources/onf-specifications/openflow/ openflow-spec-v1.0.0.pdf

OpenFlow Switch Specification Version 1.1.0. Available from: http://archive.openflow.org/documents/openflowspec-v1.1.0.pdf

OpenFlow Switch Specification Version 1.2.0. Available from: https://www.opennetworking.org/images/stories/ downloads/sdn-resources/onf-specifications/openflow/ openflow-spec-v1.2.pdf

OpenFlow Switch Specification Version 1.3.0. Available from: https://www.opennetworking.org/images/stories/ downloads/sdn-resources/onf-specifications/openflow/ openflow-spec-v1.3.0.pdf

OpenFlow Switch Specification Version 1.4.0. Available from: https://www.opennetworking.org/images/stories/ downloads/sdn-resources/onf-specifications/openflow/ openflow-spec-v1.4.0.pdf

FlowVisor. Available from: https://github.com/OPENNET WORKINGLAB/flowvisor/wiki

NOX. Available from: http://archive.openflow.org/ downloads/Workshop2009/OpenFlowWorkshopMartinCasado.pdf

POX. Available from: https://en.wikipedia.org/wiki/Pox

Beacon. Available from: https://openflow.stanford.edu/display/Beacon/Home

Ng TSE, Cai Z, Cox AL. Maestro: A system for scalable OpenFlow control. Available from: http://www.cs.rice. edu/~eugeneng/papers/TR10-11.pdf

Floodlight OpenFlow Controller- Project Floodlight. Available from: http://www.projectfloodlight.org/floodlight/

Announcing release of Floodlight with OF 1.3 support. Available from: http://sdnhub.org/releases/floodlight-plusopenflow13-support/

Ryu 3.9 documentation. Available from: http://ryu.readthedocs.org/en/latest/getting_started.html#what-s-ryu

Open day light. Available from: http://www.opendaylight. org/

Gorsansson P, Black C. Software defined networks- A comprehensive approach.1st ed. Morgan Kaufmann, an imprint of Elsevier; 2014.

Eadala SY, Nagarajan V. A review on deployment architectures of path computation element using software defined networking paradigm. Indian Journal of Science and Technology. 2016 Feb; 9(10). DOI: 10.17485/ijst/2016/ v9i10/84944.

Mandekar AV, Chandramouli K. Centralization of network using openflow protocol. Indian Journal of Science and Technology. 2015 Jan; 8(S2). DOI: 10.17485/ijst/2015/ v8iS2/61217.

Mittal P, Singh Y. Development of intelligent transportation system for improving average moving and waiting time with artificial intelligence. Indian Journal of Science and Technology. 2016 Jan; 9(3). DOI: 10.17485/ijst/2016/ v9i3/84156.

Davis B. Leveraging the load balancer to fight DDoS. Available from: http://www.sans.org/reading-room/ whitepapers/firewalls/leveraging-load-balancer-fightddos-33408

Califano A, Dincelli E, Goel S. Using features of cloud computing to defend smart grid against DDoS attacks. 10th Annual symposium on information assurance (Asia 15), ALBANY; 2015Jun. p. 44–50.

Chen-Xiao C, Ya-Bin X. Research on load balance method in SDN. International Journal of Grid and Distributed Computing. 2016; 9(1):25–36.

Ruelas AMR, Rothenberg CE. Implementation of neural switch using OpenFlow as load balancing method in data center. Campinas, Brasil: University of Campinas; 2015.

Chou L-D, Yang Y-T, Hong Y-M, Hu J-K, Jean B. A genetic-based load balancing algorithm in openflow network.Advanced Technologies, Embedded and Multimedia for Human-centric Computing. 2013; 260:411–7.

Balaguer R. Flow embedding algorithms for software defined audio networks [Master thesis]. Zurich, Switzerland: Swiss Federal Institute of Technology. Available from: http://ftp. tik.ee.ethz.ch/pub/.../MA-2014-14.pdf

Dobrijevic O, Santl M, Matijasevic M. Ant colony optimization for QoE-centric flow routing in software-defined networks. 2015 11th International Conference on Network and Service Management (CNSM); Barcelona. 2015 Nov. p. 274–8

Latah M. Solving multiple TSP problem by K-means and crossover based modified ACO algorithm. IJERT. 2016 Feb; 5(2):430–4.

Akhunzada A, Ahmed E, Gani A, Khan MK, Imran M, Guizani S. Securing the software defined networks: taxonomy, requirements, and open issues. IEEE Communications Magazine. 2015Apr; 53(4):36 –44

Jankowski D, Amanowicz M. Intrusion detection in software defined networks with self-organized maps. Journal of Telecommunications and Information Technology. 2015; 4:3–9.

Dabbagh M, Hamdaoui B, Guizaniy M, Rayes A. Softwaredefined networking security: Pros and cons. IEEE Communications Magazine. 2015; 53(6):73–9.

Bai H. A survey on artificial intelligence for network routing problems. NM,USA: University of New Mexico; 2007

Mustafa U, Masud MM, Trabelsi Z, Wood T, Al Harthi Z. Firewall performance optimization using data mining techniques. 2013 9th International Wireless Communications and Mobile Computing Conference (IWCMC); Sardinia. 2013 Jul. p. 934–40.

Mukherjee D, Acharyya S. Ant colony optimization technique applied in network routing problem. International Journal of Computer Applications. 2010; 1(15):66–73.

Dotcenko S, Vladyko A, Letenko I. A fuzzy logic-based information security management for software-defined networks. 16th International Conference on Advanced Communication Technology (ICACT); Pyeongchang. 2014 Feb. p. 167–71.

Mikians J, Barlet-Ros P, Sanjuas-Cuxart J, Sol´e-Pareta J. A practical approach to portscan detection in very highspeed links. PAM'11 Proceedings of the 12th International Conference on Passive and Active Measurement; Atlanta. 2011Mar. p. 112–21.

Williamson MM. Throttling viruses: Restricting propagation to defeat malicious mobile code. Proceedings 18th Annual Computer Security Applications Conference; Las Vegas. 2002 Dec. p. 61–8

Mehdi SA, Khalid J, Khayam SA. Revisiting traffic anomaly detection using software defined networking. RAID'11 Proceedings of the 14th International Conference on Recent Advances in Intrusion Detection; California. 2011Sep. p. 161–80.

Chen X-F, Yu S-Z. CIPA: A collaborative intrusion prevention architecture for programmable network and SDN. Computers and Security. 2016; 58:1–19.

Braga R, Mota E, Passito A. Lightweight DDoS flooding attack detection using NOX/OpenFlow. 2010 IEEE 35th Conference on Local Computer Networks (LCN); Denver, CO. 2010 Oct. p. 408–15.

Deepa SN, Devi BA. A survey on artificial intelligence approaches for medical image classification. Indian Journal of Science and Technology. 2011 Nov; 4(11). DOI: 10.17485/ijst/2011/v4i11/30291.

Yan Q, Yu FR, Gong Q, Li J. Software-Defined Networking (SDN) and Distributed Denial of Service (DDoS) attacks in cloud computing environments: a survey, some research issues, and challenges. IEEE Communications Surveys and Tutorials. 2016; 18(1):602–22.

Uzakgider T, Cetinkaya C, Sayit M. Learning-based approach for layered adaptive video streaming over SDN. Computer Networks. 2015; 92(P2):357–68.

https://www.researchgate.net/publication/284696928_Software-Defined_Networking_Using_OpenFlow_Protocols_Applications_and_Architectural_Design_Choices/figures?lo=1

Machine Learning Applications on COVID-19 Pandemic: A Systematic Literature Review

Kübra KÖKSAL[1]
Buket DOĞAN[2]
Zehra Aysun ALTIKARDEŞ[3]

Introduction

Sars-Cov-2 (Covid-19) virus, which comes from the coronavirus family such as Mers-Cov and Sars-Cov, is an enveloped RNA virus that causes respiratory failure (Alwaeli and Ibrahim, 2020: 1). The Covid-19 disease first appeared in December 2019 in Wuhan, China. This virus, which was detected to be transmitted from person to person on January 7, 2020, spread rapidly across the world. It was named as Covid-19 virus by the World Health Organization (WHO) on February 11, 2020 (Albahri et al., 2020: 2). It was declared a pandemic by WHO on 11 March 2020.

Common symptoms include fever, fatigue, loss of taste, cough, and shortness of breath. Polymerase chain reaction (PCR) is one of the common methods used for detection. In addition to this method, computed tomography (CT) images are also used as a reliable and increasingly common diagnostic method for detecting the virus.

The World Health Organization announced that by January 2021, more than 84 million people were detected as positive, approximately one million 800 thousand people died, and coronavirus cases were detected in 192 countries/territories and 26 cruise/naval ships countries. Since the disease first emerged, many studies have been conducted in the field of vaccines. A few types of vaccines used in January 2021:

1. Pfizer / BioNTech vaccine produced by Germany based BioNTech-Pfizer and the US Food and Drug Administration (FDA)

2. MRNA-1273 produced by Moderna

3. China based Sinovac vaccine

4. Russia based Sputnik V

In addition to vaccine studies, many researchers have carried out various studies in order to better analyze the characteristics of Covid-19 to apply new detection methods. Computer based

[1] Master Student, Marmara Univ., Department of Computer Engineering, 0000-0002-4252-7295
[2] Assoc. Prof., Marmara Univ., Department of Computer Engineering, 0000-0003-1062-2439
[3] Asst. Prof., Marmara Univ., Hypertension and Arteriosclerosis Center, 0000-0003-3875-1793

systems played a very important role in the fight against Covid-19 in areas such as diagnosis, detection, predicting the spreading of the virus and the number of cases in this period and aimed to alleviate the burden of health sector employees. Deep learning, machine learning and artificial intelligence methods are among the frequently used analysis methods with computer aided systems.

In this study, a systematic literature review was conducted on articles using machine learning methods for detection, diagnosis or prediction purposes and the results were evaluated. The purpose of this study is to evaluate the machine learning algorithms, datasets and the results obtained with Covid-19 and to examine how the studies conducted in this field so far have dealt with machine learn-ing methods.

This paper is structured as follows: Section 2 explains the research method used in the systematic literature review; Section 3 presents the analysis results obtained as a result of the literature review; and Section 4 provides a conclusion.

Method

The systematic literature review method applied in the study of Albahri AS, et al. was followed to determine the machine learning methods used to combat the Covid-19 virus and to perform performance analysis. The review style recommended by the Preferred Reporting Items (PRISMA) for Systematic Reviews and Meta Analyses was used (Albahri et al., 2020: 2).

Two different digital databases, IEEE and ScienceDirect, were used. IEEE Explore is a database of research articles on computer technologies, computer science, data science and medical practice. Science Direct is a platform with many publications that benefit researchers in scientific and medical issues. The steps constituting the scope of the research are as follows: determining the research protocol, determining the research questions, determining the search queries, determining the inclusion and exclusion criteria, determining the relevant literature by conducting a comprehensive research, selection of the studies, interpretation of the results. These steps will be explained in detail later in this section.Çalışmanızın yöntem bölümünü buraya yazın.

Search Strategy

English publications published between 2019-2021 using two different digital databases were examined within the scope of this study. In order to comprehensively examine the studies using the machine learning method in the fields of Covid-19 detection, diagnosis or prediction, four different search strategies consisting of selected keywords were used. Four different search queries and results used within the scope of this study are shown in Table 1 Search operations in Science Direct and IEEE digital databases were carried out using AND and OR queries. For example "sars-cov-2 AND machine learning AND (diagnosis OR prediction OR classification)

The main purpose of the review is to answer the following questions:

1.   Which machine learning algorithms were used in computer science to combat Covid-19?

2.   For what purpose were the machine learning methods used?

3.   What are the performance contributions of machine learning methods to combat Covid-19?

Table 1 – Search Queries and Results

Search Query	Result Of Databases	Total Result
Covid-19 AND machine learning AND diagnosis	Science Direct: 26 IEEE: 33	59
Covid-19 AND machine learning AND prediction	Science Direct: 55 IEEE: 29	84
Covid-19 AND machine learning AND classification	Science Direct: 25 IEEE: 46	71
Covid-19 AND machine learning	Science Direct: 131 IEEE: 136	267
Sars-Cov-2 AND machine learning	Science Direct: 38 IEEE: 13	51

Criteria For Inclusion and Exclusion

The following criteria were used to select among the studies to be examined for a systematic literature search.

1. Studies should provide experimental data on machine learning algorithms used in the Covid-19 field.

2. Research studies should have been published between 2019-2021.

3. Studies must be in English

4. Machine learning methods should be related to Covid-19 detection, diagnosis or prediction areas.

Criteria that was not included:

1. Studies are beyond the scope of machine learning algorithms and the performance impact it provides.

2. Studies that have not provided empirical data.

3. Studies examining the relationship of the virus with areas such as weather conditions, stress rate, education and other than Covid-19 detection or diagnosis are excluded.

Selection of Studies

Studies published between 2019-2021 were filtered using the specified search queries, and a total of 532 studies were obtained. A two-stage elimination process was carried out on the studies to be examined. In the first step, after the repetitive publications were removed, the abstracts and titles of the remaining studies were examined and the publications covering the determined criteria were selected. After the first step was completed, 71 out of the 532 publications remained.

In the second step, the remaining publications went through a complete reading process. At this stage, the articles suitable for the purpose of the study were selected and the title, year of publication, methods used and the results obtained were recorded in an Excel file. As a result of this process, a total of 49 articles were selected for use within the scope of the study. Figure 1 represents the steps of the applied research process.
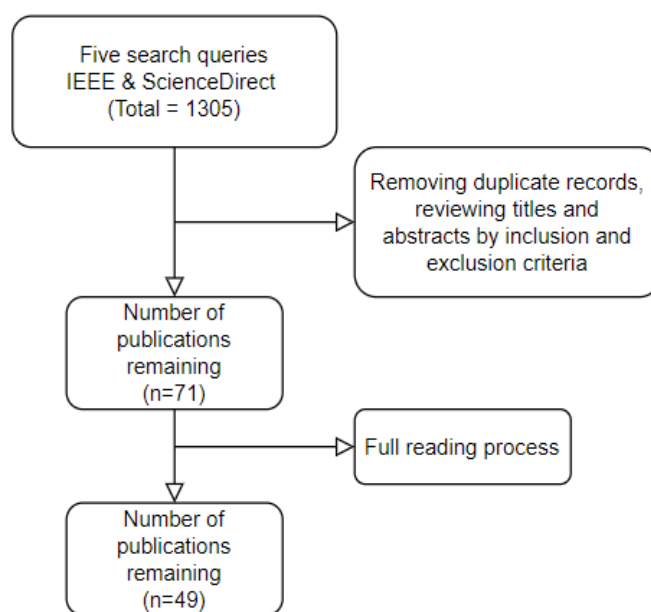

Fig. 1. Steps of the applied research process

Results

Within the scope of the research, 49 articles were examined in detail and the results obtained were analyzed under this title. Using 49 studies examined, author, country, problem type, dataset type, machine learning algorithm and obtained result information were recorded for each study. Table 4 shows this information from 49 publications. First, the distribution chart of the published articles by country was drawn. Figure 2 shows the number of scientific publications using machine learning algorithms in the Covid-19 field by geographic region. According to the chart, India ranks first with 11 publications then comes the USA with nine publications and China with seven publications.
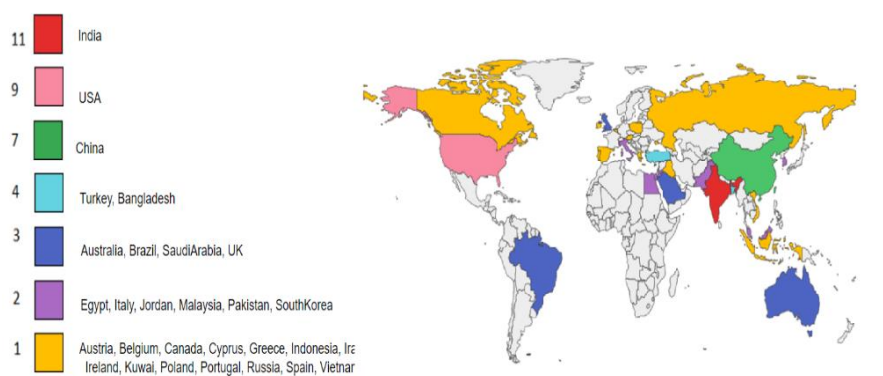
Fig. 2. Number of publications according to geographical regions.

Datasets and Resources

One of the analyzes made over the articles is to determine the types of data used. In this context, three different data types were determined. These are time series, text dataset and image dataset.

Time Series Data. Information such as the number of Covid-19 cases associated with geographic locations, the number of deaths, the number of Covid-19 tests performed or the number of people recovered are time series data. These data help researchers to predict many important information such as the growth, distribution, end time and peak time of the pandemic in the articles reviewed. In this context, many countries collect such time series information and share it publicly. Of the reviewed studies, 22 perform analysis on time series type data sets (Amar, Taha, and Mohamed, 2020: 4; Andreas et al., 2020: 1; Ballı, 2021: 2; Chakraborti et al., 2021: 3; Gambhir et al., 2020: 2; Istaiteh et al., 2020: 2; Khan, Abbas, and Truong, 2020: 4; Kuo and Fu, 2021: 2; Kurniawan et al., 2020: 2; Mandayam et al., 2020: 2; Mojjada et al., 2020: 2; Mondal et al., 2020: 1; Nikil, Dalmia, and Kumar, 2020: 2; Peng and Nagata, 2020: 1; Prakash et al., 2020: 3; Ribeiro et al., 2020: 3; Rustam et al., 2020: 2; Singh et al., 2020: 2; Wadhwa et al., 2021: 3; Wang et al., 2020: 2; Yadav, Perumal, and Srinivas, 2020: 2; Yeşilkanat, 2020: 3).

Clinical or Text Dataset. Clinical data are the main sources used in most medical research. These sources are frequently used in the diagnosis and prediction of any disease. They have also been used in the diagnosis of the Covid-19. Within the scope of the studies examined, vital values, laboratory and demographic data, comorbidities, laboratory tests, blood gas measurements, blood tests values were used as clinical data. 14 of the studied studies (Ahamad et al., 2020: 2; AlJame et al., 2020: 4; Althnian et al., 2020: 4; Arvind et al., 2021: 2; Banerjee et al., 2020: 2; Burdick et al., 2020: 2; Di Castelnuovo et al., 2020: 4; Kavadi et al., 2020: 4; Kramarenko, 2020: 3; Li et al., 2021: 2; Mondal et al., 2020: 1; Otoom et al., 2020: 3; Soltan et al., 2021: 3; Yadaw et al., 2020: 3) used machine learning algorithms on clinical data. Five studies reviewed (Althnian et al., 2020: 1; Arvind et al., 2021: 1; Burdick et al., 2020: 4; Di Castelnuovo et al., 2020: 1; Yadaw et al., 2020: 1) were used for mortality, respiratory decompensation and susceptibility estimation process, 3 studies (Kavadi et al., 2020: 1; Kramarenko, 2020: 4; Mondal et al., 2020: 11) for curve fitting procedures and the remaining 6 studies were used for diagnostic process. Table 2 shows which features are used in studies using clinical datasets.

Image Dataset. Image-based clinical data are also frequently used methods in the diagnosis of the disease. There are two types of image datasets that are frequently used in the Covid-19 diagnosis. The first of these is chest CT scans. Studies have revealed that Chest CT scans, which

have a lower false positive value than X-ray and ultrasound scans, can diagnose Covid-19. The second is X-ray scans. Although such data are less sensitive than CT scans, they have a lower dose of ionizing radiation and are more portable.

Table 2 – Features used in clinical data sets according to publication.

Ref.	Clinical features
(Arvind et al., 2021: 3)	Partial pressure of arterial CO2 (PACO2), oxygen saturation (O2 SAT), Temperature, Creatinine, Platelet count, white blood cell (WBC), systolic blood pressure (SBP), Partial pressure of arterial oxygen (PAO2), respiratory rate, Pulse and Diastolic blood pressure (DBP)
(Burdick et al., 2020: 2)	DBP, WBC, SBP, blood urea nitrogen (BUN), creatinine, platelet count, lactate, temperature, heart rate (HR), oxygen respiratory rate (RR), saturation (SpO2) and bilirubin.
(Kramarenko, 2020: 3)	Countries' population, area, urbanization rate, numbers of doctors, nurses, public funding, COVID tests, percentage of the elderly, percentage of smokers and Google's people mobility data
(Yadaw et al., 2020: 4)	Age, gender and ethnicity, comorbidities such as asthma and diabetes, smoking status of the patients, oxygen saturation level and body temperature.
(AlJame et al., 2020: 4)	100 laboratory tests including urine tests, blood tests, rt-PCR test and Sars-Cov-2 test
(Soltan et al., 2021: 3)	Point-of-care blood gas results, Blood tests, blood test results from baseline, vital signs and baseline comorbidity data (Charlson comorbidity index)
(Ahamad et al., 2020: 2)	Gender, Age, Cough, Fever, Pneumonia, Lung Infection, Muscle SorenessDiarrhea, Runny Nose, and Isolation Travel History
(Li et al., 2021: 3)	Population density, percentage of population aged <10 years life expectancy, sex ratio, prevalence of tuberculosis, prevalence of diabetes, percentage of urban population, two immunization coverages among children ages 12–23 months, percentage of population using unimproved water sources, prevalence of HIV, smoking rate, average age of childbirth, geographic location and temperature.
(Otoom et al., 2020: 4)	Symptoms, contact history with potentially infected people, and travel history.
(Althnian et al., 2020: 4)	Demographic values, result and test date, screening and confirmatory result.
(Banerjee et al., 2020: 2)	Age, full blood count and and rtPCR Sars-Cov-2 test, hematocrit, haemoglobin, eosinophils, mean corpuscular volume (MCV), leukocytes, basophils, platelets, neutrophils, mean corpuscular haemoglobin (MCH), mean platelet volume (MPV), lymphocytes, red blood cells (RBC), monocytes and red blood cell distribution, mean corpuscular haemoglobin concentration (MCHC).
(Mondal et al., 2020: 11)	RT-PCR and additional laboratory test
(Di Castelnuovo et al., 2020: 6)	Gender, age, chronic kidney disease, chronic pulmonary disease, diabetes, CRP, heart failure, hypertension, history of myocardial infarction, obesity and smoking habit.
(Kavadi et al., 2020: 4)	AgeGroupDetails, Covid_19_india, IndividualDetails, HospitalBedsIndia, StatewiseTestingDetails, ICMRTestintDetails, ICMRTestingLabs, Population.

14 of the studied studies (Brunese et al., 2020: 4; El-Kenawy et al., 2020: 1; Haritha, Praneeth, and Pranathi, 2020: 3; Hussain et al., 2021: 3; Javor et al., 2020: 1; Kang et al., 2020: 1; King et al., 2020: 1; Lai et al., 2020: 2; Mohammed et al., 2020: 8; Saha, Sadi, and Islam, 2021: 2; Sun et al., 2020: 1; Toğaçar, Ergen, and Cömert, 2020: 2; Tuncer, Dogan, and Ozyurt, 2020: 3; Ohata et al., 2021: 3) aimed to diagnose Covid-19 using machine learning algorithms on image data.

Machine Learning Applications

In this section, it has been investigated for which problem types machine learning algorithms are used in publications and the results obtained are presented.

Diagnosis of Covid-19. One of the most frequently used methods in the diagnosis of Covid-19 is RT-PCR test, as well as CT scans and X-ray scans. However, the rapid increase in the number of patients and the number of cases worldwide makes it difficult to apply these methods. For this reason, various studies have been carried out to develop computer aided solution systems. Most of the studies carried out aim to accelerate the diagnosis step by reaching accurate values close to reality. 21 of the studied studies (Ahamad et al., 2020: 1; AlJame et al., 2020: 1; Banerjee et al., 2020: 1; Brunese et al., 2020: 2; El-Kenawy et al., 2020: 5; Haritha, Praneeth, and Pranathi, 2020: 3; Hussain et al., 2021: 10; Javor et al., 2020: 1; Kang et al., 2020: 1; King et al., 2020: 1; Lai et al., 2020: 1; Li et al., 2021: 2; Mohammed et al., 2020: 5; Mondal et al., 2020: 11; Otoom et al., 2020: 3; Saha, Sadi, and Islam, 2021: 1; Soltan et al., 2021: 5; Sun et al., 2020: 3; Toğaçar, Ergen, and Cömert, 2020: 2; Tuncer, Dogan, and Ozyurt, 2020: 3; Ohata et al., 2021: 1) used the machine learning method for Covid-19 diagnosis. 14 of these studies (Brunese et al., 2020: 4; El-Kenawy et al., 2020: 1; Haritha, Praneeth, and Pranathi, 2020: 3; Hussain et al., 2021: 3; Javor et al., 2020: 1; Kang et al., 2020: 1; King et al., 2020: 1; Lai et al., 2020: 2; Mohammed et al., 2020: 8; Saha, Sadi, and Islam, 2021: 2; Sun et al., 2020: 1; Toğaçar, Ergen, and Cömert, 2020: 2; Tuncer, Dogan, and Ozyurt, 2020: 3; Ohata et al., 2021: 3) performed the diagnosis on image data sets and the remaining seven (Ahamad et al., 2020: 2; AlJame et al., 2020: 4; Banerjee et al., 2020: 2; Li et al., 2021: 2; Mondal et al., 2020: 1; Otoom et al., 2020: 3; Soltan et al., 2021: 3) studies performed the Covid-19 diagnostic procedure on non image clinical data sets.

Curve Fitting. Another important information about the Covid-19 pandemic can be obtained using time series data. By using curve fitting techniques on these data, information about the spread of the pandemic can be obtained. Using information such as the number of cases, number of deaths, the number of tests performed, the number of patients, it can be predicted when the number of cases will reach a peak, when it will end, or how it will show at certain times. This information enables countries to have information about which measures to take, when it will be better to maintain the shutdown, or how the pandemic will progress. Twenty of the studies examined in this scope (Amar, Taha, and Mohamed, 2020: 1; Andreas et al., 2020: 4; Ballı, 2021: 1; Chakraborti et al., 2021: 1; Gambhir et al., 2020: 1; Kavadi et al., 2020: 2; Kramarenko, 2020: 2-3; Kuo and Fu, 2021: 2; Mandayam et al., 2020: 1; Mojjada et al., 2020: 5; Mondal et al., 2020: 1; Peng and Nagata, 2020: 5; Prakash et al., 2020: 7; Ribeiro et al., 2020: 2-3; Rustam et al., 2020: 4; Singh et al., 2020: 2; Wadhwa et al., 2021: 3; Wang et al., 2020: 3; Yadav, Perumal, and Srinivas, 2020: 3; Yeşilkanat, 2020: 1)used machine learning algorithms for curve fitting purposes.

Prediction. In addition to Covid-19 diagnosis and prediction techniques made with curve fitting, estimation processes such as estimating the mortality rate, estimating the need for intubation can be performed and more accurate decisions can be made in the treatment process. Eight of the studied studies (Althnian et al., 2020: 1; Arvind et al., 2021: 2; Burdick et al., 2020: 3; Di Castelnuovo et al., 2020: 3; Istaiteh et al., 2020: 7; Khan, Abbas, and Truong, 2020: 1; Nikil, Dalmia, and Kumar,

2020: 2; Yadaw et al., 2020: 1) used machine learning methods for prediction. The process of estimating intubation rate in the study of Varun Arvind, et al. (Arvind et al., 2021: 4) achieves 0.83 AUC and 0.32 AUPRC value, respiratory decompensation in the study of Burdick, H. et al. (Burdick et al., 2020: 5) achieves sensitivity with a value of 0.90, mortality rate in the study of Yadaw AS (Yadaw et al., 2020: 7) achieves 0.91-0.94 AUC value and estimation of sensitivity in the study of Alhanoof Althnian et al. (Althnian et al., 2020: 6) achieves 85.6% accuracy and 0.76 AUC for decision tree algorithm.
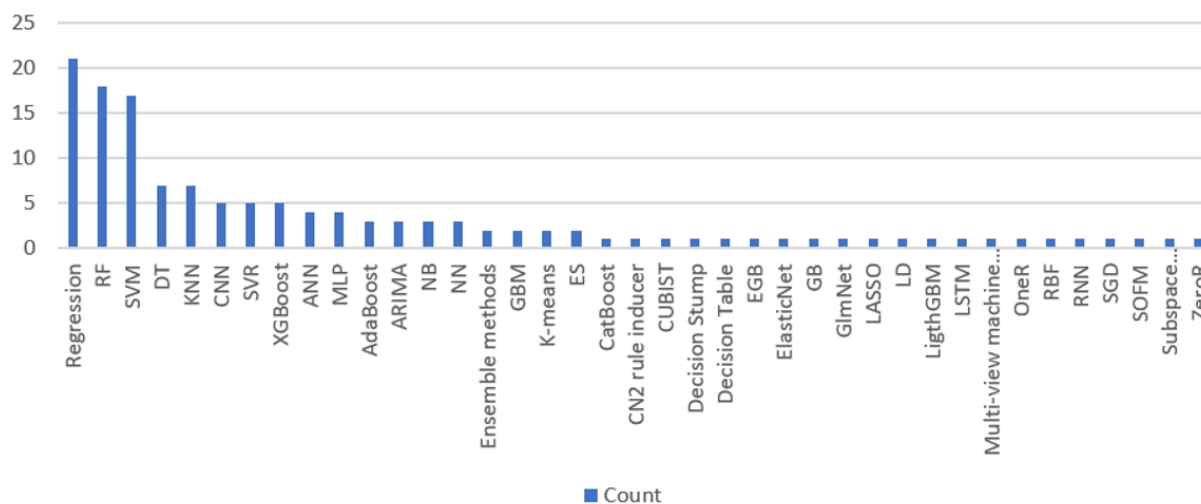

Fig. 3. Used machine learning methods and their counts.

Many different machine learning techniques have been used in the reviewed studies. Figure 3 shows the machine learning techniques used and the number of times they were used. As can be seen from the graph, regression techniques are the most commonly used machine learning method in curve fitting problems. Next comes the RF algorithm with 18 numbers and the SVM algorithm with 17 numbers. (ES: Exponential smoothing, LD: Linear discriminant) Within the scope of this study, three different use cases were determined and the examined publications were divided into at least one of these three articles. The list of machine learning algorithms used in these types determined in Table 3 is given.

Table 3 – Features used in clinical data sets according to publication.

Application type	Methods
Diagnosis	Ensemble, RF, KNN, NB, RF, MLP, SVM, CNN, NN, RBF, KNN, SGD, Regression, DT, AdaBoost, CN2 rule inducer, Multi-view machine learning technique, SOFM, XgBoost, GBM, EGB, Decision Table, Decision Stump, OneR, ZeroR, Linear discriminant (LD), subspace discriminant (SD) , Glmnet
Prediction	RF, XgBoost, K-means, ARIMA, ANN, LSTM, CNN, Regression, SVM, MLP, DT, FBM
Curve Fitting	Regression, SVM, ANN, RF, SVR, ARIMA, Elasticnet (EN), LASSO, RNN, MLP, KNN, PCR, GBM, LightGBM, DT, Ensemble, Catboost, regression tree (RT), AdaBoost, Exponential Smoothing, GB, XGBoost

Conclusions

After the removal of duplicates from 532 studies obtained as a result of the systematic literature review and the elimination process, taking into account the inclusion and exclusion criteria, 71 publications were obtained. As a second step, after the detailed examination of the publications, a total of 49 studies were determined to be examined within the scope of this study. In the analysis of these 49 studies, three data types that are frequently used were determined. These are clinical data, time series and image data. Three different categories, namely curve fitting, prediction and diagnosis, were determined as the usage situation, and all the articles examined were assigned to at least one type. While most of the data types used for the curve fitting process consisted of series, clinical data and image data were used for the diagnostic process. Studies conducted in the diagnosis category aim to accelerate this process by reaching high accuracy values and to alleviate the burden of healthcare professionals. The three most used machine learning methods in the analysis results were determined as Regression, RF and SVM. Although regression techniques are used in all three categories, it has been found to be a popular technique used for curve fitting. This study is a literature search created for future studies. It is aimed to be a guiding study for those who will work in this field by analyzing which data types are used for what purposes with which methods in the field of Covid-19 and machine learning.

In line with the results obtained, it was concluded that the most used of the 3 data types was the time series and the Covid-19 diagnosis was the most studied problem type among the 3 uses. In addition, while the most used machine learning method is Regression, it has been observed that RF and SVM methods are frequently used in the diagnosis of Covid-19. In addition to supervised learning techniques, unsupervised clustering techniques such as K-Means were also used. It has been observed that the studies examined have reached an accuracy close to manual determinations for purposes such as Covid-19 diagnosis, prediction and curve fitting.

References

Ahamad M. M., Aktar S., Rashed-Al-Mahfuz M., Uddin S., Liò P., Xu H., . . . Moni M. A. (2020). A machine learning model to identify early stage symptoms of SARS-Cov-2 infected patients. *Expert Systems with Applications*, *160*, 113661. doi:https://doi.org/10.1016/j.eswa.2020.113661

Albahri A. S., Hamid R. A., Alwan J. K., Al-Qays Z. T., Zaidan A. A., Zaidan B. B., . . . Madhloom H. T. (2020). Role of biological data mining and machine learning techniques in detecting and diagnosing the novel coronavirus (COVID-19): A systematic review. *J Med Syst*, *44*, 122. doi:10.1007/s10916-020-01582-x

AlJame M., Ahmad I., Imtiaz A., and Mohammed A. (2020). Ensemble learning model for diagnosing COVID-19 from routine blood tests. *Informatics in Medicine Unlocked*, *21*, 100449. doi:https://doi.org/10.1016/j.imu.2020.100449

Althnian A., Elwafa A. A., Aloboud N., Alrasheed H., and Kurdi H. (2020). Prediction of COVID-19 individual susceptibility using demographic data: A case study on Saudi Arabia. *Procedia Computer Science*, *177*, 379-86. doi:https://doi.org/10.1016/j.procs.2020.10.051

Alwaeli Z. A. A., and Ibrahim A. A. (2020). Predicting Covid-19 trajectory using machine learning. *2020 4th International Symposium on Multidisciplinary Studies and Innovative Technologies (ISMSIT)*, 1-4. doi:10.1109/ISMSIT50672.2020.9255149

Amar L. A., Taha A. A., and Mohamed M. Y. (2020). Prediction of the final size for COVID-19 epidemic using machine learning: A case study of Egypt. *Infectious Disease Modelling*, *5*, 622-34. doi:https://doi.org/10.1016/j.idm.2020.08.008

Andreas A., Mavromoustakis C. X., Mastorakis G., Mumtaz S., Batalla J. M., and Pallis E. (2020). Modified machine learning techique for curve fitting on regression models for COVID-19 projections. *2020 IEEE 25th International Workshop on Computer Aided Modeling and Design of Communication Links and Networks (CAMAD)*, 1-6. doi:10.1109/CAMAD50429.2020.9209264

Arvind V., Kim J. S., Cho B. H., Geng E., and Cho S. K. (2021). Development of a machine learning algorithm to predict intubation among hospitalized patients with COVID-19. *J Crit Care*, *62*, 25-30. doi:10.1016/j.jcrc.2020.10.033

Ballı S. (2021). Data analysis of Covid-19 pandemic and short-term cumulative case forecasting using machine learning time series methods. *Chaos, Solitons & Fractals*, *142*, 110512. doi:https://doi.org/10.1016/j.chaos.2020.110512

Banerjee A., Ray S., Vorselaars B., Kitson J., Mamalakis M., Weeks S., . . . Mackenzie L. S. (2020). Use of machine learning and artaificial intelligence to predict SARS-CoV-2 infection from full blood counts in a population. *International Immunopharmacology*, *86*, 106705. doi:https://doi.org/10.1016/j.intimp.2020.106705

Brunese L., Martinelli F., Mercaldo F., and Santone A. (2020). Machine learning for coronavirus covid-19 detection from chest x-rays. *Procedia Computer Science*, *176*, 2212-21. doi:https://doi.org/10.1016/j.procs.2020.09.258

Burdick H., Lam C., Mataraso S., Siefkas A., Braden G., Dellinger R. P., . . . Das R. (2020). Prediction of respiratory decompensation in Covid-19 patients using machine learning: The READY trial. *Computers in Biology and Medicine*, *124*, 103949. doi:https://doi.org/10.1016/j.compbiomed.2020.103949

Chakraborti S., Maiti A., Pramanik S., Sannigrahi S., Pilla F., Banerjee A., and Das D. N. (2021). Evaluating the plausible application of advanced machine learnings in exploring determinant factors of present pandemic: A case for continent specific COVID-19 analysis. *Science of The Total Environment*, *765*, 142723. doi:https://doi.org/10.1016/j.scitotenv.2020.142723

Di Castelnuovo A., Bonaccio M., Costanzo S., Gialluisi A., Antinori A., Berselli N., . . . Iacoviello L. (2020). Common cardiovascular risk factors and in-hospital mortality in 3,894 patients with COVID-19: survival analysis and machine learning-based findings from the multicentre Italian CORIST Study. *Nutrition, Metabolism and Cardiovascular Diseases*, *30*, 1899-913. doi:https://doi.org/10.1016/j.numecd.2020.07.031

El-Kenawy E. S. M., Ibrahim A., Mirjalili S., Eid M. M., and Hussein S. E. (2020). Novel feature selection and voting classifier algorithms for COVID-19 classification in CT Images. *IEEE Access*, *8*, 179317-35. doi:10.1109/ACCESS.2020.3028012

Gambhir E., Jain R., Gupta A., and Tomer U. (2020). Regression analysis of COVID-19 using machine learning algorithms. *2020 International Conference on Smart Electronics and Communication (ICOSEC)*, 65-71. doi:10.1109/ICOSEC49089.2020.9215356

Haritha D., Praneeth C., and Pranathi M. K. (2020). Covid prediction from X-ray Images. *2020 5th International Conference on Computing, Communication and Security (ICCCS)*, 1-5. doi:10.1109/ICCCS49678.2020.9276795

Hussain E., Hasan M., Rahman M. A., Lee I., Tamanna T., and Parvez M. Z. (2021). CoroDet: A deep learning based classification for COVID-19 detection using chest X-ray images. *Chaos, Solitons & Fractals*, *142*, 110495. doi:https://doi.org/10.1016/j.chaos.2020.110495

Istaiteh O., Owais T., Al-Madi N., and Abu-Soud S. (2020). Machine learning approaches for COVID-19 forecasting. *2020 International Conference on Intelligent Data Science Technologies and Applications (IDSTA)*, 50-57. doi:10.1109/IDSTA50958.2020.9264101

Javor D., Kaplan H., Kaplan A., Puchner S. B., Krestan C., and Baltzer P. (2020). Deep learning analysis provides accurate COVID-19 diagnosis on chest computed tomography. *European Journal of Radiology*, *133*, 109402. doi:https://doi.org/10.1016/j.ejrad.2020.109402

Kang H., Xia L., Yan F., Wan Z., Shi F., Yuan H., . . . Shen D. (2020). Diagnosis of coronavirus disease 2019 (COVID-19) with structured latent multi-view representation learning. *IEEE Transactions on Medical Imaging*, *39*, 2606-14. doi:10.1109/TMI.2020.2992546

Kavadi D. P., Patan R., Ramachandran M., and Gandomi A. H. (2020). Partial derivative nonlinear global pandemic machine learning prediction of COVID 19. *Chaos, Solitons & Fractals*, *139*, 110056. doi:https://doi.org/10.1016/j.chaos.2020.110056

Khan Y. A., Abbas S. Z., and Truong B.-C. (2020). Machine learning-based mortality rate prediction using optimized hyper-parameter. *Computer Methods and Programs in Biomedicine*, *197*, 105704. doi:https://doi.org/10.1016/j.cmpb.2020.105704

King B., Barve S., Ford A., and Jha R. (2020). Unsupervised clustering of COVID-19 chest X-Ray images with a self-organizing feature map. *2020 IEEE 63rd International Midwest Symposium on Circuits and Systems (MWSCAS)*, 395-98. doi:10.1109/MWSCAS48704.2020.9184493

Kramarenko E. R. (2020). Testing the applicability of IT Instrumentation to projecting the spread of viral epidemics. *2020 International Multi-Conference on Industrial Engineering and Modern Technologies (FarEastCon)*, 1-5. doi:10.1109/FarEastCon50210.2020.9271094

Kuo C.-P., and Fu J. S. (2021). Evaluating the impact of mobility on COVID-19 pandemic with machine learning hybrid predictions. *Science of The Total Environment*, *758*, 144151. doi:https://doi.org/10.1016/j.scitotenv.2020.144151

Kurniawan R., Abdullah S. N. H. S., Lestari F., Nazri M. Z. A., Mujahidin A., and Adnan N. (2020). Clustering and correlation methods for predicting coronavirus COVID-19 risk analysis in pandemic countries. *2020 8th International Conference on Cyber and IT Service Management (CITSM)*, 1-5. doi:10.1109/CITSM50537.2020.9268920

Lai Y., Li G., Wu D., Lian W., Li C., Tian J., . . . Jiang G. (2020). 2019 Novel coronavirus infected pneumonia on CT: A feasibility study of few shot learning for computerized diagnosis of emergency diseases. *IEEE Access*, *8*, 194158-65. doi:10.1109/ACCESS.2020.3033069

Li M., Zhang Z., Cao W., Liu Y., Du B., Chen C., . . . Wang X. (2021). Identifying novel factors associated with COVID-19 transmission and fatality using the machine learning approach. *Science of The Total Environment*, *764*, 142810. doi:https://doi.org/10.1016/j.scitotenv.2020.142810

Mandayam A. U., R A. C., Siddesha S., and Niranjan S. K. (2020). Prediction of Covid-19 pandemic based on Regression. *2020 Fifth International Conference on Research in Computational Intelligence and Communication Networks (ICRCICN)*, 1-5. doi:10.1109/ICRCICN50933.2020.9296175

Mohammed M. A., Abdulkareem K. H., Al-Waisy A. S., Mostafa S. A., Al-Fahdawi S., Dinar A. M., . . . Díez I. D. L. T. D. L. T. (2020). Benchmarking methodology for selection of optimal COVID-19 diagnostic model based on entropy and TOPSIS methods. *IEEE Access*, *8*, 99115-31. doi:10.1109/ACCESS.2020.2995597

Mojjada R. K., Yadav A., Prabhu A. V., and Natarajan Y. (2020). Machine learning models for covid-19 future forecasting. *Materials Today: Proceedings*. doi:https://doi.org/10.1016/j.matpr.2020.10.962

Mondal M. R. H., Bharati S., Podder P., and Podder P. (2020). Data analytics for novel coronavirus disease. *Informatics in Medicine Unlocked*, *20*, 100374. doi:https://doi.org/10.1016/j.imu.2020.100374

Nikil C. V. S. S., Dalmia H., and Kumar G. J. R. P. (2020). Covid-19 outbreak analysis. *2020 International Conference on Smart Technologies in Computing, Electrical and Electronics (ICSTCEE)*, 347-50. doi:10.1109/ICSTCEE49637.2020.9276790

Ohata E. F., Bezerra G. M., Chagas J. V. S. d., Neto A. V. L., Albuquerque A. B., Albuquerque V. H. C. d., and Filho P. P. R. (2021). Automatic detection of COVID-19 infection using chest X-ray images through transfer learning. *IEEE/CAA Journal of Automatica Sinica*, *8*, 239-48. doi:10.1109/JAS.2020.1003393

Otoom M., Otoum N., Alzubaidi M. A., Etoom Y., and Banihani R. (2020). An IoT-based framework for early identification and monitoring of COVID-19 cases. *Biomedical Signal Processing and Control*, *62*, 102149. doi:https://doi.org/10.1016/j.bspc.2020.102149

Peng Y., and Nagata M. H. (2020). An empirical overview of nonlinearity and overfitting in machine learning using COVID-19 data. *Chaos, Solitons & Fractals*, *139*, 110055. doi:https://doi.org/10.1016/j.chaos.2020.110055

Prakash A., Sharma P., Sinha I. K., and Singh U. P. (2020). Spread & Peak prediction of Covid-19 using ANN and regression (Workshop Paper). *2020 IEEE Sixth International Conference on Multimedia Big Data (BigMM)*, 356-65. doi:10.1109/BigMM50055.2020.00062

Ribeiro M. H. D. M., da Silva R. G., Mariani V. C., and Coelho L. d. S. (2020). Short-term forecasting COVID-19 cumulative confirmed cases: Perspectives for Brazil. *Chaos, Solitons & Fractals*, *135*, 109853. doi:https://doi.org/10.1016/j.chaos.2020.109853

Rustam F., Reshi A. A., Mehmood A., Ullah S., On B. W., Aslam W., and Choi G. S. (2020). COVID-19 future forecasting using supervised machine learning models. *IEEE Access*, *8*, 101489-99. doi:10.1109/ACCESS.2020.2997311

Saha P., Sadi M. S., and Islam M. M. (2021). EMCNet: Automated COVID-19 diagnosis from X-ray images using convolutional neural network and ensemble of machine learning classifiers. *Inform Med Unlocked*, *22*, 100505. doi:10.1016/j.imu.2020.100505

Singh S., Parmar K. S., Makkhan S. J. S., Kaur J., Peshoria S., and Kumar J. (2020). Study of ARIMA and least square support vector machine (LS-SVM) models for the prediction of SARS-CoV-2 confirmed cases in the most affected countries. *Chaos, Solitons & Fractals*, *139*, 110086. doi:https://doi.org/10.1016/j.chaos.2020.110086

Soltan A. A. S., Kouchaki S., Zhu T., Kiyasseh D., Taylor T., Hussain Z. B., . . . Clifton D. A. (2021). Rapid triage for COVID-19 using routine clinical data for patients attending hospital: development and prospective validation of an artificial intelligence screening test. *The Lancet Digital Health*, *3*, e78-e87. doi:https://doi.org/10.1016/S2589-7500(20)30274-0

Sun L., Mo Z., Yan F., Xia L., Shan F., Ding Z., . . . Shen D. (2020). Adaptive feature selection guided deep forest for COVID-19 classification with chest CT. *IEEE Journal of Biomedical and Health Informatics*, *24*, 2798-805. doi:10.1109/JBHI.2020.3019505

Toğaçar M., Ergen B., and Cömert Z. (2020). COVID-19 detection using deep learning models to exploit social mimic optimization and structured chest X-ray images using fuzzy color and stacking approaches. *Computers in Biology and Medicine*, *121*, 103805. doi:https://doi.org/10.1016/j.compbiomed.2020.103805

Tuncer T., Dogan S., and Ozyurt F. (2020). An automated residual exemplar local binary pattern and iterative relief based COVID-19 detection method using chest X-ray image. *Chemometrics and Intelligent Laboratory Systems*, *203*, 104054. doi:https://doi.org/10.1016/j.chemolab.2020.104054

Wadhwa P., Aishwarya, Tripathi A., Singh P., Diwakar M., and Kumar N. (2021). Predicting the time period of extension of lockdown due to increase in rate of COVID-19 cases in India using

machine learning. *Materials Today: Proceedings*, *37*, 2617-22. doi:https://doi.org/10.1016/j.matpr.2020.08.509

Wang P., Zheng X., Li J., and Zhu B. (2020). Prediction of epidemic trends in COVID-19 with logistic model and machine learning technics. *Chaos, Solitons & Fractals*, *139*, 110058. doi:https://doi.org/10.1016/j.chaos.2020.110058

Yadav M., Perumal M., and Srinivas M. (2020). Analysis on novel coronavirus (COVID-19) using machine learning methods. *Chaos, Solitons & Fractals*, *139*, 110050. doi:https://doi.org/10.1016/j.chaos.2020.110050

Yadaw A. S., Li Y.-c, Bose S., Iyengar R., Bunyavanich S., and Pandey G. (2020). Clinical features of COVID-19 mortality: development and validation of a clinical prediction model. *The Lancet Digital Health*, *2*, e516-e25. doi:https://doi.org/10.1016/S2589-7500(20)30217-X

Yeşilkanat C. M. (2020). Spatio-temporal estimation of the daily cases of COVID-19 in worldwide using random forest machine learning algorithm. *Chaos, Solitons & Fractals*, *140*, 110210. doi:https://doi.org/10.1016/j.chaos.2020.110210

Table 4 – Overview of Primary Studies.

	Country	Problem Category	Dataset type	Technology	Result
(Arvind et al., 2021: 4)	USA	Prediction intubation	Clinical data- vital values, laboratory and demographic data	RF	The machine learning algorithm used has 0.83 AUC and 0.32 AUPRC, which performs significantly better than the ROX index in terms of intubation risk.
(Saha, Sadi, and Islam, 2021: 8-10)	Bangladesh	Diagnosis of Covid-19	Image dataset - X-ray images	CNN based feature extraction, ensemble of ML classifiers (RF, SVM, DT, AdaBoost)	The proposed deep learning and machine learning based detection system achieved a better performance than other deep learning systems with 98.91% accuracy, 100% precision, 97.82% recall, 98.89% F1 score and 0.9894 ROC.
(Burdick et al., 2020: 3)	USA, Belgium	Prediction respiratory decompensation	Clinical data - vital values, laboratory	XGBoost	The proposed algorithm has a higher diagnostic likelihood ratio in the Modified Early Warning Score (MEWS), a higher sensitivity with a value of 0.90 than MEWS, which has a sensitivity value of 0.78.
(Sun et al., 2020: 5)	China	Diagnosis of Covid-19	Image dataset - CT images, gender, age	RF based Adaptive Feature Selection guided Deep Forest (AFS-DF)	The obtained accuracy, sensitivity, specificity, AUC, sensitivity and F1 score were 91.79%, 93.05%, 89.95%, 96.35%, 93.10% and 93.07%, respectively. The proposed method performed better than the Four commonly used machine learning models in CAP (community acquired pneumonia) classification. When compared with Lasso and ElasticNet feature selection methods, a better result was obtained with the proposed AFS-DF structure.
(Ohata et al., 2021: 5-8)	Brazil	Diagnosis of Covid-19	Image dataset - Chest X-ray images	CNN based feature extraction, KNN, NB,	SVM algorithm used with MobileNet feature extractor achieved 98.5% accuracy and F1 score value, MLP algorithm used with DenseNet201 reached an accuracy of 95.6% and F1 score value.

				RF, MLP, SVM	
(Lai et al., 2020: 5-6)	China	Diagnosis of Covid-19	Image dataset - Chest CT images	Deep convolutional neural network (DCNN), MaskR-CNN-SVM	The proposed algorithm (NCIP-Net) for the detection of normal and NCIP (novel coronavirus-infected pneumonia) reached 0.91 AUC value, 0.95 AUC value for NCIP and lung nodule detection, and 0.83 AUC value for NCIP and other pneumonia detection. It also appears to perform better than the Mask-R-CNN trained for comparison.
(Andreas et al., 2020: 3)	Cyprus, Greece, Poland, Portugal	Curve Fitting	Time series dataset	Linear, Exponential, 6th degree Polynomial Regression	Linear Regression 0.8609, Exponential Regression 0.922 and 6th degree Polynomial 0.999336 R2 values were achieved. When the results were examined, it was concluded that the 6th order polynomial regression was more suitable for the dataset. The 10th degree polynomial developed for curve fitting corresponding to cumulative infectious cases in Italy reached the value of 0.999934933 R2.
(Haritha, Praneeth, and Pranathi, 2020: 4)	India	Diagnosis of Covid-19	Image dataset - X-ray images	Transfer learning CNN with VGG	The proposed method reached 99.49% accuracy with 1.0000 sensitivity and 1.0000 specificity values for 5-class multi-class. For Covid and normal class classification, 1.0000 sensitivity, 0.9890 and specificity reached 98% accuracy.
(Mohammed et al., 2020: 1)	Iraq, Malaysia, Saudi Arabia, Spain	Diagnosis of Covid-19	Image dataset - Chest X-ray images	NN, SVM, NB, RBF, KNN, SGD, Linear R, AdaBoost, RF, DT, CN2 rule inducer, SVM(Polynomial)	By using Entropy and TOPSIS integration, the problem of selecting and comparing diagnostic models was solved effectively. SVM (linear) was chosen as the best diagnostic model for COVID19 with a proximity coefficient value of 0.9899.
(Kurniawan et al., 2020: 1)	Indonesia, Malaysia,	Predicting COVID-19 Risk Analysis	Time series dataset	K-means clustering, correlation	When the number of clusters is 5, the best cluster number performance is reached. With the cluster [Iran, France], [Spain, Germany], [United States and Italy], [Indonesia, Malaysia, Philippines] an performance about 97% has been achieved. At the same time, a suitable relation of 0.85 was predicted between total deaths and characteristics of critically infected patients.
(El-Kenawy et al., 2020: 14-16)	Egypt, Australia, South Korea	Diagnosis of Covid-19	Image dataset - CT images	SVM, NN, KNN, DT	It has been found that the highest classification accuracy can be achieved when AlexNet is used in the feature extraction stage. The used SFS Guided WOA feature selection algorithm performs better than the compared algorithms including the original WOA algorithm, and LSH-SMOTE preprocessing and the proposed PSO-Guided WOA voting classifier with the binary prediction result of 0.995 and 2.49569E- 05 It has been observed that it achieves an AUC with MSE, which outperforms other state of the art community learning.
(Istaiteh et al., 2020: 7)	Jordan	COVID-19 Forecasting, Prediction	Time series dataset	ARIMA, ANN, LSTM, CNN	Deep learning models performed better than ARIMA model in terms of three error measures (MAPE, RMSLE, MSLE). However, one dimensional CNN performed slightly better than the other two deep learning models, followed by

					ANN and LSTM models. CNN reached 3.13 MAPE, 0.13 RMSLE, 0.02 MSLE values.
(Kang et al., 2020: 8)	China	Diagnosis of Covid-19	Image dataset - Chest CT images	Multi-view machine learning technique	The multiple view representation learning technique used in the study reached 95.5% accuracy, 96.6% sensitivity and 93.2% specificity.
(Mandayam et al., 2020: 3-4)	India	Curve Fitting	Time series dataset	Linear R., SVR	It was observed that the LR model reached 99% R2 in predicting cases and the Linear Regression algorithm performed better when compared with SVR. Because the dataset is linear.
(Rustam et al., 2020: 1,10)	Pakistan, Saudi Arabia, South Korea	Curve Fitting	Time series dataset	Linear R., LASSO, SVM, ES	Three types of estimates are made, such as the number of newly infected cases, deaths and recovery over the next 10 days. While ES performed the best among all models, LASSO and LR cases performed best after ES in predicting mortality and recovery rate. It has been observed that SVM performs poorly in all forecast scenarios.
(Prakash et al., 2020: 4-10)	India	Curve Fitting	Time series dataset	Linear R., PR, ANN	Linear regression captures the data distribution, but appears to be slightly different from the actual numbers for Spain, Italy and the USA. It has been observed that linear regression catches the curve better compared to fourth order polynomial regression. However, the estimates made by the polynomial regression were far from the actual number of cases in the Spanish and Italian data. It has been seen that the predictions made with the ANN model are quite accurate; especially for the top five most affected states of India. While there was some deviation for the Top five States least affected, the Top five States moderately affected showed average modeling performance.
(King et al., 2020: 3-4)	USA	Diagnosis of Covid-19	Image dataset - Chest X-ray images	Self-Organizing Feature Maps (SOFM)	It has been shown that with the SOFM unsupervised learning technique, it can effectively extract features from Covid-19 chest x-ray images and classify the image correctly. The biggest advantage of this model is that there is no need for a labeled data requirement for training.
(Gambhir et al., 2020: 6)	India	Curve Fitting	Time series dataset	SVM, PR	With this study, the current situation of Covid-19 transmission has been successfully analyzed. The Polynomial Regression algorithm predicted a 60-day incidence increase with an accuracy of 93% compared to the SVM.
(Kramarenko, 2020: 3)	Russia	Curve Fitting	Clinical data	ANN, RNN, RF, GB, AdaBoost, Catboost, LightGBM	Gradient boosting over decision trees was chosen as the most efficient model.
(Yadaw et al., 2020: 8-9)	USA	Prediction mortality	Clinical data - comorbidities and demographic data	RF, Linear R., SVM, XGBoost	Prediction models used in the study obtained 0.91 - 0.94 AUC values in two independent verification data sets. The model obtained using only three features was as successful as the model using all features. Minimum oxygen saturation and age were chosen as the most determining features and the XGBoost produced the most accurate predictive value.

(AlJame et al., 2020: 1)	Kuwai	Diagnosis of Covid-19	Clinical data - laboratory (blood tests)	Ensemble Learning (extra trees, RF, Logistic R., XGBoost)	The proposed assembly model reached 99.88% accuracy, 99.38% AUC, 98.72% sensitivity and 99.99% specificity.
(Soltan et al., 2021: 1,6)	UK	Diagnosis of Covid-19	Clinical data - laboratory tests, blood gas measurements, and vital signs	Logistic R., RF, XGBoost	Compared to other classifiers, the XGBoost algorithm has shown the highest performance. The developed ED (emergency services) model reached 0.939 AUROC, 77.4% sensitivity, 95.7% specificity, while the acceptance model reached 0.940 AUROC, 77.4% sensitivity, 94.8% specificity. Eosinophils, basophils and CRP were chosen as the highest determinant features for the ED model.
(Mojjada et al., 2020: 5)	India	Curve Fitting	Time series dataset	Linear R., LASSO R., SVM, Exponential Smoothing	ES showed the best predictive performance depending on the size of the dataset. LR and LASSO have been successful to some extent in predicting the number of deaths. SVM showed the worst prediction performance in this study.
(Wadhwa et al., 2021: 5-6)	India	Curve Fitting	Time series dataset	Linear Regression	A machine learning model has been developed to predict the number of cases, deaths and recovery in India. Using this model, the lockout time is estimated. It has been learned that if all measures are properly implemented, the cases will begin to decrease and the lockdown will disappear on 9 September 2020.
(Ballı, 2021: 6)	Turkey	Curve Fitting	Time series dataset	Linear regression, MLP, RF, SVM	Machine learning has been used to predict the trend of the epidemic. According to the obtained results, SVM achieved the best predictive performance. SVM and linear regression have close RMSE and MAPE values. MLP ranks third in performance and RF has the worst performance. According to the information obtained, it is estimated that the epidemic will reach its peak in January 2021 and 80 million people will be infected cumulatively.
(Yeşilkanat, 2020: 1,7)	Turkey	Curve Fitting	Time series dataset	RF	Case numbers were estimated for 190 countries using RF and compared with the actual number of confirmed cases. At the end of the study, the RF algorithm obtained 0.843 and 0.995 (avg R2 = 0.959), 141.76 and 526.18 (mean RMSE = 259.38) for the test dataset. This shows that the RF algorithm is a suitable algorithm for near future case prediction.
(Ahamad et al., 2020: 1,5)	Bangladesh, USA, UK, China, Australia	Diagnosis of Covid-19, prediction symptoms	Clinical data - Demographic and symptom data	DT, RF, GBM, EGB, SVM	A machine learning model has been developed that provides features that provide high determination in the diagnosis of Covid-19 disease. The XGBoost achieved the highest accuracy (> 85%) to select features in all age groups compared to other models. The analysis showed that the most significant symptoms were cough (30.3%), fever (41.1%), runny nose (8.43%) and lung infection (13.1%).
(Hussain et al., 2021: 11)	Bangladesh, Australia	Diagnosis of Covid-19	Image dataset - Chest X-ray images	CNN	The proposed model has reached 99.1% accuracy for two (COVID and Normal) class classification, 94.2% for three (Normal, COVID and non-COVID) class classification and 91.2% for four (COVID, non-COVID viral pneumonia, Normal,

					and non-COVID bacterial pneumonia) class classification.
(Peng and Nagata, 2020: 1)	Brazil	Curve Fitting	Time series dataset	SVR	Case estimation was performed for 12 countries using the SVR algorithm and different kernel functions were tested. The Gaussian Kernel had the best within sample performance and the worst out of sample performance. The Linear Kernel function performed poorly within the sample, but achieved a good out of instance performance
(Javor et al., 2020: 3)	Austria	Diagnosis of Covid-19	Image dataset - CT images	CNN	The proposed CNN-based machine learning model classifier reached 94.5% accuracy and 0.956 AUC. The proposed algorithm has achieved superior predictive performance than two radiologists with more than 15 years of experience.
(Wang et al., 2020: 4-5)	China	Curve Fitting	Time series dataset	Logistic R., Prophet	The fastest growth point among five countries, the size of the epidemic and the time of peak was predicted. The outbreak size for the global is estimated to peak on June 21 with 3,603,111 active infections. It is learned that it will be 14.117.911 at the end of October and the fastest growth point is on May 16.
(Li et al., 2021: 3)	China, USA	Diagnosis of Covid-19, prediction symptoms	Clinical data	logistic regression	Factors associated with mortality and case rates were identified for 154 countries and 50 US states. 27 variables were selected using LASSO, and AUC values of 0.80, 0.83, and 0.81 were reached in estimates of case, death, and case fatality rates in the test set.
(Otoom et al., 2020: 7)	Jordan, Canada	Diagnosis of Covid-19	Clinical data-symptom data	SVM, NN, NB, KNN, Decision Table, Decision Stump, OneR, and ZeroR	The results showed that five algorithms achieved over 90% success. SVM achieved an accuracy of 92.95%, NN 92.89%, NB, 90.58%, KNN 92.89%.
(Althnian et al., 2020: 6-7)	Saudi Arabia, US	Prediction susceptibility	Clinical data - demographic data	MLP, SVM, DT, RF	Susceptibility describes the likelihood of an individual becoming infected. As a result of the study, DT achieved 85.6% RF 85.3%, MLP 77.2%, and SVM 74.2% accuracy. DT 0.76 and RD 0.77 performed slightly better than MLP 0.71 and SVM with AUC value of 0.77.
(Singh et al., 2020: 7-8)	India	Curve Fitting	Time series dataset	LS-SVM, ARIMA	According to the error information measured at the end of the article (MAE, MSE and RMSE), LS-SVM performed better than the ARIMA model and showed a sharp increase for one month later cases within five countries.
(Toğaçar, Ergen, and Cömert, 2020: 11)	Turkey	Diagnosis of Covid-19	Image dataset - X-ray images	SVM	In the article, a classification process in three classes (coronavirus, pneumonia, normal) was carried out. The success rate was 99.34% in Covid-19 data, 98.47% in Pneumonia data and 98.68% in normal images. The overall classification rate is 99.27%, which shows that the SMO algorithm contributes to the classification success.
(Tuncer, Dogan, and Ozyurt, 2020: 9)	Turkey	Diagnosis of Covid-19	Image dataset - X-ray images	DT, linear discriminant (LD),SVM, kkNN, subspace	SVM was chosen as the best classifier with 100.0% classification accuracy and 99% overall success rate. DT was the worst performing result.

				discriminant (SD)	
(Khan, Abbas, and Truong, 2020: 4-8)	China, Vietnam, Pakistan	Prediction mortality	Time series dataset	Gaussian Process Regression, Polynomial R.	Turkey, Spain, Sweden, France and five different models were generated using the number of deaths and cases according to the number of cases in Pakistan. According to the results, the RMSE value of GPR is lower among five countries. The Pakistan model created using GPR has an RMSE value of 1.796739, while the Swedish model has an RMSE value of 2.370486. Therefore, the Swedish model is the most suitable model for predicting Pakistan's mortality rate.
(Ribeiro et al., 2020: 7)	Brazil	Curve Fitting	Time series dataset	ARIMA, RF, SVR, cubist regression (CUBIST), ridge regression (RIDGE),stacking-ensemble learning	The article aims to estimate the daily number of cases in Brazil 1, 3 and 6 days ahead. In most scenarios, SVR and stacking-ensemble learning has achieved better performance than other algorithms. Order of algorithms by success values SVR, stacking ensemble learning, RIDGE, CUBIST, ARIMA and RF.
(Banerjee et al., 2020: 5-7)	UK	Diagnosis of Covid-19	Clinical data - laboratory (blood tests)	Logistic regression, RF, ANN, Glmnet	In the diagnostic procedure using the full blood count, ANN achieved 95%, RF 94% and glmnet 94% AUC. ANN 82%, RF 86% and glmnet 84% AUC values were obtained in the diagnosis process for patients not admitted to the hospital.
(Mondal et al., 2020: 11-12)	Bangladesh	Curve Fitting, Diagnosis of Covid-19	Clinical data - laboratory, time series	SVM, kNN, XGBoost,MLP, logistic R., DT, RF, ensemble methods, Linear R, Polynomial R.	The number of cases worldwide is modeled using regression, and classification algorithms are used to diagnose COVID-19. Among the regression models used for the number of cases, polynomial regression of degree Two cases were predicted with 98.60% accuracy and performed better than linear regression. MLP, Logistic regression and XGBoost were chosen as the best classification models with 91% accuracy. In addition, "Serum Glucose" was determined as the first best feature, Respiratory Syncytial Virus "second" Influenza A "was the third best feature.
(Nikil, Dalmia, and Kumar, 2020: 3)	India	Prediction	Time series dataset	K-means	The chart created using Tests vs. Cases contains two sets, while the Cases and Deaths chart contains three sets. In this study, it was found that different conditions and precautions should be taken for different people by cluster analysis. At this stage, regional precautions are one of the good ways to be followed, and the elderly and those with respiratory problems are more risky than other groups.
(Kuo and Fu, 2021: 5-6)	USA	Curve Fitting	Time series dataset	Elasticnet (EN), PCR, partial least squares regression (PLSR) model, KNN, regression tree (RT),	In the article, a case prediction model based on demographic, mobility and environmental data was developed at district level. All classifiers reached a value of R2> 0.81 for the number of cases per day, and a value of R2> 0.92 for the estimation of the cumulative number of cases. In addition, RF, GBM and ANN models have achieved good results in estimating the number of daily cases, while EN and GBM have obtained good results in estimating the cumulative number of cases due to low RMSE and MAE values.

				RF, GBM, ANN	
(Di Castelnuovo et al., 2020: 7-13)	Italy, USA	Prediction	Clinical data - vital values, laboratory and demographic data	RF and COX	In this study, the most determining factors were analyzed by predicting the susceptibility to death for Covid-19 patients. The RF model achieved a strong prediction success with 95.2% sensitivity, 30.8% specificity, 83.4% classification accuracy, and 90.4% F1 value. He also found that the most defining characteristics were eGFR, CRP and age. These results have been validated using Cox survival analysis.
(Yadav, Perumal, and Srinivas, 2020: 9)	India	Curve Fitting	Time series dataset	Linear R., Polinomial R.,SVR	In the study, five different analyzes such as the date the epidemic will end, the transmission rate and the growth rate were carried out. The results showed that the SVR model obtained efficient and effective results compared to other models in the estimations made for five countries.
(Amar, Taha, and Mohamed, 2020: 12)	Egypt	Curve Fitting, Prediction	Time series dataset	7 regression model	In the study, it was estimated when the epidemic would end with the number of patients to be infected. Exponential fourth-order, fifth-order, and sixth-order polynomial regression models have reached the best results for predictions over a one-month period. In addition, as a result of the logit growth regression model, it is predicted that the peak of the epidemic will be on 22 June 2020 and the end time will be on 8-September 2020.
(Brunese et al., 2020: 9)	Italy	Diagnosis of Covid-19	Image dataset - Chest X-ray images	k-NN	The method suggested in the article reached 0.965 average sensitivity and an average recall values. Compared to other categories, a precision of 0.968 and a recall value of 0.964 show that the machine learning method can distinguish between Covid-19 and other categories with good performance.
(Chakraborti et al., 2021: 3)	India, Ireland	Curve Fitting, Prediction	Time series dataset	RF, GBM	Machine learning methods were used in this study to determine the characteristics associated with the Covid-19 case and death numbers. A total of 11 variables were determined for Covid-19 cases and a total of 15 variables for their deaths. Among the variables considered, the explanatory variables discussed in this study were air pollution, demographic, migration, and economy data as the most determining factors.
(Kavadi et al., 2020: 6-7)	India	Curve Fitting	Clinical data	Partial derivative regression and nonlinear machine learning (PDR-NML)	The proposed model reduces the prediction time by 7% compared to the linear regression and 9% compared to the AI-based model, and it also increases the prediction accuracy by 2% compared to the linear regression and 3% compared to the AI-based model. This shows that the proposed method achieves better results than existing methods.

Using Various Renewable Energy Sources In Commercial Kitchens And Ensuring Energy Efficiency

Zafer KAHRAMAN[37]
Murat HACI[38]
Hakan Serhad SOYHAN[39]

Introduction

Commercial kitchen products (oven, cooker, grill, dishwasher, refrigerator, etc.) are widely used in places where there is mass food consumption (restaurants, hotels, dormitories, shopping centers, etc.). These products generally work with electricity or gas (natural gas, LPG, etc.) depending on the place of use. In addition to the increase in the population worldwide, the demands for energy are also increasing with the technological developments. Especially in fossil fuels (petroleum, natural gas, coal, etc.), the limited resources as well as the difficulties in supplying energy, fluctuations in prices and the polluting emissions of these resources in terms of the environment have emerged as important problems in recent years (Ang & et al., 2022; Ilechukwu & Lahiri, 2022; Shrestha & et al., 2022; Yang & et al., 2022; Yang, Zheng & Chang, 2022). For this reason, interest and investments in renewable energy sources (green energy) are increasing hydrogen, biogas, solar, wind, etc., which are within the scope of environmentally friendly resources. Research and development studies are also carried out intensively to expand the usage areas of energy resources (Hailemariam, Ivanovski & Dzhumashev, 2022).

Within the scope of this study, evaluations were made regarding the use of renewable energy (hydrogen, biogas, solar energy, wind energy, etc.) for various products in commercial kitchens and various studies to be carried out in the future. Innovative prototypes with original designs have been developed with activities based on R&D systematics, especially for commercial kitchen cooking products that use hydrogen and biogas from renewable energy sources. With the data in the test and evaluation stages, it has been achieved to use renewable energy sources effectively and efficiently in innovative prototypes.

Literature Review

Summaries of various literature studies on the characteristics and use of different renewable energy sources are given below.

It was emphasized that continuous improvements should be made in the research methods used in cooking studies in order to benefit the ecological environment and human health. It was stated that the literature should be systematically reviewed in order to facilitate rational design and improvements to be made in relation to cooking activities in line with sustainable development goals. While designing

---

[37] Zafer Kahraman, Dr., Öztiryakiler Madeni Eşya San. ve Tic. A.Ş, ORCID: 0000-0002-2008-0533
[38] Murat Hacı, Eng., Öztiryakiler Madeni Eşya San. Ve Tic. A.Ş, ORCID: 0000-0001-9172-8096
[39] Hakan Serhad Soyhan, Prof.Dr., Sakarya University, ORCID: 0000-0003-3723-9640

models to be simulated in commercial and residential kitchens, large-scale measurements and taking various precautions were emphasized (Li, 2021).

Due to the long-term negative effects of petrochemical use and economic crises, wind energy has emerged as a cost-effective energy source. It has been emphasized that it is emission-free, green and at the same time has the advantages of government subsidies and credits for taxes. It has various positive effects such as (i) environmental (ii) social (iii) economic and (iv) cultural effects. The potential impacts of emerging renewable technology are given in Figure 1 (Nazir & et al., 2020).
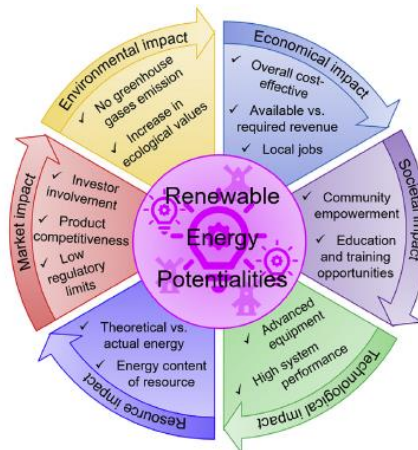
Figure 1. A view of the potential impacts of emerging renewable technology (Nazir & et al., 2020).

Renewable energies are defined as energy sources that do not run out as they are used. Renewable energy sources can be evaluated under five main headings, such as biomass obtained from plants and other wastes, wind energy, solar energy, hydroelectric energy obtained from running water and geothermal energy. Renewable energy can also be defined as clean energy as it does not produce additional pollution or waste like fossil fuel energies. Renewable energy sources have a low carbon footprint and produce less greenhouse gases. Clean energy has grown in popularity in recent years as various countries and economies are concerned to minimize their high dependence on fossil fuels. Renewable and sustainable clean energy conversions and applications are shown in Figure 2 (Jaiswal & et al., 2022).
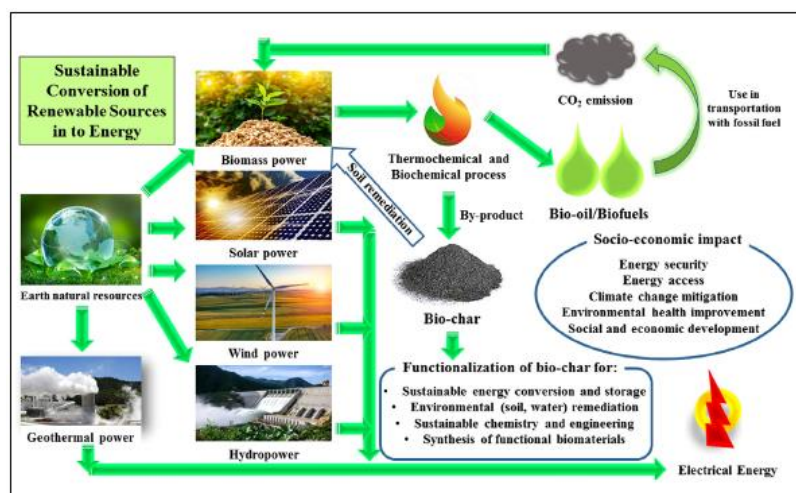
Figure 2. Renewable and sustainable clean energy conversion and applications (Jaiswal & et al., 2022).

Biomass includes bioenergy producing plant and animal materials such as bio-oil, cellulosic ethanol, renewable hydrocarbon fuels and biodiesel. Biomass includes agricultural waste, food waste, animal waste (fish, chicken waste, etc.), wood waste, food processing waste, organic waste, organic household waste and municipal waste. Various biomass feedstock sources for renewable bioenergy and biofuels are given in Table 1 (Jaiswal & et al., 2022).

Table 1. Different biomass feedstock sources for renewable bioenergy and biofuels (Jaiswal & et al., 2022).

Sources of biomass	Feedstocks	Bioenergy and biofuels	Applications
Wood by-Products	Firewood, wood chips, wood pellets, lumber, bark, furniture mill sawdust, wood processing residues	Heat energy, light energy, combined heat and power, cellulosic ethanol, electricity production, compost	Domestic use for cooking/heating, natural fertilizers, soil conditioners, agriculture mulches
Agricultural by-products	Corn cobs, fruit pits, straw, leaves, grass trimmings, lumber, bark, branches, agricultural crop residues, algae, forestry residues	Heat energy, light energy, combined heat and power, cellulosic ethanol, electricity production, compost	Domestic use for cooking/heating, natural fertilizers, soil conditioners, agriculture mulches
Solid waste	Residential and commercial garbage, paper/cardboard, vegetable/fruit peels, leftover/waste food	Heat energy, light energy, electricity production, compost	Domestic use for cooking/heating, natural fertilizers, soil conditioners, agriculture mulches
Non-crop foods plants, corn, sugarcane, agricultural residues	Cellulosic components	Bio-alcohol fuels, cellulosic ethanol, methanol, ethanol-blended petrol	Transportation vehicle usage
Landfills, leachate, manure, municipal wastewater, industrial wastewater	Biogas	Methane, liquid fuel, electricity generation, methanol production	Transportation and domestic fuel for cooking

Clean energy solutions include protecting the environment and ensuring energy security. A 3S concept including resource, system and service is being implemented. The resource specified in this concept constitutes the identification and selection of clean resources that are naturally available and whose use is technologically valid. They stated that the choice of resource depends on the natural and infrastructural situation in a particular region. The system specified in the concept includes the identification and selection of methods and systems that use environmentally friendly raw materials for clean energy production. forms. Hydrogen application of the 3S concept to obtain clean and sustainable products is given in Figure 3 (Razi & Dincer, 2022).
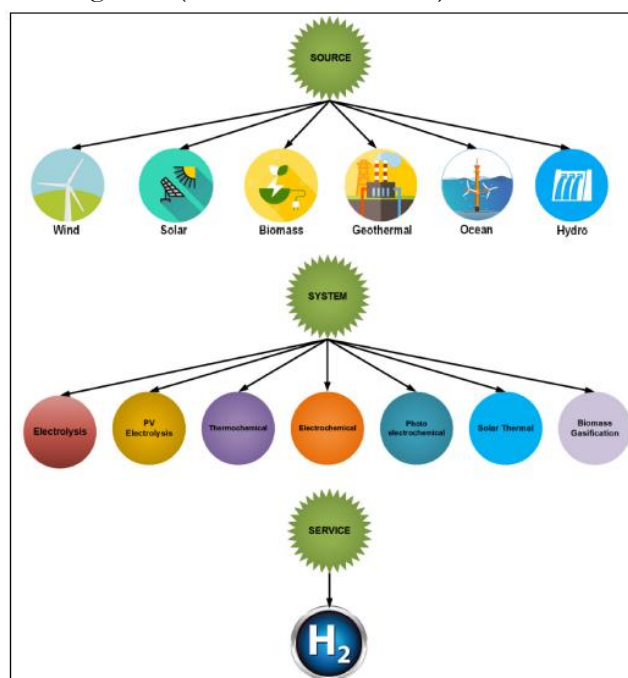

Figure 3. 3S (Source, System, Service) conceptual illustration for clean hydrogen production (Razi & Dincer, 2022).

Olabi and Abdelkareem reported that there are different obstacles to the spread of renewable energy sources as a reliable power source. The main barriers to renewable energy sources are shown in Figure 4 (Olabi & Abdelkareem, 2022).
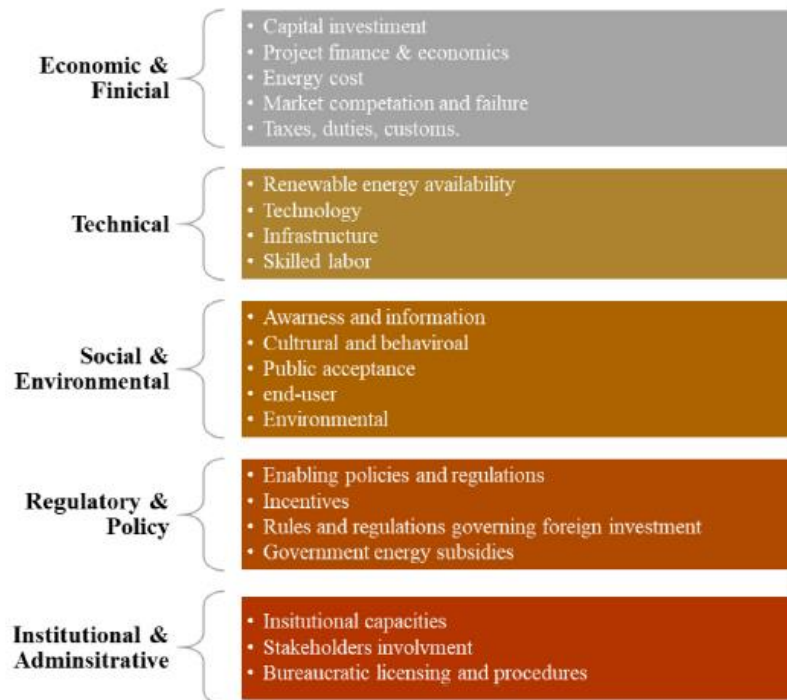

Figure 4. The main obstacles to renewable energy sources (Olabi & Abdelkareem, 2022).

While fossil fuels dominate in hydrogen production, a low amount of renewable energy sources are used. The classification of various methods used in hydrogen production is given in Figure 5 (Amin & et al., 2022).
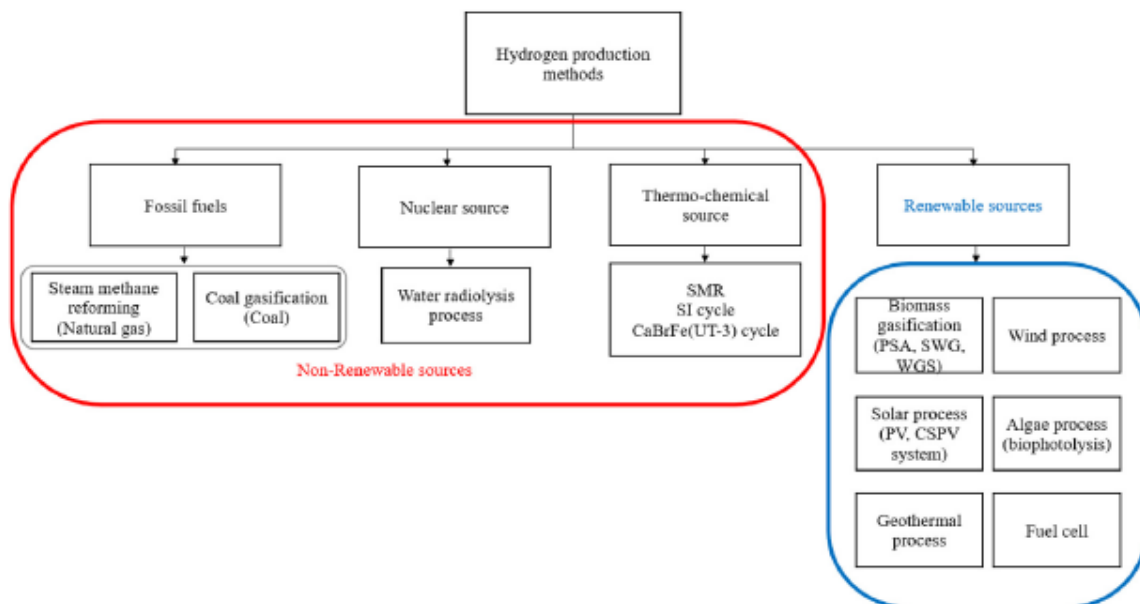
Figure 5. The classification of various methods used in hydrogen production (Amin & et al., 2022).

It was emphasized that the use of water electrolysis technology to produce hydrogen is a clean and efficient development. They emphasized that in addition to the high costs of water electrolysis technologies, the unit electric energy price also stands out as the main factor in the cost of hydrogen production by water electrolysis. The trend estimate for the main hydrogen sources is given in Figure 6 (Wang & et al., 2022).
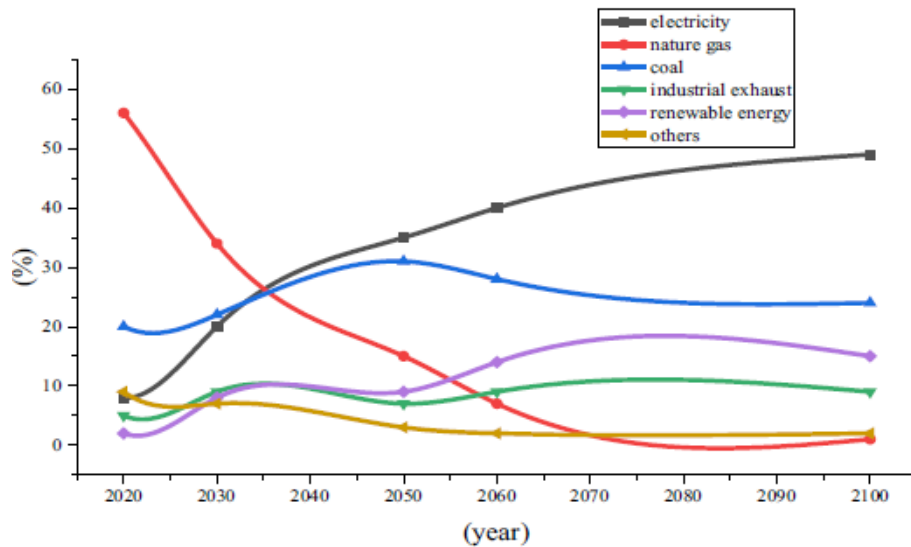
Figure 6. Trend forecast for the main hydrogen sources (Wang & et al., 2022).

The hydrogen energy industrial chain is basically divided into 3 main groups. These groups cover upstream hydrogen production, midstream hydrogen storage and distribution, and downstream integrated applications. In addition, various technologies such as material innovation, equipment production, assembly procedures and project techniques are also included in the industrial chain. Illustration of hydrogen energy industry chain is given Figure7 (Pingkue & Xue, 2022).
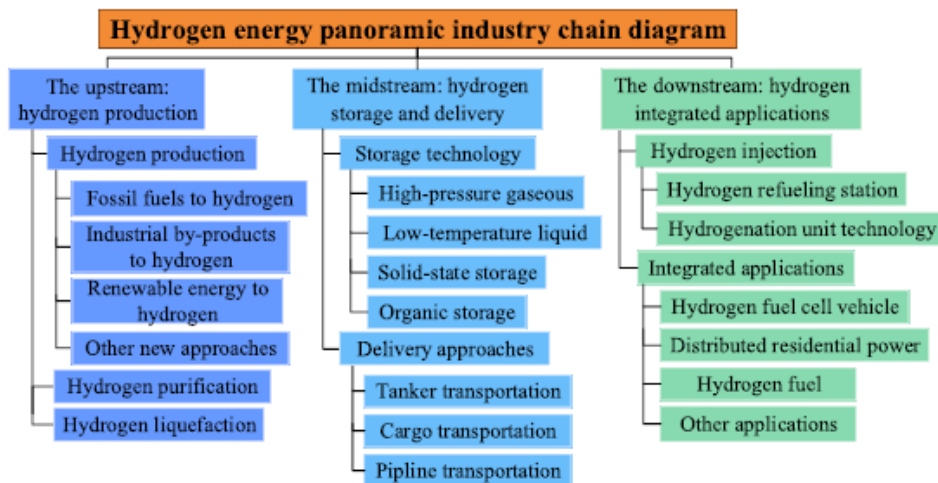

Figure 7. Illustration of hydrogen energy industry chain (Pingkue & Xue, 2022).

Arenas evaluated the design of a small-volume, folding parabolic solar reflector and the kitchen for cooking using portable solar energy, prototype production and tests. With the developed prototype, it has been reported that an average power value of 175 W and an energy efficiency of 26.6% have been achieved by using solar energy. It has been reported that a portable, inexpensive, environmentally friendly heating system has been developed for cooking, which can improve the quality of life of people in need and reduce traditional energy consumption. The environmental

changes (ambient temperature and water) in the kitchen using solar energy are given in Figure 8 (Arenas, 2007).
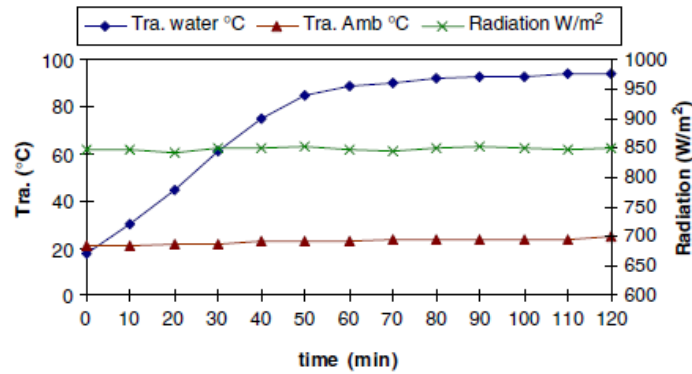

Figure 8. Variation of ambient temperature and water in the kitchen using solar energy (Arenas, 2007).

Methods

Two different innovative prototypes using hydrogen and biogas as clean energy sources for commercial kitchens have been developed with R&D systematics. Original designs were made for two different prototypes. In line with the standards for the long-term use of commercial kitchen products, the main bodies of the prototypes are made of stainless steel materials.

Original designs of various equipment (burner, injector, burner head, etc.) constituting the combustion unit of the hydrogen using commercial cooker developed specifically for the design were made. During the design verification phase, simulation studies were carried out according to various parameters, and a unique burner structure was obtained according to various hole diameters and numbers, especially on the burner head in the use of hydrogen. The commercial kitchen cooker using hydrogen is shown in Figure 9.

(a)   (b)

Figure 9. The image of the prototype of the commercial kitchen cooker using hydrogen (a) front view, (b) top view.

The photograph of the commercial cooker prototype using biogas is given in Figure 10. Food waste has been evaluated for the operation of the environmentally friendly system.

(a)   (b)

Figure 10. Photograph of the commercial cooking cooker prototype using biogas (a) front view, (b) input of food waste into the system.

After the test and evaluation stages, it has been achieved to obtain innovative prototypes (hydrogen and biogas) using two different green energy in the commercial kitchen area.

Conclusion

In this study, evaluations were made regarding the use of renewable energy (hydrogen, biogas, solar energy, wind energy, etc.) for various products in commercial kitchens and various studies to be carried out in the future. Innovative prototypes with original designs have been developed with activities based on R&D systematics, especially for commercial kitchen cooking products that use hydrogen and biogas from renewable energy sources. With the data in the test and evaluation stages, it has been achieved to use renewable energy sources effectively and efficiently in innovative prototypes. It has been provided with scientific data on innovative prototypes that can be used as alternative energy of green energy sources for commercial kitchens. In addition to the reduction of unit cooking times of hydrogen energy, significant gains have been achieved in terms of energy efficiency.

In the commercial kitchen sector, within the scope of the development of the green kitchen concept against fossil fuels, the production of innovative products using clean energy (hydrogen, biogas) has been achieved through activities based on the R&D system.

Acknowledgement

References

Amin, M., Shah, H.H., Fareed, A.G., Khan, W.U., Chung, E., Zia, A., Farooqi, Z.U.R., Lee, C. (2022). Hydrogen production through renewable and nonrenewable energy processes and their impact on climate change. *International journal of hydrogen energy, (47)*, 33112-33134.

Ang, T-Z., Salem, M., Kamarol, M., Das, H.S., Nazari, M.A., Prabaharan, N.A. (2022). A comprehensive study of renewable energy sources: Classifications, challenges and suggestions. Energy Strategy Reviews*, (43)*, 100939.

Arenas, J.M. (2007). Design, development and testing of a portable parabolic solar kitchen. *Renewable Energy, (32)*, 257–266.

Hailemariam, A., Ivanovski, K., Dzhumashev, R. (2022). Does R&D investment in renewable energy technologies reduce greenhouse gas emissions?. *Applied Energy, (327),* 120056.

Ilechukwu, N. & Lahiri, S. (2022). Renewable-energy consumption and international trade. *Renewable Energy, (8),* 10624–10629.

Jaiswal, K.K., Chowdhury, C. R., Yadav, D., Verma, R., Dutta, S., Jaiswal, K.S., SangmeshB, Karuppasamy, K.S.K. (2022). Renewable and sustainable clean energy development and impact on social, economic, and environmental health. *Energy Nexus, (7),* 100118.

Li, J. (2021). Insights into cooking sources in the context of sustainable development goals. *Sustainable Production and Consumption, (26),* 517–531.

Nazir, M.S., Bilal, M., Sohail, H.M., Liu, B., Chen, W., Iqbal, H.M.N. (2020). Impacts of renewable energy atlas: Reaping the benefits of renewables and biodiversity threats. *International journal of hydrogen energy, (45)*, 22113-22124.

Olabi, A.G., Abdelkareem, M.A. (2022). Renewable energy and climate change. *Renewable and Sustainable Energy Reviews, (158),* 112111.

Overland, I., Juraev, J., Vakulchuk, R. (2022). Are renewable energy sources more evenly distributed than fossil fuels?. *Renewable Energy, (200),* 379-386.

Pingkuo, L., Xue, H. (2022). Comparative analysis on similarities and differences of hydrogen energy development in the World's top 4 largest economies: A novel framework. *Internatioanal journal of hydrogen energy, (47),* 9485-9503.

Razi, F. & Dincer, I. (2022). Renewable energy development and hydrogen economy in MENA region: A review. *Renewable and Sustainable Energy Reviews, (168),* 112763.

Shrestha, A., Mustafa, A.A., Htike, M.M., You, V., Kakinaka, M. (2022). Evolution of energy mix in emerging countries: Modern renewable energy, traditional renewable energy, and non-renewable energy. *Renewable Energy, (199),* 419–432.

Wang, H., Zhao, X., Zhang, K., Wang, W. (2022), Economic assessment of a renewable energy-electricity-hydrogen system considering environmental benefits. *Sustainable Production and Consumption, (33),* 903–920.

Yang, Q-C., Zheng, M., Chang, C-P. (2022). Energy policy and green innovation: A quantile investigation into renewable energy. *Renewable Energy, (189),* 1166-1175.

Yang, Z., Zhang, M., Liu, L., Zhou, D. (2022). Can renewable energy investment reduce carbon dioxide emissions? Evidence from scale and structure. *Energy Economics, (112),* 106181.

References

Amin, M., Shah, H.H., Fareed, A.G., Khan, W.U., Chung, E., Zia, A., Farooqi, Z.U.R., Lee, C. (2022). Hydrogen production through renewable and nonrenewable energy processes and their impact on climate change. *International journal of hydrogen energy, (47)*, 33112-33134.

Ang, T-Z., Salem, M., Kamarol, M., Das, H.S., Nazari, M.A., Prabaharan, N.A. (2022). A comprehensive study of renewable energy sources: Classifications, challenges and suggestions. Energy Strategy Reviews*, (43)*, 100939.

Arenas, J.M. (2007). Design, development and testing of a portable parabolic solar kitchen. *Renewable Energy, (32)*, 257–266.

Hailemariam, A., Ivanovski, K., Dzhumashev, R. (2022). Does R&D investment in renewable energy technologies reduce greenhouse gas emissions?. *Applied Energy, (327),* 120056.

Ilechukwu, N. & Lahiri, S. (2022). Renewable-energy consumption and international trade. *Renewable Energy, (8),* 10624–10629.

Jaiswal, K.K., Chowdhury, C. R., Yadav, D., Verma, R., Dutta, S., Jaiswal, K.S., SangmeshB, Karuppasamy, K.S.K. (2022). Renewable and sustainable clean energy development and impact on social, economic, and environmental health. *Energy Nexus, (7),* 100118.

Li, J. (2021). Insights into cooking sources in the context of sustainable development goals. *Sustainable Production and Consumption, (26),* 517–531.

Nazir, M.S., Bilal, M., Sohail, H.M., Liu, B., Chen, W., Iqbal, H.M.N. (2020). Impacts of renewable energy atlas: Reaping the benefits of renewables and biodiversity threats. *International journal of hydrogen energy, (45)*, 22113-22124.

Olabi, A.G., Abdelkareem, M.A. (2022). Renewable energy and climate change. *Renewable and Sustainable Energy Reviews, (158),* 112111.

Overland, I., Juraev, J., Vakulchuk, R. (2022). Are renewable energy sources more evenly distributed than fossil fuels?. *Renewable Energy, (200),* 379-386.

Pingkuo, L., Xue, H. (2022). Comparative analysis on similarities and differences of hydrogen energy development in the World's top 4 largest economies: A novel framework. *Internatioanal journal of hydrogen energy, (47),* 9485-9503.

Razi, F. & Dincer, I. (2022). Renewable energy development and hydrogen economy in MENA region: A review. *Renewable and Sustainable Energy Reviews, (168),* 112763.

Shrestha, A., Mustafa, A.A., Htike, M.M., You, V., Kakinaka, M. (2022). Evolution of energy mix in emerging countries: Modern renewable energy, traditional renewable energy, and non-renewable energy. *Renewable Energy, (199),* 419–432.

Wang, H., Zhao, X., Zhang, K., Wang, W. (2022), Economic assessment of a renewable energy-electricity-hydrogen system considering environmental benefits. *Sustainable Production and Consumption, (33),* 903–920.

Yang, Q-C., Zheng, M., Chang, C-P. (2022). Energy policy and green innovation: A quantile investigation into renewable energy. *Renewable Energy, (189),* 1166-1175.

Yang, Z., Zhang, M., Liu, L., Zhou, D. (2022). Can renewable energy investment reduce carbon dioxide emissions? Evidence from scale and structure. *Energy Economics, (112),* 106181.

Evaluation of Grapefruit Peel Extract for Control of *Meloidogyne Incognita* on Tomato

Fatma Gül GÖZE ÖZDEMİR[1]

INTRODUCTION

Plants in the genus produce Citrus fruits, including important crops such as oranges, mandarins, lemons, grapefruits, pomelos, and limes. Citrus are a group of fruits that are widely produced and consumed around the world. Around 98 million tons of citrus fruits were produced in the world in 2021, 7 million tons of which was grapefruit production (USDA, 2021). Citrus fruits can be consumed fresh or processed and used as additives in fruit juices, jams, carbonated beverages and food products. Its consumption has also increased in recent years due to its potential benefits associated with antioxidant, anticancer and anti-inflammatory properties (Benavente-García ve Castillo 2008; Dosoky ve Setzer, 2018). These properties make citrus essential oils and compounds a potential and valuable alternative for the pharmaceutical and food industries. Large-scale consumption and processing of citrus fruits results in the production of large volumes of citrus peel, which is often disposed of as agro-industrial waste. Fruit peels can be used positively for oil production. However, industrial processing increases the value of citrus fruits by producing various seconder products (pectin, pulp and flavonoids etc.) (Ahmed vd., 2019). Citrus essential oils contain compounds rich in monoterpene and sesquiterpene hydrocarbons as well as their oxygenated derivatives (Gonz´alez-Mas vd., 2019). It has been reported that some compounds in the monoterpenoid group cause significant inhibition of acetylcholinesterase activity, thus affecting the nervous system of nematodes (Saad vd., 2018). In addition, different researchers have determined the nematicidal effects of citrus extracts on plant parasitic nematodes (Oyedunmade vd., 2001; Oyedunmade, 2004; Abolusoro vd., 2010). Limonene, linalool, citronellal and citral compounds found in most Citrus plants are among the monoterpenes (Liu vd., 2022).

The most common root-knot nematode species in vegetable growing areas in the world and in Türkiye are *Meloidogyne incognita* (Kofoid ve White, 1919) Chitwood, 1949 (Tylenchida: Meloidogyidae), *Meloidogyne javanica* (Treub, 1885) Chitwood, 1949, *Meloidogyne arenaria* (Neal, 1889) Chitwood, 1949, and *Meloidogyne hapla* Chitwood, 1949 (Adam vd., 2007; Uysal vd., 2017; Gürkan vd., 2019; Ghaderi ve Karssen, 2020; Maleita vd., 2021). *Meloidogyne incognita* is the most common species among root knot nematodes, it can infect almost all plants and causes significant economic damage in all subtropical-tropical regions (Hallmann ve Kiewnick, 2018; Eder vd., 2021). Root-knot nematodes feed on roots and vascular tissues, disrupt water and nutrient flow, and show symptoms such as stunning, slow growth, yellowing of leaves, wilting and early plant death in infected plants (Asaturova vd., 2022). It is seen that mostly nematicide-effective chemicals are used in the control of root-knot nematodes (Hajihassani vd., 2022). Although nematicides can effectively

[1] Dr. Öğr. Üyesi, Isparta Uygulamalı Bilimler Üniversitesi, Ziraat Fakültesi, Bitki Koruma Bölümü, Orcıd: 0000-0003-1969-4041

suppress nematodes, their use is limited due to their short-term effects. In addition, high costs, adverse health and environmental hazards, residue, negative effects on soil fauna and beneficial microflora, and phytotoxic effects on plants are other factors limiting the use of nematicides (Haydock vd., 2013; da Silva vd., 2019). This situation has made it necessary to search for alternative control methods for the control of plant parasitic nematodes. Plant extracts are inexpensive and readily available compared to conventional nematicides and are considered environmentally safe (Abolusoro vd., 2010). Natural plant products are currently the focus of research efforts due to their ability to produce chemicals that are less harmful to the environment and more effective (Javed vd., 2006). Many plants have nematicidal properties in their roots, shoots, leaves, flowers, seeds and extracts, essential oils, oilseed cake and derivatives (Regaieg vd., 2017).

Grapefruit (*Citrus paradisi*) contains various phytochemicals such as flavonoids (naringin), carotenoids, limonoids, organic acids, pectin and folate, and it is known that grapefruit has health-protecting properties thanks to these phytochemicals (Girennavar vd., 2008; Vikram vd,. 2010; Uckoo vd., 2011). The single and combined treatments of aqueous extracts of the peels of lemon, orange, grapefruit and pomegranate fruits were investigated on the mortality effect on *M. incognita* second stage juveniles (J2s) and the nematostatic effects on hatching (Göze Özdemir, 2022). The mortality effect of only the aqueous extracts of grapefruit peel on J2s was found to be 63.7% after 24 hours, and 99.0% after 48 hours *in vitro*. In addition, the percentage of suppression of the hatching of *M. incognita* 7 days after the application of the aqueous extract of grapefruit peel was reported as 54.2%. It was determined that the nematicidal effect increased in combinations of grapefruit with other fruit peels (Göze Özdemir, 2022). It is seen that studies on the use of fruit wastes or fruit peels against plant parasitic nematodes are quite scarce (Ashraf ve Khan, 2008; Tsai, 2008, Ismail, 2015; Akhtar vd., 2019). In the control of root-knot nematodes, direct mixing of fruit peels into the soil or using their extracts can provide multi-faceted benefits with both waste management and reduction of pesticide use. In present study, the effect of direct mixing of grapefruit peels into the soil and application of aqueous extract on *M. incognita* gall and egg masses was investigated.

MATERIALS AND METHODS

Fruit Peel Extraction

Five kg of grapefruit s were peeled and the peels were cut into small pieces of about 0.25 cm^2. It was sun-dried on paper for 3 days and powdered in an herbal spice grinder. It has been used in application to be mixed directly into the soil. To prepare the aqueous extract, 100 g of powdered fruit peel was weighed and 400 ml of sterilized distilled water was added to it. This mixture was then stirred at room temperature for 24 hours using a magnetic stirrer. Twenty-four hours later, it was filtered through Whatman No.41 filter paper and the extracts were pooled and concentrated under vacuum at 40 °C. This filtrate was used as 100% concentration and diluted with distilled water to obtain other concentrations (10%, 25% and 50%). It was then covered and stored in the bottles in a refrigerator at +4 °C until the experiment was set up (Regaieg vd., 2017).

Nematode Inoculum

In the study, *M. incognita* isolate, which is kept in Tueza F1 tomato cultivars and renewed every 2-3 months, was used in the climate room conditions (24±1 °C, 60%±5% RH) of ISUBU Faculty of Agriculture, Department of Plant Protection (Göze Özdemir vd., 2022).

In order to obtain *M. incognita* J2s, 2 of the galled tomato roots were selected and sterilization was carried out containing 0.5% sodium hypochlorite for 3 minutes and washed 3 times with sterile water. The egg masses was removed from these roots with the help of forceps and scalpel under a stereomicroscope and incubated for 5 days at 28°C in a 9 cm petri dish containing distilled water (Misiha vd., 2013). At the end of the five days, the hatched J2s were settling for 6 hours after taking a tape measure. Then, by counting under the light microscope, the inoculums were prepared in eppendorf tubes with 1000 J2 per pot and stored at 4°C in the refrigerator until the experiment was established.

Effect of Application of Grapefruit Peel Extracts to Tomato Roots on The Development of *Meloidogyne incognita*

Varied concentrations of dry powder (3.0, 6.0 and 9.0 g/1 kg soil) and aqueous extracts (undiluted, diluted concentration 10%, 25% and 50%) from grapefruit peels as a soil amendment were investigated on *M. incognita* in Tueza F1 tomato cv. Four-week-old tomato seedlings of tomato were transplanted into 15-cm-diameter pots containing 1 kg of sterile soil mixture (% 68 sand, % 21 silt and %11 clay). Only plants treated with nematodes were used as a control. Five replicated pots per treatment were used. The 1000 J2s were used in the nematode inoculum. Two days after nematode inoculation, different rates of powdery extracts were incorporated into the soil by sprinkling it over the soil around the plant. Fifty millilitre of aqueous extract was measured and applied to each of the pots using the various concentrations obtained. After six weeks, plants were carefully removed and the roots were excised from the shoot and washed under tap water. Then, galls and egg masses in roots were counted under the binocular stereo microscope. Evaluation was made according to the 0-5 root gall index where 0 = no galls, 1 = slight infection, 2 = moderate infection, 3 = moderately severe, 4 = severe, 5 = very severe (Regaieg, 2011).

SPSS (version 20.0) program was used for statistical analysis of the data obtained as a result of the experiment, and analysis of variance (ANOVA) was performed to test the differences between the means. Means were compared with the Tukey HSD test at $P \leq 0.05$.

RESULT and DISCUSSION

The highest number of galls (74.8) and egg masses (72.8) were found in the control. It was determined that powder and aqueous extract treatments of grapefruit decreased galls and egg masses significantly when compared to the control. While the number of galls in the treatments varied between 13.0 and 74.8, the number of egg masses varied between 12.4-72.8. In powder treatments, the number of gall and egg mass decreased as the amount added to the soil increased. The highest number of galls and egg masses was found in 3 g/kg soil powder treatment, while the lowest was found in 9 g/kg soil. In the treatment of aqueous extract, it was observed that the suppressive effect on the gall and egg mass decreased as the dilution increased. There was no statistically significant difference between the mean of galls and egg masses of undiluted concentration (100%) and 10% diluted concentration treatments. The effects of 25% and 50% diluted aqueous extract treatments on gall and egg masses were found to be similar. The lowest number of gall and egg masses was determined in of 9 g/kg soil powder treatment, undiluted and 10% diluted aqueous extract treatments (Table 1).

The gall index of the treatments varied between 2.8 and 4.0. The highest gall index were determined in 25% and 50% concentration aqueous extract and control treatments and there was no statistical difference between them. The gall index of undiluted and 10% diluted concentration treatments was found to be lower than 25% and 50% treatments. There is no statistical difference

between the gall index of the powder application doses and undiluted and 10% diluted aqueous extract treatments (Table 1).

Table 1. The effects of grapefruit peel powder and aqueous extract treatments on the development of *Meloidogyne incognita* on tomato

Treatments		The number of galls	The number of egg masses	Gall index*
		Mean±Standard error**		
Powder	3 g/ kg soil	27,0±2,4 bc	26,4±2,1 bc	3,2±0,2 b
	6 g/ kg soil	17,4±1,5 cd	16,2±1,3 cd	3,0±0,0 b
	9 g/ kg soil	14,0±1,7 d	13,0±1,4 d	2,8±0,2 b
Aqueus extract	%100	13,0±1,2 d	12,4±1,3 d	2,8±0,2 b
	%10	15,4±2,2 d	15,0±2,0 d	2,8±0,2 b
	%25	30,0±2,2 b	28,8±2,2 b	3,4±0,2 ab
	%50	38,0±3,1 b	37,2±3,0 b	4,0±0,0 a
	Control	74,8±4,0 a	72,8±4,0 a	4,0±0,0 a

*Gall index (0-5) index (Regaieg 2011); where 0 = no galls, 1 = slight infection, 2 = moderate infection, 3 = moderately severe, 4 = severe, 5 = very severe.

**Lowercase letters shown in the same column indicate statistical differences between treatments (P≤0.05)

Treatment of powder or undiluted aqueous extract of grapefruit peels was found to suppress galls and egg masses on tomato compared to control. It appears to be promising in root knot nematode control. The decrease in nematode infections is due to the toxicity of secondary products caused by the degradation of plant extracts in the soil and changes in the physical and chemical properties of the soil (Kayani vd., 2012). In some studies conducted with the essential oil of citrus peels, the main components were found to be limonene, neral, geranial, geranyl actate and geraniol (Chutia vd., 2009; Goyal vd., 2021). Nematicidal and nematotoxic monoterpenes are reported as anethole, citral, carvacrol, cymene, cineole, eugeneol, geraniol, limonene, pinene, terpineol and thymol (Liu vd., 2022). Regieg vd. (2017) reported that pomegranete powder extract was more toxic than aqueous extract. However, when the gall indexes are evaluated in this study, there is no difference between powder and aqueous extract treatments of grapefruit peel. This may be due to the difference in nematicidal compounds in pomegranate and grapefruit. Viuda-Martos vd. (2010) stated that the variety, cultivar, age, growing conditions and storage method of the plants may change the amount and efficacy of active compounds. Tsai (2008) reported that pulpified peels of lemon, orange, and grapefruit kept in the refrigerator for one week showed strong nematicidal activity as compared to extracts of fresh peels. There were significant differences in physicochemical, antioxidant properties and volatile profiles of extracted juice and oil extracted from eight grapefruit cultivars (Ahmed vd., 2019).

It was observed that the efficiency increased as the dose increased in powder treatments, while the dilution of more than 10% decreased the efficiency in the aqueous extract treatment in the study. Manju ve Sankari Meena (2015) found that the efficacy of botanicals increased with increasing doses, and generally higher dose was more effective in improving plant growth characteristics, reducing root-knot index and final soil nematode population. Ismail (2015) found

that nematode parameters showed a greater percentage reduction when higher rates of pomegranete peels were used.

This study shows that powder and aqueous extract of grapefruit can be applied to suppress root-knot nematode *Meloidogyne incognita* populations. When using only the aqueous extract, care should be taken not to dilute more than 25%. However, it is necessary to verify the nematicidal activity in field conditions as well.

The use of agro-industrial wastes for nematode control is important not only to provide an alternative to chemical nematicides, but also to assist in the disposal of agro-industrial wastes. In organic and sustainable agriculture, mixing organic wastes with soil has an important in suppressive soil formation. In this way, positive effects are obtained on beneficial soil microorganisms. For this reason, it is thought that it can also take part in the integrated control. Combining different methods in the integrated control is necessary in order to increase the success of nematode control.

REFERENCE

Abolusoro, S. A., Oyedunmade, E. A., Olabiyi, T. I. (2010). Evaluation of sweet orange peel aqueous extract (*Citrus sinensis*) as root–knot nematode suppressant. Agro Science, 9(3):170-175.

Adam, M. A. M., Phillips, M. S., Blok, V. C. (2007). Molecular diagnostic key for identification of single juveniles of seven common and economically important species of root-knot nematode (*Meloidogyne* spp.). Plant Pathology, 56: 190-197.

Ahmed, S., Rattanpal, H. S., Gul, K., Dar, R. A., Sharma, A. (2019). Chemical composition, antioxidant activity and GC-MS analysis of juice and peel oil of grapefruit varieties cultivated in India. Journal of Integrative Agriculture, 18(7), 1634-1642.

Akhtar, W., Abbasi, M.W., Rauf, A., Jahan, I, Anis, M., Javed Zaki M. (2019). Nematicidal activity of fruit pericarps against root knot nematode, *Meloidogyne javanica*. International Biology Research, 7(1): 57-65.

Asaturova, A. M., Bugaeva, L. N., Homyak, A. I., Slobodyanyuk, G. A., Kashutina, E. V., Yasyuk, L. V., Garkovenko, A. V. (2022). *Bacillus velezensis* Strains for protecting cucumber plants from root-knot nematode *Meloidogyne incognita* in a greenhouse. Plants, 11(3): 275.

Ashraf, M.S., Khan, T.A. (2008). Bio-management of reniform nematode, *Rotylenchulus reniformis* by fruit wastes and *Paecilomyces lilacinus* on chickpea. World Journal of Agriculture Sciences, 4(4): 492-494.

Benavente-Garcia, O., Castillo, J. (2008). Update on uses and properties of citrus flavonoids: new findings in anticancer, cardiovascular, and anti-inflammatory activity. Journal of agricultural and food chemistry, 56(15): 6185-6205.

Chutia, M., Bhuyan, D.P., Pathak, M.G., Sarma, T.C., Boruah. P. (2009). Antifungal activity and chemical composition of *Citrus reticulata* Blanco essential oil against phytopathogens from North East India. Food Science Technology, 42(3):777–780.

da Silva, M. N., Pintado, M. E., Sarmento, B., Stamford, N. P., Vasconcelos, M. W. (2019). A biofertilizer with diazotrophic bacteria and a filamentous fungus increases *Pinus pinaster* tolerance to the pinewood nematode (*Bursaphelenchus xylophilus*). Biological Control, 132: 72-80.

Dosoky, N. S., Setzer, W. N. (2018). Biological activities and safety of *Citrus* spp. essential oils. International journal of molecular sciences, 19(7): 1966.

Eder, R., Consoli, E., Krauss J., Dahlin, P. (2021). Polysulfides applied as formulated garlic extract to protect tomato plants against the root-knot nematode *Meloidogyne incognita*. Plants,10 (2): 394-494.

Ghaderi, R., Karssen, G. (2020). An updated checklist of Meloidogyne Göldi, 1887 species, with a diagnostic compendium for second-stage juveniles and males. Journal of Crop Protection, 9(2): 183-193.

Girennavar, B., Cepeda, M. L., Soni, K. A., Vikram, A., Jesudhasan, P., Jayaprakasha, G. K., Patil, B. S. (2008). Grapefruit juice and its furocoumarins inhibits autoinducer signaling and biofilm formation in bacteria. International journal of food microbiology, 125(2): 204-208.

González-Mas, M. C., Rambla, J. L., López-Gresa, M. P., Blázquez, M. A., Granell, A. (2019). Volatile compounds in citrus essential oils: A comprehensive review. Frontiers in Plant Science, 10: 12.

Goyal, L., Kaushal, S., Dhillon, N. K., Heena. (2021). Nematicidal potential of *Citrus reticulata* peel essential oil, isolated major compound and its derivatives against *Meloidogyne incognita*. Archives of Phytopathology and Plant Protection, 54(9-10): 449-467.

Göze Özdemir, F. G. (2022). Use of Lemon, Orange, Grapefruit and Pomegranate Fruit Peels Against Meloidogyne incognita (Kofoid and White, 1919) Chitwood, 1949. The Journal of Graduate School of Natural and Applied Sciences of Mehmet Akif Ersoy University, 13(2): 221-228.

Göze Özdemir, F. G., Tosun, B., Şanli, A., Karadoğan, T. (2022). Nematoxic activity of some Apiaceae essential oils against Meloidogyne incognita (Kofoid & White, 1919) Chitwood, 1949 (Nematoda: Meloidogynidae). Journal of Agricultural Faculty of Ege University, 59(3): 529-539.

Hajihassani, A., Marquez, J., Woldemeskel, M., Hamidi, N. (2022). Identification of Four Populations of *Meloidogyne incognita* in Georgia, United States, Capable of Parasitizing Tomato-Bearing Mi-1.2 Gene. Plant Disease, 106(1): 137-143.

Hallmann, J., Kiewnick, S. (2018). Virulence of *Meloidogyne incognita* populations and *Meloidogyne enterolobii* on resistant cucurbitaceous and solanaceous plant genotypes. Journal of Plant Diseases and Protection, 125 (4): 415-424.

Haydock, P. P. J., Woods, S. R., Grove, I. G., Hare, M. C. (2013). Chemical control of nematodes. In: Plant nematology. R. N. Perry and M. Moens, (eds.), Wallingford, CABI Publishing, 459-479.

Ismail, A.E. (2015). Management of root knot nematode *Meloidogyne javanica* on tomato by dry crushed pomegranate *Punica granatum* L. peels as a bio-fumigant in Egypt. Aichives of Phytopathology and Plant Protection, 48: 253-258.

Javed, N., Gowen, S.R., Inam-ul-Haq, M., Abdullah, K., Shahina, F. (2006). Systemic and persistent effect of neem (*Azadirachta indica*) formulations against root-knot nematodes, *Meloidogyne javanica* and their storage life. Crop Protection, 26: 911–916.

Kayani, M. Z., Mukhtar, T., & Hussain, M. A. (2012). Evaluation of nematicidal effects of *Cannabis sativa* L. and *Zanthoxylum alatum* Roxb. against root-knot nematodes, *Meloidogyne incognita*. Crop Protection, 39, 52-56.

Liu, Z., Li, Q. X., Song, B. (2022). Pesticidal Activity and Mode of Action of Monoterpenes. Journal of Agricultural and Food Chemistry, 70(15): 4556-4571.

Maleita, C., Cardoso, J. M., Rusinque, L., Esteves, I., Abrantes, I. (2021). Species-specific molecular detection of the root knot nematode *Meloidogyne luci*. Biology, 10(8): 775. https://doi.org/10.3390/biology10080775

Manju P, Sankari Meena K. 2015. Antinemic properties of the botanicals. International Journal of Security and Networks, 6(2):125–134.

Misiha, P.K., Aly, A.Z., Mahrous, M.E., Tohamy, M.R.A. (2013). Effect of culture filterates of three *Trichoderma* species, *Fusarium solani* and *Rhizoctonia solani* on egg hatching and juvenile mortality of *Meloidogyne incognita* in vitro. Zagazig Journal of Agricultural Research, 40 (3): 1-9.

Oyedunmade, E.E.A (2004). Laboratory and field toxicities of the African marigold (*Tagetes erecta*) to root-knot nematodes. The Plant Scientist, 4 (4): 115-121.

Oyedunmade, E.E.A, Ayooke, O.F, Olabiyi, T.I (2001). Comparative efficacies of soil amendment and a synthetic nematicide on growth, yield and food components of a root-knot infected soyabean (*Glycine max*.L. Merril). Nigerian Society of Experiemntal Biology, 1: 367-371.

Regaieg H. (2011).Contribution à l'étude des champignons filamenteux associés au Meloidogyne spp. Sur culture de tomate en Tunisie et évaluation de leur potentiel en tant qu'agents de lutte biologique [Contribution to the study of filamentous fungi associated with Meloidogyne spp. on tomato crop in Tunisia and evaluation of their biocontrol potential.higher agronomic institut]. Thèse de doctorat en science agronomiques. Sousse: Institut Supérieur Agronomique de Chott Mariem; p.163.

Regaieg, H., Bouajila, M., Hajji, L., Larayadh, A., Chiheni, N., Guessmi-Mzoughi, I., Horrigue-Raouani, N. (2017). Evaluation of pomegranate (*Punica granatum* L. var. Gabsi) peel extract for control of root-knot nematode *Meloidogyne javanica* on tomato. Archives of Phytopathology and Plant Protection, 50(17-18): 839-849.

Saad, M. M. G., Abou-Taleb, H. K., Abdelgaleil, S. A. M. (2018). Insecticidal activities of monoterpenes and phenylpropenes against *Sitophilus oryzae* and their inhibitory effects on acetylcholinesterase and adenosine triphosphatases. Applied Entomology and Zoology, 53(2): 173–181.

Tsai, B.Y. (2008). Effects of peels of lemon, orange and grapefruit against *Meloidogyne incognita*. Plant Pathology Bulletin, 17: 195-201.

Uckoo, R. M., Patil, B. S., Jayaprakasha, G. K. (2011, September). Separation of Furocoumarins and Polymethoxyflavones from Grapefruit Byproduct Using Flash Chromatography. In Hortscience (Vol. 46, No. 9, pp. S318-S319).

USDA, 2021, The United States Department of Agriculture, (http.//www.usda.gov).

Uysal, G., Söğüt, M.A., Elekçioğlu, İ.H. (2017). Identification and distribution of root-knot nematode species (Meloidogyne spp.) in vegetable growing areas of Lakes Region in Turkey. Turkish Journal of Entomology, 41 (1): 105-122.

Vikram, A., Jesudhasan, P. R., Jayaprakasha, G. K., Pillai, B. S., Patil, B. S. (2010). Grapefruit bioactive limonoids modulate *E. coli* O157: H7 TTSS and biofilm. International journal of food microbiology, 140(2-3), 109-116.

Viuda-Martos, M., Fernández-López, J., Pérez-Álvarez, J. A. (2010). Pomegranate and its many functional components as related to human health: a review. Comprehensive reviews in food science and food safety, 9(6), 635-654.

Convergence by Modified Post-Widder Operators Preserving e^{2ax}; a > 0

Gülten TORUN[1]

Introduction

Approximation theory is one of the main subjects in mathematics that is used by researchers. For years, many publications related to the approximation theory has made and has still being studied, too. This theory deals with the problem of approximation of continuous functions on a finite closed interval with the sequences of the linear positive operators. Linear positive operators take an important place in approximation theory, since they are monotonous operators. This property allows to proving inequalities for positive operators (Hacısalihoğlu & Hacıyev, 1995).

Widder (1941) examined the Post-Widder operators for $f \in C(0, \infty)$ is defined by

$$P_n(f; x) = \frac{1}{n!} \left(\frac{n}{x}\right)^{n+1} \int_0^\infty t^n e^{-\frac{nt}{x}} f(t) dt, \tag{1}$$

where $n \in \mathbb{N} = \{1, 2, \dots\}$, $x \in (0, \infty)$, and these operators protect only fixed functions.

Rathore & Sing (1980) defined in the following way

$$P_n^p(f; x) := \frac{1}{(n+p)!} \left(\frac{n}{x}\right)^{n+p+1} \int_0^\infty t^{n+p} e^{-\frac{nt}{x}} f(t) dt, \tag{2}$$

where p be a fixed integer. In the case of $p = 0$, the operators (2) reduce to the operators (1). In addition, for the $p = -1$ case, the operators (2) was handled by May (1976).

Rempulska & Skorupka (2009) introduced the Post-Widder and Stancu operators preserving the function x² in polynomial weighted space and showed that these operators had better approximation properties than classical Post-Widder and Stancu operators.

In recent years, the Post-Widder operators preserving test functions x^r for $r \in \mathbb{N}$ have been appropriately modified to get a better approximation. The approximation properties of the modified form of the Post-Widder operators have been studied by Gupta & Agrawal (2019) and Gupta & Tachev (2022).

In addition, the several linear operators preserving the functions constantly and e^{2ax} for fixed $a > 0$ were studied by Acar, Aral & Gonska (2017), Gürel-Yılmaz, Gupta & Aral (2017), Gürel-Yılmaz, Bodur & Aral (2018), Bodur, Gürel-Yılmaz & Aral (2018), Aral, Inoan & Raşa (2019), Sofyalıoğlu & Kanat (2019), Gupta & Maheshwari (2019), Sofyalıoğlu & Kanat (2020), Kanat & Sofyalıoğlu (2021).

---

[1] Dr. , Kastamonu University, Faculty of Education, Mathematics and Science Education

Sofyalıoğlu & Kanat (2020) has been handled the case $p = -1$ of Post-Widder operators (2) preserving the functions constant and e^{2ax} for fixed $a > 0$. For $f \in C(0, \infty)$, they constructed the modified form of Post-Widder operators as follows

$$P_{n,\theta}^*(f; x) = \frac{1}{(n-1)!}\left(\frac{n}{\theta_n(x)}\right)^n \int_0^\infty t^{n-1} e^{-\frac{nt}{\theta_n(x)}} f(t)dt, \quad n \geq 1$$

where the function $\theta_n(x)$ is defined by

$$\theta_n(x) = \frac{n}{2a}\left(1 - e^{\frac{-2ax}{n}}\right),$$

and investigated the approximation properties of these operators.

These study is organized as follows. Firstly, Stancu type Post-Widder operators are introduced, which are a modification of the Post-Widder operators that preserve the functions constant and e^{2ax} for fixed a>0. Then, uniform convergence of these modified operators for the function f on [0,∞) is examined and the convergence rate is investigated with the help of the continuity module. In addition, the Voronovskaja type asymptotic formula is obtained to examine the asymptotic behavior of these operators. Several studies were conducted on Voronovskaja type approximation for some operators by Dinlemez Kantar & Ergelen (2019), Cai, Dinlemez Kantar & Çekim (2020), Cai, Torun & Dinlemez Kantar (2021), Dinlemez Kantar & Yüksel (2022), Torun, Boyraz & Dinlemez Kantar. (2022). Finally, numerical examples and graphs are given to show the convergence of Stancu type Post- Widder operators and compared with Post Widder operators.

For $f \in C[0, \infty)$, let be defined the Stancu type Post-Widder operators as

$$G_{n,\Psi}^{\alpha,\beta}(f; x) := \frac{1}{n!}\left(\frac{n}{\Psi_n(x)}\right)^{n+1} \int_0^\infty t^n e^{\frac{-nt}{\Psi_n(x)}} f\left(\frac{nt+\alpha}{n+\beta}\right) dt, \tag{3}$$

where $n \in \mathbb{N}$, $x \in [0, \infty)$, α and β positive real numbers satisfying $0 \leq \alpha \leq \beta$. For $a > 0$, assume that operators (3) preserve the function e^{2ax}. It can be easily seen that the conditions

$$G_{n,\Psi}^{\alpha,\beta}(e^{2at}; x) = e^{2ax}$$

are satisfied. In this case, since

$$G_{n,\Psi}^{\alpha,\beta}(e^{2at}; x) = e^{2ax} = \frac{1}{n!}\left(\frac{n}{\Psi_n(x)}\right)^{n+1} \int_0^\infty t^n e^{-\frac{nt}{\Psi_n(x)}} e^{2a\frac{nt+\alpha}{n+\beta}} dt, \quad \frac{n+\beta}{\Psi_n(x)} > 2a$$

$$= \frac{e^{\frac{2a\alpha}{n+\beta}}}{n!}\left(\frac{n}{\Psi_n(x)}\right)^{n+1} \int_0^\infty t^n e^{-\frac{(n+\beta)-2a\Psi_n(x)}{(n+\beta)\Psi_n(x)}nt} dt$$

$$= e^{\frac{2a\alpha}{n+\beta}}\left(\frac{n+\beta}{n+\beta-2a\Psi_n(x)}\right)^{n+1},$$

the function $\Psi_n(x)$ is obtained as follows

$$\Psi_n(x) = \frac{n+\beta}{2a}\left(1 - \left(e^{\frac{2a(x(n+\beta)-\alpha)}{n+\beta}}\right)^{\frac{-1}{n+1}}\right). \tag{4}$$

And it can be shown that $\lim\limits_{n \to \infty} \Psi_n(x) = x$. If the function $\Psi_n(x)$ given in (4) is replaced in (3), the Stancu type Post-Widder operators take the form

$$G_n^{\alpha,\beta}(f;x) := G_{n,\Psi}^{\alpha,\beta}(f;x)$$

$$= \frac{1}{n!} \left(\frac{2an}{(n+\beta)\left(1-e^{\frac{-2a(x(n+\beta)-\alpha)}{(n+\beta)(n+1)}}\right)} \right)^{n+1} \int_0^\infty t^n\, e^{(n+\beta)\left(1-e^{\frac{-2a(x(n+\beta)-\alpha)}{(n+\beta)(n+1)}}\right)} f\left(\frac{nt+\alpha}{n+\beta}\right) dt. \, (5)$$

Some preliminary results

In this section, several lemmas and their results are given to prove the main theorem.

Lemma 1 Let $\Psi_n(x)$ be function given in (4). The operators (3) give the following equation

$$G_{n,p,\Psi}^{\alpha,\beta}(e^{\eta t};x) = e^{\frac{\eta\alpha}{n+\beta}} \left(1 - \frac{\eta \Psi_n(x)}{n+\beta}\right)^{-(n+1)}, \quad \eta \in \mathbb{R}. \tag{6}$$

Proof: Let $f(t) = e^{\eta t}, \ \eta \in \mathbb{R}.$ From the operators (3), the following equation is given by

$$G_{n,\Psi}^{\alpha,\beta}(e^{\eta t};x) = \frac{1}{n!}\left(\frac{n}{\Psi_n(x)}\right)^{n+1} \int_0^\infty t^n\, e^{-\frac{nt}{\Psi_n(x)}} e^{\eta\frac{nt+\alpha}{n+\beta}} dt$$

$$= \frac{1}{n!}\left(\frac{n}{\Psi_n(x)}\right)^{n+1} e^{\frac{\eta\alpha}{n+\beta}} \int_0^\infty t^n\, e^{-\left(\frac{1}{\Psi_n(x)} - \frac{\eta}{n+\beta}\right)nt} dt.$$

By substituting the variable $\left(\frac{1}{\Psi_n(x)} - \frac{\eta}{n+\beta}\right)nt = u$ in the integral on the right-hand side of the above equation and then using the gamma function, the proof is completed.

Lemma 2 For the test function $e_j(t) = t^j$, $j = 0,1,2,3,4,$ one has the equalities as

(*i*) $\quad G_{n,\Psi}^{\alpha,\beta}(e_0(t);x) = 1,$

(*ii*) $\quad G_{n,\Psi}^{\alpha,\beta}(e_1(t);x) = \frac{n+1}{n+\beta}\Psi_n(x) + \frac{\alpha}{n+\beta},$

(*iii*) $\quad G_{n,\Psi}^{\alpha,\beta}(e_2(t);x) = \frac{(n+2)(n+1)}{(n+\beta)^2}\Psi_n^2(x) + \frac{2\alpha(n+1)}{(n+\beta)^2}\Psi_n(x) + \frac{\alpha^2}{(n+\beta)^2},$

(*iv*) $G_{n,\Psi}^{\alpha,\beta}(e_3(t);x) = \frac{(n+3)(n+2)(n+1)}{(n+\beta)^3}\Psi_n^3(x) + \frac{3\alpha(n+2)(n+1)}{(n+\beta)^3}\Psi_n^2(x)$

$$+ \frac{3\alpha^2(n+1)}{(n+\beta)^3}\Psi_n(x) + \frac{\alpha^3}{(n+\beta)^3},$$

(*v*) $\quad G_{n,\Psi}^{\alpha,\beta}(e_4(t);x) = \frac{(n+4)(n+3)(n+2)(n+1)}{(n+\beta)^4}\Psi_n^4(x) + \frac{4\alpha(n+3)(n+2)(n+1)}{(n+\beta)^4}\Psi_n^3(x)$

$$+ \frac{6\alpha^2(n+2)(n+1)}{(n+\beta)^4}\Psi_n^2(x) + \frac{4\alpha^3(n+1)}{(n+\beta)^4}\Psi_n(x) + \frac{\alpha^4}{(n+\beta)^4}.$$

Proof: **(i)** Taking $e_j(t) = t^j$, $j = 0$ in operators $G_{n,\Psi}^{\alpha,\beta}(e_j(t); x)$, the following equation can be obtained by

$$G_{n,\Psi}^{\alpha,\beta}(e_0(t); x) = \frac{1}{n!}\left(\frac{n}{\Psi_n(x)}\right)^{n+1} \int_0^\infty t^n e^{-\frac{nt}{\Psi_n(x)}} dt.$$

If the variable $\frac{n}{\Psi_n(x)} t = u$ is changed in integral on the right side of the above equation and then gamma function is used, the following equation is obtained

$$G_{n,\Psi}^{\alpha,\beta}(e_0(t); x) = \frac{1}{n!}\left(\frac{n}{\Psi_n(x)}\right)^{n+1} \left(\frac{\Psi_n(x)}{n}\right)^{n+1} \int_0^\infty u^n e^{-u} du = \frac{1}{n!}\Gamma(n+1) = 1$$

(ii) The operators $G_{n,\Psi}^{\alpha,\beta}(e_j(t); x)$ for $j = 1$ are yielded as follows

$$G_{n,\Psi}^{\alpha,\beta}(e_1(t); x) = \frac{1}{n!}\left(\frac{n}{\Psi_n(x)}\right)^{n+1} \int_0^\infty t^n e^{-\frac{nt}{\Psi_n(x)}} \left(\frac{nt+\alpha}{n+\beta}\right) dt$$

$$=\left(\frac{n}{\Psi_n(x)}\right)^{n+1} \int_0^\infty t^{n+1} e^{-\frac{nt}{\Psi_n(x)}} dt + \frac{\alpha}{n!(n+\beta)}\left(\frac{n}{\Psi_n(x)}\right)^{n+1} \int_0^\infty t^n e^{-\frac{nt}{\Psi_n(x)}} dt.$$

From **(i)**, the value of the second sum on the right hand side of the above equation is $\frac{\alpha}{n+\beta}$. In the first integral in the above equation, by taking the variable $\frac{n}{\Psi_n(x)} t = u$ and then using the gamma function, the following equation is obtained

$$G_{n,\Psi}^{\alpha,\beta}(e_1(t); x) = \frac{n+1}{n+\beta}\Psi_n(x) + \frac{\alpha}{n+\beta}.$$

(iii) For $j = 2$, the operators $G_{n,\Psi}^{\alpha,\beta}(e_j(t); x)$ are written as follows

$$G_{n,\Psi}^{\alpha,\beta}(e_2(t); x) = \frac{1}{n!}\left(\frac{n}{\Psi_n(x)}\right)^{n+1} \int_0^\infty t^n e^{-\frac{nt}{\Psi_n(x)}} \left(\frac{nt+\alpha}{n+\beta}\right)^2 dt$$

$$= \frac{n^2}{n!(n+\beta)^2}\left(\frac{n}{\Psi_n(x)}\right)^{n+1} \int_0^\infty t^{n+2} e^{-\frac{nt}{\Psi_n(x)}} dt$$

$$+ \frac{2n\alpha}{n!(n+\beta)^2}\left(\frac{n}{\Psi_n(x)}\right)^{n+1} \int_0^\infty t^{n+1} e^{-\frac{nt}{\Psi_n(x)}} dt$$

$$+ \frac{\alpha^2}{n!(n+\beta)^2}\left(\frac{n}{\Psi_n(x)}\right)^{n+1} \int_0^\infty t^n e^{-\frac{nt}{\Psi_n(x)}} dt.$$

In the first integral on the right side of the above equation, the variable $\frac{n}{\Psi_n(x)} t = u$ is changed and then the gamma function is used. From **(i)** and **(ii)**, the following equation is found

$$G_{n,\Psi}^{\alpha,\beta}(e_2(t); x) = \frac{(n+2)(n+1)}{(n+\beta)^2}\Psi_n^2(x) + \frac{2\alpha(n+1)}{(n+\beta)^2}\Psi_n(x) + \frac{\alpha^2}{(n+\beta)^2}.$$

Similarly, the equations **(iv)** and **(v)** are proved.

Corollary 3 Let $\varphi_x^j(t) = (t-x)^j$, $j = 0,1,2,4$. The central moments of the operators (3) are given below

$$G_{n,\Psi}^{\alpha,\beta}(\varphi_x^0(t); x) = 1,$$

$$G_{n,\Psi}^{\alpha,\beta}(\varphi_x^1(t);x) = \frac{(n+1)\Psi_n(x)+\alpha}{n+\beta} - x,$$

$$G_{n,\Psi}^{\alpha,\beta}(\varphi_x^2(t);x) = \frac{(n+2)(n+1)\Psi_n^2(x)+2\alpha(n+1)\Psi_n(x)+\alpha^2}{(n+\beta)^2} - 2x\frac{(n+1)\Psi_n(x)+\alpha}{n+\beta} + x^2,$$

$$G_{n,\Psi}^{\alpha,\beta}(\varphi_x^4(t);x) = \frac{(n+4)(n+3)(n+2)(n+1)\Psi_n^4(x)+4\alpha(n+3)(n+2)(n+1)\Psi_n^3(x)}{(n+\beta)^4}$$

$$+ \frac{6\alpha^2(n+2)(n+1)\Psi_n^2(x)+4\alpha^3(n+1)\Psi_n(x)+\alpha^4}{(n+\beta)^4}$$

$$-4x\left(\frac{(n+3)(n+2)(n+1)\Psi_n^3(x)+3\alpha(n+2)(n+1)\Psi_n^2(x)+3\alpha^2(n+1)\Psi_n(x)+\alpha^3}{(n+\beta)^3}\right)$$

$$+6x^2\left(\frac{(n+2)(n+1)\Psi_n^2(x)+2\alpha(n+1)\Psi_n(x)+\alpha^2}{(n+\beta)^2}\right) - 4x^3\left(\frac{(n+1)\Psi_n(x)+\alpha}{n+\beta}\right) + x^4.$$

In addition, the following limits are obtained

(i) $\quad \lim_{n\to\infty} nG_{n,\Psi}^{\alpha,\beta}(t-x;x) = -ax^2$ $\qquad\qquad\qquad$ (7)

(ii) $\quad \lim_{n\to\infty} nG_{n,\Psi}^{\alpha,\beta}((t-x)^2;x) = x^2$ $\qquad\qquad\qquad$ (8)

(iii) $\quad \lim_{n\to\infty} n^2G_{n,\Psi}^{\alpha,\beta}((t-x)^4;x) = 3x^4$ $\qquad\qquad\qquad$ (9)

The uniform convergence of the operators $G_{n,\Psi}^{\alpha,\beta}$

The uniform convergence of a sequence of linear positive operators was demonstrated by Boyanov & Veselinov (1970). In the following theorem, the uniform convergence of the operators (3) for the function f on $[0,\infty)$ is investigated.

Let $C^*[0,\infty)$ denote the subspace of all continuous and real-valued functions on $[0,\infty)$ with the property that $\lim_{x\to\infty} f(x)$ exists and finite, equipped with the uniform norm.

Theorem 4 If the sequence $\left\{G_{n,\Psi}^{\alpha,\beta}f\right\}$ of the operators (3) satisfy

$$\lim_{n\to\infty} G_{n,\Psi}^{\alpha,\beta}(e^{-vt};x) = e^{-vx}, \quad v = 0,1,2 \qquad\qquad (10)$$

uniformly in $[0,\infty)$, then for each $f \in C^*[0,\infty)$

$$\lim_{n\to\infty} G_{n,\Psi}^{\alpha,\beta}(f;x) = f(x) \qquad\qquad (11)$$

uniformly in $[0,\infty)$.

Proof: For $v = 0$, it becomes that $\lim_{n\to\infty} G_{n,\Psi}^{\alpha,\beta}(1;x) = 1$ from (i) of Lemma 2. Now the equation (6), and the function $\Psi_n(x)$ will be used to prove the images of $f(t) = e^{-vt}$ for $v = 1,2$ respectively,

$$G_{n,\Psi}^{\alpha,\beta}(e^{-t};x) = e^{-\frac{\alpha}{n+\beta}}\left(1 + \frac{1}{2a}\left(1 - e^{\frac{-2a(x(n+\beta)-\alpha)}{(n+\beta)(n+1)}}\right)\right)^{-(n+1)}, \tag{12}$$

$$G_{n,\Psi}^{\alpha,\beta}(e^{-2t};x) = e^{-\frac{2\alpha}{n+\beta}}\left(1 + \frac{1}{a}\left(1 - e^{\frac{-2a(x(n+\beta)-\alpha)}{(n+\beta)(n+1)}}\right)\right)^{-(n+1)}. \tag{13}$$

Using the Maple software to calculate the right-hand sides of the equalities (12) and (13), the following equations are obtained, respectively,

$$G_{n,\Psi}^{\alpha,\beta}(e^{-t};x) = e^{-x} + \frac{(2a+1)e^{-x}x^2}{2n}$$
$$+ \frac{(2a+1)(3(2a+1)e^{-x}x^4 - 8(a+1)e^{-x}x^3 - 12e^{-x}x^2 - 24\alpha e^{-x}x)}{24n^2} + O\left(\frac{1}{n^3}\right), \tag{14}$$

$$G_{n,\Psi}^{\alpha,\beta}(e^{-2t};x) = e^{-2x} + \frac{2(a+1)e^{-2x}x^2}{n}$$
$$+ \frac{(a+1)(6(a+1)e^{-2x}x^4 - 4(a+2)e^{-2x}x^3 - 6e^{-2x}x^2 - 12\alpha e^{-2x}x)}{3n^2} + O\left(\frac{1}{n^3}\right). \tag{15}$$

Thus, $\lim_{n\to\infty} G_{n,\Psi}^{\alpha,\beta}(e^{-\nu t};x) = e^{-\nu x}, \nu = 0,1,2$ in the interval $[0;\infty)$. That, $\lim_{n\to\infty} G_{n,\Psi}^{\alpha,\beta}(f;x) = f$ for any $f \in C^*[0;\infty)$. That is, the sequence $\{G_{n,\Psi}^{\alpha,\beta}f\}$ uniformly converges in the interval $[0,\infty)$ for any $f \in C^*[0,\infty)$.

After Boyanov & Veslinov, the uniform convergence of a sequence of linear positive operators was studied by Holhoş (2010). In his work, he obtained the following theorem for a sequence of positive and linear operators.

Theorem 5 If $\{P_n\}$ is a sequence of linear positive operators from $C^*[0,\infty)$ to $C^*[0,\infty)$, then for each $f \in C^*[0,\infty)$, the following inequality is satisfied

$$\|P_n(f;x) - f(x)\|_{[0,\infty)} \leq \|f\|_{[0,\infty)}a_n + (2 + a_n)\omega^*(f, \sqrt{a_n + 2b_n + c_n}),$$

where a_n, b_n and c_n are defined as follows

$$\|P_n(1;x) - 1\|_{[0,\infty)} = a_n,$$

$$\|P_n(e^{-t};x) - e^{-x}\|_{[0,\infty)} = b_n,$$

$$\|P_n(e^{-2t};x) - e^{-2x}\|_{[0,\infty)} = c_n$$

and they tend to zero as n goes to infinity. The modulus of continuity ω^* is expressed by

$$\omega^*(f,\gamma) = sup_{|e^{-t}-e^{-x}|\leq\gamma; \, x,t\geq0} |f(t) - f(x)| \tag{16}$$

and this modulus has to property:

$$|f(t) - f(x)| \leq \left(1 + \frac{1}{\gamma^2}(e^{-t} - e^{-x})^2\right)\omega^*(f,\gamma), \quad \gamma > 0 \tag{17}$$

According to Theorem 5 , the uniform convergence of a sequence of linear positive operators with the help of the continuity module is given with the following theorem.

Theorem 6 Let $\left\{G_{n,\Psi}^{\alpha,\beta}f\right\}$ be a sequence of linear positive operators $G_{n,\Psi}^{\alpha,\beta}$: $C^*[0,\infty) \to C^*[0,\infty)$. For every function $f \in C^*[0;\infty)$, the following inequality is satisfied

$$\left\|G_{n,\Psi}^{\alpha,\beta}(f;x) - f(x)\right\|_{[0,\infty)} \leq 2\omega^*\left(f,\sqrt{2\sigma_n + \mu_n}\right), \tag{18}$$

where the modulus of continuity which is defined in (16) and

$$\left\|G_{n,\Psi}^{\alpha,\beta}(e^{-t};x) - e^{-x}\right\|_{[0,\infty)} = \sigma_n,$$

$$\left\|G_{n,\Psi}^{\alpha,\beta}(e^{-2t};x) - e^{-2x}\right\|_{[0,\infty)} = \mu_n,$$

Here σ_n and μ_n tend to zero as n goes to infinity and the sequence $\left\{G_{n,\Psi}^{\alpha,\beta}f\right\}$ uniformly converges to f.

Proof: From (i) of Lemma 2, $\rho_n = \left\|G_{n,\Psi}^{\alpha,\beta}(1;x) - 1\right\|_{[0,\infty)} = 0$ is obtained. To calculate σ_n and μ_n, the equalities (14) and (15) are taken, respectively,

$$\sigma_n = \left\|G_{n,\Psi}^{\alpha,\beta}(e^{-t};x) - e^{-x}\right\|_{[0,\infty)} = sup_{x\in[0;\infty)}\left|G_{n,\Psi}^{\alpha,\beta}(e^{-t};x) - e^{-x}\right|$$

$$= sup_{x\in[0;\infty)}\left|\frac{(2a+1)x^2}{2ne^x} + \frac{(2a+1)\left(3(2a+1)e^{-x}x^4 - 8(a+1)e^{-x}x^3 - 12e^{-x}x^2 - 24\alpha e^{-x}x\right)}{24n^2} + O\left(\frac{1}{n^3}\right)\right|$$

$$\leq \frac{2(2a+1)}{ne^2} + \frac{2a+1}{n^2}\left(\frac{32(2a+1)}{e^4} - \frac{9(a+1)}{e^3} - \frac{2}{e^2} - \frac{\alpha}{e}\right) + O\left(\frac{1}{n^3}\right),$$

$$\mu_n = \left\|G_{n,\Psi}^{\alpha,\beta}(e^{-2t};x) - e^{-2x}\right\|_{[0,\infty)} = sup_{x\in[0;\infty)}\left|G_{n,\Psi}^{\alpha,\beta}(e^{-2t};x) - e^{-2x}\right|$$

$$= sup_{x\in[0;\infty)}\left|\frac{2(a+1)x^2}{ne^{2x}} + \frac{(a+1)\left(6(a+1)e^{-2x}x^4 - 4(a+2)e^{-2x}x^3 - 6e^{-2x}x^2 - 12\alpha e^{-2x}x\right)}{3n^2} + O\left(\frac{1}{n^3}\right)\right|$$

$$\leq \frac{2(a+1)}{ne^2} + \frac{a+1}{n^2}\left(\frac{32(a+1)}{e^4} - \frac{\frac{9}{2}(a+2)}{e^3} - \frac{2}{e^2} - \frac{2\alpha}{e}\right) + O\left(\frac{1}{n^3}\right).$$

As a consequence, σ_n and μ_n tend to zero as n goes to infinity. Thus, the proof of the theorem is completed.

Approximation properties of the operators $G_{n,\Psi}^{\alpha,\beta}$

In this section, firstly, the convergence rate is examined with the help of the continuity module.

Let $C_B[0,\infty)$ be the space of all bounded and uniform continuous functions f on $[0,\infty)$ endowed with the norm $\|f\|_{C_B} = sup_{x\in[0;\infty)} |f(x)|$. For $\varepsilon > 0$, the Peetre K-functional is defined by

$$K_2(f,\varepsilon) = inf_{g\in C_B^2[0,\infty)} [\|f - g\| + \varepsilon\|g''\|],$$

where $C_B^2[0,\infty) = \{g \in C_B[0,\infty): g', g'' \in C_B[0,\infty)\}$.

In Theorem 2.4 (De Vore & Lorentz, 1993 : 177) , there exists an absolute constant $C > 0$ such that

$$K_2(f,\varepsilon) \leq C\omega_2(f,\sqrt{\varepsilon}), \qquad \varepsilon > 0 \tag{19}$$

where the function ω_2 is the second-order modulus of continuity of $f \in C_B[0,\infty)$ is given by

$$\omega_2(f,\sqrt{\varepsilon}) = \sup_{0<h\leq\sqrt{\varepsilon}} \sup_{x,x+h,x+2h\in[0,\infty)} |f(x+2h) - 2f(x+h) + f(x)|.$$

In addition, the first-order modulus of continuity of $f \in C_B[0,\infty)$ is defined as follows

$$\omega(f,\varepsilon) = \sup_{0<h\leq\varepsilon} \sup_{x,x+h\in[0,\infty)} |f(x+h) - f(x)|.$$

Lemma 7 For $f \in C_B[0,\infty)$, the following inequality is obtained

$$\left| G_{n,\Psi}^{\alpha,\beta}(f;x) \right| \leq \|f\|. \tag{20}$$

Proof: Taking the operators (5) and using the equation (i) of Lemma 2, it is found that

$$\left| G_{n,\Psi}^{\alpha,\beta}(f;x) \right| = \left| G_n^{\alpha,\beta}(f;x) \right|$$

$$\leq \frac{1}{n!} \left(\frac{2an}{(n+\beta)\left(1-e^{\frac{-2a(x(n+\beta)-\alpha)}{(n+\beta)(n+1)}} \right)} \right)^{n+1} \int_0^\infty t^n e^{(n+\beta)\left(1-e^{\frac{-2a(x(n+\beta)-\alpha)}{(n+\beta)(n+1)}} \right)\frac{-2ant}{}} \left| f\left(\frac{nt+\alpha}{n+\beta} \right) \right| dt.$$

$$\leq \|f\| \, G_{n,\Psi}^{\alpha,\beta}(1;x) = \|f\|.$$

Theorem 8 For $f \in C_B[0,\infty)$, there exists a positive constant L such that

$$\left| G_{n,\Psi}^{\alpha,\beta}(f;x) - f(x) \right| \leq L\omega_2\left(f, \sqrt{\frac{\xi_{n,\Psi}^{\alpha,\beta}}{8}} \right) + \omega\left(f, \left| \frac{n+1}{2a}\left(1 - e^{\frac{-2a(x(n+\beta)-\alpha)}{(n+\beta)(n+1)}} \right) + \frac{\alpha}{n+\beta} - x \right| \right),$$

where

$$\xi_{n,\Psi}^{\alpha,\beta} = \frac{(n+1)(2n+3)}{(n+\beta)^2} \Psi_n^2(x) + 4\left(\frac{\alpha(n+1)}{(n+\beta)^2} - \frac{x(n+1)}{n+\beta} \right) \Psi_n(x) + \frac{2\alpha^2}{(n+\beta)^2} - \frac{4x\alpha}{n+\beta} + 2x^2.$$

Proof: Let the auxiliary operators $\tilde{G}_{n,\Psi}^{\alpha,\beta}$ from $C_B[0,\infty)$ to $C_B[0,\infty)$ be defined as

$$\tilde{G}_{n,\Psi}^{\alpha,\beta}(g;x) = G_{n,\Psi}^{\alpha,\beta}(g;x) + g(x) - g\left(\frac{n+1}{2a}\left(1 - e^{\frac{-2a(x(n+\beta)-\alpha)}{(n+\beta)(n+1)}} \right) + \frac{\alpha}{n+\beta} \right). \tag{21}$$

From the equalities (i) and (ii) of Lemma 2 and the linearity of the operators $\tilde{G}_{n,\Psi}^{\alpha,\beta}(g;x)$,

$$\tilde{G}_{n,\Psi}^{\alpha,\beta}(t-x;x) = 0 \tag{22}$$

is obtained. Using Taylor's expansion formula for $g \in C_B^2[0,\infty)$, it can be written as

$$g(t) = g(x) + g'(x)(t-x) + \int_x^t (t-u)g''(u)du. \tag{23}$$

Applying the auxiliary operators (21) to both sides of equation (23) and using (22), it is obtained

$$\tilde{G}_{n,\Psi}^{\alpha,\beta}(g;x) = g(x) + \tilde{G}_{n,\Psi}^{\alpha,\beta}\left(\int_x^t (t-u)g''(u)du\,;x\right).$$

$$\left|\tilde{G}_{n,\Psi}^{\alpha,\beta}(g;x) - g(x)\right| \le \left|G_{n,\Psi}^{\alpha,\beta}\left(\int_x^t (t-u)g''(u)du\,;x\right)\right|$$

$$+ \left|\int_x^{G_{n,\Psi}^{\alpha,\beta}(e_1;x)}\left(G_{n,\Psi}^{\alpha,\beta}(e_1;x) - u\right)g''(u)du\right|$$

$$\le \frac{\|g''\|}{2}G_{n,\Psi}^{\alpha,\beta}((t-x)^2;x) + \frac{\|g''\|}{2}\left(\frac{n+1}{2a}\left(1 - e^{\frac{-2a(x(n+\beta)-\alpha)}{(n+\beta)(n+1)}}\right) + \frac{\alpha}{n+\beta} - x\right)^2$$

$$\le \frac{\|g''\|}{2}\left(\left(G_{n,\Psi}^{\alpha,\beta}((t-x)^2;x)\right) + \left(G_{n,\Psi}^{\alpha,\beta}(t-x;x)\right)^2\right) = \frac{\|g''\|}{2}\;\xi_{n,\Psi}^{\alpha,\beta}, \quad (24)$$

where

$$\xi_{n,\Psi}^{\alpha,\beta} = \frac{(n+1)(2n+3)}{(n+\beta)^2}\Psi_n^2(x) + 4\left(\frac{\alpha(n+1)}{(n+\beta)^2} - \frac{x(n+1)}{n+\beta}\right)\Psi_n(x) + \frac{2\alpha^2}{(n+\beta)^2} - \frac{4x\alpha}{n+\beta} + 2x^2.$$

Taking the norm of the auxiliary operators (21) and using Lemma 7, the following inequality is obtained

$$\left\|\tilde{G}_{n,\Psi}^{\alpha,\beta}(f;x)\right\| \le 3\|f\|, \quad f \in C_B[0,\infty). \tag{25}$$

Using the operators (21) and the inequalities (24) and (25), for every $g \in C_B^2[0,\infty)$, it can be written as

$$\left|G_{n,\Psi}^{\alpha,\beta}(f;x) - f(x)\right| \le \left|\tilde{G}_{n,\Psi}^{\alpha,\beta}(f-g;x) - (f-g)(x)\right|$$

$$+ \left|f\left(\frac{n+1}{2a}\left(1 - e^{\frac{-2a(x(n+\beta)-\alpha)}{(n+\beta)(n+1)}}\right) + \frac{\alpha}{n+\beta}\right) - f(x)\right| + \left|\tilde{G}_{n,\Psi}^{\alpha,\beta}(g;x) - g(x)\right|$$

$$\le 4\|f-g\| + \frac{\|g''\|}{2}\xi_{n,\Psi}^{\alpha,\beta} + \left|f\left(\frac{n+1}{2a}\left(1 - e^{\frac{-2a(x(n+\beta)-\alpha)}{(n+\beta)(n+1)}}\right) + \frac{\alpha}{n+\beta}\right) - f(x)\right|. \tag{26}$$

If the infimum on the right-hand side of (26) over all the function $g \in C_B^2[0,\infty)$ is taken, then

$$\left|G_{n,\Psi}^{\alpha,\beta}(f;x) - f(x)\right| \le 4K_2\left(f, \frac{\xi_{n,\Psi}^{\alpha,\beta}}{8}\right) + \omega\left(f, \left|\frac{n+1}{2a}\left(1 - e^{\frac{-2a(x(n+\beta)-\alpha)}{(n+\beta)(n+1)}}\right) + \frac{\alpha}{n+\beta} - x\right|\right)$$

$$\le L\omega_2\left(f, \sqrt{\frac{\xi_{n,\Psi}^{\alpha,\beta}}{8}}\right) + \omega\left(f, \left|\frac{n+1}{2a}\left(1 - e^{\frac{-2a(x(n+\beta)-\alpha)}{(n+\beta)(n+1)}}\right) + \frac{\alpha}{n+\beta} - x\right|\right),$$

where L is a positive constant. Thus, Theorem is proved.

Remark 9 Since $\lim\limits_{n\to\infty}\xi_{n,\Psi}^{\alpha,\beta} = 0$ and $\lim\limits_{n\to\infty}\left(\frac{n+1}{2a}\left(1 - e^{\frac{-2a(x(n+\beta)-\alpha)}{(n+\beta)(n+1)}}\right) + \frac{\alpha}{n+\beta} - x\right) = 0$, these limits guarantees a rate of pointwise convergence of the operators $G_{n,\Psi}^{\alpha,\beta}(f;x)$ to $f(x)$.

Finally, the Voronovskaja type asymptotic formula is given to examine the asymptotic behavior of the operators (3).

Theorem 10 For each $f \in C^*[0,\infty)$ and $x \in [0,\infty)$, the following inequality is found

$$\left| n\left(G_{n,\Psi}^{\alpha,\beta}(f;x) - f(x) \right) + ax^2 f'(x) - \frac{x^2}{2} f''(x) \right|$$

$$\leq |u_n(x)||f'(x)| + \frac{1}{2}|v_n(x)|| f''(x)| + 2\left(v_n(x) + x^2 + w_n(x)\right)\omega^*\left(f'', n^{-\frac{1}{2}}\right),$$

where f', f'' exists in $C^*[0, \infty)$, and

$$u_n(x) = nG_{n,\Psi}^{\alpha,\beta}(t - x; x) + ax^2,$$

$$v_n(x) = nG_{n,\Psi}^{\alpha,\beta}((t - x)^2; x) - x^2,$$

$$w_n(x) = \left(n^2 G_{n,\Psi}^{\alpha,\beta}((e^{-t} - e^{-x})^4; x)\right)^{\frac{1}{2}} \left(n^2 G_{n,\Psi}^{\alpha,\beta}((t - x)^4; x)\right)^{\frac{1}{2}}.$$

Proof: By Taylor's formula for a function f, the following equation can be written

$$f(t) = f(x) + f'(x)(t - x) + \frac{f''(x)}{2}(t - x)^2 + r(t, x)(t - x)^2, \tag{27}$$

where the remainder $r(t, x)$ is defined by

$$r(t, x) := \frac{f''(\tau) - f''(x)}{2}, \quad x < \tau < t.$$

By applying the operators $G_{n,\Psi}^{\alpha,\beta}(f;x)$ on both sides of the equation in (27), the equality

$$G_{n,\Psi}^{\alpha,\beta}(f;x) - f(x) = f'(x)G_{n,\Psi}^{\alpha,\beta}(t - x; x) + \frac{f''(x)}{2} G_{n,\Psi}^{\alpha,\beta}((t - x)^2; x)$$

$$+ G_{n,\Psi}^{\alpha,\beta}(r(t, x)(t - x)^2; x)$$

is obtained. Considering the Corollary 3, the following inequality can be written

$$\left| n\left(G_{n,\Psi}^{\alpha,\beta}(f;x) - f(x) \right) + ax^2 f'(x) - \frac{x^2}{2} f''(x) \right|$$

$$\leq \left| nG_{n,\Psi}^{\alpha,\beta}(t - x; x) + ax^2 \right| |f'(x)| + \frac{1}{2}\left| nG_{n,\Psi}^{\alpha,\beta}((t - x)^2; x) - x^2 \right| |f''(x)|$$

$$+ \left| nG_{n,\Psi}^{\alpha,\beta}(r(t, x)(t - x)^2; x) \right|.$$

Let $u_n(x) = nG_{n,\Psi}^{\alpha,\beta}(t - x; x) + ax^2$, and $v_n(x) = nG_{n,\Psi}^{\alpha,\beta}((t - x)^2; x) - x^2$. Then

$$\left| n\left(G_{n,\Psi}^{\alpha,\beta}(f;x) - f(x) \right) + ax^2 f'(x) - \frac{x^2}{2} f''(x) \right|$$

$$\leq |u_n(x)| |f'(x)| + \frac{1}{2}|v_n(x)| | f''(x)| + nG_{n,\Psi}^{\alpha,\beta}(|r(t, x)|(t - x)^2; x). \tag{28}$$

From the equalities (7) and (8), $u_n(x)$ and $v_n(x)$ approach zero, as n goes to infinity at any point $x \in [0, \infty)$. To calculate the term $|r(t, x)|$ in the equality (28), from inequality (17),

$$|r(t, x)| \leq \left(1 + \frac{(e^{-t} - e^{-x})^2}{\gamma^2} \right)\omega^*(f'', \gamma), \quad \gamma > 0$$

can be written and here the modulus of continuity $\omega^*(f, \gamma)$ is defined in (16). Since

$$|r(t,x)| \leq \begin{cases} 2\omega^*(f'',\gamma) & , \quad |e^{-t} - e^{-x}| \leq \gamma \\ 2\frac{(e^{-t}-e^{-x})^2}{\gamma^2}\omega^*(f'',\gamma), & |e^{-t} - e^{-x}| > \gamma \end{cases},$$

the inequality $|r(t,x)| \leq 2\left(1 + \frac{(e^{-t}-e^{-x})^2}{\gamma^2}\right)\omega^*(f'',\gamma)$ is obtained.

If the Cauchy Schwarz inequality is applied to the last term in the sum on the right-hand side of (28) and $\gamma^2 = n^{-1}$ is selected, then

$$nG_{n,\Psi}^{\alpha,\beta}(|r(t,x)|(t-x)^2;x)$$

$$\leq 2n\omega^*\left(f'',n^{-\frac{1}{2}}\right)\left(G_{n,\Psi}^{\alpha,\beta}((t-x)^2;x) + nG_{n,\Psi}^{\alpha,\beta}((e^{-t}-e^{-x})^2(t-x)^2;x)\right)$$

$$\leq 2\omega^*\left(f'',n^{-\frac{1}{2}}\right)\left(nG_{n,\Psi}^{\alpha,\beta}((t-x)^2;x)\right.$$

$$\left. + \left(n^2G_{n,\Psi}^{\alpha,\beta}((e^{-t}-e^{-x})^4;x)\right)^{\frac{1}{2}}\left(n^2G_{n,\Psi}^{\alpha,\beta}((t-x)^4;x)\right)^{\frac{1}{2}}\right)$$

$$\leq 2(v_n(x) + x^2 + w_n(x))\omega^*\left(f'',n^{-\frac{1}{2}}\right),$$

where $w_n(x) = \left(n^2G_{n,\Psi}^{\alpha,\beta}((e^{-t}-e^{-x})^4;x)\right)^{\frac{1}{2}}\left(n^2G_{n,\Psi}^{\alpha,\beta}((t-x)^4;x)\right)^{\frac{1}{2}}$.

Thus, the Voronovskaja type asymptotic formula is obtained.

Remark 11 Using the Maple software, the following equation is obtained

$$\lim_{n\to\infty} n^2G_{n,\Psi}^{\alpha,\beta}((e^{-t}-e^{-x})^4;x) = 3e^{-4x}x^4.$$

In (9), it was also given that $\lim_{n\to\infty} n^2G_{n,\Psi}^{\alpha,\beta}((t-x)^4;x) = 3x^4$.

Thus, taking into account the Remark 11, a result of Theorem 10 can be given as follows :

Corollary 12 Let $f,f',f'' \in C^*[0,\infty)$. Thus

$$\lim_{n\to\infty} n\left(G_{n,\Psi}^{\alpha,\beta}(f;x) - f(x)\right) = -ax^2 f'(x) + \frac{x^2}{2} f''(x)$$

holds for any $x \in [0,\infty)$.

Some graphical analysis

In this section, firstly, the convergence of the Stancu type Post-Widder operators $G_{n,\Psi}^{\alpha,\beta}(f;x)$ to the function $f(x) = x^3 e^{-3x}$ for different values of n, a, α and β is shown in Figure 1. It is observed that the operators $G_{n,\Psi}^{\alpha,\beta}(f;x)$ tend to the function $f(x)$ as n increases.

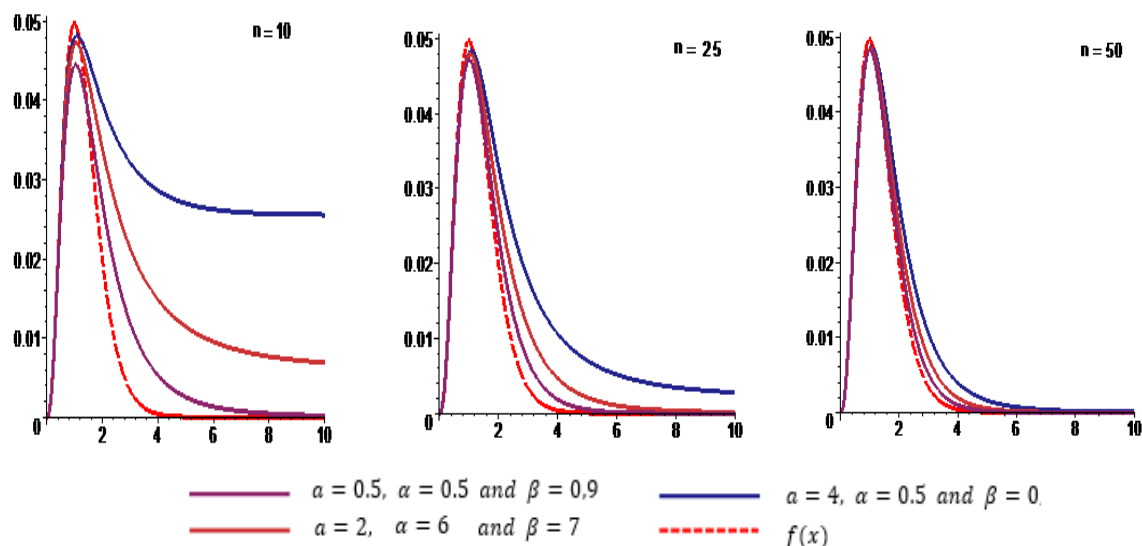**Figure 1.** *Convergence of* $G_{n,\Psi}^{\alpha,\beta}(f;x)$ *for different values of* $n, \; a, \alpha \; and \; \beta$

Secondly, the convergence of the Post-Widder Operators $P_{n,\theta}^*(f;x)$ and the Stancu type Post-Widder Operators $G_{n,\Psi}^{\alpha,\beta}(f;x)$ to the function $f(x) = x^3 \, e^{-3x}$ for $n = 50, \; a = 4$ and different values of α and β is shown in Figure 2.
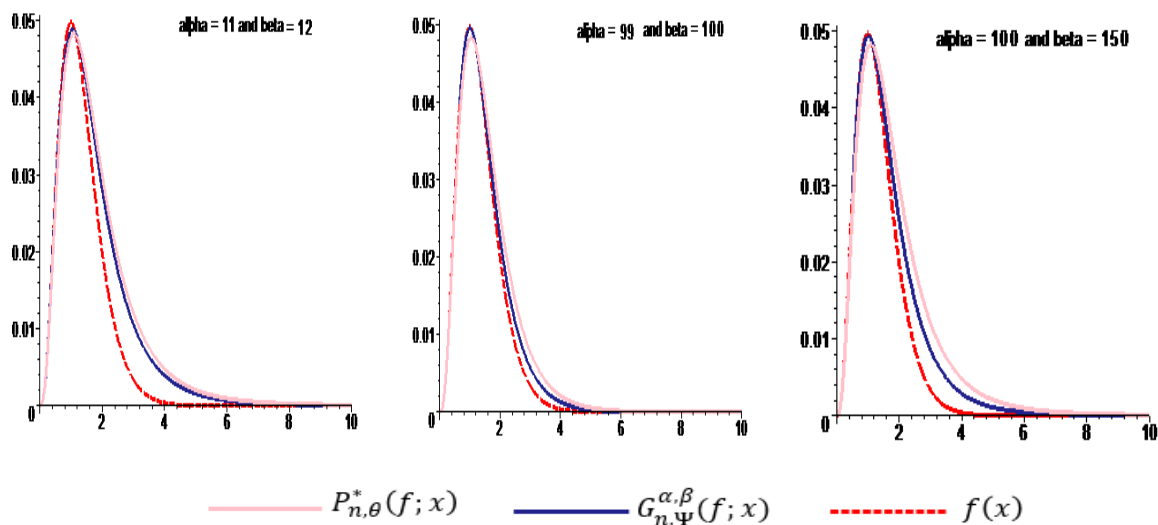
Figure 2. *Convergence of* $P_{n,\theta}^*(f;x)$ *and* $G_{n,\Psi}^{\alpha,\beta}(f;x)$ *to* $f(x)$ *for* $n = 50 \;$ *and* $\; a = 4$

References

Acar, T., Aral, A. & Gonska, H. (2017). On Szász-Mirakyan operators preserving $e^{2ax}, a > 0$. *Mediterranean J Math*, 14(6), 1-14. Doi: 10.1007/s00009-016- 0804-7

Aral, A., Inoan, D. & Raşa, I. (2019). Approximation properties of Szász-Mirakyan operators preserving exponential functions. *Positivity,* 23, 233-246. Doi: 10.1007/s11117-018- 0604-3

Bodur, M., Gürel-Yılmaz, Ö. & Aral, A. (2018). Approximation by Baskakov-Szász-Stancu operators preserving exponential functions. *Constructive Mathematical Analysis,* 1(1), 1-8. Doi: 10.33205/cma.450708

Boyanov, B.D. & Veselinov, V.M. (1970). A note on the approximation of functions in an infinite interval by linear positive operators. *Bull Math Soc Sci Math Roum,* 14(62), 9-13.

Cai, Q.B., Dinlemez Kantar, Ü. & Çekim, B. (2020). Approximation properties for the genuine modified Bernstein-Durrmeyer-Stancu operators. *Applied Mathematics-A Journal of Chinese Universities* 35 (4), 468-478. Doi: 10.1007/s11766-020-3918-y.

Cai, Q.B., Torun, G. & Dinlemez Kantar, Ü. (2021). Approximation properties of generalized λ-Bernstein–Stancu-type operators. *Journal of Mathematics*, Article ID 5590439, 1-17. Doi: 10.1155/2021/5590439

DeVore, R.A. & Lorentz, G.G. (1993). *Constructive Approximation.* (177). Berlin: Springer

Dinlemez Kantar, Ü. & Ergelen, G. (2019). A voronovskaja-type theorem for a kind of Durrmeyer-Bernstein-Stancu operators. *Gazi University Journal of Science.,* 32 (4), 1228-1236. Doi: 10.35378/gujs.513478

Dinlemez Kantar, Ü. & Yüksel, İ. (2022). Investigating (p, q)-hybrid Durrmeyer-type operators in terms of their approximation properties. *Gazi University J. Sci. Part A: Engineering and Innovation*, 1-11. Doi: 10.54287/gujsa.1029633

Gupta, V. & Agrawal, D. (2019). Convergence by modified Post-Widder operators. *RACSAM*, 113(2), 1475-1486. Doi: 10.1007/s13398-018- 0562-4

Gupta, V. & Maheshwari, P. (2019). Approximation with certain Post-Widder operators. *Publications de L'Institut Mathématique,* 105(119), 131--136. Doi: 10.2298/PIM1919131G

Gupta, V. & Tachev, G. (2022). Some results on Post-Widder operators preserving test function x^r. *Kragujevac J Math.*, 46(1), 149-165. Doi: 10.46793/KgJMat2201.149G

Gürel-Yılmaz, Ö., Bodur, M. & Aral, A. (2018). On approximation properties of Baskakov-Schurer-Szász operators preserving exponential functions. *Filomat*, 32(15), 5433-5440. Doi: 10.2298/FIL1815433Y

Gürel-Yılmaz, Ö., Gupta, V. and Aral, A. (2017). On Baskakov operators preserving the exponential function. *J Numer Anal Approx Theory*, 46(2), 150-161

Hacısalihoğlu, H. & Hacıyev, A. (1995). *Lineer Pozitif Operatör Dizilerin Yakınsaklığı.* (31). Ankara: A.Ü.F.F. Yayınları

Holhoş, A. (2010). The rate of approximation of functions in an infinite interval by positive linear operators. *Stud Univ Babes-Bolyai Math.*, 55(2), 133-142.

Kanat, K. & Sofyalıoğlu, M. (2021). On Stancu type Szász-Mirakyan-Durrmeyer operators preserving e^2ax, a>0. *Gazi University Journal of Science*, 34 (1), 196-209. Doi: 10.35378/gujs.691419

May, C.P. (1976). Saturation and inverse theorems for combinations of a class of exponential-type operators. *Canad. J. Math*, 28(6), 1224-1250. Doi: 10.4153/CJM-1976-123-8

Rathore, R.K.S. & Singh, O.P. (1980). On convergence of derivatives of Post-Widder operators. *Indian J. Pure Appl. Math*, 11(5), 547-561.

Rempulska, L., & Skorupka, M. (2009). On approximation by Post-Widder and Stancu operators preserving x². *Kyungpook Math J*, 49(1), 57-65. Doi: 10.5666/KMJ.2009.49.1.057

Sofyalıoğlu, M. & Kanat, K. (2019). Approximation properties of generalized Baskakov–Schurer–Szasz–Stancu operators preserving $e^{2ax}, a > 0$. *Journal of Inequalities and Applications,* Article number: 112(2019). Doi: 10.1186/s13660-019-2062-2

Sofyalıoğlu, M., & Kanat, K. (2020). Approximation properties of the Post-Widder operators preserving $e^{2ax}, a > 0$. *Math Meth Appl Sci*, 43:4272-4285. Doi: 10.1002/mma.6192

Torun, G., Boyraz, MM. & Dinlemez Kantar, Ü. (2022). Investigation of the Asymptotic Behavior of Generalized Baskakov-Durrmeyer-Stancu Type Operators. *Cumhuriyet Sci J*, 43 (1), 98-104. Doi: 10.17776/csj.1030637

Widder, D.V. (1941). *The Laplace Transform.* Princeton Mathematical Series, New Jersey: Princeton University Press.

.

Experimental research of hybrid thermoset composites mechanical properties

Yunus Hüseyin Erkendirci[1]
Selim Hartomacıoğlu[1]
Metin Yüksek[2]

Introduction

In hybrid composites, it is aimed to make better the composites mechanical properties by adding more than one fiber type as a reinforcement component into the matrix phase [1-2-3-4-5]. In general, fiber-reinforced hybrid composites show higher strength and hardness and higher strength to fatigue damage and corrosion compared to metal alloys [6-7]. In hybrid composites, the matrix materialcan be fiber- reinforced or particle-reinforced [8-9-10-11]. They are used to produce the components that complement each other's weaknesses [12-13] Carbon fiber has low density, tensile strength and abrasion resistance [14]. Glass fiber has high tensile strength resistance to chemicals and does not retain moisture [15] and also kevlar has low density, non-flammability and chemical resistance [16-17]. The type of fiber used as a reinforcing element in a hybrid composite is one of the important factors affecting to mechanical behavior. There are many experimental studies comparing the tension strength of hybrid and other composites, in which different fibers like carbon, glass, flax and kevlar are used as the reinforcement phase and the matrix phase is epoxy. In an experimental study conducted with hybrid and non-hybrid composites. Poyyathappan [18] concluded that fiber reinforcement materials can be listed as carbon,glass-carbon hybrid and glass,from high tolow tensile strength,in accordance with the rule of mixture (ROM). Experimental study by Vinay [19] showed that carbon-kevlar hybrid composite materials have higher strength than glass-carbon hybrid composite materials. When the tension strengths of carbon, glass & glass-carbon EHC materials produced by vacum infusion method were compared under different temperature values, it was determined better than that the tensile strength were carbon reinforced, hybrid and glass reinforced composites, respectively [20].

As can be seen from the literature review, studies on carbon fabric-glass fabric and non-wowen polypropilen composites rarely used for hybridization. In this study, two different types as 5 layers (5L) and 9 layers (9L) were produced by vacuum infusion method (VARTM).As reinforcement material; In the first material (type 1) plain woven (PW),glass fabric (GF), polypropilen mat (GN) and plain woven (PW), glass fabric (CF) and thermoset epoxy resin matrix were used. The other (type 2) 2x2 twill woven (TW) carbon fabric (CF) were used like with the other fibers and also matrix being the same. Our aim is to compare how the stacking sequence and

---
[1] Yunus Hüseyin Erkendirci, Master Strudent, Marmara University, Mechanical Engineering Department Orcid: 0000-0002-7776-088X
1 Selim Hartomacıglu Associate Professor,Marmara University Mechanical Engineering Department
2 Professor, Marmara University Textile Engineering Department

increasing the layer numbers & hence the material thickness affect the epoxy hybrid composites mechanical properties.

In this research, as mentioned above, they were subjected to tension and other test two different types of materials mechanical properties and damage behaviour to investigate and compare. Graphs were plotted for two types of materials and tables were created from the data obrained from the experiments. Afterwards, the results were compared with each other and the effects of twill and PW carbon fabric on mechanical properties and damage behaviour were exaimined. The results were supported and reported with photographs and microscope images.

Materials and Experiments

Two different types of EHC laminets of 5 and 9 layers had been produced by vacuum assisted resin transfer molding method (VARTM). Carbon, nonwoven polypropilen and E-glass fibers were supplied from Metyx (Telateks) company in Turkey. Also, epoxy resin was arranged with mixing (Resin: HEXION EPIKOTE, Curing agent: MGS RIMR 135 and HEXION EPIKURE™, Hardener: MGS BPH 137 GF, (resin/ hardener ratio is %30)) supplied from the company, Metyx Turkey. The stacking sequences of Type 1 and Type 2 EHC layers was shown in Table 1.

Types Number	Material	Carbon Glass Polypropilen Nonwoven Mat
	Number of Layer	Stacking Sequence
1	5	[G/C/NW/C/G]
1	9	[G/C/G/NW/C/G/CG]
2	5	[G/CTw/NW/CTw/G]
2	9	[G/CTw/G/CTw/NW/CTw/G/CTw/G]

Table 1. EHC laminates stacking sequences.

Carbon-Glass-Polypropilen Non Woven Glass/epoxy "HEXION EPIKOTE Resin MGS RIMR 135" EHC materials (Type 1) were produced using with PW carbon, glass fabric and non woven glass (245 gr/m^2,210 gr/m^2 and 250 gr/m^2)and then were cut into (600x600 mm) sheets. Also,Carbon-Glass-Nonwoven Polypropilen, (275 gr/m^2,210 gr/m^2 and 250 gr/m^2 then they were cut into (600x600 mm) sheets as shown Fig.1. The all various panel layers types are produced with (Resin: HEXION EPIKOTE, MGS RIMR 135" (%70 mixing rate)) epoxy resin and curing Agent (HEXION EPIKURE MGS BPH 137 GF (30% mixing rate)) hardeners with vacuum assisted transfer molding process (VARTM). All EHC materials were cured at room temperature (23 ºC) under 900 mBar vacuum pressure for 12 hours.
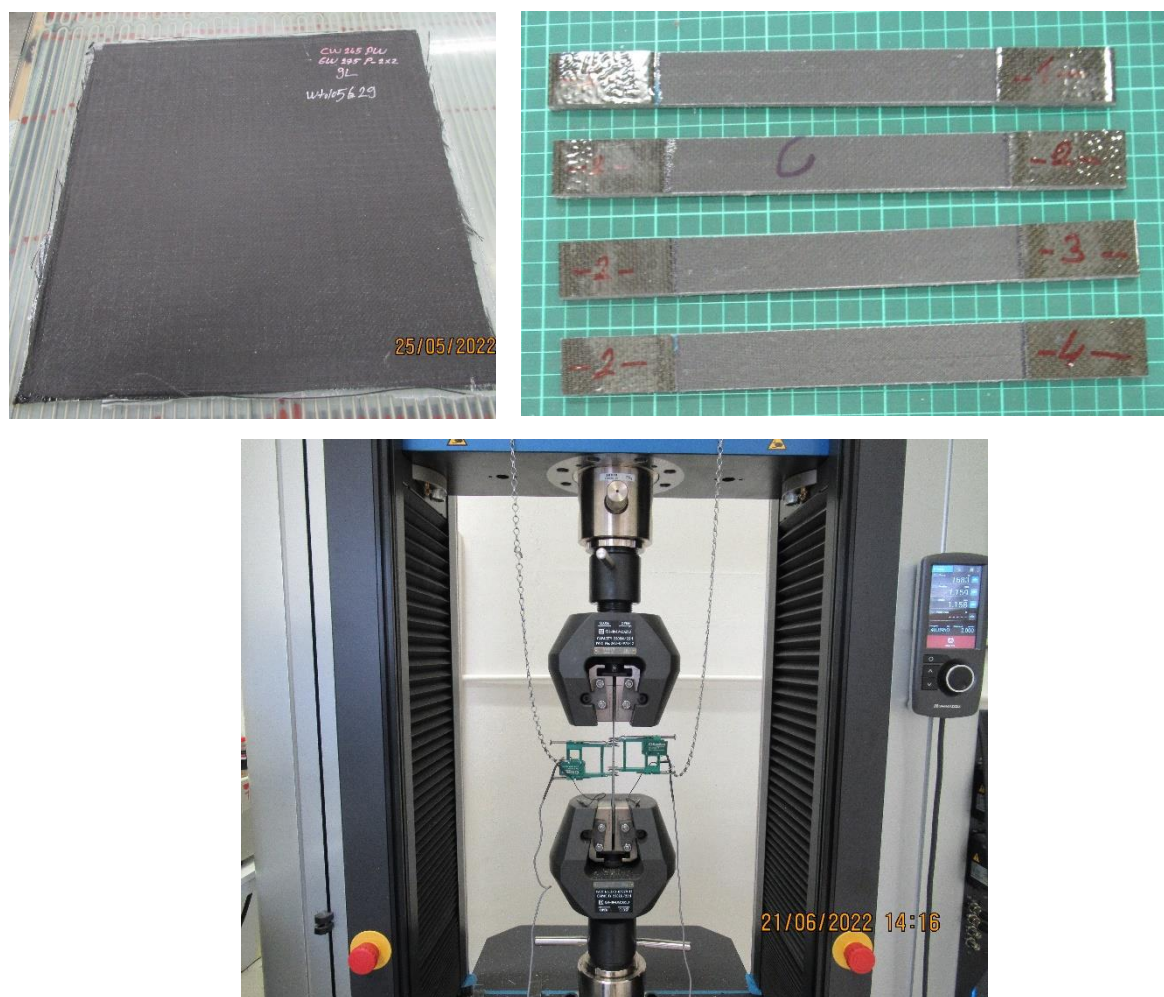
Figure 1. Photographs of sample EHC plate,test specimens & Shimadzu tensile test machine

Tension Test

The static tensile test were performed two types of EHC materials for each of them (5L and 9L) and different thickness regarding ASTM D 3039 standart. Tensile test specimens (250x250 mm) are prepared presnted in Fig.1b, tensile tests were made by the Shimadzu tensile test machine (Capacity: 250 KN) (see Fig.1c). The tensile load velocity at room temperature (RT) is 0.5 mm/min. The static tensile test results are captured & recorded with a digital camera. Throughout the recording of videos, the displacement or extension and load amounts captured with Epsilon extensometer. During the test, the displacement or extension and load amounts captured are saved and uploaded in Shimadzu tensile testing machine's data acquisiton computer. Figure 2 presents Stresss-Strain plots of all of EHC material types (PW & TW) and all layers (5L & 9L). Figure 3 are graphed to compare layers and materials. The dimensions, thickness & mass are used to compute the areal density (AD) & density of EHC materials. Fiber volume fractions (V_f) & density (ϱ) of the EHC laminates were evaluated by ASTM D2584 standart. The EHC panels areal densities are computed from the measured thickness & density of the EHC materials,

$$(AD = \rho_c{}_{H_c})$$

where, is H_c is the average thickness & ρ_c the average density of EHC material panels. EHC materials geometric and mass properties of Type 1 and Type 2 for all layers (5L and 9L) sequentially are shown at Table 2.
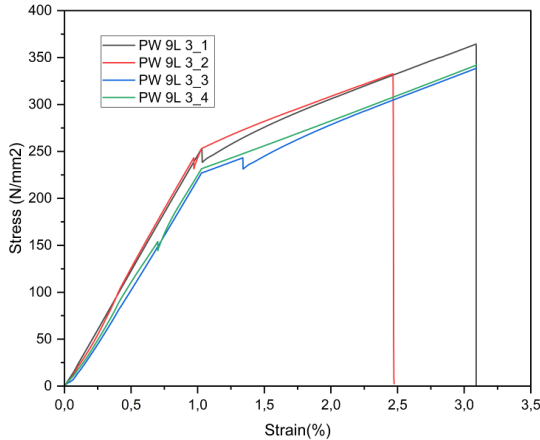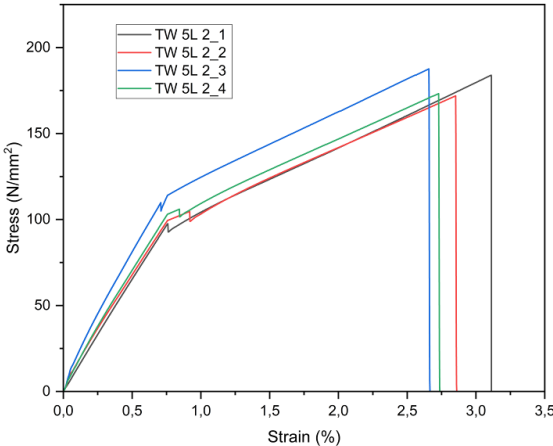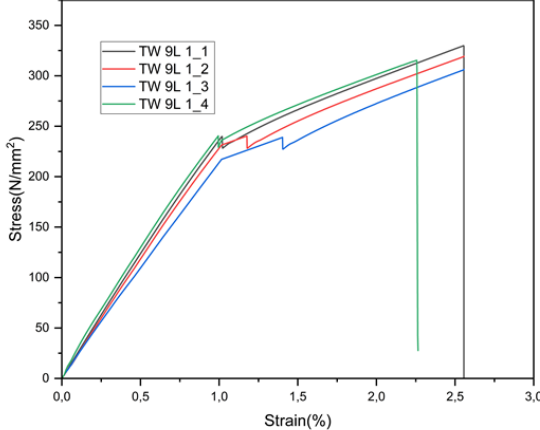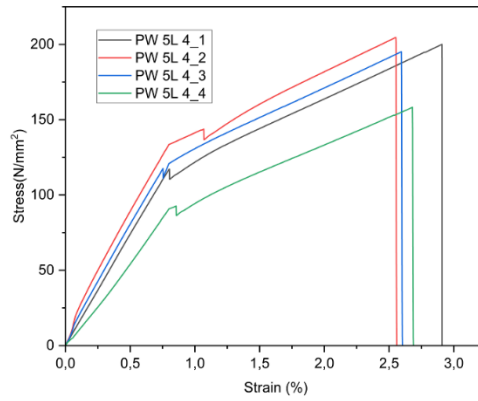
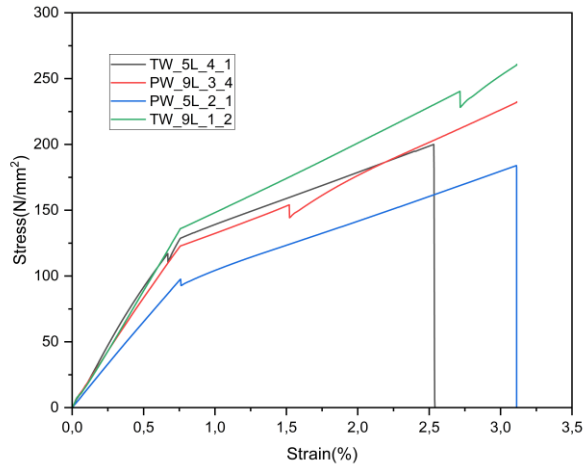**Figure 2.** Tension Stress-Strain graphs EHC materials for all types and layers

Figure 3: Stress Strain Comprasion graphs all types EHC materials

Table 2. All types EHC materials mechanical, mass and geometric properties

Hybrid Composite Materials Mechanical, Mass and Geometric Properties								
	σ_{max} (MPa)	ε %	E (MPa)	ρ_c (g/cm^3)	A_D (g/cm^2)	v_f %	H_c (mm)	B-Ratio (mm/mm)
Type1 9L	329,84	2,56	24919,22	1,29	0,41	32,23	3,17	0.0132
Type1 5L	187,58	2,94	13874,8	1,19	0,36	18,22	3,10	0,0121

Type2 9L	364,44	3,09	27421,59	1,19	0,40	33,87	3,28	0,051
Type2 5L	204,65	2,53	14336,415	1,24	0,39	18,40	3,18	0,021668

Damage Mechanism

Subsequently, the tension test, damaged specimens were investigated for understanding of damage mechanism. As a result in all types of EHC material systems brittle matrix cracks & brittle fiber fracture have been observed. Throughout the tension tests, dozens test samples were examined. For there are 96 samples, just one of them is presented in this paper as a specimen. Fiber pull out, brittle matrix cracks & brittle fiber fracture, have been occured on all types of EHC material panels. After the tension test, the fractured or damaged digital sample photographs was presented in Fig.4.

Fig. 4 The damaged digital sample photographs after the tension tests

Discussion and conclusion

In this experimental research, two types EHC materials (Type 1) plain woven (PW),glass fabric (GF), polypropilen (non-woven) fabric (GN) and plain woven (PW),glass fabric (GF) and epoxy resin as matrix were used for Type 1 of two types of EHC materials. For the other type (Type 2), twill woven (TwW) carbon fabric (CF) were used with the other fibers and matrix being the same and different layers (5L and 9L) of EHC materials laminates were researched to figure out the effect of the woven type on EHC material mechanical properties with varous thickness (i.e HC = 3.10-3.18 mm).

For EHC material (Type 1) panels were utilized as the main material & for the other types EHC material (Type 2) panels were checked with that one. Geometric properties, mechanical properties & mass of EHC materials were presented on the Table 2 to check them.Tension test were carried out to measure EHC materials elastic modulus, stress & strain for all types.

It has been determined that the stress-strain behavior of Type 2 EHC materials is different from the main Type 1 (5L and 9L), and the stress-strain graphs of EHC materials (5L and 9L) for all types and are shown in detail in the tables.

The results of this article are as follows:

1. The maximum stress of Type 1 and Type 2 EHC materials was formed in the order of Type 2 (9L), Type 1 (9L), Type 2 (5L) and Type 1 (5L). Thus, TwW Carbon fabric has been affected by the situation and its mechanical properties have increased. Elongation load capacity and stress of EHC laminates for Type 2 (5L and 9L) as shown in Table 2, Figure 2 and Figure 3.

2. Elastic modulus was determined to be thought very close to each other for all types (Type 1, 5L and Type 2, 5L& Type 1, 9L and Type 2, 9L) of EHC material panels. This presents that results are steady & the quality of production EHC materials is so good.

3. All EHC material panels densities were very close to each other.

4. The increased load capacity ratio for all EHC material panels was found to be linear with respect to EHC laminate thickness.

5. TwW carbon fabric affected EHC material panels mechanical properties of between 5% and 12%

6. Brittle matrix cracks & brittle fiber fracture have been observed in all EHC material types as expected.

References:

[1] Sun G, Zun G,Yu H,Li, et al. "Energy absorbation of metal composite and metal/composite hybrid structures under oblique crushing loding". Int J mech Sci, 2018, vol 135:458-83

[2] Gopinath A, Kumar S, Elayaperumal, "Experimental investigations of mechanical properties of jute fiber reinforced composites with polyester and epoxy resin matrices",.Procedia Engineering, 2014, 97:2052-2065

[3] Gökmen U, "Fabrication and Charecterization of Hot Extruded Hybrid Composites AI 2024 Reinforced with B4C/AI203", J. of Polytechnic, 2016, 19(4) 420-480

[4] Gökmeşe H, Karadağ H B, "IC-B4C Kompozit Hibrit MalzemelerininMikroyapı & Mekanik Özelliklerinin İncelenmesi", Gazi Üniversetesi, F. B. Dergisi, Part C:Tasarım ve Teknoloji, 2018, 6 (2): 350-435

[5] Sun G, Wang Z, Hong J, et al., .'Experimental investigation of the quais-static axial crushing behavior of filament –wound CFRP and aluminum/CFRP hybrid tubes'.Compos Struc, 2018, 190-220-35-15

[6] Davoodi MM Ahmad D Sapuan SM Ali A Khalina A Jonobi M, .Mechanical properties of hybird kenaf/glass reinforced epoxy compositesfor passangers car bumber beam Mater Des, 2010, 20;5000-22

[7] N Hashim,D.I.Amajid ,E.S.Mahdi,R Zahari,N Yidris, .Effect of fiber loading directions on the low cycle fatigue of intraply carbon Kevlar reinforced epoxy hybrid composite.Composite Structures, 2019, V.212 450-490

[8] Campbell FC,Structural composite materials.ASM Int US 2010:60

[9] Swolfs Y,Gorbatikh L,Verpoest I Fibre hybridisation in polymer composite: a review Compos Part A App Sci Manuf 2014;67:181-200

[10] Muhammad F.Ismail,Mohammed T.H Sultan Ahmad Hamdan,Ain UM Shah Mohammad Jawaid, Low Velocity İmpact Behaviour And Post-İmpact Characteristics of Kenaf/Glass Hybrid Composites With Various Ratios.Journal ofMataerials Resarch and Technology, 2019, 8(3):2500:2750

[11] Shah AUM, Sultan MTH, Jawaid M, Cardona F, Talib ARA, A review on the tensile properties of bamboo fibre reinforced polymer composites. BioRes, 2016;11:10654–76, http://dx. doi.org/10.15376/biores.11.4.Shah.

[12] Davoodi MM, Sapuan SM, Ahmad D, Ali A, Khalina A, Jonoobi M., Mechanical properties of hybrid kenaf/glass reinforced epoxy composite for passenger car bumper beam. Mater Des, 2010;31:4927–32.

[13] Sanjay M.R., Arpitha G.R., Yogesha B., 'Study on Mechanical Properties of Natural - Glass Fibre Reinforced Polymer Hybrid Composites: A Review', Materials Today: Proceedings, 2015, Volume 2, Issues 4–5, Pages 2959-2967

[14] D. Gay, SV Hoa, SW Tsai, Composite Materials Design and Applications. Boca raton FL. CRC Press LLC, 2003.

[15] S.S. Chee, M. Jawaid, M.T.H. Sultan, BioResources, 2003, 12 (2017) 7118–7132 ?

[16] J. Gustin, A. Joneson, M. Mahinfalah, J. Stone, Compos. Struct., 69 (2005) 396– 406

[17] Vinay, H.B, Experimental Study on Mechanical Properties of Polymer Based Hybrid Composite, 2016

[18] Poyyathappan, K,. Experimental Analysis and Comparative Mechanical testing on Glass- Carbon Hybrid Composites, 2019.

[19] S. Choong Woo, T. Won Kim., High Strain-Rate Failure İn Carbon/Kevlar Hybrid Woven Composites Via A Novel SHPB-AE Coupled Test. Composites Part B: Engineering, 2016, Volume 97, Pages 317-328

[20] Aklilu, G., Tensile behaviour of hybrid and non-hybrid polymer composite specimens at elevated temperatures, 2019.

Flexible Photovoltaic Applications for Non-Planar Surfaces Geometry

İbrahim GÜNEŞ[1]

Introduction

Conventional modeling takes advantage of the homogenous nature of flat surface for harvest predictions. The characteristics of a planar module yields identical performance because all cells on the module are operating under the exact same conditions. The issue arises when this homogeneity is no longer the case, producing a non- uniform gradient of incoming solar energy. The effect of this gradient remains unaddressed in the current photovoltaic modeling research.

This research takes a scale-invariant meshing approach to model the gradient of factors introduced by non-planar photovoltaic. This research develops a standardized foundation for future research in this area while investigating potential complications, detailing practical design considerations, and providing insight into nonplanar photovoltaic generation optimization.

A PV cell converts sunlight into electricity using a physical process called the photoelectric effect. Sunlight is the radiated energy from the sun. This energy can be reflected, absorbed, or just pass through a PV cell. The energy absorbed by the PV cell is then transferred to the electrons of the material. The added energy from the sunlight forces the electrons from a static position in the semiconductor material and induces a built-in electric field.

Non Planar PV Systems

The ideal single diode model is illustrated in Figure 1, considering the photocurrent and the diode current. Figure 2 is the graphical representation of which details Kirchhoff's current law at the top node of the ideal diode model. Understanding this basic principle of PV operation provides the fundamental framework vital to developing accurate models for practical applications.
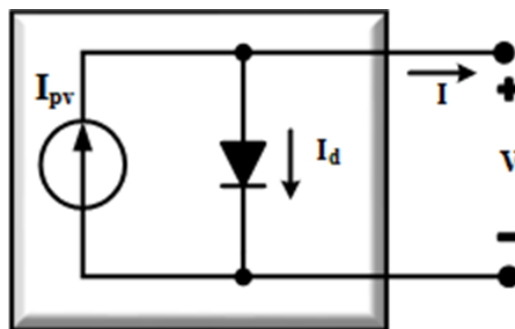

Figure 1.   *Ideal single diode model using the Shockley diode*

---

[1] Assoc. Prof. Dr. , Istanbul University Cerrahpasa Engineering Faculty Electrical Engineering Department Avcılar 34320 Istanbul Turkey,   gunesi@iuc.edu.tr
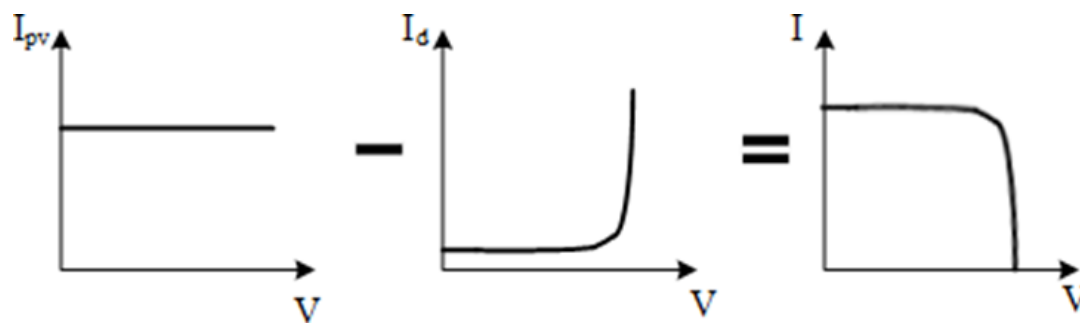
Figure 2. *Fundamental concept that defines the I-V characteristics of a PV cell.*

A simplified single diode model approach has been proposed that omits the parallel resistance. The reasoning is that when the parallel resistance is much greater than the series component, the current diverted through this element is reduced to a negligible value. This can be verified by referring to the shunt or parallel current term (Ip) for a PV cell. As parallel resistance increases, the impact of this current term approaches zero. On the other hand, the series resistance continues to correlate with the diode saturation current directly.

The result of this model provides the I-V characteristic curve expected by the PV cell, as presented in Figure 3. There are several essential characteristics on the curve that are used to evaluate the material operation. The short circuit current is the operating condition at which a difference of 0V occurs across the two PV terminals and depicts the maximum current generation ability of the PV cell at the specified insolation. Oppositely, the open circuit voltage condition describes a no-load system, corresponding to the maximum voltage at the specified insolation. These two points provide a boundary for the PV operation. The maximum power point (MPP) is the optimal operating point that delivers the most output power.
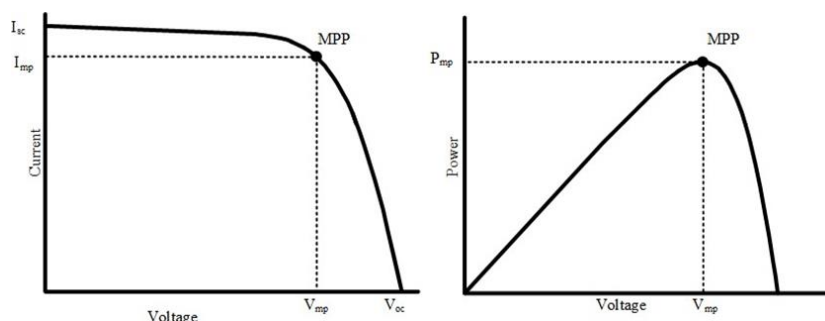

Figure 3. *I-V and P-V curve with important descriptive points.*

The only remaining parameter of the single diode model equation that does not need extraction is the operating voltage. This is because the voltage operating range is known, such that the open circuit voltage is a specified parameter in the datasheet provided by the manufacturer. To fully describe the I-V characteristics of a PV cell, the model must be computed incrementally throughout the voltage range.

Non-planar photovoltaics present three novel issues in practical applications. The most fundamental issue is the view factor gradient apparent on a curved collector. Conventional PV relies on homogeneity, so any gradient in view factor results in reduced performance. The concept of view factor will be discussed in the next section. Incoming radiation is also known as insolation and is described by W/m^2.

The concept of view factor has been used predominantly in the study of heat transfer. Since heat results from increased energy, they also provide a useful tool to translate the available solar energy into expected incident radiation on a PV collector.

Figure 4 illustrates the normal vectors of differing surface form factors. This resembles a discrete Gauss map, yielding a unit vector normal for each facet on the surface . For the flat plate, all normal vectors are homogeneous, which is ideal for achieving optimal performance. On the other hand, the semi-cylinder surface curvature yields a gradient of normal vector directions, dependent on the surface geometry.
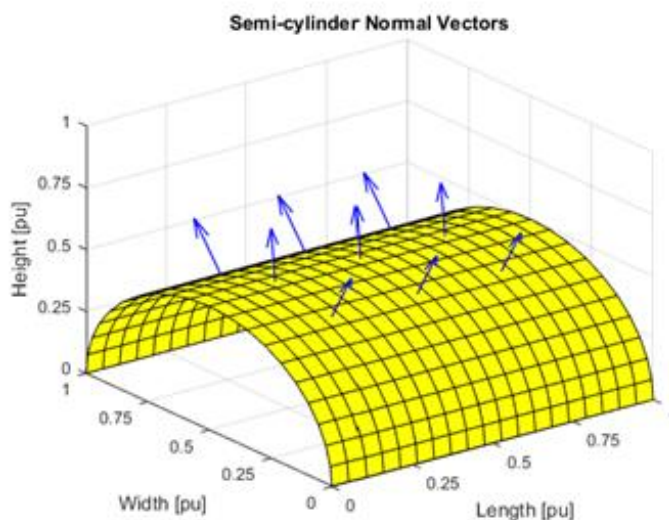

Figure 4. *Gauss map for non-planar collectors.*

The flat plate results correspond to an apparent symmetry of incoming insolation at solar noon. The top cell of the semi-cylinder is homogeneous to the planar module, and it evident in the energy profiles. While the top of the semi-cylinder is the same as the plane, the non-horizontal positions yield shifted curves.
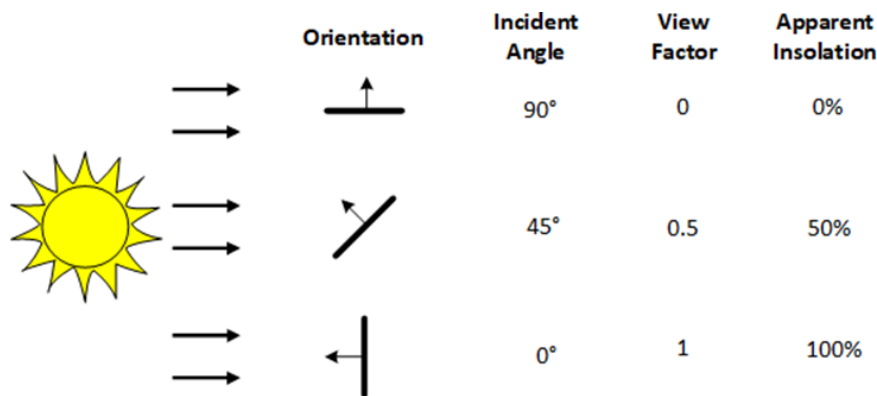

Figure 5. *Diagram of normal vector, incident angle, view factor, and apparent insolation.*

The most common deviation from homogeneity is shading. The two leading causes of a mismatch in the current generation of conventional planar solar arrays are inconsistent material degradation and shading. Since material physics lies outside the scope of this work, the focus will remain on the impact of shading. Shading of a single cell in a series connected array can drastically drop the generated output current, as illustrated in figüre 6 . When wholly shaded, the short circuit current, the photocurrent of the PV cell, drops to zero. The current from other series-connected cells must find an alternate circuit path. Instead, the current must travel through the parallel resistance, which results in power loss.

Since the parallel resistance value is assumed to be multiple orders of magnitude greater than the series resistance, this power loss can be substantial and results in localized heating of the cell. With enough upstream potential current density built up by the unshaded cells, the internal diode can be reverse biased due to the induced shunt voltage. This occurrence is highly detrimental to the performance of PV applications. Damage to the module is much more likely because it is now dissipating a significant amount of power. The shaded cell forces the upstream current produced through the internal resistances, causing hot spots.
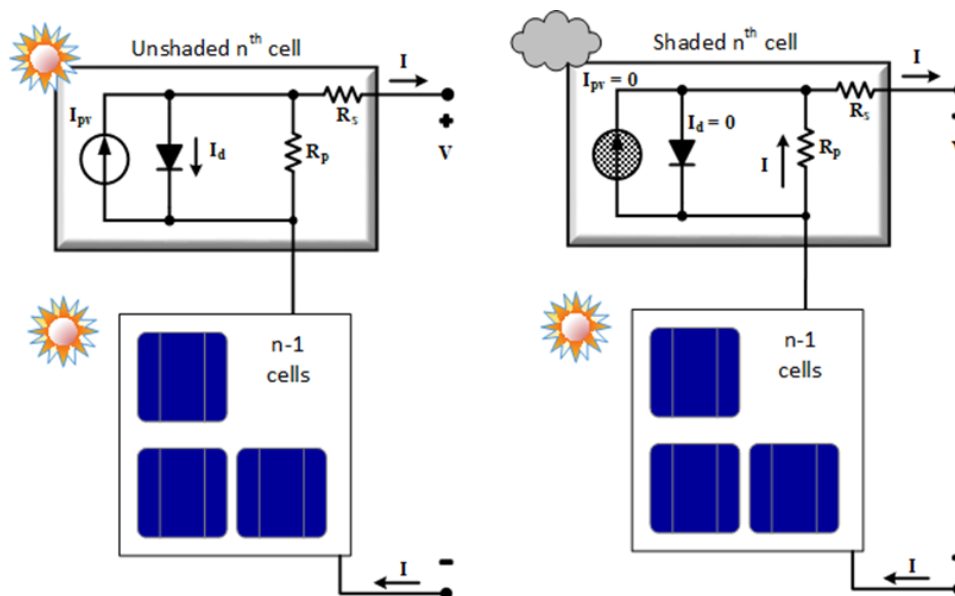

Figure 6. *Current path with and without partial shading.*

For planar PV installations, the leading cause of a mismatch current in a PV string is meteorological, like clouds or variations in the atmospheric conditions, which are stochastic. Although weather patterns can be modeled at a large scale with some confidence, the certainty of local conditions or patterns is often low. So, accurately predicting a passing cloud or non-uniform insolation for a specific PV application area is improbable.

NP-PV introduces another major cause of mismatch in the form of self-shading. Even though the unpredictable weather patterns will always be a concern for any PV applications, curved surfaces' geometric characteristics are definable. Therefore, analyzing the consistent pattern is possible. An investigation of how the curvature impacts the electrical aspects of PV must be done. Only then can the design optimization considerations be made.

The performance of PV is susceptible to high operating temperatures. Even in the most fundamental representation of the circuit equation, the relationship to temperature is evident in the diode saturation current equation in the ideal model. Temperature plays a more significant role as natural and dynamic characteristics are introduced for improved estimation.

The temperature has a significant effect on operation for every PV system, which can be seen throughout all of the modeling equations, so a thermal model is needed. In addition to defining the isolated models for electrical production and the thermal balance, it is necessary to develop an approach that couples both electrical and thermal operating models for a more accurate portrayal of realistic operational performance.

In addition to adjusting MPPT algorithms, the power electronics must also be improved for the practical use of NP-PV. A curved PV application-specific differential power processor was proposed with a flexible transformer [43]. The proposed converter design resulted in the elimination of local MPP and a slight improvement in the extracted MPP.

Geometric Design of Nonplanar PV Systems

To further improve NP-PV performance, an optimization method for the electrical design and layout of NP-PV is presented capable of modeling performance under shading and curvature. Cell dimension, interconnection, and bypass diode integration influence on module performance were investigated. The approach was applied to a double curved roof for validation. In a more general design approach, the k-means algorithm was implemented to optimize module interconnection strategies for improved electrical production on curved PV.

The analyzed surfaces are defined with a collector azimuth of 0° from the south and a tilt of 0°. This keeps the surface level on the local horizontal plane, as illustrated in Figure 7. In all plots displayed, the x-axis is oriented such that the value increases toward the south. The y-axis is oriented such that the value increases toward the east. This standardized orientation is consistent for all surfaces to narrow the scope of investigation. Because of the effect that the geometry and cell orientation have on the radiative transfer of solar energy, the morphology was presented first. The morphology techniques were conducted such that the implementation of electrical characteristics can be made on a cell level. Once electrical parameters are extracted, and the I-V curves are defined,pixelization techniques can be explored to best coordinate with the MPPT.
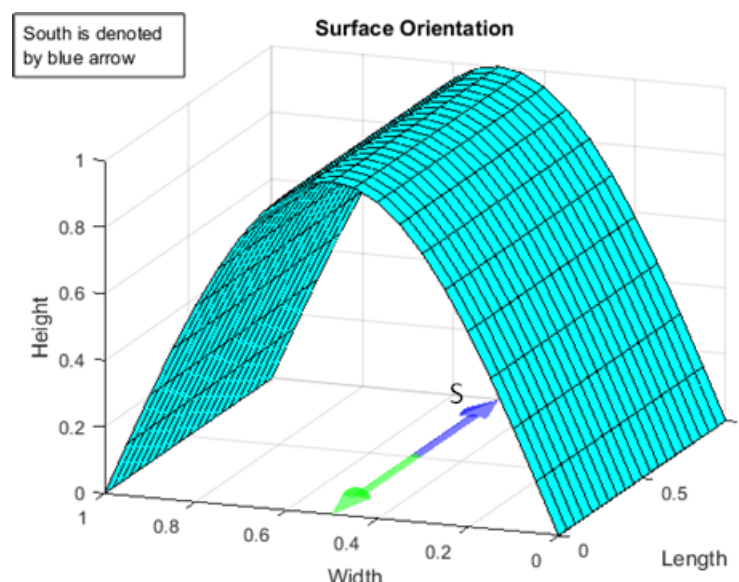

Figure 7. Orientation of defined collector geometries

Performance of Non Planar PV Systems Models

The potential performance of NP-PV is defined using three physics models. First, it is necessary to determine how much insolation the surface receives from the sun. This gives a theoretical maximum amount of energy that will strike the surface. Although perfect efficiency is not possible, comparing the insolation values with a flat surface yields valuable insight on NP-PV energy capacity, and validates further investigations. Introducing real-world efficiencies and power losses will give a more reasonable estimation of the electrical performance of the system.

The simulation conditions used in the following section are provided in Table 1. The collector orientations were selected to align the curvature of the surface with the diurnal solar. The latitude corresponds to the Tropic of Cancer, which is the northernmost latitude that experiences the sun directly overhead at solar noon.

Table 1: Parameters of Non Planar Surface

Collector Azimuth	0°
Collector Tilt	0°
Latitude	23.45°N
Day # of year	173

The flat plate serves as a control for the comparison of collection for the non-planar surfaces. The developed approach suggests that a unique power profile is produced, depending on the geometry of the curvature. The sinusoid curvature provides insight into the previously unutilized potential in that it provided three local peaks during a single day. The cells near the base of the sinusoid show little change in the rate of curvature, beginning with a tilt of about 45 degrees with respect to the planar footprint. The orientation of these cells produces the local peak in both the morning and afternoon.

The expected benefit of curved PV is that the end-user would have the ability to adjust the harvest profile as desired. If the system demands specific power curves, the surface can be designed to satisfy a practical need. The flexibility in design allows for more application-specific uses of curved photovoltaics, increasing peak available power, or a more stable harvesting profile. The evidence suggests that the geometry of the curvature is correlated to performance. Introducing an electrical model to this work provides insight into how these technologies can be optimized for applications.

Since our tuning of reflectance was based on minimizing overall error for each row, it is clear that the reflectance is not a static variable in a diurnal cycle. This introduces another factor for NP-PV applications to consider.

This analysis cannot rule out meteorological or experimental abnormalities. Therefore, the goal of this section was to establish an error bound for the model to account for significant observed impacts confidently. These results imply that this approach to thermal modeling of NP-PV provides a model capable of accurately depicting the module temperature of this surface with a margin of error expected to be within 10°C. This does not consider any variations with respect to partial shading due to meteorological events like clouds or planes.

The single diode model provides an ideal version of the operation of real cell fabrication. The double diode model would provide improved prediction accuracy of the photodiode exponential. In past work the double diode model structure has proven more precisely represent the nonlinearity of the I-V characteristics.

The short circuit current and open circuit voltage appear to be reasonably accurate. The location of the local maximum power points differs. The reason behind this deviation was determined to be due to the active diode voltage drop across the bypass diodes. The diode voltage would shift the figures to the left, depending on the diode specifications. This correction would relocate each local maximum power point to a more accurate representation of the measurements.

Some insight can be gleaned from this evaluation. Initially, it was assumed that the larger the angle difference between modules would produce equally different points of operation. This was found not to be the case. The variations of the modules with 15° angle differences were found to exceed that of the modules with a 30° change between horizontal and adjacent modules. It can be inferred that the variations in the angle from row to row have more impact with higher values of tilt. Tilt from 45°-0° experienced diminished variations on a row to row basis. This suggests the

closer to horizontal the modules are, the less deviation in production within that range. This new understanding promotes the capabilities of NP-PV applications without using bypass diodes in a design of this nature.

The traditional approach to validation is qualitative, meaning it is based on a deterministic form of analysis. Qualitative methods use graphical representations of the data to determine the significance of error, although uncertainty is not acknowledged in either the predicated or measured data. Visual interpretations may vary from person to person . Although the insight from this method of validation is flawed, the ability to visually compare data provides the ability to recognize otherwise unseen patterns. The quantitative form of analysis provides a stochastic approach to validation, considering various sources of uncertainties from the model and experiment. Both forms of validation are used within this work, each of which is intended to satisfy specific objectives.

The main objective of this study was to develop a model capable of predicting the potential generation of NP-PV applications constrained by a single axis of rotation. Insight into the theoretical energy harvest benefits regarding the traditional flat photovoltaic installations was determined using a structured quadrilateral meshing method.

In the results and conclusions made should only be associated with the specified geometry, material, location, orientation, environment, and meteorological conditions. This work is not meant to be conclusive for all NP-PV. As was established at the beginning of this research, there are many parameter combinations, so a comprehensive analysis for all cases is not feasible for one investigation. Any change in the parameters could have been investigated and probably would have exhibited different characteristics.

For a nonplanar surface, the view factor changes relative to the position of the sun and the orientation of the collector. An analysis is necessary for each cell to approximate the surface potential. A nonlinear surface would produce a nonlinear progression of average view factors instead of the linear change of a planar system. Figure 10 compares incident angles and view factors of a flat plate and semi-cylinder from Figure 8, where the length label denotes the eastward direction. The flat plate results correspond to an apparent symmetry of incoming insolation at solar noon. The top cell of the semi-cylinder is homogeneous to the planar module, and it evident in the energy profiles. While the top of the semi-cylinder is the same as the plane, the non-horizontal positions yield shifted curves.

This work has suggested many potential avenues such as water tanks, tower structural buildings, sphere, semi-sphere, cone and circle shape area to investigate in depth. Evaluating energy harvest profiles, estimating thermal impacts, predicting realistic generation, and optimizing the connection topology are all proposed within this research, suggesting potential design considerations along the way. This standardized approach promotes the use of nonplanar photovoltaic on any scale.

REFERENCES

Solar Impulse Foundation " Historic Flight Overview." https://aroundtheworld.solarimpulse.com/ (accessed Aug. 19, 2019).

H. Zhang and R. S. Balog, "Experimental verification of energy harvest from non- planar photovoltaic surfaces," in IEEE Energy Conversion Congress and Exposition, Sept. 15-19, 2013, pp. 4481-4487, doi: 10.1109/ECCE.2013.6647300.

M. Shibasaki and T. Yachi, "A power generation estimate of cylindrically-shaped flexible PV cell systems for off-grid use," in 2014 IEEE 40th Photovoltaic Specialist Conference (PVSC), June 8-13, pp. 2759-2764, doi: 10.1109/ PVSC.2014.6925500.

R. Ramchurn, "Energy Forum on Solar Building Skins," Architects' Journal, Oct. 2012, Accessed: June 3, 2018. [Online]. Available: https://www.architectsjournal.co.uk/specification/energy-forum-on-solar-building-skins

J.-P. Pelissier. "Solar France." Reuters. https://www.reuters.com/news/picture/ solar-france-idUSRTR4VM6Z (accessed Nov. 11, 2020).

A. Khaligh and O. C. Onar, Energy Harvesting: Solar, Wind, and Ocean Energy Conversion Systems (Energy, Power Electronics, and Machines). Boca Raton: Taylor & Francis, 2010.

W. Shockley, "The Theory of p-n Junctions in Semiconductors and p-n Junction Transistors," The Bell System Technical Journal, vol. 28, no. 3, pp. 435-489, 1949, doi: 10.1002/j.1538-7305.1949.tb03645.x.

S. Shi and Z. Zhou, "Applied Technology in Simulation of Photovoltaic Cell Model Based on MATLAB/Simulink," Applied Mechanics and Materials, Article no. 662, pp. 209-213, 2014, doi: 10.4028/www.scientific.net/AMM.662.209.

L. Reis, J. Camacho, and D. Novacki, "The Newton Raphson Method in the Extraction of Parameters of PV Modules," Renewable Energy and Power Quality Journal, vol. 1, pp. 634-639, 2017, doi: 10.24084/repqj15.416.

B. Tuncel, B. G. Akinoglu, T. Ozden, and R. S. Balog, "Thermal Modeling and Verification of PV Module Temperature and Energy Yield Using Outdoor Measurements for Ankara, Turkey," in 2018 International Conference on

P. Hoang, V. Bourdin, Q. Liu, G. Caruso, and V. Archambault, "Coupling Optical and Thermal Models to Accurately Predict PV Panel Electricity Production," Solar Energy Materials and Solar Cells, vol. 125, pp. 325-338, 2014, doi: 10.1016/j.solmat.2013.11.032.

O. Dupré, R. Vaillon, and M. A. Green, "A full thermal model for photovoltaic devices," Solar Energy, vol. 140, pp. 73-82, 2016, doi: 10.1016/j.solener.2016.10.033.

R. S. Balog, Y. Kuai, and G. Uhrhan, "A photovoltaic module thermal model using observed insolation and meteorological data to support a long life, highly reliable module-integrated inverter design by predicting expected operating temperature," in 2009 IEEE Energy Conversion Congress and Exposition, San Jose, CA, USA, Sept. 20-24, pp. 3343-3349, doi: 10.1109/ECCE.2009.5316107.

A. Arias-Rosales and P. R. LeDuc, "Comparing View Factor modeling frameworks for the estimation of incident solar energy," Applied Energy, vol. 277, 2020, doi: 10.1016/j.apenergy.2020.115510.

A. F. Mills, Heat Transfer, 2nd ed. Upper Saddle River, NJ, USA: Prentice Hall, 1999.

J. Appelbaum, "The role of view factors in solar photovoltaic fields," Renewable and Sustainable Energy Reviews, vol. 81, pp. 161-171, 2018, doi: 10.1016/ j.rser.2017.07.026.

T. Maor and J. Appelbaum, "View factors of photovoltaic collector systems," Solar Energy, Article vol. 86, pp. 1701-1708, 2012, doi: 10.1016/ j.solener.2012.03.017.

A. Pressley, "Curvature of surfaces," in Elementary Differential Geometry, 2nd ed. (Springer Undergraduate Mathematics Series). London: Springer, 2010, ch. 7, pp. 159-177.

G. M. Masters, Renewable and Efficient Electric Power Systems, 2nd ed. Somerset, NJ, USA: John Wiley & Sons, 2013. [Online]. Available: http:// site.ebrary.com/lib/tamu/docDetail.action?docID=10716205.

N. D. Kaushika and A. K. Rai, "An investigation of mismatch losses in solar photovoltaic cell networks," Energy, vol. 32, no. 5, pp. 755-759, 2007, doi: 10.1016/j.energy.2006.06.017.

A. McEvoy, T. Markvart, and L. Castañer, Practical Handbook of Photovoltaics, 2nd ed. (Fundamentals and Applications). Elsevier, 2012.

D. Picault, B. Raison, S. Bacha, J. de la Casa, and J. Aguilera, "Forecasting photovoltaic array power production subject to mismatch losses," Solar Energy, vol. 84, no. 7, pp. 1301-1309, 2010, doi: 10.1016/j.solener.2010.04.009.

H. Tian, F. Mancilla-David, K. Ellis, E. Muljadi, and P. Jenkins, "A cell-to- module-to-array detailed model for photovoltaic panels," Solar Energy, vol. 86, no. 9, pp. 2695-2706, 2012, doi: 10.1016/j.solener.2012.06.004.

I. Banu and M. Istrate, "Modeling and simulation of photovoltaic arrays," presented at the World Energy System Conference (WESC2012), Suceava, Romania, June 28-30, 2012.

J. A. Gow and C. D. Manning, "Development of a photovoltaic array model for use in power-electronics simulation studies," IEE Proceedings - Electric Power Applications, vol. 146, no. 2, pp. 193-200, 1999, doi: 10.1049/ip-epa:19990116.

M. Izu et al., "Lightweight flexible rooftop PV module," in 1994 IEEE 1st World Conference on Photovoltaic Energy Conversion (WCPEC), Dec. 5-9, vol. 1, pp. 990-993, doi: 10.1109/WCPEC.1994.520127.

Artificial Intelligence Based Sleep Apnea Detection with Ecg

Erdem TUNCER[1]
Çiğdem TUNCER[2]

Introduction

Sleep is one of the most important needs among our daily activities. On average, people spend about a third of their lifetime sleeping. Getting enough sleep indicates that blood pressure is regulated, heart rate is restored, and tissues are relaxed. Obstructive Sleep Apnea (OSA) is a sleep-related breathing disorder. It is characterized by repeated upper airway obstructions during sleep and subsequent waking periods (Remmers & et al. 1978). It is among the very common respiratory sleep disorders. In addition to reducing the quality of daily life of the person, OSA can also cause the development of many cardiovascular diseases. Therefore, it is important to diagnose OSA. The diagnosis of OSA plays a key role in choosing the appropriate treatment. No clinical data alone are sufficient to determine OSA. Therefore, objective tests are needed (Faal & et al. 2021, Yang & et al. 2022). The main objective test used in the diagnosis of the disease is Polysomnography (PSG). Many physiological signals are collected simultaneously with PSG all night long (Uçar 2017). These recorded signals; electroencephalography (EEG), Electrooculography (EOG) and electromyography (EMG), electrocardiography (ECG) and airflow and oximetry that provide understanding of respiratory events (Ünlü & et al. 2014, Lakadamyalı & et al. 2013).

In this study, the classification of sleep apnea data scored over ECG data was performed. The ECG signal has been preprocessed (Normalization). Then, classification was made from the windowed ECG data. At the feature extraction stage, 5 features were obtained, and ECG data were classified with Artificial Neural Network (ANN) and Support Vector Machine (SVM) classifier algorithms. As a result of the classification made between apnea and normal ECG data, a maximum success rate of 91,5% was achieved.

Materials and Method

In this study, PhysioNet-Apnea ECG database was used. Data from Phillips University, Dr. Provided by Thomas Penzel. The data set consists of a total of 70 records, divided into 35-record learning set (a01-a20, b01-b05 and c01-c10) and 35-record test set (x01-x35). Each recording contains a digitized ECG signal, expert-generated apnea note, and machine-generated QRS note. The lengths of the ECG signals vary according to the recording. Several files are associated with each record. Rnn files contain digitized ECG signals. Hea files are header files that specify the names and formats of the signal files. Apn are annotation files that contain a description for each minute of each recording indicating whether there is apnea or not. The sampling frequency of the data is 100 Hz. Amplitude values were recorded in mV. (Penzel & et al. 2000). Figure 1(a) shows an example of 10-second normalized ECG data scored normally by experts. Figure 1(b) shows an example of 10-second normalized ECG data scored as apnea. Data from 4 patients (a01, a02, a03, a04) were used in this study. For the sake of diversity, 166,66 minutes of each patient from the first

data recording were included in the study. Data are organized into 10-second windows. The number of windows and data set information obtained from the data are given in Table 1.
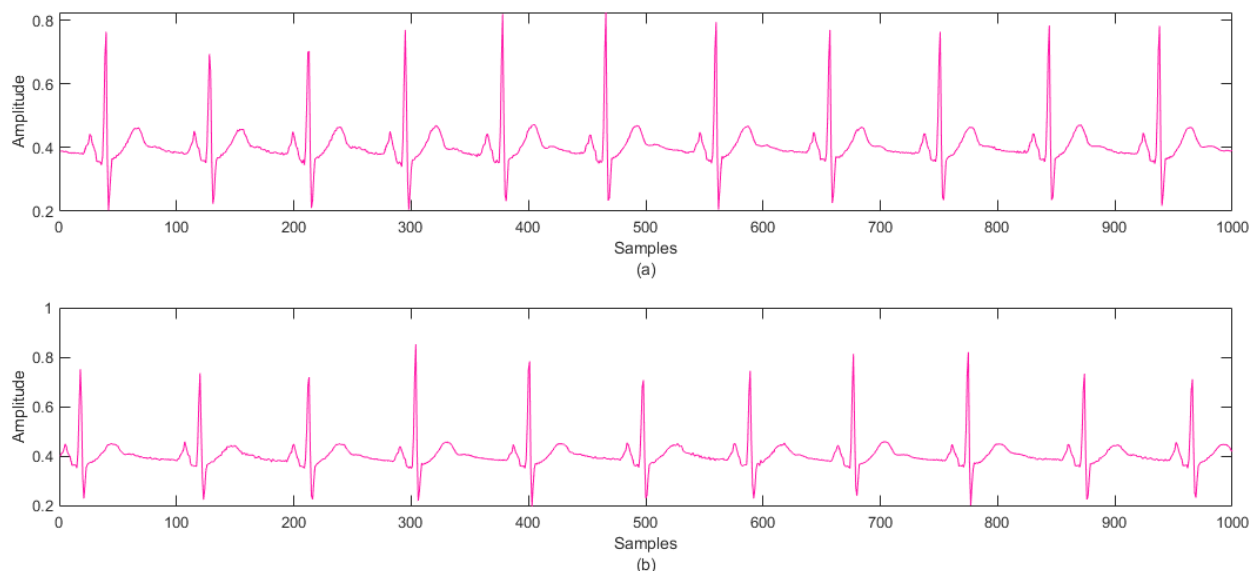

Fig 1. Typical ECG patterns of Normal (a), Apnea (b) with 1000 samples.

Table 1. ECG Dataset information

Data type	Number of epochs	Total time (Minutes)
Normal	2900	483,3
Apnea	1100	183,3
Total	**4000**	**666,6**

Mean absolute deviation, mean strength of the signal, kurtosis, skewness and variance features were obtained for each window data. The feature matrix obtained from 5 features is given as input to the classifier algorithms. Data were validated by 5-folds cross validation. ANN and SVM algorithms were used as classifier algorithms.

Artificial neural networks are information processing systems that mimic the working principles of the human brain or central nervous system in general. The generalization ability of the neural network is related to the correct selection of the network topology. The optimal architecture for the network should be large enough to learn about the problem and small enough to generalize. Therefore, the selected parameters must be carefully selected by the user. ANNs are generally divided into two as single-layer perceptrons and multi-layer perceptrons (Öztürk & et al. 2018, Mehdi & et al. 2013).

SVM is based on statistical learning theory. SVM is mainly used to distinguish the two data classes in the best possible way. For this purpose, decision boundaries or hyperplanes that can be separated linearly are determined. The algorithm determines where to draw these planes. In a nonlinear dataset, SVMs cannot plot a linear hyperplane. It therefore uses a set of mathematical functions defined as kernels. Kernel functions greatly improve performance on nonlinear data.

Different SVM algorithms use different kinds of kernel functions. These functions can be of different types such as linear, nonlinear, polynomial, radial basis kernel function. In this study, the radial basis kernel function, whose mathematical form is given in Equation (1), was used (Tuncer & et al. 2022, Melgani & et al. 2008).

$$X = (x1, x2), Y = (y1, y2) \text{ and } K(x, y) = \exp\left(-\gamma\,(x - y)^2\right) \tag{1}$$

One of the adjustable parameters given in Equation (1) γ, shows the gamma value.

Results and Discussion

In this study, the results of the two classifier algorithms were compared in order to diagnose apnea data from ECG data correctly and it was suggested to use the algorithm with high accuracy. In this study using the PhysioNet ECG dataset, normal-apnea data were classified.

ECG data is divided into windows and classified by calculating 5 features. The success rates of ANN and SVM classifier algorithms were compared. Certain network parameters are used as the basis for the ANN algorithm. In this study; The number of neurons in the input layer is 5, the number of neurons in the hidden layer is 8, the number of neurons in the output layer is 2, the learning rate is 0,03, the momentum is 0,2, and the batch size is 50. Radial basis kernel function, regularization parameter (C)=0.5, batch size=50 for the SVM algorithm. As a result of the study, a success rate of 91,5% with the ANN algorithm and 84,75% with the SVM algorithm was achieved in the correct classification of apnea diagnosis.

The diagnosis of Obstructive Sleep Apnea disease is carried out using the PSG device. In this study, an artificial intelligence-based algorithm that can diagnose from ECG signal, which will be an alternative to apnea diagnosis using PSG device, is proposed. The success rates of the two classifier algorithms were compared, and the ANN algorithm with a high success rate was proposed. Using single-channel ECG recordings with the proposed model, OSA detection in the patient will be more economical and practical. A high success rate (91,5%) was achieved with the classification made using 5 features (with the ANN algorithm).

The obtained features and the proposed classifier algorithm can be applied to larger datasets and the study can be improved by optimizing. In future studies, it is considered to carry out economic and practical solution-oriented studies with higher accuracy.

REFERENCES

Faal, M. & Almasganj, F. (2021) Obstructive sleep apnea screening from unprocessed ECG signals using statistical modelling. *Biomedical Signal Processing and Control*, *68*, 102685.

Lakadamyalı, H. (2013) Polysomnographic findings in sleep disordered breathing. *Turkish Respiratory Society*, *15*(2), 68-74.

Mehdi, B. & Khan, T. & Ali, Z. A. (2013) Artificial neural network based electrocardiography analyzer. *3rd IEEE International Conference on Computer, Control and Communication*, 1-7, DOI: 10.1109/IC4.2013.6653767.

Melgani, F. & Bazi, Y. (2008) Classification of electrocardiogram signals with support vector machines and particle swarm optimization. *in IEEE Transactions on Information Technology in Biomedicine*, *12*(5), 667-677. DOI: 10.1109/TITB.2008.923147.

Öztürk, K. & Şahin, M. E. (2018) A General view of artificial neural networks and artificial intelligence. *Takvim-i Vekayi*, *6*(2), 25-36.

Penzel, T. & Moody, G. B. & Mark, R. G. & Goldberger, A. L. & Peter, J. H. (2000) The Apnea-ECG database. *Computers in Cardiology*, *27*, 255-258.

Remmers, J. E. & Sauerland, E. K. & Anch, A. M. (1978) Pathogenesis of upper airway occlusion during sleep. *Journal of applied physiology*, *44*(6), 931-938.

Tuncer, E. & Bolat, E. D. (2022) Epileptic seizure classification from eeg signals with support vector machines. *Journal of polytechnic*, *25*(1), 239-249. DOI: 10.2339/politeknik.672077.

Uçar, M. K. (2017) Suggestions for alternative system designs for polysomnography device. *Clinical medical sciences*, *5*(3), 1-12.

Ünlü, M. & İriz, A. & Doğan, B. A. & Dinç, A. S. K. & Dursun, E. & Eryılmaz, A. & Acar, A. (2014) Relationship between obesity with symptoms and findings of obstructive sleep apnea syndrome. *Journal of Medical Updates*, 2014, *4*(1), 11-15.

Yang, Q. & Zou, L. & Wei, K. & Liu, G. (2022) Obstructive sleep apnea detection from single-lead electrocardiogram signals using one-dimensional squeeze-and-excitation residual group network. *Computers in Biology and Medicine*, *140*, 105124.

Investigation of the Effects of Third Generation Biofuel/Alcohol Mixtures on Emission and Combustion Behaviors

Erdal ÇILĞIN[1]

Introduction

The world automotive industry is one of the industries that ensures the steady growth of developed and developing countries, supports technological advances and helps many other sectors to grow. With a total size of approximately 4 trillion dollars, it constitutes approximately 5% of the world economy. In addition, the automotive industry directly and indirectly provides employment to 80 million people in the world. Global vehicle demand, which has accelerated in recent years, increased by 1.1% in 2015 compared to the previous year and reached 90.8 million units. However, the rapidly growing automotive sector, which is the 4th largest sector in the world, has a great impact on global warming, climate change and other air emissions due to fossil fuel consumption (Nowak,2019). As an example, according to data from the International Energy Agency, 99 million tons of CO_2, or 4.7% of total emissions, was generated by China's transport sector in 1990, compared to 889 million tons and 9.6% in 2018, respectively (Peterson,2020). With the growing demand, oil-derived fuel consumption is increasing and energy diversity becomes essential. Fuel property plays an important role in emission formation in the combustion process. For this reason, the concept of fuel design and diversity and the use of biofuels and biomass have come to the fore (Alam & Rahman.,2013). Biomass is non-fossil organic matter of biological origin. All natural substances of plant and animal origin are biomass energy sources, and the energy obtained from these sources is biomass energy. Biomass energy is transformed into biogas, bioethanol, biomethanol, biooil and biodiesel in modern applications. Among them, the most common use is biodiesel. Biodiesel is the mono alkyl ester of the fatty acid chain obtained from animal or vegetable oils. Biodiesel sources are classified as first generation, second generation and third generation (Ong et al., 2014). Food and edible oils such as sunflower, palm and canola are first generation biodiesel sources (Samani et al, 2021). It is stated that first generation sources reduce the amount of global food and increase its prices (Bhuiya et al., 2020). Raw materials such as domestic and commercial waste oils and inedible oils are second generation biodiesel sources. Second generation sources have reduced the dependence on edible food crops for biodiesel production. These resources are more environmentally friendly and more efficient than first generation resources (Pinzi et al., 2009). However, large fertile lands are needed to cultivate second generation resources. This creates competition as fertile lands are generally used to produce food resources. As an alternative to first and second generation biodiesel sources, third generation sources have come to the fore. Third generation sources are microalgae based sources. Microalgae describe microscopic algae (Molina et al., 2019). First of all, microalgae can be grown in fresh and salt water environments that are not suitable for first and second generation sources. They are 100 times more efficient than terrestrial-based resources. They can complete biomass formation in less than 24 hours. Microalgae do not pose a threat to terrestrial plants or to food and forage crops (Chung et al.2017). In addition, they are an effective source of biodiesel since their chemical compositions are similar to other lipid compositions. Another source of fuel diversity is alcohols. Alcohols have been seen as a suitable

---

[1] Doç. Dr, Dicle Üniversitesi

diesel fuel additive due to their liquidity and high oxygen content (**Kumar** et al,2013). Although there are many types of alcohol, short-chain alcohols have been tested by many researchers in internal combustion engines (Jamrozik et al,2019). Short-chain alcohols are alcohols containing three or fewer carbon atoms. The most important advantages of these alcohols are that they have advanced production technologies and reduce the emission levels of engines (Xingcai et al,2004). However, the use of methanol and ethanol, which are short chain alcohols, in diesel engines is difficult due to their low calorific values, miscibility problems and low cetane numbers. Ethanol causes phase formation below 10 °C when mixed with diesel or biodiesel for use in diesel engines. In addition, it cannot be mixed with diesel fuel with high mixing ratios because it causes ignition delay (ID), low calorific value and poor lubricity due to its low cetane number. As the number of carbons in alcohols increases, they can be mixed more easily with diesel and biodiesel. With the increase of carbons in alcohols, while the mass percentage of oxygen decreases, the cetane number, density and caloric value increase. In contrast to Ethanol (C_2H_5OH) and Methanol (CH_3OH), propanol (C_3H_7-OH) has a higher cetane number, calorific value and viscosity. In addition, it can be easily mixed with diesel and biodiesel due to its better solvent properties. In similar studies with propanol, it is stated that there is an improvement in diesel engine emissions, but worsening in HC emissions (Laza & Bereczky,2009) Atmanli (2016) In his study, by adding 20% propanol to the waste cooking oil biodiesel/diesel fuel mixture, he reported that the fuel with propanol added increased the specific fuel consumption by 5.28%, the CO emissions increased by 39.95% and the NOx emissions decreased by 15.05%. There are many studies in the literature investigating the performance and emission characteristics of various alcohol/diesel blend fuels. However, studies on the combustion behavior of propanol alcohol blended fuels are quite limited. Therefore, it was necessary to analyze the effects of propanol alcohol and microalgae biodiesel mixtures on combustion characteristics and exhaust emissions. The aim of the study is to examine the combustion and emission behavior of propanol alcohol blended with microalgae biodiesel and to discuss the results in the light of current literature. In this direction, biodiesel produced from microalgae was blended with 20% alcohol by volume and P-20 fuel was formed. Then, biodiesel (B-100) was blended with the reference DF fuel at a rate of 20% by volume and B-20 fuel was obtained. These fuels have been tested in a generator diesel engine at constant speed and different loads.

Experiments And Methodology

Fuel Production

Fuel production is in the form of the chemical reaction of oils, in the presence of alcohol and catalyst, to form fatty acid methyl esters and glycerine as the main product. This process is necessary for the use of vegetable oils as fuel. Because the thermal efficiency, viscosity and density of vegetable oil should be similar to diesel fuel. The most common process used for this is the transesterification reaction (Alptekin & Çanakçı,2006)

Transesterification reaction

Alcohol type, oil/alcohol molar ratio, catalyst type and amount, reaction temperature and time are important in the reaction (Azcan & Yılmaz,2011). While the use of different alcohols may slightly affect the fatty acid ester conversion rate, significant differences may occur in terms of processing costs. Methanol has been preferred because of its low cost, more polar and small molecules, easy dissolution and easy reaction. The stoichiometric ratio for alcohol: oil molar ratio is 3:1. However, since the 6:1 ratio is widely accepted as optimum, the alcohol: oil molar ratio is

6:1 in this study. The catalyst affects the efficiency and duration of the process. The catalytic activity of homogeneous alkaline catalysts is higher than that of acidic catalysts, and the reaction can be completed in an hour. Homogeneous alkaline catalyst (KOH) was used in the reaction. The reaction temperature shortens the time and increases the conversion. It was noted that the conversion took place 80% in the first 30 minutes of the reaction, and there was no remarkable increase after 60 minutes (Boz et al,2008). In this reaction, the temperature was maintained at 60ºC for 60 minutes and left to stand for 24 hours. The resulting biodiesel and glycerin were separated from gravity differences by centrifugation and excess alcohol was removed by flash evaporation. It was washed with warm water to remove residual catalyst and soaps. After the reaction of approximately 1000 g of oil with methanol, 1004.9 grams of biodiesel and 105.3 grams of glycerin were obtained. Fuel production images are given in Figure 1, and the properties of fuels are given in Table 1.

Figure 1. Fuel production visuals

Table 1. Fuel properties.

Feature	DF	1-Propanol	Biodiesel
Density (kg / m3) 15 °C	839	803	869
Viscosity (mm / s2) 40 °C	2.88	1.77	4.58
Lower Heat Value (Mj / kg)	42.44	30.65	38.62
Evaporation Heat (kj / kg)	377	727.81	-
Flash point (°C)	> 55	11.6	126

Experimental setup and test installations

The engine used: It is a four-stroke diesel generator engine with a volume of 2400 cm3 and a compression ratio of 17/1.Each of the fuels was tested at 1500 constant speed and loading of 3.6 kW, 7.2 kW and 10.8 kW. CAPELEC CAP 3200 gas device was used for emission measurements. The accuracy and uncertainty of their measurements are shown in Table 2. The schematic image of the experimental setup is given in Figure 2.

Table 2. Accuracy and uncertainty of their measurements

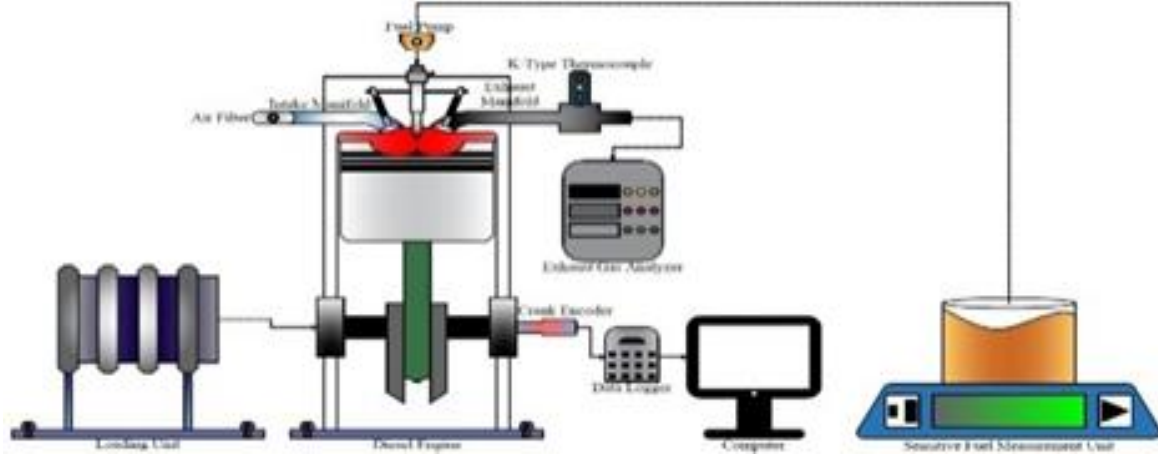| Engine Parameter	Measurement range	Accuracy
NOx	0-5000ppm	± 1 ppm
CO	0–15%	$\pm 0.001\%$
HC	0–200000 ppm	± 1 ppm
Sensor of cylinder gas pressure	0–200 bar	$\leq \pm 0.5\%$
Engine speed	0–12000 rpm	$\pm 0.1\%$ [o]

Fig. 2. Schematic image of the experimental setup

Research Findings

Specific Fuel Consumption (BSFC)

The load-dependent changes of the BSFC curves obtained by dividing the instantaneously consumed fuel volume by the power at the engine output are plotted in Figure 3.When the changes were examined, it was seen that B-20, P-20 fuels produced 2.84% and 5.13% higher g/kWh BSFC, respectively, compared to DF fuel. It is known that the energy released by the breakdown of oxygen bonds is lower than the bonds formed by hydrogen and carbon. The oxygen content of alcohols is higher than that of diesel fuel. Therefore, its thermal energy is lower (Topgül,2006). Therefore, the reason why P-20 fuel produces a high BSFC value is its high oxygen content. Fig.4 variation of the calorific value of fuels with the amount of oxygen.
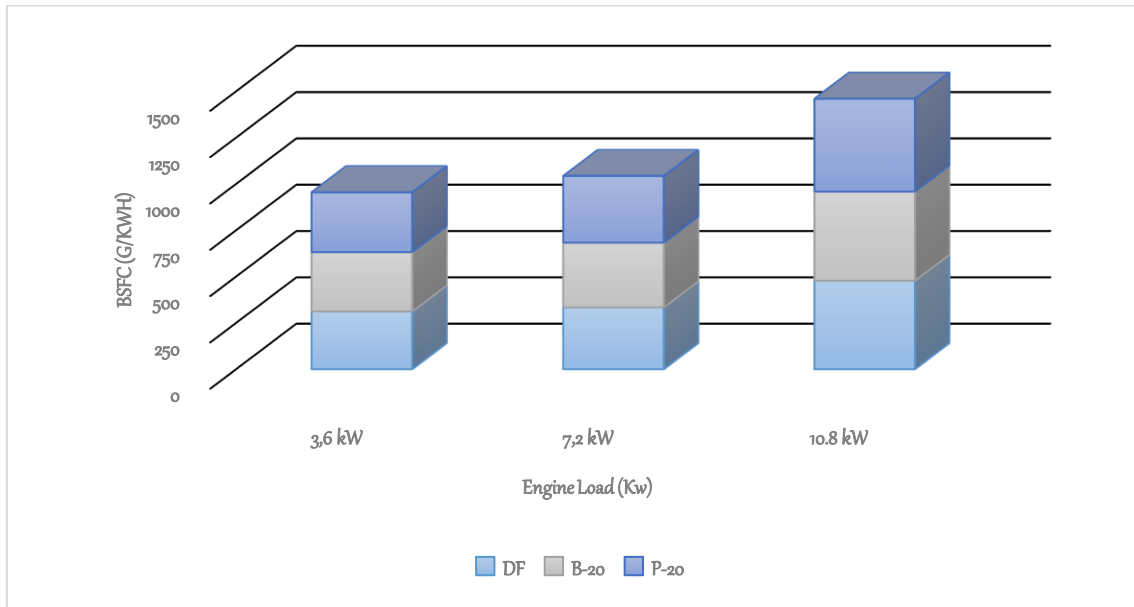
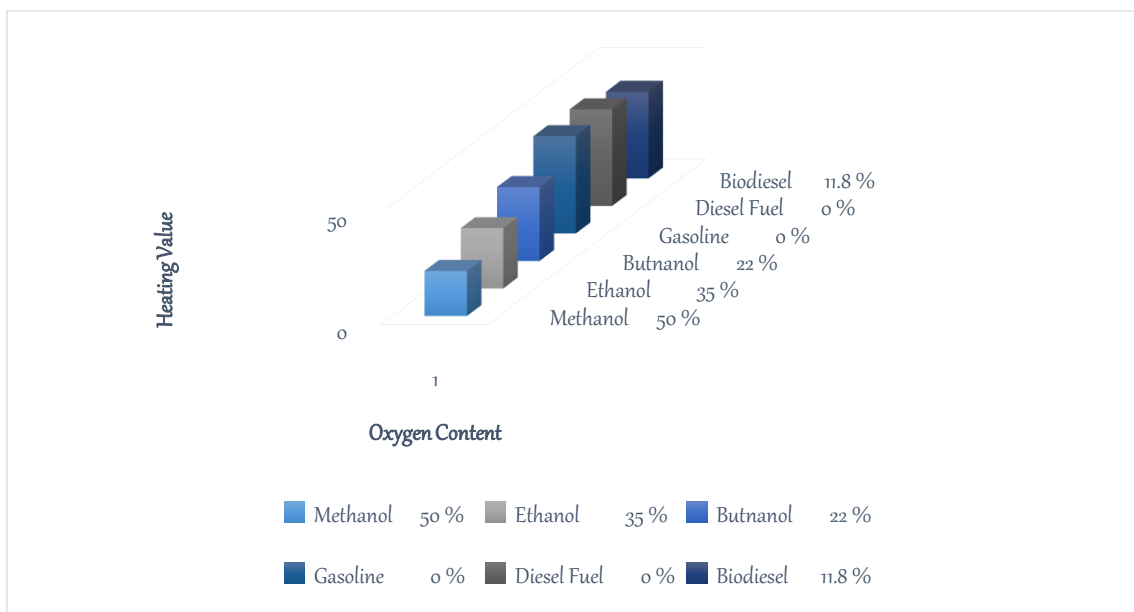*Fig 3. BSFC variation depending on load*

Fig.4 Oxygen content, calorific value amount

Exhaust Emissions

At the end of the expansion period in a 4th-stroke internal combustion engine, the exhaust valve opens and the exhaust gases pressurized in the cylinder are thrown out. CO_2, N_2, O_2 and large amounts of CO, HC, NO_x and soot are exhaust gas components in diesel engines. The composition and temperature of the exhaust gases are greatly affected by the amount of load on the diesel engine. In diesel engines, the amount of load is balanced with the amount of fuel. Therefore, the oxygen concentration in the exhaust gas differs significantly at various levels. Generally, diesel engines carry 5% oxygen in the exhaust gas at full load and 20% oxygen at idle. With increasing engine load, the amount of oxygen in the exhaust decreases, because as excess fuel

is sent, oxygen joins the combustion and more CO_2 is produced. The specific heat of exhaust gases increases (Zheng ,2004).

Carbon Monoxide Emission

Among the pollutants originating from motor vehicles, CO takes the first place with a rate of 66%. The CO changes of the experimental fuels are given in figure 5.It was observed that the CO values of B-20 fuel decreased by 7,14% on average compared to DF fuel, while the P-20 fuel decreased by 15.38%. Labeckas and Slavinskas (Labeckas et al,2016). stated in their study that the decrease in CO emissions was due to the low C atoms in the structure of biodiesel and alcohol, and the high O_2 atoms.Engines with added alcohol work with a lower air-fuel ratio due to the oxygen content, minimizing CO emissions.
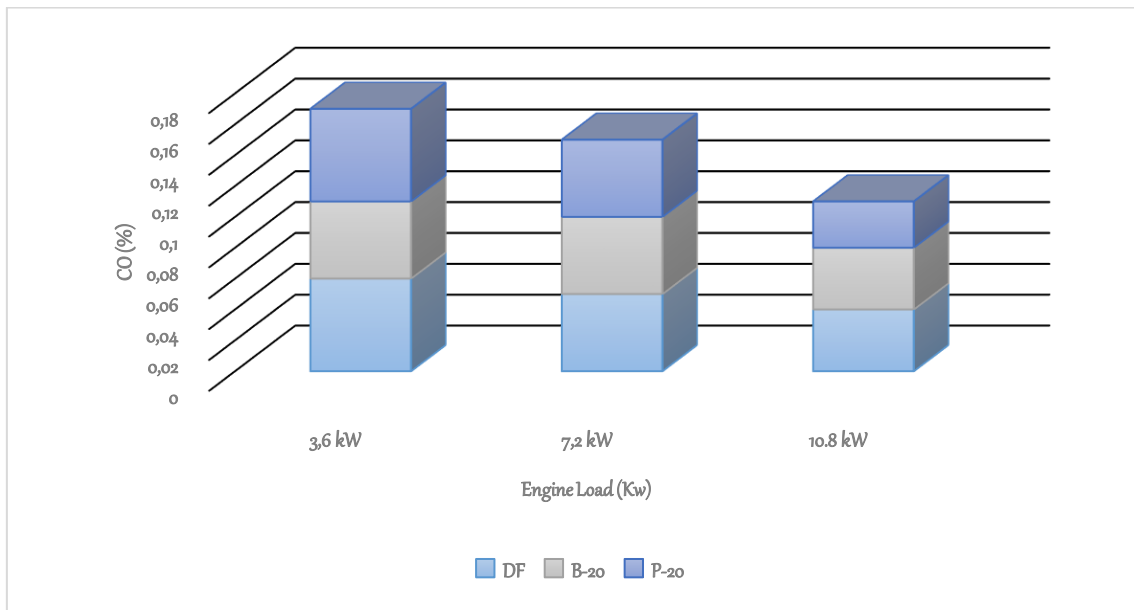

Figure 5. CO changes depending on engine load

Nitrogen Oxide Emission

High temperatures and residence times at elevated temperatures are the main causes of NO_x formation (Boruff et al,1982).NO_x is formed when nitrogen reacts with oxygen at high temperatures.It is known that in-cylinder temperatures greatly affect NO_x formation, and NO_x emissions increase as the temperature increases.When the NOx changes in Figure 6 are examined, DF fuel produced 4.28% more NOx than B-20 fuel.This high NO_x has been interpreted as being closer to complete combustion with the use of DF (İlkılıç et al,2009). It is seen that there is a 3.17% decrease in NO_x value with the use of P-20.It is thought that the high enthalpy of evaporation of propanol added to biodiesel reduces the combustion end temperatures, thus reducing NO_x emissions from high temperatures (İlkılıç et all.2015). Table 5 shows the evaporation enthalpies of the fuels
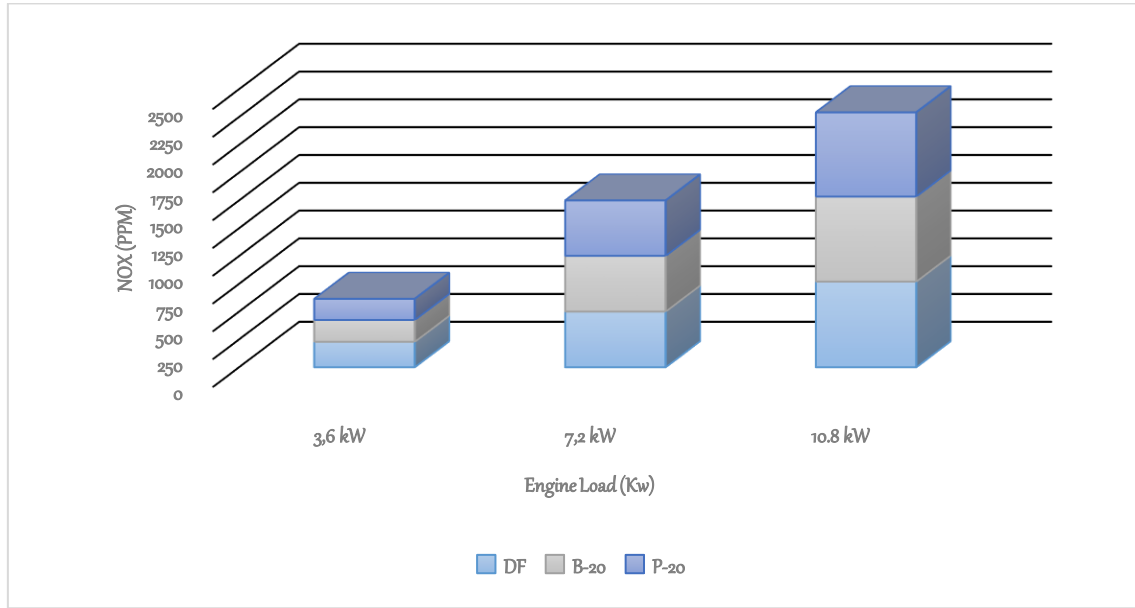
Figure 6. NOₓ changes depending on engine load

Table 5. Ignition temperatures of fuels [°C]

Fuels	Ignition Temperature [oC]
Methyl / Ethyl Alcohol	400-470
Methane	600-650
Propane	520-590
Butane	530-600
Diesel	270-350

Hydrocarbon Emission

If the Air / Fuel (A/F) ratio increases too much in internal combustion engines, the mixture becomes very weak, especially in certain areas in the combustion chamber (Adams et al,1987).Therefore, if the mixing ratio exceeds the ignition and combustion limit, HC emissions increase. Figure 7. When the HC changes were examined, it was seen that the B-20 fuel was 5.73% lower than the DF. This decrease is due to the increased oxidation of the extra oxygen in the biodiesel content (Hazar & Uyar ,2015). It is seen that there is an increase of 4.83% in P-20 fuel compared to DF fuel. The increase is due to the high latent heat of evaporation of propanol alcohol lowering the ambient temperature and the lowering temperature causing the flame to extinguish, especially near the cylinder walls (Xue et al, 2011)
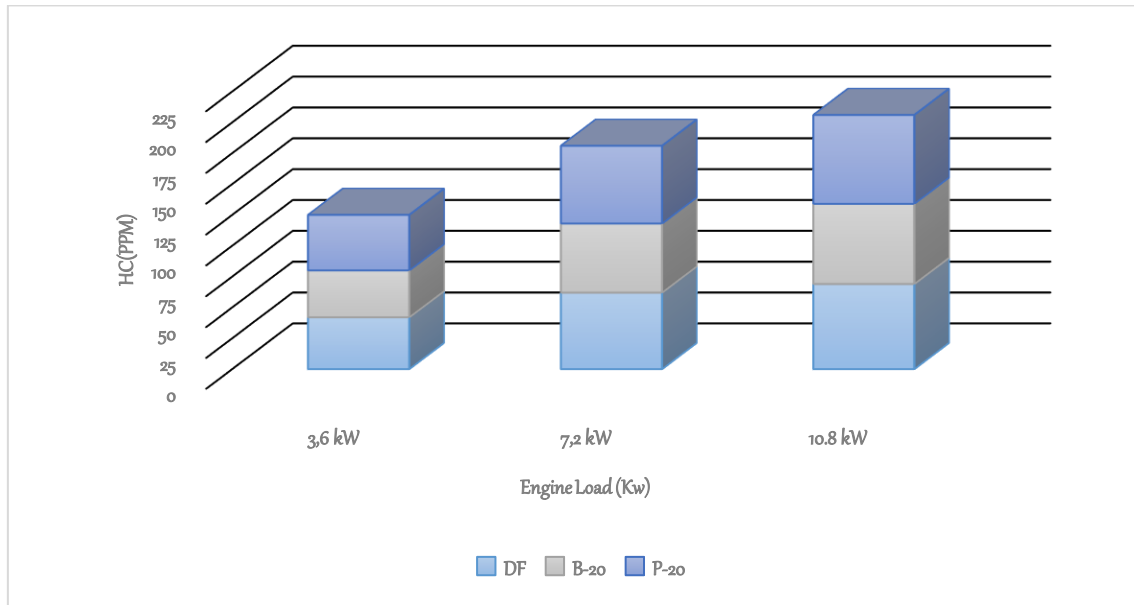
Fig.7 HC changes depending on the load

Patch Data and Burn Mechanism

The combustion process is a dynamic, physical and chemical interaction. While energy and mass transfer are associated with physical phenomena (Safgönül et al,1999). molecular interactions between fuel and oxygen are chemical reactions. During combustion, there are several parameters that affect all these relationships (Raşidova,2003). The phase, which begins with the evaporation of the injected fuel, ends with combustion and job creation (Polat, 2012). Fuel is disintegrated as a result of friction with air while being injected (Challen, 1999). Fragmentation rate is higher due to excessive friction around the fuel package (Heywood,1988). With the spraying, reactions start in the combustion chamber (Borat et al,1992). Fragmented fuel evaporates and diffusion flame is formed with ignition delay (Safgönül et al, 2008). In diesel engines, combustion is in the form of diffusion and it is local combustion zone conditions that affect combustion (Ceviz, 2005). In addition to these, air movements that occur together with heat and mass transfer in the combustion chamber are other factors affecting combustion

Combustıon Analysıs

In Combustion Analysis, the entire combustion cycle (720° KMA) can be examined, as well as a measurement range. Conditions in experimental purple from which combustion data were obtained: Specific Gas Const (kJ/kgK): 1.00, Air Density (kg/m³): 1.17, Adiabatic Index: 1.41, Polytrophic Index: 1.22, Number Of Cycles: 100, Cylinder Pressure Reference: 4, Smoothing 2, TDC Reference: 0.

Investigation of Cylinder Pressure (CP) and Heat Release Changes (NHR)

Pressure and heat release changes were generated by averaging over 100 cycles. (Figure 8.a, b, c) CP values of fuels increased with loading. Maximum values for all fuels occurred after top dead center. It was observed that B-20 fuel produced lower CP compared to DF. The decrease is thought to be due to possible consequences of the chemical and physical properties of the B-20 fuel. Because high density, viscosity and surface tension reduce the spray pressure (Ramkumar & Kirubakaran, 2016). Low spray pressure enlarges the droplet diameter (Taştan, 2018). Although

the droplet diameters are large, low penetration depths due to low pressure adversely affect the CP values (Topgül et al, 2006). In addition, the lowest cylinder pressures occurred with P-20 fuel. The high oxygen content of propanol added to the fuel content decreased the thermal efficiency of the mixed fuel and thus the cylinder pressure values. When the heat release changes were examined, it was determined that P-20 and B-20 fuels produced lower emissions than DF. The lowest heat release among fuels occurred with P-20 fuel. This decrease is due to the low thermal energy due to the fact that the energy released by the disintegration of the O2 bond in the alcohols is less than the bonds made by H and C (Enweremadu et al, 2011).
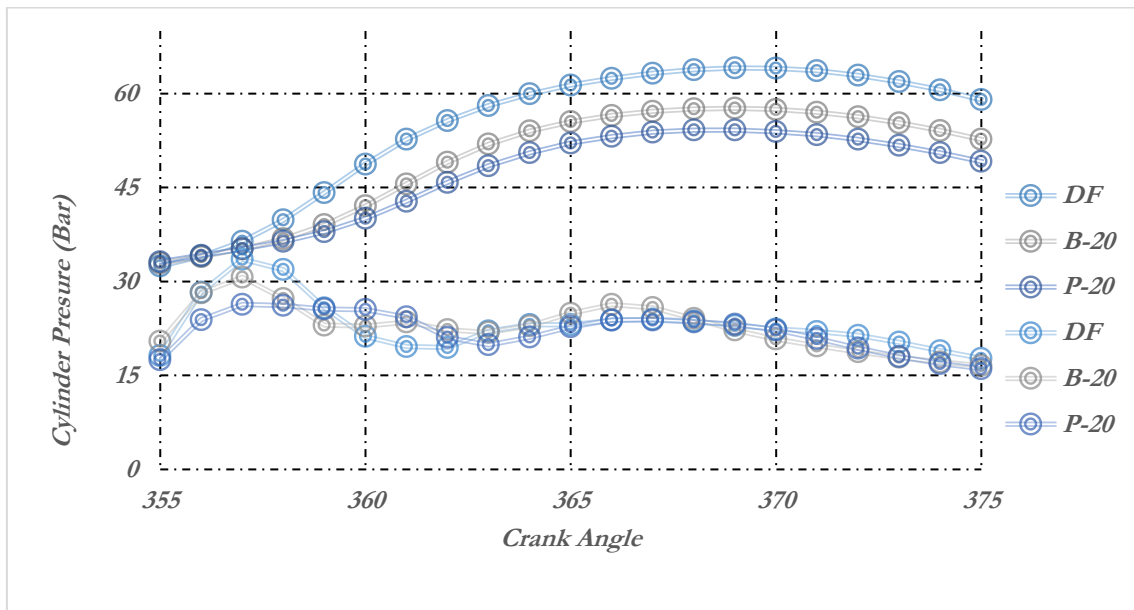

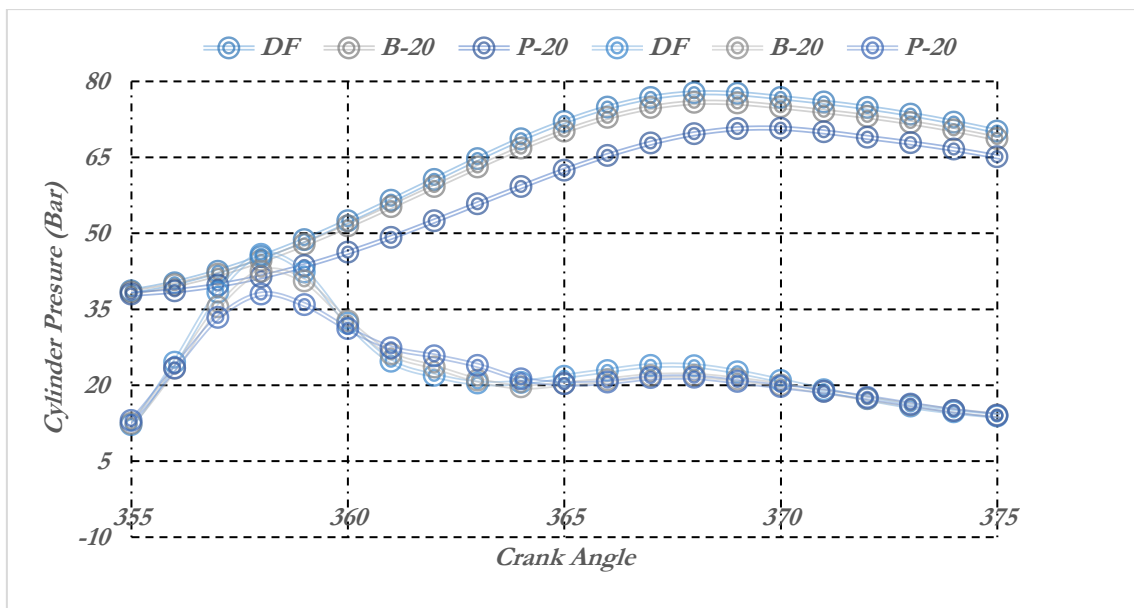*Figure 8. a Change of cylinder pressure and heat discharge rates [3.6 kw]*

Figure 8. b Change of cylinder pressure and heat discharge rates [7.2 kW]
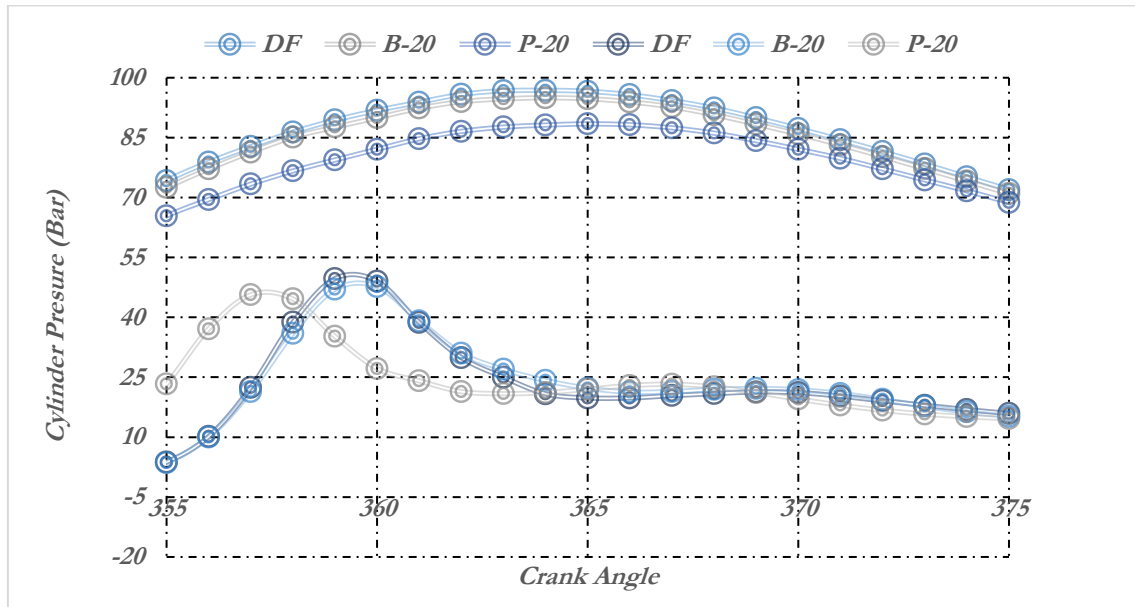
Figure 8.c Change of cylinder pressure and heat discharge rates [10.8kW]

Change of Cumulative Heat Release (CHR) and Pressure Rise Rate (RPR) Data

CHR, which is defined as the sum of instantaneous heat release rates, occurs in the form of S. It is slow in the beginning and increases rapidly until it reaches its peak value. The evaporation of the accumulated fuel during the ignition delay (ID) causes a negative value at the beginning of the curve. With its ignition, the heat emission values become positive. B-20 / P-20 fuels are fuels with low thermal values compared to DF. It is also seen in figure 9(. a,b,c) that DF produces the highest CHR. Because fuels with low heat value create low CHR curves at equal injection amounts. In addition, fuels with high CHR curves are expected to have high NO_x emissions (Aydın, 2020). DF fuel NO_x emissions were higher than P-20 and B-20 fuels. The pressure rise rate defines the load applied to the cylinder head and other combustion chamber components during the combustion process (Graboski & McCormick ,1998). In an internal combustion engine, the rate of pressure rise depends on the rate of combustion in the initial stages, which is affected by the amount of fuel involved in uncontrolled combustion. When the diagram prepared with the averages of 100 cycles was examined, it was seen that all test fuel values increased with the loading. Because the average in-cylinder gas temperatures have increased. It was observed that the maximum values progressed before the top dead center with loading. This indicates that mass and mass flow rate shorten the ignition delay. Also, these data, which seem to increase with loading, are a basic measure for monitoring the knocking of the combustion process. These higher levels that occur indicate higher NO_x emissions. When the fuels were examined, it was determined that DF fuel had a higher pressure increase compared to B-20 and P-20 fuels, despite a shorter ID time.
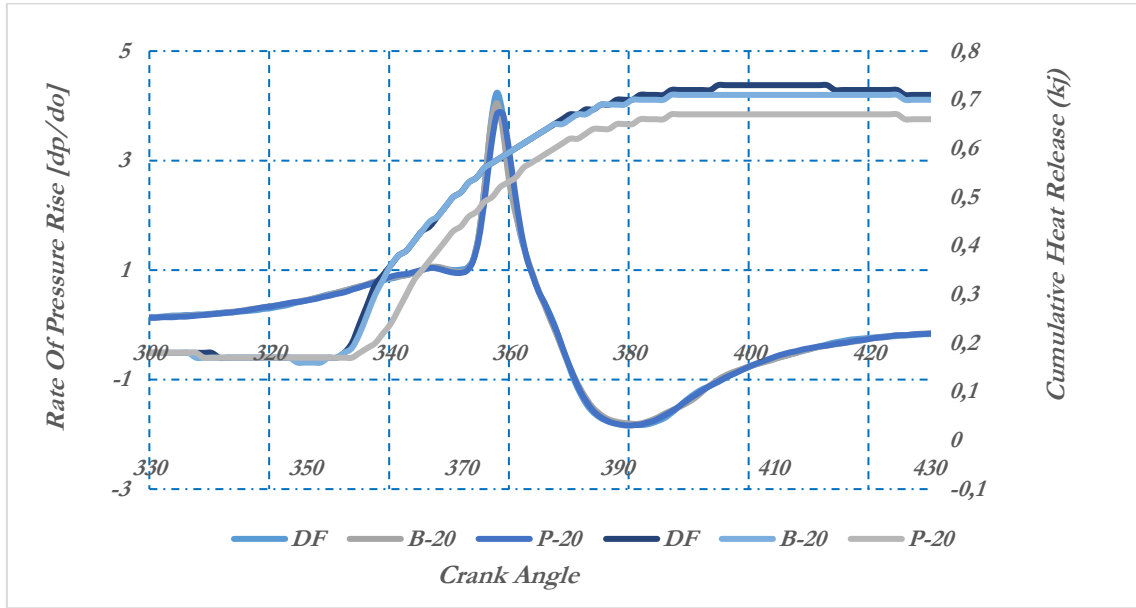
Figure 9.a. Variation of pressure mean velocity and cumulative heat release according to crank angle. [3.6kW]
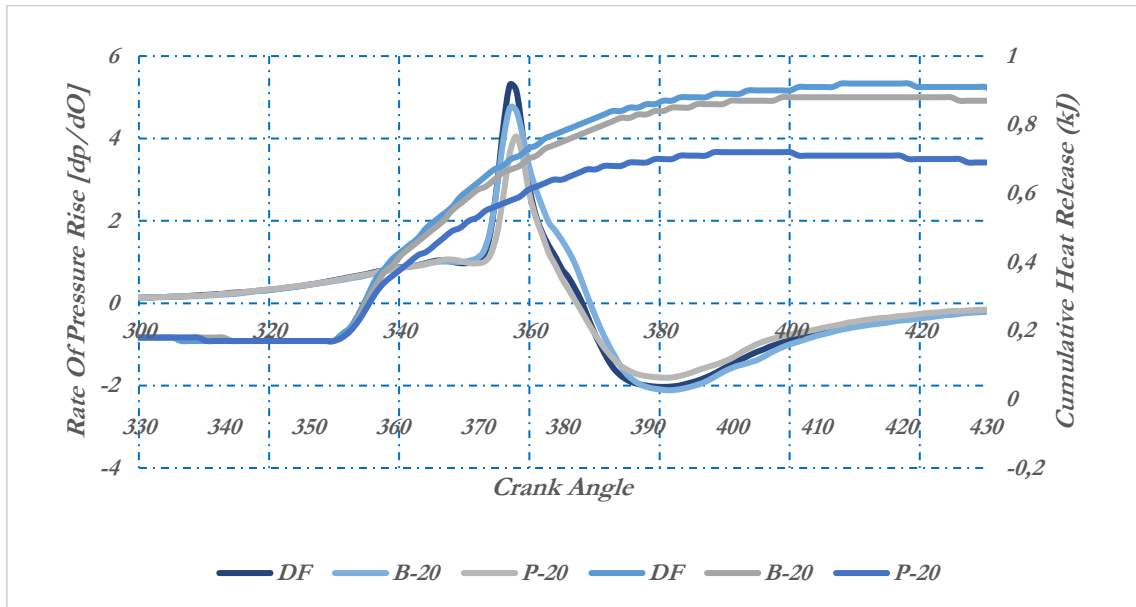

Figure 9.b. Variation of pressure mean velocity and cumulative heat release according to crank angle [7.2kW]
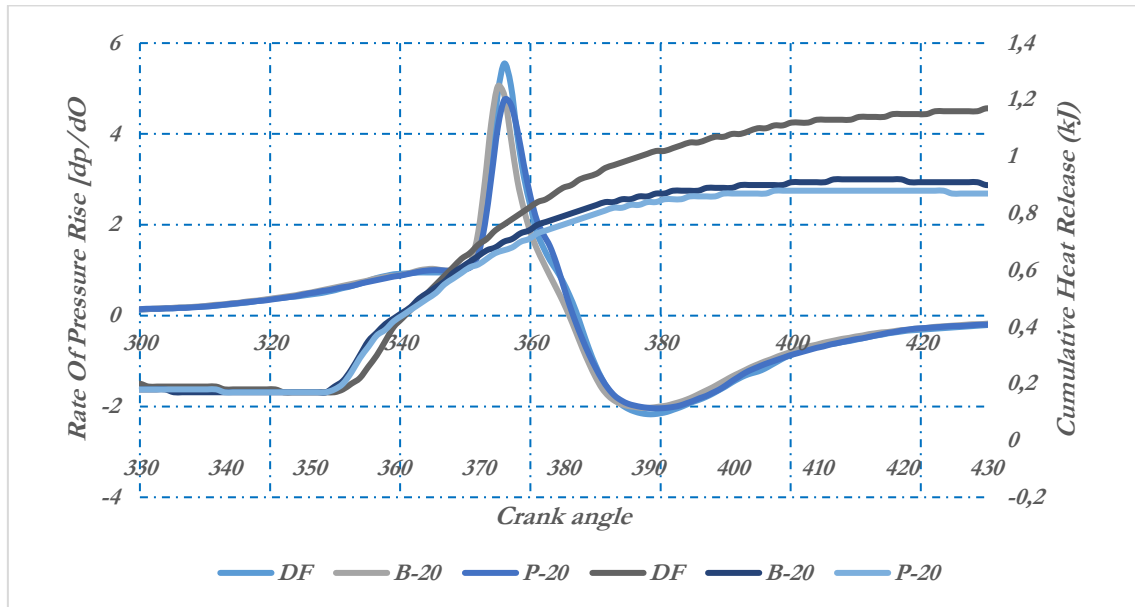
Figure 9.c. Variation of pressure mean velocity and cumulative heat release according to crank angle [10.8kW]

Average Gas Temperature (AGT)

When the figures 10a, 10b, 10c, where AGT values are given, are examined, it is seen that AGT values of all test fuels increase with loading. The maximum values occurred at a load of 10.8 kW. These were measured as 1810.84 in DF: 381CA, 1714.11 in B-20: 380CA, and 1613.45 OC in 378 CA for P-20. Combustion process in internal combustion engines is improved by the presence of oxygen (Challen ,1999). The alcohol-doped P-20 fuel mixture consisted of biodiesel and propanol. There is 20-22% oxygen in propanol alcohol and 10-12% oxygen in biodiesel. Despite these oxygen values, the lowest AGT values occurred in P-20 fuel. The reason for this was interpreted as the high molar enthalpy of vaporization and low cetane number of alcohols reduce the combustion temperature of P-20 fuel (Kuti et al,2010). Combustion data are presented in detail in table 7 and table 8.
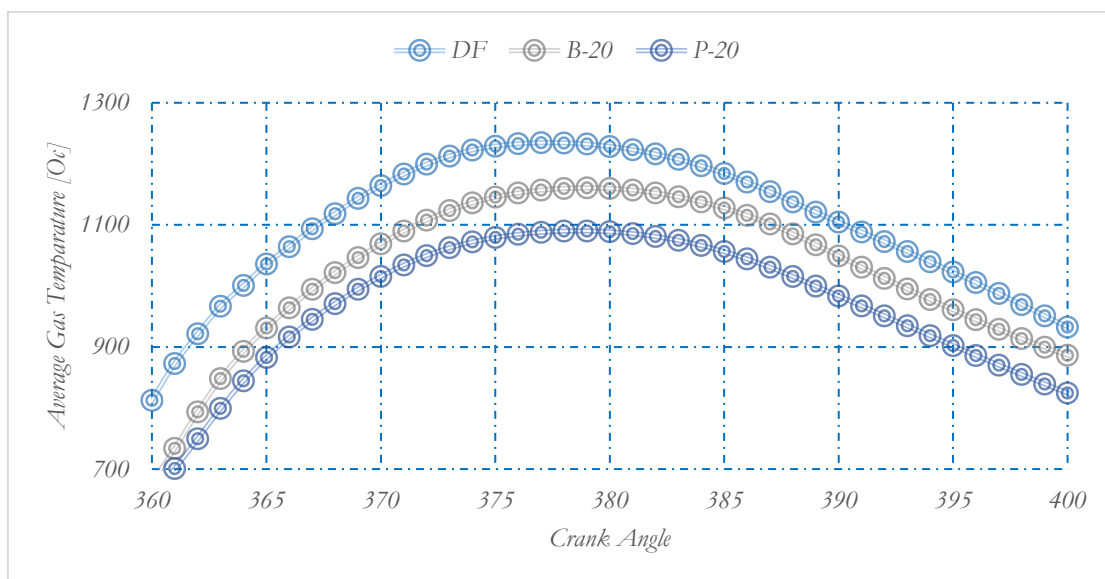
Figure 10.a Average gas temperature [3.6 kw load]
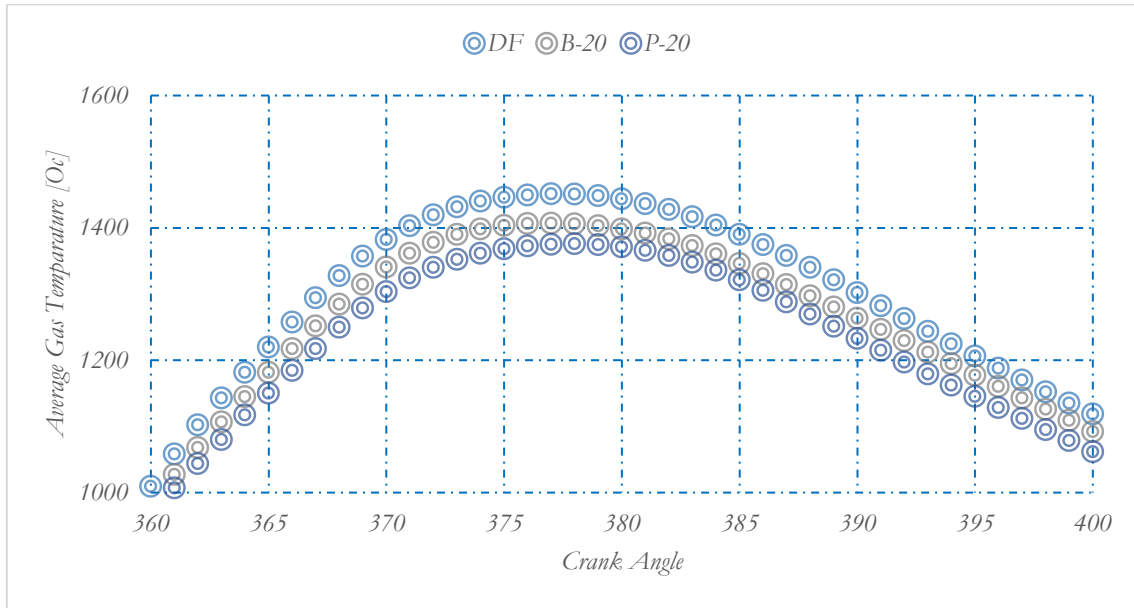
Figure 10.b Average gas temperature [7.2kw Load]
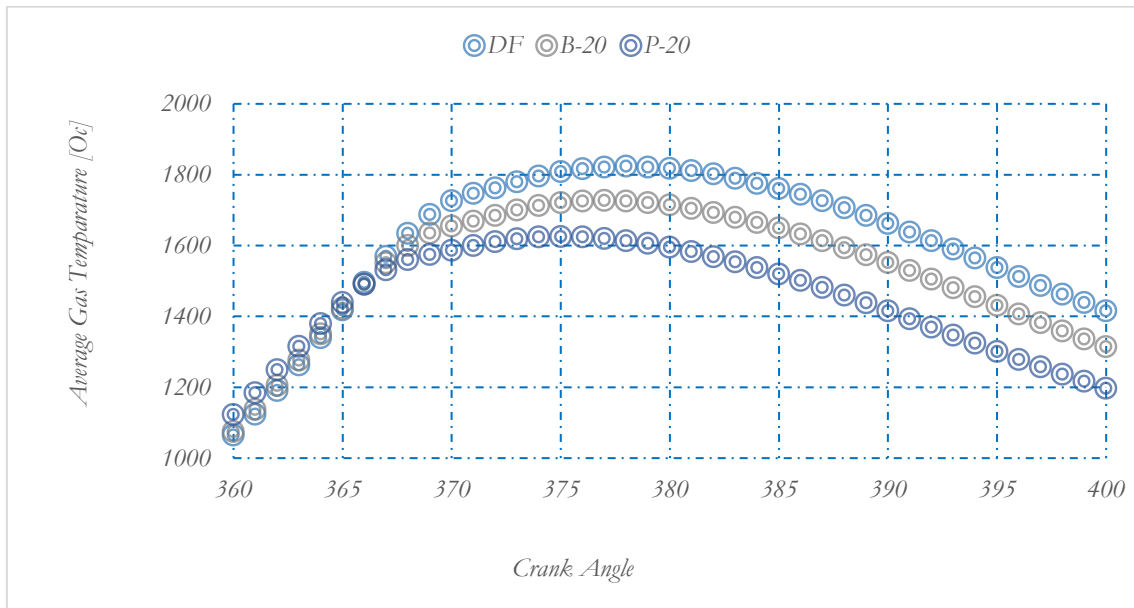
Figure 10.c Average gas temperature [10.8 kW Load]

Conclusion

The prominent results of the study conducted to see the effects of adding alcohol to microalgae on combustion and emission behaviors; First of all, the addition of alcohol decreases the cetane number, density, viscosity and calorific value of the blended fuels, while increasing the heat of evaporation. Especially the decrease in the heating value caused 5.13% g/kWh more fuel consumption in BSFC values with the use of P-20 fuel. The physical and chemical properties of the mixture fuel formed by the addition of alcohol caused a slight decrease in the combustion data.

When the effects of alcohol addition on emissions were examined, there was an increase of 4.83% in HC emissions, effective reductions of 3.17% in NOx values and 15.38% in CO values. The addition of alcohol to biodiesel indicates that it is a renewable fuel that can be used in diesel engines without modification. However, more studies are needed to determine the ideal mixing ratios.

References

Adams WH, Hinrichs HG, Adamis P. (1987). Analysis of The Combustion Process of A Spark Ignition Engine with A Variable Compression Ratio," SAE Transactions. vol.89, no.4,pp. 749-757

Atmanli A. (2016). Comparative analyses of diesel–waste oil biodiesel and propanol, n-butanol or 1-pentanol blends in a diesel engine. Fuel, 176:209-215.

Alam MM, Rahman KA. (2013) "Biodiesel from mustard oil: a sustainable engine fuel substitute for Bangladesh," Int. J. Renewable Energy Dev. Vol. 2, no.3, pp. 1-19, 2013.

Alptekin E, Çanakçı M (2006)."Biyodizel ve Türkiye'deki Durumu" Mühendis ve Makina, 47:561, 57-64.

Aydın S(2020). Detailed evaluation of combustion, performance and emissions of ethyl proxitol and methyl proxitol-safflower biodiesel blends in a power generator diesel engine." Fuel, vol.270, no.4, pp.117492.

Azcan N, Yılmaz Ö. (2011). "Yemeklik Atık Yağın Mikrodalga Destekli Transesterifikasyonu ile Biyodizel Eldesi ve Moleküler Distilasyonla Saflaştırılması" Tübitak Proje No: 110M011.

Boz N, İlgen, O, Yıldız M, Kibar ME, Kar, M, Sunal O.(2008). Atık Yemeklik Yağların ve Bitkisel Yağların Transesterifikasyon Reaksiyonu için Uygun Katalizör Tasarımı ve Kinetik Çalışmalar" Tübitak Proje No:106M04.

Bayındır H, Işık MZ, Argunhan Z, Aydın H. (2017). Combustion, performance and emissions of a diesel power generator fueled with biodiesel-kerosene and biodiesel-kerosene-diesel blends. Energy, 123, pp. 241-251

Brunt M.F.J, Rai H, Emtage AL. (1998). The calculation of heat release energy from cylinder pressure data SAE Paper No. 981052.

Bencheikh K, Atabani AE, Shobana S, Mohammed MN, Uguz G, Arpa O, Kumar G, Ayanoglu A, Bokhari A. (2019). Fuels properties, characterizations and engine and emission performance analyses of ternary waste cooking oil biodiesel–diesel–propanol blends. Sustainable Energy Technol Assess; 35:321–34.

Bhuiya M.M. K, Bhuiya M. Rasul M, Khan N, Ashwath M.(2020). Mofijur.Comparison of oil extraction between screw press and solvent (n-hexane) extraction technique from beauty leaf (Calophyllum inophyllum L.) feedstock Ind. Crop. Prod., 144, p. 112024

Borat O, Balcı M, Sürmen A (1992). İçten Yanmalı Motorlar," Gazi Üniversitesi Teknik Eğitim Fakültesi Matbaası, Ankara, pp. 85- 197.

Boruff A.W, Schwab C.E, Goering E.H. (1982). "Evaluation of Diesel Fuel - Ethanol Micro-Emulsions", Transactions of the ASAE, vol.25, no. 9, pp: 47-53.

Challen B, Baranescu R. (1999). Diesel Engine Reference Book 2nd ed.", ButterworthHeinemann, Oxford, pp.22-24.

Ceviz MA, Yüksel F (2005). Effects of ethanol–unleaded gasoline blends on cyclic variability and emissions in an SI engine." Applied Thermal Engineering vol.25, pp. 917–925, 2005.

Chung J.-W, Lee C, (2017). Molecular challenges in microalgae towards cost-effective production of quality biodiesel. Renew Sustain Energy Rev, 74, pp. 139-144

Checkel J. (1986). Dale Computerized Knock Detection from Engine Pressure Records SAE Technical Paper, 860028, 10.4271/860028

Dhanasekaran R, Ganesan S, Rajesh Kumar B, Saravanan S. (2019).Utilization of waste cooking oil in a light-duty DI diesel engine for cleaner emissions using bio-derived propanol. Fuel 2019; 235:832–7.

Enweremadu CC, Rutto HL, Oladeji JT. (2011). Investigation of the Relationship Between Some Basic Flow Properties of Shea Butter Biodiesel and their Blends with Diesel Fuel, "International Journal of the Physicsal Sciences, vol. 6, no.4, pp. 758-767.

Graboski MS, McCormick RL. (1998). Combustion of fat and vegetable oil derived fuels in diesel engines". Prog. Energy Combust. Sci, Vol.24, pp.125-164.

Hohenberg GH, (1997). Advanced approaches for heat transfer calculations SAE Paper No. 790825

Hazar H, Uyar M. (2015). Experimental Investigation of Isopropyl Alcohol (IPA)/Diesel Blends in a Diesel Engine for Improved Exhaust Emissions", International Journal of Automotive Engineering and Technologies, vol. 4, no.1, pp.1-6.

Heywood JB. (1988). InternalCombustion Engine Fundamentals", McGraw-Hill, London, pp. 486-494,1988.

İlkılıç C, Behçet R, Aydın S, Aydın H. (2009). "Nox Formatıon in diesel engines and control methods." 5. Uluslararası İleri Teknolojiler Sempozyumu, Karabük, Türkiye. 13–15 Mayıs.

İlkılıç C, Çılğın R, Aydın H. (2015). "Terebinth oil for biodiesel production and its diesel engine application. " Journal of the Energy Institute.Vol. 88, no. 3, pp. 292-303.

Jamrozik, A, Tutak W, Gnatowska R, Nowak . (2019). Comparative analysis of the combustion stability of diesel-methanol and diesel-ethanol in a dual fuel engine. Energies, 12(6):971.

Kuti OA, Xiangang WG, Zhang W, Nishida K, Huang ZH. (2010). "Characteristics of the ignition and combustion of biodiesel fuel spray injected by a common rail injection system for a direct–injection diesel engine," Proceedings of the Institution of Mechanical Engineers, Part D: Journal of Automobile Engineering, vol.224, pp.1581-1596.

Kumar S, Cho J. H, Park J, Moon I. (2013). Advances in diesel–alcohol blends and their effects on the performance and emissions of diesel engines. Renewable and Sustainable Energy Reviews, 22:46-72.

Laza, T, Bereczky Á. (2009). "Influence of Higher Alcohols on the Combustion Pressure of Diesel Engine Operated with Rape Seed Oil", Acta Mechanica Slovaca,13(3): 54-61.

Labeckas S. (2006). "The Effect of Rapeseed Oil Methyl Ester on Direct Injection Diesel Engine Performance and Exhaust Emissions", Energy Conversion and Management, vol.47, no.14, pp.1954–1967.

Molina D, Molina J.C, Carvalho A.I, Magalhães Jr C, Faulds E, Bertrand C.R. (2019). Soccol.Biological contamination and its chemical control in microalgal mass cultures Appl. Microbiol. Biotechnol., 103 (23–24), pp. 9345-9358, 10.1007/s00253-019-10193-7

Nowak, D. J. (2019) The atmospheric system: air quality and greenhouse gases" Hall. M, Balogh. S, (Eds.), Understanding Urban Ecology, Springer, Cham 2019.

Samani BH, Behruzian M, Najafi G, Fayyazi E, Ghobadian B, Behruzian A, Mofijur M, Mazlan M, Yue I.(2021). The rotor-stator type hydrodynamic cavitation reactor approach for enhanced biodiesel fuel production. Fuel, 283, p. 118821

Safgönül B, Ergeneman M, Arslan HE, Soruşbay C. (1999). İçten Yanmalı Motorlar," İstanbul Teknik Üniversitesi, Makine Fakültesi, Otomotiv Anabilim Dalı,"Birsen Yayınevi", İstanbul..

Safgönül B, Ergeneman M, Arslan HE, Sorusbay C. (2008). İçten Yanmalı Motorlar", Birsen Yayınevi, istanbul, pp. 38-41, 196-205, 2008.

Taştan M. (2018). Içten Yanmali Bir Motorda Hidrojenle Zenginleştirilmiş Metanol-Benzin Karişimlarinin Performans Ve Emisyona Etkisinin Deneysel Incelenmesi" Doktora Tezi. Ocak Kayseri.

Topgül T, Yücesu HS, Çinar C, Koca A. (2006). The Effects of Ethanol-Unleaded Gasoline Blends and Ignition Timing on Performance and Exhaust Emissions," Renewable Energy, vol.31, no. 15, pp. 2534-2542, 2006.

Topgül T. (2006). "Buji ile ateşlemeli motorlarda etil alkol-benzin karışımı kullanımında optimum çalışma parametrelerin araştırılması, " Doktora Tezi. Gazi Üniversitesi, Fen Bilimleri Enstitüsü, Türkiye

Ong H.H, Masjuki, T.M.I. Mahlia, A.S. Silitonga, W.T. Chong, K.Y.(2014). Leong.Optimization of biodiesel production and engine performance from high free fatty acid Calophyllum inophyllum oil in CI diesel engine. Energy Convers. Manag., 81 (2014), pp. 30-40

Polat S. (2013). Bir Dizel Motorunun Bilgisayar Yardımı Đle Termodinamik ve Performans Analizi." Gazi Üniversitesi Fen Bilimleri Dergisi Part: C, Tasarım Ve Teknoloji GU J Sci Part: C vol.1, no. 3, pp.139-151.

Peterson, B. (2013) "Car Ownership Statistics" (2020). Date of access: 06.10.2020. https://www.valuepenguin.com/auto-insurance/car-ownership-statistics.

Pinzi F.J, Lopez-Gimenez M.D, Luque de Castro G, Dorado M.P. (2009) Dorado The ideal vegetable oil-based biodiesel composition: a review of social, economic and technical implications. Energy Fuels, 23 (5).

Raşidova A. (2013). Vibe Fonksiyonu Kullanılarak Dizel Motorlarında Yanma Hızının Gürültü Emisyonuna Etkisinin İncelenmesi." Yüksek Lisans Tezi. İstanbul Teknik Üniversitesi.

Ramkumar S, Kirubakaran V. (2016). Biodiesel from vegetable oil as alternate fuel for C.I engine and feasibility study of thermal cracking: a critical review," Energy Conversion and Management, vol.118, pp.155-169.

Yilmaz N, Atmanli A, Vigil FM. (2018). Quaternary blends of diesel, biodiesel, higher alcohols and vegetable oil in a compression ignition engine. Fuel 2018; 212:462–9.

Zheng M, Reader GT, Hawley J.(2004). "Diesel engine exhaust gas recirculation- a review on advanced and novel concepts." Energy Conversion and Management, Energy Conversion and Management vol.45, no. 6, pp. 883- 900.

Xue J, Grift TE, Hansen AC. (2011). Effect of Biodiesel on Engine Performances and Emissions", Renewable and Sustainable Energy Reviews, vol.15, no.2, pp.1098-1116.

Xingcai, L, Zhen H, Wugao Z, Degang L (2004). The influence of ethanol additives on the performance and combustion characteristics of diesel engines. Combustion Science and Technology, 176(8):1309-1329.

Applıcation of the Rescheduling Approach in Manufacturing Systems

Ediz ATMACA

1.Introduction

A production schedule is predetermined before the execution of the manufacturing processes in the manufacturing systems. However, the unscheduled disruptions such as the delays of manufacturing processes or the addition of jobs often occur in the manufacturing systems, and an initial production schedule may not satisfy the constraints due to the disruptions. A dynamic scheduling method is therefore required to cope with the unscheduled disruptions. The reactive scheduling method is one of the dynamic scheduling methods that satisfy this requirement (Sakaguchi et al., 2008).

The changeable nature of manufacturing environments complicates the application of the very first tables and causes a decrease in table performance. To improve the performance of tables, new quests are plunged. Reactive scheduling emerges from these quests. In case of an unforeseeable incident during manufacturing, tables can be updated and new tables can be established. Every product needs different raw material and different semi-manufactured good which can be provided from various suppliers in manufacturing atmosphere. A completely reproduced table may not cover the time needed for procurement of raw material and semi-manufactured product. Sudden changes in tables raise the transportation distance, time and cost. Tables can be needed to be rescheduled in some workbenches. To avoid the deviation during application stage, alterations should be minimized in tables. Consequently, it is a healthier approach to improve tables than to start all over again (Suh et al., 1998).

Reactive scheduling is defined as the process of amending table put into practice in case of unpredictable situations in application area. Also, it is stated as the healing of table arranged before application during manufacturing operation or as the adaptation of it to process.

 In other words, it is an update operation of tables while they are in process. The algorithm of reactive scheduling repairing is presented in Figure 1 (*Raheja and* Subramaniam, 2002).
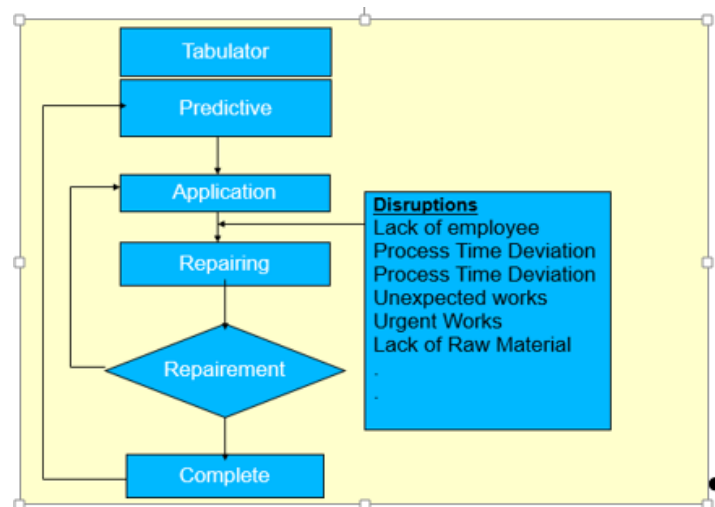

Figure 1. Reactive Scheduling Repairing.

2. Reactive Scheduling

Since reactive scheduling problems are very complicated, conventional operational research approach is not appropriate for the solution. To get healthy results, artificial intelligence and sophisticated method routine are used. Some of the operational research approaches are listed below (*Raheja and* Subramaniam, 2002).

- Right Shift Rescheduling – RSS

- is the simplest approach to reactive rescheduling. The process is formed shifting whole schedule forward and expanding them to the right to adopt the breakdowns.

- Affected Operation Rescheduling

- However, it is easy to apply; more qualified schedules appear with RSS approach. Within this algorithm, only disturbed schedules are to be rescheduled.

- A heuristic - based approaches are applicable and response to changes in an effective way but they do not assure the best result.

- Multi–Agents system in Distributed Artificial Intelligent Approaches

- These systems are for solving independent agents' problems and arranging them while they are working in this common purpose. Intelligent agents have information for scheduling and also work to improve schedule.

Knowledge-based Scheduling and Artificial Intelligent Approaches
- ❖ *Incident based thinking*
The aim of incident based thinking is to determine the best answer for breakdowns considering past events so the solutions of past events can be used for new problems.

- ❖ *Constraint based scheduling*
It is a good approach in which interactions and audit are better. Since it is based on knowledge-based and incident based module, it operates effectively than incident based scheduling.
- ❖ *Fuzzy logic*
After all corrections for constraint violation, there is a complete checking and schedule is optimized globally during correction period. Since the same modules are used for scheduling and adjustment, there is a quick reaction but the algorithm is not developed.
- ❖ *Neural networks*
The predictions are made according to past experiences and they are assuring. The reaction time is very fast to educate neural network. For correct estimation, very carefully trained sets are needed.
- ❖ *Genetic algorithm*
This algorithm considers genes' natural selection process for rescheduling. To reduce deviations on the original schedule, it needs transverse and mutation applications. Genetic algorithms are active and produce fairly good schedules however it requires high calculation effort. Demands of reactive scheduling systems can be examined in there heading given below (Vieira, 2003).

Robust: Robust approximation schedule can be valid against various corruptions. Robustness is a requested feature. It reduces decisions to approve schedule during reactive scheduling. Robustness can be improved by purifying from unnecessary reactions to failure and

underestimation. Good performance can be gained by producing small corrections and robust schedules.

Nervousness: Schedule react corruption by being restored or rescheduling. To schedule from all over again seems to be applicable but this kind of solutions may not be very successful. Reactive scheduling should be adapted to existing situations instead of high-cost and dynamic updates. In brief, Nervousness means certain changes, is opposite of stagnation. One of the goals of reactive scheduling systems must be to reduce nervousness.

Stability: It should react system failure and abide the first schedule.

Insignificant changes affect whole schedule performance. Efforts in scheduling area are constructed in scheduling and its predictive nature. In recent years, generation and control of reactive schedules not to loose its effectiveness and protection of validity are concentrated.

The procedure of schedule application, controlling, and restoring has become an important matter lately. The first studies were held in late 70s about rescheduling concept but reactive scheduling concept has appeared in early 90s with cooperation of NIST and US industry. At first they tried to solve problems about rescheduling with analytical approach. With the aid of computer technology and its progress, analytical approaches gave place to artificial intelligence techniques and knowledge-based systems. Reactive scheduling gains importance together with knowledge-based systems. Rescheduling and reactive scheduling solutions can be listed according to solution approach or corruption accruing (unpredictable incident) or can be classified. The study focused on one corruption but more than one corruption can be focused on.

Because of the nature of production area, corruptions can not be separated from each other [5].

3.Application Study

In this case study, an effort of reactive scheduling is made in a defense company's composite division for a specific job. The company has a very wide production capabilities and advanced technology. Since the manufacturing is intense and there is no scheduling because of workload, some difficulties are faced during scheduling. Because of the dynamic structure, reactive scheduling is applied. Flow-process diagram of composite division is shown in Figure 2.
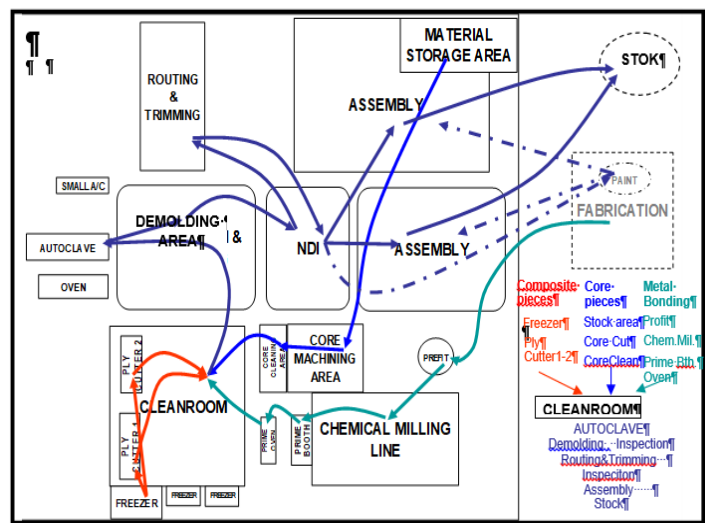

Figure 2. General Composite Flow-Process

At Cleanroom, changes in the system disturb existing schedule. Since there is no certain solution, engineers use their senses, judgments and experiences to take action. The aim of scheduling in this study is to determine the process time for composite products manufactured in Cleanroom, delivery date of products according to entrance and exit time of Autoclave and to minimize process time. The products which are impossible to repair are scraped and to they are listed in schedule in regard to delivery date to be manufactured again. For example, if the product is the last part of manufacturing it should be the first, if not it is scheduled with pieces in line with other part family going Autoclave.

Because of these inconveniences, some problem come out such as not properly using production sources, late response to clients, not corresponding delivery time, increasing in semi finished products and obeying are not used properly, overtime working.

The reason of using reactive scheduling as solution technique is that it act as coordinated effective system in spite of changes during manufacturing. In this case study, it is aimed that the main schedule is updated in Composite division, which is the main part in the factory, without letting any delay in delivery time and other troubles.

Aims of reactive scheduling are summarized as follow;

1. to establish a first schedule which can be adapted in a variety materials and products in Cleanroom.
2. to track workshop circumstances during manufacturing
3. to use workshops existing condition to activate schedule
4. to react changes around workshop while developing advanced schedule in existing workshop environment.
5. to deliver in time
6. to provide Cleanroom-autoclave coordination
7. to use sources (machine, area, personnel) effectively
8. to make long-term plan and to anticipate
9. to calculate time of needs in the basis of piece, to plan material effectively
10. to eliminate scrap materials.

In Cleanroom, end products are delivered to Autoclave. By using Visual Basic at Microsoft Excel, Macro database is developed in order to maximize labor, to minimize product stock (product size x waiting time) for updating of the schedule with troubles determined which covers machine breakdowns, urgent processes, early delivery time and late delivery time. In Figure 3, the time schedule of Cleanroom is shown. Kit No and Item No also known as item families which are determined by work planning department are registered in database. Item's registration information, footprint, personnel need and material used are indicated as constraint in software. The software operates with AC Entrance Date and Hour. The software calculates AC Exit Date and Hour, MAX and MIN Cleanroom Entrance and Exit Date and Hour by using data given and Autoclave schedule. Also the software determines Cleanroom Entrance and Exit Date and Hour which minimizes program aim function
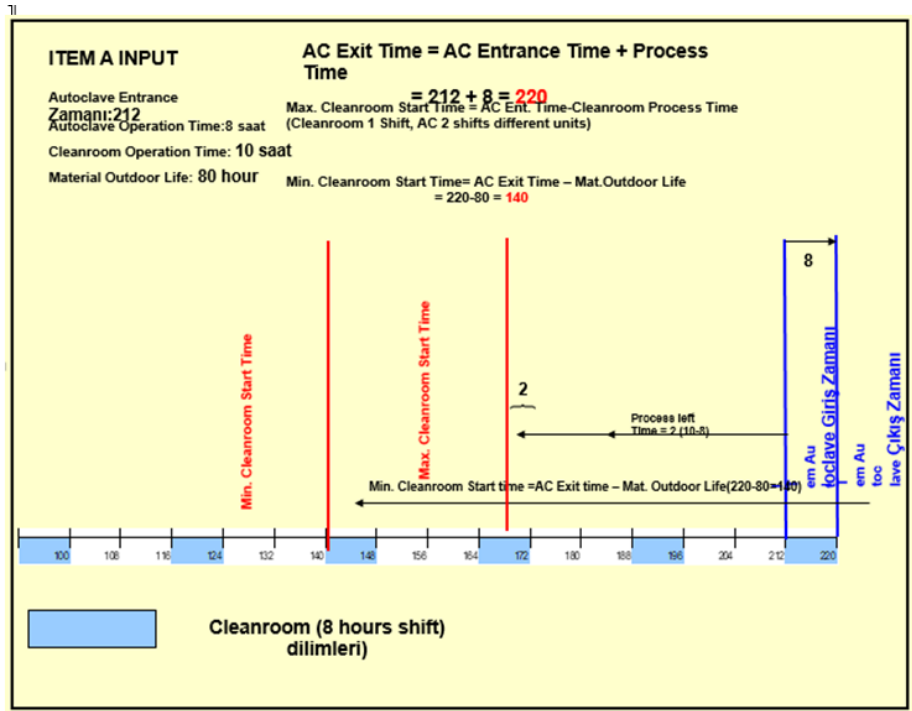
Figure 3. Autoclave - Cleanroom Schedule

The algorithm of data base stated in Figure 3 is given as following;

❖ The Cleanroom's process time of Pieces scheduled on Autoclave, number of workers and area occupied are determined.

❖ Material life is subtracted from Autoclave exit time and the result is *Minimum Cleanroom Start Time*. Process time is subtracted from Autoclave entrance time and the result gives *Maximum Cleanroom Start Time*. Scheduling must start in between these times.

❖ Items are scheduled backward starting from Maximum Cleanroom Start Time.

❖ Items' footprint, personnel and tool number are controlled instantaneously for every scheduling process.

❖ If space and personnel constraints are overcome or more tool is scheduled in both Cleanroom and Autoclave, rescheduling starts from the previous time interval and is controlled

❖ Time interval never exceeds *Minimum Cleanroom Start Time*. For this reason, if some parts are not scheduled because of time interval, personnel and tool number, new schedule is created in regard to overtime.

Some assumptions in algorithm:

❖ It is assumed that there is 1 shift per week between 08:00 and 17:00

❖ Item's life is limited by the life of material having the shortest "outdoor life time".

After algorithm Cleanroom Schedule is obtained in terms of Soir/Item date and hour. In database it is assumed that the Autoclave process time is 8 hours and Cleanroom process time is estimated in the basis of Autoclave entrance time before item life expires. Cleanroom process time is subtracted from Autoclave entrance date and Cleanroom process start time is calculated.

Rough drafts of relations for program and data flow diagram are illustrated in Figure 4. In Figure 5, 0-Degree Data Flow Diagram is shown.
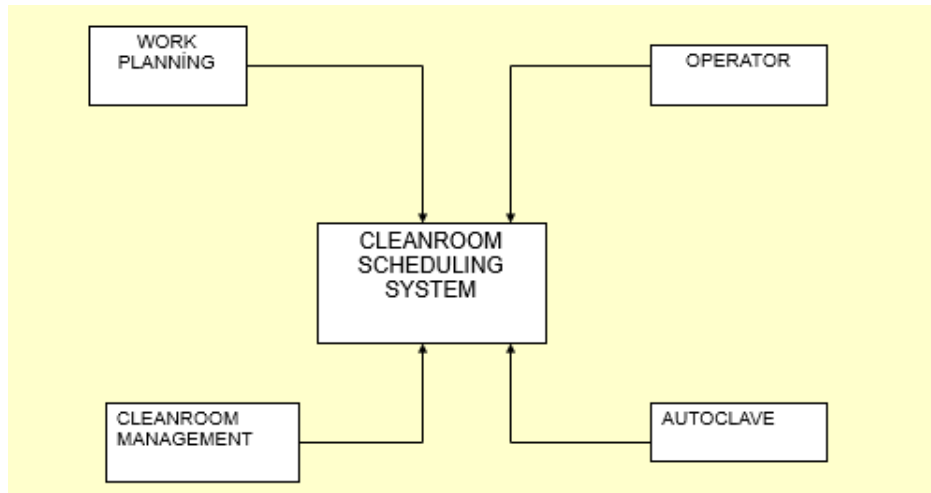
Figure 4. Rough Relation Diagram
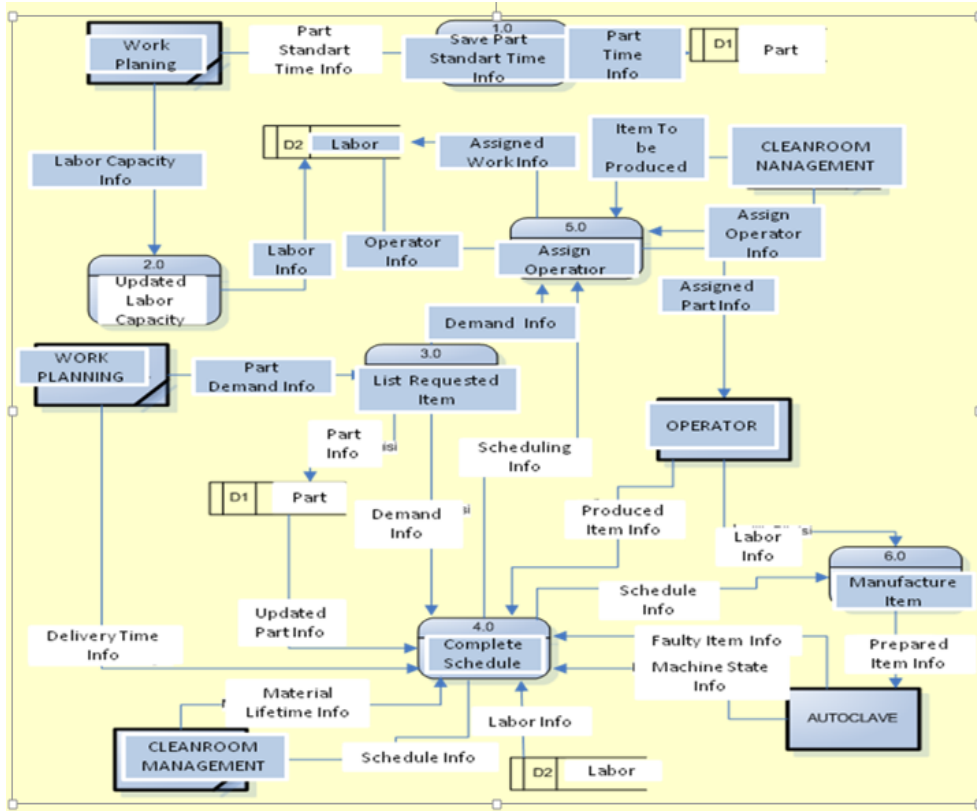
Figure 5. 0-Degree Data Flow Diagram.

As shown in Figure 4 and Figure 5, item standard time information, workload capacity, item request information and delivery date information are gained from Work Planning Department. Item standard time information is saved and sent to item data storing area. Workload capacity is updated and then sent to data storing area. Items demanded by item request information are listed and outputs are sent to data storing area. Delivery time information from Work Planning Department, material life time information from Cleanroom management, information from workload and item data storing area, machine situation and faulty product information from Autoclave and item information requested are used to produce a schedule. The schedule is used to manufacture items and assign operator to process and outputs are reported to Cleanroom Management.

To assign operators to processes some information are supplied by Cleanroom Management such as data of item to be manufactured, operators, item to be requested, and operators are assigned in the basis of workload data storing area. Assigned item information is sent to operator and assigned work is sent to workload data .Item is produced with labor information given by operator and manufactured item information is sent to Autoclave.

Conclusion

In case of unexpected events during application of schedules, update in real time is the basis of reactive scheduling. In this study, according to company's demand, a division was observed and some problems were faced on workshop scheduling. Since the problem had a dynamic structure, it was decided to apply reactive scheduling method.

In Microsoft Excel with Visual Basic, a Macro database was constituted and item scheduling was prepared. To illustrate reactive scheduling process, machine breakdown, urgent works, and early delivery time which led to a repayment on schedule were examined. Only affected items were updated without affecting the general frame of schedule. Software's interfaces were improved by MS Access for engineers to use.

References

Min Soo Suh, Albert Lee, Yung Jae Lee and Young Kwan Ko. (1998). Evaluation of ordering strategies for constraint satisfaction reactive scheduling. *Decision Support Systems,* 2(2), 187-197.

Raheja, A.S. and Subramaniam, V. (2002). Reactive Recovery of Job Shop Schedules-A Review. *Int. J. Manuf.Tech.,* 19, 756-763

Sakaguchi, T., Kamimura, T., Shirase, K. and Tanimuzu, Y.(2008). GABased Reactive Scheduling For Aggregate Production Scheduling. *The 41stCIRP Conference On Manufacturing Systems, May 26-28 2008, Tokyo,* 257-278.

Vieira,G.E., Herrmann, J.W. and Lin, E.(2003). Rescheduling manufacturing systems: a framework of strategies, policies, and methods. *Journal of scheduling,* 6, 39-62.

Irrigation and Salt Relations in Citrus

Uğur KEKEÇ
Burçak KAPUR

In irrigated agricultural lands, when there is no drainage system to remove excess water from the plant root zone after irrigation, when the constantly rising ground water evaporates from the soil surface, the dissolved salts remain in the soil and soil salinity occurs. Since irrigation is a continuous process, the salt concentration in the soil will increase in conditions where there is very little salt in the water and there is no drainage system in the land. As a result, plants will not be able to grow on the soils in these areas.

In lands that have not been irrigated before, farmers often think that overwatering will result in higher yield increases in areas that will be used for agriculture. They ignore the amount of salt added to the soil with the irrigation water and do not find it necessary to build drainage systems.

As a result, the ground water level increases and rises capillary up to a point very close to the soil surface, and the soil salinity increases (Jorenoosh & Sepaskhah, 2003). Increasing salinity of irrigation water with increasing salinization of agricultural soils hinders agricultural productivity in many semi-arid and arid regions of the world. Citrus fruits are salt sensitive plants. (Maas and Hofmann, 1977) Table 1 shows the relative resistance to salt of some fruit species by classifying them as;

1. Salt-resistant,

2. Moderately salt-resistant,

3. Salt-sensitive (Sönmez and Balaban, 1968).

Citrus varieties are among the "salt sensitive" fruits. According to the sensitivities of citrus fruits among themselves:

a- Lemon,

b-Grapefruit

c- Orange.

Table 1 Relative Salt Resistance Degrees of Some Fruit Species (Sönmez and Balaban, 1968).

FRUIT TREES		
Salt Resistant	Salt Medium Salt Resistant	Salt Sensitive
Ec= 12 ds/m	Ec= 10 ds/m	Ec= 4 ds/m
Date		
	Pomegranate	Pear
	Fig	Apple
	Olives	Orange
	Grape	Grapefruit
	Melon	Plum (for drying)
	Ece= 4 ds/m	Almond
		Apricot
		Peach
		Strawberry
		Lemon
		Avocado
		Ece= 2 ds/m

Precautions to be Taken Against the Risk of Soil Salinity in Citrus

Citrus fruits are salt sensitive plants. In many parts of the world, salinity significantly limits citrus production. Salty irrigation water reduces the yield in citrus fruits. Every 1.0 dS m-1 increase in soil extract electrical conductivity (ECe) causes about 13% yield reductions in citrus fruits (Hepaksoy., S 2000).The precautions to be taken against possible soil salinity before the citrus orchards are established are listed below (Maas, 1993; Walker et al., 1983; Zekri & Parsons, 1989).

1) Drainage conditions

2) Land leveling

3) Infiltration rate of soil

4) Applying mulch

5) Irrigation methods and water management

6) Irrigation schedule

Basic Principles to be Considered in Citrus Orchards in Terms of Irrigation, Drainage and Salinity

The necessary procedures before planting citrus orchard saplings are listed below (Çevik, 2002).

(1) The land should be cleared of weeds and bushes

(2) The soil should be loosened to a depth of at least 120 cm or more with special digging machines.

(3) Soil should be analyzed in terms of salinity and plant nutrients content.

(4) Irrigation water must be analyzed to determine its quality.

(5) The area should be leveled according to the determined irrigation methods.

(6) Large areas should be divided into sections suitable for irrigation.

(7) An irrigation plan should be prepared to ensure uniform distribution of irrigation water to all sides.

(8) Drainage system is absolutely necessary for loamy and clayey textured soils except sandy soils.

(9) In sloping areas, "prevention-turning drains" should be opened against surface flows.

(10) Protection against erosion should be provided by contour ploughing, planting and irrigation up to 15% slope on slope lands, and "terracing" on slopes higher than 15%.

(11) Establishing citrus orchards on shallow, fine-textured (heavy, dense clay) soils and lands with high ground water should be avoided.

The Quality and Classification of the Most Suitable Irrigation Water for Citrus Fruits

Irrigation waters, whether they are obtained from surface or ground water sources, contain some chemicals that they dissolve from the soil and rocks on which they flow. Concentration and natural properties of these dissolved substances determine the quality of water in terms of irrigation. The type of salt in the irrigation water is more important than the amount. For example, a small amount of boron harms or even kills the plant. If the amount of sodium in the irrigation water is high, the soil becomes unproductive over time. On the other hand, waters contain mainly plant nutrients or some useful salts that help keep the soil productive. When necessary precautions are taken in terms of irrigation and soil and drainage facilities are provided, water of poor quality can be used for irrigation without damaging the soil and plant. Careful and meticulous analysis of irrigation water shows the important salts in the water and their concentrations. Based on these analyzes, it may be possible to classify waters in terms of their suitability for irrigation and to determine the effects of water on plants and soil with confidence (Sönmez & Balaban, 1968).

Detailed water analyzes are time consuming and expensive. Therefore, it should be noted that water samples must accurately represent the water source from which they were taken. Stream samples should be taken from very distant parts of the branches and junctions of the water flowing. Well samples should be taken from wells that have been used for some time. The water samples taken should be placed in clean bottles with cork or rubber stoppers and taken to the laboratory without waiting (Sönmez & Balaban, 1968).

When determining the quality of irrigation water: It is necessary to pay attention to the total concentration of soluble salts, the relative ratio of sodium to other cations, the concentration of boron or other toxic elements.

Electrical Conductivity: The total concentration of soluble salts in irrigation waters can be expressed as electrical conductivity values for diagnostic and classification purposes. Electrical conductivity is very useful because it can be determined easily and precisely. The symbol for electrical conductivity is $ECx10^6$. In general, the classification of irrigation waters is made according to the electrical conductivity (micromhos/cm) values as follows (Zhang, 2017):

Waters with an EC x 10^6 value of 0-250 (1st Class)

Waters with an EC x 10^6 of 250-750 (Class 2)

Waters with an EC x 10^6 value of 750-2250 (Class 3)

Waters with an EC x 10^6 value greater than 2250 (Class 4) are waters.

Sodium Adsorption Rate: Since the sodium adsorption rate of the soil solution is related to the adsorption of sodium by the soil, there are obvious benefits in using this rate as an index of sodium or alkali damage of water.

Concentration of Boron or Other Potentially Toxic Elements: Boron; It is a characteristic element of compounds known as boric acid or borax. It is found in almost all natural waters. The concentration of this element ranges from trace amounts to a few ppm. Although it is one of the essential elements for plant development, it has a toxic effect on the plant when the limits to which the plants can tolerate are exceeded. According to the researches, while most of the plants develop normally in the amount of boron between 0.03-0.04 ppm, they are damaged if the amount of boron is 1 ppm.

Classification and use of irrigation water in terms of salinity.

In the classification of irrigation water, the water; It is assumed that it is used under normal conditions in terms of soil texture, infiltration rate, drainage, amount of water used, climate and salt resistance of the plant. As can be seen in the diagram used in the classification of irrigation waters; In this classification, sodium adsorption rate (SAR) is taken as an index of sodium damage and electrical conductivity (Ec x 106) values are taken as an index of salinity damage. Irrigation water classification diagram is shown in Figure 1 (Sonmez & Balaban, 1968).

As stated before, irrigation waters are divided into 4 classes according to their electrical conductivity values. The water classes in terms of salinity are given as follows on the diagram used in the classification of irrigation waters (Sönmez & Balaban, 1968).

Low Salt Water (C1): Generally, it can be used safely for irrigation of many plants in all soils. Some leaching is required, but this occurs spontaneously under normal irrigation conditions, except in soils with extremely low permeability.

Medium Salt Water (C2): It can be used in cases where there is moderate washing. Plants that are moderately resistant to salt can be grown without applying special methods of salinity control.

High Salinity Waters (C3): Special management and selection of salt-tolerant plants are needed to control salinity in soils with limited drainage.

Very High Salinity (C4): Not suitable for irrigation under normal conditions. It can sometimes be used in very rare cases. If it is used, the soils should be permeable, adequate drainage should be provided, plenty of irrigation water should be given to ensure excessive washing and plants should be selected that are very resistant to salt.

Among the water classes mentioned above, suitable areas for citrus fruits should be 1st and 2nd class waters.
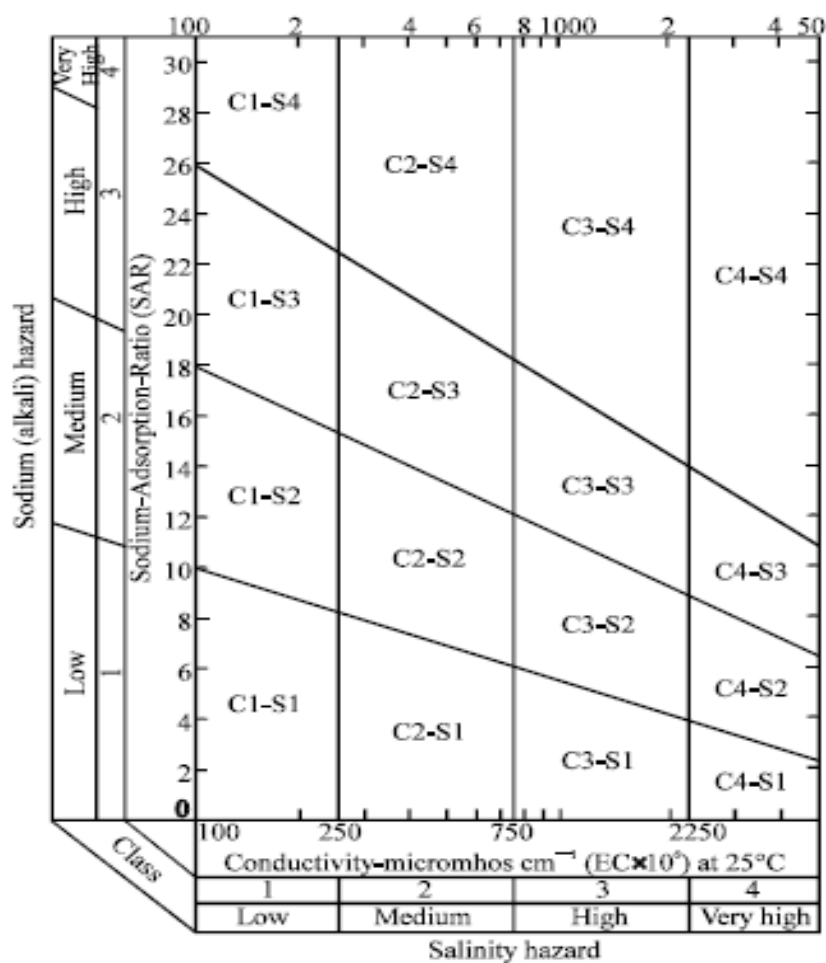
Figure 1. Water classification Scheme by USDA (1954).

Sodium Damage and Classification of Irrigation Waters According to Sodium Content.

Classification of waters according to their quality in terms of sodium damage is more complex than the classification made according to salinity damage. This problem can be addressed to some extent by reducing the degree to which soil absorbs sodium from the water and the absorption that would occur if water was introduced into the soil. The SAR (Sodium Adsorption Rate) value is used as an index of sodium damage.

Classification of irrigation waters in terms of SAR is made in terms of the effect of changeable sodium on the physical properties of the soil (Zaman, Shahid &Heng, 2018).

Water with Low Sodium (S1): It can be used as irrigation water in almost all soils with little risk of damage due to exchangeable sodium. However, plants sensitive to sodium, such as stone fruit trees, can accumulate sodium, which may be harmful to them.

Medium Sodium Waters (S2): In cases where there is no gypsum in the soil and especially under unfavorable washing conditions, it causes excessive sodium damage in fine textured soils with high cation exchange capacity. These waters can be used in coarse textured soils or organic soils with high permeability.

High Sodium Waters (S3): It often leads to the emergence of exchangeable sodium at harmful levels in soils. It requires some special soil management, such as good drainage, excess leaching and the addition of organic matter. Harmful levels of such water exchangeable sodium do not occur in gypsum soils. May require chemical amendments to remove exchangeable sodium, except where amendments cannot be applied in very high saline waters.

Very High Sodium Waters (S4): They are generally not suitable for irrigation except in low and medium salinity conditions. These waters can only be used for irrigation if there is open calcium in the soil or if improvement materials such as gypsum are used. The classification diagram of irrigation water according to sodium content is shown in Figure 2.

When irrigation water is given to calcareous soils, it dissolves excess calcium and this greatly reduces sodium damage. This should be taken into account when using C1-S3 and C1-S4 waters. For calcareous or non-calcareous soils with high pH, the sodium status of water in classes C1-S3, C1-S4 and C2-S4 can be improved by adding gypsum to the water. In case of using C2-S3 and C3-S2 waters like this, it is beneficial to periodically add gypsum to the soil.

As a result, the most suitable irrigation water for citrus fruits is first class water in the C1S1 class. However, it may not be possible to find water of this quality constantly and everywhere. For example, the quality of the water collected in the Seyhan Dam and used for irrigation is in the C2S1 class. It should be noted that when irrigation waters with higher salinity and sodium content must be used, the precautions described above are required. However, it should not be ignored that high salinity and sodium amounts for citrus fruits will be inconvenient, even if precautions are taken.
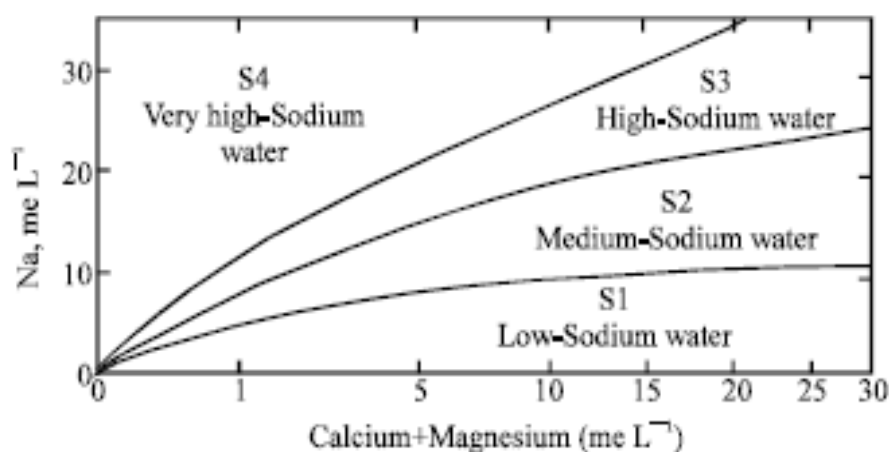

Figure 2. Sodium diagram according to Wilcox (1948)

REFERENCES

Çevik,B. (2002). "Sulama ve Drenaj." Ç.Ü. Ziraat Fakültesi, Genel Yayın No: 243, Ders Kitapları Yayın No: A-77, Adana.

Hepaksoy,S. (2000). "Effect Of Salınıty On Cıtrus" Anadolu, J. Of Aarı 10 (1) 2000, 52 - 72

Jorenush,M.H., & Sepaskhah, A.R.(2003). Modelling capillary rise and soil salinity for shallow saline water table under irrigated and non-irrigated conditions. Agricultural Water Management. Volume 61, Issue 2, 30 June 2003, Pages 125-141

Maas, E. V., & Hoffman,G.J.(1977).Crop salt tolerance current assessment. J. Irr. And Drainage Division, ASCE 103 (IR2): 115-134.

Maas, E.V. (1993). Salinity and citriculture. Tree Physiol. 12:195–216, DOI: 10.1093/treephys/12.2.195

Sönmez, N.,&Balaban, A. (1968). "Kültürteknik", Cilt II. Ankara Üniversitesi Yayınları 317, Ders Kitabı 112, Ankara,

US Salinity Lab. Staff, 1954. Diagnosis and Improvement of Saline and Alkali Soils. USDA, Washington, DC., USA

Walker, R.R.., Torokfalvy,E., Grieve, A.M., & Prior,L.D.(1983). Water relations and ion concentrations of leaves on salt stressed citrus plants. Austral. J. Plant Physiol. 10:265–277.

Wilcox, L.V. (1948). The quality of water for irrigation use. US Department of Agriculture. Tech. Bulletin 962, pp: 40.

Zaman, M., Shahid, S.A.,&Heng, L. (2018). Irrigation Water Quality. In: Guideline for Salinity Assessment, Mitigation and Adaptation Using Nuclear and Related Techniques . Springer, Cham. https://doi.org/10.1007/978-3-319-96190-3_5

Zekri, M., & Parsons, L.R.. (1989). Growth and root hydraulic conductivity of several citrus. rootstocks under salt and polyethylene glycol stresses. Physiol. Plant. 77:99–106.

Zhang H. (2017). Classification of Irrigation Water Quality. Extension Oklahoma State University.https://extension.okstate.edu/fact-sheets/classification-of-irrigation-water-quality.html , accessed 05.11.2022.

Author Identification with Artificial Neural Networks and Fuzzy Neural Networks in English Documents

Rasim CEKİK[1]
Abdullah TURAN[2]

Introduction

The rapid development of Internet technologies has brought both difficulties and convenience. The massive amount of dirty data that occurs in the Internet environment is at the root of these difficulties. However, text documents make up a large portion of this data. One of the most recent issues being researched is the extraction of meaningful information from this data. The text mining process extracts meaningful and useful information from large amounts of dirty text data. Text mining is performed on written texts to achieve various goals such as natural language processing, sentiment analysis, classification, and clustering. The most commonly used of these purposes is classification. Text classification, known as document classification and verification processes, is a sub-topic in text mining. Author identification is a document classification and verification process. Author identification can be briefly defined as the process of automatically finding which author an article belongs to, through a trained system or model. It is primarily selected features that determine success in author identification. These features should be intended to determine the author's style. Important studies in this field emerged in the 1970s as automatic indexing of documents. Some of these studies are Burrows frequency of words in the document (Burrows, 1992), Brinegar number of words and letters (Brinegar, 1963), Morton lengths of sentences (Morton, 1965), average value of Brainerd syllable numbers (Brainerd, 1974), Holmes number of words in the document and length of the document (Holmes, 1994), used as author features. In this study, the approach of Solorio et al., which accepts every word in all documents as a feature, was used. In the study, the articles of 15 authors with more than 50 articles written in English from the PAN-2011 database were discussed.

When a person comes across an article by an author he regularly reads and follows, even if he does not see the author's name, he can tell that it belongs to the author based on characteristics such as the author's style and writing style. Can this human characteristic be transferred to a system? With the rapid development of technology and the increase in success in adapting the events in nature and the biological structure of living things to technological systems, an answer to this question can be given. The most successful learner of this is Artificial Neural Networks (ANNs) (Abiodun & ark., 2019) which imitate the neural structure of the human brain. Artificial Neural Networks, inspired by the information processing method in the brain, form a network with layers and neurons within these layers. With the numerical values assigned to the neurons and the transfer functions at the outputs of the layers, the calculation is made within the system and the result is obtained from the output layer. ANN analysis was used for author identification in the study. In addition to ANN, adaptive fuzzy neural networks are also used in this study. Fuzzy neural networks

[1] Asisstant Proffesor, Department of Computer Engineering, Sirnak University, Sirnak, TÜRKİYE,
[2] Asisstant Proffesor, Department of Mechanical and Metal Technologies, Sirnak University, Sirnak, TÜRKİYE,

can be thought of as a combination of fuzzy logic and neural networks. Mamdani-type ANFIS is used as a fuzzy neural network in the study. In experimental studies, it has been observed that ANFIS provides more successful results than ANN for author identification.

Text Mining and Processes

Text Data Mining and Knowledge Discovery from Textual Databases are other names for text mining. Text mining is a subtopic of data mining, but it is not the same as data mining. It is the extraction of patterns from natural language texts rather than event-based databases in Text Mining. It does, however, provide knowledge discovery in stages similar to data mining. In conclusion, text mining is the process of focusing structured data on unstructured text data. The process of extracting meaningful and useful information from large amounts of text documents in electronic environments is known as text mining, also known as text analytics. The goal of text mining is to extract confidential information from data by processing customer comments about products, social media messages, XML documents, and website content such as news, sports, and magazines (Mecca, Raunich & Pappalardo, 2007). The data processing steps in text mining is shown in Figure-1.
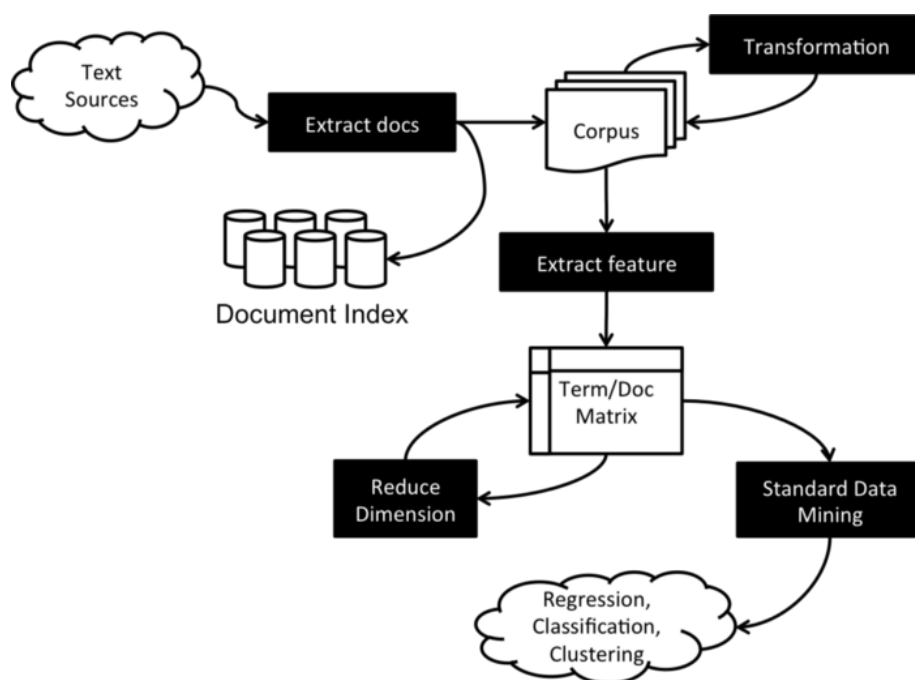
Figure 1. Basic Text Mining Flow

One of the primary tasks of text mining is text classification, which is the process of determining the category of unlabeled documents using labeled text documents. At the end of text preprocessing, feature extraction, feature selection, and weighting, this process is carried out with the help of classifiers, one of the machine learning approaches.

Extraction Author Features

In comparison to other methods, the bag of words (BoW) method, also known as N-gram, is the most widely used and simplest. The frequency and order of a word in the document are irrelevant in this approach. The only thing that matters is whether or not it is included in the document. As an attribute, the method uses the name as many words as possible. For example, if each word is considered a feature, 1-gram (unigram), if two words are considered, 2-grams (bigram),

if three words are considered, 3-grams (trigram), and so on for N-grams. In this study, Unigram was used.

The general framework of the author identification process is given in Figure 2.
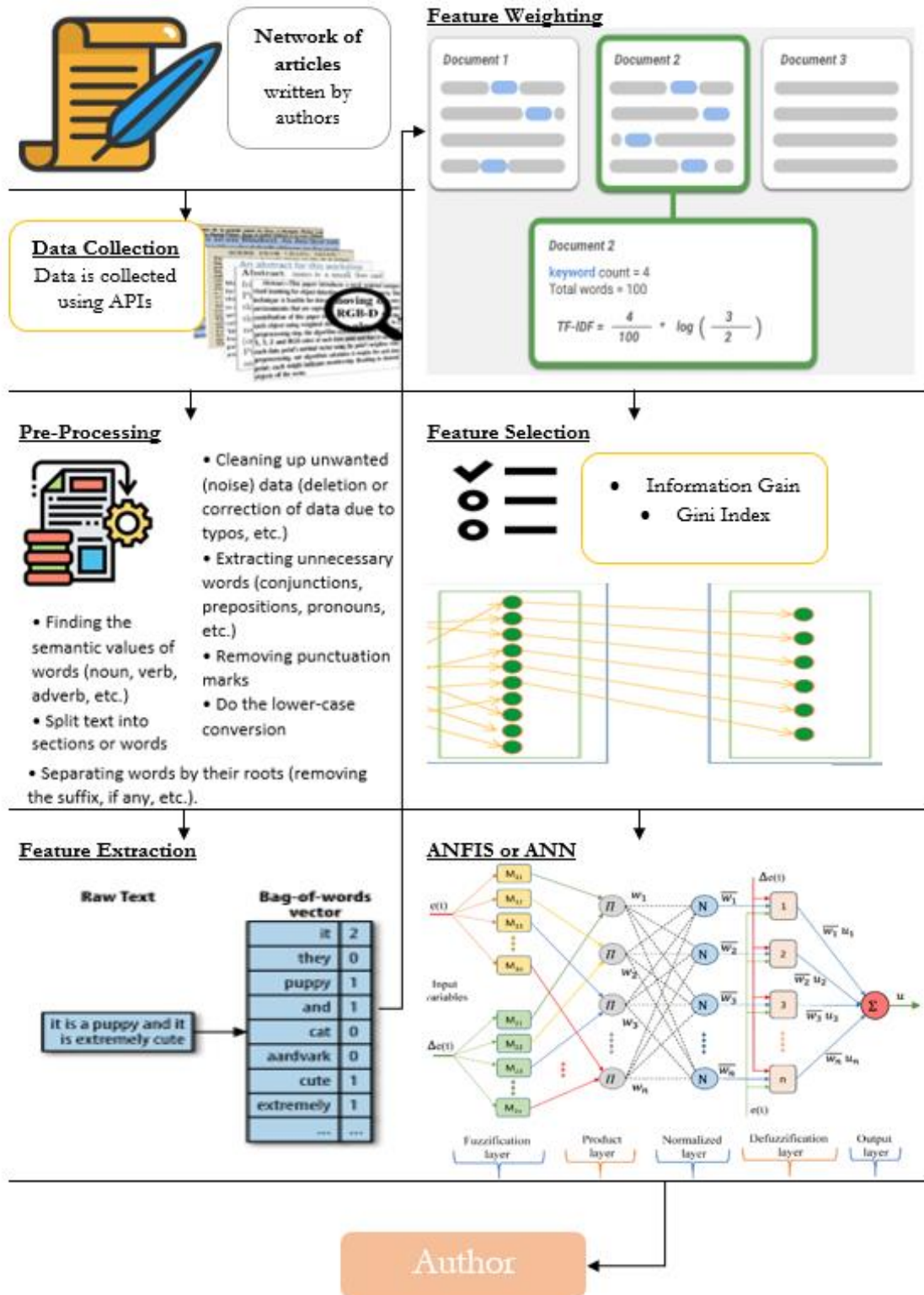
Figure 2. The general structure of the author identification system

Pre-Processing

Because each word in the documents is treated as a feature, some preprocessing is required before performing this operation. In this study, all punctuation in the documents was removed, uppercase letters were converted to lowercase letters, and unnecessary spaces were removed. Following completion of these processes, all remaining words and words or letters are assigned a feature.

Determining Value Sets of Features (Feature Weighting)

Each feature must have a set of values known as the feature space. After the features are determined, the action to be taken is to determine the value set of the features. Various value set determination methods are available for the document classification process. The most well-known of these are term frequency and inverse document frequency. These two terms are often used as term frequency - reverse text frequency (TF-IDF) (Dogan & Uysal, 2020). TF-IDF is the product of TF and IDF. This method is used more. Because it reduces the importance of the words in all documents. This method is also used in the study. This method is calculated by dividing the frequency of occurrence of terms in the document by the frequency of occurrence of terms in the entire dataset. Thus, the terms found in each document are penalized.

Let t_k show the weight of the word for the d_j document. In this case, $TF - IDF$ is expressed mathematically as Equation 1.

$$TFIDF(t_k, d_j) = TF(t_k, d_j) * log \frac{|Tr|}{|Tr(t_k)|} \tag{1}$$

Where, $TF(t_k, d_j)$ shows frequency of t_k in d_j. $|Tr|$ and $|Tr(t_k)|$ indicate total number of documents, number of documents containing t_k, respectively.

Feature Selection

The main issues in text classification are the large feature dimension space and the highly empty associated information system. This situation reduces the performance of the classifiers while increasing the computational cost. The best way to solve high dimensionality is to choose the best subset from the entire feature set. This process uses feature selection approaches. Feature selection approaches fall into three types: filter, wrapper, and embedded. After each word is determined as a feature, what needs to be done is the process of selecting the determinant features from these features. Various methods are available in the literature for this process (Cekik & Uysal, 2020; Cekik & Uysal, 2022; Parlak & Uysal, 2021a; Cekik & Uysal, 2021b). Information Gain (IG) and Gini Index (GI) are the most widely used feature selection methods in text mining (Raileanu, Laura & Kilian, 2004). Both methods are used in the study. Below are the GI and IG equations, respectively.

c: author,
m: number of authors,
t: indicates a feature;

$$IG(t) = -\sum_{i=1}^{m} p(c_i)logp(c_i/t)$$
$$+ p(t)\sum_{i=1}^{m} p(c_i)logp(c_i/t) \tag{2}$$
$$+ p(\neg t)\sum_{i=1}^{m} p(c_i/\neg t)logp(c_i/\neg t)$$

$$GI(t) = \sum_{i=1}^{m} p(t/c_i)^2 p(c_i/t)^2 \qquad (3)$$

Methods Used in The Study

In the study, two different methods were used for author recognition analysis. In other words, Multilayer Artificial Neural Networks (MLANN) and Fuzzy Artificial Neural Networks (ANFIS) were used as analysis methods that determine which article belongs to which author and classify it.

Multilayer Artificial Neural Networks (MLANN)

MLANN are densely parallel systems consisting of many processing elements connected to each other with different weights. Figure 3 shows the general structure of a three-layer MLANN. Where, i is the input layer, j is the hidden layer and k is the output layer, and W_{ij} and W_{jk} are the connection
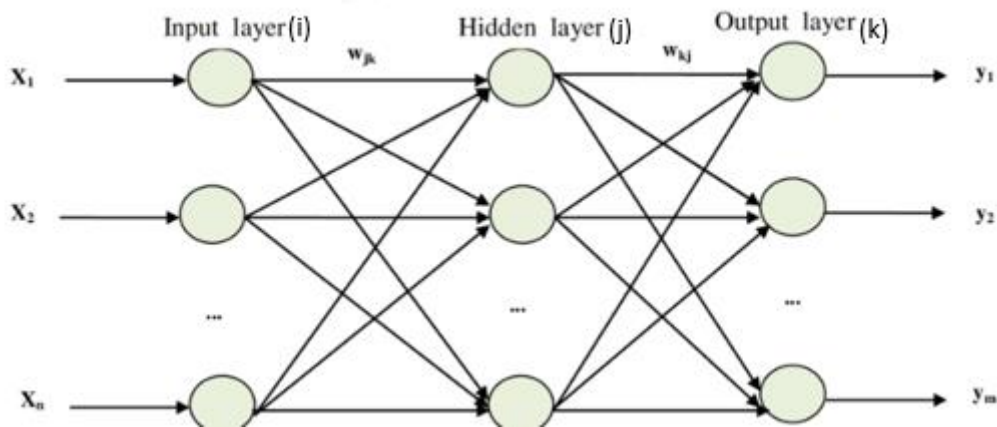
Figure 3. The general structure of a three-layer MLANN

weights between the cell layers. Initially randomly assigned weights are constantly changed during the training process by comparing the estimated outputs with the actual output values, and the errors propagate backwards (right to left in Figure 3) until the link weights that minimize the errors are adjusted. The method used to adjust the weights here is the Levenberg-Marquardt method (Marquardt, 1963). In Figure 3, each cell in layers j and k takes as input the NET-weighted aggregate outputs from the previous layer. NET value is calculated by Equation 4.

$$NET_{pj} = \sum_{i=1}^{D} W_{ij} C_{pi} + Q_j \qquad (4)$$

D is the size of the input vector, Q_j is the bias constant, W_{ij} is the set of weights between layers i and j, and C_{pi} is the output set of layer i for the p sample. Each cell in layers j and k produces the output $f(NET)$ by passing the NET value through a nonlinear description function. This commonly used depiction function is:

$$f(NET) = \frac{1}{1 - e^{-NET}} \qquad (5)$$

In the training phase, the total error Hp for the sample p is calculated by Equation 6 based on the difference of squares between the predicted and actual outputs.

$$H_p = \sum_{k=1}^{N}(G_{pk} - C_{pk})^2 \qquad (6)$$

N is the number of iterations, G_{pk} and C_{pk} are the actual and predicted output values for the p sample, respectively. Each link weight Aij is replaced by Equation 7.

$$W_{ij}^{new} = W_{ij}^{old} - [J^T J + \mu I]^{-1} J^T H_p \qquad (7)$$

where J is the Jacobian matrix containing the derivatives of the errors according to the weights; J^T transposes the Jacobian matrix; I is the unit matrix and μ is a parameter that affects the convergence rate. When the value of μ increases, the equation turns into a slope reduction algorithm, and when it gets smaller, the equation turns into a Gauss-Newton algorithm.

Fuzzy Artificial Neural Networks (ANFIS)

Adaptive fuzzy neural networks can be thought of as a combination of fuzzy logic and neural networks.
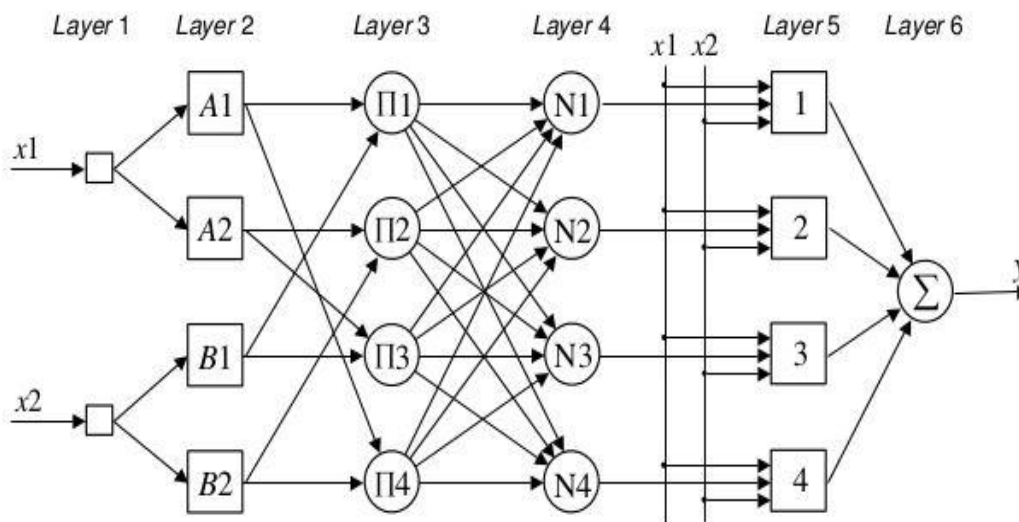
Figure 4. The general structure of a ANFIS

There are two generally known types of ANFIS. These are the Mamdani and Sugenu ANFIS. Mamdani type ANFIS was used in this study. In Mamdani type fuzzy systems, the input, that is, the information and outputs in the database, consists of fuzzy values. The most important drawback of such a fuzzy system is that the digital database cannot enter the general fuzzy system and cannot be used directly in engineering designs because the outputs are not numerical (Sen, 1999). As seen in Figure 4, there are certain layers in ANFIS. We can briefly describe these layers as follows:

- LAYER 1: It is known as the input layer.
- LAYER 2: It is the blur layer. In this layer, the membership function is determined as the activation functions of the neurons to make the blurring.
- LAYER 3: It is the layer where the fuzzy rules are determined.
- LAYER 4: It is the normalization layer. Normalized operations $i\ th$ for the node:

$$\overline{W_l} = \frac{w_i}{w_1 + w_2 \ldots w_n} \tag{8}$$

- LAYER 5: It is the defocusing layer. The weighted result values of a given rule are calculated at each node in the sharpening layer. The parameters in this layer are called result parameters. For each i node in this layer, the normalized neurons and x_1, x_2 inputs are interconnected.
- LAYER 6: In this layer, all neurons are collected with a single sum.

Experimental Works

Experiments for this study, including feature extraction, value and vector set determination, and feature selection, are carried out in JAVA using the ECLIPSE program. In other words, the information system for the analysis systems, specifically the classifiers (ANFIS and MLAAN), is written in JAVA and employs the appropriate methods to perform the author identification process. Analysis systems, on the other hand, are carried out using the appropriate MATLAB tools. MLAAN is represented by NFTOOL, and ANFSEDT is represented by ANFSEDT. The number of hidden neurons in NFTOOL is 15, and this value is been chosen after experimenting with different neuron numbers (eg 20 25 30). Below are the general structures of the selected analysis systems in Figure 5 and Figure 6.
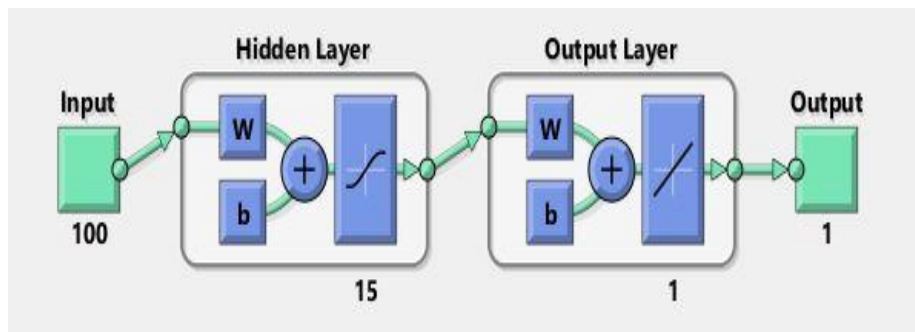
Figure 5. The general structure of the selected MLAA (This figure was taken with 100 features selected.)

If we move on to the learning algorithm of ANFIS, the hybrid algorithm, which is a combination of the least squares method and the gradient descent method, can be used. However, ANFIS also includes a back propagation algorithm. If the hybrid algorithm is selected, some operations are performed on the least squares estimator.
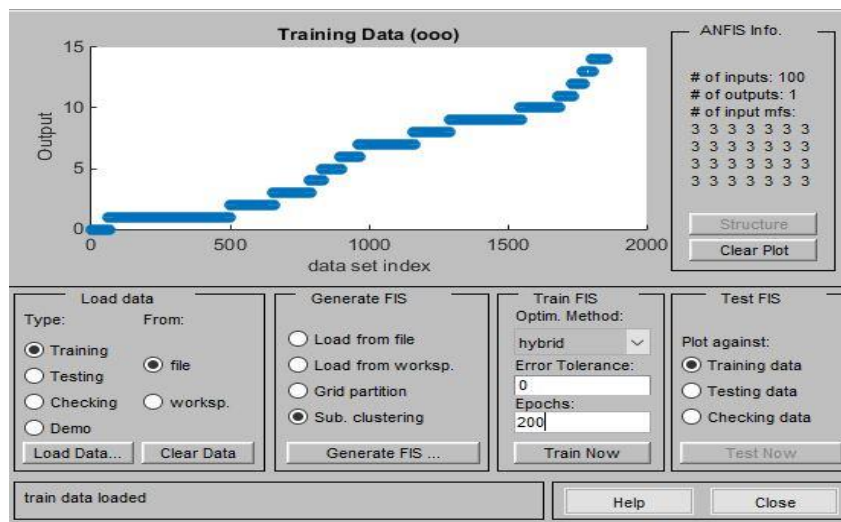

Figure 6. The general structure of the selected ANFIS (This figure was taken with 100 features selected.)

In the study, a total of 6 data sets are used according to the feature selection methods and the number of features, and their results are evaluated. Information Gain and Gini Index from the feature selection algorithms and the performance of each selection algorithm with 100, 150, and 200 features, respectively, are evaluated by analysis systems.

Accuracy Analysis

F-score and Root mean squared error (RMSE) are used as criteria for evaluating the results. The MLAAN and ANFİS performances for Information Gain are given in Table 1 and in Tables (A), (B) and (C) for each selected feature number. Likewise, this situation is expressed in Table 2 for the Gini Index.

Table 1. Information Gain results for 100, 150, and 200 feature siz

	(100)			
	Training Performance		**Test Performance**	
	f-score	**RMSE**	**f- score**	**RMSE**
MLAAN	0.6782	2.7822	0.3720	3.6126
ANFIS	0.8202	0.8907	0.4806	2.0062
	(150)			
	Training Performance		**Test Performance**	
	f- score	**RMSE**	**f- score**	**RMSE**
MLAAN	0.6782	2.9353	0.2997	3.4674
ANFIS	**0.8615**	**0.7138**	**0.5285**	**0.9823**
	(200)			
	Training Performance		**Test Performance**	
	f- score	**RMSE**	**f- score**	**RMSE**
MLAAN	0.6782	2.8730	0.2984	3.7515
ANFIS	**0.7026**	**1.0199**	**0.4108**	**1.7555**

Table 2. Gini Index results for 100, 150, and 200 feature sizes

	(100)			
	Training Performance		**Test Performance**	
	f-score	**RMSE**	**f- score**	**RMSE**
MLAAN	0.6847	3.0688	0.3136	3.7039
ANFIS	0.7956	1.2130	0.4012	1.7750
	(150)			
	Training Performance		**Test Performance**	
	f- score	**RMSE**	**f- score**	**RMSE**
MLAAN	0.6800	2.3569	0.3009	3.4758
ANFIS	0.8012	1.5138	**0.5016***	1.5010
	(200)			
	Training Performance		**Test Performance**	
	f- score	**RMSE**	**f- score**	**RMSE**
MLAAN	0.6716	2.9868	0.3055	3.7007
ANFIS	**0.8529***	**0.6138***	0.4884	**1.0158***

When Table 1 and Table 2 are examined, it is seen that the best result is obtained when 150 attributes are selected with information gain and analyzed with ANFIS. In addition, the best results for both selection algorithms are indicated in bold, and the best results for a selection algorithm in

itself are indicated with a bold * sign. For example, when 150 features are selected with gini index, it can be said that the best result for the test is obtained with ANFIS based on f-score. It is also worth noting that when the f-score was calculated for ANFIS, the results were subjected to a masking process and then the relevant calculations were made.
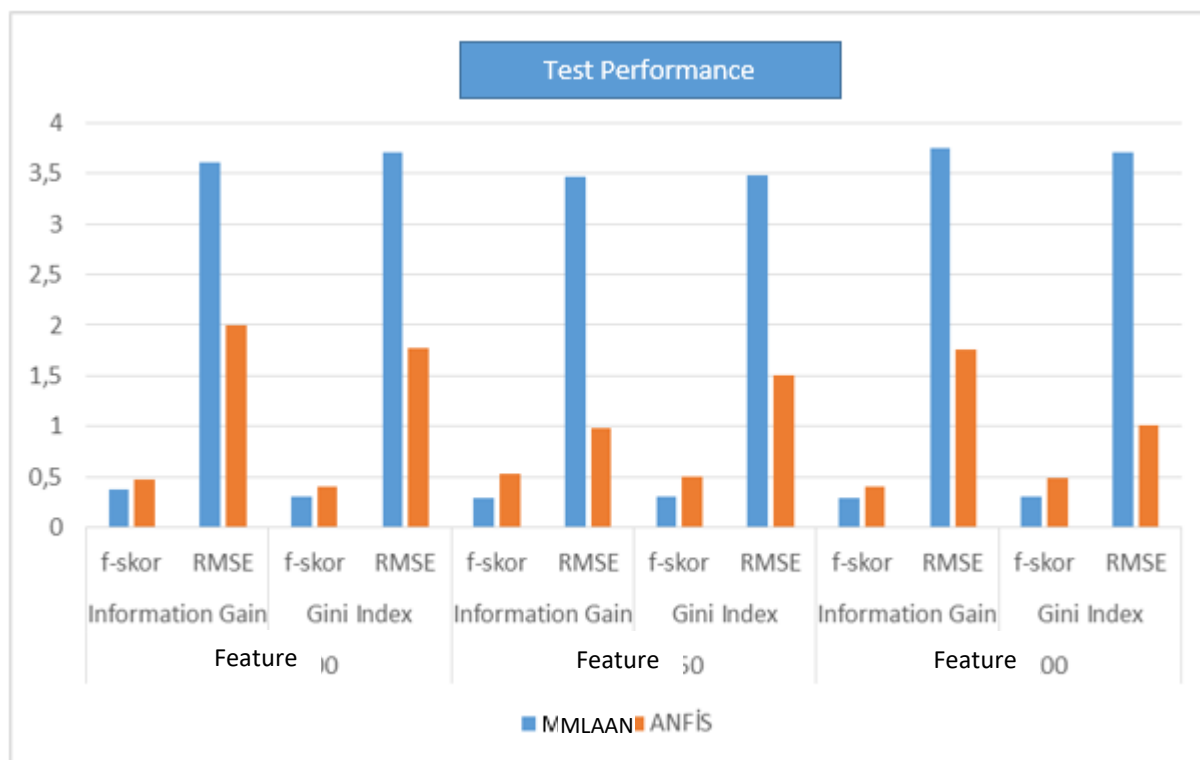
Figure 7. The general structure of a ANFIS

As a result, ANFIS gave more successful results than MLAAN for author identification. In this case, it is more convenient and understandable to see the performance of analysis systems for test data on Figure 7. Finally, it would be useful to underline that the performance may be low for analysis systems in such studies in the literature, especially in author identification processes in text mining.

Conclusion

In this study, the articles written by different authors belong to which author, using machine learning approaches ANFIS and MLAAN. After applying the Information Gain and Gini Index approaches for feature selection to the authors' documents, ANFIS and MLAAN approaches were used in the analysis part. F-score and AAA error value were used for performance evaluation. In the experimental studies, it has been seen that it gives better results with ANFISIN Information.

REFERENCES

Abiodun, O. I., Jantan, A., Omolara, A. E., Dada, K. V., Umar, A. M., Linus, O. U., ... & Kiru, M. U. (2019). Comprehensive review of artificial neural network applications to pattern recognition. *IEEE Access*, *7*, 158820-158846.

Brainerd, B. (1974). Weighting Evidence in Language and Literature: A Statistical Approach. University of Toronto Press.

Brinegar, C.S. (1963). Mark Twain and the Quintus Curtius Snodgrass Letters: A Statistical Test of Authorship. *Journal of the American Statistical Association*, 58, 85-96.

Burrows, J.F. (1992). Not unless you ask nicely: the interpretative nexus between analysis and information. *Literary Linguist Comput.* 7, 91-109.

Cekik, R. & Uysal, A. K. (2020). A novel filter feature selection method using rough set for short text data. *Expert Systems with Applications*, *160*, 113691.

Cekik, R. & Uysal, A. K. (2022). A new metric for feature selection on short text datasets. *Concurrency and Computation: Practice and Experience*. e6909.

Dogan, T. & Uysal, A. K. (2020). A novel term weighting scheme for text classification: TF-MONO. *Journal of Informetrics*, *14*(4), 101076.

Holmes, D.I. (1994). Authorship Attribution. *Comput Humanities*, 28, 87-106.

Marquardt, D. (1963). An algorithm for least squares estimation of non-linear parameters. *J.Soc.Ind. Appl.Math.*, 431-441.

Morton, A.Q. (1965). The Authorship of Greek Prose. *Journal of the Royal Statistical Society, Series A*, 128, 169-233.

Mecca, G., Raunich, S. & Pappalardo, A. (2007). A new algorithm for clustering search results. *Data & Knowledge Engineering*, *62*(3), 504-522.

Parlak, B. & Uysal, A. K. (2021a). A novel filter feature selection method for text classification: Extensive Feature Selector. *Journal of Information Science*, 0165551521991037.

Parlak, B., & Uysal, A. K. (2021b). The effects of globalisation techniques on feature selection for text classification. *Journal of Information Science*, *47*(6), 727-739.

Raileanu, R., Laura E. & Kilian S. (2004). Theoretical comparison between the gini index and information gain criteria. *Annals of Mathematics and Artificial Intelligence,* 41(1), 77-93.

Sen, Z. (1999). *Modelleme İlkeleri*, İTÜ, İnşaat Fak, İnşaat Müh.Böl., Hidrolik A.B.D., İstanbul.

Certain Curvature Tensor Fields on α-Kenmotsu Pseudo Metrıc Manifolds

Hakan ÖZTÜRK[1]
Sermin ÖZTÜRK[2]

Introduction

A systematic study of contact structures satisfying associated pseudo Riemann metric were introduced by Calvaruso and Perrone (Calvaruso & Perrone, 2010). This structure was first undertaken by Takahashi in Sasakian structures (Takashi, 1969). Contact pseudo metric structures (η, g) where η is a contact 1-form and g a pseudo Riemann metric associated to it. These structures are inherently generalization of contact metric structures.

The class of almost contact metric manifolds which are called Kenmotsu manifolds were firstly introduced by Kenmotsu (Kenmotsu, 1972). It is well known that Kenmotsu manifolds can be characterized through their Levi-Civita connection. Kenmotsu defined a structure closely related to the warped product which was characterized by tensor equations.

In recent times, a systematic study of almost Kenmotsu pseudo metric manifolds has yet to be undertaken. Wang and Liu introduced the geometry of almost Kenmotsu pseudo metric manifolds (Wang & Liu, 2016). The authors emphasized the analogies and differences in connection with the Riemannian metric tensor and obtained certain classification results related to local symmetry and nullity condition.

Locally symmetry is a strong restriction for Kenmotsu manifolds. Furthermore, if Kenmotsu structure holds the Nomizu's condition (Nomizu, 1968), i.e., $R \cdot R = 0,$ then it has negative constant curvature and if Kenmotsu manifold is conformally flat, then the manifold is a space of constant negative curvature -1 for dimension greater than 3. The notion of semi-symmetric manifold is defined by

$$R(X, Y) \cdot R = 0 \qquad (1)$$

for all vector fields X, Y on M, where $R(X, Y)$ acts as a derivation on R (Nomizu, 1968). Such a space is called "semi-symmetric space" since the curvature tensor of (M, g) at a point $p \in M, R_p$; is the same as the curvature tensor of a symmetric space (that can change with the point of p). Thus locally symmetric spaces are obviously semi-symmetric, but the converse is not true (Calvaruso & Perrone, 2002). Ogawa obtained that if a compact Kaehler manifold is semi-symmetric, then it is locally symmetric (Ogawa, 1977). These spaces were studied in the sense of a complete intrinsic classification by Szabó (Szabó, 1982).

The study is organized as follows: In introduction section, we shall give the short literature information of the study title. In preliminaries section, we shall present the concepts of the

---

[1] Assoc. Prof., Afyon Kocatepe University, Afyon Vocational School,

[2] Assoc. Prof., Afyon Kocatepe University, Faculty of Science and Literature, Department of Math.,

manifold theory and the next section is devoted to describe the basic formulas and some propositions of α-Kenmotsu pseudo metric manifolds. The last section contains the main results of the study. We shall give some results and an illustrative example of α-Kenmotsu pseudo metric manifolds satisfying certain curvature tensor conditions. Here, α is taken as a smooth function such that $d\alpha \wedge \eta = 0$ in all calculations on such manifolds.

Preliminaries

Let M be a $(2n + 1)$-dimensional smooth manifold endowed with a triple (φ, ξ, η), where φ is a type of (1,1) tensor field, ξ is a vector field, η is a 1-form on M such that

$$\eta(\xi) = 1, \varphi^2 = -I + \eta \otimes \xi, \varphi(\xi) = 0, \eta \circ \phi = 0, rank(\varphi) = 2n \qquad (2)$$

If M admits a Riemannian metric g, defined by

$$g(\varphi X, \varphi Y) = g(X, Y) - \eta(X)\eta(Y), \ \eta(X) = g(X, \xi) \qquad (3)$$

then M is called almost contact structure (φ, ξ, η, g). Also, the fundamental 2-form Φ of M is defined by

$$\Phi(X, Y) = g(X, \varphi Y) \qquad (4)$$

(Yano & Kon, 1984). If the Nijenhuis tensor vanishes, defined by

$$N_\varphi(X, Y) = [\varphi X, \varphi Y] - \varphi[\varphi X, Y] - \varphi[X, \varphi Y] + \varphi^2[X, Y] + 2d\eta(X, Y)\xi \qquad (5)$$

then (M, φ, ξ, η) is said to be normal (Blair, 1976). It is obvious that a normal almost Kenmotsu manifold is said to be Kenmotsu manifold.

Let (M, g) be an n-dimensional Riemannian manifold. We denote by ∇ the covariant differentiation with respect to the Riemann metric g. Then we have

$$R(X, Y)Z = \nabla_X \nabla_Y Z - \nabla_Y \nabla_X Z - \nabla_{[X,Y]} Z, \qquad (6)$$

The Ricci tensor of M is defined as

$$S(X, Y) = \sum_{i=1}^{n} R(X, e_i, Y, e_i) \qquad (7)$$

where $\{e_1, e_2, \ldots, e_n\}$ is a local orthonormal basis. Also, the Ricci operator Q is a tensor field of type (1,1) on M defined by

$$g(QX, Y) = S(X, Y) \qquad (8)$$

for any vector fields (Blair, 1976).

Almost contact metric manifolds such that η and Φ are closed called almost cosymplectic manifolds. Also, an almost contact metric manifold such that $d\eta = 0$ and $d\Phi = 2\eta \wedge \Phi$ is said to be an almost Kenmotsu manifold (Kenmotsu, 1972).

An almost contact metric manifold is said to be almost α-Kenmotsu if

$$d\eta = 0, d\Phi = 2\alpha(\eta \wedge \Phi). \qquad (9)$$

Here, α is a non-zero real constant (Kim & Pak, 2005). It is obvious that a normal almost α-Kenmotsu manifold is said to be α-Kenmotsu manifold.

α-Kenmotsu Pseudo Metric Manifolds

This section is devoted to give fundamental concepts of α-Kenmotsu pseudo metric manifolds. In particılar, basic curvature properties of α-Kenmotsu pseudo metric manifolds are presented. Here, α is given by a smooth function on M such that $d\alpha \wedge \eta = 0$.

A pseudo Riemannian metric g on M is said to be compatible with the almost contact structure (φ, ξ, η) if $g(\varphi X, \varphi Y) = g(X, Y) - \varepsilon\eta(X)\eta(Y)$ where $\varepsilon = \pm 1$. A smooth manifold M furnished with an almost contact structure (φ, ξ, η) and a compatible pseudo Riemannian metric g is called an almost contact pseudo metric manifold which is denoted by $(M, \varphi, \xi, \eta, g)$. It is obvious that $g(\varphi X, Y) = -g(X, \varphi Y), \eta(X) = \varepsilon g(X, \xi)$ and $g(\xi, \xi) = \varepsilon$.

An almost contact pseudo metric manifold satisfying (9) is said to be an almost α-Kenmotsu pseudo metric manifold for $\alpha \neq 0, \alpha \in R$. When an almost α-Kenmotsu pseudo metric manifold M has a normal almost contact structure, we can say that it is an α-Kenmotsu pseudo metric manifold.

Proposition 1. Let $(M, \varphi, \xi, \eta, g)$ be a $(2n + 1)$-dimensional almost contact metric manifold. If M is an α-Kenmotsu pseudo metric manifold, then we have

$$\nabla_X\xi = -\alpha\varphi^2 X = \alpha[X - \eta(X)\xi], \tag{10}$$

$$(\nabla_X\varphi)Y = \alpha[\varepsilon g(\varphi X, Y)\xi - \eta(Y)\varphi X] \tag{11}$$

for $X, Y \in \chi(M)$ (Öztürk & Öztürk, 2020).

Proposition 2. Let $(M, \varphi, \xi, \eta, g)$ be an α-Kenmotsu pseudo metric manifold. Then we have

$$R(X, Y)\xi = [\alpha^2 + \xi(\alpha)][\eta(X)Y - \eta(Y)X] \tag{12}$$

$$R(X, \xi)Y = -[\alpha^2 + \xi(\alpha)][-\varepsilon g(Y, X)\xi + \eta(Y)X] \tag{13}$$

$$R(X, \xi)\xi - \varphi R(\varphi X, \xi)\xi = 2[\alpha^2 + \xi(\alpha)][-X + \eta(X)\xi] \tag{14}$$

$$\eta(R(X, Y)Z) = \varepsilon[\alpha^2 + \xi(\alpha)][-\eta(X)g(Y, Z) + \eta(Y)g(X, Z)] \tag{15}$$

$$S(X, \xi) = -2n[\alpha^2 + \xi(\alpha)]\eta(X) \tag{16}$$

$$Q\xi = -2n\varepsilon [\alpha^2 + \xi(\alpha)] \tag{17}$$

$$(\nabla_X\eta)Y = \alpha[\varepsilon g(X, Y) - \eta(X)\eta(Y)] \tag{18}$$

$$S(\varphi X, \varphi Y) = [\alpha^2 + \xi(\alpha)](\varepsilon S(X, Y) - 2n[g(X, Y) - \varepsilon\eta(X)\eta(Y)]). \tag{19}$$

Here, α is defined by a smooth function such that $d\alpha \wedge \eta = 0$ and $\varepsilon = g(\xi, \xi)$ (Öztürk, 2017).

Definition 1. Let $(M, \varphi, \xi, \eta, g)$ be an α-Kenmotsu pseudo metric manifold. If the following condition holds

$$S(X, Y) = \lambda g(X, Y) + \varepsilon\mu\eta(X)\eta(Y) \tag{20}$$

for any $X, Y \in \chi(M)$, then M is said to be an η-Einstein α-Kenmotsu pseudo metric manifold. Here, λ and μ are the arbitrary functions on M. In particular, M becomes an Einstein manifold when $\mu = 0$ (Blair, 1976).

Proposition 3. Let $(M, \varphi, \xi, \eta, g)$ be an η-Einstein α-Kenmotsu pseudo metric manifold. Then we have

$$\lambda + \varepsilon\mu = -2n\varepsilon\alpha^2 \tag{21}$$

$$r = \lambda\varepsilon(2n+1) + \varepsilon\mu, \ \lambda = \frac{r+2n\varepsilon\alpha^2}{(2n+1)\varepsilon-1}, \ \mu = \left[\frac{2n(\alpha^2+r)+r}{(2n+1)\varepsilon-1}\right]$$

for any $X, Y \in \chi(M)$ (Öztürk & Öztürk, 2022).

Definition 2. Let (M, g) be a $(2n + 1)$-dimensional $(n \geq 2)$ Riemannian manifold. Then the D-conformal curvature tensor field on M defined as follows:

$$B(X,Y)Z = R(X,Y)Z + \frac{1}{2n-2}[S(X,Z)Y - S(Y,Z)X + g(X,Z)QY - g(Y,Z)QX$$

$$-S(X,Z)\eta(Y)\xi + S(Y,Z)\eta(X)\xi - \eta(X)\eta(Z)QY + \eta(Y)\eta(Z)Q - \frac{k-2}{2n-2}[g(X,Z)Y -$$

$$g(Y,Z)X] + \frac{k}{2n-2}[g(X,Z)\eta(Y)\xi - g(Y,Z)\eta(X)\xi + \eta(X)\eta(Z)Y - \eta(Y)\eta(Z)X]. \tag{22}$$

Here, $k = \frac{r+4n}{2n-1}$ and r is a scalar curvature of M (Chuman, 1983).

Main Results

In this section, some curvature tensor fields are investigated on α-Kenmotsu pseudo metric manifolds depending on α such that $d\alpha \wedge \eta = 0$. Thus we state the following results:

Theorem 1. Let $(M, \varphi, \xi, \eta, g)$ be a $(2n + 1)$-dimensional α-Kenmotsu D-conformal semi-symmetric pseudo metric manifold. If α is parallel along the characteristic vector field ξ and ξ is taken as time-like then M is an η-Einstein manifold. On the other hand, there exists no η-Einstein manifold if the characteristic vector field ξ is space-like.

Proof. According to the hypothesis, we assume that M is an α-Kenmotsu D-conformal semi-symmetric pseudo metric manifold. Now, let us introduce the D-conformal curvature tensor field B. If the D-conformal curvature tensor field B satisfies the following condition

$$R(X,Y) \cdot B = 0 \tag{23}$$

then M is said to be a D-conformal semi-symmetric manifold $(n \geq 2)$ (Taleshian et al., 2011). In other words, we have

$$(R(X,Y) \cdot B)(Z,U)V = 0. \tag{24}$$

Then using the definition of (23), (24) can be written as

$$R(X,Y)B(Z,U)V - B(R(X,Y)Z,U)V$$

$$-B(Z,R(X,Y)U)V - B(Z,U)R(X,Y)V = 0. \tag{25}$$

By the help of (13) and (25) with $X = \xi$, we deduce

$$[\alpha^2 + \xi(\alpha)][\eta(B(Z,U)V)Y - \varepsilon g(B(Z,U)V,Y)\xi - \eta(Z)B(Y,U)V]$$

$$+[\alpha^2 + \xi(\alpha)][\varepsilon g(Y,Z)B(\xi,U)V - \eta(U)B(Z,Y)V + \varepsilon g(Y,U)B(Z,\xi)V]$$

$$+[\alpha^2 + \xi(\alpha)][-\eta(V)B(Z,U)Y + \varepsilon g(V,Y)B(Z,U)\xi] = 0. \tag{26}$$

Taking the inner product of both sides of (26) with respect to ξ, we have

$$[\alpha^2 + \xi(\alpha)][\varepsilon\eta(B(W,V)U)\eta(Z) - g(B(W,V)U,Z) - \varepsilon\eta(W)\eta(B(Z,V)U)]$$

$$+[\alpha^2 + \xi(\alpha)][g(Z,W)\eta(B(\xi,V)U) - \varepsilon\eta(V)\eta(B(W,Z)U) + g(Z,V)\eta(B(W,\xi)U)]$$

$$+[\alpha^2 + \xi(\alpha)][-\varepsilon\eta(U)\eta(B(W,V)Z) + g(U,Z)\eta(B(W,V)\xi)] = 0. \tag{27}$$

Taking $Y = Z$ and $\xi(\alpha) = 0$ in (27), we get

$$\varepsilon\eta(B(Z,U)V)\eta(Z) - g(B(Z,U)V,Z) - \varepsilon\eta(Z)\eta(B(Z,U)V)$$

$$+g(Z,Z)\eta(B(\xi,U)V) - \varepsilon\eta(U)\eta(B(Z,Z)V) + g(Z,U)\eta(B(Z,\xi)V)$$

$$-\varepsilon\eta(V)\eta(B(Z,U)Z) + g(V,Z)\eta(B(Z,U)\xi) = 0. \tag{28}$$

Moreover, from (22) it follows that

$$\eta(B(Z,U)V = F\eta(U)g(Z,V) - F\eta(Z)g(U,V) \tag{29}$$

where F is defined by

$$F = \frac{1+\varepsilon\alpha^2(n-2)}{2n-2}. \tag{30}$$

Taking into account of (28) and (29), we obtain

$$g(B(Z,U)V,Z) = \varepsilon g(Z,Z)[F\eta(U)\eta(V) - Fg(U,V)] + \varepsilon g(Z,U)[Fg(Z,V) - F\eta(Z)\eta(V)]$$

$$-\varepsilon\eta(V)[F\eta(U)g(Z,Z) - F\eta(Z)g(Z,V)]. \tag{31}$$

Follows from (31) we have

$$g(B(Z,U)V,Z) = \varepsilon F[g(Z,U)g(Z,V) - g(Z,Z)g(U,V)]. \tag{32}$$

Now, we may take a local orthonormal φ-basis $E_j = \{e_1, \cdots, e_n, \varphi e_1, \cdots, \varphi e_n, \xi\}, j = 1, \cdots, n$. Then taking contraction in (32) with respect to $Z = E_j$, we get

$$\sum_{j=1}^{2n+1} g(B(E_j,U)V,E_j) = \varepsilon F(1 - \varepsilon(2n+1))g(U,V). \tag{33}$$

Also, considering (22), it follows that

$$\sum_{j=1}^{2n+1} g(B(E_j,U)V,E_j) = S(U,V)$$

$$+\frac{1}{2n-2}\big[2S(U,V) - \varepsilon(2n+1)S(U,V) - rg(V,U) + \varepsilon S(U,V) + r\eta(V)\eta(U) +$$

$$2n\alpha^2\eta(V)\eta(U)[\varepsilon+1]\big] - \frac{k-2}{2n-2}[g(V,U) - \varepsilon(2n+1)g(V,U)]$$

$$+\frac{k}{2n-2}[-\varepsilon g(V,U) + (1 - 2n\varepsilon)\eta(V)\eta(U)]. \tag{34}$$

Finally, using (33) and (34), it yields

$$S(U,V) = F_1 g(U,V) + F_2\eta(U)\eta(V) \tag{35}$$

where F_1 and F_2 are defined by

$$F_1 = \frac{-2r(n-1)+2(1-\varepsilon)+4n\varepsilon(k-1)-k(1+2\varepsilon)+(\varepsilon-1)(n\alpha^2-2\alpha^2-1)+2n(1-n\alpha^2\varepsilon)}{2n(\varepsilon-1)} \tag{36}$$

and

$$F_2 = \frac{r+2n\alpha^2(\varepsilon+1)+k(1-2n\varepsilon)}{2n(\varepsilon-1)}. \tag{37}$$

Thus it completes the proof by (36) and (37).

Theorem 2. Let (M,φ,ξ,η,g) be a $(2n+1)$-dimensional α-Kenmotsu Ricci D-conformal semi-symmetric pseudo metric manifold. If α is parallel along the characteristic vector field ξ, then M is an Einstein manifold with constant scalar curvature $r = -2n\alpha^2(2n+1)$.

Proof. We suppose that M is a Ricci D-conformal semi-symmetric pseudo metric manifold. It means that

$$B(X,Y) \cdot S(Z,U) = 0 \tag{38}$$

for $n \geq 2$. Thus (38) can be written as

$$S(B(X,Y)Z,U) + S(Z,B(X,Y)U) = 0. \tag{39}$$

Then putting $X = U = \xi$ in (39) we have

$$S(B(\xi,Y)Z,\xi) + S(Z,B(\xi,Y)\xi) = 0. \tag{40}$$

where $\xi(\alpha) = 0$.

Furthermore, in view of (29) we deduce

$$B(\xi,Z)U = F[\varepsilon\eta(U)Z - \xi g(Z,U)] \tag{41}$$

and

$$B(\xi,Z)\xi = F[Z - \varepsilon\eta(Z)\xi]. \tag{42}$$

Taking into account of (41) and (42) in (40) we obtain

$$S(Y,Z) = -2n\alpha^2\varepsilon g(Y,Z). \tag{43}$$

Lastly, taking contraction in (43) with respect to $Y = Z = E_j$, we get

$$r = -2n\alpha^2(2n+1).$$

Here, E_j is a local orthonormal φ-basis such that $\{e_1, \cdots, e_n, \varphi e_1, \cdots, \varphi e_n, \xi\}$, $j = 1, \cdots, n$. Thus the proof ends.

Theorem 3. Let M be a $(2n+1)$-dimensional D-conformal flat α-Kenmotsu pseudo-metric manifold. If α is parallel along the characteristic vector field ξ and ξ is time-like, then M is an η-Einstein manifold. Moreover, there exists no η-Einstein manifold where ξ is space-like.

Proof. According to the hypothesis, let us assume that M is a D-conformal flat α-Kenmotsu pseudo-metric manifold. Namely, we have

$$B(X,Y)Z = 0. \tag{44}$$

In view of (22) and (44), it follows that

$R(X,Y)Z = -\frac{1}{2n-2}[S(X,Z)Y - S(Y,Z)X + g(X,Z)QY - g(Y,Z)QX - S(X,Z)\eta(Y)\xi +$
$S(Y,Z)\eta(X)\xi - \eta(X)\eta(Z)QY + \eta(Y)\eta(Z)QX] + \frac{k-2}{2n-2}[g(X,Z)Y - g(Y,Z)X]$

$$-\frac{k}{2n-2}[g(X,Z)\eta(Y)\xi - g(Y,Z)\eta(X)\xi + \eta(X)\eta(Z)Y - \eta(Y)\eta(Z)X]. \tag{45}$$

Then taking the inner product on both sides of (45) with respect to U, we get

$g(R(X,Y)Z,U) = -\frac{1}{2n-2}[S(X,Z)g(Y,U) - S(Y,Z)g(X,U) + g(X,Z)g(QY,U) \qquad (46)$

$-g(Y,Z)g(QX,U) - \varepsilon S(X,Z)\eta(Y)\eta(U) + \varepsilon S(Y,Z)\eta(X)\eta(U) - \eta(X)\eta(Z)g(QY,U) +$
$\eta(Y)\eta(Z)g(QX,U)] + \frac{k-2}{2n-2}[g(X,Z)g(Y,U) - g(Y,Z)g(X,U)]$

$-\frac{k}{2n-2}[\varepsilon g(X,Z)\eta(Y)\eta(U) - \varepsilon g(Y,Z)\eta(X)\eta(U) + \eta(X)\eta(Z)g(Y,U) - \eta(Y)\eta(Z)g(X,U)]$

where $R(X,Y,Z,U) = g(R(X,Y)Z,U)$. From (15) and (16), (46) turns into

$$\eta(R(X,Y)Z) = -\varepsilon[\alpha^2 + \xi(\alpha)][\eta(X)g(Y,Z) + \eta(Y)g(X,Z)] = \qquad (47)$$

$$-\frac{\varepsilon}{2n-2}\{[(\varepsilon - 1)\eta(Y)S(X,Z) + (1 - \varepsilon)\eta(X)S(Y,Z)$$

$$-2n[\alpha^2 + \xi(\alpha)][\eta(Y)S(X,Z) - \eta(X)S(Y,Z)]\}$$

$$+\frac{k-2}{2n-2}[\eta(Y)g(X,Z) - \eta(X)g(Y,Z)] - \frac{\varepsilon k}{2n-2}[\eta(Y)g(X,Z) - \eta(X)g(Y,Z)]$$

for $U = \xi$. Putting $Y = \xi$ in (47) we have

$$-\frac{\varepsilon}{2n-2}[(\varepsilon - 1)\varepsilon S(X,Z) - 2n[\alpha^2 + \xi(\alpha)](\eta(X)\eta(Z) + \varepsilon g(X,Z))] \tag{48}$$

$$+\frac{(k-2)}{2n-2}\varepsilon[g(X,Z) - \eta(X)\eta(Z)] - \frac{k}{2n-2}[g(X,Z) - \eta(X)\eta(Z)]$$

$$= [\alpha^2 + \xi(\alpha)][g(X,Z) - \eta(X)\eta(Z)].$$

Next, simplifying (48) and $\xi(\alpha) = 0$, we obtain

$$S(X,Z) = \left(\frac{2n-2}{\varepsilon-1}\right)\left[\frac{\varepsilon(k-2)-k+2n\alpha^2}{2n-2} - \alpha^2\right]g(X,Z) \tag{49}$$

$$+\left(\frac{2n-2}{\varepsilon-1}\right)\left[\frac{-\varepsilon(k-2)+k+2n\varepsilon\alpha^2}{2n-2} + \alpha^2\right]\eta(X)\eta(Z).$$

So (49) becomes

$$S(X,Z) = \left[\frac{2(\alpha^2-\varepsilon)}{\varepsilon-1} + k\right]g(X,Z) \tag{50}$$

$$+\left[\frac{2(\varepsilon-\alpha^2+n\alpha^2(\varepsilon+1))}{\varepsilon-1} - k\right]\eta(X)\eta(Z).$$

Thus, considering (39), it is clear that the η-Einstein structure can not exist when the characteristic vector field ξ is chosen as space-like ($\varepsilon = g(\xi,\xi) = 1$). On the other hand, if the characteristic vector field ξ is chosen as time-like ($\varepsilon = g(\xi,\xi) = -1$), then we can state the following equation

$$S(X,Z) = \left[\frac{r+2n+1}{2n-1} - \alpha^2\right]g(X,Z) \tag{51}$$

$$+\left[-\frac{r+4n}{2n-1} + 1 + \alpha^2\right]\eta(X)\eta(Z)$$

which completes the proof.

Theorem 4. Let M be a $(2n + 1)$-dimensional α-Kenmotsu pseudo-metric manifold. If α is parallel along the characteristic vector field ξ, then there exists no ξ-D-conformal flat manifold where ξ is space-like.

Proof. In accordance with the hypothesis, we suppose that M is an α-Kenmotsu pseudo metric manifold satisfying the ξ-D-conformal flat condition. In other words, we have

$$B(X,Y)\xi = 0. \tag{52}$$

Making use of (22), (52) becomes

$$R(X,Y)\xi + \frac{1}{2n-2}[S(X,\xi)Y - S(Y,\xi)X + g(X,\xi)QY - g(Y,\xi)QX - S(X,\xi)\eta(Y)\xi$$

$$+S(Y,\xi)\eta(X)\xi - \varepsilon\eta(X)QY + \xi\eta(Y)QX] - \frac{\varepsilon(k-2)}{2n-2}[g(X,\xi)Y - g(Y,\xi)X]$$

$$+\frac{\varepsilon k}{2n-2}[g(X,\xi)\eta(Y)\xi - g(Y,\xi)\eta(X)\xi + \eta(X)Y - \eta(Y)X] = 0. \tag{53}$$

Follows from (12), (13) (16) and taking the inner product on both sides of (53) with respect to V, we deduce

$$[\alpha^2 + \xi(\alpha)][\eta(X)g(Y,V) - \varepsilon\eta(Y)g(X,V)]$$

$$+\frac{-2n[\alpha^2+\xi(\alpha)]}{2n-2}[\eta(X)g(Y,V) - \eta(Y)g(X,V)] \tag{54}$$

$$-\left(\frac{(k-2)\varepsilon}{2n-2}\right)[\eta(X)g(Y,V) - \eta(Y)g(X,V)]$$

$$+\left(\frac{\varepsilon k}{2(n-1)}\right)[\eta(X)g(Y,V) - \eta(Y)g(X,V)] = 0.$$

Then putting $Y = \xi$ and $\xi(\alpha) = 0$ in (54) we have

$$\left[\frac{\alpha^2\varepsilon-1}{n-1}\right]g(X,V) + \left[\frac{-\alpha^2\varepsilon+1}{n-1}\right]\eta(X)\eta(V) = 0. \tag{55}$$

Also, it is well known that

$$g(\varphi X, \varphi V) = g(X,V) - \varepsilon\eta(X)\eta(V). \tag{56}$$

Since $n \geq 2$ and $\alpha^2 \neq 0$, (55) takes the form

$$g(X,V) - \eta(X)\eta(V) = 0. \tag{57}$$

In view of (55) and (56) with $\varepsilon = 1$, it follows that

$$g(\varphi X, \varphi V) = 0. \tag{58}$$

However, (58) is a contradiction. Therefore, the ξ-D-conformal flat α-Kenmotsu pseudo-metric manifold does not exist when the characteristic vector field ξ is taken as space-like. Thus, the proof is completed.

Theorem 5. Let M be a $(2n + 1)$-dimensional φ-D-conformal flat α-Kenmotsu pseudo-metric manifold. If α is parallel along the characteristic vector field ξ, then M is an η-Einstein manifold.

Proof. Let us assume that M is an α-Kenmotsu pseudo metric manifold satisfying the φ-D-conformal flat condition. Thus M holds the following equation:

$$g(B(\varphi X, \varphi Y)\varphi Z, \varphi V) = 0. \tag{59}$$

By the help of (22) and (59), we have

$$g(R(\varphi X, \varphi Y)\varphi Z, \varphi V) + \frac{1}{2n-2}[S(\varphi X, \varphi Z)g(\varphi Y, \varphi V) - S(\varphi Y, \varphi Z)g(\varphi X, \varphi V)$$

$$+S(\varphi Y, \varphi V)g(\varphi X, \varphi Z) - S(\varphi X, \varphi V)g(\varphi Y, \varphi\phi Z)]$$

$$-\frac{k-2}{2n-2}[g(\varphi X, \varphi Z)g(\varphi Y, \varphi V) - g(\varphi Y, \varphi Z)g(\varphi X, \varphi V)] = 0. \tag{60}$$

Taking into account of (15), (19) and (57), (60) takes the form

$$\varepsilon[\alpha^2 + \xi(\alpha)][g(\varphi X, \varphi W)g(\varphi Y, \varphi\phi U) - g(\varphi Y, \varphi W)g(\varphi X, \varphi U)]$$

$$+\frac{[\alpha^2+\xi(\alpha)]}{2n-2}[\varepsilon S(X,Z)g(Y,V) - 2ng(X,Z)g(Y,V) + 2n\varepsilon\eta(X)\eta(Z)g(Y,V)$$

$$-S(X,Z)\eta(Y)\eta(V) + 2n\varepsilon\eta(Y)\eta(V)g(X,Z) - S(Y,Z)g(X,V)$$

$$+2ng(X,V)g(Y,Z) - 2n\varepsilon\eta(Y)\eta(Z)g(X,V) + S(Y,Z)\eta(X)\eta(V)$$

$$-2n\varepsilon\eta(X)\eta(V)g(Y,Z) + \varepsilon S(Y,V)g(X,Z) - 2ng(X,Z)g(Y,V)$$

$$+2n\varepsilon\eta(Y)\eta(V)g(X,Z) - S(Y,V)\eta(X)\eta(Z) + 2n\varepsilon\eta(X)\eta(Z)g(Y,V)$$

$$-\varepsilon S(X,V)g(Y,Z) + 2ng(X,V)g(Y,Z) - 2n\varepsilon\eta(X)\eta(V)g(Y,Z)$$

$$+S(X,V)\eta(Y)\eta(Z) + 2n\varepsilon\eta(Y)\eta(Z)g(X,V)] \tag{61}$$

$$-\frac{\varepsilon(k-2)}{2n-2}[\varepsilon g(X,Z)g(Y,V) - g(X,Z)\eta(Y)\eta(V) - g(Y,V)\eta(X)\eta(Z)$$

$$-\varepsilon g(Y,Z)g(X,V) + g(Y,Z)\eta(X)\eta(V) + g(X,V)\eta(Y)\eta(Z)] = 0.$$

Now, we may choose a local orthonormal φ-basis $E_j = \{e_1, \cdots, e_n, \varphi e_1, \cdots, \varphi e_n, \xi\}, j = 1, \cdots, n.$ Then taking contraction in (61) with respect to $X = V = E_j$ and $\xi(\alpha) = 0$, we obtain

$$-S(Y,Z) = \frac{E_1}{E_3}g(Y,Z) + \frac{E_2}{E_3}\eta(Y)\eta(Z) \tag{62}$$

Here, the functions used in (62) are as follows:

$$E_1 = \alpha^2[\varepsilon + 2(n+1)] + b(2n\varepsilon - 1) - a\alpha^2(6n + \varepsilon r) + 2na\alpha^2\varepsilon(4n+1)$$

$$E^2 = \alpha^2(2n\varepsilon - 1) - b(2n-1) + a[\alpha^2 r - 4n\alpha^4(2n-1) + 2n\alpha^2(\varepsilon + 1)]$$

$$E_3 = \left[\frac{\alpha^2(\varepsilon-n)}{n-1}\right], a = \frac{1}{2n-2}, b = \frac{k-2}{2n-2}, k = \frac{r+4n}{2n-1}.$$

As a result, the proof completes with the help of (62).

Theorem 6. Let M be a $(2n+1)$-dimensional α-Kenmotsu semi-symmetric pseudo-metric manifold. If α is parallel along the characteristic vector field ξ such that ξ is space-like, then M is a space of constant negative curvature $-\alpha^2$.

Proof. Note that (1) is equivalent to

$$R(\xi, Y) \cdot R = 0 \tag{63}$$

for all vector field Y on M, that is,

$$R(\xi,Y)R(X,Z)U - R(R(\xi,Y)X,Z)U$$
$$-R(X, R(\xi,Y)Z)U - R(X,Z)R(\xi,Y)U = 0. \tag{64}$$

Taking $X = \xi$ in (64) we get

$$R(\xi,Y)R(\xi,Z)U - R(R(\xi,Y)\xi,Z)U$$
$$-R(\xi, R(\xi,Y)Z)U - R(\xi,Z)R(\xi,Y)U = 0. \tag{65}$$

Making use of (13) and $\xi(\alpha) = 0$, (65) turns into

$$-\alpha^2 R(Y,Z)U - \alpha^4\varepsilon g(Z,U)Y + \alpha^4\varepsilon g(Y,U)Z + \alpha^4\varepsilon\eta(Y)\eta(U)Z$$

$$+\alpha^4\varepsilon\eta(Z)g(Y,U)\xi - \alpha^4\varepsilon\eta(Y)\eta(U)Z - \alpha^4\eta(Z)g(Y,U)\xi = 0. \tag{66}$$

In particular, when the vector field ξ is taken as space-like, (66) can be written

$$-\alpha^2 R(Y,Z)U - \alpha^4 g(Z,U)Y + \alpha^4 g(Y,U)Z = 0. \tag{67}$$

Moreover, we have

$$R(Y,Z)U = c[g(Z,U)Y - g(Y,U)Z] \tag{68}$$

where c is constant curvature of M. Thus from (67) and (68), the proof is completed.

Example 1. Suppose that M is a 3-dimensional manifold defined by

$$M = \{(x,y,z): \quad z \neq 0\}$$

where (x, y, z) are the standart coordinates. Let the vector fields be as follows:

$$e_1 = e^{z^2}(\partial/\partial x), e_2 = e^{z^2}(\partial/\partial y), e_3 = (\partial/\partial z).$$

Moreover, the metric tensor g is given by

$$g = e^{-2z^2}(\varepsilon_1 dx^2 + \varepsilon_2 dy^2) + \varepsilon dz^2, \ \ \eta = dz.$$

Then the following relations are held:

$$\varphi(\xi) = 0, \varphi(e_1) = e_2, \varphi(e_2) = -e_1,$$

$$\varphi^2 X = -X + \eta(X)e_3, \eta(X) = \varepsilon g(e_3, X), \eta(e_3) = g(e_3, e_3) = \varepsilon = \varepsilon_3, \tag{69}$$

$$g(\varphi X, \varphi Y) = g(X, Y) - \varepsilon\eta(X)\eta(Y), \varepsilon_i = g(e_i, e_i), i = 1,2,3.$$

According to all the equations in (69), an almost contact pseudo metric structure $(M, \varphi, \xi, \eta, g)$ exists. To check whether it is almost α-Kenmotsu pseudo metric or not, we verify the condition $d\Phi = 2\alpha(\eta \wedge \Phi)$.

On the other hand, all Φ_{ij}'s vanish except for $\Phi(e_1, e_2) = -\varepsilon_i$, we deduce

$$\Phi\left(\left(\frac{\partial}{\partial x}\right), \left(\frac{\partial}{\partial y}\right)\right) = -\varepsilon_i e^{-2z^2}$$

$$\Phi = -\varepsilon_i e^{-2z^2}(dx \wedge dy)$$

$$d\Phi = -\varepsilon_i 2z e^{-2z^2}(dx \wedge dy \wedge dz).$$

Since $\eta = dz$, we obtain

$$d\Phi = -2\varepsilon_i 2z(\eta \wedge \Phi)$$

such that $\alpha = -2\varepsilon z$. Also, we remark that $N_\varphi = 0$. Thus M is α-Kenmotsu pseudo metric one.

Discussion and Conclusion

The main purpose of this study is to investigate α-Kenmotsu pseudo metric manifolds satisfying some tensor conditions. First, the central theme that draws attention to the study is the underlying differences and similarities between the Riemannian metric and pseudo-Riemannian tensors on α-Kenmotsu manifolds such that $d\alpha \wedge \eta = 0$. Our further studies will be related to nullity distributions, (κ, μ, ν)-spaces, D-homothetic deformations, local symmetry, semi-symmetric conditions, certain parallel tensors, and the other curvature tensor fields using soliton theory on almost α-Kenmotsu pseudo metric manifolds.

References

Begawadi, C. S. & Kumar, E. G. & Venkatesha, V. (2005) On irrational D-conformal curvature tensor. *Novi Sad J. Math., 35* (2), 85-92.

Blair, D. E. (1976). *Contact manifolds in Riemannian geometry*. Lecture Notes in Math., Vol. 509, New York: Springer-Verlag, Berlin-Heidelberg.

Calvaruso, G. & Perrone, D. (2002). Semi-symmetric contact metric three-manifolds, *Yokohama Math. J., 49,* 149-161.

Calvaruso, G. & Perrone, D. (2010). Contact pseudo-metric manifolds. *Differential Geometry and its Applications, 28,* 615-634. Doi: https://doi.org/10.1016/j.difgeo.2010.05.006

Calvaruso, G. (2011). Contact Lorentzian manifolds. *Differential Geometry and its Applications, 29,* 541-551. Doi: https://doi.org/10.1016/j.difgeo.2011.04.006

Chuman, G. (1983). On the D-conformal curvature tensor. *Tensor*, 40 (2), 125-134.

De, U. C. & Pathak, G. (2004). On 3-dimensional Kenmotsu manifolds. *Ind. J. Pure Applied Math., 35,* 159-165.

Dileo, G. & Pastore A. M. (2007). Almost Kenmotsu manifolds and local symmetry. *Bulletin of the Belgian Mathematical Society-Simon Stevin, 14,* 343-354. Doi: 10.36045/bbms/1179839227

Hong, S. & Özgür, C. & Tripathi, M. M. (2006). On some special classes of Kenmotsu manifolds. *Kuwait J. Sci. Eng., 33,* 19-32.

Jun, J. B. & De, U. C. & Pathak, G. (2005). On Kenmotsu manifolds. *J. Korean Math. Soc., 42,* 435-445. Doi: https://doi.org/10.4134/JKMS.2005.42.3.435

Kenmotsu, K. (1972). A class of contact Riemannian manifold. *Tohoku Math. J., 24,* 93-103. Doi: 10.2748/tmj/1178241594

Kim, T. W. & Pak, H. K. (2005). Canonical foliations of certain classes of almost contact metric structures. *Acta Math. Sinica, Eng. Ser. Aug., 21,* 841-846. Doi: https://doi.org/10.1007/s10114-004-0520-2

Naik, D. M. & Venkatesha, V. & Kumara, H. A. (2020). Some results on almost Kenmotsu manifolds, *Note di Matematica., 40* (1), 87-100. Doi: 10.1285/i15900932v40n1p87

Nomizu, K. (1968). On hypersurfaces satisfying a certain condition on the curvature tensor, *Tôhoku Mat. J., 20,* 46-69.

Ogawa, Y. (1977). A condition for a compact Kaehlerian space to be locally symmetric, *Nat. Sci. Rep. Ochanomizu Univ., 28,* 21-23.

O'Neil, B. (1983). *Semi-Riemannian geometry with applications to relativity*. New York: Academic Press.

Öztürk, H. (2017). On α-Kenmotsu manifolds satisfying semi-symmetric conditions, *Konuralp Journal of Mathematics, 5,* 192-206.

Öztürk, S. & Öztürk, H. (2020). On α-Kenmotsu pseudo metric manifolds, *AKU Journal of Science and Eng., 20,* 975-982. Doi: 10.35414/akufemubid.803483

Öztürk, S. & Öztürk, H. (2021). Almost α-cosymplectic pseudo metric manifolds. *Journal of Mathematics, 2021,* Article ID 4106025, 10 pages. Doi: https://doi.org/10.1155/2021/4106025

Öztürk, S. & Öztürk, H. (2022). *D-konformal eğrilik tensör alanına sahip α-Kenmotsu pseudo metrik manifoldlar.* Fen ve Mühendislik Bilimlerinde Güncel Tartışmalar ve Araştırmalar 6, Ankara: Bilgin Kültür Sanat Yayınları (in press).

Perrone, D. (2014). Contact pseudo-metric manifolds of constant curvature and CR geometry. *Results in Mathematics, 66,* 213-225. Doi: https://doi.org/10.1007/s00025-014-0373-7

Szabó, Z. I. (1982). Structure theorem on Riemannian spaces satisfying $R.R = 0$, *Journal of Differential Geo., 17,* 531-582.

Takahashi, T. (1969). Sasakian manifold with pseudo-Riemannian metric, *Tôhoku Mathematical Journal, 21,* 271-290.

Taleshian, A. & Hosseinzadeh, A. A. & Khaniani, F. (2011). On D-conformal curvature tensor Sasakian manifolds. *Journal of Nonlinear Analysis and Application, 2011,* 1-5. Doi: 10.5899/2011/jnaa-00088

Wang, Y. & Liu, X. (2016). Almost Kenmotsu pseudo-metric manifolds. *Analele Stiintifice ale Universitatii Al I Cuza din Iasi -Matematica, 62,* 241-256. Doi: 10.2478/aicu-2014-0030

Yano, K. & Kon, M. (1984). *Structures on manifolds*, Series in Pure Math., Vol. 3, Singapore: World Scientific Publishing Co.

Adaptive Fuzzy Logic Based Vector Controlled Permanent Magnetic Synchronous Motor Speed Control

Mehmet KARAYEL
Çağatay ERSİN

1.Introduction

Permanent Magnet Synchronous Motors (PMSM) is one of the electric motors with the high power density and high efficiency. PMSMs are highly preferred in applications that require high speed/position accuracy and high torque/inertia. It is smaller in size and requires less maintenance than drive motors such as asynchronous motors. With these features, it is widely used in different fields [1].

Permanent Magnet Synchronous Motor (PMSM), three-phase windings in the stator; The rotor consists of surface-mounted permanent magnets. Due to the permanent magnets being inside (on the rotor surface), it provides advantages such as mechanical durability, and reduction of flux weakening and is suitable for high-speed applications.

The PMSM is driven by the rotor position-dependent synchronous sine voltage received from the position sensors. Along with the stator flux produced, the rotor flux produced by the magnets determines the torque and speed of the motor. To produce maximum torque, the phase difference between the stator flux and the rotor flux should be 90o and the sine wave voltage output should be applied to the three-phase stator windings. To achieve this, the motor must be controlled with driver circuits [2,3].

Conventional controllers are widely used in the speed/position control of PMSMs due to their simplicity of structure and sufficient efficiency in many industrial applications. However, the need for a model of the system to be controlled and the determination of the most appropriate gain values by trial and error method is the disadvantage of these controllers [4]. Conventional controllers such as proportional integral (OI) shouldn't cause overshoot and fluctuations in speed and load changes [5]. This situation has brought along more efficient searches in terms of performance and efficiency. In addition, the hardware difficulty of analogue control techniques and the necessity of complex mathematical modelling have led to the search for new approaches in control techniques. Among the developing control techniques, the fuzzy logic approach has become frequently used because it does not need complex mathematical modelling. In addition to the advantage of simple mathematical modelling, fuzzy logic control has advantages such as being flexible and conceptually easy to understand, which has increased its use in many process control systems [6,7].

Conventional PI control, when subjected to changes or deterioration of motor parameters, cannot fundamentally resolve the conflict between dynamic and static performance, and cannot meet the fast-tracking requirements of the servo system [8]. Therefore, to compensate for the disadvantages of PI control. In this study, PI control parameters were adjusted with adaptive fuzzy

logic and applied in PMSM control and the simulation of the system was established in Simulink. The result shows that the dynamics of the system using the AF-PI control have been improved.

2.Modelling of Permanent Magnet Synchronous Motors

2.1.Reference Plane Transformations

While modelling three-phase AC motors, conversion between phase planes is performed. The phase transformation is usually from the three-phase plane to the reference two-phase fixed plane (Clarke transform) or from the reference two-phase fixed plane to the polyphase plane (Inverse Clarke transform), from the reference two-phase fixed plane to the two-phase rotor plane (Park transform) 90º perpendicular to each other and 90º to each other. the reference from the two-phase rotor plane to the two-phase fixed plane (Reverse Park transform). Figure 1 shows the reference plane transformations.
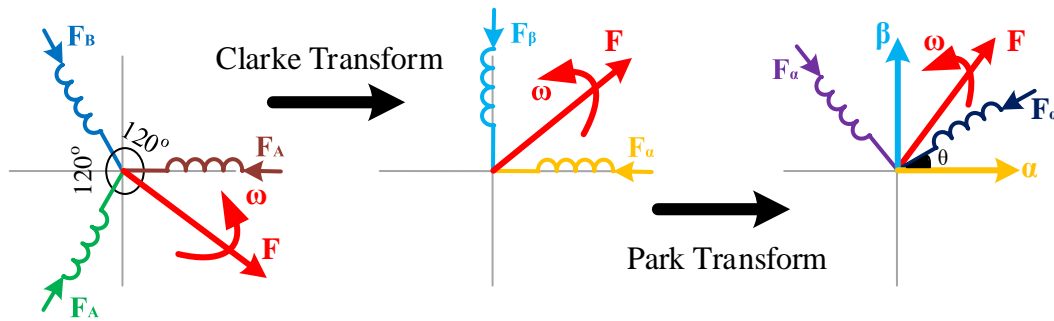
Şekil 1. Referans düzlem dönüşümleri.

2.2.Clarke Transform

When modelling three-phase AC motors, the conversion from a three-phase fixed plane to two-phase planes perpendicular to each other is called Clarke transform. With phase transformations, the number of variables in motor modelling is reduced and the solution is facilitated. Figure 2 shows the Clarke transform components. While the Clarke transform components are represented as vectorial, it is assumed that the plane of the motor phase A and the plane of the reference α phase are in the same direction. Clarke and Inverse Clarke transformation equations are given in Equations (1) and (2), respectively.
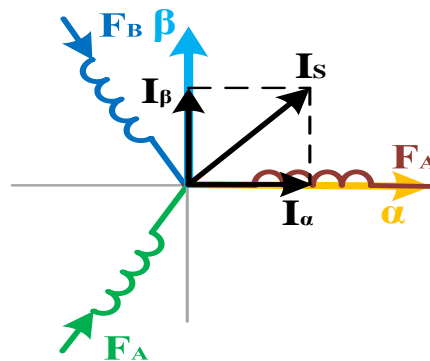
Figure 2. Components in Clarke transform.

$$\begin{bmatrix} F_\propto \\ F_\beta \\ F_0 \end{bmatrix} = \frac{2}{3} \begin{bmatrix} 1 & -\frac{1}{2} & -\frac{1}{2} \\ 0 & \frac{\sqrt{3}}{2} & -\frac{\sqrt{3}}{2} \\ \frac{1}{2} & \frac{1}{2} & \frac{1}{2} \end{bmatrix} \begin{bmatrix} F_A \\ F_B \\ F_C \end{bmatrix} \tag{1}$$

$$\begin{bmatrix} F_A \\ F_B \\ F_C \end{bmatrix} = \frac{2}{3} \begin{bmatrix} 1 & 0 & 0 \\ -\frac{1}{2} & \frac{\sqrt{3}}{2} & 0 \\ -\frac{1}{2} & -\frac{\sqrt{3}}{2} & 0 \end{bmatrix} \begin{bmatrix} F_\propto \\ F_\beta \\ F_0 \end{bmatrix} \tag{2}$$

2.3. Park Transform

The Park conversion method is used to convert from a two-phase fixed reference plane perpendicular to each other at 90o to a two-phase rotating rotor plane. Also the reverse of this situation, the reverse parking transform is used to convert from two phases rotating rotor plane to a two-phase fixed reference plane 90o to each other. Figure 3 shows the Park transform vector diagram. The Park and Inverse Park transform equations are given in (3) and (4), respectively.
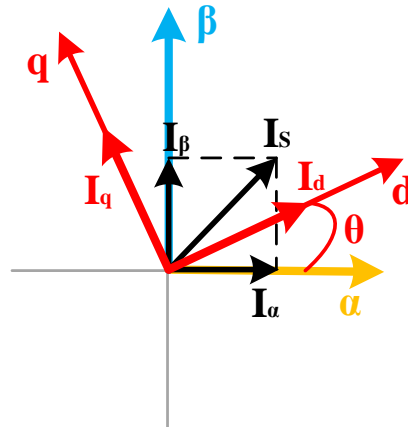
Figure 3. Components in the park transformation.

$$\begin{bmatrix} F_d \\ F_q \end{bmatrix} = \begin{bmatrix} cos\theta_r & sin\theta_r \\ -sin\theta_r & cos\theta_r \end{bmatrix} \begin{bmatrix} F_\propto \\ F_\beta \end{bmatrix} \tag{3}$$

$$\begin{bmatrix} F_\propto \\ F_\beta \end{bmatrix} = \begin{bmatrix} cos\theta_r & -sin\theta_r \\ sin\theta_r & cos\theta_r \end{bmatrix} \begin{bmatrix} F_d \\ F_q \end{bmatrix} \tag{4}$$

In equations (3) and (4), F_d and F_q denote the phasor components of the stator d-q in the rotor reference plane and θ_r the rotor angle. Here, the current and voltage variables of the d-q phasor components can be found using these equations.

2.4. Three-Phase Equivalent Circuit of Permanent Magnet Synchronous Motor

The three-phase ABC model of the PMSM is realized using the equivalent circuit shown in Figure 4. Equivalent active V_A, V_B, V_C instantaneous value of stator phase-neutral voltages, i_A, i_B, i_C instantaneous value of stator currents, R_A, R_B, R_C ohmic resistance values of stator phase windings, L_{AA}, L_{BB}, L_{CC} The total inductance values of the stator phase windings, M_{AB}, M_{BC}, M_{CA} It represents the mutual inductance values between phases of the stator phase windings.
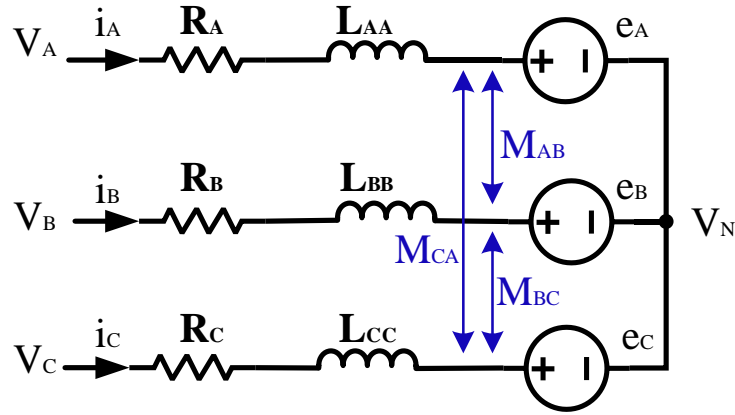
Şekil 4. PMSM üç faz stator eşdeğer devresi.

The three-phase sinusoidal voltages applied to the motor are expressed as:

$$V_A = V_m \sin\omega_e t \tag{5}$$

$$V_B = V_m \sin(\omega_e t - 2\pi/3) \tag{6}$$

$$V_C = V_m \sin(\omega_e t + 2\pi/3) \tag{7}$$

If the stator resistance, self and mutual inductance values are considered equal;

$$R_A = R_B = R_C = R_S \tag{8}$$

$$L_{AA} = L_{BB} = L_{CC} = L_S \tag{9}$$

$$M_{AB} = M_{BC} = M_{CA} = M \tag{10}$$

stator voltages;

$$\begin{bmatrix} V_A \\ V_B \\ V_C \end{bmatrix} = R_s \begin{bmatrix} i_A \\ i_B \\ i_C \end{bmatrix} + \frac{d}{dt} \begin{bmatrix} \psi_A \\ \psi_B \\ \psi_C \end{bmatrix} \tag{11}$$

phase winding currents;

$$\begin{bmatrix} \psi_A \\ \psi_B \\ \psi_C \end{bmatrix} = \begin{bmatrix} L_{AA} & M_{AB} & M_{AC} \\ M_{BA} & L_{BB} & M_{BC} \\ M_{CA} & M_{CB} & L_{CC} \end{bmatrix} \begin{bmatrix} i_A \\ i_B \\ i_C \end{bmatrix} + \psi_m \begin{bmatrix} \cos\theta_e \\ \cos(\theta_e - 2\pi/3) \\ \cos(\theta_e + 2\pi/3) \end{bmatrix} \tag{12}$$

If equation (12) is substituted in equation (11) and the equations in equation (10) are applied;

$$\begin{bmatrix} v_A \\ v_B \\ v_C \end{bmatrix} = R_s \begin{bmatrix} i_A \\ i_B \\ i_C \end{bmatrix} + L_s \frac{d}{dt}\begin{bmatrix} i_A \\ i_B \\ i_C \end{bmatrix} + \omega_e \psi_m \begin{bmatrix} \cos\theta_e \\ \cos(\theta_e - 2\pi/3) \\ \cos(\theta_e + 2\pi/3) \end{bmatrix} \tag{13}$$

obtained from the equations. Here, ψ_A, ψ_A, ψ_C represents the total flux of the phase windings, ψ_m represents the magnetic flux formed by the permanent magnets, the reduced amplitude of the magnetic flux to the stator, R_s the stator resistance, L_s the synchronous inductance, and θ_e the electrical displacement of the rotor.

Motor's electrical output power and electromagnetic torque expression;

$$P_e = e_A I_A + e_B I_B + e_C I_C \tag{14}$$

$$T_e = P_e / \omega_e \tag{15}$$

$$T_e = p\left\{ \frac{1}{2}[i_{ABC}]^T \frac{\partial[L_{ABC}]}{\partial\theta_r}[i_{ABC}] + [i_{ABC}]^T \frac{\partial[\psi_{ABC}]}{\partial\theta_r} \right\} \tag{16}$$

Here θ_r is the mechanical rotor position and p is the number of pairs of the motor.
The electrical moment equation can be expressed as:

$$T_e = T_m + J\frac{d\omega_e}{dt} + B_m\omega_e \tag{17}$$

where ω_m is the mechanical angular velocity, J is the moment of inertia, T_y is the load moment and B_m is the friction coefficient of the machine and the rotating system. The following relations can be written between θ_e electrical position and ωe electrical angular velocity.

$$\omega_e = \frac{d\theta_e}{dt} \tag{18}$$

$$\theta_r = \frac{1}{p}\theta_e \tag{19}$$

$$\omega_e = \frac{1}{p}\omega_m \tag{20}$$

2.5.dq0 Equivalent Circuit and Model of Permanent Magnet Synchronous Motor

Another method used in the modelling of PMSMs is the d-q model, which is obtained by transferring the stator sizes to the rotor plane. Computing is easier and faster in this model, which is similar to the free-excited synchronous machine model. Current and voltage variables in the

three-phase plane are transferred to the rotor reference plane by using the Clarke transform and park transform methods, respectively. Figure 5 shows the PMSM d-q equivalent circuit.
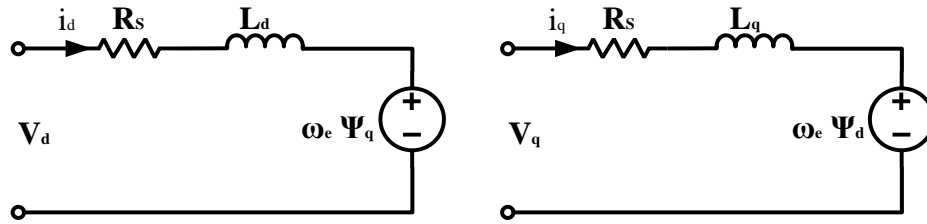
Figure 5. PMSM d-q equivalent circuit.

When Clarke and Park's transformations are applied to the voltage equations of the motor given in Equation (13);

$$V_d = r_s i_d + \frac{d}{dt}\psi_d - \psi_q \omega_e \tag{21}$$

$$V_q = r_s i_q + \frac{d}{dt}\psi_q - \psi_d \omega_e \tag{22}$$

Here, V_d and V_q show the d and q axis voltages, i_d and i_q show the d and q axis currents, and ψ_d and ψ_q show the d and q axis fluxes. D and q-axis flux expressions are given in equations (23) and (24).

$$\psi_q = L i_q \tag{23}$$

$$\psi_d = L i_d + \psi_m \tag{24}$$

If these expressions are substituted in equations (21) and (22);

$$V_d = r_s i_d + L_d \frac{d}{dt} i_d - L_q i_q \omega_e \tag{25}$$

$$V_q = r_s i_q + L_q \frac{d}{dt} i_q + L_d i_d \omega_e + \omega_e \psi_m \tag{26}$$

If necessary adjustments are made in Equations (25) and (26), the equations i_d and i_q are written as follows:

$$\frac{d}{dt} i_d = \frac{1}{L_d}\{V_d - r_s i_d + L_q i_q \omega_e\} \tag{27}$$

$$\frac{d}{dt} i_q = \frac{1}{L_q}\{V_q - r_s i_q + L_d i_d \omega_e - \omega_e \psi_m\} \tag{28}$$

The electromagnetic or induced moment expression is;

$$T_e = \frac{3}{2} p \left[\psi_m i_q + (L_d - L_q) i_d i_q\right] \tag{29}$$

After obtaining the electromagnetic torque expression, the velocity equation is obtained as follows:

$$\frac{d}{dt}\omega_m = \frac{3}{2}\frac{p}{J}\left\{\left(L_d - L_q\right)i_d i_q + i_q \psi_m\right\} - \frac{B\omega_m}{J} - \frac{T_m}{J} \tag{30}$$

3.Establishment of Simulation Model of PMSM

The creation of the control model in the MATLAB/SIMULINK environment is discussed by making use of the mathematical equations of PMSM specified in the second chapter. By using the obtained control model of PMSM, its performances will be compared by making separate controls with both the traditional PI controller and the proposed AF_PI controller.

3.1.PMSM'un Alan Yönlendirmeli Kontrol (AYK) Modeli

AYK, which is used in electrical machines, allows Alternating Current (AC) motors to be controlled independently of each other, without any relationship between the excitation circuit and armature circuit, as in Direct Current (DC) motors. Thanks to this method, high dynamic performance obtained from DC motors can also be obtained from AC motors [10,11]. The basic principle of AYK is based on the separation of the machine current into two components, expressed as d-q, one that produces torque and the other that produces flux, and these components are controlled independently of each other. AYK is easier in PMSMs compared to other electrical machines. The reason for this is that permanent magnets placed in the rotor produce a constant magnetic flux in the rotor [12]. Using equations (18), (19), (27), (28), (29) and (30), the mathematical model of PMSM is respectively; Figure 6 shows the i_q axis model, Figure 7 shows the i_d axis model, and Figure 8 shows the induced torque T_e, θe electrical position and ωe electrical angular velocity models. Figure 9 shows the final version of the PMSM mathematical model.
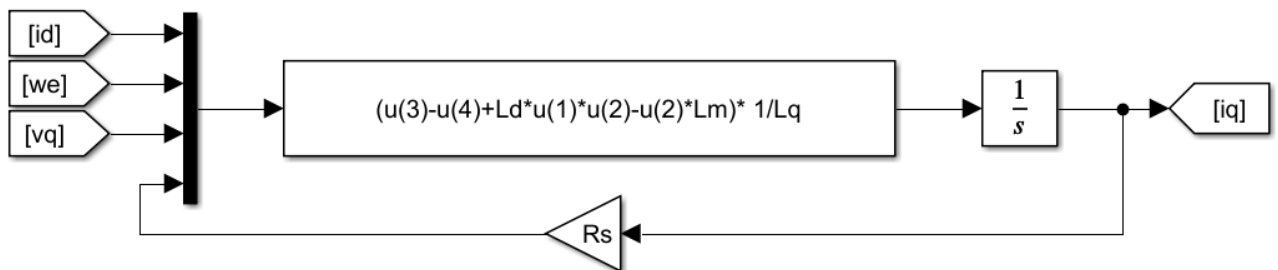
Figure 6. MATLAB/SIMULINK i_q axis model and block representation.
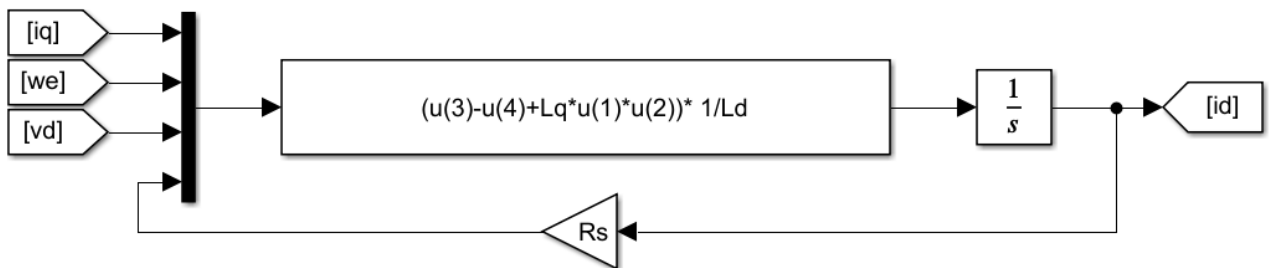
Figure 7. MATLAB/SIMULINK i_d axis model and block representation.
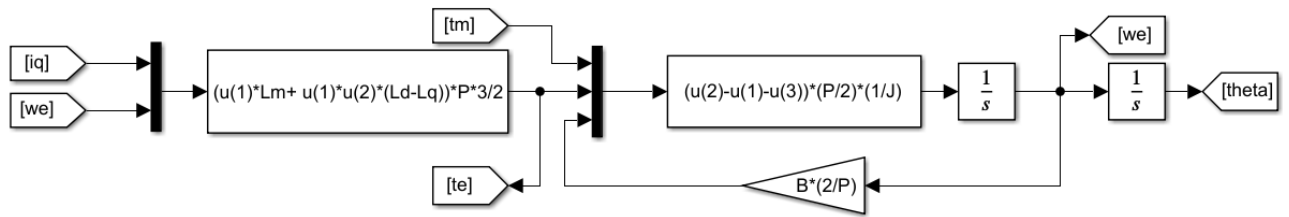
Figure 8. MATLAB/SIMULINK torque, electrical rotational speed and position model and block representation.
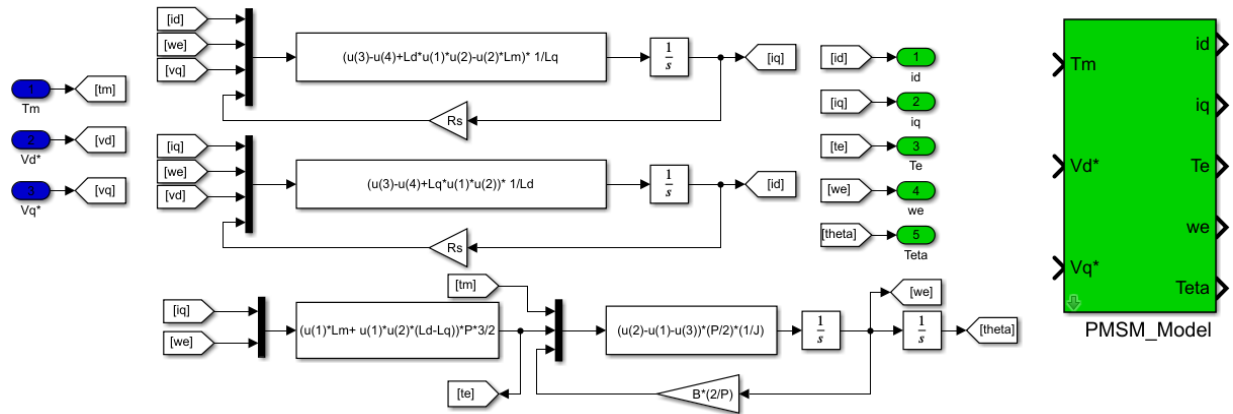
Figure 9. MATLAB/SIMULINK PMSM model and block representation.

3.2. Permanent Magnet Synchronous Motor Conversion Models

The simulations of the transformation expressions given above were performed in the MATLAB/SIMULINK environment. These transformations are shown respectively in Figure 10 Clarke transform, Figure 11 Park transform, Figure 12 Inverse Clarke transform and Figure 13 Inverse Park transform.
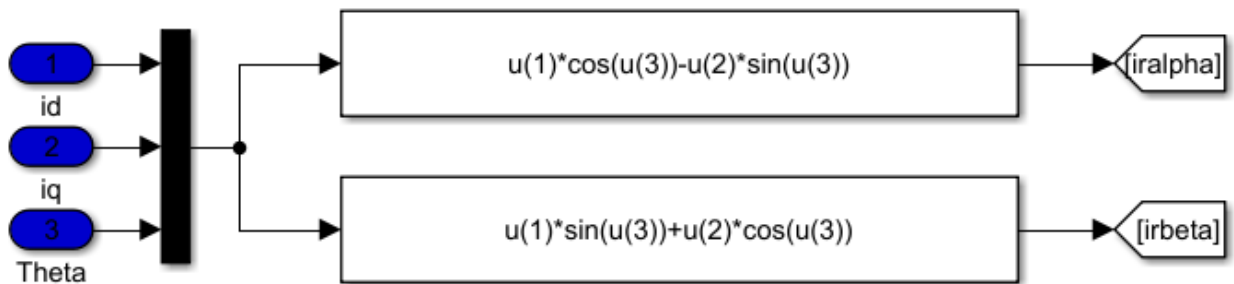
Figure 10. MATLAB/SIMULINK parking model and block representation
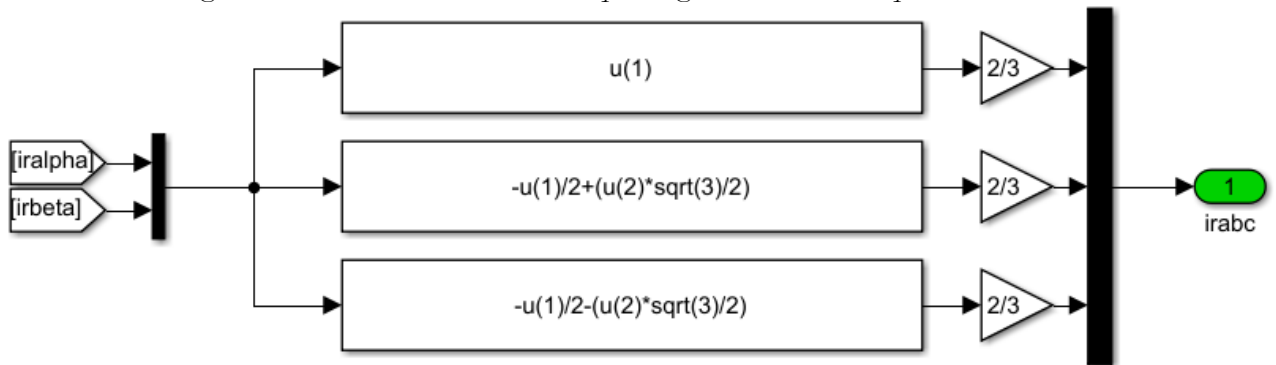
Figure 11. MATLAB/SIMULINK Clarke model and block representation.
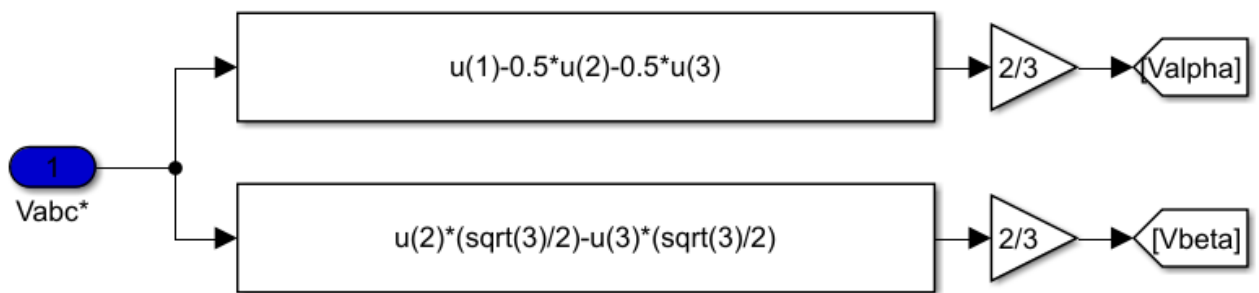
Figure 12. MATLAB/SIMULINK reverse Clarke model and block representation.
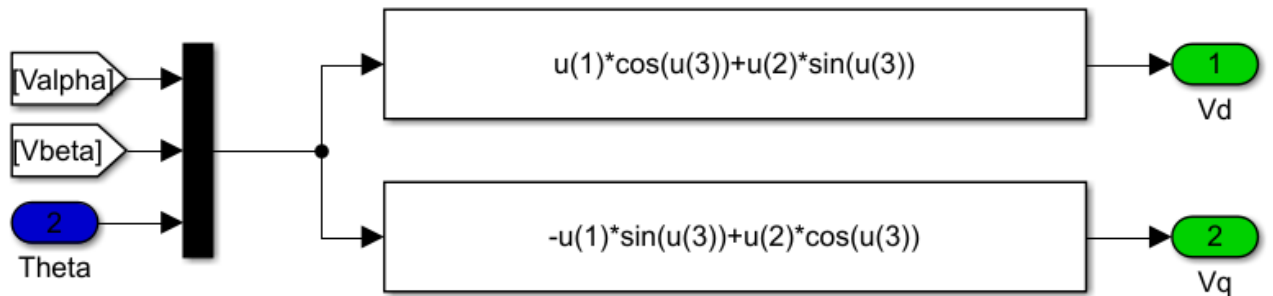
Figure 13. MATLAB/SIMULINK reverse parking model and block representation.

3.3.Inverter and Inverter Model

Current-controlled voltage source inverters have an important place in the control of AC motors. It is possible to improve the inverter performance and accordingly the performance of AC motors by improving current control methods and modulation techniques. Pulse width modulation is generally used as a modulation technique in voltage source inverters. The most commonly used current control techniques are hysteresis current control, ramp comparison control and space vector pulse width current control [13]. In this study, PMSM vector control was performed using the hysteresis current control technique, and its performance was examined under various operating conditions.

In hysteresis PWM control, it is permissible for the output to fluctuate within the predefined error band. This error band is called the hysteresis band. Figure 14 shows the hysteresis PWM control model.
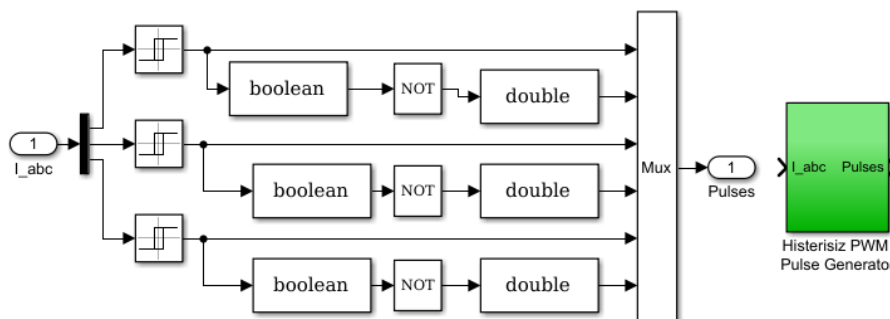
Figure 14. MATLAB/SIMULINK Hysteresis PWM control model and block representation.

A current or voltage with variable amplitude and frequency is required to supply the PMSM. This is formed by inverter circuits. A voltage source inverter is used as shown in Figure 15. The circuit is 300VDC DC voltage source and MOSFETs are used as inverter switches.
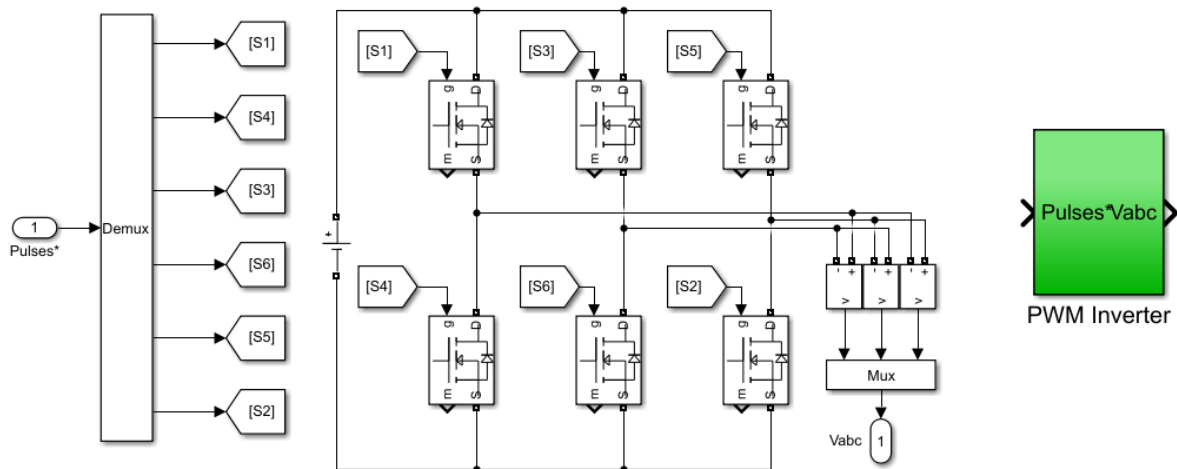
Figure 15. MATLAB/SIMULINK MOSFET switched inverter model and block representation.

The closed-loop PMSM controller model is obtained by combining the MATLAB/SIMULINK function blocks mentioned above. Figure 16 shows the traditional-PI controller applied model of PMSM. In closed loop conventional PI speed control of PMSM, the error value of the speed is obtained by taking the difference of the reference speed value and the measured speed value. The error value of the speed is applied to the conventional-PI controller and the output reference iq produced by the conventional PI controller is accepted as the current value. An error signal is generated by taking the difference of this reference iq value from the real i_q value obtained from the MATLAB model shown in Figure 6, and using this error signal, it is transferred to the PI controller and the q axis current controller. In the field-oriented control method, since the current i_d does not affect the torque, it is tried to keep the current value at zero to reduce the losses. However, flux weakening is required when operating at higher speeds than the rated speed of the motor. In this case, the current i_d needs to be set to a suitable negative value. In motor control, the value of i_d current obtained from the MATLAB model shown in Figure 7 is compared with the zero reference value and transferred to the d axis current controller by applying a PI control method [1].
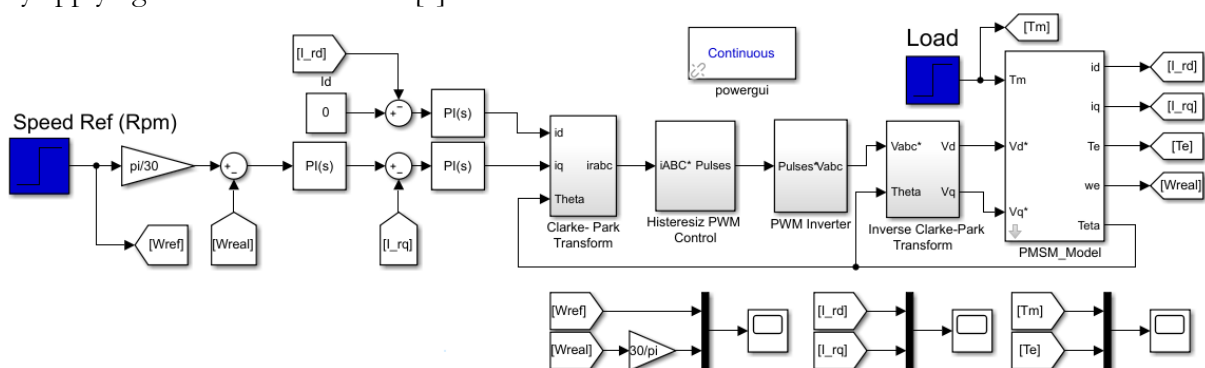
Figure 16. Field-oriented control model of MATLAB/SIMULINK PMSM with the traditional-PI controller.

4.Fuzzy Logic Control

Its basis is based on the simulation of human behaviour depending on thoughts and intuitions in controlling any system. Therefore, a person achieves the goal by applying a control strategy depending on his intuition and experience to take a system from the real situation to the desired state. Fuzzy control is based on such logical relations. For fuzzy logic, it can be called the application of mathematics to the real world [14].

When the traditional PI control is subject to the change or deterioration of the motor parameters, it cannot fundamentally resolve the conflict between dynamic and static performance, and cannot meet the fast-tracking requirements of the servo system. Therefore, to compensate for the disadvantages of PI control. As shown in the adaptive FUZZY-PI control scheme in Figure 17, the kp and ki parameters of the traditional PI controller were adjusted by adaptive fuzzy logic and implemented in the PMSM control.
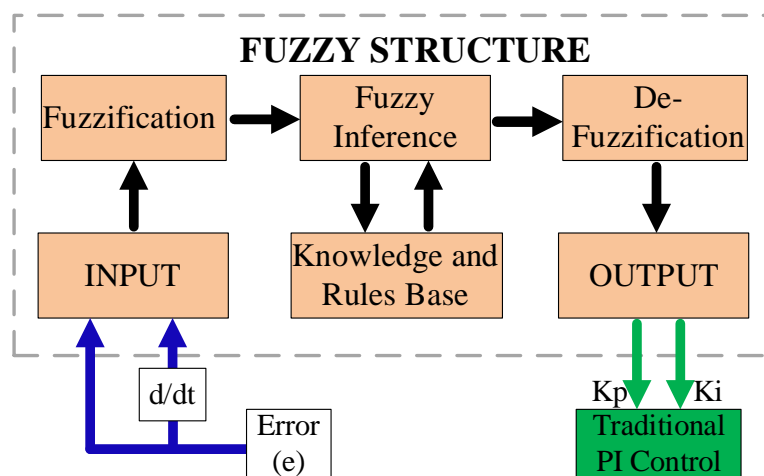
Figure 17. Adaptive FUZZY-PI control scheme.

Figure 18 shows the model of the adaptive FUZZY-PI control created in the MATLAB/SIMULINK environment. The adaptive FUZZY-PI controller consists of two separate fuzzy controllers. One of the fuzzy controllers changes the kp parameter of the PI controller and the other fuzzy controller changes the ki parameter of the PI controller depending on the speed error and the variation of the error.
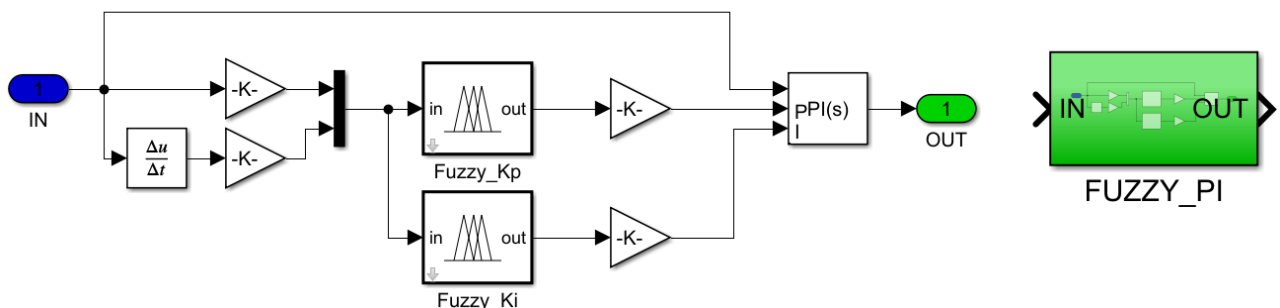
Figure 18. Adaptive FUZZY-PI controller MATLAB/SIMULINK model.

Depending on the defined rules of the fuzzy error and error variation data in fuzzy membership functions, the appropriate control output is obtained from the seven variable state

output membership function in Figure 19 for the Kp parameter of the PI controller. The rule table of the output membership function obtained for the Kp parameter is given in Table 1.

Table 1. Rule table of Kp parameter.

e / de	HN	MN	LN	ZE	LP	MP	HP
HN	HP	HP	MP	MP	LP	ZE	ZE
MN	HP	HP	MP	LP	LP	ZE	LN
LN	MP	MP	MP	LP	ZE	LN	LN
ZE	MP	MP	LP	ZE	LN	MN	MN
LP	LP	LP	ZE	LN	MN	MN	MN
MP	LP	ZE	LN	MN	MN	MN	HN
HP	ZE	ZE	MN	MN	MN	HN	HN

Triangle and trapezoidal functions are used while generating membership functions for Fuzzy-Kp and Fuzzy-Ki controllers. In the generated fuzzy membership functions, triangular and trapezoidal functions are shown with seven different symbolic values. These are HP (High Positive), MP (Medium Positive), LP (Low Positive), ZE (Zero), HN (High Negative), MN (Medium Negative), LN (Low Negative)
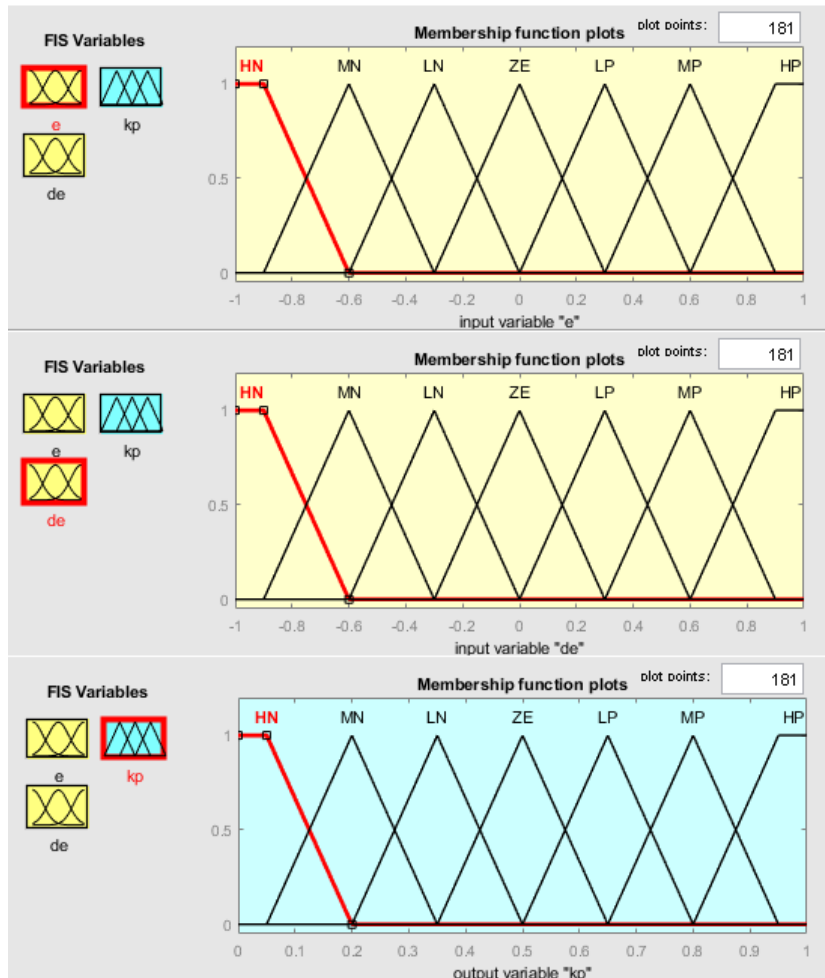
Figure 19. Input-output membership functions for the adaptive FUZZY-Kp parameter.

The appropriate control output is obtained from the seven variable state output membership function in Figure 20, the Ki parameter of the PI controller, depending on the defined rules of the blurred error and error variation data in the fuzzy membership functions. The rule table of the output membership function obtained for the Ki parameter is given in Table 2.

Table 2. Rule Table of Fuzzy_Ki.

e / de	HN	MN	LN	ZE	LP	MP	HP
HN	HN	HN	MN	MN	LN	ZE	ZE
MN	HN	HN	MN	LN	LN	ZE	LP
LN	MN	MN	MN	LN	ZE	LP	LP
ZE	MN	MN	LN	ZE	LP	MP	MP
LP	LN	LN	ZE	LP	MP	MP	MP
MP	ZE	ZE	LP	MP	MP	MP	HP
HP	ZE	ZE	LN	MP	MP	HP	HP
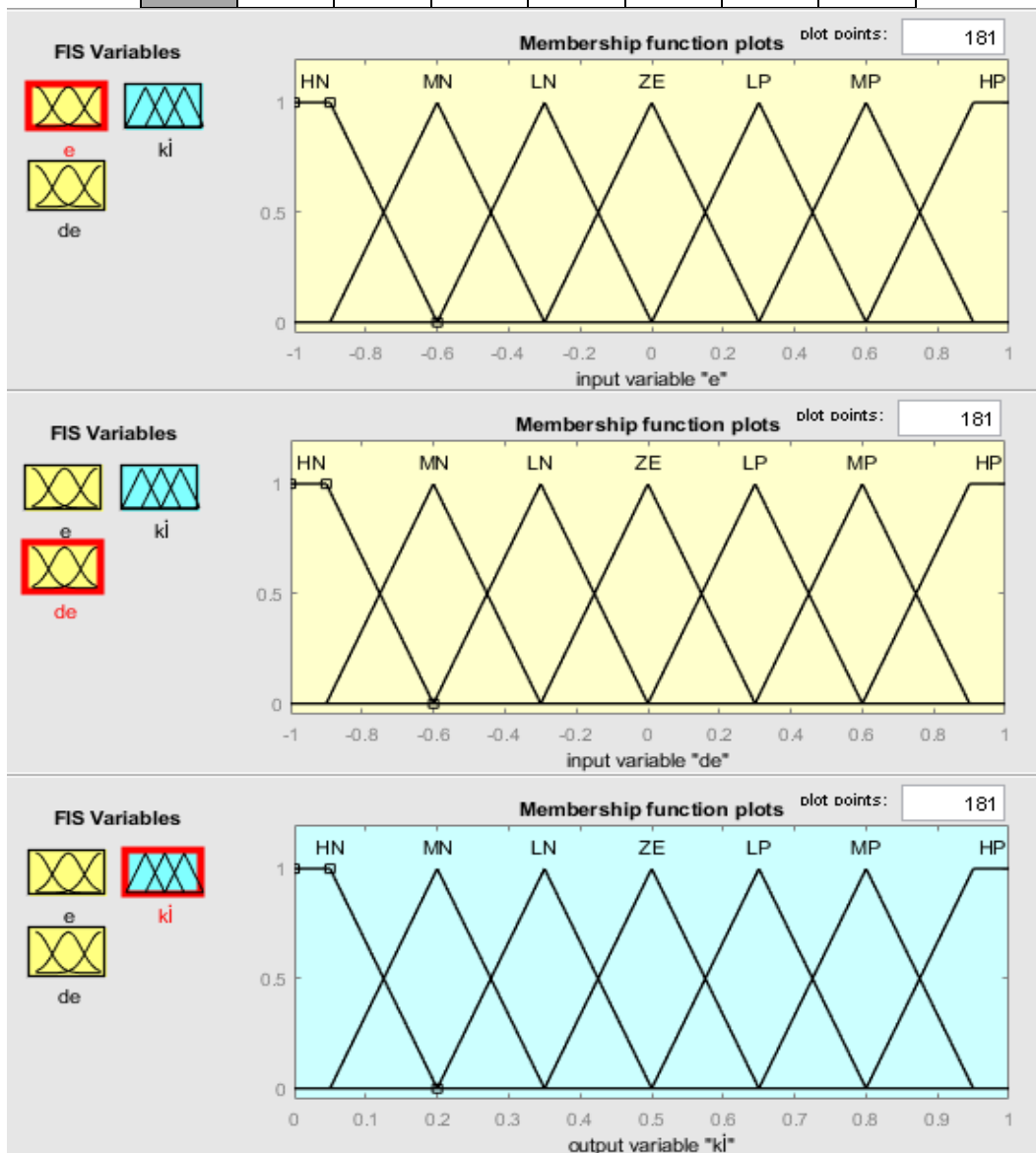
Figure 20. Input-output membership functions for the adaptive FUZZY-Ki parameter.

In Figure 21, there is a field-oriented control model of PMSM created in the MATLAB/SIMULINK environment with an adaptive FUZZY-PI controller.
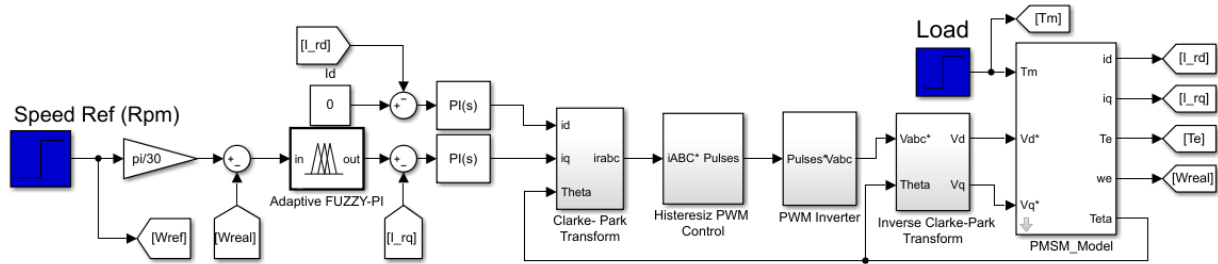
Figure 21. Field-oriented control model of MATLAB/SIMULINK PMSM with adaptive FUZZY-PI controller.

5.Simulation Results

In the simulation, the parameters of the permanent magnet synchronous motor with 8 Nm torque, 300 VDC supply and 2000 RPM speed values, which are found as a package in the Matlab/Simulink program, are created as follows.

Stator Resistance, Rs : 0.9585 Ω
Stator Inductance, Ld : 5.25 mH
Moment of Inertia, J: 0.0006329 kgm2
Coefficient of Friction, B : 0.0003035 Nm.s
Magnet Flux, ΨM : 0.1827 Weber
Number of Poles, 2p : 8

Simulation of PMSM was performed simultaneously with both conventional-PI controller and proposed adaptive FUZZY-PI controller under different speed and load conditions. I simulate. As shown in Figure 22, the reference speed value at the start time (T=0 ms) was determined as 1000rpm and the reference load value was determined as 2 Nm. The reference speed value was changed to 2000 rpm at T=50 ms. Finally, at T=85 ms, the reference load value was changed to 4 Nm. In Figure 22, the speed changes graph of conventional-PI and proposed adaptive FUZZY-PI controller in different operating states.
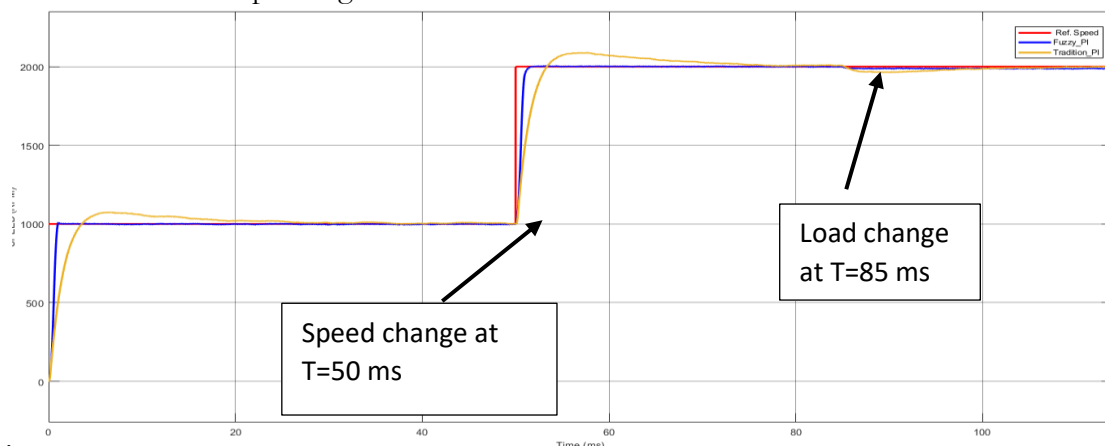
Figure 22. Graph of velocity changes of conventional-PI and proposed adaptive FUZZY-PI controllers in different states.

6.RESULT

In this study, speed control mathematical modelling and simulation of Permanent Magnet Synchronous Motor (PMSM) based on field-oriented vector control has been done using Matlab/Simulink program. In field-oriented vector control, the traditional-PI control model for speed controls and the adaptive FUZZY-PI control model are compared. The PMSM is powered by a current-controlled voltage source inverter. Hysteresis pulse-wide modulation is used to determine the current control and switching sequences of the inverter.

When the results are examined, it is seen that the proposed adaptive FUZZY-PI controller has a shorter transition time from unstable to steady state against speed and load changes compared to the traditional-PI controller, and the oscillations in the speed that occurs during the change are lower.

REFERENCES

[1]. Erken, F., (2014). Sabit mıknatıslı senkron motorda moment dalgalanması azaltılması, Doktora Tezi, Fırat Üniversitesi Fen Bilimleri Enstitüsü, Elazığ.

[2] Donsión, M. P., (2007). Parameters Influence On The Control Of A Pmsm", ISEF 2007 - XIII International Symposium on Electromagnetic Fields in Mechatronics, Electrical and Electronic Engineering, Çek Cumhuriyeti, 13-15.

[3] Akyazı, Ö., Küçükali, M., & Akpınar, A. S. (2011). Sürekli mıknatıslı senkron motorun hız denetiminin farklı bulanık üyelik fonksiyonları kullanılarak gerçekleştirilmesi. *Elektrik-Elektronik ve Bilgisayar Sempozyumu (FEEB).*

[4] Gençer, Ç, ve Gedikpınar, M., (2005). Sürekli Mıknatıslı Senkron Motorların Sayısal İşaret İşlemeTabanlı Konum Denetimi, F. Ü. Fen ve Mühendislik Bilimleri Dergisi, 17 (2), 216-223

[5] C. Elmas, M.A. Akcayol, T. Yigit, (2007). Fuzzy PI Controller For Speed Control of Switched Reluctance Motor J.Fac.Eng. Arch. Gazi Univercity, Vol 22, No 1, 65–72.

[6] G.C.D. Sousa, B.K. Bose, (1994). A Fuzzy Set Theory Based Control of a Phase-Controlled Converter DC Machine Drive, IEEE Transactions on Industry Applications, Vol. 30, No. 1, pp. 34–44.

[7] G. Feng, (2006). A Survey on Analysis and Design of Model-Based Fuzzy Control Systems, IEEE Transactions on Fuzzy Systems, Vol. 14, No. 5, pp. 676–697.

[8] Du Changqing, Zeng Hongxia, Wu Dongmei, et al. (2018). Contrastive simulation study on the control strategy of permanent magnet synchronous motor [J].Digital Manufacturing Science, 34-41.

[9] Gu, D., Yao, Y., Zhang, D. M., Cui, Y. B., & Zeng, F. Q., (2020). Matlab/Simulink based modelling and simulation of fuzzy PI control for PMSM". *Procedia Computer Science*, *166*, 195-199.

[10] Çelik, H., Kürüm, H., (2013). Sabit mıknatıslı Senkron motorun alan yönlendirmeli kontrolü, NWSA-Technological Applied Sciences, 1A0342, 8, (1), 67-85, Elazığ.

[11] Dursun, M., Karayel, M., (2020). Sabit mıknatıslı senkron motorun alan yönlendirmeli hız kontrolü, 2. Uluslararası Avrasya Bilim, Mühendislik ve Teknoloji Konferansı, 621-632, Gaziantep/Türkiye,

[12] Adam, A.A., (2007). Sabit mıknatıslı senkron motorda moment dalgalanması ve gürültünün azaltılması, Doktora Tezi, Yıldız Teknik Üniversitesi Fen Bilimleri Enstitüsü, İstanbul.

[13] Bal, G., Özgenel, M. C. ve Demirbaş, Ş., (2007) Vektör denetimli kalıcı mıknatıslı senkron motorun uzay vektör darbe genişliği modülasyonu ile performans analizi, Politeknik Dergisi, Cilt: 10, Sayı: 1, Sayfa: 7-13, Ankara.

[14] Karayel, M., Çelik, E., ve Yücedağ, İ., (2019).Bulanık Mantık Tabanlı Tek Bölgeli Yük Frekans Kontrolü, III. Uluslararası Bilimsel ve Mesleki Çalışmalar Kongresi-Mühendislik, 27-30 Haziran, Nevşehir/Türkiye,

Zinc Oxide (ZnO) – Fundemental Properties and Applications

E. Asıkuzun Tokeser

Introduction

Zinc oxide (ZnO) is an inorganic compound. The powder form is widely used as an additive to such as many materials and products plastics, ceramics, glass, cement, rubber, oil, ointments, adhesives, leather sealants, dyestuffs, foods, batteries, ferrites, flame retardants. ZnO exists as a mineral zinc stone in the earth's crust. However, most of the commercially used ZnO is produced synthetically.

Since zinc and oxygen are in II. and VI. groups of the periodic table, respectively, ZnO is often referred to as a group II-VI semiconductor in materials science. This semiconductor has some advantageous properties. Good permeability, high electron mobility, wide band gap, effective room temperature luminescence are among the most important.

What is a semiconductor?

Semiconductors are materials whose resistivity is between $\rho = 10^{-2}$ - 10^{9} ohm.cm at room temperature. The electrical properties of semiconductors can be changed by methods such as optical excitation, doping, and heat treatment. For this reason, semiconductor materials are used in many devices such as transistors, switches, diodes, detectors, thermistors and sensors.

Pure Semiconductors

At absolute zero (at 0 K), the conduction band of semiconductors is empty, the valence band is full and these bands are separated by an forbidden energy gap (E_g). The semiconductor behaves like a complete insulator at this temperature. When the temperature rises from 0 K, the thermal energy of the electrons increases and if this energy reaches the forbidden energy value, the electrons pass from the valence band to the conduction band. When electrons are displaced, holes are formed.

The hole is an opposite sign with electron but the values are the same. These gaps in the valence band are filled by other electrons in the same band, and the displaced electrons form new holes. Thus, the hole moves in lattice. In this way, electrons and holes act as free carriers and contribute to electrical conductivity.
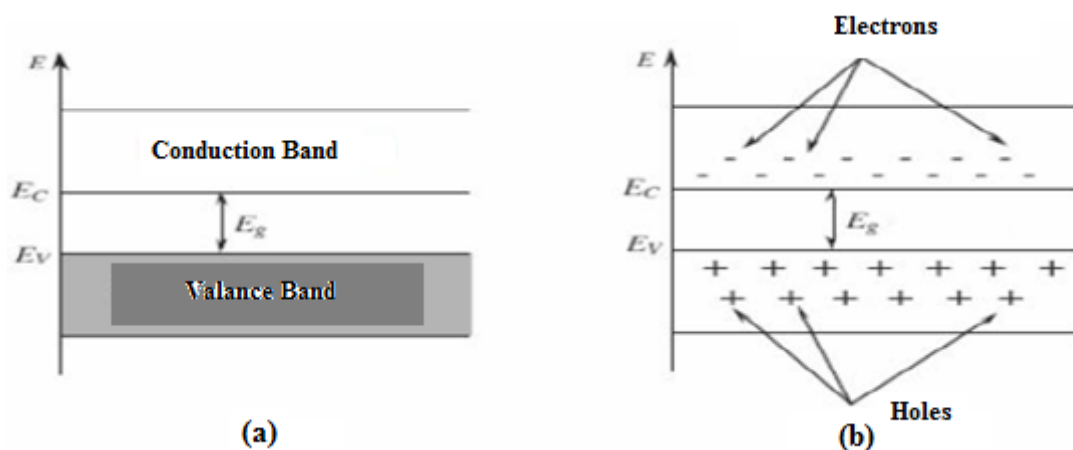
Figure 1. Energy band diagram for undoped semiconductors at different temperatures (a) $T = 0\ K$, (b) $T > 0\ K$

Doped Semiconductors

- **n-Type Semiconductors**

Silicon (Si) and germanium (Ge) in group IV A of the periodic table are semiconductors with four valence electrons. The electrons of the Si atom form covalent bonds with the electrons of other Si atoms. When VA group elements (P,As…) of the periodic table are added to this structure, impurities occur in the crystal structure. Four of the five electrons of these impurity atoms can form bonds with Si atoms. The binding energy of this non-bonding fifth electron is very low and thus begins to act as a free electron in the crystal.

Non-bonding electrons in the crystal create an energy level. This additional level is located just below the conduction band in the forbidden band gap. A very small amount of energy is needed to excite the electron from this level (for the movement of the nonbonding fifth electron). An electron moves into the conduction band with every excitation. These impurities are called donors.

Each donor electron is excited from the impurity level so that no gap is formed in the valence band. The heat energy at room temperature is sufficient to excite a large number of electrons from the donor level. In addition, transitions formed by the pure atom occur between the valence-conduction band, but this is neglected. Thus, there are more electrons in the conduction band than the number of holes in the valence band. Such materials are called n-type semiconductors.

(a) (b)
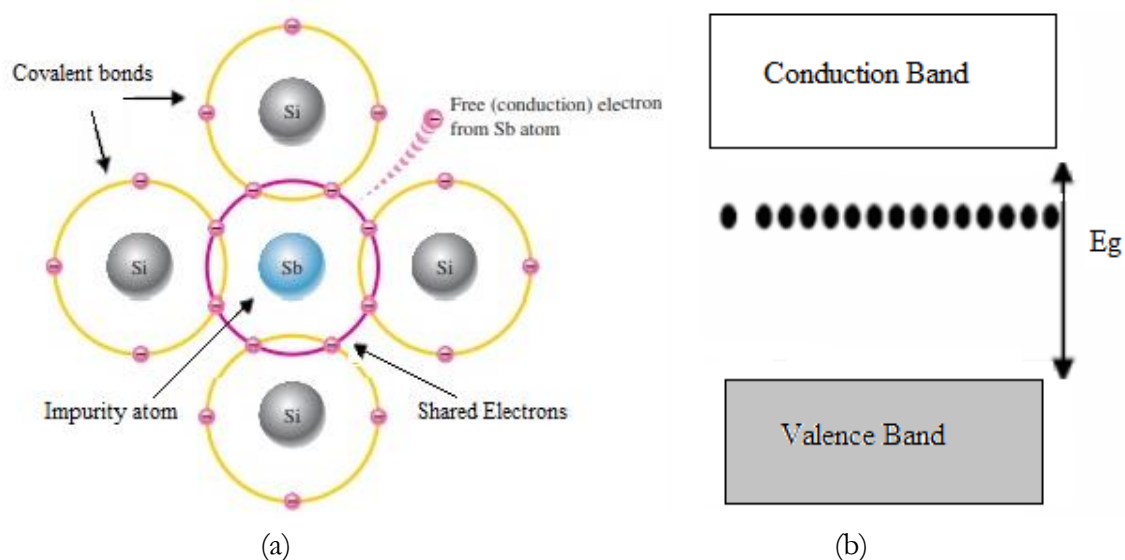
Figure 2. (a) Covalent bond formation for n-type semiconductor, (b) Impurity energy level for n-type

- **p-Type Semiconductors**

If impurities from group III A of the periodic table (such as Al, Ga…) are added to semiconductors such as Si or Ge, an electron will be deficient in the covalent bond formed. This deficiency can be seen as a void attached to the impurity atom. This vacancy can move within the impurity atom by electron transition. Such an impurity atom creates an energy level within the band gap, and this additional level is just above the valence band.

It can be thought that the gap is formed as a result of thermal excitation of an electron from the valence band to the impurity level. With this transition there is only a gap (a carrier) in the valence band. The free electron does not occur at either the impurity level or the conduction level. Such impurities are called acceptors and the additional level that occurs in the band gap is called the acceptor level. In this type of semiconductor, since the number of holes is more than the number of electrons, it is called a p-type semiconductor.
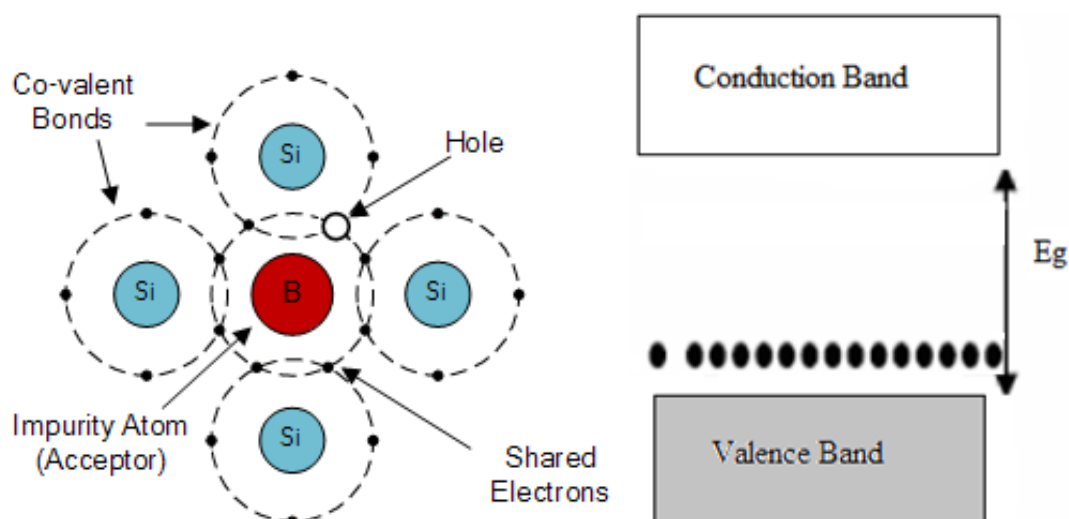
Figure 3. (a) Covalent bond formation for p-type semiconductor (b) impurity energy level for p-type

Physical and Chemical Properties of ZnO

Undoped ZnO is white at room temperature. When zinc oxide is heated up to 300°C, its color changes from white to yellow. When ZnO is heated to different temperatures, it can also take different colors such as yellow, green, brown and red. These color differences are due to the 0.02-0.03% gaps in the crystal structure.

In addition to the band gap, the carrier concentration in the structure significantly affects the surface properties of the particles. This effect has been proven by chemical sensor studies. Therefore, understanding the basic physical and chemical properties of zinc oxide samples is important for the development of future applications (Asikuzun, 2016).

Table 1. Various properties of ZnO

Properties	
Molecular Formula	ZnO
Density	5.606 g/cm^3
Melting Point	1975 °C
Boiling Point	2360 °C
Band Gap	3.3 eV (direct)
Crystal Structure	Wurtzite
Refractive Index	2.0041
Lattice Parameters (T=300 K)	
a_o	0.32495 nm
c_o	0.52069 nm
a_o/c_o	1.602
Static Dielectric Constant	8.656
Activation Energy	60 meV
Effective Electron Mass	0.24
Electron Mobility (T=300 K)	200 cm^2/V.s
Effective Void Mass	0.59

Crystal Structure

Semiconductor ZnO crystals, formed by the combination of zinc and oxygen, have a tetrahedral appearance formed by wrapping 4 oxygen atoms around each zinc atom. (Figure 2.1). The bonds that create to tetrahedral structure are typical sp^3 covalent bonds. The crystal structure of ZnO may be in the wurtzite, zinc-blende or rock salt phases. Under normal conditions, the thermodynamically stable phase is the wurtzite phase. The zinc blende phase becomes durable with

the growth of cubic structures. The rock salt phase can be observed under high pressure (Ozgur & ark., 2005).

The lattice constants are a= 3.250 Å and c= 5.206 Å. The c/a ratio is 1.60, just slightly less than the ideal 1.633. The distance between Zn and O is parallel to the c direction and is 1.992 Å and 1.973 Å in the other three directions. Its specific gravity is 5.72 gr/cm³ (Bonnell, 1995).
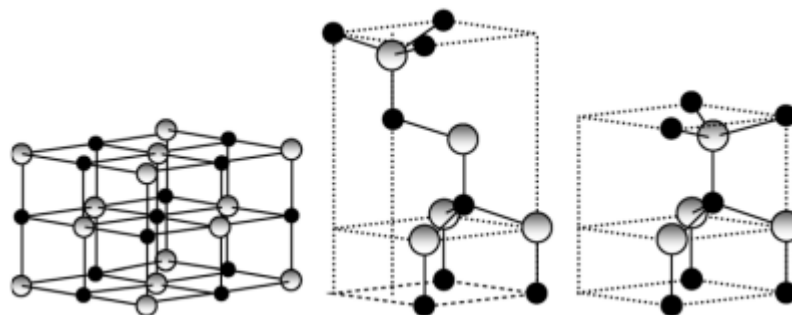
Figure 1. Representation of ZnO crystal structure (white spheres Zn atoms) (a) cubic rocksalt, (b) cubic zinc blende and (c) hexagonal wurtzite structure (Morkoc & Ozgur, 2009).

Lattice Parameters

The lattice parameters of a semiconductor generally depend on the following factors:

1. Mobility in free electron concentration with the degradation potential of the conduction band that is minimally occupied by these electrons.
2. Foreign atom and defect concentration and difference in ionic radii due to displacement with the host atom.
3. Temperature
4. External stresses (strain) can be created for example by the substrate. For many crystal materials, lattice parameters can be commonly and most accurately measured by high resolution x-ray diffraction (HRXRD) using the Bond method for symmetrical and asymmetrical reflections. Table 2.2 shows a, c and u parameters for the wurtzite structure of ZnO.

Table 2. Lattice and u parameters for ZnO

a (Å)	b (Å)	c (Å)	u
3,2496	5,2042	1,6018	0,3819
3,2501	5,2071	1,6021	0,3817
3,2860	5,2410	1,5950	0,3830
3,2498	5,2066	1,6021	
3,2475	5,2075	1,6035	
3,2497	5,5060	1,6020	

Electronic Band Structure

The most important point determined according to many studies is that zinc oxide (ZnO) has n-type character even in the undoped. It is seen that the forbidden energy range of zinc oxide changes with the doping of most oxides at different rates. The electronic structure of zinc oxide includes a fully filled 2p O^{-2} band and an empty 4s band (Zn^{-2}).

The width of the forbidden zone is approximately 3.37 eV. The character and use potential of a semiconductor is determined by its band structure. The accuracy of the information about the band structure of a semiconductor has great importance in order to be an accepted material for use in electronic circuits and device applications.

Literature Review

Transparent conductive oxides attract attention with their electrical conductivity and optical transmittance characteristics. ZnO, ITO, SnO and CdO are widely used for these applications (Akyuz, 2005).

Transparent conductive oxides find applications in many areas due to their properties. Transparent conductive oxide thin films; It is widely used in flat screen displays, laptop screens, gas sensors, solar cells. In addition, durability against environmental factors, low cost and suitability as an electronic circuit element are the factors that determine the usefulness of transparent conductive oxide material (Alexander, 2015).

Zinc oxide (ZnO) is also a very popular material in transparent conductive oxides. Zn is abundant in nature and is a non-toxic element. This has led to the widespread use of ZnO as a transparent conductive oxide material (Addonizio, 2014).

With the development of semiconductor technology, it has been seen that semiconductors such as Si and Ge are not sufficient in applications requiring high speed, high power and high frequency due to their indirect band gap structure, low mobility and conductivity. Because direct band gap semiconductors are required for optoelectronic devices. Direct band gap semiconductors are usually III-V or II-VI group compounds. III-V group semiconductors are limited to wavelengths of 500 nm and above in optoelectronic applications due to forbidden energy gaps (Singh, 1994).

II-VI group compounds have an energy band gap ranging from 1.7 to 4 eV. They are binary compounds formed between one of the II. group elements (Zn, Hg, Cd) and one of the VI. group elements (O, S, Te and Se) of the periodic table. II-VI compounds with wide band gap are used in optoelectronic devices, especially in light emitting devices. Because they have suitable direct band gap energy in the region where visible light has short wavelengths (Yuonesi & Pakdel, 2010).

Zinc oxide (ZnO) is a compound of group II-VI since zinc is in group II of the periodic table and oxygen is in group VI of the periodic table. ZnO can be found in wurtzite (hexagonal), cubic ZnS and cubic NaCl structures. The Wurtzite crystal structure is the most stable of these structures. The cubic ZnS structure can be stabilized by growing ZnO on cubic substrates. NaCl-structured ZnO can only be obtained under very high pressures (Steiner, 2004).

The wurtzite structure has a hexagonal unit cell. The lattice parameters of this structure are given as a=0.3249 nm, c=0.5205 nm (Berger, 1997). The c/a ratio of zinc oxide is 1.602 and it is close to the ideal tight-packed hexagonal structure (1,633 nm) (Steiner, 2004).

ZnO is a semiconductor that has a direct band structure and a very wide band gap (~3.3 eV) (Salam, 2013). Due to its wide band gap, it is accepted as a suitable material for LED production in the blue and ultraviolet region of the electromagnetic wave spectrum. The photoelectric, piezoelectric and thermoelectric properties of the ZnO semiconductor are very good and these are used in many applications due to these properties. These applications are; gas sensors, thin film transistors, photoelectric devices, optoelectronic devices, solar cells, UV detectors, piezoelectric transducers, surface acoustic circuits, thermoelectric devices, pH sensors, biosensors (Tsay, 2010). In addition, ZnO absorbs UV light and performs band transitions. Due to this feature, transparent conductive oxide is widely used as a thin film (Ashour & ark., 2006).

The properties of ZnO can be changed by heat treatment or by suitable doping. There are many application areas where Al, In, Ga, Li, Cu, Sn and Mg are used as doping atoms. The conductivity of zinc oxide can be increased with the contribution of ions such as Al, In, Ga. An increase in the transmittance and a decrease in the resistivity of Sn-doped ZnO thin films are observed. This is very advantageous for the construction of solar cells, on which many research

studies have been carried out recently. In addition, the forbidden energy gap value can be easily changed with the addition of Mg (Peker, Temel & Nebi, 2015).

Sol-gel method, which is one of the effective thin film forming techniques, has a wide area of use in that it can easily cover large areas and homogeneously form multi-layered films. Sol-gel method can be used in the production of most single-component or multi-component oxide films (Uhlmann & ark., 1997).

Nanostructured $Zn_{1-x}Gd_xO_\delta$ ($0 \leq x \leq 0,02$) powders were synthesized by combustion reaction method (CR) at room temperature in order to investigate its effect on structural, optical band gap, dielectric and magnetic properties. Oxygen vacancies and/or interstitial oxygen defects in Gd-doped ZnO samples play an important role in dielectric permittivity at room temperature. All Gd-doped ZnO samples exhibit typical paramagnetic behavior at room temperature (Franco & Pessoni, 2017).

The structural and thermoluminescence (TL) properties of Gd-doped ZnO nanoparticles were investigated. TL curves recorded in the 10-300 K range showed three overlapping peaks around 56, 110 and 155 K for the undoped ZnO nanoparticles (Isik & Gasanly, 2019).

Undoped, Gd-doped and (Gd, Mn) co-doped ZnO nanoparticles were produced by a hydrothermal method and their structural, morphological, optical and magnetic properties were investigated. Morphological studies showed that the synthesized nanoparticles were single and hexagonal in shape. When the diamagnetic ZnO sample is doped with Gd ions, it becomes ferromagnetic. However, this behavior was prevented with Mn ions (Poornaprakash & ark., 2017).

The structural, optical and gas sensing properties of undoped and Gd-doped ZnO nanoparticles were investigated. SEM images showed that particle diameters increased from a few nm to micrometers after Gd doping. 3% Gd-doped ZnO nanoparticles exhibited the best sensitivity (Noel & ark., 2014).

References

Addonizio, M.L. (2014). Sol–gel synthesis of ZnO transparent conductive films: the role of pH. *Applied Surface Science, 305,* 194–202.

Akyuz, İ. (2005). *Effects of Al doping and annealing on some physical properties of CdO Films*, PhD Thesis, Eskişehir Osmangazi University The graduate School of Natural and Applied Sciences, Department of Physics.

Alexander, J.N. (2015). Development and characterization of transparent and conductive InZnO films by magnetron sputtering at room temperature. *J. of Alloys and Compounds*, *633*, 157–164.

Asikuzun, E. (2016). *Characterization of ZnO Based Diluted Magnetic Semiconductor Thin Films and Nano Particles Produced By Sol-Gel Method,* PhD Thesis, Abant Izzet Baysal University, The graduate School of Natural and Applied Sciences, Department of Physics.

Ashour, M. A., Kaid, N. Z., El-Sayed and Ibrahim, A. A. (2006). Physical properties of ZnO thin films deposited by spray pyrolysis technique. *Applied Surface Science*, 252, 7844-7848.

Bonnell, D. (1995). Physical Properties of Ceramics. *MSE*, 566.

Franco, J., A., Pessoni, H. V. S. (2017). Effect of Gd doping on the structural, optical band-gap, dielectric and magnetic properties of ZnO nanoparticles. *Physica B, 506,* 145-151.

Isik, M., Gasanly, N. M. (2019). Gd-doped ZnO nanoparticles: Synthesis, structural and thermoluminescence properties. *J. of Luminescence, 207,* 220-225.

Morkoç, H., Ozgur, U. (2009). *Zinc Oxide: Fundamentals, Materials and Device Technology.* Copyright WILEY-VCH Verlag GmbH & Co. KGaA, Weinheim.

Noel, J. L., Udayabhaskar, R., Renganathan et al. (2014). Spectroscopic and fiber optic ethanol sensing properties Gd doped ZnO nanoparticles. *Spectrochimica Arta Part A: Moleculer and Biomolecular Spectroscopy, 132,* 634-638.

Ozgur , U., Alivov, I., Liu , C., Teke, A. (2005). Comprehensive review of ZnO materials and devices. *J. of Appliedd Physics*, *98*, 2-103.

Peker, D., Temel, S., Nebi, M. (2015). Mg-doped ZnO films by sol-gel spin coating method, International. *J. of Scientific and Technological Research*, *1,* 263- 269.

Poornaprakash, B., Chalapathi, U., Babu, S., Park, Si-Hyun. (2017). Structural, morphological, optical, and magnetic properties of Gd-doped and (Gd, Mn) co-doped ZnO nanoparticles. *Physica E: Low-dimensional Systems and Nanostructures*, 93.

Singh, J. (1994). *Semiconductor devices an introduction.* Mcgraw- Hill Inc. p87, 88.

Steiner, T. (2004). *Nanostructures for optoelectronic applications.* Artech House Inc., London.

Uhlmann, D.R., Suratwala, T., Davidson, K., Boulton, J.M., Teowee, G. (1997). Sol-gel derived coatings on glass. *J. of Non- Crystalline Solids, 218*, 113-122.

Yuonesi, M., Pakdel, A. (2010). Effect of low concentration of nickel on structural and optical properties of ZnO nanofilms. *Physica B, 405*, 2083–2087.

The Story of a Superconductor

E. Asıkuzun Tokeser

Introduction

Superconductivity is the properties of certain materials when they are cooled to extremely low temperatures in order to conduct direct current without encountering any resistance. In other words, materials that have zero electrical resistance under direct current when their temperature is lowered below a certain value are called superconductors. If the resistance is great, the applied voltage and the lost energy are large. But in some conductors, when the material is cooled below the critical temperature, the current carrying electrons lose their ability to convert their energy into heat and the resistance falls to zero. In this case, it is possible to create a current without applying any voltage and without losing energy. In other words, when the material is cooled below the critical temperature in an ideal metallic structure, the phonon effect disappears and the electrons move freely in the structure without any interaction with the lattice. In this case, the resistance of the structure suddenly drops to zero below the critical temperature. This material below the critical temperature is called superconducting material. In other words, in ordinary conductors, the lost energy arising from resistance and radiated as heat is prevented (between 3% and 10%). With the understanding that thousands of metal alloys can be superconducting under different conditions, new ones are added to these materials day by day.

Compared to a perfect lattice, electrons are scattered due to structural defects or impurities in the crystal. Also, lattice ions in normal modes have vibrations. These waves are called phonons. More phonons are formed in the lattice with increasing the temperature. As a result, an electron-phonon interaction, which scatters conduction electrons and causes greater resistance, occurs. Therefore, as the temperature decreases, the electrical resistance of the metal decreases. However, a residual resistance around absolute zero temperature is expected due to crystal defects. Therefore, the electrical resistivity of some solids disappears completely at sufficiently low temperatures. This situation seems extraordinary.

The behavior of electrons in a superconductor is quite different. There are impurities and lattice defects in this structure. However, the superelectrons in the conductor are not encounter any obstacles and move through the lattice. Because the electrons will not clash with any obstacle, no friction will occur, and as a result, current and energy will be transmitted without any loss.

The question of why electrons moving through the superconducting material do not encounter any obstacles has occupied scientists for years. When a material is heated, lattice vibrations increase, and when cooled, these vibrations decrease. Previous researchers believed that atomic vibrations in matter helped electrons pass more easily through the lattice. However, this was an indication that the resistance would decrease as the temperature increased. These and similar simple ideas were not sufficient to explain superconductivity. The state of superconductivity is too complex to be easily explained.

The first studies on superconductivity started with the liquefaction of helium by H. Kamerling Onnes in 1908 in Leiden. As a result of his studies in 1911, Onnes found that when solid mercury is cooled below a certain temperature called the T_c critical temperature, its electrical resistance drops to an immeasurably small value (Onnes, 1911; Kittel, 1986; Hwu & ark., 1987). As the temperature dropped below $T_c=4.2$ K, the mercury transitioned from the normal state to a

superconducting state. Since then, many other elements, compounds and alloys below critical temperatures as high as 30 K have been known as superconductors. But not all materials are superconductors. Figure 1 shows the variation of resistivity with temperature at very low temperatures for superconducting tin and non-superconducting silver. In a superconductor, current can flow for years without measurable reduction.
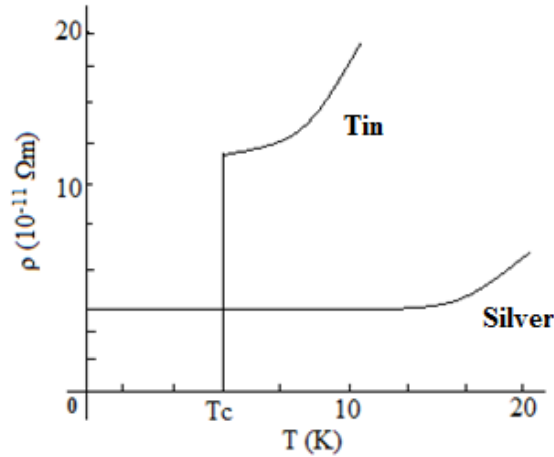
Figure 1. a) Finite resistivity curve of a normal metal at absolute temperature b) variation of resistivity ϱ of a superconductor with respect to the critical temperature Tc

In 1933, Meissner and Oschenfeld found that when a superconducting material is cooled below its critical temperature under the influence of a magnetic field, it ejects all the magnetic flux from the interior of the superconductor (Meissner & Oschenfeld, 1933). If the magnetic field is applied after the material is cooled below its critical temperature, the magnetic flux is again ejected from the superconductor (Fig. 2). Therefore, we can say that a superconducting material behaves exactly like a diamagnet. Both of the Meissner events are shown in Figure 2.

According to Lenz's law, a reduced current occurs when the magnetic flux changes in a circuit. Orbital electrons in a diamagnetic atom regulate their rotational motion to create a net magnetic moment to oppose the externally applied magnetic field. We can explain it this way: An external magnetic field cannot penetrate inside a superconductor because the conduction electrons in the superconductor adjust their motion to create a magnetic field in the opposite direction to the external field. In this case, the superconducting material behaves like a single diamagnetic atom. Thus, the two main properties of superconductors, namely the exclusion of magnetic flux and the absence of resistance to resist current, are associated with each other.
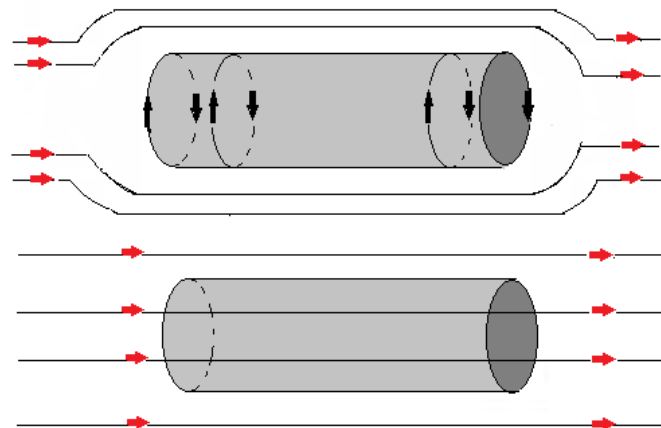
Figure 2. Schematic ejection of the magnetic field. Above is the Meissner event (Rose, 1978).

If the external field is increased above a certain value called critical B_c, it is seen that the material has no superconductivity and it becomes normal. The value of this critical magnetic field for a given metal depends on temperature (as shown for lead in Figure 3). As the external magnetic field increases, the critical temperature decreases until $B > B_c(0\ K)$. There is no superconductivity at any temperature for this metal. We can understand it like this: Suppose a magnetic field is applied on a superconductor at a temperature below T_c. The superconductor will expel this magnetic field due to the Meissner effect. The energy reduction in the magnetic field occurs as the increased energy of the electrons that creates a superconducting current. As the strength of the external magnetic field increases, the energy gained by the superconductor increases. At the critical value of B_c, the energy of the superconducting state becomes more than the energy of the normal state, so the material becomes normal.
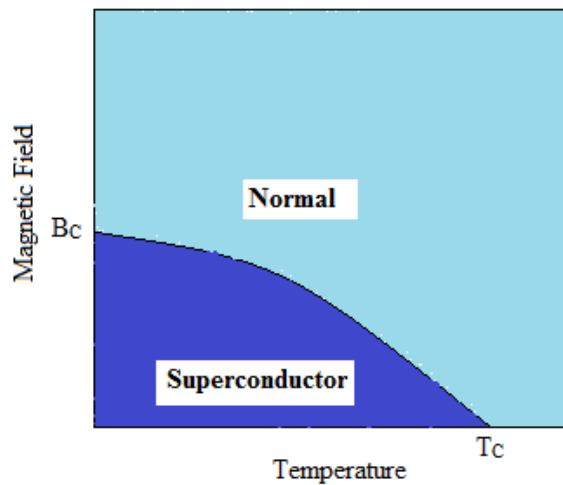
Figure 3. Change of critical B_c field with temperature (Rose, 1978)

There are many important applications of superconductivity. For example; The use of superconducting electromagnets, arising from non-resistive currents flowing inside the magnet windings, in electric motors and generators, is an obvious application. A small problem arises in this case; Magnetic fields are created in the winding wires to oppose superconductivity. This negative is eliminated using II. type superconducting materials.. There is no difference between the I. and II. types superconductors in terms of mechanism of superconductivity. Both types show similar thermal properties during the superconductor-normal transition at zero magnetic field. However, the Meissner effect is completely different. A I. type superconductor completely excludes the magnetic field, and as soon as the superconductivity disappears, the magnetic field completely penetrates. In a II. type superconductor, the magnetic field is completely ejected up to the value of H_{C1}. The field above H_{C1} is partially ejected, but the ambientis still superconducting. At a higher H_{C2} value, the flux completely enters the system and superconductivity disappears (Fig.4).
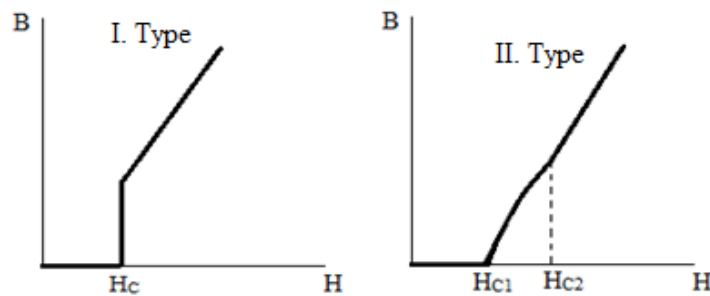
Figure 4. Behavior of I and II. type superconductors under magnetic field

Properties of Superconductors

The phenomenon of superconductivity is determined by the behavior of electrons: The phenomenon of superconductivity is determined by the behavior of electrons: The interaction of free electrons in the crystal lattice of a superconducting metal with positive ions in vicinity of its causes defects in the lattice. As a result, an indirect force of attraction is created between the electrons that would normally repel each other and thus electron pairs are formed in the metal. These electron pairs, called Cooper pairs, are difficult to separate from each other by scattering. Moreover, these pairs have anti-scattering quantum properties. These pairs are responsible for the superconductivity. Because the electrical conductivity in metals basically depends on scattering. Less scattering means the metal is better electrically conductive. In addition, superconductors can carry large amounts of current. Small superconducting coil magnets can create strong magnetic fields without consuming too much energy. Such magnets can be used as particle deflectors in the construction of airborne trains, accelerator tunnels, and nuclear magnetic resonance scanners, thanks to the magnetic field (Mikio & ark., 1987; Grant & ark., 1987).

When a superconductor is cooled to low temperatures, it shows two different properties.

1- When the electric current collides with the ion lattice forming the material structure, the current is blocked. This phenomenon creates the resistance of the material against electric current. When the same material is made into a superconductor, the ion lattice, that creates matter, supports the electric current instead of blocking it. In this way, resistance drops to zero.
2- Superconductors exclude the magnetic field.

In 1933, two German physicists, Meissner and Ochsenfeld, observed that superconductors repel magnetic field lines and do not insert them. In other words, a magnet repels a superconductor that is below its critical temperature. his event is called the Meissner Event (Tokana & ark., 1987). Experiments were carried out with cylindrical superconductors. It was seen that the sample completely repulsed the magnetic field lines at below the critical temperature and was found to be superconducting. The fact that B=0 in the material is as natural as the zero resistance of superconductors. Superconductors are also excellent diamagnets.

Zero Resistivity

The most basic property used to determine the superconducting state is the zero resistance property. The zero resistance state of superconductors can be determined by measuring the resistance against temperature. Resistance of metals is caused by the scattering of electrons from phonons, impurities, and crystal defects. In perfectly pure metals, the resistance is due to the scattering of electrons by the temperature-dependent phonons. Therefore, in pure metals, the resistance will go to zero as the temperature reaches 0 K. However, any metal always has its impure atoms. Therefore, electrons are scattered regardless of temperature, and the metal exhibits resistance even at 0 K. However, in a superconducting material, the resistance of the material decreases continuously with decreasing temperature and at critical temperature the resistance suddenly goes to zero. In the superconducting state, the electrical resistance for direct current is zero, that is, in the superconducting state, there is no loss in current. Therefore, a current can flow in the superconducting ring without loss for a very long time (Ozturk, 2007).

Resistance and magnetic susceptibility measurements have aspects that are superior to each other. Resistance measurements are preferred by researchers since these are easier. Since the magnetic field can break the interparticle bonds in granular structures. In general, resistance measurements show higher critical temperatures and sharper transitions than susceptibility measurements. In contrast, susceptibility measurements explain the magnetic behavior of superconducting material. In addition, since magnetization is a thermodynamic state variable, it can provide information about the thermodynamic behavior of the superconducting state.

Susceptibility measurements can also give information about the ratio of the superconducting phase in the material. It should also be noted that if the sample is porous, resistivity measurements cannot be occur as desired due to the problems and gaps between the particles. In an ideal homogeneous superconductor, both measurements give the same transition temperature.

How is this possible?

A microscopic theory of superconductivity is as follows.

Let's consider a metal as a lattice of positive ions (Fig. 5). Single electrons moving towards the lattice create an electric current. Normally the electrons repel each other and are scattered by the lattice and are scattered by the lattice. That is, they oppose their movements.
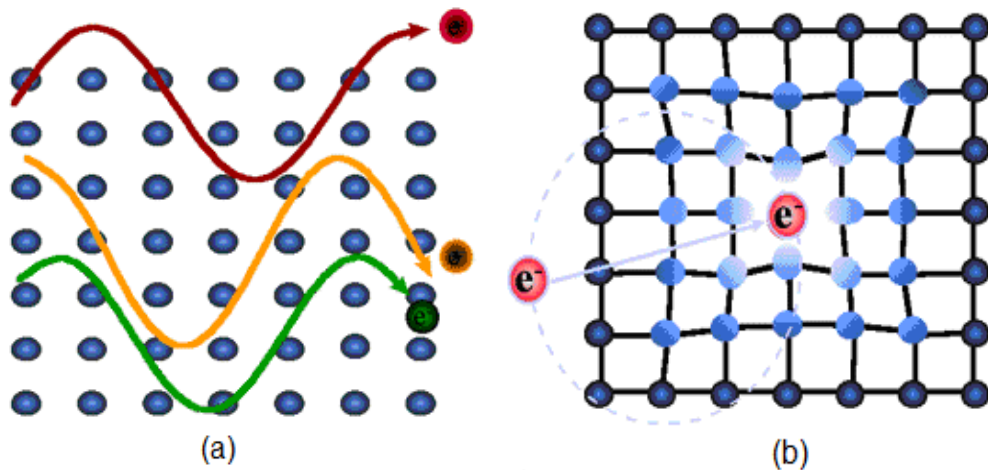
Figure 5. a) Conduction in metals and b) Formation of Cooper pairs

As an electron passes near the positive ions in the lattice, it enters the Coulomb interaction with the ions and moves slowly towards the lattice. After passing, the electrons are quickly scattered back to their original positions. When some samples and ions are cooled to low temperatures, they are not rapidly backscattered to their original positions.and form a temporary positively charged local region and form a transient positively charged local region. A second passing electron is attracted towards this positive region and follows the first electron. Thus, the two electrons move together and cross the ion lattice as a pair (Asikuzun, 2010). Electrons do not scatter when acting as a couple and they encounter a small resistance, that is, the sample has zero resistance. The current passes through the sample without resistance (Figure 6).
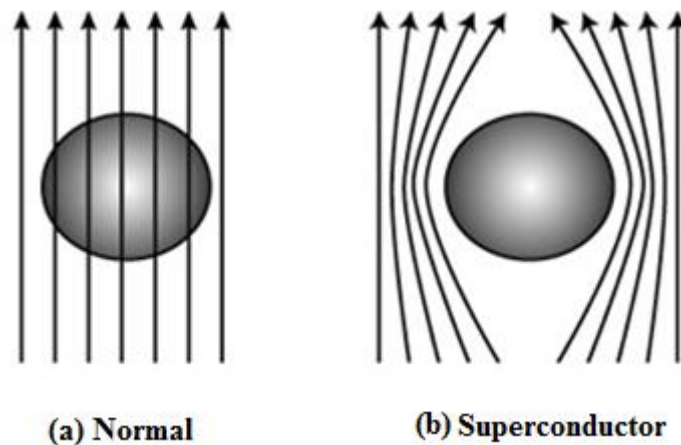
Figure 6. a) Normal and b) Magnetic flux distribution around a superconducting material

Excellent Diamagnetism

When a superconductor is cooled in a weak magnetic field, permanent currents at the surface increase at the transition temperature. These currents circulate inside and destroys the flux density. The situation is the same when a magnetic field is applied after cooling (Ibach & Luth, 1990) (Fig. 7). This phenomenon, that is, the absence of a flux density inside the superconductor, even in an applied magnetic field, is called the Meissner effect.

As is known, there are two types of superconductors that can be distinguished by their behavior under a magnetic field. These are called type I and type II. Except for Niobium (Nb) and Vanadium (V), which show superconductivity, all metallic elements are type I superconductors. Nb and V elements and all alloys and compounds showing superconductivity are II. type superconductor. All high temperature superconductors are also II. type superconductor. There is no difference in the superconductivity mechanism of I. and II. type metallic superconductors. Both have similar properties in the superconductor-normal transition at zero magnetic field. But the Meissner effect is completely different.

Type I Superconductors: After a certain magnetic field, the material recovers from the Meissner effect, returns to normal state and allows the magnetic flux to penetrate completely inside. Their critical magnetic fields are usually small.

II. Type Superconductors: In this type of materials, the material is the same as Type I until the subcritical magnetic field value called H_{c1}. Flux does not penetrate. From this value to the H_{c2} value, there is partial flux penetration. But the superconductivity continues. After the H_{c2} value, the material loses its superconductivity by transitioning to the normal phase.
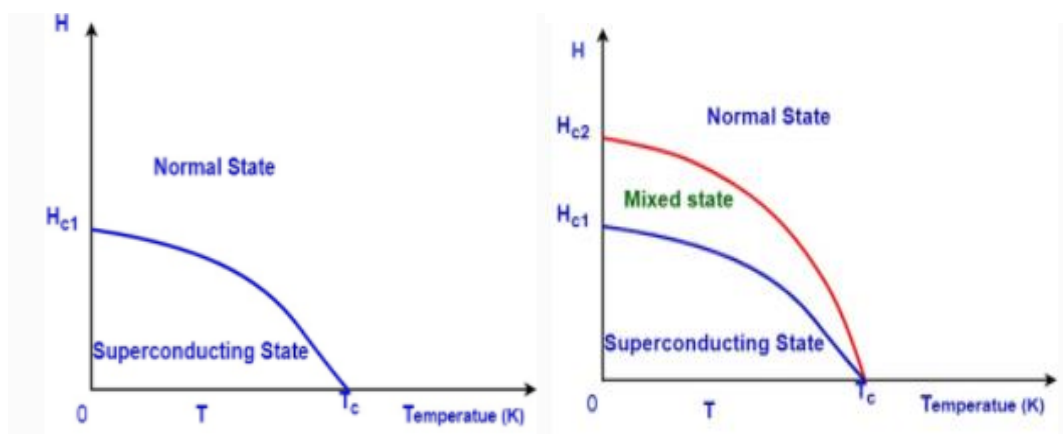
Figure 7. The magnetic behavior of a) I. type and b) II. type superconductor against the applied field.
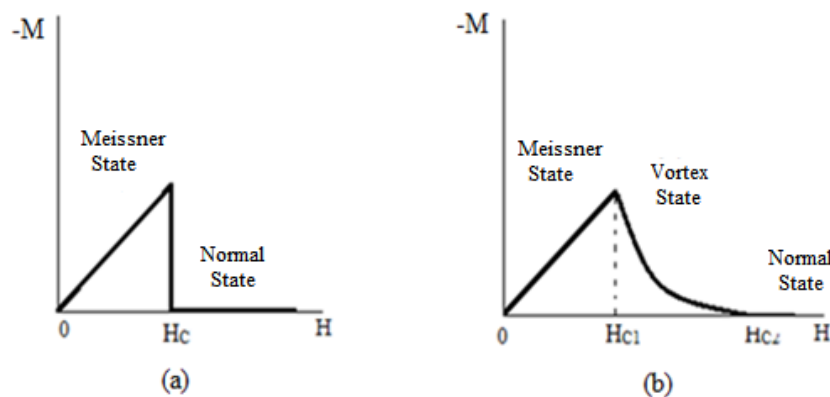
Figure 8. Magnetization of a) I. type and b) II. type superconductor

Figure 8a shows the magnetization of the I. type superconductor. The Meissner state is represented by a line with a slope of -1 in the (M,H) plane. When the transition to the normal state occurs, the slope suddenly becomes zero. Figure 8b shows the magnetization of the II. type superconductor. II. type superconductors behave completely like I. type superconductors when the applied external magnetic field value is below H_{Cl} and show excellent diamagnetism.

References

Asikuzun, E. (2010). *The Investigation of Electrical and Mechanical Properties of Pr Doped Bi-2212 Superconductor*. Master Thesis, Kastamonu University Graduate School of Natural And Applied Sciences, Department of Physics.

Grant, P.M., Beyers, M.B., Engler, E.M., Lim, G., Parkin, S.S.P., Ramirez, M.L., Lee, V.Y., Nazzal, A., Vazquez, J.E., and Sovay, R.J. (1987). Superconductivity Above 90K in the Compound $YBa_2Cu_3O_{7-x}$. *Phys. Rev. B., 35*, 7242-7244.

Hwu, S.J., Song, S.N., Thiel, J., Poeppelmeier, K.R., Ketterson, J.B., and Freeman, A.J. (1987). High T_C superconductivity in Regions of Possible Compound Formation. *Phys. Rev. B. 35*, 7119-7121.

Ibach, H., & Luth, H. (1990). *Festkorperphysik*. Third Edition.

Kittel, C. (1986). *Introduction to Solid State Physics*. John Wiley & Sons, Inc. New York, London, Sydney.

Meissner, W., Oschenfeld, R. (1933). Upper Critical Fields of High$-T_c$ Superconducting Y-Ba-Cu-O. *Nature, 132,* 931-935.

Mikio T., Jun T., Kiichi O., Hitoshi K., Yoshinari M., Yasunori I., Yoichi T.i and Hiromasa M. (1988). High-T_c Phase Promoted and Stabilized in the Bi, Pb-Sr-Ca-Cu-O System. *Japanese Journal of Applied Physics, 27,* L1041.

Onnes, H. K. (1911). Superconductivity and Magnetism. *Comm. Phys. Lab. Univ. Leiden*, 119-120.

Ozturk, O. (2007). *The effect of Au diffusion- doped on structural, superconducting and mechanical properties of $Bi_{1.8}Pb_{0.35}Sr_{1.9}Ca_{2.1}Cu_3O_y$*. Doktora Tezi, Abant İzzet Baysal Üniversitesi Fen Bilimleri Enstitüsü Fizik Anabilim Dalı.

Rose-Innes, A. C., & Rhoderic, E. H. (1978). *Introduction to Superconductivity*. New York: Pergamon, 5.

Tokana, K., et al. (1988). Properties of Pb-Doped Bi-Sr-Ca-Cu-O Superconductors. *Appl. Phys. Lett., 53,* 1329-1331.

Effect of Volcanic Basalt Fiber on Physical and Mechanical Behaviors in Mg Alloy Produced by Powder Metallurgy

Bünyamin ÇİÇEK[1]
Tuna AYDOĞMUŞ[2]

Introduction

Magnesium (Mg) metal is in the alkaline earth group in the periodic table. Being very light in terms of density increases the usage area. This metal is 1/4 times lighter than iron (Fe) and 1/2 times that of aluminum (Al). For this reason, it is frequently used in the aerospace, automotive, aviation and defense industries where lightness is at the forefront (Bamberger & Dehm, 2008; Huang, Subramani, & Chiang, 2021; Zengin, Turen, & Elen, 2019).

Many metals can be oxidized during production due to their reaction to free oxygen in the atmosphere. Mg metal has a high affinity for oxygen. For this reason, it is necessary to protect Mg metal with an atmospheric environment in production methods. While an atmosphere-controlled melting furnace is required at the casting stage, the use of an atmosphere-controlled heat treatment furnace is mandatory in powder metallurgy production. Otherwise, the reaction between Mg and oxygen develops very rapidly to form the MgO compound. Thus, the Mg element loses its known metal property (Akkaş & Boz, 2019; Bamberger & Dehm, 2008; Elen, Türen, & Koç, 2019; Matykina et al., 2016; Taleghani, 2014).

The pure Mg element, like many metals, lacks most properties while in its pure form. However, alloys produced within the framework of Hume-Rothery rules provide success in many properties. Mg element can form alloys with many elements within the framework of binary and triple phase diagrams. As a result of the alloy system, intermetallic structures and hard particles in microstructure can be formed. Thus, the alloy gains new properties with the effect of denser and harder formations than the α-Mg structure. Alloyed Mg metal is also exposed to mechanical forces, increasing many physical properties. For example, in an Mg alloy rolled for the effect of compression force, corrosion resistance shows a significant increase due to grain refinement. In a forged Mg alloy, the wear loss can decrease tens of times compared to the first sample. In addition to mechanical strength, Mg alloys give successful results in heat treatment processes and artificial aging stages. Thus, production, alloying, post-production mechanical effects and heat treatments are very important processes for Mg alloys. By applying some or all of these processes, a high-level Mg alloy can be obtained in terms of many properties (Bamberger & Dehm, 2008; B Çiçek, 2011; Elen et al., 2019; Gu et al., 2010; Yan, Bai, Liu, & Jin, 2017; Zhao, Liu, Song, & Atrens, 2008).

When Mg metal is used as a matrix, there is a letter-based proportional standard writing style for naming the alloys formed. In this writing style, the first letters are usually indicated by the initial letter of the symbol of the elements in the periodic table or by another letter. For example, the

---

[1] Dr. Lecturer, Hitit University, ORCID: 0000-0002-6603-7178
[2] Asist. Prof. Dr., Hitit University, ORCID: 0000-0002-8736-2949

letter A denotes aluminum metal, while the letter X. Integer numbers are used for the weight percentage ratio denotes calcium. For example, while the ratio of Al metal is 9 %wt and Zn metal is 1 %wt, this alloy is called AZ91 (Balasubramani, Srinivasan, Pillai, & Pai, 2007; Elen et al., 2019; Zengin et al., 2019; Zhu et al., 2021).

Apart from alloying, Mg metal can take place in a composite material as a matrix. Fiber, particle, layer etc. can create composite material with many external geometrical products. In recent years, carbon-based nanomaterials, carbides, ceramics and glassy forms can be added to the Mg matrix as additional products. Reinforcement products added to the composite material cause porosity and microstructure irregularities in the structure. For this reason, the weight percent and geometric conditions of the supplement products should be well analyzed (Sun & Ahlatci, 2011; Ye & Liu, 2004).

Density level is one of the important topics in composite materials. For this reason, the preference for the use of Mg metal is increasing. Thus, Mg metal takes its place as a matrix structure in many composite material studies. There are serious gains in the properties of composite materials with the effect of additional products. For example, by adding a Mg_2Si particle to the Mg matrix structure or forming it in the structure, the wear resistance can increase up to 40 times compared to pure Mg (B Çiçek, 2011; Lokesh, Ramachandra, Mahendra, & Sreenith, 2013; Sohag et al., 2020; Sun & Ahlatci, 2011).

One of the structures used as a composite material by-product is fiber-based products. In this context, glassy fibers, organic fibers and artificial fibers are frequently used. Fiber structures provide the composite material with an increase in yield and tensile strength. In addition, a significant increase in wear resistance is observed with the addition of certain proportions. Fiber structures are classified in terms of length, diameter and material type. Many fiber structures can be used, from the nanometer level to the millimeter level. Quartz fibers, basalt fibers (BF), fruit peel fibers, organic wood fibers, etc. products are used in composite materials (Akhlaghi, Eslami-Farsani, & Sabet, 2013; Hou et al., 2017; Rawal, 2001).

Basalt structures, one of the fiber reinforcement products added to composite materials, give successful results. BF obtained from volcanic rocks is preferred due to its high mechanical strength and wear resistance. The chemical composition differences of volcanic rocks according to geographical regions give the materials unique values. In basalt structures, Na, Al, Cl, P, Si and S elements exist in different proportions and the form of oxide compounds. In addition, structures such as Al_2O_3 and SiO_2, which are oxidized compounds of the elements that make up basalt structures, are very hard and durable ceramic compounds. Thus, BF creates a difference in many properties of a composite material to which it is added (Jamshaid & Mishra, 2016; Khalili, Daghigh, & Eslami Farsani, 2011).

BF is produced industrially. It is frequently used in ceramic structures in the industry. In addition, it takes its place in concrete additives for micro reinforcement, insulation applications, linings and increasing the mechanical strength of polymer structures. An industrially supplied BF modulus of elasticity reaches 89 GPa, while tensile strength is measured at about 5000 MPa. By adding a structure with high mechanical strength at this level to the composite, high properties can be achieved (Fiore, Scalici, Di Bella, & Valenza, 2015; Jamshaid & Mishra, 2016).

In this study, the effect of BF on the mechanical process was investigated by adding different ratios of BF to an AZ91 alloy produced by powder metallurgy method. Since BF loses its properties at high temperatures, it is produced by powder metallurgy method. The sintering heat treatment was carried out at 550°C to prevent thermal change. Sintering was applied at this temperature for 360 minutes. Afterwards, the samples were examined both physically and mechanically. BF effect was tried to be revealed by hardness and dry wear tests. Scanning electron microscopy (SEM) was used in powder-fiber mixing, microstructure phase and post-abrasion surface examinations. Energy

dispersion X-ray spectrometry (EDX) was used for the elemental determination of the structures in the SEM stage. X-ray Fluorescence (XRF) was used in the initial analysis of the powders and fiber structure and the elemental analysis after sintering. X-ray diffraction (XRD) analysis was performed to follow the microstructure phases. Thus, the effect of BF on AZ91 alloy produced by powder metallurgy has been examined with a serious investigation process.

Material Preparation and Experiments

Powder metallurgy method and process were applied in this study to obtain AZ91 material, which is Mg alloy. Differences in properties were observed with BF added to AZ91 alloy. Mg, Al and Zn metals used in this study were obtained from Nanografi Turkey. Metal powders with 99.9% purity were used. The grain sizes of metal powders are listed as D_{90} – 15.2 μm, 7.1 μm and 11.3 μm, respectively. The data obtained in the XRF (Rigaku Primus II) analysis applied before the experiments are listed in Table 1.

BF, which is used as a supplement, was purchased from Dost Kimya Turkey. The product specifications provided by the company are given in Table 2. The ready-made BF was ground in a rod mill for 1 hour for grain reduction before use. The basic SEM (Carl Zeiss Ultra Plus Gemini Fesem) images of the products used as raw materials are shown in Figure 1.

Table 1. XRF analyzes for metal powders

Elements	Mg (%wt)	Al (%wt)	Zn (%wt)	Other
Mg Powder	99.981	0.002	0.002	0.015
Al Powder	0.025	99.918	0.001	0.056
Zn Powder	0.009	0.001	99.925	0.065

Table 2. Catalogue parameters for basalt fiber

Tensile strength	4840 MPa
Elasticity module	89 GPa
Service temperatures	-260°C / +982°C
Melting Temperature	1450°C
Density	2.60-2.80 g /cm³
Fiber diameter	9-23 micrometer
Fiber length	6-12 mm
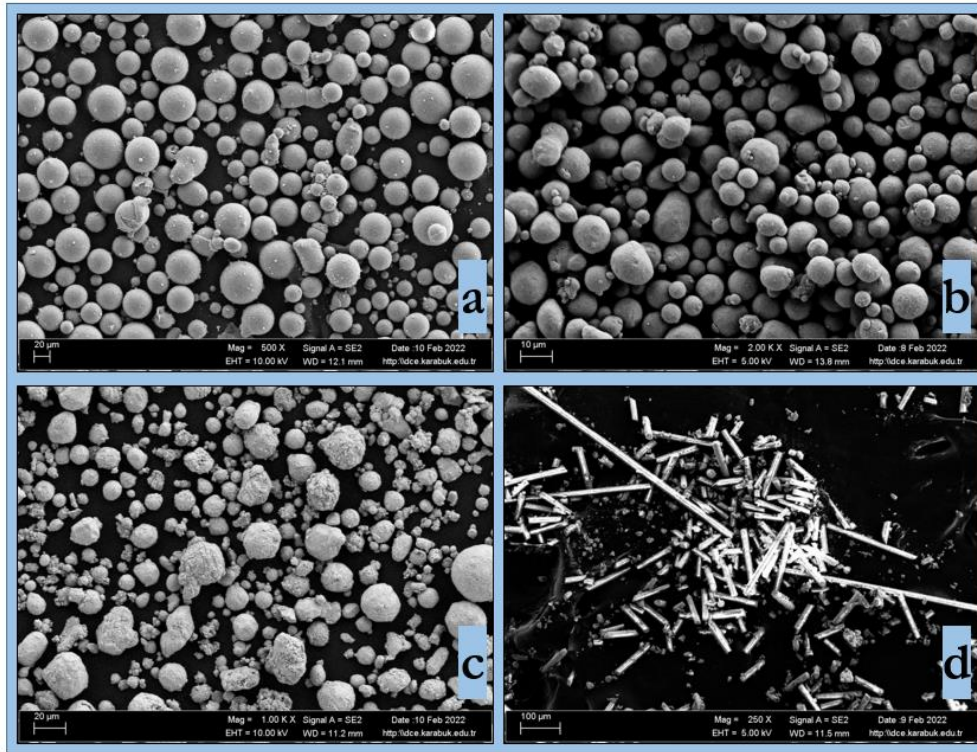
Figure 1. SEM images for raw materials; (a) Mg, (b) Al, (c) Zn, and (d) basalt fiber

Raw materials and materials were first taken into a homogeneous mixing process for the powder metallurgy process. During the mixing process, a mechanical mixing process was applied in the presence of ethanol. Mg, Al and Zn elements added to 200 ml of ethanol were mixed at 400 rpm / 1 hour. BF, on the other hand, is mixed primarily in the same details. In these initial mixing processes of powders and BF structure, agglomeration and static electrification, processes are minimized. In the mixing process applied in the magnetic stirrer, the containers were added to each other and the mixture was continued under the same conditions. After 3 hours, the liquid+powder mixture was placed on a *hydropyhobic* filter paper and dried at 70°C/24h. The resulting mixtures were used as samples. The percentage wt powder ratios in the mixtures are given in Table 3. Also, the mixing process is illustrated in Figure 2.

Table 3. Element amounts for specimens

Specimen	Mg (%wt)	Al (%wt)	Zn (%wt)	BF (%wt)
AZ91-0	90	9	1	-
AZ91-1	90	9	1	+1
AZ91-2	90	9	1	+2
AZ91-3	90	9	1	+3
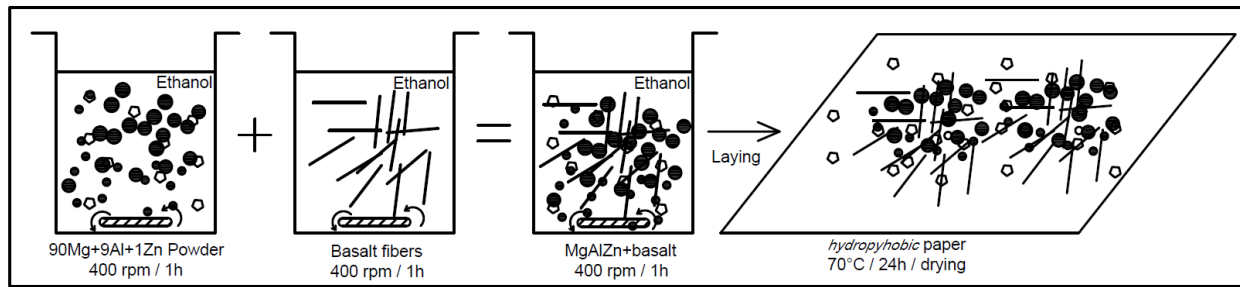
Figure 2. Powder mixing details

The powder samples obtained after the mixing process were taken into SEM analysis to control the mixing conditions. The powder samples were then taken to the pressing process. The samples were pressed in a 13 mm diameter die under a load of approximately 4 MPa/mm². The pressed samples were sintered in a Protherm brand heat treatment furnace, in a quartz glass tube with both ends blanked. In order to protect the samples placed in the glass tube from the atmosphere, the glass tube was melted with oxy-acetylene flame and the ends were blinded. The samples were sintered at 550°C for 6 hours. Photographs of the glass tube and sample after sintering were observed.

Metallic samples obtained after sintering were taken into microstructure analysis after classical metallographic preparations. A mixture of 5% picric acid+methanol was used as etching reagent in the metallographic process.

First, microstructure examinations of the samples were made under SEM microscope. In addition, EDX analysis was obtained from different structures in the AZ91-0 sample and reported. At the same time, XRD (Rigaku Ultima IV) and XRF analyzes applied for phases and elemental ratios were observed in the obtained AZ91-0 sample. For the follow-up of BF in the composite material, XRF analysis was applied to the AZ91-3 sample.

The samples were also examined by microhardness (QNESS Q10 A+) and dry wear (UTS Tribometer T10) tests. Vickers penetrating tip was used in the hardness test. The hardness test was carried out under a load of 1000 g and in five measurements. The average of the obtained values is reported.

In the dry abrasion test, the surfaces prepared with 1200 mesh sandpaper were abraded with a back-and-forth sliding motion. 316L quality 6 mm diameter balls were slid on the samples placed on a movable mechanism at a speed of 1500mm/min. A total of 100 m sliding distance was applied under 10N load. The difference between the first-last weight and the wear rate were followed. Finally, the worn surfaces were examined with SEM images.

Experimental Results and Discussions

A metal matrix composite material was obtained with the BF structure added to the AZ91 alloy produced by the powder metallurgy method during production. Composite material has been examined by many physical and mechanical based experiments and applications. SEM image analysis is given in Figure 3 for tracking the fibers added to the structure during the composite material creation process. Thus, the post-mixing process of the powder + fiber structure was monitored.
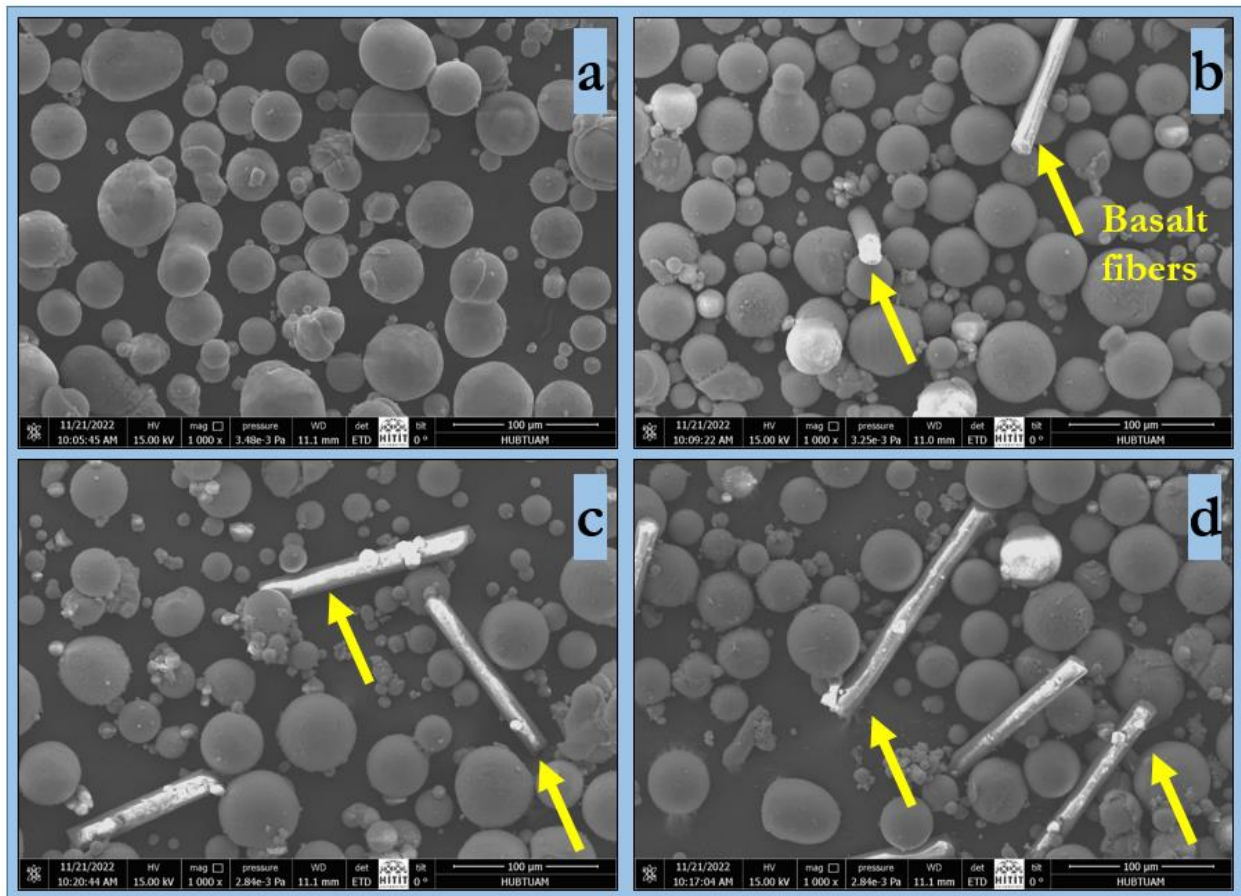
Figure 3. SEM images of mixed powder and fiber structures,

(a) AZ91-0, (b) AZ91-1, (c) AZ91-2, and (d) AZ91-3

When Figure 3 is examined, it is observed that spherical powders preserve their geometric structure in all mixtures. No oxidation or deformation was observed on the surfaces with the mixing process in alcohol. Fibers are seen in blends with BF addition. The increased BF ratio was detected in the pictures.

Pressed powder mixtures were sintered in quartz tube with blunt ends. Samples in quartz tubes after sintering are shown in Figure 4.

Figure 4. Composite materials sintered in a quartz tube

When the sintered samples are examined, it is seen that the Mg alloy can be sintered in a quartz tube with both ends closed without atmospheric environment. No oxide structures were found on

the sample surfaces. Thus, a Mg sintering process has been developed, eliminating cost and application difficulties.

After sintering, samples of basic alloy AZ91-0 material were examined in SEM environment. In Figure 5, the microstructure image of the base alloy is observed.
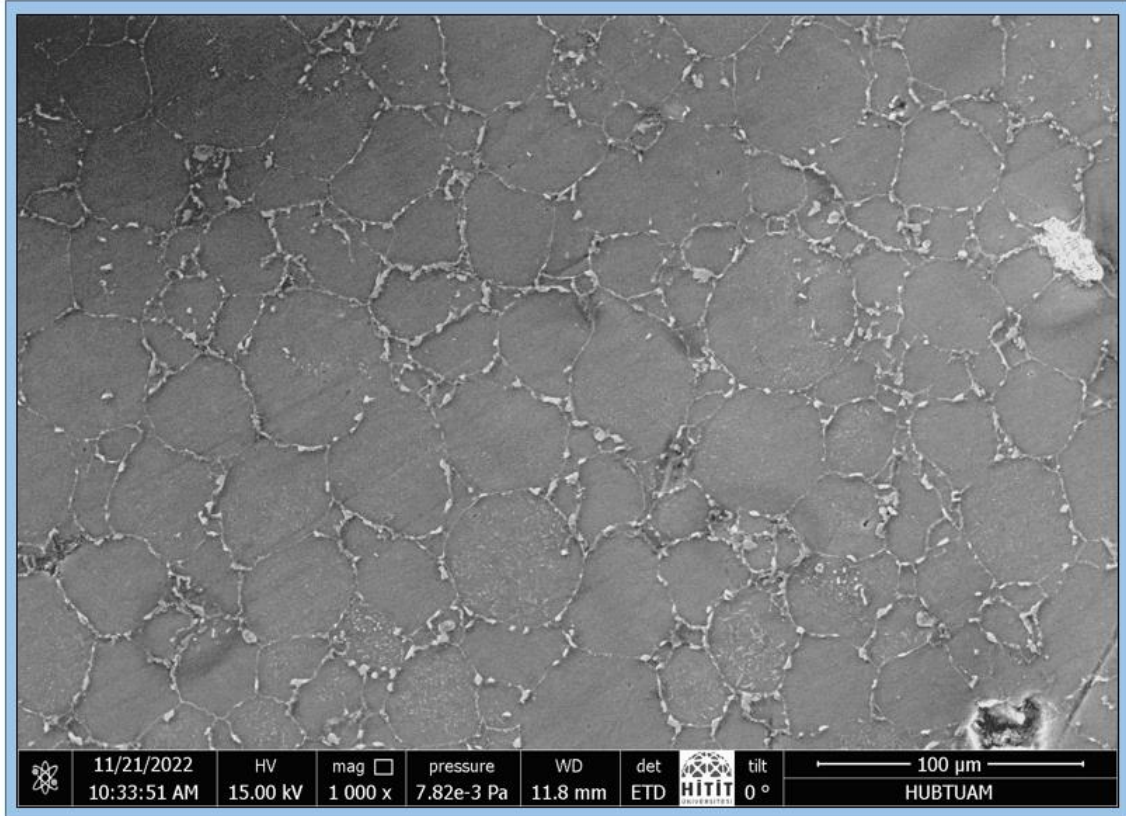
Figure 5. SEM image of AZ91-0 sintered alloy

When Figure 5 is examined, the requirements of the powder metallurgy production method are observed. Phase structures developing between dust grains are seen. Low porosity conditions have developed. Thus, the basic microstructure expected in a metallic alloy sintered without atmosphere was obtained.

In order to examine the phase structures observed between the powder grains in the AZ91-0 sample, SEM examination at high magnification was performed in Figure 6. In addition, the results of elemental EDX analysis of the phases detected in the microstructure are given in the picture.

% wt	Mg	Al	Zn
1	98.85	1.01	0.14
2	98.64	1.25	0.11
3	44.43	0.12	55.45
4	99.15	0.60	0.25
5	60.44	38.99	0.57
6	87.01	11.09	1.90
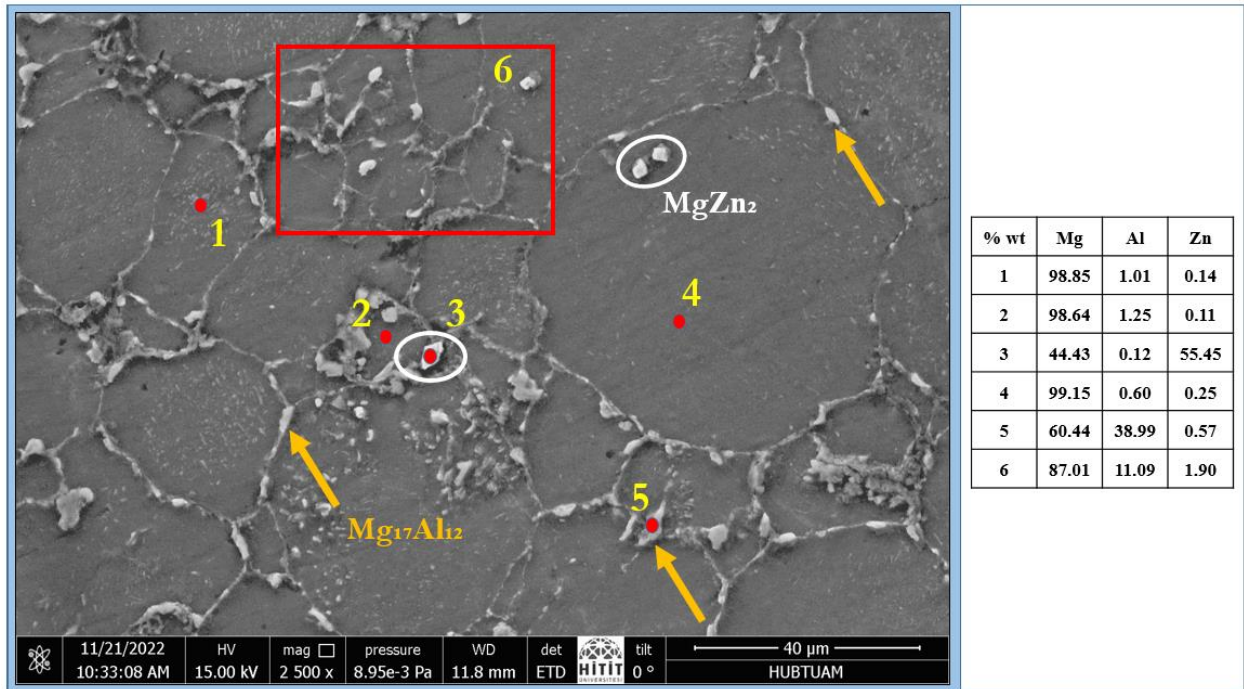
Figure 6. Microstructure analysis and EDX examination at high magnification for AZ91-0 alloy

Different phase structures observed in the microstructure were analyzed. It is seen that the expected phases in the AZ91 alloy are $Mg_{17}Al_{12}$ and $MgZn_2$, consistent with the literature. The result of the XRD analysis applied as well as the EDX analyzes of the formed phases are shown in Figure 7.
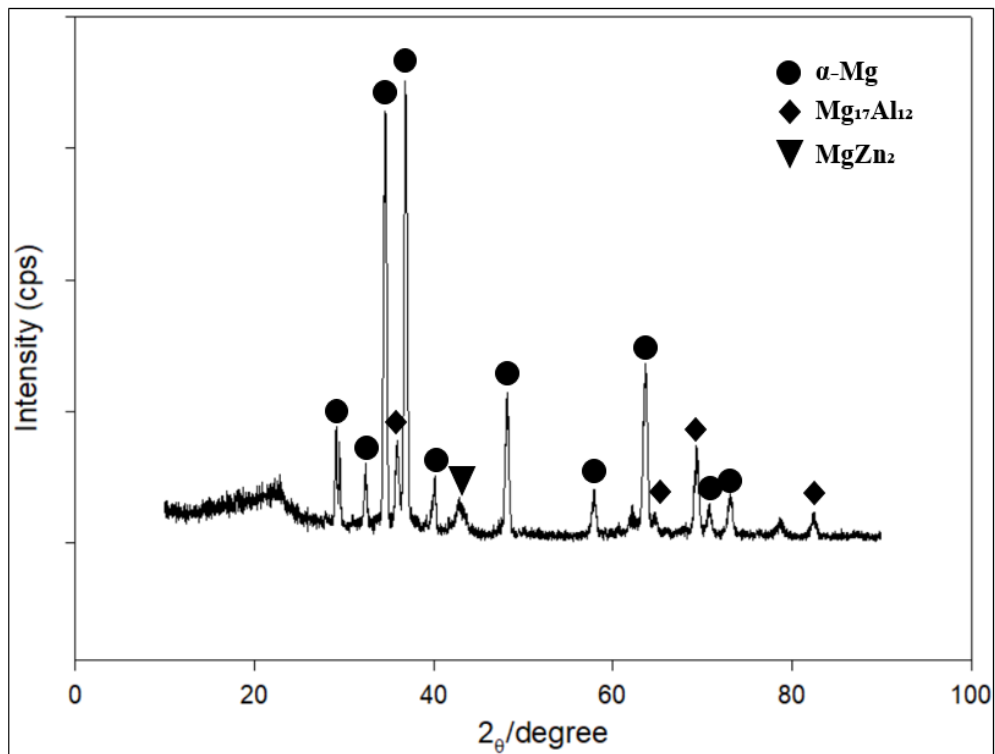
Figure 7. XRD peak for AZ91-0 alloy

When the XRD peaks given in Figure 7 were examined, the intermetallic structures shown in the microstructure were detected. Thus, it was observed that the phases expected in the AZ91 alloy were formed in the microstructure and the production method applied gave acceptable results.

The microstructure images of the composite structures obtained with the BF structure added to the AZ91-0 sample during production are given in Figure 8. Pictures are given at low and high magnification.
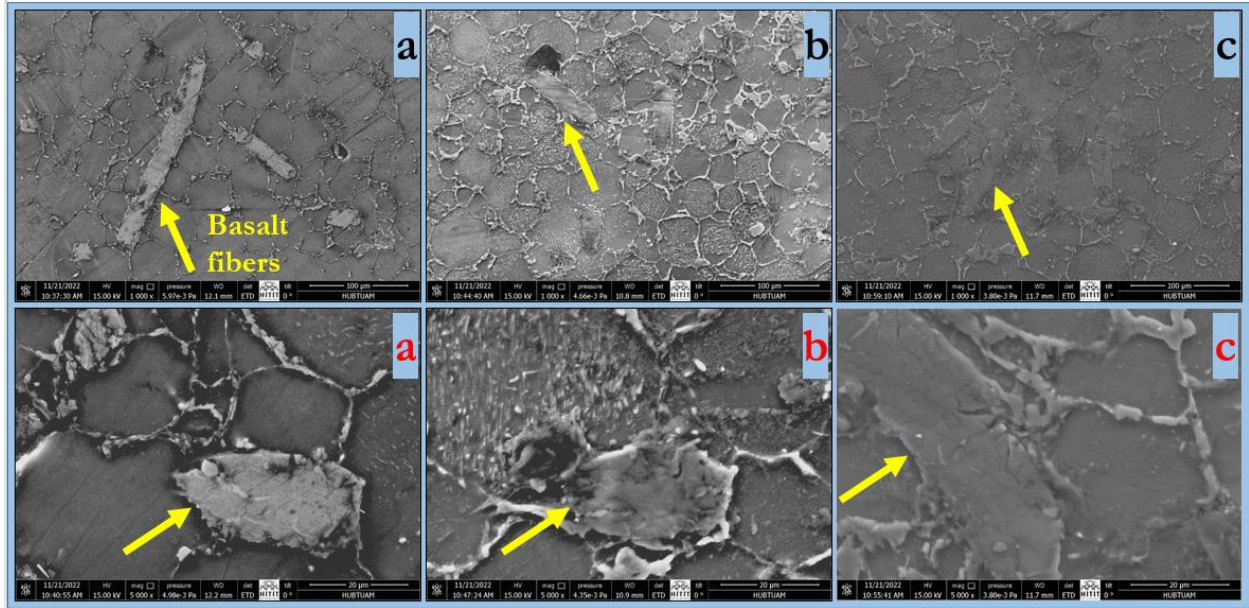
Figure 8. Microstructure images of composite materials

(a) AZ91-1, (b) AZ91-2, and (c) AZ91-3

BF structures are clearly observed in the microstructure examination of composite materials. As the BF ratio increased, the amount of detection increased. Low porosities are observed around the fiber structures. Thus, a successful metal matrix composite material was obtained with a fiber structure containing a high percentage of oxidized compounds.

XRF analyzes applied to determine the elemental ratios of alloy and composite materials are listed in Table 4.

Table 4. XRF analyzes for specimens

Specimen	Na (%wt)	Al (%wt)	Si (%wt)	S (%wt)	Cl (%wt)	Ca (%wt)	Zn (%wt)	P (%wt)	Mg (%wt)
AZ91-0	0.0083	9.5244	0.1292	0.0328	0.1187	0.0387	1.3739	0.0029	Balance
AZ91-3	0.1544	9.9093	1.9601	0.0176	0.7296	0.9378	1.0811	0.0129	Balance

According to XRF analysis, Al and Zn ratios of AZ91 alloy were found to be at the expected level. In the AZ91-3 composite material, the Al and Zn ratios were observed to be 9% and 1% by weight, respectively. In addition, Na, Si, Cl, Ca, and P elements detected in the composite material show the presence of basalt in the structure.

Vickers microhardness test was applied to the produced alloy and composite structures. The results obtained as a result of the hardness test are shown in Figure 9.
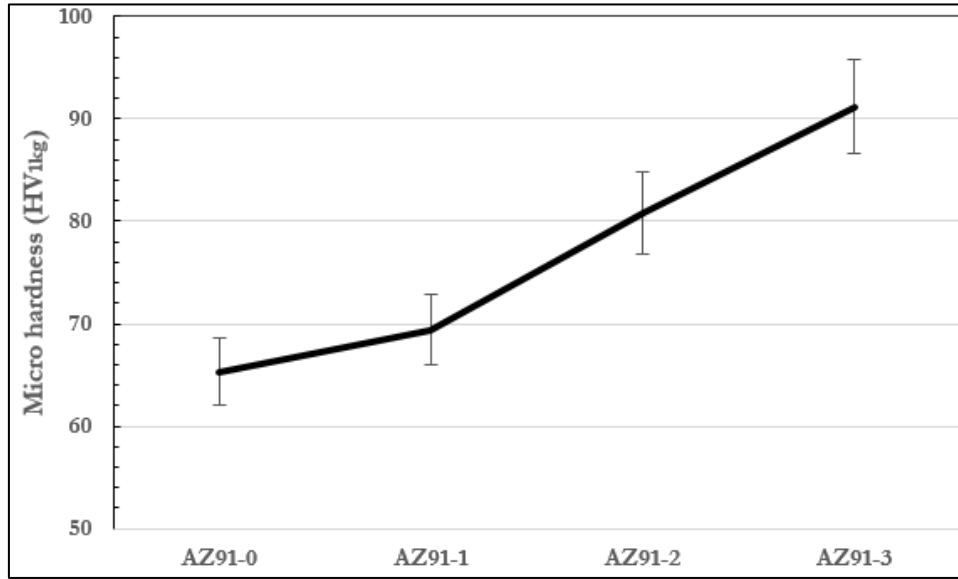
Figure 9. Hardness test results for all specimens

As a result of the hardness test, the hardness value of the composite materials increased with the addition of the BF structure to the alloy. The high strength value and modulus of elasticity of the BF structure are mainly effective in this process. In the AZ91-3 sample with the highest BF ratio, the hardness showed an increase of approximately 40% compared to the base alloy.

Worn surfaces formed as a result of the dry wear test applied to basic alloy and composite materials are shown in Figure 10 and Figure 11. Images are given at low and high magnification.
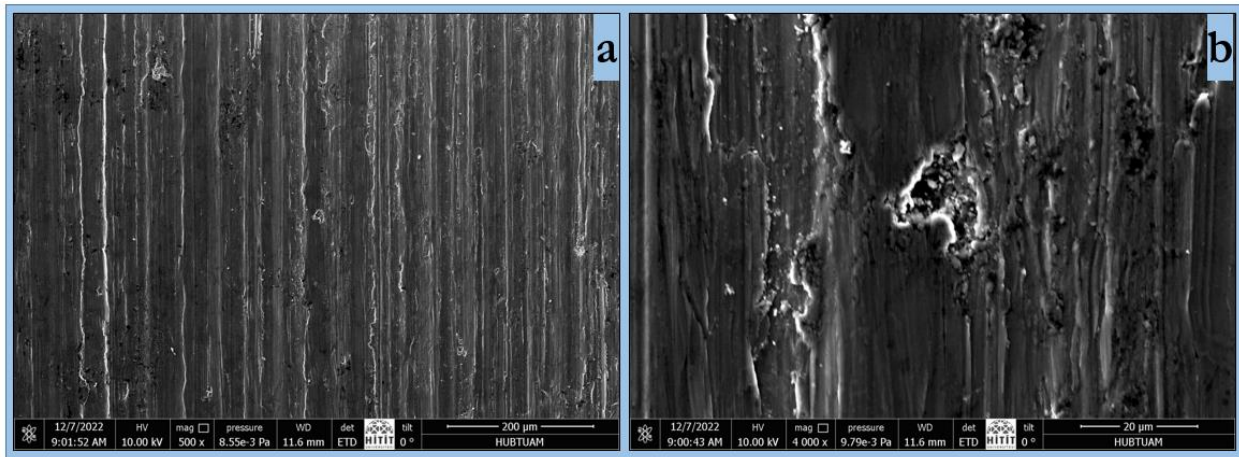
Figure 10. Worn surfaces in AZ91-0 alloy, (a) low and (b) high magnification

An adhesive wear mechanism is generally observed on the worn surface of the AZ91-0 alloy. A homogeneous image was observed on the worn surface. However, abrasive spots were detected at high magnification. The high hardness of the $MgZn_2$ particle is thought to form these abrasive spots.
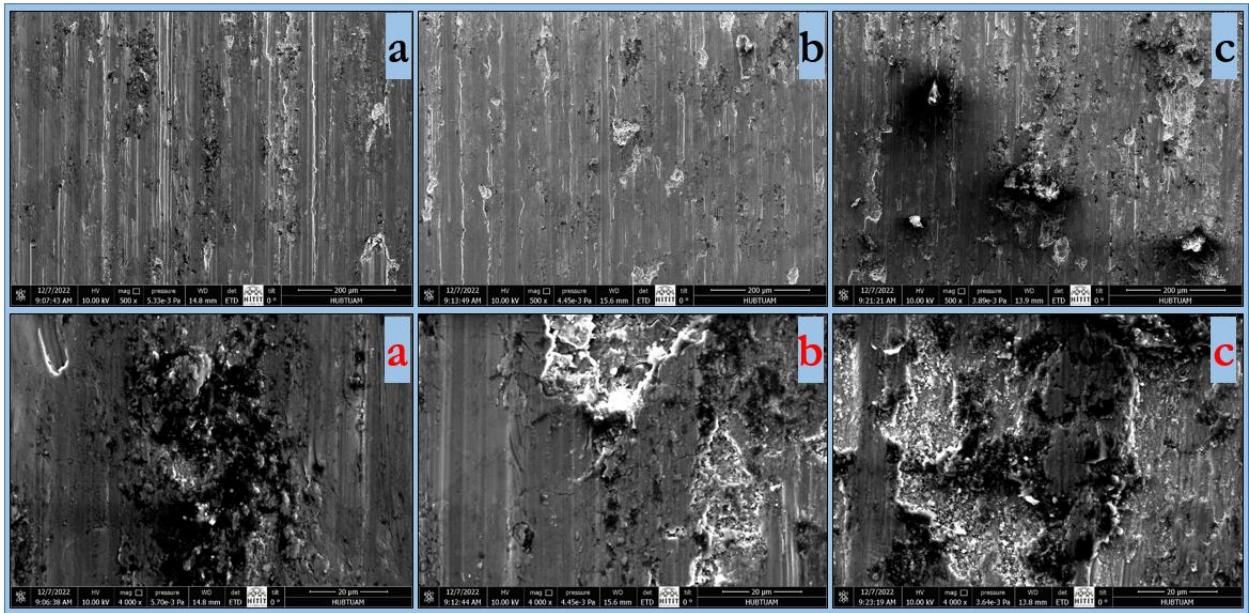
Figure 11. Worn surfaces for composite materials, (a) AZ91-1, (b) AZ91-2, and (c) AZ91-3

Worn surfaces formed in composite materials contain both wear mechanisms, adhesive and abrasive. Abrasive wear zones are observed in high magnification images. It can be said that the reinforcement fiber material causes the abrasive structure. Due to the high yield strength of the fiber material and therefore its high hardness value, the abrasive mechanism has developed. Due to the axial load applied during wear and the 316L stainless steel ball, the fiber structures are fragmented. The hard fiber particles resulting from the fragmentation deformed the softer alloy regions. Thus, as the BF ratio increased, the amount of abrasive mechanism increased.

The graph of the wear rates due to the weight loss obtained after the wear test is shown in Figure 12.
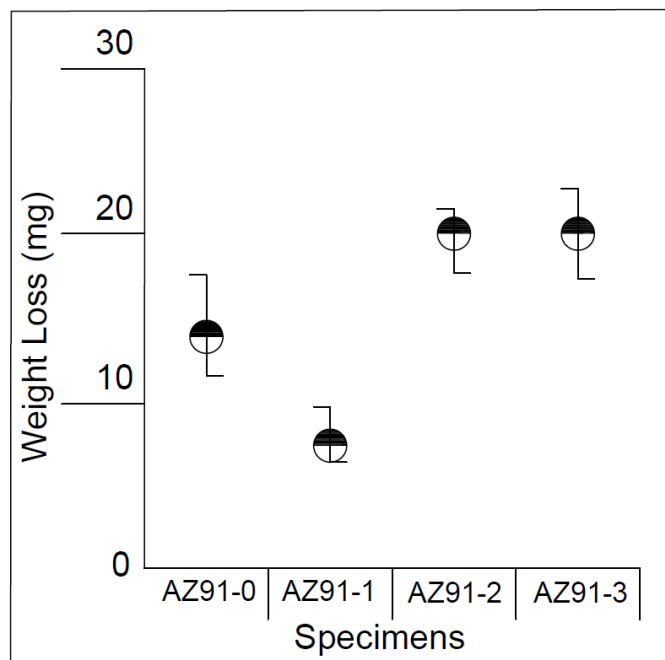
Figure 12. Weight loss rates for specimens

According to the weight loss results calculated after wear, an average of 14 mg loss occurred in the alloy sample. In the AZ91-1 composite structure, the weight loss was measured as 7 mg with an improvement rate of 50%. However, it was observed that the weight loss increased rapidly as the basalt ratio increased. In the AZ91-3 sample, the weight loss reached an average of 20 mg. Wear resistance increased with the effect of BF added at a low rate (1%). The wear rate of the structure increased with the addition of 3% BF. It is seen in Figure 11c that the fibers break and accelerate wear and develop an abrasive mechanism. Thus, while adding 1% of the BF structure was a successful result, increasing BF negatively affected the results.

According to the experimental results, the production of AZ91 Mg alloy by powder metallurgy method has been carried out successfully. General requirements for alloys produced by powder metallurgy method are provided (Cicek, Sun, Turen, & Ahlatci, 2022). In addition, it was observed that the Mg alloy, which was sintered with a unique method without atmosphere control, transitioned from oxidation to metallic form. In addition, composite materials obtained with basalt structure added to the alloy were produced.

Production of AZ91 alloy by powder metallurgy is a process that has been studied in many studies. Intermetallic phases and particles formed between dust grains were similar to the literature (Akkaş & Boz, 2019). However, atmosphere controlled sintering process is generally used in the production of Mg alloy (Akkaş & Boz, 2019; Taleghani, 2014). A new sintering step has been added to the literature with the atmosphereless method applied in this study.

The BF structure has been used frequently in the literature in recent years and has an effect on many features. It is a possible result that basalt has different chemical content depending on the geographical and volcanic region. Therefore, elemental ratios in all studies give different properties (Jamshaid & Mishra, 2016).

When the hardness test was examined, the high mechanical properties of the BF structure caused a serious increase in hardness in composite materials. This increase is an expected result with the effect of hard compounds in the BF structure. Hardness increase in BF added alloys showed similar results (Akhlaghi et al., 2013; Jamshaid & Mishra, 2016). Thus, the increase in hardness was confirmed.

The wear resistance of the composite materials formed by adding the BF structure to the alloys shows different values. As the fibers break during wear, the wear rate increases. However, fibers added at a low rate can break and fill into porosities. Thus, while the wear resistance increases at a low rate, the wear resistance decreases as the fiber content increases. The reason for this can be shown as more abrasion of the matrix alloy by the hard fibers (Bünyamin Çiçek & Aydoğmuş, 2022; Fiore et al., 2015; Jamshaid & Mishra, 2016). Finally, it has been stated in studies that abrasive wear mechanisms occur in fiber-reinforced composite materials (Amuthakkannan, Manikandan, Raja, & Rajesh, 2017; Chairman, Jayasathyakawin, Srinivasan, & Ravichandran, 2020; Guo et al., 2015). As a result, similar processes were followed in this study.

Conclusions

The production of AZ91 Mg alloy by powder metallurgy method and the process of making it into a composite material with basalt fiber addition were investigated in this study. In addition, microstructure, hardness and physical dry wear tests were applied to the samples. As a result, the following main results were obtained.

1. AZ91 alloy produced with powder forms of pure elements Mg, Al and Zn has been successfully obtained.

2. After sintering, intermetallic phases were observed among the metallic powder grains.

3. Metallic structure has been achieved without oxidation with the sintering process applied in a blanked quartz glass tube without atmosphere control.

4. Composite materials are produced with the basalt structure in the form of fiber added to the alloy.

5. With the effect of basalt fibers, the hardness level of composite materials increased by 40%.

6. In the dry wear test applied to alloy and composite materials, the structure containing 1% basalt fiber suffered the lowest weight loss.

Thus, this study was completed with both the use of a volcanic basalt fiber structure and the sintering process applied without atmospheric control. The effect of volcanic basalt fiber on wear and hardness properties has been brought to the literature. In addition, a new sintering method open to development for Mg alloys has been specifically investigated.

References

Akhlaghi, F., Eslami-Farsani, R., & Sabet, S. (2013). Synthesis and characteristics of continuous basalt fiber reinforced aluminum matrix composites. *J Compos Mater, 47*(27), 3379-3388. doi:https://doi.org/10.1177/002199831246576

Akkaş, M., & Boz, M. (2019). Investigation of the compressibility and sinterabilty of AZ91 powder production and particle production by gas atomisation method. *Journal of magnesium and alloys, 7*(3), 400-413.

Amuthakkannan, P., Manikandan, V., Raja, M. A., & Rajesh, S. (2017). Wear characterization of aluminium/basalt fiber reinforced metal matrix composites-A Novel Material. *Tribology in Industry, 39*(2), 219.

Balasubramani, N., Srinivasan, A., Pillai, U., & Pai, B. (2007). Effect of Pb and Sb additions on the precipitation kinetics of AZ91 magnesium alloy. *Materials Science and Engineering: A, 457*(1-2), 275-281.

Bamberger, M., & Dehm, G. (2008). Trends in the development of new Mg alloys. *Annu. Rev. Mater. Res., 38*, 505-533. doi:10.1146/annurev.matsci.020408.133717

Chairman, C. A., Jayasathyakawin, S., Srinivasan, D., & Ravichandran, M. (2020). Abrasive wear characteristics of bio-based jatropha oil cake incorporated basalt fiber reinforced epoxy composites. *Materials Today: Proceedings, 33*, 3947-3950.

Cicek, B., Sun, Y., Turen, Y., & Ahlatci, H. (2022). Investigation of Microstructural Evolution of Gas-assisted Metal Injection Molded and Sintered Mg-0.5 Ca Alloy. *Sci Sinter, 54*(1), 25-37. doi:https://doi.org/10.2298/SOS2201025C

Çiçek, B. (2011). *Investigation of wear and corrosion properties of Mg alloys reinforced with Mg2Si particle.* (M.Sc. Thesis), Karabuk University, Turkey.

Çiçek, B., & Aydoğmuş, T. (2022). The Effect of Basalt Fiber Addition on Physical Dry Wear in Al-Cu Alloy Used in the Automotive Industry. *International Journal of Automotive Science And Technology, 6*(4), 379-385.

Elen, L., Türen, Y., & Koç, E. (2019). AZ91 Mg alaşımına farklı oranlarda Sb ilavesi ile katılaşma hızının mikroyapı ve mekanik özelliklere etkisi. *International Journal of Engineering Research and Development, 11*(2), 451-463. doi:https://doi.org/10.29137/umagd.507264

Fiore, V., Scalici, T., Di Bella, G., & Valenza, A. (2015). A review on basalt fibre and its composites. *Composites Part B: Engineering, 74*, 74-94.

Gu, X., Zhou, W., Zheng, Y., Cheng, Y., Wei, S., Zhong, S., . . . Chen, L. (2010). Corrosion fatigue behaviors of two biomedical Mg alloys–AZ91D and WE43–in simulated body fluid. *Acta biomaterialia, 6*(12), 4605-4613. doi:https://doi.org/10.1016/j.actbio.2010.07.026

Guo, W., Guo, J., Wang, J., Yang, M., Li, H., Wen, X., & Zhang, J. (2015). Evolution of precipitate microstructure during stress aging of an Al–Zn–Mg–Cu alloy. *Materials Science and Engineering: A, 634*, 167-175.

Hou, L., Wu, R., Wang, X., Zhang, J., Zhang, M., Dong, A., & Sun, B. (2017). Microstructure, mechanical properties and thermal conductivity of the short carbon fiber reinforced magnesium matrix composites. *Journal of alloys and compounds, 695*, 2820-2826.

Huang, S.-J., Subramani, M., & Chiang, C.-C. (2021). Effect of hybrid reinforcement on microstructure and mechanical properties of AZ61 magnesium alloy processed by stir casting method. *Composites Communications, 25*, 100772.

Jamshaid, H., & Mishra, R. (2016). A green material from rock: basalt fiber–a review. *The Journal of The Textile Institute, 107*(7), 923-937.

Khalili, S., Daghigh, V., & Eslami Farsani, R. (2011). Mechanical behavior of basalt fiber-reinforced and basalt fiber metal laminate composites under tensile and bending loads. *Journal of Reinforced Plastics and Composites, 30*(8), 647-659.

Lokesh, G., Ramachandra, M., Mahendra, K., & Sreenith, T. (2013). Effect of Hardness, Tensile and Wear Behavior of Al-4.5 wt% Cu Alloy/Flyash/SiC Metal Matrix Composites. *Int J Mod Eng Res Technol, 3*(1), 381-385.

Matykina, E., Garcia, I., Arrabal, R., Mohedano, M., Mingo, B., Sancho, J., . . . Pardo, A. (2016). Role of PEO coatings in long-term biodegradation of a Mg alloy. *Appl. Surf. Sci., 389*, 810-823.

Rawal, S. P. (2001). Metal-matrix composites for space applications. *JOM, 53*(4), 14-17.

Sohag, M. A. Z., Gupta, P., Kondal, N., Kumar, D., Singh, N., & Jamwal, A. (2020). Effect of ceramic reinforcement on the microstructural, mechanical and tribological behavior of Al-Cu alloy metal matrix composite. *Mater Today: Proc, 21*, 1407-1411. doi:https://doi.org/10.1016/j.matpr.2019.08.179

Sun, Y., & Ahlatci, H. (2011). Mechanical and wear behaviors of Al–12Si–XMg composites reinforced with in situ Mg2Si particles. *Materials & Design, 32*(5), 2983-2987.

Taleghani, M. A. J. (2014). *Processing and properties of high performance 7075 Al and AZ91 Mg powder metallurgy alloys.* Universidad Carlos III de Madrid.

Yan, K., Bai, J., Liu, H., & Jin, Z.-Y. (2017). The precipitation behavior of MgZn2 and Mg4Zn7 phase in Mg-6Zn (wt.%) alloy during equal-channel angular pressing. *Journal of magnesium and alloys, 5*(3), 336-339.

Ye, H. Z., & Liu, X. Y. (2004). Review of recent studies in magnesium matrix composites. *Journal of Materials Science, 39*(20), 6153-6171.

Zengin, H., Turen, Y., & Elen, L. (2019). A comparative study on microstructure, mechanical and tribological properties of A4, AE41, AS41 and AJ41 magnesium alloys. *Journal of Materials Engineering and Performance, 28*(8), 4647-4657. doi:https://doi.org/10.1007/s11665-019-04223-8

Zhao, M.-C., Liu, M., Song, G., & Atrens, A. (2008). Influence of the β-phase morphology on the corrosion of the Mg alloy AZ91. *Corrosion Science, 50*(7), 1939-1953. doi:https://doi.org/10.1016/j.corsci.2008.04.010

Zhu, L., Qiu, F., Zou, Q., Han, X., Shu, S.-L., Yang, H.-Y., & Jiang, Q.-C. (2021). Multiscale design of α-Al, eutectic silicon and Mg2Si phases in Al-Si-Mg alloy manipulated by in situ nanosized crystals. *Materials Science and Engineering: A, 802*, 140627. doi:https://doi.org/10.1016/j.msea.2020.140627

Highway Vertical Curve Optimization with Meta- Heuristic Algorithm

Sina ASHERLOU[1]
Aref YELGHİ[2]
Erhan Burak PANCAR[3]
Şeref ORUÇ[4]

Introduction

Due to the high cost of the road, it is required careful attention. Many studies have been carried out in the world generally due to the high cost of the highway superstructure and many methods have been developed and proposed for the design of the project. Since highway design is open to innovations, research is continuing at full speed today.

A highway project consists of infrastructure and superstructure. The ground floor, which is under the leveling surface created at the end of earthworks, that is, splitting and filling works, is called infrastructure works. The performance of the pavement is directly related to the physical properties of the infrastructure. In this regard, all conditions must always be met. The superstructure, on the other hand, has a layered structure and transfers the traffic loads directly to the subgrade. The superstructure is the part that can carry traffic loads without facing major deterioration and cracking throughout its economic life (Sütaş & Öztaş, 1983).

It is an undeniable fact that optimization is everywhere, from design to implementation of all engineering fields. Mathematical optimization or programming is used in all design planning problems. In this context, the experimental result with the most economical or highest achievable performance is obtained by considering all factors. The aim of using the optimization method is to maximize production efficiency (Yang & Press, 2010). In 1988, the cost calculation was realized by considering all the geometrical features of the road class and minimizing the amount of excavation (Easa, 1988). Later, a dynamic programming model was formulated to solve two-dimensional highway location problems as defined in 1988 (Goh, Chew & Fwa, 1988). Numerical studies have been carried out to find the optimum ground line and grade line by modeling a three-dimensional road route and subjecting it to a wide variety of possible constraints (Chew, Goh & Fwa, 1989). Fwa presents an optimization program developed in 1989 to produce an optimum vertical line profile for a preselected horizontal line (Fwa, 1989). To determine the cost of excavation in the highway application, studies have been carried out on the road class chosen by the designer. The designer has an almost infinite number of viable alternatives to choose from, all of which meet the geometrical properties of the road (Moreb, 1996).

With the aid of the artificial intelligence technique of genetic algorithms, it performs route optimization analyses by making complex mathematical solutions of slopes, fixed elevation points, and horizontal-vertical curves in highway design. Considering these three constraints, the relevant

[1] Department of Civil Engineering, Avrasya University, Trabzon, Turkey
[2] Department of Computer Engineering, İstanbul Topkapı University,İstanbul, Turkey
[3] Department of Civil Engineering, Ondokuz Mayıs University, Samsun, Turkey
[4] Department of Civil Engineering, Karadeniz Technical University, Trabzon, Turkey

construction costs were examined (Fwa, Chan & Fwa, 2002). There has been some work presented on being able to significantly reduce the cost of construction. In this study, in addition to minimizing excavation works, split-fill balancing was also taken into account (Goktepe & Lav, 2003).

Considering the cost, he presented a model of a route that integrates genetic algorithms with a geographic information system, examines the effects of various costs on route selection, and explores optimization in constrained areas that realistically reflects the limits of road improvement projects (Jha & Schonfeld, 2004). Since the elevation level on the axis line of the cross-section can be misleading, it is adjusted as close as possible to the ground level on a cross-section, using the weighted ground line method. In addition, due to the difference between the original volume in a cross-section and the post-compression volume in a fill, and accordingly, not all excavated material can be used as fill material, modified excavation and fill volumes are used in the calculation of weighted ground elevations (Goktepe & Lav, 2004).

By defining a methodology for the optimization of road grade lines, using the dynamic programming approach, an optimal grade line with minimum cost was found by considering various design constraints (Goktepe, Lav & Altun, 2005). The use of a genetic algorithm is recommended to increase the efficiency of the calculation and the quality of the solutions. It is observed that the load of the data to be calculated in the geographic information system (CBS) database will be an important problem during the optimization phase of the highway design. On the other hand, through CBS, it has worked on real-world maps (Kim, Jha & Son, 2005).

A three-dimensional optimization method has been developed to automatically determine whether bridges or tunnels are preferred to fill zones (Kim et al., 2007). Since the optimization of excavations related to highway optimization will play a very important role in the total cost of projects, an excavation optimization technique based on a ground line that balances the cut-fill volumes and minimizes the total amount of excavation by developing the weighted ground line method has been developed (Goktepe, Altun & Ahmedzade, 2009).

Designers of grade line prefer an intelligent optimization tool to offer genetic algorithms for highway optimization integrated with a geographic information system (GIS) (Kang, Jha & Schonfeld, 2012).

The development of algorithms for highway optimization is increasing rapidly. Since this topic is very complex and consists of many factors, engineers have to reach different and relevant targets. Minimizing the costs of construction and excavation, adapting to environmental restrictions, and increasing the safety and comfort of users should be considered very carefully at the same time. This complex calculation can be made simple by modern artificial intelligence techniques and can be simplified and extended. In this study, a search algorithm was proposed using the partial swarm optimization method (PSO) for road optimization (Bosurgi, Pellegrino & Sollazzo, 2013).

Some work has been performed on the determination of the grade line in excavation. In this study, the grade line design affects road costs, safety, and traffic performance. grade line optimization design meets the criteria as well as the total excavation quantity which allows minimizing. generally, determining the optimum grade line starts the process. In this context, the grade line segments are assumed to be equidistant. However, these equal distances will not result in low excavation. This statement is based on a numerical approach to equalizing debt. However, the proposed approach is only available on one part of the grade line (Al-Sobky, 2014).

A general formulation of tangential lengths and circular curves appropriately associated with transition curves is presented for optimization of the horizontal route (Casal, Santamarina & Vázquez-Méndez, 2017). GA and PSO methods related to the optimization of the grade line using meta-heuristic algorithms have been used as two smart optimization tools, to find an optimized

forest path by connecting the endpoints in the forest path Profile design and cost assessment (Babapour et al., 2018).

By formulating the optimization of the grade line, height and length are considered variables in the selection of a node. To solve this optimization problem was compared using genetic algorithm (GA) and particle swarm optimization (PSO) (Ghanizadeh & Heidarabadizadeh, 2018). In the first stage of the design of highway projects, several alternative horizontal routes are usually created, and the vertical route of that road is created for each alternative horizontal route selected. Since there can be an unlimited number of vertical routes in compliance with all design rules for a selected horizontal route, an optimization method was created by the designer to obtain the most economical design and focused on optimizing the vertical route (Ozkan, Tuydes-Yaman & Acar, 2021).

In finance and application engineering, optimization algorithms are used to solve complex problems. In other words, by solving these problems, it is possible to solve other real problems in a more stable and faster manner (Yelghi & Tavangary, 2022)

To obtain an optimum grade line design by considering earthworks on the profile, the upper heuristic methods PSO, FA, and ABC have been used and very satisfactory results have been obtained thanks to these methods (Asherlou et al., 2022). If a highway project is to be fully economical, the excavation operations of that project should be minimized and at the same time, the cut-fill volumes should be equalized. To summarize this situation, to make a highway project the most economical, studies should be done on the cut-fills of that project. In this context, optimization should be made on the Profile design to equalize and at the same time minimize excavation operations.

The data on the profile are ground line and grade line. However, it will not be possible to interfere with the ground line, which shows the natural state of the land. In this case, there is only one option left for us to intervene, and that is what we call the grade line or the project line. In this context, for a highway project to be economical, the grade line of that project must be optimized.

As can be seen from the literature, excavation cost is one of the most important problems when designing a highway project. In this context, it has become an undeniable fact that some optimization methods are used for grade line design to minimize the amount of excavation and to get the cut-fill amount equal. However, only some single-objective optimization algorithms from meta-heuristic algorithms have been used in the studies on grade line so far. The methods used in this context are generally only used for horizontal path optimization.

In this study, vertical curve optimization, which is one of the most important elements apart from the straight parts of the grade line, should also be done carefully. vertical curve optimization is an undeniable fact in optimum grade line design with minimum cost. Only in this way will it be possible to solve a grade line design with a multi-stage optimization technique. However, in the studies on the grade line until now, only single-purpose methods from the metaheuristic algorithms have been used. However, with multi-objective optimization methods, it will be possible to make more detailed analyzes and develop the grade line optimization algorithm, making calculations instantly.

In this study, vertical curve optimization is performed. In this context, grade line optimization can be done using a multi-objective meta-heuristic optimization algorithm. However, nowadays only single-objective methods are generally used in grade line optimization. Since the grade line design consists of extremely complex mathematical operations, it would be more logical to use multi-objective optimization algorithms than optimization methods.

Thus, by integrating the application prepared for the optimization of the grade line and multi-purpose optimization algorithms, a more detailed analysis will be made based on two factors or

two targets for less excavation amount and Cut-fill balancing. In this context, the results obtained are more stable and reliable due to the proposed algorithm. Of course, these processes with 2000 iterations and 30 times on the X-Y axis for the meta-heuristic optimization method and compared.

As it is known during the optimization of the grade line, the grade line does not consist of only the right parts. In other words, a vertical curve must be placed between these straight segments, that is, where the point of intersections are found. However, since thousands of vertical curves will be passed during optimization, the vertical curve with the most optimum Cut-fill should be selected. In this regard, vertical curves passed through the point of intersections of the grade line can be either a stream vertical curve or a peak vertical curve, depending on the situation. In the selection of the optimum vertical curve, where the vertical curve should be, only the vertical curve at the top, which is closest to the point of intersections, out of thousands of vertical curves passed by the application, and at the same time the vertical curve at the bottom, which is the closest to the point of intersections, where the stream vertical curve should be. should be selected. Thus, all vertical curves must be optimized throughout the project to optimize the entire project in the grade line design.

Material and Method

A highway project consists of design and implementation. The finer details of the implementation of highway projects, the more attention should be paid to the design phase. In other words, just as wrong practices create unacceptable results during implementation, in projects that are not designed following the required specifications during the project design phase, implementation costs will increase and cause it to be uneconomical. In this context, by choosing one of the multi-purpose optimization algorithms and adding some coding in addition to the existing application, we will develop this algorithm for more economical grade line design. Thus, the most optimum grade line will be designed by minimizing the amount of cut and fill.

Multi-Purpose Optimization Method MOPSO (Multiple Objective Particle Swarm Optimization)

We can solve single-objective optimization problems with the PSO method and multi-objective optimization problems with the MOPSO method by developing the PSO method. It is possible to convert to MOPSO by applying some modifications to the PSO algorithm. The most important reason for this change is that the problem is multi-purpose (Coello, Pulido & Lechuga, 2004). The basis of the Particle Swarm Optimization algorithm is swarming intelligence. Factors alone cannot be effective in herd intelligence. For this reason, they reach the result by taking part in the herd and cooperating. They can't reach the result they have achieved in the form of a flock alone. To find new answers in the search area, some rules must be defined. In this context, the most important concept is the concept of movement. The first movement is considered a kind of inertia. The second move counts as nostalgic and is useless on its own. The main core of the algorithm is considered the third stage. The difference between PSO and MOPSO is in the selection of the best particle, so multi-objective optimization is focused on the definition of the best option in the algorithm. According to multi-objective optimization algorithms, the first degree of quality and then the order of the option that is not defeated is important (De Oca al., 2009).

Profile Design

The most important stage of Profile design in highway projects is the part where grade line is determined. Profile design consists of ground line and grade line. In this context, we must minimize the amount of excavation to reduce the cost. In other words, optimizing each parameter of the grade line separately in Profile design, it will have a significant effect on reducing direct costs. Thus, it is an undeniable fact that the optimum design of Profile elements will directly affect the amount of excavation. In the profile design, first of all, ground elevations and cross-section

kilometers of the axis line will be determined. The distance will be displayed on the X-axis of the profile and high on the Y-axis. In this context, an example of black and grade line design is shown in figure 1. Today, grade line is passed by determining the point of intersections in the Profile design. However, the most important factor in grade line design is the peak points of the grade line. The amount of cut and fill between the ground line and the grade line should be the least and at the same time equal. The grade line design is shown on the example ground line, that is, in figure 1.
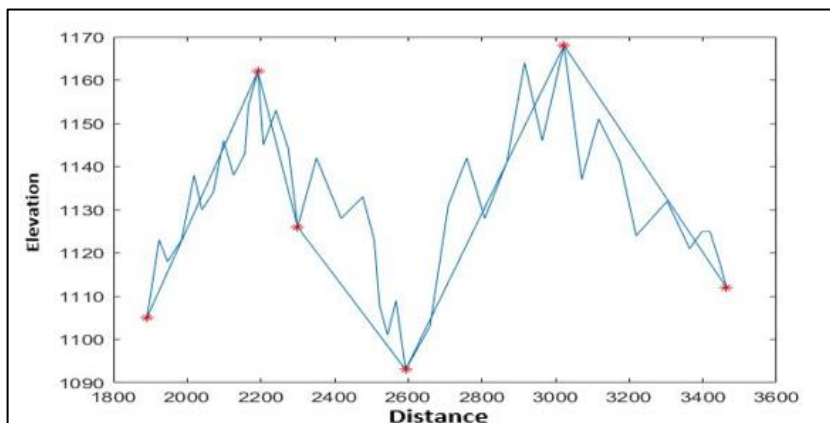
Figure 1. Profile design

Adding and Removing Points of Intersections

As shown above, it will not be entirely correct that only the intersection points along the way are selected automatically by the algorithm. In some projects, the mandatory intersection points must also be found within the scope of the project operation, as seen in figure 2, or on the contrary, there should not be any node points at certain distances for the project operation. In this context, to ensure that the application is not incomplete, at a certain stage of the design, the application designer will be asked whether there are fixed nodes, and the application will be interfered with by adding and subtracting unlimited nodes.
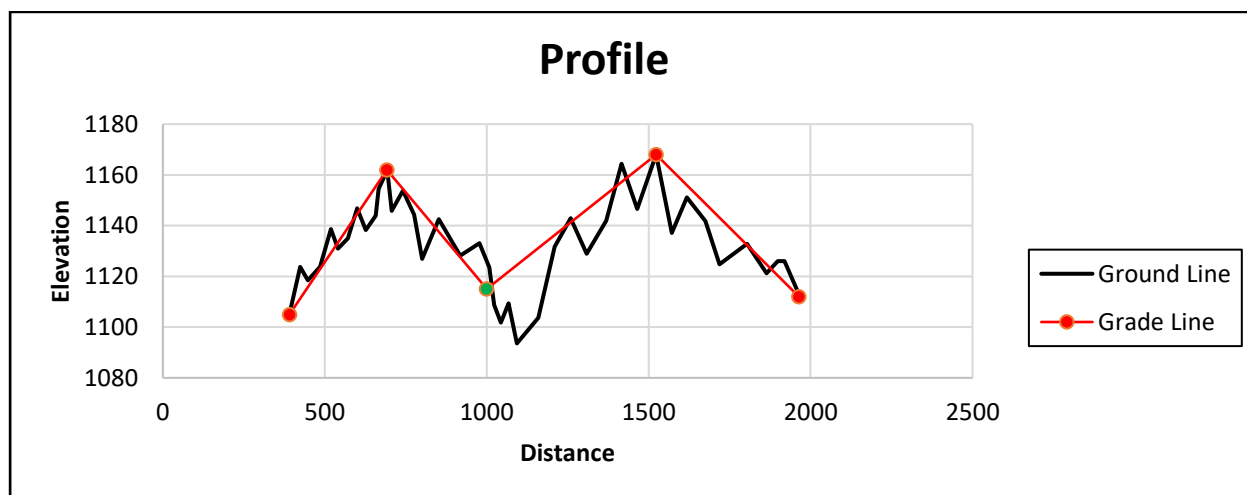
Figure 2. Addition and remuval of the intersection points

Figure 3 shows only a part of this coding. With the aid of this coding, it is first asked by the application whether there is a mandatory node that should be added in addition to the automatic knuckles found about the grade line's nodes. If the answer to the question of the node to be added is yes, the application asks for the total number of nodes to be added within the scope of the

project. After entering the number of node points that need to be added to the total, the coordinates of those node points are requested. Of course, when the X axis is asked, the kilometer where the node is located in, and when the Y axis is asked, the height code of that node is requested. Thus, the coordinates of the point of intersection that we need to add extra will be given to the application, and now a mandatory point of intersection will be added in addition to the automatically found point of intersection.

```
prompt = 'Do you want to insert peak Y/N:';
yesno = input(prompt, "s");
if yesno=='y'
number_range = input('Please input the insert number :', "s");
number_range=str2num(number_range);
user_range_insert=[];
for i=1:number_range
prompt = "please input x "+num2str(i)+" :";
number_range = input(prompt, "s");
number_rangex=str2num(number_range);
user_range_insert(i,1)=number_rangex;
prompt = "please input y "+num2str(i)+" :";
number_range = input(prompt, "s");
number_rangey=str2num(number_range);
user_range_insert(i,2)=number_rangey;
end
else
   user_range_insert=[];
end
```

Figure 3. Application coding of mandatory point of intersections addition

As seen in Figure 4 by the application, the designer will be asked whether there are the point of intersections that need to be removed first. In this way, if there are intervals where the corner points should not exist due to the project, they will be entered by the designer. Of course, at this stage, the application will need the starting and ending kilometers of the intervals where there should not be a point, and if these intervals are entered, if there is a node, it will be removed.

```
prompt = 'Do you want to remove the range data for peak Y/N:';
yesno = input(prompt, "s");
if yesno=='y'
number_range = input('please input the number of Range:', "s");
number_range=str2num(number_range);
user_range=[];
for i=1:number_range
prompt = "please input x start "+num2str(i)+" :";
number_range = input(prompt, "s");
number_rangex=str2num(number_range);
user_range(i,1)=number_rangex;
prompt = "please input x end "+num2str(i)+" :";
number_range = input(prompt, "s");
number_rangey=str2num(number_range);
user_range(i,2)=number_rangey;
end
else
   user_range=[];
end
end
```

Figure 4. Application coding required for point of intersections removal

Grade Line Slopes

Slope limits are determined for each road class in the highway specification. In this study, the maximum and minimum slopes of the grade line up and down should be determined as shown in Figure 5. In other words, a road project should be designed according to the maximum and minimum slopes and the slope of the grade line should not exceed these limits throughout the project.
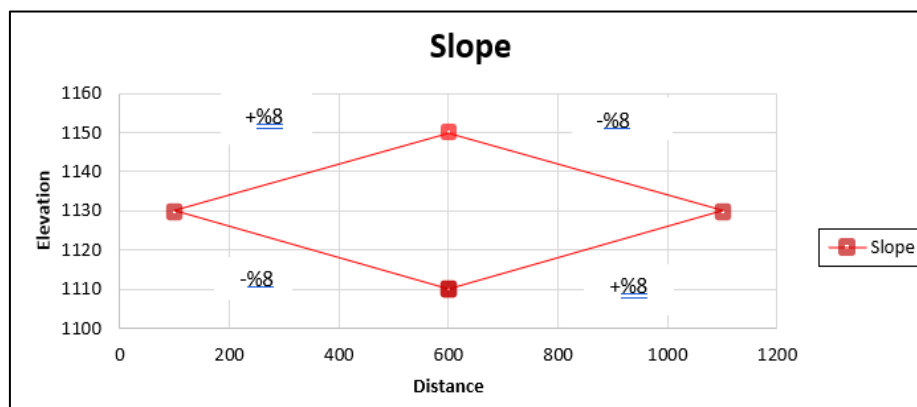
Figure 5. Maximum and minimum slope values

Maximum and minimum slopes will be asked from the designer by the designed application as shown in Figure 6. Within the scope of this study, 8% for the maximum slope of the project and 0.5% for the minimum slope will be accepted and the grade line design will be carried out between the determined slope limits. Accordingly, grade line parts outside the slope limits will be disabled and will not be included in the calculations.

```
slope_valuemax = input('please input the max slope:', "s");
% slope_valuemax=0.08;
slope_valuemax=str2num(slope_valuemax);


slope_valuemin = input('please input the min slope:', "s");
% slope_valuemin=0.005
slope_valuemin=str2num(slope_valuemin);
```

Figure 6. Application coding of maximum and minimum slopes

Cut-Fill Areas

Grade line generally consists of vertical Alignment and vertical curves. As explained above, if every element of the grade line is designed by optimizing, the amount of excavation can be minimized. In this context, the straight parts of the grade line will be passed according to the condition of the ground and the cut-fill amounts will be tried to be equal. In the red line design, first, the straight segments of the grade line will be passed in a way that equalizes the regions above and below the ground line. However, even if the correct parts to be passed at this stage are made with care, it is still almost impossible to equalize the cut fill amount exactly. Accordingly, the areas above (Cut) and below (Fill) the grade line will be calculated and equalized by the application. At the same time, we will minimize the amount of excavation by keeping the amount of these areas at

a minimum level. If the areas shown in Figure 7 are equal, it means that the most appropriate grade line design has been realized.
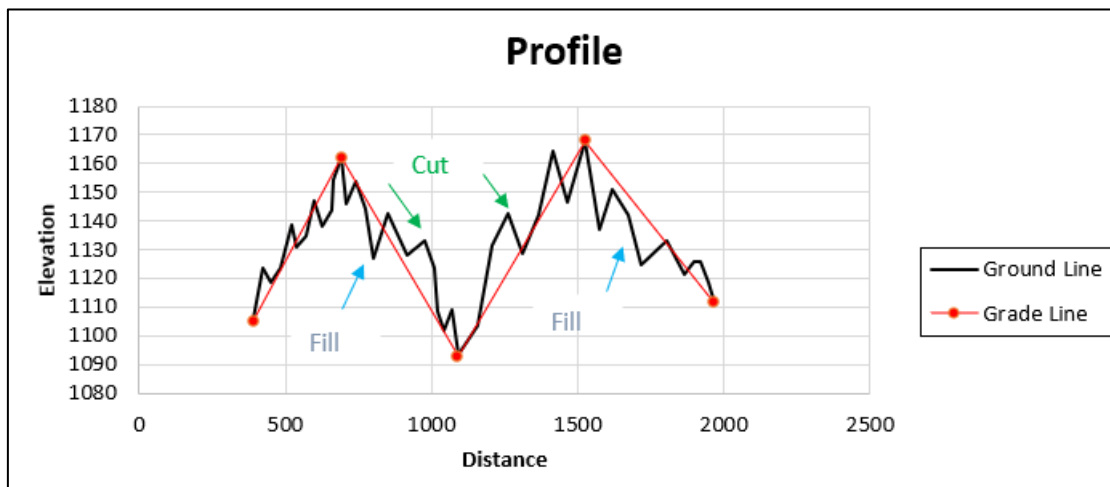
Figure 7. An example of the calculated area by using filling and cutting

Coordinate of Point of Intersections on the Ground Line

In the profile design, the places of the joint points are displaced thousands of times on both the X and Y axis, as seen in figure 8, thanks to the designed application. In this context, it becomes an undeniable fact that at every change of point of intersections, they will coincide with different places on the ground line. If we are to summarize this situation, there are different black jeans for each node. In this context, help will be taken from formula 1 in finding the black jeans for different points along the road.
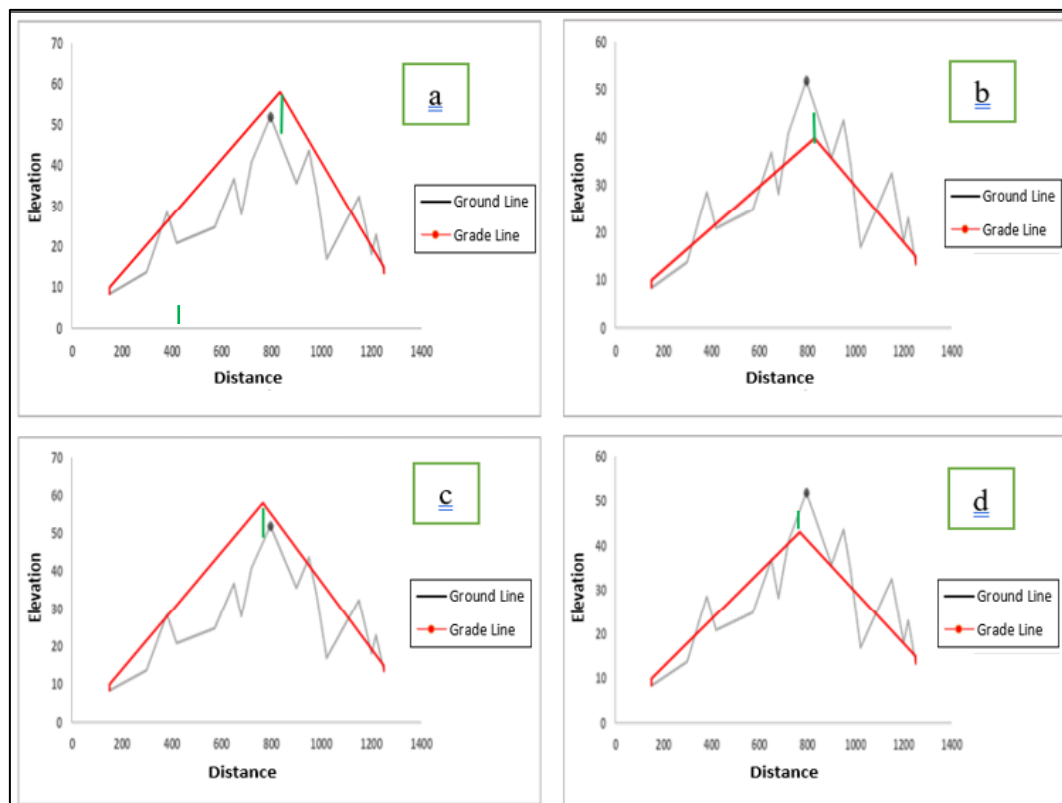
Figure 8. The situation of the point of intersection on the land

With aid of the formula 1 below, the coordinate of any node will be found on the ground line. Thus, the coordinate of the junction point on the land will be calculated as shown in Figure 9. Coordinates of points A (a, b) and B (c, d) are known from the beginning of the project as they are land elevations. Where the Point of the intersection will coincide on the ground line, that is, the X and Y coordinates are found from the formula below. Of course, at this stage, the X coordinate shows the kilometer on the Profile. In other words, the X coordinate is the same for the ground line and grade line for each node.

$$Y = \frac{X(d-b) - ad + cb}{c-a} \qquad (1)$$
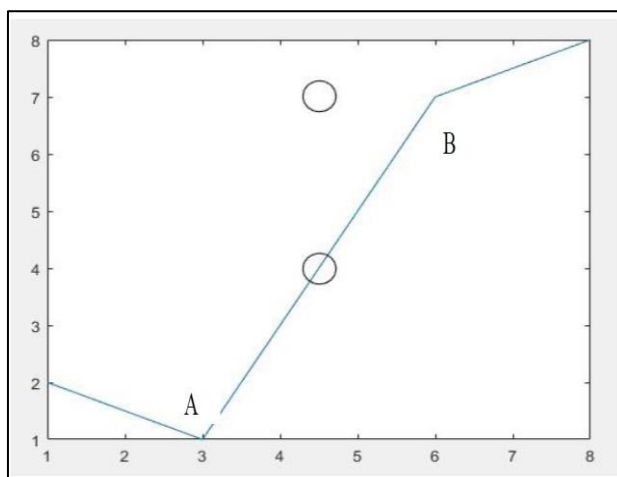
Figure 9. Ground line coordinates

Optimization of Point of Intersections of the Grade Line

Optimization over the areas described above examines the situation where the difference between the areas of the Cut-fills is zero, which is the most important point of the excavation, that is, using the excavated Cut amount in the fill areas and with almost zero excess material behind. Within the scope of this study, the intersection points of the designed grade line were examined on the X and Y axis of the coordinate system as seen in Figure 10.
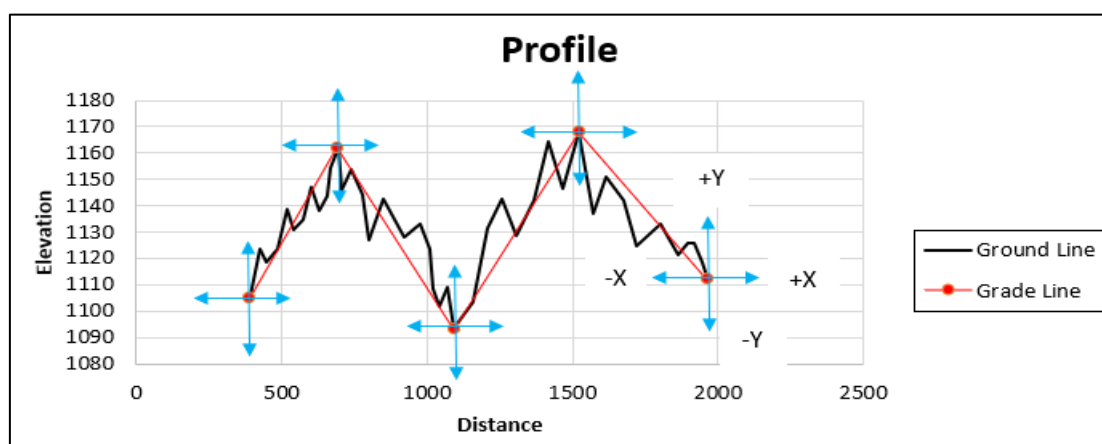
Figure 10. Controlling on the X and Y axis

For the optimization of points of intersections, examinations are made in the X and Y directions of the coordinate system by creating a matrix for each node. In other words, if we move the point of intersection up or down, maybe the Cut fill amounts will change and even cause us to

pass a more optimal grade line. In this context, since there are thousands of variables that can occur around it, points of intersections are accepted randomly by the algorithm. Of course, the higher the number of these random points, the more optimized our grade line will be designed. These areas that change in the X and Y directions will be calculated again because the Cut-fill areas change accordingly each time a change is made. Thus, it becomes an undeniable fact to use an optimization method to perform these complex calculations since there is a lot of mathematical operation involved in the realization of this method.

The application should define how much of an opening the matrix of a point of intersection will cover in the horizontal and vertical directions. In other words, a range of displacement must be specified at the point of intersections. In this coordinate system, the intervals on the X and Y axis for each node point in this coordinate system are shown with application coding in Figure 11. As seen in the application coding, the range of variability is entered separately at the start-end and mid-points. In this context, by adding a certain distance to the X and Y coordinates of each node automatically found by the application, an opening will be defined to the right, left, up, and down sides as much as that distance, and it will be possible to change the place of the node within these intervals.

```
VarMin(1)=y(1)-10;               % Lower Bound of Variables
VarMax(1)=y(1)+10;               % Upper Bound of Variables
VarMin(2)=y(cutterpeak_idx)-10;  % Lower Bound of Variables
VarMax(2)=y(cutterpeak_idx)+10;  % Upper Bound of Variables
VarMin(3)=y(end)-10;             % Lower Bound of Variables
VarMax(3)=y(end)+10;             % Upper Bound of Variables

VarMin(4)=x(1)-10;               % Lower Bound of Variables
VarMax(4)=x(1)+10;               % Upper Bound of Variables
VarMin(5)=x(cutterpeak_idx)-10;  % Lower Bound of Variables
VarMax(5)=x(cutterpeak_idx)+10;  % Upper Bound of Variables
VarMin(6)=x(end)-10;             % Lower Bound of Variables
VarMax(6)=x(end)+10;             % Upper Bound of Variables
```

Figure 11. Coding of the change interval for each point of intersection

Vertical Curve Optimization of Grade Line

In road projects, straight segments of the grade line are passed over the ground line and a vertical curve should be made at the intersections of these straight segments, that is, at the point of intersections. As seen in Figure 12, a vertical curve is placed at the intersection of the line segments that cut the ground line.
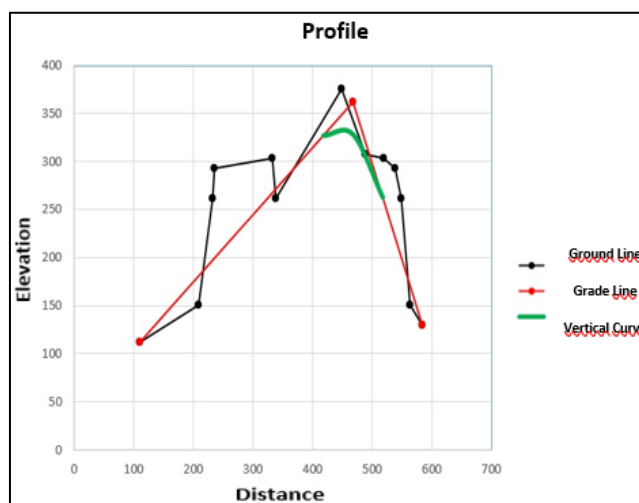
Figure 12. Placing the vertical curve at the point of intersection

The grade line visible above, as well as the vertical curve present at the nub, is more clearly shown in Figure 13.
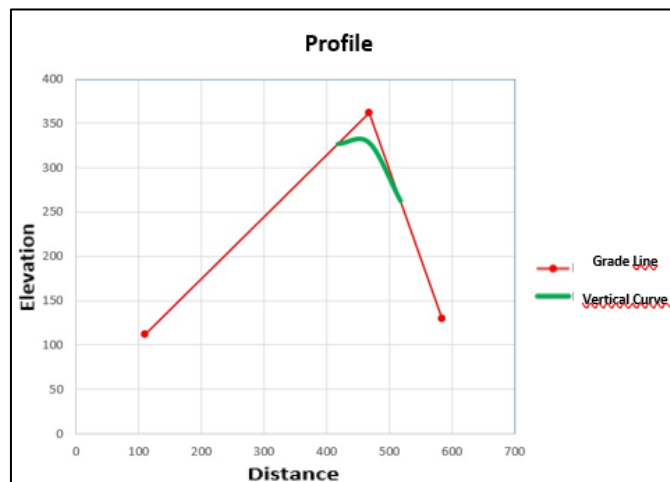
Figure 13. Vertical curve placement at the point of intersection

Vertical Curve Coding

In this context, hundreds of lines of coding must be written to integrate the same vertical victim with complex mathematical operations into the application. In Figure 14, some application related to this coding is shown in order. In this coding, which is made as an example, first, a coordinate is given to the grade line as a hypothetical. Then the slopes of this grade line will be calculated. After the slope calculation is made, the vertical curb length will be entered into the application by asking the designer. With these data, Vertical curve calculation operations will be performed very quickly by the application, even if it consists of complex operations.

```
xa=110,70
ya=111,80
xb=468,10
yb=361,40
xc=584,40
yc=130,20

x=[xa;xb;xc];
y=[ya;yb;yc];
plot(x,y)

g1=(yb-ya)/(xb-xa);
g2=(yc-yb)/(xc-xb);

G=abs(g1-g2);
prompt = 'What is the original value? ';
L = input(prompt);
T=L/2
E=(L*G)/8
KMT1=xb-T
KMT2=xb+T
KOTT1=yb-(g1*T)
KOTT2=yb+(g2*T)
KOTS=yb-E
xy=[KMT1 KOTT1;xb KOTS;KMT2 KOTT2];

hold on
fnplt(cscvn(xy'),'r',2)
hold off
```

Figure 14. Vertical curve application coding

453

Findings and Discussion

Vertical Curve Optimization Using Meta-Heuristics Algorithms

In road projects, straight segments of the grade line are passed over the ground line and a vertical curve should be made at the intersections of these straight segments, that is, at the point of intersections. As seen in Figure 15, a vertical curve is drawn at the point where the line segments intersecting the ground line intersect.
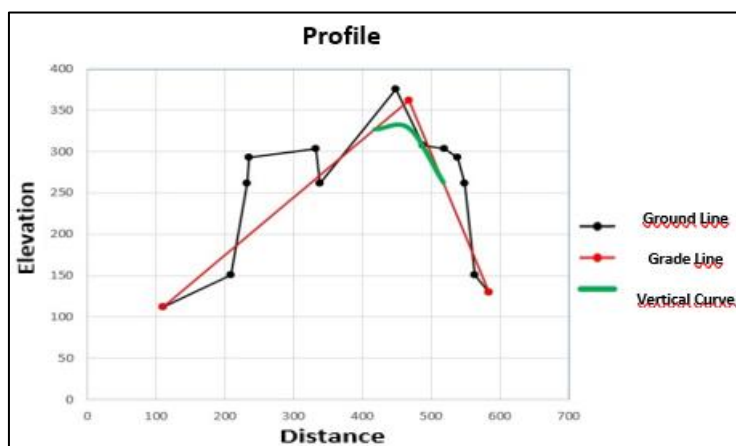
Figure 15. Placing the vertical curve at the point of intersection

Vertical Curve Implementation with Meta-Heuristics Algorithms

The grade line visible above and also the vertical curve present at the apex are shown in Figure 16 alone. In this context, lines of coding are required to integrate the vertical victim into meta-heuristic optimization algorithms.
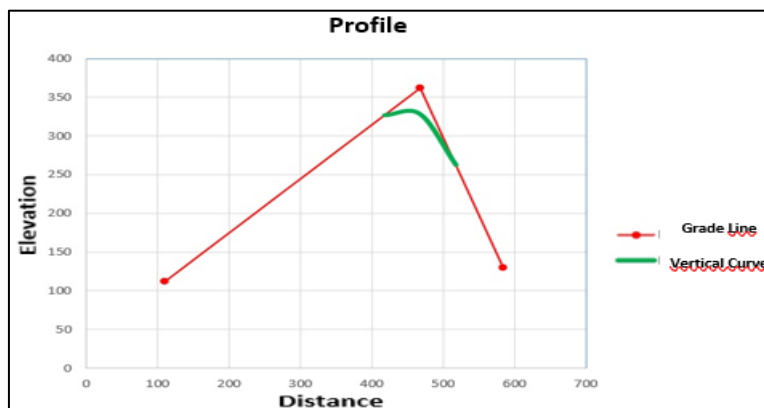
Figure 16. Vertical curve placement at the point of intersection

Vertical Curve Optimization

If vertical curve coding is integrated into the straight parts of the above-mentioned grade line, a vertical curve is passed to the grade line, which is shown in Figure 17 and exactly in Figure 18. With the aid of the application, it was possible to place a vertical curve between the straight parts of the grade line.

One vertical curve is made by the application for the grade lines drawn during the design with any optimization method, and thanks to this application, a vertical curve is passed separately for each node, despite the thousands of displacements of the node in the X and Y directions. In Figure 19, it is observed that the displacement of the junction point and the vertical curves change accordingly.
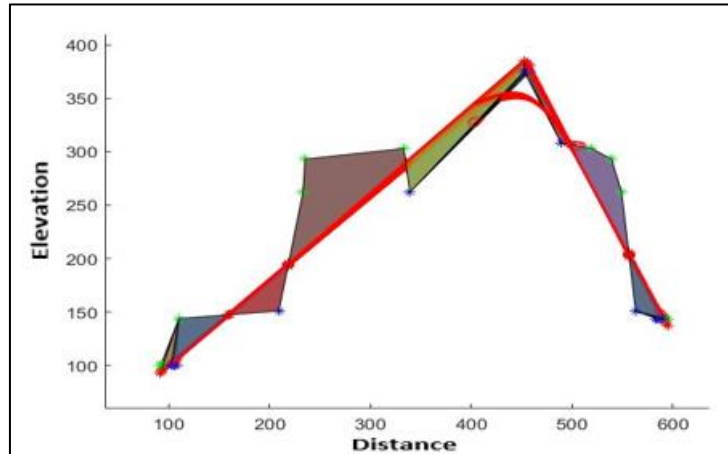
Figure 17. Vertical curves applied to grade lines
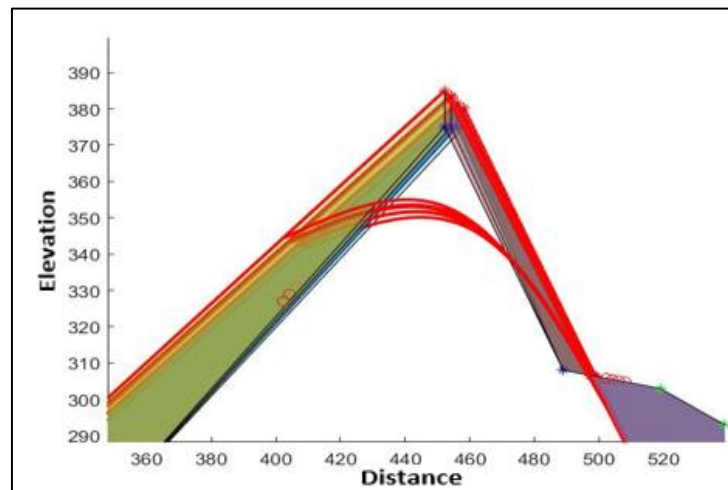
Figure 18. A separate vertical curve application for each point of intersection
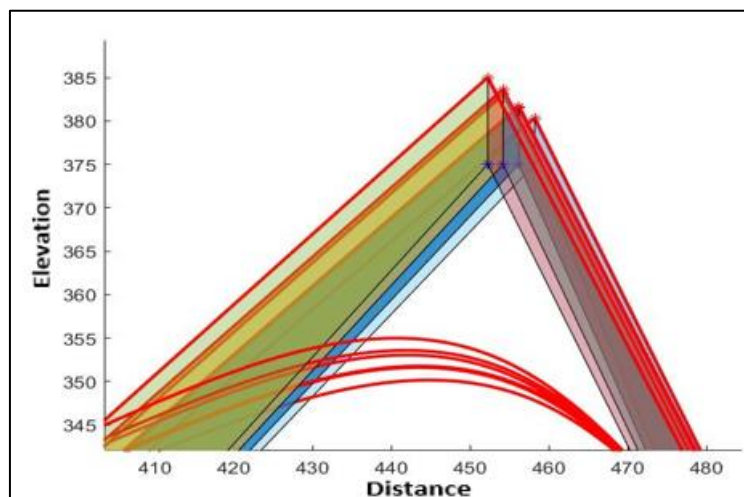
Figure 19. Displacement of the axes on the X and Y axis and the vertical curve

Elevations on the Ground Line of the Vertical Curve

In highway design, while optimizing the grade line, the vertical victim should create closed zones with the ground line. Of course, for the formation of these closed areas, this situation should be ensured by lowering the verticals from the curve start and end points to the ground line. The

height elevations of the points where these vertical lines and the ground line intersect will be found by the coding shown in Figure 20. Also, the locations of these intersection points are shown in Figure 21.

```
[KMT1,KOTT1,xs,KOTS,KMT2,KOTT2]=curve3point(xyvector(4),xyvector(1),xyvector(5),xyvector(2),xyvector(6),xyvector(3))



[pointyhat1,pointx1] = ziyaafn(y,x,[KOTT1 KMT1] )
[pointyhat2,pointx2] = ziyaafn(y,x,[KOTT2 KMT2] )
plot(pointx1,pointyhat1,'or')
plot(pointx2,pointyhat2,'or')

lx= x((pointx1<x) & (x<pointx2))
ly= y((pointx1<x) & (x<pointx2))


point_curv_x=[pointx1,pointx2]
point_curv_y=[pointyhat1,pointyhat2]


plot(point_curv_x,point_curv_y,'or')
```

Figure 20. Application coding of vertical curve and ground line relationship
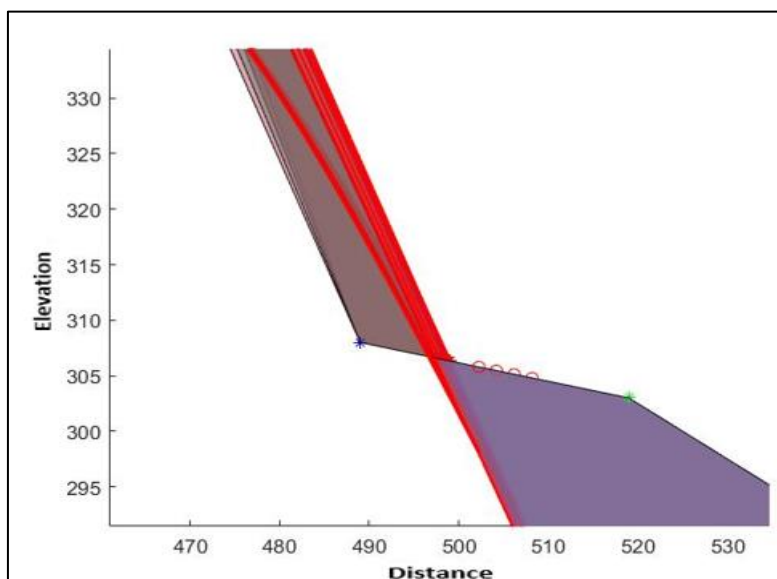
Figure 21. Height of vertical curve above ground line

Selecting the Optimum Vertical Sacrifice

As it is known during the optimization of the grade line, the grade line does not consist of just the right parts. In other words, a vertical curve must be placed between these straight segments, that is, where the point of intersections are found. However, since thousands of vertical curves will be passed during optimization, the vertical curve with the most optimum Cut fill should be selected. In this context, vertical curves passed through the point of intersections of the grade line can be either a stream vertical curve or a peak vertical curve, depending on the situation. In the selection of the optimum vertical curve, where the vertical curve should be, only the vertical curve at the top, which is closest to the point of intersection, out of thousands of vertical curves passed by the application, and at the same time, the vertical curve at the bottom, which is the closest to the point of intersection, where the stream should be vertical curve. should be selected. Thus, all vertical curves must be optimized throughout the project to optimize the entire project in the grade line design. An optimum peak vertical curve is shown in Figure 22 as an example.
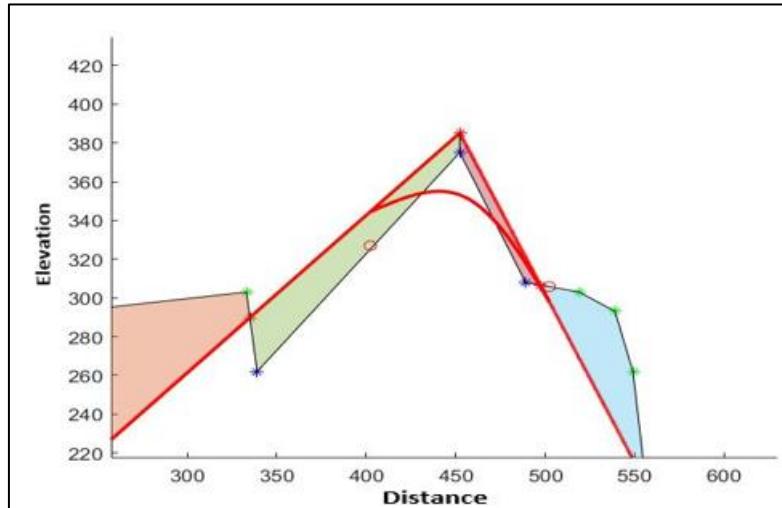
Figure 22. An example of an optimum peak vertical curve

Conclusion

In the implementation, a coordinate was given to the grade line as a hypothetical. Then, the optimization of the correct parts of this grade line has been performed. However, vertical curves must be added between these straight segments. In this context, the vertical curve length must be entered into the application. With these data, vertical curve calculation operations were performed very quickly by the application, even if it consisted of complex operations. Thus, in vertical curves, the vertical curve closest to the curve should be selected, and at the same time, the vertical curve, which is closest to the curve, is selected by the application as the most optimal vertical curve in places where there is a creek vertical curve.

References

Al-Sobky, A. S. (2014). An optimization approach for highway vertical alignment using the earthwork balance condition. World Applied Sciences Journal, 29(7), 884-891.

Asherlou, S., Yelghi, A., Pancar, E. B., & Oruç, Ş. (2022). An optimization approach for highway alignment using metaheuristic algorithms. Meta-heuristic Optimization Techniques: Applications in Engineering, 10, 11.

Babapour, R., Naghdi, R., Ghajar, I., & Mortazavi, Z. (2018). Forest road profile optimization using meta-heuristic techniques. Applied Soft Computing, 64, 126-137.

Bosurgi, G., Pellegrino, O., & Sollazzo, G. (2013). A *PSO* highway alignment optimization algorithm considering environmental constraints. Advances in Transportation Studies, (31).

Casal, G., Santamarina, D., & Vázquez-Méndez, M. E. (2017). Optimization of horizontal alignment geometry in road design and reconstruction. Transportation Research Part C: Emerging Technologies, 74, 261-274.

Chew, E. P., Goh, C. J., & Fwa, T. F. (1989). Simultaneous optimization of horizontal and vertical alignments for highways. Transportation Research Part B: Methodological, 23(5), 315-329.

Coello, C. A. C., Pulido, G. T., & Lechuga, M. S. (2004). Handling multiple objectives with particle swarm optimization. IEEE Transactions on evolutionary computation, 8(3), 256-279.

De Oca, M. A. M., Stutzle, T., Birattari, M., & Dorigo, M. (2009). Frankenstein's PSO: a composite particle swarm optimization algorithm. IEEE Transactions on Evolutionary Computation, 13(5), 1120-1132.

Easa, S. M. (1988). Selection of roadway grades that minimize earthwork cost using linear programming. Transportation Research Part A: General, 22(2), 121-136.

Fwa, T. F. (1989). Highway vertical alignment analysis by dynamic programming. Transportation Research Record, 1239(1-9), 2-3.

Fwa, T. F., Chan, W. T., & Fwa, Y. P. (2002). Optimal vertical alignment analysis for highway design. Journal of transportation engineering, 128(5), 395-402.

Ghanizadeh, A. R., & Heidarabadizadeh, N. (2018). Optimization of vertical alignment of highways in terms of earthwork cost using colliding bodies optimization algorithm. دانشگاه علم و صنعت ايران, 8(4), 657-674.

Goh, C. J., Chew, E. P., & Fwa, T. F. (1988). Discrete and continuous models for computation of optimal vertical highway alignment. Transportation Research Part B: Methodological, 22(6), 399-409.

Goktepe, A. B., & Lav, A. H. (2003). Method for balancing cut-fill and minimizing the amount of earthwork in the geometric design of highways. Journal of transportation engineering, 129(5), 564-571.

Goktepe, A. B., & Lav, A. H. (2004). Method for optimizing earthwork considering soil properties in the geometric design of highways. Journal of surveying engineering, 130(4), 183-190.

Göktepe, A. B., Altun, S., & Ahmedzade, P. (2009). Optimization of vertical alignment of highways utilizing discrete dynamic programming and weighted ground line. Turkish Journal of Engineering and Environmental Sciences, 33(2), 105-116.

Goktepe, A. B., Lav, A. H., & Altun, S. (2005). Dynamic optimization algorithm for vertical alignment of highways. Mathematical and Computational Applications, 10(3), 341-350.

Jha, M. K., & Schonfeld, P. (2004). A highway alignment optimization model using geographic information systems. Transportation Research Part A: Policy and Practice, 38(6), 455-481.

Kang, M. W., Jha, M. K., & Schonfeld, P. (2012). Applicability of highway alignment optimization models. Transportation Research Part C: Emerging Technologies, 21(1), 257-286.

Kim, E., Jha, M. K., & Son, B. (2005). Improving the computational efficiency of highway alignment optimization models through a stepwise genetic algorithms approach. Transportation Research Part B: Methodological, 39(4), 339-360.

Kim, E., Jha, M. K., Schonfeld, P., & Kim, H. S. (2007). Highway alignment optimization incorporating bridges and tunnels. Journal of Transportation Engineering, 133(2), 71-81.

Moreb, A. A. (1996). Linear programming model for finding optimal roadway grades that minimize earthwork cost. European Journal of Operational Research, 93(1), 148-154.

Ozkan, E., Tuydes-Yaman, H., & Acar, S. O. (2021, February). Vertical alignment optimisation in highway design by means of mesh adaptive direct search. In Proceedings of the Institution of Civil Engineers-Transport (pp. 1-12). Thomas Telford Ltd.

Sütaş, İ., & Öztaş, G. (1983). Karayolu inşaatında uygulama ve projelendirme. Teknik Kitaplar Yayınevi.

Yang, X. S., & Press, L. (2010). Nature-inspired metaheuristic algorithms second edition.

Yelghi, A., & Tavangari, S. (2022). Features of metaheuristic algorithm for integration with ANFIS model (No. 7594). EasyChair.

Liquid Chromatography Methods for the Determination of Beta-Carotene in Vegetable and Fruit Samples- an Evaluation of the Last Decade

Fatoş Ayça Özdemir Olgun[1]

Introduction

Carotenoids are compounds that cannot be synthesized by human-beings and animals, but are synthesized only by plants and microorganisms. An important carotenoid, β-carotene is a natural pigment found in many fruits and vegetables and also widely used in the food industry. By definition, natural pigments are pigments derived from living organisms or cells. Color can be obtained in nature from fruits, roots, seeds of plants, insects and other biological species. Beta-carotenes are high in colorful fruits and vegetables such as broccoli, brussels sprouts, bell peppers, tomatoes, spinach, carrots, sweet potatoes, zucchini, paprika, apricots, pink grapefruit, cherries, mangoes, papayas and peaches. They are also used as a coloring agent for foodstuffs such as margarine, butter and many soft drinks, as they also have natural pigment properties.

Besides being a natural colorant, β-carotene is an important antioxidant compound that acts as a precursor to vitamin A. For this reason, it has an important role in the human body as an antioxidant that can reduce the risk of cardiovascular diseases and certain types of cancer. People, low in vitamin A show histopathological changes in the pulmonary epithelium and lung parenchyma, resulting in an increased risk of lung dysfunction and respiratory disease. Various studies have reported that fruits and vegetables containing micronutrients can increase immune function. These micronutrients, such as vitamin E, vitamin C, and β-carotene (vitamin A), are antioxidants. In the COVID-19 disease, which affects the world, it has been determined that apart from the social measures taken, the nutritional habits of the people also play an important role in the course of the disease (Topuz, 2020).

Considering all the above-mentioned properties of β-carotene, it is important to determine the rates of presence in vegetables and fruits, both in terms of dietary intake of this antioxidant type, which cannot be synthesized by our body, and its use as a colorant in the food industry. Within the scope of this chapter, the chromatographic methods used for the determination of β-carotene in fruit and vegetable samples were examined and evaluated in line with the studies in the literature. I hope that this study will shed light and provide insight for future studies for researcher readers working with β-carotene.

Caretenoids

Carotenoids constitute one of the most important pigment groups found in nature with their wide distribution, structural differences, wide range of effects and functions, which function as an auxiliary pigment in photosynthesis in plants and photosynthetic bacteria, giving colors ranging from yellow to red (Olson, 2006). They also protect against photosensitization (light sensitivity) in animals, plants and bacteria. Animals store carotenoids in their tissues by modifying them because they cannot synthesize them (Rodriquez et. al., 2001). Carotenoids act only as Vitamin A

(Provitamin A) in the human body. At the same time, they can have different effects such as antioxidant activity, strengthening of the immune system, inhibition of cell mutation and transformation, non-photochemical fluorescence quenching (Olson, 1999). In adults, dietary carotene intake and blood carotene concentration provide positive health outcomes such as reduced cancer risk, prevention of cardiovascular disease, elimination of age-related stains, and improved conceptual understanding (Von Elbe et. al., 1996).

There are 600 different types of carotenoids derived from natural sources (Olson, 2006). These molecules are found in all green leafy vegetables as well as in red, yellow and orange colored fruits and vegetables. However, the chlorophyll molecule found in green leafy vegetables masked the yellow to red color of the carotenoids (Von Elbe, 1996).

Carotenoids are the molecules that belong to the isoprenoid group and have a skeletal structure of 40 carbons, which are formed as a result of covalent bonding of eight isoprene units (Figure 1) (Morrison, 1954).
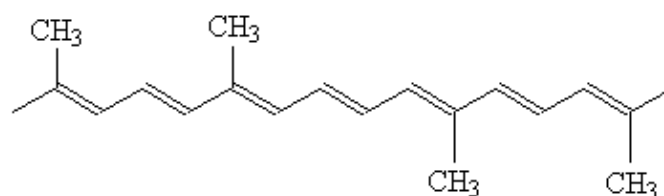
Figure 1. Polyisoprenoid structure of carotenoids

According to their chemical composition, carotenoids are divided into two main classes: "carotenes" consisting of only hydrocarbon chains and "xanthophylls", which are defined as carotenoids containing oxygen. The main ones of the carotene group consisting of hydrocarbon chains with nonpolar properties are; α-carotene, β-carotene and lycopene. Xanthophylls, on the other hand, are more polar and contain oxygen in the form of methoxy, hydroxy, keto, carboxy and epoxy 4. Examples of xanthophylls are β-cryptoxanthin, zeaxanthin, and lutein. Figure 2 shows the structure of carotenoids commonly found in foods.
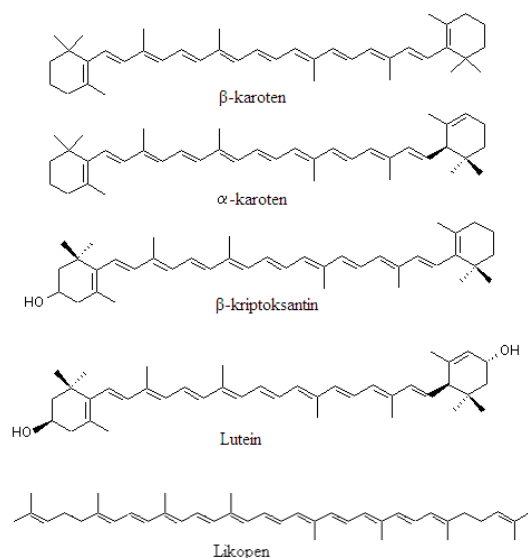
Figure 2. Some carotenoids found in foods

Different pigments are formed as a result of the cyclization of the hydrocarbon skeleton in the isoprene structure or the oxidation of the end points. Thanks to the conjugated double bond in the structure of almost all carotenoids, they absorb light in the visible region of the spectrum, and it is easy to determine their biological functions such as energy transfer and protection of cells from the harmful effects of light (Deming et. al., 1999; Krinsky, 1990). This means that they show maximum absorption at wavelengths of about 430–480 nm (Von Elbe et. al., 1996). They may be found in free form (crystalline or amorphous) or dissolved in oil in plant tissues (Von Elbe et. al., 1996) and have a boiling point varying between 130-220 °C (Britton et. al., 1995)

Of the approximately 600 different carotenoid molecules identified in nature, only 50 of those containing β-rings show provitamin A activity. All-trans-β-carotene, which has two β-rings in its structure, has the highest provitamin A activity since it is degraded to 2 molecules of retinal in the intestine. In contrast, 13-cis-β-carotene (53%) and 9-cis-β-carotene (38%) have lower provitamin A activity. Apart from provitamin A activity, isomerization also affects the antioxidant activity of carotenoids (Schieber et. al., 2005)

Tablo 1. Vitamin A Activity of β-carotene Isomers

Isomer	Activity of Vitamin A (%)
All-trans- β-carotene	100
9-cis-β-carotene	38
13-cis-β-carotene	53

The historical development of β-carotene began with its isolation from carrots by Wachenroder in 1820. After Willstaetin's molecular formula of β-carotene was determined in 1906, its chemical formula was elucidated between 1939 and 1941. After it was synthesized in the laboratory in 1953, it was produced synthetically. Since 2010, it has started to be used as a functional food additive with its antioxidant properties that support the immune system, its anticarcinogenic function against some cancers and its efficiency-enhancing effects in animals, and it still maintains its importance by today's researchers.

Beta-carotene is the precursor of vitamin A and is the most important of the provitamin A molecules. As a result of its degradation, two molecules of retinol are formed, which are then metabolized to retinol and retinoic acid. It has a skeleton containing C40 atoms in its β-carotene structure, this skeleton structure contains carbon and hydrogen atoms but no oxygen atoms. β-carotene, with the general formula $C_{40}H_{56}$ (Figure 3), consists of two beta-ionone rings at both ends of an aliphatic isoprenoid chain symmetrically linked to methyl groups (Olson, 2006).
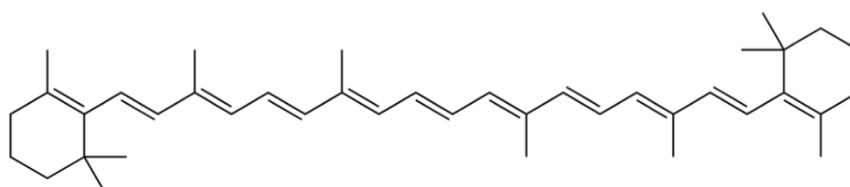
Figure 3. Chemical Structure of β-carotene

The double bond system ensures that the colors of the carotenoids are formed and the light absorbed during photosynthesis is transferred to the chlorophyll. Thanks to this feature, beta carotene reflects a bright orange-red color. In the figure below, the UV-visible molecular absorption spectrum of the β-carotene molecule is displayed, and it is obvious to see a shouldered peak between 400-500 nm. The reason for this is that the green-blue color in this region is absorbed by the molecule and reflects the red-orange color.
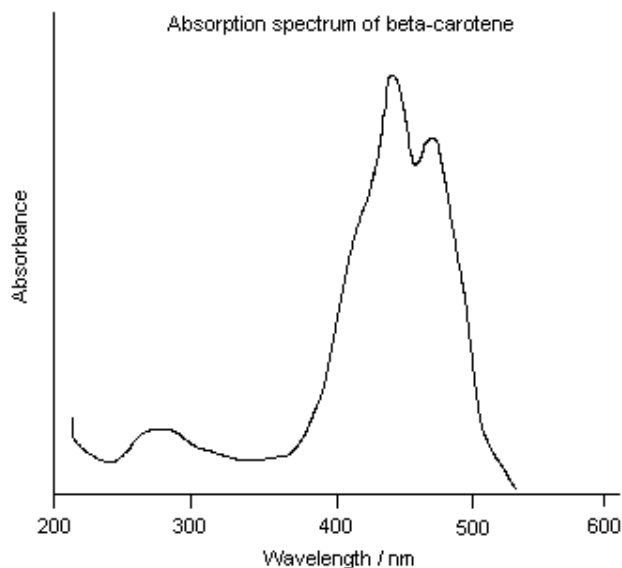
Graphic 1. UV-Visible Spectrum of beta-carotene

It also contributes to photosynthesis by transferring energy and protecting cells from the harmful effects of light (Deming et. al.,1999) Factors such as oxygen, temperature, light, pH, sulfites, water activity are effective in the oxidative breakdown of carotenoids.

With all these efficient properties, β-Carotene takes place in the food industry as a precursor to vitamin A, a natural colorant and a strong antioxidant (Shishi et. al., 2016).

Beta-Carotene

Beta carotenes are the most widely consumed plant-derived pigments. They are usually found on plants with bright orange and green colours. These include carrots, sweet potatoes, pumpkin, broccoli, even red palm oil and vitamin supplements. The amount of vitamin A obtained from beta carotenes is directly related to the source from which they are obtained. β-carotenes from citrus and vegetables are more absorbed and more biocompatible than leafy greens.

α-and β-carotenes constitute approximately 90% of the total carotenoid content present in plants. Although the amount in plants varies according to the plant species, its leaves contain 5-10 times more carotenoids than their stems (Giuffrida et. al., 2012).

As a plant source of β-carotene, there are fruits such as apricots, melons, peaches, dates, vegetables such as carrots, pumpkins, spinach, peppers, and green plants that grow naturally in meadows and pastures.

Crustaceans such as shrimp, crabs, lobsters, and fish such as salmon are sources of animal sourced carotenoids (Shahidi et. al., 1998). It is also commonly found in milk and dairy products, meat, eggs, and liver (Simpson et. al., 1985).

Functions of Beta-Carotene

Effect of Provitamin A

Among the 600 carotenoids identified in nature, there are approximately 50 carotenoids that show provitamin A activity, that is, contain a β-ring. Some known carotenoids with provitamin A activity; Alpha Carotene, Beta Carotene, Betaoxide Carotene, Semi beta Carotene, Gamma Carotene..)

Since there is a β-ion ring on each side of the β-carotene molecule, theoretically, one molecule of β-carotene has the potential to break through the middle to form two molecules of vitamin A. Two molecules of vitamin A are formed when one molecule of β-carotene is broken down in the organism by means of a special enzyme (β-carotene 15.15' dioxygenase) and other hydrolases, especially found in the intestine and liver. Therefore, the synthesis of vitamin A generally takes place in the small intestine mucosa and liver (Morrison et. al., 1954).

Antioxidant Effect

The antioxidant effect is generated by protecting cells and organisms against oxidation. In this process, as a result of the reaction with free radicals, singlet oxygen ($1O^{2}*$) decomposes as a result of direct interaction with peroxide radicals. Thus, superoxide and peroxide radicals are scavenged (Jinshi et. al., 2016).

While β-carotene shows singlet oxygen scavenging properties, it also binds free radicals. Although the chemical structure is effective in this feature of carotenoids, the most important thing is the increase in the number of conjugated double bonds.

Health Effects of Beta-Carotene

Many epidemiological studies have reported that consumption of carotenoid-rich fruits and vegetables reduces the risk of cancer (Ziegler et. al., 1989; Mc Keith et. al. 2005), cardiovascular diseases and eye diseases. (Dietmar et. al., 2001; Kalt et. al., 1999; Sulaeman et. al., 2001). It was determined that the risk of lung and stomach cancers decreased especially with β-carotene intake. In addition, it is reported that β-carotene increases lymphocyte proliferation, prevents macrophage receptor loss caused by free oxygen radicals (SOR), increases the ability of natural killer cells to kill tumor cells, and prevents the transformation of cancer cells. Since the last month of 2019, the world has faced a major public health crisis with the Covid-19 epidemic caused by the SARS-CoV-2 virus. More than 77 million cases of COVID-19 have been seen worldwide, and more than one million cases have resulted in death. Apart from social precautions, people's eating habits also play an important role in the course of the disease.

The general health status and immune system of the patients are adversely affected. This diet causes metabolic diseases such as obesity and hypertension, which are risk factors for Covid-19 infection.

With the Corona virus, quarantine has become widespread to reduce the spread of the virus all over the world. During quarantine, increased macronutrient intake may be accompanied by micronutrient deficiencies, as in obesity, which is commonly associated with impaired immune systems. Therefore, during this period, it is important to pay attention to eating habits by following a healthy and balanced diet with high amounts of minerals, antioxidants and vitamins.

Various studies have reported that fruits and vegetables containing micronutrients can increase immune function. These micronutrients, such as vitamin E, vitamin C, and B-carotene (vitamin A), are antioxidants. Beta Carotene is most commonly found in sweet potatoes, carrots and green leafy vegetables. Vitamin A deficiency has been associated with an increased risk of infection. People low in vitamin A, show histopathological changes in the pulmonary epithelium and lung parenchyma, resulting in an increased risk of lung dysfunction and respiratory disease. This is especially important considering the negative effects of COVID19 on lung function (Topuz, 2020).

Beta-Carotene in Food Processing

Uses of β-carotene in the food industry may be listed as confectionery products, beverage products, bakery products, processed cheese, butter and clarified butter obtained from cow's milk, dried fruits and vegetables, fruits and vegetables in vinegar-oil-brine, fruit and vegetable preparations and breakfast cereals. According to the Turkish Food Codex Communiqué on Colorants Used in Food, the codes in which carotenoids are used as food dyes; E160, E160b, E160c, E160d, E160e and E160f.

High Performance Liquid Chromatography (HPLC) Methods of Last Decade To Determine Beta-Carotene in Fruit and Vegetable Samples

The principle behind HPLC and the chromatographic methods, in general, is the separation between different components in a sample. This separation is performed according to a series of equilibrium stages where the injected sample components interact by partitioning or adsorption between stationary and mobile phase during movement through the system. Depending on the chemical and physical properties, the components in the sample exhibit different affinities for the mobile and stationary phase and migrate along the column at different rates.

Carotene determination studies are carried out using a High Performance Liquid Chromatography (HPLC) device. The HPLC method, which is very sensitive, gives extremely sensitive results in the separation of non-volatile or easily degradable compounds at a fixed temperature.

Many studies have been conducted to identify β-carotene contents in foods by HPLC. During the analysis of β-carotene, many different techniques with different mobile phases and column properties were used according to the compatibility of the medium. The successfull findings of the last decade was tabulated in Table 2 as a summary.

Table 2. HPLC Parameters for the Determination of β-carotene in Vegetable and Fruit Samples

Sample	Column Properties	Mobile Phase	Dedection	Beta Carotene Concentration	Reference
Banana (Thailand)	C18 column (250 × 4.6mm, 5μm)	Using isocratic run of 10% Ethylacetate :Methanol (1:1, v/v) in Acetonitrile Flow rate : 1 mLmin^{-1}	UV-Vis Dedector 450 nm	645.9- 5222.6 μg 100g^{-1}	(Tongspoodsomjit et. al., 2020)
Corn	C18 column for UPLC	methanol/acetonitrile (9 : 1 v/v),flow rate of 0.5 mLmin^{-1}	UV-Vis Dedector 448nm	0.08-2.14 mgkg^{-1}	(Satarova et. al., 2019)
Animal Feed	Venusil C8 column (250 mm × 4.6 mm, 5 μm)	The mobile phase consisted of 0.1% ammonium acetate, acetonitrile, methanol and water.	UV-Vis Dedector (450 nm)	0.12–0.2 mg kg^{-1}	(Chen et. al., 2019)
Carrot	C18 column (250.0 × 4.6 mm, 5 μm)	The mobile phase was composed of 980mL of methanol and 20mL of trichloromethane Flow rate: 0.9 mL min^{-1}	UV-Vis Dedector (454 nm)	41.06 μg g^{-1}	(Dai and Row, 2019)
Fruit Juice	SB- C18 column (250 mm × 4.6 mm, 5 μm)	The mobile phase was composed of 60% acetonitrile and 40% tetrahydrofuran. Flow rate : 1.0 mL min^{-1}	UV-Vis Dedector (445 nm)	1-5 μg mL^{-1}	(Li et. al., 2019)

Fruit Juice	C18 column (4.6 × 250 mm, 5 µm)	Mobile phase isocratic elution using dichloromethane –methanol– acetonitrile at (45 :45 : 10) Flow rate : 1mL min⁻¹	UV-Vis Dedector (450 nm)	0.3-46 mg L⁻¹	(Simpson et. al., 1985)
Water-melon	C18 column (4.6 × 250 mm, 5 µM)	Mobile phase consisted of acetonitrile l (solvent A)/dichloromethane (solvent B) and methanol (solvent C) at a Flow rate of 1 mL min⁻¹	UV-Vis Dedector (450 nm)	121.6- 454.4 µg g⁻¹	(Whong et. al., 2017)
Outer Skin of Strawberry	C18 column (200 mm ×4.6 mm, 3 lm)	binary-gradient elution using an initial composition of 75% acetone and 25% deionised water Flow rate : 1 mL min⁻¹	UV-Vis Dedector (450 nm)	10.5-14.6 µg g⁻¹	(Delgado et. al., 2016)
Raw/ Cooked Sweet Potato	C18 column (200 mm ×4.6 mm, 5µm)	Mobile phase (acetonitrile : methanol : 2-propanol in the ratio of 85:15:33 with 0.01% ammonium acetate) Flow rate : 1.7mL min⁻¹	UV-Vis Dedector (450 nm)	3.50-95.29 µg g⁻¹	(Islam et. al., 2016)

Various Types of Apples	C18 column (200 mm ×4.6 mm, 3 µm) Flow rate : 1 mL min^{-1}	Acetone: Water (75: 25)	UV-Vis Dedector (450 nm)	Flesh: 2.34- 0.17 µg g^{-1} Peel: 1-35 µg g^{-1}	(Delgado et. al., 2014)
Soy-milk	C18 column (250mm ×4.60 mm, 5 µm)	Mobile phase used was methanol: THF: water 67:27:6 (v/v/v) Flow rate : 0.8 mL min^{-1}	UV-Vis Dedector (440 nm)	20-700 µg 100mL^{-1}	(Andres et. al., 2014)
Commercial Agricultural Products	(UHPLC) C18 column (100 mm, 1.8 lm)	The solvent system consisted of (Solvent A) 75:23:2 acetonitrile, water, and hexane (v/v/v; 0.1% acetic acid v/v) and B 90:8:2 acetonitrile, butanol, and hexane (v/v/v, 0.1% acetic acid v/v). Flow rate : 0.5ml min^{-1}	UV-Vis dedector (450 nm)	1.5-55µg g^{-1}	(Mc Kevith et. al., 2005)
Food Additives	C18 (30mm × 4.6 mm, 2.7µm) Precolumn GuardCartridge RP-18e (10mm × 4.6 mm)	Washing mobile phase (methanol : water; 92:8) mobile phase consisting of 100% methanol. Flow rate: 1.5 mL min^{-1}	UV-Vis Dedector (450 nm)	6.00-30.00mg	(Brabcova et. al., 2013a)
Water-melon	C30 Column (4.6 × 150 mm, 5 µm)	1:1 (v/v) mixture of MTBE and methanol.	UV-Vis Dedector (450 nm)	12-250 µg g^{-1}	(Giuffrida et. al., 2012)

		Flow rate: 1.8mL min^{-1}			
Peach (Juice/ marmalade/ jam)	C30 column (250 mm × 4.6 mm, 5 μm)	Methanol / MTBE / water (83:15:2, v / v / v; eluent A) and methanol / MTBE / water (8:90:2, v / v / v; eluent B), Flow rate: 0.8 mL min^{-1}	UV-Vis Dedector (450 nm)	1.96-1.42 μg g^{-1}	(Brabcova et. al., 2013b)
Products from tomato paste	C18 column (75 × 2.00 mm)	A methanol-water (95:5, v/v) and component B acetonitrile-dichlormethane (90:10, v/v). Flow rate : 1mL min^{-1}	UV-Vis Dedector (450 nm)	1.5-4mg 100g^{-1}	(Radu et. al., 2012)
Red Bell Pepper, Tomatoes, Strawberry	u-HPLC C18 column (2 mm × 50 mm, 2 μm)	Mobile phase was ethylacetate: acetonitrile: acetic acid (30:68:2, v/v/v) Flow rate: 0.2 mL min^{-1}	UV-Vis Dedector (450nm)	0.5 – 140 μg mL^{-1}	(Shim et. al., 2019)
Tomato and its by-products	C30 column (3.0 mm × 150mm, 5 μm)	The mobile phase consisted of solvent A (methanol) and B (methyl- tertbutyl ether (MTBE), v/v). Flow rate: 0.5 mL min^{-1}	UV-Vis Dedector (450nm)	20-125 μg g^{-1}	(Salomon et. al., 2020)

Cladenia Species	C18 column (4.6mm ×250mm, 5 μm)	Methanol: Water: Phosphoric Acid (75: 25: 0.9 v/v/v) Flow rate: 1mL min⁻¹	PDA Dedector (200-500nm)	-	(Kocakaya et. al., 2021)
Pink grapefruit, tomato paste, fresh kiwi, apricot nectar,	C30 column (250 × 4.6 mm, 5.0 μm)	Water: Methanol: Methyl tetrabutyl ether (MTBE) Flow Rate: 1mL min⁻¹	DAD Dedector	-	(Achir et. al., 2022)
Soybean Seeds	C18 column (250 × 4.6 mm, 5.0 μm)	Gradient Elution Methanol (10mM Ammonium Acetate: MTBE	UV-Vis Dedector (450 nm)	0.10-10 µgmL⁻¹	(Gebreziabhler et. al., 2021)
Carrots, Sweet Potato	R-P HPTLC (10cm × 20 cm) glass plates precoated with silica gel	Ternary Mobile Phase Ethanol: Cyctohexane: Acetone	UV-Vis Dedector	25-1000 ng band⁻¹	(Alqarni et. al., 2021)

Conclusions And Recommendations

Caretenoids are difficult molecules to analyze due to their complex structures and isomers, especially if they had been through a food precess. As far as it is known, beta-carotene which is an important member of this family generally stands together with the other carotenoid compounds. Therefore, the accurate analysis of beta-carotene may be challenging due to this similarity among the family members. In this study, the chromotographic methods for the determination of beta carotene (which is an important type of carotenoid molecules) that were proposed at the last decade were surveyed carefully, for the first time in literature, to give a basic idea for the future studies.

As it is already known, development of a HPLC method that is suitable to seperate carotenoids with good linearity, accuracy and precision is significant. Mobile phases and the analytical columns used in the determination of beta carotene generally depends on the matrix including other molecules that are to be co-analyzed with beta carotene or the ones that may be found just as interferents. The reports and studies on HPLC method for this specific analysis is infinite and it is hardly possible to make a general standardization since it depends on several factors such as matrix effect, solvent, flow rate, temperature e.t.c. But it should be indicated that, the following parameters such as limit of detection (LOD), limit of quantification (LOQ), linearity, accuracy, repeatibility and recovery should be evaluted carefully in case of method validation.

Among the suggested methods searched in this study, we may conclude that the issues like analytical duration, installation of less hazardous chemicals, reproduction and similar chemistry consideration should be evaluated and highlighted at the installation of a chromatographic technique for the determination of beta carotene in vegetable and fruit samples.

References

Achir N., Sevent A., Soto M., Mayer C. (2022). Feasibility of Individual Carotenoid Quantification in Mixtures Using UV-Vis Spectrophotometry with Multivariate Curve Resolution Alternating Least Squares (MCR-ALS). *Hindawi Journal of Spectroscopy, 1,* 1-13. DOI: 10.1155/2022/4509523.

Alqarni M. H., Alam P., Alam A., Ali A., Foudah A., Alshehri S., Ghoneim M., Shakeel F. (2021). A Greener HPTLC Approach for the Determination of -Carotene in Traditional and Ultrasound-Based Extracts of Different Fractions of Daucus carota (L.), Ipomea batatas (L.), and Commercial Formulation*, Argonomy, 11,* 2443-2457.

Andrés V., Villanueva M. J., Tenorio M. D. (2014). Simultaneous determination of tocopherols, retinol, ester derivativesandb-carotene in milk- and soy-juice based beverages by HPLC withdiode-array detection, *Food Science Technology, 58 (2),* 557-562.

Brabcová I., Hlavackova M., Satinsky D., Solich P. (2013). A rapid HPLC column switching method for sample preparationand determination of b-carotene in food supplements, *Food Chemistry 141(2),*1433-1437. DOI: 10.1016/j.foodchem.2013.04.063.

Britton, G. (1995). Structure and properties of carotenoids in relation to function, *FASEB Journal, 9,* 1551–1558.

Chen D., Wu M., Xie S., Li X., Tao Y., Wang Z., Huang L., Pan Y., Peng D., Zonghui Y. (2019). Determination of Tartrazine, Lutein, Capsanthin, Canthaxanthin and β-Carotene in AnimalDerived Foods and Feeds by HPLC Method, *Journal of Chromatographic Science, 57 (5),* 462–468, DOI: 10.1093/chromsci/bmz019.

Dai Y., Row K. H. (2019). Isolation and Determination of Beta- Carotene in Carrots by Magnetic Chitosan Beta-Cyclodextrin Extraction and High-Performance Liquid Chromatography (HPLC), *Analytical Letters, 52(11),* 1828-1843. DOI: 10.1080/00032719.2019.1570245.

Delgado-Pelayo R., Gallardo- Guerrero L., Horrero-Mendez D. (2014). Chlorophyll and carotenoid pigments in the peel and flesh of commercialapple fruit varieties, *Food Research International, 65,* 272– 281.

Delgado-Pelayo R., Gallardo- Guerrero L., Horrero-Mendez D. (2016). Carotenoid composition of strawberry tree (Arbutus unedo L.) fruits, *Food Chemistry, 199,* 165-175. DOI: 10.1016/j.foodchem.2015.11.135.

Deming, D.M. and Erdman, J.W. (1999). Mammalian carotenoid absorption and metabolism, *Pure and Applied Chemistry, 71,* 2213–2223.

Dietmar, E.B. and Bamedi, A. (2001). Carotenoid esters in vegetables and fruits: A screening with emphasis on β-cryptoxanthin esters, *Journal of Agricultural and Food Chemistry, 49,* 2064–2067.

Fleshman M., Lester G. E., Riedl K. M., Kopec R. E., Narayanasmy S., Curley R. W., Schwartz S. J., Harrison E. H. (2011). Carotene and Novel Apocarotenoid Concentrations in Orangefleshed Cucumis melo Melons: Determinations of β-Carotene Bioaccessibility and Bioavailability, *Agricultural Food Chemistry, 59 (9),* 4448-4454. DOI: 10.1021/jf200416a.

Gebreziabhler B. S., Zhang S., Qi J., Azam M., Ghosh F., Feng Y., Huai Y., Li B., Sin J. (2021). Simultaneous Determination of Carotenoids and Chlorophylls by the HPLC-UV-VIS Method in Soybean Seeds, *Agronomy*, *11*, 758. DOI: 10.3390

Giuffrida D., Torne G., Dugo P., Dugo G. (2012). Determination of the carotenoid profile in peach fruits,juice and jam, *Fruits, Journal of Tropical and Subtropical Horticulture, 68,* 39-44. DOI: 10.1051/fruits/2012049.

Ha. J., Shim. Y., Teo H., Nam H., Ito M., Nakagawa H. (2010). Rapid Method for Determination of β-Carotene in Foods Using Ultra High Performance Liquid Chromatography, *Food Science and Biotechnology, 19,* 1199-1204.

Huang X., Liu Y., Di D., Liu J., Li C. (2010). An Improved LC-DAD Method for Simultaneous Determination of Lutein, b-Carotene and Lycopene in Tomato and Its Products, *Chromatographia, 71 (3),* 331-334. DOI:10.1365/s10337-009-1417-0.

Islam S. N., Nusrat T., Begum P., Ahsan M. (2016). Carotenoids and b-carotene in orange fleshed sweet potato: A possiblesolution to vitamin A deficiency, *Food Chemistry, 199,* 628-631.DOI: 10.1016/j.foodchem.2015.12.057.

Jacop R. A., Burri B. J. (1996). Oxidative damage and defense, *American Journal of Clinical Nutrition, 63(6)*, 985-990.

Kalt W., Forney C.F., Martin A., Prior R.L. (1999). Antioxidant capacity, vitamin C, phenolics and anthocyanins after fresh storage of small fruits, *Journal of Agricultural and Food Chemistry, 47,* 4638–4644.

Kocakaya Z., Kocakaya M., Karatoprak G. Ş. (2021). Comparative Analyses of Antioxidant, Cytotoxic, and Anti-inflammatory Activities of Different Cladonia Species and Determination of Fumarprotocetraric Acid Amounts, *KSU J. Agric Nat, 24 (6),* 1196-1207.

Kongaphisith Tongpoolsomjit K., Grandmottet F., Boonruangrod R., Krueajan A., Viyoch J. (2020). Determination of β-carotene content in Musa AA pulp (Kluai Khai) at different ripening stage and harvest period in Thailand, *Emirates Journal of Food and Agriculture. 32(6),* 443-452. DOI: 10.9755/ejfa.2020.v32.i6.2114.

Krinsky, N.I., Russet, M.D., Hendelman, G.J. and Snadderly, D.M. (1990). Structural and geometrical isomers of carotenoids in human plasma, *Journal of Nutrition, 120,* 1654–1661.

Lehman R. W. (1967). *Methods of vitamin assay.* (3rd Ed.). New York: John Wiley& Sons.

Li H., Zhao C., Tian H., Yang Y., Li W. (2019). Liquid–Liquid Microextraction Based on Acid–Base- Induced Deep Eutectic Solvents for Determination of β-Carotene and Lycopene in Fruit Juices, *Food analytical Methods, 12 (12),* 2777-2784.

Maurer M. M., Mein J. R., Chaudnuri S. K., Constant H. L. (2014). An improved UHPLC-UV method for separation and quantificationof carotenoids in vegetable crops, *Food Chemistry, 165*, 475-482. DOI: 10.1016/j.foodchem.2014.05.038.

McKevith, B. (2005). A carrot a day to keep cancer away, *Nutrition Bulletin, 30,* 117– 119.

Morrison F. B. (1954). *Feeds and Feeding—A Handbook for the Student and Stockman*. (21). New York, USA: The Morrison Publishing Company.

Olson, J.A. (1993). Vitamin A and carotenoids as antioxidants in a physiological context. *Journal of Nutritional Science Vitaminol, 39,* 57-65.

Radu G. L., Litescu S. C., Albu C., Teodor C., Truica G. (2012). Beta-carotene and lycopene determination in new enriched bakery products by HPLC-DAD method, *Romanian Biotechnological Letters*, *17 (1),* 7005-7012.

Rodriguez-Amaya, D.B. (2001). *A guide to carotenoid analysis in foods,* USA: ILSI Press.

Salamon M. V., Piccoli P., Fontana A. (2020). Simultaneous determination of carotenoids with different polarities in tomato products using a C_{30} core-shell column based approach. Microchemical Journal, 159, 105-309.

Satarova T. M., Semenova V. V., Zhang J., Jin H., Dzubetskii B. V. Cherchel V. Y. (2019). Differentiation of maize breeding samples by β-carotene content, *Regulatory Mechanisms in Biosystems, 10(1),* 63–68. DOI:10.15421/021910.

Schieber, A. and Carle, R. (2005). Occurence of carotenoid cis-isomers in food: Technological, analytical and nutritional implications, *Trends in Food Science and Technology, 16,* 416–422.

Shaidi F., Metusalach A., Brown J. A. (1998). Carotenoid pigments in seafoods and aquaculture. *Critical Reviews on Food Science. 38 (1),* 1- 67. DOI: 10.1080/10408699891274165.

Sulaeman, A., Keeler, L., Gıraud, D.W., Taylor, S.L., Wehling, R.L. and Driskell, J.A. (2001). Carotenoid content and physicochemical and sensory characteristics of carrot chips deep fried in different oils at several temperatures, *Food and Chemical Toxicology, 66,* 1257–1264.

Topuz, H. S, (2020). Covid-19 Enfeksiyonunda Beslenme, *Medical Research Reports ;3*(1), 176-180.

Whong P., Songsri P., Suriharn B., Lomthaisong K., Lertrat K. (2017). Rapid assesment of lycopene and β-carotene in spiny bitter gourd (momordica cochinensinensis (lour.) spreng), *Pakistan Journal of Botanics, 49(2),* 493-497.

Von Elbe, J.H. and Schwartz, S.J. (1996). *Colorants In "Food Chemistry".* (O.R. Fennema Ed). New York: Marcel Dekker Incoperation.

Ziegler, R.G. (1989). A review of epidemiologic evidence that carotenoids reduce the risk of cancer, *Journal of Nutrition, 119,* 116–122.

Data: Concepts and Processing

Ahmet YÜCEL[1]

Introduction

The field of processing data concepts is growing exponentially. New methods are being developed to process this data and make it useful for the future of education, health technology, and other fields. Data is being generated faster than ever before. The amount of data produced in a single day today is greater than the amount of data produced in all of human history before 1900s. In the future, this may change the way we live and learn in everything from education to healthcare. As technology advances, there are more and more data concepts that need to be processed. New methods are being developed to process Big Data. The future of education and healthcare will be greatly impacted by this new technology.

Big Data is a term used to describe large amounts of data that can be difficult to manage. As with the oil mines discovered before the Industrial Revolution, it can be difficult for societies of our time, confronted for the first time with the data phenomenon, the most important mine of this age, to understand how Big Data is used or what it is used for. In this regard, it is of great importance to developing new methods both for using data and for explaining its meaning and potential. The importance of data concepts in dealing with Big Data has never been greater. Data can be collected from many sources such as social media, mobile devices, internet searches, and more. This data is then analyzed to find patterns and trends that can be used in different areas. Big Data is a term that refers to data sets that are too large or too complex to be processed by traditional database management tools. Big Data processing is the process of analyzing Big Data and extracting useful information from it. Big Data processing requires many resources such as storage space and network speed. In addition, data processing requires knowledge of coding and programming languages such as Java and Python.

In this study, we will discuss data concepts and data processing approaches. We will explain some current concepts for each phase of these critical processes of generating, transmitting, and processing data and obtaining meaningful results.

What is Data

Data are collection or metrics expressed as written documents, numerical quantities, or multimedia content. Often the concept of data is thought to consist only of numbers, but data can also be audio recordings, images, videos, or documents. Depending on the research area, the data will have different forms. For example, if you're researching the impact of global warming on polar ice caps, your data might be satellite images. But if you're researching the proportions of graduate college students who find employment after school, your data might be the number of graduates per year and the number of students finding employment. The data will be different depending on the subject studied. There are many different approaches to categorize data. However, in general, data are expressed in two categories, either qualitative or quantitative. Quantitative data are collected on a numerical scale such as temperature, density, and length, and can be compared on this scale. Qualitative data are obtained from concepts such as verbal descriptions, photographs,

[1] Dr. Öğr. Üyesi, Finans ve Bankacılık Bölümü, Ankara Yıldırım Beyazıt Üniversitesi, orcid.org/0000-0002-2364-9449

maps, etc. Analyzing data correctly and interpreting results will help us understand patterns and trends in data, provide solutions to data-related problems, or better understand scientific facts. For example, Andrić et al. examined the qualitative data of cultural heritage works and applied pattern recognition techniques to determine the details of the origin of these cultural works (Andrić, Gajić-Kvaščev, Crkvenjakov, Marić-Stojanović, and Gadžurić, 2021). Also, Villez compared two qualitative trend analyzes based on two different data sets (Villez, 2014). Data will provide us with a powerful resource in our effort to understand the physical and sociological phenomena in our environment. For example, Gantala and Balasubramaniam simulated the propagation of ultrasound waves by applying a special data-driven physical learning model using the deep neural network method (Gantala and Balasubramaniam, 2022). Also, Chabert-Liddell et al. propose a stochastic model for the analysis of multi-level networks in the context of organizational sociology (Chabert-Liddell, Barbillon, Donnet, and Lazega, 2021).
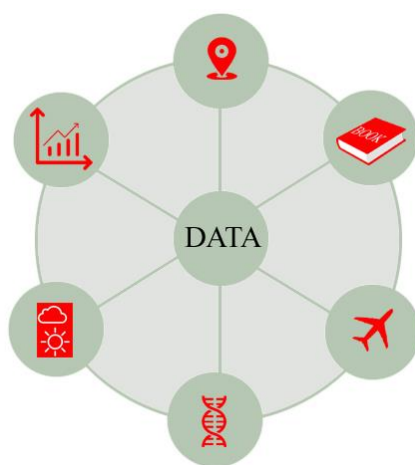
Figure 1. Data Sources

The content of data is expressed in two basic categories, quantitative and qualitative. Besides, the data can be divided into two sub-categories as structural and unstructured, depending on whether the data content is ready or not ready to be analyzed by statistical methods. Also, according to the source of the data, it can be referred to as biometric data, metadata, etc.

Structured and unstructured Data

Structured data is also known as tabular data and can be found in databases, spreadsheets, and text files. Unstructured data is any type of data that does not fall into a predefined format or classification scheme.
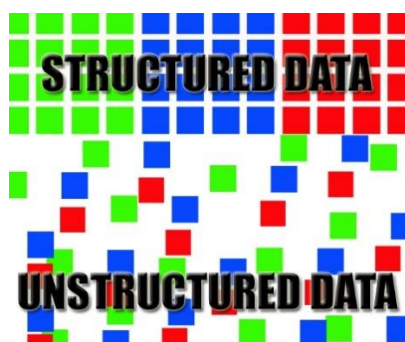
Figure 2. Structured and unstructured data

The two types of data have their own benefits and drawbacks. For example, structured data can be easily manipulated by computers. It is in a ready-to-analyze format. This can mean an

advantage or a shortened processing time. On the other hand, unstructured data provides a more natural representation of reality.

Metadata

Metadata is data that describes other data. It describes the content and format of a document. Metadata is important for many reasons. Metadata has a format that is easy to understand and interpret (McGilvray, 2008). If a person knows what metadata they are looking for, it can help them find the right document quickly and easily. Metadata also has other uses in an organization. For example, metadata helps people know when to update documents, when to archive, or where to store them (Eicken and Salganek, 2009).

Figure 3. Metadata

Biometric Data

Biometric technology, in addition to many uses, is mainly used for authentication through data based on human biometrics. Fingerprint, palm, face, etc. such that the biological characteristics of the human body are used as data. In addition, behavioral features such as voice, posture, gait, handwriting and signature are also used in biometric technology. Since each human biological characteristics are unique, unchangeable and portable, automatic biometric authentication, in particular, provides higher trust and speed compared to classical authentication. Biometric technologies scan biometric features in all their details and convert them into digital data. These data are called digital biometric codes. Produced biometric codes are transferred to microprocessors and electronic components and used for authentication purposes in system access.

Figure 4. Biometric Data

Biometric technologies, image processing, sensors, etc. are all built on digital components and artificial intelligence. Artificial intelligence is the stage that detects and interprets biometric data collected over digital components. Biometric technologies have the ability to constantly improve themselves thanks to machine learning algorithms based on artificial intelligence. Hao et al. propose an SVM-based biometric authentication system that integrates face and fingerprint data to improve the accuracy of personal identification detection (Hao et al., 2005). Machine learning processes are

basically based on big data analysis and deep learning algorithms. In this respect, biometric technologies can be thought of as a composite approach that brings together digital technologies and data science.

All over the world, countries have been investing in biometric technologies for more than 60 years (Küfeoğlu, 2022) in order to increase their market share and to be one of the pioneers of technology. Thanks to these investments, the sector continues to grow continuously and rapidly. In parallel with the development of IoT and M2M technologies, it is clear that in the coming decades, every industry based on artificial intelligence will experience significant developments and as a natural result, new investment opportunities will emerge. It is also quite clear that the market potential of the biometric technology sector, which has artificial intelligence at its center, will grow with an increasing momentum (Fairhurst, Fierrez, and Campisi, 2011).

People use the brain to see, hear, feel. It analyzes the data it collects through the senses and transforms this data into information. This information is used by the brain in decision stages, mainly for human survival. In this respect, biometric technologies produce information by imitating the methods of data collection of human senses and subsequent analysis of the brain. This process is referred to as "multi-modal biometrics" (Kumari and Thangaraj, 2020). The main goal of these technologies, based on multi-modal sensing, is for human survival and for living in safety, away from dangers. For example, the multimodal biometric approach proposed by Rajasekar et al. for smart cities, which uses biometric features such as fingerprint and iris, shows that it increases the accuracy of biometric authentication, which is critical for security (Rajasekar et al., 2022). Security is at the forefront of the use of biometric data-based technologies, but its use for purposes that facilitate human life is becoming more common day by day. From drivers' attention detection (Abate, Bisogni, Castiglione, and Nappi, 2022) to the smart city concept (Ross, Banerjee, and Chowdhury, 2020), many biometric technology application areas have begun to integrate into daily life.

What is Data Source?

Database and data warehouse

Data warehouses are a collection of databases that store the data for long periods of time. They are used to store data from different sources and provide a centralized location for analyzing and accessing the data.

A database is a set of files that stores information in tables. A table can have one or more columns, which represent fields in the database, and one or more rows, which represent records in the database. The tables are linked together by unique identifiers called keys.

Data warehouses use relational databases to store their data. These databases use SQL commands, which allow users to perform queries on their data using various clauses such as select, update, insert, delete and join.

Relational and Non-Relational Databases

Relational Databases are tables of data which are related to one another. Non-Relational Databases are not related to each other in any way and they can be easily updated.

Relational databases are the most common type of database. The data is stored in tables with rows and columns. It's organized as a series of related tables, which can be accessed by joining the tables together.

Non-relational databases don't use table-based organization to store data. They store data in a single file or document, which may contain several different types of information. This often makes them more flexible than relational databases, but they're less efficient and take up more space on the hard drive.

Data Source

Data source is a defined connection to a database, and contrary to popular belief, there is no real data in the data source. In the data source, only the database information and connection method and form are included. A database can have multiple data source connections. The available data source in the server or processor is used for data storage. The stored data can be a database or files containing tables (Oracle, 2011).

The data source is responsible for all processes from activating database connections and assigning them to the relevant database, managing them and deactivating them again. The structure in which all these connections take place is called the database connection pool. Data connection pool, which is used for effective management of database connections, which is a limited and costly tool, is widely used especially in web applications (Oracle, 2011).

Although classical approaches based on the analysis of stored data have been widely used in recent years, real-time analysis and modeling of data streams have become an urgent need in many sectors because they cannot meet the needs at the speed point. Finance, telecommunications, advertising, etc. These real-time data analysis and modeling applications are used in many industries. The ability to react quickly to rapid changes in the sectors, as well as to predict future changes, is of vital importance for every sector player.

Although data is always valuable in science, in some industries data loses its value over time. In such sectors, instead of storing and analyzing the data afterward, it is necessary to analyze the data as soon as it is formed and to use the obtained information quickly. For example, online shopping platforms such as Amazon, eBay, etc. should direct users' queries to the right products very quickly or channel the customers according to their needs by showing the right ads. At the same time, more detailed information about the needs of the customer can be produced by taking and examining the data that customers have recently created on other online platforms such as Twitter, Facebook, Instagram, Youtube, Whatsapp, etc. The data created by the same users on different platforms, user feedback, clicks, past queries, gender, age, etc. all data will be an important source of information for online commercial enterprises to meet both current customer expectations and potential customer expectations in the future. The data is analyzed quickly and the results are matched with the customer profile and used exactly when the customer needs it. For this reason, data collection and processing must be done in real-time and synchronized. Classical databases are sufficient to quickly store single-source data streams, but most of them do not support the most critical feature of data flow, "real-time data analysis".

Especially for high accuracy rates, non-real-time data analysis models are used on smaller sizes of data. In this way, guiding models and qualified information are produced to be used in real-time models. Real-time data analytics is often applied to big data, in industries where timing is critical, analyzes are performed within seconds, and results are used. Especially in the internet industry, real-time data analysis should be a source that produces uninterrupted and real-time information. For this reason, real-time data flow should occur both in parallel and simultaneously from the internet to the data source (data storage) and from the data source to the sectoral use (information based on analysis results). One of the most critical elements of the ongoing data flow, such as a circular infinite sequence, is the data recording time information. Data recording time information will allow an analysis of data by dividing it into periods, such as minute, hour, certain hours of the day, daily, weekly, monthly, certain periods of the month, annual, and certain periods of the year.

In order to meet the real-time data needs, there is a need for low-latency connection speeds, simple and reliable distributed systems (Galić, 2016) that will enable real-time data flow, and qualified application interfaces (Bornschlegl, Engel, Bond, and Hemmje, 2016) to be used in data collection. Operating in the internet industry, Facebook, LinkedIn, Cloudera, Hadoop, etc. key applications are using Scribe, Kafka, Cloudera, etc. data collection tools (Ljubenović, Pantelić, and

Simović, 2018). Many of these tools continue to operate as open sources. In classical data analysis processes, data is first stored in specified databases and then information is extracted from the data based on user interaction. In these processes, user interaction is kept passive while the database storage system actively collects data. However, this method, in which user interaction is kept passive, is used in finance, communication, trade, etc. sectors will not be enough. The "flow" management, in which calculations are made on the data as soon as the data is created, will provide higher benefits (Ke et al., 2022). System requirements for flow calculation; data collection tools compatible with data flow rate, secure and uninterrupted data query engines, maintainability (alternative systems), distributed systems, parallel computing capability.

Figure 5. Data flow

A data flow diagram (DFD) is used to represent the data flow in a computing system and refers to the process of transmitting data in the system, from storing it in a database to reporting analysis results. In DFD, abstract tasks and concrete components are expressed synchronously. DFD based on tasks (actions to be done) expresses at what stage a task should be completed, its inputs related to the task, and the expected outputs to be used in the next stage. DFD based on tangible components refers to internal and external components to perform tasks. DFD, which should be simple and understandable, supported by visuals, is also used in the processes of classifying data and distributing data according to tasks. The most common mistakes made in a DFD task step are defining the input but not defining the output, defining the output but not defining the input, or having the input and output unrelated. In this respect, DFD operates to facilitate communication between users and system designers. DFD is designed to be open to detecting deficiencies or new needs of the system and correcting or improving it by system developers, based on observations and analyses. In general, DFD is used to monitor information flow and determine system requirements.

In DFD, the initial connection must be made between the datastore and task 1. Apart from the DFD, the data store must also have a new-input connection. This external port is called an external entity. The external entity point also performs output collection tasks from the DFD. In this way, the accuracy of the system data source and new input needs are determined. The external entity connection point can be an autonomous system, as well as real people who are experts in the field. In cases where the external entity is a natural person, data entry into the system is usually done manually. The external point of existence can also be expressed as the interaction of the information system with the outside world. The background diagram shows the data flow from all external entity points and the overall concept of the system. For this reason, in the DFD drawing, the background image should not exceed one page, and the program name and the information system name should not be the same.

DFDs can be designed in different ways according to the subjects to which they will be applied. In a subject with a lot of detail, a distinction can be made from very intense to less intense, according to the task intensity. This will reveal more details. This process is called designing a DFD by flattening. In the smoothing process, first, the target system is holistically expressed in the DFD. Next, each task is broken down into possible sub-detail tasks until all sequential steps are defined

by different tasks. The most common mistake made in this process, which requires adding more layers to the DFD, is mismatching the input and output values. For consistency between DFD layers, the input and output values of each level must be equal and related. If there are many external entity points in a system, it may be necessary to first express the system and related external points in a separate DFD and then edit the remaining parts of the system's base DFD. This practice will make it easier to ensure consistency between layers.
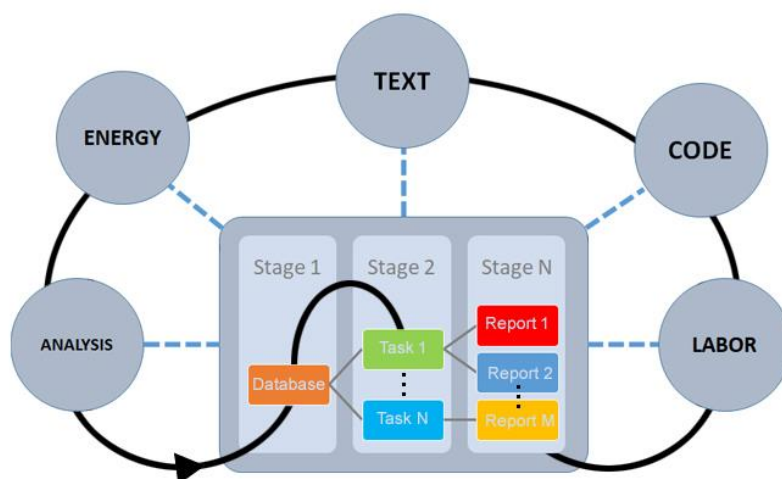
Figure 6. Data Flow Diagram

A DFD consists of tasks and concrete components. Task-based DFD essentially represents the system operation but does not say how the system will be set up and run technically. Processes such as data storage, analyzing data and transforming it into information, and reporting the results are shown in the DFD based on Tasks. Based on tangible components, DFD demonstrates the setup and operation of the system, including technical tools, computer software, files, and personnel assigned to the system. For the system to achieve its goals, DFD based on tasks and DFD based on concrete components must be implemented in a synchronized and accurate manner.

Task-based DFD shows task distributions. Therefore, it is effectively used in communication with system users. In addition, this DFD model is drawn according to the task distributions and thus determined independently of the physical components. This ensures a more stable application of the system flow. Task-based DFD enables systems analysts to better understand systemic tasks and consequently to make more solid decisions (Sutcliffe, 1989). This ensures that the task descriptions do not change frequently and thus the system is easier to maintain. While task-based DFD systems require detailed documentation, Concrete component-based DFD systems require the development of computer software.

Transactional Database

Transactional database is a real-time, dynamic, and applied database that requires high reaction speed (Cuzzocrea et al., 2015). A transactional database consists of tables in which each record represents a financial or trading transaction. As a concept, each transaction contains an original and unique ID number and a list of the transaction's stakeholders. In the transactional database, product name, transaction date, seller/buyer ID numbers, institution address, etc., can also be found in some additional tables related to the transaction content. Transactional database, which product is preferred more according to customer profile, which products' sales are related to each other, how much a product will be needed in the future, etc. It provides important product and customer-based operational information. Traditional databases do not present this information without data analysis. The way of storing datasets gives transactional databases this capability.

Figure 7. Transactional data

In a transactional database, attribute categories of data can be used for different purposes. From a statistical point of view, classification of data, content analysis and weighting of data according to content analysis are done by using attribute categories. In this way, the importance of the items can be measured. The weights of the items are formed spontaneously according to the data universe without any artificial intervention. For example, while using the customer's shopping history and profile information to identify customers in a store, some customer-specific details (inquiry history in the search engine, wedding anniversary, birthday, depending on education level, school term, etc.) might help. To determine the importance of these qualitative elements, some statistical analysis methods such as generalized linear models (GLM) are applied. In their study, Xie and Luo measured the effects of variables in the data set on insurance pricing by applying GLM (Xie and Luo, 2022).

Data mining is a dynamic research process based on data storage and the use of artificial intelligence algorithms. The "coexistence rule", which reveals the coexistence pattern of any two attributes, is one of the main purposes of data mining. For example, selling phone and phone screen protector products together can be expressed by the association rule. For example, the information that 75% of customers who buy phones also purchase screen protectors can be easily detected in the transactional database. Thanks to the association rules provided by the transactional database, determination of product variety, production planning, determination of target customer profiles, etc. Important steps can be taken in many areas. Producing association rules that about the important items is one of the most important contributions of data mining in transactional database creation processes. In their study, Yen and Lee proposed an association rule to observe the distribution of benefits and costs of products. To this end, they developed a data mining algorithm to identify useful product clusters that could be purchased (Yen and Lee, 2007).

Distributed Information Systems

Distributed systems are a collection of autonomous computers that work together to perform a task. The autonomous computers can be geographically distributed, and they are connected through a network.
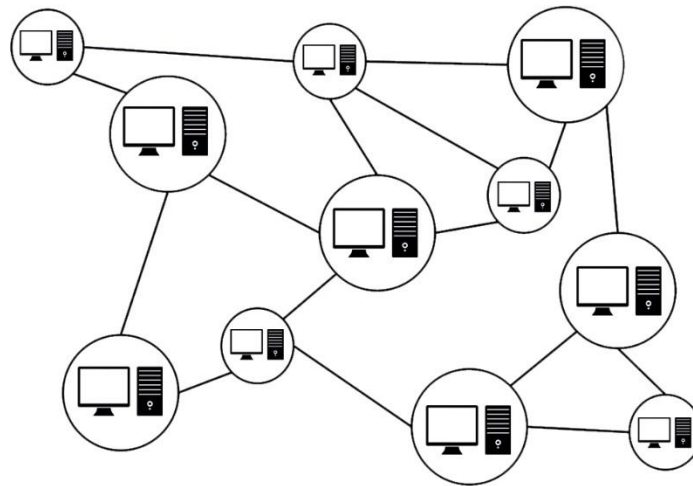
Figure 8. Distributed Information Systems

The system is designed to be tolerant of the failure of some of its components, so that it can still operate in the event that any number of its components fail. This is achieved by dividing the tasks amongst all the computer nodes in such a way that each node only performs one type of task, and each type of task is performed at least once by every node.

Extract, Transform and Load (ETL)

ETL is a process that extracts, transforms and loads data from one system to another. This process is used to extract data from a source system, transform it into the desired format and load it into a target system.

There are many software platforms available in the market that can be used for ETL processes. These platforms have different features and prices which depend on the number of users in an organization.

What is Data Science?

Data science is a set of predictive calculations that generate valuable information from existing data. It is also a multidisciplinary set of instruments and procedures that transform any data into qualified information by coordination strategies based on data science and computer science. Thanks to today's digital infrastructure, huge amounts of data are created every second. Some of this data flows in vain like a river, some of it is stored in different databases. Unfortunately, it is not possible to say that all this data is used to its full potential. Having data science will give you a unique strength and advantage in transforming data into useful and strategic information and in the ongoing competition in all sectors of real life. Thanks to data science, it will be possible to reach reliable information and decisions based on this data, produced with an approach based on facts and science, rather than just intuition and guesswork.
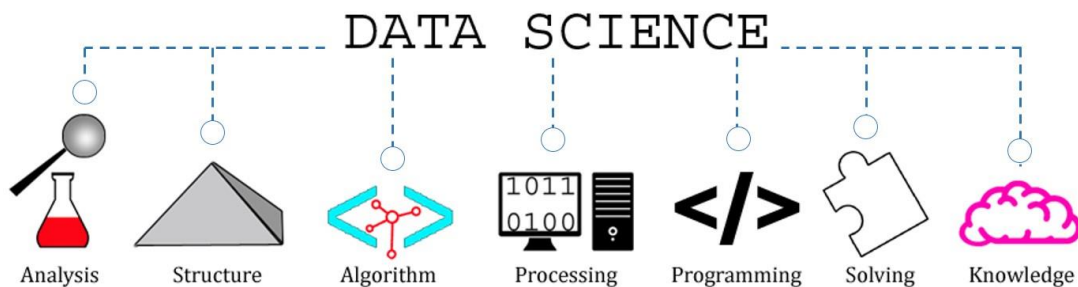
Figure 9. Data Science

Data science, one of the sub-branches of statistical theory, has been prominent for many years. However, technological advances in the last 20 years have also made industrial applications of data science possible. These new possibilities have stimulated interest and prospects in data science. This interest, the rise of big data, and its expectations can be grouped under the headings of the Internet of Things (IoT). The adoption of digital technology in business brings a wealth of information on competitors, clients, tendency of markets, and other critical factors that affect company performance. Extracting information from data is a challenging task, as this information is obtained from different structured and unstructured sources. Data can come from many sources and in different formats. Since the data may be unstructured (text, code, symbol, etc.), it is difficult or impossible for the data to be interpreted intuitively, or for industry stakeholders to manage and use the relevant data on their own.

Artificial intelligence (AI) and machine learning (ML), which were previously just science fiction concepts, have now become a part of everyday life to solve big data challenges. With the exponential growth in the amount, variety, and rate of occurrence of data, the need for data pattern detection, analysis, and prediction has gone beyond human cognitive abilities and conventional statistical methods. Today, AI and ML are a 'must' for reliable data analysis. Therefore, advanced data analytics is not possible without significant advances in computational computing power. The realization that computer processors designed to create game graphics are also very suitable for machine learning and artificial intelligence applications have triggered this development to a great extent. These advanced computer chips can handle highly complex computational algorithms, giving fast results even under the considerably tricky challenges, making them advantageous for data science applications.

Developing data storage technologies, including cloud technology, offer the ability to store all types of data at low cost and high speeds. Companies can reasonably store petabytes of data through a hybrid platform of physical and cloud storage memories. Because data science connects all aspects of an enterprise, tight integration of high-speed processes is critical. Technologies and methods designed to deliver information in real time must be able to integrate seamlessly with computational modeling capabilities that use ML algorithms to predict outcomes. These results are then used with little or no delay to decide on a topic.

There are three fields in that data scientists are proficient: statistics, computer science, and industry domain expertise. The core role of a data scientist is to control and interpret all data associated with a problem, construct and test models to provide insights and predictions, present the results to stakeholders, and then report on the computational details, including coding. In addition, data scientists are also responsible for analyzing and reporting concrete business results. Due to the many specialized skills involved, finding qualified data scientists can be overwhelming. Data science has become such a natural part of every industry that industry stakeholders and basically customers expect to receive technical support based on data analysis in product selection without demanding it. Companies that receive data science support want to understand their customers better and increase customer satisfaction and ultimately increase their sales rates and industry market shares. In addition, companies try to control costs by increasing efficiency in all processes in which the company operates and obtaining information about future trends for strategic planning. The most important aspect of this process is that decisions are based on facts rather than intuitive guesswork.

Actively investing in data science has become a necessity, not a choice, in the age of artificial intelligence and data. Data science can provide enormous financial and strategic benefits, depending on the strategic goals of companies. Boehmke et al. explain how data science can be used to meet an organization's analytical and strategic needs (Boehmke, Hazen, Boone, and Robinson, 2020). Also, using algorithms to analyze data, Yang et al. has developed a financial risk management model required for an online supply chain (Yang, Wang, and Ren, 2019). For example,

a bank can rely on real-time in-house transaction size and operating cost models to optimize online data transfer and transaction speed, thereby minimizing operating costs and energy consumption. Manufacturers may use data science to predict future demand and determine product assortment. In their study, Thomitzek et al. predict the future destinations of battery cell demand used in battery manufacturing with simulation-based modeling (Thomitzek, von Drachenfels, Cerdas, Herrmann, and Thiede, 2019). Besides, automakers are actively using data science to collect real-world driving behavior data and design autonomous driving methods through ML. Industrial factories are using data science to minimize waste and equipment downtime (França, Monteiro, Arthur, and Iano, 2020).

Overall, data science and artificial intelligence drive innovation, improvement, and efficiency in all industries. Data science can be effectively used to optimize the supply chain, streamline workforce use, understand and meet customer needs, accurately predict business metrics, monitor and improve product design and performance. Regardless of companies' strategic goals, data scientist experts can rationally gather and research available information, integrate necessary third-party data streams, apply cutting-edge analytics, and ultimately recommend actions that will lead to a forward-planning strategy relevant to companies. In addition, data scientists can help predict future results and compare confirmed outcomes by building a culture of constant learning and progress. All these data analysis capabilities will commercially secure companies both today and tomorrow.

Data science is becoming more and more automated, and it is clear that this will continue to accelerate in the future. Today, a data scientist can build an automated data analysis model on all potential varieties of thousands of data parameters, discovering the most suitable solution to an existing problem in real-time. In the past, statisticians had to manually design and adjust predictive models over a long period, combining statistical experience and their creativity. But nowadays, with the enormous increase in data volume and complexity of business problems, such tasks are extremely complex with conventional methods. Therefore, this issue needs to be addressed with AI, ML, and other digital computational techniques. While these techniques are often associated with eliminating human work, in reality, they exclusively lift the significance of data scientists and corresponding fields. When these technologies are used for the benefit of all humanity, they will offer advantages that make life easier in every field, from trade to health, and will encourage continuous innovation and development. This will require data scientists to introduce new theories and approaches to meet next-generation needs.

Big Data Analysis

To fully understand the importance and applications of big data analysis, it is necessary to first understand the concept of big data. Big data can be expressed as recorded data collected in large sizes from various sources, based on a specific goal. With the advancement of science and technology, it has become the sociological norm of the digital age to collect large-scale data to observe, analyze and extract information from all kinds of changes and new developments from social sciences to natural sciences, where human and human benefit are at the center. Big data applications are used in many areas from ordinary human life to all kinds of activities of companies or governments.
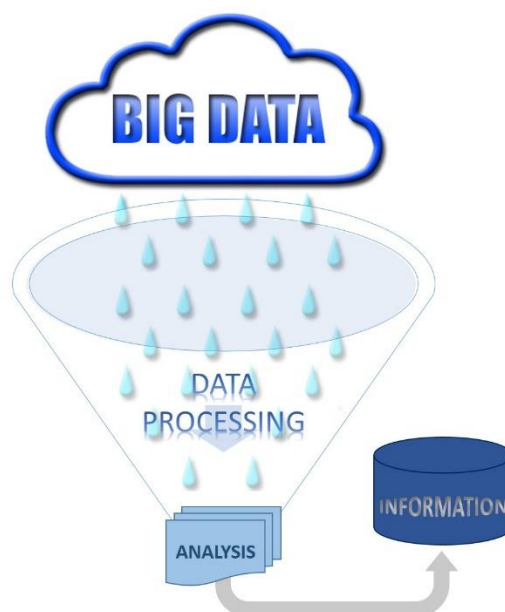
Figure 10. Big Data Analysis

Big data applications are widely used in the business world. Many large companies employ dedicated big data analysts to analyze various behaviors of customers. A company that can analyze customer data well can better understand its customers' needs and purchasing behavior (Zulu and Nkuna, 2022). This information will be a critical foundation for the company to develop strategies for both the present and the future. Through many social media and phone applications, target customers are identified, access to their phone or browser records is provided for these people to be understood more comprehensively, and very detailed and qualified data is collected. Thanks to these data, the steps to develop advertising strategies for product development for needs, to identify the deficiencies of the current product, and to market the product correctly can be taken correctly. For example, chain retail stores gain valuable insights through the analysis of big data and formulate relevant strategies to accurately predict what customers want to buy. Based on this information, they determine personalized campaigns or product prices. Based on the analysis of big data, telecommunication companies can better predict the customers and take preventive steps. Iwashita et al. propose a semantic analysis method based on information about customer requests for telecommunications services (Iwashita, Shimogawa, and Nishimatsu, 2011). With big data analysis, politicians can better understand the preferences of the voters and prepare their election propaganda according to this information.

Besides analyzing user preferences, big data can optimize the entire business process, reduce cost and accurately identify more efficient working or business models for businesses and companies Zolnowski et al. present a new approach to the cost-benefit analysis of data-driven business models (Zolnowski, Anke, and Gudat, 2017). Big data analysis is also effectively applied in processes such as the optimization of internal workflows, integration and connection of network data, optimization of logistics distribution destinations and routes, and effective management of human resources. Lucci et al. present a workflow modeling based on artificial intelligence in his study. Thanks to this model, it can provide the management and control of robotic applications (Lucci, Monguzzi, Zanchettin, and Rocco, 2022). In their study, Zheng e al. put forward an analysis approach that uses big data on traffic flow and the economic associations that cause traffic flow (Zheng, Lu, and Li, 2022). Giménez-Palacios et al. develop strategies based on data analysis for the solution of dynamic route problems that arise due to the number of vehicles or new customer demands in the distribution of logistic products (Giménez-Palacios et al., 2022). Hamilton and Sodeman presented a study on how Big Data algorithms can be used in simultaneously solving human resource management problems and determining strategies (Hamilton and Sodeman, 2020).

Big data applications can be used by large businesses or governments as well as ordinary individuals. For example, data collected by wearable technologies such as smartwatches or smart glasses are transmitted to large online databases (data clouds). Calorie intake/expenditure, duration of sleep, number of steps taken, blood pressure, etc. The data is analyzed and helps people to observe and manage their physical condition. In addition, thanks to the personal data produced during the use of both wearable and other communication technologies, artificial intelligence support can be obtained in personal decision processes. For example, in choosing a birthday gift, artificial intelligence tools will choose the most suitable options for you from the large product catalog and put them in front of you. By analyzing regional traffic data, the problems experienced in traffic and the sources of the problems can be determined. Dokuz presents an approach that scores each area of the city in terms of traffic speed, thus aiming to predict regional traffic speed, using the New York taxi trajectory dataset and the Weighted spatiotemporal trajectory and velocity big data mining approach (Dokuz, 2022). Every day, many new big data applications that aim to optimize the quality of human life come into our lives.

Another sector where the analysis of big data is used effectively is health. Diseases have very similar characteristics periodically according to the course of the disease, from the preliminary symptoms in the formation process to the effects after they appear. Understanding the data of these processes in full detail will make a contribution that increases the success both in preventive treatment and in the treatment of the disease (Chaochao et al., 2018). Thanks to the new developments in the field of biostatistics, the genetic predisposition of people to certain diseases or the duration and probability of the disease can be calculated by examining the DNA. Some big data analysis studies examine the situation of premature babies and babies born with certain genetic diseases. We can name these studies on DNA as the deciphering of DNA with big data analysis.

Sports competitions are of great importance both nationally and internationally. The sociological and economic dimensions of sportive activities, which drag large fan bases behind them, make the sport more critical than just sport. All countries and sports clubs that want to achieve success in this field apply all kinds of technical support to increase the performance of their athletes. In this way, it is possible to reach new records and new achievements. Especially football, basketball, etc. where large budgets are used. sports branches have become an industry on their own. This situation reveals that it is necessary to deal with the issue not only with sports concepts but also with scientific and technological concepts. Apart from the classical methods to achieve success, many athletes now apply big data analysis technology during training (Fury, Oh, and Berkson, 2022). For example, with the sensor technology worn on the athlete or sports equipment, the athlete's body data, performance, physical posture, and technique can be understood, and various improvement suggestions are made for better performance.

Big data analytics can make devices smarter and more autonomous. For example, Tesla uses big data collections obtained from consumers to develop self-driving cars (Kerschner and Somare, 2017). Autonomous cars are working on navigation services and artificial intelligence (AI) that collects both in-vehicle and out-of-vehicle data including other vehicles on the traffic via cameras, lidars, sensors, and internet network (Huang, 2018). The AI system processes them with simultaneous big data analysis methods. Data processing continues instantaneously and uninterruptedly, and thus, it has gained a form that constantly improves itself by debugging errors. This makes autonomous driving increasingly safe and comfortable.

Especially in recent years, the instant processing of images collected by unmanned aerial vehicles and security cameras with big data analysis methods and transforming them into intelligence information has become a very common practice in the field of security. In particular, China has installed cameras with facial recognition technology in almost every street (Chan, 2018). In addition, instant analysis of digital data such as credit card usage is used effectively in the physical tracking of suspects in some criminal investigations all over the world (Wacks, 2013). On the other

hand, there are some criticisms that in these AI supported security concepts, personal privacy is violated.

Another sector where big data algorithms are used extensively is the finance sector. Institutional or individual investors operating in the financial sector use big data models for the analysis of financial transactions (OECD, 2021). By analyzing the historical transaction records and the current data, they can make predictive, fast, and reliable investment choices that make the risks clear to a certain extent. In most of the stock buying/selling transactions, before the official buys or sells decision, it is artificial intelligence (AI) supported big data analysis algorithms, not a real financial expert, that simulates the possible decision and performs an active information flow to the investor based on the analysis.

Big Data Technologies

Collecting, storing, analyzing, and interpreting Big Data requires a range of Big Data technologies. Distributed computing methods, clustering, real-time data analysis, etc. may also be used and are also required. By using Big Data and Big Data analytics, companies can optimize costs, increase efficiency, develop new products that meet customer expectations, make smarter investment decisions, and take more accurate and risk-mitigating actions. The applications and importance of Big Data extend far beyond these examples. Examples of Big Data can be observed from all stages of life.

The ability to analyze Big Data has already passed the petabyte-second mark in real-time, and reaching the exabyte-second mark when the 6G data transmission infrastructure is ready is not a distant goal. With today's technologies, it is impossible to store and process such large amounts of data in a single database. Data of this scale should be stored in different databases, divided into subsets, and processed on different devices, and then the results should be combined. Big Data storage systems store the same data in multiple locations to ensure data security. Analyzing subsets of the same data on different devices and storing them in different repositories is called a distributed system. Some algorithms help organize how data can be stored and processed most efficiently and quickly in a distributed system.

The first step in the Big Data processing cycle is data collection. In the classical understanding of data, data is treated under three basic headings: structured, semi-structured, and unstructured. Audio, video, etc. However, data is not included in the classical understanding of data. Also network, system, device, hardware, etc. The data generated by the components are also not included in the scope of classical data. All these new forms of data are stored in the Big Data concept and analyzed together with other forms of data. Network data, links, text, images, etc. comprise the content. Device data is usually collected using devices equipped with sensors. In some cases, information related to the mechanical operation of the device (temperature level, signal strength, etc.) can also be considered device data. The collected data is transmitted and stored through data sources. During data transmission, information such as the queue ID, data subscription, data source ID, time, and serialization is used for message queue software of relevant data and synchronization of subsets collected in other sources.

Message queue middleware is mostly used in distributed big data systems. The main purpose of this software is to increase the performance of distributed data systems. In the processes from data collection to data analysis, it aims to facilitate the selection of data collected for specific purposes among other data, i.e. to ensure communication between the user and the data, thus ensuring the most effective use of the data. It also performs tasks such as scaling data, organizing new data entries, transferring data to applications, and combining data from different sources. Data subscription is a system that provides users with cumulative, uninterrupted, real-time data. Thanks to this system, users can realize business scenarios such as determining and applying asynchronous systemic task distributions and accessing data with similar content collected in different sources

and asynchronous times. Serialization, then, is the serial connection of data systems during data transmission, as in power models. In this process, objects working in the phases of data collection and production communicate through a serial connection. In the transmission of Big Data, serialized communication systems between objects provide speed, performance, and efficiency-enhancing effects in data-based workflows.

Big Data storage systems provide performance-optimized, secure storage and access to large structured and unstructured heterogeneous data. As technology and data forms change, so does the architecture of data storage. The classic physical storage points, computer main memory, flash disks, etc. are well known. But data storage (cloud databases) at different physical data storage points over the network can also be counted among the classic methods. Data storage can be classified according to the server type of the system whose data is being collected. Closed systems such as mainframe and open systems such as Windows and Linux. Open systems are divided into internal and external storage points. Distributed storage systems, such as object, block, and file storage systems, which should be used depending on the different storage points, are diversified. Distributed data storage systems, such as HDFS, Swift, Luster, etc., allow multiple users to access and share Big Data simultaneously based on multiple storage nodes.

As the size and scope of data increase, database technology continues to evolve to meet current and potential needs. The development of network technologies is an important factor that has a positive impact on the development of database technology. The access and usage methods provided by network and database technology have paved the way for more effective user activities in database processes. This database concept, in which users are as actively involved as objects, is called a relational database. Greenplum, Mycat, Aurora, etc. are well-known examples of relational databases. In a relational database, existing data is recalculated through mathematical methods based on user interaction. The weaknesses of this approach include low performance due to user speed and difficulty in scaling. In addition to storing data, the analytic database provides users with the ability to perform statistical data analysis on existing data. AnalyticDB, Clickhouse, and LucidDB are some popular analytical databases. Since the entire process is performed online in this database concept, users do not need physical components and the value of existing data can be determined without an external platform.

Big Data users use search engines to quickly and accurately find the data they need. A search engine can scale distributed data. Thus, when scanning data with specific content, the user is presented with the target data in order of importance. This feature helps optimize database performance. Elasticsearch and OpenSearch are examples of distributed search engines.

Big Data computing is the process of dividing large amounts of data into discrete subsets and computing the results by analyzing each subset synchronously with multiple computer programs. Since almost the entire process is independent of software, the application of data computing and distributed task management is maintained with high performance and reliability. In large distributed systems, when a hardware component is added to the system, the automatic operation of this physical device must be coordinated. The distributed coordination system provides coordination of all processes related to hardware components, such as commissioning replacement components, ensuring communication between components, and synchronous operation of components when a malfunction or change occurs in physical components. Examples of popular distributed coordination systems include ConfigServer, Eureka, and Chubby.

Resource management is the process of creating clusters and data centers that ensure the management and allocation of resources to ensure the most efficient use of all data sources to which the system is connected. Resource management works on the principle of dynamic allocation when there are multiple users. Ambari and Hue are examples of data resource management tools.

As the size of the system increases, so does the complexity of the workflows of the system participants and the number of problems that arise due to the complexity. This results in the need to monitor, audit, and troubleshoot workflow processes. If the definitions of the roles and responsibilities of stakeholders are not clear, this ambiguity leads to some technical problems, such as transaction deletion on metadata. At this point, the Directed Acyclic Graph (DAG) workflow management application provides important support in identifying and resolving issues. Complex workflows can be visually represented using DAG. Thanks to this graphical representation, workflows can be processed step-by-step and irreversibly from start to finish. In this workflow model, the data contained in the flow cannot be re-entered at the end of the process, and the output of each stage is treated as the input of the next stage. Airflow and Azkaban are examples of tools that provide the DAG application service.

With the development and proliferation of technology-based management systems, traditional enterprise management processes no longer meet expectations. New systems not only speed up tedious processes but also convert data generated in workflows into information. It is also possible to convert external data submitted to the system into commercial value thanks to the new approach. For example, classic database systems can provide basic services such as storing data and inserting/deleting/changing/checking data but cannot provide good decision support. For decision support, the integration of various data and historical flow structures should be considered. This highlights the importance of timing and speed. Traditional databases do not provide predictive support for future data while exploring existing data. Therefore, new information processing systems that provide decision support are gradually being deployed and their penetration is increasing.

References

Abate, A. F., Bisogni, C., Castiglione, A., and Nappi, M. (2022). Head pose estimation: An extensive survey on recent techniques and applications. Pattern Recognition, 127, 108591. doi:https://doi.org/10.1016/j.patcog.2022.108591

Andrić, V., Gajić-Kvaščev, M., Crkvenjakov, D. K., Marić-Stojanović, M., and Gadžurić, S. (2021). Evaluation of pattern recognition techniques for the attribution of cultural heritage objects based on the qualitative XRF data. Microchemical Journal, 167, 106267. doi:https://doi.org/10.1016/j.microc.2021.106267

Boehmke, B., Hazen, B., Boone, C. A., and Robinson, J. L. (2020). A data science and open source software approach to analytics for strategic sourcing. International Journal of Information Management, 54, 102167. doi:https://doi.org/10.1016/j.ijinfomgt.2020.102167

Bornschlegl, M. X., Engel, F. C., Bond, R., and Hemmje, M. L. (2016). Advanced Visual Interfaces. Supporting Big Data Applications : AVI 2016 Workshop, AVI-BDA 2016, Bari, Italy, June 7-10, 2016, Revised Selected Papers. Bari, Italy: Springer International Publishing. doi:10.1007/978-3-319-50070-6

Chabert-Liddell, S.-C., Barbillon, P., Donnet, S., and Lazega, E. (2021). A stochastic block model approach for the analysis of multilevel networks: An application to the sociology of organizations. Computational Statistics and Data Analysis, 158, 107179. doi:https://doi.org/10.1016/j.csda.2021.107179

Chan, T. F. (2018, February 13). Business Insider. Business Insider: https://www.businessinsider.com/how-china-uses-facial-recognition-technology-surveillance-2018-2 adresinden alındı

Chaochao, Y., Li, W., Lihong, K., Feng, S., Chaoyang, M., Yanjun, D., and Hua, Z. (2018). Acupoint combinations used for treatment of Alzheimer's disease: A data mining analysis. Journal of Traditional Chinese Medicine, 38(6), 943-952. doi:https://doi.org/10.1016/S0254-6272(18)30995-6

Cuzzocrea, A., Jiang, F., Leung, C. K., Liu, D., Peddle, A., and Tanbeer, S. K. (2015). Mining Popular Patterns: A Novel Mining Problem and Its Application to Static Transactional Databases and Dynamic Data Streams. A. Hameurlain, J. Küng, R. Wagner, A. Cuzzocrea, and U. Dayal içinde, Transactions on Large-Scale Data- and Knowledge-Centered Systems XXI: Selected Papers from DaWaK 2012 (s. 115-139). Springer Berlin Heidelberg. doi:10.1007/978-3-662-47804-2_6

Dokuz, A. S. (2022). Weighted spatio-temporal taxi trajectory big data mining for regional traffic estimation. Physica A: Statistical Mechanics and its Applications, 589, 126645. doi:https://doi.org/10.1016/j.physa.2021.126645

Eicken, H., and Salganek, M. (2009). Field Techniques for Sea-Ice Research. University of Alaska Press.

Fairhurst, M., Fierrez, J., and Campisi, P. (2011). Future Trends in Biometric Processing. Computer Vision IET, 5, 335-337. doi:10.1049/iet-cvi.2011.0241

França, R. P., Monteiro, A. C., Arthur, R., and Iano, Y. (2020). An Overview of the Internet of Things Technologies Focusing on Disaster Response. I. Rahimi, A. H. Gandomi, S. J. Fong, and

M. A. Ülkü içinde, Big Data Analytics in Supply Chain Management: Theory and Applications (s. 158-159). CRC Press. doi:https://doi.org/10.1201/9780367816384

Fury, M. S., Oh, L. S., and Berkson, E. M. (2022). New Opportunities in Assessing Return to Performance in the Elite Athlete: Unifying Sports Medicine, Data Analytics, and Sports Science. Arthroscopy, Sports Medicine, and Rehabilitation, 4(5), 1897-1902. doi:https://doi.org/10.1016/j.asmr.2022.08.001

Galić, Z. (2016). Spatio-temporal data streams. Springer. doi:10.1007/978-1-4939-6575-5

Gantala, T., and Balasubramaniam, K. (2022). DPAI: A Data-driven simulation-assisted-Physics learned AI model for transient ultrasonic wave propagation. Ultrasonics, 121, 106671. doi:https://doi.org/10.1016/j.ultras.2021.106671

Giménez-Palacios, I., Parreño, F., Álvarez-Valdés, R., Paquay, C., Oliveira, B. B., Carravilla, M. A., and Oliveira, J. F. (2022). First-mile logistics parcel pickup: Vehicle routing with packing constraints under disruption. Transportation Research Part E: Logistics and Transportation Review, 164, 102812. doi:https://doi.org/10.1016/j.tre.2022.102812

Hamilton, R. H., and Sodeman, W. A. (2020). The questions we ask: Opportunities and challenges for using big data analytics to strategically manage human capital resources. Business Horizons, 63(1), 85-95. doi:https://doi.org/10.1016/j.bushor.2019.10.001

Hao, Y., Liu, J., Wang, Y.-P., Cheung, Y.-m., Yin, H., Jiao, L., . . . Jiao, Y.-C. (2005). Computational Intelligence and Security : International Conference, CIS 2005, Xian, China, December 15-19, 2005, Proceedings, Part II. Xian, China: Springer-Verlag Berlin Heidelberg. doi:10.1007/11596981

Huang, B. (2018). Comprehensive geographic information systems. Amsterdam, Netherlands: Elsevier.

Iwashita, M., Shimogawa, S., and Nishimatsu, K. (2011). Semantic analysis and classification method for customer enquiries in telecommunication services. Engineering Applications of Artificial Intelligence, 24(8), 1521-1531. doi:https://doi.org/10.1016/j.engappai.2011.02.016

Iwashita, M., Shimogawa, S., and Nishimatsu, K. (2011). Semantic analysis and classification method for customer enquiries in telecommunication services. Engineering Applications of Artificial Intelligence, 24(8), 1521-1531. doi:https://doi.org/10.1016/j.engappai.2011.02.016

Ke, C., Zhang, M., Zuo, Y., Xiang, F., Zhang, D., and Tao, F. (2022). Data-driven real-time control method for process equipment in flow shop towards product quality improvement. Procedia CIRP, 908-913. doi:https://doi.org/10.1016/j.procir.2022.05.083

Kerschner, I., and Somare, M. (2017). Taxation in a global digital economy. Wien: Linde. https://worldcat.org/title/1014019256 adresinden alındı

Kumari, P., and Thangaraj, P. (2020). A fast feature selection technique in multi modal biometrics using cloud framework. Microprocessors and Microsystems, 79, 103277. doi:https://doi.org/10.1016/j.micpro.2020.103277

Küfeoğlu, S. (2022). Emerging technologies : value creation for sustainable development. Springer. doi:10.1007/978-3-031-07127-0

Ljubenović, J., Pantelić, O., and Simović, A. P. (2018). BIG DATA ANALYSIS IN SOCIAL MEDIA. N. J. Žarkić, and S. Marinković içinde, Doing business in the digital age challenges, approaches and solutions (s. 135-142). Symorg 2018.

Lucci, N., Monguzzi, A., Zanchettin, A. M., and Rocco, P. (2022). Workflow modelling for human–robot collaborative assembly operations. Robotics and Computer-Integrated Manufacturing, 78, 102384. doi:https://doi.org/10.1016/j.rcim.2022.102384

McGilvray, D. (2008). Executing Data Quality Projects: Ten Steps to Quality Data and Trusted InformationTM. San Francisco,, USA: Morgan Kaufmann Publishers Inc.

O. C. (2011). JD Edwards EnterpriseOne Tools Configurable Network Computing Implementation Guide Release 8.98 Update 4, Chapter 5.1. https://docs.oracle.com/cd/E17984_01/index.htm adresinden alındı

OECD. (2021). Artificial Intelligence, Machine Learning and Big Data in Finance: Opportunities, Challenges, and Implications for Policy Makers. OECD: https://www.oecd.org/finance/artificial-intelligence-machine-learningbig-data-in-finance.htm adresinden alındı

Rajasekar, V., Predić, B., Saracevic, M., Elhoseny, M., Karabasevic, D., Stanujkic, D., and Jayapaul, P. (2022). Enhanced multimodal biometric recognition approach for smart cities based on an optimized fuzzy genetic algorithm. Scientific Reports, 12(1), 622. doi:10.1038/s41598-021-04652-3

Ross, A., Banerjee, S., and Chowdhury, A. (2020). Security in smart cities: A brief review of digital forensic schemes for biometric data. Pattern Recognition Letters, 138, 346-354. doi:https://doi.org/10.1016/j.patrec.2020.07.009

Sutcliffe, A. (1989). Human-computer interface design. New York: Springer-Verlag New York Inc. doi:10.1007/978-1-4899-6749-7

Thomitzek, M., von Drachenfels, N., Cerdas, F., Herrmann, C., and Thiede, S. (2019). Simulation-based assessment of the energy demand in battery cell manufacturing. Procedia CIRP, 80, 126-131. doi:https://doi.org/10.1016/j.procir.2019.01.097

Villez, K. (2014). Qualitative trend analysis for process monitoring and supervision based on likelihood optimization: state-of-the-art and current limitations. (1. I. Congress, Dü.) IFAC Proceedings Volumes, 47(3), 7140-7145. doi:https://doi.org/10.3182/20140824-6-ZA-1003.01596

Wacks, R. (2013). Privacy and media freedom. Oxford: Oxford University Press.

Xie, S., and Luo, R. (2022). Measuring Variable Importance in Generalized Linear Models for Modeling Size of Loss Distributions. Mathematics 2022. doi:10, 1630. https://doi.org/10.3390/

Yang, Q., Wang, Y., and Ren, Y. (2019). Research on financial risk management model of internet supply chain based on data science. Cognitive Systems Research, 56, 50-55. doi:https://doi.org/10.1016/j.cogsys.2019.02.001

Yen, S.-J., and Lee, Y.-S. (2007). Mining High Utility Quantitative Association Rules. I. Y. Song, J. Eder, and T. M. Nguyen (Dü.), Data Warehousing and Knowledge Discovery içinde (s. 283-292). Berlin: Springer Berlin Heidelberg. doi:10.1007/978-3-540-74553-2_26

Zheng, Y., Lu, M., and Li, J. (2022). Internal circulation in China: Analyzing market segmentation and integration using big data for truck traffic flow. Economic Modelling, 115, 105975. doi:https://doi.org/10.1016/j.econmod.2022.105975

Zolnowski, A., Anke, J., and Gudat, J. (2017). Towards a Cost-Benefit-Analysis of Data-Driven Business Models. Wirtschaftsinformatik und Angewandte Informatik, 181-195.

Zulu, V. M., and Nkuna, A. M. (2022). Data modelling of subsistence retail consumer purchase behavior in South Africa. Data in Brief, 42, 108094. doi:https://doi.org/10.1016/j.dib.2022.108094

DNA Sequencing Methods: From Past to Present

K. Eren[1]
N. Taktakoğlu[2]
İ. Pirim[3]

Introduction

DNA double helix structure was first explained by Watson and Crick. The first natural polynucleotide DNA sequence was announced in 1953. Due to the development of many sequencing techniques, the entire human genome was sequenced in 2003 as a result of the Human Genome Project (Behjati & Tarpey, 2013). The goal of the Genome Project, a large-scale scientific initiative, is to investigate and evaluate the chemical sequence of the 50.000–100.000 genes that make up the human genome, or the entire collection of all genetic material. The separation and examination of the genetic code included in DNA provides the basis for this huge project. Considering the size of the human genome, scientists must have developed new techniques for DNA analysis that can quickly, cheaply, and reliably analyze massive amounts of data. DNA sequencing methods requiring large-scale application have driven technology to both enhance capacity and decrease instrument size. This demand has prompted the creation of automated equipment that speeds up and lowers the cost of biochemical processes connected to sequencing, enhances the analysis of these reactions, and makes it simpler to enter the resulting data into databases (Collins et al., 1998). It was not possible for scientists at the time to sequence nearly a full gene because they could only sequence a few base pairs per year. There was a flurry of RNA and DNA sequencing that improved procedures and provided new data, although there were difficulties in the sequencing process, the first complete genome sequencing was completed after a while. This eventually gave rise to the Maxam and Gilbert chemical degradation DNA sequencing method, which physically separates terminally tagged DNA fragments by electrophoresis and chemically cleaves specific bases of those pieces (Doğan et al., 2017). Maxam-Gilbert, called the first generation sequencing method, is based on chemical fragmentation of DNA and imaging with electrophoresis (Behjati & Tarpey, 2013). Later, a new technique with higher simplicity, reliability, and a lower hazardous level was developed. It was simply called the Sanger sequencing method. When the Human Genome Project was completed in 2003, automated Sanger DNA sequencing with fluorescent dye labels was the dominant technology (Zhong et al., 2021). Sanger technique, which uses fewer chemicals and is less harmful, is still regarded as the gold standard today.

Sequencing methods should be inexpensive, fast, accurate, and easy to implement. The inability of first-generation sequencing to meet these demands has led to new searches. The demand for less expensive and quicker sequencing techniques has grown since the first human genome sequence was completed. Massively parallel sequencing techniques avoid the scalability issues with standard Sanger sequencing by constructing micro-reactors and/or anchoring the DNA molecules to be sequenced to solid surfaces or beads. This enables millions of sequencing operations to occur simultaneously (Behjati & Tarpey, 2013). After Sanger sequencing, NGS

[1] Master Student, Izmir Katip Celebi University,
[2] Master Student, Izmir Katip Celebi University,
[3] Prof. Dr., Izmir Katip Celebi University

represents a real revolution in sequencing technology. A whole human genome may now be sequenced in a couple of days for less than $1,000, compared to many years and billions of dollars for the first human genome's Sanger sequencing (Zhong et al., 2021). Second-generation sequencing methods, also referred to as next-generation sequencing (NGS), were developed in response to this demand. The quality of genome assemblies were greatly enhanced by the use of third-generation sequencers, which generate reads of previously unprecedented sequence lengths. Field sequencing is additionally made possible by quick sequencing and simple sample preparation (Bleidorn, 2015). Massively parallel sequencing is a technique used by NGS systems in which millions of DNA fragments from a single sample are sequenced (Reis-Filho, 2009). Third-generation single molecule sequencing has been developed to lower the cost of sequencing and simplify the preparation. The procedures involved in generating libraries, amplifying DNA, and sequencing that are part of the second-generation sequencing method are not necessary in the third-generation sequencing approach.

As a result, in this review, the evolution of DNA sequencing methods from the beginning to the present were discussed in detail. It was focused on how NGS methods referring to modern high-throughput sequencing processes sequencing methods actually developed and how they carried sequencing methods forward.

1. First-Generation DNA Sequencing

First-generation DNA sequencing methods consist of two methods: Maxam-Gilbert (Chemical degradation) and Sanger (Chain termination) methods which are based on the amplification of template DNA and gel electrophoresis, emerged at approximately the same time, but the completion times differ from each other. These techniques that are crucial for sequencing the human genome, currently have a disadvantage in terms of cost and time.

Maxam-Gilbert Method

The Maxam-Gilbert method is a method based on chemical degradation introduced by Maxam and Gilbert in the late 1970s. The first step is to convert the DNA sample into a single strand. The phosphate group in the DNA sequence is removed with the help of alkaline phosphatase (Maxam & Gilbert, 1977). Polynucleotide kinase then adds a radioactive phosphate group (P^{32}) to the single helical chain's 5' end (Heather & Chain, 2016). Millions of copies of the template DNA are produced by polymerase chain reaction (PCR). The replicated template DNA is cut into pieces by cutting on the base with base-specific chemicals (Hardin, 2001). Four different chemicals are used for each base (A, G, T and C). As a result, the reaction is conducted in four different tubes, one for each base. All tubes consist of base-specific chemical and radioactively labeled template DNA. The reading of the DNA sequences can be observed by placing the reactions on different strips on the gel with the help of electrophoresis. The negatively charged DNA samples are run on the gel with an electric current. To see the bands, the gel is placed on an X-ray film. The part with the radio-labeled sequences darkens on the X-ray film. The position of the bands that become visible will differ due to the chemical cut of the DNA samples. Since the sequence with a short base length will run fast, the sequence is read from the bottom to the up (Figure 1) (Hardin, 2001).
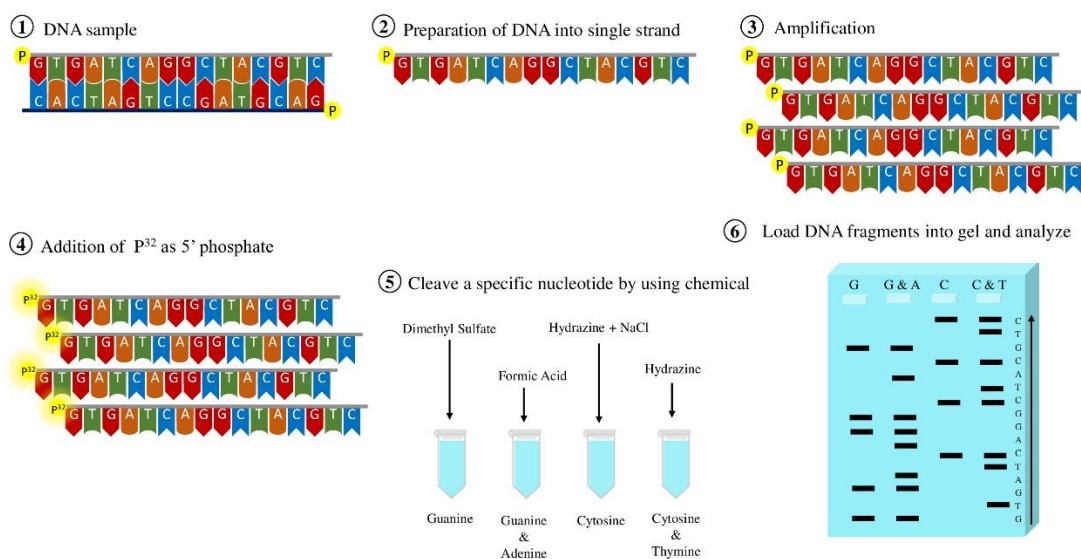
Figure 7. The basic principle of Maxam-Gilbert sequencing method. G: Guanine, A: Adenine, C: Cytosine, T: Thymine, P³²: Radioactive isotope of phosphorus.

In the Maxam-Gilbert procedure, the guanine base is cut using dimethyl sulfate, the cytosine base is cut using hydrazine and sodium chloride, the guanine and adenine bases are cut together using formic acid, and the cytosine and thymine bases are cut together using hydrazine (Hardin, 2001; Maxam & Gilbert, 1977; Rubin & Schmid, n.d.). The chemicals mentioned above methylate their specific bases. Only in high salt (NaCl) environment, hydrazine prevents methylation of the thymine base, thus making the distinction between thymine and cytosine bases easier. In addition, hot piperidine added to the medium breaks the chain of methylated DNA (Rubin & Schmid, n.d.).

The Maxam-Gilbert method isn't routinely used in the laboratory due to various disadvantages (Hardin, 2001) such as high toxicity because of the phosphate isotope and cutting chemical usage, difficulties analyzing sequences longer than 500 bp, and errors during cleavage (Franc et al., 2003).

Sanger Method

The Sanger method, which was introduced by F. Sanger in 1977, is a method based on chain elongation termination, which is used in DNA sequencing with the help of polymerase and special nucleotides (McCombie et al., 2019; Sanger et al., 1977). The elongation of the chain is terminated by synthetic ddNTPs (dideoxynucleoside triphosphate; ddCTP, ddTTP, ddGTP, ddATP), which are the monomers of the DNA chain added to the reaction (Bruijns et al., 2018; Garrido-Cardenas et al., 2017; Heather & Chain, 2016). The only difference between these ddNTPs and dNTPs (deoxynucleotide triphosphate; dCTP, dTTP, dGTP, dATP) is that they lack a hydroxyl group on the deoxyribose sugar's third carbon (Garrido-Cardenas et al., 2017). Lack of hydroxyl causes polymerization to stop, and thus, chain elongation is stopped because it cannot establish a bond with the 5' phosphate of the following dNTP (Heather & Chain, 2016). ddNTPs are designed for each nucleotide separately. Since each base corresponds to a different ddNTP reaction, the Sanger method of DNA sequencing creates a total of 4 distinct reactions for each base (Figure 2). Template DNA, polymerase, primer, ddNTP, and dNTP are all included in each tube (Bruijns et al., 2018; Hardin, 2001). Unlike dNTPs added to the reaction, the concentration of ddNTPs should be lower (Bruijns et al., 2018). When the polymerase adds one ddNTP to the elongated thread, no additional

base can be added and the elongation stops (Hardin, 2001). In this reaction carried out in parallel, loading is made into a separate well (4 different lanes) for each ddNTP on the polyacrylamide gel (Heather & Chain, 2016). In electrophoresis, the negative property of DNA is used and the positions of the DNA strands are determined (Hardin, 2001). DNA strands transferred onto the gel form a ladder image when exposed to X-rays due to their different base lengths. Since the shortest thread will advance first, the reading is performed from the bottom up (McCombie et al., 2019).
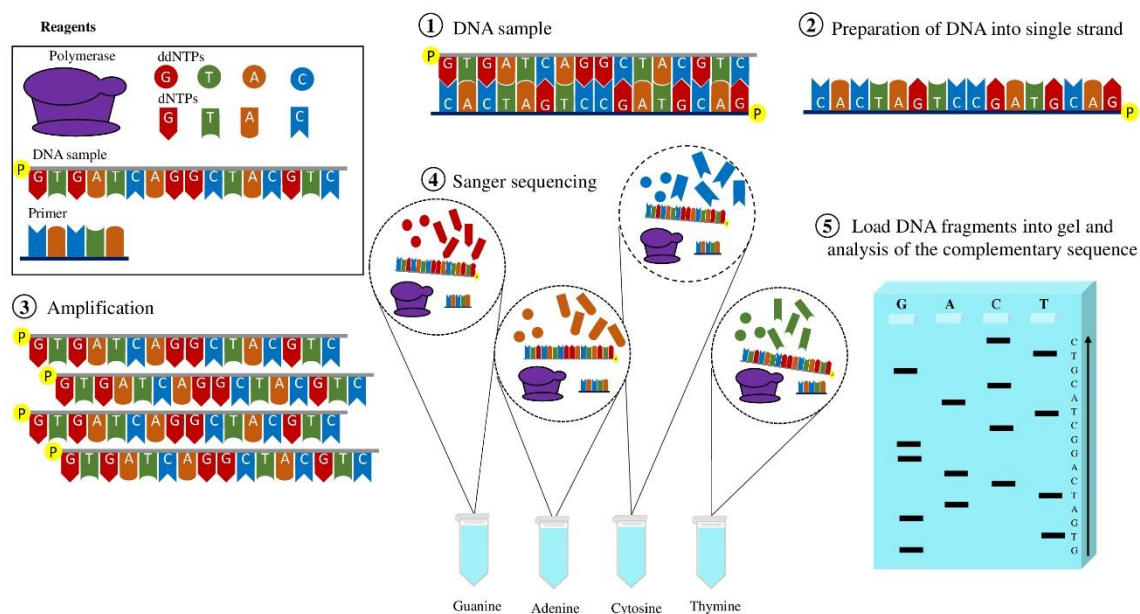
Figure 8. Schematic representation of the old Sanger method. G: Guanine, A: Adenine, C: Cytosine, T: Thymine, P: Phosphate, ddNTPs: Dideoxynucleoside triphosphate, dNTPs: Deoxyribonucleotide triphosphate.

With the advancement of technology, the Sanger method has begun to be performed with fluorescently labeled ddNTPs and capillary electrophoresis (Bruijns et al., 2018). While it was necessary to set up four different reactions for each base with the old method, the reaction is carried out only in a single tube with fluorescently labeled ddNTPs. Each ddNTP is labeled with four different base-specific fluorescent dyes (McCombie et al., 2019). These fluorescently labeled ddNTPs provide information about the last added base to the DNA strand. By capillary gel electrophoresis, DNA fragments are sorted by size difference. The fluorescent dye at the terminator of ddNTPs on the last bases of the DNA sequences undergoing electrophoresis glows with a laser. Fluorescent detection occurs through spectral detectors called CCD (Charge-Coupled Device) (Garrido-Cardenas et al., 2017). Software is required to interpret and analyze sequences (Figure 3)(Slatko et al., 2018).
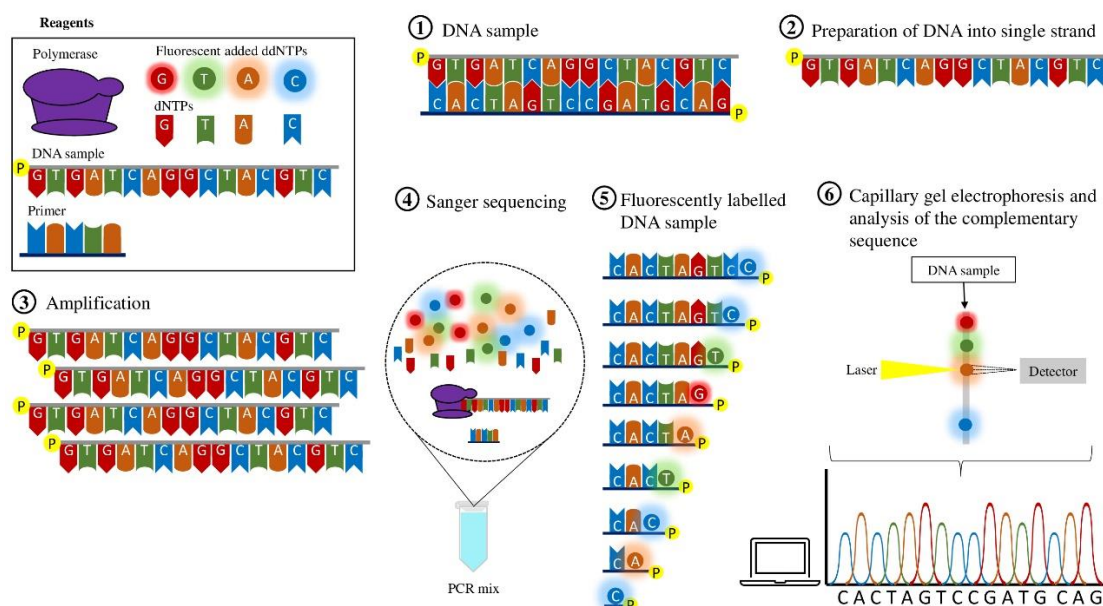
Figure 9. The new Sanger method in its simple form. G: Guanine, A: Adenine, C: Cytosine, T: Thymine, P: Phosphate, ddNTPs: Dideoxynucleoside triphosphate, dNTPs: Deoxyribonucleotide triphosphate, PCR: Polymerase chain reaction.

The Sanger sequencing method is still valid today. According to the Maxam-Gilbert method, the use of hazardous chemicals and radioactive materials is limited. Therefore, it is a less toxic method. The automated Sanger method is the most commonly used one among DNA sequencing methods (Dönmez et al., 2015). The sequence synthesized in this method constitutes the complement of the target sequence.

2. Second-Generation Sequencing

Second-generation sequencing technology allows for the rapid sequencing of whole genome. For this next- generation sequencing, there are several different kits and equipment possibilities. These tools and kits are designed to make the procedures cost-effective and time-saving. As second-generation novel sequencing techniques, it makes use of the Roche 454, Illumina, SOLiD, and Ion Torrent platforms.

Roche 454 Method

The Roche/454 GLS FLX Titanium instrument uses a platform known as pyrosequencing. Emulsion PCR and the subsequent pyrophosphate detection technique are the foundations of Roche/454 pyrosequencing (Salmaninejad et al., 2019). Nyrén et al. introduced the pyrosequencing concept for the first time in 1997 (Nyrén, 2007). It is a continuing procedure that combines magnetic beads covered with streptavidin, 3'-deficient recombinant DNA polymerase, and luciferase. 5'exonuclease activity (read-out evidence) and luminescence detection bring the process to a close (Liu et al., 2012).

The 400-600 bp DNA fragments from the sequencing sample should be divided into libraries by adding adapter sequences to both ends (Escalante et al., 2014). During the library-building process, PCR amplification by DNA polymerase lengthens each DNA fragment in the sample as nucleotides are added (Balzer et al., 2010). In this method, each nucleotide must be added one by

one to the reaction. Each amplification reaction occurs in a well containing a single DNA molecule in the form of a nanosphere or bead, oligonucleotides or probes attached to its surface, a polymerase, and other essential elements (dNTPs, buffer, MgCl$_2$, primers). The adapter sequences on the DNA fragments are complementary to the sequence of the probes. Only one DNA molecule can exist in each well for there to be a clonal amplification associated to each well. After library creation, the finished emulsion is placed in a PTP (Picotiter plate). In each of the 100,000 wells that are individually observed during the pyrosequencing procedure, PTP only supplies one bead. Each well's data will be produced for a different DNA sequence. This procedure is called Emulsion PCR (Figure 4).
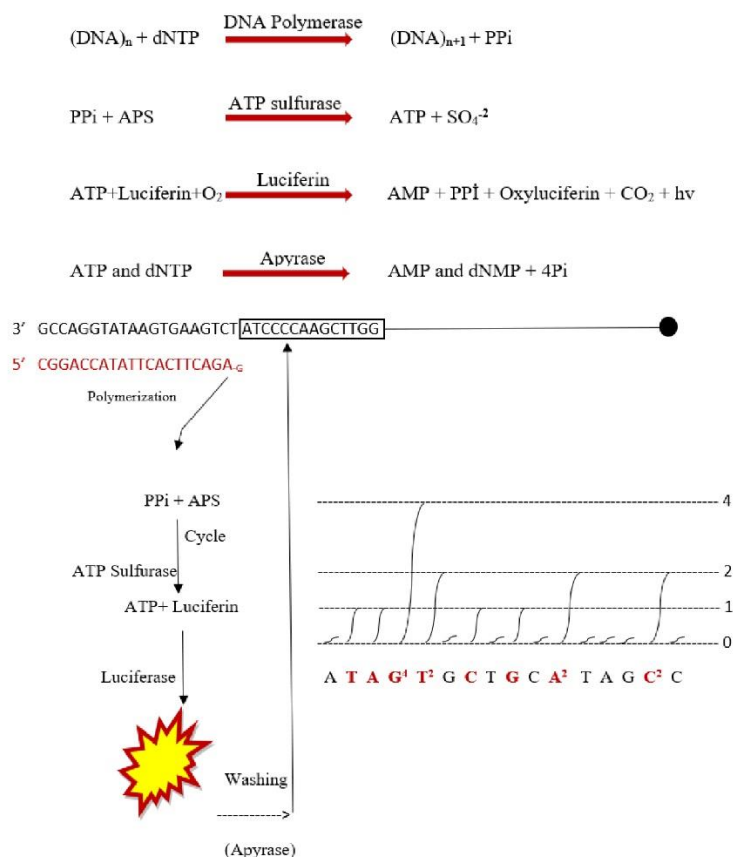
Figure 10. Principle of Roche 454 method. G: Guanine, A: Adenine, C: Cytosine, T: Thymine, dNTPs: Deoxyribonucleotide triphosphate, ATP: Adenosine triphosphate, AMP: Adenosine monophosphate, dNMP: deoxyribonucleoside monophosphate, APS: Adenosine 5'-phosphosulfate sodium salt, PPİ: Pyrophosphate, Pi: Phosphatase, hv: Emission of light.

Illumina Method

Illumina acquired the Solexa Genome Analyzer and commercialized it in 2007, and today, the HiSeq and MiSeq platforms in particular are the most successful sequencing system on the market. The amplified template DNA for sequencing creates miniature colonies called polonies by bridging PCR (Slatko et al., 2018).

In order to sequence data, Illumina uses reversible dyes. When added to DNA strands, these colors make it possible to recognize nucleotides. The blocking group and fluorescence with a distinct color for each nucleotide are revealed when the nucleotide binds. To create DNA fragment clusters, the adaptor segments are joined to single strands and put in the flow cell. Bridge

amplification is then carried out (Liu et al., 2012). The four types of nucleotides (A/T/C/G) are introduced, and each is fluorescently labeled with a different color. The unincorporated nucleotides are washed away as the four nucleotides compete for binding sites on the template DNA to be sequenced. Each synthesis is followed by the use of a laser to eliminate the fluorescent probe and blocking group. The subsequent cycle starts when one of the four bases develops a measurable fluorescent color distinct to it that allows for sequence identification. Up until the DNA molecule is sequenced, this process continues (Figure 5).
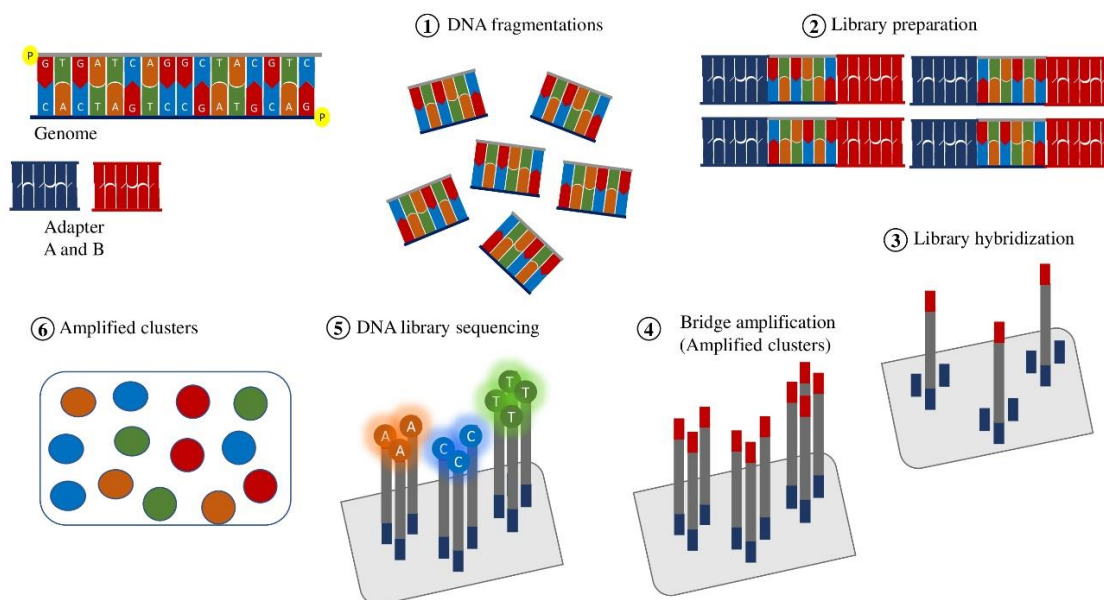
Figure 11. Library preparation and Illumina method. G: Guanine, A: Adenine, C: Cytosine, T: Thymine.

Scale differences between HiSeq and MiSeq technologies are substantial. In 10.8 days run, the HiSeq2000 produces more than 50 Gb of data and 1.6 billion base 100 dual-ended reads. MiSeq, in comparison, generates 1.5 Gb every day from 5 million 150-base paired-end reads and is intended for trials that last only one day (Slatko et al., 2018).

Compared to conventional sequencing techniques like Sanger sequencing, the Illumina approach has some advantages. Multiple sequences can be quickly sequenced at once using Illumina sequencing. Furthermore, unlike pyrosequencing, which requires expensive enzymes, this approach just employs DNA polymerase (Slatko et al., 2018). With a 0.1% error rate, Illumina's reversible terminator technology and paired-end sequencing make it the most accurate base-by-base sequencing method available (Hu et al., 2021). Sequence data outperforms most other systems in terms of throughput, read length, cost, and run time.

Solid Method

The ligation sequencing-based platform Solid Method was purchased by Applied Biosystems in 2006. A high rating of 99.85% indicates that the data collected through this platform's filtering is accurate (Liu et al., 2012).

This technique also uses the Roche 454 emulsion PCR method, which uses tiny magnetic beads. When the DNA library is finished using PCR, the magnetic beads are affixed to a glass flow cell plate. The amplified fragments are sequenced using DNA ligase. These base pairs are found on two-base coded probes that have been specially created. These sensors are a mixture composed of

an identifier base pair, a fluorescent molecule, and certain base components. Four distinct colors are defined to symbolize each base pair. The probe with the correct base pair is added to the sequence and bound to the primer by the ligase during the first cycle after the primer has been connected to the adapter. The fluorescent lights and the camera shows the light as a result of binding. Following the removal of unbound probes, imaging of the fluctuating fluorescence that distinguishes the bound probe is completed. The sequential ligation cycle is restarted when the fluorescent dye has been removed (Escalante et al., 2014).

The newly generated sequence, together with the primer, is entirely discarded, and the preceding procedures are started over with a new primer. New primer is attached to the main adapter that was previously handed to the medium one base back. The binding order in their detectors have been changed this time, which have result in various glow colors, because all of these other identifying base pairs bind one base back (n-1). During this time, the fluorescent color have been changing due to the new base pair. The nucleic acids determine according to this alteration. The known sequence is gradually completed with each cycle by shifting back a main base, and after five cycles, there is enough data to make up for any gaps in the sequence (Figure 6).
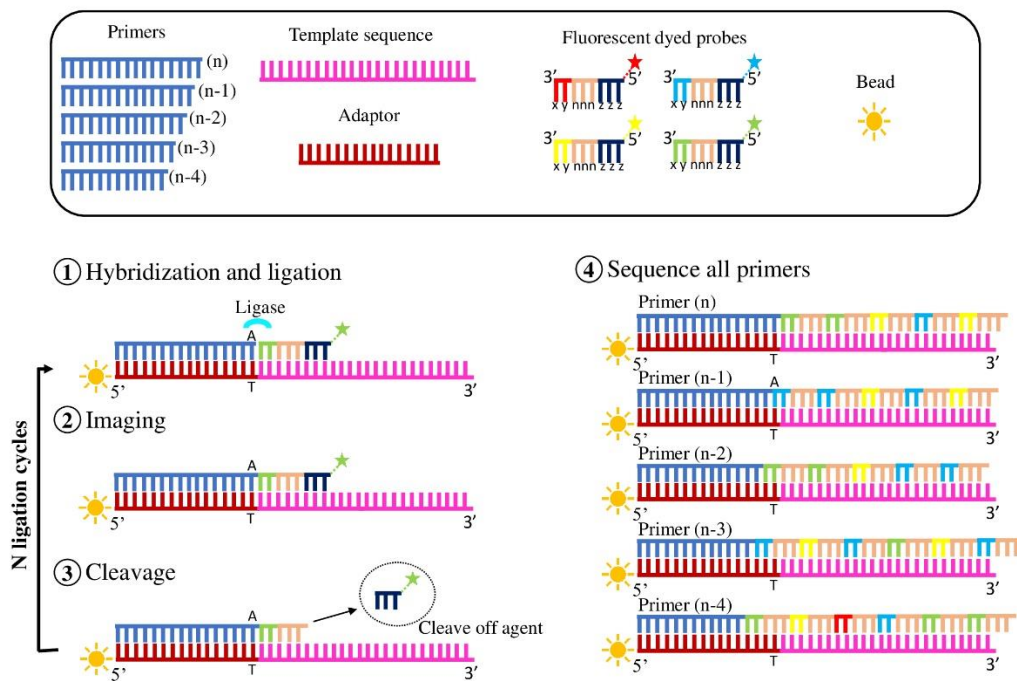
Figure 12. Stages of Solid method. G: Guanine, A: Adenine, C: Cytosine, T: Thymine, x: First base, y: Second base, n: Degenerate bases, z: Universal bases, Primer(n): GCGTAACGTAATGCTA.

5 different primers are used in the solid method. The base at the end of the primer is reduced by one, completing the sequence in 5 cycles. The reason why there are five cycles is for the detection of degenerate bases in the prepared probes in other cycles. While designing the primer, the first base of the sequence is determined by the last base of the primer. It is known that the last base of the primer is A. Considering at the color scale table, the 2nd base is determined by looking at the base corresponding to the color of the 1st base (A). The 1st base of the other probe, which is in line with with the 2nd base, is determined. The same process continues for the others, and the DNA sequence is completed (Figure 7). Solid sequencing method can be used in whole genome sequencing, targeted region sequencing, and analysis of gene expressions and small RNAs.
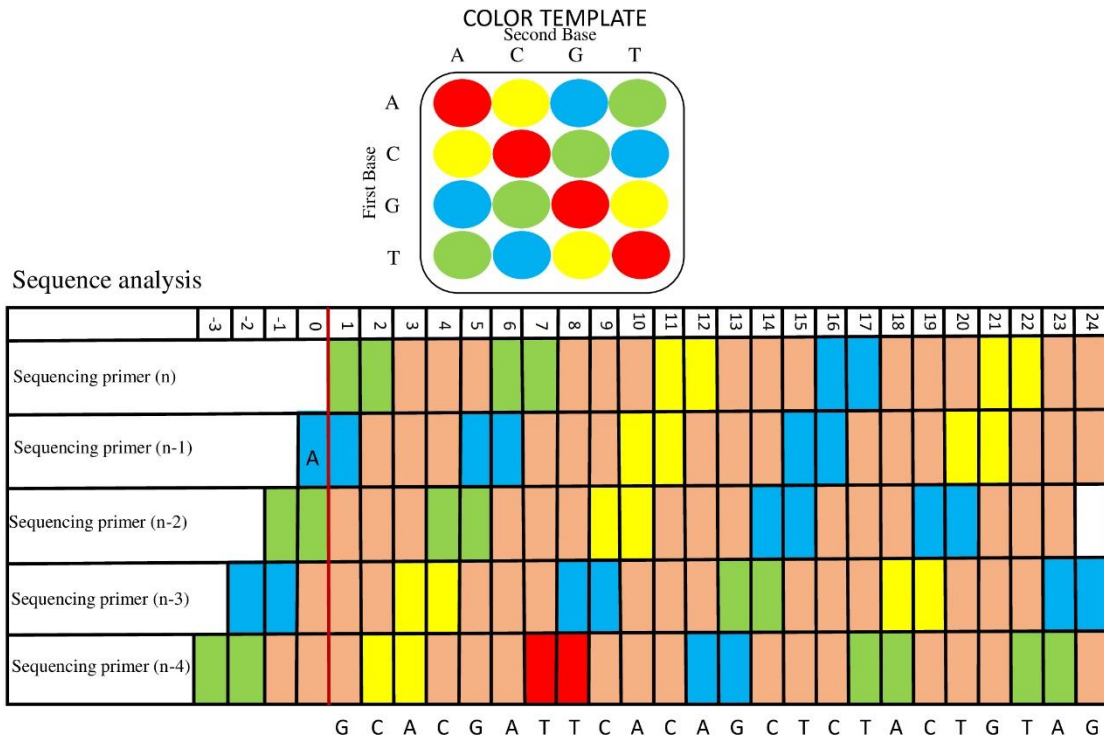
Figure 13. Analysis of DNA sequence with Solid method. G: Guanine, A: Adenine, C: Cytosine, T: Thymine, Primer(n): GCGTAACGTAATGCTA.

Solid method can complete a single run in 7 days and generate 30 Gb of data in that time. Unfortunately, its main drawback is that read lengths are short and unsuitable for many applications.

Ion Torrent Method

A primary base is shifted back in this method in each cycle, making the known sequence a little bit more complete at each step. After five cycles, there are enough information to fill in any gaps in the sequence. There are five ligation cycles in total. A reliable approach for sequencing; it can be applied to small RNA and gene expression analyses, whole genome sequencing, and targeted region sequencing (Üstek et al., n.d.).

This optics-based technique gathers photons from genome sequences and information on the appearance of the genome's base pairs. Conductive metals and software are combined in Ion Torrent (CMOS). Thus, the surface potential change of the metal oxide sensitive layer is stimulated and the potential of the terminal changes (Escalante et al., 2014).
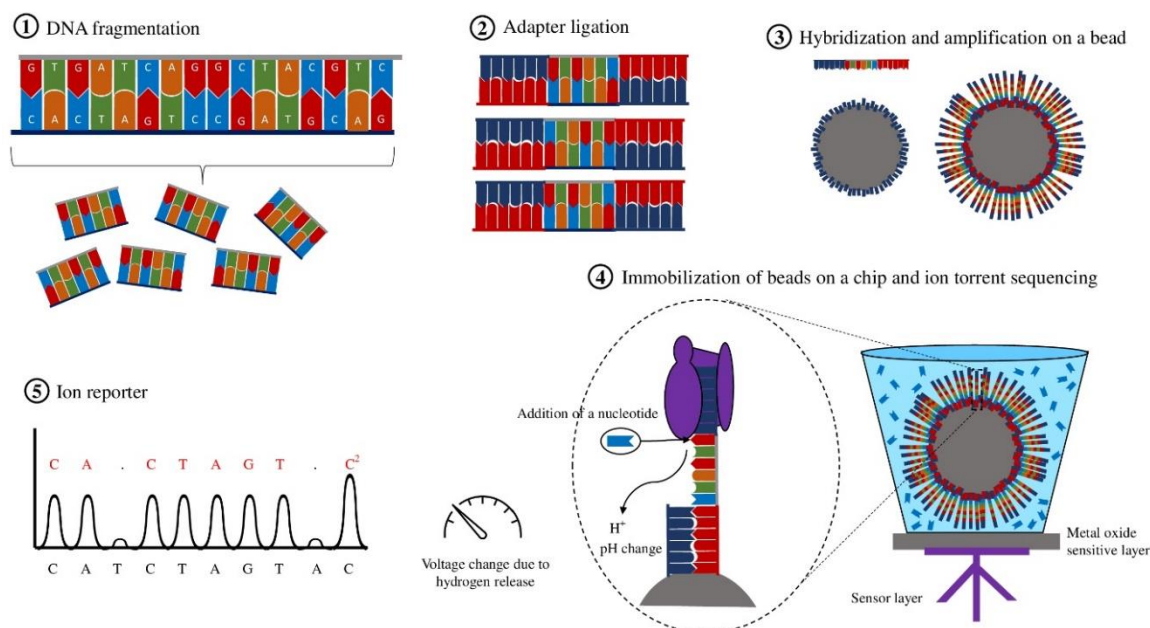
Figure 14. Ion Torrent sequencing and ion reporter. G: Guanine, A: Adenine, C: Cytosine, T: Thymine.

With the help of particular adapter sequences, fragmented DNA is joined to microbeads. Emulsion PCR beads are placed in a "chip" that has a million micro-wells, one bead in each one. A microchip with flow cells and electrical sensors below the cells hosts the sequencing reaction. Each nucleotide is incorporated and turned into an electrical signal. Protons are found using a semiconductor sensor that is ion sensitive. A voltage signal proportional to pH is created from the sensor. Protons are found using a semiconductor and ion sensitive semiconductor sensor. The sensor converts the pH fluctuations in the well into a voltage signal. Each well is integrated into the ion sensitive layer of the chip and the ion sensor, allowing for the recording of very minute voltage changes caused by nucleotide addition during DNA synthesis sequencing. One by one, dNTPs are inserted into the wells. Unlabeled dNTPs are cleaned one after the other. Hydrogen ions are released as dNTP, which is complementary to the incoming nucleotide and is added to the chain. The pH of the solution varies as the H protons are released in direct proportion to the quantity of nucleotides (Figure 8) (Escalante et al., 2014).

The major disadvantage of the system is the problems in reading homopolymer extensions and repeats. Its main advantages seem to be relatively longer read lengths, more flexible workflow, more reduced time, and a more affordable price than those provided by other platforms.

3. Third-Generation DNA Sequencing

With the increasing use of DNA sequencing methods, new technological developments are needed. Although first- and second-generation sequencing methods are revolutionary for DNA sequencing, they need to be improved in many aspects such as time, cost, and error rate. As a result of these searches, third-generation sequencing methods with longer read length, low cost and faster sequencing have been developed (Mohammadi & Bavi, 2022; Rhoads & Au, 2015). The distinguishing features of the method are the fact that it doesn't need amplification and allows real-time analysis without fragmenting the DNA (as a single molecule) (Athanasopoulou et al., 2022; Bruijns et al., 2018; Liu et al., 2012). Third-generation DNA sequencing methods are divided into two techniques as Pacific Bioscience and Oxford Nanopore Technology.

Pacific Bioscience (PacBio) Method

Pacific Biosciences' PacBio method, which was released at the end of 2010, is an SMRT-based method (Single Molecule Real Time) (Bruijns et al., 2018; Garrido-Cardenas et al., 2017; Slatko et al., 2018). It is a method used to read long-dimensional DNA sequences by making use of the components necessary for DNA synthesis (Athanasopoulou et al., 2022). In addition, the duration of preliminary preparation method is shorter than the other methods. The method involves inserting hairpin-shaped sequences known as "SMRTbell" at the beginning and end of a double-stranded DNA sample. Thanks to these sequences, the DNA becomes a circular sequence and minimizes base errors with long repetitive readings. The SMRTbell embedded DNA binds to polymerases that are immobilized to the base of a chip made of ZMW (Zero Mode Waveguides) technology (Garrido-Cardenas et al., 2017; Pareek et al., 2011). In contrast to conventional DNA sequencing techniques, which sequence DNA by wrapping the polymerase around the DNA, this technique sequences DNA by immobilizing the polymerase to the well's bottom (Athanasopoulou et al., 2022). There are thousands of picoliter ZMW wells on the chip and each well contains only one polymerase. Thus, a single DNA molecule is attached to only one well and can be analyzed in real-time. As the fluorescently labeled dNTP is incorporated into the DNA, a different colored glow appears for each base (Garrido-Cardenas et al., 2017; Liu et al., 2012; Pareek et al., 2011). The signal ends with the cleavage of the nucleotide-bound fluorescent dye pyrophosphate by the polymerase (Rhoads & Au, 2015). Imaging takes place instantaneously for each base added to the DNA (Slatko et al., 2018). An optical system with green and red lasers at the bottom of the ZMW continuously observes the radiations in milliseconds. This process takes place in other wells simultaneously and in parallel. ZMW ensures that the light is distorted exponentially. As a result, fluorescent light only illuminates the well's bottom and doesn't diffuse into neighboring wells (Figure 9) (Garrido-Cardenas et al., 2017; Slatko et al., 2018).
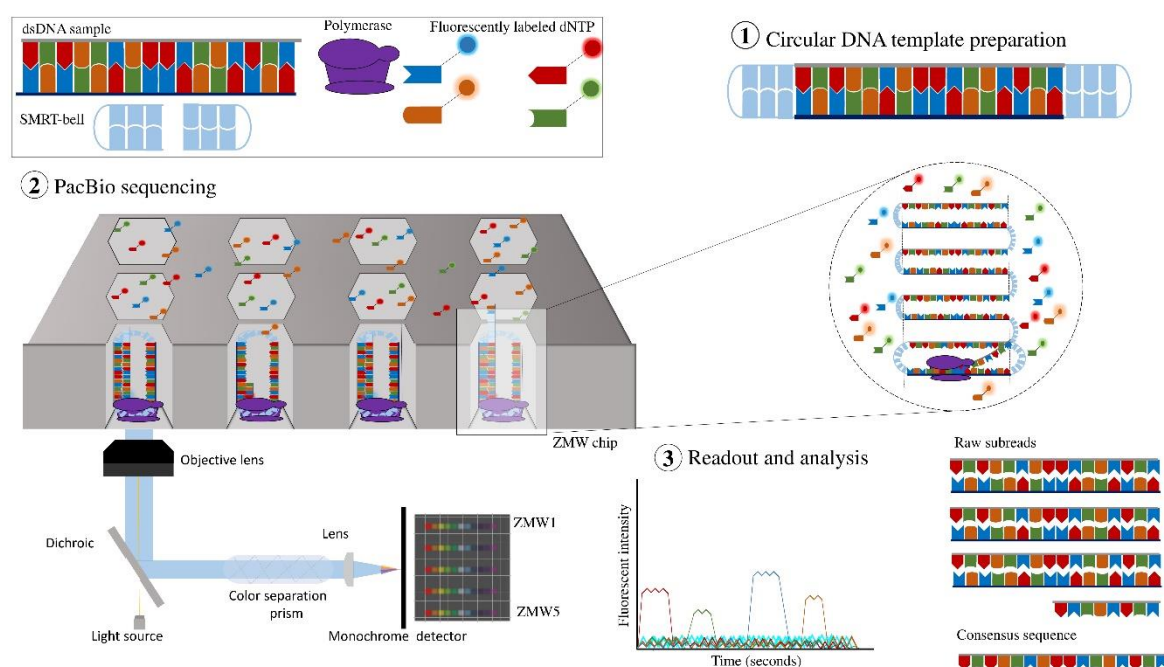
Figure 15. The basic principle of PacBio sequencing method. dsDNA: Double-stranded DNA, SMRT: Single molecule real-time, ZMW: Zero mode waveguide.

In addition to DNA sequencing, this method can detect epigenetic modifications and structural changes in the DNA sequence (Liu et al., 2012; Slatko et al., 2018). SMRT sequencing,

which is still in development, is the most commonly used platform among third-generation sequencing methods (Heather & Chain, 2016). With the use of SMRTbell, the PacBio method showed its difference compared to other methods. While this method sorts quickly, it has a high error rate. The control of this problem is provided by reading the same sequence more than once and evaluating similar templates (Slatko et al., 2018). The reading time varies depending on the length of the DNA but ranges from 0.5 to 4 hours (Rhoads & Au, 2015).

Oxford Nanopore Technology (ONT) Method

Another of the third-generation DNA sequencing methods is the ONT method developed by Oxford Nanopore Technologies. Despite the fact that this concept was first proposed in 1990, it has just recently been commercially available (Athanasopoulou et al., 2022). This technique theoretically has a much lower mistake rate because it does not involve the use of enzymes, amplification, or fluorescently tagged nucleotides. For this method, an artificial nanopore embedded in the membrane with an electric current (100 pA – 100 mV) is needed (Liu et al., 2012). This nanopore is formed by alpha-hemolysin (αHL), a 33 kD protein derived from *Staphylococcus*
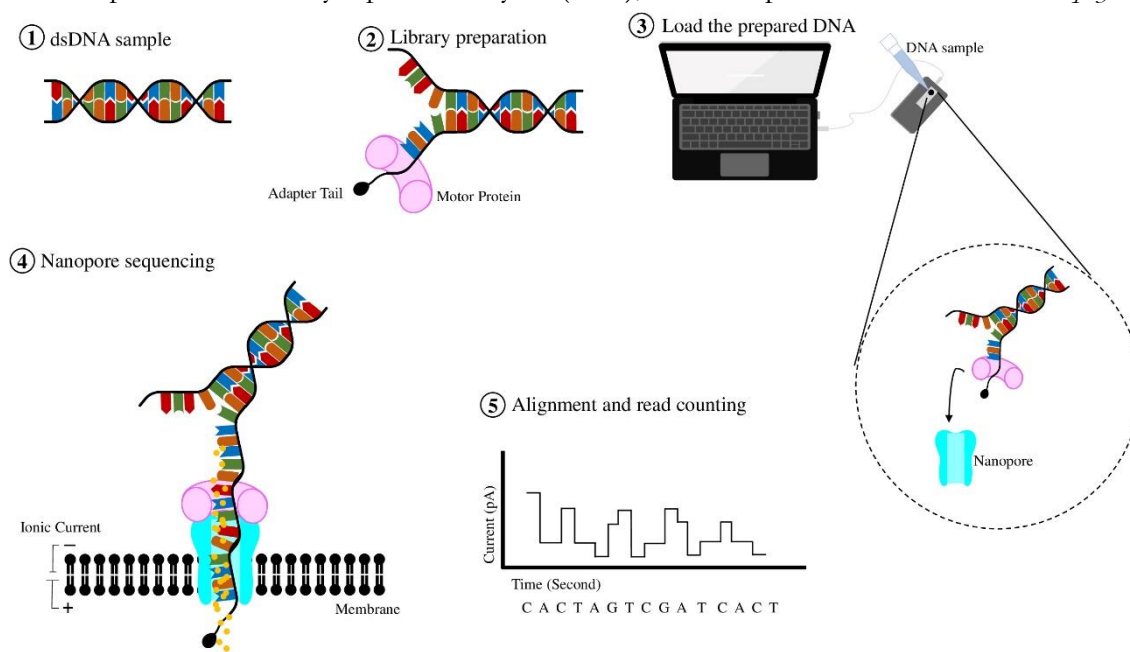
Figure 16. The Oxford nanopore technology method in its simple form. dsDNA: Double-stranded DNA, G: Guanine, A: Adenine, C: Cytosine, T: Thymine, pA: Picoampere.

aureus (Dönmez et al., 2015). Before the DNA can be sequenced, the polyA tail-containing adapter sequence needs to be introduced into it. The adapter sequence is recognized and transported to the nanopore by a motor protein. Once the nanopore detects the adapter sequence, DNA begins to pass through the nanopore as a single strand. Since DNA is negatively charged, DNA moves through the nanopore with the ionic current passing through the membrane. Each of the bases that make up the genetic material will create a different interruption on the ionic current. The characterization of the molecule passing through the nanopore according to the interruption of the current is carried out by the algorithm (Figure 10) (Feng et al., 2015).

The advantage of ONT over other methods is that it can read in a short time. In this method, analysis takes place without a secondary signal such as fluorescence, pH, or color. Since it does not need an enzyme like polymerase, it can sequence without the exposure to high temperatures. In addition, since it does not require amplification, there is no long sample preparation step (Liu et

al., 2012). In addition to being crucial for DNA sequencing, ONT is also crucial for characterizing RNAs, proteins, peptides, polymers, medicines, and macromolecules (Feng et al., 2015).

Future Approaches

Many complex diseases, including cancer, have been diagnosed and treated using sequencing techniques. Although methods such as RT-PCR, FISH, and immunohistochemistry are used in the diagnosis of diseases, sequencing methods have a greater advantage. Sequencing methods can pave the way for new perspectives in disease diagnosis and treatment. Genetic variants that are currently unknown can be identified by sequencing. In order to find alternative treatment methods, changes in DNA, RNA, or protein levels can be examined by sequencing methods, mutations in cancer signaling pathways or repair mechanisms can be detected, and genetic profiles of individuals can be narrowed by comparing transcriptome readings of genetic materials obtained from patients and healthy individuals. As a result, the disease can be diagnosed early on, paving the way for personalized treatment methods.

Multiple sequencing methods have been introduced to date. These sequencing methods differ in terms of read speed, accuracy and cost. Since DNA is a long material, the time, cost and required storage space of the sequencing method increase proportionally.

Reference

Athanasopoulou, K., Boti, M. A., Adamopoulos, P. G., Skourou, P. C., & Scorilas, A. (2022). Third-Generation Sequencing: The Spearhead towards the Radical Transformation of Modern Genomics. *Life*, *12*(1). https://doi.org/10.3390/LIFE12010030

Balzer, S., Malde, K., Lanzén, A., Sharma, A., & Jonassen, I. (2010). Characteristics of 454 Pyrosequencing Data-enabling Realistic Simulation with Flowsim. *Bioinformatics*, *26*(18), i420–i425. https://doi.org/10.1093/BIOINFORMATICS/BTQ365

Behjati, S., & Tarpey, P. S. (2013). What is next generation sequencing? *Archives of Disease in Childhood. Education and Practice Edition*, *98*(6), 236–238. https://doi.org/10.1136/ARCHDISCHILD-2013-304340

Bleidorn, C. (2015). Third generation sequencing: technology and its potential impact on evolutionary biodiversity research. *Systematics and Biodiversity*, *14*(1), 1–8. https://doi.org/10.1080/14772000.2015.1099575

Bruijns, B., Tiggelaar, R., & Gardeniers, H. (2018). Massively parallel sequencing techniques for forensics: A review. *Electrophoresis*, *39*(21), 2642. https://doi.org/10.1002/ELPS.201800082

Collins, F. S., Patrinos, A., Jordan, E., Chakravarti, A., Gesteland, R., & Walters, L. R. (1998). New goals for the U.S. Human Genome Project: 1998-2003. *Science*, *282*(5389), 682–689. https://doi.org/10.1126/science.282.5389.682

Doğan, M., Eröz, R., Yüce, H., & Özmerdivenli, R. (2017). *Yeni Nesil Dizileme (YND) Hakkında Bilinenler (Literatür Taraması) The Known about Next-Generation Sequencing (NGS) (Review of the Literature). 19*(1), 27–30.

Dönmez, D., Şimşek, Ö., & Aka Kaçar, Y. (2015). Yeni Nesil DNA Dizileme Teknolojileri ve Bitkilerde Kullanımı. *Türk Bilimsel Derlemeler Dergisi*, *8*(1), 30.

Escalante, A. E., Barbolla, L. J., Ramírez-Barahona, S., & Eguiarte, L. E. (2014). The study of biodiversity in the era of massive sequencing. *Revista Mexicana de Biodiversidad*, *85*(4), 1249–1264. https://doi.org/10.7550/RMB.43498

Feng, Y., Zhang, Y., Ying, C., Wang, D., & Du, C. (2015). Nanopore-based Fourth-generation DNA Sequencing Technology. *Genomics, Proteomics & Bioinformatics*, *13*(1), 4. https://doi.org/10.1016/J.GPB.2015.01.009

Franc, L. T. C., Carrilho, E., & Kist, T. B. L. (2003). A review of DNA sequencing techniques. *Quarterly Reviews of Biophysics*, *35*, 169–200. https://doi.org/10.1017/S0033583502003797

Garrido-Cardenas, J. A., Garcia-Maroto, F., Alvarez-Bermejo, J. A., & Manzano-Agugliaro, F. (2017). DNA Sequencing Sensors: An Overview. *Sensors (Basel, Switzerland)*, *17*(3). https://doi.org/10.3390/S17030588

Hardin, S. H. (2001). DNA Sequencing. *Encyclopedia of Life Sciences.*

Heather, J. M., & Chain, B. (2016). The sequence of sequencers: The history of sequencing DNA. *Genomics*, *107*(1), 1. https://doi.org/10.1016/J.YGENO.2015.11.003

Hu, T., Chitnis, N., Monos, D., & Dinh, A. (2021). Next-generation sequencing technologies: An overview. *Human Immunology*, *82*(11), 801–811. https://doi.org/10.1016/J.HUMIMM.2021.02.012

Liu, L., Li, Y., Li, S., Hu, N., He, Y., Pong, R., Lin, D., Lu, L., & Law, M. (2012). Comparison of Next-Generation Sequencing Systems. *Journal of Biomedicine and Biotechnology*, *2012*, 11. https://doi.org/10.1155/2012/251364

Maxam, A. M., & Gilbert, W. (1977). A new method for sequencing DNA (DNA chenistry/dimethyl sulfate cleavage/hydrazine/piperidine). *Biochemistry*, *74*(2), 560–564.

McCombie, W. R., McPherson, J. D., & Mardis, E. R. (2019). Next-Generation Sequencing Technologies. *Cold Spring Harbor Perspectives in Medicine*, *9*(11). https://doi.org/10.1101/CSHPERSPECT.A036798

Mohammadi, M. M., & Bavi, O. (2022). DNA sequencing: an overview of solid-state and biological nanopore-based methods. *Biophysical Reviews*, *14*(1), 99. https://doi.org/10.1007/S12551-021-00857-Y

Nyrén, P. (2007). 1-The History of Pyrosequencing ®. In M. Sharon (Ed.), *Pyrosequencing Protocols* (Vol. 373). Humana Press. http://link.springer.com/10.1385/1597453773

Pareek, C. S., Smoczynski, R., & Tretyn, A. (2011). Sequencing technologies and genome sequencing. *Journal of Applied Genetics*, *52*(4), 413. https://doi.org/10.1007/S13353-011-0057-X

Reis-Filho, J. S. (2009). Next-generation sequencing. *Breast Cancer Research : BCR*, *11*(Suppl 3), S12. https://doi.org/10.1186/BCR2431

Rhoads, A., & Au, K. F. (2015). PacBio Sequencing and Its Applications. *Genomics, Proteomics & Bioinformatics*, *13*(5), 278. https://doi.org/10.1016/J.GPB.2015.08.002

Rubin, C. M., & Schmid, C. W. (n.d.). *Nucleic Acids Research Pyrimidine-specific chemical reactions useful for DNA sequencing. 5*, 1980.

Salmaninejad, A., Motaee, J., Farjami, M., Alimardani, M., Esmaeilie, A., & Pasdar, A. (2019). Next-generation sequencing and its application in diagnosis of retinitis pigmentosa. *Ophthalmic Genetics*, *40*(5), 393–402. https://doi.org/10.1080/13816810.2019.1675178

Sanger, F., Nicklen, S., & Coulson, A. R. (1977). *DNA sequencing with chain-terminating inhibitors (DNA polymerase/nucleotide sequences/bacteriophage 4X174). 74*(12), 5463–5467.

Slatko, B. E., Gardner, A. F., & Ausubel, F. M. (2018). Overview of Next Generation Sequencing Technologies. *Current Protocols in Molecular Biology*, *122*(1), e59. https://doi.org/10.1002/CPMB.59

Üstek, D., Abacı, N., Sırma, S., & Çakiris, A. (n.d.). Yeni Nesil DNA Dizileme. *Deneysel Tıp Araştırmalar Dergisi*, *1*(1), 11.

Zhong, Y., Xu, F., Wu, J., Schubert, J., & Li, M. M. (2021). Application of Next Generation Sequencing in Laboratory Medicine. *Ann Lab Med*, *41*, 25–43. https://doi.org/10.3343/alm.2021.41.1.25

Nocode Machine Learning for Aplied Sciences and Engineering

Akın ÖZÇİFT[1]

Introduction

Machine Learning (ML) becomes widely used in many disciplines successfully. On the other hand, this new science at first glance needs a programming language such as Python to be applied. Preparation of data and generation of ML model may require heavy computer language based skills. Computer oriented disciplines may successfully adapt themselves easily to this trend. However, applied sciences, most of the engineering disciplines even social science originated persons may need to apply ML models to their problems. Though many universities try to teach ML based data science courses, the computer programing based approach limits usage of ML within communities.

In this aspect, there is a new trend i.e. no-code software development, targeting persons with low or no coding skills. More precisely, software development cycle requires coding skills to some degree. On the other hand, some software development phases may be defined as strictly defined steps and this routine may be repeated through "no-code" environments that needs no advanced coding skills. In this manner, newly developed no-code frameworks may allow persons to design some software routines similar to web-page design environments. With more clear terms, newly designed no-code frameworks are similar to web-design interfaces from ease of usability and they allow novice coders to develop software for a specific goal (Woo et al., 2020).

In a similar approach, ML applications may also be interpreted in a well-defined software development task and therefore non-expert users, scientists may develop their ML algorithms to analyze their data and to solve their problems. From this perspective WEKA (Bouckaert et al.) is an open-source no-code ML platform that allows scientist to experiment ML algorithms with limited or no coding skills. There are also cloud based ML frameworks such as Amazon Sage Maker (Liberty et al., 2020) that helps users to develop their ML algorithms for their own problems with minimal coding efforts.

Steps of Generation of Machine Learning Models

As we aforementioned, ML algorithm generation may be summarized in compact steps such as (i) definition of problem, (ii) collection of data, (iii) processing of data to suit ML algorithms to process, (iv) training of various ML algorithms and (v) evaluation (test) of ML algorithms. Though there may be other steps, the overall ML generation may be summarized as above. The mentioned steps may be explained as follows:

I) There are two types of ML methods that are frequently used for scientific problems. These two types are in general known as numerical (regression) forecasting or classification (label) identification. In particular numerical forecasting is used in energy generation prediction, weather prediction, solar power prediction etc. (Vinuesa et al., 2022). The other type of ML techniques are used in label prediction such as in categorization of illnesses (Alanazi et al. 2022). More precisely, the two categories may be used to solve numerical prediction problems and label identification

---

[1] Assoc. Prof., Manisa Celal Bayar University

problems. So the summarization of this step is the *identification of the problem* type as regression or classification.

II) Having defined the type of the problem, the data required to train ML algorithms should be prepared. More clearly, for the two supervised problem types, the data must be generated in a table-like style having samples (rows), column names (properties of samples regard to the problem) and the target column (forecasting). For example for solar panel energy generation prediction problem requires environment temperature, geolocation of panel, hour (minute) of the day, season (month) etc. The target column will possibly be the power produced through the solar panel at a specific time. Similarly, for a health diagnosis problem the rows are patients and corresponding columns are possibly pixel values of X-ray films and hence the target column possibly being the status of patient as "COVID-19" or "Not". Having obtained samples enough, the next step is to process the generated data. As a clarification, one should note that as the sample sizes increases the possible success of ML algorithms increases corollary. For an interested reader, it should be reminded that there are many datasets on the internet to be used for ML "learning" (Brickley et al., 2019). These datasets may be used to learn basic ML strategies or they can be used as templates to prepare users' own datasets (Marappan et al., 2022).

III) Preprocessing of collected data requires the data to be formatted suitable for ML algorithms. In general, removal of repetitive samples, insertion of values into *null* cells, removal of outliers, removal of unnecessary columns (some feature engineering) and conversion of data into numerical representation are some of the steps. However, it should be noted that these steps may be automated to some extent and they may be handled with automatic methods of no-code environments such as WEKA. For example, WEKA allows users to represent texts as bag of words and it also allows to statistically analyze data to remove outliers, to insert average values to nulls cells etc. After data processing, the task is to train various ML algorithms to solve the target problem.

IV) Train or learning step of ML algorithms is the next important step in ML-based problem solving approach. In particular, machines *learn* through data samples and their corresponding properties (columns) with optimizing a loss function (Wang et al., 2022). In particular, ML algorithms makes use of specialized loss-functions and learn while they optimize the corresponding functions. As they forward through learning a corresponding metric (subtraction of prediction and the respective real value) becomes more adequate. In other words, while an average error of regression approaching zero is acceptable, accuracy of classification approaching to 100 in percentage is becomes more adequate (Carvalho et al., 2019). ML algorithms in general trained with a percentage of data such as 80% and the remaining data is retained for evaluation or testing purposes that will be handled in the next step. There are 50-50, 60-40, 70-30 data splits for training and testing strategies respectively. There is also a cross-validation approach that will not be mentioned here. Since scope of the chapter does not let to make details of ML algorithm, some of the names of the ML algorithms supported by WEKA are Naïve Bayes, Support Vector Machine, Linear Regression, Logistics Regression and Random Forests (Roy et al., 2022). As a summary, having generated suitable data (for a problem type), the dataset should be divided with a split (i.e. 80-20) and some corresponding ML algorithms to be modelled with the training split.

V) Evaluation of ML models requires a metric such as Mean Squared Error (MSE) or Accuracy. MSE measures the quality of ML model in forecasting a numerical value and it is more valuable as it tends to zero for a ML algorithm. Accuracy metric measures true prediction quality of an ML algorithm and specifically it is better as it approaches to a hundred in percentage. Having selected the evaluation metrics, the ML models trained in step (iv) should be tested and compared against each other. This step determines the most valuable ML model that will be used in the solution of the designed problem.

Determination of the best ML algorithm may be extended to ensemble ML algorithms such as boosting and bagging. In this context, Gradient Boosting Trees and XG-Boost are so well-known ensembles that are used in regression and classification algorithms (Kavzoglu et. al, 2022).

Nocode Machine Learning Platforms

There are many ML frameworks that offer model development with no programming experience but only the knowledge of ML processing pipeline. Name to a few, MakeML, Obviously AI, SuperAnnotate, Teachable Machine, PyCaret (a low-code framework), MonkeyLearn, KNIME, Rapid Miner and WEKA for personal usages. Furthermore, Amazon's Sage Maker, Microsoft's Azure and Google's AutoML and BigML are cloud based ML platforms that require no-code or low-code skills to develop ML models.

In this context, we will summarize properties of WEKA that offers a wide variety of ML tools ranging from data processing to ML algorithms in an open source manner. Furthermore, this ML model development tool serves a baseline to learn other no-code platforms easily.

WEKA, is developed in Java at the University of Waikato, New Zealand. The platform contains data visualization, processing tools and related ML algorithms ranging from simple regression-classification algorithms to advanced ensemble generation methods such as boosting, bagging and stacking (Graczyk et al., 2010). One of the main advantages of the environment is that it has a user friendly Graphical User Interface (GUI) that allows user to apply ML model development tasks with some button clicks. Having installed WEKA on the computer, it is easy to observe the most widely used tool "Explorer" in Figure 1.

Figure 1. WEKA Interface

The remaining three buttons have other properties that are scope of this study. The interested reader may refer to WEKA manual and to the related tutorials through internet search.

As it was mentioned above, data statistics, visualization and processing is an important part of ML model development cycle. In this aspect, the WEKA explorer provides user with visual statistics about the dataset ingested on the "Preprocess" tab in Figure 2.
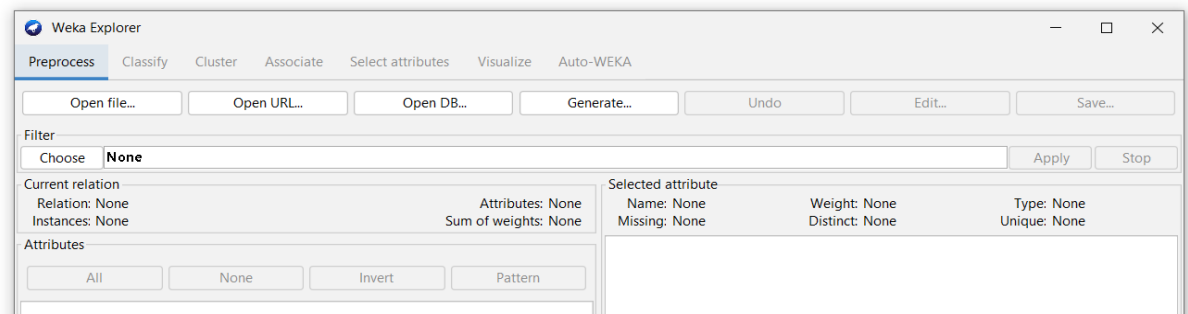
Figure 2. Explorer and related tabs in WEKA.

As it is drawn from Figure 2, the dataset (most of the time a csv or WEKA's arff file) is ingested through "open file" command and processed afterwards. Preprocessing of data may include normalization, outlier detection, feature (attribute) extraction, insertion of data into null values, removal of repetitions etc.

Following from Figure 2, "Classify" tab is the most widely used tab in WEKA and it allows user to choose ML models and train-test splits for the last two steps of ML model generation (Singhall et al., 2013). These two steps will be conducted in the following section with a case study.

A Case Study: Identification of Hypothyroidism Disease on WEKA

As it was underlined that WEKA provides users with no-code ML development environment having many advanced ML functionalities such as data processing (including feature engineering), algorithm design and advanced ensemble algorithms. Even an Auto-ML option, i.e. a high level automatic ML model development strategy, is provided with a GUI approach without requirement of code. In this case study a medical hypothyroid diagnosis problem (based on the dataset placed in the data directory under WEKA) is used to summarize whole no-code ML development cycle. Hypothyroidism is a disease that is defined as the reduction in the thyroid hormones release (Guleria et al., 2022). There is a dataset (hypothyroid.arff) inside data directory under WEKA and this dataset has the following properties given in Figure 3 (Quinlan et al., 1987).
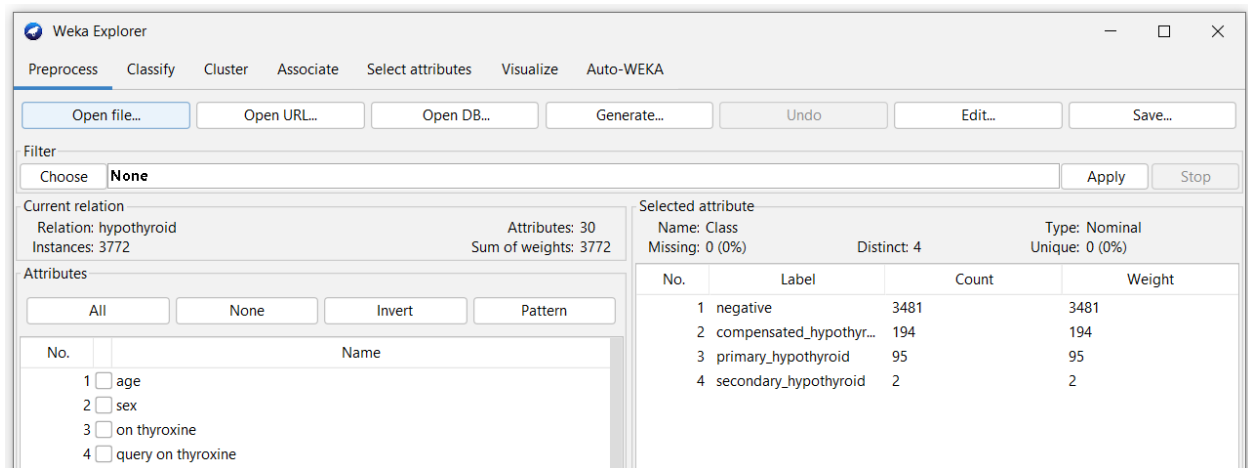
Figure 3. The properties of hypothyroid.arff dataset opened with explorer "open file".

From Figure 3, it is observed that the dataset 3772 samples (patients) with 30 attributes (defining columns such as age, sex etc.) and 4 classes (3481 healthy, 194, 95 and 2 patients with three types of thyroid dysfunctions).

This data was designed for identification of disease status of patients and hence it is a classification problem. Therefore, the classification algorithm (Naïve Bayes), train-test split (80-20) and accuracy (performance of Naïve Bayes) will be selected under "Classify" tab. All of the selections and the result of the classifier performance is presented in Figure 4 respectively.
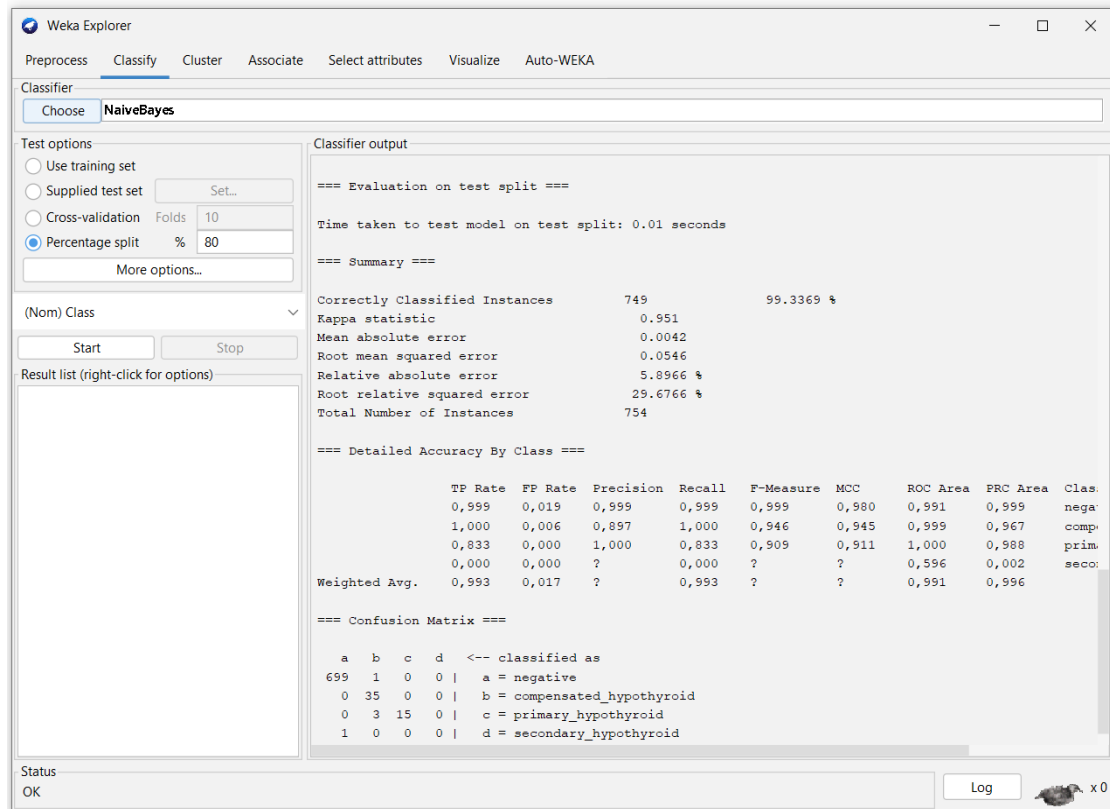
Figure 4. No-code Hypothyroid Disease Classification with Naïve-Bayes

The corresponding accuracy result of this ML model for 20% test (754 patients) is 99.33% in Figure 4. Naïve Bayes may identify the status of the patients just with single error prediction.

Conclusion

In this study, no-code ML modelling frameworks were reviewed and a sample framework (WEKA) was presented with a case ML development sample. As the technology improves, alternative no-code software development strategies are also generated. ML as an emergent data science is also used in many science disciplines ranging from engineering, health to social sciences. However, classical ML production pipelines require coding skills such as python or R. This requirement may decrease productivity and weakens focus on ML concepts. On the other hand, no-code environments such as WEKA may help focusing on ML concepts and experiments while increasing productivity. One another benefit of no-code ML software is undoubtedly to extent usage of ML concepts to a large user community including just curious persons.

As a recommendation, a ML practitioner may start with an open-source environment such as WEKA and he/she may use built-in datasets through learning. Furthermore, a search as "arff datasets" may provide the user with many datasets ready to work with. The experience with WEKA suit will be hoped that to be advantageous to learn other ML environments.

REFERENCES

Alanazi, A. (2022). Using machine learning for healthcare challenges and opportunities. *Informatics in Medicine Unlocked*, 100924.

Bouckaert, R. R., Frank, E., Hall, M. A., Holmes, G., Pfahringer, B., Reutemann, P., & Witten, I. H. (2010). WEKA---Experiences with a Java Open-Source Project. *The Journal of Machine Learning Research*, *11*, 2533-2541.

Brickley, D., Burgess, M., & Noy, N. (2019, May). Google Dataset Search: Building a search engine for datasets in an open Web ecosystem. In *The World Wide Web Conference* (pp. 1365-1375).

Carvalho, D. V., Pereira, E. M., & Cardoso, J. S. (2019). Machine learning interpretability: A survey on methods and metrics. Electronics, 8(8), 832.

Graczyk, M., Lasota, T., Trawiński, B., & Trawiński, K. (2010, March). Comparison of bagging, boosting and stacking ensembles applied to real estate appraisal. In *Asian conference on intelligent information and database systems* (pp. 340-350). Springer, Berlin, Heidelberg.

Guleria, K., Sharma, S., Kumar, S., & Tiwari, S. (2022). Early prediction of hypothyroidism and multiclass classification using predictive machine learning and deep learning. *Measurement: Sensors*, *24*, 100482.

Kavzoglu, T., & Teke, A. (2022). Predictive Performances of ensemble machine learning algorithms in landslide susceptibility mapping using random forest, extreme gradient boosting (XGBoost) and natural gradient boosting (NGBoost). *Arabian Journal for Science and Engineering*, 1-19.

Liberty, E., Karnin, Z., Xiang, B., Rouesnel, L., Coskun, B., Nallapati, R., ... & Smola, A. (2020, June). Elastic machine learning algorithms in amazon sagemaker. In *Proceedings of the 2020 ACM SIGMOD International Conference on Management of Data* (pp. 731-737).

Marappan, R., & Bhaskaran, S. (2022). Datasets Finders and Best Public Datasets for Machine Learning and Data Science Applications. *COJ Rob Artificial Intel*, *2*(1).

Quinlan, J. R., Compton, P. J., Horn, K. A., & Lazarus, L. (1987, October). Inductive knowledge acquisition: a case study. In *Proceedings of the Second Australian Conference on Applications of expert systems* (pp. 137-156).

Roy, S., & Ganguli, R. (2022). Comparative Analysis of Machine Learning Classification Algorithms for Predictive Models Using WEKA. In *Emerging Technologies in Data Mining and Information Security* (pp. 173-183). Springer, Singapore.

Singhal, S., & Jena, M. (2013). A study on WEKA tool for data preprocessing, classification and clustering. *International Journal of Innovative technology and exploring engineering (IJItee)*, *2*(6), 250-253.

Singhal, S., & Jena, M. (2013). A study on WEKA tool for data preprocessing, classification and clustering. *International Journal of Innovative technology and exploring engineering (IJItee)*, *2*(6), 250-253.

Vinuesa, R., & Brunton, S. L. (2022). Enhancing computational fluid dynamics with machine learning. *Nature Computational Science*, *2*(6), 358-366.

Wang, Q., Ma, Y., Zhao, K., & Tian, Y. (2022). A comprehensive survey of loss functions in machine learning. *Annals of Data Science*, *9*(2), 187-212.

Woo, M. (2020). The rise of no/low code software development—No experience needed?. *Engineering (Beijing, China)*, *6*(9), 960.

Sms Spam Filtering For Turkish and English Dataset

Bekir PARLAK[1]

Giriş

Short Message Service (SMS) has become one of the most common communication methods due to the rapid increase in the number of mobile phone users around the world. This rapid increase attracted the attention of unwanted (spam) senders and caused the problem of SMS spam messages, just like unsolicited (spam) e-mails. Unfortunately, most of the SMS messages that come to mobile phones today are irritating spam messages such as the credit facilities of banks, discount announcements of stores, and new tariffs of communication service providers.

SMS is one of the important services frequently used by all important applications such as banking or municipal transactions that require authentication. For this reason, it is important to use the service reliably rather than completely shutting it down. This is because SMS is one of the most preferred tools, especially for product or service advertisements and announcements, due to its low cost and easy use.

Simple techniques including whitelisting and blacklisting methods cannot perform well for classifying spam SMS messages. Worse still, a blacklisted phone number can send regular messages as well as spam SMS. For example, a bank might send a spam SMS message with new loan opportunities and a regular message including an online banking password. In this case, it is necessary to resort to smarter techniques such as content-based classification. Despite the desire to filter spam messages with the e-commerce law in effect as of May 1, 2015 in Turkey, spam SMS sending via foreign service providers without user requests still continues. Therefore, the detection and filtering of spam SMS messages that disturb users are among the subjects studied.

In the literature, there are studies on SMS filtering in English(Roy et al., 2020; Xia and Chen, 2021) and studies on SMS filtering in Turkish(Karasoy and Ballı, 2017, 2021; Uysal et al., 2012a). Ballı and Karasoy(Karasoy and Ballı, 2017) carried out a deep learning-based study for SMS detection. Attribute tags that can affect the classification performance of SMSs compiled from different regions and age groups are included in the SMS dataset. A model was created for this dataset, which was created with the help of the Word2Vec library. Through this deep learning-based model, new features are revealed for each SMS in the dataset. As a result of the experiments, it was observed that Word2Vec and Random Forest classifier achieved the highest performance. In another study(Ballı and Karasoy, 2019), a content-based classification model using machine learning is proposed to filter out spam messages. The model to be used in classification is created from the selected dataset with the help of Word2Vec word embedding tool. Thanks to this model, two new features are emerging for calculating the distances of messages to spam and raw words. Considering these two new features, the performances of classification algorithms are compared. The Random Forest classifier was successful with an accuracy rate of 99.64%. A higher percentage of correct classification is achieved compared to other studies using the same dataset. In addition, Ballı and Karasoy(Karasoy and Ballı, 2021) made content-based SMS classification for Turkish using machine learning and deep learning methods to filter out spam. TurkishSMS dataset was

---

[1] Dr. Bekir Parlak, Amasya Üniversitesi, bekir.parlak@amasya.edu.tr

prepared by collecting messages from different age groups and regions of people. There are five different structural features in the TurkishSMS dataset, two new features found with Word2Vec, and 45 features created with the word index values of each message. The feature matrix, consisting of 52 features in total, was evaluated with deep learning algorithms as well as traditional machine learning algorithms and the results were compared. As a result, the convolutional neural network was found to be the most successful algorithm with the highest classification performance.

Uysal et al.(Uysal et al., 2012a) proposed a new scheme for classifying SMS messages, so that informative features are first searched using two different feature selection techniques based on chi-square and information gain, and Bayesian classification algorithms are then used together with the selected feature sets to classify the SMS. In addition, a real-time mobile application has been developed for SMS spam filtering using the proposed classification scheme. Moreover, a real-time mobile application for SMS spam filtering using the proposed classification scheme has been developed based on the Android application previously introduced in(Uysal et al., 2012c). The filtering framework was evaluated on a large dataset of legitimate and spam English SMS messages. Experimental results clearly show that very high accuracy is achieved in filtering SMS spam messages. Uysal et al.(Uysal et al., 2012b) conducted a comprehensive analysis of the effects of various feature extraction and feature selection methods together on SMS filtering in two different languages, Turkish and English. The entire feature set of the filtering scheme consists of attributes originating from the bag of words (BoW) model[10] as well as a set of structural attributes adopted for the spam problem. Distinguishing features based on the word bag model are determined using chi-square and Gini index based feature selection methods. The selected features are then combined with structural features and fed with two different pattern classification algorithms, k-nearest neighbor and support vector machine, to classify SMS messages as spam or normal. The filtering framework is evaluated on two separate SMS message datasets consisting of Turkish and English messages, respectively. For this purpose, as part of the study, the first publicly available collection of SMS messages in Turkish was created and also a dataset available in English was used. Extensive experimental analysis on both datasets revealed that combinations of word bags and structural features yield better classification performance than bag-of-word features alone. However, the effectiveness of feature selection methods differed slightly in each language.

In this study, the effect of various feature selection methods on filtering spam messages of Turkish and English language short message service (SMS=Short Message Service) was investigated. During the filtering phase, the entire feature set was created from the features exposed by the bag of words (BoW) model. Distinctive features in the BoW are determined using feature selection methods. It is then fed with classification algorithms commonly used to classify SMS messages. The filtering framework was evaluated on the Turkish and English SMS dataset. Extensive experimental analysis on the respective datasets revealed that combinations of Multinomial Naïve Bayes(MNB) classifier and EFS(Extensive Feature Selector) feature selection methods provide better classification performance. The effectiveness of the feature selection methods used varies slightly in each classifier.

Datasets

Although many e-mail datasets(Ahmed, 2020; Bhowmick and Hazarika, 2018; Venkatraman et al., 2020) have been made available to researchers, only a limited number of publicly available SMS datasets are available in the literature. Especially for Turkish language, the number of datasets is quite low. Therefore, within the scope of this study, a previously created SMS message collection in Turkish, which is one of the agglutinative languages widely used all over the world, was used. This is very important as it is the first Turkish SMS dataset(Uysal et al., 2012b) in the academic literature. The dataset consists of 420 spam and 430 regular messages collected from volunteers. In the experiments, 50% of the dataset was used for training and 50% for testing. In addition, 2086

features are revealed before the training dataset pre-processing steps in the experiments, while a total of 1728 features are revealed after the pre-processing steps. We have shown the number of documents in the training and testing part of the dataset in Table 1. Since the total number of documents in the ham and spam categories is close to each other, the dataset can be counted as a balanced dataset. The second English dataset is the SMS Spam Collection. A collection of SMS-tagged messages known as the SMS Spam Collection was gathered for SMS Spam study. It has a single batch of 5,574 English SMS messages that have been classified as spam or ham (legal) messages. The SMS Spam Collection contains 747 (13.4%) spam messages and 4,827 (86.6%) legal SMS messages. In the experiments, 50% of the dataset was used for training and 50% for testing. In addition, 5038 features are revealed before the training dataset pre-processing steps in the experiments, while a total of 4286 features are revealed after the pre-processing steps. We have shown the number of documents in the training and testing part of the dataset in Table 2. Since the total number of documents in the ham and spam categories is different to each other, the dataset can be counted as a unbalanced dataset.

Table 1. Turkish SMS Dataset

	Train	Test
Ham	215	215
Spam	210	210

Table 2. English SMS Collection

	Train	Test
Ham	2414	2413
Spam	374	373

Feature Extraction

Many text classification studies use the Bag-of-Words model(Li et al., 2020) to represent text documents in which the exact order of words or terms in the documents is ignored but the frequency of the terms is considered. Each different term in a document collection ultimately creates an attribute on its own. Specific weights are assigned to terms to represent their importance in a particular document(Salton and Buckley, 1988). The most common weighting scheme, Term Frequency-Inverse Document Frequency (TF-IDF=Term Frequency- Inverse Document Frequency), brings the frequency of a term into a certain range by considering the number of documents containing that term in a document(Schütze et al., 2008). Therefore, a document is represented by a multidimensional feature vector; where each dimension of the vector corresponds to the weight value of a different word in the document collection, also known as the vector space model(Al-Anzi and AbuZeina, 2018).

Even if spam SMS filtering can be treated as a traditional text classification task, the nature of spam messages can differ significantly from official texts. Since the size of an SMS message is limited to only 160 characters, both the length of the message and the number of terms are of great importance. Also, the use of upper or lower case letters can be an indication of spam. Similarly, some non-alphanumeric characters (for example, "!", "$") and numeric characters (for example, phone numbers) are common in spam messages. Additionally, internet(URL=Uniform Resource Loader) links are often observed in spam SMS messages. Such attributes are defined as structural attributes. However, in this study, only the features in the word bag model were studied.

It should also be noted that deletion of alphanumeric characters, tokenization, stemming, removal of redundant words, and lowercase conversion are performed as pre-processing steps during feature extraction. Since only Turkish and English datasets are used in this study, the stemming phase is specific to Turkish and English languages. While Zemberek algorithm is applied for Turkish messages, Porter-Stemmer algorithm is used for English messages [19]. Tokenization or fragmentation is the process of dividing a text into words, phrases or other meaningful parts, i.e. tokens.

Feature Selection

Although there are filters, wrappers, and embedded feature selection methods, researchers prefer filter-based methods to select distinctive features, especially in text classification problems, due to the filters' classifier independence and relatively low computation time(Parlak and Uysal, 2021). The filter methods used in this study are Gini Index(GI)(Singh et al., 2010), Normalized Difference Measure(NDM)(Rehman et al., 2017) and Extensive Feature Selector(EFS)(Parlak and Uysal, 2021). All three methods have proven to be quite successful in previous text classification studies.

Table 3. Preliminaries for feature selection methods

Notation	Meaning
$p(t\|C_j)$	Probability of term t when class C_j exists
$p(\bar{t}\|C_j)$	Probability of absence of term t when class C_j exists
$p(t\|\overline{C_j})$	Probability of absence of of term t when class C_j does not exists
$p(\bar{t}\|\overline{C_j})$	Probability of term t when class C_j does not exists
$p(C_j\|t)$	Probability of class C_j when t term is present
$p(\overline{C_j}\|t)$	Probability of absence of class C_j when t term is present
$p(C_j\|\bar{t})$	Probability of class C_j when t term is not present
$p(\overline{C_j}\|\bar{t})$	Probability of absence of class C_j when t term is not present

Gini Index

GI, orijinal olarak karar ağaçlarındaki niteliklerin en iyi alt kümesini bulmak için kullanılan yöntemin geliştirilmiş bir versiyonu olan başarılı bir öznitelik seçim yöntemidir(Singh et al., 2010). Aşağıda verildiği gibi nispeten daha basit bir hesaplamaya sahiptir:

$$GI(t) = \sum_{j=1}^{M} P(t|c_j) * P(c_j|t) \tag{1}$$

Normalized Difference Measure (NDM)

It is used as a new attribute ranking metric for text classification(Rehman et al., 2017). NDM offers the minimum document frequency as a modifier to the balanced accuracy measure (ACC2). For NDM, we divide the ACC2 metric by min(tpr, fpr). Mathematically, NDM is defined as:

$$NDM(t) = \sum_{j=1}^{M} \frac{|P(t|c_j) - P(t|\overline{c_j})|}{\min{(P(t|c_j), P(t|\overline{c_j}))}} \tag{2}$$

Extensive Feature Selector (EFS)

The filter-based EFS method[22] selects more distinctive attributes by using both class-based and collection-based possibilities of the attribute. Its formula is a bit more complicated than other methods:

$$EFS(t) = \sum_{j=1}^{M} \left(\frac{P(t|C_j)}{P(\bar{t}|C_j) + P(t|\overline{C_j}) + 1} \right) \cdot \left(\frac{P(C_j|t)}{P(\overline{C_j}|t) + P(C_j|\bar{t}) + 1} \right) \tag{3}$$

Classifiers

Support Vector Machines (SVM) is one of the most efficient classifiers in text classification studies. There are two versions of the SVM(Haryanto and Mawardi, 2018) classifier, linear and nonlinear. The focus of the SVMclassifier is the margin concept. Hyperplanes have been used by classifiers to separate classes. For SVM with linear kernel, the LibSVM library is used.

Decision Tree (DT) is one of the best classifiers in text classification domain. A non-linear classifier and multistage decision system, DT(Subasi et al., 2018) rejects classes one at a time until a logical class is found.

Naive Bayes (NB)(Zhao et al., 2016) classifier is linear in the number of variables (features/predictors) in a learning problem, making them extremely scalable. Instead of using an expensive iterative approximation, as is the case for many other types of classifiers, maximum-likelihood training can be accomplished in linear time by evaluating a closed-form expression.

Experimental Study

In the experimental study, the effects of feature extraction, feature selection and pattern classification methods on the filtering of Turkish and English spam SMS messages were investigated. While the total number of features was 1728 while preprocessing in the experiments, 2086 features were revealed without preprocessing for Turkish SMS dataset. While the total number of features was 4286 while preprocessing in the experiments, 5038 features were revealed without preprocessing for English SMS dataset. In addition, it was observed how the performance changed in 5 different dimensions: 50, 100, 300, 500 and 1000.

The feature sets are then fed with NB, DT and SVM classifiers. The well-known F score(Goutte and Gaussier, 2005) was used to evaluate classification performance, as the dataset was also balanced (ie, the number of SMS messages in the spam and normal classes was almost equal). Classification results are presented in Table 4-9 for the Turkish and English dataset, respectively. The results were partitioned into 50%-50% of the training and testing sections to objectively evaluate the dataset.

For the Turkish SMS dataset, considering the highest weighted average F scores, in most cases the GI and NDM methods show the highest performance in different dimensions and classifier. However, the highest score was 0.943 with the combination of NDM method, 300 dimensions and SVM classifier. As the dimensions increase, the performance generally increases up to a certain size. However, performance decreases after certain dimensions. In terms of classifiers, SVM outperformed DT and NB classifier in most cases. On the other hand, the NB classifier showed higher performance than the DT classifier in most cases.

Table 4. F Scores for Turkish SMS Dataset with SVM Classifier

Turkish SMS	50	100	300	500	1000
GINI	0.891	0.924	0.941	0.936	0.922
NDM	0.924	0.924	**0.943**	0.927	0.929
EFS	0.917	0.927	0.936	0.936	0.922

Table 5. F Scores for Turkish SMS Dataset with DT Classifier

Turkish SMS	50	100	300	500	1000
GINI	0.858	0.858	0.870	**0.887**	**0.887**
NDM	0.787	0.810	0.872	0.863	0.870
EFS	0.848	0.858	0.860	0.867	0.867

Table 6. F Scores for Turkish SMS Dataset with NB Classifier

Turkish SMS	50	100	300	500	1000
GINI	0.894	0.911	**0.927**	0.922	0.925
NDM	0.910	0.922	0.920	0.906	0.925
EFS	0.884	0.901	0.907	0.912	0.925

For the English SMS dataset, given the highest weighted average F scores, in most cases the GI, NDM and EFS methods show the highest performance in different dimensions and classifier. However, the highest score was 0.978 with the combination of GINI method, 500 dimensions and SVM classifier. As the dimensions increase, the performance generally increases up to a certain size. However, performance decreases after certain dimensions. In terms of classifiers, SVM outperformed DT and NB classifier in most cases. On the other hand, the NB classifier showed higher performance than the DT classifier in most cases. The top 10 features according to the Feature Selection Methods are shown in Table 10-11. For the Turkish SMS dataset, the top 10 features are the same even if the GI and EFS feature scores are different. In addition, the NDM method produced several features similar to these two methods. But for the English SMS dataset, there are differences among the top 10 attributes of GINI, NDM and EFS methods. From this, it is seen that the feature selection methods and data sets have a serious effect on the ranking of the features.

Table 7. F Scores for English SMS Dataset with SVM Classifier

English SMS	50	100	300	500	1000
GINI	0.964	0.971	0.973	**0.978**	0.976
NDM	0.953	0.966	0.973	0.972	0.977
EFS	0.961	0.971	0.975	0.976	0.974

Table 8. F Scores for English SMS Dataset with DT Classifier

English SMS	50	100	300	500	1000
GINI	0.946	0.949	0.951	0.956	0.955
NDM	0.915	0.937	0.947	0.945	0.949
EFS	0.945	0.949	0.956	**0.958**	0.955

Table 9. F Scores for English SMS Dataset with NB Classifier

English SMS	50	100	300	500	1000
GINI	0.955	0.957	0.957	0.956	0.956
NDM	0.940	**0.961**	**0.961**	0.957	0.955
EFS	0.957	0.957	0.955	0.955	0.955

Tablo 10. Top-10 features according to Feature Selection Methods for Turkish SMS dataset

Turkish SMS	GINI	NDM	EFS
1	tl	indir	tl
2	com	ozel	com
3	indir	firsati	indir
4	icin	ay	icin
5	ozel	taksit	ozel
6	sadece	**hemen**	sadece
7	firsati	**gonderin**	firsati
8	ay	**cardfinans**	ay
9	taksit	com	taksit
10	ye	**yazip**	ye

Tablo 11. Top-10 features according to Feature Selection Methods for English SMS dataset

Turkish SMS	GINI	NDM	EFS
1	txt	www	txt
2	call	txt	call
3	free	service	free
4	claim	**landlin**	claim
5	mobil	claim	www
6	www	**pound**	mobil

7	uk	**music**	uk
8	prize	**camera**	prize
9	**stop**	**po**	**box**
10	**win**	**urgent**	service

Results and Conclusions

In this study, the effect of feature selection methods on spam SMS filtering for Turkish and English language has been extensively investigated in terms of classification accuracy. Only the bag-of-words approach was used while creating the feature vector. On the other hand, the effectiveness of feature selection strategies was tested in three different classifiers. The schemas showing the highest performance were determined in both datasets.

Besides the bag-of-words approach, examining new structural features, evaluating other feature selection and classification methods in SMS spam filtering problem will remain as interesting studies in the future. It can also be included in the spam SMS filtering task by including different pattern classifiers.

KAYNAKÇA

Hampden-Thompson, G. & Galindo, C. (2017) School–family relationships, school satisfaction and the academic achievement of young people. *Educational Review, 69* (2), 248-265. Doi: 10.1080/00131911.2016.1207613

Kline, B. R. (2005). *Principles and practice of structural equation modeling* (Second edit). NY: The Guilford Press.

Nal, M. (2018*). Hastanelerde acil yardım ve afet yönetimi.* Ankara: Akademisyen Kitabevi

Ahmed, B. (2020) Wrapper Feature Selection Approach Based on Binary Firefly Algorithm for Spam E-mail Filtering. *Journal of Soft Computing and Data Mining* 1, 44-52.

Al-Anzi, F.S., AbuZeina, D. (2018) Beyond vector space model for hierarchical Arabic text classification: A Markov chain approach. *Information Processing & Management* 54, 105-115.

Ballı, S., Karasoy, O. (2019) Development of content-based SMS classification application by using Word2Vec-based feature extraction. *IET Software* 13, 295-304.

Bhowmick, A., Hazarika, S.M., (2018) E-Mail Spam Filtering: A Review of Techniques and Trends, Advances in Electronics, *Communication and Computing. Springer*, pp. 583-590.

Goutte, C., Gaussier, E., (2005) A probabilistic interpretation of precision, recall and F-score, with implication for evaluation, *European conference on information retrieval. Springer*, pp. 345-359.

Haryanto, A.W., Mawardi, E.K. (2018) Influence of word normalization and chi-squared feature selection on support vector machine (svm) text classification, *2018 International Seminar on Application for Technology of Information and Communication. IEEE*, pp. 229-233.

Karasoy, O., Ballı, S. (2017) Classification Turkish SMS with deep learning tool Word2Vec, *2017 International Conference on Computer Science and Engineering (UBMK). Ieee*, pp. 294-297.

Karasoy, O., Ballı, S. (2021) Spam SMS detection for Turkish language with deep text analysis and deep learning methods. *Arabian Journal for Science and Engineering*, 1-17.

Li, P., Mao, K., Xu, Y., Li, Q., Zhang, J. (2020) Bag-of-Concepts representation for document classification based on automatic knowledge acquisition from probabilistic knowledge base. *Knowledge-Based Systems* 193, 105436.

Parlak, B., Uysal, A.K. (2021) A novel filter feature selection method for text classification: Extensive Feature Selector. *Journal of Information Science*, 0165551521991037.

Rehman, A., Javed, K., Babri, H.A. (2017) Feature selection based on a normalized difference measure for text classification. *Information Processing & Management* 53, 473-489.

Roy, P.K., Singh, J.P., Banerjee, S. (2020) Deep learning to filter SMS spam. *Future Generation Computer Systems* 102, 524-533.

Salton, G., Buckley, C. (1988) Term-weighting approaches in automatic text retrieval. *Information processing & management* 24, 513-523.

Schütze, H., Manning, C.D., Raghavan, P. (2008) *Introduction to information retrieval.* Cambridge University Press.

Singh, S.R., Murthy, H.A., Gonsalves, T.A. (2010) Feature Selection for Text Classification Based on Gini Coefficient of Inequality. *Fsdm* 10, 76-85.

Subasi, A., Alzahrani, S., Aljuhani, A., Aljedani, M. (2018) Comparison of decision tree algorithms for spam e-mail filtering, 2018 1*st International Conference on Computer Applications & Information Security (ICCAIS). IEEE*, pp. 1-5.

Uysal, A.K., Gunal, S., Ergin, S., Gunal, E.S., (2012a) A novel framework for SMS spam filtering, *2012 International Symposium on Innovations in Intelligent Systems and Applications. IEEE*, pp. 1-4.

Uysal, A.K., Gunal, S., Ergin, S., Sora Gunal, E., (2012b) The impact of feature extraction and selection on SMS spam filtering. *Elektronika ir Elektrotechnika* 19, 67-72.

Uysal, A.K., Günal, S., Ergin, S., Günal, E.Ş., (2012c) Detection of SMS spam messages on mobile phones, *2012 20th Signal Processing and Communications Applications Conference (SIU).* Ieee, pp. 1-4.

Venkatraman, S., Surendiran, B., Kumar, P.A.R. (2020) Spam e-mail classification for the internet of things environment using semantic similarity approach. *The Journal of Supercomputing* 76, 756-776.

Xia, T., Chen, X. (2021) A weighted feature enhanced Hidden Markov Model for spam SMS filtering. *Neurocomputing* 444, 48-58.

Zhao, L., Huang, M., Yao, Z., Su, R., Jiang, Y., Zhu, X. (2016) Semi-supervised Multinomial Naive Bayes for text classification by leveraging word-level statistical constraint, *Proceedings of the Thirtieth AAAI Conference on Artificial Intelligence.* AAAI Press, pp. 2877-2883.

Sulfur Isotope Fractionation During Sulfate Reduction in Organic-Rich Cayirhan Oil Shales (Cos) (Beypazari, Ankara / Turkey)

Berna YAVUZ PEHLIVANLI[1]

1. Introduction

Middle Miocene age, organic-material rich oil shales which are exposed in the area between Beypazarı and Nallıhan towns in the city of Ankara have been investigated by means of differentiation of organic-material bearing geologic units, basin tectonism, organic material content of rocks and their economic potential (Zieglar, 1939; Aziz, 1976; Akkuş et al., 1982; Şener and Sengüler, 1991; ÖzCelik, 2002; Gülbay and Korkmaz, 2005; Sarı and Aliyev, 2006, Yavuz Pehlivanlı 2011, Yavuz Pehlivanlı et al., 2014).

It is estimated that study area hosts a possible reserve consisting of 300 million tons of oil shales with calorific value of more than 1000 k cal/kg and another 900 million tons with calorific value between 100-1000 k cal/kg (Zieglar, 1939; Aziz, 1976). In this respect, assessment of oil shales in the area is crucially important. In this work, COS are systematically studied geochemical paleoredox variations dependent upon depth of all samples and prevailed during the deposition of these shales are essentially determined.

Oil shales is one of the most important industrial raw materials for the future. In this respect, assessment of oil shales in the study area is crucially important. In this work, geochemical characteristics of COS are systematically studied and sulfur isotope characteristicsprevailed during the deposition of these shales are essentially determined.

Both chemical and biological processes influence the sulfur geochemistry of sedimentary rocks during deposition and diagenesis (Krouse, 1977a,b; Postgate, 1979; 1983; Berner, 1984). These processes are constrained by availability of sulfur and organic matter (Aizenshtat et al., 1983; Berner and Raiswell, 1983; Mango, 1983; Orr, 1974;1986; Canfield and Berner, 1987; Morse and Cornwell, 1987; Canfield, 1989; Morse and Emeis, 1990; Tuttle et al., 1990). As part of a program to document sedimentary sulfur geochemistry of saline lacustrine environments, we studied theMiocene Hırka Formation in Beypazarı, Ankara, Turkey. Our study evaluated the sulfur geochemistry during deposition anddiagenesis of the HırkaFormation sediment usingabundances of sulfur and organic carbon; distribution of forms of sulfur and their isotopic composition.

2. Geologic setting and stratigraphy

The study area is located at west of Beypazarı and north of Yeni Cayırhan. The area in Bole H27-d quadrangle covers an area of 30 km^2 at northeast of Cayırhan (Figure 1).Paleocene Kızılbayır formation is the oldest unit in the study area. It is unconformably overlain by middle Miocene

[1] Yozgat Bozok Üni.Müh.-Mimarlık Fak.Jeoloji Müh.Böl./Yozgat 0000-0003-0127-8525

sedimentary units which consist of, from bottom to the top, Boyalı, Hırka, Karadoruk and Sarıağıl formations. These units are cut by Teke volcanites. Pliocene Softa formation and alluvium cover all these units (Figures 1).

The Cayırhan oil shales under investigation are formed within the Hırka formation which conformably overlies the Boyalı formation with lateral and vertical transitions. Typical section of formation is around the Hırka village where laminated sandstone, claystone, oil shale, carbonaceous shale, dolomitic limestone, tuff, trona and local intraformational breccia occur. Oil shales of Hırka formation in colors changing from gray to light-dark brown are very thin bedded. Oil shales of 8-22 m thickness are interlayered with dolomitic limestone and tuffs. This unit contains leaf fossils, trunk pieces, gastropod and ostracode fossil fragments.

3. Material and methods

In this study a total of 40samples were examined which were collected from outcrops (B and C measured stratigraphic sections-MSS), gallery (CG gallery) and boreholes (S, PS, PK, PM and PR boreholes). Samples were taken from measured stratigraphic sections, core boxes of boreholes drilled in the area and in coal galleries from levels cutting oil shales of the Hırka formation. Samples with locations given in Figure 1 were subjected to organic geochemical and isotopic analyses.
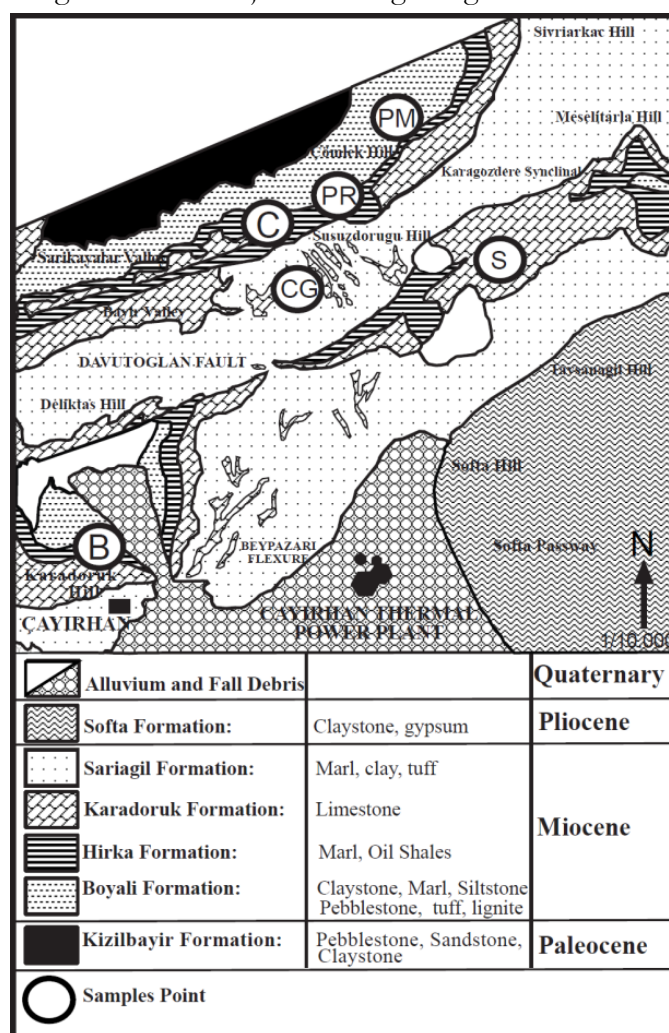
Figure 1. Geological map of the study area (İnci et al. 1988).

Total organic carbon (TOC wt %), maturity levels, kerogen types, HI, OI and Tmax (°C) values were determined by Rock-Eval pyrolysis method. Rock-Eval pyrolysis analysis was carried out with the Rock Eval-VI device at the TPAO laboratories. IFP 160000 (Institüt FranCais Petrole) was used as the standard.

The δ³⁴S isotope values were produced using Thermo Quest Finnigan Delta Plus XLa Europa elemental analyser and mass spectrometer at Iso-Analytical, Cheshire, UK. For the δ³⁴S measurements collagen samples of approximately 10 mg were used, in duplicate, to produce the data given in Table 2. Samples were compared to the NBS-127 BaSO4 standard. Aliquots of the IAEA-S1 standard and the NBS-127 standard were also measured in the sample runs and the N34S standard deviations were þ 0.46x for IAEA-S1 (n= 8, 0.2 mg), and þ 0.37x for NBS-127 (n = 10, 0.2 mg).The calibration is linear between -10 to +30 per mil. Accuracy was measured to be ± 0.15repeated and internal standard.

4. Results and Discussion

4.1. Sulfur isotopes

The sulfur isotope composition (in situ sulfur isotope analyses) of 40 samples of sediments are shown in Table. 2. Cayırhan oil shales (COS) has sulfur isotopic values between -6,37 ‰ and 26,55 ‰ in basin (average value 13,86‰). Bmeasured stratigraphic sections-MSS has isotopic value between -6,37‰ and +22,29‰; C measured stratigraphic sections-MSS has isotopic value between 9,46‰ and21,09‰; CG gallery has isotopic value between 5,65 ‰ and 20,42‰; PK boreholes has isotopic value between -4,46‰and 23,77‰; PM boreholes has isotopic value between 14,11‰ and26,55‰; PR boreholes has isotopic value between 13,25 ‰ and 17,91 ‰; PS boreholes has isotopic value between -1,15 ‰ and 17,49‰ and S S boreholes has isotopic value between 0,87‰and 23,06‰ (Figure 4).

Acoording to change intervals of samples; forsulfurisotopevaluesare extremely wide range, there can be interpretedto be effectiveby thetwo ormore sourcesof sulfur (**Figure 4**). δ34S (‰) histogram of samples are concentrated in between +17 and 21 (Figure 5).

Table 1. Results of the pyrolis analysis of COS (B and C MSS, CG Gallery, PK, PM, PR, PS and S boreholes).

Sample No	Total Organic Carbon (%TOC)	S1 (mg HC/g)	S2 (mgHC/g)	S3 (mgCO2/g)	HI	OI	Tmax (C°)
B55	12,74	4,4	104,34	4,53	819	36	424
B50	11,58	3,94	105,86	3,03	914	26	438
B42	9,34	0,63	76,13	3,68	815	39	438
B34	14,36	1,09	128,26	5,08	893	35	441
C33	13,2	1,81	120,26	5,02	911	38	443
C30	9,51	2,95	74,32	3,2	781	34	430
C28	6,00	0,87	47,23	3,47	787	58	442
C15	4,92	1,02	37,42	2,11	761	43	438
CG-19	5,32	nd	nd	nd	nd	nd	nd
CG11	21,59	3,33	195,16	6,73	904	31	447
CG1	23,29	0,58	29,19	15,52	125	67	420
PR28	5,73	2,61	46,02	1,77	803	31	442
PR20	8,65	4,02	73,15	1,67	846	19	421
PR11	3,46	0,76	21,25	1,12	614	32	433
PM34	11,81	7,47	92,84	3,32	786	28	437
PM28	11,00	7,25	92,6	2,38	842	22	439
PM24	9,17	6,07	74,13	1,57	808	17	431

PM18	9,64	4,36	85,68	1,7	889	18	421
PM17	12,74	5,12	106,84	2,5	839	20	434
PM13	16,37	3,64	126,93	4,21	775	26	428
S19	6,41	1,76	49,72	2,35	776	37	443
S77	12,85	5,20	104,13	3,12	810	24	424
S-79	12,10	nd	nd	nd	nd	nd	nd
S83	11,17	2,75	94,91	1,75	850	16	421
average	10,96	3,26	85,74	3,63	788,55	31,68	433,41

Table 2. $\delta^{34}S$ isotope resut of COS

	$\delta^{34}S_{CDT}$(‰)
B-14	5,20
B-17	-6,37
B-18	-0,06
B-21	1,98
B-30	16,49
B-36	22,29
C-1 (a)	9,46
C-2	16,04
C-11	19,93
C-18 (a)	21,09
C-25	16,91
CG-1	5,65
CG-5	16,24
CG-7	20,42
CG-12	19,78
CG-15	19,09
CG-20	19,60
PK-1	-4,46
PK-5	15,39
PK-10	20,08
PK-12	23,77
PK-22	11,87
PM-13	22,13
PM-17	26,55
PM-21	23,15
PM-24	14,11
PR-4	13,25
PR-5	17,10
PR-11	14,98
PR-23	17,91
PS-1	10,83
PS-2	8,87
PS-3	17,49
PS-10	14,91
PS-14	-1,15
S-54	23,06
S-79	10,56
S-85	0,87
S-89	13,07
S-92	16,31
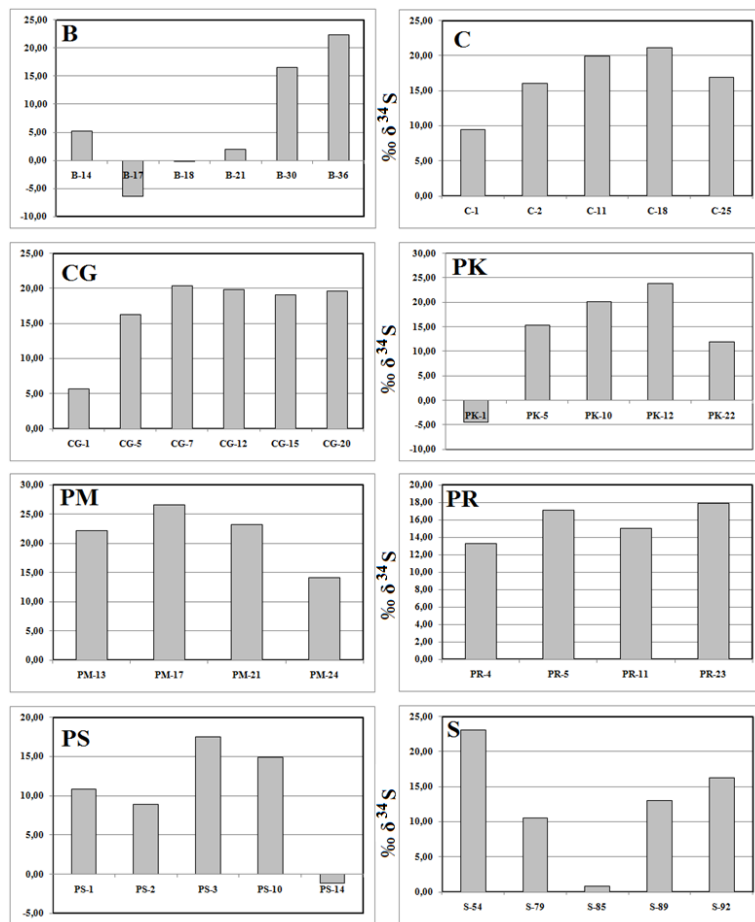
Figure 4. δ34S Graphs of the samples.
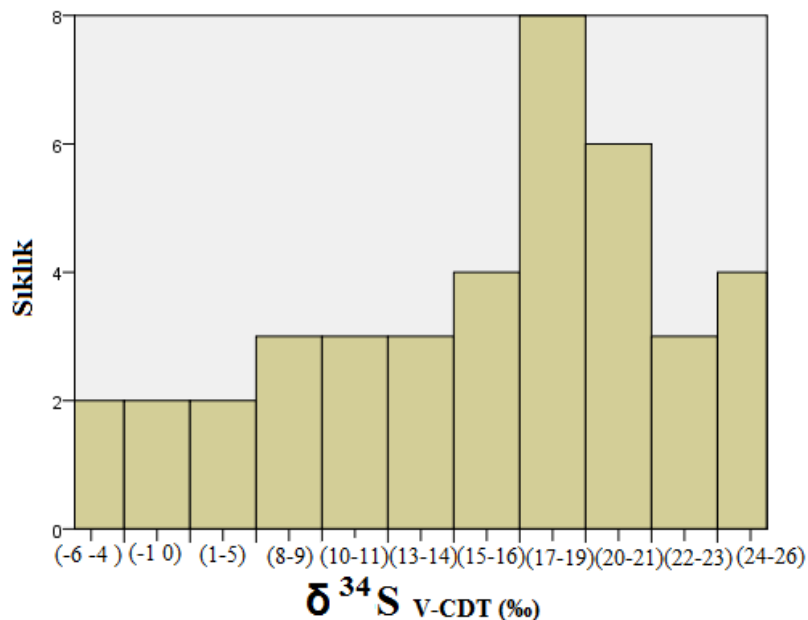
Figure 5 Distribution of δ34S of the samples.

The S-isotopic composition may give information about the occure of environment. The change of isotopic ratios from negative to positive indicates that sediment water and bacterial

activities are effective. The presence of oxygen in the pores in the sediments of the sediments in seawater makes the isotope ratios constant. S-isotope data support the presence of a reducing (anoxic) water column. Sulfate usually represents oxidized sulfite. Many studies suggest that pH and $fO2$ (oxygen fugacity) are effective on δ34S values. However, geological, mineralogical and geochemical factors are also effective here. Positive (+) δ34S values represent environments where pH values decrease; negative (-) δ34S values indicate an increase in $fO2$ (oxygen fugocity). Therefore, the change between high positive and low negative values of δ34S values in the study area may be affected by pH and $fO2$ of the environment. In the low fO2 and pH region, sulfide 34S contents may be similar to δ34S to ΣS (Thode et al. 1958, Sakai, 1968, Hartmann and Nielsen 1969, Krouse, 1977a,b Jőrgensen, 1978, Nielsen, 1979, Ohmoto and Rye1979.a, b, Subiaset al,1997, Hoefs 2009)

The δ34S results of the samples were compared with the various geological environments and ore types in Figure 6, and the δ34S values of atmospheric sulfur components from different sources in Figure 7. Although it is a problem for interpretation that the reference values, which are in a very wide range, fall into a similar area with most of these comparisons, knowing the geological features of the evaluated samples provides convenience in this regard. Considering the geological environment and oil shale formation, the variation between ‰-6.37 and ‰26.55 determined in the samples is consistent with the variation range of biogenic sulfide and sedimentary rocks (Figure 6). In addition, the fact that the range of H2S of both terrestrial and marine origin is close in terms of variation intervals according to the δ34S values compared in Figure 6 does not constitute a discrimination criterion. However, previous studies, field observations, petrographic-mineralogical findings and elemental analysis studies in the study area point to the terrestrial lake environment of the samples. In addition, it can be argued that the variation range of organic origin SO2 according to the δ34S values of SO2 origin is quite compatible with the evaluated samples.
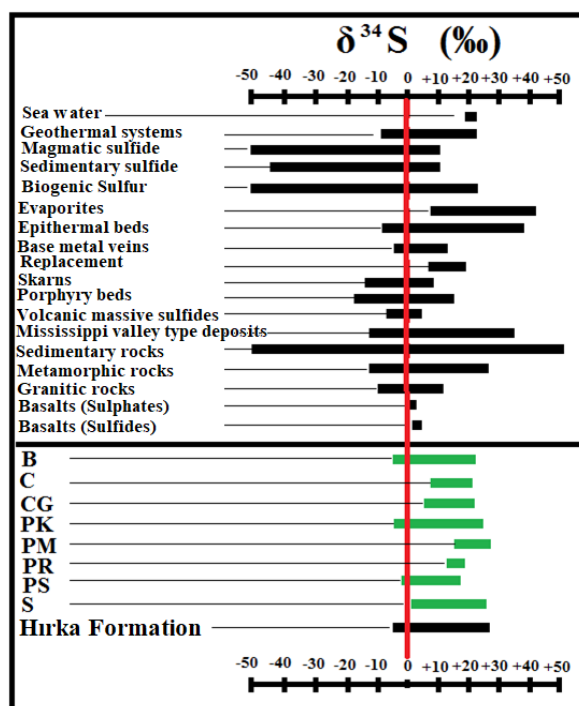
Figure 6 δ34S values for various geological environments and ore types (B Measured Stratigraphic Section (MSS), C MSS, CG Gallery, PK, PM, PR, PS and S Drilling) (Ohmoto and Rye 1979.a,b, Claypool et al. 1980, Ohmoto 1986, Hoefs 2009).
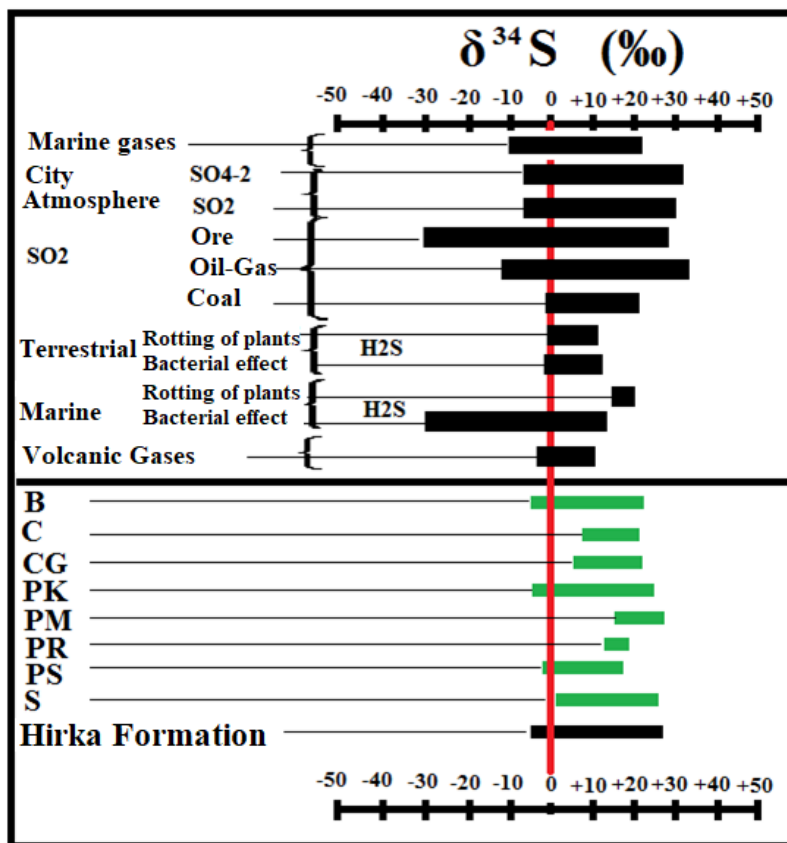
Figure 7 δ34S changes of atmospheric sulfur components in different sources (B -MSS, C - MSS, CG Gallery, PK, PM, PR, PS and S Drilling) (Faure and Mensing 2005).

5. Results

1. Based on average TOC values (10,96 % wt), CBS has very good/perfect source rock potential. Kerogen types (Type-I) mostly characterize lacustrine environment. Tmax values (413-447 °C) indicate that the maturity level of CBS is from immature to advance mature.

2. Cayırhan oil shales (COS) has sulfur isotopic values between -6,37 ‰ and 26,55 ‰ in basin (average value 13,86‰).

3. The isotopic ratios range from negative (-6,37 ‰) to positive (+26,55‰). If seawater is trapped in the sediment under oxidizing conditions as pore water, its isotopic ratio should have been preserved.

4. $\delta^{34}S$ values could be effective on pH and $fO2$ of the environment. In some studies, a slight decrease in pH values $\delta^{34}S$ values due to positive values, while negative values $fO2$ (oxygen fugacity) suggested that without increasing. Therefore wide range of $\delta^{34}S$ values of COS in the study area could be affected by $fO2$ and pH.

REFERANCES

Aizenshtat, Z., Stoler, A., Cohen, Y., Nielsen, H., 1983. The Geochemical sulphur enrichment of recent organic matter by polysulfides. In: Bjoroy, M. et al. (Eds.), The Solar Lake Advances in Organic Geochemistry 1981. Wiley & Sons, Chichester, pp. 279–288

Akkuş, İ., Sümer, A., Şengüler, İ., Taka, M., Pekatan, R. ve Işık, A. 1982. Beypazarı Cayırhan yöresinin jeoloji ve bitümlü şeyl olanakları. MTA Rapor No: 7837.

Aziz, A. 1976. Beypazarı Yeni Cayırhan ve Karaköy arasındaki sahanın jeolojisi ve bitümlü şist olanakları. MTA Rapor No: 5732.

Berner R. A. and Raiswell R. (1983) Burial of organic carbon and pyrite sulfur in sediments over Phanerozoic time: A new theory. Geochim. Cosmochim. Acta 47,855-862.

Berner, R. A. 1984: Sedimentary pyrite formation: An update, Geochim. Cosmochim. Ac., 48(4), 605–615.

Canfield, D. E. and Berner, R. A. 1987.Dissolution and pyritization of magnetite in anoxic marine sediments, Geochim. Cosmochim. Ac., 51, 645–659,

Canfield, D.E., 1989. Reactive iron in marine sediments. Geochimica et Cosmochimica Acta 53, 619–632.

Claypool, G.E., Holser, W.T., Kaplan, I.R., Sakai, H., Zak, I., 1980. The age curves of sulfur and oxygen isotopes in marine sulfate and their mutual interpretation. Chem. Geol. 28, 199–260.

Espitalie, J., Deroo, G. and Marquis, F. 1985. La pyrolyse Rock-Eval et ses applications: Revue de rinstitut FranCais du Petrole., Vol. 40, pp. 139-1162.

Espitalie, J., Madec, M. and Tissot, B. 1977. Source rock characterization, 9th offshore tecnology conference, pp. 439-444.

Faure, G. and Mensing, T.M. 2005. Isotopes "principles and applications". third edition. john wiley &sons, pp. 897.

Gülbay, R. ve Korkmaz, S. 2005. Kuzeybatı Anadolu'daki Bitümlü Şeyllerin Organik Jeokimyasal özellikleri ve Çökelme Ortamları. Türkiye Jeoloji Bülteni, Sayı 2, s. 21-41.

Hartmann M. and Nielsen, H. (1969). δ34S-Werte in rezenten Meeressedimenten und ihre Deutung am Beispiel einiger Sedimentprofile aus der westlichen Ostsee, Geol. Rundsch. 58, 621.

Hoefs, J., 2009. Stable Isotope Geochemistry, Sixth Revised and Updated Edition. SpringerVerlag, Berlin 75–76.

İnci, U., Helvacı, C. and Yağmurlu, F. 1988. Stratigraphy of Beypazarı Neogene basin, Central Anatolia, Turkey. Newsl.Stratigr., Vol. 18, pp. 165-182.

Jarvie, D.M. 1991. Total Organic Carbon TOC Analysis. Merrill, R.K., ed., Source and Migration Processes and Evaluation Techniques, Tulsa, American Association of Petroleum Geologists., pp. 113-118.

Jörgensen, B.B. 1978. A comparison of methods for the quantification of bacterial sulfate reduction in coastal marine sediments, I. Measurement with radiotracer techniques, Geomicrobiol. 1.1 (1978) 11; II. Calculations from mathematical models, Geomicrobiol. J. (1978) 29; III. Estimation from chemical and bacteriological field data, Geomicrobiol. J. 1 (1978) 49.

Kraus, G.P. and Parker, K.A.1979. Geochemical evalution of petroleum source rock in Bonaparte Gulftimor sea region, NW Australia. A.A.P.G. Bull.,Vol. 63, pp. 2021-2041.

Krouse HR (1977a) Sulphur isotope studies and their role in petroleum exploration, pp. 189-211. In Hitchon B. (editor), Application of Geochemistry to the Search for Crude Oil and Natural Gas, Special Issue J. Geochem. Explor. I. Elsevier, New York.

Krouse HR (1977b) Sulphur isotope abundances elucidate uptake of atmospheric sulphur emissions by vegetation. Nature 265:45–46.

Mango, F.D., 1983. The diagenesis of carbohydrates by hydrogen sulfide. Geochimica et Cosmochimica Acta 47, 1433–1441

Morse J. W. and Cornwell J. C. (1987) Analysis and distribution of iron sulfide minerals in recent anoxic sediments. *Mar Chem.* **22**, 55-69.

Morse J. W. and Emeis K. C. (1990) Controls on C/S ratios in hemipelagic sediments. Amer. J. Sci. 290, 1117- 1135

Nelson M. B. (1978) *Kinetics and Mechanisms of the Oxidation of Ferrous Sulfide.* Ph.D. dissertation, Stanford University.

Nielsen, H. (1979). Sulfur Isotopes. In: Jäger, E., Hunziker, J.C. (eds) Lectures in Isotope Geology. Springer, Berlin, Heidelberg. https://doi.org/10.1007/978-3-642-67161-6_24.

Ohmoto, H and Rye, O. 1979a. Isatopes of sulfur and carbon (In: Barnes, H. L. (edt.), Geochemistry of hydrothermal ore deposits, Wiley, Newyork, pp. 506-567.

Ohmoto, H. 1986. Stable isotope geochemistry of ore deposits (In; Valley et all. (Edts.); Stable isotopes in high temperature geological processes, Reviews in mineralogy, Vol. 16, pp. 491-559.

Ohmoto, H. and Rye, R. O. 1979b. Sulfur and carbon isotopes and ore genesis: a review. Econ. Geol, 69, 826-842.

Orr WL (1974) Changes in sulfur content and isotopic ratios of sulfur during petroleum maturation—study of Big Horn basin Paleozoic oils. Bull. Am. Assoc. Petrol. Geol. 50:2295–2318.

Orr, W.L., 1986. Kerogen/asphaltene/sulfur relationships in sulfur-rich Monterey oils. In: Leythaeuser, D., Rullkötter, J. (Eds.). Advances in organic geochemistry vol. 10, 499–516.ÖzCelik, O. 2002. Beypazarı Ankara Kuzeyinde Miyosen Yaşlı Bitümlü Birimlerin Organik Jeokimyasal Özellikleri. Türkiye Jeoloji Bülteni, Cilt 45, s. 1-17.

Peters, K.E. and Cassa, M.R. 1994. Applied source rock geochemistry. In: The petroleum system- from source to trap, L.B. Magoon and W.G. Dows eds., AAPG Memoir Vol. 60, pp. 93-117.

Postgate, J. R., 1983. The Sulfate-Reducing Bacteria (2nd Edition) X + 208 S., 20 Abb., 4 Tab. University Press, Cambridge.

Postgate, J. R.1979. The sulphate-reducing bacteria. Cambridge [Eng.] ; New York : Cambridge University Press, viii, 151 p. : ill. ; 23 cm.

Sakai, H. 1968. Isotopic properties of sulfur compounds in hydrothermal processes. Geochem. J., 2, 29-49.

Sarı,A., Aliyev, S.A., 2006. Organic Geochemical Characteristics of the Paleocene-Eocene Oil Shales in the Nallıhan Region, Ankara, Turkey. Petroleum Science and Engineering.53,123-134 (SCI).

Subías, I., Recio, C., Fanlo, I., Fernandez-Nieto, C., 1997. Stable isotope composition of F-Pb-Zn mineralization in the Valle de Tena (Spanish Central Pyrenees). Miner. Deposita 32, 180–188.

Şener, M. and Şengüler, İ. 1991. Beypazarı Bitümlü Marnlarının jeolojisi ve ekonomik kullanım alanları MTA Rapor No: 9202.

Thode HG, Monster J, and Dunford HB (1958) Sulphur isotope abundances in petroleum and associated materials. Am. Assoc. Petrol. Geol. Bull. 42:2619–2641.

Tissot, B. and Welte, D.H. 1984. Petroleum formation and occurrence: 2.edition Springer-Verlag, Berlin, pp. 699.

Tuttle, M.L.W., Charpentier, R.R., and Brownfield, M.E. (1990), The Niger Delta petroleum system; Niger Delta Province, Nigeria, Cameroon, and equatorial Guinea, Africa. US Geological Survey Open-file Report 99-50-H. https://doi.org/10.3133/ofr9950H.

Yavuz Pehlivanlı B. 2011. Hırka formasyonu (Beypazarı, Ankara, Türkiye) bitümlü şeyllerinin inorganik element depolanmaları ve organik-inorganik elementler arasındaki kökensel ilişkiler Ankara Üniversitesi, Fen Bilimleri Enstitüsü Doktora Tezi, 540s.

Yavuz Pehlivanlı B.,.KoC Ş. and Sari A .2014. Carbon isotope ($\delta 13C$) characteristics of middle Miocene Cayirhan oil shales (Beypazari, Ankara/Turkey): Implications on paleoenvironment and paleoclimate Fuel, 135, 427-434.

Zieglar, J. 1939. Eskişehir-Ankara-Bolu-Cankırı civarında yapılan jeolojik etüt. MTA Enerji Hammadde Etüt ve Arama Hırka Beypazarı ve Karaköy Nallıhan Havalisindeki Bitümlü Şistler, Rapor No: 983, MTA.

A Sequential CNN Architecture for Early Detection of Alzheimer's Disease From MRI Images

Gaffari ÇELİK[1]

Introduction

Alzheimer's Disease (AD) is an incurable neurodegenerative disease that is mostly seen in the elderly and causes progressive deterioration in the cognitive abilities of patients. This disease, which is mostly seen in people aged 65 and over, increases exponentially with age. About 50 million people worldwide suffer from this disease. AD is the fourth most common cause of death after heart disease, cancer, and cerebral hemorrhage. In addition, AD is the most common among the different types of Dementia and covers 70% of dementia (loss of memory and cognition) cases. Dementia is expected to affect 82 million people by 2030 and 152 million by 2050 (Farina et al., 2020; Khojaste-Sarakhsi et al., 2022; EL-Geneedy et al., 2023; Alorf & Khan, 2022; Cassani et al., 2018).

It is estimated that Alzheimer's disease begins with small and unnoticeable changes in the brain at least 20 years before symptoms appear (Alberdi et al., 2016). Patients live for years without noticing symptoms. Changes in the brain cause damage and destruction of nerve cells in some parts of the brain, causing symptoms such as memory loss and language problems in patients. As time progresses, the symptoms tend to increase and individuals become unable to perform their daily activities (Association, 2019).

Although the definitive diagnosis of Alzheimer's disease is possible by examining the brain tissue after death, it can be diagnosed in living patients as a result of the combination of positron emission tomography (PET) biomarkers and cerebrospinal fluid (CSF) with several clinical criteria (Budson and Solomon, 2012). However, since there is no cure for this disease yet, current methods are used to stop the progression of the disease and delay the symptoms with drugs (Farina et al., 2020; Weller & Budson, 2018). Delayed treatment for AD will not prevent disease progression. However, effective treatment can be achieved if early detection of dementia stages is provided. For this, early diagnosis with imaging methods is required between the stages of dementia. The use of fully automated reliable imaging techniques will help better than the manual and semi-automatic techniques used so far. In addition, automatic techniques that do not require human intervention and that can distinguish the stages of dementia associated with a cognisant live score or clinical scale will be more helpful (Subramanyam Rallabandi & Seetharaman, 2023). The stages of dementia were classified using various machine learning (ML) techniques and structural magnetic resonance imaging (sMRI) tools (Prakash et al., 2021; Chang et al.,2021).

AD has three stages, namely Pre-clinical AD, Mild Cognitive Impairment (MCI), and Dementia due to AD, which are stated below.

- Pre-clinical AD: It is the initial stage of AD. Changes begin in the brain, blood, and CSF. However, since there are no symptoms at this stage, the beginning of this stage has not

yet been detected. It is assumed that this stage may precede any symptom manifestation 20 years (Cassani et al., 2018; Alberdi et al., 2016; Riley et al., 2005; Sperling et al., 2011).

- Mild Cognitive Impairment (MCI): The second stage of AD disease is called MCI. At this stage, the patient can work independently. However, the patient may have difficulty in pronouncing the correct word and locating/remembering something known. There may even be symptoms such as memory loss. Family members or friends may notice these symptoms. Not all subjects diagnosed with MCI at this stage are diagnosed with AD. However, 10-15% of these develop AD each year. The reason why AD does not occur in others is still unknown (McEvoy et al., 2009; O'Dwyer et al., 2012).

- Dementia due to AD: Dementia due to AD: This stage, which is the last stage of AD, is usually the longest stage. In this phase, changes occur in the patient's behaviors, bodily functions (such as walking and swallowing), cognitive abilities, and memory. The person may have trouble remembering himself, paying bills, dressing, controlling his bowels, and fulfilling his daily needs such as the bladder. Also, at this stage, psychological symptoms begin to appear. Even in severe patients, memory and cognitive abilities are severely affected and the person loses interaction with the environment. Care is needed at this stage (Khojaste-Sarakhsi et al., 2022; Cassani et al., 2018; Alberdi et al., 2016).

Although Alzheimer's disease is not seen as the cause of death, the disease may result in death because it triggers psychiatric diseases in patients (Alorf & Khan, 2022). Therefore, early diagnosis of AD is extremely important in terms of increasing the quality of life of patients (Khojaste-Sarakhsi et al., 2022).

Despite the recent clinical studies that have developed AD, the possible errors that may occur in the examination of neuroimages, the increase in the number of patients, and the brain degeneration that may occur with aging make it difficult to diagnose. Computer-aided methods have been actively used more and more in order to minimize possible errors that may occur in the diagnosis of AD, to facilitate diagnosis, and to support specialist physicians. He made a significant contribution to the development and advancement of clinical decision support systems with computer-aided methods such as neuroimaging, deep learning (DL), and machine learning (ML). The development of DL-based architectures for AD diagnosis has rapidly increased using the increasing number of data and datasets provided by the Alzheimer's Disease Neuroimaging Initiative (ADNI) with the advancing technology (Khojaste-Sarakhsi et al., 2022; Alorf & Khan, 2022). Most of these architectures are based on the use of images in different modalities obtained from brain MRI scans (Khojaste-Sarakhsi et al., 2022).

Related Works

There are many studies in the literature using DL and ML techniques for AD diagnosis. For example, Zhang et al. proposed a CNN-based DL architecture for AD diagnosis. In the proposed architecture, the properties obtained after successive convolution and pooling operations were applied, the first three fully connected layers, and then the classification process was carried out with the softmax process. They achieved an accuracy of 88.20% in the dual classification (mild cognitive impairment (MCI) and AD) performed with MRI and PET images (Zhang et al., 2019). Neffati et al. proposed an ML-based architecture that is a combination of Downsized Kernel Principal Component Analysis (DKPCA) and Support Vector Machine (SVM) architectures. After the features were normalized with the DKPCA approach, classification was performed with the SVM algorithm. They used the OASIS dataset for testing. They achieved 92.5% accuracy, 95% specificity, and 88% sensitivity with their proposed architecture (Neffati et al., 2019). Duc et al. developed a 3-D CNN technique for the diagnosis of AD. With the developed technique, they obtained 85.27% accuracy by using the feature map obtained from the s-FMRI images grouped as AD and NC (Duc et al., 2020). Islam and Zhang proposed different models based on a deep CNN

to diagnose AD and its stages. In the study using the Open Access Series of Imaging Studies (OASIS) dataset, they obtained 93.18%, 92% f1-score, 93% recall, and 94% precision (Islam and Zhang, 2018).

In another study by Sarraf and Tofighi, they used a transfer learning method based on LeNet-5 and CNN architecture. With their proposed method, the two-class dataset containing AD and NC data showed 96.86% success (Sarraf & Tofighi, 2016). Liu et al. proposed a deep CNN model for AD diagnosis using the ADNI dataset. In the proposed architecture, the classification process is carried out with the feature maps obtained as a result of the segmentation process. In the dataset, there are MRI images taken at 449 T1 shots, 97 AD, 233 MCI, and 119 Normal Control (NC). With their proposed method, they achieved an accuracy of 88.9% in classifying AD vs. NC and an accuracy of 76.2% in classifying MCI vs. MCI (Liu et al., 2020). Buvaneswari and Gayathri proposed a combination of principal component analysis (PCA) and support vector regression (SVR) for the detection of AD and MCI using the ADNI dataset. To reduce the feature size with PCA, classification was also performed with SVR. In the study, they provided 98.53% accuracy (Buvaneswari and Gayathri, 2021).

Ahmed et al. used a dataset prepared by the Gwangju National Dementia Research Center (GARD). They proposed the CNN model for AD diagnosis. They performed feature extraction with the CNN model and classification with softmax. With this approach, they achieved 90.05% accuracy (Ahmed et al. 2019). In another study by Kam et al., they used a 3D CNN-based method. With this method, they achieved an accuracy of 76.07% in the diagnosis of AD (Kam et al., 2020). Khan et al. used a VGG-based transfer learning technique. They achieved a success increase of 4% and 7% in the study using the ADNI dataset (Khan et al., 2019). Lee et al. proposed an AlexNet-based architecture. They performed binary classification (AD and NC) and multiple classifications (AD, NC, and MCI) using the ADNI and OASIS datasets. The proposed method achieved a classification accuracy of 99.35% in the OASIS dataset and 98.74% in the ADNI dataset for binary classification. They achieved 98.06% accuracy using ADNI data for multiclassification (Lee, Ellahi, & Choi, 2019).

In another study performed by Ning et al. for the estimation of AD, they proposed an association-induced multimodal method. This method consists of a combination of dimension integration reductions representation learning and classification models. With their proposed approach, they classified AD and NC samples with 96.9% accuracy (Ning et al., 2021). Wang et al. used the ML-based AdaBoost architecture using an fMRI dataset containing AD, MCI, and NC samples. First, they extracted feature maps with correlation coefficients using the regions of interest (ROIs) technique. Then, they used the proposed linear discriminant analysis (LDA) method to reduce noise effects. Finally, they achieved 75.8% accuracy by performing classification with the AdaBoost method (Wang et al., 2018).

Jia et al. obtained a new fMRI-based dataset with the first mean amplitude of low-frequency amplitude (mALFF) transformation and mean regional homogeneity (mReHo) image transformation methods. Then, they extracted feature vectors with their proposed 3DPCANet model and canonical correlation analysis (CCA) method. Using the vectors of the features they obtained, they achieved success rates of 91.30%, 92.00%, and 95.00% at different stages with the ML-based SVM algorithm (Jia et al., 2021). In the study performed by Loddo et al., AD diagnosis was performed using three different datasets (OASIS, ADNI, and KAGGLE). As a method, they proposed a method that combines ResNet101, AlexNet, and InceptionResNetV2 techniques. The method they proposed showed 98.51% accuracy on the two-class dataset and 98.67% accuracy on the multi-class datasets containing all datasets (Loddo et al., 2022).

Qureshi et al. used a 3D-CNN model to divide 133 AD patients with dementia grades between 0.5 and 3 into two classes based on dementia grade. There were 77 patients in the very mild/mild

group with dementia grade 0.5 to 1 and 56 patients in the moderate/severe group with dementia grade 2 to 3. At the end of the study, they obtained 0.923 ± 0.042 accuracy, 0.946 ± 0.019 specificity, and 0.896 ± 0.077 sensitivity (Iqbal Qureshi et al., 2019). Ju et al. performed early MCI detection from fMRI time series data using the stacked autoencoder method. They achieved an accuracy of 64.71% on time series data and 86.47% on link data, an improvement of 31.21% over traditional classification methods (Ju et al., 2019).

In addition, field transfer learning (Cheng et al., 2015), multitasking learning (Yu et al., 2016) and semi-supervised multimodal manifold order transfer learning (Cheng et al., 2015), Deep Belief Networks (DBP) (Ortiz et al., 2016), auto-encoder (Liu et al., 2014), and Fully Connected Networks (FCN) (Lian et al., 2020) and CNN (Payan & Montana, 2015))(Liu et al., 2018) based different models have been developed. In addition, different methods have been developed for MCI classification and estimation of AD progression (Grueso & Viejo-Sobera, 2021), AD, and MCI classification (Amini et al., 2021).

Material

This study for Alzheimer's disease is taken from Kaggle (Shastri, 2022), a public platform. The main purpose of sharing this dataset is to enable researchers to design and develop the right architecture for Alzheimer's Disease diagnosis. The data consists of MRI images from various websites, public repositories, and hospitals. In Table 1, the classes in the dataset, the number of images, and the resolution information about the images are given. The dataset contains a total of 6400 MRI images, with 896 images of Mild Dementia, 64 images of Moderate Dementia, 3200 of No Dementia, and 2240 images of Very Mild Dementia. All images are in 128x128 resolution. Some class-based sample images in the dataset are given in Fig. 1. The sample images given are images that would not be distinguishable by a normal person but can be distinguished by an expert or by ML and DL techniques.

Table 1. Alzheimer's disease Kaggle dataset

Class	Number of images	Resolution
Mild Demented	896	128x128
Moderate Demented	64	128x128
Non Demented	3200	128x128
Very Mild Demented	2240	128x128
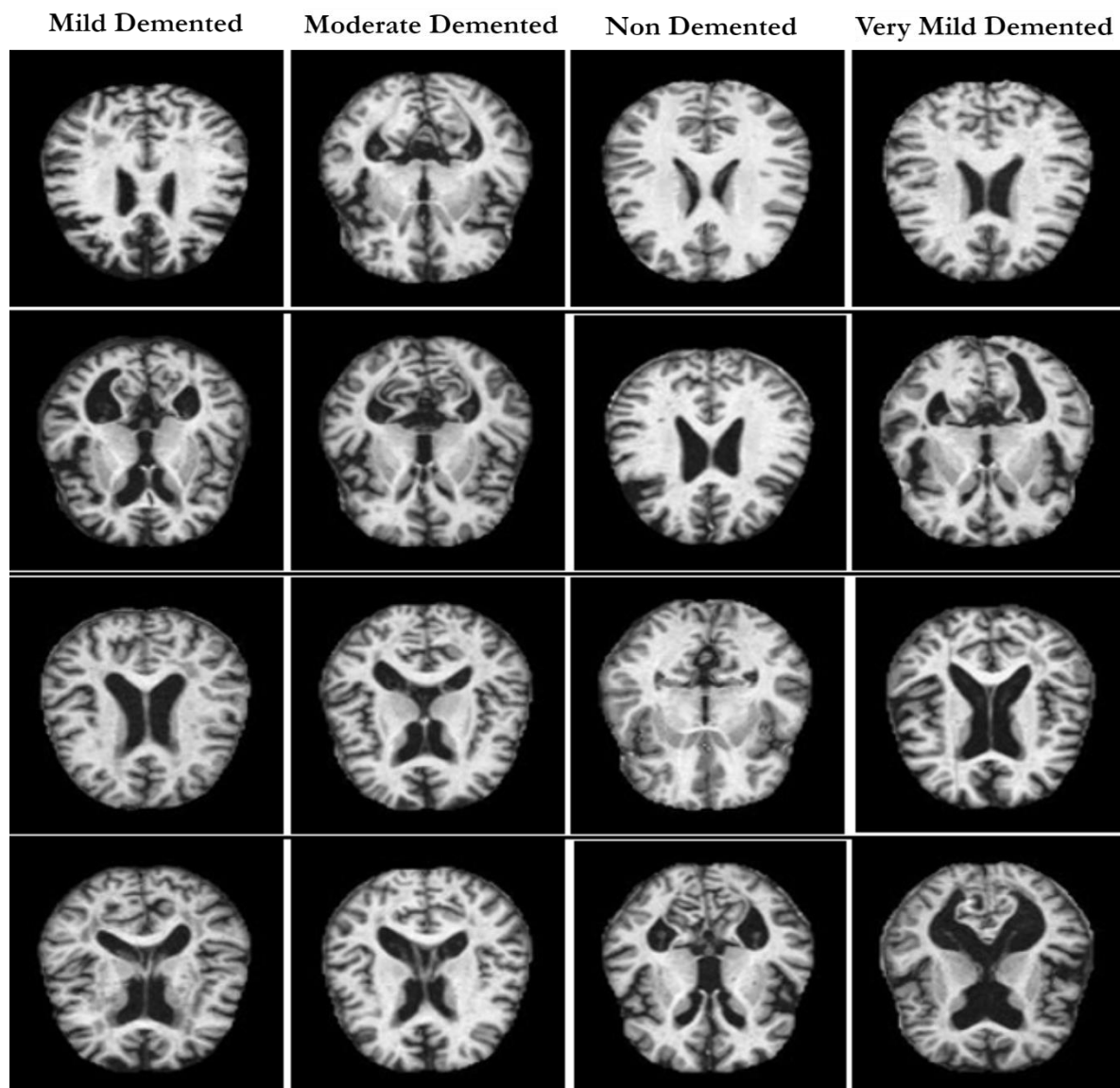
Figure 1. Some sample images according to the stages of Alzheimer's disease in the dataset

Method

In this study, a convolutional neural network-based (CNN) architecture is proposed to predict AD stages (see Fig. 3). CNN is a kind of feedforward neural network that can extract important features from input data by convolution operations. CNN architectures are considered to be one of the most representative architectures in the field of deep learning, as they have shown successful results in many areas such as autonomous vehicles, computer vision, self-service supermarkets, facial recognition of people, and intelligent medical treatments (Manavi et al., 2023; Li et al., 2021). In particular, the features of the CNN architectures given below have made CNNs one of the most basic architectures in the field of DL. These features (Li et al., 2021):

- Local connections: Each neuron in a layer is connected to only a certain number of neurons in the previous layer; It is not connected to all neurons. This plays an important role in accelerating convergence and reducing the number of parameters.
- Weight sharing: Connections in a group can use the same weights parameters. This reduces the number of parameters.

- Downsampling size reduction: A pooling layer preserves important/injured information while removing unimportant information. This reduces the data size and reduces the number of parameters.

As shown in Fig. 2, basically four components are needed to build a CNN architecture. The convolution operation is used for feature extraction, the pooling operation is used to avoid losing information at the boundary, and the stride operation is used to control the convolution density. In addition, average pooling or maximum pooling is applied to eliminate the fit problem that may occur after the convolution process (Li et al., 2021; Hawkins, 2004).
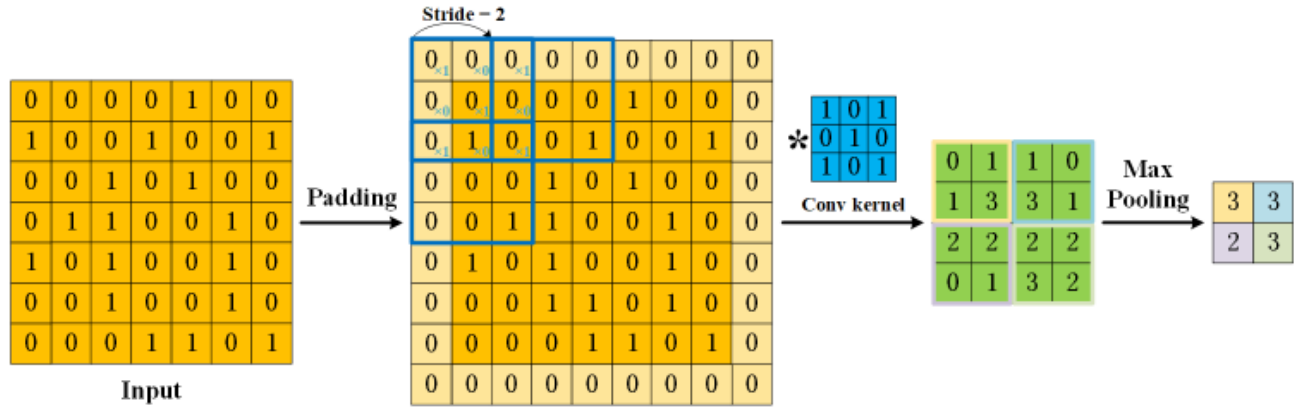
Figure 2. Basic units and processing of 2D CNN architecture (Li et al., 2021)

Proposed Method

The methodology of the proposed architecture is given in Fig. 3. The 128x128 resolution MRI data taken as input is given to the SequentialCNN architecture. The SequentialCNN architecture is normalized with the Rescaling layer of the image it receives. After this process, two Convolution layers, MaxPooling, and Dropout layers are applied respectively. After repeating the same operations three times, the convolution layer is connected. The feature maps obtained from the last convolution layer are vectorized with the Flatten layer. Finally, three dense layers are applied and the final dense layer is estimated AD disease stage. Except for the last dense layer, the Relu activation function is applied after the dense layer and all convolutional layers. The properties obtained in the last dense layer are classified with the softmax activation function. The Adam algorithm was used for the weight update of the proposed architecture. Cross entropy (L_{CE}) is used as the cost function of the SequentialCNN architecture. In order to minimize the cost function, the cost is spread into layers with the backpropagation algorithm. Cross entropy cost function:

$$L_{CE} = -\sum_{i=1}^{n} y_i \, log(\hat{y}_i) \tag{1}$$

Here y_i denotes the real class and $(\hat{y}_i)$ denotes the probability value of the ith class. The convolution operation is mathematically defined as follows (Ahamed et al., 2021):

$$(I * K)(i,j) = \sum_{m}\sum_{n} I(i + m, j + n)K(m,n) \tag{2}$$

Where K is the two-dimensional filter, m and n are the filter size, I is the input data. Relu activation mathematically (Gu et al., 2018; Nair & Hinton, 2010):

$$f(x)_{Relu} = max\,\{0, x_{i,j,k}\} \tag{3}$$

Here, $x_{i,j,k}$ is the input information of the activation function in the (i,j) position in the kth channel. Softmax function used for classification estimation (Gao & Pavel, 2017):

$$Z^k = \frac{e^{x^k}}{\sum_{i=1}^{n} e^{x^n}} \qquad (4)$$

Here, n is the number of classes, x is the input vector, Z is the output vector, and values up to $k = 1 \dots n$.

To update the weights in the proposed SequentialCNN architecture, the Adam (Kingma & Ba, 2015; Seyyarer et al., 2020) optimization algorithm is used. Adam optimization algorithm:

$$w_{t+1}^j = w_t^j - \eta \frac{v_t}{\sqrt{s_t + \varepsilon}} \times g_t \qquad (5)$$

$$v_t = \beta_1 \times v_{t-1} - (1-\beta_1) \times g_t \qquad (6)$$

$$s_t = \beta_2 \times s_{t-1} - (1-\beta_2) \times g_t^2 \qquad (7)$$

Where, w weights, time t, η learning coefficient represent hyperparameters β_1 and β_2. s_t and v_t represent the exponential mean of the squares of the gradients along w_t. The gradient at time t is expressed by g_t.
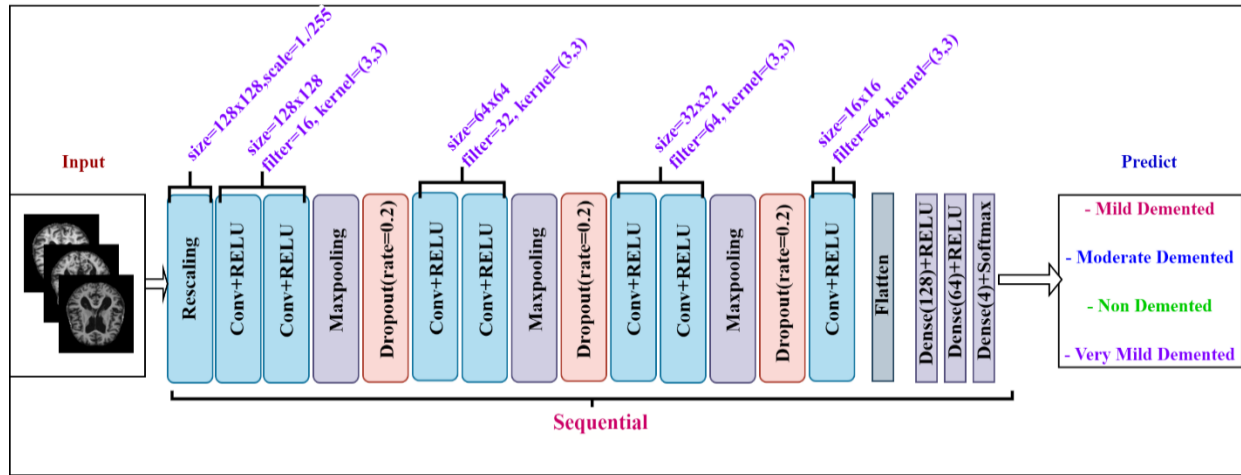
Figure 3. The methodology of the proposed architecture (Sequential CNN)

The layers of the SequentialCNN architecture are given in Table 2. Initially, the images given as input are normalized with the Rescaling layer and the image pixel values are scaled to the range of 0-1. In the Parameters column, the values of the parameters given in the layers are given. The output sizes of the layers are given in the Output_shape column and the param column. The total number of parameters of the proposed architecture is 2214804.

Table 2. Layers of the proposed architecture

Layer	Layer (type)	Parameters	Output Shape	Param
1	Rescaling	scale=1./255	128x128x3	0
2	Conv2D	filters=16, kernel_size=(3,3), activation='relu'	128x128x16	448
3	Conv2D	filters=16, kernel_size=(3,3), activation='relu'	128x128x16	2320
4	MaxPooling2D	pool_size=(2,2)	64x64x16	0
5	Dropout	rate=0.2	64x 64x16	0
6	Conv2D	filters=32, kernel_size=(3,3), activation='relu'	64x64x32	4640
7	Conv2D	filters=32, kernel_size=(3,3), activation='relu'	64x64x32	9248
8	MaxPooling2D	pool_size=(2,2)	32x32x32	0
9	Dropout	rate=0.2	32x32x32	0
10	Conv2D	filters=64, kernel_size=(3,3), activation='relu'	32x32x64	18496
11	Conv2D	filters=64, kernel_size=(3,3), activation='relu'	32x32x64	36928
12	MaxPooling2D	pool_size=(2,2)	16x16x64	0
13	Dropout	rate=0.2	16x16x64	0
14	Conv2D	filters=64, kernel_size=(3,3), activation='relu'	16x16x64	36928
15	Flatten	-	16384	0
16	Dense	Output filter size=128, activation='relu'	128	2097280
17	Dense	Output filter size=64, activation='relu'	64	8256
18	Dense	Output filter size=4, activation='softmax'	4	260
		Total params		2.214.804

Evaluation metrics

Accuracy, Precision, Sensitivity, Specificity, G-Mean, and AUC evaluation metrics were used to evaluate the performance of the proposed method. The necessary parameters to define these metrics, true positive (TP), true negative (TN), false positive (FP), and false negative (FN), are defined as follows (Manavi et al., 2023; Zahid et al., 2020; Wang et al. al., 2022; Aminu et al. al., 2021):

- True positive (TP): Number of correctly predicted samples.
- True negative (TN): The number of correctly predicted incorrect instances.
- False positive (FP): The number of incorrectly guessed correct samples.
- False negative (FN): The number of incorrectly guessed incorrect samples.

$$Accuracy = \frac{TP + TN}{TP + TN + FP + FN} * 100 \tag{8}$$

$$Precision = \frac{TP}{TP + FP} * 100 \tag{9}$$

$$Recall/Sensitivity = \frac{TP}{TP + FN} * 100 \tag{10}$$

$$Specificity = \frac{TN}{TN+FP} * 100 \tag{11}$$

$$G - Mean = \sqrt{Sensitivity \ x \ Specificity} * 100 \qquad (12)$$

Another evaluation metric, The receiver operating characteristic (ROC) curve, is used to find the true positive (TPR) rate versus the false positive rate (FPR) value. The area under the ROC is defined as the Area Under the ROC Curve (AUC) (Subramanian et al. 2022).

$$FPR = \frac{FP}{FP+TN} \qquad (13)$$

$$TPR = \frac{TP}{TP+FN} \qquad (14)$$

$$AUC = \int_{-\infty}^{+\infty} TP_{rate}(t) \, FP_{rate}(t) dt \qquad (15)$$

Where TP_{rate} denotes true positive and FP_{rate} denotes false positive rate. t is a parameter that takes a value in the range of [0,1].

Confusion matrix (see Table 3) is another metric used in classification problems. It shows the class in which the data is included as a result of the classification (Gunduz, 2019; Celik, 2023).

Table 3. Confusion matrix

Actual /Predicted	Positive	Negative
Positive	True Positive (TP)	False Negative (FN)
Negative	False Positive (FP)	True Negative (TN)

Findings and Discussion

In this section, the findings obtained as a result of the experimental studies carried out for the diagnosis of AD are shared. Studies were carried out on Google Colaboratory platform and using Keras / Tensorflow libraries. The necessary parameters for the education of architectures are given in Table 4. Each model has trained 100 epochs, Cross entropy is used as the loss function and the batch size value is given as 128.

Table 4. Training parameters of the models

Parameter name	Value
Number of epochs for training of architectures	100
Loss	Cross entropy
Batch size	128

The flow chart of the experimental study process is given in Fig. 4. 80% of the AD dataset is reserved for training and 20% for testing. First, an experimental study was carried out to select the appropriate optimization algorithm, which greatly affects the performance of the models. For this, the proposed architecture (SequentialCNN) was trained for 100 epochs separately for each optimization algorithm, and their performance was evaluated according to the test dataset, and the results are presented in Table 5. After the selection of the appropriate optimization algorithm, the proposed model and the current CNN models were trained for 100 epochs each, and their performances were compared according to the test dataset, and the findings are given in Table 6.
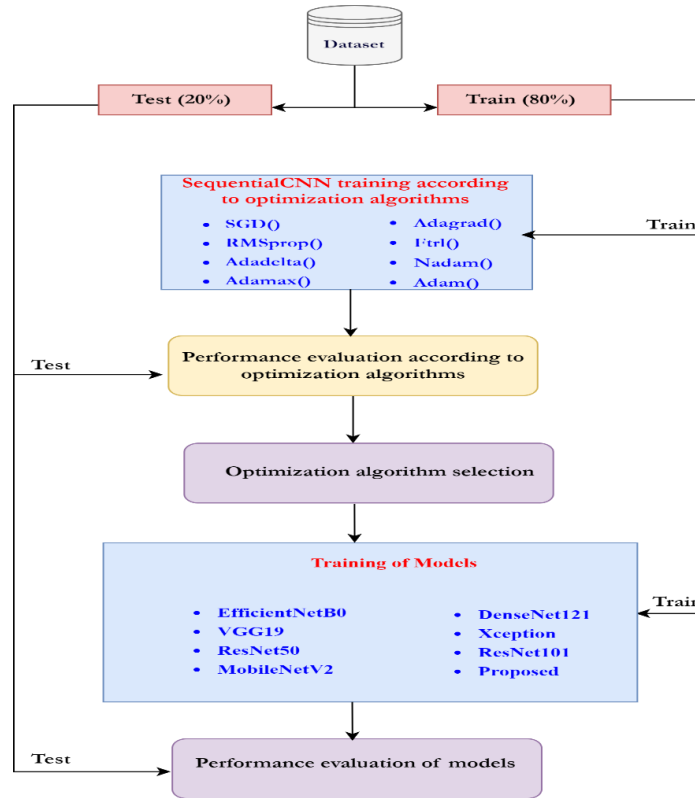
Figure 4. Flow chart of the experimental study process

First, an experimental study has been carried out for the selection of the appropriate optimization method that affects the success of the CNN models. After training each optimization method 100 epochs with the SequentialCNN architecture, the findings obtained according to the test dataset are presented in Table 5. When the results are examined, the Adam algorithm showed the best success with a performance of 99.69% and 100%, respectively, according to the accuracy and specificity metrics of the Adam method. According to Precision, recall, and F1-Score metrics, Adam, Nadam and RmsProp show 100% success. According to G-Mean and AUC metrics, we can say that the RMSprop algorithm shows the highest performance with 99.66% and 99.75% rates. When examined in general, the Adam algorithm was chosen as the optimization method in the training of architectures in other applications, since a higher performance was obtained with the Adam optimization algorithm.

Table 5. Success rates according to the optimization algorithm

Optimezer	Accuracy	Precision	Recall	F1-Score	Specificity	G-Mean	AUC
SGD	79.61	84.00	81.00	83.00	84.12	80.15	86.19
RMSprop	99.61	**100.00**	**100.00**	**100.00**	99.71	**99.66**	**99.75**
Adadelta	51.09	13.00	25.00	17.00	0.00	0.00	50.00
Adamax	99.45	**100.00**	**100.00**	**100.00**	99.71	99.59	99.68
Adagrad	55.93	35.00	31.00	29.00	1.18	0.00	38.31
Nadam	99.53	100.00	100.00	100.00	99.71	99.64	99.73
Ftrl	51.09	13.00	25.00	17.00	0.00	0.00	50.00
Adam	**99.69**	100.00	100.00	100.00	100.00	99.61	99.74

After determining the best-performing optimization method for the training of the architectures, the proposed architecture and current CNN models are trained. Then, the successes of the models according to the test data set are presented in Table 6. When the findings were examined, the recommended architecture showed the highest performance with 99.69%, 100%, 99.61%, and 99.74%, respectively, according to accuracy, specificity, G-Mean, and AUC metrics. Similarly, when the results are analyzed according to the Precision, recall, and F1-Score metrics, we can say that the SequentialCNN architecture shows 100% success.

Table 6. Performance results of architectures

Method	Accuracy	Precision	Recall	F1-Score	Specificity	G-Mean	AUC
EfficientNetB0	98.67	99.00	99.00	99.00	97.94	98.54	99.00
VGG19	97.57	98.00	96.00	97.00	94.39	96.00	97.52
ResNet50	99.06	99.00	99.00	99.00	99.41	99.23	99.43
MobileNetV2	92.81	96.00	88.00	92.00	84.93	87.67	92.26
DenseNet121	97.18	98.00	96.00	97.00	97.62	96.27	97.62
Xception	99.06	99.00	99.00	99.00	99.12	99.12	99.36
ResNet101	99.21	99.00	99.00	99.00	98.24	98.95	99.33
Proposed (SequentialCNN)	**99.69**	**100.00**	**100.00**	**100.00**	**100.00**	**99.61**	**99.74**

In addition, the training times of the models and the number of parameters are shown in Table 7. We can say that the SequentialCNN model is faster than other architectures with a training time of 09.27 minutes. At the same time, it is seen that the SequentialCNN model has the lowest parameter. It is possible to say that the proposed model has a simpler architecture compared to other models.

Table 7. Training times (min.) of architectures and number of parameters

Method	Train time (min.)	Number of parameters
EfficientNetB0	29.37	4.049.571
VGG19	55.19	20.024.384
ResNet50	34.58	23.587.712
MobileNetV2	22.41	2.257.984
DenseNet121	37.39	7.037.504
Xception	57.14	20.861.480
ResNet101	54.08	42.658.176
Proposed (SequentialCNN)	**09.27**	**2.214.804**

The confusion matrix results obtained according to the test dataset with the SequentialCNN architecture are given in Fig. 5. It is possible to say that you have shown a high success by predicting only four images from 1280 MRI images in the test dataset you are examining.

	Mild Demented	Moderate Demented	Non Demented	Very Mild Demented
Mild Demented	170	0	1	1
Moderate Demented	0	13	0	0
Non Demented	0	0	652	1
Very Mild Demented	0	0	1	441

Figure 5. Confusion matrix results of the proposed architecture

Some sample MRI images and estimation results are given in Fig. 6. When the results are examined, it is seen that the stage of AD disease is predicted correctly in the sample images.
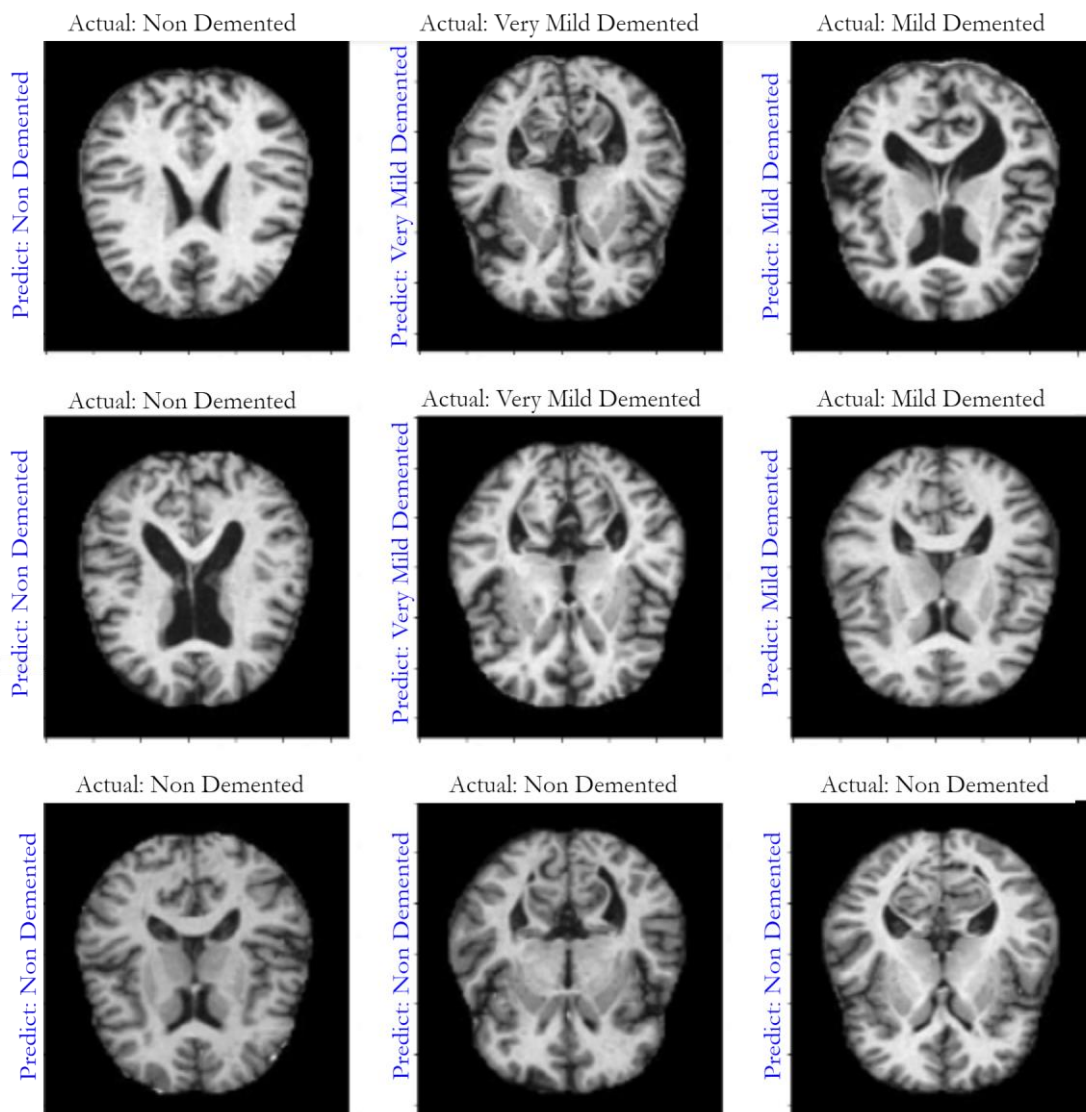
Figure 6. Estimation of sample MRI images

Conclusion

Alzheimer's Disease (AD) is one of the most difficult diseases to treat and causes loss of cognition in patients. AD is estimated to begin at least 20 years before symptoms appear. This disease causes diseases such as loss of cognition and language problems in patients. Although the definitive diagnosis of Alzheimer's disease is possible as a result of the combination of several clinical criteria, there is no cure yet. For AD, which has no definitive treatment, the progression rate of the disease is stopped and the symptoms are delayed by normal methods. However, since delayed treatment for AD does not prevent the progression of the disease, the results can be fatal. This percentage is important in AD disease. Computer-assisted deep learning methods, which have recently been developed in order to facilitate the diagnosis of AD and assist specialist physicians in this field, have made significant contributions. In the literature, studies with these methods have yielded important results in the diagnosis of AD.

In this study, a deep learning-based convolutional neural network (CNN)-based model (SequentialCNN) was proposed for the diagnosis of AD disease stages. Accuracy, precision, recall, and F1-Score, specificity, G-Mean, and AUC metrics were used to evaluate success rates. Firstly, the success of different optimization algorithms was examined by making a study for the selection of optimization parameters, which have a significant effect on the success of CNN models. In the application, the highest performance was achieved with the Adam optimization algorithm in general. In the second application, a comparative study was carried out to show the success of the proposed architecture among current CNN architectures. The proposed architecture showed the highest performance compared to other architectures with 99.69% accuracy, 100% specificity, 99.61% G-Mean, and 99.74% AUC. In addition, according to precision, recall, and F1-Score metrics, SequentialCNN architecture achieved the highest success with a 100% success rate. When the speed and complexity of the architectures are examined, we can say that the proposed architecture has fewer parameters and is faster than other architectures.

REFERENCES

Ahamed, K. U., Islam, M., Uddin, A., Akhter, A., Paul, B. K., Yousuf, M. A., Uddin, S., Quinn, J. M. W., & Moni, M. A. (2021). A deep learning approach using effective preprocessing techniques to detect COVID-19 from chest CT-scan and X-ray images. *Computers in Biology and Medicine*, *139*(October), 105014. https://doi.org/10.1016/j.compbiomed.2021.105014

Ahmed, S., Choi, K. Y., Lee, J. J., Kim, B. C., Kwon, G. R., Lee, K. H., & Jung, H. Y. (2019). Ensembles of Patch-Based Classifiers for Diagnosis of Alzheimer's Diseases. *IEEE Access*, *7*, 73373–73383. https://doi.org/10.1109/ACCESS.2019.2920011

Alberdi, A., Aztiria, A., & Basarab, A. (2016). On the early diagnosis of Alzheimer's Disease from multimodal signals: A survey. *Artificial Intelligence in Medicine*, *71*, 1–29. https://doi.org/10.1016/j.artmed.2016.06.003

Alorf, A., & Khan, M. U. G. (2022). Multi-label classification of Alzheimer's disease stages from resting-state fMRI-based correlation connectivity data and deep learning. *Computers in Biology and Medicine*, *151*(PA), 106240. https://doi.org/10.1016/j.compbiomed.2022.106240

Amini, M., Pedram, M. M., Moradi, A., Jamshidi, M., & Ouchani, M. (2021). Single and Combined Neuroimaging Techniques for Alzheimer's Disease Detection. *Computational Intelligence and Neuroscience*, *2021*. https://doi.org/10.1155/2021/9523039

Aminu, M., Ahmad, N. A., & Mohd Noor, M. H. (2021). Covid-19 detection via deep neural network and occlusion sensitivity maps. *Alexandria Engineering Journal*, *60*(5), 4829–4855. https://doi.org/10.1016/j.aej.2021.03.052

Association, A. (2019). 2019 Alzheimer's disease facts and figures. *Alzheimer's & Dementia*, *15*(3), 321–387. https://doi.org/10.1016/j.jalz.2019.01.010

Budson, A. E., & Solomon, P. R. (2012). New criteria for Alzheimer disease and mild cognitive impairment: Implications for the practicing clinician. *Neurologist*, *18*(6), 356–363. https://doi.org/10.1097/NRL.0b013e31826a998d

Buvaneswari, P., & Gayathri, R. (2021). Detection and Classification of Alzheimer's disease from cognitive impairment with resting-state fMRI. *Neural Computing and Applications*, *2*. https://doi.org/10.1007/s00521-021-06436-2

Cassani, R., Estarellas, M., San-Martin, R., Fraga, F. J., & Falk, T. H. (2018). Systematic review on resting-state EEG for Alzheimer's disease diagnosis and progression assessment. *Disease Markers*, *2018*. https://doi.org/10.1155/2018/5174815

Celik, G. (2023). Detection of Covid-19 and other pneumonia cases from CT and X-ray chest images using deep learning based on feature reuse residual block and depthwise dilated convolutions neural network. *Applied Soft Computing*, *133*, 109906. https://doi.org/10.1016/j.asoc.2022.109906

Chang, C. H., Lin, C. H., & Lane, H. Y. (2021). Machine learning and novel biomarkers for the diagnosis of alzheimer's disease. *International Journal of Molecular Sciences*, *22*(5), 1–12. https://doi.org/10.3390/ijms22052761

Cheng, B., Liu, M., Suk, H. Il, Shen, D., & Zhang, D. (2015). Multimodal manifold-regularized transfer learning for MCI conversion prediction. *Brain Imaging and Behavior*, *9*(4), 913–926. https://doi.org/10.1007/s11682-015-9356-x

Cheng, B., Liu, M., Zhang, D., Munsell, B. C., & Shen, D. (2015). Domain Transfer Learning for

MCI Conversion Prediction. *IEEE Transactions on Biomedical Engineering*, *62*(7), 1805–1817. https://doi.org/10.1109/TBME.2015.2404809

Duc, N. T., Ryu, S., Qureshi, M. N. I., Choi, M., Lee, K. H., & Lee, B. (2020). 3D-Deep Learning Based Automatic Diagnosis of Alzheimer's Disease with Joint MMSE Prediction Using Resting-State fMRI. *Neuroinformatics*, *18*(1), 71–86. https://doi.org/10.1007/s12021-019-09419-w

EL-Geneedy, M., Moustafa, H. E.-D., Khalifa, F., Khater, H., & AbdElhalim, E. (2023). An MRI-based deep learning approach for accurate detection of Alzheimer's disease. *Alexandria Engineering Journal*, *63*, 211–221. https://doi.org/10.1016/j.aej.2022.07.062

Farina, F. R., Emek-Savaş, D. D., Rueda-Delgado, L., Boyle, R., Kiiski, H., Yener, G., & Whelan, R. (2020). A comparison of resting state EEG and structural MRI for classifying Alzheimer's disease and mild cognitive impairment. *NeuroImage*, *215*(March). https://doi.org/10.1016/j.neuroimage.2020.116795

Gao, B., & Pavel, L. (2017). *On the Properties of the Softmax Function with Application in Game Theory and Reinforcement Learning*. 1–10. http://arxiv.org/abs/1704.00805

Grueso, S., & Viejo-Sobera, R. (2021). Machine learning methods for predicting progression from mild cognitive impairment to Alzheimer's disease dementia: a systematic review. *Alzheimer's Research & Therapy*, *13*(1), 162. https://doi.org/10.1186/s13195-021-00900-w

Gu, J., Wang, Z., Kuen, J., Ma, L., Shahroudy, A., Shuai, B., Liu, T., Wang, X., Wang, G., Cai, J., & Chen, T. (2018). Recent advances in convolutional neural networks. *Pattern Recognition*, *77*, 354–377. https://doi.org/10.1016/j.patcog.2017.10.013

Gunduz, H. (2019). Deep Learning-Based Parkinson's Disease Classification Using Vocal Feature Sets. *IEEE Access*, *7*, 115540–115551. https://doi.org/10.1109/ACCESS.2019.2936564

Hawkins, D. M. (2004). The Problem of Overfitting. *Journal of Chemical Information and Computer Sciences*, *44*(1), 1–12. https://doi.org/10.1021/ci0342472

Iqbal Qureshi, M. N., Ryu, S., Song, J., Ho Lee, K., & Lee, B. (2019). Evaluation of functional decline in Alzheimer's dementia using 3D deep learning and group ICA for RS-fMRI measurements. *Frontiers in Aging Neuroscience*, *10*(FEB), 1–9. https://doi.org/10.3389/fnagi.2019.00008

Islam, J., & Zhang, Y. (2018). Brain MRI analysis for Alzheimer's disease diagnosis using an ensemble system of deep convolutional neural networks. *Brain Informatics*, *5*(2). https://doi.org/10.1186/s40708-018-0080-3

Jia, H., Wang, Y., Duan, Y., & Xiao, H. (2021). Alzheimer's Disease Classification Based on Image Transformation and Features Fusion. *Computational and Mathematical Methods in Medicine*, *2021*. https://doi.org/10.1155/2021/9624269

Ju, R., Hu, C., Zhou, P., & Li, Q. (2019). Early Diagnosis of Alzheimer's Disease Based on Resting-State Brain Networks and Deep Learning. *IEEE/ACM Transactions on Computational Biology and Bioinformatics*, *16*(1), 244–257. https://doi.org/10.1109/TCBB.2017.2776910

Kam, T. E., Zhang, H., Jiao, Z., & Shen, Di. (2020). Deep Learning of Static and Dynamic Brain Functional Networks for Early MCI Detection. *IEEE Transactions on Medical Imaging*, *39*(2), 478–487. https://doi.org/10.1109/TMI.2019.2928790

Khan, N. M., Abraham, N., & Hon, M. (2019). Transfer Learning with Intelligent Training Data

Selection for Prediction of Alzheimer's Disease. *IEEE Access*, *7*, 72726–72735. https://doi.org/10.1109/ACCESS.2019.2920448

Khojaste-Sarakhsi, M., Haghighi, S. S., Ghomi, S. M. T. F., & Marchiori, E. (2022). Deep learning for Alzheimer's disease diagnosis: A survey. *Artificial Intelligence in Medicine*, *130*(May), 102332. https://doi.org/10.1016/j.artmed.2022.102332

Kingma, D. P., & Ba, J. L. (2015). Adam: A method for stochastic optimization. *3rd International Conference on Learning Representations, ICLR 2015 - Conference Track Proceedings*, 1–15.

Lee, B., Ellahi, W., & Choi, J. Y. (2019). Using deep CNN with data permutation scheme for classification of Alzheimer's disease in structural magnetic resonance imaging (SMRI). *IEICE Transactions on Information and Systems*, *E102D*(7), 1384–1395. https://doi.org/10.1587/transinf.2018EDP7393

Li, Z., Liu, F., Yang, W., Peng, S., & Zhou, J. (2021). A Survey of Convolutional Neural Networks: Analysis, Applications, and Prospects. *IEEE Transactions on Neural Networks and Learning Systems*, *33*(12), 1–21. https://doi.org/10.1109/tnnls.2021.3084827

Lian, C., Liu, M., Zhang, J., & Shen, D. (2020). Hierarchical Fully Convolutional Network for Joint Atrophy Localization and Alzheimer's Disease Diagnosis Using Structural MRI. *IEEE Transactions on Pattern Analysis and Machine Intelligence*, *42*(4), 880–893. https://doi.org/10.1109/TPAMI.2018.2889096

Liu, M., Li, F., Yan, H., Wang, K., Ma, Y., Shen, L., & Xu, M. (2020). A multi-model deep convolutional neural network for automatic hippocampus segmentation and classification in Alzheimer's disease. *NeuroImage*, *208*(August 2018). https://doi.org/10.1016/j.neuroimage.2019.116459

Liu, M., Zhang, J., Adeli, E., & Shen, D. (2018). Landmark-based deep multi-instance learning for brain disease diagnosis. *Medical Image Analysis*, *43*, 157–168. https://doi.org/10.1016/j.media.2017.10.005

Liu, S., Liu, S., Cai, W., Pujol, S., Kikinis, R., & Feng, D. (2014). Early diagnosis of Alzheimer's disease with deep learning. *2014 IEEE 11th International Symposium on Biomedical Imaging (ISBI)*, 1015–1018. https://doi.org/10.1109/ISBI.2014.6868045

Loddo, A., Buttau, S., & Di Ruberto, C. (2022). Deep learning based pipelines for Alzheimer's disease diagnosis: A comparative study and a novel deep-ensemble method. *Computers in Biology and Medicine*, *141*(October 2021), 105032. https://doi.org/10.1016/j.compbiomed.2021.105032

Manavi, F., Sharma, A., Sharma, R., & Tsunoda, T. (2023). CNN-Pred : Prediction of single-stranded and double-stranded DNA-binding protein using convolutional neural networks. *Gene*, *853*(November 2022), 147045. https://doi.org/10.1016/j.gene.2022.147045

McEvoy, L. K., Fennema-Notestine, C., Roddey, J. C., Hagler, D. J., Holland, D., Karow, D. S., Pung, C. J., Brewer, J. B., & Dale, A. M. (2009). Alzheimer Disease: Quantitative Structural Neuroimaging for Detection and Prediction of Clinical and Structural Changes in Mild Cognitive Impairment. *Radiology*, *251*(1), 195–205. https://doi.org/10.1148/radiol.2511080924

Nair, V., & Hinton, G. E. (2010). Rectified Linear Units Improve Restricted Boltzmann Machines. *Proceedings of the 27th International Conference on International Conference on Machine Learning, ICML'10*, 807–814.

Neffati, S., Ben Abdellafou, K., Jaffel, I., Taouali, O., & Bouzrara, K. (2019). An improved machine learning technique based on downsized KPCA for Alzheimer's disease classification. *International Journal of Imaging Systems and Technology*, *29*(2), 121–131. https://doi.org/10.1002/ima.22304

Ning, Z., Xiao, Q., Feng, Q., Chen, W., & Zhang, Y. (2021). Relation-Induced Multi-Modal Shared Representation Learning for Alzheimer's Disease Diagnosis. *IEEE Transactions on Medical Imaging*, *40*(6), 1632–1645. https://doi.org/10.1109/TMI.2021.3063150

O'Dwyer, L., Lamberton, F., Bokde, A. L. W., Ewers, M., Faluyi, Y. O., Tanner, C., Mazoyer, B., O'Neill, D., Bartley, M., Collins, D. R., Coughlan, T., Prvulovic, D., & Hampel, H. (2012). Using support vector machines with multiple indices of diffusion for automated classification of mild cognitive impairment. *PLoS ONE*, *7*(2). https://doi.org/10.1371/journal.pone.0032441

Ortiz, A., Munilla, J., Górriz, J. M., & Ramírez, J. (2016). Ensembles of Deep Learning Architectures for the Early Diagnosis of the Alzheimer's Disease. *International Journal of Neural Systems*, *26*(07), 1650025. https://doi.org/10.1142/S0129065716500258

Payan, A., & Montana, G. (2015). *Predicting Alzheimer's disease: a neuroimaging study with 3D convolutional neural networks*. http://arxiv.org/abs/1502.02506

Prakash, J., Wang, V., Quinn, R. E., & Mitchell, C. S. (2021). Unsupervised machine learning to identify separable clinical alzheimer's disease sub-populations. *Brain Sciences*, *11*(8). https://doi.org/10.3390/brainsci11080977

Riley, K. P., Snowdon, D. A., Desrosiers, M. F., & Markesbery, W. R. (2005). Early life linguistic ability, late life cognitive function, and neuropathology: Findings from the Nun Study. *Neurobiology of Aging*, *26*(3), 341–347. https://doi.org/10.1016/j.neurobiolaging.2004.06.019

Sarraf, S., & Tofighi, G. (2016). *Classification of Alzheimer's Disease Structural MRI Data by Deep Learning Convolutional Neural Networks*. 8–12. http://arxiv.org/abs/1607.06583

Seyyarer, E., Ayata, F., Uçkan, T., & Karci, A. (2020). Derin Öğrenmede Kullanilan Optimizasyon Algoritmalarinin Uygulanmasi ve Kiyaslanmasi. *Anatolian Journal of Computer Sciences*, *5*(2), 90–98. https://dergipark.org.tr/en/download/article-file/1148741

Shastri, S. (2022). *Alzheimer MRI Preprocessed Dataset*. (Accessed from https://www.kaggle.com/datasets/sachinkumar413/alzheimer-mri-dataset on 16/09/2022).

Sperling, R. A., Aisen, P. S., Beckett, L. A., Bennett, D. A., Craft, S., Fagan, A. M., Iwatsubo, T., Jack, C. R., Kaye, J., Montine, T. J., Park, D. C., Reiman, E. M., Rowe, C. C., Siemers, E., Stern, Y., Yaffe, K., Carrillo, M. C., Thies, B., Morrison-Bogorad, M., … Phelps, C. H. (2011). Toward defining the preclinical stages of Alzheimer's disease: Recommendations from the National Institute on Aging-Alzheimer's Association workgroups on diagnostic guidelines for Alzheimer's disease. *Alzheimer's and Dementia*, *7*(3), 280–292. https://doi.org/10.1016/j.jalz.2011.03.003

Subramanian, N., Elharrouss, O., Al-Maadeed, S., & Chowdhury, M. (2022). A review of deep learning-based detection methods for COVID-19. *Computers in Biology and Medicine*, *143*, 105233. https://doi.org/10.1016/j.compbiomed.2022.105233

Subramanyam Rallabandi, V. P., & Seetharaman, K. (2023). Deep learning-based classification of healthy aging controls, mild cognitive impairment and Alzheimer's disease using fusion of MRI-PET imaging. *Biomedical Signal Processing and Control*, *80*(P1), 104312.

https://doi.org/10.1016/j.bspc.2022.104312

Wang, L., Mao, Z., Xuan, H., Ma, T., Hu, C., Chen, J., & You, X. (2022). Status diagnosis and feature tracing of the natural gas pipeline weld based on improved random forest model. *International Journal of Pressure Vessels and Piping*, *200*(July), 104821. https://doi.org/10.1016/j.ijpvp.2022.104821

Wang, Z., Zheng, Y., Zhu, D. C., Bozoki, A. C., & Li, T. (2018). Classification of Alzheimer's disease, mild cognitive impairment and normal control subjects using resting-state fmri based network connectivity analysis. *IEEE Journal of Translational Engineering in Health and Medicine*, *6*(March), 1–9. https://doi.org/10.1109/JTEHM.2018.2874887

Weller, J., & Budson, A. (2018). Current understanding of Alzheimer's disease diagnosis and treatment. *F1000Research*, *7*(0), 1161. https://doi.org/10.12688/f1000research.14506.1

Yu, G., Liu, Y., & Shen, D. (2016). Graph-guided joint prediction of class label and clinical scores for the Alzheimer's disease. *Brain Structure and Function*, *221*(7), 3787–3801. https://doi.org/10.1007/s00429-015-1132-6

Zahid, L., Maqsood, M., Durrani, M. Y., Bakhtyar, M., Baber, J., Jamal, H., Mehmood, I., & Song, O. Y. (2020). A Spectrogram-Based Deep Feature Assisted Computer-Aided Diagnostic System for Parkinson's Disease. *IEEE Access*, *8*, 35482–35495. https://doi.org/10.1109/ACCESS.2020.2974008

Zhang, F., Li, Z., Zhang, B., Du, H., Wang, B., & Zhang, X. (2019). Multi-modal deep learning model for auxiliary diagnosis of Alzheimer's disease. *Neurocomputing*, *361*, 185–195. https://doi.org/10.1016/j.neucom.2019.04.093

Performance Evaluation of Energy-Efficient Torque Distribution Method for the Autonomous Vehicle with Different Road Conditions

Hakan BASARGAN[1]
András MIHÁLY[2]
Péter GÁSPÁR[1,2]

Introduction

This research deals with the evaluation of the developed energy optimal control allocation of an in-wheel electric vehicle with autonomous trajectory tracking in different slopes and road conditions. The developed method is based on a multi-criteria torque distribution considering the power consumption of the electric in-wheel motors. This method aims to increase battery state-of-charge and by this means extending the range of the autonomous electric vehicle. The objective of this method is to minimize power consumption by creating an optimal distribution between yaw moment and steering angle. Eight electric motor models which are based on the Simscape model with regenerative energy ability and the basic Li-Ion battery model have been built and implemented in an attempt to simulate the operation of the autonomous four-wheel independently actuated vehicle. Several road conditions such as different degrees of slope, road roughness are considered during simulations. This developed method is evaluated and compared with a different method in different road conditions and slopes. These tests are validated in the Trucksim which is an advanced dynamical vehicle simulation environment. Results show that this developed method is more efficient in several road conditions.

The driving range of electric vehicles is one of the most popular topics nowadays, thus many researchers in both academic and industrial areas work on this problem. At the same time, in-wheel motor vehicles are in the scope of research for both academic and industry for automotive. The benefits of the in-wheel motors have already been studied recently (Chen et al., 2016, Jain and Williamson 2009, Watts et al. 2010). As known, in-wheel motor doesn't have transmission inside, thus we are able to control each motor separately without external mechanical integration. Due to controlling each in-wheel motor individually, it is possible to design optimal torque distribution for each motor. This control can distribute driving torque between driving wheels according to driving conditions and provide energy flow optimization in order to save energy. The vehicle safety integration control, such as an electronic stability program and traction control system needs proper condition while this individually controllable in-wheel motor can provide it.

There are numerous studies related to the torque distribution method for in-wheel driven vehicles, while these studies have used different models and methods in the process of the torque

[1] Department of Control for Transportation and Vehicle Systems,
Budapest University of Technology and Economics, Müegyetem rkp. 3, H-1111 Budapest, Hungary; hakan.basargan@kjk.bme.hu
[2] Systems and Control Laboratory, Institute for Computer Science and Control (SZTAKI), Eötvös Loránd Research Network (ELKH), H-1111 Budapest, 13–17 Kende street, Hungary; [mihaly.andras

distribution. The proposed method of (Lin (2019)) consist of a multi-objective optimal torque distribution method by considering energy consumption and vehicle stability. Their energy efficiency control allocation model reduces the total power loss by 9.29% over the New European Driving Cycle method. The strategy of (Guo et al., 2020) is based on the extremum optimization algorithm, where the four wheels work with high efficiency and the vehicle consumes the low power, and compared with torque average distribution strategy. (Jin et al., 2020) adopted the deep deterministic policy gradient algorithm to optimize the distribution of the drive torque in order to reduce energy consumption. Hu and colleagues (Hu et al., 2019) proposed method on wheel torque optimization distribution method during the steering. Their control scheme with optimal motor efficiency as the objective function is constructed to improve the economy. The results have been compared with the conventional stability control strategy and it is shown that method reduces the energy consumption while ensuring vehicle stability. The study of (Guo et al., 2019) has a similar method under emergency conditions. Their torque distribution algorithms have 3 layers: upper controller, where the diamond shape method was used to define the stable area, middle controller, where sliding mode control method was used, and lower controller, where an optimization-based method was used to distribute the torque to the independent four wheels. (Song et al., 2020) proposes a torque distribution strategy regardless of whether the same or different motors are equipped in the rear and front wheels and verified the proposed strategy using an urban dynamometer driving schedule. They used four permanent magnet synchronous motors like our study and (Wu et al., 2018). The study of (Peng et al., 2019) proposes the method, which takes into account both safety and energy-saving performances with hierarchical control. The torque values are calculated directly by using the model predictive control method then compare the control effects between non-hierarchical and hierarchical torque distribution strategy. Xu and his colleagues (Xu et al., 2018) introduces a braking torque distribution strategy with regenerative braking system. The strategy is based on model predictive control theory. Their proposed controller can maximize the regeneration efficiency by determining the hydraulic and motor braking torque. This research paper (Park et al., 2018) has been used fuzzy control approach in the torque distribution strategy. Our previous publication (Mihály et al., 2019) has introduced the energy optimal control method with 2 different control levels, which are multi-objective wheel torque distribution method (low-level) and minimization of the cornering resistance (high-level), while my Master's thesis (Hakan, 2018) introduces the fundamental of this multi-objective torque distribution method. The book chapter (Gáspár et al., 2020) consist of a reconfigurable trajectory-tracking control design with maximizing battery state-of-charge by using multi-objective method.

This paper evaluates the earlier-proposed energy optimal torque distribution method in different road conditions and slopes with a trajectory tracking controller. This method has been developed with a multi-objective in-wheel motor torque optimization for considering electric motor efficiency characteristics along with safety aspects of the vehicle. The trajectory tracking controller has been developed with Linear Parameter-Varying (LPV) framework and integrated to this study instead of using driver model.

The paper is organized as follows: Trajectory Tracking Control section consists introduction of the vehicle model and trajectory controller. The Battery Model introduces the battery model for this research, configuration, and parameters of the battery. The Motor Model section describes the parameter and configuration of the motor model and usage in this research. The Torque Distribution Method section includes description of normal distribution and earlier-proposed efficient torque distribution method. Simulation Results shows the efficiency of the energy-efficient torque distribution method in the TruckSim simulation environment. Finally, a couple of conclusive remarks are listed in Conclusion section.

Trajectory Tracking Control

Lateral and longitudinal dynamics of the vehicle are necessary to be formulated to design a trajectory tracking controller. Here, the two-wheeled bicycle model is used for vehicle modeling, see Figure 1. The motion equations are given as:

$$J\ddot{\psi} = c_1 l_1 \alpha_1 - c_2 l_2 \alpha_2 + M_b r$$
$$m\dot{\xi}(\dot{\psi} + \dot{\beta}) = c_1 \alpha_1 + c_2 \alpha_2$$
$$m\ddot{\xi} = F_l - F_d$$
$$\ddot{y}_v = \dot{\xi}(\dot{\psi} + \dot{\beta})$$

(1)

where l_1 and l_2 are geometric parameters, m is the mass, J is yaw-inertia of the vehicle, and c_1 and c_2 are cornering stiffnes. The yaw of the vehicle is expressed as ψ, while the side-slip angle is β. $\dot{\xi}$ is the longitudinal and $\ddot{y}_v$ is lateral acceleration. The brake yaw moment M_{br} longitudinal force F_l and the front steering angle δ are the inputs of the system. For the side slip angles of the wheels, the following notations are used:

$$\alpha_1 = \delta - \beta - (\dot{\psi} l_1)/\dot{\xi}$$
$$\alpha_2 = -\beta + (\dot{\psi} l_2)/\dot{\xi}$$

(2)

Lateral and longitudinal position tracking must be guaranteed in the design. The calculated vehicle's lateral position in both coordinate systems y_v and y_{gl} is shown in Figure 1. Eventually, in the reference road geometry, rotation of vehicle calculation is considered as below:

$$y_{(v,r)} = -\sin(\psi)\, x_{gl,r} \cos(\psi)\, y_{gl,r}$$

(3)

where $x_{gl,r}$ is longitudinal and $y_{gl,r}$ is lateral coordinates of the reference road geometry in the world coordinate system, $y_{v,r}$ is the lateral position of the reference road geometry in the coordinate system of vehicle.

Assumption: $x_{gl,r}$ and $y_{gl,r}$ are are given in look-up tables for different road courses, or can be calculated with coordinate transformation from GPS data of the selected road.
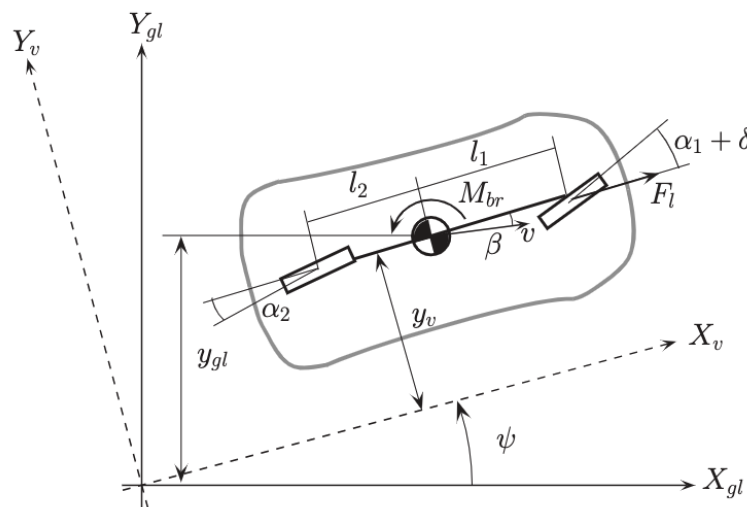
Figure 1. Single track bicycle model

The trajectory tracking control through the LPV technique has already been introduced in (Mihály et al., 2019); hence here only a brief explanation is given. The state-space representation form of the vehicle motion equation can be expressed as follows from Equation 1.

$$\dot{x} = A(\rho)x + B_1\, w + B_2\,(\rho)u \qquad (4)$$
$$z = Cx + Dw$$
$$y = Cx + Dw$$
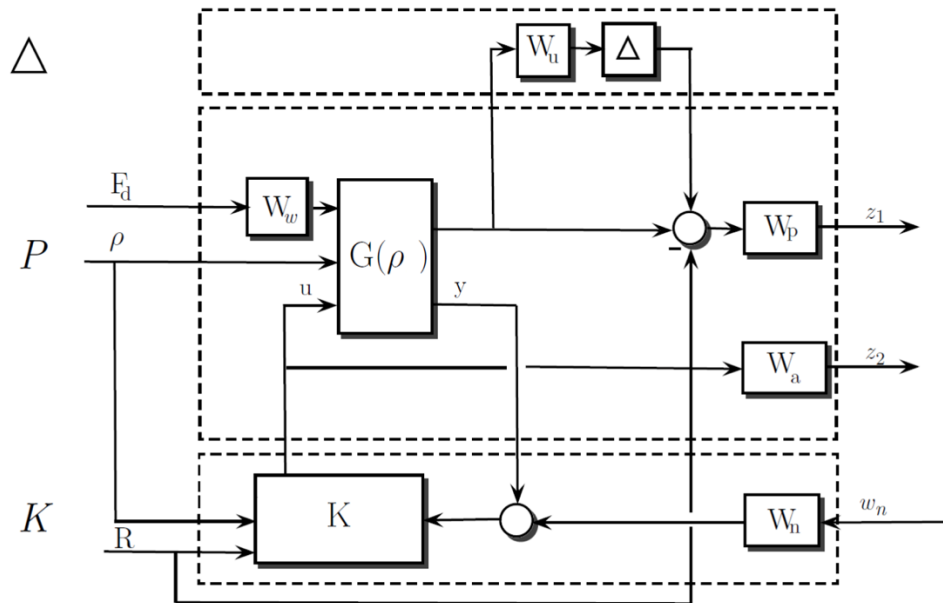
Figure 2. Closed-loop interconnection structure

The state vector of the system can be written as $x = \begin{bmatrix} \dot{\xi} \ \xi \dot{\psi} \ \beta \ \dot{y}_v \ y_v \end{bmatrix}^T$ containing the displacement of the vehicle, the longitudinal velocity, the side-slip angle, the yaw-rate, the lateral velocity and position of the vehicle. The control inputs of the system are the longitudinal force, the front steering angle and the brake yaw-moment, which are given in an input vector as: $x = [F_l\ \delta\ M_{br}]^T$.

The proper velocity tracking must be provided in longitudinal direction: $z_\xi = \left| \dot{\xi_{ref}} - \dot{\xi} \right|$. This can be formulated as an optimization criterion: $z_\xi \to 0$. Then, minimization is needed in the difference between the vehicle lateral position and reference position $z_y = \left| y_{v,r} - y_v \right|$, which can be formulated as the following optimization criterion $z_y \to 0$. These performances are built in a performance vector: $z_1 = \begin{bmatrix} z_\xi\ z_y \end{bmatrix}^T$.

Simultaneously, actuator saturations must be handled while they are formulated as performance criteria: $z_2 = [\delta\ M_{br}]^T$ in control design.

The velocity is assumed to be measured or estimated (Song et al., 2002) The nonlinear model can be transformed into an LPV model using a scheduling variable of $\rho = \dot{\xi}$ The velocity and the lateral position are measured output of the system, i.e. $y = \begin{bmatrix} \dot{\xi}\ y_v \end{bmatrix}^T$. The controller design is based on the weighting strategy, which is formulated via a close-loop interconnection structure, it can be seen in Figure 2.

Battery Model

Lithium-Ion battery compared to other battery types have several advantages such as greater efficiency, energy density, increased nominal voltages, lower specific weight, smaller size, increased lifetime, faster and more efficient charging, maintenance-free usage, and greater resistance for the external conditions (Han et al., 2014). Due to its advantages, they are preferred in the automotive industry. Thus, the Li-ion battery model is used for this study. The parameters of the battery for simulation are shown in Table 1.

Table 1. Paramaters of the battery model.

Parameters	Value	Unit
Battery type	*Lithium-iom*	-
Nominal voltage	*400*	*V*
Rated capacity	*58.5*	*Ah*
Initial state-of-charge	*80*	*%*
Battery response type	*30*	*s*
Initial resistance	*0.0687*	*ohm*
Capacity	*52.9*	*Ah*
Maximum capacity	*58.5*	*Ah*

A Li-ion battery is built up in parallel (to increase current), in series (to increase voltage), or in combined configurations by connected primary Li-ion cells. Multiple battery cells can be integrated as a battery module. More than one battery module can be converted into a battery pack. Typically, a basic Li-ion cell consists of a cathode (positive electrode) and an anode (negative electrode) that are contacted with an electrolyte containing a lithium-ion. Rate discharge, charge, discharge temperature and cycle characteristics of Li-Ion battery can be seen in Figure 3 (Co, 2010).
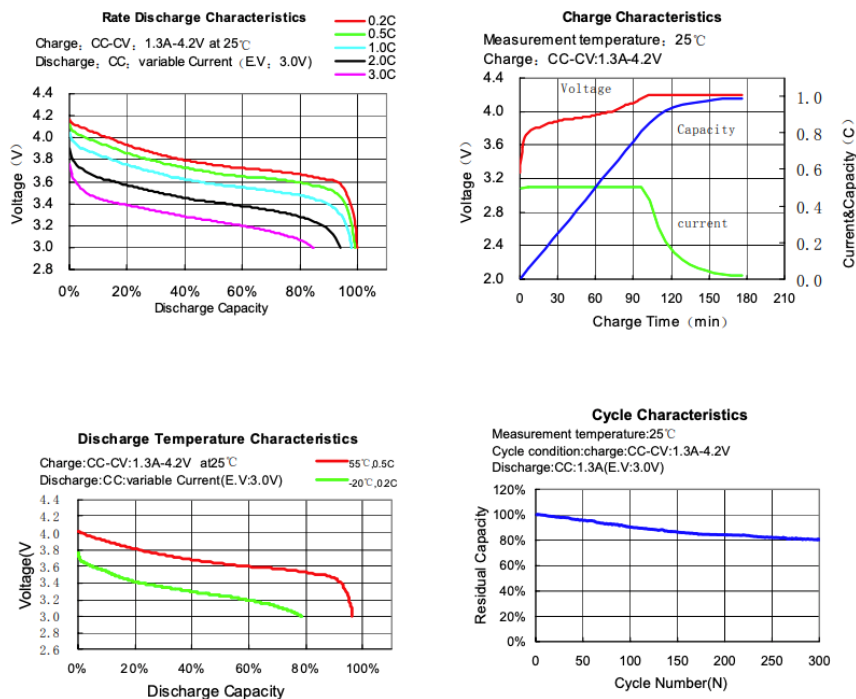
Figure 3. Characteristics of Lithium Ion battery

In this paper, battery discharge and charge can be formulated as (5) and (6) (Shepherd, 1965)

$$f_1(it, i*, i, Exp) = E_0 - K.\frac{Q}{Q - it}.i* - K\frac{Q}{Q - it}.it + Laplace^{-1}\left(\frac{Exp(s)}{Sel(s)}.0\right) \tag{5}$$

$$f_1(it, i*, i, Exp) = E_0 - K.\frac{Q}{|it| + 0.1.Q}.i* - K\frac{Q}{Q - it}.it + Laplace^{-1}\left(\frac{Exp(s)}{Sel(s)}.\frac{1}{s}\right) \tag{6}$$

where i_t is extracted capacity, i is battery current, i^* is low frequency current dynamics, K is polarization constant, E_0 is constant voltage, A is exponential voltage, Q is maximum battery capacity and B is exponential capacity.

Motor Model

Permanent Magnet Synchronous Motor (PMSM) was used as a consequence of its advantage and easy of control. The technology of in-wheel motor provides a solution for many problems such as producing power equally to internal combustion engine (ICE) alternatives and controlling is easy. In addition to this, in-wheel motors have great advantages such as decreasing the number of vehicle parts, reduce complexity and cost, be the future of combined power electronics, give freedom to complete the design. Furthermore, the regenerative braking potential can be increased by using in-wheel motors and that can reduce battery cost and battery size or rising range. Commonly, these advantages provide a huge opportunity for hybrid and electric vehicles, including full-size SUVs and sedan vehicles, which are more desired by the customers who want also are profitable for manufacture (Watts et al., 2010, Itoh et al., 2011)

The PMSM is an electrical machine that has the stator phase windings and motor permanent magnets. Three-phase stator windings create a turning magnetic field through the three-phase AC. The rotor is furnished with a superior permanent magnet on the surface or within ferromagnetic materials, for example, neodymium iron, boron, or uncommon earth magnetic materials to acquire a solid magnetic field (Boby et al., 2013).

PMSM block in Simulink is used to simulate the torque distribution method. PMSM works in both generator or motor mode by determining the sign of the mechanical torque (positive for engine mode, negative for generator mode), and by means of this regeneration, energy can be applied. Equations (7) are described in the rotor reference frame.

$$\frac{d}{dt} i_d = \frac{1}{L_d} V_d - \frac{R}{L_d} i_d + \frac{L_q}{L_d} p w_m i_q \tag{7}$$
$$\frac{d}{dt} i_d = \frac{1}{L_d} V_d - \frac{R}{L_d} i_d + \frac{L_d}{L_q} p w_m i_d - \frac{\lambda p w_d}{L_q}$$
$$T_e = 1.5 p [\lambda i_q + (L_d - L_q) i_d i_q]$$

where, A is signify resistance of stator windings, L_q and L_d express inductances of q and d axis, i_q and i_d are currents of axis of q and d, λ is flux induced, V_q and V_d are voltage of q and d axis, w_m is angular velocity of rotor, p number of pole pairs and T_e express electromagnetic torque.

There is no variation in the phase inductance for a round motor. The inductances of d and q given by below formulas for the salient round motor:

$$L_q = L_d = \frac{L_{ab}}{2} \tag{8}$$

$$L_q = \frac{\min(L_{ab})}{2} \quad L_d = \frac{\max(L_{ab})}{2}$$

For the mechanical system of 3 phases permanent magnet synchronous machine, the angular velocity of the rotor which is mechanical speeds are expressed as follows:

$$\frac{d}{dt} w_m = \frac{1}{J} (T_e - T_f - F w_m - T_m) \tag{9}$$

$$\frac{d\theta}{dt} = w_m$$

where J is combined inertia of rotor and load, F is combined viscous friction of rotor and load, θ is rotor angular position, T_m is shaft mechanical torque, T_f is shaft static friction torque and ω_m is rotor's angular velocity.

The motor model needs an inverter, speed controller, and vector controller where they have been implemented in the motor model. The complete motor model has eight motors, four of them are for the recharging process and the other four motors are for the charging process in case of negative torque.

Torque Distribution Method

In this section, optimal torque distribution method is presented, while the non-optimal torque distribution method is also presented here in order to compare with optimal torque distribution.

Non-optimal torque distribution

In the non-optimal torque distribution method, if the longitudinal force which is given by high-level controller F_l is more than zero, and yaw moment M_{br} is more or equal than zero, Equation (10) is used with positive sign in F_{fR} and F_{rR} equations and negative sign in F_{fL} and F_{rL} equations. If longitudinal is bigger than zero and yaw moment is less than zero, (10) is used with negative sign in F_{fR} and F_{rR} equations and positive sign in F_{fL} and F_{rL} equations. In case of braking, (11) and in high braking pressure, the torques are distributed equally as $F_{fL} = F_{fR} = F_{rL} = F_{rR} = \frac{F_l}{4}$.

$$F_{fL} = F_{fL} \pm \frac{2|M_{br}|}{4b_f} \tag{10}$$

$$F_{fR} = F_{fR} \pm \frac{2|M_{br}|}{4b_f}$$

$$F_{rL} = F_{rL} \pm \frac{2|M_{br}|}{4b_r}$$

$$F_{rR} = F_{rR} \pm \frac{2|M_{br}|}{4b_r}$$

$$F_{front} = \frac{F_{fL} + mgl_2{}^2}{2h} - \frac{mgl_2{}^2}{2h} \frac{h}{mg(l_1 + l_2)} \tag{11}$$

$$F_{rear} = F_l - F_{front}$$

$$F_{fl} = F_{fr} = \frac{F_{front}}{2}$$
$$F_{rl} = F_{rr} = \frac{F_{rear}}{2}$$

Optimal torque distribution

The main aim of the torque distribution of the in-wheel motor drive system is to improve the energy efficiency and performance of the vehicle. Efficient torque distribution is based on the minimization of the power consumption and to do it with satisfying the longitudinal force and yaw moment, the pattern search algorithm is used. This distribution method has been introduced in (Mihály et al., 2019).

The power of in-wheel motors are directly related to their torque. Therefore, possible to write force related power equation. Therefore, the power consumption of in-wheel motor P_{ij} , $i \in [f = front, r = rear], j \in [L = left, R = right]$ are calculated:

$$P_{ij} = \sqrt{F_{ij} w_{ij} P_{in}} \tag{12}$$

where w_{ij} is the rotational speed of each motor and P_{in} is equalized input power which is defined as allocated equalized power of one motor. It is calculated as total power consumption of motors per motor equally.

The maximum vertical wheel loads $F_{z,ij}$ are calculated (Kiencke&Nielsen, 2005)

$$F_{z,ij} = m \left(\frac{l_{[1,2]} g \pm h a_x}{L} \right) \left(0.5 \pm \frac{h a_y}{b_{\{f,r\}g}} \right) \tag{13}$$

where $L = l_1 + l_2$, h is the height of the mass center, a_x and a_y is longitudinal and lateral accelerations measured by inertial sensors and g is the gravitational constant. The front-wheel loads $i = f$ are calculated using l_2 and b_f with a negative sign in the first bracket, whereas the rear wheel loads $i = r$ are calculated with l_1 and b_r with positive sign in the first bracket. Moreover, right wheel loads $j = R$ with a positive sign, while left wheel loads $j = L$ are defined with a negative sign in the second bracket. The maximum and minimum longitudinal traction wheel force which transmissible for each wheel is given as: $\left| F_{ij}^{max} \right| = \mu F_{z,ij}$ and $\left| F_{ij}^{min} \right| = -\mu F_{z,ij}$. The upper and lower bound can be expressed as:

$$-\mu F_{z,ij} \leq F_{z,ij} \leq \mu F_{z,ij} \tag{14}$$

M_z is the yaw moment which given by high level controller achieved by wheel forces generated by in-wheel motors. Therefore, the yaw moment M_z^{veh} generated by F_{ij} which is longitudinal wheel forces can be calculated as:

$$M_z^{veh} = \left(-F_{fL} + F_{fR} \right) \frac{b_f}{2} + \left(-F_{rL} + F_{rR} \right) \frac{b_r}{2} \tag{15}$$

Two equalities need to satisfy the demands of the high-level controller, where this equation is (16).

$$M_z^{veh} = M_z \tag{16}$$

In the meantime, a nonlinear constraint is presented in order to ensure the performance of velocity tracking and the sum of the wheel forces have to be equal to the longitudinal force F_L by Equation (17), and the objective function is found in (18).

$$\sum F_{ij} - F_l = 0 \tag{17}$$

$$J = \min P_{total} = \sum_{\substack{i=f,r \\ j=L,R}}^{4} P_{ij} \tag{18}$$

Therefore, the wheel force distribution optimization problem is solved, where the objective function given in (18) is minimized with the lower and upper bounds calculated by (14), (16) and (17) are satisfied. Finally, the torques for the in-wheel motors can be expressed as:

$$T_{ij} = R_{eff} F_{ij} \tag{19}$$

The relation between determined and generated wheel torque is described as below (Tahami et al., 2003):

$$T_{motor}(s) = \frac{T(s)\,(1+\eta)}{1+2\zeta+2\zeta^2} \tag{20}$$

where T_{motor} is the electric motor torque, T is the determined torque, while ζ and η represents the dynamic response and steady state error of the electric hub motors.

Simulation Results

The simulation vehicle is a compact utility truck with a half-tonne of payload. The geometry of the road course is shown in Figure 4. As can be seen, the paths of the vehicle have different slope values. Note that several vehicle dynamic signals can be measured in real vehicles using widespread wheel speed sensors and gyroscopes; thus vehicle velocity, yaw rate, and longitudinal and lateral accelerations are also measured in TruckSim. The goal of the simulation is to compare the results of the torque distribution method in 3 different slopes.
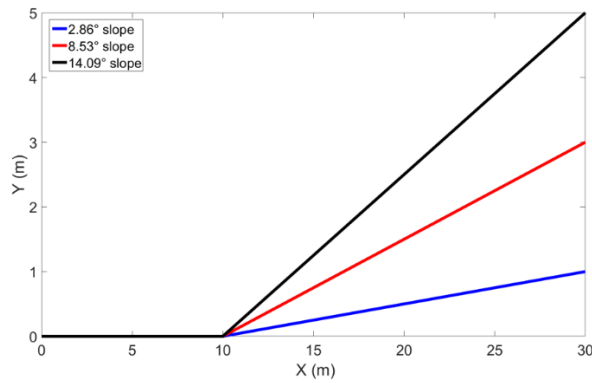
Figure 4. Road courses

The simulation results are shown for 2.86°, 8.53° and 14.09° slopes in Figure 5,6 and 7 respectively. Results show that in high slope, usage of the battery is higher and efficiency in the proposed method is better. The usage of state-of-charge is considered in the calculation of efficiency. Efficiency of the slopes 2.86°, 8.53° and 14.09° are 2.75, 4.4 and 5.5%.
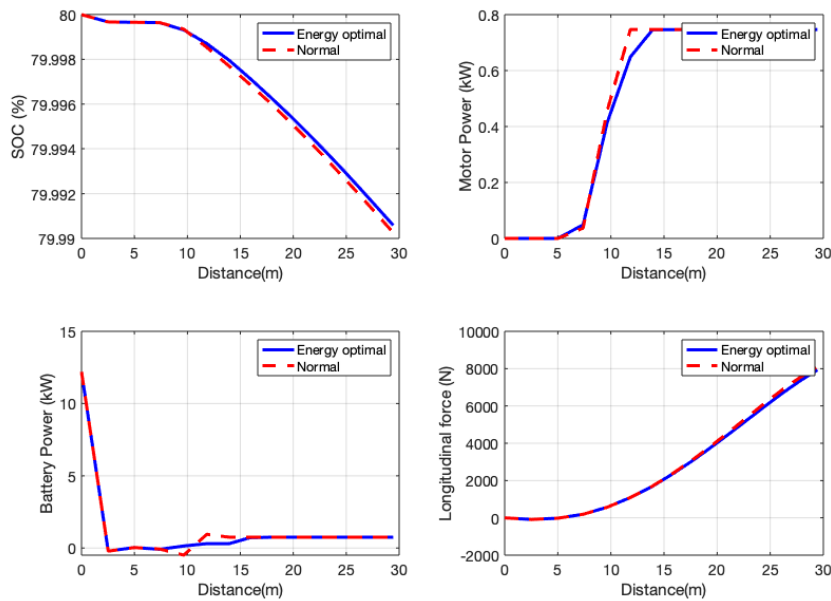
Figure 5. Results of 2.86 ° slope road simulation

It is well demonstrated, that although longitudinal force differences between energy optimal and normal cases are quite similar, the prescribed longitudinal force is smaller with the proposed energy optimal method. It can be seen also in the results of motor power and battery power, the proposed efficient torque distribution model is more efficient than the non-optimal method.
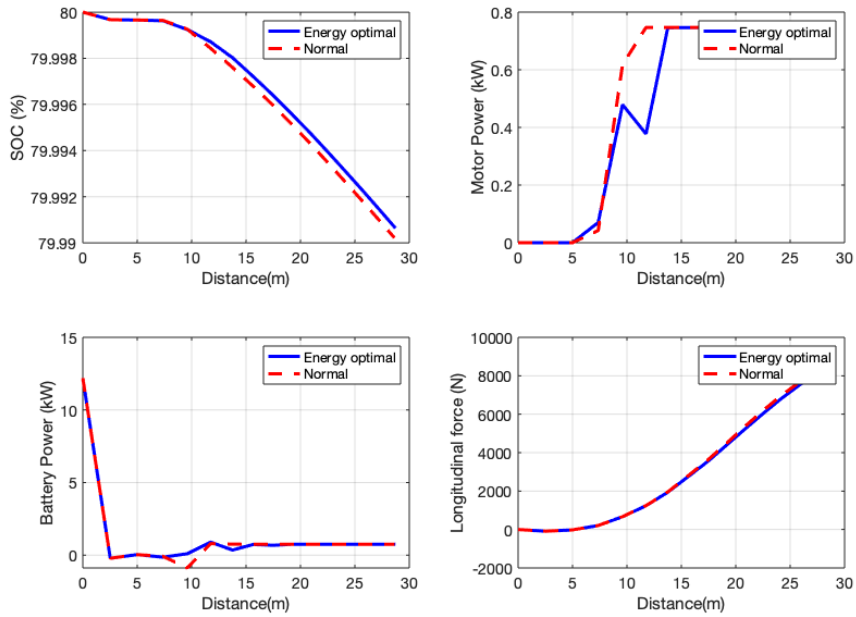
Figure 6. Results of 8.53 ° slope road simulation
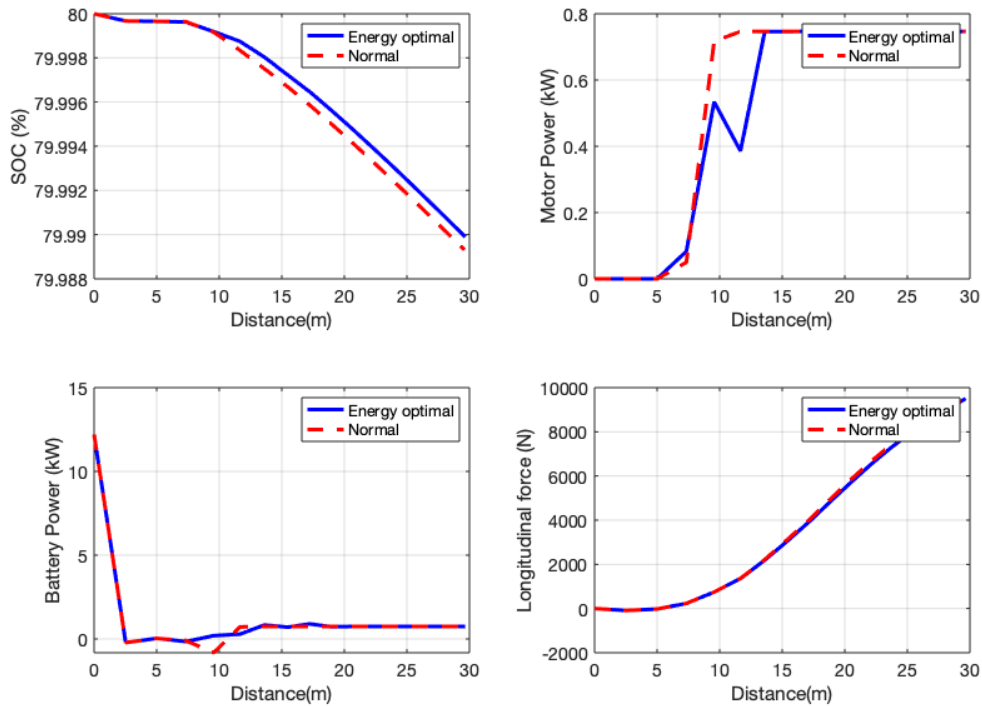
Figure 7. Results of 14.09 ° slope road simulation

The torque distribution method has also been validated in Waterford Michingan race track, see Figure 8(a,b) (Gáspár et al., 2020).

(a) Race track

(b) Altitude

(c) State-of-charge
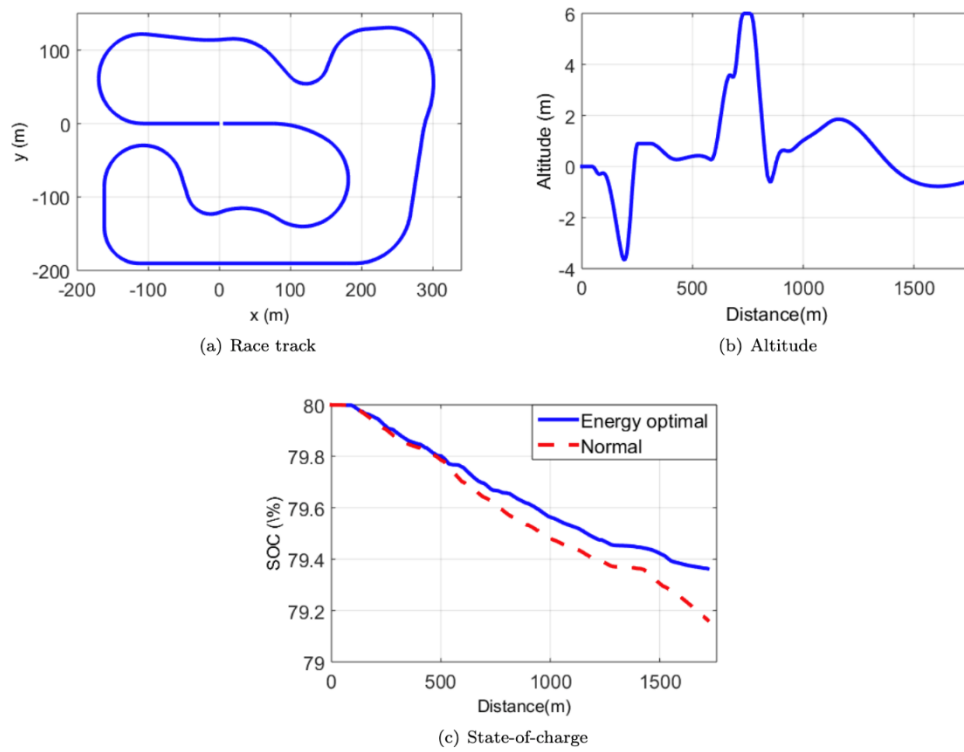
Figure 8. Previous simulation

The efficiency of the proposed method in the race track is validated by comparing battery SOC values, as depicted in Figure 8(c). With the proposed energy optimal reconfiguration method, the initial SOC value of 80% has dropped down to only around 79.4% while in the normal case battery SOC value decreased to around 79.2% which shows a significant difference.

Conclusion

The paper introduced an evaluation of the proposed energy optimal torque distribution method and non-optimal torque distribution method for an autonomous in-wheel driven vehicle with four independent electric motors. The complete lithium-ion battery model and in-wheel electric motor model with regenerative braking ability have been built in order to demonstrate the operation of the autonomous four-wheel independently-actuated vehicle. Different road courses have been built with different slopes. Simulation in the TruckSim vehicle dynamics simulation environment on different road courses has shown the effectiveness of the proposed energy optimal torque distribution method.

KAYNAKÇA

Basargan, H. (2018). Trajectory tracking control of independent in-wheel motor driven autonomous electric vehicle with efficient torque distribution. Master's thesis, Budapest University of Technology and Economics, Budapest, Hungary.

Boby, K., Kottalil, A. M., and Ananthamoorthy, N. (2013). Mathematical modelling of pmsm vector control system based on svpwm with pi controller using matlab. International Journal of Advanced Research in Electrical, Electronics and Instrumentation Engineering, 2(1).

Chen, Q., Liao, C., Ouyang, A., Li, X., and Xiao, Q. (2016). Research and development of in-wheel motor driving technology for electric vehicles. International Journal of Electric and Hybrid Vehicles, 8(3):242–254.

Co., E. (2010). Lithium-Ion Battery LIR18650 2600mAh Datasheet. Co., EEMB, pages 1–9.

Gáspár P., Mihály, A., and Basargan, H. (2020). Fault-tolerant trajectory tracking control of in-wheel motor vehicles with energy-efficient steering and torque distribution.

Guo, L., Ge, P., and Sun, D. (2019). Torque distribution algorithm for stability control of electric vehicle driven by four in-wheel motors under emergency conditions. IEEE Access, 7:104737–104748.

Guo, L., Xu, H., Zou, J., Jie, H., and Zheng, G. (2020). Torque distribution strategy of four-wheel independent drive electric vehicle based on optimal energy consumption. In 2020 IEEE 3rd International Conference on Electronics Technology (ICET), pages 252–256. IEEE.

Han, X., Ouyang, M., Lu, L., Li, J., Zheng, Y., and Li, Z. (2014). A comparative study of commercial lithium ion battery cycle life in electrical vehicle: Aging mechanism identification. Journal of Power Sources, 251:38–54.

Hu, J., Tao, J., Xiao, F., Niu, X., and Fu, C. (2019). An optimal torque distribution control strategy for four-wheel independent drive electric vehicles considering energy economy. IEEE Access, 7:141826–141837.

Itoh, Y., Sakai, K., and MAKINO, Y. (2011). In-wheel motor system. NTN technical Review, (79).

Jain, M. and Williamson, S. S. (2009). Suitability analysis of in-wheel motor direct drives for electric and hybrid electric vehicles. In 2009 IEEE Electrical Power & Energy Conference (EPEC), pages 1–5.

Jin, L., Tian, D., Zhang, Q., and Wang, J. (2020). Optimal torque distribution control of multi-axle electric vehicles with in-wheel motors based on DDPG algorithm. Energies, 16(3).

Kiencke, U. and Nielsen, L. (2005). Automotive control systems: for engine, driveline, and vehicle. Springer Science & Business Media.

Lin, C., Liang, S., Chen, J., & Gao, X. (2019). A multi-objective optimal torque distribution strategy for four in-wheel-motor drive electric vehicles. IEEE Access, 7, 64627-64640.

Mihály, A., Gáspár, P., and Basargan, H. (2019). Maximizing autonomous in-wheel electric vehicle battery state of charge with optimal control allocation. In 2019 18th European Control Conference (ECC), pages 250–255. IEEE.

Park, J., Jang, I. G., and Hwang, S.-H. (2018). Torque distribution algorithm for an independently driven electric vehicle using a fuzzy control method: Driving stability and efficiency. Energies, 11(12):3479.

Peng, H., Wang, W., Xiang, C., Li, L., and Wang, X. (2019). Torque coordinated control of four in-wheel motor independent-drive vehicles with consideration of the safety and economy. IEEE Transactions on Vehicular Technology, 68(10):9604–9618.

Shepherd, C. M. (1965). Design of primary and secondary cells ii. an equation describing battery discharge. Journal of the Electrochemical Society, 112(7):657–664.

Song, C., Uchanski, M., and Hedrick, J. (2002). Vehicle speed estimation using accelerometer and wheel speed measurements. Proc. of the SAE Automotive Transportation Technology, Paris.

Song, Z., Hofmann, H., Li, J., Wang, Y., Lu, D., Ouyang, M., and Du, J. (2020). Torque distribution strategy for multi-pmsm applications and optimal acceleration control for four-wheel-drive electric vehicles. Journal of Dynamic Systems, Measurement, and Control, 142(2).

Tahami, F., Kazemi, R., and Farhanghi, S. (2003). A novel driver assist stability system for all-wheel-drive electric vehicles. IEEE Transactions on Vehicular Technology, 52:683–692.

Watts, A., Vallance, A., Whitehead, A., Hilton, C., and Fraser, A. (2010). The technology and economics of in-wheel motors. SAE International Journal of Passenger Cars-Electronic and Electrical Systems, 3(2010-01-2307):37–55.

Wu, D., Li, Y., Zhang, J., and Du, C. (2018). Torque distribution of a four in-wheel motors electric vehicle based on a pmsm system model. Proceedings of the Institution of Mechanical Engineers, Part D: Journal of Automobile Engineering, 232(13):1828–1845.

Xu, W., Chen, H., Zhao, H., and Ren, B. (2019). Torque optimization control for electric vehicles with four in-wheel motors equipped with regenerative braking system. Mechatronics, 57:95–108.

Design and Implementation of a Steer-by-Wire Control System for Autonomous Vehicles

Karem AL-BADRI[1]
Hakan BASARGAN[2]

1. Introduction

A technological revolution has occurred in several markets due to the development of technology. One of the most significant sectors is automotive, while this improvement makes out the autonomous driving technology (Başargan, H., 2019). Autonomous driving is a hot topic for both industry and academia and one of the key subjects is steering control. Steering by Wire is a vehicle technology in which an Electronic Control Unit (ECU) transfers a steering command from an operational element (the steering wheel) to an actuator at the driven wheels through an electrical signal. These systems' steering and driving wheels are not mechanically connected. The most challenging issue for Steer by Wire systems is ensuring safety and dependability standards while putting in acceptable effort. This alteration is expected to provide many benefits, but there are still certain technical and safety issues that need to be solved. There have been a variety of control mechanisms utilized to control the steer-by-wire system. Some of these strategies, along with their outcomes, are explained in the literature review.

The performance of the steering system can be improved, and the steering ratio can be adjusted to meet the needs by using SbW technology. Because this technology uses electric connections to replace the steering system's mechanical link, it has several advantages over traditional steering systems, including being fuel-free, environmentally friendly, requiring less space, allowing the steering system's position to vary according to requirements, and improving low-speed handling. The maintenance and power costs of a steer-by-wire system are disadvantages. Although steer-by-wire will theoretically require more power than the existing technology, the electricity cost will be negligible when compared to the power usage of power steering. There may potentially be more electrical failures, although SbW systems are expected to survive longer due to fewer mechanical parts, which will increase safety and save total maintenance costs (Kader, 2006).

The steering wheel and front wheel blocks in the SbW system are two separate blocks. The components that make up the steering wheel block are as follows. A steering wheel that controls the direction of a vehicle, a steering wheel angle sensor that transmits the steering wheel's rate of turn, wheel angle, and other important data to the vehicle's computer (ECU), and a steering wheel feedback motor that provides feedback torque to the driver to improve road sensation while

---

[1] 1.Affiliation still missing: Systems and Control Laboratory, Institute for Computer Science and Control (SZTAKI), Eötvös Loránd Research Network (ELKH), H-1111 Budapest, 13–17 Kende street, Hungary; [mihaly.andras],[gaspar.peter]@sztaki.mta.hu,

[2] Department of Control for Transportation and Vehicle Systems, Budapest University of Technology and Economics, Müegyetem rkp. 3, H-1111 Budapest, Hungary;

driving. The front-wheel block, on the other hand, is made up of a steering motor that generates steering torque and a gear head assembly that amplifies torque and passes it to the front wheel. Pinion angle sensor that sends a signal to the steering wheel block's feedback motor. Additionally, a rack and pinion gearbox comprise a circular gear (the pinion) engaging a linear gear (the rack) to convert rotational action into linear motion. The rack is driven linearly once the pinion is rotated, followed by the two front wheels. The major input signal for the steering actuator comes from the feedback angle sensor, whereas the primary signal for the feedback motor comes from the pinion angle sensor(Zhe Sun, 2017).

MATLAB/ SIMULINK simulation environments are used in this study to evaluate the performance of the chosen controllers. The results are addressed in the last part, where the model in the loop is successfully implemented. The lane change and double lane-changing maneuvers are demonstrated using the MIL Matlab Simulink bicycle model. The results show that the LQR controller was able to compensate for the inaccuracy in the steering wheel motor angle, while the MPC controller was able to achieve high wheel synchronization and directional control tracking performance.

Several studies have been presented on steer-by-wire control with different control methods. In (Fu et al., 2009), a general feedback control approach is used to build a conventional SbW controller. SbW control was demonstrated using the Integral Partition PID Control method. While in (Mohd Tumari et al., 2017), the development of a PID control approach for directional control and wheel synchronization in a VSBW system is discussed where Two PID controllers regulate the steering wheel angle and front-wheel angle. Because it can provide closed-loop control of the front wheel corner, PID and Fuzzy control were chosen as the steering system's control algorithm (M. Li & Chang, 2018). According to (Zaidi Mohd Tumari et al., 2019), the PID controller is utilized to manage the angle of the front wheel as well as the returnability of the steering wheel. Also, the steering wheel's returnability is controlled by a fuzzy logic controller. In (Paolo Falcone, 2007), An MPC strategy is provided that will be used to operate an active front steering system in a self-driving car. The study (Huang et al., 2019)proposes a Sliding Mode Predictive Tracking Control (SMPC) strategy for an SbW system with uncertain dynamics to improve the MPC's resiliency in the face of modeling uncertainty and disruptions in the steering control procedures. A traditional SMC is used for the sbw system because it provides various advantages such as precise tracking and robustness against disturbances and unpredicted flaws that are frequent in systems like sbw. According to the (Wang et al., 2014) research, a robust sliding mode control approach for SbW systems with unexpected dynamics is established. In comparison to previous approaches, the suggested robust Sliding Mode Learning Control (SMLC) system offers various advantages which are mentioned in (Do et al., 2014). The article (Im et al., 2007) examines a general bilateral control system that employs a disturbance observer. An experiment using an electronic car demonstrates the efficacy of this study. For (Y. ran Li et al., 2012), Based on analyzing the dynamic model of the steering performing system, Second Order Active Disturbance Rejection Controller (SOADRC) has been used to perform the steering angle following control of the SbW system. Using a Composite Nonlinear Feedback (CNF) controller, the study (Saruchi et al., 2014) presents a novel SbW control technique to assure steering wheel and front wheel synchronization. CNF is a feedback control law that combines linear and nonlinear rules. The steer-by-wire control can be easily implemented into the trajectory tracking control (Basargan et al., 2021)(Basargan H., 2018) (Gáspár et al., 2020).

This article is organized as follows: Section 2 contains the modeling of the steer-by-wire system, Section 3 introduces the formulation of the LQR and MPC controller design, while the implementation of the controller's design is proposed in Section 4 with passive and controlled

simulation results to demonstrate the efficiency of the proposed method. Finally, Section 5 contains the concluding remarks and future works.

2. Mathematical model

The steering wheel and the front axle system are the two subsystems that make up the SBW system as shown in Figure 1. The modeling of both systems will be discussed in detail in this part. In addition, a 2-DOF bicycle linear model is used to test the performance of the controllers and as the vehicle plant for the simulation assessment.
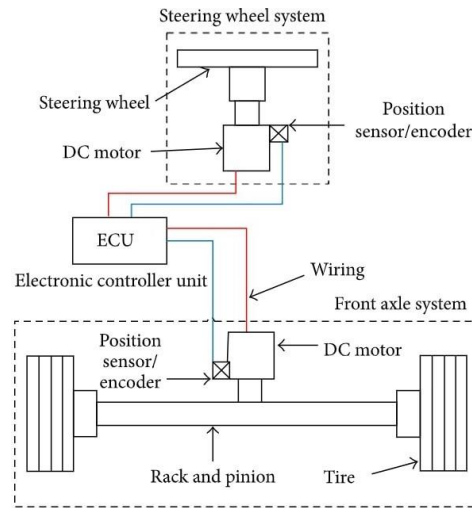
Figure 1. Steer by wire system (Sheikh Muhammad Hafiz Fahami et al., 2015).

The steering wheel motor's primary function is to create steering feedback torque for the driver's steering sensation. The system schematic for the steering wheel system is shown in Figure 2. The steering wheel angle(δ_{sw}) generated by the driver torque represents the system's input, while the rate change of the steering wheel motor angle ($\dot{\delta}_{m1}$), the steering motor angle (δ_{m1}), and the current of the steering wheel motor (i_{a1}) are the system's outputs. Table 1 displays the specifications of the steering wheel mechanism.
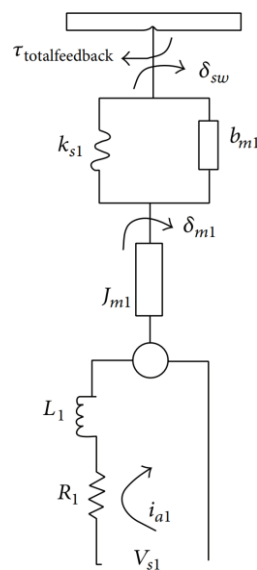
Figure 2. Steering wheel subsystem diagram (Sheikh Muhammad Hafiz Fahami et al., 2015).

Table 1. Steering wheel system parameter

Parameters	Description	Value	Unit
R_1	Motor resistance	5.64	ohm
L_1	Motor inductance	0.017	henry
K_{sm}	Motor constant	0.024	Nm
J_{m1}	Motor inertia	0.0036	kgm²
b_{m1}	Motor damping	0.0068	Nm/(rad/s)
k_{s1}	Lumped torque stiffness	3500	Nm/rad
V_{s1}	Voltage source	…	Volt

The mathematical equations of steering wheel are written as follows:

The steering motor angle is:

$$\ddot{\delta}_{m1} = -\left(\frac{b_{m1}}{J_{m1}}\right)\dot{\delta}_{m2} + \left(\frac{k_{s1}}{J_{m1}}\right)i_{a1} \dots (1)$$

And the current equation is:

$$i_{a1} = -\left(\frac{R_1}{L_1}\right)i_{a1} - \left(\frac{k_{sm}}{L_1}\right)\dot{\delta}_{m1} + \left(\frac{V_{s1}}{L_1}\right) \dots (2)$$

As a result, the state equation of the steering wheel subsystem is given as follows:

$$\dot{x}_{sm} = A_{sm}x_{sm} + B_{sm}u_{sm} \dots (3)$$

$$y_{sm} = C_{sm}x_{sm} \dots (4)$$

$$x_{sm}^T = [\dot{\delta}_{m1} \quad \delta_{m1} \quad i_{a1}] \dots (5)$$

Where, u_{sm} is the steering wheel motor's input, whereas the output is the rate of change of steering wheel motor angle $\dot{\delta}_{m1}$, steering wheel motor angle δ_{m1}, and steering wheel motor current i_{a1}. The following is the list of parameter states:

$$A_{sm} = \begin{bmatrix} -\left(\frac{b_{m1}}{J_{m1}}\right) & 0 & \left(\frac{k_{s1}}{J_{m1}}\right) \\ 1 & 0 & 0 \\ -\left(\frac{k_{sm}}{L_1}\right) & 0 & -\left(\frac{R_1}{L_1}\right) \end{bmatrix} \dots (6)$$

$$B_{sm} = \begin{bmatrix} 0 \\ 0 \\ \left(\dfrac{1}{L_1}\right) \end{bmatrix} \dots (7)$$

$$C_{sm} = [0 \quad 1 \quad 0] \dots (8)$$

$$D_{sm} = [0] \dots (9)$$

$$u_{sm} = \delta_{sw} = V_{s1}$$

The aim of front axle system is to make sure that the front tire angle matches the steering wheel motor angle instruction based on the steering ratio. A front axle DC motor, rack and pinion, and tire model make up the front axle subsystem. Figures 3 and 4 illustrate the front axle system diagram and the subsystem block diagram, respectively. The steering wheel motor angle δ_{m1} is the system's input, while the front tire angle δ_f is the system's output. Table 2 shows the specifications of the front axle system, and the mathematical model of this system is based on the assumptions mentioned in the (Sheikh Muhammad Hafiz Fahami et al., 2015) paper.
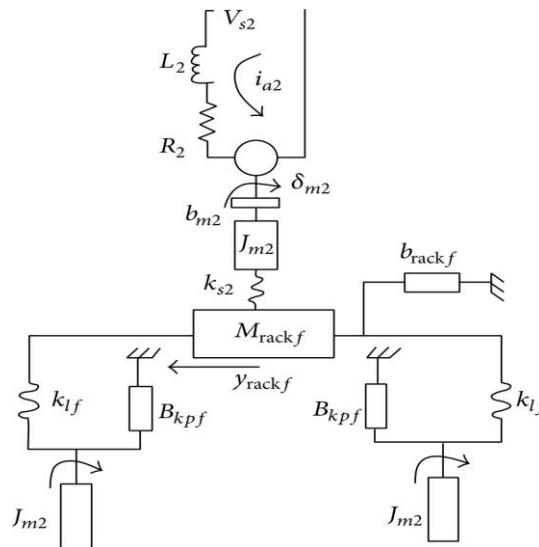
Figure 3 Front axle subsystem diagram (Ancha et al., 2007).
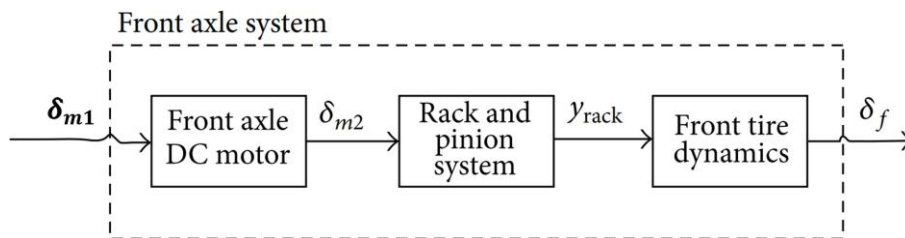
Figure 4. Front axle subsystem block diagram.

Table 2. Front axle system parameter.

Parameters	Description	Value	Unit
R_2	Motor resistance	4.64	ohm
L_2	Motor inductance	0.015	henry
K_{fm}	Motor constant	0.032	Nm
J_{m2}	Motor inertia	0.0062	kgm²
b_{m2}	Motor damping	0.0036	Nm/(rad/s)
k_{s2}	Lumped torque stiffness	3500	Nm/rad
B_{rack}	Rack damping coefficient	0.015	henry
M_{rack}	Rack lumped mass	0.032	Nm
k_{lf}	Rack linkage stiffness	2600	Nm/rad
r_L	Offset of king pin axis	0.00036	m
r_P	Pinion gear radius	0.025	m
B_{kp}	King pin damping coefficient	0.00062	kgm²
I_f	Lumped front wheel inertia	0.00036	kgm²

The front axle DC motor's basic equation is given as follows:

The angle of the front axle motor is:

$$\ddot{\delta}_{m2} = -\left(\frac{b_{m2}}{J_{m2}}\right)\dot{\delta}_{m2} + \left(\frac{k_{s2}}{J_{m2}}\right)i_{a2} \ldots (10)$$

And the equation for the current in the front axle motor is:

$$\dot{i}_{a2} = -\left(\frac{R_2}{L_2}\right)i_{a2} - \left(\frac{k_{fm}}{L_2}\right)\dot{\delta}_{m2} + \left(\frac{V_{s2}}{L_2}\right) \ldots (11)$$

As a result, the front axle motor's state equations are as follows:

$$\dot{x}_{fm} = A_{fm}x_{fm} + B_{fm}u_{fm} \ldots (12)$$

$$y_{fm} = C_{fm}x_{fm} \ldots (13)$$

$$x_{fm}^T = [\dot{\delta}_{m2} \quad \delta_{m2} \quad i_{a2}] \ldots (14)$$

And u_{fm} is the front axle motor's input, whereas the output is the rate of change of front axle motor angle $\dot{\delta}_{m2}$, front axle motor angle δ_{m2}, and front axle motor current i_{a2}. The following is the list of parameter states:

$$A_{fm} = \begin{bmatrix} -\left(\dfrac{b_{m2}}{J_{m2}}\right) & 0 & \left(\dfrac{k_{s2}}{J_{m2}}\right) \\ 1 & 0 & 0 \\ -\left(\dfrac{k_{fm}}{L_2}\right) & 0 & -\left(\dfrac{R_2}{L_2}\right) \end{bmatrix} \ldots (15)$$

$$B_{fm} = \begin{bmatrix} 0 \\ 0 \\ \left(\dfrac{1}{L_2}\right) \end{bmatrix} \ldots (16)$$

$$u_{fm} = \delta_{m1} = V_{s2}$$

The model for the rack and pinion system will be described in the following equation:

$$\ddot{y}_{rack} = \frac{1}{M_{rack}}\left[\left(\frac{2k_{lf}y_{rack}}{r_L^2}\right) - \left(\frac{2k_{s2}y_{rack}}{r_p^2}\right) - B_{rack}\dot{y}_{rack} + \left(\frac{k_{s2}\delta_{m2}}{r_p}\right)\right] \dots (17)$$

As a result, the rack and pinion's state equations are as follows:

$$\dot{x}_{yrack} = A_{yrack}\,x_{yrack} + B_{yrack}\,u_{yrack} \dots (18)$$

$$y_{yrack} = C_{yrack}\,x_{yrack} \dots (19)$$

$$x_{yrack}^T = [\dot{y}_{rack} \quad y_{rack}] \dots (20)$$

Where the rack and pinion system's input is u_{yrack}, and the output is rack displacement y_{rack}, with the following parameter states:

$$A_{yrack} = \begin{bmatrix} -\left(\dfrac{B_{rack}}{M_{rack}}\right) & \left[\left(\dfrac{2k_{lf}y_{rack}}{M_{rack}r_L^2}\right) - \left(\dfrac{2k_{s2}y_{rack}}{M_{rack}r_p^2}\right)\right] \\ 1 & 0 \end{bmatrix} \dots (21)$$

$$B_{yrack} = \begin{bmatrix} \left(\dfrac{k_{s2}}{M_{rack}\,r_p}\right) \\ 0 \end{bmatrix} \dots (22)$$

$$u_{yrack} = \delta_{m2}$$

The model for front tire dynamic system will be described in the following equation:

$$\ddot{\delta}_f = \frac{1}{I_f}\left[\left(-k_{lf}\delta_f + \left(\frac{k_{lf}y_{rack}}{r_L}\right) - B_{kp}\dot{\delta}_f\right)\right] \dots (23)$$

As a result, the Front tire dynamic's state equations are as follows:

$$\dot{x}_{tire} = A_{tire}\,x_{tire} + B_{tire}\,u_{tire} \dots (24)$$

$$y_{tire} = C_{tire}\,x_{tire} \dots (25)$$

$$x_{tire}^T = [\dot{\delta}_f \quad \delta_f] \dots (26)$$

Where the front tire dynamic's input is u_{tire}, while the output for this system is δ_f front tire angle and the parameter's state is:

$$A_{tire} = \begin{bmatrix} -\left(\dfrac{B_{kp}}{I_f}\right) & -\left(\dfrac{k_{lf}}{I_f}\right) \\ 1 & 0 \end{bmatrix} \dots (27)$$

$$B_{tire} = \begin{bmatrix} \left(\dfrac{k_{lf}}{I_f r_L}\right) \\ 0 \end{bmatrix} \dots (28)$$

$$u_{tire} = y_{rack}$$

The final states of the front axle system can be generated according to (Saruchi et al., 2015) using all three system equations previously mentioned, where the input to this system is δ_{m1} while the final output is δ_f with the following state parameters:

$$x_{fa} = \begin{bmatrix} \dot\delta_{m2} & \delta_{m2} & i_{a2} & \dot y_{\text{rack}} & y_{\text{rack}} & \dot\delta_f & \delta_f \end{bmatrix} \dots (29)$$

$$A_{fa} = \begin{bmatrix}
-\left(\dfrac{b_{m2}}{J_{m2}}\right) & 0 & \left(\dfrac{k_{s2}}{J_{m2}}\right) & 0 & 0 & 0 & 0 \\
1 & 0 & 0 & 0 & 0 & 0 & 0 \\
-\left(\dfrac{k_{fm}}{L_2}\right) & 0 & -\left(\dfrac{R_2}{L_2}\right) & 0 & 0 & 0 & 0 \\
0 & \left(\dfrac{k_{s2}}{M_{\text{rack}}\, r_p}\right) & 0 & -\left(\dfrac{B_{\text{rack}}}{M_{\text{rack}}}\right) & \left[\left(\dfrac{2k_l y_{\text{rack}}}{M_{\text{rack}}\, r_L^2}\right) - \left(\dfrac{2k_{s2} y_{\text{rack}}}{M_{\text{rack}}\, r_p^2}\right)\right] & 0 & 0 \\
0 & 0 & 0 & 1 & 0 & 0 & 0 \\
0 & 0 & 0 & 0 & \left(\dfrac{k_{lf}}{I_f r_L}\right) & -\left(\dfrac{B_{kp}}{I_f}\right) & -\left(\dfrac{k_{lf}}{I_f}\right) \\
0 & 0 & 0 & 0 & 0 & 1 & 0
\end{bmatrix} \dots (30)$$

$$B_{fa} = \begin{bmatrix} 0 \\ 0 \\ \left(\dfrac{1}{L_2}\right) \\ 0 \\ 0 \\ 0 \\ 0 \end{bmatrix} \dots (31)$$

$$C_{fa} = \begin{bmatrix} 0 & 0 & 0 & 0 & 0 & 0 & 1 \end{bmatrix} \dots (32)$$

$$D_{fa} = [0] \dots (33)$$

$$u_{fa} = \delta_{m1}$$

Before going into the model classification, it's important to note that there are two forms of vehicle motion control: path following and trajectory tracking. The lateral and longitudinal control for the vehicle is considered independently in path following. For longitudinal control, basic cruise control may be employed, while for lateral control, waypoint references can be provided. These waypoints can be defined as array references, and the controller's job is to go to the closest waypoint using the steering system's intervention. The trajectory tracking solution will be the subject of this work. The fundamental distinction is that we must specify our trajectory as a function of time in trajectory tracking (position and heading reference in function of time). In another world, a significant contrast exists between a path and a trajectory. A path is a spatial construct that describes how to move from point A to point B in the world without using time as a constraint. A trajectory is a path with a timetable attached to it. It informs us how fast we should walk along the path and when we should arrive at each stop along the way. As a result, time is a restriction while following a trajectory. The models that we developed for controller design may be used to classify vehicle motion control systems. The geometric approach, the kinematic model,

and the dynamic model are the three sorts of modeling approaches. The geometric technique is the simplest, in which the vehicle wheelbase and corner radius are utilized to define the relationships according to the control job. Path following controllers, such as pure pursuit controllers and Stanley controllers, commonly employ such models. The schematic for the geometric approach is shown in Figure 5.
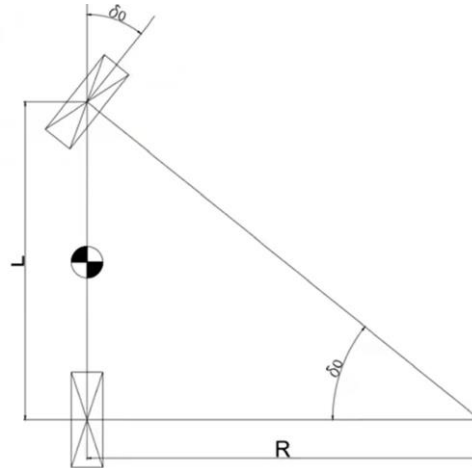
Figure 5. Schematic of the bicycle geometric approach.

Depending on the purpose, both kinematic and dynamic model-based vehicles can be used. When we want to handle extremely dynamic vehicle motion, fiction, or handling constraints, we need to utilize dynamic models with various degrees of complexity. The dynamic model-based is shown in Figure 6. A truck model, bicycle model, two truck models, and many types of tire models can be used as well. However, kinematic models will be the focus area of this paper for simplicity's sake.
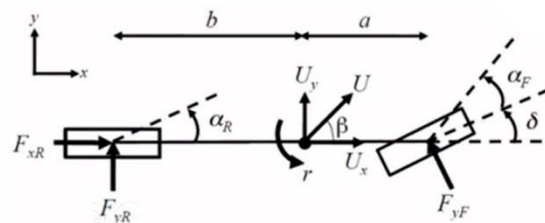
Figure. 6. The bicycle dynamic model.
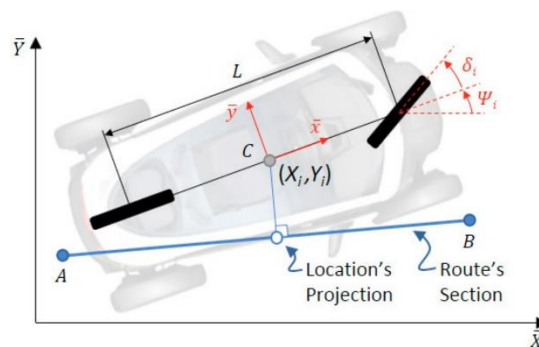
Figure 7. The simplified bicycle kinematic model-based (Matute et al., 2019).

If the goal is to control the vehicle at low speeds and lateral accelerations, a kinematic model that ignores the forces and moments occurring on the vehicle body can be used. However, driving at a low speed will not result in a significant error. As a result, three differential equations may be used to determine the vehicle kinematics, which are listed below. The simplified bicycle kinematics model is shown in Figure 7. The car's heading angle (yaw angle) is represented as ψ, and its front axle angle is represented as δ_f .

$$\dot{X} = v_x * \cos\psi \dots (34)$$

$$\dot{Y} = v_x * \sin\psi \dots (35)$$

$$\dot{\psi} = \left(\frac{v_x * \tan \delta_f}{L}\right) \dots (36)$$

The controller takes into account the vehicle's kinematic bicycle model, as described in Figure 7. The equations are based on mathematical relationships and do not take any forces into account. At points A and B, which represent the front and back ends of the vehicle wheelbase (L), the two left and right wheels are presented as two individual wheels. The vehicle's center of gravity is at point C, which determines the vehicle's position. The vehicle is considered to go in a straight line. The vehicle's motion is described by its position coordinates and orientation (X,Y, ψ). The longitudinal speed and lateral acceleration of the vehicle are parallel and perpendicular, respectively, to the longitudinal axis. The two inputs to this model are longitudinal speed (v_x) and front-wheel angle (δ_f) (Matute et al., 2019). Table 3 describe the parameters used in this model.

Table 3. Bicycle kinematic model parameters.

Parameters	Description	Value	Unit
v_x	*longitudinal speed*	*10*	*m/s*
L	*vehicle wheelbase*	*3*	*m*

3. Controller design

This part consists of designing controllers for steer by wire system. For the Wheel synchronization and direction control, two controllers will be designed. The first controller is responsible for compensating of the steering wheel motor angle inaccuracy δ_{m1}. Then δ_{m1} is supplied into the front axle system's input (Sheikh Muhamad Hafız Fahami et al., 2012, 2013). The front-wheel system's second controller will manage wheel synchronization and direction control to guarantee that the system is following the input signal. The decision to implement an LQR controller for the steering wheel system and an MPC controller for the front axle system will be discussed. In order to control a steer by wire system, many primary conditions must be met as follow:

(1) Wheel synchronization and direction control the front wheel must obey the driver's input command from the steering wheel.

(2) The angle of the steering wheel in relation to the angle of the front wheel called Steering ratio which can be changed. For example , if the steering ratio is 15:1, this means that The front tire wheel should turn to a 1-degree angle by turning the steering wheel to a 15-degree angle. İn this work, The mathematical expression of hyperbolic tangent is used as variable steering ratio (VSR) by adjusting the steering ratio. The usage of hyperbolic tangent idea will not only improves

agility at lower speeds but also decreases the driver's load on the steering wheel (Sheikh Muhammad Hafiz Fahami et al., 2014).

(3) The capability to return the steering wheel or have free control. If the driver's hands are removed or released from the steering wheel, the steering wheel shall automatically return to the center.

(4) Variable steering feel that can be adjusted. The driver of the car relies on steering feel to perceive the force of the condition of the road with tire-to-earth contact and keep vehicle control. The scope of this paper will focus on designing controllers to achieve the first two conditions while other points will be discussed in future works.

Steering Wheel System Controller Design

The (LQR) design approach is well-known in current optimal control theory and has been applied in a variety of applications. In this work, it will be used for the Steering wheel system to compensate for the steering wheel motor angle inaccuracy. An LQR design technique is used to determine the best closed-loop pole positions. The benefits of using LQR are that it is simple to build and that it improves the accuracy of state variables by estimating them. When compared to pole placement, the LQR control has the advantage of specifying a set of performance weights rather than needing to define where eigenvalues should be positioned, which may be more obvious. To stabilize the system, the state feedback control K is designed to minimize the cost function J. A feedback gain matrix is used in LQR control systems to establish a compromise between the usage of control effort, the magnitude, and the speed of response that would provide a stable system. The LQR controller's control block diagram is shown in Figure 8 (Mohamed & Albatlan, 2014).
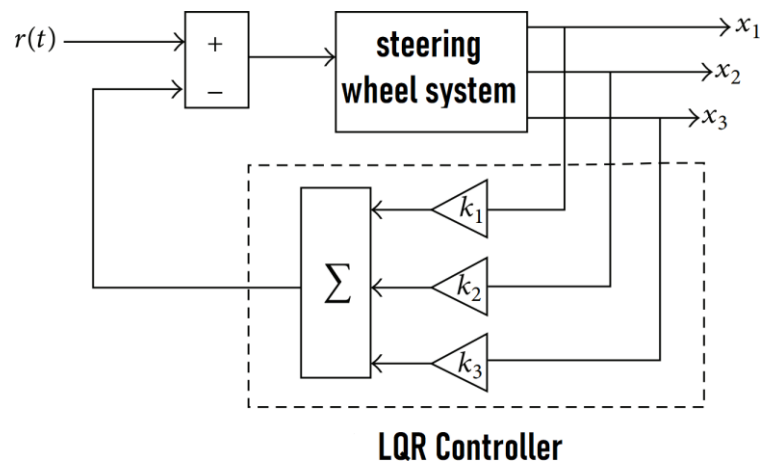
LQR Controller

Figure 8. Basic structure of LQR controller.

The following equation represents the cost function J that needed to be minimized:

$$J = \int_0^\infty (X^T Q X + U^T R U)dt \dots (37)$$

Where X^T and U^T are the inverses of the state and input vector, accordingly. The weighting factors are Q and R. An LQR optimization approaches heavily relies on the weighting matrices Q and R. The following equation represents the Riccati equation that can be used to solve this problem:

$$PA + A^T P - PBR^{-1}B^T P + Q = 0 \ldots (38)$$

P represents a symmetric positive definite matrix. The regulator gain and control signal are calculated using the following two equations:

$$k_c = R^{-1}B^T P \ldots (39)$$
$$u = -k_c X = R^{-1}B^T PX \ldots (40)$$

The gain matrix K is calculated using Matlab software. The controller gains are calculated using the Matlab LQR function and the state-space model parameters that were modeled in section 2. Return recurrence to the lowest value of the performance index determines the weighting parameter values. The chosen weighting parameters are described in equations (41) and (42). while the generated parameters of control feedback gain matrix K are mentioned in (43).

$$Q = \begin{bmatrix} 0 & 0 & 0 \\ 0 & 1 & 0 \\ 0 & 0 & 0 \end{bmatrix} \ldots (41)$$

$$R = [1] \ldots (42)$$

$$K = [0.0003 \quad 1.0000 \quad 0.7475] \ldots (43)$$

so the control input signal will be :

$$u(t) = 0.0003X_1 + 1.0000X_2 + 0.7475X_3 \ldots (44)$$

The simulation experiments are done to see if the linear quadratic regulator controller is a superior solution for system stability.

Front Axle Wheel Controller Design

The front axel wheel angle has different names like steering angle, heading angle, and frontwheel angle. The controller's purpose is to compute the plant's input variables in such a way that the plant's output tracks the output of Variable Steering Ratio (VSR). MPC controller has been chosen to ensure that the front axle angle can track the steering wheel motor angle. Model Predictive Control (MPC), a multi variable control approach that can deal with the inter-connections of the variables in the desired system, solves this challenge. Autonomous vehicle systems must also achieve a high degree of safety. An MPC controller can offer this, as it can manage restrictions like keeping a safe distance from other vehicles. The goal of this paper is to obtain optimum MPC controller implementation by boosting computing speed in order to minimize optimization execution time. To maintain an autonomous vehicle on the proper course, an MPC is employed to regulate the front axle system. When the plant dynamics do not vary, or when the speed is fixed, a standard MPC controller is utilized to regulate the system (Ahmad Reda, Ahmed Bouzid, 2020). The connection between inputs and outputs makes the Autonomous Vehicle steering system, which is a Multi Input Multi Output (MIMO) system, difficult to build using standard controllers. Before starting the design of controllers, it should be mentioned that the MPC controller will work with the SISO system in this paper due to the fact that the longitudinal velocity will be constant at 10 m/s. To compute the input, MPC uses a future prediction technique. The MPC controller employs an optimizer to verify that the plant's output matches the intended reference input. The prediction method is based on the MPC controller simulating the front axle angle with a plant model in the next P time steps, where P is the prediction horizon, which represents time, and the MPC controller forecasts by looking forward in time. The optimizer then chooses the optimum scenario that produces the smallest error between the reference and expected trajectories after the Model Predictive Controller has carefully simulated

multiple future scenarios. The predicted trajectory scenario with the lowest cost function has the smallest error, indicating that it is the best alternative (D. M. Abhishek and C. Mariappan, 2021).

Figure 9 illustrates a traditional MPC controller, while Figure 10 represent the future prediction approach in which each scenario simulates a sequence of steering wheel rotations to follow the reference trajectory, with the best scenario obtaining the least costly function, as stated previously. The scenario with the least cost function J = 20, which provides the best reference trajectory tracking, is the preferred solution. A "state estimator" is used by the MPC controller to estimate the state of the system and provide input to the controller. The static Kalman Filter (KF) is applied in the MPC controller to update the controller states (plant model state, measurements noise model state, and disturbance model state).
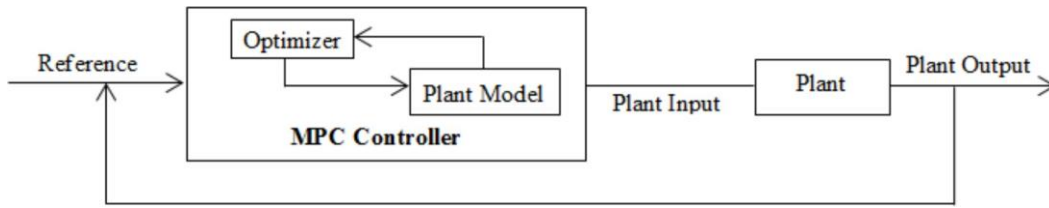
Figure 9. Basic structure of mpc controller.
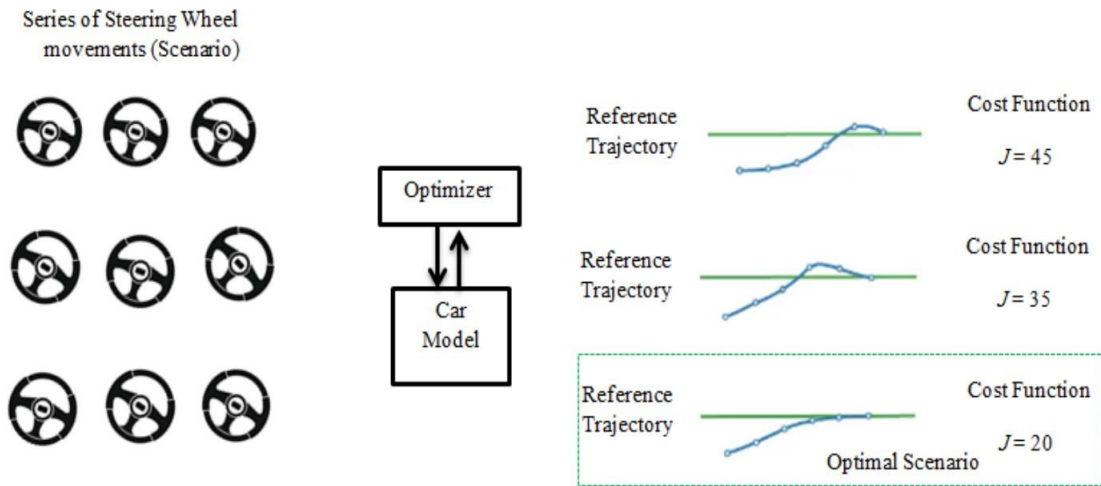
Figure 10. Strategy for Predicting the Future of an Optimization Problem (mathworks, 2018).

The MPC controller provides an online objective function, which is a Quadratic Problem (QP) in this case, at each control interval. Some of the characteristics of the optimization problem are as follows: The cost function is used to evaluate the controller's performance, with the purpose of lowering the cost. The cost Function is also called the objective function. Also, there are soft and hard constraints, such as physical limitations, must be met for the system to work effectively. The MPC controller must calculate control inputs driving the plant's output that are extremely near to the intended reference in order to accomplish optimization. By using various scenarios and reducing the cost function of the optimization problem, this procedure is carried out in a structured way (Ahmad Reda, Ahmed Bouzid, 2020). The cost function J of the steering system of an autonomous vehicle may be written as:

$$J = \sum_{i=1}^{p} w_e e_{k+i}^2 + \sum_{i=0}^{p-1} w_{\Delta u} \Delta u_{k+i}^2 \dots (45)$$

Where (w_e) is the expected error weight (e_{k+i}) and ($w_{\Delta u}$) is the steering angle increases weight Δu_{k+i} . The purpose of the cost function is to reduce both the inaccuracy between the anticipated and reference trajectory as well as the variation in steering angle between time steps. The lowest value of the cost function corresponds to the ideal solution. Decision: Change the controllable variables to reduce the cost function and meet the constraints. The MPC controller calculates the controlled variable by solving the quadratic problem with a particular QP solver that changes the linear optimization problem into the basic form of the QP problem.

The basic constraints, such as the steering angle limits, are taken into account while designing the MPC controller. The major parameters and terms of the MPC controller are shown in Figure 11, with the following definitions: Ts is the Control Time Step, while k is the current sampling step. Prediction Horizon (P): the number of time steps on which the MPC controller predicts by looking forward in time. Control Horizon (M): the number of control motions that can be made in time step k+P. The design parameters of the MPC controller are important because they affect the optimization problem's efficiency and computing complexity. So, a good balance between computing complexity and performance should be achieved. Several broad guidelines may be used to determine the parameters.
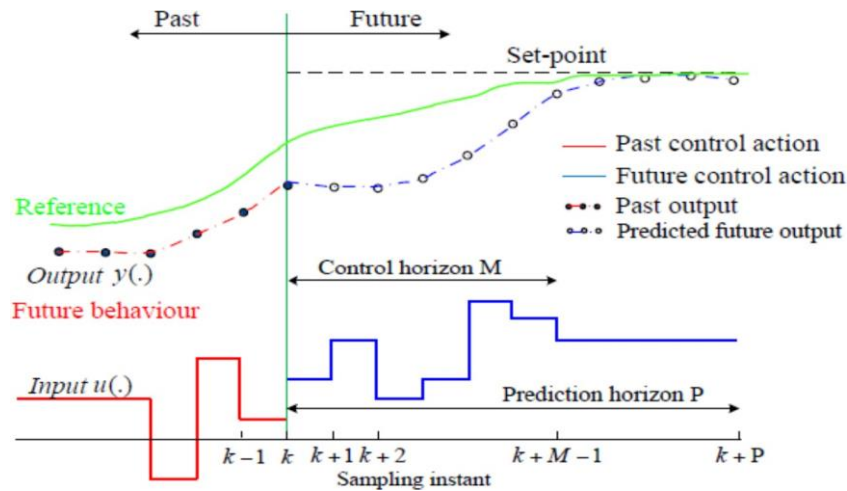
Figure 11. Schematic of the main terms in MPC controller (wikiwand, 2020).

The Simulink model was constructed based on the MPC control diagram. The necessary blocks (front axle model and Reference model) were first added to the MATLAB workspace and connected to the MPC block. The measured output is the first input to the controller, followed by the reference trajectory built with MATLAB's signal builder. The internal plant model and scenarios were specified in MPC Designer. The MPC controller concept for linear systems is shown in Figure 12 (unchanging dynamics system with fixed speed). The chosen parameters for MPC controllers are shown in Table 4.
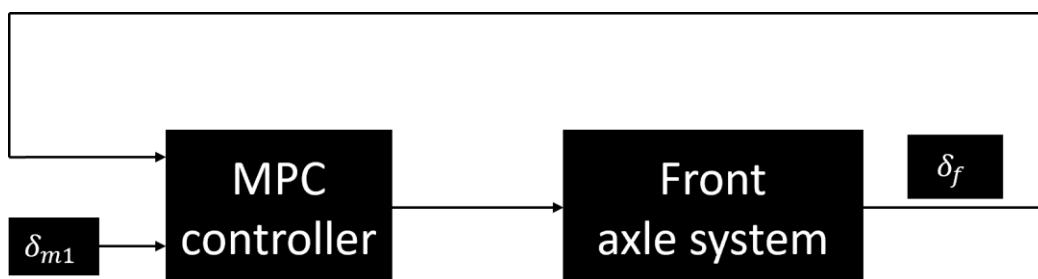
Figure 12. Model of MPC controller for linear system.

Table 4. MPC controller parameters with constaints.

Parameters	Value	Constraints	value
Sampling time	0.01	Steering wheel angle	±30
Prediction horizon	10	Changing rate (steering wheel angle)	±15
Control horizon	3		

4. Simulation results and discussion

In this section, the simulation results are explained, as well as how the model in the loop is implemented. The lane change and double lane-changing maneuvers are demonstrated using the Model-in-Loop(MIL) Matlab Simulink bicycle model.

MIL is the testing of individual or combined modules in a model-based development environment like Mathworks' MATLAB Simulink or ETAS' ASCET. The reduced chance of a hazardous incident occurring is quantified using MIL ratings. It is required to dive into the details of compliance claimed by manufacturers in order to evaluate specific devices for eligibility for inclusion in a safety system. In this section, the results of two scenarios will be discussed in detail and applied to the Bicycle model.

The first simulation is a single lane change task for the autonomous vehicle. In 2018, the UN R79 rule set the standards for the first semiautomated steering functions (Journal et al., 2015). A combination of the lane-keeping assist and the lane-changing system is required for this operation. The electronics take over driving during an autonomous lane change, and the driver is simply required to "follow" the steering wheel. When the system's limits are reached, the driver must retake control of the vehicle. As a result, the driver must keep a constant eye on the lateral and/or longitudinal guidance. Figure 13 shows the lane-changing scenario.
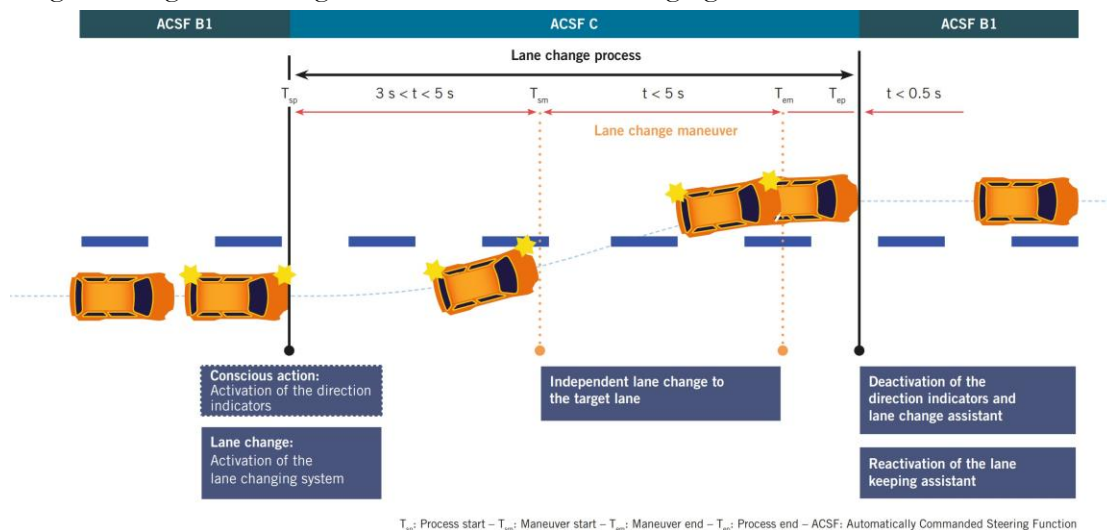
Figure 13. Lane changing scenario (Jürgens et al., 2021).

The Kinematic bicycle model has been used in the Simulink model to evaluate the performance of the steer by wire control system. The Simulink connection between the SbW system and with bicycle model is shown in the Figure 14. In the bicycle model Figure 15 shows Steering wheel performance for lane change tracking with the LQR control signal. Due to the fact

that LQR control utilizes quadratic state and control costs to achieve optimum control of the linear system, the output response is identical to the steering wheel input reference. The driver applied 26 degrees as the steering wheel angle at the seventh second to start the lane-changing process. The lane-changing process ends at second 12 and goes straight after that.
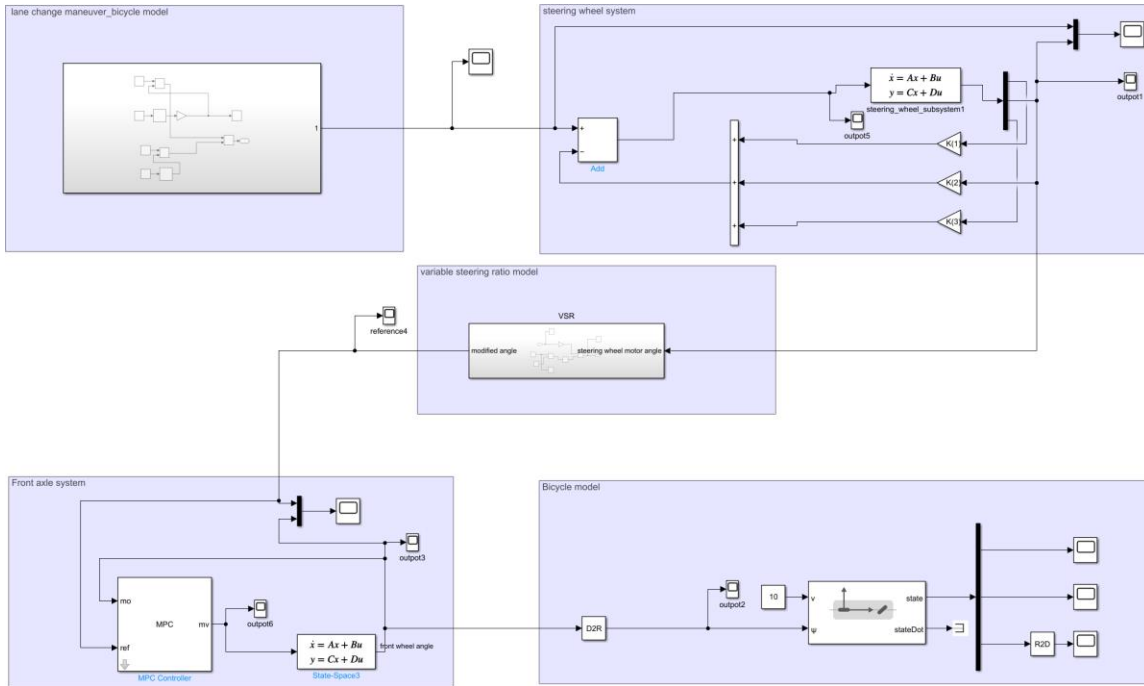
Figure 14. The connection between the SbW system and the bicycle model in Simulink.
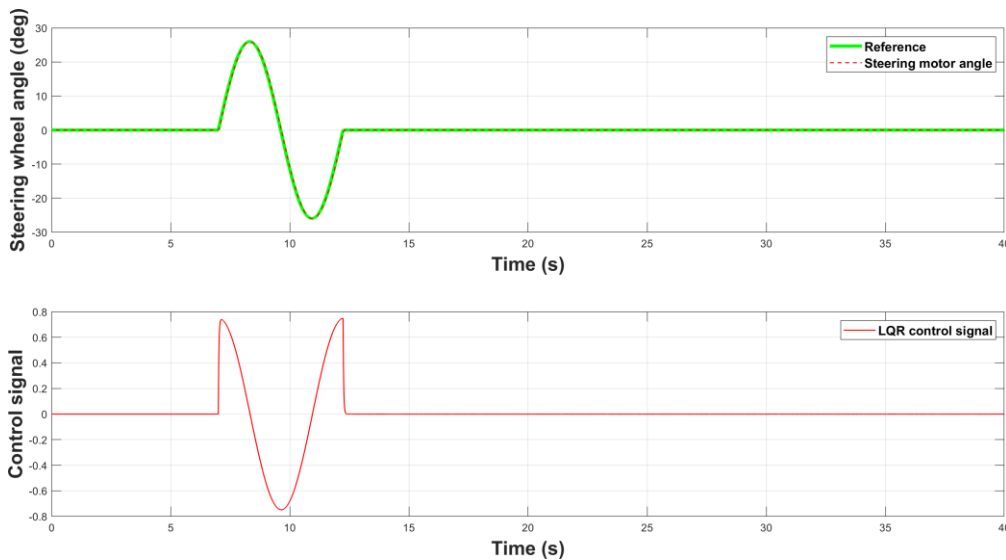
Figure 15. Steering wheel simulink response for lane change scenario.

Figure 16 illustrates the input signal for the Variable Steering Ratio and the updated steering motor angle which decreased by (14.4%) approximately depending on the applied velocity (36 km/h). The updated steering motor angle represents the input for the front axle system. While for the front axle system, Figure 17 is used to show the tracking performance for the MPC controller with the control signal. According to the results, the performance of MPC tracking can be definitely guaranteed. When the angle is positive (counter-clockwise) this means that the direction of the

wheel is going to the left, while when the angle is negative (clockwise) this means that the direction of the wheels is going to the right.
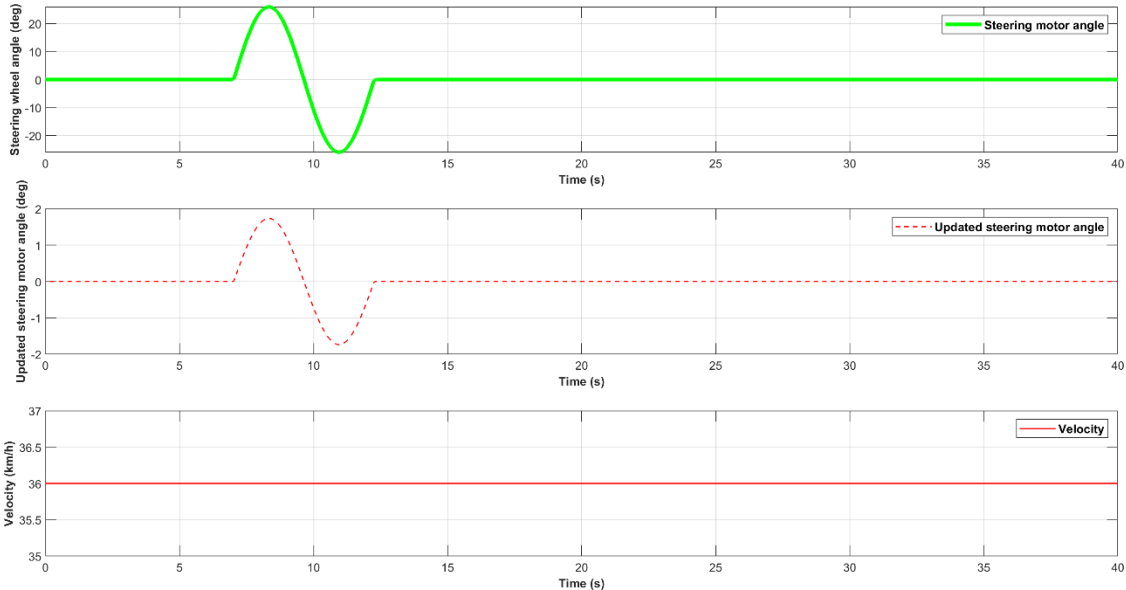
Figure 16. VSR response for lane change scenario
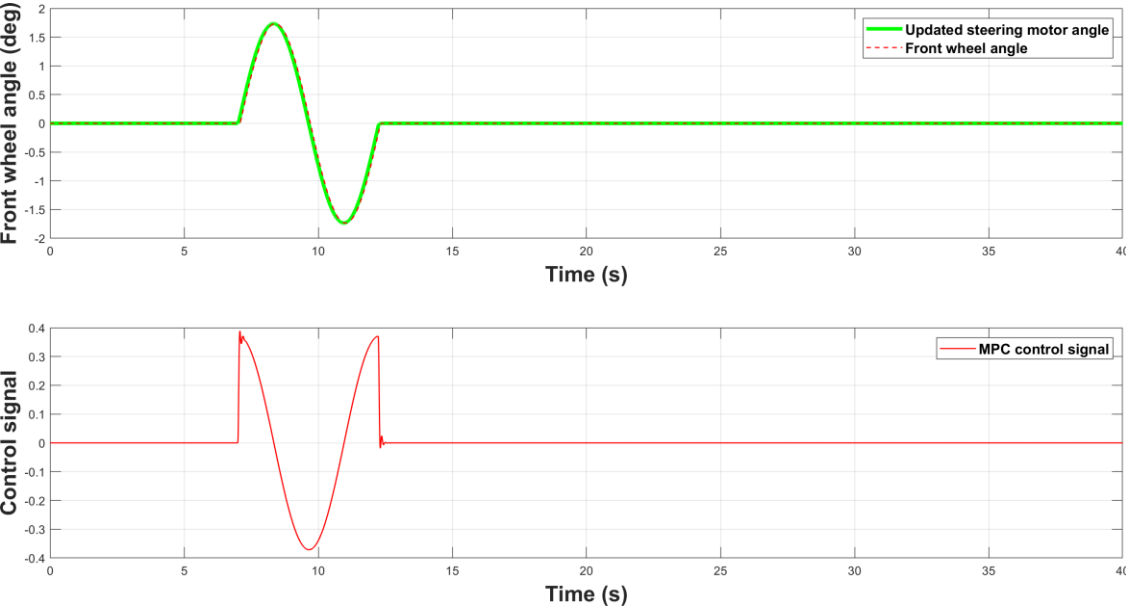
Figure 17. Front axle system response for lane change scenario.

The mathematical modeling of this system has been mentioned previously in section 2 with its parameters. Figure 18 shows X-coordinate, vehicle path, and yaw angle for the lane change scenario. The results show that the vehicle was able to implement the lane change perfectly according to the assumption that the width of the road is 5 m. The driver starts the lane change after 70 m of driving and needs 50 m to end this scenario and go straight. The longitudinal distance (X-coordinate) always increases while the lateral distance (Y-coordinate) is changing according to the implemented scenario. Finally, the yaw angle, which is the angle formed by a line traveling in the direction of travel and the x-axis of the vehicle, starts with zero and back to zero when the vehicle finishes the implementation of the scenario successfully
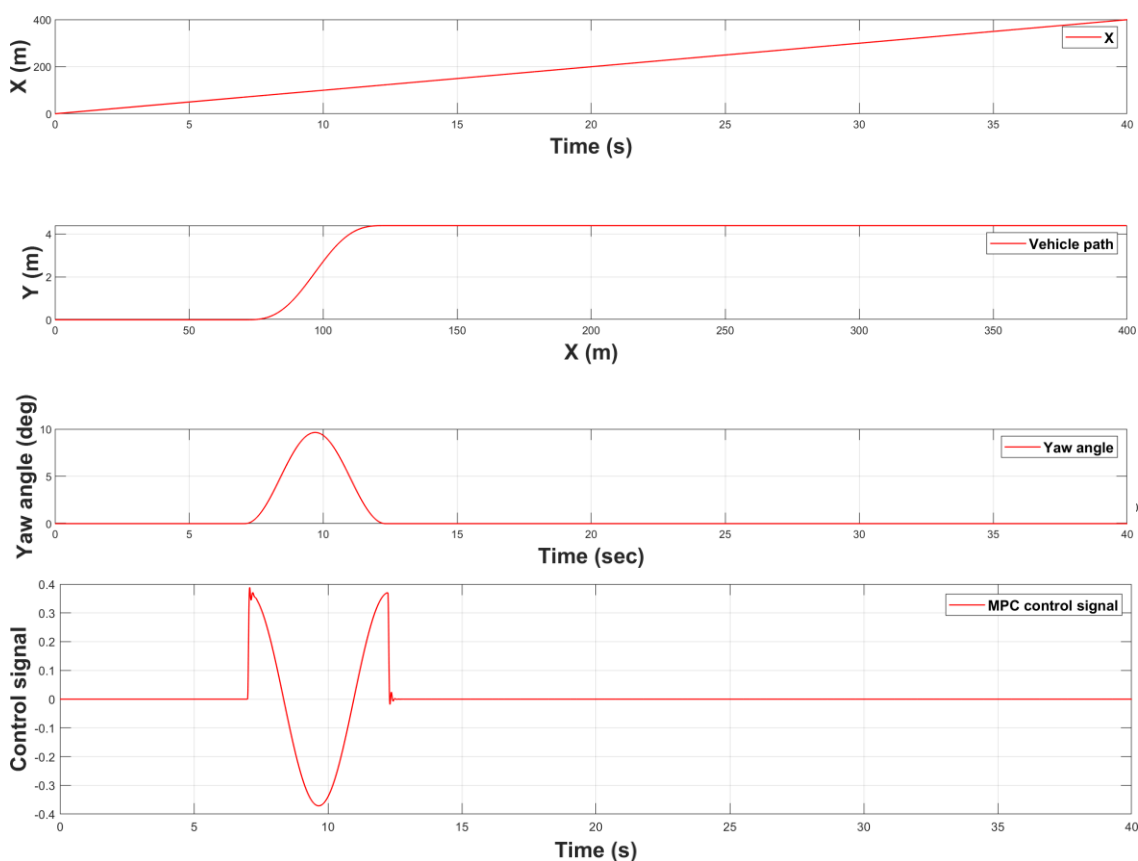
Figure 18. Bicycle model response for lane change scenario.

Next, the double lane change maneuver scenario has been simulated. The Double Lane Change (DLC) maneuver is based on a closed-loop test in which the vehicle must be maneuvered to follow a predetermined course with sufficient precision. Because there are no published assessments for autonomous vehicle driving skills, the automotive industry's tests must be implemented. The ISO 3888-1 test course standard provides a double lane change maneuver, as depicted in Figure 19, that is used to subjectively evaluate vehicle dynamics performance (ISO, 2018). Because it measures just a tiny portion of a vehicle's handling features and is primarily dependent on driver input, the test is subjective. The test's adaptability to evaluating driving competence in autonomous ground vehicles is due to its dependency on driver ability (Jamaluddin et al., 2012). The Kinematic bicycle model in Simulink has been used as well to test the performance of the steer by wire control system in the situation of a double lane change maneuver. Figure 20 shows the DLC steering wheel performance with the LQR control signal. The driver applied 26

degrees as the steering wheel angle at the seventh second to start the lane-changing process from the left lane to the right lane. The lane-changing process ends at second 12 and goes straight after that for 4 seconds. The last part of the double lane change scenario will be applied at 16 seconds to change the lane from right to left. This scenario will end at 21 seconds and complete straight in the right lane.
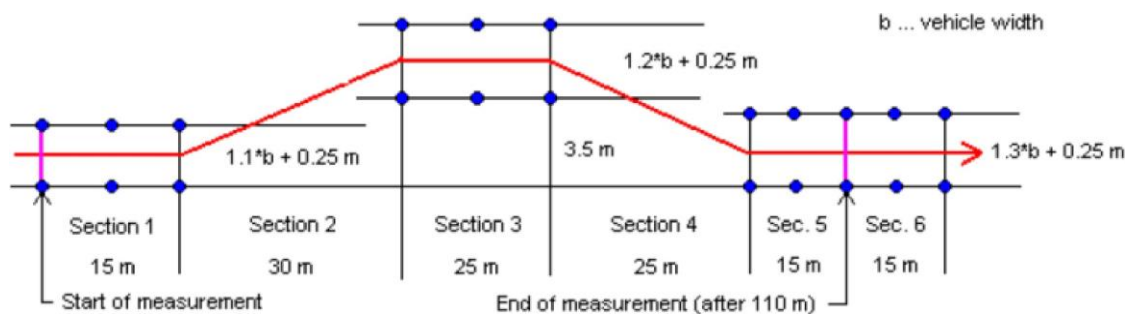
Figure 19. ISO 3888-1 DLC test scenario (Jamaluddin et al., 2012).
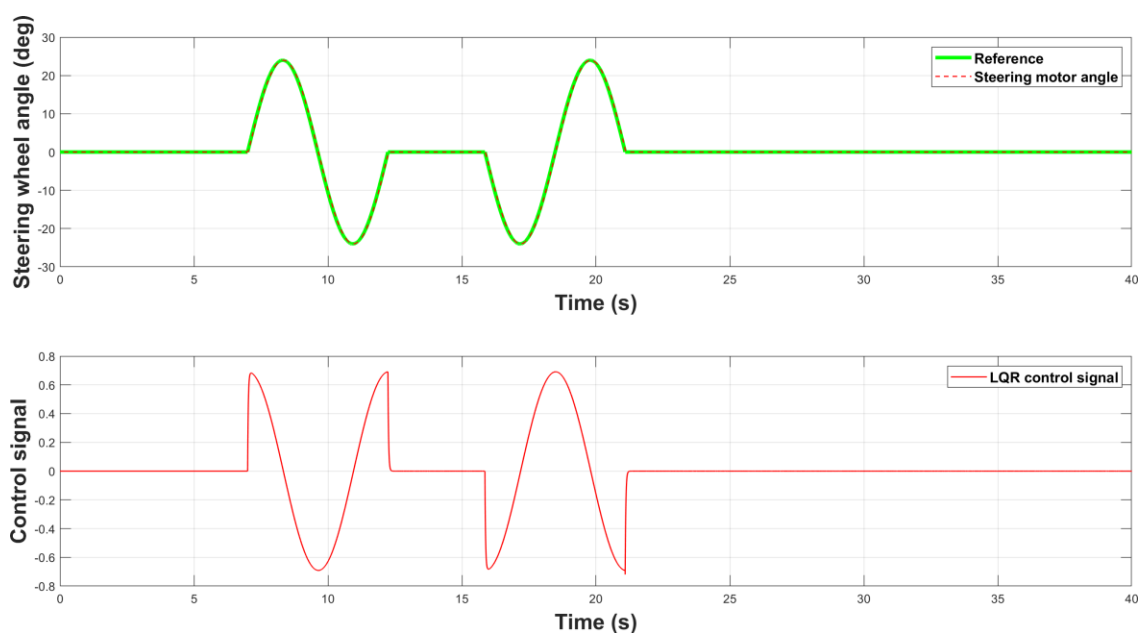
Figure 20. Steering wheel simulink response for double lane change scenario.

Figure 21 shows the VSR input signal and the modified steering motor angle, which decreased by (14.4%) approximately depending on the applied velocity (36 km/h). The modified steering motor angle represents the input for the front axle system, Figure 22 demonstrates the MPC controller's tracking performance with the front axle system's control signal. The performance of MPC tracking can be confirmed, according to the results. The control signal refers to the signal sent to the plant. It is the signal produced by the MPC controller. The plant's output is actually the response. So, The engineer can change the output by changing the plant's input and the MPC controller's parameters.
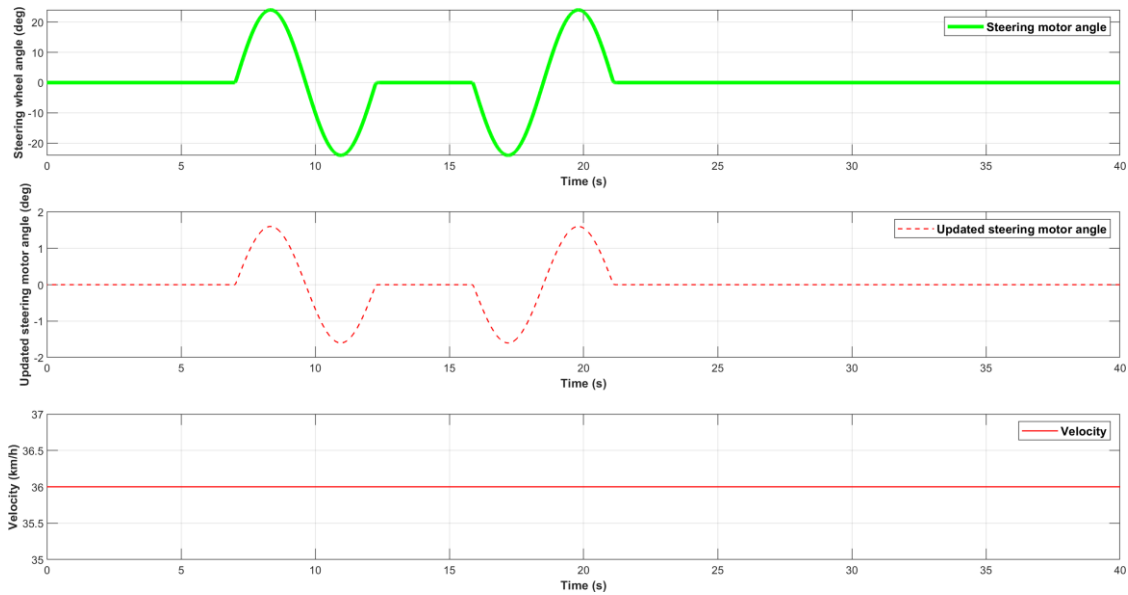
Figure 21. VSR response for double lane change scenario.
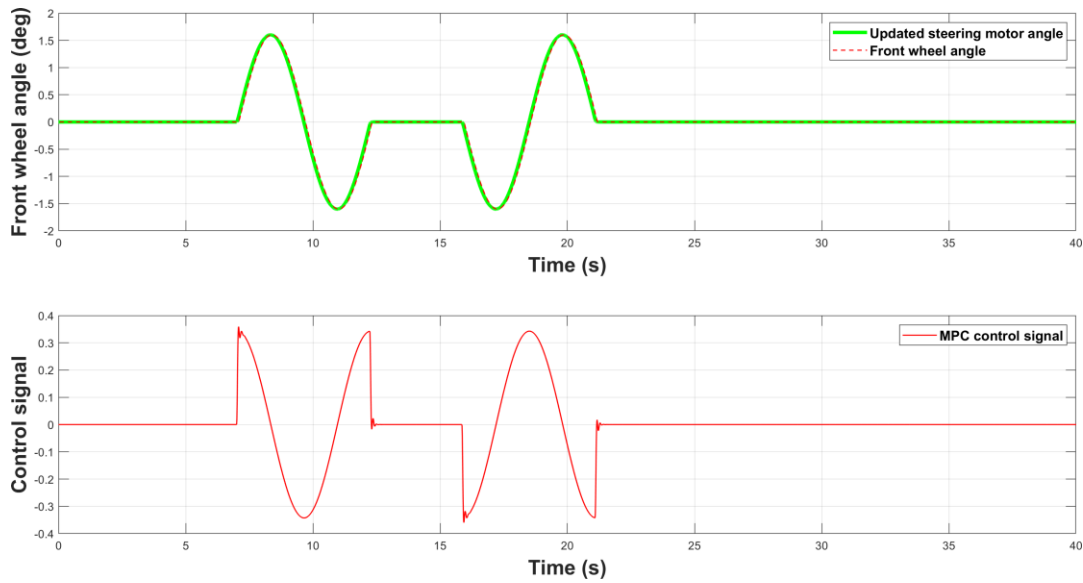
Figure 22. Front axle system response for double lane change scenario.

As mentioned before, the mathematical modeling of this system has been mentioned previously in section 2 with its parameters. Figure 23 shows X-coordinate, Y-coordinate, vehicle path, and yaw angle for the double lane change scenario.
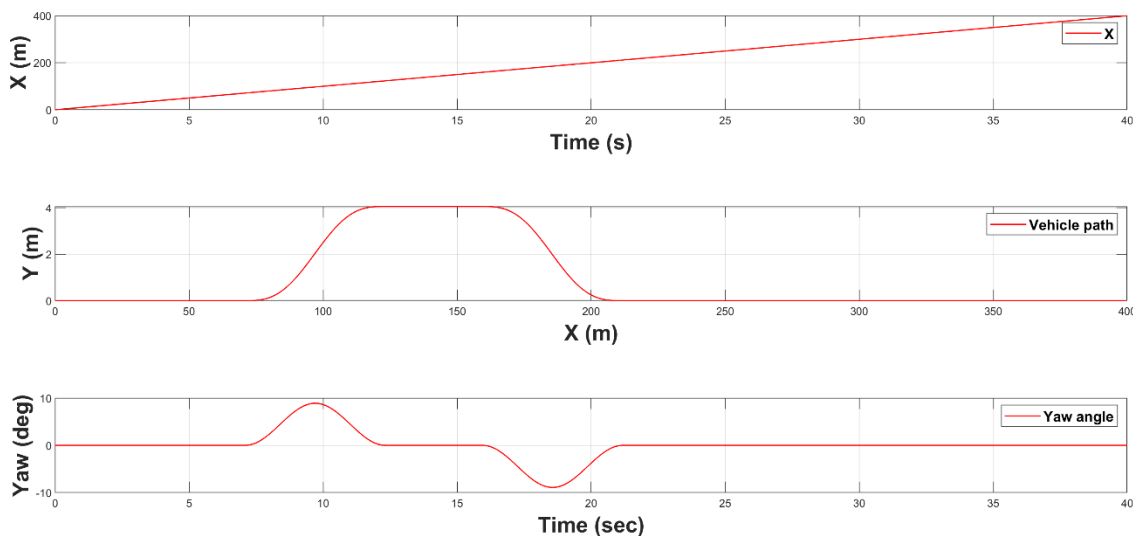
Figure 23. Bicycle model response for double lane change scenario.

The findings show that the vehicle executed the double lane change smoothly under the expectation that the road width is 5 meters. The car started to change its position from left to right lane after 75 meters then it keep going straight for 50 meters before going back to the left lane again. According to the implemented double lane change scenario, the longitudinal distance (X-coordinate) always rises, whereas the lateral distance (Y-coordinate) changes. Finally, the yaw angle, which is the angle created by a line going in the direction of motion and the vehicle's x-axis, begins at zero and returns to zero when the vehicle successfully completes the scenario execution. For that reason, it can be seen that the yaw angle is changing when the driver is activating the lane-changing scenario. If the driver is going in a straight line without steering, the yaw angle will still be zero.

5. Conclusion and future works

The primary ideas presented in this article can be summarized in different sections. The first part includes an introduction to the steer-by-wire system, as well as components, benefits, drawbacks, and The literature review of the most common controllers used to control steer-by-wire systems, such as PID, FLC, MPC, and SMC. A full explanation of the mathematical modeling of the steering wheel system, front-wheel system, and bicycle model is discussed in the second part. The LQR and MPC controller designs are addressed in part 3 along with the reasons behind this decision. Section four contains the implementation of steer-by-wire control system in Matlab/Simulink, where the model in the loop is effectively implemented. Two examples are illustrated using the MIL Matlab Simulink bicycle model: lane change and double lane-changing maneuver. The results show that the controllers were able to achieve high tracking performance for wheel synchronization and directional control.

In the future development, the described systems will employ various control algorithms to imitate the force feedback torque of a steer-by-wire system, which will provide the driver with an artificial sensation similar to that of driving a conventional car. Another controller will be designed to ensure that the steering wheel will return to the center automatically if the driver's hands are removed or released from the wheel. In addition, the suggested control algorithm will be tested on real-time Hardware in the loop HIL in order to check its efficacy. Also, different Variable steering ratio VSR algorithms will be performed and evaluated in various driving situations so that the optimum approach may be used in vehicles.

Refrences

Ahmad Reda, Ahmed Bouzid, J. V. (2020). *Model predictive controller in an autonomous vehicle*. https://doi.org/10.12700/APH.17.7.2020.7.9

Ancha, S., Baviskar, A., Wagner, J. R., & Dawson, D. M. (2007). Ground vehicle steering systems: Modelling, control, and analysis of hydraulic, electric and steer-by-wire configurations. *International Journal of Vehicle Design*, *44*(1–2), 188–208. https://doi.org/10.1504/IJVD.2007.013225

Basargan, H., Mihaly, A., & Gaspar, P. (2021). Fault-Tolerant Trajectory Tracking Control for Autonomous Vehicle Based on Camera and GPS. *2021 European Control Conference, ECC 2021*, 473–478. https://doi.org/10.23919/ECC54610.2021.9655065

Başargan, H. (2019). Driver and pedestrian trust analysis on integration of autonomous vehicles to infrastructure of turkey. Alphanumeric Journal, 7, 25-36.

Basargan, H. (2018). Trajectory Tracking Control of Independent In-Wheel Motor-Driven Autonomous Electric Vehicle with Efficient Torque Distribution [Master's Thesis, Budapest University of Technology and Economics].

D. M. Abhishek and C. Mariappan. (2021). *Model predictive controller in an autonomous vehicle*.

Do, M. T., Man, Z., Zhang, C., Wang, H., & Tay, F. S. (2014). Robust Sliding Mode-Based Learning Control for Steer-by-Wire Systems in Modern Vehicles. *IEEE Transactions on Vehicular Technology*, *63*(2), 580–590. https://doi.org/10.1109/TVT.2013.2280459

Fahami, Sheikh Muhamad Hafiz, Zamzuri, H., Mazlan, S. A., & Zakaria, M. A. (2012). Modeling and simulation of vehicle steer by wire system. *SHUSER 2012 - 2012 IEEE Symposium on Humanities, Science and Engineering Research*, 765–770. https://doi.org/10.1109/SHUSER.2012.6268992

Fahami, Sheikh Muhamad Hafiz, Zamzuri, H., Mazlan, S. A., & Zulkarnain, N. B. (2013). The design of vehicle active front steering based on steer by wire system. *Advanced Science Letters*, *19*(1), 61–65. https://doi.org/10.1166/asl.2013.4706

Fahami, Sheikh Muhammad Hafiz, Zamzuri, H., & Mazlan, S. A. (2015). Development of estimation force feedback torque control algorithm for driver steering feel in vehicle steer by wire System: Hardware in the loop. *International Journal of Vehicular Technology*, *2015*. https://doi.org/10.1155/2015/314597

Fahami, Sheikh Muhammad Hafiz, Zamzuri, H., Mazlan, S. A., & Saruchi, S. A. (2014). The variable steering ratio for vehicle steer by wire system using hyperbolic tangent method. *Applied Mechanics and Materials*, *575*(June), 781–784. https://doi.org/10.4028/www.scientific.net/AMM.575.781

Fu, X., Kong, F., & Fu, L. (2009). Research of automotive steer-by-wire control based on integral partition PID control. *3rd International Conference on Genetic and Evolutionary Computing, WGEC 2009*, 561–564. https://doi.org/10.1109/WGEC.2009.21

Gáspár, P., Mihály, A., & Basargan, H. (2020). Fault-tolerant trajectory tracking control of in-wheel motor vehicles with energy-efficient steering and torque distribution. *Fault Diagnosis and*

Fault-Tolerant Control of Robotic and Autonomous Systems, 213–234. https://doi.org/10.1049/PBCE126E_ch10

Huang, C., Naghdy, F., & Du, H. (2019). Sliding mode predictive tracking control for uncertain Steer-by-Wire system. *Control Engineering Practice*, *85*(October 2018), 194–205. https://doi.org/10.1016/j.conengprac.2018.12.010

Im, J. S., Ozaki, F., Matsunaga, N., & Kawaji, S. (2007). Control of steering-by-wire system using bilateral control scheme with passivity approach. *ICCAS 2007 - International Conference on Control, Automation and Systems*, 1488–1493. https://doi.org/10.1109/ICCAS.2007.4406574

ISO. (2018). *Passenger cars — Test track for a severe lane-change manoeuvre — Part 1: Double lane-change.* https://www.iso.org/obp/ui/#iso:std:iso:3888:-1:ed-2:v1:en

Jamaluddin, H., Ping, E. P., & Hudha, K. (2012). Hardware-in-the-loop simulation of automatic steering control for double lane change and sine steer manoeuvres. *International Journal of Vehicle Autonomous Systems*, *10*(1/2), 67. https://doi.org/10.1504/ijvas.2012.047695

Journal, O., Union, E., Application, S. D., Specifications, A., Services, T., Approval, T., & Appendix, A. (2015). *Acts Adopted By Bodies Created By. 78*, 30–59.

Jürgens, F., Ehrich, H., & Schulte, L.-E. (2021). Approval Requirements for Automated and Connected Vehicles. *ATZ Worldwide*, *123*(1), 44–49. https://doi.org/10.1007/s38311-020-0599-9

Kader, A. (2006). *Steer-by-Wire Control System. May*, 32.

Li, M., & Chang, J. (2018). *The Development of Steering Control Strategy on Engineering Vehicles Steer-by-Wire System. 164*(Icmse), 214–217. https://doi.org/10.2991/icmse-18.2018.42

Li, Y. ran, Huang, J. ming, & He, Z. ming. (2012). A nonlinear control method of steering angle following used in steer-by-wire system. *Applied Mechanics and Materials*, *190–191*, 890–893. https://doi.org/10.4028/www.scientific.net/AMM.190-191.890

mathworks. (2018). *Understanding Model Predictive Control, Part 2: What Is MPC?* https://www.mathworks.com/videos/understanding-model-predictive-control-part-2-what-is-mpc--1528106359076.html

Matute, J. A., Marcano, M., Diaz, S., & Perez, J. (2019). Experimental Validation of a Kinematic Bicycle Model Predictive Control with Lateral Acceleration Consideration. *IFAC-PapersOnLine*, *52*(8), 344–349. https://doi.org/10.1016/j.ifacol.2019.08.085

Mohamed, E. S., & Albatlan, S. A. (2014). Modeling and Experimental Design Approach for Integration of Conventional Power Steering and a Steer-By-Wire System Based on Active Steering Angle Control. *American Journal of Vehicle Design*, *2*(1), 32–42. https://doi.org/10.12691/ajvd-2-1-5

Mohd Tumari, M. Z., Saealal, M. S., Abd Rashid, W. N., Saat, S., & Mohd Nasir, M. A. (2017). The vehicle steer by wire control system by implementing PID controller. *Journal of Telecommunication, Electronic and Computer Engineering*, *9*(3–2), 43–47.

Paolo Falcone, F. B. (2007). Predictive Active Steering Control for Autonomous Vehicle Systems. *IEEE TRANSACTIONS ON CONTROL SYSTEMS TECHNOLOGY*, *15*(3), 37–126. https://doi.org/10.1002/9781119771876.ch3

Saruchi, S. A., Zamzuri, H., Mazlan, S. A., Ariff, M. H. M., & Nordin, M. A. M. (2015). Active front steering for steer-by-wire vehicle via composite nonlinear feedback control. *2015 10th Asian Control Conference: Emerging Control Techniques for a Sustainable World, ASCC 2015*. https://doi.org/10.1109/ASCC.2015.7244432

Saruchi, S. A., Zamzuri, H., Mazlan, S. A., Fahami, S. M. H., & Zulkarnain, N. (2014). Wheel synchronization control in steer-by -wire using composite nonlinear feedback. *Applied Mechanics and Materials*, *575*, 762–765. https://doi.org/10.4028/www.scientific.net/AMM.575.762

Wang, H., Kong, H., Man, Z., Tuan, D. M., Cao, Z., & Shen, W. (2014). Sliding mode control for steer-by-wire systems with AC motors in road vehicles. *IEEE Transactions on Industrial Electronics*, *61*(3), 1596–1611. https://doi.org/10.1109/TIE.2013.2258296

Wikiwand. (2020). *Model predictive control*. https://www.wikiwand.com/en/Model_predictive_control

Zaidi Mohd Tumari, M., Azidi Mohd Nasir, M., Saat, S., Shamsul Rahimi A. Subki, A., Norhisyam Abd Rashid, W., Helmi Suid, M., & Riduwan Ghazali, M. (2019). The Control Schemes of Vehicle Steer by Wire System by using Fuzzy Logic and PID Controller. *Research Journal of Applied Sciences*, *13*(2), 137–145. https://doi.org/10.36478/rjasci.2018.137.145

Zhe Sun. (2017). *Robust Control Design for Vehicle Steer-by-Wire Systems*. https://www.nhtsa.gov/sites/nhtsa.dot.gov/files/811998-targcrashsafbenestmethpedcrashavmitsys.pdf

Feature Extraction Methods in Electroencephalography (EEG) Based Brain-Computer Interface Systems

Hanife GÖKER[1]

Introduction

The brain-computer interface (BCI) systems permit the communication between the user and the computer/machine via an interface, by analyzing the changes in brain activity and turning it into a command that the computer can understand. BCI systems record brain signals and send these signals to the computer system (Khalid et al., 2009). The signals are used to control a device or to express an idea or a thought. BCI systems establishes a channel of communication between the outside world and the human brain. These systems are able to transmit information from human brains and translate their inaudible thoughts. So, they can assist those who have disabilities in communicating their ideas and opinions in a number of ways, such as semantic categorization, spelling applications, or silent speech. Robots with BCI systems can assist people with disabilities in their daily lives and careers and encourage cooperation in building their communities. BCI systems also contribute to the detection of diseases such as neurodegenerative diseases, abnormal brain structure, seizures, and sleep disorders.

Human brain activity is measured by invasive, partial invasive, or non-invasive approaches. Invasive techniques implant electrodes beneath the scalp. These techniques measure brain activity either using electrocorticography (ECoG) on the cortical surface or intracortically through the motor cortex. ECoG improves the quality of the obtained signal, it is best at providing high temporal and spatial resolution. However, this technique has many disadvantages. In addition to the usability problems arising from the introduction of the surgical procedure, problems with the output of the system have emerged. Once implanted, the electrodes cannot be slid to detect brain activity in another part of the brain. Medical complications can also result from the body's unsuccessful adaptation to the new object. Moreover, there may also be problems with the implants' stability and infection. Therefore, the use of invasive techniques in the real world is often limited to very few BCI-based medical applications.

In general, non-invasive devices are considered the safest and least costly device type. These devices can only capture weak human brain signals due to skull occlusion (Fred et al., 2022). Most BCI systems obtain relevant information on brain activity using the EEG device. EEG signals are low-amplitude electrical signals that measure the electrical activity between scalp electrodes and neurons in the brain. Electrodes positioned on the scalp enable the detection of brain activity. In clinical practice, EEG is the most often employed method due to simplicity, portability, low cost, convenience, low risk to users, and high temporal resolution. EEG signals are used to provide detailed information about brain function and structure, and to better understand its neural correlates.

[1] Assistant Professor, Department of Electrical Electronics Engineering, Faculty of Simav Technology, Kutahya Dumlupinar University

The EEG signal has a wide frequency band between 0-100 Hz, this frequency range is divided into five frequency bands: delta (δ) waves, theta (θ) waves, alpha (α) waves, beta (β) waves, and gamma (γ) waves (Aydemir & Kayıkçıoğlu, 2009; Kalin et al., 2020):

Delta (δ) waves have amplitudes of 20 - 400 µV and frequencies of 0 - 4 Hz. It occurs under general anesthesia or deep sleep, that is, when the brain is at very low activity.

Theta (θ) waves have amplitudes of 5 - 100 µV and frequencies of 4 - 7 Hz. It occurs in healthy people when their brain activity is low, such as during restless sleep, stressful conditions, or medium-level anesthesia.

Alpha(α) waves have amplitudes of 2 - 10 µV and frequencies of 8-12 Hz. Individuals who are awake; They are seen when they are physically and mentally at full rest, without external stimuli, and when the eyes are closed.

Beta (β) waves have frequencies of 12 - 30 Hz. Their amplitudes range from 1-5 µV. Mental workload, rapid eye movements encountered during sleep, focused attention and sensory information processing are encountered in the Beta phases. Beta waves correspond to the highest level of activity.

Gamma (γ) waves have frequencies of 30 Hz and above and amplitudes less than 1 mV. This rhythm is typically associated with perception and consciousness. Gamma waves correspond to the highest operating state (high brain activity).

Frequency is the most commonly used method to classify EEG waveforms. The four frequency waves are given in Figure 1.
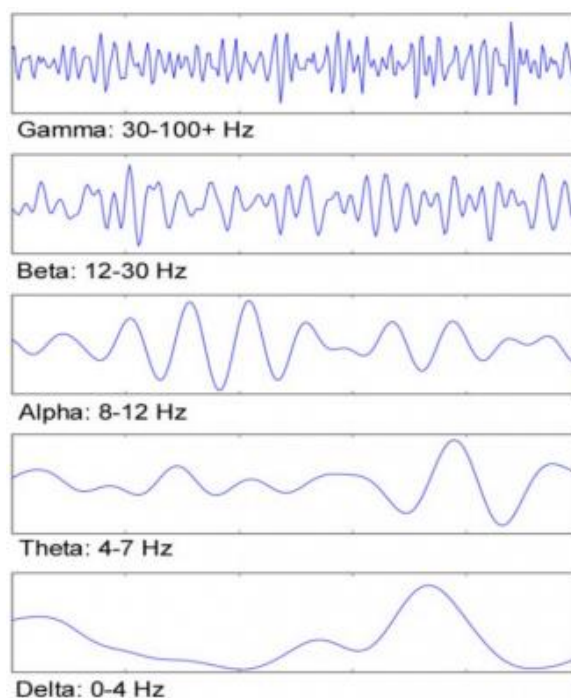
Figure 1. Frequency waves

Clinical and physiological interest is concentrated between 0.1 and 30 Hz.

EEG-Based BCI Systems

EEG-based BCI systems consist of five main stages: signal acquisition, signal preprocessing, feature engineering (feature selection and feature extraction), classification, and application interface. The block diagram of the EEG-based BCI system is given in Figure 2:
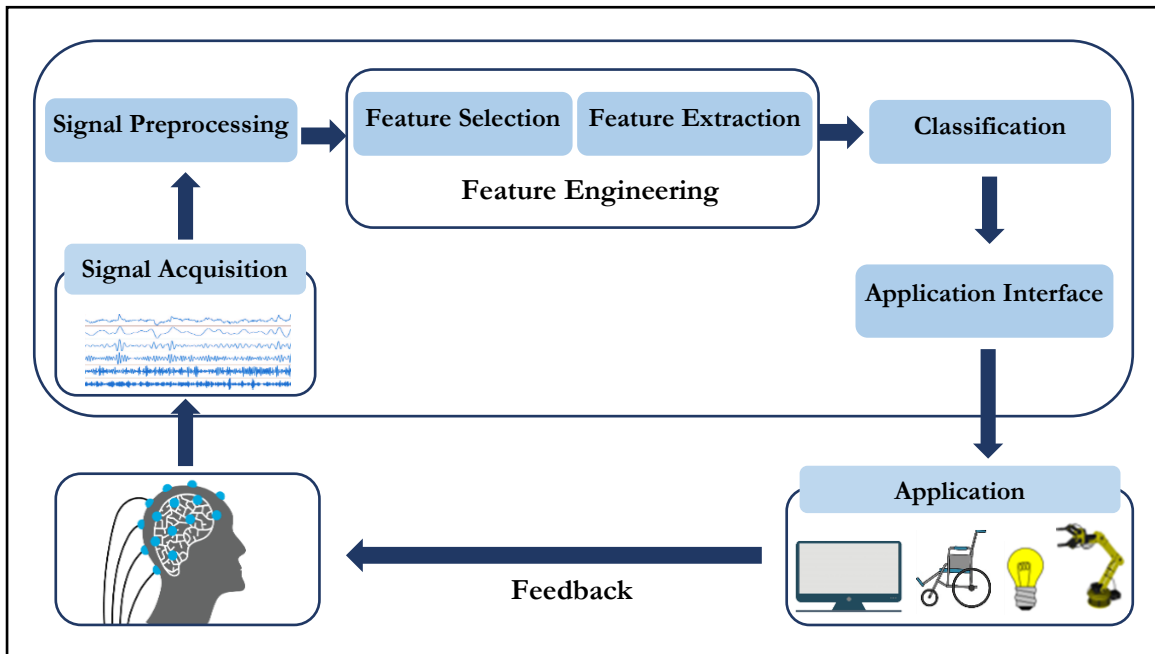
Figure 2. The Block Diagram of the EEG-Based BCI Systems

a) Signal Acquisition

EEG signals from the brain are captured directly, in the signal acquisition stage. Due to its safety, high temporal resolution, and simplicity of use, EEG is the most popular signal acquisition technique. By using the EEG device, the electrical activities of the brain can be recorded, in accordance with the internationally accepted mapping process, in certain standards, in digital media or by printing on paper. The 10-20 international standard electrode placement is used in EEG signal acquisition (Lakshmi, Prasad & Prakash, 2014). The electrode layout of the 19-channel EEG device is given in Figure 3:
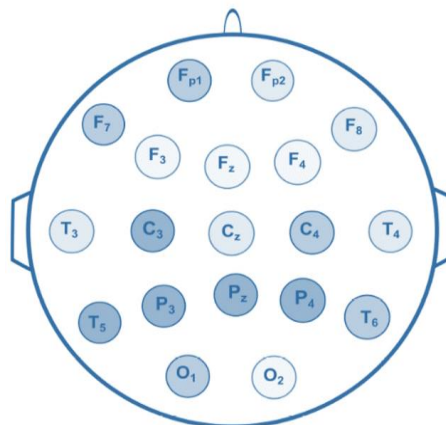
Figure 3. Electrodes positioning for the international 10-20 system

Electrodes placed near the regions of the brain, which perform different operations, allow us to obtain information about that region. EEG signals are non-stationary in nature and they are sensitive to artifacts from eye movements, muscle activities, heartbeat, and power line interference (Hochberg & Donoghue, 2006).

b) Signal Preprocessing

Signal preprocessing includes digitizing signals for analysis of signals, filtering to remove artifact or noise from raw EEG signals, segmenting, or amplifying signals. EEG signals can be analyzed by digitizing. Artifacts originating from various environments outside the brain during EEG recordings prevent accurate measurements. Artifacts can occur for a variety of reasons. These artifacts are biological artifacts (such as eye movements, ECG and pulsation, sweating, and muscle contraction), motion artifacts, electrode-related artifacts, network-related artifacts (such as radio waves, electrostatic artifact, city current noise), and artifacts originating from the EEG device. For more efficient analysis of EEG signals, these artifacts must be removed from the signal before analysis of the signals. Various filter structures such as high-pass filter or low-pass filter are used in order to remove the interference factors such as artifacts and network noises that directly affect the signals from the signals. The amplitudes of the EEG signals are very low. EEG signals at the microvolt (µV) level can be amplified by amplifying them to millivolts (mV) or volts (V) in order to make them suitable for signal processing systems and to be analyzed in more detail. The purpose of the signal preprocessing is to prepare the signals for feature extraction stage. It can also be used for noise removal, artifact processing, etc. operations are performed.

c) Feature Engineering

Feature engineering is a collection of methods that includes main topics such as feature extraction, or feature selection to improve predictive learning performance (Dong and Liu, 2018). Feature selection is the process of selecting the most useful features from the dataset or eliminating the unimportant features. It selects a subset of predictive variables to construct a model and reduces the dimensionality of the data. The advantages of feature selection are that it reduces the size of the feature set and the amount of memory, increases the speed of the algorithm, eliminates irrelevant data and noisy data, improves data quality, makes the dataset simpler to describe, visualize and understand, and improves the success of the model (Ladha and Deepa, 2011).

Feature selection methods are categorized into three types: filter-type feature selection, wrapper-type feature selection, and embedded-type feature selection:

- The filter-type feature selection method takes into account the feature relevance to the response and feature variance and determines the importance of the feature accordingly.
- The wrapper-type feature selection method considers a subset of the features and begins training. After, a feature is then either added or removed using a selection criterion. The addition or removal of a feature changes the success of the model, and this is directly measured by the selection criterion. The method iteratively trains and improves a model until the halting criteria are met.
- The embedded-type feature selection method gains the significance of the feature as part of the model learning process. When the model is trained, the significance of the features in the model is get.

Feature extraction transforms raw EEG data into digital features that can be processed, provided the information in the original dataset is preserved. It produces better results than giving

EEG raw data as direct input to machine learning or deep learning algorithms, which causes information redundancy, computational complexity, and high data rate. Features are extracted from the signals in the feature extraction stage, and feature vectors that can be classified are created. Feature extraction techniques are categorized: time domain, frequency domain, time-frequency domain, and complexity measures & non-linear parameters (Aboalayon et al., 2016). Feature extraction techniques are given in Figure 4.

Time Domain	Frequency Domain	Time – Frequency Domain	Complexity Measures- Non-linear

– Statistical parameters
– Hjorth parameters
– Average power
– Root mean squared
– Energy
– Curve length
– Zero crossing
– Local extremum
– Detrended fluctuation analysis
– Shannon entropy
	– Power spectral density
	  • Non-parametric analysis
	  • Parametric analysis
	– Mean frequency
	– Median frequency
	– Spectral edge frequency
	– Higher-order spectrum
	– Higher-order crossover
	– Spectral entropy
	– etc.
		– Short-time Fourier transform
		– Wavelet transform
		– Empirical mode decomposition
		– Hilbert-Huang transform
		– Time-frequency ridges
		– etc.
			– Hurst exponent
			– Lyapunov exponent
			– Approximate Entropy
			– Sample Entropy
			– Permutation entropy
			– Multiscale Entropy
			– etc.

Figure 4. Feature extraction methods

Time-domain features are extracted from raw EEG signals or decomposed signals performed on a time domain (Boonyakitanont et al., 2020).

- *Statistical parameters* are mean, median, minimum and maximum values, standard deviation, variance, kurtosis, skewness, mode, trimmed mean, coefficient variation, and quartile (Q1, Q2, Q3) on a time domain. They are explained with mathematical expressions in the following equations:

Mean
$$= \frac{1}{N} \sum_{n=1}^{N} X(n) \tag{1}$$

Median
$$= \frac{(\frac{N}{2})^{th}\ value + (\frac{N}{2}+1)^{th}\ value}{2} \tag{2}$$

Min
$$= min[x_n] \tag{3}$$

Max
$$= max[x_n] \tag{4}$$

Standard deviation
$$= \sqrt{\frac{1}{N} \sum_{N}^{n=1} (X(n) - mean)^2} \tag{5}$$

Variance
$$= \frac{\sum_{n=1}^{N} (x_n - mean)^2}{N} \tag{6}$$

Kurtosis
$$= \frac{\sum_{n=1}^{N} (x_n - mean)^4}{(N-1)\ standard\ deviation^4} \tag{7}$$

Skewness	$=\dfrac{\sum_{n=1}^{N}(x_n - mean)^3}{(N-1)\,standard\ deviation^3}$	(8)
Mode	= The value in the dataset that occurs most frequently	(9)
Trimmed mean	$=\dfrac{\sum_{i=p+1}^{n-p} X_{(i)}}{n-2p}$	(10)
Coefficient variation	$=\dfrac{Standard\ deviation}{Mean}$	(11)
Quartile 1 (Q1)	$=\frac{1}{4}(n+1)^{th}\ term$	(12)
Quartile 2 (Q2)	$=\frac{2}{4}(n+1)^{th}\ term$	(13)
Quartile 3 (Q3)	$=\frac{3}{4}(n+1)^{th}\ term$	(14)

- The three *Hjorth parameters* are activity, mobility, and complexity. Hjorth parameters is frequently performed for feature extraction in biological signals and computes signal complexity in the time domain (Safi and Safi, 2021). They are explained with mathematical expressions in equation 15, equation 16, and equation17.

Activity	$= var\ (y(t))$	(15)
Mobility	$=\sqrt{\dfrac{var\ (y'(t))}{var\ (y(t))}}$	(16)
Complexity	$=\dfrac{mobility\ (y'(t))}{mobility\ (y(t))}$	(17)

- The *average power, energy, root mean square (RMS)* are mutually pertinent with the amplitude measurements defined as the maximum level of the signal wave in a periodic motion. The RMS, also known as quadratic mean, is the average power's square root, and the average power is the signal mean square, the energy is a summation of a squared signal (Boonyakitanont et al., 2020).

- *Curve length*, also known as line length, is useful for estimating the stability of a signal's values. If the value of this feature is low in a certain range, it is an indication that the signal is stable, otherwise the signal is unstable. It is calculated as in equation 18.

L(X)	$=\sum_{i=1}^{N-1}|X_{i+1} - X_i|$	(18)

- *The zero crossing number* is a measure of the morphological features of a signal and reflects significant changes throughout the signal. This feature refers to occur when there is a sign change between samples. If the zero crossing number is large, EEG signals contain uncertainty and have high-frequency components (Boonyakitanont et al., 2020).

- *The local extremum number* is the total number of local maximums and minimums in a signal. It resembles the zero crossing number, which denotes the frequency measurement of the signal inferentially (Boonyakitanont et al., 2020).

- *Detrended fluctuation analysis (DFA)* is an effective mathematical technique for examining the power law of long-term correlations of non-stationary time series. DFA is used to determine the features of the local fluctuations at various time scales (Márton et al., 2014). It is calculated as in equation 19 (Goshvarpour, Abbasi & Goshvarpour, 2013).

$$\text{DFA} = \sqrt{\frac{1}{N}\sum_{k=1}^{N}[y(k) - y_n(k)]^2} \tag{19}$$

In the time series with N samples, the y coordinate of the straight line segments is represented by $y_n(k)$. The integrated time series y(k) is subtracted from the trend by subtracting the local trend $y_n(k)$ from each box.

- Entropy is a measure of uncertainty and complexity and is used to reveal the complexity of a dynamic system. *Shannon entropy* (ShEn) is the most basic measure used to analyze system complexity. ShEn measures the predictability of future amplitude values of the EEG based on the currently observed probability distribution of the amplitude values in the signal. It is calculated as in equation 20 (Yol et al., 2018)

$$\text{ShEn} = \sum_{i=1}^{n} p(x_i) \log_a \frac{1}{p(x_i)} \; a > 1 \tag{20}$$

using random variable x that has the values x1, x2, …, xn, and p(xi) is the probability of random variable x values x_i.

- *Tsallis entropy* (TsEn) uses the non-exhaustive parameter q to measure information of certain events. TsEn and Renyi entropy are considered generalized and more advantageous concepts of entropy compared to ShEn (Liang et al., 2015). TsEn(q) entropy is the degree of uncertainty around the i event. It is calculated as in equation 21 (Yol et al., 2018):

$$\text{TsEn (q)} = 1 - \frac{\sum_{i=1}^{n}(p_i)^q}{q-1} \tag{21}$$

- Renyi entropy (RenEn) is utilized to calculate the spectral complexity of the time series. It is calculated as in equation 22 (Kar, Bhagat & Routray, 2010):

$$\text{RenEn} = \frac{1}{q-1} \log\left[\sum_j p_j^q\right] \tag{22}$$

where p_j is the relative energy and q is known as the entropic index. The parameter q gives generality to this measure of information.

Frequency-domain features are extracted by transforming the signals in the time domain to the frequency domain (Wang and Wang, 2021).

- *Power spectral density,* defines the power distribution of a signal over the frequency range. It is applied to determine the distribution of the power of signals in frequency space and to interpret their characteristics. It is expressed in watts per hertz (W/Hz). Power spectral density methods can be categorized as non-parametric and parametric analysis:

- *Non-parametric analysis* adopts the assumption that there is no knowledge of the structure of the signals. Spectrum estimation is applied directly to signals. Periodogram, Barlett, Welch, and Blackman-Tukey are the most well-known non-parametric spectrum estimation methods. Periodogram method is the most basic form of non-parametric methods. Actually, periodogram method is equal to the smoothed sample power spectral density. Bartlett method is the average of the periodograms. Bartlett method divides the signal into equal parts, and these separated parts do not overlap each other. After the signal is divided into equal parts, spectrum estimation is found with the periodogram method. Welch method divides the signal into multiple segments, instead of analyzing the signal as a whole and calculates the power spectral density of the signal by overlapping these segments a certain number of times. Welch method is an average of periodograms across time. The Blackman-Tukey method is an average of modified periodograms across time. Blackman-Tukey provides the smoothing of periodograms.
- *Parametric analysis* adopts the assumption that the signal has a certain pattern. Parametric methods provide higher performance than non-parametric methods, when the signal length is short. Yule-Walker, Burg, and modified covariance methods are the most well-known parametric spectrum estimation methods. Yule-Walker power spectrum estimation solves the signal using the least squares method. Yule-Walker method applies the window to the data. It performs well for large datasets as well as other parametric methods, and produces a stable model. The Burg method is based on minimizing forward and backward prediction errors. Unlike other parametric methods, the Burg method directly estimates the reflection coefficients and avoids calculating the autocorrelation function. The modified covariance method aims to minimize forward and backward prediction errors in terms of least squares. The modified covariance method provides high resolution for short data records, but can produce unstable models.

- *Mean frequency (MF)* or *intensity-weighted mean frequency,* provides the mean of the frequency distribution using normalized power spectral density. It is calculated as in equation 23.

$$MF(X) = \sum_k x[k] \, f[k] \tag{23}$$

where x[k] is an EEG epoch's normalized power spectral density at frequency f[k].

- *Median frequency* can be expressed as the frequency of a power spectrum where half the power is at lower frequencies and half at higher frequencies. So, the median frequency gives a simple way to analyze the power spectrum and can be easily computed.

- *Spectral edge frequency* indicates the frequency at which the total power of the normalized power spectral density. It is computed from the power in the frequency ranges, similar to the median frequency. Firstly, the AUC of the power spectrum is computed. The frequency that separates 90% of the area from 10% of the area is then determined (Tonner and Bein, 2006).

- *Higher-order spectrum (HOS)* represents to the moments and the cumulants of a signal. HOS can be used to identify higher-order moments or complaints that provide more details about the phase characteristics and accurate information about the EEG signal (Wang & Wang, 2021).

- *Higher-order crossover (HOC)* is the associated sequence of zero crossing numbers when a certain filter sequence is applied to a time series. Various types of HOC sequences can be computed with the right filter design according to the desired spectral and discrimination analysis (Petrantonakis & Hadjileontiadis, 2009).

- *Spectral entropy (SE)* is based on information entropy and is a measure of its spectral power distribution. It treats the normalized power distribution of the signal in the frequency domain as a probability distribution. Spectral entropy is used to determine the degree of regularity in complex signals. If the signal has uniform probabilities, it has high entropy, but if it has irregular probabilities, it has low entropy. Spectral entropy, unlike entropy, calculates the probability values of the power spectral density. It is calculated as follows (Schmierer, Li & Li, 2022):

$$SE_n(t) = \sum_{n=1}^{N} P(t,n) \log_2 P(t,n) \tag{24}$$

Time-frequency domain features simultaneously have localized analysis capabilities in the time-frequency domain due to integrating time-domain and frequency-domain information. Time domain information of the original signal will not be lost during frequency domain analyses of EEG signals, and this analysis process can guarantee a higher-resolution (Wang and Wang, 2021).

- *Short-time Fourier transform* (STFT) adds a time-fixed window function and is frequently used. The non-stationary process is considered to be the overlap of a series of short-term stationary signals. It is calculated as follows (Wang & Wang, 2021):

$$X(t,f) = \int_{-\infty}^{+\infty} x(u)\, w(u-t) e^{-j2\pi fu} du \tag{25}$$

$w(u-t)$ represents the short-term window function. The shape and fixed size of the window function cannot meet the low-frequency subdivision requirements and high-frequency time subdivision.

- *Wavelet transform (WT)* is widely used to reduce size and extract distinctive features from signals or images for training machine and deep learning models. WT shows which frequency component the signal contains at which time. It converts signals into sub-signals by gradually breaking them into high and low frequency components. The main purpose of the conversion process is to obtain the signal coefficients and recombine the obtained coefficients to obtain the linear combination of the signal. By means of these wavelet coefficients, the signal can be analyzed at different resolutions and frequency ranges.

The main advantages of WT are that it has a varying window size that is wide at low frequencies and narrow at high frequencies, it is suitable for analysis of sudden and transient signal changes, and for analyzing irregular data patterns, i.e. impulses that exist in different time samples (Behbahani, Ahmadieh, Rajan, 2021).

- *Empirical mode decomposition (EMD)* can decompose the signal into different the intrinsic mode functions (IMFs). IMFs must meet two conditions: Firstly, in this method, the minimum and maximum values of the x(t) signal are determined. The maximum value of the signal amplitude is equal to how many zero crossings there are over the whole signal time domain, or the maximum difference is 1. The average value of the envelope formed by the minimum and maximum amplitudes of the signal is zero. Secondly, when the value is at its maximum, the cubic spline interpolation function uses it to fit the upper envelope $e_{max}(t)$; when it is at its minimum, it uses it to fit the lower envelope $e_{min}(t)$. Then the mean m(t) between the two envelopes is then calculated as follows (Ji et al., 2019):

$$m(t) = \frac{e_{max}(t) + e_{min}(t)}{2} \tag{26}$$

Then the mean (m(t)) is subtracted from the signal (x(t)) to produce the modal function c(t):

$$c(t) = x(t) - m(t) \tag{27}$$

It is verified whether $c(t)$ satisfies the condition of the IMF. If $c(t)$ satisfies, it is an IMF component and the original signal is $x_{n+1}(t)$:

$$xn+1(t) \quad = x_n(t) - c(t) \tag{28}$$

Finally, when the resulting signal is less than the two extremes, the residual component $r(t)$ is reserved and parsing ends. The original signal is parsed into n IMFs and the residual component is $r(t)$:

$$x(t) \quad = \sum_{i=1}^{n} c_i(t) + r(t) \tag{29}$$

- *Hilbert-Huang transform (HHT)* used to analyze non-stationary and non-linear data such as EEG signals. EMD is an adaptive time-frequency analysis method pioneered by Huang. This method will increase the multicomponent signal to several IMFs using the elimination process. The elimination process indicates the process that removes the low frequency and in the end it remains only the high frequency. The first step of HHT is applying EMD to the signals. In this step, any complex dataset is decomposed into a finite and usually small number of sub-signals (IMFs). Then, the instantaneous frequency defined using the Hilbert transform shows the physical meaning of the local phase change better than any other non-IMF time series for the obtained IMFs (Zhang et al., 2015).

- *Time-frequency ridges* are curves in the time-frequency plane that represent the instantaneous frequency of the signal component. These curves are found by maximizing the absolute value of the time-frequency matrix at each time point. Time-frequency ridges contain important information as they detect areas of the time-frequency plane where most of the energy of the EEG signal is concentrated (Bahador et al., 2021).

Complexity Measures- Non-linear Parameters

- *Hurst exponent (HE)* measures the correlation of sequences in a time series. It is used to evaluate the absence or presence of long-range correlations and their extent in a time series. Long-range correlation sequences are denoted by $HE > 0.5$, while long-range anti-correlation and anti-persistent sequences are denoted by $HE < 0.5$. It is estimated using rescaled interval analysis (R/S) and calculated as in equation 30 (Madan et al., 2018).

$$HE \quad = \frac{\log(R/S)}{\log T} \tag{30}$$

where S denotes the standard deviation of the time series, R is the difference between the minimum and maximum of deviation, and T denotes the duration of the sample data.

- *Lyapunov exponent* can be expressed as the average exponential rate of divergence or convergence. It used for diagnostic measurement of any chaotic system (Saikia et al., 2019). Lyapunov exponents provide an opportunity to qualitatively evaluate their local stability attractant properties. Let's consider the phase trajectory $x(t)$ of the dynamic system originating from the point x (0) and the orbit close to it (Yakovleva et al., 2020):

$$x_1(t) \quad = x(t + \vec{\varepsilon}(t)) \tag{31}$$

Consider the function;

$$\lambda[\vec{\varepsilon}(0)] = \lim_{t \to \infty} \frac{\ln[|\vec{\varepsilon}(t)| / |\vec{\varepsilon}(0)|]}{t} \tag{32}$$

For all possible rotations of the first displacement vector in N-dimensional phase space in n directions, function (equation 32) will change in hops and take a finite set of values $\lambda_1, \lambda_2, \lambda_3, \ldots, \lambda_n,$. These function values are referred to as Lyapunov exponents. Positive Lyapunov exponents serve as a measure of the mean exponential deviations of neighboring orbits, and negative ones serve as a measure of the mean exponential convergence of the orbits to the attractor.

- *Approximate entropy* (ApEn) estimates the approximate entropy of a uniformly sampled time domain signal by reconstructing the phase space. It is used to measure correlation and persistent patterns. Also evaluates the degree of disorder or randomness in a time series of length N. A large ApEn value indicates disorder and unpredictability, while a low ApEn value indicates greater predictability. With r representing the tolerance factor, d representing the maximum difference between the distance x(i) and x(j), the correlation sum of the vector x(i) is calculated as follows (Assaf, Charif, & Demir, 2022):

$$C_i^m = \frac{number\ of\ j\ such\ that\ d\ [x^m\ (i),\ x^m\ (j)] \le r}{N-m+1} \tag{33}$$

Given r, the $C_i^m(r)$ measures the regularity of patterns similar to a given one of window length m. $C_i^m(r)$ measures the summed correlation of vector x(i) with all other vectors. Then, taking the natural logarithm of $C_i^m(r)$, the mean logarithmic correlation sum can be obtained as:

$$\Phi^m(r) = (N - m + 1)^{-1} \sum_{i=1}^{N-m+1} \log C_i^m(r) \tag{34}$$

then the ApEn is calculated as:

$$ApEn(m, r, N) = \Phi^m(r) - \Phi^{m+1}(r) \tag{35}$$

- *Sample entropy* (SampEn) measures the complexity of two different time series. The higher the autocorrelation between the series, the smaller the SampEn values. m fixes a positive integer and r fixes a positive real number. Given a regularly sampled time series U(t), a sequence of vectors $x^m(1), x^m(2), ..., x^m(N - m + 1) \in R^m$ is formed. For each i defines $1 \le i \le N - m + 1$ (Holzinger et al., 2014):

$$C_i^m = \frac{number\ of\ j\ such\ that\ d\ [x^m\ (i),\ x^m\ (j)] \le r\ and\ i \ne j}{N-m+1} \tag{36}$$

Furthermore, define:

$$\Phi^m(r) = (N - m)^{-1} \sum_{i=1}^{N-m} C_i^m\ (r) \tag{37}$$

then the SampEn is calculated as:

$$SampEn(m, r, N) = log(\Phi^m\ (r)) - log(\Phi^{m+1}\ (r)) \tag{38}$$

- Permutation entropy (PE), which has the advantages of simplicity, robustness, low computation, and invariance over nonlinear uniform transformations, is a method for analyzing the complexity of the signal (Rajabi et al., 2022). The time series signal can be subsets as $X_i = [x_i, x_{i+\tau}, ..., x_i + (m-1)_\tau]$ using the embedded dimension m and time-delayed τ. There is m! possible order pattern. The PE is calculated as (Şeker et al., 2021):

$$H_{PE}(m) \qquad = \sum_{m=1}^{m!} p(\pi) \ln p(\pi) \qquad (39)$$

- Multiscale entropy (MSE) measures the complexity of a physiological signal by measuring entropy on multiple time scales using a coarse-grained procedure. Coarse graining the data basically means averaging different numbers of consecutive points to create different scales or resolutions of the signal. The MSE is calculated as (Narayan, 2018):

$$y_i(\tau) \qquad = \frac{1}{\tau} \sum_{i=(j-1)\tau+1}^{j\tau} x_i, 1 \le j \le N/\tau \qquad (40)$$

where τ is the time scale. A time series with a lot of fluctuations produces higher entropy values. Therefore, it can be considered a signal with higher complexity. Similarly, signals with a high degree of regularity have lower entropy values (Narayan, 2018).

d) Classification

After the feature extraction stage, the signals are classified using various classification algorithms. Classification is the process of estimating which group belongs to the new data whose class is not labeled, using existing data labeled as a class. Many classification algorithms have been developed since there cannot be one that works perfectly on every dataset and the process of deciding which class the signals belong to is expected to be both fast and accurate. K-nearest neighbors, decision trees, support vector machine, random forest, naive bayes, and linear discriminant analysis are widely used machine learning classification algorithms. Recurrent neural networks, deep belief networks, convolutional neural networks, long-short term memory, and bidirectional long-short term memory are widely used deep learning classification algorithms.

e) Application Interface and Feedback

The classified signals are finally translated into useful commands for any connected device, such as a computer, robot, or wheelchair in the control interface stage. Finally, the user is provided with feedback on the detected activity. The purpose of this process is to help the user control their brain activities, thus increasing user performance (Siuly et al., 2016).

Conclusion

EEG-based BCI systems are systems that can directly collect EEG signals, which measure electrical activity between neurons in the brain and have low amplitude, and analyze these signals and send them as commands to a computer, assistive device, or prosthesis. EEG signal analysis can explain how the brain works, which regions of the brain are active and how the active regions communicate with each other. EEG-based BCI systems consist of signal acquisition, signal preprocessing, feature engineering (feature extraction and feature selection), classification, and application interface stages. The characteristics of EEG signals are extracted by taking into account the advantages that are basically revealed based on amplitude, frequency and sometimes phase structure. In this study, a clear representation of the signal processing steps in EEG-based BCI systems was presented, with a particular focus on feature extraction methods. Feature extraction is the process of converting raw EEG data into smaller and digital features, provided the information in the original dataset is preserved. Feature extraction is the most basic and most difficult issue in

EEG-based BCI systems. The feature vector should be obtained by extracting the most important features of the EEG signals in feature extraction. Because the success of the system is related to their classification based on extracted features.

REFERENCES

Aboalayon, K. A. I., Faezipour, M., Almuhammadi, W. S. & Moslehpour, S. (2016) Sleep stage classification using EEG signal analysis: a comprehensive survey and new investigation. *Entropy, 18*(9), 272. Doi: 10.3390/e18090272

Assaf, A., Charif, H. & Demir, E. (2022) Information sharing among cryptocurrencies: Evidence from mutual information and approximate entropy during COVID-19. *Finance Research Letters, 47*, 102556. Doi: 10.1016/j.frl.2021.102556

Aydemir, Ö. & Kayıkçıoğlu, T. (2009) EEG tabanlı beyin bilgisayar arayüzleri. *Akademik Bilişim, 9*, 11-13.

Bahador, N., Jokelainen, J., Mustola, S., & Kortelainen, J. (2021) Multimodal spatio-temporal-spectral fusion for deep learning applications in physiological time series processing: A case study in monitoring the depth of anesthesia. *Information Fusion, 73*, 125-143. Doi: 10.1016/j.inffus.2021.03.001

Behbahani, S., Ahmadieh, H., & Rajan, S. (2021) Feature extraction methods for electroretinogram signal analysis: A review. *IEEE Access.* 116879-116897. Doi: 10.1109/ACCESS.2021.3103848

Boonyakitanont, P., Lek-Uthai, A., Chomtho, K., & Songsiri, J. (2020) A review of feature extraction and performance evaluation in epileptic seizure detection using EEG. *Biomedical Signal Processing and Control, 57*, 101702. Doi: 10.1016/j.bspc.2019.101702

Dong, G., & Liu, H. (2018) *Feature engineering for machine learning and data analytics.* CRC Press.

Fred, A. L., Kumar, S. N., Kumar Haridhas, A., Ghosh, S., Purushothaman Bhuvana, H., Sim, W. K. J., Vimalan, V., Givo, F. A. S., Jousmäki, V., Padmanabhan, P., & Gulyás, B. (2022) A Brief Introduction to Magnetoencephalography (MEG) and Its Clinical Applications. *Brain Sciences, 12*(6), 788. Doi: 10.3390/brainsci12060788

Goshvarpour, A., Abbasi, A., & Goshvarpour, A. (2013) Analysis of electroencephalogram signals in different sleep stages using Detrended fluctuation analysis. *International Journal of Image, Graphics and Signal Processing, 5*(12), 49. Doi: 10.5815/ijigsp.2013.12.07

Hampden-Thompson, G. & Galindo, C. (2017) School–family relationships, school satisfaction and the academic achievement of young people. *Educational Review, 69* (2), 248-265. Doi: 10.1080/00131911.2016.1207613

Holzinger, A., Hörtenhuber, M., Mayer, C., Bachler, M., Wassertheurer, S., Pinho, A. J., & Koslicki, D. (2014) *On entropy-based data mining.* In Interactive Knowledge Discovery and Data Mining in Biomedical Informatics (pp. 209-226). Springer, Berlin, Heidelberg.

Hochberg, L. R., & Donoghue, J. P. (2006) Sensors for brain-computer interfaces. *IEEE Engineering in Medicine and Biology Magazine, 25*(5), 32-38. Doi: 10.1109/MEMB.2006.1705745

Huang, N. E. (2014). Huang, N. E. (2014). *Hilbert-Huang transform and its applications.* World Scientific. (pp. 1-26).

Ji, N., Ma, L., Dong, H., & Zhang, X. (2019). EEG signals feature extraction based on DWT and EMD combined with approximate entropy. *Brain Sciences, 9*(8), 201. Doi: 10.3390/brainsci9080201

Kalin, F., Akinci, T. C., Türkpence, D., Seker, S., & Korkmaz, U. (2020). *Detection of epileptic seizure using STFT and statistical analysis.* In Advances in Neural Signal Processing. IntechOpen.

Kar, S., Bhagat, M., & Routray, A. (2010). EEG signal analysis for the assessment and quantification of driver's fatigue. *Transportation Research Part F: Traffic Psychology and Behaviour, 13*(5), 297-306. Doi: 10.1016/j.trf.2010.06.006

Kline, B. R. (2005). *Principles and practice of structural equation modeling* (Second edit). NY: The Guilford Press.

Khalid, M. B., Rao, N. I., Rizwan-i-Haque, I., Munir, S., & Tahir, F. (2009, February). Towards a brain computer interface using wavelet transform with averaged and time segmented adapted wavelets. *In 2009 2nd International Conference on Computer, Control and Communication* (pp. 1-4). IEEE.

Ladha, L., & Deepa, T. (2011). Feature selection methods and algorithms, *International Journal on Computer Science and Engineering, 3*(5), 1787-1797.

Lakshmi, M. R., Prasad, T. V., & Prakash, D. V. C. (2014). Survey on EEG signal processing methods. *International Journal of Advanced Research in Computer Science and Software Engineering, 4*(1). 84-91.

Liang, Z., Wang, Y., Sun, X., Li, D., Voss, L. J., Sleigh, J. W., Hagihira, S., & Li, X. (2015). EEG entropy measures in anesthesia. *Frontiers in Computational Neuroscience, 9*, 16. Doi: 10.3389/fncom.2015.00016

Madan, S., Srivastava, K., Sharmila, A., & Mahalakshmi, P. (2018). A case study on Discrete Wavelet Transform based Hurst exponent for epilepsy detection. *Journal of Medical Engineering & Technology, 42*(1), 9-17. Doi: 10.1080/03091902.2017.1394390

Márton, L. F., Brassai, S. T., Bakó, L., & Losonczi, L. (2014). Detrended fluctuation analysis of EEG signals. *Procedia Technology, 12*, 125-132. Doi: 10.1016/j.protcy.2013.12.465

Nal, M. (2018*). Hastanelerde acil yardım ve afet yönetimi.* Ankara: Akademisyen Kitabevi

Narayan, P. S. (2018). Understanding multiscale entropy, Washington, DC, USA:Sapien Labs. (On 05/12/2022 Retrieved from: https://sapienlabs. org/understanding-multiscale-entropy/)

Petrantonakis, P. C., & Hadjileontiadis, L. J. (2009). Emotion recognition from EEG using higher order crossings. *IEEE Transactions on information Technology in Biomedicine, 14*(2), 186-197. Doi: 10.1109/TITB.2009.2034649

Rajabi, S., Azari, M. S., Santini, S., & Flammini, F. (2022). Fault diagnosis in industrial rotating equipment based on permutation entropy, signal processing and multi-output neuro-fuzzy classifier. *Expert Systems with Applications, 206*, 117754. Doi: 10.1016/j.eswa.2022.117754

Safi, M. S., & Safi, S. M. M. (2021). Early detection of Alzheimer's disease from EEG signals using Hjorth parameters. *Biomedical Signal Processing and Control, 65*, 102338. Doi: 10.1016/j.bspc.2020.102338

Saikia, A., Hussain, M., Barua, A. R., & Paul, S. (2019, March). Significance of Lyapunov exponent in Parkinson's disease using electroencephalography. *In 2019 6th International Conference on Signal Processing and Integrated Networks (SPIN)* (pp. 791-795). IEEE.

Schmierer, T., Li, T., & Li, Y. (2022). A novel empirical wavelet SODP and spectral entropy based index for assessing the depth of anaesthesia. *Health Information Science and Systems, 10*(1), 1-14. Doi: 10.1007/s13755-022-00178-8

Siuly, S., Li, Y., & Zhang, Y. (2016). *Significance of EEG signals in medical and health research*. In EEG Signal Analysis and Classification (s. 23-41). Springer, Cham.

Şeker, M., Özbek, Y., Yener, G., & Özerdem, M. S. (2021). Complexity of EEG dynamics for early diagnosis of Alzheimer's disease using permutation entropy neuromarker. *Computer Methods and Programs in Biomedicine, 206,* 106116. Doi: 10.1016/j.cmpb.2021.106116

Tonner, P. H., & Bein, B. (2006). Classic electroencephalographic parameters: median frequency, spectral edge frequency etc. *Best Practice & Research Clinical Anaesthesiology, 20*(1), 147-159. Doi: 10.1016/j.bpa.2005.08.008

Wang, J., & Wang, M. (2021). Review of the emotional feature extraction and classification using EEG signals. *Cognitive Robotics, 1*, 29-40. Doi: 10.1016/j.cogr.2021.04.001

Yakovleva, T. V., Kutepov, I. E., Karas, A. Y., Yakovlev, N. M., Dobriyan, V. V., Papkova, I. V., Zhigalov, M. V., Saltykova, O. A., Krysko, A. V., Yaroshenko, T., Y., Erofeev, N. P., & Krysko, V. A. (2020). EEG analysis in structural focal epilepsy using the methods of nonlinear dynamics (Lyapunov exponents, Lempel–Ziv complexity, and multiscale entropy). *The Scientific World Journal (2020).* 1-13. Doi: 10.1155/2020/8407872

Yol, S., Ozdemir, M. A., Akan, A., & Chaparro, L. F. (2018, November). Detection of epileptic seizures by the analysis of EEG signals using empirical mode decomposition. *In 2018 Medical Technologies National Congress (TIPTEKNO)* (pp. 1-4). IEEE.

Zhang, F., Han, C., Li, L., Zhang, X., Xie, J., & Li, Y. (2015). Research on high-frequency combination coding-based SSVEP-BCIs and its signal processing algorithms. *Shock and Vibration (2015).*1-12. Doi: 10.1155/2015/194230

The Relationshıp of Structure-Activity and Antioxidant Effects of Phenolic Compounds and Carotenoıds

Hatice Banu KESKİNKAYA[1]

Introduction

Phenolic compounds commonly found in plants are secondary metabolites synthesized during aromatic amino acid metabolism. The amounts of phenolic compounds found in almost every fruit and vegetable vary between 0.1-1.0% (Friedman and Jürgens, 2000; Escarpa and Gonzalez, 2001; Coşkun, 2006).

Today, the structures of thousands of phenolic compounds have been defined and new defined phenolics are constantly being added to them. These compounds, which come to the fore among phytochemicals, have important physiological and morphological importance in plants. Phenolic compounds are found naturally in the structure of plants as well as can be formed as a result of chemical reactions such as Maillard reactions (Bravo, 1998; Karovičová and Šimko, 2000; Alasalvar et al., 2001; Naczk and Shahidi, 2004; Luthria, 2008).

Carotenoids are organic pigments in tetraterpenoid structure produced by various plants, algae, photosynthetic bacteria, molds and yeasts (Ramesh and Muthuraman, 2018). Today, about 750 natural carotenoids have been identified and 50 of them are; in some foods consumed by humans and 20 of them; It is found in human blood and tissues (Arathi et al., 2015; Kot et al., 2018).

Usually carotenoids; carotenes (hydrocarbon carotenoids) such as β-carotene and lycopene, consisting only of carbon and hydrogen, and xanthophylls (oxygens) containing functional groups epoxy (violaxanthin, neoxanthine, fuxoxanthin), hydroxy (lutein and zeaxanthin), keto (astaxanthin, cantaxanthin) and methoxy (spirilloxanthin) containing carotenes).

1. Phenolic Compounds and Antioxidant Properties

Structurally, phenolic compounds have an aromatic ring bearing one or more hydroxyl groups. This structure can vary from a simple phenolic molecule to complex highly polymerized compounds (Bravo, 1998). Phenols containing a (-OH) group in their structure (C6H5OH) form the simplest phenolic compound and all other compounds are derived from phenol. Phenolic compounds containing more than one (-OH) are called "polyphenols" (Harborne, 1989; Shahidi and Naczk, 1995; Harborne et al., 1999).

There is a natural defense mechanism in the body against free radical molecules that occur as a result of different mechanisms. All of the compounds that make up this defense mechanism are called "antioxidants". Antioxidants include macromolecules (ferritin, myoglobin, transferrin, ceruloplasmin, haptoglobilin) enzymes; (glutathione peroxidase-GP, glutathione reductase, catalase-CAT, cytochrome-C-oxidase, superoxide dismutase-SOD, hydroxyperoxidase) and micromolecules (vitamin C-vitamin A-vitamin β-carotene, vitamin E, thiol containing, glutathione

[1] Asisst Prof., Necmettin Erbakan University,

(GSH)), tocopherols, ubiguinon, N-acetyl cysteine, captopril, methionine, such compounds are counted (Hilmi, 1994).

1.1. Classification of Phenolic Compounds

Phenolic compounds are divided into two main groups as "simple phenolic substances" and "polyphenols" according to the number of carbon atoms they contain. Phenolic substances commonly found in fruits and vegetables are examined in three parts: hydroxybenzoic acids, hydroxycinnamic acids and flavonoids.

Flavonoids are divided into five subgroups: catechins, anthocyanins, flavonols, flavanones and proanthocyanidins (leuicoanthocyanidins) (Figure 1.1) (Reis Giada, 2013). Among these, phenolic acids, flavonoids and tannins are considered as the main dietary phenolic compounds (King and Young, 1999).

Figure 1.1. Classification of phenolic compounds (Vermerris and Nicholson, 2008).

Phenolic acids consist of two subgroups, hydroxybenzoic and hydroxycinnamic acids. Hydroxybenzoic acids such as gallic acid, p-hydroxybenzoic, protocatechic, vanillic and syringic acid have the (C6-C1) structure in common. On the other hand, hydroxycinnamic acids such as caffeic, ferulic, p-coumaric and sinapic acid are aromatic compounds with a three-carbon side chain (C6-C3) (Table 1.1). (Saldamli, 2007).

Table 114. Chemical structures of hydroxycinnamic acid and hydroxybenzoic acid groups (Bravo, 1998)

Connecting group and its location	Hydroxycinnamic acid	Hydroxybenzoic acid
	o-coumaric acid	
2- OH		Salicylic acid
		m- Hydroxybenzoic acid
3- OH		
4- OH		*p*- Hydroxybenzoic acid
	p- coumaric acid	

2,3-di-OH		Pyrocatechic acid
2,4-di-OH		Resorsilicic acid
2,5-di-OH		Gentisic acid
3,4-di-OH	Caffeic acid	Protocatechic acid
3,5-di-OH		*a-* Resorsilicic acid
3,4,5-tri-OH		Gallic acid
3-OCH₃, 4-OH	Ferulic acid	Vanillic acid
3-OH, 4-OCH₃	Isoferulic acid	Isovanilic acid
3,5-di-OCH₃,4-OH	Sinapic acid	Syringic acid

Flavonoids constitute the largest group of plant phenolics, with more than half of the 8000 natural phenolic compounds (Harborne and Williams, 2000). Flavonoids; They are low molecular weight compounds that are arranged in the C6-C3-C6 configuration and contain 15 carbon atoms. Its basic structure consists of two aromatic rings (A and B) connected by 3 carbon bridges in the form of a heterocyclic ring (C).

The (A) aromatic ring is obtained by acetate/malonate, while the (B) ring is obtained from phenylalanine by shikimic acid (Bohm, 1998; Merken and Beecher, 2000). According to the linkage change in the (C) ring, flavonoid classes such as flavonols, flavones, flavanones, flavanols or catechins, isoflavones, flavanols and anthocyanidins are formed (Hollman and Katan, 1999). Flavones and flavonols are the most common and structurally diverse classes of flavonoids. Changes such as oxygenation, alkylation, glycosylation, acylation and sulfation in the (A) and (B) rings can cause the formation of different flavonoids within each class (Figure 1.2).
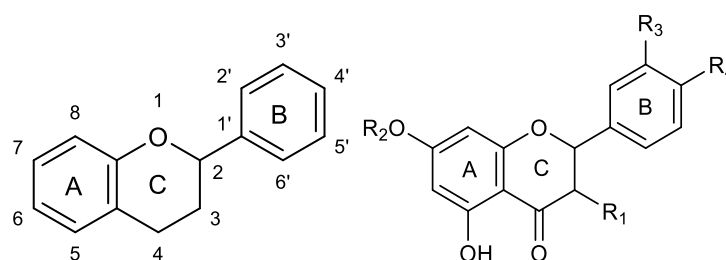
Figure 1.2. Basic structure (a) and some components (b) of flavonoids

In general, flavanones are found in citrus fruits, flavones in spices, isoflavonoids in legumes, anthocyanins and catechins in fruits, and flavonols in all fruits and vegetables (Figure 1.3).
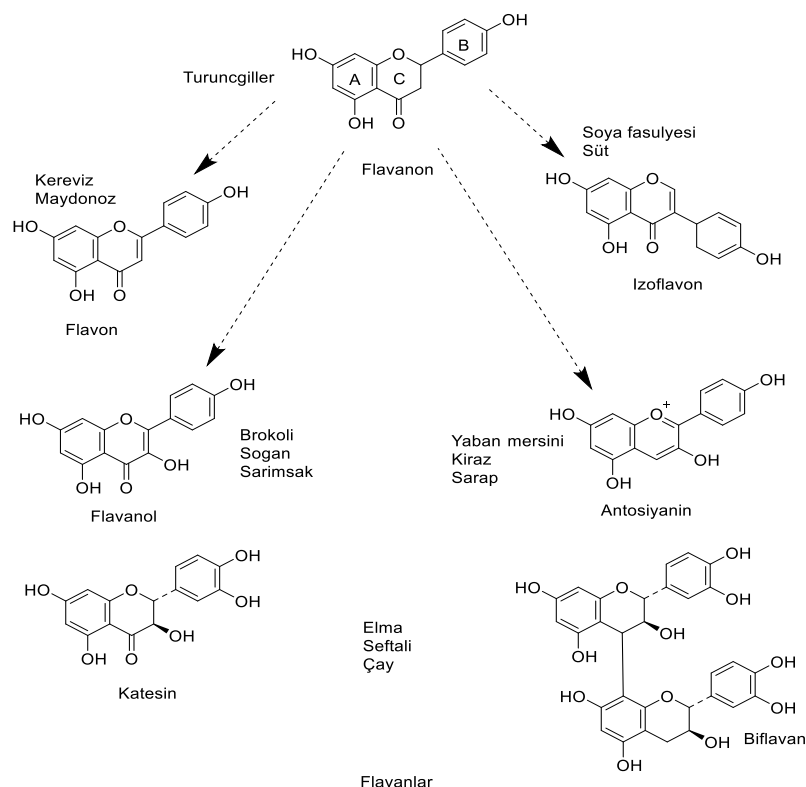
Figure 1.3. Chemical structure of flavonoids

Phenolic compounds are the name given to a group of compounds containing hydroxyl (-OH) on an aromatic hydrocarbon ring. Polyphenols found in macroalgae are tannins, catechins, flavonoids, phlorotannins, and some phenolic acids. These phenolic compounds have such significant pharmaceutical properties as antiproliferative, antibacterial, antidiabetic, antikoagulan, antiviral, antihelmintik, anti-inflammatory, anti-HIV, antioxidant, antiparasitic, antiallergic, and anti-tumoral ones (Keskinkaya et al.,2022).

Tannins, which form the third important group of phenolic compounds, are found in various tissues and plant essences of higher plants such as bark, wood, fruit, fruit seed, leaf, root. Molecular weights vary between 500-3000 daltons, and tannins with a molecular weight of 20000 daltons have been defined in the literature (Hagerman, 2002). It contains a large number of hydroxyl groups and functional groups, and their chemical structures are highly variable. Except for some high molecular weight structures, it can dissolve in water and form cross-links with protein and other macromolecules. Tannins; It causes a decrease in the nutritional value of foods by forming a complex with proteins, minerals, starch and digestive enzymes (Aydın and Üstün, 2007; Ergezer and Çam, 2008). According to their molecular structures, they are divided into two groups as hydrolyzable tannins (elajitannins) and non-hydrolyzable tannins (condensed tannins, proanthocyanidins) (Figure 1.4) (Seeram and Nair, 2002; Vermerris and Nicholson, 2008). A third subgroup, the fluorotannins containing phloroglucinol, has been isolated from several species of brown algae, but they are generally not important for human nutrition (Ragan and Glombitza, 1986).
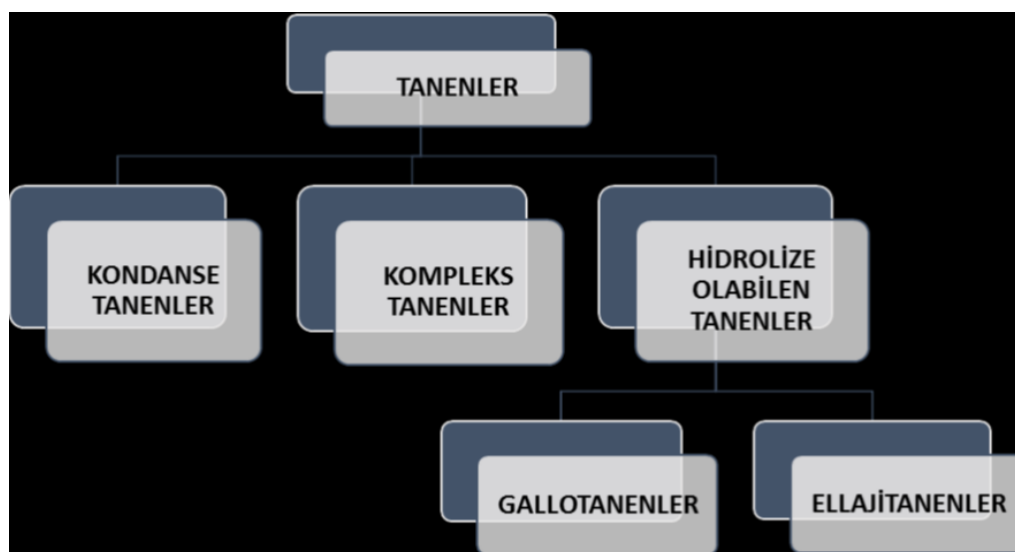
Figure 1.4. Classification of tannins

Condensed tannins, also known as proanthocyanidins, are polymeric components consisting of polyhydroxyflavan-3-ol monomer (catechin or leukoanthocyanidin) of flavonoids (Figure 1.5.) (Hagerman, 2002). Polymerization takes place under enzyme catalysis with the effect of temperature and acidity. Depending on the degree of polymerization, the ability of proanthocyanidins to precipitate proteins also increases (Schofield et al., 2001; Vermerris and Nicholson, 2008).
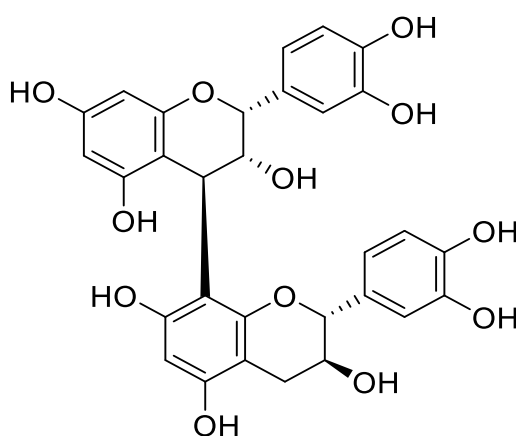
Figure 1.5. Proanthocyanidin B2 consisting of epicatechin and catechin unit (Harborne, 1989).

1.2. Metabolism of Phenolic Compounds and Structure-Activity Relationship

The antioxidant activity of phenolic compounds is due to their ability to bind free radicals, donate hydrogen atoms or electrons, or chelate metals (Afanas' ev et al., 1989; Amarowicz et al., 2004). The structure of phenolic compounds is an important determinant of their radical scavenging and metal chelating activity. This situation is called "structure-activity relationship (SAR/LAI)". For example, antioxidant activity in phenolic acids depends on the number and position of hydroxyl groups on the carboxyl functional group (Rice-Evans et al., 1996; Robards et al., 1999). While monohydroxybenzoic acids with a hydroxyl (-OH) group in the ortho- or para-

position on the carboxyl group do not show any antioxidant activity, m-hydroxybenzoic acid with a hydroxyl group in the meta-position has antioxidant properties.

Hydroxycinnamic acids show higher antioxidant activity than hydroxybenzoic acids (Andreasen et al., 2001). The high activity of hydroxycinnamic acid is associated with the presence of a CH=CH-COOH group, which allows radical stabilization and high H-donation compared to the -COOH group in hydroxybenzoic acids (Rice-Evans et al., 1996).

2. Carotenoids and Antioxidant Properties

Nutritionally, carotenoids are considered to be important bioactive compounds, and the only way humans and animals can meet their needs; It is stated that there is an intake from food sources through digestion (Arathi et al., 2015).

Unlike many plant-derived bioactive substances such as flavonoids, anthocyanins and vitamin C, carotenoids are hydrophobic; they are well soluble in oil, organic solvents such as acetone, alcohol, ethyl ether, chloroform and ethyl acetate. They are little or no soluble in water, they need to be dissolved by lipoprotein, fat droplet or bile salt in order to be absorbed in the human body (Rodriguez-Amaya, 2001; Palozza et al., 2006). The long polyene structure of carotenoids enables them to absorb ultraviolet light and increase their oxidation susceptibility, thus carotenoids have the feature of being a strong antioxidant. Carotenoids can prevent peroxidation of fats (De Ancos et al., 2006).

It is stated that carotenoids reactivate the body's immune system and accelerate the healing of wounds. It is stated that carotenoids should be added to foods as supplements because the human body cannot synthesize these compounds. Carotenoids are an important group of pigments that are widely distributed in nature and have many properties (Woutersen et al., 1999).

Carotenoids are often characterized by polyene chains of 35-40 carbons terminated in ring structures. Its main biochemical functions are based on long conjugated double bonds, which are also responsible for their color. As the number of these bonds increases, the electrons interacting with the conjugated systems find more displacement opportunities and consume less energy. In this way, lower energy level light is absorbed. This can be explained by the fact that carotenoid compounds are often red in color (Meléndez-Martínez et al., 2007).

It is stated that there are conjugated double bonds in the long acyclic C40H56 structure that forms the skeleton of carotenoids (Figure 1.6). All carotenoids; It is stated that this chain structure is formed by hydrogenation, dehydrogenation, cyclization, oxidation reactions, their combinations, or the breakdown of this basic carbon skeleton structure or the combination of these structures (Pfander, 1992).
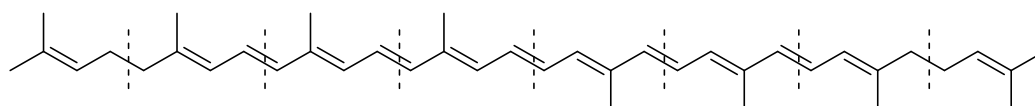
Figure 1.6. Basic acyclic C40H56 structure involved in carotenoid formation

It is known that carotenoids also undergo isomerization and decomposition at low temperature storage conditions. For example, in a study, it was determined that this is also true for lycopene and β-carotene (Lin and Chen, 2005). It is stated that β-carotene functions as a very effective chain-breaking antioxidant, but the antioxidant effect of β-carotene decreases with increasing oxygen

pressure. Since the oxygen concentration differs from tissue to tissue, carotenoids play different roles in different tissues (El-Agamey et al., 2004).

Many factors affect the carotenoid content in plants. It is reported that factors such as climate, pesticide use and soil type affect the formation of carotenoids. Since light, which is one of the most important of these factors, promotes the biosynthesis of carotenoids, the degree of exposure of the plant to light is an important factor affecting the carotenoid concentration. Some microalgae synthesize significant amounts of secondary carotenoids such as astaxanthin, canthaxanthin and echineone (carotenogenesis) under abnormal environmental conditions (Rise et al., 1994).

Carotenoids show high antioxidant activity due to the conjugated double bonds in their structures. Due to these structural features, they have the effect of removing singlet oxygen species and scavenging free radicals directly (Krinsky and Johnson, 2005). It is thought that carotenoids with conjugated double bond system also show activity accelerating the oxidation of lipid and similar substrates under certain conditions (Cheeseman et al., 1984).
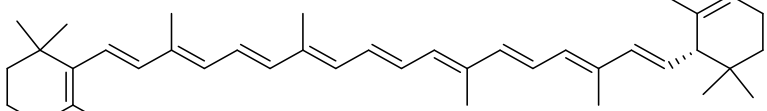
Antioxidants; They are structures that protect tissues and cell components against free radical damage. Most of the carotenoids have antioxidant activity and these pigments are also important for enhancing the immune response, carcinogenic metabolism, enzyme activity and regular cell growth (Palozza et al., 2006; Fiedor and Burda, 2014).

Some factors affecting the antioxidant activities of carotenoids in biological systems can be listed as follows;

• The structure (size, nature, position, number of groups, etc.) and physical form (clustered, monomeric, etc.) of the carotenoid,
• The active site or localization of the carotenoid molecule in the cell,
• Potential for interaction with other carotenoids or antioxidants
  • Concentration of carotenoid in the environment,
• Ambient oxygen pressure (Britton, 1995).

2.1.   Classification of Carotenoids

More than 85% of natural compounds obtained from green algae are terpenes (Blunt et al., 2005). The isoprene units of terpenes are straight chain or ringed. It is found in the structure of biological pigments, vitamins A, D, E and K, electron 10 carriers; Phytol, consisting of 4 isoprene, is found in the structure of chlorophyll combined with the porphyrin ring. Squalene containing 6 isoprene rings is an intermediate in cholesterol synthesis. with 8 isoprene rings; hepene, lycopene, carotene. Carotenoids are generally classified as only hydrocarbon carotenes (lycopene, β-carotene and α-carotene) and their oxygenated derivatives xanthophylls (zeaxanthin, spirilloxanthin, myxoxanthophyll, anteroxanthin and torularhodin) (Goodwin, 1980). In carotenes; 4 isoprene in chains; the other 4 are ringed as two isoprene units at both ends of this chain (ionone ring). Classification of carotenoids is given in Figure 2.1. (Bağdatlıoğlu and Demirbuker, 1999).

I. Carotenes (Hydrocarbon structures)	α−karoten	

	β−karoten	
	γ−karoten	
	δ−karoten	
	Lutein	
II. Xanthophylls (Carotenoid alcohols)	α−kriptoksantin	
	β−kriptoksantin	
	Lutein	
	Flavoksantin	
	Violaksantin	
III. Carotenoid ketones	Astaksantin	
	Kapsantin	
	Fukoksantin	
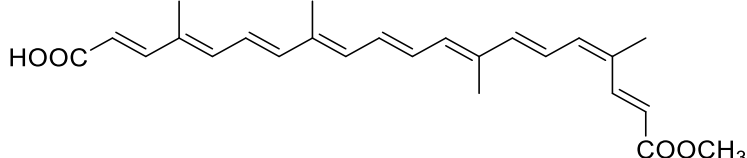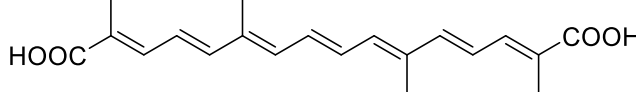
IV. Carotenoid acids	Biksin	
	Krosetin	

Figure 2.1. Classification of carotenoids

2.1.1. Beta-carotene Metabolism

β-carotene; It is one of the lipophilic and yellow-orange natural pigments in the carotene group with a tetraterpenoid structure (Liaaen-Jensen, 2004; Erdal and Ökmen, 2013). β-carotene is widely found in plants and microorganisms. Animals that cannot synthesize β-carotene need these plants. Its chemical formula is C4OH56, molecular weight; It is known that β-carotene, which is stated as 536.9 g/mol, is insoluble in water and ethyl alcohol, and its solubility is not very good in vegetable oils. The maximum spectrophotometric absorption of the solution of this substance in chloroform; It is stated to be between 466 and 496 nm (Ötles and Çagindi, 2007). Nutritional studies report that β-carotene is beneficial in the fight against many cancers and other types of diseases, thanks to its antioxidant and vitamin A precursor properties (Bhosale and Gadre, 2001). Since vitamin A cannot be synthesized by the body without its precursor, it is known as a vitamin that must be taken externally for humans and all mammals. Deficiency of this vitamin; It is stated that it adversely affects body development, cell renewal and the body's resistance to infections (Ötleş and Atlı, 2011). It is reported that β-carotene has the highest provitamin A activity (Kot et al., 2016).

β-carotene is one of the most common pigments found in nature. The most important feature of β-carotene, one of the most studied carotenoids, is its metabolism to vitamin A. The presence of a β-ionone ring at both ends of the β-carotene chain structure causes it to have higher provitamin A activity than other carotenoids (Krinsky and Johnson, 2005). The chemical structure of β-carotene consists of a central skeleton of eight isoprene units with 40 carbons, with two rings at the end of the conjugated double bond chain, as shown in Figure 2.2 (Ribeiro et al., 2008).
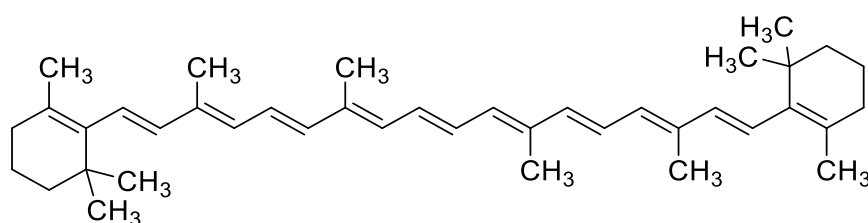
Figure 2.2. Chemical structure of β-carotene

It is a pigment that dissolves in oil but emulsifies in aqueous solutions, giving it a yellow-orange color. They are obtained commercially from algae (Barth et al., 1995). Dunaliella salina and Dunaliella bardawil have been reported to accumulate high amounts of β-carotene under a combination of high light sensitivity and high salt and nutrient stress (Cowan et al., 1995).

While β-carotene scavenges free radicals under low oxygen partial pressure under physiological conditions, it has a prooxidant effect at high oxygen pressure and especially at high concentrations (Cadenas and Packer, 2002).

It has been shown that β-carotene, by showing antioxidant properties, reduces the harmful effects of free radicals, prevents diseases such as cancer forms, coronary artery diseases, premature aging, arthritis and about 60 harmful factors (Törnwall et al., 2004).

Among the carotenoids, β-carotene is known to have the highest provitamin A activity. The reason for this; Unlike other carotenoids, it is stated that there is a β-ionone ring at both ends of the β-carotene chain structure (Türkcan and Ökmen, 2012). It is stated that carotenoids without β-ionone ring do not show provitamin activity (Bogacz-Radomska and Harasym, 2018).

β-carotene is one of the vitamin A precursor carotenoids and is mostly found in yellow-orange-green vegetables and fruits such as sweet potatoes, pumpkin apricots, carrots, red peppers, mangoes, collard greens, spinach, broccoli (Farré et al., 2010). . Unlike other vitamin A precursor carotenoids, 2 moles of vitamin A emerge from one mole of β-carotene (Tang, 2010). β-carotene; It contributes to the antioxidant defense system with many mechanisms such as quenching free radicals in the body, neutralizing the single (singlet) oxygen that causes the formation of these radicals, and increasing the activity of other antioxidants such as α-tocopherol and phenolic compounds. It is also very important for eye health, bone and tooth development (Kiokias and Gordon, 2004).

β-carotene is one of the most important food additives and is widely used as a natural colorant in margarine, baking oils and beverages (Chen et al., 2016).

REFERENCES

Friedman, M. ve Jürgens, H. S., 2000, Effect of pH on the stability of plant phenolic compounds, *Journal of agricultural and food chemistry*, 48 (6), 2101-2110.

Escarpa, A. ve Gonzalez, M., 2001, An overview of analytical chemistry of phenolic compounds in foods, *Critical Reviews in Analytical Chemistry*, 31 (2), 57-139.

Coşkun, F., 2006, Gıdalarda bulunan doğal koruyucular, *Gıda teknolojileri elektronik dergisi*, 2, 27-33.

Bravo, L., 1998, Polyphenols: chemistry, dietary sources, metabolism, and nutritional significance, *Nutrition reviews*, 56 (11), 317-333.

Karovičová, J. ve Šimko, P., 2000, Determination of synthetic phenolic antioxidants in food by high-performance liquid chromatography, *Journal of Chromatography A*, 882 (1-2), 271-281.

Alasalvar, C., Grigor, J. M., Zhang, D., Quantick, P. C. ve Shahidi, F., 2001, Comparison of volatiles, phenolics, sugars, antioxidant vitamins, and sensory quality of different colored carrot varieties, *Journal of agricultural and food chemistry*, 49 (3), 1410-1416.

Naczk, M. ve Shahidi, F., 2004, Extraction and analysis of phenolics in food, *Journal of Chromatography A*, 1054 (1-2), 95-111.

Luthria, D. L., 2008, Influence of experimental conditions on the extraction of phenolic compounds from parsley (Petroselinum crispum) flakes using a pressurized liquid extractor, *Food Chemistry*, 107 (2), 745-752.

Harborne, J., 1989, General procedures and measurement of total phenolics, *Methods in plant biochemistry*, 1, 1-28.

Shahidi, F. ve Naczk, M., 1995, Food phenolics, Technomic Pub. Co., p.

Harborne, J., Baxter, H. ve Moss, G., 1999, Tannins, Chapter 45, In: Phytochemical Dictionary. A Handbook of Bioactive Compounds from Plants, Eds, *United Kingdom*: Taylor & Francis, p. 570-581.

Reis Giada, M. d. L., 2013, Food phenolic compounds: main classes, sources and their antioxidant power. U: Morales-Gonzales (ur.) Oxidative stress and chronic degenerative diseases: a role for antioxidants, Intech.

King, A. ve Young, G., 1999, Characteristics and occurrence of phenolic phytochemicals, *Journal of the American dietetic association*, 99 (2), 213-218.

Harborne, J. B. ve Williams, C. A., 2000, Advances in flavonoid research since 1992, *Phytochemistry*, 55 (6), 481-504.

Bohm, B. A., 1998, Introduction to flavonoids, Harwood academic publishers, p.

Merken, H. M. ve Beecher, G. R., 2000, Measurement of food flavonoids by high-performance liquid chromatography: a review, *Journal of agricultural and food chemistry*, 48 (3), 577-599.

Hollman, P. ve Katan, M. B., 1999, Dietary flavonoids: intake, health effects and bioavailability, *Food and chemical toxicology*, 37 (9-10), 937-942.

Keskinkaya, H. B., Deveci, E., Güneş, E., Okudan, E. Ş., Akköz, C., Gümüş, N. E. ve Karakurt, S., 2022, Chemical composition, in vitro antimicrobial and antioxidant activities of marine macroalgae codium fragile (suringar) hariot, *Commagene Journal of Biology*, 6 (1), 94-104.

Hagerman, A. E., 2002, Tannin chemistry, http://www.users.muohio.edu/hagermae/tannin.pdf: [15.07.2022].

Aydın, S. ve Üstün, F., 2007, Tanenler 1 kimyasal yapıları, farmakolojik etkileri, analiz yöntemleri, *İstanbul Üniversitesi Veteriner Fakültesi Dergisi*, 33 (1), 21-31.

Ergezer, H. ve Çam, M., 2008, Tanenler: Sınıflandırma, yapıları ve sağlık üzerine etkileri. Türkiye 10. Gıda Kongresi: 229-232.

Seeram, N. P. ve Nair, M. G., 2002, Inhibition of lipid peroxidation and structure− activity-related studies of the dietary constituents anthocyanins, anthocyanidins, and catechins, *Journal of agricultural and food chemistry*, 50 (19), 5308-5312.

Vermerris, W. ve Nicholson, R., 2008, Families of phenolic compounds and means of classification, In: Phenolic Compound Biochemistry, Eds: Springer, p. 1-34.

Ragan, M. ve Glombitza, K., 1986, Phlorotannins, brown algal polyphenols, *Progress in Phycological Research*, 4, 129-241.

Schofield, P., Mbugua, D. ve Pell, A., 2001, Analysis of condensed tannins: a review, *Animal feed science and technology*, 91 (1-2), 21-40.

Afanas' ev, I. B., Dcrozhko, A. I., Brodskii, A. V., Kostyuk, V. A. ve Potapovitch, A. I., 1989, Chelating and free radical scavenging mechanisms of inhibitory action of rutin and quercetin in lipid peroxidation, *Biochemical pharmacology*, 38 (11), 1763-1769.

Rice-Evans, C. A., Miller, N. J. ve Paganga, G., 1996, Structure-antioxidant activity relationships of flavonoids and phenolic acids, *Free radical biology and medicine*, 20 (7), 933-956.

Robards, K., Prenzler, P. D., Tucker, G., Swatsitang, P. ve Glover, W., 1999, Phenolic compounds and their role in oxidative processes in fruits, *Food Chemistry*, 66 (4), 401-436.

Andreasen, M. F., Landbo, A.-K., Christensen, L. P., Hansen, Å. ve Meyer, A. S., 2001, Antioxidant effects of phenolic rye (Secale cereale L.) extracts, monomeric hydroxycinnamates, and ferulic acid dehydrodimers on human low-density lipoproteins, *Journal of agricultural and food chemistry*, 49 (8), 4090-4096.

Ramesh, M. ve Muthuraman, A., 2018, Flavoring and coloring agents: Health risks and potential problems, In: Natural and Artificial Flavoring Agents and Food Dyes, Eds: Elsevier, p. 1-28.

Arathi, B. P., Sowmya, P. R.-R., Vijay, K., Baskaran, V. ve Lakshminarayana, R., 2015, Metabolomics of carotenoids: The challenges and prospects–A review, *Trends in food science & technology*, 45 (1), 105-117.

Kot, A. M., Błażejak, S., Gientka, I., Kieliszek, M. ve Bryś, J., 2018, Torulene and torularhodin:"new" fungal carotenoids for industry?, *Microbial Cell Factories*, 17 (1), 1-14.

Rodriguez-Amaya, D. B., 2001, A guide to carotenoid analysis in foods, ILSI press Washington, p.

Palozza, P., Muzzalupo, R., Trombino, S., Valdannini, A. ve Picci, N., 2006, Solubilization and stabilization of β-carotene in niosomes: delivery to cultured cells, *Chemistry and physics of lipids*, 139 (1), 32-42.

De Ancos, B., Sánchez-Moreno, C., De Pascual-Teresa, S. ve Cano, M., 2006, Fruit freezing principles, In: Handbook of fruits and fruit processing, Eds: Hui, Y. H., *New Jersey*: Blackwell Publishing, p. 59-79.

Woutersen, R., Wolterbeek, A., Appel, M., Berg, H. v. d., Goldbohm, R. ve Feron, V., 1999, Safety evaluation of synthetic β-carotene, *Critical Reviews in Toxicology*, 29 (6), 515-542.

Meléndez-Martínez, A. J., Britton, G., Vicario, I. M. ve Heredia, F. J., 2007, Relationship between the colour and the chemical structure of carotenoid pigments, *Food Chemistry*, 101 (3), 1145-1150.

Pfander, H., 1992, Carotenoids: an overview, *Methods in enzymology*, 213, 3-13.

Lin, C. ve Chen, B., 2005, Stability of carotenoids in tomato juice during storage, *Food Chemistry*, 90 (4), 837-846.

El-Agamey, A., Lowe, G. M., McGarvey, D. J., Mortensen, A., Phillip, D. M., Truscott, T. G. ve Young, A. J., 2004, Carotenoid radical chemistry and antioxidant/pro-oxidant properties, *Archives of biochemistry and biophysics*, 430 (1), 37-48.

Rise, M., Cohen, E., Vishkautsan, M., Cojocaru, M., Gottlieb, H. E. ve Arad, S. M., 1994, Accumulation of secondary carotenoids in Chlorella zofingiensis, *Journal of plant physiology*, 144 (3), 287-292.

Krinsky, N. I. ve Johnson, E. J., 2005, Carotenoid actions and their relation to health and disease, *Molecular aspects of medicine*, 26 (6), 459-516.

Cheeseman, K. H., Burton, G. W., Ingold, K. U. ve Slater, T. F., 1984, Lipid peroxidation and lipid antioxidants in normal and tumor cells, *Toxicologic Pathology*, 12 (3), 235-239.

Fiedor, J. ve Burda, K., 2014, Potential role of carotenoids as antioxidants in human health and disease, *Nutrients*, 6 (2), 466-488.

Britton, G., 1995, Structure and properties of carotenoids in relation to function, *The FASEB Journal*, 9 (15), 1551-1558.

Goodwin, T., 1980, Biosynthesis of carotenoids, In: The biochemistry of the carotenoids, Eds: Springer, p. 33-76.

Bağdatlıoğlu, N. ve Demirbuker, B., 1999, Gıda işlemede karotenoidlerde meydana gelen gelişmeler, *Gıda*, 9, 48-51.

Liaaen-Jensen, S., 2004, Basic carotenoid chemistry, *Oxidative Stress and Disease*, 13, 1-30.

Erdal, P. ve Ökmen, G., 2013, Gıdalarda kullanılan mikrobiyal kaynaklı pigmentler, *Türk Bilimsel Derlemeler Dergisi* (2), 56-68.

Ötles, S. ve Çagindi, Ö., 2007, Carotenoids as Natural Colorants, In: Food colorants: chemical and functional properties, Eds: Socaciu, C.: Routledge, p.

Bhosale, P. ve Gadre, R., 2001, β-carotene production in sugarcane molasses by a Rhodotorula glutinis mutant, *Journal of Industrial Microbiology and Biotechnology*, 26 (6), 327-332.

Ribeiro, H. S., Chu, B.-S., Ichikawa, S. ve Nakajima, M., 2008, Preparation of nanodispersions containing β-carotene by solvent displacement method, *Food Hydrocolloids*, 22 (1), 12-17.

Barth, M. M., Zhou, C., Kute, K. M. ve Rosenthal, G. A., 1995, Determination of optimum conditions for supercritical fluid extraction of carotenoids from carrot (Daucus carota L.) tissue, *Journal of agricultural and food chemistry*, 43 (11), 2876-2878.

Cowan, A., Logie, M., Rose, P. ve Phillips, L., 1995, Stress induction of zeaxanthin formation in the β-Carotene accumulating alga dunaliella salina teod, *Journal of plant physiology*, 146 (4), 554-562.

Cadenas, E. ve Packer, L., 2002, Handbook of antioxidants, Marcel Dekker New York, p.

Törnwall, M. E., Virtamo, J., Korhonen, P. A., Virtanen, M. J., Taylor, P. R., Albanes, D. ve Huttunen, J. K., 2004, Effect of α-tocopherol and β-carotene supplementation on coronary heart disease during the 6-year post-trial follow-up in the ATBC study, *European heart journal*, 25 (13), 1171-1178.

Türkcan, O. ve Ökmen, G., 2012, Mikrobiyal karotenoidler, *Türk Bilimsel Derlemeler Dergisi* (1), 115-122.

Bogacz-Radomska, L. ve Harasym, J., 2018, β-Carotene—properties and production methods, *Food Quality and Safety*, 2 (2), 69-74.

Farré, G., Sanahuja, G., Naqvi, S., Bai, C., Capell, T., Zhu, C. ve Christou, P., 2010, Travel advice on the road to carotenoids in plants, *Plant Science*, 179 (1-2), 28-48.

Tang, G., 2010, Bioconversion of dietary provitamin A carotenoids to vitamin A in humans, *The American journal of clinical nutrition*, 91 (5), 1468S-1473S.

Kiokias, S. ve Gordon, M. H., 2004, Antioxidant properties of carotenoids In Vitro and In Vivo, *Food Reviews International*, 20 (2), 99-121.

Chen, X.-W., Fu, S.-Y., Hou, J.-J., Guo, J., Wang, J.-M. ve Yang, X.-Q., 2016, Zein based oil-in-glycerol emulgels enriched with β-carotene as margarine alternatives, *Food Chemistry*, 211, 836-844.

Determination of Organic Acids Content in Plum (*Prunus Cerasifera*) Puree from Malatya Region by Ion Chromatography

Hatice Çağlar Yılmaz[1]
Sema Erdemoglu[1]
Şeref Güçer[2]

Introduction

Plums (genus Prunus of the Rosaceae family) are a famous juicy and nutritious fruit cultivated worldwide and are well adapted to a wide variety of ecogeographic conditions, as evidenced by the worldwide species diversity (Sarıdaş & et al., 2016). The species such as P. salicina Lindl., Prunus domestica L., P. cerasifera Ehrh, P. insititia L., P. americana Marsh. and P. spinosa L. are cultivated around the world. These species are often used in regionally diverse industries (Liu, Nisar & Wan, 2020). The species identified in Turkey include Prunus spinosa L., Prunus cerasifera, Prunus domestica L., P. simonii Carr., Prunus institia L. and P. salicina Lindl. (Davis, 1972). Plums belonging to P. cerasifera are well adapted to various ecogeographic conditions with their cultivated and wild forms in the Anatolian region (Asian part of Turkey), spreading from southeast to Central Anatolia and Aegean and Mediterranean regions. After harvesting, the plums are dried in hot air at 85 to 90°C for 18 hours and processed as plum juice, puree or other plum product. Dried prunes have ~6.1 g of dietary fiber per 100 g, prune juice is dietary fiber-free due to straining before bottling. Both prunes and prune juice have a high sorbitol content (14.7 and 6.1 g/100 g, respectively), which provides a laxative effect. Prunes are a good source of energy in the form of simple sugar and do not cause a rapid increase in blood sugar concentration due to their high fiber, fructose and sorbitol content. Prunes or purees contain large amounts of phenolic compounds (184 mg/100 g). Antioxidants can play an important role in reducing the risk of certain pathological diseases. Antioxidants neutralize free radicals and other reactive substances that cause degenerative reactions in the body with the diseases (Cai, 2004; Chun, 2003). Additionally, plums have a high potassium content (745 mg/100 g), and potassium may be beneficial for cardiovascular health. Prunes play an important role in the prevention of osteoporosis due to the boron in their structure. A portion of prunes (100 g) can meet the daily boron requirement (2-3 mg)(Sapuntzakis, 2001). One of the other important properties of plums is their levels of fiber, sorbitol, and malic acid. Both fiber and sorbitol help absorb and retain moisture, while malic acid helps strengthen the flavor. Fresh plum puree is an excellent choice for those who want to add nutritional value to their daily diet. Plums or purees are one of the best sources of fiber, vitamin A, potassium and naturally occurring antioxidants.

Many study have been reported on the determination of acid in beverages. For this purpose, various analytical methods such as high-performance liquid chromatography (HPLC) procedures are used. These techniques are time-consuming and use large amounts of reagents, which makes them expensive. But the speed and selectivity of liquid chromatography methods make them more useful for the analysis of juices (Masson, 2000).

Organic acids are generally by an ion exclusion column in a HPLC and detected by either performance liquid chromatograph and detected by either a refractive index (RI) or an ultraviolet (UV) detector. Organic acids elution occurs with increasing pKa values, but other variables, eg

additional hydrophobicity, hydrogen bonding and adsorption of acids, can slightly alter the elution order. The small molecules, such as propylene glycol, soluble sugars have retention times similar to those of malonic, malic and citric on an exclusion column. These compounds cause problems in the elution of the above-mentioned organic acids. For this reason, detection becomes more difficult with the RI detector, which has poor selectivity and low sensitivity. Some organic acids generate very low signal in the UV region. In mixed matrices, this is even more of a problem (Alcazar & et al., 2003; Qiu & Jin, 2002). For the reasons mentioned above, conductivity detector provides more sensitivity in analysis than UV or RI detector in determination of organic acids. Some studies have given the analysis of aromatic acids (eg malalic acids), alcoholic sugars (eg methanol with sucrose) and various weak acids (eg succinic acids) by IEC (ion exclusion chromatography) using the conductivity detector. IC using suppressed conductivity presents highly specific and sensitive detection, which minimizes interference and sample clean up (Chen & et al., 2001; Soufleros & et al., 2010).

Plum puree is made locally in the houses by using the plums cultivated in the region of Malatya, Turkey and it is generally used by adding directly into a variety of meals or salad sauces in order to enhance the flavorof them. The purpose of this study is to analyses the organic acids found in this traditional meal by using IC after an appropriate sample preparation procedure was applied. Because the most important organic acids especially the malic acid containing in the plum puree and the malic acid helps potentiate flavor. Organic acids are known to affect flavor quality in fruit juice and puree. For this reason fast and accurate measurements methods would be then extremely helpful in agronomy studies and quality control of plum juice or puree. In addition microbial changes in acidic foods (pH<4.5) such as fruit juices and purees, generally do not involve toxicological hazard (with the exception of mycotoxin formation in the presence of some types of mould), but they can cause degradation in quality, with notable commercial damages (Trifiro & et al., 1997).

If plum puree is dissolved in deionize water, sugar, tannens, large phenolic groups, minerals, etc. except of carboxylic acids pass in to solution. Prior to ICE analysis sample were subjected to a solid phase extraction on ion-exchange cartridges in order to remove matrix compounds that might overlap with the compounds of interest. While organic acids were determined by IC, some pretreatments were applied on sample for to prevent plugged of ICE separator column. Thus, ICE separator column is used longer time for organic acids analysis. At this study, the samples were passed from C_{18}Baker-10SPE (solid phase extraction) columns for removal matrices as sugars and then the samples were injected to ion chromatograph for organic acid analysis.

Experimental

Reagents

The ultrapure water with resistivity above 0.05 μS obtained from a Mili Q (Milipore, Milford, MA, USA) system was used throughout the experiments. All chemicals used in this study were analytical reagent grade and deionized water was used to prepare all solutions. Hydrochloride acid (HCI) and tetrabutylammonium hydroxide (TBAOH) were of ion chromatography grade (Sigma, Germany). Tartaric acid (Merck, Germany), DL-malic acid and propionic acid (Sigma, Germany) were prepared 1000 mg/L stock solutions. The working standard solutions were prepared daily by diluting 1000 mg/L standard solutions of each organic acid, i.e., 2.5-50 mg/L for tartaric acid and 5-50 mg/L for malic and propionic acids. Total sugar in plum puree was determined as glucose by Antron solution prepared by dissolving 0.75 g of Antron (Merck, Germany) in 100 mL of 72% H_2SO_4 at cold. Glucose (Merck, Germany)was prepared as 500 mg/L stock solution, and then the stock solution was diluted between 2-10 mg/L in Daily.

Instrumentation

A QIC Dionex Analyzer (CA, USA) system with an attached conductivity detector and a 40 μL sample loop was used in this study. Dionex ICE-AS1 separator column (AC, USA) and Dionex ICE MMS suppressor column (AC, USA) were used for determination of carboxylic acids. Analytical column was packed with sulfonated sytrene divinilbenzene resin in the H^+ form. Data acquisition was accomplished using a Spectra Physics 4290 integrator.

Total sugar in plum puree were determined with Simadzu 2100 Model (Tokyo, Japan) UV-visible spectrophotometer with 1 cm quartz cell at room temperature. Branson model ultrasonic bath was used to degas the eluent and regenerate solutions.

Operating Conditions

The regenerate solutions were prepared with 3-day intervals, since TBAOH converts to tetrabutilammoniumcarbonate due to CO_2 in air and tetrabutilammoniumcarbonate precipitates slightly in ICE-AMMS column, if medium is acidic. Therefore, 0.1 mol/L of boric acid solution was passed with 2 mL/min, flow rate is for 30 min to clean up the supressor column. The operating conditions were given in Table 1.

Table 1. The analysis conditions of the ion chromatographic measurements.

Column	Dionex ICE-AS1
Eluent	1.0×10^{-3} mol/L HCl
Eluent flow rate	2 mL/min
Supressor column	Dionex ICE-MMS
Regenerant	1.0×10^{-2} mol/L TBAOH
Regenerant flow rate	2 mL/min
Detector	Supressed conductivity
Full scale	30 μS

Sample

Traditional plum puree sample is prepared as follows: The washed plums are stewed in boiling water until syrup of the right consistency is obtained. After cooling and straining, stewed plums are squeezed; seeds and other residues like hulls are discarded. The puree is then allowed to dry in sunlit to increase thickness and to gain durability. Thus, a dense, dark colored sour puree is obtained. It is stored in the glass jars after a little table salt is added to prevent spoiling.
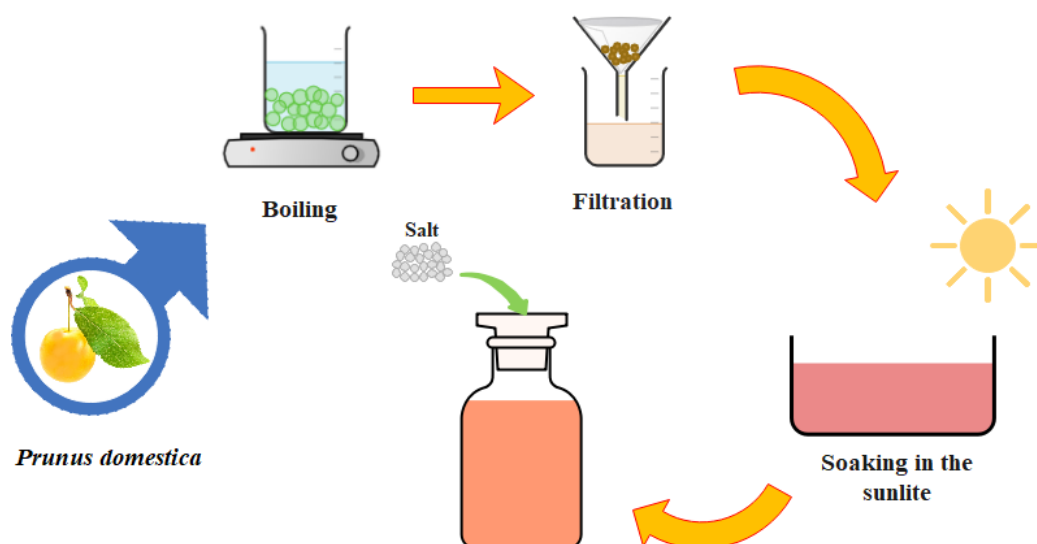
Figure 1. The sample preparation of *prunus domestica.*

Sample preparation and pretreatment

To determine the organic acids in plum puree, the samples were treated with IC by two methods: In the first method, 1.000 g of puree was dissolved in 100 mL of deionised water. The mixture was centrifuged twice at 5000 rpm and then filtered using 0.45 μm filters. The decanted solution was diluted 10 times and it was directly injected to IC. In the second method, 10 mL of the solution diluted 10 times in the first method was allowed to pass through the C_{18}Baker-10SPE column, filtered with 0.45 μm filters, and then it was injected to IC. Beforehand the C_{18}Baker-10SPE was activated with 15 mL of deionized water, and then the 10 mL of sample dilution were passed through with 0.5 mL flow rate. All cartridges are disposable.
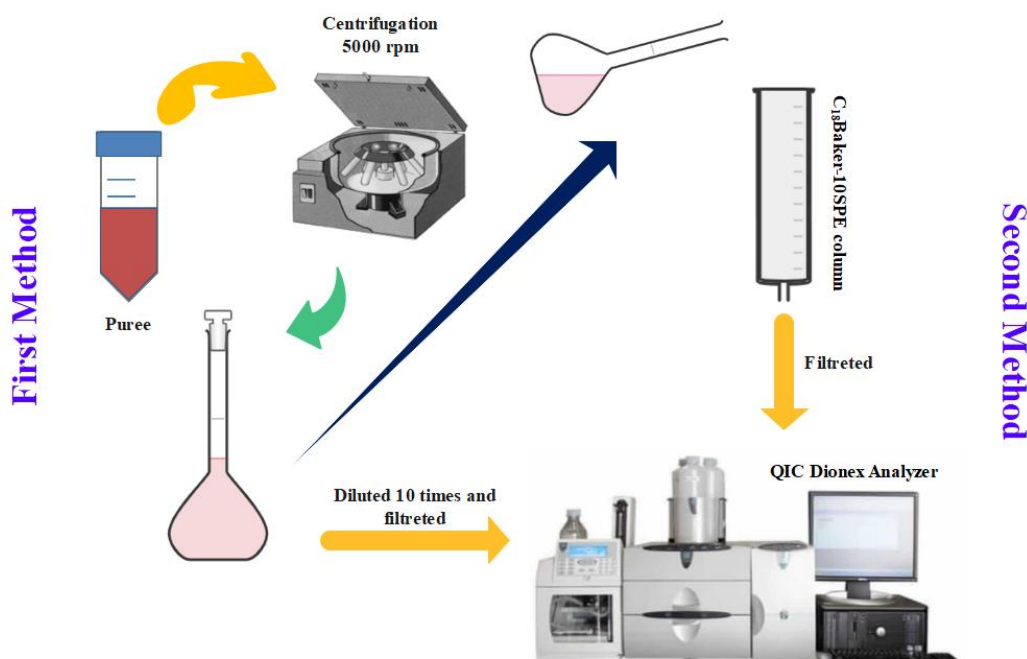
Figure 2. The sample preparation and pretreatment.

Determination of total sugar

5 mL of Antron solution was added to 10 mL of each standard solution of glucose prepared in the concentration range of 2-10 mg/L and to blank solution. These solutions were held in closed tubes in a water bath at 100°C for 12 min, after the agitation with a vortex agitator for 2 min. The absorbance of cooled standard solutions was measured at 620 nm wavelengths. Above treatments were applied on 10 mL of sample solution diluted 1/10 directly and after pass through C_{18}Baker-10SPE. Then absorbance of samples was measured at 620 nm wavelengths. Total sugar was determined directly and after passing from C_{18}Baker-10SPE columns for six replicates.

Spike recovery studies

Also organic acids may retain on the C_{18}Baker-10SPE columns used for removal of carbohydrates as sugar. In order to control the losses of this type, a synthetic solution containing 10 mg/L of glucose, 10 mg/L of tartaric and propionic acids and 50 mg/L of malic acid was prepared. 10 mL of the synthetic solution was passed, in 2 mL portions, through C_{18}Baker-10SPE columns with 0.5 mL/min flow rate. Thus, the efficiency of the C_{18}Baker-10SPE columns was tested on the synthetic solution. Organic acids concentration of the synthetic solution was determined directly and after treatment with C_{18}Baker-10SPE columns by IC. The amount of total sugar as glucose was also determined spectrometrically.

Results and Discussion

A calibration curve for each organic acid was calculated by regressing the peak area against the corresponding acid concentration from six standards (5-50 mg/L) in triplicate. The calibration curve for each acid was linear and determination coefficients ranged from 0.9990 to 1.000. The set of data obtained in two calibration experiments, one with standard solution (namely standard calibration SC) and another one with standard additions (AC) were used for each organic acids. The comparing both the analytes, content in different calibrations tested the coefficients of the analytical results. The results from SC and AC are not significantly different, so calculated of concentration of organic acids in plum puree can be carried out directly by the SC method. The results were calculated by using the calibration curve obtained from the injection of aqueous organic acid standard solutions directly to the IC, since there were no any significant change in the peak areas and retention times of chromatograms obtained by injection of organic acid standard solutions treated with C_{18}Baker-10SPE to the IC.

Shown in Fig. 3a is the chromatogram obtained by direct injection of standard solution containing 50 mg/L of each tartaric, malic and propionic acids to the IC. The retention times and pKa constants of these acids are given in Table 2.

(a)

Malic acid

Tartaric acid

Propionic acid

Conductivity

Time (min)

(b)

Malic acid

Tartaric acid

Propionic acid

Conductivity

Time (min)

(c)

Malic acid

Tartaric acid

Propionic acid

Time (min)
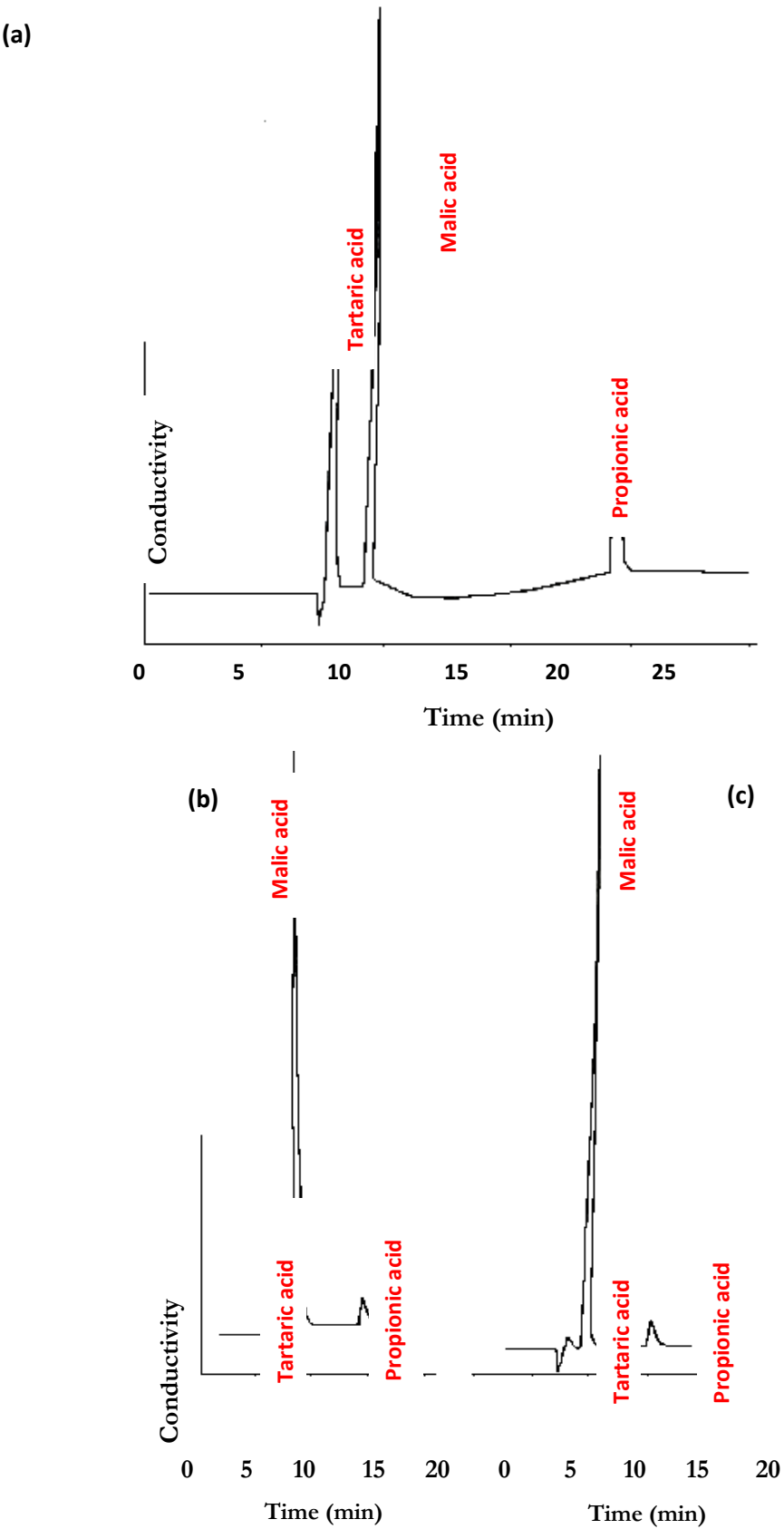
Figure 3. (a) The IC chromatograms for the organic acids mixture with each of 50 mg/L, (b) 1/10 diluted plum puree sample injected directly (c) for that injected after the treatment with C_{18}Baker-10SPE column.

Table 2. The pKa and retention times of organic acid with the concentration of 50 mg/L.

Organic acid	pKa1	pKa2	Retention time (min)
Tartaric acid	3.03	4.37	8.27
Malic acid	3.50	5.05	9.32
Propionic acid	4.87	-	16.20

As seen from Table 2, the smaller the pKa value of the organic acid, the shorter retention time. Because the mechanism for separation of these carboxylic acids is primarily ion exclusion. IEC has developed into a very useful technique for separating relatively weak bases, small weak acids, and hydrophilic molecular species such as lower alcohols and the carbohydrates. The analytical method actually involves the separation of molecular species rather than ions. Of course, ions can often be readily converted into molecular species as when anions of weak acids as acidified. Ionic material is rejected by anion or cation exchange resin and pass through quickly, but non-ionic substances are held up and come through slowly. An acid with a large alkyl group would have a greater hydrophobic attraction and thus a longer retention time. In IEC, stronger acids (lower pKa) are eluted more rapidly than weaker acids, presumably because the stronger acids are incompletely converted to molecular form. If this were the case, coexistence of the ionic and molecular forms might produce broader peaks; however, these compounds produce very sharp peaks. A better explanation might be that stronger acids are more polar, and therefore interact less strongly with the resin matrix.

Fort he removal of molecules as sugar, solid phase extraction on C_{18}Baker-10SPE cartridges were selected, then the best conditions to perform the procedure were chosen always by taking into account the idea of obtaining the highest recoveries. The efficiency of the C_{18}Baker-10SPE was tested on synthetic solution. Experiments were always performed six times and the results are summarized in Table 3.

Table 3. The efficiency of the C_{18}Baker-10SPE column (n=6)

Compound	Initial conc. (mg/L)	Conc. after treatment with C_{18}Baker (mg/L±sd)	Recovery (%)
Glucose	10.0	4.10±0.30	40
Tartaric acid	10.0	10.40±1.70	104
Malic acid	50.0	49.80±1.85	99.6
Propionic acid	10.0	9.00±1.54	90

As seen from Table 3, while 60% of total sugar as glucose in synthetic solution is held on C_{18}Baker-10SPE columns, 40% of it does not retain and passes the columns. Nevertheless, tartaric acid and malic acid are hardly held with the recoveries of 104% and 99.6%, respectively. The recovery of propionic acid is found as 90%. These results reveal that C_{18}Baker-SPE column is suitable for analysis of organic acids by IC, used for removal of matrices as sugar.

Total sugar as glucose determined in the plum puree solution (1.000 g/100 mL of deonised water) was 14.7%±1.20, whereas it was found 5.80%±1.0 after the treatment with C_{18}Baker-10SPE column. In other words, 8.9% of sugar was retained on the column. The chromatograms obtained for the 1/10 diluted samples injected directly to IC and injected after the treatment with C_{18}Baker-10SPE column were given in Fig. 3b,c. If these are compared, it is seen that there are no any difference at the peaks of organic acids after the treatment of sample solution with C_{18}Baker-10SPE column. Exceptionally, there is a small decrease at the peak overlaps resulted from the matrix, even in the direct injection of the samples. However, the samples often contain both organic acids and carbohydrates (sugars), and it is desirable to perform the analysis in the same run. Wines, for

example, contain organic acid, residual sugars and alcohols can be analyzed using ion exclusion type columns. Mono, di- and polysaccharides, alcohols, sugar and organic acids are often present together in food and drink. However, the matrix compounds, such as sugar, plugs the separation column and shorten the column life. Consequently, background problems are encountered and baseline signal increases, causing gradual losses of accuracy of the results; however employing a C_{18}Baker-10SPE column could alleviate these problems.

The organic acids concentrations were calculated by using peak areas from the IC chromatograms obtained by direct injection of the plum puree solution diluted 10 times and by injection after treatment with C_{18}Baker-10SPE column are given in Table 4 and Figure 4 which depicts the results of the plum puree solution diluted 10 times and for 100 g of sample. It was found that when the plum puree samples were subjected to IC analysis without any treatment, standard deviation is higher than treatment with C_{18}Baker-10SPE column. In addition, it was determined that plum puree is very rich in malic acid which is very important because of helps potentiate flavor.

Table 4. The organic acids conc. of plum puree, determined by direct injection after treatment with C_{18}Baker-10SPE column (n=6).

Organic acids	Direct injection (mg/L±sd)	After treatment with C_{18}Baker-10SPE column (mg/L±sd)	In 100 g of sample (mg±sd)
Tartaric acid	10.83±1.08	10.00±0.53	1000±53
Malic acid	77.90±5.62	78.27±1.70	7827±170
Propionic acid	18.15±1.26	17.10±0.60	1710±60
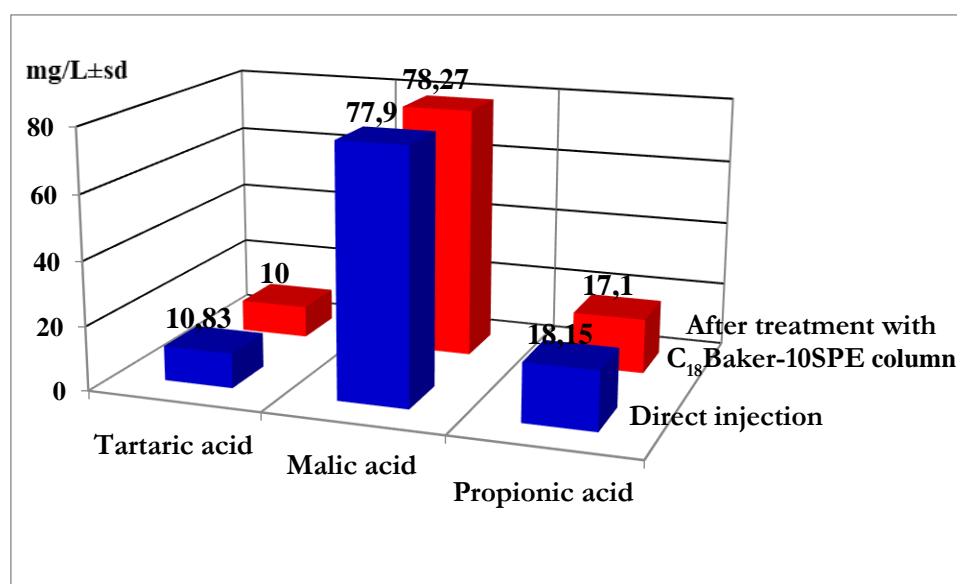
Figure 4. The organic acids conc. of plum puree, determined by direct injection after treatment with C_{18}Baker-10SPE column (n=6)

As a conclusion, it may be stated that the proposed treatment with C_{18}Baker-10SPE column method, for removal of matrices as sugar, simple, improves recovery and has repeatibility in the organic acids analysis by IC. This method could be helpful in improving routine quality control for organic acid analysis in fruit juice and puree.

References

Alcázar, A., Fernández-Cáceres, P.L., Martı, M.J., Pablos, F. & González, A.G. (2003) Ion chromatographic determination of some organic acids, chloride and phosphate in coffee and tea. *Talanta, 61(2)*, 95-101. https://doi.org/10.1016/S0039-9140(03)00244-3.

Cai, Y., Luo, Q., Sun, M. & Corke, H. (2004). Antioxidant activity and phenolic compounds of 112 traditional Chinese medicinal plants associated with anticancer. *Life Sciences, 74,* 2157-2184. https://doi.org/10.1016/j.lfs.2003.09.047.

Chen, Q.C. & Wang, J. (2001). Simultaneous determination of artificial sweeteners, preservatives, caffeine, theobromine and theophylline in food and pharmaceutical preparations by ion chromatography. *Journal of Chromatography A, 937*, 57-64. https://doi.org/10.1016/S0021-9673(01)01306-1.

Chun, O.K., Kim, D, Moon, H.Y., Kang, H.G. & Lee, C.Y. (2003). Contribution of individual polyphenolics to total antioxidant capacity of plums. *Journal of Agricultural and Food Chemistry, 51,* 7240-7245. https://doi.org/10.1021/jf0343579.

Davis PH (1972). Flora of Turkey and the East Aegean Islands, vol. IV. Edinburgh, UK: Edinburgh University Press.

Lui, W., Nisar, M.F. & Wan, C. (2020). Characterization of Phenolic Constituents from *Prunus cerasifera* Ldb Leaves. *Journal of Chemistry, 5976090*, 5 pages. https://doi.org/10.1155/2020/5976090.

Masson, P. (2000). Influence of organic solvents in the mobile phase on the determination of carboxylic acids and inorganic anions in grape juice by ion chromatography. *Journal of Chromatography A, 881,* 387-394. https://doi.org/10.1016/S0021-9673(00)00164-3.

Qui, J. & Jin, X. (2002). Development and optimization of organic acid analysis in tobacco with ion chromatography and suppressed conductivity detection. *Journal of Chromatography A, 950,* 81-88. https://doi.org/10.1016/S0021-9673(02)00034-1.

Sapuntzakis, M., Bowen, P.E., Hussain, E.A., Wood, B.D. & Farnsworth, N.R. (2010). Chemical Composition and Potential Health Effects of Prunes: A Functional Food?. *Critical Reviews in Food Science and Nutrition, 41,* 251-286. https://doi.org/10.1080/20014091091814.

Sarıdaş, M.A., Kafkas, E., Zarıfıkhosroshahı, M., Bozhaydar, O. & Paydaş Kargı, S. (2016). Quality traits of green plums (*Prunus cerasifera* Ehrh.) at different maturity stages. *Turkish Journal of Agriculture and Forestry, 40,* 655-663. doi:10.3906/tar-1603-45.

Soufleros, E.H., Pissa, I., Petridis, D., Lygerakis, M., Mermelas, K., Boukouvalas, G. & Tsimitakis, E. (2001). Instrumental analysis of volatile and other compounds of Greek kiwi wine; sensory evaluation and optimisation of its composition. *Food Chemistry, 75*, 487-500. https://doi.org/10.1016/S0308-8146(01)00207-2.

Trifirò, A., Saccani, G., Gherardi, S., Vicini, E., Spotti, E., Previdi, M.P., Ndagijimana, M., Cavalli & S., Reschiotto, C. (1997). Use of ion chromatography for monitoring microbial spoilage in the fruit juice industry. *Journal of Chromatography A, 770,* 243-252. https://doi.org/10.1016/S0021-9673(97)00049-6.

Climate Change and Livestock Production

Müge ERKAN CAN[1]

Introduction

It is widely predicted that climate and weather variability would rise as the earth warms. Humans, animals, and environmental systems will all be significantly impacted by changes in climate events and weather patterns. It is anticipated that an increase in the frequency of heat stress, drought, and floods events will have a negative impact on many different industries around the world.

The production of livestock has a significant impact on environmental factors, particularly climate change. Increases in temperature have a detrimental effect on animal reproduction, growth, meat and milk yield and quality, well-being, and immune response. The livestock industry interacts with many other industries, plays a significant part in agriculture in emerging countries, and there is a growing demand for animal-derived products worldwide. It is obvious that the cattle sector needs to grow. Extreme weather's negative impacts have a harmful influence on livestock. There is considerable doubt that the effects of climate change on livestock performance will be negative in many areas, as predicted by the majority of models. The viability of cattle systems around the world is seriously threatened by climate change. Scholars have come to acknowledge the truth of climate change and its effects. Even though global warming's effects won't be felt uniformly, severe issues can be averted by recognizing climate change early enough.

Based on these reasons, the consequences of climate change on livestock production are discussed in this review article, along with some recommendations for production methods.

Climate Change

The globe is experiencing numerous difficulties, including feeding the expanding population and deal with serious environmental problems including the depletion of natural resources and catastrophic climate change. With a few exceptions, the majority of studies that look at the future of the food system recommend that food security and sustainable agriculture should be the main goals of any global or national plan. One of the biggest threat to the world is climate change, which affects crop yields, water availability, and land use at a time when people are rapidly expanding, some times occuring to food crisis. Increased temperatures throughout the growing season can have a significant influence on farm income, food security, and agricultural output (Battisti & Naylor, 2009).

Numerous variables contribute to climate change, which has a variety of effects on human and animals systems. Recent assessments provide a broad overview of the current and projected effects of climate change, highlighting the extensive degradation of ecosystems, the planet's dwindling capacity to adapt to these impacts, as well as the negative socioeconomic repercussions. Ecosystems on land and in the ocean have already seen catastrophic extinctions of species, some

---

[1] Asst. Prof., Çukurova University, Agricultural Structures and Irrigation

of which are permanent. Across all evaluated regions, adverse climate change consequences on agriculture and crop output are noticeable.

The economic sectors that constitute the foundation of our food supply (fisheries, agriculture, freshwater, forestry), as well as a crucial source of livelihood for the poor, are being negatively impacted by ongoing environmental devastation. We rely on key ecosystems all around the world, yet 60% of them have already undergone degradation, pollution, or unsustainable use. These ecosystems include soils, waters, forests, and fisheries (MEA, 2005). Ecosystems will be directly impacted by climate change in a variety of ways, such as changes to the productivity and growth regions of cultivated and non-cultivated vegetation. Additionally, it is anticipated to alter the frequency of extreme climatic occurrences, posing hazards to ecosystems. Many species, especially those already in danger because of things like low population numbers, restricted or unsteady habitats, and narrow climatic ranges, are predicted to face greater extinction risks as a result of climate change. Climate change is expected to further adversely affect key development challenges. The problems and risks mentioned about climate change are summarized in the Table 1 below under the main headings (Adapted from MEA, 2005).

Table 1. Different subjects affected by the climate changes

Subjects	Way of affecting	Expected risk level
Exacerbate the loss of biodiversity	Increasing the likelihood of extinction for many species, especially those already in danger because of things like low populations, patchy habitats, and restricted climatic ranges	Medium - high certainty
Water quality	In many arid and semiarid areas, it is expected that water supply and quality would decline. Pollution and depletion of clean water resources	High certainty
Natural disasters	It is projected that the risk of floods and droughts is increase	High certainty
Natural events	It is projected that sea level rise by 8–88 centimeters	-
Undesirable possibilities	In some areas, it is anticipated that biomass production and hydropower would become less reliable	High certainty
Undesirable possibilities	Along with extreme weather-related traumatic injury and death, heat stress mortality and dangers to poor nutrition in other places	High certainty
Undesirable possibilities	In many areas, it is expected that the prevalence of waterborne illnesses like cholera as well as vector-borne illnesses like malaria and dengue will rise	Medium - high certainty
Decreasing agricultural productivity	In the tropics and subtropics areas, agricultural productivity is predicted to decline for nearly any amount of warming	Low to medium certainty
Decreasing fisheries	Projected adverse effects on fisheries	-
Undesirable possibilities	The projected changes in climate are may when combined with changes in land use and the spread of exotic or alien species, they are likely to have a negative impact on species' ability to migrate and to survive in fragmented habitats	Medium - high certainty
Global warming	There will be a significant net harmful impact on ecosystems (ecosystem services) worldwide if global mean surface temperature increases more than certain levels.	Medium certainty

Greenhouse gas (GHG) emissions	The amount of heat that would come from any stabilized greenhouse gas concentration is subject to a wide range of uncertainty, but according to IPCC forecasts, this would necessitate an eventual CO_2 stability level of less than 450 parts per million carbon dioxide.	Medium certainty
Food supply shortage	Access to clean water and food will become more difficult	Low - medium certainty

The poorest and most vulnerable individuals will suffer the most as a result of climate change and will touch everyone. Researchers concurred that one of the causes of rural poverty and one of the issues it needs to solve is climate change. Despite being a global issue, impoverished people in developing nations that significantly rely on the natural resource base for their livelihoods are more severely affected by climate change's negative effects. The most climate-sensitive economic sectors, agriculture and livestock raising, are extremely important to rural poor populations' ability to survive.

Climate change and livestock

According to research, up to 34% of current lands used for growing crops and raising livestock may no longer be appropriate by the end of the century if temperatures rise as predicted. The areas which are most at-risk are regions where the world's top livestock-producing countries are located such as Brazil, China and India (Reintjes, 2022). Crops and agricultural production are small part of how climate change may affect the production of food. The impact of climate change on grassland and rangeland productivity will have significant effects on the production of dairy, meat, and wool. Loss of resources will result from a lack of water and an increase in the frequency of drought in some nations. As a result, already-existing food insecurity and violence over limited resources would worsen, as seen numerous African countries (IFAD, 2009).

According to the IPCC, the increase in the average global surface temperature by 2100 might range from 1.8°C to 4.0°C. About 20 to 30% of plant and animal species are predicted to be in danger of going extinct with temperature increases of 1.5° C to 2.5° C (FAO, 2007) which will have devastating effects on food security in developing nations (IPPC, 2007). Animals suffering from heat exhaustion will consume less food at a slower rate, which will have a negative impact on their ability to grow (Rowlinson & et al., 2008).

The link between cattle production and climate change is becoming increasingly obvious. Farming animals is extremely harmful to the environment and the health of the earth overall since it requires a tremendous quantity of water, destroys forests, and emits a significant amount of greenhouse gases. According to research, there are a number of changes that may be made to reduce food-related climate emissions, including dietary changes. Farm animal production for food production has a significant negative impact on the environment. Animal agriculture contributes to water pollution, the destruction of forests and other wild areas that assist to control the planet's atmosphere, and the emissions of greenhouse gases like nitrous oxide and methane. The sustainable intensification of industrial systems, which has significant effects on the wellbeing of billions of animals as well as the environment, is frequently the focus when livestock systems are mentioned.

Methane and nitrous oxide are the two primary greenhouse gases produced by the practice of raising farmed animals. It is estimated that animal agriculture accounts for at least 16.5 percent of greenhouse gas pollution worldwide. Cattle, goats, and sheep, which are ruminant animals frequently reared for food, release methane during the enteric fermentation process that occurs while they digest their meal. Microbes in the animals' digestive systems break down and ferment plant materials like cellulose, starches, sugars, and fiber throughout this process. This method is

quite efficient. The "rumen," the largest stomach chamber of ruminants like cows, allows them to consume plants and crop waste that humans are unable to. Methane, a hazardous gas produced by this process and mostly discharged into the atmosphere via animal burps, is a byproduct. Another source of emissions is methane from livestock manure, which is particularly important in concentrated animal feeding operations or in hogs and dairy cattle that store waste as a liquid. Globally, there is an urgent need to maintain the biodiversity that supports food production and cut greenhouse gas (GHG) emissions that contribute to climate change by at least 80% in wealthy nations.

Impact of climate change on livestock

Livestock output has already been impacted by climate change, both directly and indirectly through the effects of heat stress on animal productivity. Its effects on grassland, species distribution, and illnesses have indirectly impacted cattle output as well. As the world's temperatures rise, these effects will worsen. Livestock may be more susceptible to infections because zoonotic diseases - ailments that spread from animals to humans - are more sensitive to climate change than pathogens that only affect humans or other animals. As the climate warms, the ranges of disease-carrying insects and other arthropods will grow, and more extreme weather events brought on by climate change will also accelerate the spread of illness.

Changes in the production and quality of feed crops and forage e (Chapman & et al., 2012; IFAD, 2010; Polley & et al., 2013; Thornton & et al., 2009), water availability (Henry & et al., 2012; Nardone & et al., 2010; Thornton & et al., 2009), animal breeding and milk production (Henry & et al., 2012; Nardone & et al., 2010; Thornton & et al., 2009), illnesses (Nardone & et al., 2010; Thornton & et al., 2009), reproduction (Nardone & et al., 2010), and biodiversity (Reynolds & et al., 2010) are just a few of the potential effects of climate chance on livestock (Rojas-Downing & et al., 2017).

The factors classified according to the direct and indirect effects of climate change are given in Table 2 (Adapted from Cheng & et al., 2022).

Table 2. Direct and indirect effects of climate change

Impact	Potential Results	Main Reasons
Direct	Reduced/Decline/Negatively affected: Feed intake, animal yield (milk, meat etc), reproductive, immune functions Increased: Mortality	Rising temperatures Heat stress
Indirect	Changes: Crop yields, composition of pastures, quality of forage	Increase in atmospheric CO_2 levels and temperature
	Increasing water consumption, decreasing water resources	Rising temperatures Heat stress
	Greater seasonal fluctuation in the availability of resources	Extreme climatic events occurring more frequently
	Increasing pest, parasite and disease	Temperature rise and alters to the precipitation pattern

Collier & et al., 2019 reported that climate changes impacts on livestock both direct and indirect ways. Lacetera, 2019 stated that direct and indirect impacts of heat stress to the health of farm animals. Increased temperatures, as well as the frequency and severity of heat waves, are the

main causes of the direct consequences. Through metabolic disturbances, oxidative stress, and immunological suppression that result in infections and death, these environmental factors can have an impact on livestock health. The indirect consequences include those related to changes in feedstock supply and water quality as well as the persistence and spread of diseases and/or their vectors. Wittmann & et al., 2001 simulated a 2 °C rise in temperature, and under these circumstances, their model showed that Culicoides imicola, the main vector of the bluetongue virus, might spread widely.

The primary climatic component that impacts animal production is the thermal environment. Air temperature, humidity, and airflow are all involved in this (Ames, 1980). The thermal comfort zone is a term used to describe the connection that best describes these situations. Animals exhibit at their peak efficiency and use the least amount of energy in this region (Nardone & et al, 2006). Being homeotherms, livestock must maintain their body temperature within a relatively small range in order to stay healthy and productive. Animals experience stress due to environmental temperatures that are either below or above the thermoneutral range. Adult cattle are reported to performance best in a range of temperatures between 5 °C and 15 °C (Hahn, 1999). Dairy cattle have a lower upper critical temperature than other types of animals (Wathes & et al. 1983).

When the ambient temperature veers outside of their thermal comfort range, animals experience thermal stress. Acclimatization refers to an animal's phenotypic reaction to a certain stressor (Fregly, 2011; Nardone & et al., 2006). Compared to cold stress, heat stress is more detrimental and has a bigger impact. Climate change is almost certainly raising temperatures as well, which will afterwards cause more heat stress and less cold stress (Collier & et al., 1982; Maibam & et al., 2018). As a result, while discussing thermal stress, heat stress has been the main subject (Cheng, 2022).

The cycle showing the relationship between animal production and heat stress is given in the Figure.1 (Adapted from Singh, 2022).
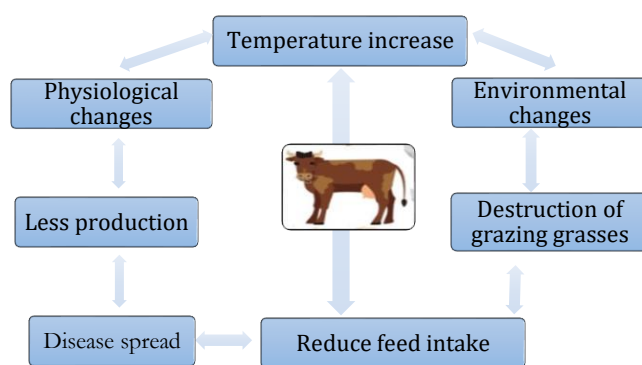
Figure 1. Cycle of heat stress impact on livestock

Heat stress in cows is result of hot, humid weather conditions. Increasing ambient temperature reduces the gradients driving convective, radiation, and conductive heat loss for air temperatures below an animal's skin surface temperature, which increases reliance on evaporative cooling (sweating and panting) to remove body heat. However, in hot, humid summer weather, the animal cannot sufficiently expel body heat, causing body temperature to rise. High relative humidity limits the effectiveness of evaporative cooling. Heat stress alters behavior and metabolism, resulting in decreased feed intake and metabolic activity, which lowers productivity (NRC 2001; Sirohi & Michaelowa, 2007). Animal functions can be hampered by the stress at least temporarily that results

when the magnitudes (intensity and duration) of adverse environmental conditions reach threshold limits with little or no possibility for relief (recovery) (Hahn & Becker 1984; Hahn, 1999; Sirohi & Michaelowa, 2007). Even extreme short-term events, such as summer heat waves and winter storms, can kill the weak animals (Balling, 1982; Hahn & Mader 1997), which can have a significant financial impact on livestock farmers (Sirohi & Michaelowa, 2007).

Researchers (Lacetera & et al., 1996; Nardone & et al., 1997; Ronchi & et al., 1995, 1997, 1999, Itoh & et al., 1998a,b; Moore & et al., 2005; O'Kelly, 1987; Sano & et al., 1983, 1985; Vizcarra & et al., 1997) clearly stated that heat-stressed altered glucose, protein and lipid metabolism and also liver functionality of subjects'. According to Wolfenson & Roth (2019), hot summer weather interferes with a number of reproductive processes, which lowers the conception rate in dairy cows all over the world. A significant impairment of reproductive processes, including disruption of oocyte developmental competence, attenuated embryonic growth and early embryonic death due to impaired hormone secretion, alteration of ovarian follicular growth dynamics, suboptimal corpus luteum development, and attenuated uterine endometrial responses, may occur when body temperature reaches 39.5 °C. Lin & et al. (2006) indicated that, broiler chickens' oxidative stress reaction to heat exposure should be taken into account.

One reaction to high ambient temperatures is decreased feed intake. Under severe heat stress, ruminants exhibit decreased hunger, gut motility, and rumination (Baile & Forbes, 1974; Yadav & et al., 2013). As ambient temperatures increase over 25–26 °C, lactating dairy cows show a decrease in feed intake, and this decrease happens more quickly above 30 °C (Kadzere & et al., 2002). Compared to other ruminants, goats are less vulnerable to heat stress. However, when the ambient temperature is more than 10 °C over their thermal comfort zone, their feed intake decreases naturally (Lu, 1989; Cheng, 2022).

Forages and grain/oil crop products make up the majority of the feed for livestock. Climate has an impact on both the production of those items as well as the availability of water for irrigation and soil moisture. As a result, the effects of climate change are primarily felt indirectly through its effects on the water and feed supply (Cheng, 2022). The effects of climate change on livestock are classified and given in the Table 3 (Adapted from Rojas-Downing & et al., 2017).

Table 3. Impacts of Climate Change on Livestock

Subject to be adversely affected	Main Reasons	Potential effects and potential possibilities
Quality and quantity of feeds	Increase in atmospheric CO_2 levels and temperature[1] (1.Chapman & et al., 2012, 2. IFAD, 2010, 3. Thornton & et al., 2008, 4. Thornton & et al., 2009, 5.Thornton & et al., 2015, 6. Baruch & Mérida, 1995)	Location, livestock system, and species all affect the quantity and quality of feeds as a result of climate change[2] By changing the dynamics of species competition as a result of changes in optimal growth rates, it will modify the composition of pastures[2,3,4,5] Extreme weather conditions (floods etc.), can change the shape and structure of roots, leaf growth and reduce overall output[6]
Diseases	Rising temperatures[7] (7.Nardone & et al., 2010, 8. Tubiello & et al., 2008)	Morbidity and death Spreading pathogens or parasites[7,4,8] Feed and water scarcity[7,4,8]
Water	As sea level rises salination[9] adds to chemical and biological contaminants and high concentrations of heavy metals in freshwater aquifers[7]	Water scarcity and depletion Salination may affect digestion, metabolism, fertility. Other chemicals and heavy metals may damage respiratory, cardiovascular, excretory,

	(9. Karl & et al., 2009)	skeletal, nervous systems, and impair hygienic standards[7] This situation will affect both livestock drinking water sources, and also pasture yield and feed production systems of livestock.	

Heat stress

Feed intake and nutrient utilization	Heat stress (10. Mader, 2003, 11.Chase, 2006, 12. Mader & Davis, 2004, 13. Wyman & et al., 1962,14. Lacetera & et al., 1996, 15. Lacetera & et al., 2003)	Impair metabolic and digestive functions[10] Increasing respiration rates[11] Thermal stress decreases feed intake[12,4,13] Negative energy balance and reduced weight gain[14,15]	
Animal production	Heat stress	Decreased production[7] Significant economic losses	
Reproduction	Heat stress (16.Hansen, 2007, 17. Wolfenson & et al., 2000, 18. Karaca & et al., 2002, 19. Mathevon & et al., 1998, 20.Kunavongkrita & et al., 2005	Impairment of embryo development, Reduced pregnancy rate[16,7,17] Lower sperm concentration and quality[18,19,20]	
Health	Heat stress	Severe health problems and illnesses	
Mortality	Heat stress	Heat stress could affect livestock mortality	

Rust (2019) demonstrates clearly how climate change by focus on adaptation impacts both extensive and intensive cattle production systems. It is crucial to have better understanding of how different livestock systems are affected by climate change and how to adapt to it. Varied adaptation methods must be put in place since the climate change will have different effects on extensive and intensive animal production systems (Bernabucci, 2019). For better disease prevention in the future, as well as for better mitigating and adapting responses of animals to heat stress, new methodologies, tools, and techniques should be developed and applied to link climatic data with disease surveillance systems (Lacetera 2019; Bernabucci, 2019).

It is clear that animal husbandry has a intensely negative impact on climate change. Greenhouse gas emissions can be shown as the main source of this negative effect. Various measures should be taken and scientific activities should be continued in order to break the circle caused by the negative interaction between livestock and climate change. Techniques for reducing greenhouse gas emissions from livestock have been compiled and presented in the Table 4 (Adapted from Llonch & et al., 2017).

Table 4. The main mitigation techniques for greenhouse gas (GHG) emissions described in literature

Approaches	Potential to reduce greenhouse gas emissions	Potential effects on welfare	
Antimethanogens		**Negative**	**Positive**
Chemical inhibitors	%33[1] - %50[2] - %5 ~ %91[3] (1.Abecia & et al., 2012; 2.Tomkins & et al., 2009; 3.Mitsumori & et al., 2012)	Hazards associated with the usage of halogenated chemicals, such as hepatotoxic, nephrotoxic, and carcinogenic effects (but exclude the use of 3-nitrooxypropanol)	IEE* as they reduce energy loss as a result of lower methane emissions uses to all direct antimethanogenic strategies
Electron receptors (nitrates)[(RR)]	%16[4] - %27[5]- >%30[6] - %17[7] (4.Van Zijderveld & et al., 2011; 5.Hulshof & et al., 2012; 6.Gerber & et al., 2013; 7.Troy & et al., 2015)	Toxicity	IEE*

Ionophores (monensin)[RR]	%3 ~ %5[8] %8 ~ %9[9] >%10[6] and %27 ~ %30[10] (8.Beauchemin & et al., 2010; 9.Appuhamy & et al., 2013; 10.Guan & et al., 2006)	Toxicity	Acidosis (LR) Rumen bloat (LR) Emphysema (LR) IEE
Dietary lipids[RR]	%3,8 (%1 - FI)[11] %5.4 (%1 - FI)[12] %10 ~ %30[6] and up to %40[13] (11. Martin & et al., 2010; 12.Beauchemin & et al., 2008; 13.Machmüller, 2006)	THBCS***** IDF**	Negative energy balance (LR) IEE*
DEI ***			
IDD[AA]****	%6.5[14] %10 ~ %16[15] %17[16] and %10 ~ %30[6] (14.Beauchemin & et al., 2011; 15.Lovett & et al., 2006; 16.Hales & et al.,2012)	THBCS***** Acidosis Higher risk of bloated rumen and Laminitis	Negative energy balance (LR)
Intensive housing[AA]	%8 ~ %9[17] %10 ~ %30[6] (17.Pinares-Patino & et al., 2007)	Increased social stress Inability to display natural behavior. Greater potential for disease spread	Reduced parasite loads
Enhancing welfare and health[AA]	%3% ~ %6 (by a %28 ~ 55%)[18] (18.Hospido & Sonesson, 2005)		Improved health A longer lifespan Reduction in the prevalence of mastitis in dairy cattle[18]
Boosting reproductive effectiveness[AA]	%4[14] (14.Beauchemin & et al., 2011)	Increased metabolic demand Poor body condition	Improved natal survival
Intensive breeding[AA]	%17 ~ %24[19] and %10 ~ %20[1] %19 ~ %23[2] (19. Garnsworthy, 2004.)		Poor health characteristics and metabolic disorders

LR: Lower risk	FI: Fat increase	AA: for all animals	RR: for restricted to ruminants.
*IEE: Improved energy efficiency		**IDF: Impaired digestive function	
***DEI: Decrease emission intensity (Ei)		**** IDD: Increase diet digestibility	***** THBCS: Too high body condition score

Livestock can be a key component of both adaptation and mitigation strategies. Technical and management approaches to lower livestock-related GHG emissions as well as the incorporation of animals into larger environmental services could all be considered mitigation measures (IFAD, 2009).

Applying effective cooling is a requirement and prerequisite to reducing heat stress. However, occasionally reducing summertime heat stress is insufficient to maintain reproductive function even after the stressor has passed. It is suggested that in order to increase fertility, cooling must be used in conjunction with other therapies. To increase the fertility of heat-stressed dairy cows, it may be necessary to use procedures such as improved ovulation timing, enhanced removal of damaged follicles, induction of ovulation in healthy follicles, embryo transfer, and progesterone supplementation before and after artificial insemination (Wolfenson & Roth, 2019; Bernabucci, 2019).

Responses to climate change include mitigation, which lessens the long-term impact of climate change, and adaptation, which lessens the vulnerability of people and ecosystems to climatic changes. But neither mitigation nor adaptation by themselves can completely counteract the effects of climate change. In order to address this concern, efforts must be concentrated on both adaptation and mitigation, or reducing the amount of gases that contribute to global warming that are released into the atmosphere. Presently, relatively few development plans encouraging sustainable livestock and agriculture practices have specifically mentioned taking action to help

local populations prepare for or mitigate the effects of climate change. To improve their capacity to adapt and respond to new threats, rural communities will need to engage in activities targeted at boosting their resilience (IFAD, 2009).

Crops and agricultural production are only a small part of how climate change may affect the production of food. The impact of climate change on grassland and rangeland productivity will have significant effects on the production of dairy, meat, and wool. Loss of resources will result from a lack of water and an increase in the frequency of drought in some nations. As a result, already-existing food insecurity and violence over limited resources would worsen, as seen numerous African countries (IFAD, 2009).

Results

In order to best manage the decline in production efficiency and the quality of animal products, the expansion of land desertification, and the deteriorating of animal health among the anticipated effects of climate change in the coming decades, decision-makers and institutions must support livestock sector.

There is a lot of research to support the idea that animals under heat stress perform significantly worse and producers be suffered significant economic losses. If systematic data is provided on the effect assessment of climate change on livestock productivity this situation may be very helpful to create appropriate adaptation and mitigation strategies to sustain livestock production in the changing climate scenario.

Since livestock is a significant source of income, it is crucial to identify appropriate solutions in order to preserve this industry as a profitable business while simultaneously enhancing profitability and lowering environmental pollution by minimizing the negative consequences of climate change.

REFERENCES

Abecia, L., Toral, P.G., Martín-García, A.I., Martínez, G., Tomkins, N.W., Molina-Alcaide, E., Newbold, C.J. & Yaňez-Ruiz, D.R. (2012). Effect of bromochloromethane on methane emission, rumen fermentation pattern, milk yield, and fatty acid profile in lactating dairy goats. *Journal of Dairy Science*, 95, 2027-2036.

Ames, D. (1980). Thermal Environment Affects Production Efficiency of Livestock. *BioScience*, 30, 457-460.

Appuhamy, R.N., Strathe, A.B., Jayasundara, S., Wagner-Riddle, C., Dijkstra, J., France, J. & Kebreab, E. (2013). Anti-methanogenic effects of monensin in dairy and beef cattle: a meta-analysis. *Journal of Dairy Science,* 96, 5161-5173.

Baile, C.A. & Forbes, J.M. (1974). Control of feed intake and regulation of energy balance in ruminants. *Physiol. Rev.*, 54, 160-214.

Balling, R.C. Jr. (1982). Weight gain and mortality in feedlot cattle as influenced by weather conditions: refinement and verification of statistical models. *In Center for Agricultural Meteorology and Climatology Report 82–1.* University of Nebraska-Lincoln, Lincoln, NE, USA, p 52.

Baruch, Z. & Mérida, T. (1995). Effects of drought and flooding on root anatomy in four tropical forage grasses. *Int. J. Plant Sci.* 156, 514-521.

Battisti, D.S. & Naylor, R.L. (2009). Historical Warnings of Future Food Insecurity with Unprecedented Seasonal Heat. *Science*, 323 (5911), 240-244.

Beauchemin, K.A., Janzen, H.H., Little, S.M., McAllister, T.A. & McGinn, S.M. (2011). Mitigation of greenhouse gas emissions from beef production in western Canada; evaluation using farm-based life cycle assessment. *Animal Feed Science and Technology* 166, 663–677.

Beauchemin, K.A., Janzen, H.H., Little, S.M., Mcallister, T.A. & Mcginn, S.M. (2010) Life cycle assessment of greenhouse gasemissions form beef production in western Canada: a casestudy. *Agric Syst.* 103(6), 371-379.

Beauchemin, K.A., Kreuzer, M., O'Mara, F. & McAllister, T. A. (2008). Nutritional management for enteric methane abatement: a review. *Australian J. Expt. Agric.* 48, 21-27.

Bernabucci, U. (2019). Climate change: impact on livestock and how can we adapt. *Anim Front.* 9(1), 3-5. Doi: 10.1093/af/vfy039

Chapman, S.C., Chakraborty, S., Dreccer, M.F. & Howden, S.M. (2012). Plant adaptation to climate change: opportunities and priorities in breeding. *Crop Pasture Sci.* 63, 251-268.

Chase, L.E. (2006). Climate change impacts on dairy cattle. Fact sheet, *Climate Change and Agriculture: Promoting Practical and Profitable Responses*, pp. 17-23.

Cheng, M., McCarl, B. & Fei, C. (2022). Climate Change and Livestock Production: A Literature Review. *Atmosphere*, 13, 140. Doi: 10.3390/atmos13010140

Collier, R.J., Beede, D.K., Thatcher, W.W., Israel, L.A. & Wilcox, C.J. (1982). Influences of environment and its modification on dairy animal health and production. *J. Dairy Sci.*, 65, 2213-2227.

Collier, R.J., Baumgard, L.H., Zimbelman, R.B. & Xiao, Y. (2019). Heat stress: Physiology of acclimation and adaptation. *Anim. Front.* 9, 12-19.

FAO (2007). Adaptation to Climate Change in Agriculture, Forestry, and Fisheries: perspective, framework and priorities. FAO, Rome.

Fregly, M.J. (2011). Adaptations: Some general characteristics. *In Comprehensive Physiology; American Cancer Society*: Atlanta, GA, USA pp. 3–15. https://onlinelibrary.wiley.com/doi/abs/10.1002/cphy.cp040101

Garnsworthy, P.C. (2004). *Livestock yield trends: implications for animal welfare and environmental impact*. In Yields of Farmed Species (Eds J. Wiseman and R. Sylvester-Bradley), Nottingham University Press, Nottingham.

Gerber, P.J., Vellinga, T., Opio, C. & Steinfeld, H. (2011). Productivity gains and emissions intensity in dairy systems. *Livestock Science*, 138, 100-108.

Guan, H., Wittenberg, K.M., Ominski, K.H. & Krause, D.O. (2006). Efficacy of ionophores in cattle diets for mitigation of enteric methane. *J. Anim. Sci.* 84, 1896-1906.

Hahn, G.L. (1999). Dynamic responses of cattle to thermal heat loads. *J Anim Sci.* 77(2), 10-20.

Hahn, G.L. & Mader, T.L. (1997). Heat waves in relation to thermoregulation, feeding behavior, and mortality of feedlot cattle. In: Proceedings *5th International Livestock Environment Symposium*, Minneapolis, MN, (pp. 563-571).

Hales, K.E., Cole, N.A. & MacDonald, J.C. (2012). Effects of corn processing method and dietary inclusion of wet distillers grains with solubles on energy metabolism, carbon-nitrogen balance, and methane emissions of cattle. *Journal of Animal Science*, 90, 3174-3185.

Hansen, P.J. (2007). Exploitation of genetic and physiological determinants of embryonic resistance to elevated temperature to improve embryonic survival in dairy cattle during heat stress. *Theriogenology*, 68(4), 242-249.

Hospido, A. & Sonesson, U. (2005). The environmental impact of mastitis: a case study of dairy herds. *Science of the Total Environment*, 343, 71-82.

Hulshof, R.B.A., Berndt, A., Gerrits, W.J.J., Dijkstra, J., Van Zijderveld, S.M., Newbold, J.R. & Perdok, H.B. (2012). Dietary nitrate supplementation reduces methane emission in beef cattle fed sugarcane-based diets. *Journal of Animal Science*, 90, 2317-2323.

IFAD (2010). Livestock and climate change. International Fund for Agricultural Development. (Accessed from https://www.ifad.org/en/on 16/06/2015).

IFAD (2009). International Fund for Agricultural Development. Livestock Thematic Papers. (Accessed from https://w w w.ifad.org/lrkm/index.htm on 16/06/2015).

IPCC (2007). Intergovernmental Panel on Climate Change. Fourth Assessment Report (Accessed from https://www.ipcc.ch/site/assets/uploads/2018/03/ar4_wg2_full_report.pdf on 16/06/2015).

Itoh, F., Obara, Y., Rose, M.T., Fuse, H. & Hashimoto, H. (1998a). Insulin and glucagon secretion in lactating dairy cows during heat exposure. *J. Anim. Sci.* 76, 2182-2189.

Itoh, F., Obara, Y., Rose, M.T. & Fuse, H. (1998b). Heat influences on plasma insulin and glucagon in response to secretogogues in non-lactating dairy cows. *Dom. Anim. Endocrinol.* 15, 499-510.

Kadzere, C.T., Murphy, M.R., Silanikove, N. & Maltz, E. (2002). Heat stress in lactating dairy cows: A review. *Livest. Prod. Sci.*, 77, 59-91.

Karaca, A.G., Parker, H.M., Yeatman, J.B. & McDaniel, C.D. (2002). Role of seminal plasma in heat stress infertility of broiler breeder males. *Poult. Sci.* 81, 1904-1909.

Karl, T.R., Melillo, J.M. & Peterson, T.C. (2009). *Global Climate Change Impacts in the United States*. U.S. Global Change Research Programme. Cambridge University Press.

Kunavongkrita, A., Suriyasomboonb, A., Lundeheimc, N., Learda, T.W. & Einarsson, S. (2005). Management and sperm production of boars under differing environmental conditions. *Theriogenology*, 63, 657-667.

Lacetera, N., Bernabucci, U., Ronchi, B. & Nardone, A. (1996). Body condition score, metabolic status and milk production of early lactating dairy cows exposed to warm environment. *Riv. Agric. Subtrop. Trop.* 90, 43-55.

Lacetera, N., Bernabucci, U., Ronchi, B. & Nardone, A. (2003). Physiological and productive consequences of heat stress: The case of dairy ruminants. Proc. of the *Symposium on Interaction between Climate and Animal Production: EAAP Technical Serie*, (pp. 7, 45-60).

Lacetera N. (2019). Impact of heat stress on animal health and welfare. *Anim. Front.*, 9(1), 26-31.

Llonch, P., Haskell, M. J., Dewhurst, R. J. & Turner, S. P. (2017). Review: current available strategies to mitigate greenhouse gas emissions in livestock systems: an animal welfare perspective. *Animal*, 11 (2), 274-284. Doi: 10.1017/S1751731116001440

Lovett, D.K., Shalloo, L., Dillon, P. & O'Mara, F.P. (2006). A systems approachto quantify greenhouse gas fluxes from pastoral dairy production asaffected by management regime. *Agricultural Systems*, 88, 156-179. Doi: 10.1016/j.agsy.2005.03.006

Lu, C.D. (1989). Effects of heat stress on goat production. *Small Rumin. Res.*, 2, 151-162.

Lin, H., Decuypere, E. & Buyse, J. (2006). Acute heat stress induces oxidative stress in broiler chickens. *Comp. Biochem. Physiol. A. Integr. Physiol.*, 144, 11-17.

Machmuller, A. (2006). Medium-chain fatty acids and their potential to reduce methanogenesis in domestic ruminants. *Agric. Ecosyst. Environ.*, 112, 107-114.

Mader, T.L. (2003). Environmental stress in confined beef cattle. *J. Anim. Sci.* 81, 110-119.

Mader, T.L. & Davis, M.S. (2004). Effect of management strategies on reducing heat stress of feedlot cattle: Feed and water intake. *J. Anim. Sci.*, 82, 3077-3087.

Martin, C., Morgavi, D.P. & Moreau, D. (2010). Methane mitigation in ruminants: From microbe to the farm scale. *Animal*, 4, 351-365.

Maibam, U., Hooda, O.K., Sharma, P.S., Upadhyay, R.C. & Mohanty, A.K. (2018). Differential level of oxidative stress markers in skin tissue of zebu and crossbreed cattle during thermal stress. *Livest. Sci.*, 207, 45-50.

Mathevon, M., Buhr, M.M. & Dekkers, J.M. (1998). Environmental, management, and genetic factors affecting semen production in Holstein bulls. *J. Dairy Sci.* 81, 3321-3330.

MEA (2005). *Ecosystem and Human Well-being: Synthesis. Millennium Ecosystem Assessment*. Island Press, Washington, DC.

Moore, C.E., Kay, J.K., VanBaale, M.J., Collier, R.J. & Baumgard, L.H. (2005). Effect of conjugated linoleic acid on heat stressed Brown Swiss and Holstein cattle. *J. Dairy Sci.* 88, 1732-1740.

Mitsumori, M., Shinkai, T., Takenaka, A., Enishi, O., Higuchi, K., Kobayashi, Y., Nonaka, I., Asanuma, N., Denman, S.E. & McSweeney, C.S. (2012). Responses in digestion, rumen fermentation and microbial populations to inhibition of methane formation by a halogenated methane analogue. *British Journal of Nutrition,* 108, 482-491.

Nardone, A., Ronchi, B., Lacetera, N., Ranieri, M.S. & Bernabucci, U. (2010). Effects of climate change on animal production and sustainability of livestock systems. *Livest. Sci.* 130, 57-69.

Nardone, A., Ronchi, B., Lacetera, N. & Bernabucci, U. (2006). Climatic Effects on Productive Traits in Livestock. *Vet. Res. Commun.* 30, 75-81.

Nardone, A. & Villa, E. (1997). Characterization, utilization and conservation of cattle germoplasm in the Mediterranean Area. *EAAP Publication*, 85, 109-122.

NRC (2001) *Nutrient requirement of dairy cattle.* National Research Council, National Academy Press, Washington, DC.

O'Kelly, J.C. (1987). Influence of dietary fat on some metabolic responses of cattle to hyperthermia induced by heat exposure. Comp. *Biochem. Physiol.* 87A, 677-682.

Pinares-Patino, C.S., Hour, D., Jouany, J.P. & Martin, C. (2007). Effects of stocking rate on methane and carbon dioxide emissions from grazing cattle. *Agriculture, Ecosystems and Environment*, 121, 30-46.

Reintjes, E. (2022). Food Systems and Livestock Production Under Climate Change: The IPCC's Sixth Assessment (Accessed from https://www.fairr.org/article/food-systems-and-livestock-production-under-climate-change/on 17/06/2015).

Rust J.M. (2019). The impact of climate change on extensive and intensive livestock production systems. *Anim. Front.* 9(1), 20-25.

Rowlinson, P., Steel, M. & Nefzaoui, A. (2008). Adapting Livestock Production Systems to Climate Change – Temperate Zones. Livestock and Global Change conference proceeding. Cambridge University Press, Tunisia. (pp. 61-63).

Ronchi, B., Bernabucci, U., Lacetera, N., Nardone, A. & Bertoni, G. (1995). Effetti dello stress termico sullo stato metabolico di vitelle di razza Frisona. *Zoot. Nutriz. Anim.* 21, 209-221.

Ronchi, B., Bernabucci, U., Lacetera, N. & Nardone, A. (1997). Effetti dello stress termico sullo stato metabolico-nutrizionale di vacche Frisone in lattazione. *Zoot. Nutriz. Anim.* 22, 351-363.

Ronchi, B., Bernabucci, U., Lacetera, N., Verini Supplizi, A. & Nardone, A. (1999). Distinct and common effects of heat stress and restricted feeding on metabolic status in Holstein heifers. *Zoot. Nutriz. Anim.* 25, 71-80.

Sano, H., Takahashi, K., Ambo, K. & Tsuda, T. (1983). Turnover and oxidation rates of blood glucose and heat production in sheep exposed to heat. *J. Dairy Sci.* 66, 856-861.

Sano, H., Ambo, K. & Tsuda, T. (1985). Blood glucose kinetics in whole body and mammary gland of lactating goats exposed to heat. *J. Dairy Sci.* 68, 2557-2564.

Sirohi, S & Michaelowa, A. (2007). Sufferer and cause: Indian livestock and climate change. *Climatic Change.* 85, 285-298. Doi: 10.1007/s10584-007-9241-8

Singh, R. (2022). Impact Of Climate Change On Livestock. Pashudhan Praharee. (Accessed from https://www.pashudhanpraharee.com/impact-of-climate-change-on-livestock-2/on 18/06/2015).

Thornton, P.K., Herrero, M., Freeman, A., Mwai, O., Rege, E., Jones, P. & McDermott, J. (2008). *Vulnerability, climate change and livestock: Research opportunities and challenges for poverty alleviation.* International Livestock Research Institute (ILRI), Kenya.

Thornton, P.K., Boone, R.B. & Ramirez-Villegas J. (2015). Climate change impacts on livestock. CGIAR Resrach program on Climate Change, Agriculture and Food Security (CCAFS), Working Paper No. 120.

Thornton, P.K., Van de Steeg, J., Notenbaert, A. & Herrrero, M. (2009). The impacts of climate change on livestock and livestock systems in developing countries: A review of what we know and what we need to know. *Agric. Syst.* 101, 113-127.

Tomkins, N.W., Colegate S.M. & Hunter R.A. (2009). A bromochloromethane formulation reduces enteric methanogenesis in cattle fed grain-based diets. *Animal Production Science*, 49, 1053-1058. Doi: 10.1071/EA08223

Troy, S.M., Duthie, C.A., Hyslop, J.J., Roehe, R., Ross, D.W., Wallace, R.J., Waterhouse, A. & Rooke, J.A. (2015). Effectiveness of nitrate addition and increased oil content as methane mitigation strategies for beef cattle fed two contrasting basal diets. *Journal of Animal Science* 93, 1815-1823.

Tubiello, F., Schmidhuber, J., Howden, M., Neofotis, P.G., Park, S., Fernandes, E. & Thapa, D. (2008). *Climate Change Response Strategies for Agriculture: Challenges and Opportunities for the 21st Century.* The World Bank, Washington, DC.

Van Zijderveld, S.M., Gerrits, W.J.J., Dijkstra, J., Newbold, J.R., Hulshof, R.B.A. & Perdok, H.B. (2011). Persistency of methane mitigation by dietary nitrate supplementation in dairy cows. *Journal of Dairy Science.* 94, 4028-4038.

Vizcarra, J.A., Wettemann, R.P., Spitzer, J.C. & Morrison, D.G. (1997). Body condition at parturition and post partum weight gain influence luteal activity and concentrations of glucose, insulin, and nonesterified fatty in plasma of primipaourus beef cows. *J. Anim. Sci.* 76, 927-936.

Wathes, C.M., Jones, C.D.R. & Webester, A.J.F. (1983) Ventilation, air hygiene and animal health. *Vet Rec*, 113(24), 554-559.

Wolfenson, D., Roth, Z. & Meidan, R. (2000). Impaired reproduction in heat-stressed cattle: basic and applied aspects. *Anim. Rep. Sci.*, 6(1-3), 535-547.

Wolfenson D., & Roth, Z. (2019). Impact of heat stress on cow reproduction and fertility. *Anim. Front.*, 9(1), 32-38.

Wyman, O., Johnson, H.D., Merilan, C.P. & Berry, I.L. (1962). Effect of ad libitum and force feeding of two rations on lactating dairy cows subject to temperature stress. *J. Dairy Sci.*, 45, 1472-1478.

Wittmann, E.J., Mellor, P.S. & Baylis, M. (2001). Using climate data to map the potential distribution of Culicoides imicola (Diptera: Ceratopogonidae) in Europe. *Rev. Sci. Tech.* 20, 731-740.

Yadav, B., Singh, G., Verma, A.K., Dutta, N. & Sejian, V. (2013). Impact of heat stress on rumen functions. *Vet. World.*, 6, 992-996.

Thermodynamic Investigation on the Effects of Fouling Factor For Residantial Heating System

Nail Burak ELİBOL [1]
Oğuz ARSLAN [2]

Introduction

The energy demand arising from the demands has been attempted to be met by means of fossil fuels in direct proportion to overpopulation and technological developments, but this has resulted in a decrease in fossil fuel reserves over time. Due to decreasing resources, the demand for fossil fuels has increased, leading to new energy technologies and more effective and efficient energy use. Given the rising demand for energy and the desire to lessen the environmental impact of fossil fuels, more effective energy utilization has assumed significance. For this reason, it has created a new energy issue in terms of the efficient use of energy. Therefore, it has become a necessity to improve energy efficiency in individual heating systems and to use and research more efficient systems. For example, in buildings that need heating in Europe, the average heating requirement is 40%. In addition, the amount of energy demanded is greater than 70%. Heating is an important need, and indirectly evaluating panel radiators and other heating devices in terms of efficiency in the energy consumption of the related heating need, as well as conducting research on this subject, has created a significant focus of attention on energy efficiency(Gelis, 2021). Many researchers have studied the factors that have an impact on how effectively heating systems perform in specific homes and may result in excessive energy consumption as a result of these effects in order to meet all of these heating needs. These researchers have focused on using energy sources that are less harmful to the environment and more environmentally friendly for use in specific heating systems(Gelis, 2021).

The parameters of sediment, accumulation and fouling formed by exposing the heat exchanger to lake water were investigated, and the changes in the fluid temperature, fluid flow rate and surface area to which the heat exchanger is exposed along with the time the heat exchanger is left in the fluid water are analyzed. As a result, in this study, the fouling conditions were examined by keeping the heat exchanger waiting for a minimum of 45 days, and it has also been stated that low speed and high temperature adversely affect the amount of fouling (Kukulka & Devgun, 2007).Differences between metal foam heat exchangers and common heat exchangers were investigated. The thermal performance of the system against particulate fouling during the flow rate, fluid type and heat transfer was investigated. As a result, it has been understood that the efficient thermo-physical properties of the porous metal foam are more preferable than the finned heat exchangers used in other industries. It was concluded that more research should be done to reduce the fouling factors of the metal foamed heat exchanger and to prevent particulate fouling (Kuruneru, Vafai, Sauret, & Gu, 2020). Research has been done on the fouling effects of calcium carbonate. For this, the surface of the heat exchanger was examined under the physical steam method of Ti SS316L as a coating material. As a result of the experimental study, it was seen that

---

[1] M.Sc. Student, Bilecik Seyh Edebali University,
[2] Prof.Dr., Bilecik Seyh Edebali University,

the heat transfer coefficient is higher, the fouling time is slower and the corrosion resistance is higher on the titanium coated heat exchanger surfaces. Thus, it is stated that the thermal efficiency of the heat exchanger can become more effective and long-lasting (Wang, Tang, He, Kulacki, & Yu, 2019). A system is analyzed depending on the composite fouling of $CaCO_3$ and $CaSO_4$ in plate heat exchangers in various ways, flow rate, strip angle and temperature factors. As a result, it was observed that $CaCO_3$ had better adhesion than $CaSO_4$, and the fouling resistance decreased with the increase of the Re value, considering the increasing fouling removal rate. In line with these conditions, it was concluded that empirical changes such as temperature, Re values, fluid densities of $CaCO_3$ and $CaSO_4$, geometric strip angles of plates, flow rates are a very obvious cause of composite fouling (K. S. Song, Lim, Yun, Kim, & Kim, 2019). In heat recovery systems, a study was made on the thermal heat transfer efficiency of the system by using various types of heat exchangers in environments containing dirt and dust. As a result, it has been stated that H-type fins can reduce the heat transfer performance as well as reduce the fouling (Wang et al., 2019). Experiments with model systems reconstructing whey proteins from whey isolated powder (WPI) have been described. As a result, β-lactoglobulin (BLG) denaturation of Casein / WPI at the molecular level and fouling on pilot scale plate heat exchangers were taken into account in the pasteurization process. A large effect of casein/WPI on fouling was observed, indicating that casein has an effect on mineral and protein effects in case of fouling (Liu et al., 2020). A statistical model has been prepared that can be accurately predicted and measured by the parameters commonly used in industrial areas. As a result, it was stated in this study that fouling estimation is a clear method in terms of the use of industrial heat exchangers (Sundar et al., 2020). The causes of fouling factors in various systems have been examined and discussed. It is said that the causes of fouling can be in gaseous and liquid fluids or in bulk fluids, it seriously affects the surface heat transfer performance of the system over time. Consequently, considering the reviews, designers should examine more widely the non-fouling factors to achieve a higher degree of thermal efficiency: in line with these factors, it has been suggested that the design of the heat exchangers should be taken care of and thus, the efficiency performance can be improved further (Awais & Bhuiyan, 2019). The importance of protein fouling and control in the heating phase of whey powder concentrate (WPC) has been explained. For this purpose, based on the weight of protein-based fouling in whey, a dimensionless analysis method was applied to the experimental study, and the amount of fouling of the experimental heat exchanger was evaluated empirically. As a result, in the study evaluated by dimensional analysis, it is said that there is a different guide to the effects of fouling in plate heat exchangers (Gu et al., 2019). Excessive amount of impurities in the production of phosphoric acid by the dihydrate process, pipe clogging, acid temperatures reaching critical points, and fouling in the heat exchanger, affecting the operating performance for less than 5 days, were investigated. As a result, in this study, among 75 topologies showing the best results, a 7-neuron hidden layer network using the tangential sigmoid transfer function for the hidden and output layers was obtained. The ANN model optimized for thermal efficiency is said to reflect net results with variability in measurements AARD = 0.0639%, MSE = 0.00003, RMSE = 0.00573 and r^2ALL = 0.9998 (Aguel, Meddeb & Jeday, 2019). Calcium sulfate fouling was based on the process of analyzing the thermal fouling resistance of the heat exchanger in the fluid-solid fluidized bed heating process caused by forced particle-free and cylindrical particles in heat transfer. As a result, in this study, it was understood that the absolute mean percent relative error was between 0.6 and 22.8 compared to the fouling status and the data in the modeling proposed (Maddahi, Hatamipour & Jamialahmadi, 2019). To investigate the heat transfer efficiency of Na_2SO_4 mixtures at several different concentrations, a circulating fluidized bed model in three phases, solid-liquid and vapor phase, was designed and produced. Glass bead particles were determined as chemically inactive solid particles. As a result, it is mentioned that the heat transfer coefficient in the high density solution has less heat transfer conductivity than the low solution under the same conditions with the effect of physical conditions. The factors that will increase the heat transfer to the maximum

and their weights are 16.7% and 33.3%, respectively. The experimental range for Na_2SO_4 solutions is said to be 8.8% and 10.7% (Yang et al., 2020).In the industrial use of stack gases, the accumulation of particles and ash on the surface of the heat exchangers in large quantities was analyzed. In this modeling, it was stated that the increase in the stack gas inlet velocity and decrease in its concentration decreased the total mass amount of fly ash particles. It was stated that the total fouling mass decreased with increasing the particle wall temperature of $5\mu m$ size, whereas the total fouling mass of $9\mu m$-$15\mu m$ size particles remained constant despite the increase in the wall surface temperature (Xu et al., 2019).In general, it is aimed to improve the heat transfer surfaces, reduce resistance and finalize the relations in soot blowing effect. As a result, they observed that the absolute deviation between the estimated data and the results of the study was 4% (Tang et al., 2019). A study was conducted on the thermal efficiency of a chevron-type plate heat exchanger using CuO/water nanofluid. As a result, it has been concluded that using high low frequency vibration reduces the formation of fouling and decreases the thermal resistance. When exposed to vibration continuously, fouling delay was observed. At the same time, the total particle weight is said to be optimum 0.3% (Sarafraz et al., 2017). The design and modeling of the heat exchanger has been taken into account on the flow, thermal heat transfer and fouling resistances in the heat exchange pipes of the heat pump systems due to the sewage. In the modeling, an asymptotically distributed contamination was observed. It has been analyzed that this asymptotic value is inversely proportional to the square of the initial flow rate. This data is said to have a linear and decreasing correlation with the initial flow rate (Song et al., 2017). A study was carried out for the mineral and sediment accumulation layer on the different pipe surfaces of the heat exchanger. It has been observed that the effect of these five different materials increases the potential for fouling over time. It is said that the reason for this is that the accumulation is directly proportional to the increase in the thermal conductivity coefficient of the metal surfaces. The finding in SS316 metal is that the increase in the concentration with temperature increased the precipitation and since the shear stress linearly increased with the flow rate, it was also observed that the fouling decreased (Teng et al., 2017).In refineries where intense inorganic concentrations are followed, a thermo-hydraulic method was used to examine the fouling character in heat exchangers. As a result, it was stated in the study that it is an advanced model for the fouling problem and its diagnosis (Diaz-Bejarano et al., 2017).A common problem in environments with high particulate fouling in plate heat exchangers in aircrafts have been considered. As a result, it has been stated with statistical indexes that this modeling maximizes the incoming substances and provides the opportunity to better measure and understand the fouling status and that it is a reliable model in conditions where fouling estimation is difficult (Palmer et al., 2016).The fouling behavior of pure salt (Na_2SO_4) and mixed (Na_2SO_4 and NaCl) salt in a heat exchanger was considered. In this study, it is mathematically explained that sodium sulfate is the main pollutant in thermal fouling and that as the amount of sodium chloride in the mixed salt solution increases, the thermal fouling resistance gradually decreases (Lv, Lu & Ren, 2020).It was aimed to develop a method by replacing SUS304 with micro/nano scale holes by using electrical etching method in a stainless steel modified surface chevron plate heat exchanger. As a result of this experiment, as the working time increased, the $CaCO_3$ particles accumulated on the surface of the heat exchanger, therefore the fouling increased proportionally. It is said that the fouling behavior is at the minimum level in the heat exchanger whose surface is modified with PMMA (Ahn et al., 2019).An experimental study was carried out on crystallization fouling for rough and smooth surfaces in a double tube heat exchanger. In this experimental study, it was stated that turbulence occurred in the surface revision, increased the heat transfer coefficient and decreased fouling. It was stated that the additional wire pipe used on the outer surface of the inner pipe under the effect of fouling increased the heat transfer rate up to 180% and reduced the fouling by 86% (Hasan, Jwair & Craig, 2017).A study was conducted on the fouling effects on the plate heat exchanger of the most common bacterial species, sludge-forming bacteria (SFB) and iron bacteria (IB) in the fluidized water in the system. As a result, it was observed

that while the value and duration of the fouling resistance decreased with the increase of the flow rate, it also increased with the increase of the solution concentration. It has been said that the fouling resistance of SFB bacteria is maximum at 35°C (Xu et al., 2016).In order to better understand the thermal fouling resistance, a method in shell and tube heat exchanger was presented. As a result, these data were verified by taking the data of a heat exchanger used in a raw distillation unit with a value of 800t/h. Thus, the improved approach is said to allow for long-term monitoring of variables in HEN efficiency (Markowski, Trafczynski & Urbaniec, 2013).Long-term fouling test at different wastewater velocities and a fouling test with various mounting locations of the heat exchanger according to the pump was created through real pig farm wastewater. In the study, it was observed that the particle diameters accumulated on the surfaces were between 1.5-88 µm. In addition, it has been observed that there is negative fouling resistance in the fouling initial stage at medium and low fluid velocity. It is stated that the pump used in the study has higher fouling resistance values and average particle fouling size of the heat exchanger mounted at the suction inlet than the heat exchanger mounted at the ignition outlet. Thus, it is said that contamination with ash constitutes 71% by mass of total contamination on pipe surfaces (Shen et al., 2014).Studies have been carried out on plate heat exchangers. In the model examined, a model design was investigated on the amount of fouling in plate heat exchangers and the resulting slip stresses. As a result, in this study, the flow rate and flow rate of the water in the layer formed with the contamination thicknesses between 0.8mm and 2.5mm and the pollution thermal conductivity of 1.03W/mK were investigated. It is said that the model made is compatible with the design in the literature and the model used can be used for cooling water fouling analysis in industrial systems as well (Arsenyeva et al., 2013a).It has been mentioned that fouling in heat exchangers can create many equipment and investment costs if it is not done correctly for performance analysis. It was mentioned that the developed system allows detailed monitoring of contamination formation within the system boundaries in closed loop control. It is mentioned that thermal performance and pressure drops are better analyzed in the combined system. As a result, it is said that even if the thermal and flow parameters of this proposed system change, the contamination in the system can be observed without being affected by these changes. In this way, it is mentioned that unnecessary economic losses are avoided and the cleaning of the heat exchanger can be done more conveniently (Patil, Srinivasan & Srinivasan, 2022).The effects of contamination for the shell chamber in tube heat exchangers used in textile companies were investigated. Model tubes used in the chimney outlet of the ram machine, which is constantly exposed to stack gas, were placed and it was said that the fouling thickness reached 0.5mm within 3 months.As a result of the economic analysis, it was mentioned that the R value, which they determined as the ratio of the unit cost of natural gas to the cost of electricity, is above 15 and that fouling creates economic variability (Ceylan & ÇINAR, 2020).The flow around the finned tube group was analyzed using a cross-flow two-row heat exchanger of the waste gas/water type. As a result, in this study, which was carried out due to pollution, while it was stated that the heat transfer coefficient of the pipes in the first row was higher than the pipes in the second row, it has been stated that the fouling in the inner part of the pipe caused a change on the temperature, the fouling on the outside of the pipe affected the transfer coefficient very little, and the temperature change was greater with the increase in fouling (Łopata & Ocłoń, 2015a).A linear and time-invariant thermal analysis method has been developed due to fouling in a heat exchanger. As a result, it was stated that this method provided an idea that can determine more efficiently the temperature of the fluid liquid, the turbulence effect and the pipe surface roughness and the flow rates of the water entering the system and leaving the system in case of fouling (Al Hadad, Schick & Maillet, 2019).

In this study, the model investigated in individual heating systems is combi boiler and radiator connected heating system.The same type of fluid water at different temperatures passing through the main heat exchanger in the panel radiator and the boiler causes corrosion and sediment formation over time, causing the initial efficiency performance to be lost. For the 4.5kW house

taken in the design, the pollution parameters were 0,1-0,7-1,5mm in case of internal fouling and 0,1-0,3-0,5mm for external pollution, and calculations were made by combining them with each other (Al Hadad et al., 2019),(Łopata & Ocloń, 2015b),(Ceylan & Çınar, 2020),(Patil et al., 2022),(Arsenyeva et al., 2013b). At this point, depending on the fouling, the energy desired to be provided to the neighborhood cannot meet the heating need. This situation results in the pump circulation in the boiler to work more and the pressure losses to increase. In this study, efficiency analyzes will be examined depending on the fouling in the panel radiator and combi heat exchanger(Elibol, n.d.).

Material and Method

In this study, the changes in heat transfer and heat coefficients, which are used in the heat circuit of the houses and occur first in clean conditions and then depending on the fouling parameters, are explained in the system designed on the existing system. In our system, all calculations are presented with reference to the heat power of the radiator panels and the heat exchanger of combi boiler. As given in Figure 1. the flow diagram of the system is as shown below.
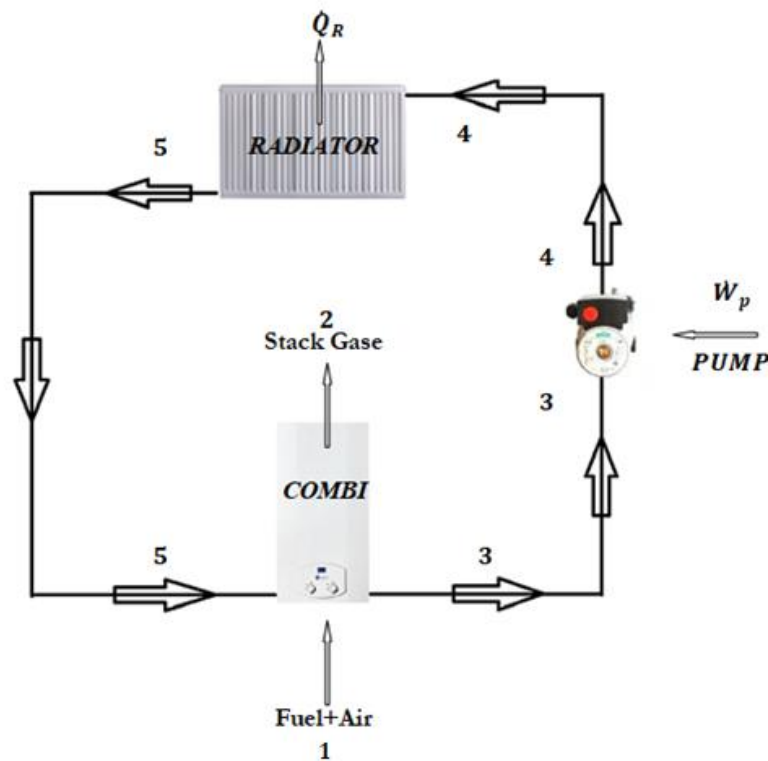
Figure 1. *Flow diagram of the heating system for a residance.*

Panel radiators through which hot flowing water passes are widely used in home, business and industrial areas. The heat generated by the panel radiators, the temperature of the water entering and leaving the radiator, as well as the type of the panel radiator, the number of fins, the model of the cross-section through which the fluid passes, and the fouling status cause differences in efficiency. Hot water passes through sections with different geometric shapes and is transferred to the air by means of heat, radiation and natural convection through the panel surface and fin. For this reason, it is very important to optimize the design and weight of panel radiators (Calisir, Yazar & Baskaya, 2019).

In the study, different fouling values were considered to form the cases. In total, 28 cases were taken into account, including the clean ones. The fouling values for the radiator with a conductivety of 0.8 W/mK were determined to be 0.1, 0.7, and 1.5 mm. For the heat exchanger of the combi

boiler, the internal fouling values were taken as in the radiator, whereas the external fouling values were taken as 0.1, 0.3, and 0.5 mm with a conductivity value of 0.1 W/mK (Al Hadad et al., 2019),(Łopata & Ocłoń, 2015b),(Ceylan & ÇINAR, 2020), (Patil et al., 2022), (Arsenyeva et al., 2013b). The formed cases are presented in Our model was designed by calculating the average distance of 1.2m between the combi boiler and the radiator in our system flow.

Table 1. *Formed cases related fouling of components.*

Cases	Raidator fouling (m)	Internal fouling (m)	External fouling (m)
1	-	-	-
2	0.0001	0.0001	0.0001
3			0.0003
4			0.0005
5		0.0007	0.0001
6			0.0003
7			0.0005
8		0.0015	0.0001
9			0.0003
10			0.0005
11	0.0007	0.0001	0.0001
12			0.0003
13			0.0005
14		0.0007	0.0001
15			0.0003
16			0.0005
17		0.0015	0.0001
18			0.0003
19			0.0005
20	0.0015	0.0001	0.0001
21			0.0003
22			0.0005
23		0.0007	0.0001
24			0.0003
25			0.0005
26		0.0015	0.0001
27			0.0003
28			0.0005

In Table 1, the whole fouling situation is given in detail.

Modeling of the Heating System Components

Aluminum panel radiators with a nominal height of 600 mm were used in the heating system. The structure of the radiator is given in Figure 2(O Arslan, 2008:117). In this context, a panel radiator with a unit length includes 30 heating channels equipped with finned surfaces.
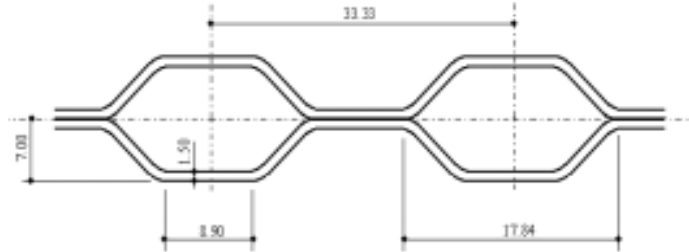
Figure 2. *Cross-sectional view of the used raditor panel.*

In the modeling of the radiator, the inlet temperature of the working fluid water was considered to be 60 °C, whereas the outlet temperature was taken as 45 °C for low-temperature heating applications in residences. The results of the model were compared with the value (1087 W) of the producer(Mec Tesisat, 2014). In the calculations, the indoor temperature was assumed to be 22 °C. The heat transferred to the indoor space from the radiator channels in the system is given as:

$$\dot{Q} = \dot{m}_{water} C_{p,water} \cdot \Delta T \tag{1}$$

In this part, while $\dot{m}_{water}$ refers to the mass flow rate of fluid water, $C_{p,water}$ refers to the specific heat of fluid water, ΔT indicates the difference between the inlet and outlet temperatures of fluid water. The cross-section of our radiator panel is referenced as indicated in Figure 3.
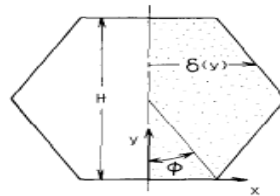
Figure 3. *Cross section for hexagonal pipes*

The velocity of the fluid as it passes through a radiator channel is:

$$v = \frac{\dot{m}}{\rho \cdot A} \tag{2}$$

Here: ṁ is the flow rate through a channel, ρ is the density of the fluid, A refers to the channel area. The hydraulic diameter in the radiator channels is given by:

$$D_h = \frac{4xA}{C} \tag{3}$$

Here: C refers to the channel circumference. The characteristics of heat transfer phenomena depend on the flow conditions, and it is expressed through the Reynolds number:

$$\text{Re} = \frac{v\,D_h\,\rho}{\mu} \tag{4}$$

Here (μ) refers to the kinematic viscosity of the fluid. The heat transfer rate is given by the Nusselt number (Nu). In the case of laminar flow ($Re<2300$)(Genceli, 2005a:312).It was obtained as 3.35 from the literature (Yutaka, Hiroshi & Faghri, 1988:2590–93).So, the convective heat transfer coefficient of the internal flow is given by:

$$h_i = \frac{Nu \cdot k_a}{d_h} \tag{5}$$

Here, k_a is the thermal conductivity of the fluid. The convective heat transfer coefficient of the outer flow (h_o) was accepted as 7.7 W/m²K (TMMOB Mechanical Engineers 2019). Total heat transfer coefficient is then given by:

$$U = \frac{1}{\frac{1}{h_i} + \frac{1}{h_o} + \frac{l}{k_{Al}} + \frac{l_{fouling}}{R_{fouling}}} \tag{6}$$

Here: k_{Al} is the conductivity for aluminum panels. It is taken as 200W/mK (Wellini, n.d.). $l_{fouling}$ is the thickness of the fouling, $R_{fouling}$ is the fouling resistance. Finally, the transferred heat from the base radiator is given by:

$$\dot{Q}_R = U \cdot A \cdot \Delta T \tag{7}$$

Since the panel radiators are equiped with finned surfaces, the heat transfer occured from this surfaces should also be taken into account. The total number of fins was calculated as 42 per unit radiator lenght. The fin conductivity was accepted as 240 W/mK(Halici, 2016:164). The fin structure of used radiator is given in Figure 4.
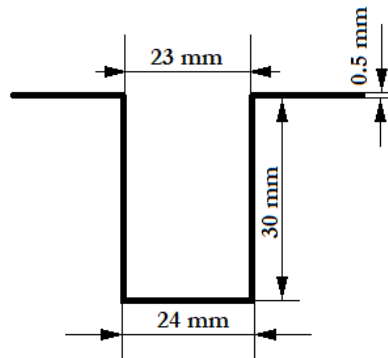
Figure.4. *Fin structure of the used panel radiator.*

The heat transfer occurs by natural convection through the fin structure. In this regard, the Grashof number (Gr) is issued. It is expressed by:

$$Gr = \frac{g \cdot \beta \cdot L_c^3 \, (T_Y - T_\infty)}{V^2} \tag{8}$$

Here: T_Y is the average temperature of the fluid. T_∞ is the ambient temperature. L_c is the panel radiator height. β refers to the coefficient of thermal expansion:

$$\beta = \frac{1}{T_f} \tag{9}$$

Here: (T_f) refers to the film temperature. Here, air is regarded as the ideal gas. The other important parameter is the Rayleigh number (Ra) since it determines the flow characteristic. *Ra* is given by:

$$Ra = Pr \times Gr \tag{10}$$

When Rayleigh number is $10^{-1} < Ra < 10^9$, the flow is assumed as laminar. The dimensionless heat transfer (Nu) is can be calcultes by Churchill and Chu relation for $10^{-1} < Ra < 10^{12}$ (Halici, 2016: 362):

$$Nu = \left[0.825 + \frac{0.387 Ra^{1/6}}{\left(1 + (0.492/Pr)^{9/16}\right)^{8/27}} \right]^2 \tag{11}$$

Here, Pr refers to the prandtl number. So, the convective heat transfer coefficient of the fins is given by:

$$h_f = \frac{Nu.k_{air}}{L} \tag{12}$$

Here, k_{air} is the conductivity of the air at the film temperature of T_f. With the assumption of insulated fins, the fin efficiency calculation is given by:

$$\eta_f = \frac{\tanh(mL)}{mL} \tag{13}$$

Here: L refers to the circumference and area multiplication. m is given by:

$$m = \sqrt{\frac{h_f P}{k A_f}} \tag{14}$$

Here, A_f refers to the fin area. h_f is fin heat transference coefficient, and P is the fin circumference. k is conductivity of the aluminum fin, and it was taken as 240W/mK(Halici, 2016: 164).The total heat transference rate is then given by:

$$\dot{Q}_f = \eta_f . h_f . P. L. \Delta T \tag{15}$$

Here: Δ_T is the difference between the fin surface temperature and the indoor temperature. So, the Eq. (7) is given as:

$$\dot{Q}_d = U(H - Nt)b(\Delta_T - T_\infty) \tag{16}$$

Here: H is the total fin length. *(N)* if the number of fins, *(t)* is the fin thickness, and b refers to the fin height. The expression of the total heat transfer with fins and panels is as follows:

$$\dot{Q}_{R,total} = \dot{Q}_f + \dot{Q}_d \tag{17}$$

According to this, the calculated value of the model was validated with the reference values of the producer. The comparison results are shown in Table 2.

The reference radiator channel heat power is as given in Table 2. When the panel radiator is evaluated at 22°C indoor temperature, the heat power in the manufacturer's model has been calculated. The heat power of the reference and designed model is given in Table 2.

Table 2. Model validation.

T$_{indoor}$ (°C)	$\dot{Q}_{reference}$ (W)	$\dot{Q}_{total}$ (W)
22	1087	1087.12

According to Table 2, the calculated value by the propsed model is in good agreement with the value of producer. The deviaiton is only 0.01104%.So, the propsed model can be used with a high accuracy.

For the panel radiator, the friction factor in the laminar flow is taken into account in the calculation of the pressure losses:

$$f_{Rad} = \frac{64}{Re}$$

(18)

It is used for both laminar and turbulent flow. When calculating the pressure loss in the panel radiator, it was calculated with 30 channels. It is given with the following equation:

$$\sum \Delta P_{Rad} = 30 f_{Rad} \frac{L_c}{d_h} \frac{\rho.v_{Rad}^2}{2} \quad (19)$$

Here, L_c is the radiator height. d_H refers to the hydraulic diameter of the radiator, v is the flow rate, g denotes gravity.

The total power required for the pump is given with $W_{\Delta P}$:

$$W_{\Delta P} = \frac{\dot{m} \sum \dot{\Delta P}_{Rad}}{\rho_{ave}\,\eta_p} \quad (20)$$

η_p is the efficiency of the pump, and it was taken as 84.5% constant throughout the entire design (Ucar & Arslan, 2021a:4). ρ_{ave} is the density of the average fluid water.

Table 3. Technical characteristics of aluminum panel radiator for the clean case.

PARAMETERS	UNIT	$T_{indoor}(°C)$
-	-	22
$\dot{Q}_{fin}$	W	547.91
$\dot{m}_{water}$	kg/s	0.0801717
A	m^2	0.6
μ	kg/ms	0.000524421
ρ	kg/m^3	986.95
ka	W/mK	0.645
Nu	-	3.350
Cp	J/kgK	4182.202
$V_{fouling}$	m/s	0.003984
Re	-	95.22

$A_{min,fouling}$	m^2	0.0001469
$d_{h,fouling}$	m	0.0127
h	$W/m^2 K$	170.1378
f_{rad}	-	0.6721
Δ_p	Pa	34.52
$\dot{W}_p$	kW	0.0000039822
$L_{fouling}$	m	-
$K_{fouling}$	W/mK	-
$R_{fouling}$	$W/m^2 K$	-
$L_{fouling}$	m	-
$K_{fouling}$	W/mK	-
$R_{fouling}$	$W/m^2 K$	-
$U_{fouling}$	$W/m^2 K$	7.3662
$\dot{Q}_R$	W	1087.12
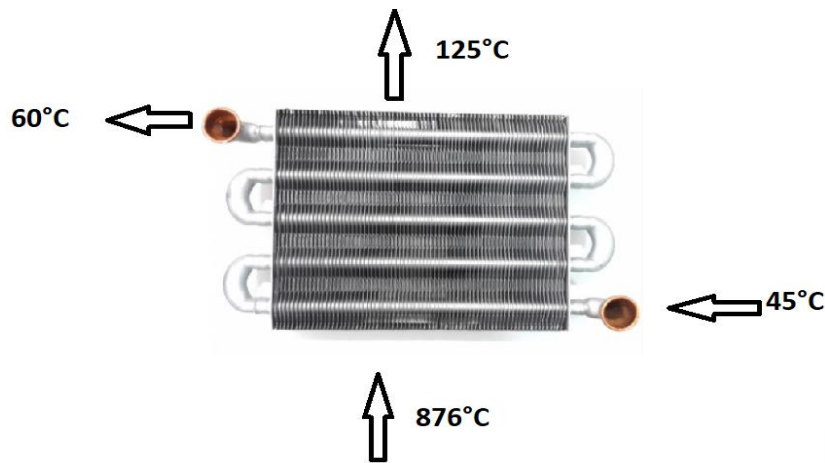
Figure 5. *Combi Heat Exchanger Model Diagram*

Natural gas consumption, which plays an important role especially in individual heating needs, meets 24% of energy use today (Akmercan Gaz Doğalgaz, n.d.).As a result of this circumstance, efficiency improvements in natural gas and fuel combi boilers are favored heating equipment when both cost and environmental conditions are considered. Using combi heat exchangers, we can meet both household heating and hot water demands. The primary heat exchanger was made to be the intended compact heat exchanger. The heat power of the reference model is 24 kW(Ucar & Arslan, 2021a). In our developed model, the heat exchanger's heating power was determined to be 22.8 kW. The fluid water moving in the heat exchanger of a combi has intake and outlet temperatures of 45°C and 60°C, respectively.The technical parameters of the combi heat exchanger are: The pipe through which the liquid water flows has an inner diameter of 0.016 m and an outside diameter of 0.022 m (Çelik, 2016:29), The height of the combi heat exchanger was measured at 0.04 m. After examination, the length of a sample heat exchanger for a combi is 0.18 m. The fin thickness was determined to be 0.005 m, and the number of fins was calculated to be 113. In the reaction of

chemical combustion, the stack gas's entrance and output temperatures are 876 °C and 125 °C, respectively(Ucar & Arslan, 2021b:3).The following calculation are used to calculate the area of compact finned heat exchangers:

The internal area estimate of the pipe through which the fluid water moves is provided in Equation 21.

$$A_i = \pi \, r^2 \tag{21}$$

Total outer fin area is used as stated in Equation 22. In this case, δ is the distance between the two fins.

$$A_{d,f} = [8\pi(r_4{}^2 - r_3{}^2) + 2\pi r_4 t][L/\delta] \tag{22}$$

The area of the outer pipe without fins was calculated using equation 23.

$$A_{do} = 2\pi r_3 (s - t) \, [L/\delta] \tag{23}$$

The entire exterior area was computed using equation 24.

$$A_d = A_{d,f} + A_{do} \tag{24}$$

The thermal conductivity of the combi compact heat exchanger's outer tube is 50 W/mK, while the thermal conductivity of the fin section is 250 W/mK(Genceli, 2005a:208).

The average temperature of the fluid water moving in the clean heat exchanger of the combi has been determined to be 52.5°C.

The equation 25 is used to calculate the average of the circulating liquid in the pipe portion of the heat exchanger.

$$T_{m,w} = \frac{T_{water,in} + T_{water,out}}{2} \tag{25}$$

If the flow state is Re>10000, the flow is turbulent and is expressed in equation 26(Genceli, 2005b:312).

$$Nu = 0.023 Re^{0,8} \, Pr^n \tag{26}$$

Here, n water in internal flow is calculated by taking 0.4 in case of heating or 0.3 in case of cooling (Genceli, 2005b:312).

Calculation of thermal conductivity coefficient of water in internal flow is given in equation 27.

$$h_{in} = \frac{Nuk_a}{d_h} \tag{27}$$

k_a: here the conductivity coefficient of the fluid is given as constant and it is given 0.645 W/mK using the thermodynamic table(Cimbala & Çengel, 2020:942).Here, (d_h) refers to the hydraulic diameter.

The fins on the outside of the heat exchanger of combi cause it to become a compact heat exchanger.Therefore, the stack gases formed as a result of combustion moved between these fins increase the heat transfer.

The average temperatures of the stack gases entering and outering the designed heat exchanger of combi are specified in equation 28.

$$T_{mg} = \frac{T_{gas,in} + T_{gas,out}}{2}$$
(28)

The gas flow rate of the model combi boiler with a heating power of 22.8 kW is calculated as in equation 29 by:

$$\dot{Q} = \dot{m}_{t,fuel} \cdot c_{gas} \cdot \Delta T_{m,g}$$

(29)

The calculation of the combi boiler heat power is the same as the radiator. Here: Δ_T is taken as the average logarithmic temperature difference of the inlet and outlet temperatures of stack gas and fluid water to the heat exchanger of combi boiler. So, the Eq. (7) is given as.

The logarithmic temperature difference expression is as given in equation 30

$$\Delta_T = \frac{(T_{w,i} - T_{g,o}) - (T_{w,o} - T_{g,i})}{\ln\left(\frac{(T_{w,i} - T_{g,o})}{(T_{w,o} - T_{g,i})}\right)}$$

(30)

The gas flow rate through a single channel is calculated from equation 31 by:

$$\dot{m}_{gas} = \frac{\dot{m}_{t,fuel}}{113}$$

(31)

The velocity of the stack gas passing through a single channel is given in equation 32 by:

$$V = \frac{\dot{m}_{gas}}{\rho_{ave,gas} A_{min,E}}$$

(32)

In the equation 32 specified, $\rho_{ave,gas}$ is the density of the stack gas at the average temperature value, $A_{min,E}$ indicates the area through which the stack gas passes through a channel.

As stated in Equation 33, the hydraulic diameter of the region where the stack gas passes is given in the equation below.

$$d_h = 4 \frac{L \, A_{min,E}}{A_d}$$

(33)

Here: L is the length of the heat exchanger of combi. The Nusselt value of the stack gas is constant. If it is accepted that the rectangular fins are fully developed in terms of hydrodynamics, it is 8.23 the average nusselt value, which is accepted as a constant heat flux along the perimeter in the laminar flow direction(Genceli, 2005c:317).

The total pressure loss for the heat exchanger of combi boiler is given in equation 34.

$$\Delta_P = \frac{\left(\frac{\dot{m}}{A_{min,E}}\right)^2}{\rho_i} \left\{ \left[\varsigma_d + 1 - \left(\frac{A_{min,E}}{A_{front}}\right)^2\right] + 2\left(\frac{\rho_i}{\rho_o} - 1\right) + \lambda_s \frac{A}{A_{min,E}} \frac{\rho_i}{\rho_{ave}} - \left[1 - \varsigma_g - \left(\frac{A_{min,E}}{A_{front}}\right)^2\right] \frac{\rho_i}{\rho_o} \right\}$$

(34)

Here: (ς_d) is the local loss in contraction, (ς_g) is the local loss in expansion. (A_{front}) is the front input section area of the heat exchanger, (ρ_i), (ρ_{ave}), (ρ_o) are the inlet, average, and outlet densities of the fluid, respectively. Since the heat exchanger of combi is a 5-pass pipe, the total area of the pipe is expressed as A and λ_s is the coefficient of friction (Genceli, 2005d:166).

The required pump power due to the pressure loss of the fluid in combi compact heat exchangers is given in equation 35.

$$\dot{W} = \frac{\dot{m} \Sigma (Ap)_t}{\rho \eta_p}$$

(35)

Here: $\Sigma(Ap)_t$ is the total pressure loss in the heat exchanger. (η_p) is the pump or fan efficiency (Genceli, 2005d:167).

Table 4. *Technical Characteristics of Combi Boiler Clean for the Clean Case.*

PARAMETERS	UNIT	$T_{indoor}(°C)$
-	-	**22**
$\dot{m}_{gas}$	kg/s	0.03862
$\dot{m}_{water}$	kg/s	0.08017
A	m^2	5.4417
μ	kg/ms	0.00000357
ρ	kg/m^3	0.4579
k_a	W/mK	0.645
Nu	-	8.23
C_p	J/kgK	1181.0362
$V_{fouling}$	m/s	1686.898886
Re	-	1431.49
$A_{min,fouling}$	m^2	0.0000500
$d_{h,fouling}$	m	0.000006616
h	$W/m^2 K$	433.20115
$\lambda_{s,gas}$	-	0.35812
$\Delta_{p,gas}$	Pa	3497202.291
$W_{\Delta p,gas}$	W	349078.5
f_{water}	-	0.03008
$\Delta_{p,water}$	Pa	109.1218
$W_{\Delta p,water}$	k W	0.00001049
$L_{in,fouling}$	m	0
$K_{in,fouling}$	W/mK	0.8
$L2_{in,fouling}$	m	0
$K2_{in,fouling}$	W/mK	0.8
$L_{out,fouling}$	m	0
$K_{out,fouling}$	W/mK	0.1
$R_{fouling}$	$W/m^2 K$	0
$U_{fouling}$	$W/m^2 K$	0.10272
$\dot{Q}_C$	W	22829.53

It is in acceptable agreement with a 5.13% deviation between our reference model with a thermal power of 24 kW and the model we designed with a value of 22.8 kW.

Energy Analysis

The first law of thermodynamics expresses energy analysis. According to the first rule, energy is an absolute constant, which means that it cannot be generated or destroyed. Energy transforms from one state to another. It says that in the cycle state of a system, heat exchange and work exchange must be equal in the same unit system and correspondingly in separate units. It refers that the fluid in the control volume flows continuously in continuous flow systems. The fluid feature varies from one point to the next, but it does not alter over time at any point. Mass, heat, and work interactions do not alter over time in a continuous flow system(Çengel & Boles, 2008:45–230).

$$\Sigma \dot{m}_{in} = \Sigma \dot{m}_{out} \tag{36}$$

Heat, work, and mass in a control volume continuous flow system are equal to energy input and output energy per unit time. In the control volume, total energy is constant. The change in the system's kinetic and potential energy per unit time in the control volume is '0'(Çengel & Boles, 2008: 45–230).

$$\dot{E}_{in} - \dot{E}_{out} = \frac{dE_{sis}}{d_t}$$

$$\dot{E}_{in} = \dot{E}_{out} \tag{37}$$

The total energy change in continuous flow systems is specified in equation 37 to be "0." Kinetic and potential energy changes are ignored in the system, as seen in Equation 38.

$$\dot{Q}_{in} - \dot{W}_{in} + \Sigma_{in}\dot{m}h = \dot{Q}_{out} - \dot{W}_{out} + \Sigma_{out}\dot{m}h \tag{38}$$

Equation 39 calculates the energy efficiency expression:

$$\eta = \frac{\dot{Q}_{out}}{\dot{Q}_{in}} \tag{39}$$

The following equation specifies the energy balance of the combustion reaction in the combi boiler:

$$\dot{Q}_{fuel} = \Sigma_{in} \dot{n} \left(\bar{h}_{ol}^{\circ} - \bar{h}_T - \bar{h}_{298}^{\circ} \right) - \Sigma_{out} \dot{n} \left(\bar{h}_{ol}^{\circ} - \bar{h}_T - \bar{h}_{298}^{\circ} \right) \tag{40}$$

Here, $\dot{n}$ is the mole ratio of fuel, $\bar{h}_{ol}^{\circ}$ is the enthalpy of formation, $\bar{h}_T$ enthalpy of temperature at state conditions and $\bar{h}_{298}^{\circ}$ is the absolute reference enthalpy at 298K.
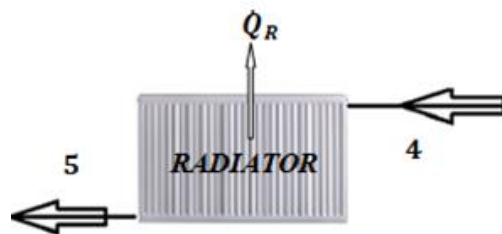
Figure 6. *Radiator Flow Diagram*

Considering the continuous flow condition, the mass balance for the radiator is expressed by the following equation 41:

$$\dot{m}_4 = \dot{m}_5 \tag{41}$$

The temperatures of the incoming water fluid are 60°C at points 4 and 5, while the temperatures of the exiting water fluid are 45°C. There are no work entry and exit points here. While the input water had an enthalpy value of 251.25 kJ/kg, the output water had an enthalpy value of 188.42 kJ/kg. The following is the energy balance for the radiator diagram in a continuous flow system:

$$\dot{Q}_{rad} = \dot{m}_{in,water} h_{in,water} - \dot{m}_{out,water} h_{out,water} \tag{42}$$

The energy transferred from the radiator to the indoor is denoted by $\dot{Q}_{rad}$. In the equation below, the pump power for the radiator panel is supplied by:

$$\dot{W}_{\Delta P_{rad}} = \frac{\dot{m}_{water} \ \Sigma \Delta P_{rad}}{\rho_{ave,water} \ \eta_p}$$

(43)

$\Sigma \Delta P_{rad}$ denotes the overall pressure loss for the radiator. The input and output water flow rates are expressed by $\dot{m}_{water}$, η_p denotes the pump's efficiency. Efficiency for the radiator is given as:

$$\eta_R = \frac{\dot{E}_{out}}{\dot{E}_{in}} \tag{44}$$

2
Stack Gase

COMBI

5   **3**

Fuel+Air
1
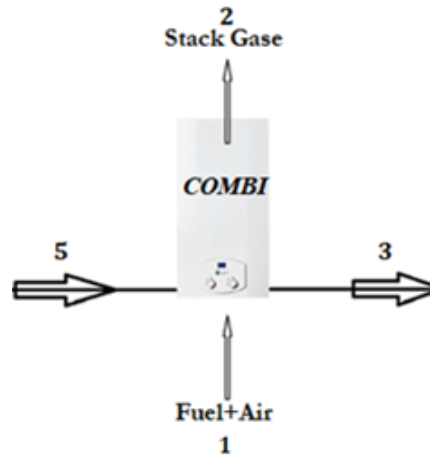
Figure 7. *Combi Flow Diagram*

Considering the continuous flow condition, the mass balance for the boiler is expressed by the following equation:

$$\dot{m}_5 = \dot{m}_3 \tag{45}$$

$$\dot{m}_{fuel} + \dot{m}_{air} = \dot{m}_{stack,gas}$$

Here, The temperatures of the input and output water fluid at points 5 and 3 are 45° and 60°C, respectively. Here, there is no $\dot{W}_{work}$ input and output. $\dot{Q}_{stack \ gas}$ is the heat composed. While the enthalpy value of the input water is 188.42 kJ/kg, the output water is calculated as 251.25 kJ/kg. The total flow rate of the reacting fuel and air is calculated as 0.000255kg/s. The energy balance for the diagram in the continuous flow system is given below:

$$\dot{Q}_C = \dot{m}_{fuel} h_{fuel} + \dot{m}_{in,water} h_{in,water} - \dot{m}_{out,water} h_{out,water} - \dot{m}_{stack,gas} h_{stack,gas}$$

(46)

The pump power fluid gas through in the heat exchanger of combi boiler is given in the equation below:

$$\dot{W}_{\Delta P} = \frac{\dot{m}_{gas} \ \sum \dot{\Delta P}_{combı}}{\rho_{ave,gas} \ \eta_f} \tag{47}$$

Here: $\sum \Delta P_{combi}$ is the total pressure loss of the gas, $\dot{m}_{gas}$ refers to the mass flow rate of the total gas, $\rho_{ave,gas}$ is the average density of the input and output gas. η_f is the fan efficiency.

The pump power fluid water through in the heat exchanger of combi boiler is given in the equation below:

$$\dot{W}_{\Delta P} = \frac{\dot{m}_{water} \ \dot{\sum} \Delta P_{combı}}{\rho_{ave,water} \ \eta_C} \tag{48}$$

Here: $\sum \Delta P_{combi}$ is the total pressure loss for the water in the heat exchanger of boiler. $\dot{m}_{water}$ expresses the input and output water flow rate.

Efficiency for the boiler is given as:

$$\eta_C = \frac{\dot{E}_{out}}{\dot{E}_{in}} \tag{49}$$
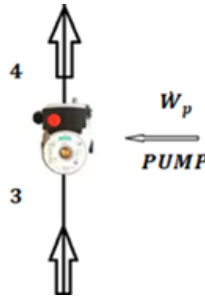
Figure 8. Pump Flow Diagram

If the mass flow equation is expressed for the pump, the following equation is used:

$$\dot{m}_3 = \dot{m}_4 \tag{50}$$

Here, the temperatures of the input and output water fluid at points 3 and 4 are 60°C. Here, there is $\dot{W}_p$ work entry. The energy balance for the diagram in the continuous flow system is given below:

$$\dot{Q}_{rad} = \dot{m}_{in,water} h_{in,water} - \dot{m}_{out,water} h_{out,water} + \frac{\dot{m}_{water}(\Delta P)}{\rho.\eta_p} \tag{51}$$

Here: ΔP is the pressure loss of the total water circulating in the boiler and raditor.

Pump efficiency is expressed by the following equation:

$$\dot{W} = \frac{\dot{m}_{water}(\Delta P)}{\rho.\eta_p}$$

(52)

Combustion Reaction Energy Calculation of Natural Gas

The properties of the stack gases are taken as reference by considering the combustion results of natural gas as the thermophysical properties of the average stack gases.

The combustion reaction equation of natural gas is given detail in equation 53.

$$CH_4 + \lambda 2(O_2 + 3.76N_2) \rightarrow CO_2 + 2H_2O + 0.2O_2 + 8.272N_2 \tag{53}$$
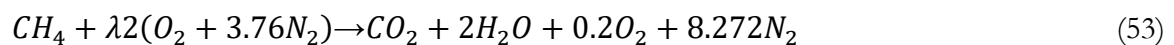
The λ of the chemical reaction with the complete combustion of 1mol of methane gas indicates the excess air coefficient and is 1.1 (Ucar & Arslan, 2021b:3).

The fuel enthalpy was calculated based on the average thermodynamic properties of the stack gases formed after combustion as given in Graphic 1(Aralsan, 2019).
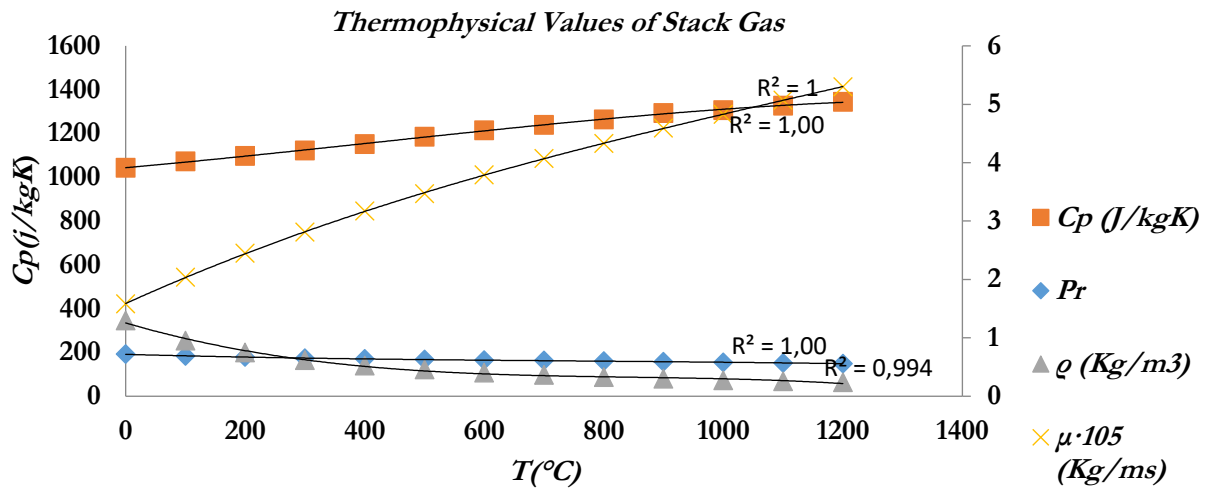
Graph 1. *Average Thermophysical Properties of Stack Gases.*

The total input and output enthalpies of the chemical reaction resulting from complete combustion are given in Table 5 and Table 6 below respectively.

Table 5. *Total Enthalpies of Fuel at Inlet Temperature.*

Compound	Mole	h(formation)	h(1149K)	h(398K)	h(298K)	Result
CH_4	1	-74850	0	0	0.00	-74850.000
O_2	2.2	0	0	0	8682	-19100.400
N_2	8.27	0	0	0	8669	-71692.630
					h_{in}	165643.030

The enthalpy values of fuel and air at 25°C inlet temperature of natural gas are given in Table 6. The result is 165643.030 kJ/kmol.

Table 6. *Total Enthalpies of Stack Gas entering the Heat Exchanger of combi boiler*

Compound	Mole	h(formation)	h(1149K)	h(398K)	h(298K)	Result
CO_2	1	-393520	45447.1	0	9364	-448331.10
H_2O	2	-241820	42167.9	0	9904	-587783.80
N_2	8.27	0	35061.5	0	8669	-361651.23
O_2	0.2	0	36633.05	0	8682	-9063.01
					h_{out}	1406829.145

The stack gas resulting from the inlet combustion reaction of the calculated 0.000255kg/s fuel with dry air and the stack gase with a temperature of 876°C are the products input the heat exchanger of combi boiler. Here: While the total enthalpy of the reaction at 25°C is 165643.030 kJ/kmol, the total enthalpy of the 876°C stack gas resulting from the reaction is 1406829.145 kJ/kmol. Here, the mass of methane entering 1 kmol was calculated as 16 kg/kmol. The total

enthalpy values of stack gase with exit temperature of 125°C from heat exchanger of Combi boiler are given in Table 7.

Table 7. *Total Enthalpies of Stack Gas Resultant the Heat Exchanger of combi boiler*

Compound	Mole	h(formation)	h(1149K)	h(398K)	h(298K)	Result
CO_2	1	-393520	0	13289.6	9364	-416173.600
H_2O	2	-241820	0	13287.6	9904	-503468.000
N_2	8.27	0	0	11581.4	8669	-167470.808
O_2	0.2	0	0	11650.6	8682	-4066.520
					$h_{stack\ gases}$	-1091178.928

Given as in Table 7,The energy of the stack gas leaving the heat exchanger of combi boiler was calculated as -1091178.928 kJ/kmol. As a result, it was calculated that the stack gas transferred to the combi heat exchanger was transferred with an energy of 5.02kW. The total amount of energy required for individual residences was accepted as 4.5kW (Arslan & Arslan, 2022:23). The amount of heat required for a 22°C in case conditions was calculated as 5.02 kW.

Table 8. *System Energy Cycle in Clean State*

Cycle	Fluid	m	T_{indoor}	T	h	s	$\dot{E}$
-		kg/s	°C	°C	kJ/kg	kJ/kgK	kW
1	Aır+fuel	0.000255	22	25	19728.138	2267.00	5.0307
2	Stack Gas	0.000255	22	25	-68198.683	2826.79	17.39
3	Water	0.0801717	22	60	251.25	0.8322	20.143
4	Water	0.0801717	22	60	251.25	0.8322	20.143
5	Water	0.0801717	22	45	188.42	0.6383	15.11

In the clean state cycle.The air entering at point 1 is the fuel inlet, and the stack gas outlet is at point 2. Fluid water coming out of the combi boiler at point 3 passes directly through the pump inside the combi boiler. Here, the pressure is assumed to be constant, and the fluid entering the radiator at 60 °C from the 4th point loses heat and transfers it to the indoor while the 45 °C water leaving the radiator at the 5th point returns to the heat exchanger of the combi boiler.

Table 9. *Clean State Energy Data.*

Compound	Ei	Eo	Q	W	η
22°C	kW	kW	kW	kW	
Radiator	20.14	15.10	5.03	-	%99.85
Pump	20.14	20.14	-	0.0000144722	%84.50
Combi	5.03	5.03	0	-	%100.00
Whole System					**%100**

As Given at Table 9:The total efficiency of the system. which at clean state is at 22°C indoor temperature and resulted in 100%.

Exergy Analysis

Exergy is defined as the highest possible work potential from a system when a system or a control volume experiences a reversible state shift from a certain beginning state to the state of its surroundings. so that there is no violation of thermodynamic laws. When a system is in balance with its environment, it is said to be in its "dead state." Exergy is also affected by environmental (dead-state) circumstances in addition to the system. A system in a dead state has the same pressure and temperature values as the surrounding environment. In environmental settings, it is not the same as potential or kinetic energy. It has no effect on these energies. Likewise. It has no influence on magnetic or electrical fields. Exergy is similar to energy. Heat, mass, and work are transferred in three separate ways(Çengel & Boles, 2008:424–457).

The continuous flow equation is generally given as follows:

$$\sum \dot{Ex}_{in} - \sum \dot{Ex}_{out} = \sum \dot{Ex}_d$$
(54)

The expressions in equation 54 are given in detail in equation 55 by:

$$\sum \dot{Ex}_{heat}^{Q} + \sum \dot{Ex}_{work}^{W} + \sum \dot{Ex}_{i.m} - \sum \dot{Ex}_{o.m} = \sum \dot{Ex}_d$$
(55)

As stated in Equation 55. while heat induced exergy is given as $\sum \dot{x}_{heat}$ exergy from work effect is given as $\sum \dot{x}_{work}$ Another exergy comes from mass flow. This exergy is defined as $\sum \dot{Ex}_{mass,in}$ and $\sum \dot{Ex}_{mass,out}$ The general equations of these expressions are as follows:

Exergy transferred by heat:

$$\sum \dot{Ex}_{heat} = \sum 1 - \left(\frac{T_0}{T}\right) \dot{Q}$$
(56)

Exergy transferred by mass flow:

$$\sum \dot{Ex}_{mass.in} = \sum \dot{m}_{mass.in} \, \dot{\psi}$$
(57)

$$\sum \dot{Ex}_{mass.out} = \sum \dot{m}_{mass.out} \, \dot{\psi}$$
(58)

Exergy transferred by work effect:

$$\sum \dot{Ex}_{work} = \dot{W}$$
(59)

In general. the physical exergy flux is defined by the equation in 60:

$$\Psi = (h - h_0) - T_0(S - S_0)$$
(60)

At this point, the points h and s specify the order of enthalpy and entropy, respectively. At certain temperatures. The sub-indexes with 0 expresses the conditions in 298K.

The exergy of the combi boiler and stack gas resulting from the combustion reaction are given in equations 61 and 62, respectively.

$$\dot{Ex}_{fuel} = \left(1 - \frac{T_0}{T_{m,fuel}}\right) \dot{Q}_{fuel} + \dot{Ex}^{ch}{}_{fuel} - \dot{I}$$
(61)

$$\dot{E}x_{s,g} = \left(1 - \frac{T_0}{T_{s,g}}\right)\dot{Q}_{s,g} + \dot{E}x^{ch}{}_{s,g} - \dot{I} \tag{62}$$

Here: $T_{m,fuel}$ indicates the average temperature of the boiler in the combustion chamber. $\dot{E}x^{ch}$ expresses the chemical exergy of the fuel. Here: $\dot{Q}_{fuel}$ and $\dot{Q}_{s,g}$ are the energies of the combi boiler and stack gas respectively. Here, $\dot{I}$ gives irreversibility. The chemical exergy of the fuel entering the heat exchanger of combi at 876°C is as given in equation 63 and irreversibility is expressed in 64.

$$\dot{E}x^{ch}{}_{fuel} = \sum_i (x_i ex_i)_{product} - \sum_i (x_o ex_o)_{reactant} \tag{63}$$

$$I = \dot{E}x_{d.k} = T_0 S_{ii} \tag{64}$$

Here: x_i is the mole fraction of the molar chemical exergy for substance i. The entropy generation that occurs during instantaneous combustion in the combustion chamber region is indicated by S_{ii}:

$$S_{ii} = S_p - S_r + \frac{\dot{Q}_{CC}}{T_{cc}} \tag{65}$$

$T_{cc} \cdot \dot{Q}_{CC}$, S_p and S_r expresses the condition temperature, heat losses, product entropy and reaction entropy in the combustion chamber, respectively.

$$S_i = N_i\left[\bar{S}_i^{\circ}(T.P_0) - R_u \ln y_i P_{toplam}\right] \tag{66}$$

Here: Equation 66 is given for the substance i component which is the subscript in the ideal gas mixture. Standard molar enthalpy is $\bar{S}_i^{\circ}$. Universal gas constant is given as R_u. y_i is the molar fraction and P_{total} refers to the total pressure.

The stack gas exits heat exchanger of combi boiler at 125°C and its chemical exergy is given in equation 67.

$$\dot{E}x^{ch}{}_{s,g} = \dot{R}\,T_0 \sum y_i \left(\ln y_i / y\right) = \sum_i y_i^{-ch.i} + \dot{R}T_0 \sum_i y_i \ln y_i \tag{67}$$

The standard molar chemical exergy equation of water is given in equation 68, assuming 1 atm pressure and 25°C.

$$\dot{E}x^{ch}{}_{water} = \dot{R}T_0 \left(\ln P_{saturation}(T_0)/P_{oo}\right) \tag{68}$$

Here: P_{oo} is standard partial pressure of water. $P_{saturation}$ is expresses saturation of water at 25°C. It indicates the saturation pressure at 3.169 kpa (Y. A. Çengel & Boles. 2008:890).

Exergy Analysis of Natural Gas in Combustion Reaction

The thermophysical values and mole fractions of the incoming and outgoing substances of the formation entropy of natural gas during the chemical reaction are given in the table 10 and table 11 below by.

Table 10. Total Entropy input

Compound	N_i	Y_i	S_i(1atm)	$R_{un} \ln Y_i\, P$	$N_i S_i$
CH_4	1	1	186.16	0	186.16
O_2	2.2	0.21	205.04	12.975	479.63
N_2	8.272	0.79	191.61	1.959	1601.21
				S_{in}	2267.00

Table 11. *total entropy output*

Compound	N_i	Y_i	S_i(1atm)	$R_{un} \ln Y_i P$	$N_i S_i$
CO_2	1	0.0872	276.867	20.282	297.15
H_2O	2	0.1744	248.831	14.520	526.70
O_2	0.2	0.0174	248.358	33.682	56.41
N_2	8.27	0.7210	232.652	2.720	1946.53
				S_{out}	2826.79

While taking into account the entropy produced during the chemical reaction.In this case, the producted entropy was calculated as 967.87kJ/kmolK.Here:(T_0) is the reference temperature of 298K

The irreversibility that occurs in this case is given in equation 69.Here: $\dot{I}$ *is* the irreversibility.

$$\dot{I} = S_{\ddot{U}} \times T_0$$
(69)

$$\dot{I} = 4.5967 kW$$

irreversibility has been calculated as 4.60kW at 22°C clean state condition.

Referring to Figure 6,the expression for the radiator specific physical exergy flux by mass input and output is as follows.

$$\Psi_4 = (h_4 - h_0) - T_0(S_4 - S_0) \tag{70}$$
$$\Psi_5 = (h_5 - h_0) - T_0(S_5 - S_0) \tag{71}$$

The specific exergy of the heat transferred to the medium is expressed as:

$$\sum \dot{E}x_R = \sum 1 - \left(\frac{T_0}{T_{m,R}}\right) \dot{Q}_R \tag{72}$$

Here: $\sum \dot{E}x_R$ is the exergy of the radiator panel. $\dot{Q}_R$ represents the energy of the radiator. The general exergy expression for the radiator is as follows:

$$\sum \dot{X}_{d.R} = \dot{m}\psi_4 - \dot{m}\psi_5 - \left(1 - \frac{T_0}{T_{m,R}}\right)\dot{Q}_R$$
(73)

Table 12. *Thermophysical characteristics of heat exchanger combi.*

Point	Fluıd	Flow rate	T_{indoor}	T	h	s	I	$\dot{E}x_{ch}$	$\dot{E}x_{ph}$
-	-	kg/s	°C	°C	kJ/kg	kJ/kgK	kW	kW	kW
1	Aır+Fuel	0.000255	22	25	19728.138	2267	4.60	5.23	-1.51
2	Stack Gas	0.000255	22	125	-68198.683	2826.79	4.60	0.01274	-3.11
3	Water	0.0801717	22	60	251.25	0.8313	-	-	0.6293
4	Water	0.0801717	22	60	251.25	0.8313	-	-	0.6293
5	Water	0.0801717	22	45	188.42	0.6386	-	-	0.2247

With reference to Figure 7. the physical specific exergy flux equivalence of fluid water for the combi boiler is expressed as follows:

$$\Psi_5 = (h_5 - h_0) - T_0(S_5 - S_0) \tag{74}$$

$$\Psi_3 = (h_3 - h_0) - T_0(S_3 - S_0) \tag{75}$$

The heat exergy of the fuel entering the boiler is generally expressed as:

$$\sum \dot{E}x_{combi.fuel} = \sum \left(1 - \left(\frac{T_0}{T_{m,f}}\right)\dot{Q}_f\right) - \dot{I} \tag{76}$$

The exergy of the stack gas outer from the combi boiler is expressed as follows by:

$$\sum \dot{E}x_{combi.stack\ gas} = \sum 1 - \left(\frac{T_0}{T_{s,g}}\right)\dot{Q}_{stack\ gas} - \dot{I} \tag{77}$$

The general exergy in the boiler is expressed as follows:

$$\sum \dot{X}_d = \dot{m}\psi_{water.in} - \dot{m}\psi_{water.out} + \left(1 - \frac{T_0}{T_{m,f}}\right)\dot{Q}_{fuel} - \dot{I} - \left(1 - \frac{T_0}{T_{s,g}}\right)\dot{Q}_{s.g} - \dot{I} \tag{78}$$

The physical specific exergy flux balance of the fluid water entering the pump is the same at points 3 and 4 and is expressed as follows:

$$\Psi_3 = (h_3 - h_0) - T_0(S_3 - S_0)$$
(79)

$$\Psi_4 = (h_4 - h_0) - T_0(S_4 - S_0)$$
(80)

In general. the exergy of the pump is expressed as follows:

$$\sum \dot{X}_d = \dot{m}\psi_3 - \dot{m}\psi_4 + \dot{W}_p \tag{81}$$

Table 13. *Clean State Combi Exergy Data.*

Compounds	Exi	Exo	Exd	ɛ
22°C	kW	kW	kW	
radiator	0.6293	0.4245	0.2048	%67.45
combi	3.9377	0.6511	3.28660	%16.53
pump	0.6511	0.6511	0.0104941122	%84.50
whole system				%11.41

The total exergy efficiency of the system which was clean at 22°C indoor temperature resulted as 11.41%.

Results and Discussion

Given In Graphs2,in Case 2,the energy efficiency is 99.84713% in the clean condition at 22°C indoor temperature. In Graphic 2, the thickness of the internal fouling originating from the radiator is (0.1),(0.7),(1.5)mm, the thickness of the internal fouling originating from the heat exchanger of combi is the same as the radiator. From Case 2 to Case 28, energy efficiency ranges to decrease from 99.74812% at the maximum to 98.50752% at the minimum. The energy transferred to the indoor was found to be 5.0294kW.
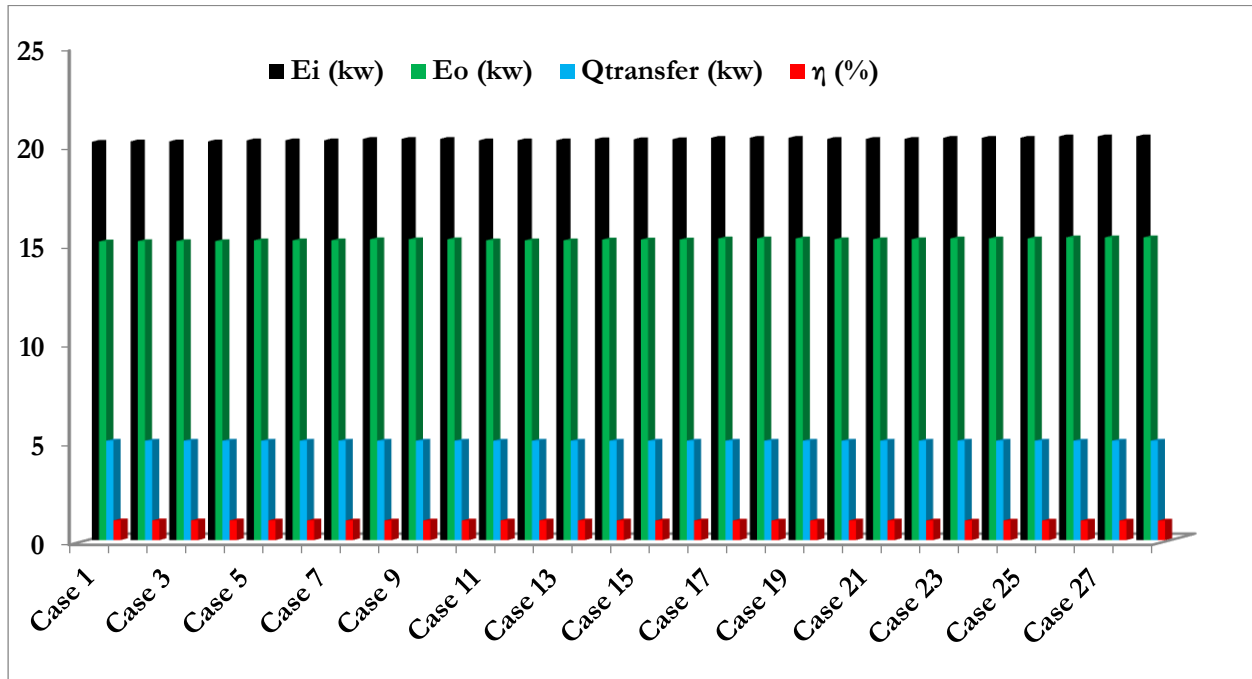
Graph 2. Case 1-Case28 Radiator Energy Analysis.

Given In Graphs3,in Case 2,the exergy efficiency is 67.45590%. In the clean condition at 22°C indoor temperature. In Graphic 3, the thickness of the internal fouling originating from the radiator is (0.1),(0.7),(1.5)mm, the thickness of the internal fouling originating from the heat exchanger of Combi is the same as the radiator. From Case 2 to Case 28, exergy efficiency ranges to decrease from 67.38095% at the maximum to %66.54648 at the minimum.
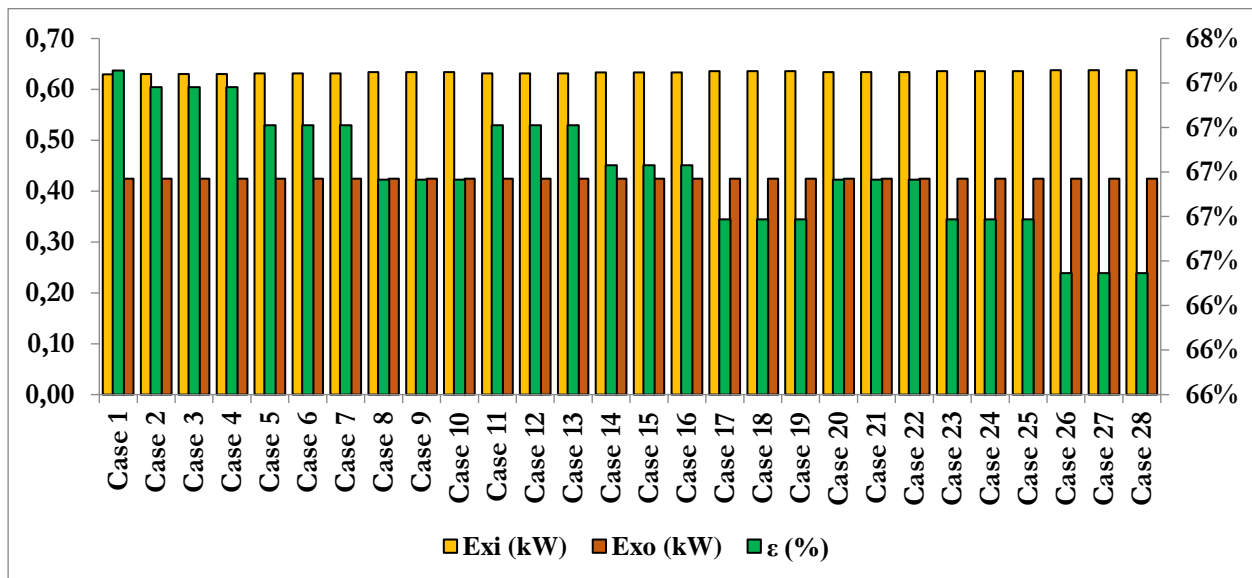
Graph 3. Case1-28 Radiator Exergy Analysis.

Given In Graphs4,in Case 2,the energy efficiency is 100% in the clean condition at 22°C indoor temperature. In Graphic 4, the thickness of the internal fouling originating from the radiator is (0.1),(0.7),(1.5)mm, the thickness of the internal fouling originating from the heat exchanger of combi is the same as the radiator. The value outernal fouling from the combi boiler is (0.1),(0.3),(0.5)mm.From Case 2 to Case 28, energy efficiency ranges to decrease from 58.88694% at the maximum to %8.71909 at the minimum.
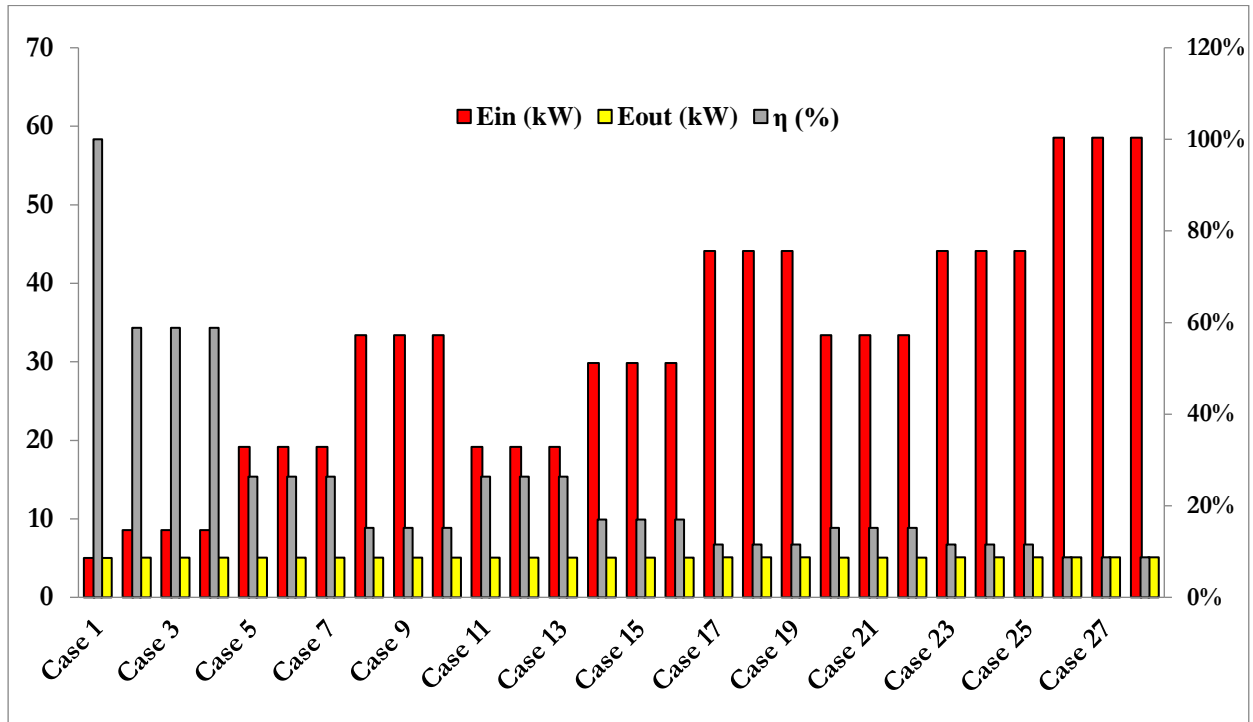
Graph 4. Case 1-Case28 Combi Boiler Energy Analysis.

Given In Graphs5,in Case 2,the exergy efficiency is 16.53503% in the clean condition at 22°C indoor temperature. In Graphic 5, the thickness of the internal fouling originating from the radiator is (0.1),(0.7),(1.5)mm, the thickness of the internal fouling originating from the heat exchanger of combi is the same as the radiator. The value outernal fouling from the combi boiler is (0.1),(0.3),(0.5)mm.From Case 2 to Case 28, exergy efficiency ranges to decrease from 9,93763% at the maximum to 1.51316% at the minimum.
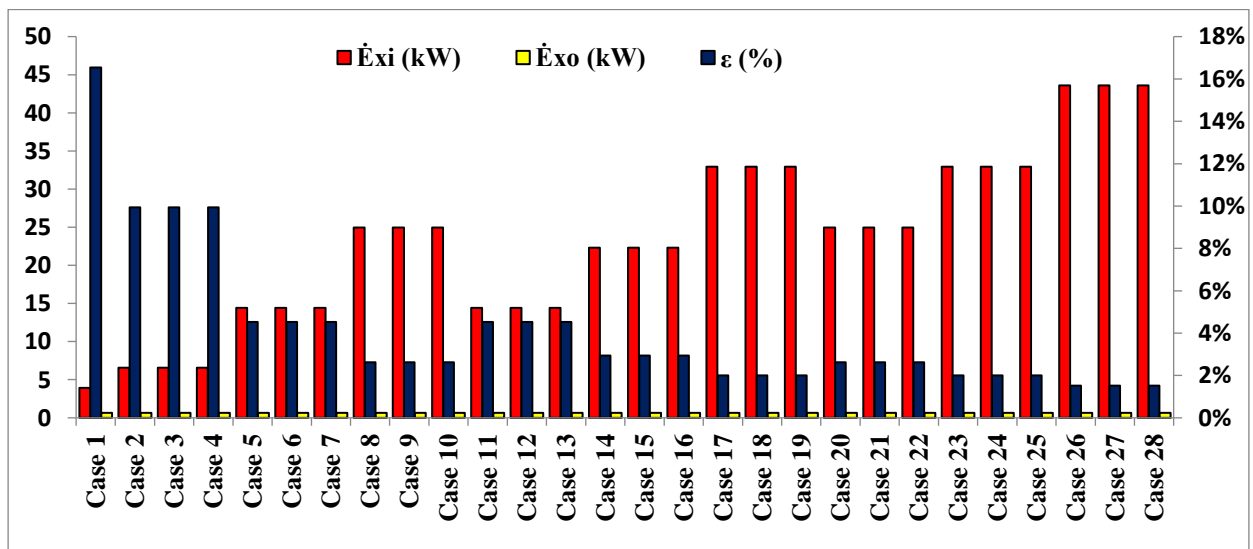
Graph 5. Case 1-Case28 Combi Boiler Exergy Analysis.

In Graph 6. Case 1. the pump power of the radiator and the combi boiler at 22°C were found to be 0.00000398 and 0.00001049 respectively. In Graph 6. at 22°C indoor temperatures. thickness results of the internal fouling from the radiator are (0.1),(0.7),(1.5)mm, the thickness of the internal

fouling originating from the heat exchanger of combi is the same as the radiator and combi boiler
external fouling values are (0.1),(0.3),(0.5)mm. From Case 2 to Case 28. the pump powers of the
radiator and the boiler vary to increase 0.0000205355kW and 0.0001003900kW at the maximum,
0.0000064279kW and 0.00001187kW at the minimum, respectively
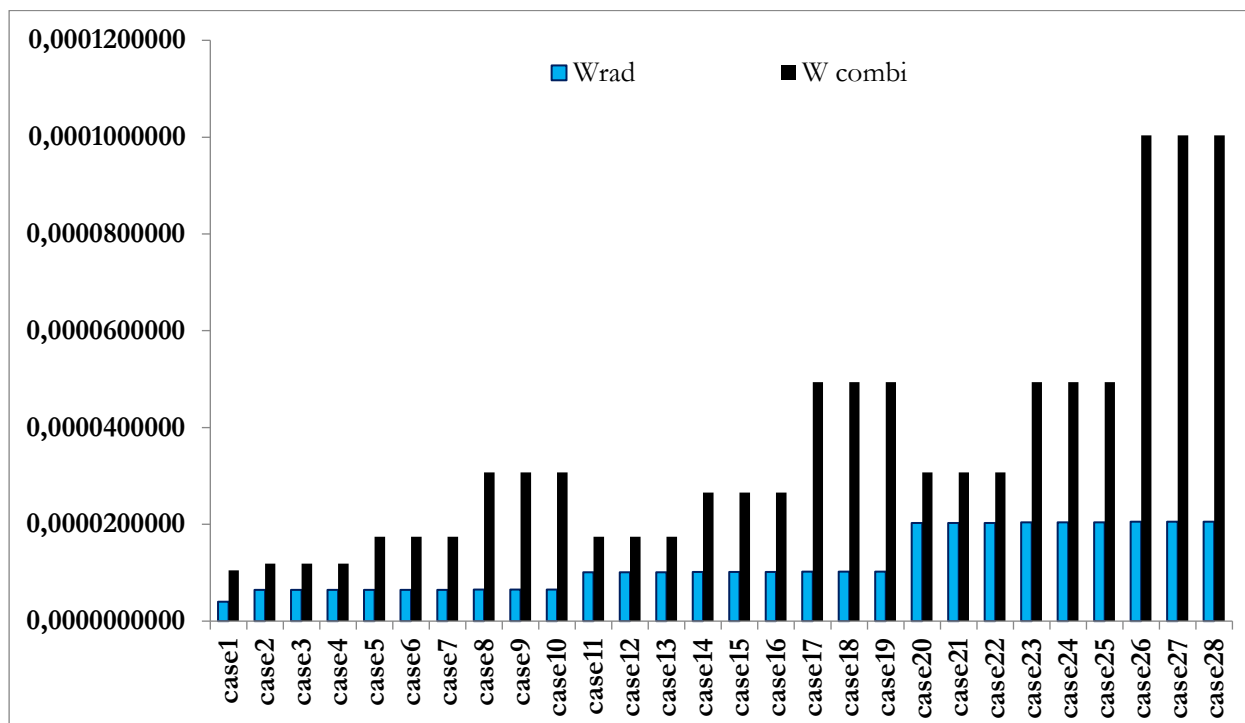
Graph 6. Case 1-Case28 Pump Power Data.

Conclusion

In this study. which was carried out in 28 models. 3 different internal fouling and 3 different
external fouling were taken into account. resulting in total efficiency and exergy analyzes of the
whole system. As a result. It was determined that it decreased from maximum 100% efficiency to
minimum 8.7196% efficiency depending on the fouling state. In the exergy efficiency analysis. the
maximum exergy efficiency of the whole system was 11.4112%. and it was concluded with a
minimum decrease of 0.9783% depending on the fouling state.This situation reveals that by
increasing the pump power. it will cause more fuel consumption and electricity consumption. For
this purpose. pollution and its effect on energy and exergy efficiency are very important. It reveals
that cleaning and maintenance should be done in the most accurate way in order to prevent
efficiency reduction. By doing more work in this area. a boiler and radiator model can be developed
that will reduce the amount of fouling.

List of abbreviations and symbols

$\dot{m}_{gas} = gas\ mass\ flow\ rate\ \left(\frac{kg}{s}\right)$

$\dot{m}_{water} = water\ mass\ flow\ rate\ \left(\frac{kg}{s}\right)$

$\dot{m}_f = flue\ mass\ flow\ rate\ \left(\frac{kg}{s}\right)$

$\dot{m}_{t.f} = mass\ flow\ rate\ of\ fuel\ at\ average\ temperature\ \left(\frac{kg}{s}\right)$

$\dot{m}_{s,g} = stack\ gas\ mass\ flow\ rate\ \left(\frac{kg}{s}\right)$

$\dot{Q}_n = standard\ Heat\ Power(W)$

$\dot{Q}_d = Outer\ Total\ Heathhhh\ Power(W)$

$\dot{Q}_f = finnet\ hHeat\ Power(W)$

$\dot{Q}_C = Combi\ Rated\ Power(W)$

$\dot{Q}_{fuel} = heat\ of\ fuel(W)$

$F = capacitive\ value$

$\dot{Q} = required\ heat\ Power(W)$

$c_{p.water} = specific\ gravity\ of\ water\ (J/kgK)$

$c_{p.gas} = specific\ gravity\ of\ gas\ (J/kgK)$

$\Delta_T = average\ temperature(°C)$

$v = speed\ (\frac{m}{s})$

$\rho = density\ (kg/m^3)$

$\rho_{ave} = average\ density\ (kg/m^3)$

$\rho_i = input\ density\ (kg/m^3)$

$\rho_o = output\ density\ (kg/m^3)$

$A = area\ (m^2)$

$A_f = fin\ area\ (m^2)$

$A_{min} = minumum\ area\ (m^2)$

$A_{front} = front\ input\ area\ (m^2)$

$A_{min.Eşa} = minimum\ cross-sectional\ area\ of\ the\ heat\ exchanger(m^2)$

$dh = hydraulic\ diameter\ (m)$

$dh_{min} = minimum\ hydraulic\ diameter(m)$

$C = environment(m)$

$\mu = dynamic\ viscosity(kg/ms)$

$Re = Reynolds\ number$

$h_i = internal\ conductivity\ coefficient\ (W/m^2K)$

$h_f = fin\ conductivity\ coefficient\ (W/m^2K)$

$h = conductivity\ coefficient\ (W/m^2K)$

$h_d = external\ conductivity\ coefficient\ (W/m^2K)$

$ka = coefficient\ of\ thermal\ conductivity\ of\ water(W/mK)$

$Nu = Nusselt\ number$

$L_c = panel\ radiator\ height(m)$

$L = length\ (m)$

$L_{fouling} = fouling\ thickness\ (m)$

$R_{fouling} = fouling\ transport\ coefficient(W/mK)$

$k_{Al} = Thermal\ conductivity\ coefficient\ of\ aluminum(W/mK)$

$k_{air} = coefficient\ of\ thermal\ conductivity\ of\ air\ (W/mK)$

$U = total\ conductivity\ coefficient\ (W/m^2K)$

$T_y = surface\ average\ temperature\ (°C)$

$T_F = Film\ temperature\ (°C)$

$T_\infty = ambient\ temperature\ (°C)$

$T_{water.in} = entering\ water\ temperature\ (°C)$

$T_{water,out} = leaving\ water\ temperature\ (°C)$

$T_{m,g} = average\ gas\ temperature\ (°C)$

$T_{s,g} = stack\ gase\ temperature\ (°C)$

$T_m = average\ temperature\ (°C)$

$T_{cc} = condition\ temperature\ (°C)$

$\beta = thermal\ expansion\ \left(\frac{1}{°C}\right)$

$Ra = Rayleigh\ number$

$Pr = prandtl\ number$

$Gr = Grashof\ number$

$P = Fin\ circumference\ (m)$

$\Lambda = aluminum\ thermal\ conductivity\ coefficient\ \ (W/mK)$

$L = Area\ multiplication\ of\ fin\ circumference\ (m^3)$

$N = number\ of\ fin$

$t = fin\ thickness\ (m)$

$\delta = distance\ between\ two\ fin\ (mm)$

$\dot{Q}_R = \ total\ radiator\ heat\ output\ (W)$

$\dot{Q}_{s,g} = stack\ gas\ heat\ power\ (W)$

$\dot{Q}_d = outer\ surface\ heat\ transfer\ (W)$

$\bar{h}_T^° = enthalpy\ at\ state\ conditions\ (kJ/kg)$

$\bar{h}_{298}^° = Enthalpy\ at\ 298K\ conditions\ (kJ/kg)$

$\bar{h}_{ol}^° = enthalpy\ of\ formation\ (kJ/kg)$

$v_{rad} = radiator\ flow\ rate\ \left(\frac{m}{s}\right)$

$A_i = interior\ area\ (m^2)$

$A_{d,f} = outer\ fin\ area\ (m^2)$

$A_{do} = outer\ finless\ area\ (m^2)$

$A_d = outer\ total\ area\ (m^2)$

$f_{rad} = friction\ factor$

$\lambda_s = coefficient\ of\ friction$

$\Delta_P = pressure\ drop\ (bar)$

$\dot{W}_{rad} = required\ pump\ power\ (W)$

$m = average$

$\eta_f = tip\ insulated\ fin\ efficiency$

$\eta_{fan} = fan\ efficiency$

$\eta_R = Radiator\ efficiency$

$\eta_C = combi\ efficiency$

$T_0 = absolute\ temperature(°C)$

$\dot{m}_t = average\ temperature\ mass\ flow\ rate(kg/s)$

$g = gravitational\ acceleration$

$\Psi = exergy\ flux$

$\dot{E}x_{CH} = chemical\ exergy$

$\dot{E}x_{PH} = physical\ exergy$

$\dot{E}i = input\ energy\ (kW)$

$\dot{E}o = output\ energy(kW)$

$\dot{s}_{üre} = generated\ entropy(\frac{kJ}{kgK})$

$I = irreversibility(kW)$

$\varsigma_d = local\ loss\ in\ contraction$

$\varsigma_g = local\ loss\ in\ expansion$

$\dot{Q}_{cc} = heat\ loss\ due\ to\ the\ reaction(W)$

$s = entropy\ (\frac{kJ}{kgK})$

$\dot{s}_P = product\ entropy\ (\frac{kJ}{kgK})$

$\dot{W} = work(kW)$

$s_0 = dead\ state\ entropy(\frac{kJ}{kgK})$

$\Delta_{P_{rad}} = radiator\ pressure\ drop(bar)$

$\Delta_{P_C} = combi\ pressure\ drop(bar)$

$\Delta_{P_f} = fan\ pressure\ drop(bar)$

$r = radius$

REFERENCES

Aguel, S., Meddeb, Z., & Jeday, M. R. (2019). Parametric study and modeling of cross-flow heat exchanger fouling in phosphoric acid concentration plant using artificial neural network. *Journal of Process Control*, *84*, 133–145. https://doi.org/10.1016/j.jprocont.2019.10.001

Ahn, H. S., Kim, K. M., Lim, S. T., Lee, C. H., Han, S. W., Choi, H., … Wongwises, S. (2019). Anti-fouling performance of chevron plate heat exchanger by the surface modification. *International Journal of Heat and Mass Transfer*, *144*, 118634. https://doi.org/10.1016/j.ijheatmasstransfer.2019.118634

Akmercan Gaz Doğalgaz. (n.d.). Akmercan Gaz Doğalgaz. Retrieved October 12, 2022, from https://www.akmercangaz.com.tr/tr/bilgi-bankasi/dogalgaz-nedir/

Al Hadad, W., Schick, V., & Maillet, D. (2019). Fouling detection in a shell and tube heat exchanger using variation of its thermal impulse responses: Methodological approach and numerical verification. *Applied Thermal Engineering*, *155*, 612–619. https://doi.org/10.1016/J.APPLTHERMALENG.2019.04.030

Aralsan. (2019, September 16). Aralsan. Retrieved October 16, 2022, from https://www.aralsan.com/baca-gazi-fiziksel-ozellikleri

Arsenyeva, O. P., Crittenden, B., Yang, M., & Kapustenko, P. O. (2013a). Accounting for the thermal resistance of cooling water fouling in plate heat exchangers. *Applied Thermal Engineering*, *61*(1), 53–59. https://doi.org/10.1016/J.APPLTHERMALENG.2013.02.045

Arsenyeva, O. P., Crittenden, B., Yang, M., & Kapustenko, P. O. (2013b). Accounting for the thermal resistance of cooling water fouling in plate heat exchangers. *Applied Thermal Engineering*, *61*(1), 53–59. https://doi.org/10.1016/J.APPLTHERMALENG.2013.02.045

Arslan, O. (2008). *Kütahya-Simav Jeotermal Kaynaklarının Hassas Değerlendirmesi: Entegre Sistem Tasarımı ve Enerji-Ekserji Analizleri*. Dumlupınar Üniversitesi Fen Bilimleri Enstitüsü, Doktora Tezi, Kütahya.

Arslan, Oguz, & Arslan, A. E. (2022). Performance evaluation and multi-criteria decision analysis of thermal energy storage integrated geothermal district heating system. *Process Safety and Environmental Protection*, *167*, 21–33. https://doi.org/10.1016/J.PSEP.2022.08.073

Awais, M., & Bhuiyan, A. A. (2019, October 1). Recent advancements in impedance of fouling resistance and particulate depositions in heat exchangers. *International Journal of Heat and Mass Transfer*, Vol. 141, pp. 580–603. Elsevier Ltd. https://doi.org/10.1016/j.ijheatmasstransfer.2019.07.011

Calisir, T., Yazar, H. O., & Baskaya, S. (2019). Thermal performance of PCCP panel radiators for different convector dimensions – An experimental and numerical study. *International Journal of Thermal Sciences*, *137*, 375–387. https://doi.org/10.1016/J.IJTHERMALSCI.2018.12.007

Çelik, H. S. (2016). *Reküperatör boru konstrüksiyonunun verime olan etkisinin deneysel ve sayısal yöntemlerle araştırılması* (p. 29). p. 29. Fen Bilimleri Enstitüsü.

Çengel, Y. A., & Boles, M. A. (2008). *TERMODİNAMİK* (No. 5; A. Pınarbaşı, Ed.). İZMİR: güven bilimsel.

Ceylan, H., & ÇINAR, B. (2020). The Effect of Fouling on the Baffle Spacing of a Shell and Tube Heat Exchanger. *Süleyman Demirel Üniversitesi Fen Bilimleri Enstitüsü Dergisi*, *24*(3), 584–592.

Ceylan, H., & Çınar, B. (2020). The Effect of Fouling on the Baffle Spacing of a Shell and Tube Heat Exchanger. *Süleyman Demirel Üniversitesi Fen Bilimleri Enstitüsü Dergisi*, *24*(3), 584–592.

Cimbala, J. M., & Çengel, Y. A. (2020). *Akışkanlar mekaniği* (No. 3; koza matba). ankara: palme yayınevi.

Diaz-Bejarano, E., Behranvand, E., Coletti, F., Mozdianfard, M. R., & Macchietto, S. (2017). Organic and inorganic fouling in heat exchangers – Industrial case study: Analysis of fouling state. *Applied Energy*, *206*, 1250–1266. https://doi.org/10.1016/j.apenergy.2017.10.018

Elibol, N. burak. (n.d.). *Kirlilik faktörünün Konut Isıtma Devrelerindeki Etkilerinin Termodinamik İncelemesi*. Bilecik Şeyh Edebalı Üniversitesi, Fen Bilimler Enstitüsü, Bilecik (Devam eden Yüksek Lisans Tezi).

Gelis, K. (2021). Factorial experimental design for second law analysis of panel radiators as a function of radiator dimension. *Journal of Building Engineering*, *43*, 102872. https://doi.org/10.1016/J.JOBE.2021.102872

Genceli, O. F. (2005a). *Isı değiştiricileri*. İstanbul: Birsen Yayınevi.

Genceli, O. F. (2005b). *Isı değiştiricileri*. İstanbul: Birsen Yayınevi.

Genceli, O. F. (2005c). *Isı değiştiricileri*. İstanbul: Birsen Yayınevi.

Genceli, O. F. (2005d). *Isı değiştiricileri*. İstanbul: Birsen Yayınevi.

Gu, Y., Bouvier, L., Tonda, A., & Delaplace, G. (2019). A mathematical model for the prediction of the whey protein fouling mass in a pilot scale plate heat exchanger. *Food Control*, *106*, 106729. https://doi.org/10.1016/j.foodcont.2019.106729

Halici, F. (2016). *Örneklerle isi geçisi : isi transferi*. Istanbul: Birsen Yayınevi.

Hasan, B. O., Jwair, E. A., & Craig, R. A. (2017). The effect of heat transfer enhancement on the crystallization fouling in a double pipe heat exchanger. *Experimental Thermal and Fluid Science*, *86*, 272–280. https://doi.org/10.1016/j.expthermflusci.2017.04.015

Kukulka, D. J., & Devgun, M. (2007). *Fluid temperature and velocity effect on fouling*. https://doi.org/10.1016/j.applthermaleng.2007.03.024

Kuruneru, S. T. W., Vafai, K., Sauret, E., & Gu, Y. T. (2020, December 31). Application of porous metal foam heat exchangers and the implications of particulate fouling for energy-intensive industries. *Chemical Engineering Science*, Vol. 228, p. 115968. Elsevier Ltd. https://doi.org/10.1016/j.ces.2020.115968

Liu, W., Chen, X. D., Jeantet, R., André, C., Bellayer, S., & Delaplace, G. (2020). Effect of casein/whey ratio on the thermal denaturation of whey proteins and subsequent fouling in a plate heat exchanger. *Journal of Food Engineering*, *289*, 110175. https://doi.org/10.1016/j.jfoodeng.2020.110175

Łopata, S., & Ocłoń, P. (2015a). Numerical study of the effect of fouling on local heat transfer conditions in a high-temperature fin-and-tube heat exchanger. *Energy*, *92*, 100–116. https://doi.org/10.1016/j.energy.2015.03.048

Łopata, S., & Ocłoń, P. (2015b). Numerical study of the effect of fouling on local heat transfer conditions in a high-temperature fin-and-tube heat exchanger. *Energy*, *92*, 100–116. https://doi.org/10.1016/J.ENERGY.2015.03.048

Lv, Y., Lu, K., & Ren, Y. (2020). Composite crystallization fouling characteristics of normal solubility salt in double-pipe heat exchanger. *International Journal of Heat and Mass Transfer*, *156*, 119883. https://doi.org/10.1016/j.ijheatmasstransfer.2020.119883

Maddahi, M. H., Hatamipour, M. S., & Jamialahmadi, M. (2019). A model for the prediction of thermal resistance of calcium sulfate crystallization fouling in a liquid–solid fluidized bed

heat exchanger with cylindrical particles. *International Journal of Thermal Sciences*, *145*, 106017. https://doi.org/10.1016/j.ijthermalsci.2019.106017

Markowski, M., Trafczynski, M., & Urbaniec, K. (2013). Validation of the method for determination of the thermal resistance of fouling in shell and tube heat exchangers. *Energy Conversion and Management*, *76*, 307–313. https://doi.org/10.1016/j.enconman.2013.07.052

Mec Tesisat. (2014). Mec Tesisat. Retrieved October 11, 2022, from http://www.mectesisat.com/img/kalde-radyator-teknik-katalog_212.pdf

Palmer, K. A., Hale, W. T., Such, K. D., Shea, B. R., & Bollas, G. M. (2016). Optimal design of tests for heat exchanger fouling identification. *Applied Thermal Engineering*, *95*, 382–393. https://doi.org/10.1016/j.applthermaleng.2015.11.043

Patil, P., Srinivasan, B., & Srinivasan, R. (2022). Monitoring fouling in heat exchangers under temperature control based on excess thermal and hydraulic loads. *Chemical Engineering Research and Design*, *181*, 41–54. https://doi.org/10.1016/J.CHERD.2022.02.032

Sarafraz, M. M., Nikkhah, V., Madani, S. A., Jafarian, M., & Hormozi, F. (2017). Low-frequency vibration for fouling mitigation and intensification of thermal performance of a plate heat exchanger working with CuO/water nanofluid. *Applied Thermal Engineering*, *121*, 388–399. https://doi.org/10.1016/j.applthermaleng.2017.04.083

Shen, C., Cirone, C., Yang, L., Jiang, Y., & Wang, X. (2014). Characteristics of fouling development in shell-and-tube heat exchanger: Effects of velocity and installation location. *International Journal of Heat and Mass Transfer*, *77*, 439–448. https://doi.org/10.1016/j.ijheatmasstransfer.2014.05.031

Song, J., Liu, Z., Ma, Z., & Zhang, J. (2017). Experimental investigation of convective heat transfer from sewage in heat exchange pipes and the construction of a fouling resistance-based mathematical model. *Energy and Buildings*, *150*, 412–420. https://doi.org/10.1016/j.enbuild.2017.06.025

Song, K. S., Lim, J., Yun, S., Kim, D., & Kim, Y. (2019). Composite fouling characteristics of CaCO3 and CaSO4 in plate heat exchangers at various operating and geometric conditions. *International Journal of Heat and Mass Transfer*, *136*, 555–562. https://doi.org/10.1016/j.ijheatmasstransfer.2019.03.032

Sundar, S., Rajagopal, M. C., Zhao, H., Kuntumalla, G., Meng, Y., Chang, H. C., … Salapaka, S. (2020). Fouling modeling and prediction approach for heat exchangers using deep learning. *International Journal of Heat and Mass Transfer*, *159*, 120112. https://doi.org/10.1016/j.ijheatmasstransfer.2020.120112

Tang, S. Z., Li, M. J., Wang, F. L., & Liu, Z. Bin. (2019). Fouling and thermal-hydraulic characteristics of aligned elliptical tube and honeycomb circular tube in flue gas heat exchangers. *Fuel*, *251*, 316–327. https://doi.org/10.1016/j.fuel.2019.04.045

Teng, K. H., Kazi, S. N., Amiri, A., Habali, A. F., Bakar, M. A., Chew, B. T., … Khan, G. (2017). Calcium carbonate fouling on double-pipe heat exchanger with different heat exchanging surfaces. *Powder Technology*, *315*, 216–226. https://doi.org/10.1016/j.powtec.2017.03.057

TMMOB Makine Mühendisleri. (2019, July). TS 825. Retrieved December 8, 2022, from http://www1.mmo.org.tr/resimler/dosya_ekler/cf3e258fbdf3eb7_ek.pdf

Ucar, M., & Arslan, O. (2021a). Assessment of improvement potential of a condensed combi boiler via advanced exergy analysis. *Thermal Science and Engineering Progress*, *23*, 100853. https://doi.org/10.1016/J.TSEP.2021.100853

Ucar, M., & Arslan, O. (2021b). Assessment of improvement potential of a condensed combi boiler via advanced exergy analysis. *Thermal Science and Engineering Progress*, *23*, 3. https://doi.org/10.1016/J.TSEP.2021.100853

Wang, F. L., Tang, S. Z., He, Y. L., Kulacki, F. A., & Yu, Y. (2019). Heat transfer and fouling performance of finned tube heat exchangers: Experimentation via on line monitoring. *Fuel*, *236*, 949–959. https://doi.org/10.1016/j.fuel.2018.09.081

Wellini. (n.d.). Kurumsal / Alüminyum Radyatörlerin Genel Özellikleri. Retrieved April 4, 2021, from http://www.wellini.co/sayfa-alminyum-radyatrlerin-genel-zellikleri-46.html

Xu, Z., Han, Z., Sun, A., & Yu, X. (2019). Numerical study of particulate fouling characteristics in a rectangular heat exchange channel. *Applied Thermal Engineering*, *154*, 657–667. https://doi.org/10.1016/j.applthermaleng.2019.03.142

Xu, Z., Wang, J., Jia, Y., Geng, X., & Liu, Z. (2016). Experimental study on microbial fouling characteristics of the plate heat exchanger. *Applied Thermal Engineering*, *108*, 150–157. https://doi.org/10.1016/j.applthermaleng.2016.07.110

Yang, M., Jiang, F., Qi, G. peng, & Li, X. lun. (2020). Heat transfer performance of a vapor–liquid–solid three-phase circulating fluidized bed evaporation system with different concentrations of Na2SO4 solutions. *Applied Thermal Engineering*, *180*. https://doi.org/10.1016/j.applthermaleng.2020.115833

Yutaka, A., Hiroshi, N., & Faghri, M. (1988). Developing laminar flow and heat transfer in the entrance region of regular polygonal ducts. *International Journal of Heat and Mass Transfer*, *31*(12), 2590–2593.

Green Energy Production and Sustainable Carbon Reduction Potential of Poultry Waste in Turkey

Zuhal AKYÜREK[1]

Introduction

Energy security is one of the main drivers of sustainable development. Growing population, technological and economic developments in the last decades have created a steady increase in global demand for energy. The world energy mix heavily depends on fossil fuels. Backwards of fossil fuel energy such as uncertainty in supply, fluctuations in fossil fuel prices and climate change concerns give impetus to transition to low carbon energy.

Biomass is an abundant and carbon neutral source of renewable energy production. It is the only renewable energy source that can produce electricity, provide heating, cooling and can be converted into fuels in form of solid, liquid and gas (Sahoo et al., 2018; Magnhanaki et al., 2013, Akyürek, 2019a). Biomass refers to organic materials that is derived from animals or plants, present in nature or generated from agricultural and industrial activities and urban wastes (Ferreira et al., 2018; Mao et al., 2015). Biomass energy highly depends on availability of the resources as well as their utilization through sustainable conversion technologies (Terrapan-Pffaff et al., 2012).

Biomass can be converted to green energy through combustion, gasification, pyrolysis, anaerobic digestion technologies (Panwar et al., 2012). Depending on the fuel properties, suitable technologies are applied for waste treatment and renewable energy recovery purposes. Compared with other bioenergy conversion technologies, biogas is a mature and commercialized technology for waste utilization (Li et al., 2016). Biogas can be produced from landfills, wastewater treatment plants, sewage treatment plants and anaerobic digestion plants processing organic waste. Anaerobic digestion describes the robust process of organic material decomposition in oxygen-free medium to produce biogas, which is composed of methane, carbon dioxide, ammonia and traces of other gases, volatile fatty acids, and water (Lyytimaki, 2018; Yentekakis and Grammatiki, 2017). Natural gas has become one of the most widely used energy forms in the recent decades (Demirbaş, 2010).

The biogas produced from the anaerobic digestion of organic waste can be used for electricity and heat production in energy sector. Biogas generally used in power and CHP plants in economically developed regions, while in rural it is mostly used for heating or cooking purposes (Scarlat et al., 2018; Akyürek, 2018). Biogas can also be upgraded to bio-methane to be used as fuel in transport sector to replace with oil and diesel fuel. Bio-methane can be compressed or liquefied to increase its volumetric energy density. Bio-methane has been shown to be more environmentally beneficial than liquid biofuels in road transport sector to contribute the climate change combat (Patterson et al., 2011).

Turkey is one of the fast-growing economies in Europe and is a candidate country for European Union Membership. In the EU, political targets for climate and energy in 2030 are 40% reductions in greenhouse gas emissions. In longer term, the EU has ambition for transition to low carbon economy and to reach CO_2 reduction of 80-95% by 2050 (Scarlat et al., 2018). In Turkey, power generation and industrial activities are responsible for most of the total greenhouse gas

---

[1] Assoc. Prof. Dr., Dept. of Energy Systems Engineering, Burdur Mehmet Akif Ersoy University

emissions (Figure 1). According to Turkey's Intended Nationally Determined Contribution covering the period 2012-2030, total greenhouse gas emissions will be reduced up to 21% by 2030 with the improvements in energy, industrial processes and products use, agriculture, land use land-use change and forestry, and the waste sectors. From this point of view, biogas energy can contribute significantly to reach the emission reduction targets of Turkey.
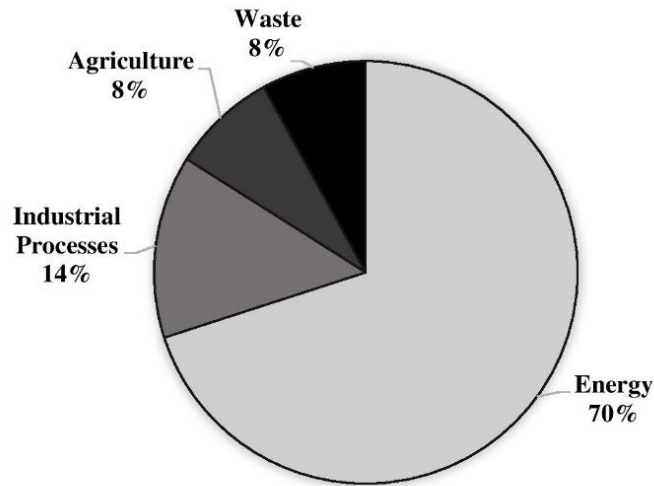
Figure 1. Sectoral distribution of the generated greenhouse gas emissions in Turkey.

Figure 2 shows the European countries with highest biogas production capacity. Biogas production in EU-28 Countries have reached to 15887 TOE in 2015. Germany has the highest share (50%) in total biogas production in Europe (Meyer et al., 2017) followed by United Kingdom, Italy, Czechia and France.
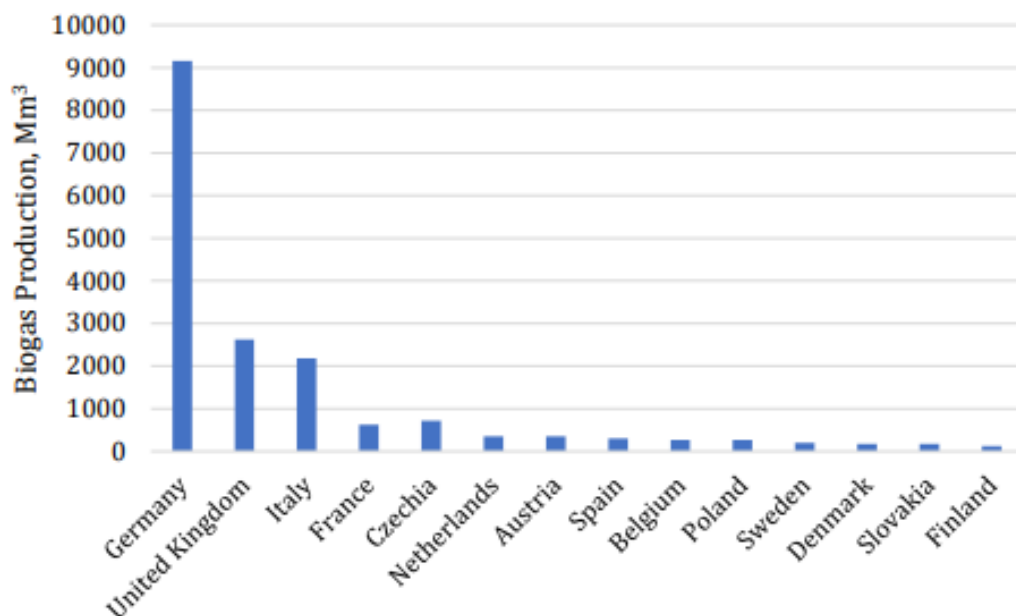
Figure 2. Biogas production capacity in Europe (Eurostat, 2015).

According United Nations (UN), food demand will rise by 70 % worldwide by 2050. In this context, the poultry sector will gain global importance for supplying protein foods (Ferreira et al., 2019). Over the last decades, the poultry industry has grown tremendously in order to meet the huge demand for cheap and safe meat and eggs supply. However, the projections towards intensification of the sector on the other hand, have risen the environmental concerns on waste management (Gerber et al., 2007). Managing poultry waste is challenging and results in financial burden for livestock farms. Intensive chicken breeding causes production of high nitrogen content in manure, which hinders poultry waste to be directly used as fertilizer in farmlands (Cavalaglio et al., 2018). Council Directive of 12 December 1991 concerning the protection of waters against pollution caused by nitrates from agricultural sources (91/676/EEC) restricts the use of nitrates to 170 kg/ha.

In Turkey, poultry farming has high economic value and the poultry industry is a prospective and progressive sector. A huge amount of waste is produced from this sector annually. Traditionally, livestock manure is used to fertilize the local farmland. However, severe negative impacts to the environment may occur when manure is directly stored on the farmland; for instance, provoking greenhouse gas emissions, causing animal and human health problems, reducing soil fertility, eutrophication of surface waters due to runoff of excess nitrate and phosphate and spreading of pathogens, antibiotics, heavy metals, etc. in the groundwater, etc. (Ten et al., 2014; Motew et al., 2018; Fuchs et al., 2018).

Anaerobic digestion can be an efficient solution for handling the environmental problems associated with treatment of poultry manure through biogas production. Poultry manure is a highly bio-degradable organic waste which is rich in organic matter and hence an efficient substrate for energy recovery (Altınbaş and Çiçek, 2019). Moreover, poultry manure had higher biogas potential compared to dairy manure with loading rate of solids below 5 % under mesophilic conditions (Itoda and Awulu, 1999) . There are many studies available in literature that have pointed out poultry manure as a potential source of renewable energy (Batzias et al., 2005; Ribeiro et al., 2018; Akyürek and Coşkun, 2019), however, there are no detailed studies available on estimation of the poultry waste derived biogas production in Turkey. Therefore, this study attempts to identify the biogas potential of regions of Turkey considering poultry manure capacity by using the recent data. The assessment of energy and electricity generation capacities and carbon emission reduction potential have carried out.

Materials and Methods

Turkey is a Eurasian country with a minor portion located in South Eastern Europe and the major portion (Anatolia) of is located in Asia Continent. Turkey has 78 million ha total land area. Turkey is composed of seven geographic regions, each having different climate and geographical properties. Turkey's population has reached to 84.34 million in 2020. Agricultural activities and livestock industry have significant role in Turkish Economy. Livestock farming has also great importance in terms of solution to socio-economic problems in the country such as preventing the immigration from rural areas to cities.

Poultry Population

Biogas potential from poultry waste is determined for the seven regions in Turkey. The total number of total poultry population provided from Turkish Statistical Institute (TUIK, 2021) is shown in Figure 3. As can be seen from the figure, most of the poultry population is accumulated in Aegean, Marmara, Black Sea, Central Anatolia and Mediterranean Regions.
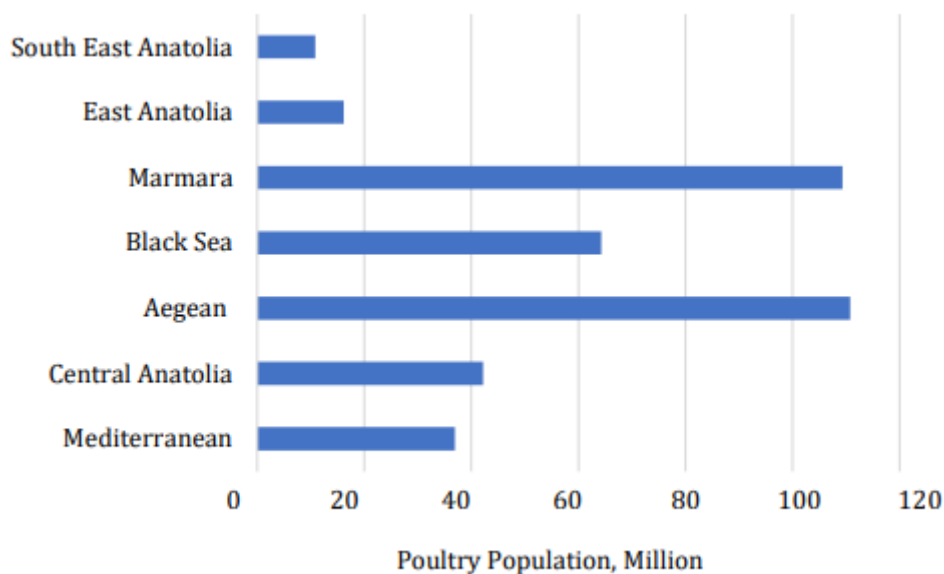
Figure 3. Poultry population (Broiler and Egg Chicken) distribution in Regions of Turkey, 2021.

Poultry Waste Potential

Poultry waste mainly refers to the organic waste consisting of a mixture of manure, bedding material, litter, feed waste, broken eggs and feathers removed from poultry hutches (Kelleher et al., 2002). Table 1 shows the typical waste characteristics of the poultry waste and Figure 4 shows the available poultry waste production in Turkey year 2021.

Table 1. Characterization of Poultry Manure (Özyurt 2010; Kelleher et al., 2002; Özer, 2017)

Total solids (TS), %	44
Volatile total solids (VTS), %	89
C/N	12.24
pH	8.8
Total Nitrogen (dry, %)	3.56
P_2O_5 (dry, %)	0.71
K_2O_5 (dry, %)	3.79
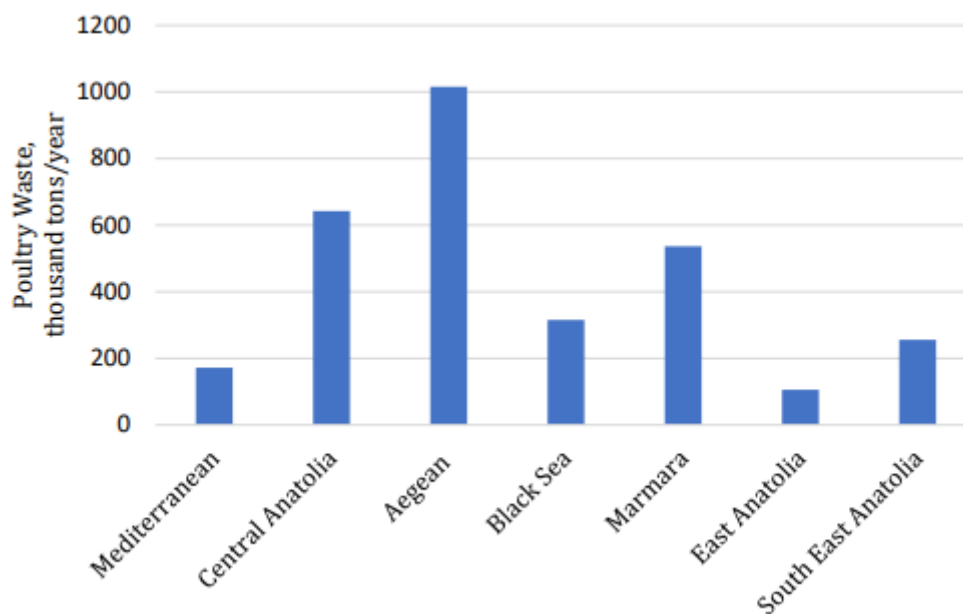
Figure 4. Distribution of poultry waste from egg chicken in Regions of Turkey, 2021.

Biogas Potential

Biogas potential is affected by are many factors such as type of the animal, body weight, total solids ratio, volatile solids ratio, the availability ratio of waste and operating conditions of the anaerobic digestion process. Excess ammonia content, high temperature and/or pH levels are some of the operational obstacles that can hinder the methane production in anaerobic digesters (Kelleher et al., 2002).

The egg chicken wastes are considered to be feasible for anaerobic digestion operation for efficiently producing biogas and organic fertilizer than broiler chicken wastes (MoENR), therefore the theoretical potential of biogas production has calculated from the amount of waste derived from egg chickens.

Theoretical biogas production potential is calculated as follows (Abdeshahian et al., 2016):

$$TBP = M * TS\% * VTS\% * AC * EB_{VTS} \tag{1}$$

where TBP denotes the theoretical potential of biogas (m³/year),

M is the total amount of the poultry manure produced for each region (kg/year)

TS represents the ratio of the total solids of the poultry manure, %

VTS is the ratio of total volatile solids in the poultry manure, %

AC denotes the availability ratio, %

EB_{VTS} is the quantity of estimated biogas produced per kg of the volatile total solids (m³/kg VTS).

In the current study, the availability of the poultry has taken as 99 % due to high residence time of poultry in the hens. The quantity of estimated biogas produced per kg of the volatile total solids is in the range of 300-450 l/kg VTS for poultry (Avcıoğlu and Türker, 2012).

Energy Recovery

The amount of energy produced from bio-methane (kWh/year) is calculated based on Equation 2;

$$E_M = TBP * M_p * E_{CH_4} \qquad (2)$$

M_P represents the methane production ratio of biogas %

E_{CH4} is the energy content of methane (36 MJ/m^3 CH$_4$)

Electricity generation from bio-methane is calculated from Equation 3;

$$E_{Me} = E_M * \eta \qquad (3)$$

η denotes electricity conversion of bio-methane energy depending on the power generation plant (40 %).

Greenhouse Gas (GHG) Emissions

Potential savings of GHG emissions are estimated by considering the on-land deposition of manure, biogas production from anaerobic digestion process and fossil fuel displacement. On-farm deposition of fresh poultry manure results in methane emissions due to organic content of the waste. The methane emission due to unprocessed poultry manure is calculated by Equation 4 (IPCC, 2006):

$$E_{CH4} = 0.67 * N * VS * B_o * MCF \% \qquad (4)$$

Where N is the number of poultry,

VS denotes the volatile solids, kg dry manure/year,

B_o is the biodegradability of the organic matter: 0.24 (kg CH4/kg VS),

MCF is the methane conversion factor for poultry litter in an open pit: 65 %.

Indirect nitrous oxide emissions occur via nitrification and denitrification of nitrogen content in the manure during outdoor storage. Nitrous oxide emission during natural processing of poultry manure can be formulated by [IPCC, 2007] Equation 5:

$$E_{N2O} = N * N_{ex} * MS * EF_{N2O-D} * 1.57 \qquad (5)$$

Where N is the number of poultry,

N_{ex} is annual average nitrogen excretion/poultry, 0.6 kg N/year,

MS is the fraction of litter stockpiled, 1 for outdoor storage,

EF_{N2O-D} is the emission factor for direct N$_2$O emissions in 0.002 kgN$_2$O-N/kg N.

Total amount of uncontrolled release of biogas to the atmosphere is calculated as,

$$B_{CO2} = E_{CH2} + E_{N2O} \qquad (6)$$

In contrast to fossil fuel produced CO$_2$, emission from biogas have much shorter carbon cycle among atmospheric CO$_2$ to plant, plant to poultry, poultry to manure (Cornejo and Wilkie, 2010). Emission factor of 0.8 kW$_e$/CO$_2$ is defined for electricity generation from biogas while it is 1 kW$_e$/CO$_2$ for electricity generation from coal (Murphy et al., 2004);

$$B_{e,CO2} = E_M * 0.8 \qquad (7)$$

The average efficiency of the conversion from coal to electricity is used as 0.33 in Equation (8) to evaluate the coal displacement with biogas.

$$C_{e,CO2} = \frac{E_M}{0.33} * 1.0 \tag{8}$$

Total savings of GHG emission from electricity generation from biogas on behalf of coal is obtained from the following equation (Özer, 2017):

$$TES_{CO2} = B_{CO2} + C_{e,CO2} - B_{e,CO2} \tag{9}$$

Organic Fertilizer Production

The residue of the anaerobic digestion process is the organic fertilizer which is a valuable product to be used for agricultural, landscaping and horticultural applications. The slurry retained after digestion process is a thick sludge with a moisture content of about 80-90 % which can be dewatered by simple filtration before it is sold as solid fertilizer.

The amount of the organic residual that can be obtained after biogas processing is calculated by Equation 10;

$$F = M * AC * TS\% * NVTS\% * OS\% \tag{10}$$

where F is the amount of fertilizer produced from digester, ton/year,
NVTS is the ratio of non-volatile total solids in poultry manure, %
OS is the ratio of organic solids in non-volatile total solids.

Results and Discussion

Animal waste derived from the livestock farms and processing industries has high organic content that can lead to environmental pollution. These wastes are generally characterized by their high nitrogen and phosphorus contents and generally used as fertilizer by means of spreading on the farmlands. Direct application of animal waste to farmlands results in nutrient imbalance in the soil and triggers environmental contamination due to transfer of pathogens, diseases, antibiotics, heavy metals and hormones (Abdeshahian et al., 2016; Mainali et al., 2017). Suitable treatment of livestock manure by means of anaerobic digestion provides getting rid of negative environmental impacts of manure to air, soil and water resources, protecting human health, preventing bad odors and stabilizing the manure to form organic fertilizer (Hol-Nielsen et al., 2009; Gebrezgabher et al., 2010).

In this study, the potential of poultry population in Turkey is evaluated in terms of energy production from biogas, waste management and climate change impacts. The share of poultry population and poultry waste potential in Turkey is demonstrated in Figure 5. As can be seen from the figure, poultry population has the highest share (85%) in the animal stock of Turkey, whereas it has the lowest manure production potential (9%). The biogas conversion yield of poultry on the other hand, is much greater than those of cattle and small ruminants' manure. Therefore, poultry waste becomes a favorable substrate for biogas production in anaerobic digesters.
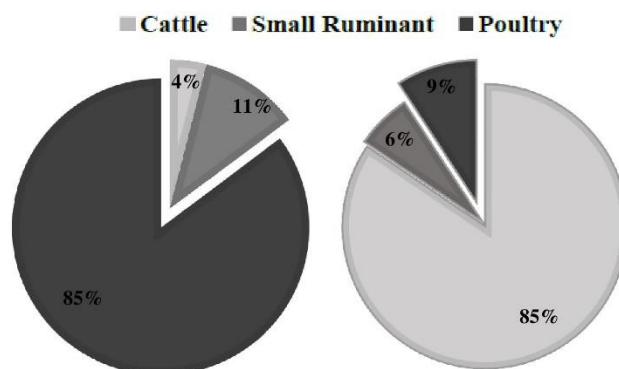
Figure 5. Comparison of the animal population (a) and available waste production potential by animal type (b) in Turkey (2021).

The results of the calculations revealed that total theoretical biogas production potential from poultry manure in Turkey is 327.8 Million m3/year. Biogas and bio-methane production potential in different regions of Turkey are illustrated in Figure 6. As expected from the amount of waste inventories, Aegean Region has shown the highest biogas production potential from poultry waste in Turkey.
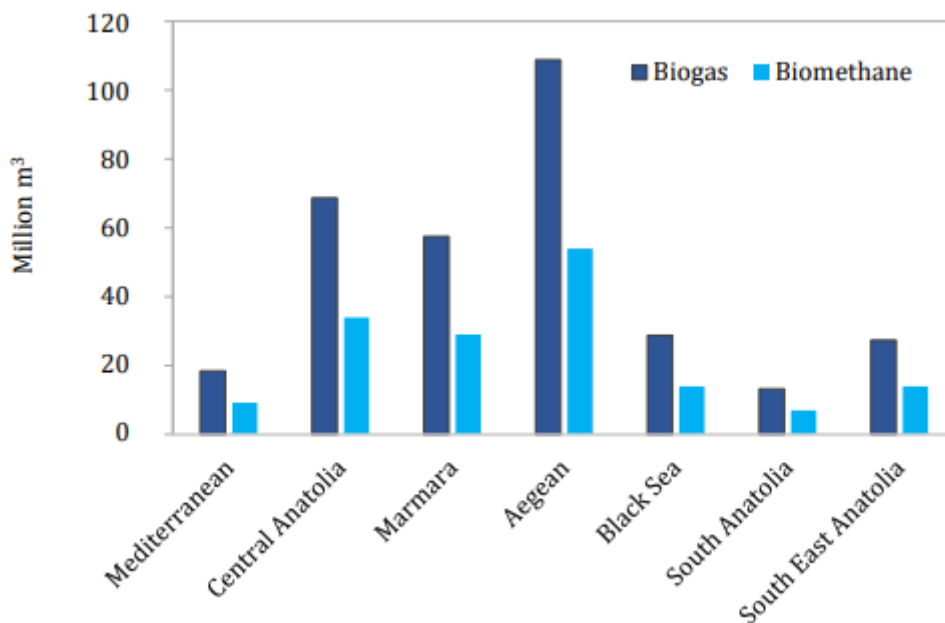
Figure 6. Contribution of each region to biogas and bio-methane production.

Estimated potential of energy and electricity productions from poultry manure are presented in Table 2. Total annual potential of energy production from poultry waste derived biogas in Turkey accounts for ˜1639 GWh.

Table 2. Annual Energy, electricity production potential from poultry waste.

Region	GWh	GWe
Mediterranean	92.03	33.13
Central Anatolia	343.35	123.61
Marmara	287.67	103.56
Aegean	543.88	195.80
Black Sea	168.99	60.84
South Anatolia	66.23	23.84
South East Anatolia	136.94	49.30
Total	1639	590

Total annual electricity generation potential of poultry derived biogas can contribute to 590 GWe to the electricity production from renewable sources. As an energy importing country, energy production from local sources especially from organic waste is of great importance for Turkey. Biogas production not only contributes to energy supply but also helps to reduce greenhouse gas emissions via avoiding CH_4 and N_2O emissions from on-farm depositing. Figure 7 shows the potential of the regions of Turkey in terms of total greenhouse gas (GHG) emission savings.
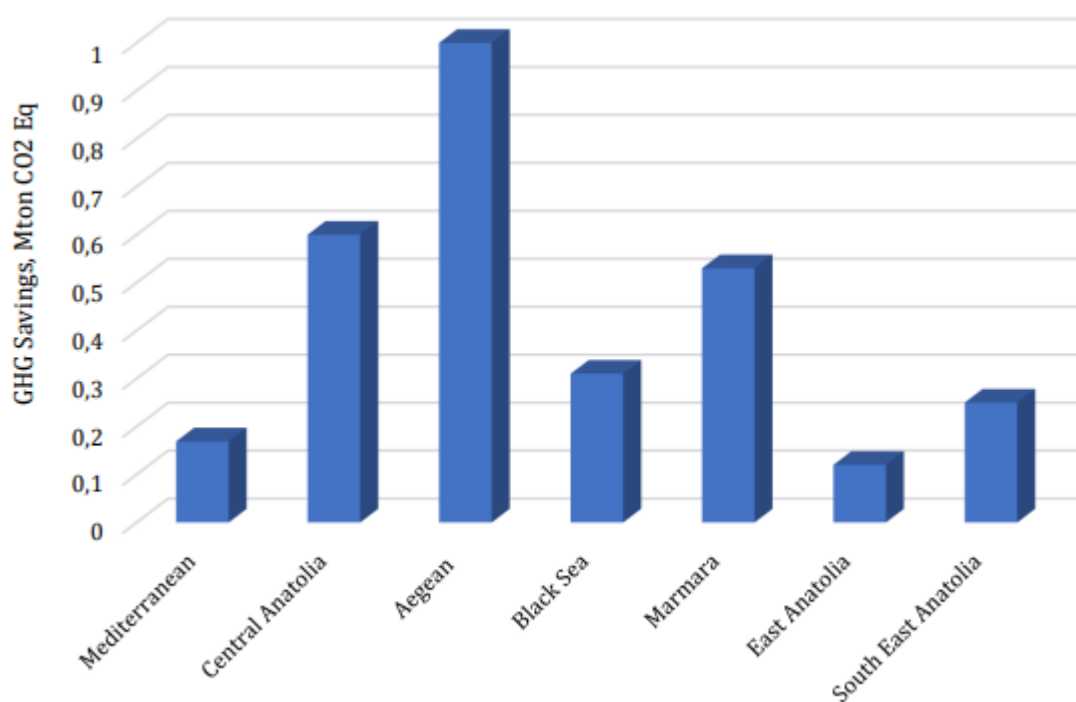
Figure 7. Total GHG emission savings in each region.

The by-product of the anaerobic digestion process is the digestate which has high fertilizing potential compared to unprocessed animal manure. During the process of anaerobic digestion, in contrast to composting, the amount of nutrient content of the feedstock stays almost the same. However, the form of nutrients in the manure changes. Nitrogen, Phosphorous and Potassium are the key nutrients in the organic fertilizers. Small amount of nitrogen is emitted within biogas whereas the high amount of total nitrogen (>99%) retains within the bio-slurry in the digester (Wysocka-Czubaszek, 2019). About 50 % of the organic nitrogen of manure is converted to ammonia which is readily available for uptake by plants (Kamal et al., 2011). Therefore, high

nitrogen availability in the digestate makes it more suitable for fertilizer application compared to untreated poultry manure to act as a substitute to Synthetic-N fertilizers.

The composition of the poultry derived organic fertilizer is reported to have 1.8-2.7 % of Nitrogen, 0.8-3.3 % of Phosphorous and 0.5-0.8% of Potassium (K) contents (Kamal et al., 2011; Islam, 2006). On farm application trials of the digestate from poultry waste have shown that the organic fertilizer has superior impact on the yield of agricultural crops (Cabbage, tomato, etc.) compared to synthetic fertilizers (Alburquerque et al., 2012). The stability of the bio-slurry determines the dynamics of nitrogen in soil; hence before applying directly to the field, some aerobic post treatment methods such as curing and maturing may be required to stabilize the product. From the calculations (Equation 10), total 0.251 million ton/year organic fertilizer production can be achieved by using anaerobic digestion technology in Turkey.

The estimated potentials of production of energy and GHG emissions are summarized in two different scenarios and illustrated in Figure 8. In the figure, the first scenario represents the emissions from on farm deposition of poultry manure and coal combustion for electricity generation. In the second scenario, on the other hand, poultry waste is deposited in storage tanks and utilized in anaerobic digestion plant to produce biogas and GHG emissions only resulted from biogas combustion to produce the same amount of electricity. As can also be seen from the illustration, biogas production is a feasible route for poultry sector to reduce the risk of methane and nitrous oxide emissions to atmosphere. Environmental hazard can considerably be reduced if poultry waste is anaerobically digested instead of spreading as raw fertilizer onto farmlands.

Renewable power is of great importance in Turkey. Most of the investments in renewable electricity generation is accumulated in solar and wind energy. However, bio-waste is abundant organic source and has significant potential to contribute to renewable energy mix. In Turkey, renewable energy investments are supported via guaranteed feed-in tariff system. Feasibility studies on biogas power shows the payback periods in the range of 2-3 years (Çoban et al., 2016) that poultry waste valorization via biogas production can be considered as a worthwhile energy option in Turkey.
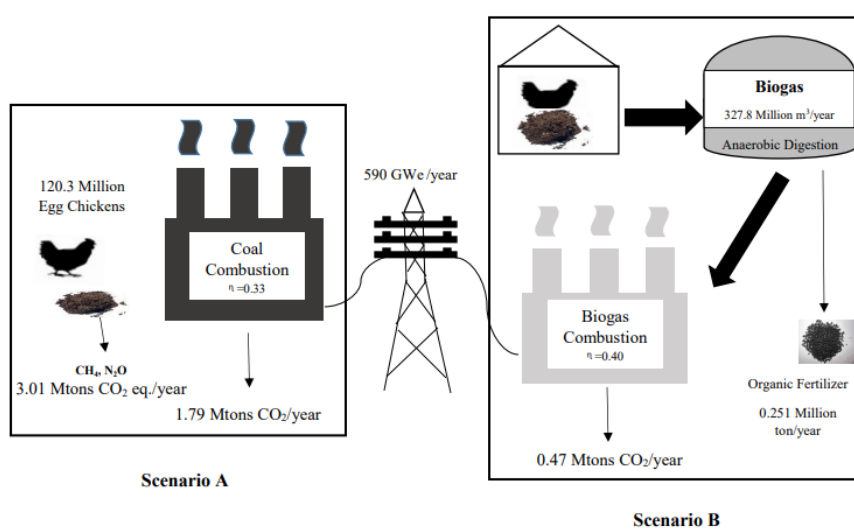
Fіgure 8. Schematic description of the inputs and outputs of (A) on farm manure deposition and coal combustion (B) biogas production.

Concluding Remarks

In Turkey, high amount of biodegradable poultry waste generates. As an energy importing country, Turkey needs to focus and invest on utilization of her renewable sources for providing energy security and for reaching the envisaged emission reduction targets for 2030. The estimation study of environmental impact and energy potential of biogas production from poultry waste has revealed that egg chicken waste has 327.8 million m^3/year biogas production potential corresponding to annual 590 GWe electricity generating capacity and about 3 Mt CO2 equivalent emission mitigation. The residual of biogas production process has annual 251 thousand tons of organic fertilizer production potential for agricultural, landscaping and horticultural applications.

REFERENCES

Abdeshahian, P., Lim, J. S, Ho, W.S., Hashim, H., Lee, C.T. (2016) Potential of biogas production from farm animal waste in Malaysia. Renew. Sust. Energ. Rev., 60, 714-723. DOI: 10.1016/j.rser.2016.01.117

Alburquerque J.A., de la Fuente C., Bernal M.P. (2012) Chemical properties of anaerobic digestates affecting C and N dynamics in amended soils. Agr Ecosyst Environ 160, 15–22. https://doi.org/10.1016/j.agee.2011.03.007

Akyürek, Z., (2018) Potential of Biogas Energy from Animal Waste in the Mediterranean Region of Turkey, *J Energ Sys.* 2(4), 159-167, (2018). DOI: 10.30521/jes.455325

Akyürek, Z., (2019a) Sustainable valorization of animal manure and recycled polyester: co-pyrolysis synergy, *Sustainability*, 11(8), 2280. https://doi.org/10.3390/su11082280

Akyürek, Z. (2019b) Energy Recovery from Animal Manure_Biogas Potential of Burdur, Turkey, *Eskişehir Tech. Uni. J Sci. Tech., Part A: Appl. Sci. Eng.,* 20(2), 161-170. DOI:10.18038/aubtda.456873

Akyürek, Z, Coşkun, S. (2019) Determination of Biogas Energy Potential of Aegean Region Based on Animal Waste. *Celal Bayar Uni. J Sci.* 15(2), 171-174. Doi: 10.18466/cbayarfbe.492880

Altinbas, M., Cicek, A.O. (2019) Anaerobic co-digestion of chicken and cattle manures: Free ammonia inhibition, *Energ Source Part A,* 41(9), 1097-1109. https://doi.org/10.1080/15567036.2018.1539143

Avcioğlu, A.O., Türker, U. (2012) Status and potential of biogas energy from animal wastes in Turkey, *Renew. Sust. Energ. Rev.,* 16, 1557–1561. https://doi.org/10.1016/j.rser.2011.11.006

Batzias, F.A., Sidiras, D.K., Spyrou, E.K. (2005) Evaluating livestock manures for biogas production: a GIS based method. *Renew Energ.,* 30, 1161–76. https://doi.org/101016/j.renene.2004.10.001

Cavalaglio, G., Coccia, V., Cotana, F., Gelosia, M., Nicolini, A., Petrozzi, A. (2018) Energy from poultry waste: An Aspen Plus-based approach to the thermo-chemical processes, *Waste Manag.* 73, 496-503. http://dx.doi.org/10.1016/j.wasman.2017.05.037

Cornejo, C., Wilkie, A.C. (2010) Greenhouse gas emissions and biogas potential from livestock in Ecuador. Energy Sustain Dev., 14, 256-266. https://doi.org/10.1016/j.esd.2010.09.008

Coban, V., Cagman, S., Eyidogan M., Kılıc Canka, F., Kaya, D. (2016) Economic Analysis of Biogas Production from Chicken Manure, In the Proceedings of 8th International Ege Energy Symposium and Exhibition.

Demirbaş, A. (2010) *Methane Gas Hydrate*, Springer, 57-76. ISBN: 978-1-84882-871-1

Eurostat database (2019) https://ec.europa.eu/eurostat/data/database

Ferreira, L.R.A., Otto, R.B., Silva, F.P., De Souz, S.N.M., De Souz S.S., Ando Junior, O.H. (2018) Review of the energy potential of the residual biomass for the distributed generation in Brazil, *Renew. Sust. Energ. Rev,* 94, 440–455. https://doi.org/10.1016/j.rser.2018.06.034

Fuchs, W., Wang, X., Gabauer, W., Ortner, M., Li, Z. (2018) Tackling ammonia inhibition for efficient biogas production from chicken manure: Status and technical trends in Europe and China, *Renew. Sust. Energ. Rev.,* 97, 186–199. https://doi.org/10.1016/j.rser.2018.08.038

Gerber, P., Opio, C., Steinfeld, H. (2007) Poultry production and the environment – a review, *Poultry in the 21st Century.* http://www.fao.org/Ag/Againfo/home/events/bangkok2007/docs/part2/2_2.pdf Jönsson, O., Polman, E., Jensen, J.K., Eklund, R., Schyl, H., Ivarsson, S. (2003) Sustainable Gas Enters the European Gas Distribution System, http://www.dgc.eu/sites/default/files/filarkiv/documents/C0301_sustainable_gas.pdf

Gebrezgabher, S.A., Meuwissen, M.P.M., Prins, B.A.M., Lansink, A.G.J.M.O. (2010) Economic analysis of anaerobic digestion – a case of Green power biogas plant in The Netherlands". *NJAS – Wageningen J Life Sci* 57, 109–115. https://doi.org/10.1016/j.njas.2009.07.006

Guerra-Rodriguez, E., Diaz-Ravina, M., Vazquez, M. (2001) Co-composting of chestnut burr and leaf litter with solid poultry manure, Bioresour. Tech. 78, 107-109, PII: S0960-8524(00)00159-0

Hol-Nielsen JB, Al-Seadi T, Oleskowicz P. (2009) The future of anaerobic digestion and biogas utilization". *Bioresour. Technol.* 100, 5478–5484. https://doi.org/10.1016/j.biortech.2008.12.046

IPCC. Guidelines for national greenhouse gas inventories. Chapter 10: emission from livestock and manure management. (2006). https://www.ipcc-nggip.iges.or.jp/public/2006gl/

IPCC. Climate change 2007: synthesis report. Contribution of working groups I, II and III to the fourth assessment report of the intergovernmental panel on climate change. Geneva, Switzerland: IPCC; (2007) https://www.ipcc.ch/report/ar4/syr

Islam, M.S. (2006) Use of Bioslurry as Organic Fertilizer in Bangladesh Agriculture", International Workshop on the Use of Bioslurry Domestic Biogas Programmes. http://www.bibalex.org/search4dev/files/338830/172330.pdf

Itoda, I.N., Awulu, J.O. (1999) Effects of total solids concentrations of poultry, cattle, and piggery waste slurries on biogas yield, *Transactions of the ASABE* 42, 1853-1855,. Doi:10.13031/2013.13350

Kamal, A., Rabbani, G., Islam, S. (2011) Processing of Grameen Shakti Jaibo Sar as Organic Fertilizer and Its Uses. http://www.bibalex.org/search4dev/files/338830/172330.pdf

Kelleher, B.P., Leahy, J.J., Henihan, A.M., O'Dwyer, T.F., Sutton, D., Leahy, M.J. (2002) Advances in poultry litter disposal technology – a review, Bioresour. Tech. 83, 27–36. PII: S0960-8524(01)00133-X

Li, K., Liu, R., Sun, C. (2016) A review of methane production from agricultural residues in China, *Renew. Sust. Energ. Rev.,* 5, 857–865. http://dx.doi.org/10.1016/j.rser.2015.10.103

Lyytimäki, J. (2018) Renewable energy in the news: Environmental, economic, policy and technology discussion of biogas. *Sustain Pro Consump.* 15, 65-73. https://doi.org/10.1016/j.spc.2018.04.004

Maghanaki, M.M., Ghobadian, B., Najafi, G., Galogah, R.J., (2013) Potential of biogas production in Iran. *Renew. Sust. Energ. Rev,* 28, 702–714. http://dx.doi.org/10.1016/j.rser.2013.08.021

Mainali, B., Emran, S.B., Silveira, S. (2017) Greenhouse gas mitigation using poultry litter management techniques in Bangladesh, Energ., 127, 155-166. http://dx.doi.org/10.1016/j.energy.2017.03.103

Mao, C., Yongzhong, F., Xiaojiao, W., Guangxin, R., (2015) Review on research achievements of biogas from anaerobic digestion, *Renew. Sust. Energ. Rev.,* 45, 540-55. https://doi.org/10.1016/j.rser.2015.02.032

Meyer, A.K.P., Ehimen, E.A., Holm-Nielsen, J.B. (2017) Future European biogas: animal manure, straw and grass potentials for a sustainable European biogas production. *Biomass Bioenerg.,* 111, 154-164. https://doi.org/10.1016/j.biombioe.2017.05.013

Motew, M., Booth, E.G., Carpenter, S.R., Chen, X., Kucharik, C.J. (2018) The synergistic effect of manure supply and extreme precipitation on surface water quality, *Environ Research Letters* 13, 044016. https://doi.org/10.1088/1748-9326/aaade6

Murphy, J.D., McKeogh, E., Kiely, G. (2004) Technical/economic/environmental analysis of biogas utilisation. Appl Energy 77, 407-427. https://doi.org/10.1016/j.apenergy.2003.07.005

Ozyurt, O. (2010) Energy issues and renewables for sustainable development in Turkey, Renew. Sust. Energ. Rev., 14, 2976-2985. https://doi.org/10.1016/j.rser.2010.08.002

Özer, B. (2017) Biogas Energy Opportunity of Ardahan City of Turkey, Energ., 139, 1144-1152. https://doi.org/10.1016/j.energy.2017.07.052

Patterson, T., Esteves, S., Dinsdale, R., Guwy, A. (2011) An evaluation of the policy and techno-economic factors affecting the potential for biogas upgrading for transport fuel use in the UK, *Energ Policy,* 39, 1806–1816. doi:10.1016/j.enpol.2011.01.017

Panwar, N.L., Kothari, R., Tyagi, V.V. (2012) Thermo Chemical Conversion of Biomass–Eco Friendly Energy Routes, *Renew. Sust. Energ. Rev.,* 16, 1801-16. https://doi.org/10.1016/j.rser.2012.01.024

Ribeiro, E.M., Barros, R.M., Filho, G.L.T., Santos, I.F.S., Sampaio, L.C., Santos, T.V., Silva F.G.B., Silva, A.P.M., Freitas, J.V.R. (2018) Feasibility of biogas and energy generation from poultry manure in Brazil, *Waste Manag. Research,* 36, 221-235. https://doi.org/10.1177/0734242X177518

Sahoo, K., Mania, S., Das, L., Bettinger, P. (2018) GIS-based assessment of sustainable crop residues for optimal siting of biogas plants, *Biomass Bioenerg,* 110, 63–74. https://doi.org/10.1016/j.biombioe.2018.01.006

Scarlat, N., Fahl, F., Dallemand, J.F., Monforti, F., Motola, V. (2018) A spatial analysis of biogas potential from manure in Europe, *Renew. Sust. Energ. Rev.,* 94, 915–930. https://doi.org/10.1016/j.rser.2018.06.035

Terrapon-pfaff, J.C., Fischedick, M., Monheim, H. (2012) Energy potentials and sustainability— the case of sisal residues in Tanzania, *Energy Sustain Dev.,* 16, 312–319. https://doi.org/10.1016/j.esd.2012.06.001

Ten Hoeve, M., Hutchings, N.J., Peters, G.M., Svanström, M., Jensen, L.S., Bruun, S. (2014) Life cycle assessment of pig slurry treatment technologies for nutrient redistribution in Denmark. *J Environ. Manag.*, 132, 60–70. https://doi.org/10.1016/j.jenvman.2013.10.023

Turkish Statistical Institute (TUIK) 2021. http://tuik.gov.tr

Yentekakis, I.V. and Grammatiki, G. (2017) Biogas Management: Advanced Utilization for Production of Renewable Energy and Added-value Chemical, *Front Environ Sci.*, 5, 1-18. https://doi.org/10.3389/fenvs.2017.00007

Wysocka-Czubaszek, A. (2019) Dynamics of Nitrogen Transformations in the Soil Fertilized with Digestate from Agricultural Biogas Plant, *J Ecolog Eng.* 20(1), 108-117. https://doi.org/10.12911/22998993/93795

Essential Oils and Their Antimicrobial Effects

Ayşen ALTINER[1]
Tanay BİLAL[2]

Introduction

Aromatic plants and essential oils obtained from them have been used for centuries in our country, as well as all over the world, for the treatment of diseases, and as a preservative and flavoring in food products. Reasons such as the synthetic additives, the use of which has increased in parallel with the developing technology, have many side effects on health and the resistance of microorganisms to synthetic antimicrobials have reintroduced the use of medicinal and aromatic plants and essential oils and extracts from them and have accelerated the studies onthe development of these products for use in food, animal feed and organic farming applications (Bayaz, 2014).

Essential oils are highly concentrated, aromatic, volatile, easily crystallizable and hydrophobic liquids produced by different plant materials such as roots, fruits, wood, herbs, bark, branches, leaves, seeds, buds, rhizomes and flowers of any botanical species. Strong odor is one of the prominent characteristic features of essential oils (Wani et al., 2021). Essential oils are obtained from various aromatic plants that grow in the geography between the warm tropical countries and the temperate Mediterranean region countries (Bakkali et al., 2008). Essential oils produced for industrial purposes are mainly extracted from orange, corn, eucalyptus, citronella, peppermint and lemon, but the more commonly used essential oils are obtained from lavender, chamomile, peppermint, tea tree, geranium, jasmine, rose, rosemary, frankincense and sandalwood (Djilani & Dicko, 2012).

Although essential oils are defined as oils because they are insoluble in water and dissolve in organic solvents, they are different from fixed oils (Bayaz, 2014). They are hydrophobic, soluble in alcohol, non-polar or weakly polar solvents, waxes and oils, but very slightly soluble in water, and most are colorless or pale yellow, liquid, and have a lower density than water (except essential oils of sassafras, vetiver, cinnamon and clove) (Martín et al., 2010). Due to their molecular structure (the presence of olefinic double bonds and functional groups such as hydroxyl, aldehyde, ester), essential oils can be easily oxidized by light, heat and air, and their colors darken (Djilani & Dicko, 2012). Therefore, to prevent oxidation, essential oils should be stored in a cool and dark place and best suited in amber glass containers (Wani et al., 2021).

The composition and amounts of essential oils vary depending on the type of plant, the part of the plant obtained from, the mode of production, the geographical structure of the region where it is grown and the climate (Bayaz, 2014). The components of essential oils can be broadly classified as volatile and non-volatile fractions. The general chemical composition of the volatile fraction of

[1] Prof. Dr. İstanbul Üniversitesi-Cerrahpaşa, Veteriner Fakültesi, Biyokimya Anabilim Dalı
[2] Prof. Dr. İstanbul Üniversitesi-Cerrahpaşa, Veteriner Fakültesi, Hayvan Besleme ve Beslenme Hastalıkları Anabilim Dalı

the aromatic oil includes mono- and sesquiterpene components, alcohols, aliphatic aldehydes and esters, as well as various oxygenated derivatives. On the other hand, 1-10% by weight of the isolated essential oil consists of carotenoids, fatty acids, flavonoids and waxes classified as non-volatile residues (Hussain et al., 2008). Terpenoids and phenylpropanoids are the main components of essential oils. In addition, few aromatic and aliphatic components are also present (Kürekci & Sakin, 2017). In the essential oil complex, phenylpropanoids are present in lesser amounts than terpenoids. Terpenoids constitute the largest group of plant active components and the most important elements are monoterpenoids (Figure 1) and sesquiterpenoids. Thymol and carvacrol in thyme, limonene in orange, pinene in laurel and menthol in mint are the most important examples of terpenoids (Çayıroğlu, 2015). Examples of phenylpropanoids are anethole in fennel, eugenol in cinnamon, cinnemaldehyde in cinnamon and buckthorn (Şahan, 2012).
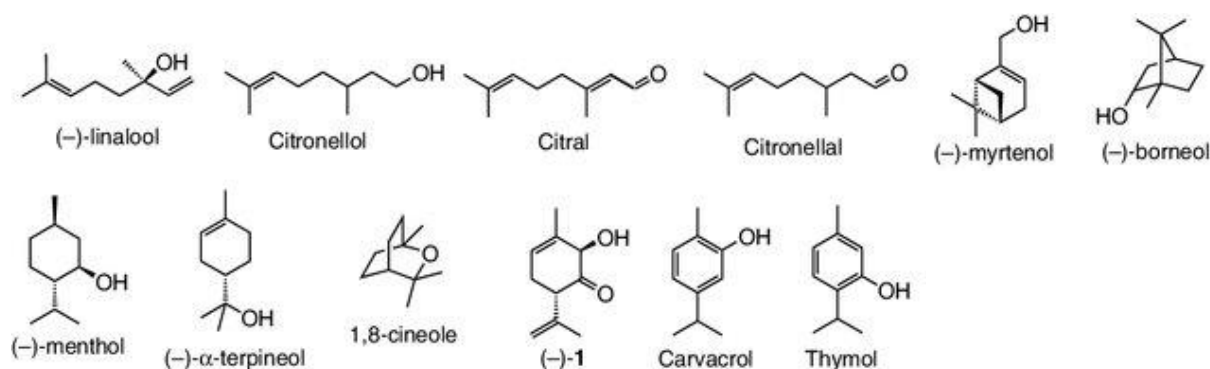
Figure 1. Structures of monoterpenoids

Of the approximately 3000 known essential oils, about 300 are of commercial importance, and they or some of their components are used in pharmacology, agricultural applications, preservatives and flavorings in the food industry, alcoholic beverages, animal nutrition, sanitation, cosmetics, perfumery products and folk medicine as a natural therapeutic (Perry et al., 2003). These essential oils are of notable importance as insecticides in agriculture, as preservatives and flavorings in food technology, in beverages, foods and spices, as perfumes in the perfumery industry, as healers in pharmacy and aromatherapy (Fernandez-Lopez & Viuda-Martos, 2018). These plant extracts play a role in preserving food due to their strong antimicrobial activities along with their antioxidant properties. Essential oils can also serve as natural ingredients in cosmetics for microbial protection (Wani et al., 2021). In studies on the use of essential oils in animal nutrition, it is stated that the addition of these oils to feed and water significantly improves feed consumption, feed efficiency and carcass quality (Güler & Dalkılıç, 2005).

Essential oils of aromatic plants have become the focus of research because they increase the taste and consumption of foods, stimulate the secretion of digestive enzymes, increase gastrointestinal motility, have antimicrobial, antiviral, antiparasitic, antifungal, immunomodulatory, antioxidant and anti-inflammatory effects (Giannenas et al., 2013). Studies have shown that essential oils have antiviral, antioxidant, antibacterial, antidiabetic and anticancer properties due to the phenolic hydroxyl groups, ketones, aldehydes, hydrocarbons, ether, α-tocopherol and monoterpenes they contain (Lammari et al., 2021). In the pharmaceutical industries, drugs in the form of capsules, syrups, ointments, creams and sprays contain certain essential oil compositions and their production numbers are constantly increasing (Aziz et al., 2018).

Essential oils are also used in various combinations in the treatment of many diseases such as digestive problems, headaches, muscle and joint pains, respiratory tract infections, wounds, burns, hair loss, eczema and some other skin disorders, and psychological disorders such as anxiety, depression, attention and concentration problems, and insomnia (Kurt & Tatlı Çankaya, 2021). In

a study, it was reported that inhalation of eucalyptus essential oil every 30 minutes for 3 days after total knee replacement significantly reduced pain and inflammatory responses (Kim et al., 2014).

Antimicrobial Effects of Essential Oils

Essential oils have strong potential as antimicrobial agents. In studies, the effectiveness of essential oils obtained from various plants against different foodborne pathogens, bacteria and viruses that cause disease in humans has been demonstrated by in-vitro experiments (Kürekci & Sakin, 2017). It is reported that the antimicrobial effect occurs with the lipophilic properties of the oils and the presence of a number of terpenoid and phenolic compounds in their chemical structures. The antimicrobial activities of these essential oils are attributed to their rich chemical contents such as p-cymene, ogenol, cinnamic aldehyde, thymol and carvacrol (Wani et al., 2021).

Essential oils show their effects by destroying pathogenic microorganisms in the digestive systems of animals and/or by increasing the beneficial microorganism population that provides better digestion and absorption of nutrients. It is also suggested that essential oils limit the growth of microorganisms by inhibiting the effects of enzymes that synthesize the microorganism cell wall (Canbolat et al., 2011). Factors that alter the antimicrobial effects of essential oils are their chemical content, concentration, interactions between primary active ingredients, and vulnerability of microorganisms. The presence of both minor and major components of essential oils can produce synergistic or antagonistic effects, leading to altered activity (Nascimiento et al., 2018). Many essential oils show synergistic antimicrobial activity when used in combination (Kürekci & Sakin, 2017).

For example, eucalyptus essential oil is used to relieve asthma, bronchitis, cough, cold and flu symptoms in the respiratory tract. Rose essential oil has antibacterial, antiviral, antifungal, antiseptic, antioxidant, analgesic, anti-inflammatory and wound healing effects (Mohebitatar et al., 2017). Myrrh (Figure 2) essential oil is used safely in recommended doses for colds, flu, sinusitis, cough, sore throat, gum problems and skin disorders (Grbic et al., 2018). Garlic has been used as medicine for centuries to treat colds, influenza, and other types of infections (Asif et al., 2020). The problem of pathogens in food and meat products has been tried to be solved by applying low doses of essential oils (Aziz et al., 2018).
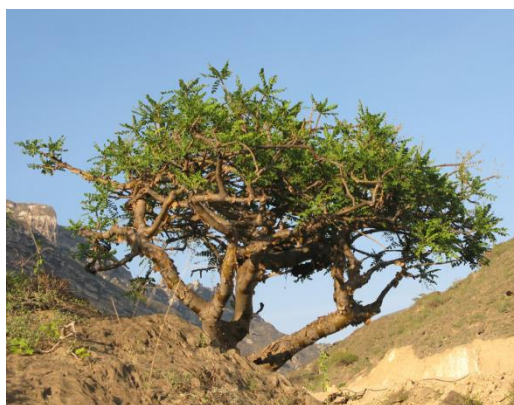
Figure 2. Myrrh tree

Antibacterial Effects of Essential Oils

The application of aromatic herbs as antibacterial agents to prevent bacterial growth and rot has been going on since ancient times (Aziz et al., 2018). Essential oils have antibacterial properties for many types of bacteria, including rumen bacteria, thanks to the active components in their structure. It is thought that essential oils can turn the fermentation profile in favor of the animal

by suppressing Gram (+) bacteria in the rumen (Demirtaş et al., 2011). It has been noted that essential oils containing phenolics and aldehydes generally exhibit better antibacterial activity. The antibacterial properties of essential oils may vary depending on factors such as the geographical conditions of the plant from which the essential oil is obtained, the harvest time, the method of obtaining, the type and chemical structure of the active substance in its structure (Şahan, 2012).

Essential oils have antibacterial effects on many microorganisms, including Gram (-) and Gram (+) bacteria. It was determined that essential oils of *Tanacetum santolinoides* plant collected from the Sinai Peninsula in Egypt showed antibacterial activity against Gram (+) and Gram (-) bacteria (El-Shazly, Dorai & Wink, 2002). Examples of bacteria targeted by essential oils are *Listeria monocytogenes*, *Bacillus sphaericus*, *Enterobacter aerogenes*, *Escherichia coli*, *Pseudomonas aeruginosa*, *Staphylococcus aureus*, *Staphylococcus epidermidis*, *Salmonella typhi*, *Shiguella flexneri* and *Yersinia enterocolitica* (Ramsey et al., 2020). Al-Howiriny (2003) extracted the essential oil of *Salvia lanigera* (Figure 3) and reported that this extract has a very good inhibitory effect against *Bacillus subtilis*, *Staphylococcus epidermidis*, *Proteus mirabilis*, *Mycobacterium smegmatis*, *Candida albicans* and *Candida vaginalis* microorganisms, and however, reported that *Escherichia coli* and *Pseudomonas aeruginosa* were resistant to this essential oil. İlçim, Dığrak & Bağcı (1998) reported that extracts of lichen, myrtle and clove plants inhibited at different rates the growth of *Bacillus megaterium*, *Bacillus subtilis*, *Bacillus brevis*, *Escherichia coli*, *Klebsiella pneumoniae*, *Enterobacter aerogenes*, *Pseudomonas aeruginosa*, *Staphylococcus aureus* and *Listeria monocytogenes* bacteria.

Figure 3. Salvia lanigera

In an *in vitro* study by Sutili et al. (2015), essential oils from *Hesperozygis ringens*, *Ocimum gratissimum* (African basil) and *Ocimum americanum* (American basil) showed potent inhibitory effects against *Aeromonas hydrophila*. An *in vitro* study conducted by Thanissery, Kathariou & Smith (2014) showed that essential oils of clove, rosemary, and mixed thyme-orange inhibited *Campylobacter* and *Salmonella enterica*. The antibacterial activities of essential oils from thyme, rosemary, clove, allspice and cinnamon against *Pseudomonas aeruginosa*, *Staphylococcus aureus* and *Salmonella typhi* have been confirmed (Wani et al., 2021). Lambert et al. (2001) investigated the effects of thymol and carvacrol on *Staphylococcus aureus* and *Pseudomonas aeruginosa* and proved that these substances have better effects when used together than when used alone.

Mitsch et al. (2004) concluded that when essential oil mixtures containing thymol + carvacrol + ogenol + curcumin + piperine are added to the diet, the colonization and growth of *Clostridium perfringens* in the gut of broilers can be controlled. Likewise, Evans, Plunkett & Banfield (2001) reported that a mixture of clove + thyme + peppermint + lemon essential oils reduced the number

of *Clostridium perfringens* in broilers. In addition, it was determined that the addition of essential oils significantly increased the number of *Bifidobacteria* and *Lactobacillus* in the intestine and significantly reduced the number of intestinal *Escherichia coli* and *Salmonella* (Kürekci & Sakin, 2017). Kim, Marshall & Wei (1995) reported that essential oils obtained from medicinal and aromatic plants are rich in ogenol, carvacrol and thymol, all of which strongly inhibit foodborne pathogens such as *Vibrio vulnificus*, *Listeria monocytogenes*, *Salmonella typhimurium* and *Escherichia coli*. Gram (-) bacterial strains of *Escherichia coli* and *Pseudomonas aeruginosa* are strongly targeted by essential oils from *Piper guineense* (West African black pepper) and *Piper caldense* roots (Wani et al., 2021).

It has been reported that the antimicrobial effect concentrations of essential oils differ between bacterial species and that *Pseudomonas* and *Proteus* species are the most resistant bacterial species when compared to other tested species (Kürekci & Sakin, 2017). Garlic, lemon myrtle and tea tree oils have been found to be very effective against methicillin-resistant *Staphylococcus aureus* (Hayes & Markovic, 2003). It has been reported that oils of laurel, clove, lemongrass and thyme are inhibitory on *Escherichia coli* at concentrations of 0.02, 0.04, 0.06 and 0.05 %, respectively. It was determined that basil and eucalyptus oils inhibit *Staphylococcus aureus* at 1% concentration, while thyme, rosemary, peppermint, lemongrass, clove and laurel oils have the potential to inhibit *Staphylococcus aureus* at 0.05% concentration (Kürekci & Sakin, 2017). Brum et al. (2017) investigated the effects of adding African basil (*Ocimum gratissimum*) and ginger (*Zingiber officinale*) essential oils to the diets of Nile tilapia fish on growth, immunological blood parameters, and survival rate in infection with *Streptococcus agalactiae*. While the control group had 2.86% mortality after infection, 100% relative survival was determined only in the 0.5% ginger diet group.

Oregano oil showed maximum inhibition against *Salmonella*. It has been reported that essential oils obtained from thyme have strong antibacterial activities against *Pseudomonas fluorescens*, *Listeria monocytogenes*, *Bacillus thermosphacta* and *Escherichia coli* (Wani et al., 2021). The antibacterial activity of Mexican thyme essential oil was revealed and it was determined that the inhibition activity of this essential oil was due to the main component called carvacrol (Aziz et al., 2018). Mohiti-Asli & Ghanaatparast-Rashti (2018) found that the addition of thyme oil to the ration decreased the number of ileal *Escherichia coli* in broilers statistically when compared to the control group, but the number of *Lactobacillus* was not affected by oregano oil added to the ration. Lavender essential oil is obtained by steam distillation of the fresh flowering parts of the *Lavandula angustifolia* plant. The main active ingredients in its content are linalool and linalyl acetate. Other active ingredients are limonene, camphor, terpinen-4-ol, lavandulol, lavandulil acetate and 1,8-cineol (Figure 4). Lavender essential oil is a strong antibacterial effective against many types of bacteria (Kurt & Tatlı Çankaya, 2021).
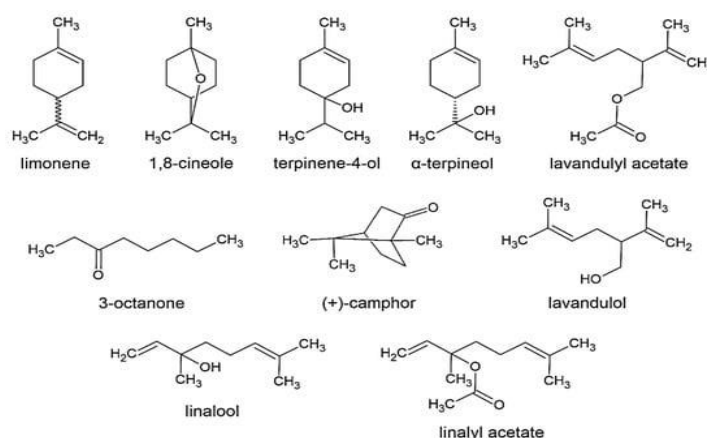
Figure 4. Chemical composition of Lavandula angustifolia

Essential oils from blue eucalyptus (*Eucalyptus globulus*) have traditionally been used to treat various respiratory ailments such as pharyngitis, bronchitis and sinusitis (Asif et al., 2020). Antimicrobial activity of blue eucalyptus essential oil against *Escherichia coli* and *Staphylococcus aureus* bacteria found in foods, intestines and respiratory tract has been investigated. The results showed that the essential oil has the power to inhibit both bacterial activities. It has been reported that the ability of this essential oil to inhibit bacterial growth may be due to chemical components such as 1,8-cineole, citronellal, citronellol, citronellyl acetate, p-cymene, eucamalol, limonene, linalool, β-pinene, γ-terpinene, α-terpinol, alloocimene and aromadendrene (Aziz et al., 2018). Due to the good potential of blue eucalyptus essential oil as an antimicrobial agent, it has been suggested to be a natural antibiotic for the treatment of various infectious diseases (Rashid et al., 2013).

Geranium essential oil is used in the treatment of dysentery and hemorrhoids as well as reducing pain due to postherpetic neuralgia (Greenway et al., 2003). This essential oil has the ability to inhibit strains of *Escherichia coli*, *Pseudomonas aeruginosa*, *Staphylococcus aureus*, *Bacillus subtilis*, *Salmonella enteritidis*. The most susceptible species is *Staphylococcus aureus* (Aziz et al., 2018). *Acinetobacter* species are an important cause of nosocomial infections. The antibacterial effect of geranium essential oil together with cinnamon and lavender essential oils against these bacteria has been studied and it has been emphasized that the formulation prepared to provide hygiene and disinfection of the hospital environment can be used effectively in the fight against infections caused by *Acinetobacter* genus bacteria (Sienkiewicz et al., 2014). Palmarosa (*Cymbopogon martinii*) essential oil is used as a skin tonic in aromatherapy due to its antimicrobial effect. It has also been shown to be effective on *Cutibacterium acnes*, which is the cause of acne (Kurt & Tatlı Çankaya, 2021). In a study, it was reported that myrrh (*Commiphora myrrha*) essential oil showed a strong antibacterial effect against *Borrelia burgdorferi*, a vector-borne Lyme disease spirochete that is difficult to eradicate by existing antibiotics (Feng et al., 2018).

It was determined that Gram (-) *Haemophilus influenzae* and Gram (+) *Streptococcus pneumoniae* are the most sensitive strains to *Artemisia annua* (sweet wormwood) essential oil. *Artemisia annua* also has the ability to inhibit *Micrococcus luteus* strains. Kamazeri et al. (2012) studied the essential oils of *Curcuma aeruginosa*, *Curcuma mangga* (mango ginger) and *Zingiber cassumar* plants from Malaysia for their antimicrobial activity against *Bacillus cereus*, *Staphylococcus aureus*, *Escherichia coli* and *Pseudomonas aeruginosa*. The strongest activity was exerted by *Curcuma mangga* essential oil. *Curcuma aeruginosa* had moderate activity, while *Zingiber cassumunar* showed no activity against most of the microorganisms tested. The most susceptible bacterium was *Staphylococcus aereus*, as it was inhibited by the three essential oils. It has been reported that the essential oil of Chinese cinnamon (*Cinnamomum cassia*) has potent antibacterial activities against *Pseudomonas fluorescens*, *Listeria monocytogenes*, *Bacillus thermosphacta* and *Escherichia coli* (Wani et al., 2021). In an *in vitro* study, it was observed that cinnamaldehyde extract obtained from cinnamon inhibited *Clostridium perfringens* and *Bacteroides fragilis* strongly, and moderately inhibited *Bifidobacterium longum* and *Lactobacillus acidophilus* (Lee & Ahn, 1998).

Antibacterial Effect Mechanism of Essential Oils

The antibacterial activity of essential oils can be bacteriostatic or bactericidal (Ramsey et al., 2020). The main mode of action of these oils is due to the disruption of the membrane integrity of Gram (+) and Gram (-) bacteria (Kürekci & Sakin, 2017). Due to the presence of a peptidoglycan layer outside the cell membrane in gram-positive bacteria, essential oils show maximum activity against them. Gram-negative bacteria carry a bilayer phospholipid membrane outside the inner membrane and are attached to the inner membrane by lipopolysaccharides (Wani et al., 2021). The antibacterial mechanism of action is facilitated by a series of biochemical reactions within the bacterial cell, depending on the type of chemical components present in the essential oil (Ramsey et al., 2020). One of the possibilities for the antibacterial mechanism of action of essential oils is the irreversible damage to the membranes of bacterial cells, which promotes cytoplasmic material

losses, ion leaks, loss of energy substrates such as glucose and ATP, and ultimately leads to lysis and death of bacteria. Interactions of essential oils and their components with polysaccharides, fatty acids and phospholipids make bacterial membranes more permeable so that loss of ions and cellular contents leads to cell death (Saad, Muller & Lobstein, 2013). The phenolic structure of essential oils also elicits an antimicrobial response against bacteria. Their mechanism of action may be related to ability to change microbial cell membrane permeability of phenolic compounds, damage to cytoplasmic membranes, interfere with the cellular energy (ATP) production system and ability to disrupt proton pump activity strength. Phenolic compounds inhibit the functional properties of the cell by disrupting the cell membrane and eventually cause the contents of the cell to leak (Bajpai, Baek & Kang, 2012). Because the compounds they contain are lipophilic, essential oils easily penetrate bacterial cell membranes and disrupt critical processes of the cell membrane, such as nutrient processing, synthesis of structural molecules, emission of growth regulators, energy production, and cell-cell communication quorum sensing network (Swamy, Akhtar & Sinniah, 2016).

Another possible mechanism of action includes degradation of cytoplasmic proteins and inactivation of cellular enzymes leading to bacterial cell death. The mechanism is inhibition of amylase and protease production, which stops toxin production and electron flow, resulting in coagulation of the cell contents (Bakkali et al., 2008). It has been reported that while carvacrol and thymol break the bacterial membrane and allow membrane-related materials to come out of the cell, terpenoids and phenylpropanoids penetrate the bacterial wall and reach the inner parts of the cell thanks to their lipophilic properties (Bayaz, 2014). In a study, carvacrol and thymol caused the breakdown of the outer membrane of Gram (-) bacteria, the release of lipopolysaccharides, and increased permeability of the cytoplasmic membrane to ATP (Burt, 2004). It has been reported that the essential oil obtained from *Eucalyptus globulus* induces strong growth inhibitory effects on Gram (+) *Escherichia coli* and Gram (-) *Staphylococcus aureus* (Wani et al., 2021). The main component of tea tree essential oil is terpinen-4-ol. This essential oil has been shown to penetrate the cell wall and cytoplasmic membrane of all tested bacterial strains (Kurt & Tatlı Çankaya, 2021).

Antiviral Effects of Essential Oils

It has been documented that essential oils have potent antiviral effects against many DNA and RNA viruses such as herpes simplex virus type-1 and type-2, dengue virus type-2, Junin virus, influenza virus, adenovirus type-3, polio virus, rhinovirus and coxsackievirus B1 (Ramsey et al., 2020). It is known that enveloped viruses are also sensitive to essential oils (Asif et al., 2020). The essential oil components (*E*)-Nerolidol, (*E,E*)-farnesol and (*E,E*)-a-farnesene, in admixture or alone, can inhibit viral replication. The compounds geranyl formate, (*E,E*)-farnesol, (*E*)-*β*-farnesene, (*E,E*)-a-farnesene, eremanthin and (*E*)-cinnamyl acetate had a high effectiveness against spike proteins of SARS-CoV-2 (Wani et al., 2021). Sharma & Kaur (2020) also determined the anti-proteinase activity of 1,8-cineole (eucalyptol), the active component of eucalyptus oil. According to the researchers, 1,8-cineole can bind with Mpro and thus inhibit viral reproduction. The complex mixture of essential oils, with the exception of *β*-caryophyllene, one of the most famous antiviral compounds found in many different essential oils from different plant families, often shows higher antiviral activity than the individual compounds, probably due to the phenomenon of synergism (Djilani & Dicko, 2012).

In vivo and *in silico* studies have drawn attention to the potential role of carvacrol, menthol and eugenol against COVID-19. Various components of essential oils, such as phenylpropanes, sesquiterpenes, and triterpenes, have demonstrated potent antiviral activities against rhinovirus and herpes viruses (Tragoolpua & Jatisatienr, 2007). It has been reported that isoborneol is a potent antiviral agent against the herpes simplex virus (Wani et al., 2021). Eugenol has been shown to have antiviral activity against herpes simplex virus type-1 and type-2 (Asif et al., 2020). It has been shown that carvacrol and its isomer, thymol, obtained from thyme, inhibit viral host cell fusion

through depletion of viral cholesterol from human immunodeficiency virus type-1 envelope membranes, which prevents the virus from entering the host system. It has been reported that carvacrol has antiviral activities against acyclovir-resistant herpes simplex virus type-1, human respiratory syncytial virus and human rotavirus (Kamalabadi, Astani & Nemati, 2018). In SARS-CoV-2, carvacrol markedly suppressed viral replication through inhibition of Mpro (Wani et al., 2021). Pilau et al. (2011) reported that the essential oil of *Lippia graveolens* (Mexican oregano) (Figure 5) inhibited 5 of 5 DNA and 3 RNA viruses, and its main component, carvacrol, inhibited 3 of these 5 viruses. Anethole, cinnamaldehyde, carvacrol, geraniol, cinnamyl acetate, L-4-terpineol, thymol, and pulegone have shown good potential to inhibit the S1 subunit of viral S proteins. It has been found that cinnamaldehyde has more favorable binding properties compared to other compounds (Asif et al., 2020). These essential oil components have been found to be active against a wide variety of viruses such as influenza virus, human herpes viruses, human immunodeficiency virus, yellow fever virus and avian influenza (Ma & Yao, 2020).

Figure 5. Lippia graveolens

It has been found that treatment with essential oils from *Illicium verum* (star anise), *Melaleuca alternifolia* (tea tree), *Leptospermum scoparium* (manuka) and *Matricaria recutita* (chamomile) inhibited the ability to infect of acyclovir-susceptible and -resistant strains of herpes simplex virus, indicating the enormous antiviral potential of these essential oils (Schnitzler, Astani & Reichling, 2011). An *in vitro* study has shown that essential oils and monoterpene ingredients of tea, eucalyptus and thyme are highly active against herpes simplex virus type-1. These essential oils provided almost 96% inhibition of herpes simplex virus type-1 and the monoterpenes showed approximately 80% inhibition against the virus (Wani et al., 2021). It has been reported that essential oils obtained from thyme oil, manuka oil, Australian eucalyptus oil and tea tree oil have antiherpes activities. Essential oils from *Glechon spathulata*, *Artemisia arborescens* (tree wormwood) and *Glechon marifolia* showed potent antiviral activity against herpes simplex virus type-1 (Venturi et al., 2015). It has been shown that essential oils obtained from Colombian medicinal and aromatic plants such as *Ocimum campechianum*, *Hyptis mutabilis*, *Lepechinia vulcanicola*, *Minthostachys mollis* and *Lepechinia salviifolia* have great activity against type-1 and type-2 herpes viruses. It has been reported that these essential oils prevent viral infections in the early stages (Brand et al., 2016). The essential oil obtained from *Melissa officinalis* (lemon balm) contains two main components, citronellal and citral, and these components inhibit the replication of the herpes simplex type-2 virus (Wani et al., 2021). Lemon balm oil prevented disease formation from herpes simplex type-1 and type-2 viruses in a dose-dependent manner. It also almost completely eliminated viral infectivity at higher concentrations. It is reported that eucalyptus oil has *in vitro* antiviral activities against virus strains such as enveloped mumps viruses and herpes simplex type-1 and type-2 viruses (Lau et al., 2010). In addition, 1,8-cineole has been shown to protect mice against the herpes simplex type-2 virus (Asif et al., 2020).

The vapors of essential oils obtained from *Citrus bergamia* (bergamot orange) and *Eucalyptus globulus* (blue gum) and their isolated compounds, namely citronellol and eugenol, showed rapid

anti-influenza virus effects (Asif et al., 2020). Anti-avian influenza virus H5N1 activity has been reported with essential oils obtained from the leaves and fruits of *Fortunella margarita* (Wani et al., 2021). Pourghanbari et al. (2016) reported that various concentrations of lemon balm essential oil delayed the replication process in H9N2 virus. Brochot et al. (2017) reported that eucalyptus oil and its active ingredient 1,8-cineole (eucalyptol) inactivate the free influenza A (H1N1) virus and disrupt the envelope structures of the virus. It has been found that the essential oil components of *Pogostemon cablin* (patchouli) are active against H2N2 influenza-A virus (Wani et al., 2021). Elaissi et al. (2012) investigated the antiviral activities of eight types of eucalyptus essential oil against coxsakievirus B3 incubated with the Vero cell line, a generative replication of influenza B viruses. The results showed that essential oils of *Eucalyptus sideroxylon*, *Eucalyptus lehmannii*, *Eucalyptus leucoxylon* and *Eucalyptus odorata* did not inhibit viral infections, essential oils of *Eucalyptus bicostata* and *Eucalyptus astringens* had significant antiviral activity, followed by *Eucalyptus cinerea* and *Eucalyptus maidenni*. The antiviral activities of these essential oils are variable and dose dependent. The antiviral activities were also decreased by decreasing the concentrations of these essential oils.

It has been reported that essential oils obtained from *Citrus sinensis* (sweet orange), *Anthemis hyalina* (chamomile) and *Nigella sativa* have significant activity against the replication of coronaviruses and the levels of transient receptor potential gene expressions (Wani et al., 2021). Treatment with a mixture of oleoresins and essential oils from different aromatic and medicinal plants reduced the severity of the symptoms and clinical lesions of the coronavirus infectious bronchitis virus in chickens, as well as reduced the amount of viral RNA in the chicken's trachea (Jackwood et al., 2010). Garlic has been used as medicine for centuries to treat colds, influenza, and other types of infections (Asif et al., 2020). Thuy et al. (2020) reported that garlic oil has great potential to treat COVID-19 patients. Garlic essential oils and their components (particularly diallyl sulfide) have the potential to prevent entry of the COVID-19 virus into host cells and activate molecular antioxidant pathways that reduce the secretion of culprit pro-inflammatory cytokines (Asif et al., 2020). All of the components of *Juniperus oxycedrus* (cade juniper) essential oil have shown remarkable inhibitory activity against the SARS-CoV-1 coronavirus (Wani et al., 2021).

Essential oils from *Eupatorium patens* and *Artemisia douglasiana* (California mugwort) have been found to be active against dengue virus (Wani et al., 2021). Zeedan et al. (2014) report that essential oil from *Achillea fragrantissima* exhibits anti-ORF virus (a parapox virus) activity. Bammi, Khelifa & Remmal (1997) found that five different essential oils act on Epstein-Barr virus. Trachyspermum oil has been reported to produce remarkable antiviral potential against Japanese encephalitis virus. Essential oils of *Lippia junelliana* (moldenke) and *Lippia turbinata* have shown potent antiviral activity against Junin virus (Wani et al., 2021). It was found that the essential oil obtained from *Melaleuca alternifolia* (tea tree) showed remarkable antiviral activity against tobacco mosaic virus and suppressed lesion formation in *Nicotiana glutinosa* plant within 10 days after application (Bishop, 1995). It has been reported that essential oils from oregano and clove have remarkable antiviral properties against some non-enveloped DNA and RNA viruses such as adeno virus type-3, coxsackie virus B-1 and polio virus (Wani et al., 2021). It has been reported that the essential oil obtained from *Eucalyptus globulus* (blue gum) is slightly toxic to the epidemic parotitis virus (Schnitzler, Wiesenhofer & Reichling, 2008).

Antiviral Effect Mechanism of Essential Oils
Essential oils have the potential to interfere with the lipid bilayer of the viral envelope due to their lipophilic nature. The fluidity of the membranes is then altered and at higher concentrations the membranes even rupture (Wink, 2020). The main mechanisms by which essential oils induce antiviral effects are direct effects on free viruses, inhibition of steps involved in virus attachment, penetration, intracellular replication and release from host cells, and inhibition of vital viral enzymes (Ma & Yao, 2020). Essential oils and the phytochemicals that make up it disrupt viral replication. Essential oils can interfere with the designed virion envelope for inhibition of virus replication by

inhibiting the entry into human host cells, synthesis of viral proteins, early gene expression process, glycosylation of viral proteins and cellular DNA polymerase (Pusztai et al., 2008). Carvacrol has the potential to inhibit Mpro and therefore can stop viral replication. The proposed mechanisms are that essential oils interfere with the virus envelope by inhibiting specific processes in the viral replication cycle or by masking viral components required for adsorption and entry into host cells, thereby inhibiting virus diffusion from cell to cell (Saddi et al., 2007).

The antiviral activity of essential oils is mainly due to direct virucidal effects that denature viral structural proteins or glycoproteins (Djilani & Dicko, 2012). The main components of essential oils, eugenol, menthol and carvacrol, have binding affinities to SARS-CoV-2 spike protein, main protease Mpro, RNA-dependent RNA polymerase and human ACE-2 proteins, respectively. (*E,E*)-*a*-farnesene, (*E,E*)-farnesol and (*E*)-nerolidol showed better binding with SARS-CoV-2 Mpro (main viral proteases), showing that these essential oil components can inhibit viral replication when administered alone or in a mixture (Silva et al., 2020). The best binding with human ACE2 was observed with *a*-bulnenene, eremanthin, (*E,E*)-*a*-farnesene, (*E*)-*β*-farnesene, (*E,E*)-farnesol, (*E*)-nerolidol, *β*-sesquiphellandrene and (*Z*)-spiroether, respectively. In the case of SARS-CoV-2 spike proteins, comparatively better binding was observed with (*E*)-cinnamyl acetate, eremanthin, (*E,E*)-*a*-farnesene, (*E*)-*β*-farnesene, (*E,E*)-farnesol and geranyl formate, respectively. Overall, (*E,E*)-*a*-farnenene, (*E*)-*β*-farnenene and (*E,E*)-farnesol showed better binding potentials with target proteins (Asif et al., 2020).

Antiseptic Effects of Essential Oils

Eucalyptus (Figure 6) oil has also been shown to have disinfecting properties and inhibit the growth of viruses in various kitchen utensils and filter devices (Asif et al., 2020). Karpanen et al. (2010) combined eucalyptus essential oil with chlorhexidine digluconate as a skin antiseptic drug to increase efficacy during topical application and showed that the combination between chlorhexidine digluconate and essential oil could increase the penetration of chlorhexidine digluconate into the skin. The use of tea tree essential oil in the treatment of acne vulgaris, seborrheic dermatitis and chronic gingivitis is recommended. It also speeds up the wound healing process (Satchell et al., 2002). It has been determined that the essential oil of *Boswellia sacra* (frankincense) was used in the mummification process in ancient Egypt. Frankincense essential oil is known to have antiseptic, astringent, cicatrizing, sedative and pain-relieving effects in rheumatism. It is one of the best skin healing oils used in skin diseases among essential oils. It has a promising potential in relieving inflammation in the skin and remodeling the tissue (Han, Rodriguez & Parker, 2017).

Figure 6. Eucalyptus

The components of *Mentha x piperita* (peppermint) essential oil include menthol, menthyl acetate, limonene, isomentone, menthone and carvone. The external use of peppermint essential oil benefits from its antipruritic, astringent and antiseptic effects. It has been shown that the essential oil of *Vetiveria zizanioides* (vetiver) can help in the treatment of acne with its antimicrobial effect (Orchard et al., 2018). *Pogostemon cablin* (patchouli) essential oil is preferred for acne, eczema, inflamed, cracked and irritated skin problems. *Pelargonium graveolens* essential oil is one of the most preferred skin repairing oils. With its anti-inflammatory effect, it suppresses inflammatory symptoms that develop with neutrophil accumulation and edema on the skin and is recommended as a new candidate to be used as a wound healer, especially in skin infections associated with Methicillin-resistant *Staphylococcus aureus* (Maruyama et al., 2005). The use of *Commiphora myrrha* (myrrh) essential oil dates back to the making of embalming balms and ointments in the ancient Egyptian Civilization. Myrrh essential oil is applied topically by inhalation, massage and bath as well as topically for skin/wound care as analgesic, antiseptic, antioxidant, anti-inflammatory, astringent, antispasmodic and carminative (Grbic et al., 2018).

Antifungal Effects of Essential Oils

Essential oils from plants such as basil, clove, citrus, garlic, fennel, lemongrass, oregano, rosemary and thyme have shown significant antifungal activities against a wide range of fungal pathogens. Some of the fungal pathogens affected are *Candida acutus*, *Candida albicans*, *Candida apicola*, *Candida catenulata*, *Candida inconspicua*, *Candida tropicalis*, *Rhodotorula rubra*, *Sacharomyces cerevisae*, *Trignopsis variabilis*, *Aspergillus parasiticus*, and *Fusarium moniliforme* (Swamy, Akhtar & Sinniah, 2016). Vazquez et al. (2001) investigated the antifungal effects of eugenol and thymol on the production and development of citrine synthesized by *Penicillium citrinum* in various Spanish cheeses and culture medium. It has been shown that 200 μg/ml eugenol completely inhibits the growth of *Penicillium citrinum* and that citrine cannot be detected at concentrations above 100 μg/ml (Bayaz, 2014). Wendorff & Wee (1997) reported that the use of phenolic compounds in Cheddar cheese stopped the growth of mold, which is a spoilage factor, and that high concentrations of thymol had an inhibitory effect on fungal growth and mycotoxin production. It is understood that these essential oils or their effective compounds can be used to prevent unwanted molds in cheese such as *Penicillium verrucosum*, *Penicillium citrinum*, *Penicillium expansum* instead of chemical agents (Bayaz, 2014).

Rosmarinus officinalis (rosemary) and *Thymus vulgaris* (thyme) essential oils potently inhibited the growth of *Aspergillus parasiticus* and the production of aflatoxin (Bayaz, 2014). It has been determined that peppermint and rosemary essential oils are effective against two strains of *Saccharomyces cerevisiae*, while thyme oil has an inhibitory effect against *Aspergillus niger* by disrupting cell organelles, cell membrane and cell wall (Schelz, Molnar & Hohmann, 2006). It has been reported that essential oils from Oregano and thyme inhibit the growth of molds such as *Aspergillus niger* and *Aspergillus flavus* (Wani et al., 2021). Tea tree essential oil has been shown to penetrate the cell wall and cytoplasmic membrane of all tested fungal strains. It has also been reported to be effective on tinea pedis (foot fungus) (Satchell et al., 2002). *Pelargonium graveolens* essential oil is antifungal. Myrrh essential oil has strong antifungal activity against skin dermatophyte fungi (Kurt & Tatlı Çankaya, 2021). Clove essential oils have been reported to have significant inhibition against *Botrytis cinerea* (Wani et al., 2021). *Artemisia annua* (sweet wormwood) has the ability to inhibit *Candida krusei* strains (Aziz et al., 2018).

Antifungal Effect Mechanism of Essential Oils

Similar to the effects on bacteria, essential oils have the ability to enter and interrupt the homeostasis of the fungal cell wall and cytoplasmic membranes, and especially of the mitochondria (Ramsey et al., 2020). One of the proposed mechanisms involves essential oils penetrating mitochondrial membranes and altering electron flow through the electron transport system, so that

essential oils degrade the lipids, proteins, and nucleic acid content of fungal cells (Arnal-Schnebelen et al., 2004). Another proposed mechanism is depolarization of mitochondrial membranes, which reduces membrane potential and affects ion channels and proton pumps to lower pH. This leads to apoptosis and necrosis of the fungal cell (Yoon et al., 2000). Two phenomena that inhibit the action of yeasts by essential oils are the creation of a pH gradient across the cytoplasmic membrane and the blocking of energy production leading to membrane disruption (Djilani & Dicko, 2012).

Antiparasitic Effects of Essential Oils

Essential oils have been shown to have significant antinematocidal activity. Barbosa et al. (2010) reported the antinematocyte activities of essential oils obtained from *Thymus caespititius*, *Thymus capitatus*, *Satureja montana* (winter savory), *Origanum vulgare* and *Chamaespartium tridentatum* against *Bursaphelenchus xylophilus* (pine wood nematode). Allen, Lydon & Danforth (1997) stated that the inclusion of 1,8-cineol and camphor components of essential oil obtained from *Artemisia annua* (sweet wormwood) plant in the diet of chicks inoculated with *Eimeria acervulina* and *Eimeria tenella* played a preventive role in the fight against coccidiosis.

It is known that tea tree essential oil is effective on mites. The effect of this essential oil against *Sarcoptes scabiei* (skabies) has also been demonstrated (Kurt & Tatlı Çankaya, 2021). In a study conducted with tea tree, clove, eucalyptus and palmarosa essential oils, it was foreseen that these oils are effective against *Sarcoptes scabiei* (scabies) and can be evaluated in alternative therapy for this purpose, and that clove and palmarosa essential oils can also be used for control of mites because it was determined that they kill all mites within 20 and 50 minutes (Fang et al., 2016). Gomez-Rincon et al. (2014) showed that tea tree essential oil inhibited the growth of *Anisakis simplex* L3 larvae. In another study, it was reported that *Origanum syriacum* (Syrian oregano) essential oil induced protective effects against gastrointestinal parasite *Anisakis simplex* (herring worm) and mosquito vector *Culex quinquefasciatus* (southern house mosquito). It has been reported that essential oil obtained from *Origanum compactum* induces 100% mortality in *Anisakis simplex* L3 larvae isolated from *Micromesistius poutassou* (blue whiting) (Lopez et al., 2018).

REFERENCES

Al-Howiriny, T. A. (2003). Composition and antimicrobial activity of the essential oil of *Salvia lanigera. Pakistan Journal of Biological Sciences, 6* (2), 133-135. Doi: 10.3923/pjbs.2003.133.135

Allen, P. C., Lydon, J., & Danforth, H. D. (1997). Effects of components of *Artemisia annua* on coccidia infections in chickens. *Poultry Science, 76* (8), 1156-1163. Doi: 10.1093/ps/76.8.1156

Arnal-Schnebelen, B,, Hadji-Minaglou, F., Peroteau, J. F., Ribeyre, F., & de Billerbeck, V. G. (2004). Essential oils in infectious gynaecological disease: a statistical study of 658 cases. *International Journal of Aromatherapy, 14* (4), 192-197. Doi: 10.1016/j.ijat.2004.09.003

Asif, M., Saleem, M., Saadullah, M., Yaseen, H. S., & Al-Zarzour, R. (2020). COVID-19 and therapy with essential oils having antiviral, anti-inflammatory, and immunomodulatory properties. *Inflammopharmacology, 28* (5), 1153-1161. Doi: 10.1007/s10787-020-00744-0

Aziz, Z. A. A., Ahmad, A., Setapar, S. H. M., Karakucuk, A., Azim, M. M., Lokhat, D., Rafatullah, M., Ganash M., Kamal, M. A., & Ashraf, G. (2018). Essential oils: Extraction techniqes, pharmaceutical and therapeutic potential - A review. *Current Drug Metabolism, 19* (13), 1100-1110. Doi: 10.2174/1389200219666180723144850

Bajpai, V. K., Baek, K. H., & Kang, S. C. (2012). Control of *Salmonella* in foods by using essential oils: A review. *Food Research International, 45* (2), 722-734. Doi: 10.1016/j.foodres.2011.04.052

Bakkali, F., Averbeck, S., Averbeck, D., & Idaomar, M. (2008). Biological effects of essential oils – A review. *Food and Chemical Toxicology, 46* (2), 446-475. Doi: 10.1016/j.fct.2007.09.106

Bammi, J., Khelifa, R., & Remmal, A. (1997). Etudes de l'activité antivirale de quelques huiles essentielles. In Proceedings of *the International Congress Aromatic Medicinal Plants & Essential Oils*, Benjilali, B., Ettalibi, M., Ismaili-Alaoui, M., Zrira, S. (eds). Actes Editions, Rabat, Morocco, (pp. 502).

Barbosa, P., Lima, A. S., Vieira, P., Dias, L. S., Tinoco, M. T., Barroso, J. G., Pedro, L. G., Figueiredo, A. C., & Mota, M. (2010). Nematicidal activity of essential oils and volatiles derived from Portuguese aromatic flora against the pinewood nematode, *Bursaphelenchus xylophilus. Journal of Nematology, 42* (1), 8-16.

Bayaz, M. (2014). Esansiyel yağlar: Antimikrobiyal, antioksidan ve antimutajenik aktiviteleri. *Akademik Gıda, 12* (3), 45-53.

Bishop C. D. (1995). Antiviral activity of the essential oil of *Melaleuca alternifolia* (maiden amp; betche) cheel (tea tree) against Tobacco mosaic virus. *Journal* of *Essential Oil Research*, 7 (6), 641-644. Doi: 10.1080/10412905.1995.9700519

Brand, Y. M., Roa-Linares, V. C., Betancur-Galvis, L. A., Duran-Garcia, D. C., & Stashenko, E. (2016). Antiviral activity of Colombian Labiatae and Verbenaceae family essential oils and monoterpenes on Human Herpes viruses. *Journal* of *Essential Oil Research,* 28 (2), 130-137. Doi: 10.1080/10412905.2015.1093556

Brochot, A., Guilbot, A., Haddioui, L., & Roques, C. (2017). Antibacterial, antifungal, and antiviral effects of three essential oil blends. *Microbiologyopen, 6* (4), e00459. Doi: 10.1002/mbo3.459

Brum, A., Pereira, S. A., Owatari, M. S., Chagas, E. C., Chaves, F. C. M., Mouriño, J. L. P., & Martins, M. L. (2017). Effect of dietary essential oils of clove basil and ginger on Nile tilapia (*Oreochromis niloticus*) following challenge with *Streptococcus agalactiae. Aquaculture, 468* (1), 235-243. Doi: 10.1016/j.aquaculture.2016.10.020

Burt, S. (2004). Essential oils: Their antibacterial properties and potential applications in foods - A review. *International Journal of Food Microbiology*, 94 (3), 223-253. Doi: 10.1016/j.ijfoodmicro.2004.03.022

Canbolat, Ö., Kalkan, H., Karaman, Ş., & Filya, İ. (2011). Esansiyel yağların sindirim, rumen fermantasyonu ve mikrobiyal protein üretimi üzerine etkileri. *Kafkas Üniversitesi Veteriner Fakültesi Dergisi, 17* (4), 557-565. Doi:10.9775/kvfd.2011.4006

Çayıroğlu, H. (2015). Süt sığırlarında esansiyel yağların yem değerlendirme, sindirilebilirlik, rumen fermantasyonu ile süt verimi ve bileşimi üzerine etkileri. *Türk Tarım – Gıda Bilim ve Teknoloji Dergisi, 3* (7), 522-528. Doi: 10.24925/turjaf.v3i7.522-528.341

Demirtaş, A., Öztürk, H., Pişkin, İ., Demirkıran, D., Salgırlı, Y., Fidancı, U. R., & Emre, B. (2011). Biberiye ve adaçayı ekstraktlarının ruminal fermantasyon üzerine etkilerinin rumen simülasyon tekniği (RUSITEC) ile araştırılması. *İstanbul Üniversitesi Veteriner Fakültesi Dergisi, 37* (2), 127-134.

Djilani, A., & Dicko, A. (2012). The therapeutic benefits of essential oils. In J. Bouayed & T. Bohn Eds.), *Nutrition, well-being and health* (pp. 155-178). Rijeka: InTech.

Elaissi, A., Rouis, Z., Ben Salem, N. A., Mabrouk, S., Ben Salem, Y., Salah, K. B. H., Aouni, M., Farhat, F., Chemli, R., & Harzallah- Skhiri, F. (2012). Chemical composition of 8 eucalyptus species' essential oils and the evaluation of their antibacterial, antifungal and antiviral activities. *BMC Complementary and Alternative Medicine,* 12, 81. Doi: 10.1186/1472-6882-12-81

El-Shazly, A., Dorai, G., & Wink, M. (2002). Composition and antimicrobial activity of essential oil and hexane-ether extract of *Tanacetum santolinoides* (dc.) Feinbr. and Fertig. *Zeitschrift für Naturforschung C, 57* (7-8), 620-623. Doi: 10.1515/znc-2002-7-812.

Evans, J. W., Plunkett, M. S., & Banfield, M. J. (2001). Effect of an essential oil blend on coccidiosis in broiler chicks. *Poultry Science, 80* (suppl. 1), 258 (abstract).

Fang, F., Candy, K., Melloul, E., Bernigaud, C., Chai, L., Darmon, C., Durand, R., Botterel, F., Chosidow, O., Izri, A., Huang, W., & Guillot, J. (2016). *In vitro* activity of ten essential oils against *Sarcoptes scabiei. Parasites & Vectors, 9*, 594. Doi: 10.1186/s13071-016-1889-3

Feng, J., Shi, W., Miklossy, J., Tauxe, G. M., McMeniman, C. J., & Zhang, Y. (2018). Identification of essential oils with strong activity against stationary phase *Borrelia burgdorferi. Antibiotics (Basel), 7* (4), 89. Doi: 10.3390/antibiotics7040089

Fernandez-Lopez, J., & Viuda-Martos, M. (2018). Introduction to the special issue: Application of essential oils in food systems. *Foods, 7* (4), 56. Doi: 10.3390/foods7040056.

Giannenas, I., Bonos, E., Christaki, E., & Florou-Paneri, P. (2013). Essential oils and their applications in animal nutrition. *Medicinal & Aromatic Plants, 2* (6), 140. Doi: 10.4172/2167-0412.1000140.

Gomez-Rincon, C., Langa, E., Murillo, P., Valero, M. S., Berzosa, C., & Lopez, V. (2014). Activity of tea tree (*Melaleuca alternifolia*) essential oil against L3 larvae of *Anisakis simplex. BioMed Research International, 2014*, 549510. Doi: 10.1155/2014/549510.

Grbic, M. L., Unković, N., Dimkić, I., Janaćković, P., Gavrilović, M., Stanojević, O., Stupar, M., Vujisić, L., Jelikić, A., Stanković, S., & Vukojević, J. (2018). Frankincense and Myrrh essential oils and burn incense fume against micro-inhabitants of sacral ambients. Wisdom of the ancients? *Journal of Ethnopharmacology, 219*, 1-14. Doi: 10.1016/j.jep.2018.03.003.

Greenway, F. L., Frome, B. M., Engels, T. M., & McLellan, A. (2003). Temporary relief of postherpetic neuralgia pain with topical geranium oil. *American Journal* of *Medicine, 115* (7), 586-587. Doi: 10.1016/s0002-9343(03)00434-0.

Güler, T., & Dalkılıç, B. (2005). Aromatik bitkilerin organik (ekolojik) hayvancılıkta kullanım imkânı. *Fırat Üniversitesi Doğu Araştırmaları Dergisi, 3* (2), 13-20.

Han, X., Rodriguez, D., & Parker, T. L. (2017). Biological activities of frankincense essential oil in human dermal fibroblasts. *Biochimie Open, 4*, 31-35. Doi: 10.1016/j.biopen.2017.01.003.

Hayes, A. J., & Markovic, B. (2003). Toxicity of Australian essential oil *Backhousia citriodora* (lemon myrtle). Part 2. Absorption and histopathology following application to human skin. *Food* and *Chemical Toxicology, 41* (10), 1409-1416. Doi: 10.1016/s0278-6915(03)00159-5.

Hussain, A. l., Anwar, F., Sherazi S. T. H., & Przybylski, R. (2008). Chemical composition, antioxidant and antimicrobial activities of basil (*Ocimum basilicum*) essential oils depends on seasonal variations. *Food Chemistry, 108* (3), 986-995. Doi: 10.1016/j.foodchem.2007.12.010.

İlçim, A., Dığrak, M., & Bağcı, E. (1998). Bazı bitki ekstraktlarının antimikrobiyal etkilerinin araştırılması. *Turkish Journal of Biology, 22*, 119-125.

Jackwood, M. W., Rosenbloom, R., Petteruti, M., Hilt, D. A., McCall, A. W., & Williams, S. M. (2010). Avian coronavirus infectious bronchitis virus susceptibility to botanical oleoresins and essential oils *in vitro* and *in vivo*. *Virus Research, 149* (1), 86-94.

Kamalabadi, M., Astani, A., & Nemati, F. (2018). Anti-viral effect and mechanism of carvacrol on herpes simplex virus type 1. *International Journal of Medical Laboratory, 5* (2), 113-122.

Kamazeri, T. S. A. T., Samah, O. A., Taher, M., Susanti, D., & Qaralleh, H. (2012). Antimicrobial activity and essential oils of *Curcuma aeruginosa*, *Curcuma mangga*, and *Zingiber cassumunar* from Malaysia. *Asian Pacific Journal of Tropical Medicine, 5* (3), 202-209. Doi: 10.1016/S1995-7645(12)60025-X

Karpanen, T. J., Conway, B. R., Worthington, T., Hilton, A. C., Elliott, T .S. J., & Lambert, P. A. (2010). Enhanced chlorhexidine skin penetration with eucalyptus oil. *BMC Infectious Diseases, 10*, 278. Doi: 10.1186/1471-2334-10-278

Kim, J., Marshall, M. R., & Wei, C. (1995). Antibacterial activity of some essential oil components against five foodborne pathogens. *Journal of Agricultural Food Chemistry, 43* (11), 2839-2845. Doi: 10.1021/jf00059a013

Kim, K.Y., Seo, H. J., Min, S. S., Park, M., & Seol, G. H. (2014). The effect of 1,8-cineole inhalation on preoperative anxiety: A randomized clinical trial. *Evidence-Based Complementary* and *Alternative Medicine, 2014*, 820126. Doi: 10.1155/2014/820126

Kurt, N., & Tatlı Çankaya, İ. İ. (2021). Aromaterapi uygulamaları ve uçucu yağlar. *Lokman Hekim Dergisi, 11* (2), 230-241. Doi: 10.31020/mutftd.882997

Kürekci, C., & Sakin, F. (2017). Uçucu Yağlar: Antimikrobiyal açıdan uçucu yağlar: In-vitro ve in-vivo çalışmalar. *Türkiye Klinikleri Hayvan Besleme ve Beslenme Hastalıkları Dergisi - Özel Konular, 3* (1), 15-20.

Lambert, R. J., Skandamis, P. N., Coote, P. J., & Nychas, G. J. (2001). A study of the minimum inhibitory concentration and mode of action of oregano essential oil, thymol and carvacrol. *Journal of Applied Microbiology, 91* (3), 453-462. Doi: 10.1046/j.1365-2672.2001.01428.x

Lammari, N., Demautis, T., Louaer, O., Meniai, A. H., Casabianca, H., Bensouici, C., Devouassoux, G., Fessi, H., Bentaher, A., & Elaissari, A. (2021). Nanocapsules containing *Saussurea lappa* essential oil: Formulation, characterization, antidiabetic, anti-cholinesterase and anti-inflammatory potentials. *International Journal of Pharmaceutics 593*, 120138. Doi: 10.1016/j.ijpharm.2020.120138

Lau, S. K. P., Poon, R. W. S., Wong, B. H. L., Wang, M., Huang, Y., Xu, H., Guo, R., Li, K. S. M., Gao, K., Chan, K. H., Zheng, B. J., Woo, P. C. Y., & Yuen, K. Y. (2010). Coexistence of different genotypes in the same bat and serological characterization of *Rousettus* bat coronavirus HKU9 belonging to a novel *Betacoronavirus* subgroup. *Journal of Virology, 84* (21) 11385-11394. Doi: 10.1128/jvi.01121-10

Lee, H. S., & Ahn, Y. J. (1998). Growth-inhibiting effects of *Cinnamomum cassia* bark-derived materials on human intestinal bacteria. *Journal of Agricultural and Food Chemistry, 46* (1), 8-12. Doi: 10.1021/jf970548y

Lopez, V., Cascella, M., Benelli, G., Maggi, F., Gomez-Rincon, C. (2018). Green drugs in the fight against *Anisakis simplex*-larvicidal activity and acetylcholinesterase inhibition of *Origanum compactum* essential oil. *Parasitology Research, 117* (3), 861-867. Doi: 10.1007/s00436-018-5764-3

Ma, L., & Yao, L. (2020). Antiviral effects of plant-derived essential oils and their components: An updated review. *Molecules, 25* (11), 2627. Doi: 10.3390/molecules25112627

Martín, A., Varona, S., Navarrete, A. & Cocero, M. J. (2010). Encapsulation and co-precipitation processes with supercritical fluids: Applications with essential oils. *The Open Chemical Engineering Journal, 4*, 31-41. Doi: 10.2174/1874123101004010031

Maruyama, N., Sekimoto, Y., Ishibashi, H., Inouye S., Oshima , H., Yamaguchi , H., & Abe, S. (2005). Suppression of neutrophil accumulation in mice by cutaneous application of geranium essential oil. *Journal of Inflammation (London), 10*, 2 (1), 1-11. Doi: 10.1186/1476-9255-2-1

Mitsch, P., Zitterl-Eglseer, K., Köhler, B., Gabler, C., Losa, R., & Zimpernik, I. (2004). The effect of two different blends of essential oil components on the proliferation of *Clostridium perfringens* in the intestines of broiler chickens. *Poultry Science, 83* (4), 669-675. Doi: 10.1093/ps/83.4.669

Mohebitabar, S., Shirazi, M., Bioos, S., Rahimi, R., Malekshahi, F., & Nejatbakhsh, F. (2017). Therapeutic efficacy of rose oil: A comprehensive review of clinical evidence. *Avicenna Journal* of *Phytomedicine*, *7* (3), 206-213.

Mohiti-Asli, M., & Ghanaatparast-Rashti, M. (2018). Comparing the effects of a combined phytogenic feed additive with an individual essential oil of oregano on intestinal morphology and microflora in broilers. *Journal of Applied Animal Research, 46* (1), 184-189. Doi: 10.1080/09712119.2017.1284074

Nascimiento, M.N.G., Junqueira, J.G.M., Terezan, A.P., Severino, R.P., Silva, T.S., Martins, C. H.G., & Severino, V.G.P. (2018). Chemical composition and antimicrobial activity of essential oils from Xylopia aromatic (Annonaceae) flowers and leaves. *Revista Virtual de Quimica, 10* (5), 1578-1590. http://dx.doi.org/10.21577/1984-6835.20180107

Orchard, A., van Vuuren, S. F., Viljoen, A. M., & Kamatou, G. (2018). The *in vitro* antimicrobial evaluation of commercially essential oils and their combinations against acne. *International Journal of Cosmetic Sciences, 40* (3), 226-243. Doi: 10.1111/ics.12456

Perry, N. S. L., Bollen, C., Perry, E. K., & Ballard, C. (2003). Salvia for dementia therapy: Review of pharmacological activity and pilot tolerability clinical trial. *Pharmacology Biochemistry and Behaviour, 75* (3), 651-659. Doi: 10.1016/s0091-3057(03)00108-4

Pilau, M. R., Alves, S. H., Weiblen, R., Arenhart, S., Cueto, A. P., & Lovato, L. T. (2011). Antiviral activity of the Lippia graveolens (Mexican oregano) essential oil and its main compound carvacrol against human and animal viruses. *Brazilian Journal of Microbiology, 42* (4), 1616-1624. Doi: 10.1590/S1517-838220110004000049

Pourghanbari, G., Nili, H., Moattari, A., Mohammadi, A., & Iraji, A. (2016). Antiviral activity of the oseltamivir and *Melissa officinalis* L. essential oil against avian influenza A virus (H9N2). *VirusDisease, 27* (2), 170-178. Doi: 10.1007/s13337-016-0321-0

Pusztai, R., Hohmann, J., Rédei, D., Engi, H., & Molnár, J. (2008). Inhibition of human cytomegalovirus IE gene expression by dihydro-beta-agarofuran sesquiterpenes isolated from Euonymus species. *In Vivo (Athens, Greece), 22* (6), 787-792.

Ramsey, J. T., Shropshire, B. C., Nagy, T. R., Chambers, K. D., Li, Y., & Korach, K. S. (2020). Essential oils and health. *Yale Journal of Biology and Medicine, 93* (2), 291-305.

Rashid, S., Rather, M. A., Shah, W. A., & Bhat, B. A. (2013). Chemical composition, antimicrobial, cytotoxic and antioxidant activities of the essential oil of *Artemisia indica* Willd. *Food Chemicals, 138* (1), 693-700.

Saad, N. Y., Muller, C. D., & Lobstein, A. (2013). Major bioactivities and mechanism of action of essential oils and their components. *Flavour and Fragrance Journal, 28* (5), 269-279. Doi: 10.1002/ffj.3165

Saddi, M., Sanna, A., Cottiglia, F., Chisu, L., Casu, L., Bonsignore, L., & De Logu, A. (2007). Antiherpevirus activity of *Artemisia arborescens* essential oil and inhibition of lateral diffusion in Vero cells. *Annals of Clinical Microbiology and Antimicrobials, 6*, 10. Doi: 10.1186/1476-0711-6-10

Satchell, A. C., Saurajen, A., Bell, C., & Barnetson, R. S. C. (2002). Treatment of interdigital tinea pedis with 25% and 50% tea tree oil solution: A randomized, placebo-controlled, blinded study. *Australas Journal of Dermatology, 43*, (3), 175-178. Doi: 10.1046/j.1440-0960.2002.00590.x

Schelz, Z., Molnar, J., & Hohmann, J. (2006). Antimicrobial and antiplasmid activities of essential oils. *Fitoterapia, 77* (4), 279-285. Doi: 10.1016/j.fitote.2006.03.013

Schnitzler, P., Wiesenhofer, K., & Reichling, J. (2008). Comparative study on the cytotoxicity of different Myrtaceae essential oils on cultured Vero and RC-37 cells. *Pharmazie - International Journal of Pharmaceutical Sciences, 63* (11), 830-835. Doi: 10.1691/ph.2008.8597

Schnitzler, P., Astani, A., & Reichling, J. (2011). Antiviral effects of plant-derived essential oils and pure oil components. In H. Thormar (Ed.) *Lipids and essential oils as antimicrobial agents* (pp. 239-251). West Sussex: John Wiley and Sons, Ltd. Doi: 10.1002/9780470976623.ch10

Sharma, A. D., & Kaur I. (2020). Jensenone from eucalyptus essential oil as a potential inhibitor of COVID 19 corona virus infection. *Research & Reviews in Biotechnology & Biosciences, 7* (1), 59-66. Doi: 10.5281/zenodo.3748477

Sienkiewicz, M., Głowacka, A., Kowalczyk, E., Wiktorowska-Owczarek, A., Jóźwiak-Bębenista, M., & Łysakowska, M. (2014). The biological activities of cinnamon, geranium and lavender essential oils. *Molecules, 19* (12), 20929-20940. Doi: 10.3390/molecules191220929

Silva, J. K. R. da, Figueiredo, P. L. B., Byler, K. G., & Setzer, W. N. (2020). Essential oils as antiviral agents. Potential of essential oils to treat SARS-CoV-2 infection: An *in-silico* investigation. *International Journal of Molecular Sciences, 21* (10), 3426. Doi: 10.3390/ijms21103426

Sutili, F. J., de Lima Silva, L., Gressler, L. T., Gressler, L. T., Battisti, E. K., Heinzmann, B. M., de Vargas, A. C. & Baldisserotto, B. (2015). Plant essential oils against *Aeromonas hydrophila*: *In vitro* activity and their use in experimentally infected fish. *Journal of Applied Microbiology, 119* (1), 47-54. Doi: 10.1111/jam.12812

Swamy, M. K., Akhtar, M. S., & Sinniah, U. R. (2016). Antimicrobial properties of plant essential oils against human pathogens and their mode of action: An updated review. *Evidence-Based Complementary* and *Alternative Medicine, 2016*, 3012462. Doi: 10.1155/2016/3012462

Şahan, Z. (2012). Bazı bitki uçucu yağlarının enerji, protein ve lif kaynağı yemlerin in vitro gerçek sindirilebilirliğine ve yüksek verimli süt sığırlarında süt verimi ve süt kompozisyonlarına etkileri. Çukurova Üniversitesi Fen Bilimleri Enstitüsü, Doktora Tezi, (pp. 1-147) Adana.

Thanissery, R., Kathariou, S., & Smith, D. P. (2014). Rosemary oil, clove oil, and a mix of thyme-orange essential oils inhibit *Salmonella* and *Campylobacter in vitro. Journal of Applied Poultry Research, 23* (2), 221-227. Doi: 10.3382/japr.2013-00888

Thuy, B. T. P., My, T. T. A., Hai, N. T. T., Hieu, L. T., Hoa, T. T., Loan, H. T. P., Triet, N. T., Anh, T. T. V., Quy, P. T., Tat, P. V., Hue, N. V., Quang, D. T., Trung, N. T., Tung, V. T., Huynh, L. K., & Nhung, N. T. A. (2020). Investigation into SARS-CoV-2 resistance of compounds in garlic essential oil. *ACS Omega, 5* (14), 8312-8320. Doi: 10.1021/acsomega.0c00772

Tragoolpua, Y., & Jatisatienr, A. (2007). Anti-herpes simplex virus activities of *Eugenia caryophyllus* (Spreng.) Bullock & S. G. Harrison and essential oil, eugenol. *Phytotherapy Research, 21* (12), 1153-1158. Doi: 10.1002/ptr.2226

Vazquez, B. I., Fente, C., Franco, C. M., Vazquez, M. J., & Cepeda, A. (2001). Inhibitory effects of eugenol and thymol on *Penicillium citrinum* strains in culture media and cheese. *International Journal of Food Microbiology, 67* (1-2), 157-163. Doi: 10.1016/s0168-1605(01)00429-9

Venturi, C. R., Danielli, L. J., Klein, F., Apel, M. A., Montanha, J. A., Bordignon, S. A. L., Roehe, P. M., Fuentefria, A. M., & Henriques, A. T. (2015). Chemical analysis and *in vitro* antiviral and antifungal activities of essential oils from *Glechon spathulata* and *Glechon marifolia. Pharmaceutical Biology, 53* (5), 682-688. Doi: 10.3109/13880209.2014.936944

Wani, A. R., Yadav, K., Khursheed, A., & Rather, M. A. (2021). An updated and comprehensive review of the antiviral potential of essential oils and their chemical constituents with special focus on their mechanism of action against various influenza and coronaviruses. *Microbial Pathogenesis, 152*, 104620. Doi: 10.1016/j.micpath.2020.104620

Wendorff, W. L., & Wee, C. (1997). Effect of smoke and spice oils on growth of molds on oil-coated cheeses. *Journal of Food Protection, 60* (2), 153-156. Doi: 10.4315/0362-028X-60.2.153

Wink, M. (2020). Potential of DNA intercalating alkaloids and other plant secondary metabolites against SARS-CoV-2 causing COVID-19. *Diversity, 12* (5), 175. Doi: 10.3390/d12050175

Yoon, H. S., Moon, S. C., Kim, N. D., Park, B. S., Jeong, M. H., & Yoo, Y. H. (2000). Genistein induces apoptosis of RPE-J cells by opening mitochondrial PTP. *Biochemical and Biophysical Research Communications, 276* (1),151-156. Doi: 10.1006/bbrc.2000.3445

Zeedan, G. S. G., Abdalhamed, A. M., Ottai, M. E., Abdelshafy, S., & Abdeen, E. (2014). Antimicrobial, antiviral activity and GC-MS analysis of essential oil extracted from *Achillea fragrantissima* plant growing in Sinai peninsula, Egypt. *Journal* of *Microbial* and *Biochemical Technology, S8,* 6. Doi: 0.4172/1948-5948.S8-006

Diabetes Mellitus in Cats and Dogs

Fatmanur YOLDAŞ[1]
Burcu Menekşe BALKAN[2]

Diabetes mellitus (DM) is a common disease encountered in canine and feline medicine (Behrend & ark., 2018). It is a chronic metabolic disease, is caused by the absence or insufficiency of insulin. In diabetes, glucose utilization is impaired and hyperglycemia and glycosuria occur. The disease is rarely detected in sheep, cattle, pigs and horses (Karagül & ark., 2000). Yoon & ark., 2020 found that, breeds at most risk included Australian terriers and Siberian huskies as previously reported, as well as, for the first time, English springer spaniels. In contrast to other populations where there is female predisposition for DM, desexed male dogs in Australia were at increased risk for DM compared with both entire males and desexed females.

Normal Insulin Physiology And Glucose Balance

A good understanding of metabolism is essential for understanding the pathogenesis of DM. Glucose provides the basic energy requirement for all body tissues. The brain can utilize up to 50% of total glucose, especially at times of high demand. The brain's energy stores are insufficient; therefore, it needs a constant supply of glucose to function as it should. Therefore, blood glucose levels must be maintained within the range of 60-120 mg/dl to avoid adverse effects on the central nervous system. Insulin is the most important hormone regulating blood glucose levels; in addition to this role, it also controls the rate of glucose uptake by muscle, fat and liver cells (Guthrie & Guthrie, 2009). In mammals, insulin is synthesized in the β cells of the endocrine pancreas; in the fetus, it is biosynthesized in the liver and vitellus sac (yolk sac) (Rhodes, Shoelson & Halban, 2005). Normal glucose balance is maintained by the following interrelated events: the production of glucose in the liver, its utilization by skeletal muscle and other peripheral tissues, and the action of balancing hormones such as insulin and glucagon. The main metabolic function of insulin is to increase the rate at which glucose enters specific cells. These specific cells are largely striated muscle cells and to a lesser extent fat cells. In the brain and other peripheral tissues, the entry of glucose into the cell occurs independently of insulin. Insulin exerts an anabolic effect in the body, stimulating the production of glycogen, lipids and proteins and conversely reducing their breakdown (Kumar, Abbas & Aster, (2013). An increase in insulin secretion is balanced by an increase in insulin synthesis (Rhodes, Shoelson & Halban, 2005).

Etiology

Diabetes is a chronic metabolic disease characterized by partial or complete insulin deficiency that is common in animals. The causative factors are usually severe pancreatitis or conditions associated with islet cell destruction. DM can develop as primary or secondary. In humans, primary DM can occur in two different forms: insulin-dependent (IDDM, type-1), which occurs in young and thin people, or insulin-independent (NIDDM, type-2), which occurs mostly in obese adults. There is also a secondary (type-3) type of DM. Although all 3 types of DM in humans are observed

---

[1] DVM
[2] Assoc. Prof. Dr., Department of Biochemistry, Faculty of Veterinary Medicine, University of Burdur Mehmet Akif Ersoy,

in animals (especially dogs), type-3 DM is more common. Type-3 (secondary) DM is caused by pancreatic disease or damage, antogonist hormones, drug toxicity (alloxan, streptozotocin), auto-antibodies against insulin in beta cells, hyperadrenocorticism and acromegaly (Hypersomatotropism) (Başoğlu & Sevinç, 2004).

The animal form of type-1 DM is similar to type-1 DM in humans and involves autoimmune destruction of beta cells. This type of DM is characterized by low insulin levels in the blood and an inadequate insulin response after glucose ingestion. Insulin administration is indicated in these patients, and ketoacidosis develops (Nelson, 1985). Histologic examination of the pancreas in dogs with type-1 diabetes revealed that pancreatic islets were destroyed and replaced by fibrous tissue in approximately 30% of cases (Başoğlu & Sevinç, 2004).

Type-2 DM is caused by insulin insensitivity. Especially obesity predisposes to insulin resistance in animals (Nelson, 2000; Başoğlu & Sevinç, 2004; Khan, 2005; Martin et al., 2006). Long-term administration of corticosteroids and progesterone stimulates growth hormone release, resulting in hyperglycemia and insulin resistance (Turgut & Ok, 2001).

Type-3 (secondary) DM is the most common form of diabetes in animals. The most common endocrinopathies involved in the development of the disease are hyperadrenocorticism and acromegaly (hypersomatotropism). Other causes of secondary diabetes in dogs are pancreatic damage and persistent progesterone release. Progestin treatments account for the majority of DM cases in cats (Stogdale, 1986). In this type of DM; after treatment of the primary disease, the disorder improves and glucose homeostasis returns to normal (Başoğlu & Sevinç, 2004).

Factors that are effective in the development of DM can be expressed as stress, glucocorticoid applications, megestrol acetate, obesity, pancreatitis, estrus and pregnancy, genetic, hormonal and immunologic causes, and infectious causes (Nelson, 1985). It has been revealed that obesity has an important role in the formation of diabetes and is effective in type-2 diabetes, which mostly develops due to insulin resistance (Khan, 2005). It is possible that synthetic progestin administration and endogenous progesterone may stimulate growth hormone synthesis in dogs and subsequently cause acromegaly and insulin resistance (Selman et al., 1994). It is known that some drug therapies or some drugs administered for experimental purposes may cause diabetes. A 9-year-old neutered cat treated with chronic methylprednisolone therapy developed DM with symptoms of polyphagia, polydipsia and polyuria, hyperadrenocorticism developed and hypercalcemia was detected in the following periods (Smith et al., 2002).

Estrogen and progesterone reduce the sensitivity of target organs to insulin, predisposing to type-2 diabetes. Therefore, females are more susceptible to diabetes than males. Symptoms of diabetes in females occur frequently during estrus and diestrus periods (Davison et al., 2005). Generally, DM is associated with hyperadrenocorticism. Because chronic hypercortisolemia causes insulin resistance (Nicola & Edgar, 2007).

Some autoimmune diseases have an important role in the development of DM. In such patients, mononuclear cells accumulate intensively in pancreatic islets and spontaneous DM develops due to decreased insulin secretion (Başoğlu & Sevinç, 2004).

After the use of streptozotocin-derived agents, it has been reported that permanent diabetes may develop due to damage to beta cells (Arai et al., 2002). Tiftik et al. (1992) induced DM in dogs by administering alloxan monohydrate intravenously at a dose of 0.6-0.7 mmol/kg. It was determined that hyperglycemia, decrease in plasma insulin level, glycosuria, ketonuria and proteinuria and decrease in urine pH were observed in all dogs that developed diabetes.

Classiffication of DM

Insulin Dependent Diabetes (Type 1 Diabetes)

The most common pancreatic disorder in dogs with type 1 diabetes is the decrease in the

number and size of islets of Langerhans. In addition, swelling of β-cells by taking water is also among the findings. In mild cases, β-cells are destroyed and degranulated, whereas in severe cases islets may be so destroyed that they cannot be seen (Manns & Martin, 1972).

Immunologic tolerance to β-cells is reduced in insulin-dependent diabetes. Cellular and humoral immunity against activated β-cell antigens is stimulated and β-cells are destroyed by a mechanism involving T lymphocytes. Type 1 diabetes is therefore referred to as an organ-specific immune disease. The markers associated with the disease are circulating autoantibodies (Mandrup-Poulsen et al., 1989).

Type 1 diabetes is a disease with a genetic basis. Autoantibodies are formed directly against cytoplasmic components of β-cells, the cell surface or insulin. In the majority of cases of canine diabetes, atrophy or fibrosis occurs. Diabetes in dogs is often not detected until clinical signs appear with hyperglycemia (Hoenig, 1995).

Non-Insulin Dependent Diabetes (Type 2 Diabetes)

It is a type of diabetes characterized by insufficient insulin secretion, hyperglycemia and insulin resistance. The pathogenesis of the disease is characterized primarily by deficiency in insulin secretion and secondarily by insulin toxicity or amyloid deposition. There may also be excess insulin secretion in type 2 diabetes. In the early stage of the disease (e.g. in obesity not complicated by glucose intolerance) there is actually a true excess insulin release. But blood glucose is still normal. In the later stages of the disease, by some unknown mechanism, insulin release is insufficient to control glucose concentration and blood insulin levels increase. Because blood glucose levels are constantly high, β-cells are subjected to constant and severe stimulation. This results in loss of function in β-cells (Warram et al., 1990).

Secondary (Type-3) Diabetes

It is diabetes that develops due to other conditions or factors. Endocrine disorders such as hyperadrenocorticosism (Peterson, 1984) and progesterone-activated growth hormone disorders play an important role in secondary diabetes in dogs. These hormones oppose the action of insulin and cause insulin resistance (Kahn et al., 1993).

Gestational diabetes (Gestational Diabetes)

They are rare cases in dogs. It is usually observed in middle-aged dogs in the 2nd half of pregnancy. If diabetes persists after the end of pregnancy or diestrus, it should be classified as Type 1 diabetes or another specific diagnosis. In clinical studies in dogs, more cases of diabetes have been observed in winter pregnancies (Hoenig, 2002).

Pathogenes

DM occurs as a result of insulin insufficiency or insulin resistance due to lesions in the pancreas. DM begins to form with the increase in glucagon, catecholamines, glucocorticoids and growth hormone, which oppose the effect of insulin, and changes in insulin activity (Reusch et al., 2006; Rand et al., 2004).

Insulin plays an important role in metabolism by acting on liver, muscle and adipose tissues, causing acceleration of glucose utilization, glycogen storage, fat synthesis, amino acid uptake and protein synthesis (Özyener, 1998; Karagül & ark., 2000; Guyton & Hall, 2000). Insulin stimulates the entry of amino acids into muscle cells (Aytuğ, 1998) and increases glucose entry into muscle and adipose tissue.

Glycolysis is reduced in the absence of insulin, and glycogenesis and lipogenesis are also inhibited. In insulin insufficiency in diabetic patients, 5% of the glucose load taken into the body is converted into fat (Guyton & Hall, 2000) increased lipase activity causes lipolysis to accelerate and free fatty acid concentrations to increase (Karagül & ark., 2000; Guyton & Hall, 2000).

Insulin facilitates the transport of amino acids across the cell membrane and generally shows an anabolic effect on protein metabolism. Based on this, it can be said that protein anabolism decreases and protein catabolism increases in the absence of insulin (Karagül & ark., 2000).

Glucose ingested with food or resulting from hepatic gluconeogenesis cannot be used in fat and muscle tissue or in the liver itself due to insufficient insulin in cells and accumulates in the blood (Karagül & ark., 2000; Kaymak, 1996; İmren & Şahal, 1996). When the glucose accumulated in the blood exceeds the renal threshold, it passes into the urine and causes glycosuria (Lust, 2002; Guyton & Hall, 2000; İmren & Şahal, 1996), which in turn causes osmotic diuresis and leads to polyuria. Polyuria leads to polydipsia by stimulating the thirst center in the hypothalamus (Lust, 2002; Turgut, 2000; Schaer, 2003). Despite hyperglycemia, polyphagia occurs because the body is actually starving. Weight loss is observed with polyuria, polydipsia and polyphagia (Lust, 2002; Guyton & Hall, 2000).

Since the body cannot metabolize glucose, the energy required for the body is provided by using fat stores. Insulin deficiency causes an increase in its antagonist epinephrine and glucagon (Karagül & ark., 2000). Ketosis may occur as a result of excessive breakdown of fatty acids (Schaer, 2003; Guyton & Hall, 2000).

The uptake and transport of amino acids in the surrounding tissues slows down, but the circulating levels of alanine and other amino acids involved in gluconeogenesis increase (Karagül & ark., 2000).

Some metabolic changes are observed in the organism due to diabetes. In the mild form of DM (normal fasting blood glucose with abnormal glucose tolerance), the current plasma glucose level is unable to generate an insulin response. This inadequate response develops due to impaired insulin secretion or insulin resistance of the liver (Greenbaum, 2002).

Diabetes is often associated with dyslipidemia. Diabetic patients usually have decreased levels of high-density lipoprotein (HDL) and increased levels of low-density lipoprotein (LDL) and triglycerides (TG). The increased LDL in the blood in cases of diabetes is small and concentrated LDL, which is more susceptible to oxidation and more arterogenic (can damage the vascular endothelium) (Kreisberg, 1998). In addition, hyperglycemia facilitates the glycosylation of LDL and other lipoproteins, causing them to oxidize more rapidly and to show more arterogenic activity. This particular condition is the disturbance in metabolism caused by diabetes, which is responsible for dyslipidemia. In diabetic patients, free fatty acids increase in circulation due to increased release from adipose tissue and decreased uptake from skeletal muscles. The liver responds to the increase in free fatty acid levels by increasing very low density lipoprotein (VLDL) and cholesteryl ester synthesis. This results in hypertriglyceridemia in diabetic patients. Hypertriglyceridemia and low HDL in insulin resistance are risk factors for cardiovascular diseases (Aguilar-Salinas et al., 2004).

In the severe form of diabetes (Type-1, absolute insulin insufficiency), increased blood glucose concentration cannot stimulate insulin secretion. Because there is no or insufficient insulin to regulate glucose release from the liver (Başoğlu & Sevinç, 2004).

It is characterized by severe insulin insufficiency, negative nitrogen balance and breakdown of body proteins. The amount of alanine and other amino acids used by the liver for glucose production increases, while plasma alanine levels decrease. As a consequence, muscle proteins are catabolized and metabolic disorders occur with denaturation of proteins. A large amount of free fatty acids from the breakdown of fat cells from adipose tissue for energy are released into the bloodstream. The removal of the suppressive effect of insulin on lipase and adipose tissue leads to

a rapid breakdown of fats. Therefore, triglycerides are formed in the liver as a result of esterification of free fatty acids. If the concentration of free fatty acids exceeds the esterification level of the liver, hepatic lipidosis and hypertriglyceridemia develop (Dimski, 1997). Ketonemia occurs as a result of fat metabolism disorders due to severe insulin insufficiency. Under normal conditions, insulin inhibits lipolysis and prevents the conversion of fatty acids into ketone bodies (Chiasson et al., 2003).

Imbalances between reactive oxygen production and antioxidant protection mechanisms lead to oxidative stress. Oxidative stress is an important factor in the development of DM and its complications. In the diabetic period, reactive oxygen groups may cause systemic inflammation. Studies have shown that antioxidant preparations prevent the development and progression of systemic inflammation (Chiasson et al., 2003).

In one case of hypophosphatemia developed experimentally in dogs and cats, severe hemolysis, infection, hemorrhages, respiratory depression, encephalopathy, hepatic problems, cardiomyopathy and myopathy developed. It was also observed that six of the dogs and one of the cats developed severe diabetes. As a result, an association between diabetes and hypophosphatemia was reported. It has been reported that severe erythrocyte hemolysis and death may occur in humans and animals when serum phosphorus concentrations fall below 1 mg/dl (Willard et al., 1987).

Coronary artery disease develops 2 to 4 times more frequently in diabetic patients. Acute coronary syndromes can be detected years before the onset of type-2 diabetes during periods of impaired glucose tolerance and impaired fasting glucose (Doğan & Ergin, 2006).

In a study on endogenous serum insulin concentrations, it was observed that endogenous serum insulin concentrations were significantly lower in diabetic dogs with ketoacidosis compared to uncomplicated diabetes (Parsons et al., 2002; Burski et al., 2004).

In a study, it was found that there is a link between anti-psychotic drugs and DM. The reason for this was reported to be the deterioration of blood glucose balance and increased risk of developing DM after the use of anti-psychotic drugs (Holt & Peveler, 2006). On the other hand, it has been reported that arteriosclerosis is more common in dogs with DM and hypothyroidism than in dogs with hyperadrenocorticism (Hess et al., 2003).

In another study conducted in terms of protein metabolism, it was reported that leucine and arginine administered with insulin combination stimulated protein synthesis more (Nolles et al., 2006). Hormonal studies have shown that obesity causes changes in the blood levels of hormones involved in energy metabolism. It has been revealed that an increase in body weight causes an increase in cortisol, insulin and insulin-like growth hormone (IGF-1) levels and a decrease in growth hormone synthesis, and that sterilization causes excessive food consumption and a decrease in metabolic rate (Martin et al., 2006).

Complications of DM

Diabetic animals have decreased resistance to bacterial and fungal diseases and are prone to suppurative cystitis, prostatitis, bronchopneumonia and dermatitis. Impaired chemotactic, phagocytic and microbicidal functions and dysfunction of polymorphous nuclear leukocytes due to poorly controlled diabetes have been implicated in the predisposition to these diseases. Radiologically detected cases of emphysematous cystitis are often related to DM. Gas accumulation in the urinary bladder wall and lumen is caused by infection with glucose-fermenting bacteria. In some diabetic dogs, gas formation in the gallbladder wall has also been observed (Charles, 2007; La Perle & Capen, 2007).

Diabetic animals have decreased resistance to bacterial and fungal diseases and are prone to

suppurative cystitis, prostatitis, bronchopneumonia and dermatitis. Impaired chemotactic, phagocytic and microbicidal functions and dysfunction of polymorphous nuclear leukocytes due to poorly controlled diabetes have been implicated in the predisposition to these diseases. Radiologically detected cases of emphysematous cystitis are often related to DM. Gas accumulation in the urinary bladder wall and lumen is caused by infection with glucose-fermenting bacteria. In some diabetic dogs, gas formation in the gallbladder wall has also been observed (Charles, 2007; La Perle & Capen, 2007).

Hepatomegaly may be seen due to fatty deposits in the liver. Lipids accumulate in the liver as a result of increased fat mobilization and damage to hepatocytes by ketonemia. Cirrhosis may develop with prolonged and widespread lipid accumulation. In progressive cases, cirrhosis is accompanied by icterus and bilirubinuria (Charles, 2007; La Perle & Capen, 2007; Şahinduran et al., 2016).

Dogs with poorly controlled diabetes often develop cataracts and when the disease becomes chronic, diffuse and often bilateral lens opacities are observed (Charles, 2007; La Perle & Capen, 2007; Bennett & Knowlwe, 2005).

Other extra hepatic diabetic lesions include chronic kidney disease due to microangiopathy characterized by thickening of the capillary basement membrane, blindness and gangrene. Dogs with long-term, poorly controlled spontaneous diabetes develop nodular or diffuse glomerulosclerosis characterized by Periodic acid-Schiff (PAS)-positive glycoprotein deposits as round nodules within the glomerular capillary bundle. Other renal lesions include intracytoplasmic glycogen deposits in Henle's loop and intranuclear glycogen deposits in distal convolute tubules (Ciobotaru, 2013; La Perle & Capen, 2007; Cusumano et al., 2002).

Biochemical Basis of Complications

To date, many studies have been conducted to explain the biochemical basis of the complications of diabetes. Despite numerous experimental studies using animal models, it has not been possible to explain exactly how all of the complications arise. The reason for this has been shown to be that complications arising from diabetes affect a large number of organs. Prolonged high blood glucose levels cause structural changes in tissues. Among the causes of tissue damage, nonenzymatic glycolization of proteins plays an important role. Glycolyzed proteins are unable to perform their biological functions (Ekmetzoglou & Zografos, 2006).

As is known, in healthy individuals with blood glucose concentrations between reference values, a very small amount of glucose is metabolized via the polyol pathway and sorbitol is released (Ekmetzoglou & Zografos, 2006). In diabetic individuals, increased glucose concentration stimulates the synthesis of aldose reductase, the key enzyme of the polyol pathway, resulting in the accumulation of large amounts of sorbitol in cells. Since sorbitol is a component that cannot cross the cell membrane, sorbitol accumulation is observed in cells. Sorbitol accumulated in cells causes an increase in intracellular osmotic pressure. Increased osmotic pressure creates stress in cells. Due to this stress, some diabetes-induced complications arise (Ekmetzoglou & Zografos, 2006).

Some of the sorbitol released as a result of the increase in the polyol pathway is metabolized by sorbitol dehydrogenase and fructose is released. During sorbitol formation, aldose reductase requires nicotinamide adenine dinucleotide phosphate (NADPH+H) and significant levels of NADPH+H are utilized. However, some enzymes involved in the elimination of free radicals released during oxidative stress (such as glutathione reductase) also require NADPH+H (Kinoshita & Nishimura, 1988). In hyperglycemia, when the polyol pathway is overworked, a large amount of NADPH+H is used. As a result, NADPH+H' deficiency is observed. When enzymes involved in the elimination of free radicals cannot find enough NADPH+H', free radicals cannot be scavenged. The free radicals accumulating in the cells increase the oxidative stress of the organism and thus

many different complications are encountered as a result of the changes observed in the molecules attacked by free radicals in all tissues (Trueblood & Ramasamy, 1998).

As a result of hyperglycemia, the polyol pathway is greatly accelerated and NADPH+H consumption is increased. On the other hand, excessive production of superoxide stimulated by hyperglycemia inhibits glucose-6-phosphate dehydrogenase enzyme. Glucose-6-phosphate dehydrogenase is the rate-limiting enzyme of the pentose phosphate pathway. When not enough glucose-6-phosphate dehydrogenase is synthesized, NADPH+H' synthesized in the pentose phosphate pathway cannot be produced. Consequently, NADPH+H' deficiency becomes more pronounced. Elimination of free radicals released during metabolism becomes difficult and oxidative stress on the organism increases (Rolo & Palmeire, 2006).

Previous studies have reported that hyperglycemia increases the de novo synthesis of diacylglycerol. As known, diacylglycerol is an endogenous activator for protein kinase C. Protein kinase C is involved in many metabolic events such as cell proliferation, cell contraction and intracellular calcium uptake. In cases of prolonged hyperglycemia, metabolic disorders are observed due to excess diacylglycerol (Koya & King, 1998).

When cells do not receive enough glucose, fats are used as an energy source. If fatty acids used in the synthesis of cell membranes are used to meet the energy needs of the cell, cell membrane synthesis is disrupted. This is also the case in individuals with diabetes. This is why diabetic patients have delayed wound healing. In order for acetyl-CoA, which is released in the mitochondria as a result of β-oxidation of fatty acids, to enter the citric acid cycle, oxaloacetate, one of the products released by the breakdown of glucose, is needed. In other words, carbohydrates are needed for fats to be used by the organism. Since the cells of diabetic individuals do not receive enough glucose, an increase in acetyl-CoA synthesis is observed. There is a parallel between the rate of fatty acid breakdown and the rate of synthesis of chemical compounds called ketone bodies (acetoacetic acid, β-hydroxybuturic acid and acetone) and cholesterol. This leads to ketosis and a decrease in blood pH. Decreased blood pH has negative effects on the whole organism (Ekmetzoglou & Zografos, 2006).

Due to insulin deficiency, glucose passes into the urine and glucosuria is observed as a result of inadequate utilization of carbohydrates, excessive glycogen breakdown and elevated blood glucose level due to gluconeogenesis. Since the presence of glucose in the urine causes an increase in osmotic pressure, polyuria is also observed in diabetics. Along with the large amount of water lost from the body through urine, potassium is also lost and as a result, hypokalemia usually occurs in diabetic individuals. Due to the lack of potassium ions, which play an essential role in muscle contraction, coordination disorders occur in diabetics (Ekmetzoglou & Zografos, 2006).

Clinical and Laboratory Findings

Clinical Findings

The term DM describes a multiple syndrome associated with abnormal carbohydrate metabolism resulting in hyperglycemia. Individual metabolic lesions in diabetic patients sometimes result in relative suppression of insulin secretion with varying degrees of peripheral resistance to insulin, resulting in characteristic clinical manifestations such as polyuria, polydipsia, polyphagia and weight loss.

Glucosuria occurs when hyperglycemia (>200 mg/dl in dogs) exceeds tubular reabsorption capacity. Polyuria is due to the osmotic diuretic effect of glucose in the renal tubules. Polydipsia develops to compensate for polyuria. Increased appetite, hunger is governed by the satiety center in the hypothalamus. The presence of insulin is necessary for glucose to enter this area. In the

absence of insulin, there is a constant feeling of hunger.

There is weight loss in patients with long-standing diabetes due to urinary calorie loss, but some diabetics may become obese.

Hepatomegaly due to fat mobilization and hepatitis lipidosis; muscle weakness due to inhibition of cellular glucose transport; urinary and respiratory system infections; ulcerative skin lesions; cutaneous xanthomata; and pancreatitis in cases where diabetes cannot be controlled (Vurkaç & Şahinduran, 2018).

In advanced cases, the accumulation of ketone bodies, metabolic acidosis and therefore depression, anorexia, vomiting, rapid dehydration, severe hypovolemia, circulatory collapse, coma and death may occur. Most dogs develop cataracts 6 months after diagnosis. Hypertension is caused by the accumulation of glucose compounds in the endothelium. Diabetic nephropathy, proteinuria, glomerulosclerosis, renal failure, diabetic retinopathy and retinal hemorrhage may also occur (Aytuğ, 2011).

Laboratory Findings

The most common laboratory abnormalities in DM are hyperglycemia, glycosuria, increased liver enzymes, hypercholesterolemia and hyperproteinemia. Complications usually occur due to chronic hyperglycemia and less commonly due to ketoacidosis (Aytuğ, 1998; Fleeman et al., 2001; Schaer, 2003). While blood glucose level is usually above 200 mg/dl in symptomatic patients, blood glucose level is between 125-180 mg/dl in asymptomatic diabetic patients (Aytuğ, 1998). When the blood glucose level exceeds the renal threshold (180 mg/dl in dogs and 200 mg/dl in cats), glycosuria is observed, but glycosuria is not observed in all diabetic patients, especially in those fed carbonhydrate-poor diets (Aytuğ, 1998). Serum insulin level is below 26 µU/ml in patients with type 1 DM (Turgut, 2000). Lipemia may develop in patients with diabetes due to increased fat mobilization (Catchpole et al., 2005). Plasma is cloudy in fasting samples. Cholesterol level in the blood hovers around 300 mg/dl in the acute phase of the disease. As the disease becomes chronic, it can reach 900 mg/dl. In severe cases, triglyceride, lipoprotein and free fatty acid levels in the blood increase with the increase in cholesterol level (Turgut, 2000; Başoğlu & Sevinç, 2004). Serum (Alanine Aminotransferase) ALT and (Alkaline Phosphatase) ALP activities may increase as a result of hepatic lipidosis in patients. If diabetic ketoacidosis develops, ketonemia and ketonuria are observed (Reusch et al., 2006). A decrease in blood pH is observed due to metabolic acidosis that may develop in DM (Hoenig, 2002). Along with this disturbance in acid-base balance, fluid-electrolyte disorders are also observed. In animals with diabetes, blood urea and creatinine levels are normal unless there is also primary renal failure and prerenal uremia (Aytuğ, 2011). Serum lipase and amylase levels are high in dogs with pancreatitis. However, serum amylase and lipase levels may also be elevated in chronic inflammation and renal failure. In diabetic patients, proteinuria may be detected in urine examinations as a result of secondary urinary tract infections. As a result of hyperglycemia in diabetic animals, calcium absorption from the intestines decreases, while urinary excretion of calcium and phosphorus increases. In addition, vitamin D and osteocalcin levels in the blood decrease and parathyroid hormone secretion increases as a result. Although hemogram results of patients with diabetes are generally normal in uncomplicated cases, impairments in the structure and function of erythrocytes, leukocytes and platelets may be observed as a result of hematologic complications of diabetes (Aytuğ, 1998).

Methods used in Diagnosis

The diagnosis of the disease is based on anamnesis, clinical findings and especially laboratory findings. The most important laboratory finding in the diagnosis of the disease is persistent fasting hyperglycemia and glycosuria. Fasting blood glucose in healthy cats and dogs is 75- 120 mg/dl.

Fasting blood glucose levels above 200 mg/dl should be considered abnormal. Repeated measurements of fasting blood glucose above 200 mg/dl and accompanying glycosuria are diagnostic findings for diabetes (Turgut, 2000; Akalın, 2007). In all dogs with DM, besides a significant hyperglycemia, a decrease in plasma insulin levels, glycosuria, ketonuria and proteinuria and a decrease in urine pH were observed. It was determined that serum glucose level (16.7 mmol/l) was significantly increased and serum malate dehydrogenase (MDH) concentration was significantly decreased in dogs experimentally induced diabetes with streptozotocin and it was reported that MDH parameter may be an important marker in the evaluation of glycemic control and diabetes (Arai et al., 2002).

Detection of blood glucose levels may not always be sufficient to diagnose diabetes. In this case, Intravenous Glucose Tolerance Test (IVGTT) is recommended. Animals with mild hyperglycemia do not show clinical signs of DM and in this case, the impaired glucose tolerance is assessed by IVGTT to determine whether insulin treatment is needed. Two hours after the IVGTT test in healthy animals, blood glucose levels fall to the lower limit or lower, whereas in diabetic animals, glucose levels remain elevated. An Oral Glucose Tolerance Test (OGTT) can also be used for diagnostic purposes. The glucose tolerance test is often used to diagnose diabetes in cats and dogs. It is especially indicated for the diagnosis of patients with persistent hyperglycemia (120-175 mg/dl) but no glycosuria and, to a lesser extent, for the diagnosis of patients with glycosuria but no hyperglycemia. Glucose tolerance testing may give different results due to diet, medications, non-pancreatic diseases, stress and other factors. Test protocols should be followed to minimize inaccuracies in test results. For this purpose, diet and activity should be regulated. OGTT is preferred if there is no gastro-intestinal problem that may prevent absorption in the intestines. In this test, 25% glucose solution is administered to the patient at a dose of 1.75 g/kg in the morning on an empty stomach. Venous blood samples are collected at 30, 60, 90, 120 and 180 minutes before and after administration, respectively. In non-diabetic patients, blood glucose levels return to normal between the 60th and 90th minutes. In diabetic patients, after 90 minutes, blood glucose level remains above normal values (Turgut, 2000; Başoğlu & Sevinç, 2004; Khan, 2005).

Glucagon Response Test is another test used in the diagnosis of diabetes. With this test, information about insulin secretion capacity can be obtained and insulin insensitive animals can also be identified (Başoğlu & Sevinç, 2004). Kirk et al. (1993) examined serum insulin levels in cats by injecting glucagon at a dose of 0.5 mg/kg. They found significant increases in serum insulin levels at the 5th, 10th, 15th and 30th minutes. It was observed that serum insulin concentrations started to return to normal values 60 minutes after injection. In addition to the above-mentioned diagnostic methods, routine urine analysis should be performed along with complete blood count, biochemical measurements of insulin, creatinine, Blood Urea Nitrogen (BUN), ALP, Aspartate Aminotransferase (AST), ALT, calcium (Ca), potassium (K), phosphorus (P), total protein, albumin and ketone bodies (Nelson, 2000; Khan, 2005; Fracassi et al., 2007). If vomiting, diarrhea and lethargy are also present, serum amylase, lipase, blood gases and serum electrolyte levels should also be checked. In addition, thoracic and abdominal radiographs may be used. Hypophosphatemia that may develop as a result of diabetic ketoacidosis may lead to serious problems that may result in death (Willard et al., 1987).

In ketoacidosis, a complication of diabetes in dogs, endogenous insulin levels are significantly reduced (Parsons et al., 2002). The development of diabetic ketoacidosis occurs as a result of two basic metabolic disorders. These metabolic disturbances can be expressed as a relative or absolute decrease in endogenous serum insulin levels and an increase in blood levels of glucagon, catecholamine, cortisol and growth hormones that suppress insulin secretion (Powers, 2001; Feldman & Nelson, 2004).

Increased glucose molecules in the blood bind to hemoglobin through an irreversible, non-enzymatic reaction and HbA1c is formed (Marca et al., 1999). Normally, a small proportion of total

hemoglobin is found glycosylated in erythrocytes. The amount of glycosylated hemoglobin varies depending on the serum glucose level and the half-life of erythrocytes. The HbA1c level indicates the 60-90 day glucose level in humans and dogs (Denise et al., 1997).

HbA1c is not affected by short-term fluctuations in blood glucose and is a relatively accurate indicator of blood glucose control in diabetes. In veterinary medicine, stress-induced hyperglycemia can be seen, especially during blood sampling from cats and dogs. HbA1c levels are not affected by stress-induced hyperglycemia (Taşçene & Karagül, 2008). HbA1c constitutes 3% of total hemoglobin in humans. While this rate varies between 6-10% in humans with diabetes (Trivelli et al., 1971), this rate varies between 3-7% in dogs (Wood & Smith, 1980). In patients with diabetes, HbA1c concentration increases 2-3 times higher than normal. Wood & Smith (1980) measured the minor hemoglobin concentrations, glycosylated hemoglobin B fraction (HbA1b) and HbA1c by chromatogrophic method in healthy and diabetic dogs and found that HbA1c concentration was significantly higher in diabetic dogs. He revealed that these parameters have important benefits in monitoring blood glucose levels and determining insulin efficacy.

An important parameter in the diagnosis of the disease is fructosamine. Fructosamines are formed as a result of non-enzymatic bonding of glucose in hyperglycemic blood with amino groups of proteins (Behrend & ark., 2018).

Thus the serum fructosamine test measures a pool of glycated proteins, including glycated albumin, which comprises the bulk of the measured fructosamine concentration (Welsh, Kirkman & Sacks, 2016). Studies have shown that fructosamine levels have an important place in the diagnosis of diabetes. Normally, the synthesis and elimination of fructosamine in the blood continues as a continuous process and is kept in balance in this way. However, after the development of hyperglycemia, this balance is disrupted and fructosamine concentration increases rapidly (Jensen, 1993). Davison et al. (2005) reported that fructosamine concentration increased significantly in dogs with DM. On the other hand, Martin et al. (2006) reported that fructosamine concentration (> 340 µmol/L) was significantly increased in obese dogs, and Reusch et al. (2002) reported that fructosamine level was increased in obese dogs with hypothyroidism and this may be a precursor of type-2 diabetes.

In their study, Norris & Schermerhorn (2022), investigated the use of HbA1C in the clinical monitoring of diabetes. Their results showed that HbA1c is a more consistent parameter than serum fructosamine concentration in clinical monitoring of diabetes. Briefly, they emphasized that the determination of HbA1c levels in the evaluation of glycemic status in diabetic dogs would be beneficial, but HcA1C should be used together with other tests in the follow-up of clinically stable diabetic dogs (Norris & Schermerhorn, 2022).

There are many similarities between diabetic cats with and diabetic humans in case of Islet amyloidosis. In this case, progressive damage is seen especially in β- and α-cells, while the number of δ-cells is normal. Similar features of islet amyloidosis are seen in more than 90% of Type-2 DM (non-insulin-dependent) humans and diabetic cats. Acute pancreatic necrosis (APN) may occur as a result of predisposing factors such as insulin antagonism, insulin resistance, changes in glucose tolerance, obesity, hyperadrenocorticism, and continuous use of glucocorticoids. In such cases, it is important to address the etiological agent, risk factors, diagnosis of diabetes, hormonal and drug interactions, and to apply appropriate treatment (herbal) protocols. At this point, it should be kept in mind that the protocols used for the diagnosis and treatment of human DM are not suitable for animals. More research is needed on diabetic status in domestic and wild animals (Niaz & et al., 2018).

DM is a syndrome caused by various etiologies. It should be noted that the clinical manifestations of DM do not indicate the cause of the disease. However, clinical signs can provide information about the disease process and severity. It is important that the studies to be carried

out are aimed at diagnosing and classifying the factors affecting the formation of the disease in diabetic dogs and cats, and for the early diagnosis, prevention and treatment of these factors (Gilor & ark., 2016).

REFERENCES

Aguilar-Salinas, C., Assis-Luores-Vale, A., Stockins, B., Rengifo, H. M., Filho, J. D., Neto, A. A., Rabelo, L. M., Torres, K. P., Oliveira, J. E. P., Machado, C. A., Reyes, E., Saavedra, V., Florenzano, F., Hernández, M. V., Jiménez, S. H., Ramírez, E., Vazquez, C., Salinas, S., Hernández, I., Medel, O., Moreno, R., Lugo, P., Alvarado, R., Mehta, R., Gutierrez, V. & Pérez, F. J. G. (2004). Ciprofibrate Therapy İn Patients With Hypertriglyceridemia And Low High Density Lipoprotein (Hdl)-Cholesterol: Greater Reduction Of Non-Hdl Cholesterol İn Subjects With Excess Body Weight. *Cardiovascular Diyabetology.* 3,8-9.

Akalın, P. (2007). *Beta-Endorfinin Kan Glikoz Düzeyine Etkiler.* Doktora Tezi. S.Ü. Sağlık Bilimleri Enstitüsü, Konya/Türkiye.

Arai, T., Nakamura, M., Magori, E., Fukuda, H., Mizutani, H., Kawakami, E. & Sako, T. (2002). Changes İn Activities Of Enzymes Related To Energy Metabolism İn Peripheral Leukocytes Of Diyabetic Dogs With Glycemic Control By İntensive İnsulin Treatment. *Res. Vet. Sci.* 73, p. 183-186.

Aytuğ, N. (1998). *Kedi Ve Köpek Hastalıkları.* Metabolizma Hastalıkları, İmren Hy (Editör), Medisan Yayınları, Ankara. s. 345-346.

Aytuğ, N. (2011). *Köpek Ve Kedilerin İç Hastalıkları*, 1. Baskı, F. Özsan Matbaacılık, Bursa. S. 370-378.

Başoğlu, A. & Sevinç, M. (2004) *Evcil Hayvanlarda Metabolik Ve Endokrin Hastalıklar.* S.Ü. Vakfı Yayınları, Konya. s. 264-271.

Behrend, E., Holford, A., Lathan, P., Rucinsky, R., & Schulman, R. (2018). 2018 AAHA Diabetes Management Guidelines for Dogs and Cats. *Journal of the American Animal Hospital Association*, *54*(1), 1–21. https://doi.org/10.5326/JAAHA-MS-6822

Bennett, P. H. & Knowler, W. C. (2005). Definition, Diagnosis And Classification Of Diabetes Mellitus And Glucose Homeostasis. In: Kahn Cr, Weir Gc, King Gl, Jacobson Am, Moses A C, Smith Rj, Editors. *Joslin's Diabetes Mellitus.* p. 331-339, London: Lippincott, Williams And Wilkins.

Burski, K., Ueland, T. & Maciejewski, R. (2004). Serum Amylase Activity Disorders İn The Course Of Experimental Diabetes İn Rabbits. *Vet. Med. Czech.* 49, 197-200.

Catchpole, B., Ristic, J. M. & Fleeman, L. M., Et Al (2005). Canine Diabetes Mellitus: Can Old Dogs Teach Us New Tricks? *Diabetologia. 48* (10): 1948-1956.

Charles, J. A. (2007). Diabetes Mellitus. In: Maxie Mg, Editor. Jubb, *Kennedy And Palmer's Pathology Of Domestic Animals*, 5th Ed. p. 414-418. Philadelphia: Saunders Elsevier.

Chiasson, J.L., Jilwan, N. A., Bélanger, R., Bertrand, S., Beauregard, H., Ékoé, J. M., Fournier, H. & Havrankova, J. (2003). *Diagnosis And Treatment Of Diyabetic Ketoacidosis And The Hyperglycemic Hyperosmolar State.* Canadian Medical Association. 168, 7-8.

Ciobotaru, E. (2013). Spontaneous Diabetes Mellitus İn Animals. In: Oo Oluwafemi, Editör. *Diabetes Mellitus - Insights And Perspectives.* p. 271-296. Rijeka, Croatia; Intech.

Cusumano, A. M., Bodkin, N. L., Hansen, B. C., Lotti, R., Owens, J., Klotman, P. E. & Kopp, J. B. (2002). Glomerular Hypertrophy İs Associated With Hyperinsulinemia And Precedes Overt Diabetes İn Aging Rhesus Monkeys. *Am J Kidney Dis.* 40: 1075–1085.

Davison, L. J., Herrtage, M. E. & Catchpole, B. (2005). Study Of 253 Dogs İn The United Kingdom With Diabetes Mellitus. *Vet. Rec.* 156, 467-471.

Denise, A.E., Richard, W. N., Edward, C. F. & Larry, A. N. (1997). *Glycosylated Haemoglobin Concentrations İn The Blood Of Healty Dogs And Dogs With Naturally Developing Diabetes Mellitus, Pancreatic B-Cell Neoplasia, Hyperadrenocorticism And Anemia.* Javma, 211, 723- 727.

Dimski, D. S. (1997). Feline Hepatic Lipidosis. *Semin Vet Med Surg (Small Anim).* 12, 28-33.

Doğan. A. & Ergin, A. (2006). *Diyabet Ve Akut Koroner Sendromlar.* Medical Network. Erişim Adresi: Http://Www.Medicalnetwork.Com.Tr/Web/Konu.Asp?Goster=1&Metin=276

Ekmetzoglou, A. & Zografos, C. G. (2006). A concomitant Review Of The Effects Of Diabetes Mellitus And Hypothyroidism In Wound Healing. *World Journal Of Gastroenterology*, *12* (17), p. 2721-2729.

Feldman, E. C. & Nelson, R. W. (2004). *Canine And Feline Endocrinology And Reproduction.* 3rd. Edn. W.B. Saunders, Philadelphia.

Fleeman, L.M. & Rand, J. S. (2001). Management Of Canine Diabetes. *Vet Clin North Am Small Anim Pract. 31* (5): 855-880.

Fracassi, F., Mandrioli, L., Diana, A., Hilbe, M., Grinwis, G. & Gandini, G. (2007). Pituitary Macroadenoma İn A Cat With Diabetes Mellitus, Hypercortisolism And Neuroligical Signs. *J.Vet. Med. A.* 54, 359-363.

Gilor, C., Niessen, S. J., Furrow, E. & DiBartola, S. P. (2016). What's in a Name? Classification of Diabetes Mellitus in Veterinary Medicine and Why It Matters. *J Vet Intern Med.*, 30(4):927-940. doi:10.1111/jvim.14357

Greenbaum, C. J. (2002). *Patients With Type 1 Diabetes Who Have Normal Fasting Glucose.* American Diabetes Association. 51, 951-957.

Guthrie, D. W. & Guthrie, R. A. (2009). *Management Of Diabetes Mellitus A Guide To The Pattern Approach,* 6 Th Edition, New York: Springer Publishing Company, 3-120.

Guyton, A. C. & Hall, J. E. (2000). *Textbook Of Medical Physilogy.* 10th Ed, Wb Saunders, Philadelphia.

Hess, R. S., Kass, P. H. & Winkle, T. J. V. (2003). Association Between Diabetes Mellitus, Hypothyroidism Or Hyperadrenocorticism And Atherosclerosis İn Dogs. *J. Vet. Intern. Med.* 17, 489-494.

Hoenıg, M. (1995). Pathophysiology Of Canine Diabetes. *Veterinary Clinics Of North Merica: Small Animal Practice*, *25* (3), 553-561.

Hoenig, M. (2002). Comparative Aspects Of Diabetes Mellitus İn Dogs And Cats, *Mol Cell Endocrinol,* p. 221-229.

Holt, R. I. G. & Peveler R. C. (2006). Association Between Antipsychotic Drugs And Diabetes. *Diabetes, Obesity And Metabolism.* 8, 125-135.

İmren, H. Y. & Şahal, M. (1996). Veteriner İç Hastalıkları, 4. Baskı, Medisan Yayınları, Ankara.

Jensen, A. L. (1993). Various Protein And Albumin Corrections Of The Serum Fructosamine Concentrations İn The Diagnosis Of Canine Diabetes Mellitus. *Vet. Res. Comm.* 17, 13-23.

Kahn, S. E., Horber, F. F. & Prıgeon, R. L. (1993). Effect Of Glucocoricoids And Growth Hormone Treatment On Proinsulin Levels İn Humans. *Diabetes*, 42, 1082- 1085.

Karagül, H., Fidancı, U. R., Altıntaş, A. & Sel, T. (2000). *Klinik Biyokimya*, 1. Baskı, Medisan Yayınları, Ankara.

Khan, C. M. (2005). *Merck Veterinary Manual.* Ninth. Edition, National Publishing Inc. Philadelphia.

Kınoshıta, J. H. & Nıshımura, C. (1988). The İnvolvement Of Aldose Reductase İn Diabetic Complications, *Diabetes Metab Rev,* 4, p. 323-337.

Kirk, C. A., Feldman, E. C. & Nelson, R. W. (1993). Diagnosis Of Naturally Acquired Type-1 And Type-2 Diabetes Mellitus İn Cats. *Am. J. Vet. Res.* 54, 463-467.

Koya, D. & King, G. L. (1998). Protein Kinase C Activation And The Development Of Diabetic Complications. *Diabetes*, 47, p. 859-866.

Kreisberg, R. A. (1998). Diyabetic Dyslipidemia. *Am J Cardiol.* 82, 89-90

Kumar, V., Abbas, A. K. & Aster, J. C. (2013). *Robbins Basic Pathology (Robbins Temel Patoloji).* Çev: Tuzlalı S, Güllüoğlu M, Çevikbaş U., İstanbul, Nobel Tıp Kitapevi, s. 715-763.

La Perle, K. M. D. & Capen, C. C. (2007). Hypofunction Of Pancreatic İslet Cells: Diabetes Mellitus. In: Mcgavin Md, Zachary Jf, Editors. *Pathologic Basis Of Veterinary Disease.* 4th Ed. P. 734-737. China: Mosby Elsevier.

Lust, E. (2002). Diabetes Mellitus İn Canines And Felines. *U.S Pharmacist.* Vol. 27: 11.

Mandrup-Poulsen, T., Helqvıst, S. & Molvıg, J. (1989). Cytokines As İmmune Effector Molecules İn Autoimmune Endocrine Diseases With Special Reference To İnsulin-Dependent Diabetes Mellitus. *Autoimmunity*, 4, 191-218.

Manns, J. G. & Martın, C. L. (1972). Plasma İnsulin, Glucagon, And Nonesterified Fatty Acids İn Dogs With Diabetes Mellitus. *Am J Vet Res*, 33, 981-985.

Marca, M. C., Loste, A., Unzueta, A. & Perez, M. (1999). Blood Glycated Haemoglobin Evalution İn Sick Dogs. *Can J Vet Res*, 64, 141-144.

Martin, L. J. M., Siliart, B., Dumon, H. J. V. & Nguyen, P. G. (2006). Hormonal Disturbances Associated With Obesity İn Dogs. *J.Anim. Phy. And Anim. Nutr.* 90, 355-360.

Nelson, R. W. (1985). Disorders Of Glucose Metabolism İn The Dog-1: Diabetes Mellitus. *Vet. Med*, 80, 27-36.

Nelson, R. W. (2000). Diabetes Mellitus. In *Textbook Of Veterinary Internal Medicine* 5th Edn. Eds. S.J. Ettinger, E.C. Feldman, W.B. Saunders Company, Philadelphia. p. 1438-1460.

Niaz, K., Maqbool, F., Khan, F., Hassan, F. I., Momtaz, S., & Abdollahi, M. (2018). Comparative occurrence of diabetes in canine, feline, and few wild animals and their association with pancreatic diseases and ketoacidosis with therapeutic approach. *Veterinary world*, *11*(4), 410–422. https://doi.org/10.14202/vetworld.2018.410-422

Nicola, R. P. & Edgar, P. F. (2007). Insulin Resistance Is Associated With Hypercortisolemia İn Polynesian Patients Treated With Antipsychotic Medication. *Diabetes Care*. 30, p. 1425-1429.

Nolles, J. A., Van-Straten, E. M. E., Bremer, B. I., Koopmanschap, R. E., Verstegen, M. W. A. & Schreurs, V. V. A. M. (2006). Dietary Amino Acids Fed İn Free Form And As Protein Components Do Not Differently Affect Postprandial Plasma İnsulin, Glucagon, Growth Hormone And Corticosterone Responses İn Rats. *Journal Of Animal Physiology And Animal Nutrition*. 90, 289-299.

Norris, O., & Schermerhorn, T. (2022). Relationship between HbA1c, fructosamine and clinical assessment of glycemic control in dogs. *PloS one*, *17*(2), e0264275. https://doi.org/10.1371/journal.pone.0264275

Özyener, F. (1998). Karbonhidrat Metabolizması. (Alınmıştır) *Tıp Öğrencileri İçin Klinik Biyokimya,* Ulukaya E (Çeviri Editörü). Nobel&Güneş Yayınları, Bursa. s. 1-20.

Parsons, S. E., Drobatz, K. J., Lamb, S. V., Ward, C. R. & Hess, R. S. (2002). Endogenous Serum İnsulin Concentration İn Dogs With Diyabetic Ketoacidosis. *J. Vet. Emergency And Critical Care*. 12, 147-152.

Peterson, M. E. (1984). Decreased İnsulin Sensitivity And Glucose Tolerance İn Spontaneous Canine Hyperadrenocorticism. *Res Vet Sci*, 36, 177-182.

Powers, A. C. (2001). Diabetes Mellitus. In Braunwald E, Fauci Anthony, Kasper D, Hauser S,Longo D, & Jameson Jl (Eds.), *Harrison's Principles Of İnternal Medicine.* New York: Mcgraw-Hill Companies. p. 2109-2137.

Rand, J. S., Fleeman, L. M. & Farrow, H. A. Et Al (2004). *Canine And Feline Diabetes Mellitus Nature Or Nuture, J. Nutr*. 134: p. 2072-2080.

Reusch, C. E., Gerber, B. & Boretti, F. S. (2002). Serum Fruktozamin Concentrations İn Dogs With Hypothyroidism. *Vet. Res. Commin*. 26, 531-536.

Reusch, C. E., Tschour, F. & Kley, S. Et Al (2006). *Diabetes Mellitus İn The Cat: A Review*. Schweiz Arch Tierheilkd. 148: 130-138.

Rhodes, C. J., Shoelson, S. & Halban, P. A. (2005). Insulin Biosynthesis, Processing, And Chemistry. In: Kahn Cr, Weir Gc, King Gl, Jacobson Am, Moses Ac, Smith Rj. (Eds), *Joslin's Diabetes Mellitus.* 14th Edition, Boston: Lippincott Williams & Wilkins, p. 65-82.

Rolo, P. A. & Palmeıra, M. C. (2006). Diabetes And Mitochondrial Function Role Of Hyperglycemia And Oxidative Stress, *Toxicology And Applied Pharmacology*, 212, 167-178.

Schaer, M. (2003). Diabetes Mellitus, *Clinical Medicine Of The Dog & Cat*. Manson Publishing Ltd, London.

Selman, P. J., Mol, J. A., Rutteman, G. R., Gardenen, E. & Rijnberk, A. (1994). Progestin-İnduced Growth Hormone Excess İn The Dog Originates İn The Mammary Gland. *Endocrinology*. 134, 287-292.

Smith, S. A., Freeman, L. C. & Swanson, M. B. (2002). Hypercalcemia Due To İatrogenic Secondary Hypoadrenocorticism And Diabetes Mellitus İn A Cat. *J.Amer. Anim. Hosp. Assoc.* 38, 41-44.

Stogdale, L. (1986). Definition Of Diabetes Mellitus. *Cornell Vet*. 76, 156-174.

Şahinduran, Ş., Özmen, Ö. & Sevgisunar, N. (2016). Multi-Organ Damage İn A Cow With Diabetes Mellitus. *Ankara Üniv Vet Fak Derg*, 63: 77-81.

Taşçene, N. & Karagül, H. (2008). Diyabetli Köpeklerde Kan HbA1c Düzeyleri, *Ankara Üniv. Vet. Fak. Derg.* 55, 75-78.

Tiftik, A. M., Turgut, K., Gürbilek, M. & Sevinç, M. (1992). Köpeklerde Alloksan İle Oluşturulan Experimental Diyabet Üzerinde Araştırmalar. *S.Ü. Vet. Fak. Derg.* 8, 18-21.

Trivelli, L. A., Ranney, H. M. & Lai, H. T. (1971). Hemoglobin Compenents İn Patients With Diabetes Mellitus. *N. Engl. J. Med.* 284, 354-357.

Trueblood, N. & Ramasamy, R. (1998). Aldose Reductase İnhibition İmproves Altered Glucose Metabolism Of İsolated Diabetic Rat Hearts. *Am J Physiol*, 275, 75-83.

Turgut, K. (2000). *Veteriner Klinik Laboratuar Teşhis*.1. Baskı, Bahçıvanlar Basım Sanayi Aş, Konya.

Turgut, K. & Ok, M. (2001). *Kedi Ve Köpek Gastroenterolojisi*. Bahcıvanlar Basım Sanayi. A.Ş. Konya.

Vurkaç, N. & Şahinduran, Ş. (2018). Köpeklerde Diabetes Mellitus, *MAKÜ Sag. Bil. Enst. Derg. 6* (1): 43-50. ISSN: 2148-2837

Warram, J. H., Martın, B. C. & Krolewskı, L. S. (1990). Slow Glucose Removal Rate And Hyperinsulinemia Preceede The Development Of Type Iı Diabetes İn The Offspring Of Diabetic Parents. *Ann Intern Med*, 113, 909-915.

Welsh, K. J., Kirkman, M. S., & Sacks, D. B. (2016). Role of Glycated Proteins in the Diagnosis and Management of Diabetes: Research Gaps and Future Directions. *Diabetes care*, *39*(8), 1299–1306. https://doi.org/10.2337/dc15-2727).

Willard, M. D., Zerbe, C. A., Schall, W. D., Johnson, C., Crow, S. E. & Jones, R. (1987). Severe Hypophosphatemia Associated With Diabetes Mellitus İn Six Dogs An One Cat. *Javma*. 190, 1007-1010.

Wood, P. A. & Smith, J. E. (1980). Glycosylated Hemoglobin And Canine Diabetes Mellitus. *Javma*. 176, 1267- 1268.

Yoon, S., Fleeman, L. M., Wilson, B. J., Mansfield, C. S., & McGreevy, P. (2020). Epidemiological study of dogs with diabetes mellitus attending primary care veterinary clinics in Australia. *The Veterinary record*, *187*(3), e22. https://doi.org/10.1136/vr.105467

The Importance of Procalcitonin with Soluble Trigger Receptor-1 Expressed By Myeloid Cells in Veterinary Medicine

Mert SEZER[1]

Definition and Importance of the Concept of Biomarker

Molecules that provide information about the healthy and pathological state of the living thing, are found in blood or other body fluids and can be measured are called biomarkers. Biomarkers provide very important information in evaluating the effectiveness of treatment, distinguishing whether the fire is infectious or non-infectious, and evaluating the diagnosis and prognosis of diseases (Miguel & et al., 2011; Akyüz & Gökce, 2021; Sezer & Gökce, 2021). Acute phase proteins, oxidative stress parameters, and biomarkers were evaluated separately or together in the diagnosis and prognosis of different diseases. Biomarkers in respiratory system diseases (Akyüz & et al., 2022b), traumatic reticuloperitonitis of cattle (Akyüz & Aydın, 2022), rats with kidney damage (Akyüz & et al., 2021), calves with diarrhea (Erkılıç & et al., 2019), cattle with paratuberculosis (Akyüz & et al., 2022d) provided very valuable information.

Sepsis occurs during the course of many diseases. Sepsis is a complicated condition that affects living things (Akyüz & et al., 2017; Akyüz & et al., 2022c). In the case of sepsis, there is an interaction between the organism and the pathogen causing the disease. As a result, the release of biomarkers occurs. The most effective way to combat diseases is early diagnosis and effective intervention. The use of biomarkers for early diagnosis has been emphasized in recent years (Su & et al., 2011; Sezer & Gökce, 2021).

Desirable Properties of an Ideal Biomarker

It should be biochemically stable and work in a small amount of blood, can be measured quickly and at low cost with a simple analysis method, its sensitivity should be ≈100% and its specificity >85% (Sönmezer & Tülek, 2015). It should be used in the follow-up of the patient's prognosis and treatment. Distinguish between infectious and non-infectious conditions. It should be able to distinguish whether the pathogen in the etiology of the disease is bacterial or viral (Abd Elmouttaleb & et al., 2016). Apart from this, it should be objective and provide information about the mortality rate of the disease (Valenzulea-Sanchez & et al., 2016; Sezer & Gökce, 2021).

Construction and Biosynthesis of Procalcitonin

Procalcitonin (PCT) is the precursor of the calcitonin hormone and is synthesized by C cells in the thyroid gland (Matur & et al., 2017; Akyüz & Gökce, 2021; Akyüz & et al., 2022a). Apart from this, pancreas, liver, spleen, adrenal gland, lung, kidney, brain, spinal cord, testis stomach, small intestines, visceral part of the colon, skin, peritoneal macrophages and leukocytes are also

---

[1] Assistant Professor., Institution: Kafkas University Faculty of Veterinary Medicine, Department of Internal Medicine

synthesized from muscle and adipose tissue (Müller & et al., 2001; Carrol, 2002; Akyüz & et al., 2022a; Akyüz & et al., 2022b).

Bracq & Machason, (1993); Oberhoffer & et al., (1999) and Nijsten & Olinga, (2000) stated that PCT is produced by macrophages and monocytes in many organs, especially the liver, in response to infections. Morgenthaler et al., (2003) also gave similar information on the subject. Therefore, hormokine (since it is synthesized from both endocrine glands and tissues) is characteristic (Christ-Crain & Muller, 2007). In healthy conditions, its blood level is low (Matur & et al., 2017). Its half-life is 22-26 hours, and it is secreted within 2-4 hours (Carrol, 2002) in all inflammatory conditions with tissue damage (Chivate & et al., 2016; Matur & et al., 2017). It is broken down and removed from the circulation by proteolysis (Meisner & et al., 2000). The increase in procalcitonin level is especially associated with bacterial endotoxin and cytokines such as TNF, IL-1, IL-6. Procalcitonin release occurs as a result of the cell-mediated immune response stimulated by these (Nakamura & et al., 2013).

The molecular weight of procalcitonin is 13 kDa and it is a polypeptide containing 116 amino acids in its structure (Jin & Khan, 2010; Günal & et al., 2011). Ghillani et al., (1989) first stated that procalcitonin is produced in the thyroid gland and that it is the precursor of the calcitonin hormone (Aouifi & et al., 1999).

Procalcitonin synthesis is controlled by calcitonin gene 1 (CALC-1). When the structure of this gene was examined, it was seen that it consisted of 6 exons and 5 introns (Matur & et al., 2017; Akyüz & et al., 2022a). Procalcitonin is synthesized as follows. First, there is the synthesis of catacalcin, which contains 21 amino acids in its structure. Afterwards, calcitonin consisting of 32 amino acids and N-procalcitonin consisting of 57 amino acids are synthesized, respectively. N-procalcitonin is usually located in adipose tissue and neuroendocrine cells and is involved in maintaining energy balance in the body. Calcitonin, on the other hand, has an antagonist effect on the parathyroid gland and takes part in the metabolism of calcium and phosphorus. Katacalcin also has a similar role to calcitonin and is especially involved in the structure and functions of the skeletal system (Matur & et al., 2017).

Procalcitonin is synthesized by neuroendocrine cells in the respiratory and digestive systems in inflammatory conditions (Mitaka, 2005). It has been observed that there is a significant increase in the level of thyroid and lung cancers, especially in the human field. In addition, the determination of procalcitonin levels is used to evaluate the prognosis of patients with sepsis and pneumonia (Matur & et al., 2017; Akyüz & Gökce, 2021; Akyüz & et al., 2022b). Procalcitonin levels provide very important information in the grading of whether there is sepsis or if sepsis is dominant. If procalcitonin levels are between 0.2 ng/mL-2 ng/mL, it indicates that there is no sepsis, between 2-10 ng/mL, sepsis is dominant, and above 10 ng/mL, severe sepsis is present (Chivate & et al., 2016; Matur & et al., 2017). It has been stated that procalcitonin does not increase in cases of viral infections in studies conducted in the human field, and it is reported that due to this feature, it provides very important information in differentiating bacterial and viral infections. It has been reported that cytokines called IFN-γ reduce the level of procalcitonin in viral infections (Linscheid & et al., 2004). It provides valuable information about the severity of diseases according to the level of procalcitonin (Müller & et al., 2001; Matur & et al., 2017).

In recent years, biomarkers have been frequently used in the evaluation of the prognosis of diseases. One of these biomarkers is procalcitonin (Aslan & et al., 2011). In the evaluation of the prognosis of respiratory and circulatory system diseases of bacterial origin, especially in the human field (Christ-Crain & et al., 2004; Sandek & et al., 2004; Aslan & et al., 2011; Shin & et al., 2019; Akyüz & et al., 2022b), the follow-up of the condition of patients with sepsis (Schröder & et al.,

1999; Aslan & et al., 2011; Akyüz & Gökce, 2021). It has been stated that it gives better results than many biomarkers, including C-reactive protein, especially in patients with traumatic sepsis (Balcı & et al., 2009; Aslan & et al., 2011).

The Role and Importance of Procalcitonin in Veterinary Medicine

Studies on calcitonin in the veterinary field were first conducted experimentally in dogs in 1962. Later, studies on procalcitonin were carried out in rats. Procalcitonin, which is used in the follow-up of sepsis in intensive care patients in the human field, has started to be used in the veterinary field in the follow-up of the prognosis of diseases (Copp & Cheney, 1962; Matur & et al., 2017).

The neonatal period is the first 28-day period after birth, and it is the period when diseases are most common in animals and the death rate due to sepsis is the highest (Akyüz & et al., 2016; Akyüz & Gökce, 2021). Therefore, biomarkers play an important role in the follow-up of sepsis occurring in the neonatal period. One of the most important diseases seen in this period is diarrhea. Infectious (viral, bacterial and protozoan causes) and non-infectious (adverse environmental conditions, not giving colostrum after birth, not giving umbilical care, etc.) reasons play a role in the etiology of diarrhea. Sepsis, dehydration due to fluid and electrolyte loss, and metabolic acidosis are the main causes of death in diarrhea caused by the aforementioned causes (Akyüz, 2020). Akyüz & Gökce (2021), stated that procalcitonin is important for the prognosis of the disease in their study on calves with sepsis. Especially in neonatal calves, PCT level was found to be quite high in case of sepsis caused by E. coli.

Another important problem seen in cattle breeding enterprises is respiratory system diseases. Cattle are very sensitive to respiratory system diseases due to their anatomical structure. Inflammation of the lungs is called pneumonia and results in loss of productivity and death, especially in young animals. Aspiration pneumonia is frequently encountered, especially in calves, due to faulty milk drinking, etc. (Akyüz & et al., 2022b). Akyuz & et al., (2022b) stated that procalcitonin level is important in the diagnosis of the disease in their study on calves with aspiration pneumonia.

In studies conducted with experimental animals (golden hamsters), it was found that procalcitonin was produced only in the lung and thyroid gland in the healthy group; In the hamster group with sepsis, they also reported that there was procalcitonin production from many tissues such as liver, spleen, pancreas, gastrointestinal system, kidneys, skin, brain, adrenal gland, and testis, and thus the procalcitonin level increased (Müller & et al., 2001; Matur & et al., 2017). Similarly, Giunti & et al., (2010) detected the CALC-1 gene in different tissues except thyroid tissue in the study they conducted in dogs with sepsis diagnosed with parvoviral enteritis and revealed the presence of procalcitonin (Giunti & et al., 2010; Matur & et al., 2017).

In another study conducted in dogs, it was stated that procalcitonin levels in the serum were high in the patient group infected with Babesia canis (Brkjacic & et al., 2014). In a study conducted in dogs, it was reported that PCT levels were higher in dogs with various diseases compared to the healthy group (Kuzi & et al., 2008).

In studies conducted in horses, it has been reported that procalcitonin levels increase (from 28.5 ng/mL to 271 ng/mL) at the 24th hour after LPS administration (Costa & et al., 2015). In diseases such as pneumonia in horses, it has been reported that the procalcitonin level is higher in diseases where sepsis occurs compared to the healthy group (Bonelli & et al., 2015; Barton & et al., 2016). Rieger & et al., (2014) found that procalcitonin levels were between 2,593 ng/mL and 198.520

ng/mL in septic horses and 47 ng/mL in the healthy group. Similarly, in another study conducted in foals with sepsis, it was reported that procalcitonin levels were higher in the patient group compared to the control group (Pusterla & et al., 2006). It has been stated in studies that procalcitonin has an important place in the diagnosis of sepsis and that the mortality rates of patients with sepsis and PCT levels are parallel (Chivate & et al., 2016; Matur & et al., 2017).

The Importance of Trigger Receptor (sTREM-1) Expressed by Myeloid Cells in Veterinary Medicine

The biomarker called trigger receptor (TREM)-1 expressed from myeloid cells (Latour-Perez & et al., 2010) was discovered in 2000 by Bouchon et al. (Smok & et al., 2020). This biomarker is approximately 30 kDa in size and has a glycoprotein structure. It is located on the surface of monocytes, neutrophils, macrophages and endothelial cells, and its level increases by being released from the specified places, especially in acute inflammatory conditions where endotoxemia occurs (Adly & et al., 2014). TREM-1 is a member of the immunoglobulin family and acts as a cell surface receptor (Petric & et al., 2018). This marker gives the first signals of the inflammatory response through the protein called DAP12 on the cell surface and is released as a result of the binding of bacterial products to Toll-like receptors (TLR 2 and TLR 4). In this case, it also stimulates the production of cytokines and chemokines (IL 1β, TNF α, IL 8) (Zhang & et al., 2011; Smok & et al., 2020). The soluble form of this biomarker is sTREM 1 (Su & et al., 2011). sTREM 1 is present in cerebrospinal fluid, urine, bronchoalveolar fluid, pleural fluid and plasma. It is released when phagocytes are activated (Smok & et al., 2020).

Studies in patients with sepsis have reported that its level varies in the form of increase and decrease (Palmiere & Augsburger, 2014). In some studies, it has been reported that TREM 1 levels are high in patients with sepsis (Gamez-Diaz & et al., 2011; Su & et al., 2011) and that its level increases only by being released from the relevant places in case of illness (Adly & et al., 2014). It is released into body fluids and blood in diseases such as arthritis, pneumonia, meningitis, peritonitis, pleural effusion and metritis accompanied by sepsis (Su & et al., 2011; Sönmezer & Tülek, 2015). In recent years, it has been reported that sTREM-1 levels are quite high in some cases with high mortality rates (such as pneumonia and sepsis) (Latour-Perez & et al., 2010; Jin Jeong & et al., 2012).

Studies have shown that sTREM-1 levels provide important information in the evaluation of the prognosis and diagnosis of diseases and in distinguishing between non-infectious and sepsis (Wu & et al., 2012). It has been stated that sTREM-1 values are between 0-144 ng/mL in non-infectious patients and 30-428 ng/mL in patients with sepsis (Sönmezer & Tülek, 2015). sTREM -1 levels increase as a result of the damage to the tissues caused by the proteolytic enzymes released by the pathogenic agents that cause disease in living things. Therefore, it is stated that monitoring serum sTREM-1 levels will provide useful information about the prognosis of diseases (Bayram & et al., 2015).

Acute renal failure often develops in patients with sepsis. The detection of an increase in the level of sTREM-1 in the urine 2 days before the development of renal failure (Bonventre & Zuk, 2004) shows that this biomarker may be useful in the early diagnosis of sepsis. In patients with a high mortality rate. It has been stated that the level of sTREM-1 increased (Samraj & et al., 2013), and the level of sTREM-1 decreased in patients whose fire was brought under control with the treatment. Therefore, monitoring of sTREM-1 levels is very useful in evaluating the response to treatment (Gamez-Diaz & et al., 2011; Adly & et al., 2014; Su & et al., 2016).

The reason for the high levels of sTREM-1 in deceased patients is due to cellular damage (Zhang & et al., 2011). Studies have shown that sTREM-1 is more advantageous than C-reactive protein in the evaluation of sepsis (Adly & et al., 2014). In determining the severity of diseases, the level of sTREM-1 was compared with some biomarkers and it was stated that sTREM-1 is a better biomarker (Su & et al., 2016; Petric & et al., 2018). In patients with sepsis in the neonatal period, the sensitivity of sTREM-1 was found to be 100% and the specificity was 97% (Smok & et al., 2020). In a statistical study, it was reported that the specificity of sTREM-1 in bacterial infections is 95% (Zhang & et al., 2011).

In some studies, it was determined that sTREM-1 levels decreased in patients. It has been stated that the activity of sTREM-1 decreases and its levels decrease especially in digestive system infections. It has been stated that sTREM-1 shows a negative acute phase response in cases of inflammation and damage in the digestive system. The reason for this situation is that when inflammation occurs in the digestive tract, neutrophil migration occurs especially in the intestinal crypts and damage occurs in the intestinal mucosa. When neutrophils adhere to this tissue, serum sTREM-1 levels decrease (Kutlu & et al., 2021). Sezer & Gökce, (2021) found that serum sTREM-1 levels in the patient group decreased compared to the healthy group in their study on calves with diarrhea-induced sepsis in the neonatal period.

As a result, the use of PCT and sTREM-1 biomarkers in veterinary medicine in the clinical diagnosis and follow-up of diseases will provide important information. In addition to helping in the diagnosis of diseases, the evaluation of PCT and sTREM-1 in the follow-up of the patient will enable the physician to make a more accurate decision. We believe that this information will shed light on the evaluation of different biomarkers in different diseases in the future.

References

Abd Elmouttaleb, AT & Aly, HA & Bayomy, EM & Abdelhamed, MR & Esmael, NF. (2016). Plasma procalcitonin and proadrenomedullin concentrations as predictive markers for early onset neonatal sepsis. *American Journal of Biochemistry and Biotechnology*, 6 (1), 6-15.

Adly, AAM & Ismail, EA & Andrawes, NG & El-Saadany, MA. (2014). Circulating soluble triggering receptor expressed on myeloid cells-1 (sTREM-1) as diagnostic and prognostic marker in neonatal sepsis. *Cytokine*, 65, 184-191. Doi: 10.1016/j.cyto.2013.11.004

Akyüz, E & Kükürt, A & Makav, M & Gökçe, E & Eroğlu, HA & Deveci, HA & Gökce, G & Karapehlivan, M. (2022d). Evaluation of total sialic acid, paraoxonase activity and malondialdehyde in cows with subclinical paratuberculosis. *Journal of the Hellenic Veterinary Medical Society*, 73 (3), 4283-4288.

Akyüz, E & Aydın, U. (2022). Prognostic Value of haptoglobin and ceruloplasmin levels determined in cows with adhesive and non-adhesive traumatic reticuloperitonitis. *Kafkas Üniversitesi Veteriner Fakültesi Dergisi*, 28 (3), 337-344.

Akyüz, E & Coşkun, A & Şen, İ. (2016). Deneysel endotoksemi oluşturulan buzağılarda sıvı tedavisinin hemodinamik parametreler üzerine etkisi. *Eurasian Journal of Veterinary Sciences*, 32 (4), 246-254.

Akyüz, E & Gökce, G. (2021). Neopterin, procalcitonin, clinical biochemistry, and hematology in calves with neonatal sepsis. *Tropical Animal Health and Production*, 53, 354. Doi: 10.1007/s11250-021-02779-z

Akyüz, E & Sezer, M & Gökce, G. (2022a). Some İmportant Biomarkers and Clinical Significance. Hülya Çiçek, Zeliha Selamoğlu, Hasan Akgül (Eds.), Gece Kitaplığı-Current Research in Health Sciences, İçinde (s. 15-30). Ankara: Gece Kitaplığı.

Akyüz, E & Makav, M & Kuru, M & Bayram, P. (2021). The effect of Tarantula cubensis extract on gentamicin-induced acute kidney injury in ovariectomized rats. *Kafkas Üniversitesi Veteriner Fakültesi Dergisi*, 27 (5), 559-566.

Akyüz, E & Merhan, O & Aydın, U & Sezer, M & Kuru, M & Karakurt, E & Yıldız, U & Bozukluhan, K & Batı, YU & Yıldız, A & Gökce, G. (2022b). Neopterin, procalcitonin, total sialic acid, paraoxonase-1 and selected haematological indices in calves with aspiration pneumonia. *Acta Veterinaria Brno*, 91, 115-124.

Akyüz, E & Sezer, M & Kuru, M & Naseri, A. (2022d). Changes in hematology, some clinical biochemical parameters and mineral levels in neonatal calves with sepsis due to diarrhea. *Van Veterinary Journal*, 33 (1), 26-30.

Akyüz, E. (2020). Kars Bölgesindeki Neonatal Buzağılarda Sıklıkla Karşılaşılan İshal Kaynaklı Sepsis Nedenleri. Pınar Ayvazoğlu Demir (Ed.), Tüm Yönleri İle Kuzey Doğu Anadolu Bölgesinde Hayvancılık, İçinde (s. 401-423). Ankara: Iksad Publications.

Akyüz, E & Naseri, A & Erkılıç, EE & Makav, M & Uzlu, E & Kırmızıgül, AH & Gökce, G. (2017). Neonatal buzağı ishalleri ve sepsis. *Kafkas Üniversitesi Fen Bilimleri Enstitüsü Dergisi*, 10 (2), 181-191.

Aouifi, A & Piriou, V & Blanc, P & Bouvier, H & Bastien, E & Chiari, P & Rousson, P & Evans, R & Lehotet, JJ. (1999). Effect of cardiopulmonary bypass on serum procalcitonin and C-reactive protein concentrations. *British Journal of Anaesthesia*, 83 (4), 602-607. Doi: 10.1093/bja/83.4.602

Aslan, A & Demir, M & Atay, A & Köseoğlu, MH & Kaya, M. (2011). Correlation between the levels of procalcitonin and C-reactive protein. *Türk Klinik Biyokimya Dergisi,* 2, 61-66.

Balci, C & Sivaci, R & Akbulut, G & Karabekir, HS. (2009). Procalcitonin levels as an early marker in patients with multiple trauma under intensive care. *International Journal of Medical Research*, 37 (6), 1709-1717. Doi: 10.1177/147323000903700606

Barton, AK & Pelli, A & Rieger, M & Gehlen, H. (2016). Procalcitonin as a biomarker in equine chronic pneumopathies. *BMC Veterinary Research*, 12 (685), 5-7. Doi: 10.1186/s12917-016-0912-4

Bayram, H & Tünger, Ö & Çivi, M & Yüceyar, MH & Ulman, C & Horasan, GD & Çetin, ÇB. (2015). Diagnostic and prognostic value of procalcitonin and sTREM-1 levels in sepsis. *Turkish Journal of Medical Sciences*, 45, 578-586.

Bonelli, F & Meucci, V & Divers, TJ & Jose-Cunilleras, E & Corazza, M & Tognetti, R & Guidi, G & Intorre, L & Sgorbini, M. (2015). Plasma procalcitonin concentration in healthy horses and horses affected by systemic inflammatory response syndrome. *Journal of Veterinary İnternal Medicine*, 29 (6), 1689-1691. Doi: 10.1111/jvim.13640

Bonventre, JV & Zuk, A. (2004). Ischemic acute renal failure: an inflammatory disease? *Kidney International*, 66 480-485. Doi: 10.1111/j.1523-1755.2004.761_2.x

Bracq, S & Machason, M. (1993). Calcitonin gene expression in normal hu8man liver. *The European Journal of Biochemistry*, 331, 14-18. Doi: 10.1016/0014-5793(93)80288-6

Brkljacic, M & Torti, M & Pleadin, J & Mrljak, V & Smit, I & Kis, I & Mayer, I & Crnogaj, M & Matijatko, V. (2014). The concentrations of inflammatory markers the amino-terminal portion of C-type pronatriuretic peptide and procalcitonin in canine babesiosis caused by babesia canis. *Veterinarski Arhiv*, 44 (6), 575-589.

Carrol, ED & Thomson, APJ & Hart, CA. (2002). Procalcitonin as a marker of sepsis. *International Journal of Antimicrobial Agents*, 20 (1), 1-9. Doi: 10.1016/s0924-8579(02)00047-x

Chivate, CG & Belwalkar, GJ & Limaye, RP & Patil, RV. (2016). Procalcitonin as a marker for the diagnosis of sepsis. *International Journal of Research in Medical Sciences*, 4 (4), 1216-1218.

Christ-Crain, M & Jaccard-Stolz, D & Bingisser, R & Gencay, MM & Huber, PR & Tamm, M. (2004). Effect of procalcitoninguided treatment on antibiotic use and outcome in lower respiratory tract infections: Cluster-randomised, Single-blinded İntervention Trial. *Lancet*, 363 (9409), 600-607. Doi: 10.1016/S0140-6736(04)15591-8

Christ-Crain, M & Muller, B. (2007). Biomarkers in respiratory tract infections: Diagnostic guides to antibiotic prescription prognostic markers and mediators. *European Respiratory Journal*, 30 (3), 556-573. Doi: 10.1183/09031936.00166106

Copp, DH & Cheney, B. (1962). Calcitonin-a hormone from the parathyroid which lowers the calcium-level of the blood. *Nature*, 193, 381-382. Doi: 10.1038/193381a0

Costa, MC & Silva, G & Ramos, LV & Staempfli, HR & Arroyo, LG & Kim, P & Weese, JS. (2015). Characterization and comparison of the bacterial microbiota in different gastrointestinal tract compartments in horses. *Veterinary Journal*, 245 (1), 74-80. Doi: 10.1016/j.tvjl.2015.03.018

Erkılıç, EE & Merhan, O & Kırmızıgül, AH & Öğün, M & Akyüz, E & Çitil, M. (2019). Salivary and Serum Levels of Serum Amyloid A, Haptoglobin, Ceruloplasmin and Albumin in Neonatal Calves with Diarrhoea. *Kafkas Universitesi Veteriner Fakultesi Dergisi*, 25, 4, 583-586.

Gamez-Diaz, LY & Enriquez, LE & Matute, JD &Velásquez, S & Iván, DG & Toro, F & Ospina, S & Bedoya, V & Arango, CM & Valencia, ML & De La Rosa, G & Gómez, CI & García, A & Patiño, PJ & Jaimes, FA. (2011). Diagnostic accuracy of HMGB-1, s-TREM-1, and CD64 as markers of sepsis in patients recently admitted to the emergency department. *Academic Emergency Medicine*, 18, 807-815. Doi: 10.1111/j.1553-2712.2011.01113.x

Giunti, M & Peli, A & Battilani, M & Zacchini, S & Militerno, G & Otto, CM. (2010). Evaluation of CALC-I gene (CALCA) expression in tissues of dogs with signs of the systemic inflammatory response syndrome. *Journal of Veterinary Emergency and Critical Care*, 24 (5), 523-527. Doi: 10.1111/j.1476-4431.2010.00575.x

Günal, Ö & Ulutan, F & Erkorkmaz, Ü. (2011). Sepsisli hastalarda prokalsitoninin prognostik değeri. *Klimik Dergisi*, 24 (1), 31-35.

Jin, M & Khan, AI. (2010). Procalcitonin: uses in the clinical laboratory for the diagnosis of sepsis. *Laboratory Medicine*, 41 (3), 173-177.

Jin Jeong, S & Goo Song, Y & Oh, KC & Won, KH & Su, KN & Han, SH & Choi, JY & Kim, JM. (2012). Measurement of plasma strem-1 in patients with severe sepsis receiving early goal-directed therapy and evaluation of its usefulness. *Shock*, 37 (6), 574-578. Doi: 10.1097/SHK.0b013e318250da40

Kutlu, Y & Toprak, İD & Gokden, Y & Eruzun, H & Arman, Y & Yoldemir, ŞA &Toprak, Z & Tukek, T. (2021). The relationship between sTREM-1 and activation of inflammatory bowel diseases. *Journal of Istanbul Faculty of Medicine*, 84, 318-323.

Kuzi, S & Aroch, I & Peleg, K & Karnieli, O & Klement, E & Dank, Gillian. (2008). Canine procalcitonin messenger RNA expression. *Journal of Veterinary Diagnostic Investigation*, 20 (5), 629-33. Doi: 10.1177/104063870802000516

Latour-Pérez, J & Alcalá-López, A & García-García, MÁ & Sánchez-Hernández, JF & Abad-Terrado, C & Viedma-Contreras, JA & Masiá, M & González-Tejera, M & Arizo-León, D & Broch Porcar, MJ & Bonilla-Rovira, F & Gutiérrez, F. (2010). Diagnostic accuracy of sTREM-1 to identify infection in critically ill patients with systemic inflammatory response syndrome. *Clinical Biochemistry*, 43, 720-724. Doi: 10.1016/j.clinbiochem.2010.03.001

Linscheid, P & Seboek, D & Schaer, DJ & Zulewski, H & Keller, U & Müller B. (2004). Expression and secretion of procalcitonin and calcitonin gene-related peptide by adherent monocytes and by macrophage-activated adipocytes. *Critical Care Medicine*, 32 (8), 1715-1721. Doi: 10.1097/01.ccm.0000134404.63292.71

Matur, E & Eraslan, E & Çötelioğlu, Ü. (2017). Biology of procalcitonin and its potential role in veterinary medicine. *Journal of Istanbul Veterinary Sciences*, 2 (1), 16-27.

Meisner, M & Schmidt, J & Hüttner, H & Tschaikowsky, K. (2000). The natural elimination rate of procalcitonin in patients with normal and impaired renal function. *Intensive Care Medicine*. 26 (2), 212-216. Doi: 10.1007/BF02900740

Miguel, D & Prieto, B & Costa, M & Coto, D & Alvarez, FV. (2011). Cord blood plasma reference intervals for potential sepsis markers: Pro-adrenomedullin, pro-endothelin, and pro-atrial natriuretic peptide. *Clinical Biochemistry*, 44, 337-341. Doi: 10.1016/j.clinbiochem.2010.12.012

Mitaka, C. (2005). Clinical laboratory differentiation of infectious versus non-infectious systemic inflammatory response syndrome. *Clinica Chimica Acta*, 351 (1-2), 17-29. Doi: 10.1016/j.cccn.2004.08.018

Morgenthaler, NG & Struck, J & Chancerelle, Y & Weglöhner, W & Agay, D & Bohuon, C & Suarez-Domenech, V & Bergmann, A & Müller B. (2003). Production of procalcitonin (PCT) in non-thyroidal tissue after LPS injection. *Hormone and Metabolic Research*, 35 (05), 290-295. Doi: 10.1055/s-2003-41304

Muller, B & White, JC & Nylen, ES & Snider, RH & Becker, KL & Habener, JF. (2001). Ubiquitous expression of the Calcitonin-I gene in multiple tissues in response to sepsis. *Journal of Clinical Endocrinology and Metabolism*, 86 (1), 396-404. Doi: 10.1210/jcem.86.1.7089

Nakamura, M & Kono, R & Nomura, S & Utsunomiya, H. (2013). Procalcitonin: mysterious protein in sepsis. *Journal of Clinical Medicine*, 2 (1), 7-11.

Nijsten, MW & Olinga, P & Vries, EG & Koops, HS & Groothuis, GM & Limburg, PC & ten Duis H J & Moshage H & Hoekstra HJ & Bijzet & Zwaveling JH. (2000). Procalcitonin behaves as a fast responding acute phase proteinin vivoandin vitro. *Critical Care Medicine*. 28 (2), 458-461. Doi: 10.1097/00003246-200002000-00028

Oberhoffer, M & Stonans, I & Russwurm, S & Stonane, E & Vogelsang, H & Junker, U & Jäger, L & Reinhart, K. (1999). Procalcitonin expression in human peripheral blood mononuclear cells and its modulation by lipopolysaccharides and sepsis-related cytokines in vitro. *The Journal of Laboratory and Clinical Medicine*, 134 (1), 49-55. Doi: 10.1016/s0022-2143(99)90053-7

Palmiere, C & Augsburger, M. (2014). Markers for sepsis diagnosis in the forensic setting: State of the art. *Croatian Medical Journal*, 55, 103-114. Doi: 10.3325/cmj.2014.55.103

Petric, V & Brkic, S & Lendak, D & Mihajlovic, D & Mikic, AN & Komazec, SL. (2018). The significance of sTREM-1 as a diagnostic biomarker of sepsis in the context of Sepsis-3 definition. *Signa Vitae*, 14 (1), 65-70.

Pusterla, N & Magdesian, KG & Mapes, S & Leutenegger, CM. (2006). Expression of molecular markers in blood of neonatal foals with sepsis, *American Journal of Veterinary Research*, 67 (6), 1045-1049. Doi: 10.2460/ajvr.67.6.1045

Rieger, M & Kochleus, C & Teschner, D & Rascher, D & Barton, AK & Geerlof, A & Kremmer, E & Schmid, M & Hartmann, A & Gehlen, H. (2014). A new ELISA for the

quantification of equine procalcitonin in plasma as potential inflammation biomarker in horses. *Analytical and Bioanalytical Chemistry*, 406 (22), 5507-5512. Doi: 10.1007/s00216-014-7944-z

Samraj, RS & Zingarelli, B & Wong, HR. (2013). Role of biomarkers in sepsis care. *Shock*, 40: 358-365. Doi: 10.1097/SHK.0b013e3182a66bd6

Sandek, A & Springer, J & Habedank, D & Brunkhorst, F & Anker, SD. (2004). Procalcitonin-guided antibiotic treatment in heart failure, *Lancet*, 363 (9420), 1555. Doi: 10.1016/S0140-6736(04)16165-5

Schröder, J & Staubach, KH & Zabel, P & Stüber, F & Kremer, B. (1998). Procalcitonin as a marker of severity in septic shock. *Langenbeck's Archives of Surgery*, 384 (1), 33-38. Doi: 10.1007/s004230050170

Sezer, M & Gökce, G. (2021). Sepsis Şüpheli Buzağılarda sTREM-1, MR-Pro Adrenomedullin, Klinik Biyokimya ve Hematoloji Üzerine Araştırmalar. *Kafkas Üniversitesi Sağlık Bilimleri Enstitüsü*, Doktora Tezi, İç Hastalıkları Anabilim Dalı, Kars.

Shin, H & Kim, JG & Kim, W & Lim, TH & Jang, BH & Cho, Y & Choi, KS & Ahn, C & Lee, J & Na, MK. (2019). Procalcitonin as a prognostic marker for outcomes in post-cardiac arrest patients: A systematic review and meta-analysis. *Resuscitation*, 138: 160-167. Doi: 10.1016/j.resüsitasyon.2019.02.041

Smok, B & Domagalski, K & Pawłowska, M. (2020). Diagnostic and prognostic value of IL-6 and sTREM-1 in SIRS and sepsis in children. *Mediators of Inflammation*, 8201585. Doi: 10.1155/2020/8201585

Sönmezer, MÇ &Tülek, N. (2015). Bakteriyel infeksiyonlarda ve sepsiste biyobelirteçler. *Klimik Dergisi*, 28(3), 96-102.

Su, L & Feng, L & Zhang, J & Xiao, Y & Jia, Y & Yan, P & Feng, D & Xie, L. (2011). Diagnostic value of urine sTREM-1 for sepsis and relevant acute kidney injuries: A prospective study. *Critical Care*, 15, 2-10. Doi: 10.1186/cc10508

Su, L & Liu, D & Chai, W & Liu, D & Long, Y. (2016). Role of sTREM-1 in predicting mortality of infection: a systematic review and meta-analysis. *British Medical Journal*, 6 (5), e010314. Doi: 10.1136/bmjopen-2015-010314

Valenzuela-Sánchez, F & Valenzuela-Méndez, B & Rodríguez-Gutiérrez, JF & Estella-García, Á & González-García, MÁ. (2016). New role of biomarkers: Mid-regional pro-adrenomedullin, the biomarker of organ failure. *Annals of Translational Medicine*, 4 (17), 329. Doi: 10.21037/atm.2016.08.65

Wu, Y & Wang, F & Fan, X & Bao, R & Bo, L & Li, J & Deng, X. (2012). Accuracy of plasma sTREM-1 for sepsis diagnosis in systemic inflammatory patients: a systematic review and meta-analysis. *Critical Care*, 16: R229. Doi: 10.1186/cc11884

Zhang, J & She, D & Feng, D & Jia, Y & Xie, L. (2011). Dynamic changes of serum soluble triggering receptor expressed on myeloid cells-1 (sTREM-1) reflect sepsis severity and can predict prognosis: a prospective study. *BMC İnfectious Diseases*, 11, 53. Doi: 10.1186/1471-2334-11-53

Comparison of Equivalent, Similar Matrices and Regular Matrices

Hasan KELEŞ[1]

Introduction

This section is on the similarity and equivalence of two matrices. Similar matrices associated with the bases of spaces do the same job. Comparisons of new lemma, theorem and properties were made over the definitions of equivalence and similarity, which are related to the multipliers of the martris. In addition, the connection between equivalence and similarity was expressed. Any regular matrix is divisible by integer and remainder. This property of regular matrices is evaluated by similarity. New results are obtained.

Let $\mathbb{F}$ be a field and $M_n(\mathbb{F}) = \left\{ \left[a_{ij} \right]_n \Big| a_{ij} \in \mathbb{F}, n \in \mathbb{Z}^+ \right\}$. Suppose $A, B, C \in M_n(\mathbb{F})$. Then

    i. A is similar to A. (Reflexive)
    ii.   If A is similar to B, then B is similar to A. (Symmetric)
    iii.   If A is similar to B and B is similar to C, then A is similar to C. (Transitive)
    iv.   If A is regular matrix, for $i \in \mathbb{Z}^+$, $\exists A_i, B_i, C_i \in M_n(\mathbb{F}) : A = A_i B_i = A_i C_i$, where $B_i \neq C_i$. (Escort)

Similarity is an Equivalence Relation. The fact that similarity is an equivalence relation is not emphasized here. Briefly, in this study, the necessary and sufficient conditions of similarity are investigated. Obtained property, lemma and theorems are given. An infinite similar matrix is written to any matrix. The situation same is true for equivalent matrices in [1].

In this section $M_n(\mathbb{F})$ is taken as the set of regular matrices. $\mathbb{F} = \mathbb{R}$ is taken when giving samples. Operations are performed on the $\mathbb{R}$ number field.

Is there a matrix $\exists A, B \in M_n(\mathbb{F})$ for $\forall F \in M_n(\mathbb{F})$ such that, $AB = F$? Also, are these A, B matrices unique? This question is a topic worth researching for many years.

If $B \big| F$ then $\exists A \in M_n(\mathbb{F})$ such that,

$$BA = F, \ F = BA.$$

Except for special cases in matrix multiplication, $AB \neq BA$.

---

[1] Lecturer, Karadeniz Technical University

The following definition is given, which is defined by interchanging the columns and rows of two regular matrices. More detailed information has been given in many studies on rational matrices. Only some contributions of rational matrices to equivalence and similarity are discussed here. The algorithms used in the solution of some linear equations are related to similar and equivalent matrices. This situation is provided the new theorems, lemma, and properties to the literature. Preliminary studies of the situation concerning the department are given in previous related articles and references. The study is carried out with the summary part of these studies.

Definition 1.1. Let $\mathbb{F}$ be a field and $M_n(\mathbb{F}) = \left\{ \left[a_{ij} \right]_n \middle| a_{ij} \in \mathbb{F}, n \in \mathbb{Z}^+ \right\}$. A rational matrix is defined by

$$- : M_n(\mathbb{F}) \times M_n(\mathbb{F}) \to M_n(\mathbb{F})$$

$$(B, F) \to \frac{F}{B} := \left[\frac{\left({}_B^F i_j \right)_{ji}}{|B|} \right]_{n \times n}.$$

i.   The $\left[\left({}_B^F i_j \right)_{ji} \right]_n$ matrix obtained here is the *column co-divisor matrix* of the F matrix on the B matrix.

The $\left[\left({}_B^F i_j \right)_{ji} \right]_n$ matrix is the determinant of the matrix obtained by writing the ith column of the F matrix into the jth column of the B matrix in [2].

ii.   The determinant of the new matrix obtained by writing on the jth row of the matrix B the ith row of the matrix A is called the *co-divisor by row* of the matrix A by the row on the matrix B. It is denoted by $\underset{ij}{AB}$. Their number is n^2. The matrix co-divisor by row is

$$\left[\left(\underset{ij}{AB} \right)_{ij} \right] \text{ in [3].}$$

The followings theorem and lemma are given without proof.

Theorem 1.2.([3]). Let $\frac{A}{B} \in \mathbb{Q}(M_n)$. Then, for least the regular matrix $A_1 \in M_n(\mathbb{F})$ exists such that $A = A_1 A_2$ and $B = A_1 B_2$ it satisfies equation,

$$\frac{A}{B} = \frac{A_1 A_2}{A_1 B_2} = \frac{A_2}{B_2}, \text{ where } A_2, B_2 \in M_n(\mathbb{F}) \text{ are regular.}$$

Lemma 1.3. Let $A, B \in M_n(\mathbb{F})$ two regular matrices. Then

$$\left(\frac{A}{B} \right)^{-1} = \left(\frac{B^T}{A^T} \right)^{-1}.$$

Equivalent and Similar Matrices

In this section, some properties between similar, equivalent, transposed and inverse matrices are given.

Definition 2.1. Two families $(A_i)_{i \in I}$ and $(B_i)_{i \in I}$ of matrices of $M_n(\mathbb{F})$ indexed over the same set I are said to be simultaneously similar when there exists $P \in GL_n(\mathbb{F})$ such that

$$\forall i \in I, \ PA_iP^{-1} = B_i$$

(such a matrix P will then be called a base change matrix with respect to the two families) in [4]. B_i similiar to A_i denoted as by $B_i \approx A_i$.

Two families $(A_i)_{i \in I}$ and $(B_i)_{i \in I}$ of matrices of $M_{n,p}(\mathbb{F})$ indexed over the same set I are said to be simultaneously equivalent when there exists a pair $(P,Q) \in GL_n(\mathbb{F}) \times GL_n(\mathbb{F})$ such that

$$\forall i \in I, \ PA_iQ = B_i \quad \text{in [4]}.$$

B_i equivalen to A_i denoted as by $B_i \sim A_i$.

Lemma 2.2. Let $A_i, B_i \in M_n(\mathbb{F})$ be any two regular matrices. Then

$$B_i \approx A_i \Leftrightarrow B_i \sim A_i.$$

Proof. Let $A_i, B_i \in M_n(\mathbb{F})$ be two regular matrices. If $B_i \approx A_i$ then,

$$\exists P \in M_n(\mathbb{F}): B_i = PA_iP^{-1}$$

If $Q := P^{-1}$ then,

$$\exists P,Q \in M_n(\mathbb{F}): B_i = PA_iQ \Rightarrow B_i \sim A_i.$$

Lemma 2.3. Let $A_i, B_i \in M_n(\mathbb{F})$ be any two regular matrices with $B_i \approx A_i$. Then $\exists P^{-1} := \dfrac{B_i}{A_i}$,

$$\dfrac{P^{-1}}{A_i} = C_i \in M_n(\mathbb{F}):$$

$$B_i \approx C_i.$$

Proof. Let $A_i, B_i \in M_n(\mathbb{F})$ be two regular matrices. Then

$$A_i \big| B_i \overset{\exists P \in M_n(\mathbb{F})}{\Leftrightarrow} B_i = A_iP$$

$$P^{-1} \big| A_i \overset{\exists C_i \in M_n(\mathbb{F})}{\Leftrightarrow} A_i = P^{-1}C_i$$

$$B_i = A_iP = P^{-1}C_iP$$

$$\Leftrightarrow B_i \approx C_i.$$

Property . If $B \approx A \Leftrightarrow B = PAP^{-1}$

i. $\quad A_1 = \dfrac{B}{A}, A_2 = \dfrac{A_1}{A} \Leftrightarrow B = A_1^{-1}A_2A_1 \Leftrightarrow B \approx A_2$.

ii. $\left(\dfrac{\dfrac{B}{A}A}{B}\right)^{T} = \dfrac{\left(\dfrac{B}{A}\right)^{T}B^{T}}{A^{T}}$.

Example 2.4. $B = \begin{bmatrix} 1 & 2 \\ 3 & 4 \end{bmatrix}, A = \begin{bmatrix} 1 & -1 \\ 2 & 1 \end{bmatrix}$

$$A\big|B \Leftrightarrow B = \begin{bmatrix} 1 & 2 \\ 3 & 4 \end{bmatrix} = \underbrace{\begin{bmatrix} 1 & -1 \\ 2 & 1 \end{bmatrix}}_{A}\underbrace{\begin{bmatrix} 0 & 3 \\ \frac{1}{2} & -2 \end{bmatrix}}_{P^{-1}} = AP^{-1}$$

$$P^{-1} = \begin{bmatrix} 0 & 3 \\ \frac{1}{2} & -2 \end{bmatrix} \Rightarrow P = \begin{bmatrix} \frac{4}{3} & 2 \\ \frac{1}{2} & 0 \end{bmatrix}$$

$$P\big|A \Leftrightarrow A = PC_{i} = \begin{bmatrix} 0 & 3 \\ \frac{1}{2} & -2 \end{bmatrix}\begin{bmatrix} \frac{16}{3} & \frac{2}{3} \\ \frac{1}{3} & -\frac{1}{3} \end{bmatrix} = \begin{bmatrix} 1 & -1 \\ 2 & 1 \end{bmatrix}$$

$$B = \begin{bmatrix} 0 & 3 \\ \frac{1}{2} & -2 \end{bmatrix}\begin{bmatrix} \frac{16}{3} & \frac{2}{3} \\ \frac{1}{3} & -\frac{1}{3} \end{bmatrix}\begin{bmatrix} \frac{4}{3} & 2 \\ \frac{1}{2} & 0 \end{bmatrix} = PC_{i}P^{-1} = \begin{bmatrix} 1 & 2 \\ 3 & 4 \end{bmatrix}$$

$$\Leftrightarrow B_{i} \approx C_{i}\,.$$

$$A\big|C_{i} \Leftrightarrow C_{i} = AD_{i} = \begin{bmatrix} 1 & -1 \\ 2 & 1 \end{bmatrix}\begin{bmatrix} \frac{17}{9} & \frac{1}{9} \\ -\frac{31}{6} & -\frac{5}{6} \end{bmatrix} = \begin{bmatrix} \frac{16}{3} & \frac{2}{3} \\ \frac{1}{3} & -\frac{1}{3} \end{bmatrix}$$

$$B = PC_{i}P^{-1} = PAD_{i}P^{-1}$$

If $Q := D_{i}P^{-1}$ then,

$$\begin{bmatrix} 0 & 3 \\ \frac{1}{2} & -2 \end{bmatrix}\begin{bmatrix} \frac{16}{3} & \frac{2}{3} \\ \frac{1}{3} & -\frac{1}{3} \end{bmatrix}\begin{bmatrix} \frac{4}{3} & 2 \\ \frac{1}{2} & 0 \end{bmatrix} =$$

$$= \underbrace{\begin{bmatrix} 0 & 3 \\ \frac{1}{2} & -2 \end{bmatrix}}_{P}\underbrace{\begin{bmatrix} 1 & -1 \\ 2 & 1 \end{bmatrix}\begin{bmatrix} \frac{17}{9} & \frac{1}{9} \\ -\frac{31}{6} & -\frac{5}{6} \end{bmatrix}\begin{bmatrix} \frac{4}{3} & 2 \\ \frac{1}{2} & 0 \end{bmatrix}}_{Q} = \begin{bmatrix} 1 & 2 \\ 3 & 4 \end{bmatrix}$$

$$\Rightarrow PAQ = B \Rightarrow B \sim A.$$

The following Lemma 2.5 is given which is easy to prove.

Lemma 2.5. If $A, B \in M_n(\mathbb{F})$ are any two regular matrices, then

   i. $B = AC,\ A = BC^{-1}$, where $C \in M_n(\mathbb{F})$.

   ii. $A = KS + R,$ where $K, S, R \in M_n(\mathbb{F})$.

   iii. $\left(\dfrac{B}{A} \right)^T = \dfrac{\left(A^T \right)^{-1}}{\left(B^T \right)^{-1}}.$

   iv. $\dfrac{B}{A} = \left(\dfrac{\left(A^T \right)^{-1}}{\left(B^T \right)^{-1}} \right)^T.$

   v. $\dfrac{A}{B} = \left(\dfrac{B^T}{A^T} \right)^{-1}.$

Two regular matrices produce the similar matrix is given. The following theorem is given that a regular matrix is similar to the sum of two different matrices.

Theorem 2.6. Let $A_i, B_i \in M_n(\mathbb{F})$ be any two regular matrices. There are exists $M_i, C_i, N_i, D_i \in M_n(\mathbb{F})$ that $M_i \approx C_i, N_i \approx D_i$. Then

$$B_i \approx M_i + N_i.$$

Proof. Let $A_i, B_i \in M_n(\mathbb{F})$ any two regular matrices.
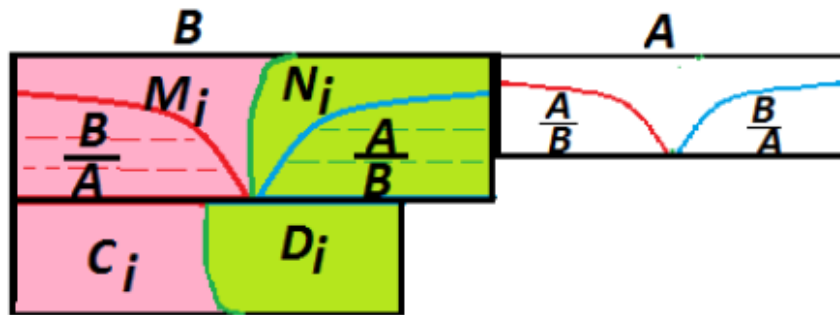
Figure 1. Factors and Similar Spaces

$$P = \frac{B}{A_i}, A_i = KS + R, \exists K, S, R \in M_n(\mathbb{F})$$

$$B_i = (KS + R)P = KSP + RP$$

$$K = P^{-1}K_i, R = P^{-1}D_i$$

$$B_i = KSP + RP = P^{-1}K_i SP + P^{-1}D_i P$$

$$M_i = M\,P^{-1}\underbrace{K_i\,SP}_{C_i} \Leftrightarrow M_i \approx C_i$$

$$N_i = P^{-1}D_iP \Leftrightarrow N_i \approx D_i.$$

$$B_i = M_i + N_i\,.$$

Example 2.7. Let $B = \begin{bmatrix} 1 & 2 \\ 3 & 4 \end{bmatrix}, A = \begin{bmatrix} 1 & -1 \\ 2 & 1 \end{bmatrix}$ be two regular matrices.

$$A = \begin{bmatrix} 2 & 1 \\ 5 & 3 \end{bmatrix}\begin{bmatrix} 3 & -1 \\ 2 & 1 \end{bmatrix} + \begin{bmatrix} -7 & 0 \\ -19 & 3 \end{bmatrix} = \begin{bmatrix} 1 & -1 \\ 2 & 1 \end{bmatrix}$$

$$P = \frac{B}{A} = \begin{bmatrix} \dfrac{4}{3} & 2 \\ \dfrac{1}{2} & 0 \end{bmatrix}$$

$$B = \left(\begin{bmatrix} 2 & 1 \\ 5 & 3 \end{bmatrix}\begin{bmatrix} 3 & -1 \\ 2 & 1 \end{bmatrix} + \begin{bmatrix} -7 & 0 \\ -19 & 3 \end{bmatrix}\right)\begin{bmatrix} \dfrac{4}{3} & 2 \\ \dfrac{1}{2} & 0 \end{bmatrix}$$

$$B = \begin{bmatrix} 2 & 1 \\ 5 & 3 \end{bmatrix}\begin{bmatrix} 3 & -1 \\ 2 & 1 \end{bmatrix}\begin{bmatrix} \dfrac{4}{3} & 2 \\ \dfrac{1}{2} & 0 \end{bmatrix} + \begin{bmatrix} -7 & 0 \\ -19 & 3 \end{bmatrix}\begin{bmatrix} \dfrac{4}{3} & 2 \\ \dfrac{1}{2} & 0 \end{bmatrix}$$

$$= \begin{bmatrix} 0 & 3 \\ \dfrac{1}{2} & -2 \end{bmatrix}\underbrace{\begin{bmatrix} \dfrac{38}{3} & \dfrac{22}{3} \\ \dfrac{2}{3} & \dfrac{1}{3} \end{bmatrix}\begin{bmatrix} 3 & -1 \\ 2 & 1 \end{bmatrix}\begin{bmatrix} \dfrac{4}{3} & 2 \\ \dfrac{1}{2} & 0 \end{bmatrix}}_{C_i} + \begin{bmatrix} 0 & 3 \\ \dfrac{1}{2} & -2 \end{bmatrix}\underbrace{\begin{bmatrix} -\dfrac{142}{3} & 6 \\ -\dfrac{7}{3} & 0 \end{bmatrix}\begin{bmatrix} \dfrac{4}{3} & 2 \\ \dfrac{1}{2} & 0 \end{bmatrix}}_{D_i}$$

$$\begin{bmatrix} 2 & 1 \\ 5 & 3 \end{bmatrix}\begin{bmatrix} 3 & -1 \\ 2 & 1 \end{bmatrix}\begin{bmatrix} \dfrac{4}{3} & 2 \\ \dfrac{1}{2} & 0 \end{bmatrix} = \begin{bmatrix} \dfrac{31}{3} & 16 \\ \dfrac{82}{3} & 42 \end{bmatrix} = M_i$$

$$\begin{bmatrix} -7 & 0 \\ -19 & 3 \end{bmatrix}\begin{bmatrix} \dfrac{4}{3} & 2 \\ \dfrac{1}{2} & 0 \end{bmatrix} = \begin{bmatrix} -\dfrac{28}{3} & -14 \\ -\dfrac{73}{3} & -38 \end{bmatrix} = N_i$$

$$M_i \approx C_i, N_i \approx D_i$$

$$B = M_i + N_i\,.$$

Theorem 2.8. If $A, B \in M_n(\mathbb{F})$ any two regular matrices, then

$$B = PAQ \Leftrightarrow P = \frac{B}{A}, Q = \left(\frac{A^2}{BA}\right)\frac{B}{A}.$$

Proof. Let $A, B \in M_n(\mathbb{F})$ be any two regular matrices.

$\Leftarrow$ If $P = \dfrac{B}{A}, Q = \left(\dfrac{A^2}{BA}\right)\dfrac{B}{A}$, then

$$PAQ = \left(\dfrac{B}{A}\right)A\left(\dfrac{A^2}{BA}\right)\dfrac{B}{A} = B.$$

$$\Rightarrow: B = PAQ = \underbrace{\left(\dfrac{B}{A}\right)}_{P}A\underbrace{\left(\left(\dfrac{A^2}{BA}\right)\dfrac{B}{A}\right)}_{Q} \Rightarrow P := \dfrac{B}{A}, Q = \left(\dfrac{A^2}{BA}\right)\dfrac{B}{A}.$$

Discussions.

Column co-dividers are used in the study. Similar operations are performed for row co-dividers. In this case, the existence of different situations apart from the same features is left as a discussion.

REFERENCES

Serre, D. (2002) *Matrices:Theory and Applications*, New York: Springer-Verlag,.

Keleş, H. (2022). *On Results Divisibility and Multipliers of Regular Matrices of Order nth ,* 4th International CEO Communication, Economics, Organization & Social Sciences Congress.

Keleş, H. (2022). *On Some Results Row Co-Division in Regular Square Matrices,* 4. International Palandöken scientific studies congress, Erzurum.

Pazzis de S. C. (2010). Invariance of simultaneous similarity and equivalence of matrices under extension of the ground field, Linear Algebra and its Applications , 433, 618–624.

Bapat, R. B. (1998). Graphs and Matrices, New York: Springer, American Mathematical Society,

Volume 126, (4), Pages 1005-1015, S 0002-9939(98)04368-8.

Keleş, H. (2022). Poloids and Matrices, The Aligarh Bulletin of Mathematics, Volume 41, (1) , p. 41-52.

Pandemics

Cihat Furkan Göv
Hülya Çelik[1]

1. INTRODUCTION

The emergence and spread of infectious diseases with pandemic potential has occurred regularly throughout history. Many infectious diseases that lead to pandemics are caused by zoonotic pathogens transmitted to humans due to increased contacts with animals through breeding, hunting and global trade activities. Understanding the mechanisms of transmission of pathogens to humans allowed the creation of methods of preventing and controlling infections. For centuries, the implementation of public health measures such as isolation, quarantine and border control have helped control the spread of infectious diseases and maintain the community structure. Global friction programs of waterborne pathogens, vector-borne diseases and zoonotic spreads in the animal-human interface are of primary importance for rapidly detecting the emergence of infectious threats. In the event of a pandemic, new technologies are needed for rapid diagnostic tests, contact monitoring, reuse of drugs, biological markers of disease severity, and new platforms for the development and production of vaccines. In this research project, we review the major pandemics that have affected humanity throughout history, such as plague, cholera, influenza and coronavirus diseases, how they were contained in the past and how these diseases are managed today.

Virüs

The virus is a small agent that causes infection with only one of the deoxyribo nucleic acid or ribonucleic acids packaged in the protective sheath, which consists of a protein or complex structure. Viruses are not considered alive because they need host cells to grow and multiply. Since viruses do not independently have proliferation mechanisms and molecules, they depend on host cells for reproduction and are considered parasitic cells. Viruses often have a limited host range that they can infect, and viruses can only infect certain bacteria, plants or animals. Viruses depend on the metabolic molecules of the host cell. Viruses alter the host's normal metabolic reactions, allowing new virus particles to form. In order for viruses to survive, they must infect a cell and synthesize their own viral proteins and genetic material by capturing the mechanisms of the cell (Takz,2019).

Ways Viruses Are Transmitted

-Direct contact

-Injection of blood or contaminated liquids

-Tissue transplants

---

[1] Ağrı Ibrahim Cecen University, Faculty of Pharmacy Basıc Pharmaceutıcal Scıences Department / Fundamental Scıences of Pharmacy1,2 03200 Agri/TURKEY

-Respiratory tract

-Fecal-oral pathway

Factors Affecting The Ways Viruses Are Transmitted

-Source of the virus

-Resilience of the virus

-Environmental conditions

-How the virus reaches the target tissues of the body (Basustaoglu,2010).

Proliferation of Viruses

When viruses encounter a host cell that can multiply by entering the body of the living creature, they activate their proliferation mechanisms. When the virus encounters a suitable host cell where it can multiply, it immediately clings to it. After viruses cling to the host cell, certain enzymes are used to break down the cell membrane and transfer genetic material into the cell. This genetic material can be a chain of ribonucleic acid or deoxyribonucleic acid, which contains information that provides the synthesis of proteins necessary to initiate the process of developing new viruses. The genetic material of the virus captures the mechanisms of the cell through enzymes belonging to the virus. The mechanisms of the cell are used to create new genetic material belonging to the virus and to create protein sheaths. New viruses in the cell usually come out when the cell breaks down. When the cell disintegrates, the cell dies. This cycle, which viruses use to multiply and cause the cell to die, is called a lytic (disruptive) cycle.

Viruses with membranes on protein bristles do not choose the way to break down the body in order to multiply. Unlike other viruses, such viruses pass through the cell membrane and enter the cell. These viruses, which enter the cell as a whole, multiply and then come out without breaking down the cell. Once the virus enters the cell, it stores its genetic material as part of the cell deoxyribonucleic acid. In this way, the virus continues to transfer genetic material to the baby cells every time the cell multiplies without revealing its presence to the cell. It can secretly transfer the genetic material of the virus from cell to cell without causing any signs of disease, and suddenly the virus starts the cycle of proliferation. This cycle is called the lysogenic cycle (Freudenric and Kiger 2020).

Pandemi

The word pandemic is derived from the ancient Greek words pan and demos, and 'pan' means 'demos' and people mean (Pandemic). Wikipedia, free encyclopedia,2022).

The effect is not a specific country or region; Infectious diseases that are effective all over the world are called pandemics. According to the World Health Organization, the pandemic is a rapidly spreading and unseasonal infectious disease in which the human population does not have immunological resistance (Qiu et al.2017).

General Characteristics of Pandemics

- Appearance in various geographical areas

- The emergence of many diseases that can be a precursor to infectious diseases

- Caused by mutated viruses

- Inadequate or no social immunity

- Formation of diseases resulting in death

- Causing changes and measures in the lifestyles of society

- Spreading without seasonal conditions (Özkoçak et al. 2020).

Major Pandemics in Human History

Amvâs Tâ:

The plague, which occurred in the Palestinian settlement of Amvâs during the reign of Omar, spread rapidly and was also seen in the territory of Syria and Iraq. Syria was the most common settlement of the epidemic.

The plague of cucumbers spreading in Amvâs is the most common of the plague species. It is defined by the Arabs as a blessing.

Since it appeared in Amvâs, the epidemic was called Amvâs tuânu.

There are three types of this plague, bubonic, septicaemia and pneumonic, caused by a bacterium called Yersinia pestis, which passes from one rodent infected with fleas to another. Tâun is a bubonic species also known as cucumber, which is one of the plague species.

The bacterium pestis, which enters the human body with the bite of fleas, causes the lymph node to become inflamed and stretched.

In the later stage of the disease, with the growth of lymph nodes, inflamed and severe pain-causing bulges appear in the body

Swelling is more common in the armpits, behind the ear, earlobe and groin areas where the skin is thin in the body

Swellings can be red, yellow, black in color. In the mildest type of the disease, the silus is red in color. With the increase in disease severity, the swellings turn yellow and then black.

In the Middle Ages, medical examiners did not know much about the treatment of taun disease. If the swellings in the bodies of those infected with Taun's disease spontaneously exploded without intervention and the blood and pus in the boil emptied out, the patient had a chance of recovery. Otherwise, patients usually die within three days.

According to the imam shafi, he thought that the patient would be healthy by applying the ointment obtained by crushing the violet flower in the treatment of taun disease or by boiling the violet and containing it in the patient (Genghis,2020).

Black Plague

The disease was seen between 1347 and 1351. The disease is called black plague because of the appearance of black swelling in the body (Glitter, 2020).

Yersinia pesticide is the cause of the plague epidemic that has killed many people in Europe (Jarus,2020).

Doctors who treated the plague also wore some special costumes. The protective costume consisted of a polished fabric coat, a beak-shaped mouthpiece usually filled with herbs, straw and spices, and a mask with a glass eye part. These doctors studied ways to treat blood draw, frog or leech (Byfield, 2010).

Cholera

Cholera is an infection whose factor is Vibrio Cholerae, which causes the body to lose high rates of water, showing signs of diarrhoea that starts suddenly and suddenly intensifies. When the bacteria, which is resistant to stomach acid, is taken into the body at high rates with liquid, the bacteria escapes stomach acid and reaches the intestines, causing infection (Undored and Altinbas 2020).

The outbreak was seen in Japan in 1817, Moscow in 1826, Berlin in 1831, Paris and London, Hamburg in 1892 and Canada. Many people have lost their lives in these outbreaks. Treatment for cholera, which has a high mortality rate, is quite simple.

Cholera patients recover in a short time with oral fluid treatment. Salt and glucose mixtures are given to eliminate the lack of electrolytes such as sodium, potassium, chlorine and bicarbonate lost in the treatment and to provide the necessary energy in patients with nutritional problems. In patients whose condition is too severe to meet the nutritional needs, the mixture is applied into the vein. In even more serious and urgent cases, tetracycline and tetracycline-like antibiotics are used (Aslan,2020).

Spanish Flu

The influenza epidemic, a subtype of H1N1 virus, was the cause of the H1N1 virus between 1918 and 1921. The surprising thing about the epidemic is that it affects more healthy young adults than the weak, the elderly and children. The reason the outbreak is called spanish flu is because Spain did not take part in World War I and there was no mention of the outbreak in other European states due to censorship, and the Spanish press brought up the outbreak for the first time (Aslan,2020).

Doctors used vaccines against the hemophilus influenzae and pneumococcal species to treat the outbreak. They gave oxygen to the patients. Although they resorted to ancient applications such as bleeding the patient, they could not find a definitive treatment in every intervention.

In order to reduce the spread of the epidemic, measures such as quarantine, isolation, mask use, closure of public areas were taken but were unsuccessful.

The vaccines and drugs used in the treatment were not effective. Although blood transfer from recovering patients to new patients was a silver lining, there was no definitive solution (Temel, 1918).

Hong Kong Flu

The disease was first seen in Hong Kong. It is the influenza epidemic that caused the deaths of nearly 1 million people between 1968 and 1969.

The disease-causing type A H3N2 virus is derived from the H2N2 virus with an antigenic deviation called the merger of many subtypes of the virus to produce different viruses than the original.

The new type of virus carries the genes of H2N2, one of the bird flu virus variants (Aslan, 2020).

Symptoms of Hong Kong flu include fever, muscle pain, weakness. These symptoms usually lasted 4-6 days. The mortality rates of children and elderly patients with Hong Kong flu are high. Although a vaccine for the virus was produced, it benefited after the outbreak affected people on a global scale (Hsieh et al.2006).

Smallpox

Variola virus is the cause of smallpox. Variola virus is in the Poxviridae family. When a case of smallpox is encountered, it is obligatory to be reported internationally. Smallpox falls into the group of infectious diseases among the types of diseases (Özer and Suna 2020).

The first vaccine produced in history is the smallpox vaccine (Badur,2020).

In 1966, as a result of the campaign led by the World Health Organization, the use of smallpox vaccines was mandatory worldwide. The World Health Organization has reported that the infection that causes smallpox worldwide has ceased permanently. The World Health Organization has recommended that the smallpox vaccine be removed from routine practice after the end of the disease. Smallpox is the only disease that has ever ended among human infectious diseases (Özer and Suna 2020).

Swine influenza

The cause of the disease is a virus in the family Orthomyxoviridae. The other name of the disease is "swine influenza virus", i.e. SIV.

Known swine flu types are usually Influenzavirus A, which is rarely type C influenza virus.

Swine flu is constantly changing its structure to spread among humans.

In 2009, an outbreak of swine flu was observed. The outbreak, which began in 2009, originated in Mexico and affected 191 countries worldwide. The outbreak that started in Mexico was caused by H1N1, a subspecies of influenza A virus.

The disease is transmitted to humans from those who come into contact with poultry and pigs closely and without protective clothing. When the meat of the sick animal is cooked under favorable conditions, the disease is not transmitted (Kara, 2010).

Symptoms of the disease are fever, cough without phlegm beats, unbearable pain throughout the body, fever, weakness, shortness of breath and sudden symptoms with a temperature of 38.30 °C. Sudden symptoms are high fever, pain, ache, diarrhea, which develop between 3-6 hours. Although these symptoms vary from person to person, they can usually vary between 4-7 days.

Oseltamivir or zanamivir drugs used to treat flu can be used in the treatment. These drugs should be used within the first 2 days after the onset of symptoms. Drugs should be administered under the supervision of a doctor and used in accordance with risk groups. Paracetamol should be used instead of aspirin as a painkiller. It is not recommended to consume medicines when going abroad for pandemic prevention purposes (Sanli,2010).

Bird Flu

Bird flu is a deadly disease transmitted from animals with the virus. Other names of the disease are Avian Influenza, Pestis Avium, Bird Flu, Avian Flu, Chicken Plague. The type of virus that is deadly to humans is H5N1 (Aslan,2020).

Bird flu is an infectious disease caused by influenza viruses found in birds. Disease-causing viruses are carried in the intestines of birds, are found in their feces and often do not show symptoms of the disease.

The virus that causes bird flu has been proven to be transmitted between pigs and humans, between chickens and humans, but there is no certainty about whether there is transmission between wild birds and humans (Goldrick and Goetz 2007).

Symptoms of the disease include fever, cough, sore throat, muscle aches and pain in the lung. Cases with pneumonia and respiratory distress are at risk of death. The disease is called blue death because the body begins to turn blue when not enough oxygen enters the cells.

There is no definitive treatment for the disease. Protection is provided by vaccination. Animals with disease factors need to be killed. Due to antigen changes in influenza virus, the activity of the virus should be monitored and the content of influenza vaccines should be updated every year (Aslan,2020).

Ongoing Pandemics

. Hiv/Aids

The hiv virus is the cause of the disease. Hiv virus is known as the human immunodeficiency virus. Hiv virus affects the mechanisms of the immune system in humans, causing the system to collapse. The disease that hiv virus is a factor in is called AIDS. AIDS is known as acquired immunodeficienicience syndrome. AIDS is an infectious disease in the zoonotic group (Undored and Altinbas 2020).

HIV virus, which is a factor in AIDS disease, is the virus that causes the collapse of the immune system by affecting cells involved in vital functions such as T cells, macrophages and dendritic cells, which are auxiliary cells in the human immune system (Özer and Suna 2020).

Ways hiv/aids are transmitted

HIV virus, which is a factor in AIDS disease, is found in the blood of people infected with the highest rates. Genital secretions, phlegm, breast milk, saliva, tears and cerebral spinal fluid may also be a disease factor. The most important factors that are effective in the transmission of the disease factor are blood, genital secretions and breast milk.

Stages and Cemptons of HIV Infection

Primary Infection

Hiv virus, which is a factor in AIDS disease, first acts on macrophage/dendritic cells in submucosal layers;

Approximately 87% of people infected with HIV 2-4 weeks after entering the body show flu-like symptoms. . People infected with this stage have high rates of HIV in their genital fluids and have a high amount of transmission (Lewthwaite and Wilkins 2009).

Serokonversiyon

This period, known as seroconversion, is the stage at which the body begins to produce antibodies to the virus (Card et al.2008).

Asymptomatic Infection

The stage of asymptomatic infection is known as the latent period. At this stage, the disease progresses quite insidiously. It does not show symptoms or symptoms. The duration of this period varies from person to person. The reason for the difference in duration is due to the difference in the health status and immune system functions of the person (Lever,2009).

Advanced HIV Infection/ Clinical AIDS

It is the stage where there is a significant reduction in immune system mechanisms, increased proliferation of HIV virus, cessation of antigen production and increased susceptibility to infections (Hazenberg et al.2003).

HIV /AIDS Treatment

The aim of the treatment, known as antiretroviral, is to suppress HIV replication and increase immune functions by using drugs that control the proliferation of HIV virus, to keep the life expectancy of infected people at normal level and to normalize the quality of life. Effective viral suppression has a positive effect on the general health of the community by reducing the risk of disease transmission among individuals (Akgül et al. 2018).

Drugs Used to Treat HIV/ AIDS

Nükleozid Revers Transkriptaz İnhibitörleri (NRTİ)

Nucleoside Revers Transcriptase Inhibitors interact with the catalytic region of the revers transcripttase enzyme found in the HIV virus, a cause of AIDS disease (De Clercq,2007).

Nucleoside Revers Transcripttase Inhibitors have analogues 2',3'-dideoxynucleosine (ddN), and the effects of drugs in this group are similar. After nucleoside Revers Transcriptal Inhibitors enter the cell, they turn into 5'-monophosphate (ddNMP), 5'-diphosphate (ddNDP) and 5'-triphosphates (ddNTP), respectively. The transformation process occurs before ddNMP acts as a competiative inhibitor/alternative substrate of normal deoxynucleosite triphosphate (dNTP).

As a compelling inhibitor of the normal substrate, ddNTP inhibits the merging of the normal substrate with the DNA chain and participates in this chain as an alternative substrate in the form of ddNMP. Thus, it acts as a de-chain terminator (De Clercq,2009).

Non-Nükleozid Revers Transkriptaz Enzim İnhibitörleri (NNRTİ)

The first two classes of Non-Nucleoside Reversal Transcardase Enzyme Inhibitors are known as 1-[(2hydroxytoxy)methyl]-6-(phenylticyo)timin-structured compounds i.e. 4,5,000 with HEPT6.7-tetrahydro-5-methylimidazo[4,5,1-jk][1,4]benzodiazepin-2(1H)-on, i.e. TIBO derivatives (Pauwels et al. 1990).

Compounds of this nature primarily interact with the allosteric region of HIV-1 revers transcriptasis. The drugs in this gup are also called specific inhibitors of HIV-1 (De Clercq,2004).

Protease Inhibitors (PI)

Protease Inhibitors carry a hydroxyetylene skeleton opened by the HIV protease enzyme, which resembles a peptide bond but cannot be opened itself. The mechanism of action of drugs in this group prevents HIV protease from performing its normal function; thus, the proteolytic process of precursor viral proteins to mature viral proteins is prevented (Madruga et al.2007).

Fusion Inhibitors (FI)

Hiv virus, which is a factor of AIDS disease, creates fusion with normal cells thanks to gp41 in the membrane, transferring its viral RNA and viral enzymes to normal cells. Enfuvirtite, a physio intibiary, was produced to prevent this fusion (Matthews et al. 2004).

The mechanism of action of drugs in this group is to prevent the virus molecule from fusing with the outer cell membrane (De Clercq,2009).

Co-receptor Inhibitors (CRİ)

Co-receptor inhibitors must enter the target cells to show their effects, and the correlators used in M (macrophage)-tropical and T (lymphocyte)-tropical HIV lineages) should interact with CCR5 or CXCR4. The mechanism of action of drugs in this group is the interaction of the co-receptor and viral glycoprotein gp120, the interaction of gp120 with the CD4 receptor and the fusion of gp41 and the outer cell membrane (Westby and van der Ryst 2005)

The only CRİ drug approved for use is maravirocytose (Perros, 2007), an antagonist ccr5.

Integrators (II)

The enzyme integral has attracted attention in the development of drugs against hiv virus. The first clinically approved integral inhibitor (II) is raltegravir. The effect of raltegarvirin is on thread transfer. This is the effect of elvitegravir. Elvitegravirin is effective in reducing viral loading in people infected with HIV (Sulukan et al. 2009).

Covid-19

Coronaviruses are single-chain, positive polarity, enveloped RNA viruses in the Coronavirinae subfamily of the Coronaviridae family in the Nidovirales class. The reason these viruses are called coronaviruses is due to the latin word "corona", which means "crown" due to the bar-shaped extensions found on the surface of the virus (Chen et al.2020).

The four structural proteins found in coronaviruses - the S (Spike) protein, the E (Envelope) protein, the M (Membrane) protein and the N (Nucleocapsid) protein -- are responsible for the formation of mature virus particles (virions) and the emergence of infection. The S protein is responsible for the formation of spikes on the surface of the coronavirus. The protrusions on the surface are responsible for the virus's adhesion to the host cell septators and its entry into the cell M protein, which allows the virus particle to form with three different transmembrane regions, to allow the virus to curve the cell membrane and bind to the nucleocap. Protein E is involved in the packaging and release of the virus and viral pathogenesis. The N protein contains regions connected to the viral genome in the RNA structure (Alpine and Unal 2020).

Ways Covid-19 Is Transmitted

The main way of transmission of coronavirus is the droplet path. The virus found in respiratory secretions can make the healthy individual sick by direct contact with the mucous membrane, while the infected individual coughs, sneezes or speaks through droplets. In finding a new host for the virus, the contact of another individual is effective with the droplets that the sick individual emits through coughing and sneezing (Gürsu,2020).

Stages and Cemptons of Covid-19 Infection

The severity of infection is divided into 5 groups: asymptomatic infection, mild form, moderate form, severe infection, critical infection.

Asymptomatic Infection

It is defined for cases that have tested positive for coronavirus and do not show clinical symptoms. Asymptomatic infection plays an important role in social transmission. This is due to the absence of clinical symptoms in those infected.Babies and children who do not show clinical symptoms play an important role in interpersonal transmission.

Mild Form Symptoms

Fever, fatigue, muscle pain, cough, sore throat, runny nose, sneezing, symptoms of acute upper respiratory tract

Symptoms of Medium Form

Pneumonia, usually fever and cough, wheezing in some cases

Symptoms of Severe Infection

Dyspnea, central cyanosis, decreased oxygen saturation, hypoxemia

Critical Signs of Infection

Acute respiratory distress syndrome, respiratory failure, multiple organ failure (Happy, 2020).

Covid-19 Treatment

The main goal in the treatment of coronavirus is supportive and symptomatic treatment. First of all, the infected persons should be removed from the community and quarantined. Cases with mild symptoms should be managed by home counseling without going to health centers. In treatment, the body's water and electrolyte level should be kept to a certain extent, nutrition should be taken care of, fever and cough should be checked. In cases where the body does not receive enough oxygen, the face mask, high-flow nasal cannula, oxygen should be provided through non-invasive ventilation. Mechanical ventilation and oxygen support may be required, and kidney replacement therapy may be required in some patients. Antibiotics and antifungal should be used in cases with two or more infections in the body at the same time (Jin et al. 2020).

Vaccines are the most effective way to prevent epidemics in the form of infections. This is because it takes both costly and a long time to develop drugs suitable for treatment. Vaccines are both a way to be used in the prevention of global epidemic diseases (DG et al. 2020).

Drugs Used to Treat Covid-19

Klorokin (CQ), Hidroksiklorokin (HCQ)

Although chloroquine has not been approved by the FDA in the treatment of coronavirus, it has allowed use if doctors deem it appropriate. The FDA has not approved any therapeutic agents or drugs for the treatment and prevention of coronavirus. Clinical efficacy and safety of chloroquine in the treatment of coronavirus is unclear. Since doctors are successful in the treatment of different diseases, they have approved the use of chloroquine.

Hydroxychloroquine is a chloroquine-derived drug.The mechanism of action of the drug inhibits the enzyme polymerase, preventing the merger by interfering with the glucocytion of the virus and cell receptors by increasing the ph of the place where the intracellular digestion of the substance formed and taken by the combination of phagosome and lysosome occurs.

Hydroxychloroquine is recommended in patients who will be monitored with outpatient treatment and treated by hospital in the coronavirus treatment guide of the Ministry of Health in our country.

Favipiravir

Favipiravir RNA viruses have an effect by inhibiting the enzyme RNA-dependent RNA polymerase. Favipiravir is an antiviral drug. Favirpiravir forms favipiravir ribofuranosyl-5B-triphosphate, an active form of the body. For this activation process, favipiravir intraselecular phosphoribosylasion occurs. Favipiravir ribofuranosyl-5B-triphosphate is a substrate of RNA-dependent RNA polymerase and inhibits RNA polymerase enzyme activity. Since the RNA-dependent RNA polymerase enzyme is found in many RNA viruses, favipiravir expands its spectrum by affecting this enzyme.

Remdesivir

Remdesivir is in the antiviral drug group. It is used in the treatment of Ebola and marburg virus infections. This drug is the precursor to nucleotide analoma, which is metabolized into the intracellar adenosine triphosphate analogue, which inhibits the enzyme viral RNA polymerase. Remdesivir is a wide-spectrous drug. It has a preventive and therapeutic effect in non-clinical studies against coronaviruses.

Lopinavir/ritonavir(LPV/R)

Lopinavir, a combination of ritonavir, is used to treat HIV infection. It is a protease inhibitor, one of the drugs used to treat AIDS. The enzyme protease plays a role in the processing of coronavirus polyprotein. Lopinavir and rheaavirin have contrasting effects against coronavirus separately and together.

Nitazoksanid

The drug nitazoksanid has strong in vitro activity against coronavirus. Apart from the coronavirus, this drug has broad-spectrum antiviral activity against influenza, respiratory sysnsityal virus, parainfluenza, rotavirus and norovirus The mechanism of action of the drug is associated with the pathways regulated with the host during the proliferation of the virus.

Tosilizumab

The effect of the drug tosilizumab is caused by monoclonal antibodies due to membrane or inhibiting soluble interleukin-6 receptors (rIL-6). This drug has been approved for use in the treatment of rheumatoid arthritis patients.

İvermektin

Ivermectin is a broad-spectrum FDA-approved drug effective against parasites. It has had an effect on many viruses in studies on the drug. The mechanism of action of the drug ivermectin inhibits the nuclear intake of the host and viral proteins. Ivermectin both acts on some Rna virus

infections and has an effect on some DNA viruses. In studies on the drug, the coronavirus has a reducing effect on its effectiveness (Mutlu et al. 2020).

Factors Affecting Viral Pandemics

Vaccines

Viral pandemics can be effectively prevented with inexpensive and effective vaccination strategies. Vaccines protect against pathogens by stimulating primary defense mechanisms.

Vaccination is the process of applying a small amount of an infectious agent, such as viruses or bacteria, to stimulate the immune system to recognize and respond to this agent. Vaccines are often used to prevent infectious diseases. Vaccines are administered by injection. Vaccines are often designed to stimulate the production of antibodies, proteins that neutralize foreign invaders in the body.

To improve the specific immunological system through vaccination, the human body can produce white blood cells (B and T cells) that can fight the pathogen (especially) in response to the immune system, allowing the adaptive immune system to grow.

Since the disease is mostly a new type of virus in virus-induced pandemics, it is impossible to produce a vaccine before the pandemic begins.

In the production of vaccines against pandemics, the disease factor is primarily stated. After the disease factor is determined, it is replicated in the cultural environment and the vaccine is produced. The spread of pandemics increases in the time spent in vaccine production. The vaccine produced is specific to the disease factor determined. Vaccines are effective on the black virus. The treatment of the infected person with the vaccine is limited (Şahin and Demir 2020).

Antiviral Drugs

Antiviral drugs are used in virus-induced infections. It is used in the prevention and treatment of virus-induced infections. In viral pandemics, the treatment of the disease is either through the application of vaccines or the use of antiviral drugs to prevent the disease before the disease occurs (Carrasco et al. 2011).

Virus-Related Protein Use

The protein associated with the virus contains anti-idiotypical antibodies, natural ligands of the receptor and anti-receptor antibodies. The mechanism of action prevents the virus from binding to host cell receptors and entering the cell before the viral infection begins.

Reverse Transcription Inhibitors/ Revers Transcription Inhibitors

Nucleotide or nucleoside analogues, similar to the building blocks of ribonucleic acid or Deoxyribo nucleic acid, are used as antiviral drugs. Since the mechanism of action is not 3'OH in analogues, viral Ribonucleic acid or Deoxyribo blocks enzymes that synthesize nucleic acid.

Antisense

When the virus genome becomes active in the host cell, it produces mRNA molecules that play a role in the synthesis of viral proteins. mRna production begins by proteins. Antisensors are

drugs made from short segments of DNA or RNA that can bind to their viral genomes as a complement and prevent transcription of the viral genome.

Ribozim

When the virus genome becomes active in the host cell, it produces mRNA molecules that play a role in the synthesis of viral proteins.mRna production begins by proteins. Antisensors are drugs made from short segments of DNA or RNA that can bind to their viral genomes as a complement and prevent transcription of the viral genome.

Protease Inhibitors

Protease inhibitors developed for the treatment of HIV/ AIDS and hepatitis C are widely used in the treatment of these diseases. Some viruses break down viral protein chains after translation with the enzyme protease within the target cell, creating virions and spreading them in cells that are not infected with disease factors. Protease inhibitors take effect by inhibiting the enzyme viral protease.

İnterferonlar

Interferons suppress the disease-causing virus factor by strengthening the body's immune system instead of attacking the disease-causing virus factor.Interferon viruses prevent their proliferation.Interferons are signaling proteins produced due to the presence of several viruses in the body.Interferons are cytokines synthesized by cells in viral infection. It shows its effect by enabling communication between cells to strengthen the immune system against disease-causing factors.Interferons have opposite effects on the proliferation of viruses by protecting cells from virus infections.

Conventional Plasma Treatment

Conventional plasma therapy, which is used to treat and prevent epidemic diseases, is the treatment of the disease by taking blood from people who have suffered from the disease, separating antibodies and giving them to sick people (Şahin and Demir 2020).

3. RESULTS AND RECOMMENDATIONS

Pandemiler epidemics that are effective worldwide. An epidemic pandemic not only is it widespread and the mortality rate is high, but it is also contagious must be high. Affecting human history pandemilere Although various methods have been applied in the treatment of related diseases for centuries, there is no definitive treatment method. Her pandemiye there is a unique way of treating the disease. These semptomatik and supportive treatment, lac treatment and vaccination of healthy people pandeminin to reduce the effects. Pandemileri investments in preventing factors increase,Ar-Thanks to the development of ge studies, we may face in the future pandemic we strengthen our hand in their dangers.

Acknowledgement

REFERENCES

AKGÜL, Ö., ÇALŞKAN, R., & ÖNER, YA (2018). HIV/AIDS: Current Approaches. Journal of Medical School Clinics , 1 (1), 19-31.

ALP, S., & ÜNAL, S. (2020). Pandemic caused by the new coronavirus (SARS-CoV-2): developments and current situation. Flora Magazine, 25.

Aslan, R. (2020). From history to the present, epidemics, pandemics and Covid-19. Journal of Detail, 8(85), 35-41.

Badur, S. (2010). H1N1 epidemiology and virus. ANKEM Derg , 24 , 190-5.

Basustaoglu,A.C,2010.Medical Microbiology.Atlas Bookseller Tic.Ltd.Sti,947,Ankara

Byfield T. (2010) . Renaissance: God in Man, A.D. 1300 to 1500: But Amid Its Splendors, Night Falls on Medieval Christianity, Christian History Project, p. 37.

Card, J.J., Amarillas, A., Conner, A., Akers, D.D., Solomon, J., DiClemente, R.J. (2008). TheComplete HIV/AIDS Teaching Kit: With CD-ROM, Springer Publishing Company, New York, 25-71.

Carrasco, LR, Lee, VJ, Chen, MI, Matchar, DB, Thompson, JP and Cook, AR (2011). Antiviral stockpiling strategies for future influenza pandemics: a global epidemic-economic perspective. Journal of the Royal Society Interface , 8 (62), 1307-1313.

Genoa, E. (2020). Amvas taunu and its effects that occurred during the Period of Omar. Journal of Caucasus University Faculty of Theology, 7(13), 129-150.

Chen, Y., Liu, Q., & Guo, D. (2020). Emerging coronaviruses: genome structure, replication, and pathogenesis. Journal of medical virology, 92(4), 418-423.

Craig Freudenrich, PhD & Patrick J. Kiger "How Viruses Work" 2020. https://science.howstuffworks.com/life/cellular-microscopic/virus-human.htm

 (Accessed:14 February 2022)

De Clercq, E. (2004). Non-nucleoside reverse transcriptase inhibitors (NNRTIs): past, present, and future. Chemistry & biodiversity, 1(1), 44-64.

De Clercq, E. (2007). "Anti-HIV drugs" Verh. K. Acad. Healed. Belgian, 69, 81-104.

De Clercq, E. (2009). Anti-HIV drugs: 25 compounds approved within 25 years after the discovery of HIV. International journal of antimicrobial agents, 33(4), 307-320.

DG, A., HJ, S., & MH, K. (2020). Lee S, Kim HS, Myoung J, et al. Current Status of Epidemiology, Diagnosis, Therapeutics, and Vaccines for Novel Coronavirus Disease 2019 (COVID-19). J Microbiol Biotechnol [Internet], 30(3), 313-24.

Goldrick, BA and Goetz, AM (2007). Pandemic flu: what infection control specialists need to know. American journal of infection control , 35 (1), 7-13.

GÜRSU,E. (2020). CoronavirusPandemisi. https://www.researchgate.net/profile/ElifGuersu/publication/341599760_Koronavirus_Pandemisi_ve_SarsCoV2_Virusune_Genel_Bakis/links/5ec95c0392851c11a8820702/Koronavirues-Pandemisi-ve-Sars-CoV-2-Viruesuene-Genel-Bakis.pdf

Hazenberg, MD, Otto, SA, van Benthem, BH, Roos, MT, Coutinho, RA, Lange, JM, ... & Miedema, F. (2003). Permanent immune activation in HIV-1 infection is associated with progression to AIDS. Aid , 17 (13), 1881-1888.

Hsieh, YC, Wu, TZ, Liu, DP, Shao, PL, Chang, LY, Lu, CY, ... & Huang, LM (2006). Flu outbreaks: past, present and future. Journal of formosan Medical Association , 105 (1), 1-6.

Jarus O. 20 of the worst epidemics and pandemics in history. Live Science, All About History March 20, 2020. https://www.livescience.com/worst-epidemics-and-pandemics-in-history.html

 (Access 16.02.2022)

Jin, YH, Cai, L., Cheng, ZS, Cheng, H., Deng, T., Fan, YP, ... & Wang, XH (2020). A quick recommendation guide to the diagnosis and treatment of pneumonia (standard version) infected with the new coronavirus (2019-nCoV) in 2019. Military Medical Research , 7 (1), 1-23.

Kara, A. (2010). Swine Flu (Pandemic Influenza 2009, Influenza 2009 H1N1). Journal of Child Health and Diseases, 53(1).

Kutlu, R. (2020). What we have learned about the new coronavirus pandemic, current approaches to diagnosis and treatment and the situation in Turkey. Turkish Journal of Family Medicine and Primary Care, 14(2), 329-344.

Lever, AM (2009). HIV: virus. Medicine , 37 (7), 313-316.

Lewthwaite, P. and Wilkins, E. (2009). Natural history of HIV/AIDS. Medicine , 37 (7), 333-337.

Madruga, J. V., Cahn, P., Grinsztejn, B., Haubrich, R., Lalezari, J., Mills, A., ... & DUET-1 Study Group. (2007). Efficacy and safety of TMC125 (etravirine) in treatment-experienced HIV-1-infected patients in DUET-1: 24-week results from a randomised, double-blind, placebo-controlled trial. The Lancet, 370(9581), 29-38.

Matthews, T., Salgo, M., Greenberg, M., Chung, J., DeMasi, R., & Bolognesi, D. (2004). Enfuvirtide: the first therapy to inhibit the entry of HIV-1 into host CD4 lymphocytes. Nature reviews Drug discovery, 3(3), 215-225.

MUTLU, O., UYGUN, İ., & ERDEN, F. (2020). Drugs used to treat coronavirus disease (COVID-19). Kocaeli University Journal of Health Sciences, 6(3), 167-173.

Özer, M., & Suna, H. E. (2020). Covid-19 pandemic and education. Şeker, Özer, A. and C. Korkut (Der.), Anatomy of the global epidemic: Within the future of man and society, 171-192.

Özkoçak, V., Koç, F., & Gültekin, T. (2020). Anthropological View of Pandemics: Example of coronavirus (Covid-19). Electronic Turkish Studies , 15 (2).

Pandemic.Wikipedia, liberation. https://tr.wikipedia.org/wiki/Pandemi(Access:14.02.2020)

Glitter, H. (2020). Infectious disease outbreaks in history. Tepecik Education and Research Hospital Journal, 30, 19-26.

Pauwels, R., Andries, K., Desmyter, J., Schols, D., Kukla, M. J., Breslin, H. J., ... & Janssen, P. A. (1990). Potent and selective inhibition of HIV-1 replication in vitro by a novel series of TIBO derivatives. Nature, 343(6257), 470-474.

Perros, M. (2007). CCR5 antagonists for hiv infection and AIDS treatment. Advances in Antiviral Drug Design , 5 , 185-212.

Qiu, W., Rutherford, S., Mao, A., & Chu, C. (2017). Pandemic and its effects. Health, culture and society , 9 , 1-11.

SULUKAN, E. E., KÜÇÜKOĞLU, K., & GÜL, H. İ. (2009). AIDS and the drugs used to treat it. Ankara Faculty of Pharmacy Journal,38 (1) 47- 78.

Şahin, F., & Demir, S. (2020). Viruses, Factors and Consequences Affecting Viral Pandemics. Muzaffer Şeker, Ali Özer and Cem Korkut. Turkish Academy of Sciences, 55-76.

Sanli, K. (2010). Influenza virus and swine flu. Istanbul Legal Sultan Suleyman Medical Journal (IKSST), 2(1), 4-12.

Don't wear it, S. (2019). Review of Virus Subject in Secondary Education from the Point of View of Program, Teacher and Student. Master's Thesis, Hacettepe University Institute of Educational Sciences, Ankara.

UNMASKED, Ö. L., & ALTINBAS, SK (2020). Microorganisms existed long ago on the blue planet: the history of pandemics. Turkish Journal of Women's Health and Neonatology , 2 (2), 53-69.

Temel, M. K. (1918). Flu Pandemic. Istanbul University Institute of Health Sciences Master's Thesis, Istanbul.

Westby, M., & van der Ryst, E. (2005). CCR5 antagonists: host-targeted antivirals for the treatment of HIV infection. Antiviral chemistry and chemotherapy, 16(6), 339-354.

Design and Implementation of High-Speed Fpga-Based Complex e^X Calculation Unit

Günay TEMÜR

Introduction

FPGA chips are preferred in applications that require high processing power and performance due to their low cost, reprogram ability and high frequency operation. FPGAs first appeared in the mid-1980s and were first used in the telecommunications and networking industry. They were originally developed to create prototypes of ASIC designs and perform functional validation on them through simulation . However, their place in the final product range has increased over time due to their low development costs and their ability to be put on the market in a short time. Towards the end of the 1990s, it started to be used in other sectors as well (Temür 2013). After production, FPGA chips can be reprogrammed according to their functionality needs. These features make them different from ASICs designed for a specific application or task. In addition, these features enable hardware designs to be upgraded and reconfigured during or after the implementation (Babu ve Parthasarathy 2021).

FPGA chips today are an inevitable hardware element for designs to be used in the calculation of mathematical functions which are extremely difficult to calculate precisely with digital circuits in the context of medical imaging (Almekkawy, Xu, ve Chirala 2014), (Rasu, Sundaram, ve Santhiyakumari 2015), image processing (Raut vd. 2019; Chaple, Daruwala, ve Gofane 2015), robotics (Wan vd. 2021), voice recognition (Rodríguez-Orozco vd. 2018; Sun, Li, ve Luo 2011), encryption (Ismail vd. 2017), (Adil Yazdeen vd. 2021), bioinformatics (Surendar 2017), space technology (Wan vd. 2021), (Cosmas ve Kenichi 2020), vehicle technology (Acosta Lúa vd. 2021), (Tatar ve Bayar 2019) and artificial neural networks (Şahin ve Temür 2016). One of these mathematical functions to be calculated is Exponential Function (ex). The ability of this function to provide accurate results is crucial for the successful operation of function-dependent designs. It is also expected that the function yields results as quickly as it gives correct results. For this reason, various methods have been described in the literature in order to calculate the ex function logically. Some of the methods used to calculate the ex function are the Look Up Table (LUT) use, Taylor Series expansion and COordinate Rotation DIgital Computer (CODIC) based approaches (Arar 2017). Examples of the studies on FPGA chips implemented using these methods are given below.

Wielgosz et al. presented an implementation of the double sensitive ex function. This application is an application created by a LUT Table structure together with Taylor series expansion. The application is built for 64-bit numbers and provides low latency and low space consumption on the FPGA chip when compared to 32-bit applications. Thanks to the parallel operation logic of the FPGA chips and the low space cost of the module, it was stated that the results obtained using two modules on the same chip were satisfactory (Wielgosz, Jamro, ve Wiatr 2008).

Sujitha and Reddy created a design that can calculate log and ex functions for CORDIC-based 16-bit numbers. As a disadvantage to this design, they suggested that it can be used in decoding algorithms and communication systems (J Sujitha 2014).

Koyuncu and Sahin designed a CORDIC-based ex calculation unit for FPGA chips. The unit was designed to work with 32-bit data in IEEE 754-1985 floating-point number format. The results produced by the unit were compared with the actual results and it was observed that the unit can calculate with at least four-digit sensitivity (Şahin ve Koyuncu 2011).

Wang et al. have designed a model to provide scalable application capabilities for an overall hardware architecture, computational precision, and degree of interpolation. Eight complex reciprocal and eight complex exponential design examples are applied to validate the proposed architecture. The ASIC and FPGA-based experimental results show that the proposed scheme can efficiently approach complex reciprocal and exponential functions up to 16-bit precision, and also achieves a significant reduction in memory requirements compared to traditional two-part and multi-part schemes (Wang, Ercegovac, ve Xiao 2014).

Hosseiny and Jaberipur used rectangular multipliers for hardware realization of complex exponential functions (CEF). Compared to previous studies, they achieved more than 30% speedup and 75% lower cost (Hosseiny ve Jaberipur 2020).

Another study was carried out by Doss et al. with the LUT and Taylor Series expansion on FPGA. In the study, data processing speed was compared with a PC and high speed gains were obtained (Doss ve Riley 2004).

In this study, a complex ex calculator module was designed, differently from other studies. The designed module works with the 64-bit IEEE 754-1985 floating-point number format. The module was coded in VHDL and synthesized for the FPGA Virtex-6 XC6VLX75T chip with Xilinx's ISE 14.7 EDA tool. The results produced by the module were compared with the actual results and the sensitivity of the module was determined.

General information about the subject was given in the following sections of the article. In the second part, the general structure of FPGA chips, CORDIC algorithm and ex calculation method are explained. Then in the third part, the ex calculation method applied in this work were explained consecutively. In the fourth part, the architectural structure and operation of the designed module were explained in detail. In the fifth part, the test studies and the results obtained from these studies were presented. In the last part, the results were discussed and recommendations were given about future studies.

Background Information

FPGA Chips

FPGA chips are integrated circuits that provide designers great convenience with their reprogrammable structure and ability to perform parallel operations. In recent years, the use of FPGAs in real-time and high-performance data processing applications has become quite widespread.

Input/Output Blocks (IOBs), interconnecting networks, and configurable logic blocks (CLBs) in the FPGA chips (the general structure shown in Figure 1) can be programmed according

to the circuit that the user designs. These chips are usually mounted on computer systems in the form of an electronic card with other circuit elements.
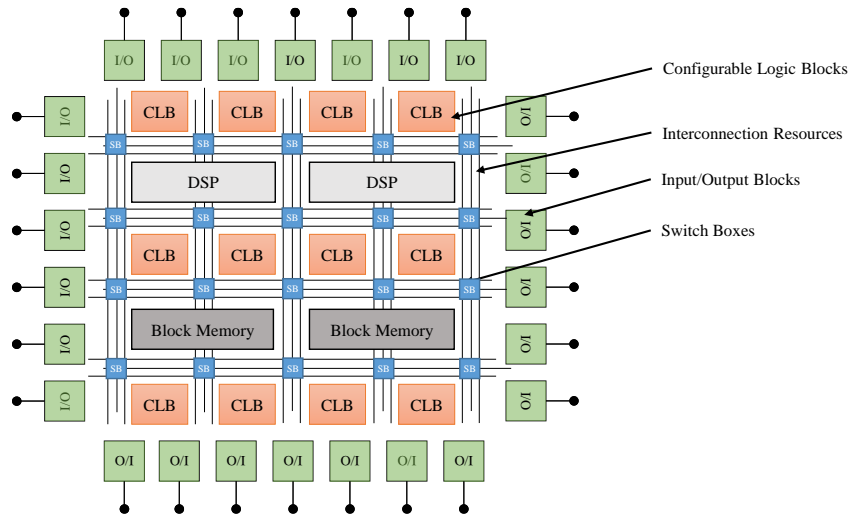
Figure 1. FPGA Architecture (Hoe, Deepthi Bollepalli, ve Martinez 2013)

Programmable Logic Blocks

CLBs consist of LUT Carry Logic and Flip-Flops, as can be seen in figure 2. a typical FPGA chip may contain tens of thousands of CLBs and flip-flops. The size of an FPGA chip can be expressed as the number of inputs and outputs of CLBs, the number of transistors used in the formation of CLBs, or the number of logical functions that CLBs can perform. Memory capacity (LUT) is limited by the number of entries. CLBs provide functional elements for the logic circuit the user wants to build. The flexibility and symmetry of the CLB architecture allows applications to be deployed with ease (Temür 2013).
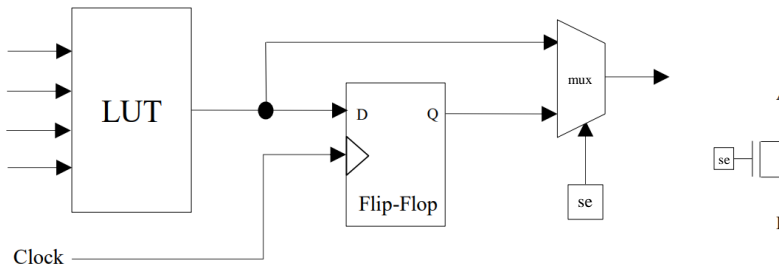
Figure 2. Structure of Configurable Logic Block (Temür 2013)

Programmable I/O Blocks

As seen in figure 3, IOBs act as a programmable interface between the internal signal lines and pins of the chip. Thanks to IOBs, the pins of FPGAs can be programmed as input, output or bidirectional. Depending on the type of FPGA chips, the number of IOBs in a chip can reach 1000s .
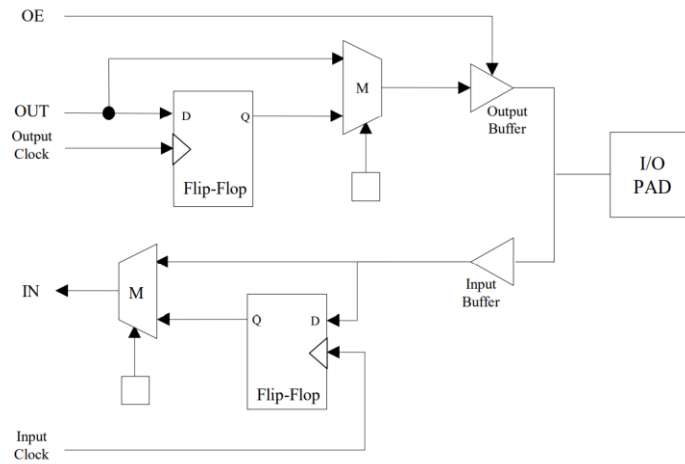
Figure 3. I/O Block Diyagram (Temür 2013)

Interconnection Resources

These units, shown in the clear diagram in Figure 4, are used to configure connections both between CLBs and between CLBs and IOBs. Since they are programmable, they have a very flexible structure. There are matrix switches at the junction of the horizontal and vertical channels. These switches have a six-transistor steering mechanism inside. Thanks to these programmable switches, it can be directed to the other three neighboring parties from the input side (Temür 2013).
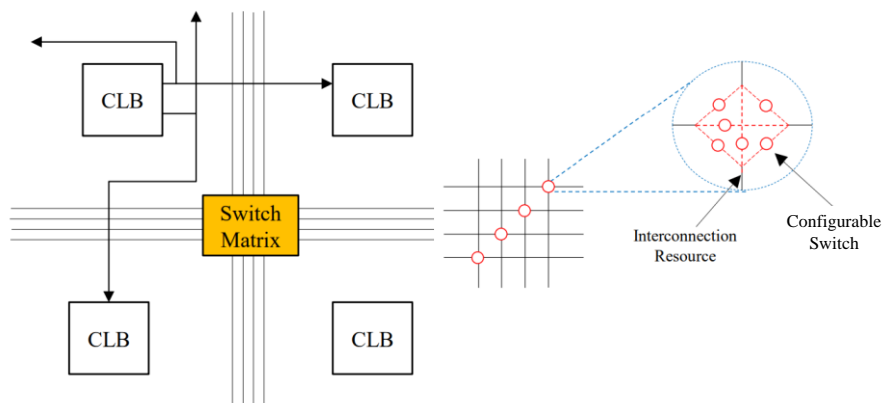
Figure 4. Configurable Interconnection Resources ("FPGA Architecture for the Challenge")

Methods of e^x Calculation

There are different methods used to calculate the e^x function in the literature. These functions can be expressed as standard basic approaches and modern approaches. Taylor series expansion is one of the standard basic approaches.

e^x value calculation formula with the Taylor Series expansion is given in equation (1).

$$e^x = 1 + \frac{x^1}{1!} + \frac{x^2}{2!} + \frac{x^3}{3!} + \frac{x^4}{4!} + \cdots + \frac{x^n}{n!}$$

(1)

This method is an iterative approach method. Taylor approximation presents a major disadvantage, which resides in uniformity of the convergence time. As the number of iterations in

the formula increases, the calculated value gets closer to the actual ex value. Since this method is a calculation method that needs the nth power of x, it is not preferred in digital circuit designs.

On the other hand, the little-known LUT and CORDIC algorithms are modern methods used to calculate the e^x function in the literature. The LUT method is the pre-tabled version of the fixed ex values that are predicted to be needed in the calculation. In this method, e^x values in a wide range cannot be calculated. This method is used for results that will correspond to fixed input values and does not give the desired output with the desired precision. In cases where precise calculations are required, very large tables are needed.

Another modern method, the CORDIC method is a calculation method created with the help of trigonometric functions. It is shown by Walther [6] that the CORDIC algorithm can be used to compute hyperbolic functions. As given in equation (2), the value of e^x is calculated by the adding of *Sinh(x)* to *Cosh(x)* values calculated by CORDIC.

$$e^x = Sinh(x) + Cosh(x)$$

(2)

This architecture does not need a LUT since the values for the angle accumulator are fixed and hardwired as constants to each adder and subtractor in the angle accumulator chain. Also the barrel   shifters can be eliminated, since non-combinatorial hardwired shifts can be applied to the adder and subtractor in each stage (Pouyan, Hertz, ve Nilsson 2011).

As can be seen in the flow diagram of the CORDIC algorithm given in Figure 5, the main purpose is to bring the output value of the Z variable closer to zero.
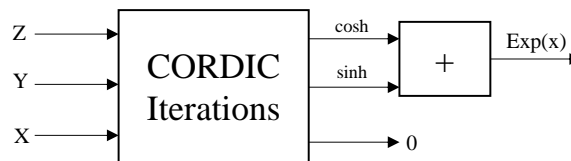
Figure 5. Expential function entity (Boudabous vd. 2004)

This process, in the rotation mode given in figure 6, circular angle transformation, vector *i.* with position *(i+1)*. It is formed by performing the shift operations until the angle value "*θ*" between its current position is reset.
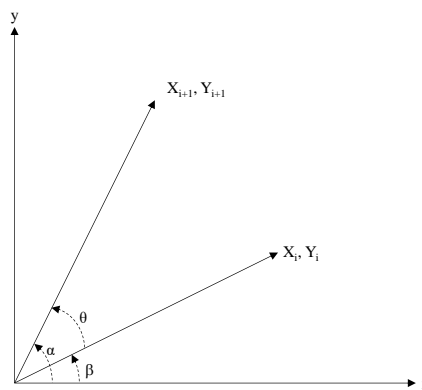
Figure 6. Circular angle conversion in rotation mode (Considine 1989)

The biggest disadvantage of this method is that the current CORDIC unit can only calculate the *Sinh(x)* and *Cosh(x)* values in the range of $-\pi/4$ to $\pi/4$. Therefore, CORDIC can only calculate between $e^{-0.7853981}$ and $e^{0.7853981}$.

Proposed e^x Calculation Method

The e^x calculation method proposed in this study is given as $e^{x.y}$. (x) represents the desired integer part, and (y) represents the decimal part. The formula used in the calculation is given in equation (3) and the flow chart of the proposed model is given in figure 7.

$$e^{x.y} = LUT(x) * [Sinh(.y) + Cosh(.y)]$$
(3)
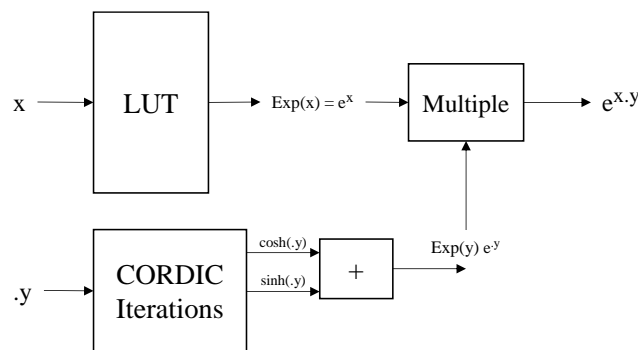
Figure 7. flow chart of the proposed model

This module consists of 2 channels designed as a complex structure in which the CORDIC and LUT methods are used together. The first channel is the part of the CORDIC design that calculates the exponential function $e^{.y}$ of the decimal part of the number to be calculated. The current CORDIC structure is able to compute values of *Sinh(y)* and *Cosh(y)* only in the range $-\pi/4$ to $\pi/4$. Therefore, CORDIC can only calculate between $e^{0.7853981}$ and $e^{0.7853981}$. At this point, the maximum decimal value for the module is fixed to 0.75 in order not to deal with odd operations. For this reason, our module contains 2 CORDICs. With the first CORDIC, only 0.75 and lower values are calculated. If the desired calculation value is 0.75 or less, then 0 is transferred to the other CORDIC unit. CORDIC produces a value of 1 that will not change the final value in the multiplication operation against the input value of 0. If the desired decimal value of the module is greater than 0.75, then 0.75 is subtracted from the value to be calculated and the other CORDIC enters for the remaining value. Then, by multiplying the results from both CORDIC units, the value of e^y can be calculated. With this design, the exponential function values of a maximum decimal number such as 0.99 can also be calculated.

The LUT design consisting of the other-channel is the part where the desired integer e^x values are calculated. The formula used in the calculation is given in equation no.(4). For these values, a control structure was created with VHDL codes and provision for desired values is transferred as power of e to the corresponding module. The equations used in determining the desired values are given in (5) and (6). d in equation (5) represents both the negative and positive values of x (0-9), which is desired to be calculated in equation (5) represents both the negative and positive values of x (0-9), which is desired to be calculated. When the value (d) obtained by a mode operation is subtracted from the value (x), negative and positive values of t:10-20-…-90 representing the value (x) are transferred to the module output as power of e. These exponential numbers are transferred to *ContA* and *ContB* units, which consist of another unit. In these units, e^x output values created in

response to incoming exponential values are transferred to the output of the units. Finally, the obtained values of e^d and e^t are multiplied as shown by the equation (4) to obtain e^x value.

$$e^x = e^d * e^t = e^{d+t} \tag{4}$$

$$d = x \bmod 10 \tag{5}$$

$$t = x - d \tag{6}$$

e^x Calculator Module Design

In this work, a hardware module calculating the ($e^{x,y}$) exponential value of a given decimal (*x.y*) value, which can be used for FPGA chips has been designed. The module has been designed to work with numbers in the IEEE 754-1985 floating-point number standard and can calculate values between $e^{-99.99}$ ve $e^{99.99}$. The module produces more definite values between $e^{-89.99}$ ve $e^{89.99}$ since the result for the values greater than e^{90} is infinite while it is 0 for the values less than e^{-90}. The module was coded in VHDL and synthesized for the FPGA Virtex-6 XC6VLX75T chip with Xilinx's ISE 14.7 EDA tool. The operational structures used in the design were also created with Xilinx's IP Core Generator.

Figure 8 shows the top level block diagram of the designed module. The module has 64-bit data input and output paths. *Enable* and *Ready* signals are used to provide synchronization (hand-shaking) between the module's timing and the module and the other units to which the module is connected. When valid data is present at the input of the module, the *Enable* signal is activated and the data begins to be processed as the module starts to read it. When the module generates the result, it activates the *Ready* signal to warn the next unit.

The module has been designed with 47 clock pipelined structures. This means that the module can read a new (*x.y*) value for each period to calculate. The result of the first reading is produced after 47 periods, and at each subsequent period, other results corresponding to the new (*x.y*) input can be respectively generated.
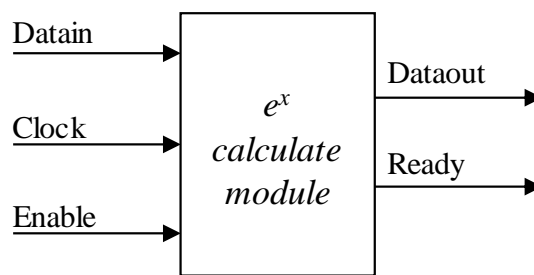
Figure 8. e^x Calculation Module, Top Level Block Diagram

Figure 9 shows the second level block diagram of the e^x calculation unit. The 64-bit *(x.y)* number that comes to the unit is first converted from "floating point" number format to "fixed-point" number format. The first 11 bits of this number are the integer (*x*) while the remaining 53-bit are the decimal (*.y*) and parts.

Figure 9. e^x Calculation Module Second Level Block Diagram

After this step, the *(x)* and *(.y)* parts of the number advance in the unit from two different channels. While the integer *(x)* part runs from the 1st channel, the operation of the *(mod10)* given in the equation (5) is applied by the *(mod)* unit. The aim of this unit is to learn the value of the units digit for a two-digit integer. Then the value obtained with mod10 is transferred to the output unit. *(x)* number is transferred to the output unit as another entry. The value at the output unit is obtained as 10 and multiples of our count. By entering into *ContA* and *ContB* units, these two numerical values obtained are able to produce *(e^x)* output that is fixedly introduced to the system. The *ContA* and *ContB* units are a unit created with a simple "if" block. This unit generates constant output values according to the input values. These constant values are given in table 1 on the following page. The output of the *ContA* and *ContB* units is multiplied by the "multiple controller out" unit as indicated by equation (4). The output of this unit gives us the *e^x* value of the number *(x)*. The result obtained is then stored in a delay unit up to 19 clock cycles for the calculation of the *(.y)* value as *e^y* , which is to come from the 2nd channel.

Table 1. e^x Output values for x integer inputs (LUT)

ContA Input Dec	ContA Input Binary	64bit e^x HEX OUT	ContB Input Dec	ContB Input Binary	64bit e^x HEX OUT
0	00000000000	3FF0000000000000	0	00000000000	3FF0000000000000
1	00000000001	4005BF0A80000000	10	00000001010	40D5829DC0000000
2	00000000010	401D8E64C0000000	20	00000010100	41BCEB0880000000
3	00000000011	403415E5C0000000	30	00000011110	42A3704700000000
4	00000000100	404B4C9020000000	40	00000101000	438A220D40000000
5	00000000101	40628D38A0000000	50	00000110010	44719103E0000000
6	00000000110	407936DC60000000	60	00000111100	45579DBCA0000000
7	00000000111	4091228860000000	70	00001000110	463FBFD220000000
8	00000001000	40A749EA80000000	80	00001010000	47255779C0000000
9	00000001001	40BFA71580000000	90	00001011010	7FF0000000000000
-1	11111111111	3FD78B5635FDCF09	-10	11111110110	3F07CD79B55EE42F
-2	11111111110	3FC152AAA33D6D85	-20	11111101100	3E21B48655E34457
-3	11111111101	3FA97DB0C9A5BFB1	-30	11111100010	3D3A56E0C2AE6E18
-4	11111111100	3F92C155BA0A9722	-40	11111011000	3C5397924995539C
-5	11111111011	3F7B993FE01D6A27	-50	11111001110	3B6D257D54805FC4

-6	11111111010	3F644E51D8CBEFBE	**-60**	11111000100	3A85AE191A9C9281
-7	11111111001	3F4DE16BAF146EE7	**-70**	11110111010	39A02057D125F45E
-8	11111111000	3F35FC229D30496B	**-80**	11110110000	38B7FD974D400187
-9	11111110111	3F202CF3D3F7B960	**-90**	11110100110	37D1D8508FA83B20

The (.y) value advancing through the 2nd channel is the 53-bit portion that comes from *floattofix* converter unit. However, since CORDIC works with a maximum of 48-bit input, the last 5 bits, which are considered to be insignificant, are ignored. The remaining 48-bit (.y) value primarily enters into the *cordic input* unit. This unit also has a fixed 48-bit "fixed" 0.75 number. This fixed 0.75 number is determined as it is the maximum number that the CORDIC can calculate. In this unit, we have created a block that compares whether the decimal number is greater than the constant 0.75 input. Thanks to this unit, as in channel 1, our value is again two numbers. If the decimal number is greater than 0.75, 0.75 is subtracted from our number as shown in equation (7), the remaining difference (*w*) and 0.75(*f*) are transferred to the output unit as two separate outputs. If the number is equal to or less than 0.75, then 0 (*w*) to 0.75 (*f*) values are passed to the output to be sent to the CORDIC units. These two values are applied to two different CORDIC units in the module, and *Sinh(w), Cosh(w)* and *Sinh(f)* and *Cosh(f)* values corresponding to these values are calculated simultaneously. These values calculated by CORDICs are collected separately to yield fixed results. After these fixed results are passed through a *fixtofloat* converter, these two values are multiplied in the last multiplier of the second channel, yielding the value of e^y.

$$.y > 0.75 \begin{pmatrix} w = .y - 0.75 \\ f = 0.75 \end{pmatrix}$$
$$.y \leq 0.75 \begin{pmatrix} w = 0 \\ f = 0.75 \end{pmatrix} \tag{7}$$

After this stage, the resulting e^y value will be transferred to two separate units. The goal here is to perform an additional calculation depending on the likelihood of the datain *(x.y)* number to be negative. For this reason, the *divider* unit has been used. The process is to obtain the e^y value that comes from CORDICs divided by 1. This obtained value is applied to a "mux" unit together with the e^y value. The 64th bit of the incoming 64-bit datain value gives us whether the number is negative or positive. This is the 64th bit *mux* it is designed to determine the output value of our unit as a selector. If our number is negative, then the value from *divider* is transferred to the output. If the number is positive, the e^y value is transferred to the output. After this step, the final multiple unit, where the e^x value is multiplied by e^y as the last stage, gives us the counterpart of $e^{x \cdot y}$ value as *dataout*.

Test Results Of Fpga-Based e^x Calculator Module

The designed e^x unit was synthesized for the Virtex-6 FPGA XC6VLX75T chip and the determined data processing time was obtained using the ISE simulation program. The usage statistics on the specified FPGA chip after the synthesis of the module are given in Table 2. From the chip statistics provided, it is possible that 3 copies of the module can be placed in a single chip, to the smallest capacity model of Virtex-6, and can be run in parallel. The high IOB value in the statistics does not prevent the module copy from being placed. That is because the data input/output to the chips is provided via a single data path .

Table 2. Module's FPGA chip statistics

Number of Slice Registers / %	Number of Slice LUTs / %	Number of bonded IOBs / %	Max Clock Speed (Mhz)
17141 / 18	15007 / 32	131 / 54	56,460

Table 3 gives the comparison of the actual results with the results produced by the e^x unit for some sample test values. The values in the first column are the selected test values (x.y). The values in the second and third columns are the values generated by the Excel program and the Module. In the last column, the precision between the Excel values and the values produced by the designed Module is given by specifying the number of digits in different colors. According to the results obtained, the designed module can produce results with precision up to 7-8 digits.

The module has been designed with a 47 clock pipelined structure and can be operated at 56.460 MHz. The module runs for the first 47 periods after the first data entry is made, and the result is generated at the end of the 47th period. A new data can be entered with every clock pulse at the input, and this data is calculated consecutively after the first 47 periods of waiting and then sent to the output. When the unit is used in this way, it can perform 56458 e^x calculations per second.

Table 3. e^x Comparative Results of the Module

Input Value	Output Excel Exp	Output Module Exp	Output Precision
-89.899	9.06484477E-40	9.06484454E-40	9.06484477E-40
-88.599	3.32616047E-39	3.32616039E-39	3.32616047E-39
-80.199	1.47916576E-35	1.47916574E-35	1.47916576E-35
-71.679	7.41661665E-32	7.41661664E-32	7.41661665E-32
-63.400	2.92233398E-28	2.92233395E-28	2.92233398E-28
-57.800	7.90276278E-26	7.90276275E-26	7.90276278E-26
-42.270	4.38906740E-19	4.38906727E-19	4.38906740E-19
-36.357	1.62313828E-16	1.62313830E-16	1.62313828E-16
-25.145	1.20133810E-11	1.20133811E-11	1.20133810E-11
-14.836	3.60418493E-07	3.60418495E-07	3.60418493E-07
-7.700	4.52827183E-04	4.52827175E-04	4.52827183E-04
5.300	2.00336810E+02	2.00336814E+02	2.00336810E+02
12.850	3.80788735E+05	3.80788724E+05	3.80788735E+05
33.440	3.33278636E+14	3.33278625E+14	3.33278636E+14
43.650	9.05636953E+18	9.05636968E+18	9.05636953E+18

69.150	1.07513605E+30	1.07513606E+30	1.07513605E+30
76.300	1.36983724E+33	1.36983729E+33	1.36983724E+33
89.000	4.48961282E+38	4.48961293E+38	4.48961282E+38

Conclusion

The exponential function (e^x) is a function highly needed in various fields that require intensive calculation. However, it is difficult to calculate this function logically and it requires high processor power. For such areas requiring high processing speed, FPGA chips are a fast, high-capacity hardware element that has proven its usability. In this study, an e^x calculator module has been designed that can be used in digital designs, making use of the fact that FPGA chips are a cheap and flexible alternative for applications requiring high computational power. The designed module works with the 64-bit IEEE 754-1985 floating-point number format. The module was coded in VHDL and synthesized for the FPGA Virtex-6 XC6VLX75T chip with Xilinx's ISE 14.7 EDA tool. According to the results obtained, the designed module can produce results with precision up to 7-8 digits. Considering that the IEEE 754-1985 floating point number representation is sensitive to a maximum of 7-8 bits, the accuracy of the results produced by the designed module can be argued to be excellent. In addition, the designed module can be operated at maximum 56.460 MHz. In the future, the clock speed can be increased by using a memory structure which is different from the kad structure for the module. Considering the amount of hardware the unit uses, it can be seen as a disadvantage that FPGA uses too much space for the smallest chip. For this, more replicas can be created for the larger-capacity FPGA chips that the module can be run in parallel.

REFERENCES

Acosta Lúa, Cuauhtémoc, Stefano Di Gennaro, Antonio Navarrete Guzmán, ve Jorge Rivera Domínguez. 2021. "Digital sliding mode controllers for active control of ground vehicles". *Asian Journal of Control* 23 (5): 2129–44. https://doi.org/10.1002/asjc.2627.

Adil Yazdeen, Abdulmajeed, Subhi R. M. Zeebaree, Mohammed Mohammed Sadeeq, Shakir Fattah Kak, Omar M. Ahmed, ve Rizgar R. Zebari. 2021. "FPGA Implementations for Data Encryption and Decryption via Concurrent and Parallel Computation: A Review". *Qubahan Academic Journal* 1 (2): 8–16. https://doi.org/10.48161/qaj.v1n2a38.

Almekkawy, Mohamed, Jingwei Xu, ve Mohan Chirala. 2014. "An optimized ultrasound digital beamformer with dynamic focusing implemented on FPGA". *2014 36th Annual International Conference of the IEEE Engineering in Medicine and Biology Society, EMBC 2014*, 3296–99. https://doi.org/10.1109/EMBC.2014.6944327.

Arar, Steve. 2017. "An Introduction to the CORDIC Algorithm". 2017. https://www.allaboutcircuits.com/technical-articles/an-introduction-to-the-cordic-algorithm/.

Babu, Praveenkumar, ve Eswaran Parthasarathy. 2021. "Reconfigurable FPGA Architectures: A Survey and Applications". *Journal of The Institution of Engineers (India): Series B* 102 (1): 143–56. https://doi.org/10.1007/s40031-020-00508-y.

Boudabous, Anis, Fahmi Ghozzi, M Wajdi Kharrat, ve Nouri Masmoudi. 2004. "Implementation of Hyperbolic Functions Using CORDIC Algorithm". *IEEE*, 738–41.

Chaple, Girish N., R. D. Daruwala, ve Manoj S. Gofane. 2015. "Comparisions of Robert, Prewitt, Sobel operator based edge detection methods for real time uses on FPGA". *Proceedings - International Conference on Technologies for Sustainable Development, ICTSD 2015*, sayı 1: 4–7. https://doi.org/10.1109/ICTSD.2015.7095920.

"CLB(Configurable Logic Block) Wiki - FPGAkey". y.y. Erişim 13 Ocak 2022. https://www.fpgakey.com/wiki/details/51.

Considine, Vincent. 1989. "CORDIC trigonometric function generator for DSP". *ICASSP, IEEE International Conference on Acoustics, Speech and Signal Processing - Proceedings* 4: 2381–84. https://doi.org/10.1109/icassp.1989.266946.

Cosmas, Kiruki, ve Asami Kenichi. 2020. "Utilization of fpga for onboard inference of landmark localization in cnn-based spacecraft pose estimation". *Aerospace* 7 (11): 1–25. https://doi.org/10.3390/aerospace7110159.

Doss, Christopher C., ve Robert L. Riley. 2004. "FPGA-based implementation of a robust IEEE-754 exponential unit". *Proceedings - 12th Annual IEEE Symposium on Field-Programmable Custom Computing Machines, FCCM 2004*, 229–38. https://doi.org/10.1109/FCCM.2004.38.

"FPGA Architecture for the Challenge". y.y. Erişim 13 Ocak 2022. https://www.eecg.utoronto.ca/~vaughn/challenge/fpga_arch.html.

Hoe, David H.K., L. P. Deepthi Bollepalli, ve Chris D. Martinez. 2013. "FPGA fault tolerant arithmetic logic: A case study using parallel-prefix adders". *VLSI Design* 2013. https://doi.org/10.1155/2013/382682.

Hosseiny, Adel, ve Ghassem Jaberipur. 2020. "Complex exponential functions: A high-precision hardware realization". *Integration* 73 (February): 18–29. https://doi.org/10.1016/j.vlsi.2020.02.005.

Ismail, Samar M., Lobna A. Said, Ahmed A. Rezk, Ahmed G. Radwan, Ahmed H. Madian, Mohamed F. Abu-Elyazeed, ve Ahmed M. Soliman. 2017. "Generalized fractional logistic map encryption system based on FPGA". *AEU - International Journal of Electronics and Communications* 80: 114–26. https://doi.org/10.1016/j.aeue.2017.05.047.

J Sujitha, V Ramohan Reddy. 2014. "Implementation of Log and Exponential Function in FPGA". *International Journal of Engineering Research Technology* 3 (11): 1–4. https://www.ijert.org/view-pdf/11860/implementation-of-log-and-exponential-function-in-fpga.

Pouyan, Peyman, Erik Hertz, ve Peter Nilsson. 2011. "A VLSI implementation of logarithmic and exponential functions using a novel parabolic synthesis methodology compared to the CORDIC algorithm". *2011 20th European Conference on Circuit Theory and Design, ECCTD 2011* 4 (1): 709–12. https://doi.org/10.1109/ECCTD.2011.6043642.

Rasu, R., P. Shanmuga Sundaram, ve N. Santhiyakumari. 2015. "FPGA based non-invasive heart rate monitoring system for detecting abnormalities in Fetal". *International Conference on Signal Processing and Communication Engineering Systems - Proceedings of SPACES 2015, in Association with IEEE*, 375–79. https://doi.org/10.1109/SPACES.2015.7058287.

Raut, Sushil, Kohei Shimasaki, Sanjay Singh, Takeshi Takaki, ve Idaku Ishii. 2019. "Real-time high-resolution video stabilization using high-frame-rate jitter sensing". *ROBOMECH Journal* 6 (1). https://doi.org/10.1186/s40648-019-0144-z.

Rodríguez-Orozco, Eduardo, Enrique Efren García-Guerrero, Everardo Inzunza-Gonzalez, Oscar Roberto López-Bonilla, Abraham Flores-Vergara, Jose Ricardo Cárdenas-Valdez, ve Esteban Tlelo-Cuautle. 2018. "FPGA-based chaotic cryptosystem by using voice recognition as access key". *Electronics (Switzerland)* 7 (12): 1–16. https://doi.org/10.3390/electronics7120414.

Şahin, İbrahim, ve İsmail Koyuncu. 2011. "FPGA ÇİPLERİ İÇİN CORDIC TABANLI ex HESAPLAMA ÜNİTESİ TASARIMI". *E-journal of New World Sciences Academy*, sayı September.

Şahin, İbrahim, ve Günay Temür. 2016. "A Controller Desıgn Tool Development For Automatıcally Mappıng Artıfıcıal Neural Networks". *SDU International Journal of Technological Science* 8 (1): 34–52.

Sun, Yan, Le Li, ve Hong Luo. 2011. "Design of FPGA-based multimedia node for WSN". *7th International Conference on Wireless Communications, Networking and Mobile Computing, WiCOM 2011*, 4–8. https://doi.org/10.1109/wicom.2011.6040365.

Surendar, A. 2017. "FPGA based parallel computation techniques for bioinformatics applications". *International Journal of Research in Pharmaceutical Sciences* 8 (2): 124–28.

Tatar, Guner, ve Salih Bayar. 2019. "FPGA Based Bluetooth Controlled Land Vehicle". *International Symposium on Advanced Electrical and Communication Technologies, ISAECT 2018 - Proceedings*, 1–6. https://doi.org/10.1109/ISAECT.2018.8618830.

Temür, Günay. 2013. "Yapay Sinir Ağlarının Otomatik Olarak Fpga Çipine Uygulanması İçin Denetleyici Tasarım Aracı". *Düzce Üniversitesi*. Düzce Üniversitesi.

Wan, Zishen, Bo Yu, Thomas Yuang Li, Jie Tang, Yuhao Zhu, Yu Wang, Arijit Raychowdhury, ve Shaoshan Liu. 2021. "A Survey of FPGA-Based Robotic Computing". *IEEE Circuits and Systems Magazine* 21 (2): 48–74. https://doi.org/10.1109/MCAS.2021.3071609.

Wang, Dong, Milo D Ercegovac, ve Yang Xiao. 2014. "Two-Dimensional Interpolation" 63 (12): 2948–60.

Wielgosz, MacIej, Ernest Jamro, ve Kazimierz Wiatr. 2008. "Highly efficient structure of 64-Bit exponential function implemented in FPGAs". *Lecture Notes in Computer Science (including subseries Lecture Notes in Artificial Intelligence and Lecture Notes in Bioinformatics)* 4943 LNCS: 274–79. https://doi.org/10.1007/978-3-540-78610-8_28.

Turgutlu Sanayisinin Gelişim Süreci ve Sektörel Yapısı

Ferhat ARSLAN[1]

Giriş

Arapça şanai kelimesinden türeyen ve Türkçede "Ham maddeleri işlemek, enerji kaynaklarını yaratmak için kullanılan yöntemlerin ve araçların bütünü, işleyim, uran, endüstri" (TDK, 2019) anlamına gelen sanayi terimini "hammaddenin işlenerek yeni bir ürün haline getirilme faaliyeti" (Arslan, 2018: 168) şeklinde tanımlamak mümkündür.

Günümüzde gelişmekte olan ülkelerin ekonomik gelişmişliklerini tamamlamak adına sanayi ve sanayileşmeye önem verdiği bilinmektedir. Ünal (2010)'ın ifadesiyle sanayi, toplumların en temel ve ekonomik faaliyetlerindendir ve kalkınma ile küreselleşmenin de yapı taşlarından birisidir (s. 1). Karadeniz ve Yılmaz (2021) da sanayileşmenin bütün ülkelerin gelişmesinde temel amaçlardan biri olduğunu; bu nedenle toplumların kalkınması ile sanayileşmenin eş değer görüldüğü üzerinde durmuştur (s. 1819). Bu açılardan bakıldığında sanayi ile kalkınma düzeyinin paralel yönde ilerlediği ve ekonomik açıdan kalkınmak isteyen ülkelerin sanayileşme kapsamında politikalar belirlediği söylenebilir.

Sanayinin bir bölgede yoğunlaşmasında farklı etmenler etkilidir. Doğanay ve Çavuş (2016), Türkiye'de sanayinin kuruluş koşullarını etkileyen faktörleri hammadde, enerji kaynakları, sermaye, iş gücü, ulaşım ve pazar olarak belirtmişlerdir. Temurçin (2012) bir bölgede, bir ilde ya da ilçede sanayinin gelişmesinde ulaşımın etkili olduğunu söyleyerek hammaddenin temini ve mamul maddenin taşınmasının kolay ve ucuz sağlanmasının sanayinin gelişmesinden ana faktör olduğu üzerinde durmuştur. Kaygalak (2011) ise son 30 yıldır esnek üretim ilişkilerinin yaygınlaşmasıyla birlikte, sanayinin mekânsal dağılışında da köklü dönüşümler yaşandığını ve küresel ekonomik ilişkilerin bir neticesi olarak gelişen "bölgeselleşme" eğilimlerinin sanayinin küresel ölçekte yeniden mekânsal dağılımını sağladığını ve sanayideki yapısal dönüşümün de yeni yer seçimi eğilimleri yarattığını ifade etmiştir (s. 170).

Şehirler, fonksiyon özellikleri ve arazi kullanım biçimleri ile kırsal yerleşmelerden ayrılır (Özdemir vd. 2020). Bu fonksiyon özelliklerinden birisi olan sanayi sektöründe yeni yer arayışları beraberinde Turgutlu gibi büyükşehirlere yakın olup ana ulaşım yolları üzerindeki yerleşmelerin yeni sanayi merkezleri haline gelmesini sağlamıştır. Turgutlu'da tuğla sanayisi ile başlayan bu süreç günümüzde farklı sektörlerden firmaların yer aldığı bir noktaya gelerek Turgutlu'nun küçük çaplı atölye tipi işletmelerden büyük çaplı istihdam sağlayan bir merkez haline gelmesini sağlamıştır. Turgutlu'da sanayileşme ile birlikte diğer faktörlerin de etkisiyle mekânsal büyümesinin bu kızla devam edeceği tahmin edilmektedir (Deniz vd. 2018; Üzülmez ve Yılmaz, 2021). Bu çalışmada Turgutlu'nun yaşadığı bu mekânsal büyümenin önemli aktörlerinden birisi olan sanayileşme sürecindeki değişimin sektörel bazda ele alınarak gelecek için bir senaryo çizebilmek amaçlanmıştır.

Çalışma Sahasının Yeri Ve Konumu

Manisa il sınırları içerisinde yer alan Turgutlu'nun kuzey batısında Manisa, kuzeyinde Saruhanlı, doğusunda Ahmetli, güneyinde Ödemiş ve Bayındır, güney batısında Kemalpaşa yer alır. İzmir – Ankara kara yolu ile İzmir-Uşak demiryolu üzerinde bulunan Turgutlu Manisa'ya 30 km, İzmir'e 54 km uzaklıkta bulunur (Şekil 1). Gediz Havzası içerisinde yer alan Turgutlu'nun kuzeyinde

---

[1]Doç. Dr. Manisa Celal Bayar Üniversitesi, Fen-Edebiyat Fakültesi, Coğrafya Bölümü ferhat.arslan@cbu.edu.tr

Gediz Ovası, güneyinde Bozdağlar yer alır. Örgen vd. (2009)'nin ifadesiyle Turgutlu'nun morfolojik yapısını dört farklı birime ayırmak mümkündür. Gediz Nehri'nin getirdiği alüvyonlarla oluşan ova tabanı, güneye doğru ova tabanı ile Bozdağlar arasındaki Tmolos depoları, güneyde uzanan Bozdağlar ve kuzeyde ovayı sınırlayan alçak platodur (s. 19).

Şekil 1. Çalışma Sahası Lokasyon Haritası

Turgutlu Sanayisinin Gelişimi ve Sektörel Yapısı

Turgutlu Sanayisinin Gelişim Süreci

Turgutlu verimli Gediz Ovası üzerinde kurulu olması, iklim ve toprak şartlarının uygunluğu, İzmir-Ankara kara yolu üzerinde olması, Anadolu'nun ilk demir yollarından olan İzmir-Kasaba demir yolu hattının varlığı ve İzmir Limanı'na doğrudan bağlantı kurulabilir olması sahada sanayileşmenin hızlanmasını sağlamıştır. Bölgesinde önemli bir yerleşim alanı olan Turgutlu'da sanayi faaliyetlerinin tarımsal üretime ve doğal kaynaklarına bağlı olduğunu söylemek mümkündür. 1927 Türkiye Salnamesi'ne göre Turgutlu'da 3 pamuk, 1 susam, 1 tuğla, 1 un, 1 kereste fabrikası ile değirmen (Bilgi, 2019:292) bulunması bu durumu kanıtlar niteliktedir.

1935 Genel Nüfusu Sayımlarında Turgutlu'da çalışan nüfusun sektörel dağılımının verildiği bölümde Turgutlu sanayisi ile ilgili fikir edinmek mümkündür. Buna göre Turgutlu'da 5.432 kişinin çalıştığı toprak mahsulleri sektöründe çalışanların 4.065'i erkek 1.367'si ise kadındır. Sanayi ve küçük sanatlar olarak sınıflandırılan bölümde ise 1.721'i erkek 434'ü kadın toplam 2.155 kişi çalışırken, bu bölümde en çok istihdamın olduğu sektör toplam 493 kişi ile elbise sanayisidir (416 erkek 77 kadın). Elbise sanayisini 310 kişi (274 erkek 36 kadın) ile gıda, içki ve türün sanayisi izlerken, 213 kişinin (tamamı erkek) çalıştığı demir sanayisi ise üçüncü sırada yer alır. Toplam 193 kişinin (159 erkek 34

kadın) çalıştığı ağaç işleme sanayisi ve 122 kişinin çalıştığı ve 83 kadın çalışan ile kadın istihdamının en yüksek olduğu dokuma sanayisi de diğer önemli sanayi alanlarıdır (s. 85).

Turgutlu sanayisinde önemli bir yeri olan tuğla ve kiremit sanayisinin tarihsel gelişimi Cumhuriyet Dönemi öncesinde kadar dayanır. 1925 yılında Turgutlu Kooperatif Şirketi tarafından Kısmalı mevkiinde kurulan tuğla fabrikası 75.000 tığla ve 4.000 kiremit üretimi yapılmıştır (Akça, 1997: 87). Ancak endüstriyel anlamda Turgutlu'da kurulan ilk tuğla fabrikası Almanların 1935 yılında Kısmalı'da kurdukları fabrikadır. Almanların kurduğu bu tesisin bir özelliği de yöredeki yabancı sermaye ile kurulan ilk tesis olmasıdır. Tesisin Kısmalı yöresinde kurulmasının nedenini, burada bulunan zengin toprak madeni oluşturmaktadır (Özdemirden, 1997: 8). Kısmalı yöresindeki toprağın miktar olarak azalması ve niteliğini kaybetmesi tuğla ve kiremit sanayisi için yeni yer arayışlarını getirmiş ve 1958 – 1981 yılları arasında Çatalazmağı bölgesinde hammadde alımı gerçekleşmiştir. Ancak tarımsal arazi bölgesinde yer alan bölgede aşırı hammadde kullanımı sonucunda arazinin zarar görmesi sonucunda İmar-İskân Bakanlığı, Manisa Bölgesi Toprak Su Gediz Planlama Müdürlüğü'nün el atması ile bölgeden toprak alımı durdurulmuştur (Kaya, 2013: 376). Başbakanlığın 07.07.1981 tarih ve 10/01694 sayılı emri ile Manisa Toprak Su Bölge Müdürlüğü tarafından tarım dışı alan olarak tespit edilen 12 bölgede MTA tarafından kil hammaddesi sağlanması amacıyla yapılan aramalar sonucunda 217.945.000 ton hammadde rezervi saptanmıştır (Güney, 1995: 341).

1995 yılında 80 tuğla - kiremit fabrikası bulunduğu Turgutlu ve çevresinde 540 dekarı kapalı 1.595 dekarı açık olmak üzere toplam 2.135 dekar tesis alanı söz konusudur (Tomar, 1995: 262). Marmara Depremi'nin gerçekleştiği 1999 yılına kadar 80 civarında tuğla – kiremit fabrikasının bulunduğu Turgutlu'da depremden sonra getirilen kısıtlamalar nedeniyle bu sayısı 2014 yılında 35'e (Görçiz, 2014) günümüzde ise 13'e düşmüştür (TUKSAD, 2022).

Turgutlu Organize Sanayi Bölgesi (TOSB)'nin Kuruluşu

Turgutlu'da sanayileşme için gerekli koşulların varlığı ve sanayileşme sürecinin planlama ekseninde gerçekleştirilmesine olan farkındalık sahada bir organize sanayi bölgesi kurulması fikrini getirmiştir. Hem önemli ulaşım aksları üzerinde olması, iş gücünün fazlalığı, önemli sermaye alanlarına yakınlık gibi faktörler Turgutlu'da bir organize sanayi bölgesi kurulmasını hızlandırmıştır.

Bu faktörlerin de etkisiyle sahada bir organize sanayi bölgesi kurulması 1995 yılında gerçeklemiştir. 22159 sayılı resmi gazetede ilan edilerek yatırım programı içerisine dahil edilen TOSB, 11.01.1996 tarihinde Turgutlu ilçe merkezinde 7 km, Manisa il merkezine 26 km, İzmir limanına 45 km, İzmir – İstanbul Otobanı bağlantı noktasına 3 km, Turgutlu Tren İstasyonu'na 4 km uzaklıktaki Çepnidere mevkiinde kurulmuştur (TOSB, 2021) (Foto 1). Yukarıda bahsedilen merkezlere ve bağlantı noktalarına yakınlığı TOSB'u yerli ve yabancı yatırımcılar için cazip kılarken, bölgede yeni planlama çalışmalarını zorunlu kılmıştır (Şekil 2). 3.420.000 m² lik bir alanda kurulu bulunan TOSB, 2019 yılında içinde bulunan 99 firma sayısı ile bölgesinde hızlı bir ilerleme gösteren bir OSB olması ile dikkat çekmiştir. 64 firmanın aktif olarak faaliyetine devam ettiği TOSB'da 5 firma gayri faal tesis niteliğinde iken 15 firma ise yapım aşamasında olarak belirtilmektedir (Manisa Valiliği, 2019).

Foto 1. TOSB Yerleşim Alanı Kaynak: Turgutlu Belediyesi (2022)
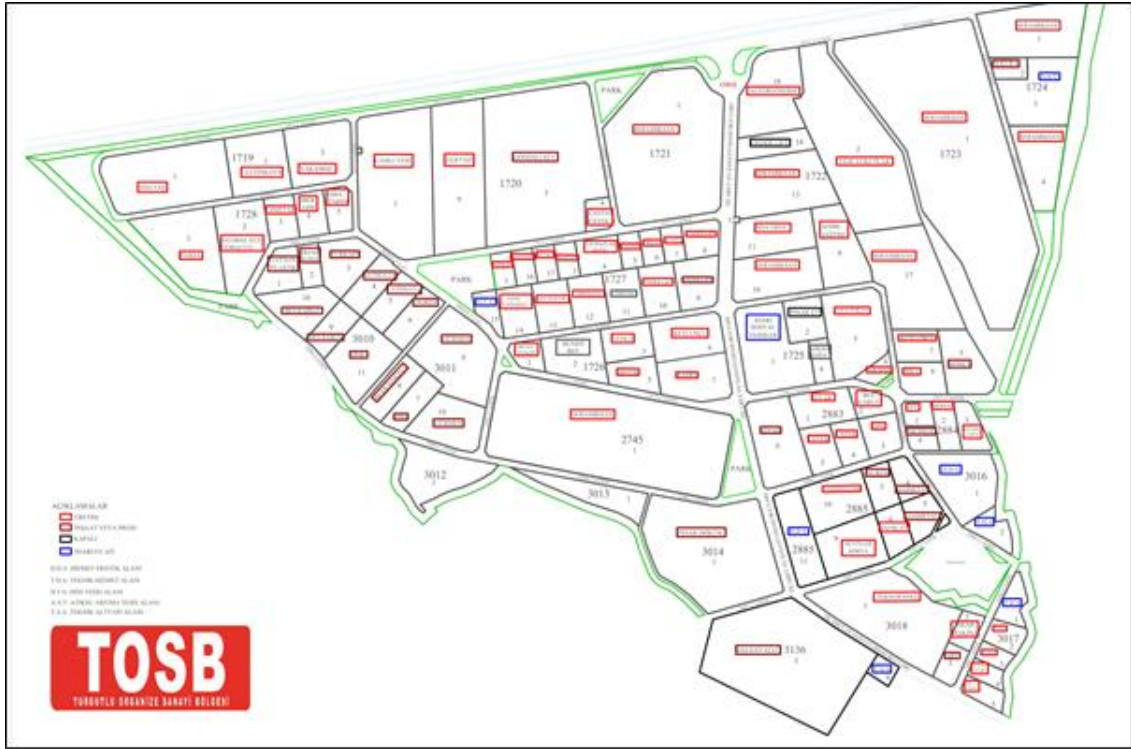
Şekil 2. Tahsise Uygun Parseller ve Güncel İmar Planı Kaynak: TOSB (2021)

Turgutlu Küçük Sanayi Sitesi (TKSS)

1988 yılında faaliyete geçen TKSS, Turgutlu şehrinden geçen İzmir – Ankara kara yolu güzergahında yer alır. Şehrin ara sokaklarında dağınık bir halde bulunan işletmelerin neden olduğu çevre kirliliği ve gürültüden halkın rahatsız olması nedeniyle öncü ustaların bir araya gelmesi ile 1968 yılında TKSS'nin kurulması için ilk adımlar atılmıştır. 1983 yılına kadar üye kayıtları ve arsa alım çalışmaları yapılan TKSS'nin ilk temelleri 1985 yılında atılmış ve 143 adet iş yeri ve hizmete giren sosyal tesis ile hizmete başlamıştır. Küçük sanayi işletmelerini planlı bir şekilde bir araya getirmeyi amaçlayan TKSS'nin 1987 yılında hizmete açılan birinci bölümünde 143 iş yeri bulunurken, 1991 yılında temeli atılan ve 1997 yılında hizmete giren ikinci kısmında 439, 2002

yılında açılan üçüncü kısımda ise 335 iş yeri faaliyete geçmiştir. 2022 itibariyle 917 iş yerinin faaliyette olduğu TKSS'de 6 bin kişi istihdam edilmektedir (Kaya, 2013; TKSS, 2022)

Turgutlu Sanayisinin Sektörel Yapısı

Geçmişten günümüze tuğla ve kiremit sanayisi ile anılan Turgutlu'da İzmir-Ankara kara yolunun her iki tarafında sanayi bölgeleri planlanması sahanın farklı sanayi sektörlerinin de tesis kurmasını sağlamıştır.

Toprak sanayisinin yoğun olduğu bölgede sektörel anlamda çeşitlilik kazanmasında TOSB'un etkisinin olduğunu söylemek mümkündür. 2002 yılında sanayi siciline kayıtlı firma sayısı 49 iken 2017 yılında 327 firmaya çıkması ve sanayide istihdam edilen kişi sayısının da 2002 yılında 3.388 iken 2017 yılında 10.267 kişiye yükselmesi TOSB'un kurulmasına bağlanmaktadır (Turgutlu Belediyesi, 2019) (Tablo 1).

Tablo 1: Turgutlu'da Sanayi İşletmesi ve Sanayi İstihdamının Gelişimi

| Yıl	Sanayi Siciline Kayıtlı İşyeri	Sanayi İstihdam
2000	75	3539
2002	49	3388
2004	79	3550
2007	121	4940
2013	242	6640
2014	295	7011
2015	331	9264
2016	330	10102
2017	327	10267

Kaynak: Turgutlu Belediyesi, 2019

Tablo 2 ve Şekil 4, TOSB'taki firmaların 2021 yılı itibariyle sektörel dağılımını göstermektedir. Toplamda 76 firmanın yer aldığı TOSB'ta en çok firmanın yer aldığı sektör 28 firma ilse makine sektörüdür. 19 firmanın yer aldığı gıda sektörü ikinci sırada yer alırken, onu 7 firma ile seramik ve yapı elemanları sektörü izlemektedir.

Tablo 2. Turgutlu Organize Sanayi Bölgesinde Firmaların Sektörel Dağılımı

Sektör Adı	Firma Sayısı
Makine	28
Gıda	19
Seramik ve Yapı Elemanları	7
Metal İşleme	5
Elektrik Malzemeleri	4
Sağlık Ürünleri	3
Ambalaj Malzemeleri	2
Ağaç Ürünleri	2
Diğer	6
Toplam	76

Kaynak: TOSB (2021)

779
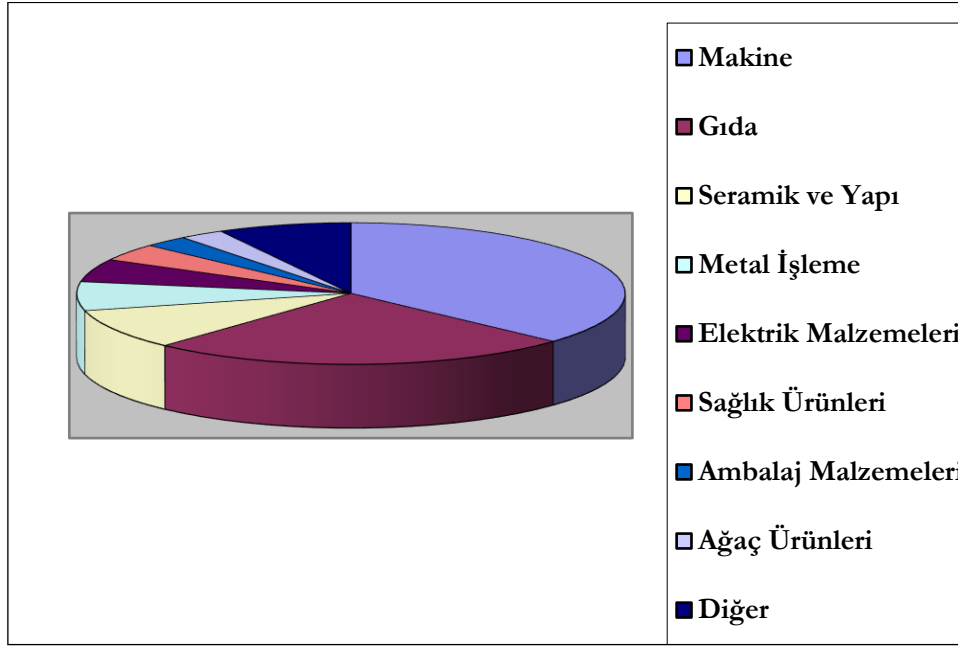
Şekil 4. Turgutlu Organize Sanayi Bölgesinde Firmaların Sektörel Dağılımı

Sonuç

Turgutlu sanayisinin gelişim sürecini ve sektörel dağılımını incelemeyi amaçlayan bu çalışma sonucunda Turgutlu sanayisinin gelişim süreci ortaya çıkarılmıştır. Verimli tarım alanları, elverişli iklim koşulları ve önemli ulaşım güzergahları üzerinde olması nedeniyle önemli bir şehir olma statüsünü her dönem korumayı başarmış Turgutlu'da sanayi sektöründe değişimler söz konusudur.

Türkiye'de uzun yıllar tuğla ve kiremit sanayisinin merkezi konumunda yer almış Turgutlu'da hem hammadde temininde yaşanan sorunlar hem de sektörün yaşadığı ekonomik sıkıntılar bölgedeki tuğla-kiremit sektörünün de dar boğaza girmesine neden olmuştur. Ancak bu dar boğaz Turgutlu Organize Sanayi Bölgesi'nin kurulması ile bölgedeki sanayinin farklı bir kulvara girmesi ile aşılmış görülmektedir.

İzmir – Ankara kara yolu üzerinde olması, İzmir Limanı'na, İzmir Adnan Menderes Havaalanı'na ve Manisa Organize Sanayi Bölgesi ile Kemalpaşa Organize Sanayi Bölgesi'ne yakınlığı nedeniyle hem yerli hem de yabancı firmaların yatırım yaptığı TOSB, Turgutlu sanayisinde de sektörel çeşitliliği sağlamıştır. Bir tuğla ve kiremit sanayisi alanı olan Turgutlu, TOSB'un kurulması ile özellikle makine ve gıda sektöründe faaliyette bulunan firmalara ev sahipliği yapar hale gelmiştir. Bu duruma Turgutlu'nun büyükşehirlere yakınlığının da etkili olduğu görülmektedir.

Sonuç olarak Turgutlu, 19. ve 20. yüzyıllarda atölye tipi imalat yapan küçük sanayi tesislerinden geniş çaplı üretim yapan firmaların bulunduğu bir konuma yükselmiş görülmektedir. Şehrin bulunduğu coğrafi konumun yanında bölgede yaşayan yatırımcıların da yönlendirmesi ile Turgutlu'nun ileriki dönemlerde önemli bir sanayi şehri olması kaçınılmaz görülmektedir.

Kaynakça

Akça, B. (1997), Cumhuriyetin İlk Yıllarında Turgutlu. Turgutlu Sosyo - Ekonomik Tarihi Sempozyumu 4 -5 Eylül 1995. Turgutlu: Turgutlu Belediyesi, s. 82-89.

Arslan, F. (2018). Türkiye'de Sürdürülebilir Üretimde Organize Sanayi Bölgelerinin Rolü: Manisa Organize Sanayi Bölgesi (MOSB) Örneği. Marmara Coğrafya Dergisi, (37) , 167-182.

Bilgi, N. (2019). Cumhuriyet'in İlk Yıllarında Turgutlu (1923 – 1928): İmar, İnşa, İktisat ve Ziraat. 20. Yüzyılda Turgutlu İçinde (Ed. Gülmez, N. ve Bilgi, N.). s. 259 – 295. Turgutlu: Turgutlu Belediyesi Kültür Yayınları.

Deniz, M., Kocaman, E., Topuz, M. (2018). Uşak şehrinde aile sağlığı merkezlerine erişilebilirliğin CBS ile Analizi. Turkish Studies, International Periodical for the Languages, Literature and History of Turkish or Turkic, 13(26), 475-491.

Doğanay, H. ve Çavuş, A. (2016). Türkiye Ekonomik Coğrafyas, Ankara: Pegem Akademi.

Görçiz, G. (2014). http://www.konuttimes.com/genel/turkiye-tugla-ve-kiremit-imalatinin-yuzde-20si-turgutluda/36282 (06.11. 2022 tarihinde erişilmiştir)

Güney, N. C. (1995). Gediz Havzasında Amaç Dışı Arazi Kullanımı. I. Gediz Havzası Erozyon ve Çevre Sempozyumu, 10 - 11 Ekim 1995. Salihli, 1995. 339-343

Karadeniz, V ve Yılmaz, Y. (2021). Sanayi Coğrafyası Açısından Bir İnceleme: Erzincan Organize Sanayi Bölgesi. Atatürk Üniversitesi Sosyal Bilimler Enstitüsü Dergisi, 25 (4), 1818-1852.

Kaya, A. (2013). Turgutlu İlçesinin Coğrafyası. (Yayınlanmamış Doktora Tezi). Afyonkarahisar: Afyon Kocatepe Üniversitesi Sosyal Bilimler Enstitüsü.

Kaygalak, İ. (2011). Türkiye'de Sanayi Kümelenmesi ve Sanayinin Yer Seçimindeki Yeni Eğilimler. TÜCAUM VI. Coğrafya Sempozyumu, 169-180, Ankara.

Manisa Valiliği (2019). Sayılarla Manisa. http://manisa.gov.tr/kurumlar/manisa.gov.tr/ documents/Sayilarla_Manisa_2019.pdf (15.11.2022 tarihinde erişlmiştir)

Meşe, K.I. (2005). Turgutlu Tarihi Kent Dokusunun İncelenmesi. (YayınlanmamışYüksek Lisans Tezi). Dokuz Eylül Üniversitesi, İzmir.

Ölgen, M. K., Erdal, Ü. ve Sökmen, Ö. (2009). Turgutlu – Salihli Arasında Organik Tarım Faaliyetlerinin Toprak Üzerindeki Etkileri. Ege Coğrafya Dergisi, 18 (1-2) , 17-30.

Özdemir, H. M. , Özav, L. ve Yasak, Ü. (2020). Örnek Köyden Şehire Dönüşen Etimesgut'ta Şehirsel Fonksiyonlar Ve Arazi Kullanımının Değişimi . Doğu Coğrafya Dergisi, 25 (44) , 163-182 .

Özdemirden, M (1997). Turgutlu Toprak Sanayi Bitirme Projesi, Manisa: Celal Bayar Üniversitesi Turgutlu Meslek Yüksek Okulu.

TCBİGD. (1937). Genel Nüfus Sayımı (Manisa), 20 İlkteşrin 1935. İstanbul: Devlet Basımevi.

Temurçin, K. (2012). Bağcılar (İstanbul) İlçesi'nde Sanayinin Gelişimi ve Yapısı. Süleyman Demirel Üniversitesi Fen-Edebiyat Fakültesi Sosyal Bilimler Dergisi, 2012 (26) , 105-123.

TKSS (2022). Turgutlu Küçük Sanayi Sitesi. http://turgutlukss.org.tr/ (18.11.2022 tarihinde erişilmiştir)

Tomar, A. (1995). Gediz Havzası Turgutlu Yöresinde Tarım Topraklarının Amaç Dışı Kullanımının Çevresel ve Ekonomik Etkileri. I. Gediz Havzası Erozyon ve Çevre Sempozyumu, 10- 11 Ekim 1995. Salihli,

TOSB (2021). https://www.turgutluosb.org.tr/hakkimizda (11.11.2022 tarihinde erişilmiştir.)

Turgutlu Belediyesi (2019). Turgutlu Belediyesi 2020-2024 Stratejik Planı. https://www.turgutlu.bel.tr/app/files/5415_8617_4865-StratejikPlan20202024.pdf (15.11.2022 tarihinde erişilmiştir)

Turgutlu Belediyesi (2022). https://www.turgutlu.bel.tr/kurumsal/haberler/turgutlu-kabina-sigmiyor-osb-seffaflikla-buyuyor (11.11.2022 tarihinde erişilmiştir.)

Ünal, Ç. (2010). Türkiye'de Sanayi Tarihi Gelişimi ve Bugünü Yapısı. Erzurum: Mega Ofset.

Üzülmez, M., Yılmaz, A. (2021). Turgutlu Şehrinin Mekânsal Gelişiminin Tarım Arazileri Üzerindeki Etkisi. Ege Coğrafya Dergisi , 30 (1) , 73-83 .

CURRENT DEBATES ON NATURAL AND ENGINEERING SCIENCES

5